Edited by
E. Schöll and H. G. Schuster

Wiley-VCH

Handbook
of Chaos Control

Second, Completely Revised and Enlarged Edition

Handbook of Chaos Control

Edited by
Eckehard Schöll and Heinz Georg Schuster

2nd, completely revised and enlarged edition

Handbook of Chaos Control

Edited by
Eckehard Schöll and
Heinz Georg Schuster

Related Titles

Gao, J.-B.

Signal Processing with Random Fractals

2007
ISBN: 978-0-471-65470-4

Pain, J.

The Physics of Vibrations and Waves

2005
ISBN: 978-0-470-01296-3

Schuster, H. G., Just, W.

Deterministic Chaos
An Introduction

2005
ISBN: 978-3-527-40415-5

Gilmore, R., Lefranc, M.

The Topology of Chaos
Alice in Stretch and Squeezeland

2003
ISBN: 978-0-471-40816-1

Thompson, J. M. T., Stewart, H. B.

Nonlinear Dynamics and Chaos

2002
ISBN: 978-0-471-87684-7

Handbook of Chaos Control

Edited by
Eckehard Schöll and Heinz Georg Schuster

2nd, completely revised and enlarged edition

The Editors

Prof. Dr. Eckehard Schöll, Ph.D.
Technische Universität Berlin
Institut für Theoretische Physik
Hardenbergstr. 36
10623 Berlin
Germany
schoell@physik.tu-berlin.de

Prof. Dr. Heinz Georg Schuster
Christian-Albrechts-Universität Kiel
Institut für Theoretische Physik und Astrophysik
Olshausenstr. 40
24118 Kiel
Germany
schuster@theo-physik.uni-kiel.de

Cover Picture
The front cover shows the stabilization (upper part) of a chaotic spatio-temporal pattern (lower part) by time-delayed feedback control, cf. Fig. 24.10 in Chapter 24.

Contents

Preface

During the last decade, control of complex irregular dynamics has evolved as one of the central issues in applied nonlinear science. The number of papers published in this field has been steadily growing since the first pioneering papers appeared in 1990, and has reached an annual number between 600 and 700 during the past few years.

The seminal article by Ott, Grebogi, and Yorke (1990), in which they demonstrated that small time-dependent changes in the control parameters of a nonlinear system can turn a previously chaotic trajectory into a stable periodic motion, alone was cited much more than 2000 times. Nowadays the notion of chaos control has been extended to a much wider class of problems involving stabilization of unstable periodic or stationary states in nonlinear dynamic systems. Within the last few years major progress has been made in this field, in particular with respect to

- extending the methods of chaos control to spatiotemporal patterns;
- extending the methods of control of deterministic dynamic systems to stochastic and noise-mediated systems;
- development of novel control schemes;
- deepened understanding and analytic insight into different control schemes;
- applications to various areas, e.g., biological, medical, technological systems.

Since its first publication in 1999, the *Handbook of Chaos Control* has become the standard reference in this field. Eight years after the first edition, there is need to present the new material which has been accumulated, and to set new trends and identify new promising directions of research.

The present volume is the second completely revised and enlarged edition, and includes only articles which have been newly written for this volume. It aims at presenting a comprehensive overview of the state-of-the-art in this growing field; containing chapters written by the leading scientists who are active in this area. The focus is put on recent developments like novel control schemes, analytical insights, control of chaotic space–time patterns, control of noisy nonlinear systems and noise-induced dynamics, secure communication with chaos, and applications of chaos control to physics, chemistry, biology, medicine, and engineering. Furthermore, the overlap of chaos control with the traditional field of control theory in the engineering community is identified.
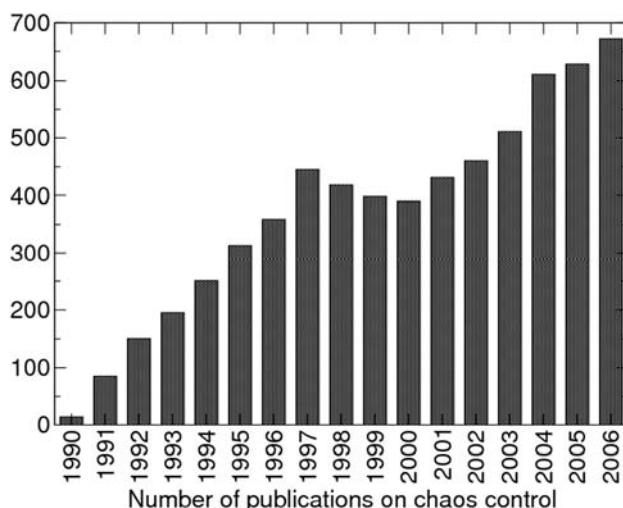
The chapters of the book are state-of-the-art review articles and should be of interest to graduate students and researchers; theoretical and experimental physicists, applied mathematicians, electronic engineers, nonlinear scientists from interdisciplinary fields, e.g., chemistry, biology, medicine, control theory, and engineering. The 36 chapters are grouped into nine parts, where the first four parts deal with basic aspects and extension of methods; controlling space–time chaos; controlling noisy motion; communicating with chaos and chaos synchronization, and the last five parts contain applications to optics, to electronic systems, to chemical reaction systems, to biology and medicine, and to engineering. Among the topics are, for instance, secure communication with chaotic semiconductor lasers, control of communication networks, noninvasive time-delayed feedback control of laser diodes, electronic circuits, and semiconductor nanostructures, control of chemical turbulence and electrochemical oscillators, suppression of synchronization as therapeutic tools for neural diseases like Parkinson and epilepsy, and control of cardiac dynamics.

We hope that this volume will stimulate further developments in this still thrilling area which is centered on the overlap of basic research and far-reaching applications.

We would like to thank all authors who have contributed to this volume as well as the publishers for their excellent cooperation. Special thanks are due to Philipp Hövel for his technical assistance.

Berlin and Kiel, June 2007   *Eckehard Schöll* and *Heinz G. Schuster*

Number of publications on chaos control

List of Contributors

Henry Abarbanel
University of California
Marine Physical Laboratory
Scripps Institution of Oceanography
9500 Gilman Drive
San Diego, CA 0402
USA

Vadim Anishchenko
Institute of Nonlinear Dynamics
Physics Department
Saratov State University
Astrakhanskaya street 83
Saratov 410012
Russia

Vladimir Astakhov
Laboratory of Nonlinear Dynamics
Radiophysics Chair
Department of Physics
Saratov State University
Astrakhanskaya 83
Saratov 410071
Russia

Alexander Balanov
University of Nottingham
Room B103 Physics and Mathematics
University Park
Nottingham, NG7 2RD
UK

Eshel Ben-Jacob
Tel Aviv University
School of Physics and Astronomy
69978 Tel Aviv
Israel

Hartmut Benner
Technische Universität Darmstadt
Institut für Festkörperphysik
Hochschulstraße 6
64289 Darmstadt
Germany

Jonathan N. Blakely
U.S. Army Research
Development
and Engineering Command
AMSRD-AMR-WS-ST
Redstone Arsenal
Alabama 35898
USA

Bernd Blasius
Universität Potsdam
Institut für Physik
Am Neuen Palais 10
14469 Potsdam
Germany

Stefano Boccaletti
Istituto Nazionale di Ottica Applicata
Làgo E. Fermi 5
50125 Firenze
Italy

Thomas L. Carroll
US Naval Research Laboratory
Code 6341
Washington, D.C. 20375
USA

Chol-Ung Choe
Department of Physics
University of Science
Kwahak-Idong, Unjong District
Pyongyang
DPR Korea

David J. Christini
Weill Cornell Medical College
Division of Cardiology
1300 York Ave.
New York, NY 10065
USA

Jens Christian Claussen
Universität Kiel
Institut für Theoretische Physik
und Astrophysik
Leibnizstraße 15
24098 Kiel
Germany

Jim Collins
Boston University
Department of Biomedical
Engineering
44 Cummington Street
Boston, MA 02215
USA

Cornelia Denz
Institute of Applied Physics
and Center for Nonlinear Science
Westfälische Wilhelms-Universität
Münster
Corrensstraße 2–4
48149 Münster
Germany

Harald Engel
Institut für Theoretische Physik
Technische Universität Berlin
Hardenbergstraße 36
10623 Berlin
Germany

B. Fiedler
Institut für Mathematik I
FU Berlin
Arnimallee 2–6
14195 Berlin
Germany

William Firth
University of Strathclyde
Department of Physics
107 Rottenrow
Glasgow, G4 0NG
Scotland
UK

V. Flunkert
Technische Universität Berlin
Institut für Theoretische Physik
Hardenbergstraße 36
10623 Berlin
Germany

Alexander Fradkov
Russian Academy of Sciences
The Institute for Problems
of Mechanical Engineering
61 Bolshoy ave. V.O.
199178 St. Petersburg
Russia

Nicoleta Gacin
Advanced Technology Institute
and Department of Physics
Faculty of Engineering
and Physical Sciences
University of Surrey
Guildford, Surrey
GU2 7XH
UK

Daniel J. Gauthier
Duke University
Department of Physics
Box 90305
Durham, North Carolina 27708
USA

Edeltraud Gehrig
Advanced Technology Institute
and Department of Physics
Faculty of Engineering
and Physical Sciences
University of Surrey
Guildford, Surrey
GU2 7XH
UK

M. Georgi
Freie Universität Berlin
Institut für Mathematik I
Arnimallee 2–6
14195 Berlin
Germany

Celso Grebogi
Universidade de São Paulo
Instituto de Física
Caixa Postal 66318
05315-970 São Paulo SP
Brazil

Roman Grigoriev
Georgia Tech
837 State Street
Atlanta, GA 30332-0430
USA

Björn Gütlich
Institute of Applied Physics and
Center for Nonlinear Science
Westfälische Wilhelms-Universität
Münster
Corrensstraße 2–4
48149 Münster
Germany

Ortwin Hess
Advanced Technology Institute
and Department of Physics
Faculty of Engineering
and Physical Sciences
University of Surrey
Guildford, Surrey
GU2 7XH
UK

Takashi Hikihara
Kyoto University
Department of Electrical Engineering
Katsura, Nishikyo
Kyoto 615-8510
Japan

Klaus Höhne
Technische Universität Darmstadt
Institut für Festkörperphysik
Hochschulstraße 6
64289 Darmstadt
Germany

Philipp Hövel
Institut für Theoretische Physik
Technische Universität Berlin
Hardenbergstraße 36
10623 Berlin
Germany

Jack Hudson
Department of Chemical Engineering
University of Virginia
102 Engineers' Way
P.O. Box 400741
Charlottesville, VA 22904-4741
USA

Henri Huijberts
Queen Mary University of London
School of Engineering and
Materials Science
Mile End Road
London E1 4NS
UK

Lucas Illing
Duke University
Department of Physics
PO Box 90305
Durham, NC 27708
USA

Natalia Janson
Loughborough University
Department of Mathematical Sciences
Loughborough, LE11 3TU
UK

Peter N. Jordan
Weill Cornell Medical College
Division of Cardiology
1300 York Ave.
New York, NY 10065
USA

Wolfram Just
Queen Mary University of London
School of Mathematical Sciences
Mile End Road
London, E1 4NS
UK

Ido Kanter
Bar-Ilan University
Minerva Center and
Department of Physics
52900 Ramat-Gan
Israel

Wolfgang Kinzel
University of Würzburg
Institute for Theoretical Physics
and Astrophysics
Am Hubland
97074 Würzburg
Germany

Achim Kittel
Carl-von-Ossietzky University
Oldenburg
Energy and Semiconductor
Research Laboratory
Institute of Physics
Carl-von-Ossietzky Straße 9–11
26129 Oldenburg
Germany

Trine Krogh-Madsen
Weill Cornell Medical College
Division of Cardiology
1300 York Ave.
New York, NY 10065
USA

Jürgen Kurths
Universität Potsdam
Institut für Physik
Am Neuen Palais 10
PF 601553
14415 Potsdam
Germany

Anna Lin
Duke University
Physics Department
Durham, NC 27708
USA

Clemens von Loewenich
Technische Universität Darmstadt
Institut für Festkörperphysik
Hochschulstraße 6
64289 Darmstadt
Germany

Andre Longtin
University of Ottawa
Department of Physics
150 Louis Pasteur
Ottawa
Ontario K1N 6N5
Canada

Elbert E. N. Macau
Instituto Nacional de Pesquisas
Espaciais
Laboratório Associado de
Computação e Matemática
Aplicada – LAC
INPE 12227-010
São José dos Campos
Brazil

Cristina Masoller
Universidad Politècnica
de Catalynya
Departament de Fisica
i Enginyeria Nuclear
Colom 11
Terrassa 08222, Barcelona
Spain

Igor Mezic
University of California
Department of Mechanical
Engineering
ENGR II, Room 2339
Santa Barbara, CA 93106
USA

Alexander Mikhailov
Fritz-Haber-Institut
der Max-Planck-Gesellschaft
Abteilung Physikalische Chemie
Faradayweg 4–6
14195 Berlin
Germany

Erik Mosekilde
Technical University of Denmark
Complex Systems Group
Department of Physics
Building 309
2800 Kongens Lyngby
Denmark

Stefan C. Müller
Otto-von Guericke-Universität
Magdeburg
Institut für Experimentelle Physik
Abteilung Biophysik
PF 4120
39016 Magdeburg
Germany

Hiroyuki Nakajima
Kinki University
Department of Electronic Engineering
and Computer Science
Faculty of Engineering
1, Takaya-Umenobe
Higashi-Hiroshima 739-2116
Japan

Alexander Neiman
Ohio University
Department of Physics
and Astronomy
Athens, OH 45701
USA

Henk Nijmeijer
Eindhoven University of Technology
Department of
Mechanical Engineering
P.O. Box 513
5600 MB Eindhoven
The Netherlands

Maciej Ogorzalek
Jagiellonian University
Department of Information
Technologies
Faculty of Physics, Astronomy
and Applied Computer Science
ul. Reymanta 4
30-059 Krakow
Poland

Junji Ohtsubo
Shizuoka University
Faculty of Engineering
Hamamatsu, 432-8561
Japan

Jordi Garcia Ojalvo
Escola Tecnica Superior d'Enginyeria
Industrial de Terrassa
Colom 11
08222 Terrassa, Barcelona
Spain

Alan V. Oppenheim
Department of Electrical Engineering
and Computer Science
Room 36-615
77 Massachusetts Avenue
Cambridge, MA 02139
USA

Gian-Luca Oppo
University of Strathclyde
Department of Physics
107 Rottenrow
Glasgow, G4 0NG
Scotland

UK

Ulrich Parlitz
Universität Göttingen
Drittes Physikalisches Institut
Friedrich-Hund-Platz 1
37077 Göttingen
Germany

Louis M. Pecora
Naval Research Laboratory
Code 6341
Washington, D.C. 20375
USA

Arkady Pikovsky
Universität Potsdam
Institut für Physik
PF 601553
14415 Potsdam
Germany

Alexander Pogromsky
Eindhoven University of Technology
Department
of Mechanical Engineering
P.O. Box 513
5600 MB Eindhoven
The Netherlands

Martin Popp
Qimonda Dresden GmbH & Co. OHG
Device Development (QD DR D)
P.O. Box 10 09 64
01079 Dresden
Germany

Kestutis Pyragas
Semiconductor Physics Institute
Solid State Physics Laboratory
A. Gostauto 11
01108 Vilnius
Lithuania

Viktoras Pyragas
Semiconductor Physics Institute
Solid State Physics Laboratory
A. Gostauto 11
01108 Vilnius
Lithuania

Tatjana Pyragien
Semiconductor Physics Institute
Solid State Physics Laboratory
A. Gostauto 11
01108 Vilnius
Lithuania

Nikolaj Rulkov
University of California, San Diego
Institute for Nonlinear Science
9500 Gilman Drive
La Jolla, CA 92093-0402
USA

Jan Schlesner
Institut für Theoretische Physik
Technische Universität Berlin
Hardenbergstr. 36
10623 Berlin
Germany

Eckehard Schöll
Technische Universität Berlin
Institut für Theoretische Physik
Hardenbergstraße 36
10623 Berlin
Germany

Heinz Georg Schuster
Universität Kiel
Institut für Theoretische Physik
und Astrophysik
Leibnizstr. 15
24098 Kiel
Germany

Hiroyuki Shirahama
Faculty of Education
Ehime University
Bunkyo-cho 3
Matsuyama 790-8577
Japan

K. Alan Shore
University of Wales
School of Informatics
Division of Electronic Engineering
Bangor Dean Street
Bangor, LL57 1UT
UK

Kenneth Showalter
West Virginia University
Department of Chemistry
Morgantown, WV 26506-6045
USA

Sitabhra Sinha
The Institute of
Mathematical Sciences
CIT Campus, Taramani
600113 Chennai
India

Joshua Socolar
Duke University
Physics Department
Durham, NC 27708
USA

Mark L. Spano
NSWC, Carderock Laboratory
West Bethesda
Maryland, MD 20817
USA

S. Sridhar
The Institute of
Mathematical Sciences
CIT Campus, Taramani
600113 Chennai
India

Peter Tass
Forschungszentrum Jülich
Institut für Medizin (MEG)
52425 Jülich
Germany

Theo Tschudi
Technische Universität Darmstadt
Institut für Angewandte Physik
AG Licht- und Teilchenoptik
Hochschulstraße 6
64289 Darmstadt
Germany

Lev Tsimring
Institute for Nonlinear Science
University of California
San Diego
La Jolla, CA 92093-0402
USA

Hans-Jürgen Wünsche
Humboldt-Universität zu Berlin
Institut für Physik
Newtonstr. 15
12489 Berlin
Germany

Kohei Yamasue
Kyoto University
Venture Business Laboratory
Katsura, Nishikyo
Kyoto 615-8510
Japan

Zhanybai T. Zhusubaliyev
Kursk State Technical University
Department of Computer Science
50 Years of October Str. 94
305040 Kursk
Russia

Vladimir Zykov
Institut für Theoretische Physik
Technische Universität Berlin
Hardenbergstr. 36
10623 Berlin
Germany

Part I
Basic Aspects and Extension of Methods

1
Controlling Chaos

Elbert E. N. Macau and Celso Grebogi

1.1
Introduction

The concept of "control" is associated with the idea of implementing actions to guarantee that a system behaves as desired. Nature is prodigal in presenting sophisticated control strategies that regulated phenomena that take place in all scales of time and space [13, 18, 35, 49]. These mechanisms reach the ultimate level of efficacy and refinement on biological systems in which they are responsible for the emergence of the sustainable phenomenon of life. A careful and systematic investigation performed on mechanisms Nature uses for system control uncover that they are based on the following concepts: stability, feedback, and flexibility.

Stability can be defined as the system's ability for keeping itself working properly even when perturbations act on it. This is the main goal to be achieved by the control strategy that is embedded in the system. Every system is supposed to operate properly inside well-defined regions. During its lifetime operation, a system suffers all kinds of internal and external perturbations. In order to continue its appropriate operation, a system must be stable enough to those perturbations. This ability can be seen around us in natural processes and is closely related to the concept of feedback [18, 49], which can be defined as the mechanism whereby part of the system output is returned (back) to be used as input of the control strategy, providing self-regulation. Through this mechanism, a system regulates itself by monitoring its own output to keep it stable and operating properly. To accomplish that, control strategies presented in Nature exploit another key property of the Nature: flexibility. The idea behind this concept is that it is not necessary to stress the system and drive it brutally to the desired operation point immediately or directly. In contrast, it is more efficient, reliable, and realizable to control the system by letting it to fluctuate and eventually change its dynamics as little as possible to drive it to the desired state without applying intense forces. An excess of control may result in energy waste and eventually could imply in system damage. Thus, the concepts of stability, feed-

back and flexibility are wisely combined and exploited by Nature through control strategies that allow it to opportunistically accomplish its process with remarkable efficiency.

Let us now explore how this scenario, inspired from Nature, fits on the concept of chaos control [21, 22, 33, 39]. At first, it is necessary to properly understand the meaning of chaotic dynamics [2, 14]. The sensitive dependence on initial condition is the main characteristic of chaotic behavior. It means that two trajectories that are initialized very close to each other separate exponentially in time. Because of this typical behavior, which is known as the "butterfly effect," long time prediction of a chaotic trajectory based on finite precision measurements is impossible. However, this characteristic also implies that a chaotic trajectory is extremely sensitive to the effect of perturbations. As so, just a small perturbation applied at a given time is enough to change the trajectory's future evolution, directing its way to other regions of the chaotic invariant set [25]. Another key characteristic of the chaotic system is that there are an infinite variety of behaviors embedded on it. A chaotic system contains a dense orbit on the invariant set, which is a chaotic trajectory that recurrently passes infinitely close to any point of that set. A third characteristic is that the chaotic invariant set contains an infinite number of unstable periodic orbits of all periods, which coexist with the chaotic motion. These orbits are unstable in the sense that small deviation from the periodic orbit grows exponentially rapidly in time, and the system quickly moves away from the periodic orbit in a chaotic trajectory. The combination of these three characteristics makes chaotic systems as one of the most flexible systems that can be found in Nature. It is exactly these characteristics that are explored in the scenario of chaos control.

Chaos control is based on the idea of exploiting the key dynamical characteristics just presented to control the system as desired [21, 22, 33, 39]. As so, the sensitive dependence on the initial condition is used both to stabilize chaotic behavior in periodic orbits [21, 22, 33, 39] and to direct trajectories to a desired state [30, 34, 44–46]. Small perturbations applied to control parameters can be used to stabilize chaos, keeping the parameters in the neighborhood of their nominal values. This idea that came about in the context of the OGY method of control of chaos [39] and its feasibility has been experimentally demonstrated in several experiments [1, 4, 5, 8, 15, 17, 26, 37, 41]. Besides, a carefully chosen sequence of small perturbations applied to some control parameter can also be used to rapidly direct trajectories to some desired final state [44–46]. This strategy of guiding trajectories in chaotic systems, called targeting, also had its feasibility experimentally demonstrated [7]. On both these approaches we can verify how the fundamental idea of the chaos control is applicable: the system flexibility is paramount and opportunistically exploited so that the perturbations do not significantly change the system dynamics, but just enable the intrinsic system dynamics to accomplish the desired control task. In some sense, the control of chaos mimics the way that Nature implements its control strategy to opportunistically accomplish its goals. Furthermore, to extremely exploit the flexibility presented on chaotic systems, the controller that implements the chaos control

strategy must preserve the chaotic dynamics at all time. As so, the feedback concept, when used, is applied just locally, in the neighborhood of a specific chaotic trajectory, and implemented so that just small perturbations are applied on the chaotic trajectory with the goal of keeping the whole system stable and operating properly.

Over the years, the concept of control of chaos has been successfully applied on a variety of systems and on a multitude of circumstances. However, the horizon of applicability is still wider. In a typical application, we see a control of chaos strategy applied in a situation in which the chaotic dynamics develops on a chaotic attractor. However, chaotic dynamics are present not only on chaotic attractors [25, 48], but also on nonattracting chaotic sets, giving rise to important phenomena with remarkable physical consequences for the dynamical system in which they are present. These are the cases of chaotic transients [24, 28], chaotic scattering [9, 27], and fractal basing boundaries [20, 23]. In these phenomena, a typical trajectory presents over time different behaviors in which a chaotic behavior is followed by a nonchaotic one. The dynamics is understood by the presence of chaotic saddles. A chaotic saddle is an invariant chaotic set that can be envisioned as the intersection of its stable and unstable manifolds, where the stable and unstable manifolds each consist of a Cantor set of surfaces. As so, it is a fractal object and it has chaotic trajectories that never leave the set. It can be understood by the horseshoe model, introduced by Smale [48], who, by using symbolic dynamics, showed that this invariant set has a dense orbit, exhibits the sensitivity to initial condition property, and embedded in it there is a countable infinity set of unstable periodic orbits of arbitrary high periods. Let us consider a system in which a nonattracting chaotic saddle Γ coexists in the phase space with others nonchaotic attractors. As there are other attractors in the phase space, all initial conditions, except for a set of measure zero made up of the chaotic saddle Γ and its stable manifold, generate trajectories that asymptote to one of the attractors. Trajectories starting from random initial conditions may wander near the chaotic saddle Γ for a finite time before settling down into one of the attractors. During the time interval in which a trajectory suffers the influence of the chaotic saddle, it behaves as a chaotic trajectory. Furthermore, the closer the initial condition of a trajectory to the stable manifold of Γ, longer the trajectory stays near the chaotic saddle, exhibiting a chaotic-like behavior.

If we have a chaotic system whose dynamics is governed by a chaotic saddle, control of chaos strategy can be combined with classic control methods to give rise to a powerful control approach that exploits the flexibility that the combined methods can offer. It can be accomplished as follows: for an ordinary trajectory, whenever it behaves as a chaotic one, a control of chaos strategy is applied. As soon as the trajectory leaves the region of the phase space in which it behaves as a chaotic one, control of chaos is switched off and a classic control mechanism starts to be in effect. With this approach that we could call as *opportunistic chaos control*, we have the most effective control approach in action for each of the conceivable dynamical behaviors that a system may present. In fact, this hy-

pothetical situation is very common in Nature and in technological systems. In this chapter, we present some key examples that show the efficiency of this approach. Therefore, we proceed as follows. In the next two sections, we review the OGY method of chaos control as it was originally proposed and our targeting strategy that can be applied even to higher dimensional systems. After that, we show an application example where a classic control method is used in association with the OGY to properly control an electronic system. In the subsequent section, our targeting method is associated with the classic control method to efficiently control a system with a very elaborated dynamics. Finally, we end this chapter with remarks about the concept of control of chaos.

1.2
The OGY Chaos Control

The key ingredient for the control of chaos [38, 39] is the observation that a chaotic invariant set has embedded on it an infinite and enumerable set of unstable periodic orbits of all periods. Counting on ergodicity [25], another intrinsic property of the chaotic behavior, we wait for a natural passage of the chaotic trajectory close to the desired periodic behavior and then a small judiciously chosen controlling perturbation is applied. This small perturbation is enough to stabilize the system in the desired periodic behavior. Through this mechanism, the system can operate on a large number of different set points (theoretically, an infinite number of them), with a great flexibility in switching among them.

In this section, we review the main points related to the originally proposed algorithm. As so, our scenario is a chaotic dynamical system whose attractor is a three-dimensional state space. A Poincaré section [2] can be introduced transversal to the chaotic flow so that the system dynamics on this Poincaré section can be described by a two-dimensional invertible map as

$$x_{n+1} = \mathbf{F}(x_n, p), \tag{1.1}$$

where $x_n \in R^2$, $\mathbf{F}$ is a smooth function of its variables, and $p \in R$ is an externally accessible control parameter. Following the idea of using small perturbations to control the system, parameter allowed variations must be small,

$$|p - \bar{p}| < \delta, \tag{1.2}$$

where $\bar{p}$ is the nominal parameter value, and $\delta \ll 1$ defines the allowable range of parameter variation. We wish to program the parameter p so that a chaotic trajectory is stabilized when it enters in a neighborhood of the target periodic orbit.

Let $x_\mathbf{F}(\bar{p})$ be one of the fixed points of the map (1.1) at the nominal parameter value $\bar{p}$ that we wish to stabilize. (The extension of the method for unstable periodic points of period larger than 1 is straightforward.) The location of the fixed

point in the phase space depends on the control parameter p. Upon application of small perturbation Δp, we have $p = \bar{p} + \Delta p$. Since Δp is small, we expect $x_F(p)$ to be close to $x_F(\bar{p})$. We write

$$x_F(p) \approx x_F(\bar{p}) + g\Delta p, \tag{1.3}$$

where the vector g is given by

$$g \equiv \frac{\partial x_F}{\partial p}\Big|_{p=\bar{p}} \approx \frac{x_F(p) - x_F(\bar{p})}{\Delta p}. \tag{1.4}$$

The system dynamics of any smooth nonlinear system is approximately linear in a small ε-neighborhood of a fixed point. Thus, near $x_F(\bar{p})$, we can use the linear approximation for the map:

$$[x_{n+1} - x_F(p)] \approx M[x_F(p)] \cdot [x_n - x_F(p)], \tag{1.5}$$

where $M[x_F(p)]$ is the 2×2 Jacobian matrix of the map $F(x, p)$ evaluated at the fixed point $x_F(p)$, which is defined as follows:

$$M[x_F(p)] = \frac{\partial F}{\partial x}\Big|_{x_F(p)} \approx M[x_F(\bar{p})] + \frac{\partial M}{\partial p}\Big|_{p=\bar{p}}\Delta p. \tag{1.6}$$

Note that $\Delta p \sim \varepsilon$ and $||[x_n - x_F(p)]|| \sim \varepsilon$, where ε is the size of the small neighborhood in which the linear approximation (1.5) is valid. Writing $x_F(p) \approx x_F(\bar{p}) + g\Delta p$ (from Eq. (1.4)), substituting this relation and Eq. (1.6) into Eq. (1.5), and keeping only terms which are first order in ε, we obtain

$$x_{n+1} - x_F(\bar{p}) \approx g\Delta p + M[x_F(\bar{p})] \cdot [x_n - x_F(\bar{p}) - g\Delta p]. \tag{1.7}$$

In Eq. (1.7), the Jacobian matrix M is evaluated at the fixed point $x_F(\bar{p})$ of the unperturbed system, which is the one to be stabilized. Since $x_F(\bar{p})$ is embedded in the chaotic attractor, it is unstable and it has one stable and one unstable direction [4]. Let e_s and e_u be the stable and unstable unit eigenvectors at $x_F(\bar{p})$, respectively, and let f_s and f_u be two unit vectors that satisfy $f_s \cdot e_s = f_u \cdot e_u = 1$ and $f_s \cdot e_u = f_u \cdot e_s = 0$, which are the relations by which the vectors f_s and f_u can be determined from the eigenvectors e_s and e_u. The vectors f_s and f_u are contravariant basis vectors associated with the eigenspace e_s and e_u. The Jacobian matrix $M[x_F(\bar{p})]$ can then be written as:

$$M[x_F(\bar{p})] = \lambda_u e_u f_u + \lambda_s e_s f_s, \tag{1.8}$$

where λ_s and λ_u are the stable and unstable eigenvalues in the eigendirections e_s and e_u, respectively.

When the trajectory point x_n falls into small ε-neighborhood of the desired fixed point $x_F(\bar{p})$ so that Eq. (1.5) applies, a small parameter perturbation Δp_n is

applied at time n to make the fixed point shift slightly so that at the next iteration $(n+1)$, x_{n+1} falls on the stable direction of $x_F(\bar{p})$. Thus, we choose the parameter control Δp_n such that

$$f_u \cdot [x_{n+1} - x_F(\bar{p})] = 0. \tag{1.9}$$

If x_{n+1} falls on the stable direction of $x_F(\bar{p})$, we can then set the control perturbation to zero, and the trajectory for subsequent time will approach the fixed point at the geometrical rate λ_s. Thus for sufficiently small $[x_n - x_F(\bar{p})]$, we can substitute Eq. (1.7) into Eq. (1.9) to obtain $\Delta p_n = c_n$:

$$c_n = \frac{\lambda_u f_u \cdot [x_n - x_F(\bar{p})]}{(\lambda_u - 1) f_u g} \equiv C[x_n - x_F(\bar{p})]. \tag{1.10}$$

We assume in the above that the generic condition $g \cdot f_u \neq 0$ is satisfied so that $c_n \sim |x_n - x_F(\bar{p})|$, which is small. The considerations above apply only to a local small neighborhood of $x_F(\bar{p})$. Globally, we can specify the parameter perturbation Δp_n by setting $\Delta p_n = 0$ if $|c_n|$ is too large, since the range of the parameter perturbation is limited by Eq. (1.2). Thus, practically, we can take Δp_n to be given by

$$\Delta p_n = \begin{cases} c_n & \text{if } |c_n| < \delta \\ 0 & \text{if } |c_n| \geq \delta, \end{cases} \tag{1.11}$$

where in the definition of c_n in Eq. (1.10), it is not necessary to restrict the quantity $|x_n - x_F(\bar{p})|$ to be small.

This method can be extended to higher dimensional systems.

1.3
Targeting–Steering Chaotic Trajectories

The inherent exponential sensitivity of chaotic time evolution to perturbations can be intelligently exploited to direct the dynamics of the system to some desired state using a carefully chosen sequence of small perturbations to some system parameter. This approach, which is of fundamental interest for the control system, is called *targeting* [45].

The targeting idea came about as a way to get around an excessive transient time associated with the use of the OGY method of chaos control to higher dimensional systems. As we saw in the previous section, this method relies on the topological transitivity of the system on the invariant set Λ to bring a chaotic orbit close enough to a neighborhood of the periodic orbit on which we want to stabilize the system. This procedure works. Nevertheless, it presents a significant problem: the *transport time* can be excessively long. Besides, this time depends sensitively on the initial conditions and on the system's dimension. In

dissipative chaotic systems, for randomly chosen initial conditions, the *average transport time* is typically ε^{-D}, where ε is the linear dimension of the neighborhood about the periodic orbit, and D is the pointwise dimension at the periodic point [29]. For low values of D, this time can be acceptably small. However, for systems of higher dimension, it may have a prohibitively large value.

Let us consider a discrete time dynamical system,

$$\mathbf{X}_{i+1} = \mathbf{F}(\mathbf{X}_i, p), \tag{1.12}$$

where $\mathbf{X}_i \in \Re^n$, $p \in \Re$ is an externally controllable parameter that can be externally modified, and $\mathbf{F}$ is a smooth function in both variables. The nominal value of the parameter is $p = \bar{p}$, for which $\mathbf{F}$ is chaotic on a compact, invariant set $\Lambda \subset \Re^n$. Suppose we have two points $\mathbf{X}_s$ and $\mathbf{X}_t$ in Λ. Consider $B_\varepsilon(\mathbf{X}_s)$ a ball of radius ε around $\mathbf{X}_s$, and another ball $B_\varepsilon(\mathbf{X}_t)$ of radius ε about $\mathbf{X}_t$. The *targeting goal* is to find a *constructive orbit* that goes from a point $\mathbf{p}_{\mathbf{X}_s} \in B_\varepsilon(\mathbf{X}_s)$ to a point $\mathbf{p}_{\mathbf{X}_t} \in B_\varepsilon(\mathbf{X}_t)$. Through that constructive orbit, the inherent exponential sensitivity of a chaotic time evolution to perturbations is intelligently exploited to direct trajectories to a desired state in the shortest possible time, by the use of a carefully chosen sequence of small perturbation to some control parameter. Furthermore, since these perturbations are sufficiently small, they do not significantly change the system's dynamics, but enable the intrinsic system dynamics to drive the trajectory to the desired state.

Our technique is subdivided into two sequential parts [34]. In the first one, we find the previously described points $\mathbf{p}_{\mathbf{X}_s}$ and $\mathbf{p}_{\mathbf{X}_t}$ so that there is an orbit (real) that goes from $\mathbf{p}_{\mathbf{X}_s}$ to $\mathbf{p}_{\mathbf{X}_t}$.

In the second part, this orbit is used to build a constructive orbit (virtual) that allows the transport from $\mathbf{p}_{\mathbf{X}_s}$ to $\mathbf{p}_{\mathbf{X}_t}$ using smaller number of elements, i.e., of real orbits. In this process, small perturbations to the control parameter are used to move among the real orbits. The effect of these perturbations is to change the system's evolution from one real orbit to another, resulting in a constructive orbit that allows the transfer from $\mathbf{p}_{\mathbf{X}_s}$ to $\mathbf{p}_{\mathbf{X}_t}$ in a faster time. Thus, the overall effect of this procedure is to produce a suboptimal solution that is gotten by the elimination of parts of the orbit where *recurrences* occur with the use of small perturbations.

1.3.1
Part I: Finding a Proper Trajectory

The main idea of the first part of our technique is as follows [45, 46]: consider a line segment $\overline{a_1 b_1} \subset B_\varepsilon(\mathbf{X}_s)$, so that $\mathbf{X}_s$ is its middle point. To find $\mathbf{p}_{\mathbf{X}_s}$, $\overline{a_1 b_1}$ is iterated in the forward direction, while the region $B_\varepsilon(x_t)$ is iterated in the backward direction, until the forward iterated segment intersect the backward iterated region at the point $\mathbf{p}_I$. It is important to say that it is again the transitivity of a chaotic system that assures that $\mathbf{p}_I$ will be found. When the intersection is found, there is a trajectory that goes from $\mathbf{p}_{\mathbf{X}_s} \in \overline{a_1 b_1}$ to $B_\varepsilon(\mathbf{X}_t)$ through the in-

tersection $\mathbf{p}_I$. Note that $\mathbf{p}_{\mathbf{X}_s}$ can be found by iterating $\mathbf{F}$ in the backward direction from $\mathbf{p}_I$. The point $\mathbf{p}_{\mathbf{X}_s}$ is then used to determine the value $\widetilde{p}$ of the parameter that must be applied to the system to bring it from $\mathbf{X}_s$ to $\mathbf{p}_{\mathbf{X}_s}$. The following algorithm describes how that technique can be implemented:

Step 1: Define a direction Θ in space and using this direction construct a line segment $\overline{a_1 b_1} \subset B_\varepsilon(\mathbf{X}_s)$, so that $\mathbf{X}_s$ is its middle point. Call a_1 as c_0, and b_1 as c_{n_p}.

Step 2: Generate N random points $\{d_j\}_{j=1}^N$ inside $B_\varepsilon(\mathbf{X}_t)$.

Step 3: Create a partition of n_p subsets in $\overline{c_0 c_{n_p}}$ using a sequence of $n_p - 1$ interior points $\{c_j\}_{j=1}^{n_p-1}$.

Step 4: Using $\{d_j\}_{j=1}^N$, construct a Delaunay triangulation (Watson 1981; Varosi et al. 1987) T, which has the sequence of cells $\{F_j\}_{j=1}^M$.

Step 5: Iterate in the forward direction $\{c_j\}_{j=1}^{n_p-1}$ and use linear interpolation to approximate the resultant curve delimited by each pair of iterated points.

Step 6: Iterate in the backward direction $\{d_j\}_{j=1}^N$ and use linear interpolation to approximate the iterated cells of the Delaunay triangulation T.

Step 7: Continue the iteration described in steps 5 and 6 until finding the intersection $\mathbf{p}_I$ between $\overline{\mathbf{F}^l(c_k)\mathbf{F}^l(c_{k+1})}$ and $\mathbf{F}^{-l}(F_h)$, where this one is the backward iterated cell found by linear interpolation of the backward iteration of the points that delineate the cell F_h.

Step 8: Consider the middle point c_{md} of the segment $\overline{c_k c_{k+1}}$. Identify if the intersecting segment is $\overline{c_k c_{\mathrm{md}}}$ or $\overline{c_{\mathrm{md}} c_{k+1}}$. In the first case, assign the value of c_{md} to c_{k+1}; otherwise, assign the value of c_{md} to c_k. Applying a similar procedure, find a new cell F_h which is smaller than the previous one, but still contains in its face p_{x_t}.

Step 9: If $d[c_k, c_{k+1}] > \delta_l$, where δ_l is a specified limit on the precision, then repeat step 8. Otherwise, $\mathbf{p}_{\mathbf{X}_s}$ is equal to c_k.

Step 10: Using $\mathbf{p}_{\mathbf{X}_s}$, determine the value of $\widetilde{p}$ that drives the system from $\mathbf{X}_s$ to $\mathbf{p}_{\mathbf{X}_s}$. When the system gets $\mathbf{p}_{\mathbf{X}_s}$, return the parameter to its nominal value, i.e., $\bar{p}$. From there, the system dynamics will conduct the system evolution to a point $\mathbf{p}_{\mathbf{X}_t} \in B_\varepsilon(x_t)$ in $2 * l$ iterates.

With the use of this procedure, the average transport time to go from the source point to the target point typically scales logarithmically with the inverse of the size of the target region [45], which contrasts with the exponential increasing that takes place if this algorithm is not used.

1.3.2
Part II: Finding a Pseudo-Orbit Trajectory

Part I of our method produces an orbit that goes from $\mathbf{p}_{\mathbf{X}_s}$ to $\mathbf{p}_{\mathbf{X}_t}$. Let us represent that orbit by the following sequence of points $\{\mathbf{X}_i\}_{i=0}^N$ in $\Re^n$, where $\mathbf{X}_0 = \mathbf{p}_{x_s}$, and $\mathbf{X}_N = \mathbf{p}_{\mathbf{X}_t}$. As that orbit belongs to a chaotic trajectory in a compact invariant set Λ, it might have recurrent points [10, 11, 32, 34]. In Part II,

we look for those *recurrent points* by using a sequential search [31]. If $\mathbf{X}_r$ is a recurrent point, it means that it belongs to a sequence of points $\{\ldots, \mathbf{X}_r, \mathbf{X}_{r+1}, \ldots, \mathbf{X}_{r+n}, \ldots\}$ such that $d[\mathbf{X}_r, \mathbf{X}_{r+n}] < \delta$, making up a kind of *loop*. If none of the points inside the loop is located in $B_\varepsilon(\mathbf{X}_t)$, that loop does not effectively conduct the trajectory to the targeting point. Thus, after being identified, our method replaces that loop by a smaller orbit that is backward asymptotic to $\mathbf{X}_r$ and forward asymptotic to $\mathbf{X}_{r+n}$ [6, 29]. By creating patches like that to the recurrent points of the original orbit, we build a *constructive orbit* or a *pseudo-orbit* that allows the transportation from $\mathbf{p}_{\mathbf{X}_s}$ to $\mathbf{p}_{\mathbf{X}_t}$ with considerably less iterations than the original orbit. However, to accomplish that, perturbations must be introduced in order to switch the trajectory along the pseudo-orbits, as described next [10, 11, 32, 34].

In a hyperbolic situation, it is known that if the distance between $\mathbf{X}_r$ and $\mathbf{X}_{r+n}$ is sufficiently small, say less than $\delta_{\lim}$, then the unstable manifold of $\mathbf{X}_r$, $W_\varepsilon^u(\mathbf{X}_r)$ and the stable manifold or $\mathbf{X}_{r+n}$, $W_\varepsilon^s(\mathbf{X}_{r+n})$ intersect each other in a point $\mathbf{q}$. This fact can be exploited to accomplish our goal if a proper perturbation is applied to the sequence of points of the original orbit that passes through $\mathbf{X}_r$. In fact, according to the theorem of Hirsh and Pugh (Arrowsmith 1994), $\mathbf{q} \in W_\varepsilon^u(\mathbf{X}_r) \cap W_\varepsilon^s(\mathbf{X}_{r+n})$ implies that forward iterations of $\mathbf{q}$ converge to forward iterations of $\mathbf{X}_{r+n}$, i.e., $\lim_{k\to\infty} d[\mathbf{F}^k(\mathbf{q}), \mathbf{F}^k(\mathbf{X}_{r+n})] = 0$, and backward iterations of q converges to backward iterations of $\mathbf{X}_r$, i.e., $\lim_{k\to\infty} d[\mathbf{F}^{-k}(\mathbf{q}), \mathbf{F}^{-k}(\mathbf{X}_r)] = 0$. Thus, if we consider a point $\mathbf{X}_{r-m}$ that precedes $\mathbf{X}_r$ in the original trajectory, and a point $\mathbf{X}_{r+n+t}$ that succeeds $\mathbf{X}_{r+n}$ in the original trajectory, we have $d[\mathbf{F}^t(\mathbf{q}), \mathbf{F}^t(\mathbf{X}_{r+n})] = \varepsilon_{r+n+t}$, and $d[\mathbf{F}^{-m}(\mathbf{q}), \mathbf{F}^{-m}(\mathbf{X}_r)] = \varepsilon_{r-m}$. Furthermore, as $W_\varepsilon^u(\mathbf{X}_r)$ can be locally approximated by $E_{\mathbf{X}_r}^u$, which is the unstable subspace of the tangent space at $\mathbf{X}_r$, while $W_\varepsilon^s(\mathbf{X}_{r+n})$ can be locally approximated by $E_{x_{r+n}}^s$, which is the stable subspace of the tangent space at $\mathbf{X}_{r+n}$, and that approximation is continuously preserved over the iterations by the Jacobian of $\mathbf{F}$, i.e., $D\mathbf{F}(\cdot)$ calculated at the iteration point [25]. It follows that ε_{r-m} is located in the direction of $E_{\mathbf{X}_{r-m}}^u$, and ε_{r+n+t} is located in the direction of $E_{\mathbf{X}_{r+n+t}}^s$. Thus, if the proper perturbation ε_{r-m} is applied in the direction of $E_{\mathbf{X}_{r-m}}^u$, it produces a perturbed orbit that passes through $\mathbf{q}$, and converges to the original trajectory after $\mathbf{X}_{r+n}$. Consequently, that procedure generates the desired patch that avoids the recurrent loop of the original trajectory. In addition, that argument indicates that the perturbation ε_{r-m} can be calculated by solving the following equation:

$$\mathbf{F}^{m+t}(\mathbf{X}_{r-m} + \varepsilon_{r-m} E_{\mathbf{X}_{r-m}}^u, \bar{p}) = \mathbf{X}_{r+n+t} + \varepsilon_{r+n+t} E_{\mathbf{X}_{r+n+t}}^s. \tag{1.13}$$

This equation can be solved by using the Newton-secant method.

We should emphasize that the values of m and t in Eq. (1.13) can be adequately adjusted for each system by an empirical procedure. Also, Hirsh and Pugh's theorem provides us with a proper way to use the approximation of the tangent subspace $E_{\mathbf{X}_i}^s$ and $E_{\mathbf{X}_i}^u$ at a point. According to that theorem, if we consider an orbit $\{\mathbf{X}_k\}_{k=1}^n$ which contains $\mathbf{X}_i$, any variation near $\mathbf{X}_{i-m}$ will expand

along the unstable manifold of $\mathbf{X}_i$ if m is chosen large enough. A similar statement can be made regarding the stable manifold of $\mathbf{X}_i$ for variations near $\mathbf{X}_{i+m}$ iterated in the backward direction.

That procedure can be used in the attempt to eliminate the recurrence in the original path from $\mathbf{p}_{\mathbf{X}_s}$ to $\mathbf{p}_{\mathbf{X}_t}$ that are less than $\delta_{\lim}$. Higher priority in the elimination should be assigned to the longest loops. A patch is accepted as usable if the perturbation ε_{r-m} to be applied, in order to implement it, is less than a pre-assigned limit value $\varepsilon_{\lim}$. Our method spawns a sequence of perturbations $\{\varepsilon_i\}_{i=1}^K$ and directions $\{\boldsymbol{E}_i\}_{i=1}^K$ to be respectively applied to a sequence of points $\{\mathbf{X}_{n_i}\}_{i=1}^K$ of the original trajectory. To apply each perturbation, it is necessary to calculate the value $\widetilde{p_{\mathbf{X}_{n_i}}}$ of the parameter to be used in $\mathbf{X}_{n_i}$ to change the system state from $\mathbf{X}_{n_i}$ to $\mathbf{X}'_{n_i} = \mathbf{X}_{n_i} + \varepsilon_i \boldsymbol{E}_{x_i}$. The overall result of our method is a suboptimal constructive trajectory or a suboptimal pseudo-orbit that allows the transfer from $\mathbf{p}_{\mathbf{X}_s}$ to $\mathbf{p}_{\mathbf{X}_t}$.

The previous arguments can be consolidated in the following algorithm:

Step 1: Starting from the original transfer trajectory from $\mathbf{p}_{\mathbf{X}_s}$ to $\mathbf{p}_{\mathbf{X}_t}$, find all the recurrent points whose distance from it to its recurrent point is less than $\delta_{\lim}$. Sort them out by the size of the loop in decreasing order.

Step 2: Take from the list its first point and find a patch for the loop using Eq. (1.13). If the resulting perturbation is less than $\varepsilon_{\lim}$, accept the patch. Put in the solution list the points in which the perturbation should be applied, together with the perturbations and the direction values.

Step 3: Take the next point in the list that is located after the previous found patch.

Step 4: Find a patch for the loop using Eq. (1.13). If the resulting perturbation is less than $\varepsilon_{\lim}$, accept the patch. Put in the solution list the points in which the perturbation should be applied, together with the perturbations and the direction values.

Step 5: Go back to step 3 until all the points of the list have been considered.

Step 6: Use the solution list and the original trajectory to compute the pseudo-orbit that allows the suboptimal transfer from $\mathbf{p}_{\mathbf{X}_s}$ to $\mathbf{p}_{\mathbf{X}_t}$.

1.3.3
The Targeting Algorithm

The algorithm that results from the combination of parts I and II can be applied to general situations [31]. In fact, individually, each part has been successfully applied to numerical and laboratory experiments in mechanics [29, 46] and in situations involving spacecraft guidance [11]. Furthermore, with delay coordinate embedding, the algorithm is applicable to experimental situations in which no *a priori* analytical knowledge of the system dynamics is available [46].

The power of our method is due to the sequential combination of both parts. However, we must stress the fact that the second part has the objective of reducing the length of long trajectories that present recurrence to get a smaller trajectory. We can have situations where that algorithm does not succeed because

there is no recurrence in the trajectory for the specified limit values for the perturbation and the proximity between the recurrent points. In other situations, the trajectory found by the first part of the algorithm is short enough and already satisfies our goals.

1.4
Applying Control of Chaos and Targeting Ideas

In this section we apply the control of chaos concept in association with classical control methods. The proper combination of these two approaches gives rise to what we call the opportunistic chaos control strategy. We demonstrate this strategy by analyzing three very significative examples. In these examples, the chaotic invariant sets are nonattractive. In the first case, we consider a simple electronic circuit operating in a regime in which an attracting periodic orbit coexists with a chaotic saddle. As so, initial conditions not located on the periodic orbit generate trajectories that undergo a chaotic transient behavior until they eventually settle to the periodic orbit. In this system, a classic control steering method is used in association with the OGY to make the system behave periodically, and with a period that is different of the originally presented by the system after its transient interval.

In the second example, we analyze a very involved scenario with the presence of chaotic and no-chaotic behaviors that are entwined in state space in a very complicated way. Here our opportunistic chaos strategy combines the chaotic targeting approach and classic control methods to steer trajectories through the phase space and also to stabilize the system on periodic behaviors from time to time.

1.4.1
Controlling an Electronic Circuit

Let us consider an electronic circuit composed of an AC voltage source, a resistor, an inductor, and a diode as the nonlinear element, as shown in Fig. 1.1.

Applying the Kirchhoff voltage law, the voltage across the diode is related to the input voltage generator (V_{in}) and the circuit current by

$$L\frac{dI}{dt} = V_0 \sin(2\pi ft) - RI - V_d, \tag{1.14}$$
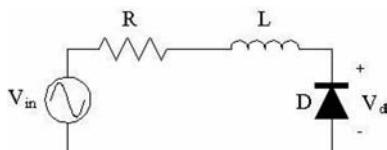
Fig. 1.1 Diode circuit: the diode circuit is composed of an AC voltage source V_{in}, a resistor R, an inductor L, and a diode; V_d is the voltage across the diode.

where V_0 is the voltage amplitude and f is the frequency.

For the diode, we consider its high-frequency model for the voltage across it, which is given by [19, 40]

$$V_d = \frac{|q|(C_j - C_d)}{2C_jC_d} + \frac{q(C_j + C_d)}{2C_jC_d} + E_0, \tag{1.15}$$

where q is the diode accumulated charge, C_j is the junction capacitance, and C_d is the diffusion capacitance.

Our system model equation can be converted to the following system of first-order autonomous differential equations:

$$\begin{cases} \dfrac{dq}{dt} = I \\[2mm] L\dfrac{dI}{dt} = V_0 \sin(\theta) - RI - \left(\dfrac{|q|(C_j - C_d)}{2C_jC_d} + \dfrac{q(C_j + C_d)}{2C_jC_d} + E_0 \right) \\[2mm] \dfrac{d\theta}{dt} = 2\pi f \end{cases} \tag{1.16}$$

For this work, we use the diode DIN1206C, which, according to the specifications, has for the parameters of its high-frequency model the values $453pF$ for the diffusion capacitance (C_d), 30 nF for the junction capacitance (C_j), and 0.52 V as the junction voltage (V_j). The circuit parameter values are $L = 0.18$ mH, and $R = 4.5\,\Omega$. For the input voltage generator, i.e., $V_{in} = V_o \sin(2\pi ft)$, we set $f = 333$ kHz, and V_0, the input voltage amplitude, is used as the variable parameter.

In Fig. 1.2, we show the system bifurcation diagram obtained by using a time-$2\pi f$ stroboscopic map.

Let us now look at the system dynamics inside the period-3 window. For this purpose and for $V_0 = 2.3$ V, we take a random initial condition located outside the period-3 window attractor and we obtain its trajectory. This trajectory, as it is observed in the previously defined time-$2\pi f$ stroboscopic map, appears in Fig. 1.3, while Fig. 1.4 shows the associated time series plot for the circuit current I. We can see that the system initially has a chaotic-like behavior. After this transient time, the trajectory finally settles on a period-3 periodic behavior. Further analysis indicated that this is a chaotic transient, which happens for this value of V_0 due to the presence of a nonattracting chaotic saddle that coexists with the period-3 attractor. Thus, trajectories starting from random initial conditions typically wander chaotically near this chaotic saddle for a finite time before settling down into the period-3 attractor. During the time interval in which the trajectory wanders chaotically, this trajectory presents in essence all the characteristics that are typical of a real chaotic trajectory. As so, during this time interval, it shows a sensitive dependence to changes in initial condition, as one of its finite-time Lyapunov exponents is greater than zero. Furthermore, embedded in the chaotic saddle, there are an infinite but numerable sets of unstable periodic orbits (UPO) of all periods.

Bifurcation Diagram

x10^{-9} C
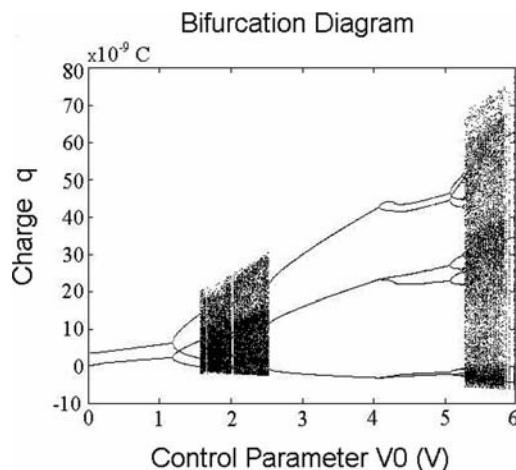
Fig. 1.2 Bifurcation diagram: diode circuit bifurcation diagram defined by a time-$2\pi f$ stroboscopic map; the time-$2\pi f$ mapped charge q against the control parameter V_0 varying from 0 to 5.8 V.

Period-3 Orbit Chaotic Transient
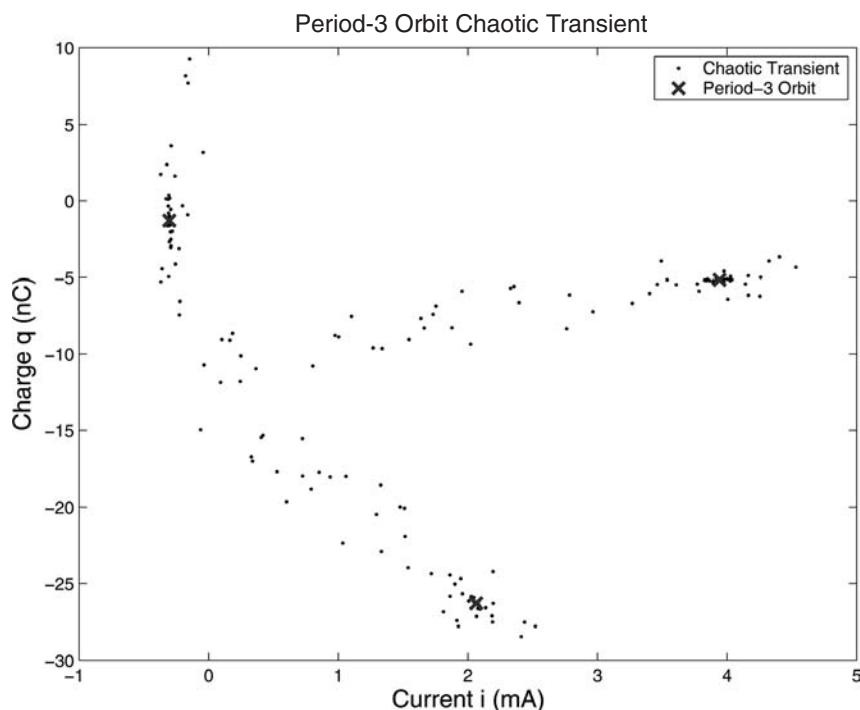
Fig. 1.3 Chaotic transient: chaotic transient before convergence to the period-3 orbit at $V_0 = 3.8$ V and $f = 333$ kHz.
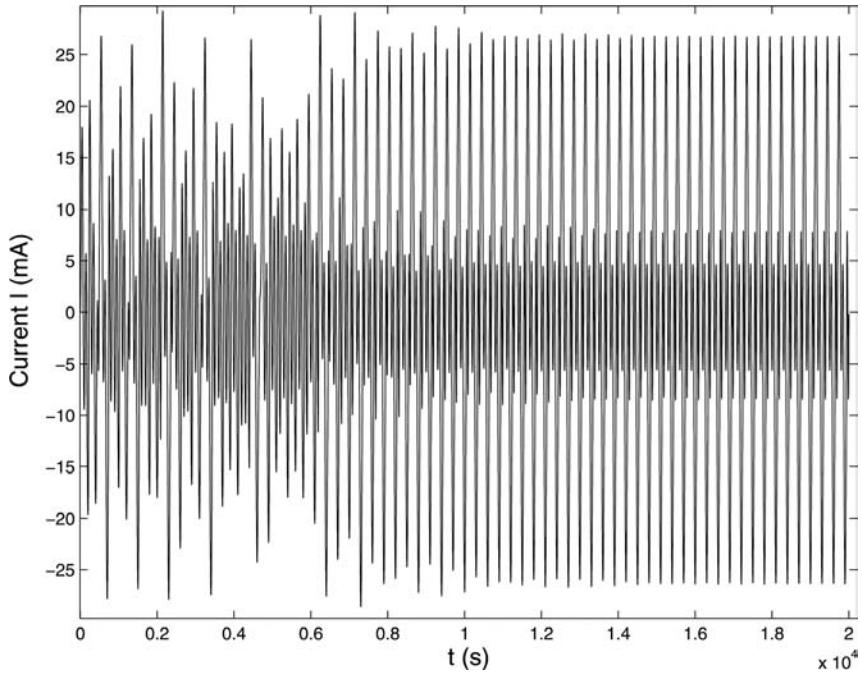
Fig. 1.4 Chaotic transient time series: Current *I* (mA) versus time transient before convergence to the period-3 orbit at $V_0 = 3.8$ V and $f = 333$ kHz.

Let us now assume that we want to stabilize the system in one of these *UPO*. The original OGY method depends on ergodicity to bring a chaotic trajectory sufficiently close to the desired *UPO* so to stabilize the system. However, we are now dealing with a system in which the behavior is not chaotic, but it is a chaotic transient. As so, a typical trajectory might not pass close to the desired unstable periodic orbit embedded in the chaotic saddle. To overcome this diffi-culty related to accessibility of the unstable periodic orbits by a chaotic transient trajectory, we use our opportunistic chaos control strategy: a classical nonlinear control method is strategically associated with the *OGY* chaos control strategy. The classical method is used first, just to drive the trajectory to the neighbor-hood of the *UPO*. From these point on, the *OGY* strategy is then applied so that the system is kept stabilized by using small perturbations.

This classical nonlinear control method, called *input–output linearization* [47], works as follows: consider a guiding control problem and a nonlinear system,

$$\dot{\mathbf{x}} = \mathbf{f}(\mathbf{x}, u) \tag{1.17}$$
$$, y = h(\mathbf{x}),$$

where u is the control parameter.

Assume that our goal is to make the output $y(t)$ follows the desired output $y_d(t)$, where $y_d(t)$ is well known and limited (not diverging). Note that the output $y(t)$ is not directly related to the control parameter u. Consequently, in general, it is not easy to find out how the input u should be designed to control and guide the output $y(t)$. However, in many situations it is possible to find out a simple and direct functional relationship between the output $y(t)$ and the control parameter u.

In our system model, represented by Eq. (1.16), let us redefine its variable as follows: $q = x_1$, $I = x_2$, $y = x_1$, $\theta = x_3$, and $V_0 = u$, so that the system is now described by the following equations:

$$\begin{cases} \dfrac{dx_1}{dt} = x_2 \\[2mm] L\dfrac{dx_2}{dt} = u\sin(x_3) - Rx_2 - \left(\dfrac{|x_1|(C_2 - C_1)}{2C_2C_1} + \dfrac{x_1(C_2 + C_1)}{2C_2C_1} + E_0 \right) \\[2mm] \dfrac{dx_3}{dt} = 2\pi f \\[2mm] y = x_1 \end{cases} \qquad (1.18)$$

To find a functional relation between the output y and the input u, we differentiate the output y twice

$$\ddot{y} = ((1/L)\sin(x_3))u + f_1(\mathbf{x}), \qquad (1.19)$$

where $f_1(x)$ is a state function defined by

$$f_1(\mathbf{x}) = (1/L)\left(-Rx_2 - \left(\dfrac{|x_1|(C_2 - C_1)}{2C_2C_1} + \dfrac{x_1(C_2 + C_1)}{2C_2C_1} + E_0 \right) \right). \qquad (1.20)$$

Equation (1.19) is a direct relation between the output y and the input u. Now, if we choose the input control as follows

$$u = \dfrac{L}{\sin(x_3)}(v - f_1), \qquad (1.21)$$

where v is the new input to be determined, the nonlinearity presented in Eq. (1.19) is canceled and we get a linear relationship between the output and the new input v:

$$\ddot{y} = v. \qquad (1.22)$$

Let us make $e = y(t) - y_d(t)$ the guiding error. We choose the new input control as follows:

$$v = \ddot{y}_d - k_1 e - k_2 \dot{e}, \tag{1.23}$$

where k_1 and k_2 are positive constants.

From Eqs. (1.22) and (1.23), we get the closed loop guiding error differential equation

$$\ddot{e} + k_1 e + k_2 \dot{e} = 0. \tag{1.24}$$

This equation can be transformed to its characteristic form

$$\lambda^2 + k_1 \lambda + k_2 = 0 = (\lambda - p_1)(\lambda - p_2). \tag{1.25}$$

As so, it is possible to choose the appropriates constants k_1 and k_2 to properly allocate the poles of the linearized system. Thus, at each iteration the constants k_1 and k_2 are properly chosen and the new input value is estimated in accordance with the desired output $y_d(t)$ and the current error $e(t)$.

In Fig. 1.5, we show the results of applying our opportunistic chaos control method for this system in an extreme situation. The system is initially on the period-3 periodic orbit. Our method is successively used to stabilize the system on unstable periodic orbits of periods 1, 2, 4, and 8.
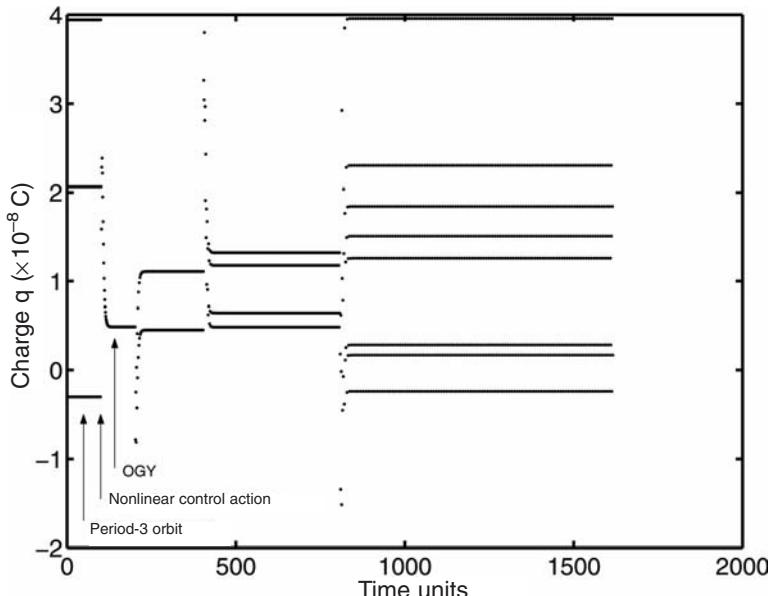
Fig. 1.5 Control in chaotic saddles: the figure shows the system period-3 regime followed by a transient classic control that conducts the orbit to an ε-neighborhood of the desired fixed point (periodic point) when the OGY control is applied.

1.4.2
Controlling a Complex System

To construct a complex dynamical system, let us consider the kicked single rotor, which describes the time evolution of a mechanical pendulum that is being kicked at times $nT, n = 1, 2, \ldots$, with a constant force f_0. From the differential equation for this mechanical system one can derive a Poincaré map which is related to the state of the system just after each successive kick [43]:

$$x_{k+1} = x_k + y_k (mod 2\pi) \qquad (1.26)$$
$$y_{k+1} = (1 - v) * y_k + f_0 \sin(x_k + y_k),$$

where x corresponds to the phase and y to the angular velocity. f_0 is the force parameter, and v is the damping parameter, measuring the energy dissipation of the system. The parameter v varies between 0, for a Hamiltonian situation, with no damping, and 1, in the case of a very strong damping. The dynamics lies on the cylinder $[0, 2\pi) \times \Re$.
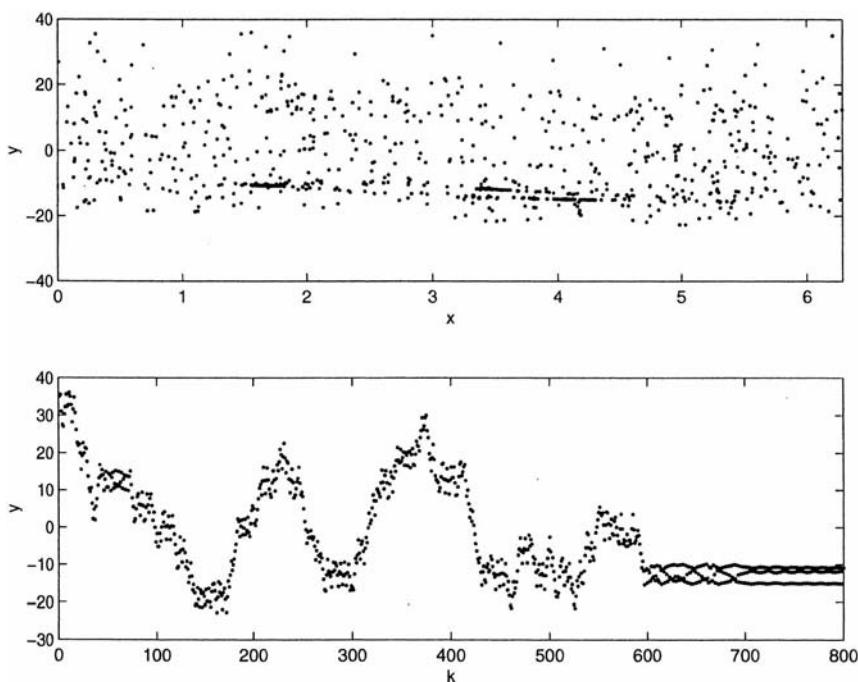
Fig. 1.6 Typical trajectory of the kicked single rotor with the parameters $f_0 = 4.0$ and $v = 0.02$. The y variable represents the angular velocity, x represents the phase, and k represents the iteration number. In both graphs, all plotted quantities are dimensionless.
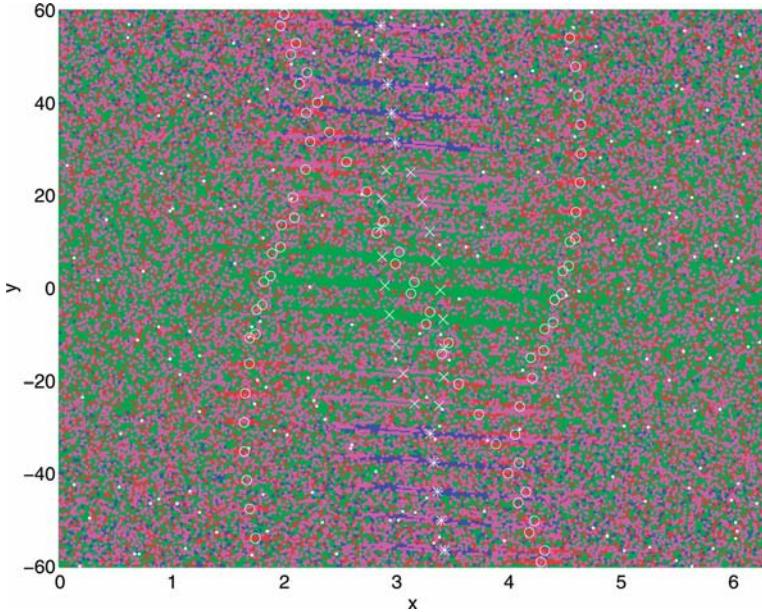
Fig. 1.7 Basin of attraction for the kicked single rotor. The colors identify the periodicity of the orbits, while the characters identify the location of the attracting periodic orbits. In the figure, "*" indicates the position of attracting period one points, "x" the posi- tion of attracting period two orbits, and "o" the position of attracting period three orbits. This picture is for the following parameters: $f_0 = 4.0$ and $v = 0.02$. All quantities plotted are dimensionless.

In the Hamiltonian case (no damping, $v = 0$), we have the area-preserving standard map, which was studied by Chirikov [12] and by many other authors [36, 42]. It has stable and unstable periodic orbits, Kolmogorov-Arnol'd-Moser (KAM) surfaces, and chaotic regions. Depending on the nonlinear parameter f_0, the regions of regular motion and the regions of chaotic motion are complexly interwoven. As the second equation of the map is also taken to be modulo 2π, the map of the cylinder reduces now to the map of the torus $[0, 2\pi) \times [0, 2\pi)$ to itself. As a consequence, each of the periodic orbits represents, in fact, a family of overlapping periodic orbits in which the velocity y differs by integer multiples of 2π. Because of the modulo 2π, all periodic orbits of the same family are located at the same location on the torus.

If we now consider the Hamiltonian case but introduce a very small amount of dissipation (v value close to zero), the motion again takes place on the cylinder $[0, 2\pi) \times \Re$ in order to preserve the invariant structure. The periodic orbits become sinks and the chaotic Hamiltonian sets become saddle chaotic invariant sets embedded in the basin boundaries separating the various sinks. The chaotic motion is hence replaced by long chaotic transients that occur before the trajectory is eventually asymptotic to one of the sinks [16], as can be seen in a typi-
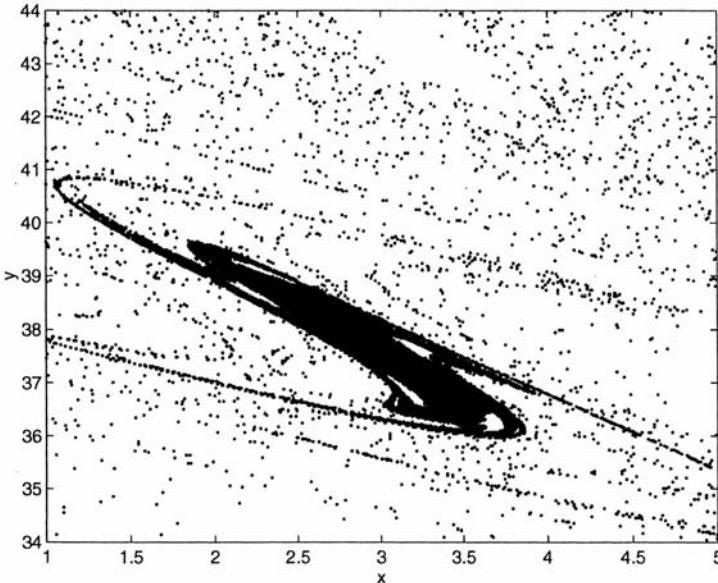
Fig. 1.8 Enlargement of the basin of attraction for a period-1 attracting orbit. Points located inside the region $[1.0, 5.0] \times [34.0, 44.0]$ that go to this period-1 attracting orbit are plotted. All quantities plotted are dimensionless.

cal trajectory that appears in Fig. 1.6. Furthermore, the dissipation leads to a separation of the overlapping periodic orbits, which belong to a given family, with increasing modulo of the velocities on the cylinder. However, there is a bounded cylinder which contains all of the attractors [16]. This cylinder is given as $[0, 2\pi) \times [-y_{max}, y_{max}]$, where $y_{max} = f_0/v$, and all trajectories are eventually trapped inside this region [16]. Consequently, for values of v close to zero, there is a large, but finite, number of coexisting periodic orbits of increasing period. Figure 1.7 is a picture in the space of initial conditions showing the basins of attraction for all attractors of periods 1 to 3. The periodicity of the attractors in the picture is distinguished by gray scales, while the locations of the attracting periodic orbits are identified by special characters that are mentioned in the figure caption.

Figure 1.8 shows a typical basin of attraction for the period-1 attracting orbit at $y = 6\pi$. The black points are attracted to this attractor. The basins of attraction have fractal boundaries, with the box counting dimension d of the basin boundary equal to $d = 1.999$. This means that the dimensions of the basin boundaries is nearly the dimensions of the state space, and they are organized in a complexly interwoven structure, with chaotic saddles embedded in these basin boundaries [23]. Furthermore, extremely small changes in the initial conditions may shift a trajectory from one basin to another, which means that the system has high sensitivity to the final state. Thus, which attractor is eventually
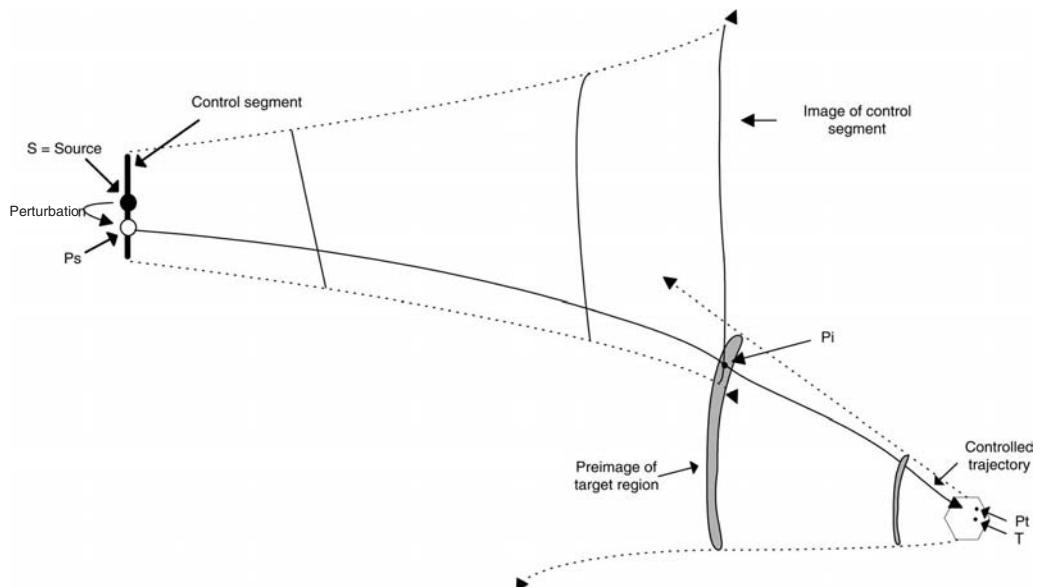
Fig. 1.9 Schematic representation of the scenario involving the use of part I of our targeting procedure for a two-dimensional system.

reached by a trajectory of the system depends strongly on the initial conditions. In this scenario, typical trajectories, starting with arbitrary initial conditions, experience periods of long chaotic transients due to the saddle chaotic invariant sets, before approaching one of the periodic attractors.

Let us consider two points x_s and x_t, both of which located in the neighborhood of the fractal basin boundary. Our objective is to apply our targeting procedure to find a pseudo-orbit that goes from a point $p_{x_s} \in B_\varepsilon(x_s)$ to a point $p_{x_t} \in B_\varepsilon(x_t)$, where ε is a specified small value. The scenario involving the use of part I, as described in Section 1.3, of the targeting algorithm is depicted in Fig. 1.9. In this case, the dimension of the space is 2. To apply part I of the targeting algorithm, we uniformly distribute random points in the interior of the circle $B_\varepsilon(x_s)$. In this case, the result of a Delaunay triangulation is a polygon, which is iterated backward, while the "control segment" is iterated forward. The result of this procedure can be seen in Fig. 1.10. For this particular situation, part I of the algorithm is able to find a trajectory that takes just 30 iterations to reach $p_{x_t} \in B_\varepsilon(x_t)$. We consider this result good enough and decide that it is not necessary to apply part II of the algorithm. It is important to reaffirm that for low dimension systems, in general, just part I produces a good result.

The procedure just described works for points located in the neighborhood of the fractal basin boundaries. It works because of the inherent exponential sensitivity of the chaotic time evolution to perturbations. Therefore, the source point x_s and the targeting point x_t *must* both be in the same neighborhood of the
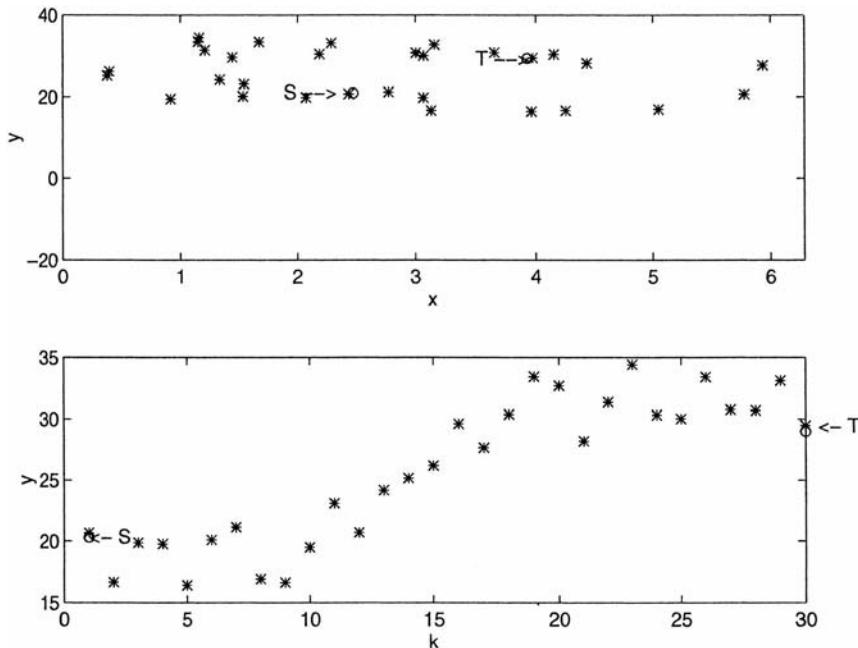
Fig. 1.10 By exploring the chaotic behavior of the system, our targeting procedure rapidly steers the trajectory from *S* to *T*. The asterisks represent the trajectory obtained by applying our targeting procedure to drive the system from the point *S* to the point *T*. The *y* variable represents the angular velocity, *x* represents the phase, and *k* represents the iteration number. In both graphs, all quantities plotted are dimensionless.

chaotic invariant set. This is the case for the points x_s and x_t of the previous example. However, if the system is evolving in a regular regime (not chaotic), the condition of being located in the same chaotic invariant set is not satisfied. Furthermore, the time evolution is "ordered," and the inherent exponential sensitivity to perturbations does not apply. However, we show next that if the objective is to bring the trajectory from one stable state to another stable state, we can first guide the trajectory to the basin boundary structure, where the chaotic saddles are located, and there apply our targeting method. Thus, the idea, which is illustrated in Fig. 1.11, is as follows: (i) remove the trajectory from the basin of attraction of the initial stable periodic orbit, (ii) apply the targeting procedure in the basin boundary to bring the trajectory to the neighborhood of the basin of attraction of the desired stable periodic orbit and finally (iii) bring the trajectory to the desired stable periodic orbit. We can accomplish this guidance task inside the basin of attraction of the stable periodic orbits (i) and (iii) by using a classical technique from the system control theory and outside the basins of attraction (in the chaotic invariant region) (ii) using the targeting procedure just described. This approach stresses the powerful tool that we developed by combining classical control techniques with chaos control methods.
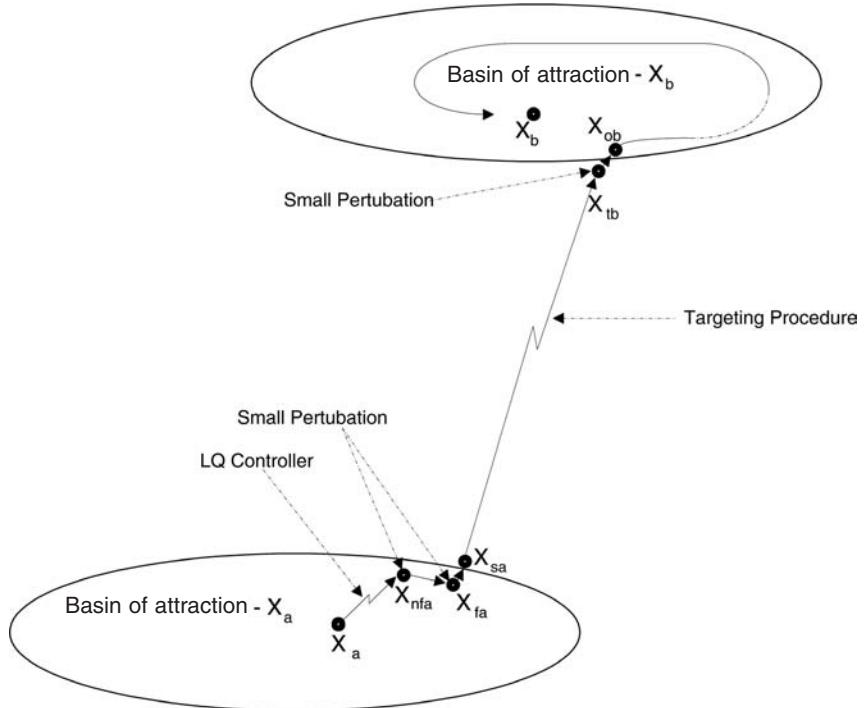
Fig. 1.11 Schematic representation of our complete targeting procedure. The system was evolving in a periodic orbit X_a. Our goal is to steer it to another periodic orbit X_b. The *LQ controller* drives the trajectory from X_a to a point X_{nfa} near X_{fa}. In X_{nfa} a small perturbation is applied, and the system moves to the state X_{fa}. Another perturbation is applied, and the system moves to the state X_{fa}. Our chaotic targeting procedure is then used to stir the system to X_{tb}. Another small perturbation drives the system to the point X_{ob}, that belongs to the basin of attraction of X_b. From this point, the system's natural dynamics drives the trajectory to the desired stable periodic orbit X_b.

To accomplish (i), we can use, for example, a classical optimal control method, such as the *LQ controller* [3]. As the basin of attraction of the stable periodic orbits is small open regions around the periodic orbits, it is possible to linearize the system about the points $\{x_i\}_{i=1}^{n_p}$ of the orbit, which gives

$$z_{k+1} = A(x_i)z_k, \tag{1.27}$$

where $A(x_i)$ is $Df(x_i)$. To change the state of the system, it is necessary to introduce an input term to Eq. (1.27) as

$$z_{k+1} = Az_k + Bu_k, \tag{1.28}$$

where u_k is the vector of inputs and B is a constant matrix that states how the inputs influence the state of the system. The objective is to pick u_k so that the "cost function"
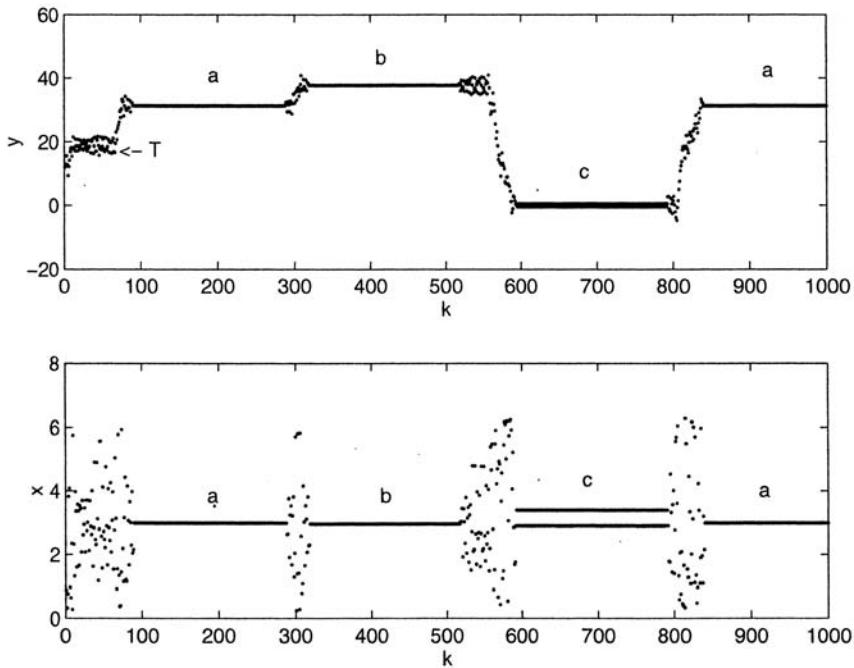
Fig. 1.12 Results of applying our combined method of control to change the system evolution among stable periodic orbits. The *y* variable represents the angular velocity, *x* represents the phase, and *k* represents the iteration number. In both graphs, all quantities plotted are dimensionless.

$$J = 1/2 \sum_{k=0,N} (z_k^t Q_1 z_k + u_k^t Q_2 u_k) \qquad (1.29)$$

is minimized. Q_1 and Q_2 are symmetric and positive definite weighting matrices to be selected based on the relative importance of the various states and controls. The well-known solution technique can now be applied (see [3]).

As our targeting procedure, applied in (ii), is able to drive the trajectory to the neighborhood of the basin of attraction of the desired stable periodic orbit, just a small perturbation can be used to send the orbit from that point to the interior of the basin of attraction. Once there, the system dynamics is enough to drive the trajectory to the desired stable periodic orbit. Thus, (iii) can be easily accomplished. However, another control system technique could be applied, if desired.

In Fig. 1.12 we show the results of applying that combined method to change the system evolution among the desired stable periodic orbits. When our targeting method is applied, the perturbations that are necessary to create the pseu-

do-orbit and send the orbits to the interior of the basin of attraction of the stable periodic orbits are less than 0.1.

1.5
Conclusion

In 1990, the concept of controlling chaos came about showing that not only the chaotic evolution could be controlled, but also the complexity inherent on the chaotic dynamics could be exploited to provide a unique level of flexibility and efficiency in technological uses of chaotic systems. Over the years, we have witnessed a variety of applications for this concept in almost all areas of knowledge. In parallel, new methods appear, each one tailored to specific situations or trying to improve previously released control of chaos methods. Despite this tremendous development and research, the fundamental ideas embedded in this concept must be kept in focus. With this chapter, we envisage not only the assessment of those fundamental ideas but also to point out paths to be followed in future development. As so, we summarize it with the following:

- Controlling of chaos is based on small perturbations applied to sensitive systems in order to opportunistically exploit its dynamics. It is based on the flexibility that such a system can provide. Feedback strategies may be used, but just locally to a particular trajectory.
- Controlling of chaos can be applied wherever chaos is present. This means that its application is not only restricted to attracting sets, but can also be used in nonattracting ones, situations in which we can produce interesting results.
- Control of chaos strategies can be combined with classic control strategies to convey powerful, opportunistic, and efficient control mechanisms that exploit the limits of flexibility that the system can provide.

References

1 F. T. Arecchi, R. Meucci, G. Puccioni, and J. Tredicce. Experimental evidence of subharmonic bifurcations, multistability, and turbulence in a q-switched gas laser. *Phys. Rev. Lett.*, 49:1217–1220, 1982.

2 D. K. Arrowsmith and C. M. Place. *An Introduction to Dynamical Systems*. Cambridge University Press, 1990.

3 K. J. Aström and B. Wittenmark. *Computer Controlled System: Theory and Design*. Prentice-Hall, Englewood Cliffs, NJ, 1984.

4 A. Azevedo and S. M. Rezende. Controlling chaos in spin-wave instabilities. *Phys. Rev. Lett.*, 66:1342–1345, 1991.

5 G. L. Baker. Control of the chaotic driven pendulum. *Am. J. Phys.*, 63(9):832–838, 1995.

6 E. Barreto, E. J. Kostelich, C. Grebogi, E. Ott, and J. A. Yorke. Efficient switching between controlled unstable orbits in higher dimensional chaotic systems. *Phys. Rev. E,* 51:4169–4172, 1995.

7 E. Belbruno, *Capture and Chaotic Motions in Celestial Mechanics: with Applications to the Construction of Low Energy Transfer.* Princeton University Press, 2004.

8 S. Bielawski, D. Derozier, and P. Glorieux. Controlling unstable periodic orbits by a delayed continuous feedback. *Phys. Rev. E,* 49:971–974, 1994.

9 S. Bleher, C. Grebogi, and E. Ott. Bifurcation to chaotic scattering. *Physica D,* 46:87–121, 1990.

10 E. M. Bollt and J. D. Meiss. Controlling chaotic transport through recurrence. *Physica D,* 81:280–294, 1995.

11 E. M. Bollt and J. D. Meiss. Targeting chaotic orbits to the moon through recurrence. *Phys. Rev. A,* 204:373–378, 1995.

12 B. V. Chirikov. A universal instability of many-dimensional oscillator systems. *Phys. Rep.,* 52:265–379, 1979.

13 D. L. DeAngelis, W. M. Post, and C. C. Travis. *Positive Feedback in Natural Systems.* Springer, Berlin, 1986.

14 R. Devaney. *An Introduction to Chaotic Dynamical Systems.* Persus Books, Cambridge, MA, 1989.

15 W. L. Ditto, S. N. Tauseo, and M. L. Spano. Experimental control of chaos. *Phys. Rev. Lett.,* 65:3211–3214, 1990.

16 U. Feudel, C. Grebogi, B. Hunt, and J. A. Yorke. Map with more than 100 coexisting low-periodic attractors. *Phys. Rev. E,* 54:71–81, 1996.

17 A. Garfinkel, M. L. Spano, W. L. Ditto, and J. N. Weiss.Controlling cardiac chaos. *Science,* 257:1230–1233, 1992.

18 J. L. Gouze. Positive and negative circuits in dynamical systems. *J. Biol. Systems,* 6:11–15, 1998.

19 P. E. Gray and C. L. Searle. *Princípios de Eletrônica.* Livros Técnicos and Científicos Ed. S.A, 1977.

20 C. Grebogi, E. Kostelich, E. Ott, and J. A. Yorke. Multi-dimensioned interwined basin boundaries: Basin structure of the kicked double rotor. *Physica D,* 25:347–360, 1987.

21 C. Grebogi and Lai. Controlling chaotic dynamical systems. *Syst. Control Lett.,* 31:307–312, 1997.

22 C. Grebogi, Y. C. Lai, and S. Hayes. Control and applications of chaos. *J. Franklin Inst.,* 334B:1115–1146, 1997.

23 C. Grebogi, E. H. Nusse, E. Ott, and J. A. Yorke. Basic sets: Sets that determine the dimensions of basin boundaries. In J. C. Alexander, editor, *Lecture Notes in Mathematics,* vol. 1342, pp. 220–250. Springer, Berlin, 1988.

24 C. Grebogi, E. Ott, and J. A. Yorke. Crises, sudden changes in chaotic attractors, and transient chaos. *Physica D,* 7:181–200, 1983.

25 J. Guckenheimer and P. Holmes. *Nonlinear Oscilations, Dynamical Systems, and Bifurcations of Vector Fields.* Springer, Berlin, 1983.

26 S. Hayes, C. Grebogi, and E. Ott. Communicating with chaos. *Phys. Rev. Lett.,* 70:3031, 1993.

27 G. H. Hsu, E. Ott, and C. Grebogi. Strange saddles and the dimensions of their invariant manifold. *Phys. Lett. A,* 127(4):199–204, 1988.

28 H. Kantz and P. Grassberger. Repellers, semi-attractors, and long-lived chaotic transients. *Physica D,* 17:75–86, 1985.

29 E. J. Kostelich, C. Grebogi, E. Ott, and J. A. Yorke. Higher-dimensional targeting. *Phys. Rev. E,* 47:305–310, 1995.

30 E. E. N. Macau. Targeting in chaotic scattering. *Phys. Rev. E,* 57:5337–5346, 1998.

31 E. E. N. Macau and C. Grebogi. Driving trajectories in complex systems. *Phys. Rev. E,* 59:4062–4069, 1999.

32 E. E. N. Macau. Using chaos to guide a spacecraft to the moon. *Acta Astronautica,* 47:871–878, 2000.

33 E. E. N. Macau. Exploiting unstable periodic orbits of a chaotic invariant set for spacecraft control. *Celes. Mech. Dyn. Sys.,* 87:291–305, 2003.

34 E. E. N. Macau and C. Grebogi. Driving trajectories in chaotic systems. *Int. J. Bifurcat. Chaos,* 11:1423–1442, 2001.

35 K. S. McCann. The diversity-stability debate. *Nature,* 405:228–233, 2000.

36 J. D. Meiss, J. R. Lary, J. D. Crawford, C. Grebogi, A. N. Kaufway, and H. D. I. Abrabanel. Correlations of periodic, area-preserving maps. *Physica D,* 6:375–384, 1983.

37 R. Meucci, W. Gadomski, M. Ciofini, and F. T. Arecchi. Experimental control of chaos by means of weak parametric perturbations. *Phys. Rev. E,* 49:2528–2531, 1994.

38 E. Ott, C. Grebogi, and J. A. Yorke. Controlling chaotic dynamical systems. In D. Campbell, editor, *CHAOS/XAOC, Soviet-Amer. Perspective on Nonlinear Science,* pp. 153–172. Amer. Inst. Phys., 1990.

39 E. Ott, C. Grebogi, and J. A. Yorke. Controlling chaos. *Phys. Rev. Letts.*, 64(11): 1196–1199, 1990.

40 J. F. Pierce. *Dispositivos de Junção Semicondutores*. Ed. USP, 1972.

41 S. J. Schiff, K. Jerger, D. H. Duong, T. Chang, M. L. Spano, and W. L. Ditto. Controlling chaos in brain. *Nature*, 370:615–620, 1994.

42 G. Schmidt. Stochasticity and fixed-point transitions. *Phys. Rev. A,* 22:2849–2854.

43 G. Schmidt and B. W. Wang. Dissipative standard map. *Phys. Rev. A,* 32:2994–2999, 1985.

44 T. Shinbrot, W. Ditto, C. Grebogi, E. Ott, M. Spano, and J. A. Yorke. Using the sensitive dependence of chaos (the "butterfly effect") to direct trajectories in an experimental chaotic system. *Phys. Rev. Lett.,* 68:2863–2866, 1992.

45 T. Shinbrot, E. Ott, C. Grebogi, and J. A. Yorke. Using chaos to direct trajectories to targets. *Phys. Rev. Lett.*, 65:3215–3218, 1990.

46 T. Shinbrot, E. Ott, C. Grebogi, and J. A. Yorke. Using chaos to direct orbits to targets in systems describable by a one-dimensional map. *Phys. Rev. A*, 45:4165–4168, 1992.

47 E. Slotine and W. Li. *Applied Nonlinear Control.* Prentice-Hall, Englewood Cliffs, NJ, 1991.

48 S. Smale. Differentiable dynamical systems. *Bull. Amer. Math. Soc.*, 73:747–817, 1967.

49 R. Thomas and R. D'Ari. *Biological Feedback*. CRC Press, Boca Raton, FL, 1990.

2
Time-Delay Control for Discrete Maps

Joshua E. S. Socolar

This chapter is intended as a pedagogical introduction to discrete time delayed feedback methods. It is neither a comprehensive review, nor a presentation of dramatic new results. It does, on the other hand, organize known results in a self-contained manner that emphasizes the conceptual points that have proven to be important, where much of the original literature focuses on historically important points and rigorous mathematical proofs. The present work also contains examples and one generalization that have not appeared elsewhere. The goal is to provide a conceptual foundation for readers who wonder whether discrete time delay feedback methods are up to the task they have in mind. Since the study of discrete methods foreshadows many (but not all!) of the important questions that arise in studies of continuous versions of delayed feedback control, the present chapter may also serve as a useful prequel to chapters on continuous methods.

2.1
Overview: Why Study Discrete Maps?

When chaotic oscillations degrade the performance of a natural or engineered system, control strategies are often aimed at creating stable, periodic behavior. If it is important to alter the intrinsic dynamics of the system as little as possible, either because those dynamics are the object of study or because the energy available for control is limited, the possibility of stabilizing an unstable periodic orbit (UPO) embedded in the chaotic dynamics becomes highly attractive. A conceptually simple scheme for accomplishing this is to continuously monitor a system variable and adjust an available parameter with the goal of making the system do the same thing in the present that it was doing one period in the past [1]. In principle, all one needs to know is the period of the UPO. One can then inject a feedback signal proportional to the measured difference between current and past values of a system variable. For some range of feedback gains, the UPO will be a stable orbit of the compound system with feedback. And

when the system is on this orbit, the feedback signal will vanish – the observed behavior will be an embedded periodic orbit intrinsic to the uncontrolled system and the power dissipated in the feedback loop will become arbitrarily small.

The comparison of a current measurement to a measurement made some appreciable time in the past in order to generate a control signal is termed "time delayed feedback" (TDF). TDF can often be easier to implement than control schemes that rely on detailed knowledge of the desired orbit and/or significant amounts of computation to determine the feedback signal. Its principal benefit is that the controller does not require prior knowledge of the values of the system variables in the UPO – there is no need to measure the distance of the system from the UPO itself. The simplification comes with a cost, however: the introduction of a time delay into the system can give rise to unanticipated instabilities. Much work has been done to elucidate the nature of these instabilities and develop analytical methods for determining feedback parameter choices that will do the desired job, most often for delay times chosen to coincide with the period of the desired UPO. (See chapters by the authors Just, Pyragas, Clausen, Parlitz, Janson, Masoller, Schöll, Illing, Wünsche, Christini, Schuster, and Hikihara of this volume.)

Discrete-time systems described by maps rather than differential equations provide a platform for gaining fundamental analytical insights into time delay control methods. Though certain subtleties inherent in continuous control schemes, such as latency effects [2–4] or infinite sets of perturbation modes and associated Floquet multipliers [5, 6], are not captured in the discrete map models, the trends discovered through analysis of discrete maps are a good starting point for developing intuition about the behavior of continuous systems. Moreover, in systems with sufficiently slow dynamics, the schemes for controlling discrete maps may be directly implemented. An interesting example is the control of cardiac alternans, where the control signal is constructed from measurements of the duration of the action potential (the time required for the transmembrane voltage to drop below a threshold value after an activating stimulus is applied) [7, 8]. In that case, one works directly with the empirically observed map rather than constructing it from underlying differential equations.

The TDF controllers studied to date generate a feedback signal that is linearly proportional to a measured difference between current and past values. The analysis of variations about the desired behavior in the controlled system therefore involves only linear stability analysis. The time delay introduces a complication, however, that can lead to nontrivial constraints on the types of UPOs that can be stabilized by a given feedback scheme. We show below that almost all of these constraints can be overcome in principle, so that almost any orbit that can be stabilized using standard methods of proportional control based on a discrete-map description can also be stabilized using TDF.

An important question about any control scheme is how sensitive it is to noise in the system. This question can be addressed analytically in the context of discrete maps. We show below one way of estimating the noise level that a TDF controller can tolerate.

2.2
Theme and Variations

The simplest system one might wish to control is an unstable fixed point of a single-variable map. The map may represent the piercings of a Poincaré section of a two-variable continuous system subject to periodic driving, for example, with the section defined by the phase of the drive and the value of one of the variables. The periodic drive ensures that the time delay between piercings of the Poincaré section is always the same. (For subtleties associated with more general Poincaré sections, see Chapter 6 by Claussen of this volume.) Let the dynamics of the remaining system variable y be governed by a map

$$y_{t+1} = f(y_t; \kappa_t), \tag{2.1}$$

where the integer index t represents time and the real number κ is the value of a system parameter that can be altered by an external signal. We assume that $f(y; \kappa_0)$ has a fixed point y^*.

Control of y^* is to be attempted by constructing a feedback signal that adjusts κ based on the difference between the current and past values of y. The simplest approach is to let

$$\kappa_t = \kappa_0 + \gamma \left(y_t - y_{t-1} \right), \tag{2.2}$$

where γ is a (real) constant of proportionality [9]. A complete analysis of this elementary system reveals many of the key features of TDF. After describing these, we will turn to extensions involving recursive use of past values of x and generalizations to many dimensions.

The general form of TDF considered here may be written as follows:

$$\mathbf{y}_{t+1} = \mathbf{f}(\mathbf{y}_t; \, \boldsymbol{\kappa}_0 + \hat{\mathbf{B}}_0 \hat{\mathbf{G}} \cdot \mathbf{u}_t) \tag{2.3}$$

$$\mathbf{u}_t = \sum_{s=0}^{\infty} \hat{\mathbf{R}}^s \cdot (\mathbf{y}_{t-s} - \mathbf{y}_{t-s-1}). \tag{2.4}$$

Here lowercase boldface quantities are ℓ-dimensional vectors; uppercase boldface indicates a vector with k elements, where k is the number of parameters accessible for control; and a hat indicates a matrix quantity. $\mathbf{f}(\mathbf{y}_t)$ is the uncontrolled map; $\mathbf{u}_t$ is the control signal; $\boldsymbol{\kappa}_0$ is the vector of nominal values of the adjustable parameters; $\hat{\mathbf{B}}_0$ is an $\ell \times k$ matrix that specifies the coupling of the control signal to the adjustable parameters; and $\hat{\mathbf{G}}$ and $\hat{\mathbf{R}}$ are matrices we are free to choose in order to transform the measured variables into one or more nonzero control signals. Equations (2.1) and (2.2) are the special case $\ell = k = 1$ and $\hat{\mathbf{R}} = 0$.

Equation (2.3) does not cover all possible strategies for including information from many past iterates of the map. One could, for example, average signals collected from some fixed number of past iterates [9, 10]. The method of

Eq. (2.3) is sufficiently general, however, to allow stabilization of any fixed point that can be controlled by the proportional control techniques described in control theory textbooks [11]. The infinite series appearing here is less of a problem than one might first imagine. It can easily be implemented experimentally using a recursive scheme that requires only a single delay element [12–14].

2.2.1
Rudimentary Time-Delay Feedback

For the simplest case, the success of a proposed controller is determined by linear stability analysis of Eqs. (2.1) and (2.2). We make the following definitions:

$$x_t \equiv \gamma_t - \gamma^*; \quad u_t \equiv \gamma_t - \gamma_{t-1}, \quad v \equiv \left.\frac{df}{d\gamma}\right|_{\gamma=\gamma^*}, \quad \beta \equiv \gamma\left.\frac{\partial f}{\partial \kappa}\right|_{\kappa=\kappa_0}. \tag{2.5}$$

The $\partial f/\partial \kappa$ term in the definition of β characterizes the sensitivity of the dynamics to changes in κ. One must be careful to clearly define what is meant by κ. For example, suppose a parameter k appears in the differential equations that define the dynamics. The discrete (map-based) controller may function, for example, by adjusting the value of k smoothly up and down during the time interval between measurements of x_t, or by rapidly adjusting it at some time during that interval and holding it fixed until the next adjustment is made. The value of β then is not simply determined by $\partial f/\partial k$. In the former case, κ would be the amplitude of the modulation of k; in the latter, β would depend on the time chosen for switching as well as the size of the adjustment of k.

In the vicinity of γ^*, Eqs. (2.1) and (2.2) then take the form

$$x_{t+1} = vx_t + \beta u_t \quad u_t = x_t - x_{t-1}, \tag{2.6}$$

or

$$\begin{pmatrix} x_{t+1} \\ u_{t+1} \end{pmatrix} = \begin{pmatrix} v & \beta \\ v-1 & \beta \end{pmatrix} \begin{pmatrix} x_t \\ u_t \end{pmatrix}. \tag{2.7}$$

Straightforward eigenvalue analysis leads to the picture shown in Fig. 2.1. Stable operation of the system occurs if both eigenvalues μ_1 and μ_2 of the matrix in Eq. (2.7) have magnitudes less than unity. We will refer to the eigenvalues as *Floquet multipliers* to emphasize their relation to the underlying continuous dynamical system. If the largest value of $|\mu|$ is greater than unity, control will be unsuccessful.

Several points are worth noting. First, this basic scheme, sometimes referred to as "time delay autosynchronization" (TDAS), cannot stabilize unstable fixed points with $v > 1$ or $v < -3$. Since the system is stable when $|v| < 1$ even with for $\beta = 0$ (no control), TDAS is useful only for $-3 < v < -1$. The $v > -3$ constraint can be lifted using the technique described in Section 2.2.2. Control of a
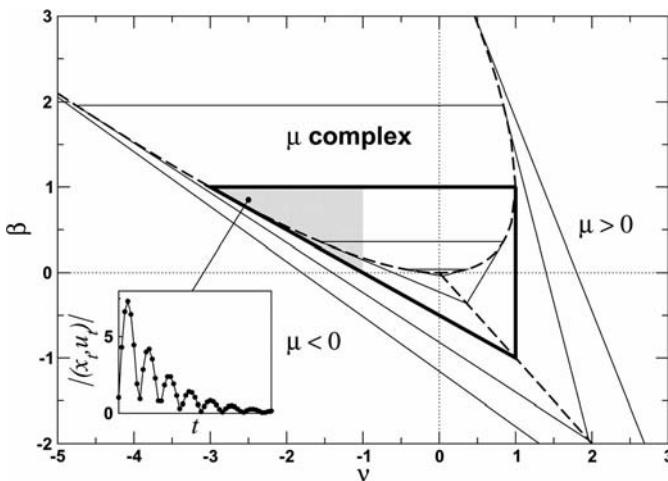
Fig. 2.1 Stability diagram for the rudimentary TDF scheme. Triangles are contours representing constant values of $|\mu|$, the largest Floquet multiplier of the controlled system. The thick triangle corresponds to $|\mu| = 1$; systems in its interior converge to the fixed point. The thick dashed lines separate regions of qualitatively different types of instability or convergence. The shaded region is where control is useful. Inset: transient growth followed by convergence to the fixed point for successful control corresponding to the labeled point in the gray region.

fixed point that has a positive Floquet multiplier greater than unity requires the use of higher dimensional schemes, as shown in Section 2.2.3.

Second, the nature of the instability that occurs as parameters are varied across the stability boundary depends on which boundary is crossed. (We assume that the full system includes a quadratic nonlinearity at the fixed point.) For fixed v, increasing β generates a Hopf bifurcation, with μ_1 and μ_2 becoming complex conjugates before the instability occurs. Decreasing β leads to a period-doubling instability. A drift in the system parameter v to positive values greater than unity while β remains fixed leads to a monotonic instability (no oscillations).

Third, the contours near the period-doubling boundary vary much more rapidly than those near the Hopf boundary. The system will generally be less sensitive to parameter drift for larger values of β in the domain of control.

Finally, due to the non-normality of eigenvectors and nondegeneracy of eigenvalues of the mapping matrix, convergence to the fixed point from a randomly selected initial condition need not be monotonic. There can be a large transient that moves the system farther from the fixed point before convergence sets in. This is illustrated the inset, where the distance from the fixed point is plotted for a trajectory beginning at $(x_0, u_0) = (1,0)$ for $v = -2.5$ and $\beta = 0.85$. This type of transient growth plays an important role in determining how much noise the controlled system can tolerate (see Section 2.3).

2.2.2
Extending the Domain of Control

In order to extend the utility of TDF to stronger instabilities in a practical manner (and without resorting to standard feedback schemes that rely on knowledge of the fixed point), values of the system variable from further in the past can be incorporated into the feedback signal. The simplest way to do this, from both an analytical and experimental perspective, is to replace Eq. (2.6) with

$$x_{t+1} = vx_t + \beta u_t; \quad u_t = \sum_{s=0}^{\infty} R^s \cdot (x_{t-s} - x_{t-s-1}), \tag{2.8}$$

where R is a real parameter we are free to choose. An advantage of this scheme over other methods of incorporating past values of x is that the sum can be formed recursively by rewriting u_t as

$$u_t = x_t - x_{t-1} + R\,u_{t-1}. \tag{2.9}$$

The stability analysis of this system is then quite similar to the above analysis of TDAS. The linearization about the fixed point now reads

$$\begin{pmatrix} x_{t+1} \\ u_{t+1} \end{pmatrix} = \begin{pmatrix} v & \beta \\ v-1 & \beta+R \end{pmatrix} \begin{pmatrix} x_t \\ u_t \end{pmatrix}. \tag{2.10}$$

Writing expressions for the Floquet multipliers of this map, one can see that they are related to the TDAS Floquet multipliers above by the parameter transformation

$$v \to \frac{v-R}{1-R}, \quad \beta \to \beta - R\frac{v-R}{1-R}. \tag{2.11}$$

Thus Fig. 2.7 simply gets sheared for nonzero R, as shown in Fig. 2.2, where we display the cases $R < 1$ and $R > 1$ separately so that v is always increasing to the right.

The notable features of these pictures are the extensions of the domain of control to arbitrary values of v. Values of R just below 1 allow control of arbitrarily strong oscillatory instabilities (large, negative values of v). Values of R just above 1 allow control of arbitrarily strong monotonic instabilities ($v > 0$).

The latter possibility may be counter-intuitive because $R > 1$ leads to increasingly large weighting of past deviations, which would seem to imply larger and larger feedback signals. The analysis shows, however, that the system arranges for cancellation of these large effects and x and u do both converge to zero [15].

There is one special case where ETDAS is likely to fail, as would any TDF method that does not refer explicitly to the fixed point value of a system variable: the case $v = 1$, which corresponds to a *stationary mode*. The linearized sys-
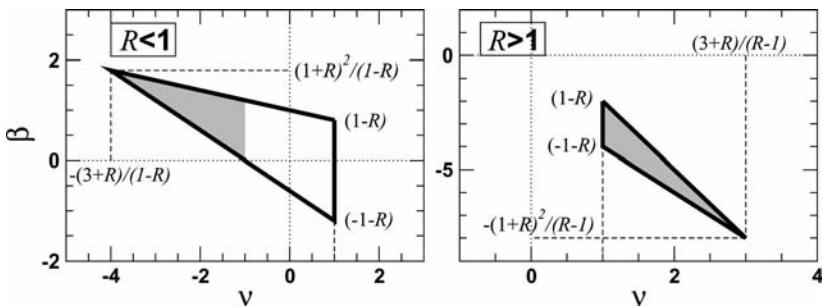
Fig. 2.2 Stability diagram for the extended scheme. The system is stable in the interior of the triangle. The shaded area indicates the regime where control is necessary for stability.

tem in this case has a continuum of fixed points, and TDF cannot choose between them. That is, if the system begins at some distance from the desired fixed point, it will return to the initial point and therefore will always produce $u = 0$. The stability of the full (nonlinear) system will then depend upon the nature of the nonlinearity near the fixed point. A nonlinear stability analysis of maps controlled by TDF has not yet been carried out. Experience with high-dimensional systems, however, shows that marginal Floquet multipliers tend to destabilize controlled systems in the presence of noise (see below).

The use of nonzero R, referred to as "extended TDAS" (ETDAS) allows for stabilization of any fixed point (with no stationary mode) of a one-dimensional map. Direct implementation of this conceptual scheme requires sample-and-hold hardware that is triggered upon detection of passage through a Poincaré section, but does *not* require holding any signal for more than one period of the desired UPO.

The performance of discrete ETDAS is illustrated in Fig. 2.3 for the Rössler system. The system equations are

$$\dot{x} = -y - z + \eta_x, \tag{2.12}$$
$$\dot{y} = x + c_1 y + \eta_y, \tag{2.13}$$
$$\dot{z} = \kappa - z(x - c_2) + \eta_z, \tag{2.14}$$

where c_1 and c_2 are constants, κ is the parameter assumed to be available for control, and η_i is a bounded noise term. More precisely, we introduce the noise through an additive term in a simple Euler integrator:

$$x(t + \delta) = x - (y - z + \varepsilon_x)\delta, \tag{2.15}$$
$$y(t + \delta) = y + (x + c_1 y + \varepsilon_y)\delta, \tag{2.16}$$
$$z(t + \delta) = z + (\kappa - z(x - c_2) + \varepsilon_z)\delta, \tag{2.17}$$
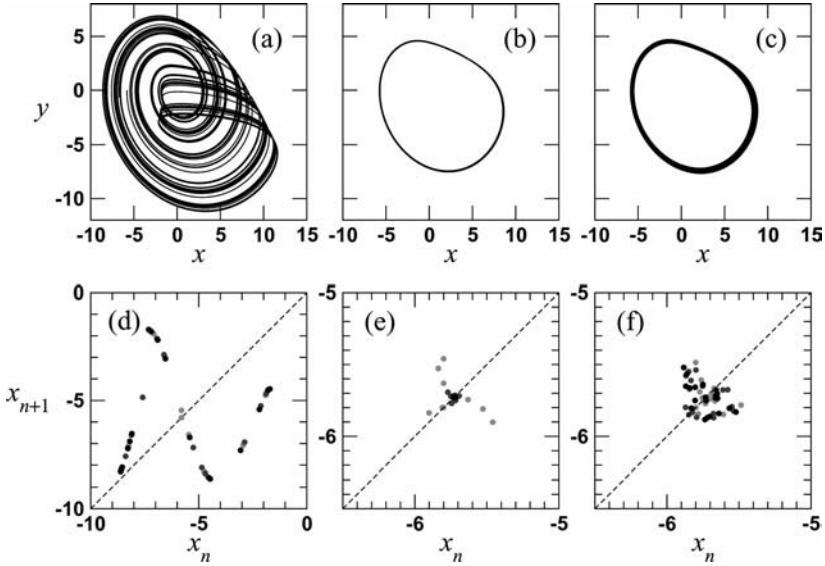
Fig. 2.3 ETDAS stabilization of the Rössler oscillator. (a) The uncontrolled system, with zero noise. (b) The controlled system, with zero noise. (c) The controlled system, with noise. (d), (e), (f) show return maps for x constructed from the trajectories of (a), (b), (c), respectively. Lighter dots indicate earlier times. Note the different scales.

where ε_i is a random number drawn from a uniform distribution over the interval $[-\eta_{\max}, \eta_{\max}]$.

We take the Poincaré section to be defined as the plane $y = 0$ and consider the piercings with $\dot{y} < 0$ and defining x_n as the value of x on the nth passage through the Poincaré section. The control signal is constructed as follows:

$$u_n = x_n - x_{n-1} + Ru_{n-1}; \tag{2.18}$$
$$\kappa = \kappa_0 + \gamma u_n \text{ for times between piercings } n \text{ and } n+1, \tag{2.19}$$

where γ and R are constants. The parameter values used for the figure are: $c_1 = 0.3$; $c_2 = 5$; $\kappa_0 = 0.3$; $\eta_{\max} = 0.1$; $\delta = 0.01$; $\gamma = 0.25$ (or 0 for no control); and $R = 0.5$.

From Fig. 2.3 (a), one can see that the fixed point is strongly unstable; the slope v of the return map at the fixed point is less than -3, which means that stabilization cannot be achieved with the simple $R = 0$ scheme. The middle panels show that there is a periodic orbit that is stabilized by ETDAS with $R = 0.5$. (Though not shown here, the feedback signal u does decay to zero.) The right panels show that the control is robust with respect to bounded noise. The points on the return map remain close to the fixed point and the orbit stays close to the periodic orbit of the middle panel.

2.2.3
High-Dimensional Systems

The previous two subsections introduced the basic idea of discrete TDF in the context of maps with a fixed point that has just one unstable direction. To stabilize systems consisting of many dynamical variables and periodic orbits with multiple unstable directions, we may need to monitor several system variables and provide feedback signals to several parameters. A theoretical investigation of a powerful way to do this was introduced by Yamamoto et al. [16]. Here we describe a generalization of ETDAS (called GETDAS) that, while technically representing a special case of the general method [17], has been shown to retain enough generality to cover almost all classically controllable fixed points [14].

Let $\mathbf{x}_t$ be an ℓ-dimensional vector of deviations of system variables from their fixed point values on the Poincaré section; let κ now represent k parameters that are accessible for adjustment; and let $\hat{\mathbf{A}}$ be the matrix that maps $\mathbf{x}_t$ to $\mathbf{x}_{t+1}$ in the uncontrolled system at κ_0. We assume that $\hat{\mathbf{A}}$ has full rank. Otherwise we could choose a smaller set of variables to describe the system near the fixed point.

The ETDAS parameter β is now best thought of as a product of two matrices: a factor $\hat{\mathbf{G}}$ that we are free to adjust and a factor $\hat{\mathbf{B}}$ that contains the information about which k parameters are adjustable and how small changes in them affect the map. ($\hat{\mathbf{G}}$ is the analog of γ in Eq. (2.2) and $\hat{\mathbf{B}}$ is the analog of $\partial f / \partial \kappa$ in Eq. (2.5). Note that the information in $\hat{\mathbf{B}}_0$ of Eq. (2.3) is included in $\hat{\mathbf{B}}$.)

For purposes of analysis, it is convenient to include $\hat{\mathbf{G}}$ in the definition of the control signal $\mathbf{u}$ so that the linearized version of Eq. (2.3) becomes

$$\mathbf{x}_{t+1} = \hat{\mathbf{A}} \cdot \mathbf{x}_t + \hat{\mathbf{B}} \cdot \mathbf{u}_t , \tag{2.20}$$

$$\mathbf{u}_t = \sum_{s=0}^{\infty} \hat{\mathbf{R}}^s \hat{\mathbf{G}} \cdot (\mathbf{x}_{t-s} - \mathbf{x}_{t-s-1}) \tag{2.21}$$

$$= \hat{\mathbf{G}} \cdot (\mathbf{x}_t - \mathbf{x}_{t-1}) + \hat{\mathbf{R}} \cdot \mathbf{u}_{t-1}. \tag{2.22}$$

A schematic diagram of a GETDAS controller is shown in Fig. 2.4. For implementation of the discrete controllers shown here, the output of $\hat{\mathbf{B}}$ is sampled once every period and the sampled value determines the feedback signal.

The design problem for such a controller is to choose $\hat{\mathbf{G}}$ and $\hat{\mathbf{R}}$ given $\hat{\mathbf{A}}$ and $\hat{\mathbf{B}}$. (We assume $\hat{\mathbf{A}}$ has full rank.) One convenient approach is to make use of well-known design methods for standard proportional control systems in which the feedback signal is determined by the difference between the current variable values and their fixed point values. When the fixed point values are available for reference, the (linearized) controlled system takes the form

$$\mathbf{x}_{t+1} = \hat{\mathbf{A}} \cdot \mathbf{x}_t + \hat{\mathbf{B}} \cdot \mathbf{u}_t , \tag{2.23}$$

$$\mathbf{u}_t = -\hat{\mathbf{K}} \cdot \mathbf{x}_t , \tag{2.24}$$
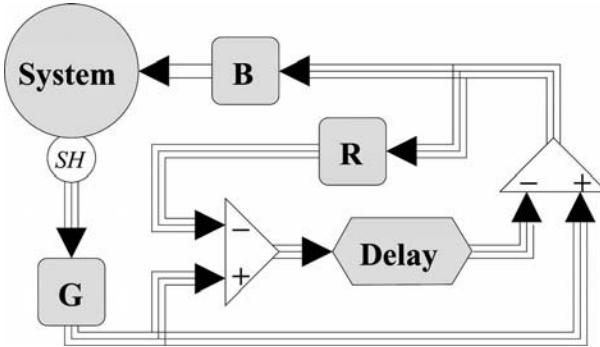
Fig. 2.4 Schematic circuit diagram for implementing GETDAS to control a dynamical system. Triple lines indicate multiple signals that are fed into each element in the loop. The hexagon represents an element whose only effect is a time delay of all incoming signals. Triangles represent devices that form the difference of each pair of incoming signals. Each labeled square represents a device that performs a linear transformation on its inputs. The square labeled **B** may be considered as a part of the system that cannot be changed and may have fewer outputs than the full number of system variables. The circle labeled *SH* is a sample-and-hold element.

where $\hat{\mathbf{K}}$ is a matrix that can be chosen using techniques of discrete state optimal control theory if and only if $\hat{\mathbf{A}}$ and $\hat{\mathbf{B}}$ satisfy a controllability condition. (See [11] for a detailed discussion of controllability.)

Equations (2.20) and (2.23) can both be cast in the form

$$\begin{pmatrix} \mathbf{x} \\ \mathbf{u} \end{pmatrix}_{t+1} = \hat{\mathbf{Q}} \begin{pmatrix} \mathbf{x} \\ \mathbf{u} \end{pmatrix}_t, \tag{2.25}$$

where we have

$$\hat{\mathbf{Q}} \equiv \begin{pmatrix} \hat{\mathbf{A}} & \hat{\mathbf{B}} \\ \hat{\mathbf{G}}[\hat{\mathbf{A}} - \hat{\mathbf{I}}] & \hat{\mathbf{G}}\hat{\mathbf{B}} + \hat{\mathbf{R}} \end{pmatrix} \quad \text{or} \quad \begin{pmatrix} \hat{\mathbf{A}} & \hat{\mathbf{B}} \\ -\hat{\mathbf{K}}\hat{\mathbf{A}} & -\hat{\mathbf{K}}\hat{\mathbf{B}} \end{pmatrix}. \tag{2.26}$$

A comparison of these two forms immediately reveals that the GETDAS scheme has the same stability properties as the standard method if we choose

$$\hat{\mathbf{G}} = -\hat{\mathbf{K}}\left[\hat{\mathbf{A}} - \hat{\mathbf{I}}\right]^{-1}\hat{\mathbf{A}} \quad \text{and} \quad \hat{\mathbf{R}} = \hat{\mathbf{K}}\left[\hat{\mathbf{A}} - \hat{\mathbf{I}}\right]^{-1}\hat{\mathbf{B}}. \tag{2.27}$$

(Note that $\left[\hat{\mathbf{A}} - \hat{\mathbf{I}}\right]^{-1}\hat{\mathbf{A}} - \left[\hat{\mathbf{A}} - \hat{\mathbf{I}}\right]^{-1} = \hat{\mathbf{I}}$ and that $\left[\hat{\mathbf{A}} - \hat{\mathbf{I}}\right]^{-1}$ commutes with $\hat{\mathbf{A}}$.) This construction breaks down only if $[\hat{\mathbf{A}} - \hat{\mathbf{I}}]$ is singular, which occurs if and only if the system has one or more stationary mode, as may have been expected from the analysis of the one-dimensional version.

Assuming no stationary modes, every choice of $\hat{\mathbf{K}}$ can be mimicked by a choice of $\hat{\mathbf{G}}$ and $\hat{\mathbf{R}}$ [14]. According to Eq. (2.27), the matrices thus obtained satisfy the relation $\hat{\mathbf{R}} = -\hat{\mathbf{G}}\hat{\mathbf{A}}^{-1}\hat{\mathbf{B}}$. Any choice of $\hat{\mathbf{G}}$ and $\hat{\mathbf{R}}$ that do not satisfy this rela-

tion corresponds to GETDAS schemes that are not equivalent to any standard proportional controller. Yamamoto introduced a further generalization of TDF control in which a vector $\mathbf{w}$ of dynamical variables is added to the system as part of the control mechanism and the feedback signal is generated from it as follows [16]:

$$\mathbf{u}_t = \hat{\mathbf{G}}_1(\mathbf{x}_t - \mathbf{x}_{t-1}) + \hat{\mathbf{R}}_1\mathbf{w}_t, \tag{2.28}$$

$$\mathbf{w}_t = \hat{\mathbf{G}}_2(\mathbf{x}_{t-1} - \mathbf{x}_{t-2}) + \hat{\mathbf{R}}_2\mathbf{w}_{t-1}. \tag{2.29}$$

The method is called *dynamical delayed feedback control* (DDFC). Nakajima noted that GETDAS is a special case of DDFC in which $\hat{\mathbf{G}}_2 = \hat{\mathbf{I}}$ and $\hat{\mathbf{R}}_1 = \hat{\mathbf{G}}_1\hat{\mathbf{R}}_2$, with the GETDAS parameters being $\hat{\mathbf{G}} = \hat{\mathbf{G}}_1$ and $\hat{\mathbf{R}} = \hat{\mathbf{R}}_2$ [17]. The relations between the various TDF methods and the standard proportional controllers are summarized in Fig. 2.5.

To illustrate two points about GETDAS control, we study the fixed point of a two-dimensional system with two unstable Floquet multipliers. We consider two variables coupled symmetrically with parameter values set such that the fixed point of the coupled system has two unstable Floquet multipliers, and we assume that the parameter accessible for control affects only one of the maps. The behavior of the system near the fixed point is given by

$$\hat{\mathbf{A}} = \begin{pmatrix} v_1 & c \\ c & v_2 \end{pmatrix}; \quad \hat{\mathbf{B}} = \begin{pmatrix} 1 & 0 \\ 0 & 0 \end{pmatrix}. \tag{2.30}$$

Inspection of the eigenvalues of $\hat{\mathbf{A}} - \hat{\mathbf{K}}\hat{\mathbf{B}}$ (expressed in terms of arbitrary elements K_{ij}) reveals that the following choice drives the system to the fixed point in finite time (achieves deadbeat control):
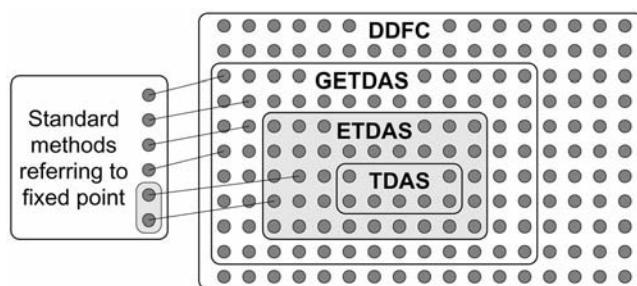
Fig. 2.5 Relations between time delay methods and standard proportional control methods. Each disk represents a choice of control parameters. Disks joined by lines generate identical $\hat{\mathbf{Q}}$ matrices and hence identical Floquet multipliers at the controlled fixed point. Shaded regions indicate one-dimensional maps.

$$\hat{\mathbf{K}} = \begin{pmatrix} v_1 + v_2 & (c^2 + v_2^2)/c \\ 0 & 0 \end{pmatrix}. \tag{2.31}$$

For purposes of illustration, we choose $\hat{\mathbf{K}}$ slightly different from this, so that control is still successful but the convergence rate is finite. Because the general expressions for $\hat{\mathbf{G}}$ and $\hat{\mathbf{R}}$ are rather long and unilluminating, we consider the specific case

$$v_1 = -2, \quad v_2 = 1.5, \quad c = 0.5, \quad \text{and} \quad \hat{\mathbf{K}} = \begin{pmatrix} 0.5 & 4.0 \\ 0 & 0 \end{pmatrix}. \tag{2.32}$$

With this choice, the uncontrolled system $\hat{\mathbf{A}}$ has two unstable Floquet multipliers $(-2.0700, 1.5700)$ and the (successfully) controlled system $\hat{\mathbf{Q}}$ has only stable Floquet multipliers $(\sqrt{1/2}, -\sqrt{1/2}, 0, 0)$. Equation (2.27) then tells us that a GETDAS controller with

$$\hat{\mathbf{G}} = \begin{pmatrix} -0.7857 & -10.7143 \\ 0 & 0 \end{pmatrix} \quad \text{and} \quad \hat{\mathbf{R}} = \begin{pmatrix} 1.2857 & 0 \\ 0 & 0 \end{pmatrix} \tag{2.33}$$

will stabilize the system, yielding the same convergence rate $-\mu = \sqrt{1/2} \approx 0.7071$. It is interesting to note, however, that the convergence rate can be improved without changing $\hat{\mathbf{R}}$. If we take, for example,

$$\hat{\mathbf{G}} = \begin{pmatrix} -0.4857 & -9.7143 \\ 0 & 0 \end{pmatrix}, \tag{2.34}$$

the Floquet multipliers become $(0.581952, -0.466233, 0.184281, 0)$. The largest μ has been reduced at the expense of increasing one of the zero multipliers by a small amount. In addition, the elements of $\hat{\mathbf{G}}$ have decreased in magnitude, which may be an advantage in some applications. This GETDAS scheme is not equivalent to any choice of $\hat{\mathbf{K}}$. For the system considered here, improving the convergence rate by choosing a different $\hat{\mathbf{K}}$ leads to larger matrix elements of $\hat{\mathbf{G}}$. Thus we see that there is a potential benefit to exploring GETDAS parameter choices that do not map directly onto a standard control scheme.

The above example is a case where the uncontrolled system has a single real, unstable Floquet multiplier. As may have been expected from the one-dimensional analysis, the required $\hat{\mathbf{R}}$ has an eigenvalue greater than unity.

Control of rings of many identical coupled maps have been studied in some detail using standard proportional control techniques [18, 19] and time delay methods [14]. In addition to being examples of control in higher dimensional systems, these studies emphasize the role that symmetries play in the design and robustness of the controllers.

2.3
Robustness of Time-Delay Stabilization

The effect of bounded, unbiased, and uncorrelated noise on the performance of a discrete controller of any of the types defined above can be calculated to linear order in the deviations from the fixed point. The purpose of such a calculation is to give a heuristic picture of the robustness of the controller. When a noise term $\mathbf{h}_t$ is added to the right-hand side of Eq. (2.20), the iterates of the map will form an elliptical cloud of points centered at the fixed point with axis lengths larger than the widths of the distributions of the components of $\mathbf{h}$, as observed in Fig. 2.3 (f). (Note that $\mathbf{h}$ is the noise in the discrete map presumably due to the microscopic noise η_i in the underlying differential equations but not easily calculated from it.) As the size of $\mathbf{h}$ is increased, the nonlinearity in the map will eventually lead to a discontinuous jump in the cloud to a size limited only by nonlinear saturation effects, signaling a loss of control. The noise level at which this happens can be estimated as follows.

In the linear system, the introduced noise $\mathbf{h}$ will be amplified by the system's dynamics [18, 19]. We assume that noise enters the system in the form of an independent random addition h_i to x_i on every time step, with h_i drawn from a bounded distribution with variance σ^2. Equation (2.20) becomes

$$\mathbf{x}_{t+1} = \hat{\mathbf{A}} \cdot \mathbf{x}_t + \hat{\mathbf{B}} \cdot \mathbf{u}_t + \mathbf{h}_t, \tag{2.35}$$

$$\mathbf{u}_t = \sum_{s=0}^{\infty} \hat{\mathbf{R}}^s \hat{\mathbf{G}} \cdot (\mathbf{x}_{t-s} - \mathbf{x}_{t-s-1}) \tag{2.36}$$

with

$$\langle (h_j)_t \rangle_a = 0 \; \forall \, j, t \tag{2.37}$$
$$\langle (h_i)_t (h_j)_{t'} \rangle_a = \sigma^2 \delta_{ij} \delta_{tt'}$$

Here the notation $\langle \, \rangle_a$ represents an ensemble average.

For notational convenience, we define $\bar{\mathbf{x}}$ to be the 2ℓ-dimensional vector $(\mathbf{x}, \mathbf{u})$ and $\bar{\mathbf{h}}$ to be $(\mathbf{h}, \hat{\mathbf{G}} \cdot \mathbf{h})$. In terms of $\hat{\mathbf{Q}}$ as defined in Eq. (2.25), Eq. (2.35) becomes

$$\bar{\mathbf{x}}_{t+1} = \hat{\mathbf{Q}} \cdot \bar{\mathbf{x}}_t + \bar{\mathbf{h}}_t . \tag{2.38}$$

Iterative substitution for $\bar{\mathbf{x}}$ on the right-hand side yields

$$\bar{\mathbf{x}}_{t+1} = \hat{\mathbf{Q}}^{n+1} \cdot \bar{\mathbf{x}}_{t-n} + \sum_{s=0}^{n} \hat{\mathbf{Q}}^s \bar{\mathbf{h}}_{t-s} . \tag{2.39}$$

In the $n \to \infty$ limit, the first term on the right-hand side vanishes because $\hat{\mathbf{G}}$ and $\hat{\mathbf{R}}$ have been chosen such that all eigenvalues of $\hat{\mathbf{Q}}$ have magnitude less than unity.

To estimate the size of the cloud of points around the fixed point, we calculate the average magnitude of $\bar{\mathbf{x}}_{t+1}$ over many realizations of the noise. Using Eq. (2.37) and the fact that the first ℓ components of $\bar{\mathbf{h}}$ are related to the last ℓ through $\hat{\mathbf{G}}$, one gets

$$\langle \bar{\mathbf{x}}_{t+1} \cdot \bar{\mathbf{x}}_{t+1} \rangle_a = \sum_{s=0}^{\infty} \mathrm{Tr}\left[(\hat{\mathbf{Q}}^{\top})^s \cdot \hat{\mathbf{Q}}^s \cdot \hat{\mathbf{H}} \right], \tag{2.40}$$

where $\hat{H}_{ij} \equiv \langle (\bar{h}_i)_t (\bar{h}_j)_t \rangle_a$, which can be evaluated using Eq. (2.37) and expressed as

$$\hat{\mathbf{H}} = \sigma^2 \begin{pmatrix} \hat{\mathbf{I}} & \hat{\mathbf{G}}^{\top} \\ \hat{\mathbf{G}} & \hat{\mathbf{G}} \cdot \hat{\mathbf{G}}^{\top}, \end{pmatrix} \tag{2.41}$$

where $\hat{\mathbf{I}}$ is the $\ell \times \ell$ identity matrix. In the case where $\hat{\mathbf{G}}$ and $\hat{\mathbf{R}}$ can be obtained from $\hat{\mathbf{K}}$ via Eq. (2.27), the algebra can be simplified [14]; and in the one-dimensional case where $\hat{\mathbf{G}}$ and $\hat{\mathbf{R}}$ are scalars, further simplification is possible; but here we retain the fully general expressions.

To carry out the infinite sum in Eq. (2.40), define $\bar{\mathbf{v}}^{(i)}$ and $\bar{\mathbf{e}}^{(i)}$ to be the left and right eigenvectors, respectively, of $\hat{\mathbf{Q}}$ corresponding to the eigenvalue μ_i and normalized such that $\bar{\mathbf{v}}^{(i)} \cdot \bar{\mathbf{e}}^{(j)} = \delta_{ij}$. Using

$$\left[(\hat{\mathbf{Q}}^{\top})^s \cdot \hat{\mathbf{Q}}^s \right]_{pq} = \sum_{i,j=1}^{2\ell} \left(\mu_i \mu_j \right)^s \left(\bar{\mathbf{e}}^{(i)} \cdot \bar{\mathbf{e}}^{(j)} \right) \left(\bar{v}_p^{(j)} \bar{v}_q^{(i)} \right) \tag{2.42}$$

and performing the sum over s, we get

$$\langle \bar{\mathbf{x}}_{t+1} \cdot \bar{\mathbf{x}}_{t+1} \rangle = \sum_{i,j=1}^{2\ell} \frac{\left(\bar{\mathbf{e}}^{(i)} \cdot \bar{\mathbf{e}}^{(j)} \right) \left(\bar{\mathbf{v}}^{(j)} \cdot \hat{\mathbf{H}} \cdot \bar{\mathbf{v}}^{(i)} \right)}{1 - \mu_i \mu_j}, \tag{2.43}$$

which can be evaluated numerically given $\hat{\mathbf{A}}$, $\hat{\mathbf{B}}$, $\hat{\mathbf{G}}$, $\hat{\mathbf{R}}$, and hence $\hat{\mathbf{Q}}$ and $\hat{\mathbf{H}}$. From this expression, we see again that a stationary mode ($\mu = 1$) will cause trouble. We also see that a pair of complex marginally stable modes ($|\mu| = 1$) may cause trouble if the numerator associated with them does not vanish.

We define the (linear) noise amplification factor γ as the ratio of the standard deviation of the distribution of states around the fixed point in the controlled system to the standard deviation of the intrinsic noise:

$$\gamma \equiv \sqrt{\frac{\langle \bar{\mathbf{x}}_{t+1} \cdot \bar{\mathbf{x}}_{t+1} \rangle_a}{2\ell}}. \tag{2.44}$$

The denominator used here implies an admittedly rough assumption that the cloud of points around the fixed point is spherical. We are seeking here only an order-of-magnitude estimate.

In a nonlinear system, the standard deviation of the cloud around the fixed point is roughly $\gamma\sigma$ for very small σ, but increases rapidly as σ crosses some threshold $\sigma_{\max}$. (An illustration of this behavior can be found in [14].) To estimate $\sigma_{\max}$, we make the rough assumption that nonlinearities introduce uncorrelated errors and treat them as an additional source of noise with standard deviation σ_{nonlin}. The total standard deviation Δ from the fixed point, averaged over the 2ℓ components of $\bar{\mathbf{x}}$, is then

$$\Delta = \gamma\sqrt{\sigma^2 + \sigma_{\mathrm{nonlin}}^2}\,. \tag{2.45}$$

Assuming that the quadratic nonlinearity does not vanish, we expect σ_{nonlin} to be roughly the size of the nonlinear contribution near the fixed point: $\sigma_{\mathrm{nonlin}} \approx f''\Delta^2/2$, where f'' is ℓ times the average magnitude of the coefficient of $x_i x_j$ in the expansion of the map about the fixed point. The threshold is then determined by a self-consistency condition on Δ:

$$\Delta = \gamma\sqrt{\sigma^2 + \frac{1}{4}f''\Delta^4}\,. \tag{2.46}$$

A real solution for Δ exists if and only if

$$\sigma < \sigma_{\max} = \frac{1}{\gamma^2 f''}\,. \tag{2.47}$$

As a test of this formula, consider the effect of adding a quadratic term to numerical example of GETDAS described above. We take the system to be the nonlinear map

$$\mathbf{x}_{t+1} = \hat{\mathbf{A}}\cdot\mathbf{x}_t + \hat{\mathbf{B}}\cdot\mathbf{u}_t + 2f''(x_1^2, x_2^2) + \mathbf{h}_t, \tag{2.48}$$

$$\mathbf{u}_t = \sum_{s=0}^{\infty}\hat{\mathbf{R}}^s\hat{\mathbf{G}}\cdot(\mathbf{x}_{t-s} - \mathbf{x}_{t-s-1}) \tag{2.49}$$

with $f'' = 1$ and other parameters specified by Eqs. (2.32)–(2.34). Evaluating γ and $\sigma_{\max}$ according to the above formulas, we find $\gamma = 12.6$ and predict that loss of control should occur for $\sigma \gtrsim 0.006$. Direct iteration of the controlled map shows that the standard deviation in $\bar{\mathbf{x}}\cdot\bar{\mathbf{x}}$ is exactly $\gamma\sigma$ for $\sigma \ll 0.006$, grows slightly faster than linearly with σ for $\sigma \sim 0.006$, and abruptly diverges at $\sigma \approx 0.009$. Example calculations of $\sigma_{\max}$ and detailed comparisons to numerical simulations for a higher dimensional system of coupled maps may be found in [14].

2.4
Summary

Discrete time delay feedback methods can be a useful tool for stabilizing unstable periodic orbits of continuous systems or fixed points of discrete maps. In addition to being amenable to analysis, the extended scheme that makes recursive use of past iterates of the feedback signal is particularly practical, as it can be implemented in hardware with a single delay element and in principle enables control of any fixed point that is controllable via standard proportional control techniques. Moreover, experience suggests that many of the features brought to light in the analysis of discrete, recursive time delayed feedback systems are present as well in continuous systems, as the reader will notice in perusing other chapters in this volume. As research in chaos control continues to turn up new situations requiring theoretical analysis and new applications in natural and engineered systems, the concepts and basic phenomenology of discrete time delayed feedback control should be put to good use.

Acknowledgments

References

1 K. Pyragas and A. Tamasevicius, "Experimental control of chaos by delayed self-controlling feedback," Phys. Lett. A, **180**, 99–102 (1993).

2 W. Just, D. Reckwerth, E. Reibold, and H. Benner, "Influence of control loop latency on time delayed feedback control," Phys. Rev. E **59**, 2826 (1999).

3 J. N. Blakely, L. Illing, and D. J. Gauthier, "Controlling fast chaos in delay dynamical systems," Phys. Rev. Lett. **92**, 193901 (2004).

4 P. Hövel and J. E. S. Socolar, "Stability domains for time delay feedback control with latency," Phys. Rev. E **68**, 036206 (2003).

5 M. E. Bleich and J. E. S. Socolar, "Stability of periodic orbits controlled by time delay feedback," Phys. Lett. A **210**, 87–94 (1996).

6 W. Just, T. Bernard, M. Ostheimer, E. Reibold, and H. Benner, "Mechanism of time delayed feedback control," Phys. Rev. Lett. **78**, 203–206 (1997).

7 E. G. Tolkacheva, M. M. Romeo, M. Guerraty, and D. J. Gauthier, "Condition for alternans and its control in a two-dimensional mapping model of paced cardiac dynamics," Phys. Rev. E **69**, 031904 (2004).

8 K. Hall, D. J. Christini, M. Tremblay, J. J. Collins, L. Glass, J. Billette, "Dynamic control of cardiac alternans," Phys. Rev. Lett. **78**, 4518–4521 (1997).

9 J. E. S. Socolar and D. J. Gauthier, "Analysis and comparison of multiple-delay schemes for controlling unstable fixed points of discrete maps," Phys. Rev. E **57**, 6589–6595 (1998).

10 G. W. Flake, G.-Z. Sun, Y.-C. Lee, and H.-H. Chen, in *Advances in Neural Information Processing,* edited by J. D. Cowan, G. Tesauro, and J. Alspector (Morgan Publishers, San Mateo, CA, 1994).

11 K. Ogata, *Discrete-Time Control Systems* (Prentice-Hall, Englewood Cliffs, 1987).

12 J. E. S. Socolar, D. W. Sukow, and D. J. Gauthier, "Stabilizing unstable periodic orbits in fast dynamical systems," Phys. Rev. E **50**, 3245–3248 (1994).

13 M. E. Bleich, D. Hochheiser, J. V. Moloney, and J. E. S. Socolar, "Controlling extended systems with spatially filtered, time delayed feedback," Phys. Rev. E **55**, 2119 (1997).

14 I. Harrington and J. E. S. Socolar, "Design and robustness of delayed feedback controllers for discrete systems," Phys. Rev. E **69**, 056207 (2004).

15 K. Pyragas, "Control of chaos via an unstable delayed feedback controller," Phys. Rev. Lett. **86**, 2265 (2001).

16 S. Yamamoto, T. Hino and T. Ushio, "Dynamic delayed feedback controllers for chaotic discrete-time systems," IEEE Trans. Circuits Syst. I, Fundam. Theory Appl. **48**, 785–789, (2001).

17 H. Nakajima, "A generalization of the extended delayed feedback control for chaotic systems," Proc. Control Oscillations Chaos, **2**, 209–212 (2000).

18 R. O. Grigoriev, M. C. Cross and H. G. Schuster, "Pinning Control of Spatiotemporal Chaos," Phys. Rev. Lett, **79**, 2795–2798 (1997).

19 D. A. Egolf and J. E. S. Socolar, "Failure of linear control in noisy coupled map lattices," Phys. Rev. E, **57**, 5271–5275 (1998).

3
An Analytical Treatment of the Delayed Feedback Control Algorithm

Kestutis Pyragas, Tatjana Pyragienė, and Viktoras Pyragas

3.1
Introduction

Although the delayed feedback control (DFC) method [1] was introduced more than one decade ago, it is still one of the most active fields in applied nonlinear science [2, 3]. The method allows a noninvasive stabilization of unstable periodic orbits (UPOs) of dynamical systems in the sense that the control force vanishes when the target state is reached. The DFC algorithm is reference free and makes use of a control signal obtained from the difference between the current state of the system and the state of the system delayed by one period of the target orbit. The block diagram of the method is presented in Fig. 3.1. The method allows us to treat the controlled system as a black box; no exact knowledge of either the form of the periodic orbit or the system of equations is needed. The DFC algorithm is especially superior for fast dynamical systems, since it does not require any real-time computer processing.

Successful implementation of the DFC algorithm has been attained in diverse experimental systems, including electronic chaotic oscillators [4–7], mechanical pendulums [8, 9], lasers [10–12], gas discharge systems [13–15], a current-driven ion acoustic instability [16], a chaotic Taylor-Couette flow [17], chemical systems [18, 19], high-power ferromagnetic resonance [20], helicopter rotor blades [21], and a cardiac system [22].

The DFC method has been verified for a large number of theoretical models from different fields. The problem of stabilizing high-speed semiconductor lasers was considered in [23–25]. Batlle et al. [26] implemented the DFC in a model of buck converter. The problem of controlling chaotic solitons by a time delayed feedback mechanism was considered in [27]. Galvanetto [28] demonstrated the delayed feedback control of chaotic systems with dry friction. Bleich and Socolar [29] demonstrated that the DFC can stabilize regular behavior in a paced, excitable oscillator described by Fitzhugh-Nagumo equations. Rappel et al. [30] used the DFC for stabilization of spiral waves in an excitable media as a model of cardiac tissue in order to prevent the spiral wave breakup. The DFC
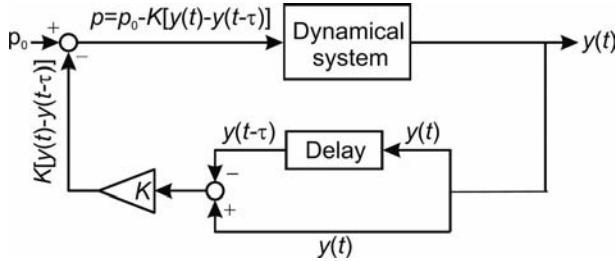
Fig. 3.1 Block diagram of the delayed feedback control method. $y(t)$ is an output variable, p is a control parameter, p_0 is its value at which the dynamical system possesses an unstable periodic orbit with a period τ, and K is the feedback gain.

was also implemented in a model of a car-following traffic [31] and in economical models [32, 33]. Tsui and Jones [34] investigated the problem of chaotic satellite attitude control. Mensour and Longtin [35] proposed the DFC as a method to store information in delay-differential equations. Mitsubori and Aihara [36] suggested rather exotic application of the DFC, namely, the control of chaotic roll motion of a flooded ship in waves. Rosenblum and Pikovsky [37, 38] considered the influence of the DFC on the synchronization in an ensemble of globally coupled oscillators and discussed a possibility of using this approach to suppression of pathological brain rhythms.

Several modifications of the original delayed feedback scheme have been proposed to improve the control performance. Among those are extended DFC (EDFC) schemes employing multiple delays to stabilize strongly unstable orbits [39, 40] or unstable DFC (UDFC) schemes using an unstable degree of freedom in a feedback loop [41–43] to overcome the so-called odd number limitation from which usual delayed feedback control suffers [44–46].

Although the DFC method is popular in experimental investigations, its theory is still in infancy. Systems with time delay are hard to handle because the dynamics takes place in infinite-dimensional phase spaces. Even linear analysis of such systems is difficult due to the infinite number of Floquet exponents (FEs) characterizing the stability of controlled orbits. The linear and nonlinear analysis of such systems is usually performed numerically. In this context, a reasonable way for further development of the delayed feedback control theory is to look for problems allowing an analytical treatment. Our idea for the analytical approach is to consider dynamical systems close to bifurcation points of periodic orbits.

Most investigations in the theory of the DFC are devoted to the stabilization of unstable periodic orbits embedded in chaotic attractors of low-dimensional (usually three-dimensional) systems. The leading Floquet multipliers (FMs) of such orbits are real valued and lie outside the unit circle in the complex plane (Fig. 3.2 (a) and (b)). The orbits with the negative real multiplier arise from a
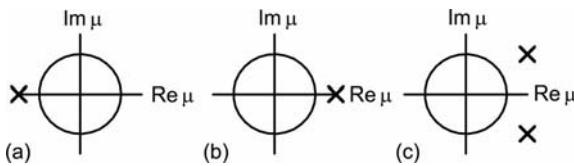
Fig. 3.2 Leading Floquet multipliers of unstable periodic orbits arising from different bifurcations: (a) period doubling, (b) tangent or subcritical Hopf, and (c) Nejmark-Sacker (discrete Hopf) bifurcations. The unit circle defines the region of stability.

period-doubling bifurcation and are typical, for example, for the Rössler system. The mechanism of stabilization of such orbits by delayed feedback is well understood [44, 47]. The orbits with the positive real multiplier come, for example, from a tangent or a subcritical Hopf bifurcation and are typical, for instance, for the Lorenz system. They satisfy the odd number limitation and it has been assumed for a long time that they cannot be stabilized by the usual delayed feedback method, see, however, chapter 4, for a correction of this view. The mechanism of stabilization of such orbits by the UDFC is described in [41–43]. In addition to the above-mentioned orbits, there exists a large class of unstable periodic orbits with the complex conjugate pair of leading FMs (Fig. 3.2 (c)). Such orbits arise from a Nejmark-Sacker (discrete Hopf) bifurcation and cannot appear in low-dimensional chaotic attractors. However, such orbits may appear in low-dimensional nonchaotic systems.

Our aim is to describe an analytical treatment of the DFC algorithm for orbits arising in the three different bifurcations. Note that all three types of orbits have different topological properties. The orbits with the negative real multiplier flip their neighborhood during one turn. We consider them in Section 3.3. The orbits with the complex conjugate pair of the multipliers have a finite torsion and the orbits with the positive real multiplier have no torsion. We consider their stabilization in Sections 3.4 and 3.5, respectively. In Section 3.2, we describe a relationship between the FEs of periodic orbits controlled by proportional and delayed feedback algorithms. This relationship is an essential tool of our analytical approach. We also utilize the methods of bifurcation theory and asymptotic methods of nonlinear dynamics, such as method of averaging, the center manifold theory, and a near identity transformation.

3.2
Proportional Versus Delayed Feedback

Consider a dynamical system described by ordinary differential equations

$$\dot{x} = f(x, p, t), \tag{3.1}$$

where the vector $x \in R^m$ defines the dynamical variables and p is a scalar parameter available for an external adjustment. We imagine that a scalar variable

$$y(t) = g\big(x(t)\big) \tag{3.2}$$

that is a function of dynamic variables $x(t)$ can be measured as the system output. Let us suppose that at $p = p_0 = 0$ the system has an UPO $x_0(t)$ that satisfies $\dot{x}_0 = f(x_0, 0, t)$ and $x_0(t + T) = x_0(t)$, where T is the period of the UPO. Here the value of the parameter p_0 is fixed to zero without a loss of generality. To stabilize the UPO we consider two continuous time feedback techniques, the proportional feedback control (PFC) and the DFC, both introduced by Pyragas [1].

The PFC uses the periodic reference signal

$$y_0(t) = g\big(x_0(t)\big) \tag{3.3}$$

that corresponds to the system output if it would move along the target UPO. For chaotic systems, this periodic signal can be reconstructed from the chaotic output $y(t)$ by using the standard methods for extracting UPOs from chaotic time series data [48, 49]. The control is achieved via adjusting the system parameter by a proportional feedback

$$p(t) = G[y_0(t) - y(t)], \tag{3.4}$$

where G is the control gain. If the stabilization is successful the feedback perturbation $p(t)$ vanishes. The experimental implementation of this method is difficult since it is not simple to reconstruct the UPO from experimental data.

More convenient for experimental implementation is the DFC method, which can be derived from the PFC by replacing the periodic reference signal $y_0(t)$ with the delayed output signal $y(t - T)$ [1]:

$$p(t) = K[y(t - T) - y(t)]. \tag{3.5}$$

Here we exchanged the notation of the feedback gain for K to differ it from that of the proportional feedback. The delayed feedback perturbation (3.5) also vanishes provided the target UPO is stabilized. The DFC uses the delayed output $y(t - T)$ as the reference signal and the necessity of the UPO reconstruction is avoided. This feature determines the main advantage of the DFC over the PFC.

Hereafter, we consider a more general (extended) version of the delayed feedback control, the EDFC, in which a sum of states at integer multiples in the past is used [39]:

$$p(t) = K\left[(1-R)\sum_{n=1}^{\infty} R^{n-1}y(t-nT) - y(t)\right]. \tag{3.6}$$

The sum represents a geometric series with the parameter $|R| < 1$ that determines the relative importance of past differences. For $R = 0$ the EDFC transforms to the original DFC. The extended method is superior to the original in that it can stabilize UPOs of higher periods and with larger FEs. For experimental implementation, it is important that the infinite sum in Eq. (3.6) can be generated using only single time delay element in the feedback loop.

The success of the above methods can be predicted by a linear stability analysis of the target orbit. For the PFC method, the small deviations from the UPO $\delta x(t) = x(t) - x_0(t)$ are described by variational equation

$$\delta\dot{x} = [A(t) + GB(t)]\delta x, \tag{3.7}$$

where $A(t) = A(t+T)$ and $B(t) = B(t+T)$ are both T-periodic $m \times m$ matrices

$$A(t) = D_1 f(x_0(t), 0, t), \qquad B(t) = D_2 f(x_0(t), 0, t) \otimes Dg(x_0(t)). \tag{3.8}$$

Here D_1 (D_2) denotes the vector (scalar) derivative with respect to the first (second) argument. The matrix $A(t)$ defines the stability properties of the UPO of the free system and $B(t)$ is the control matrix that contains all the details on the coupling of the control force.

Solutions of Eq. (3.7) can be decomposed into eigenfunctions according to the Floquet theory,

$$\delta x = \exp(\Lambda t)u(t), \quad u(t) = u(t+T), \tag{3.9}$$

where Λ is the FE. The spectrum of the FEs can be obtained with the help of the fundamental $m \times m$ matrix $\Phi(G, t)$ that is defined by equalities

$$\dot{\Phi}(G, t) = [A(t) + GB(t)]\Phi(G, t), \quad \Phi(G, 0) = I. \tag{3.10}$$

For any initial condition x_{in}, the solution of Eq. (3.7) can be expressed with this matrix, $x(t) = \Phi(G, t)x_{in}$. Combining this equality with Eq. (3.9) one obtains the system $[\Phi(G, T) - \exp(\Lambda T)I]x_{in} = 0$ that yields the desired eigensolutions. The characteristic equation for the FEs reads

$$\det[\Phi(G, T) - \exp(\Lambda T)I] = 0. \tag{3.11}$$

It defines m FEs Λ_j (or Floquet multipliers $\mu_j = \exp(\Lambda_j T)$), $j = 1, \ldots, m$ that are the functions of the control gain G:

$$\Lambda_j = F_j(G), \quad j = 1, \ldots, m. \tag{3.12}$$

The values $F_j(0)$ are the FEs of the free system. By assumption, at least one FE of the free UPOs has a positive real part. The PFC is successful if the real parts of all eigenvalues are negative, $\text{Re}F_j(G) < 0$, $j = 1, \ldots, m$, in some interval of the parameter G.

Consider next the stability problem for the EDFC. The variational equation in this case reads

$$\delta\dot{x} = A(t)\delta x(t) + KB(t)\left[(1 - R)\sum_{n=1}^{\infty} R^{n-1}\delta x(t - nT) - \delta x(t)\right]. \tag{3.13}$$

The delay terms can be eliminated due to Eq. (3.9), $\delta x(t - nT) = e^{-n\Lambda T}\delta x(t)$. As a result the problem reduces to the system of ordinary differential equations similar to Eq. (3.7),

$$\delta\dot{x} = [A(t) + KH(\Lambda)B(t)]\delta x, \tag{3.14}$$

where

$$H(\Lambda) = \frac{1 - \exp(-\Lambda T)}{1 - R\exp(-\Lambda T)} \tag{3.15}$$

is the transfer function of the extended delayed feedback controller. Equations (3.7) and (3.14) have the same structure defined by the matrices $A(t)$ and $B(t)$ and differ only by the value of the control gain. The equations become identical if we substitute $G = KH(\Lambda)$. The price one has to pay for the elimination of the delay terms is that the characteristic equation defining the FEs of the EDFC depends on the FEs itself:

$$\det\left[\Phi\big(KH(\Lambda), T\big) - \exp(\Lambda T)I\right] = 0. \tag{3.16}$$

Nevertheless, we can take advantage of the linear stability analysis for the PFC in order to predict the stability of the system controlled by time delayed feedback. Suppose that the functions $F_j(G)$ defining the FEs for the PFC are known. Then the FEs of the UPO controlled by time delayed feedback can be obtained through the solution of the transcendental equations

$$\Lambda = F_j\big(KH(\Lambda)\big), \quad j = 1, \ldots, m. \tag{3.17}$$

We emphasize the physical meaning of the functions $F_j(G)$, namely, these functions describe the dependence of the Floquet exponents on the control gain in the case of the PFC.

3.3
Controlling Periodic Orbits Arising from a Period Doubling Bifurcation

In this section, we consider the theory of the DFC for periodic orbits arising from a period doubling bifurcation. Such orbits flip their neighborhood during one turn. More specifically, we consider UPOs whose leading Floquet multiplier is real and negative (Fig. 3.2 (a)) so that the corresponding FE obeys $\mathrm{Im} F_1(0) = \pi/T$. It means that the FE is placed on the boundary of the "Brillouin zone." Such FEs are likely to remain on the boundary under various perturbations and hence the condition $\mathrm{Im} F_1(G) = \pi/T$ holds in some finite interval of the control gain $G \in [G_{\min}, G_{\max}]$, $G_{\min} < 0$, $G_{\max} > 0$.

Let us introduce a dimensionless function

$$\phi(G) = F_1(G)T - i\pi \tag{3.18}$$

that describes the dependence of the real part of the leading FE on the control gain G for the PFC and denote by

$$\lambda = \Lambda T - i\pi \tag{3.19}$$

the dimensionless FE of the EDFC shifted by the amount π along the complex axes. Then from Eqs. (3.15) and (3.17) we derive

$$\lambda = \phi(G), \tag{3.20a}$$

$$K = G\frac{1 + R\exp(-\phi(G))}{1 + \exp(-\phi(G))}. \tag{3.20b}$$

These equations define the parametric dependence λ versus K for the EDFC.

To demonstrate the benefit of Eqs. (3.20) let us derive the stability threshold of the UPO controlled by the extended delayed feedback. The stability of the periodic orbit is changed when λ reverses the sign. From Eq. (3.20a) it follows that the function $\phi(G)$ has to vanish for some value $G = G_1$, $\phi(G_1) = 0$. The value of the control gain G_1 is nothing but the stability threshold of the UPO controlled by the PFC. Then from Eq. (3.20b) one obtains the stability threshold for the EDFC:

$$K_1 = G_1(1 + R)/2. \tag{3.21}$$

It is interesting to note that the stability threshold for the DFC ($R = 0$) is equal to the half of the threshold in the case of the PFC, $K_1 = G_1/2$. In the following

we demonstrate the use of the parametric equations (3.20) for a specific example of the Rössler system.

3.3.1
Example: Controlling the Rössler System

Let us consider the problem of stabilizing the period-one UPO of the Rössler system [50]:

$$
\begin{pmatrix} \dot{x}_1 \\ \dot{x}_2 \\ \dot{x}_3 \end{pmatrix} = \begin{pmatrix} -x_2 - x_3 \\ x_1 + ax_2 \\ b + (x_1 - c)x_3 \end{pmatrix} + p(t) \begin{pmatrix} 0 \\ 1 \\ 0 \end{pmatrix}.
\tag{3.22}
$$

Here we suppose that the feedback perturbation $p(t)$ is applied only to the second equation of the Rössler system and the dynamic variable x_2 is an observable available at the system output, i.e., $y(t) = g(\boldsymbol{x}(t)) = x_2(t)$.

For parameter values $a = 0.2$, $b = 0.2$, and $c = 5.7$, the free ($p(t) \equiv 0$) Rössler system exhibits chaotic behavior. Linearizing Eq. (3.22) around the UPO one obtains explicit expressions for the matrices $A(t)$ and $B(t)$ defined in Eq. (3.8).

First we consider the system (3.22) controlled by proportional feedback, when the perturbation $p(t)$ is defined by Eq. (3.4). By solving Eqs. (3.10) and (3.11) we obtain three FEs Λ_1, Λ_2, and Λ_3 as functions of the control gain G. The real parts of these functions are presented in Fig. 3.3 (a). The values of the FEs of the free ($G = 0$) UPO are $\Lambda_1 T = 0.876 + i\pi$, $\Lambda_2 T = 0$, $\Lambda_3 T = -31.974 + i\pi$. Thus the first and the third FEs are located on the boundary of the "Brillouin zone." In Fig. 3.3 (a), we restricted ourselves to a small interval of the parameter $G \in [0, 0.67]$ in which all FEs do not change their imaginary parts. Information on the behavior of the leading FE Λ_1 or, more precisely, of the real-valued function $\phi(G) = \Lambda_1 T - i\pi$ in this interval will suffice to derive the main stability properties of the system controlled by delayed feedback.
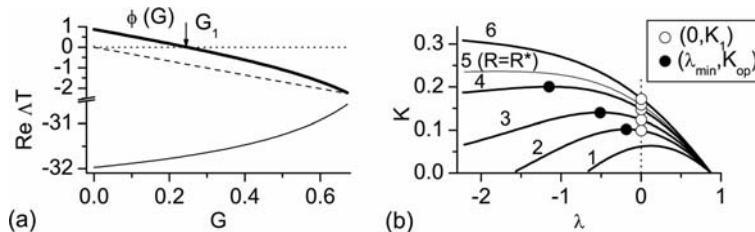
Fig. 3.3 (a) FEs of the Rösler system under PFC as functions of the control gain G. Thick solid, thin broken, and thin solid lines represent the functions $\Lambda_1 T - i\pi$, $\Lambda_2 T$ (zero exponent), and $\Lambda_3 T - i\pi$, respectively. (b) Parametric dependence K versus λ defined by Eqs. (3.20) for the EDFC. The numbers mark the curves with different values of the parameter R: (1) -0.5, (2) -0.2, (3) 0, (4) 0.2, (5) 0.28, (6) 0.4. Solid dots show the maxima of the curves and open circles indicate their intersections with the line $\lambda = 0$.

The main information on the EDFC performance can be gained from para-
metric equations (3.20). They make possible a simple reconstruction of the rele-
vant Floquet branch in the (K, λ) plane. This Floquet branch is shown in
Fig. 3.3 (b) for different values of the parameter R. Let us denote the dependence
K versus λ corresponding to this branch by a function ψ, $K = \psi(\lambda)$. It reads

$$\psi(\lambda) = \phi^{-1}(\lambda) \frac{1 + R \exp(-\lambda)}{1 + \exp(-\lambda)}, \tag{3.23}$$

where ϕ^{-1} denotes the inverse function of $\phi(G)$. The maximum in the region
$\lambda < 0$ defines the minimal value of the leading FE $\lambda_{\min}$ for the EDFC and
$K_{\mathrm{op}} = \psi(\lambda_{\min})$ is the optimal value of the control gain at which the fastest con-
vergence of the nearby trajectories to the desired orbit is attained. From
Fig. 3.3 (b) it is evident that the delayed feedback controller should gain perfor-
mance through the increase of the parameter R since the maximum of the
$\psi(\lambda)$ function moves to the left. At $R = R^* \approx 0.28$ the maximum disappears.
For $R > R^*$, it is difficult to predict the optimal characteristics of the EDFC. In
this case the value $\lambda_{\min}$ is determined by the intersection of different Floquet
branches.

An evaluation of the right boundary K_2 of the stability domain is a more intri-
cate problem. Nevertheless, for the parameter $R < R^*$ it can be successfully
solved by means of an analytical continuation of the function $\psi(\lambda)$ on the com-
plex region. For this purpose we expand the function $\psi(\lambda)$ at the point $\lambda = \lambda_{\min}$
into power series

$$\psi(\lambda) = K_{\mathrm{op}} + \sum_{n=2}^{N+1} a_n (\lambda - \lambda_{\min})^n. \tag{3.24}$$

We evaluate numerically the coefficients a_n by the least-squares fitting. Here we
take the real values of λ. To extend the Floquet branch to the region $K > K_{\mathrm{op}}$
we have to solve the equation $K = \psi(\lambda)$ for the complex argument λ.

Figure 3.4 shows the dependence of the leading FEs on the control gain K for
the EDFC. The thick solid line represents the most important Floquet branch
that conditions the main stability properties of the system. It is described by the
function $K = \psi(\lambda)$ with the real argument λ. For $R < R^*$, this branch originates
an additional sub-branch, which starts at the point $(K_{\mathrm{op}}, \lambda_{\min})$ and spreads to
the region $K > K_{\mathrm{op}}$. The sub-branch results from an analytical continuation of
the function $\psi(\lambda)$ on the complex plane. As seen from the figures the Floquet
sub-branches obtained by means of an analytical continuation are in good agree-
ment with the "exact" solutions evaluated from the complete system of
Eqs. (3.10), (3.15), and (3.16).

For $R > R^*$, the maximum in the function $\psi(\lambda)$ disappears and the Floquet
branch originated from the eigenvalues $\lambda = \ln R \pm i\pi$ of the controller becomes
dominant in the region $K > K_{\mathrm{op}}$. This Floquet branch and the intersection point

(a)

(b)

(c)

(d)
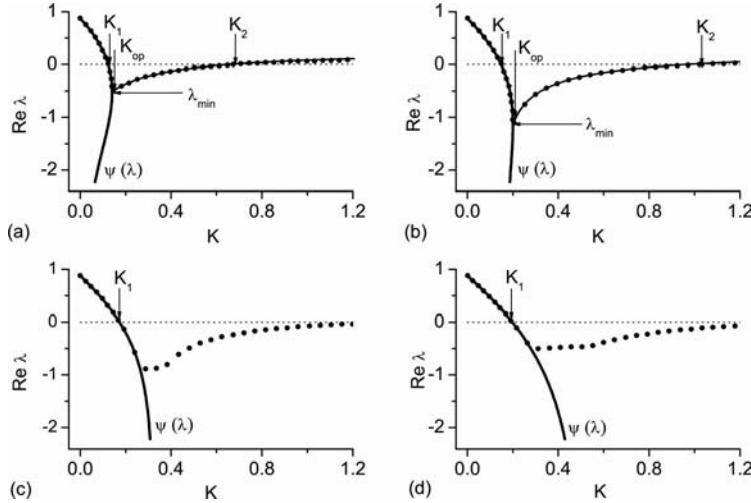
Fig. 3.4 Leading FEs of the Rösler system under EDFC as functions of the control gain K for different values of the parameter R: (a) 0.1, (b) 0.2, (c) 0.4, (d) 0.6. Thick solid lines symbolized by $\psi(\lambda)$ show the dependence $K = \psi(\lambda)$ for real λ. Solid lines in the region $K > K_{op}$ are obtained by analytical continuation of Eq. (3.24). The number of terms in series (3.24) is N = 15. Solid black dots denote the "exact" solutions obtained from the complete system of Eqs. (3.10), (3.15), (3.16).

(a)

(b)
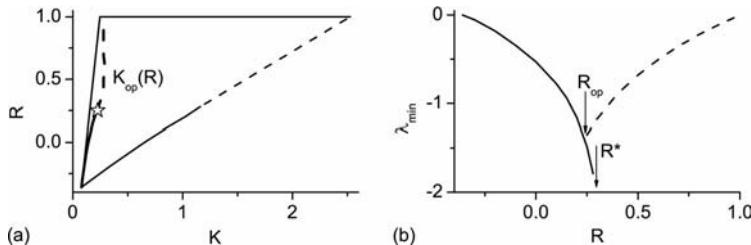
Fig. 3.5 (a) Stability region of the period-one UPO of the Rössler system under EDFC. The thick curve inside the region shows the dependence K_{op} versus R. The star marks the optimal point (K_{op}, R_{op}). (b) Minimal value λ_{min} of the leading FE as a function of the parameter R. In both figures solid and broken lines denote the solutions obtained from Eqs. (3.20) and Eqs. (3.10), (3.15), (3.16), respectively.

(K_{op}, λ_{min}) are unpredictable via a simple analysis. It can be determined by solving the complete system of Eqs. (3.10), (3.15), (3.16). In Fig. 3.4 (c) and (d) these solutions are shown by dots.

Figure 3.5 demonstrates how much of information one can gain via a simple analysis of parametric equations (3.20). These equations allow us to construct the stability domain in the (K, R) plane almost completely. Figure 3.5 (b) shows how the decay rate λ_{min} attained at the optimal value of the control gain K_{op} depends on the parameter R.

3.4
Control of Forced Self-Sustained Oscillations

In this section, we consider the problem of controlling UPOs with the complex conjugate pair of leading FMs (Fig. 3.2(c)). Such orbits may appear in low-dimensional nonchaotic systems, e.g., in a nonautonomous self-sustained oscillator exhibiting a quasiperiodic motion. We demonstrate an analytical treatment on the specific physical example of a weakly nonlinear van der Pol oscillator subjected to a periodic force and the DFC [51]. Without control, the oscillator can be synchronized by the periodic force only in a certain region of parameters. However, outside this region the system has UPOs that can be stabilized by the DFC. The feedback perturbation vanishes if the stabilization is successful and thus the region of synchronization can be extended noninvasively. By taking advantage of the fact that the system is close to a Hopf bifurcation, we derive a simplified averaged equation which can be treated analytically even in the presence of the delayed feedback. As a result we obtain simple analytical expressions defining the region of synchronization of the controlled system as well as an optimal value of the control gain.

3.4.1
Problem Formulation and Averaged Equation

Consider a weakly nonlinear van der Pol oscillator under the action of external periodic force and delayed feedback perturbation,

$$\ddot{x} + \omega_0^2 x + \varepsilon(x^2 - 1)\dot{x} = a\sin(\omega t) + k(x - x_T). \tag{3.25}$$

The parameter ω_0 is the characteristic frequency of self-sustained oscillations, and ε is responsible for the strength of nonlinearity of the oscillator. The first term on the right-hand side is an external periodic force and the second term describes the delayed coupling due to control. The parameter k is the feedback gain, $x_T \equiv x(t - T)$, and $T = 2\pi/\omega$ is the period of the external force. We suppose that ε is a small parameter, $\varepsilon \ll \omega_0$. Moreover, we assume that the amplitude a, the frequency detuning $\omega - \omega_0$ as well as the control perturbation $k(x - x_T)$ are proportional to the small parameter ε.

We apply the method of averaging. First we rewrite Eq. (3.25) as a system

$$\dot{x} = y, \tag{3.26 a}$$
$$\dot{y} = -\omega_0^2 x - \varepsilon(x^2 - 1)y + a\sin(\omega t) + k(x - x_T). \tag{3.26 b}$$

As Eq. (3.25) or system (3.26) is close to that of a linear oscillator, we can expect that the solution has a nearly harmonic form. Since there is a forced system we look for a solution with the characteristic frequency ω

$$x = (A(t)e^{i\omega t} + A^*(t)e^{-i\omega t})/2, \tag{3.27 a}$$

$$y = i\omega(A(t)e^{i\omega t} - A^*(t)e^{-i\omega t})/2. \tag{3.27 b}$$

Here $A(t)$ is a new variable, a slowly varying complex amplitude. Substituting Eqs. (3.27) in system (3.26) we obtain the equation for the complex amplitude, which after averaging over the period T of fast oscillations takes the form

$$\dot{A} = \frac{\omega^2 - \omega_0^2}{2i\omega}A - \frac{\varepsilon}{2}A\left(\frac{|A|^2}{4} - 1\right) - \frac{a}{2\omega} + \frac{k}{2i\omega}(A - A_T). \tag{3.28}$$

By choosing an appropriate scale for the amplitude

$$A = 2z \tag{3.29}$$

and introducing new parameters

$$a = \frac{a}{2\varepsilon\omega}, \quad v = \frac{\omega^2 - \omega_0^2}{\varepsilon\omega} \approx 2\frac{\omega - \omega_0}{\varepsilon}, \quad \kappa = \frac{k}{\varepsilon\omega}. \tag{3.30}$$

Equation (3.28) can be simplified to

$$(2/\varepsilon)\dot{z} = -ivz - z(|z|^2 - 1) - a - i\kappa(z - z_T). \tag{3.31}$$

The parameters a, v, and κ are proportional respectively to the amplitude of external force, the frequency detuning, and the delayed feedback gain.

3.4.2
Periodic Orbits of the Free System

The bifurcation diagram of Eq. (3.31) for several values of the parameter κ is shown in Fig. 3.6. Since it is symmetrical with respect to the v and a axis, only the part $v \geq 0$, $a \geq 0$ is presented. First we discuss this diagram for the free system when $\kappa = 0$. We start the analysis with finding the stationary solutions. Setting $\dot{z} = 0$ and $z = z_0$, we obtain

$$-ivz_0 - z_0(|z_0|^2 - 1) - a = 0. \tag{3.32}$$

We introduce the notations

$$s = |z_0|^2, \quad f_v(s) = s\left[(s - 1)^2 + v^2\right]. \tag{3.33}$$

Then the values of s can be found by solving the cubic equation

$$f_v(s) = a^2 \tag{3.34}$$
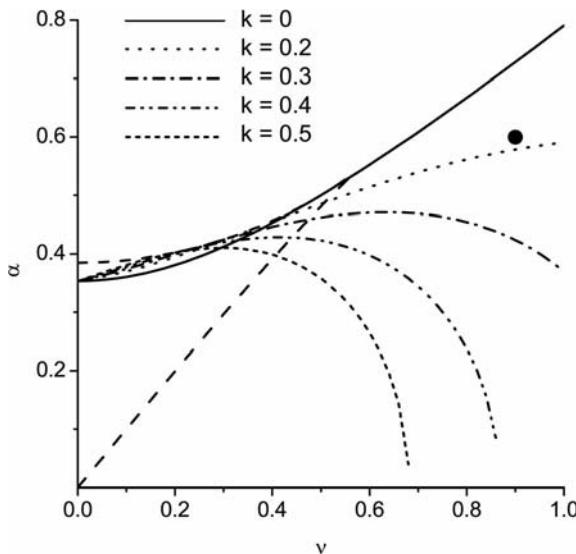
Fig. 3.6 The bifurcation diagram for the van der Pol oscillator controlled by delayed feedback. In the region between two dashed lines there are three periodic orbits. Outside this region there is only one periodic orbit. The solid line defines the Hopf bifurcation for the uncontrolled system, and broken lines are defined by Eq. (3.44). Above these lines the oscillator is synchronized with the external force. The solid dot $(v, a) = (0.9, 0.6)$ shows the set of parameters which we use in Section 3.4.3 to demonstrate the DFC performance.

with respect to s. Knowing s, from Eq. (3.32) one can determine the steady state value of z,

$$z_0 = -a/(s - 1 + iv). \tag{3.35}$$

Solutions of the cubic equation (3.34) define stationary periodic orbits of the forced system. The period of these orbits coincides with the period T of the external force, and the amplitude (the radius in the (x, y) plane) is

$$|A_0| = 2|z_0| = 2\sqrt{s}. \tag{3.36}$$

Equation (3.34) has three real roots provided

$$a_1^2(v) < a^2 < a_2^2(v), \tag{3.37a}$$

$$a_{1,2}^2(v) = \frac{2}{27} \left[9v^2 + 1 \mp (1 - 3v^2)^{3/2} \right] \tag{3.37b}$$

or one real root otherwise. Thus the forced van der Pol oscillator has either three or one periodic orbit(s). The region with three orbits is between broken lines in Fig. 3.6. Outside this region there is only one periodic orbit.

To determine the stability of periodic orbits of the free system, we have to linearize Eq. (3.31) for $\kappa = 0$. This leads to the characteristic equation

$$\left(\frac{2\lambda}{\varepsilon}\right)^2 - 2(1 - 2s)\frac{2\lambda}{\varepsilon} + f_v'(s) = 0. \tag{3.38}$$

Here λ is the Floquet exponent of the periodic orbit, and

$$f_v'(s) = (3s - 1)(s - 1) + v^2 \tag{3.39}$$

is the derivative of the function $f_v(s)$. The stability of a periodic orbit depends on the amplitude of the orbit. For $f_v'(s) = 0$ we have a tangent (saddle-node) bifurcation, and for $s = 1/2$ a Hopf bifurcation arises. The condition $f_v'(s) = 0$ defines the boundaries $a^2 = a_{1,2}^2(v)$ of the region with three periodic orbits in the (v, a) plane (broken lines in Fig. 3.6). When crossing into this region two additional orbits of saddle and node types occur. The condition of the Hopf bifurcation $s = 1/2$ defines the minimal amplitude of the stable orbit $A_{min} = \sqrt{2}$. The orbits with amplitude $|A_0| < A_{min}$ are unstable. In the (v, a) plane, this condition defines the hyperbola

$$a^2 = f_v(1/2) = v^2/2 + 1/8, \tag{3.40}$$

which is shown by a solid line in Fig. 3.6. Above this line the oscillator is synchronized with the external force. Below this line, in the region of one periodic orbit, we usually have a quasiperiodic behavior. The orbits losing their stability through the Hopf bifurcation have a pair of complex conjugate exponents with the positive real part. In the next section, we analyze their stability under the action of the DFC.

3.4.3
Linear Stability of the System Controlled by Delayed Feedback

We now analyze Eq. (3.31) for $\kappa \neq 0$. The term $\kappa(z - z_T)$ does not change the steady state solutions of this equation, but can change their stability. The characteristic equation now reads

$$\left(\frac{2\lambda}{\varepsilon}\right)^2 - 2(1 - 2s)\frac{2\lambda}{\varepsilon} + (3s - 1)(s - 1) + \left[v + \kappa(1 - e^{-\lambda T})\right]^2 = 0. \tag{3.41}$$

We can expect that close to the Hopf bifurcation the leading Floquet exponents will be proportional to the small parameter ε. This assumption allows the approximation $e^{-\lambda T} \approx 1 - \lambda T$, which simplifies Eq. (3.41),

$$(1 + K^2)\left(\frac{2\lambda}{\varepsilon}\right)^2 - 2(1 - 2s - vK)\frac{2\lambda}{\varepsilon} + f_v'(s) = 0. \tag{3.42}$$

Here we use the notation

$$K = \kappa T \varepsilon / 2 = k\pi / \omega^2. \tag{3.43}$$

This approximation is equivalent to that of replacing the delay term in Eq. (3.31) by the first derivative, $z_T = z(t - T) \approx z(t) - T\dot{z}$.

From Eq. (3.42) we see that the delayed feedback changes the condition of the Hopf bifurcation, $1 - 2s - vK = 0$, which now depends on the delayed feedback strength K. The relation between K, v, and a is

$$a^2 = \frac{1}{8}(1 - vK)\left[(1 + vK)^2 + 4v^2\right]. \tag{3.44}$$

In Fig. 3.6, these relations are presented by curves in the (v, a) plane for different fixed values of K. These curves define the boundaries of synchronization for the controlled oscillator. Above these curves the oscillator is synchronized with the periodic force. We see that the delayed feedback perturbation extends the synchronization region. Employing Eq. (3.43) and relation $s = |A_0|^2 / 4$ the threshold of the Hopf bifurcation can be presented in the form

$$k_0 = \frac{\omega^2}{\pi} K_0 = \frac{\omega^2}{\pi v}\left(1 - \frac{|A_0|^2}{2}\right). \tag{3.45}$$

To demonstrate how the FEs depend on the control gain k we specify the parameters (v, a) to be $(0.9, 0.6)$. This set of parameters is marked by a solid dot in Fig. 3.6. We have calculated the leading FEs of the initially unstable orbit using three different methods, namely, (i) solving transcendental equation (3.41), (ii) using the quadratic equation (3.42), and (iii) solving variational equations derived from the exact system (3.26). The results of the above analysis for $\varepsilon = 0.01$ are presented in Fig. 3.7. The exact values of the leading FEs are shown by dots. There are two branches (the left-hand and the right-hand) defining the interval of stability $k_0 < k < k_1$ in which the real part of the leading FE is negative.

First we discuss the results for the left-hand branch. Figure 3.7 (a) shows that all the above three methods give quantitatively coinciding results. Thus for small ε the leading FE of the left-hand branch can be reliably obtained from the simple quadratic equation (3.42), which yields

$$\text{Re}\lambda = \frac{\varepsilon}{2}\frac{1 - |A_0|^2/2 - vk\pi/\omega^2}{1 + (k\pi/\omega^2)^2}, \tag{3.46}$$

and the threshold k_0 of the Hopf bifurcation is well described by Eq. (3.45).

The right-hand branch of the FE defining the upper threshold k_1 cannot be quantitatively well described by Eq. (3.41). This is because the term $k(x - x_T)$ responsible for the control in the system (3.26) is not small in this case, and the
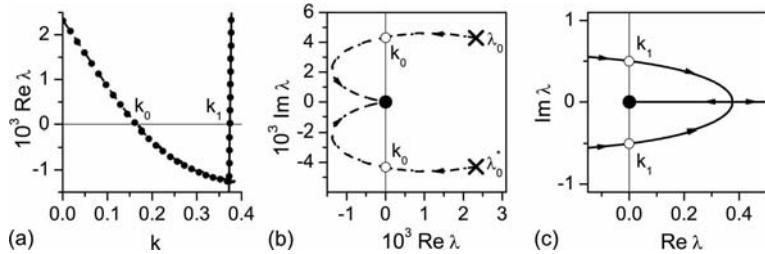
Fig. 3.7 Leading Floquet exponents as functions of the control gain for $(v, a) = (0.9, 0.6)$. Here and in all numerical demonstrations below we take $\omega_0 = 1$. (a) Reλ versus k for $\varepsilon = 0.01$. For the given values of parameters v, a, and ε, we have $\omega \approx 1.00451$ and $a \approx 0.01205$. The amplitude of the unstable orbit is $|A_0| \approx 1.034$ and its FEs for $k = 0$ are $\lambda_0 \approx (2.327 \pm 4.297i) \times 10^{-3}$. Solid dots are the values of the FEs obtained from variational equations derived from exact equations (3.26). The dashed and dotted lines calculated respectively from Eqs. (3.41) and (3.42) (or Eq. (3.46)) approximate the left-hand branch. The solid line calculated from Eq. (3.49) approximates the right-hand branch. (b) Root loci of Eq. (3.41) (dotted line) and Eq. (3.42) (dashed line) as k varies from 0 to ∞ for the same parameter value as in (a). Crosses and black dot denote the location of the roots for $k = 0$ and $k = \infty$, respectively. (c) Root loci of Eq. (3.47).

averaging procedure performed with this system is not valid. For the right-hand branch, the nonlinear terms in Eq. (3.41) are small in comparison with the control term. Setting $\varepsilon = 0$ in the exact variational equations we obtain the characteristic equation

$$\lambda^2 + \omega_0^2 - k(1 - e^{-\lambda T}) = 0. \tag{3.47}$$

The root loci diagram of the relevant branch for this equation when varying k is shown in Fig. 3.7 (c). The pair of complex conjugate roots intersects the imaginary axes at the points $\lambda = \pm i\pi/T = \pm i\omega/2$. This intersection appears for $k = k_1$, where

$$k_1 = \frac{1}{2}\left(\omega_0^2 - \frac{\omega^2}{4}\right) \tag{3.48}$$

defines the upper threshold of stability. For $k = k_1$, the orbit loses stability by a period doubling bifurcation. Expanding the solution of Eq. (3.47) in Taylor series close to the threshold $k = k_1$, we obtain an approximate analytical expression

$$\text{Re}\lambda = \frac{4\pi k_1/\omega}{\omega^2 + (2\pi k_1/\omega)^2}(k - k_1) \tag{3.49}$$

that describes well the Reλ versus k dependence for the right-hand branch (Fig. 3.7 (a)).

Although here we have presented the analytical results only for the case of the DFC algorithm, the theoretical approach described in this section can be easily extended for the case of the EDFC [51].

3.4.4
Numerical Demonstrations

To verify the validity of the linear theory we have numerically investigated the original nonlinear differential equations (3.26). Without control the system experiences a quasiperiodic motion (Fig. 3.8 (a)). The DFC perturbation stabilizes an unstable UPO and we have a periodic motion synchronized with an external force (Fig. 3.8 (b)). Whenever the synchronization is established the feedback perturbation vanishes (Fig. 3.8 (c)). The envelopes of the transient are well described by the averaged amplitude equation (3.31). This confirms the validity of the averaging procedure applied to the time delay system (3.26).

3.5
Controlling Torsion-Free Periodic Orbits

It has been widely assumed that the conventional DFC can stabilize only a certain class of periodic orbits characterized by a finite torsion. More precisely, the limitation was thought to be that any UPOs with an odd number of real Floquet multipliers greater than unity can never be stabilized by the DFC. This statement was first proved by Ushio [52] for discrete time systems. Just et al. [44]
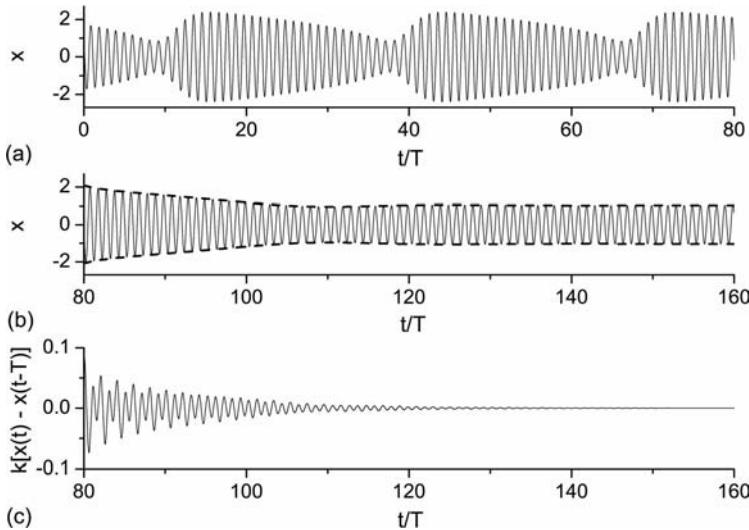
Fig. 3.8 Results of numerical integration of delay-differential equations (3.26) for $(v, a) = (0.9, 0.6)$, $\varepsilon = 0.1$. (a) Dynamics of the x variable without control. (b) and (c) Dynamics of the x variable and perturbation $k[x(t) - x(t - T)]$ when the control is switched on. The broken line (an envelop) in (b) is the dynamics of the complex amplitude $|A(t)| = 2|z(t)|$ obtained from the averaged equation (3.31). The strength of the feedback gain is $k = 0.34$.

and Nakajima [45] proved the same limitation for the continuous time DFC, and then this proof was extended for a wider class of delayed feedback schemes, including the EDFC [46]. Hence it seems hard to overcome this inherent limitation, see, however, chapter 4 for a recent correction of this view, where this proof is refuted.

In [41], we have proposed to supplement the feedback loop with an additional unstable degree of freedom in order to overcome the odd number limitation. The idea of an unstable controller can be demonstrated with the simple example. Consider an unstable discrete time system $y_{n+1} = \mu_s y_n$, $\mu_s > 1$ controlled by the EDFC:

$$y_{n+1} = \mu_s y_n - K F_n, \tag{3.50a}$$
$$F_n = y_n - y_{n-1} + R F_{n-1}. \tag{3.50b}$$

The free system $y_{n+1} = \mu_s y_n$ has an unstable fixed point $y^* = 0$ with the only real Floquet multiplier $\mu_s > 1$ and, in accordance with the above limitation, cannot be stabilized by the EDFC for any values of the feedback gain K. This is so indeed if the EDFC is stable, i.e., if the parameter R in Eq. (3.50b) satisfies the inequality $|R| < 1$. However, it is easy to verify that the unstable controller with the parameter $R > 1$ can stabilize this system. Using the ansatz $y_n, F_n \propto \mu^n$ one obtains the characteristic equation

$$(\mu - \mu_s)(\mu - R) + K(\mu - 1) = 0 \tag{3.51}$$

defining the FMs μ of the closed loop system (3.50). The system is stable if both roots $\mu = \mu_{1,2}$ of Eq. (3.51) are inside the unit circle of the μ complex plain, $|\mu_{1,2}| < 1$. Figure 3.9 (a) shows the characteristic root-locus diagram for $R > 1$, as the parameter K varies from 0 to ∞. For $K = 0$, there are two real eigenvalues greater than unity, $\mu_1 = \mu_s$ and $\mu_2 = R$, which correspond to two independent subsystems (3.50a) and (3.50b), respectively; this means that both the con-
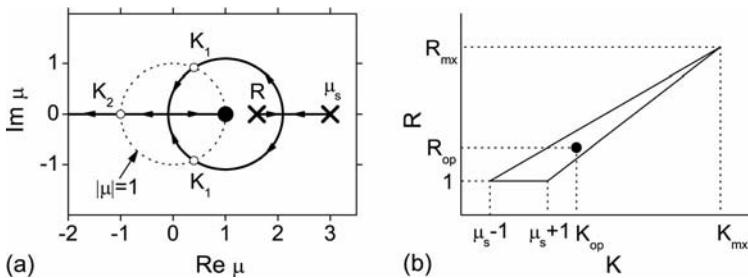
Fig. 3.9 (a) Root loci of Eq. (3.51) at $\mu_s = 3$, $R = 1.6$ as K varies from 0 to ∞. The crosses and black dot denote the location of roots at $K = 0$ and $K \to \infty$, respectively. (b) Stability region of Eqs. (3.50) in the (K, R) plane; $K = (\mu_s + 1)^2/(\mu_s - 1)$, $R = (\mu_s + 3)/(\mu_s - 1)$.

trolled system and controller are unstable. With the increase of K, the eigenvalues approach each other on the real axes, then collide and pass to the complex plain. At $K = K_1 \equiv \mu_s R - 1$ they cross symmetrically the unite circle $|\mu| = 1$. Then both eigenvalues move inside this circle, collide again on the real axes and one of them leaves the circle at $K = K_2 \equiv (\mu_s + 1)(R + 1)/2$. In the interval $K_1 < K < K_2$, the closed loop system (3.50) is stable. By a proper choice of the parameters R and K one can stabilize the fixed point with an arbitrarily FM μ_s. Figure 3.9 (b) shows the stability region in the plane of parameters (K, R). For a given value μ_s, there is an optimal choice of the parameters $R = R_{op} \equiv \mu_s/(\mu_s - 1)$, $K = K_{op} \equiv \mu_s R_{op}$ leading to zero eigenvalues, $\mu_1 = \mu_2 = 0$, such that the system approaches the fixed point in finite time.

Note that the idea of using an unstable EDFC with the parameter $R > 1$ fails for continuous time systems, since such a controller involves an infinite number of unstable modes. An appropriate controller for continuous time systems can be constructed on the basis of usual EDFC with the parameter $|R| < 1$. A required additional greater than unity real FM can be gained via supplementing the feedback loop by an additional unstable mode. The performance of such a controller has been numerically demonstrated for the Lorenz system [41] as a representative of systems with torsion-free UPOs. Later on it has been realized that the unstable DFC allows an analytical treatment if the system is close to a subcritical Hopf bifurcation. First such a treatment has been performed for a simple nonlinear second-order electronic circuit modeling a subcritical Hopf bifurcation [42]. Then this approach has been extended for wider class of dynamical systems with an arbitrary large phase space dimension [43]. Below we briefly describe this approach for the Lorenz system.

3.5.1
Example: Controlling the Lorenz System at a Subcritical Hopf Bifurcation

We consider the Lorenz system [53]

$$\dot{x} = \sigma(y - x) \tag{3.52a}$$
$$\dot{y} = rx - y - xz \tag{3.52b}$$
$$\dot{z} = xy - bz \tag{3.52c}$$

for fixed values of the parameters $\sigma = 10$, $b = 8/3$, and variable parameter r. For $0 < r < 1$, the Lorenz system has a unique stable steady state (a stable node) at the origin $C^0 : (0, 0, 0)$. For $r = 1$, the origin becomes a saddle and two additional symmetrical stable fixed points $C^{\pm}$,

$$(x_f^{\pm}, y_f^{\pm}, z_f) = \left(\pm\sqrt{b(r - 1)}, \pm\sqrt{b(r - 1)}, r - 1 \right) \tag{3.53}$$

appear. For $r = r_H$, the steady states $C^{\pm}$ become unstable. The value

$$r_H = \frac{\sigma(\sigma + b + 3)}{\sigma - b - 1} \tag{3.54}$$

represents the point at which the subcritical Hopf bifurcation occurs. Just below this bifurcation point, for

$$r = r_H - \Delta r, \quad 0 < \Delta r << r_H, \tag{3.55}$$

there are two small unstable limit cycles surrounding the stable steady states $C^{\pm}$. Moreover, at the same values of the parameter r there exists a strange attractor. Thus the system is multistable and depending on initial conditions the phase trajectory may either be attracted to the one of the steady states or exhibit a chaotic behavior on the strange attractor.

Our aim is to stabilize the unstable limit cycles arising at the Hopf bifurcation using the DFC technique. In particular, we are interested in analytical treatment of this problem. Note that the periodic orbits arising at this bifurcation are torsion free and we need an unstable controller. Specifically, we consider the following control algorithm:

$$\dot{x} = \sigma(y - x) \tag{3.56a}$$
$$\dot{y} = rx - y - xz + \varepsilon w(y - y_f) \tag{3.56b}$$
$$\dot{z} = xy - bz \tag{3.56c}$$
$$\dot{w} = \varepsilon \lambda_c w + k[y - y(t - \tau)]. \tag{3.56d}$$

We suppose that y is an observable and apply the control perturbation $w(y - y_f)$ only to the second equation of the Lorenz system. We use a nonlinear perturbation. For definiteness, we consider the control of the periodic orbit surrounding the fixed point C^+ and take $y_f \equiv y_f^+ = \sqrt{b(r-1)}$.

Equation (3.56 d) describes an unstable delayed feedback controller, which supplements the system with an additional unstable Floquet mode and eliminates the odd number limitation. The positive parameter $\lambda_c > 0$ defines the value of the additional FE introduced with the controller. The parameter k denotes the strength of the feedback gain. The delay time τ in Eq. (3.56 d) is equal to the period of the unstable periodic orbit such that the controller does not change the periodic solution of the Lorenz system. Finally, the parameter

$$\varepsilon = \sqrt{b(r_H - 1)} - \sqrt{b(r - 1)} \approx \sqrt{b/(r_H - 1)}\Delta r/2 \tag{3.57}$$

defines the closeness of the system to the bifurcation point $r = r_H$. This is the main control parameter, whose smallness we exploit in the perturbation theory. Below we describe only the main steps of our analytical approach; for details we refer to our recent paper [43].

Generally Eqs. (3.56) represent a rather complicated system of nonlinear delay-differential equations. The dynamics of the system takes place in an infinite-dimensional phase space and reduction of the phase space dimension via the

center manifold theory is a nontrivial task. To overcome the problem of an infinite-dimensional phase space we use the relationship between the FEs of the DFC and PFC algorithms described in Section 3.2. In Eq. (3.56 d) we replace the delay term $y(t - \tau)$ with the periodic solution of the free Lorenz system $y_0(t)$ corresponding to the unstable limit cycle, which we intend to stabilize. Then instead of the DFC problem described by delay-differential equations (3.56) we get a nonautonomous system of four ordinary differential equations for the PFC problem. To transform the nonautonomous PFC problem to the autonomous we write an additional free Lorenz system with the initial conditions taken on the stable manifold of the desired UPO, such that it generates the signal $y_0(t)$ required for the PFC algorithm. As a result we get an autonomous system of seven ordinary differential equations for the PFC problem. Using the closeness of the system to a subcritical Hopf bifurcation we apply the center manifold theory and reduce the system dimension. Then we simplify this system by using the near identity transformation and averaging. Linearization of the simplified system around the desired UPO leads to a characteristic equation of the PFC problem. Finally, using the relationship between the FEs of the PFC and DFC algorithms we derive an analytical characteristic equation for the DFC algorithm:

$$\lambda^2 - (\lambda_0 + \lambda_c)\lambda + \lambda_0\lambda_c + Qk[1 - \exp(-\varepsilon\lambda\tau)] = 0. \tag{3.58}$$

Here $\lambda_0 = \Lambda_0/\varepsilon \approx 0.360675991$ and $\lambda = \Lambda/\varepsilon$ are the rescaled values of the FEs Λ_0 and Λ of the free and DFC controlled UPO, respectively. An approximate value of the parameter Q is 1.743243862.

For $\varepsilon|\lambda|\tau \ll 1$, we can use an approximation $\exp(-\varepsilon\lambda\tau) \approx 1 - \varepsilon\lambda\tau$, which transforms Eq. (3.58) to the simple quadratic equation

$$\lambda^2 - (\lambda_0 + \lambda_c - kQ\varepsilon\tau)\lambda + \lambda_0\lambda_c = 0. \tag{3.59}$$

In Fig. 3.10 (a), we compare the leading FEs of the controlled system determined by three different methods: (i) solving the quasipolynomial equation (3.58), (ii) using the solutions of the quadratic equation (3.59), and (iii) by solving the exact system of variational equations derived from Eqs. (3.56). All above three results are in good quantitative agreement, as viewed in Fig. 3.10 (a). Thus the leading FEs are reliably predicted by the simple quadratic equation (3.59).

The mechanism of stabilization is evident from Fig. 3.10 (b). For $k = 0$, two real positive solutions of Eq. (3.59), $\lambda = \lambda_0$ and $\lambda = \lambda_c$, describe an unstable eigenvalue of the free system and the free controller, respectively. With increasing k, the eigenvalues approach each other on the real axis, and then collide and pass to the complex plane. For $k = k_0$, where

$$k_0 = (\lambda_0 + \lambda_c)/Q\varepsilon\tau, \tag{3.60}$$
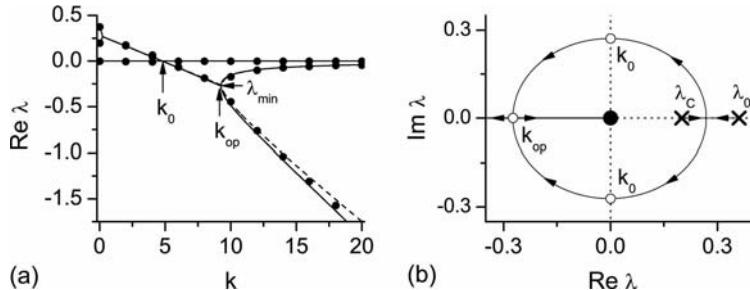
Fig. 3.10 (a) Real parts of leading Floquet exponents of the controlled limit cycle as functions of the control gain for $\varepsilon = 0.1$, $\lambda_c = 0.2$. Dashed and solid lines show the solutions of the characteristic equations (3.59) and (3.58), respectively. Dots correspond to the values of Floquet exponents obtained from the exact variational equations derived from Eqs. (3.56). (b) Root loci of Eq. (3.58) as k varies from 0 to ∞ for the same parameter values as in (a). Crosses and black dot denote the location of the roots for $k = 0$ and $k = \infty$, respectively.

they cross the imaginary axis and move symmetrically into the left half plane, i.e., both the system and the controller become stable. An optimal value of the control gain is

$$k_{op} = k_0 + 2\sqrt{\lambda_0 \lambda_c}/Q\varepsilon\tau, \tag{3.61}$$

since it provides the fastest convergence to the stabilized limit cycle with the characteristic rate $\lambda_{min} = -\sqrt{\lambda_0 \lambda_c}$.

The validity of the linear theory is confirmed by numerical analysis of the original system of nonlinear delay-differential equations (3.56) presented in Fig. 3.11. In numerical simulations, the controller is switched on only when the system is close to the desired periodic orbit and switched off when it is far away from the orbit. Without control ($t < \tau$), the Lorenz system demonstrates a chaotic behavior on the strange attractor. For $t > \tau$, the control algorithm starts to act and after a transient process the controlled system approaches a previously unstable limit cycle, and the feedback perturbation vanishes.

3.6
Conclusions

The aim of this chapter was to review recently developed theoretical methods allowing an analytical treatment of some delayed feedback control problems. The key idea is to consider the control problems close to bifurcation points of periodic solutions. We managed to treat analytically the delayed feedback control algorithm at three different bifurcations, namely, the period doubling, the discrete Hopf, and the subcritical Hopf bifurcations. All three types of bifurcations are characterized by different topological properties of periodic orbits. The orbits
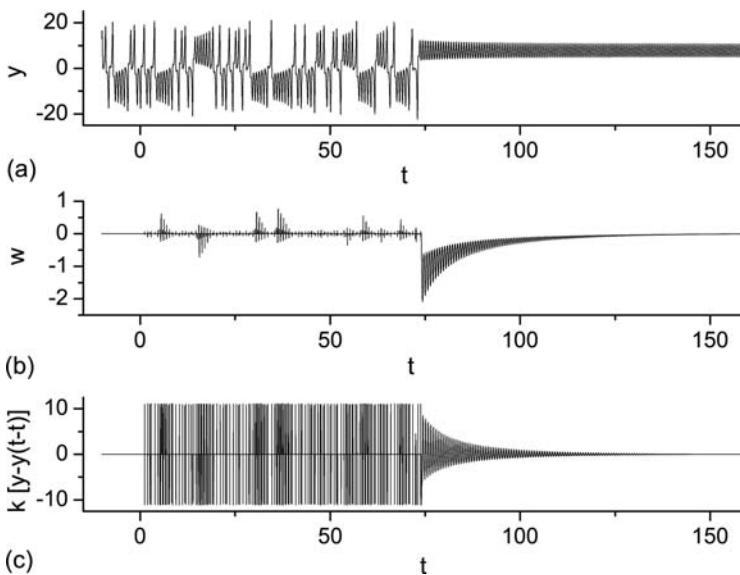
Fig. 3.11 Dynamics of (a) variable y, (b) controller variable w, and (c) delayed feedback perturbation $k[y - y(t - \tau)]$. The initial conditions are $x(-15\tau) = 8.109559459$, $y(-15\tau) = 13.03719946$, $z(-15\tau) = 14.27465065$, $w(-15\tau) = 0$. $y(t) = 0$ for $-15\tau < t \leq -14\tau$. The control is initiated at $t = \tau$. The values of the parameters are $\varepsilon = 0.1$, $\lambda_c = 0.2$, $\tau = 0.67398328$, $k = 0$ for $-15\tau \leq t < \tau$ and $k = 9.25$ for $t \geq \tau$. For $|y - y(t - \tau)| > Y_{max} = 1.2$, the controller is off.

without torsion are particularly difficult to control. To stabilize such orbits we need an unstable controller.

In our analytical approaches, we use the classical tools of nonlinear dynamics and bifurcation theory, such as the method of averaging, the center manifold theory, and the near identity transformation. We also utilize the relationship between Floquet exponents of the proportional and delayed feedback control algorithms, which allows us to reduce the delayed feedback problems to finite-dimensional phase spaces.

The analytical approaches are demonstrated for paradigmatic models of the Rössler system, the forced van der Pol oscillator, and the Lorenz system. We have obtained simple analytical expressions for the dependence of leading Floquet exponents on the control gain and determined the lower and upper thresholds of stability as well as optimal values of the control gain. The main results and the approaches are of general importance since they are relevant to any systems close to the associated bifurcation points.

We believe that the developed analytical methods are important contributions to the theory of the delayed feedback control. They give not only a better insight into the mechanism of the delayed feedback control technique, but they are also important for optimizing the control algorithm. We hope that the ideas presented in this chapter will stimulate the search for further modifications of the

delayed feedback control technique aiming at the improvement of the control performance.

References

1 Pyragas, K., *Phys. Lett. A 170* (**1992**) p. 421

2 Schuster, H.G., *Handbook of Chaos Control,* Wiley-VCH, Weinheim, **1999**

3 Pyragas, K., in: *Synchronization: Theory and Application,* Kluwer, Dordrecht, **2003**, p. 187

4 Pyragas, K. and Tamasevicius, A., *Phys. Lett. A* 180 (**1993**) p. 99

5 Kittel, A., Parisi, J., Pyragas, K. and Richter, R., *Z. Naturforsch.* 49 a (**1994**) p. 843

6 Gauthier, D. J., Sukow, D. W., Concannon, H. M. and Socolar, J. E. S., *Phys. Rev. E* 50 (**1994**) p. 2343

7 Celka, P., *Int. J. Bifurcation Chaos Appl. Sci. Eng.* 4 (**1994**) p. 1703

8 Hikihara, T. and Kawagoshi, T., *Phys. Lett. A* 211 (**1996**) p. 29

9 Christini, D. J., In, V., Spano, M. L., Ditto, W. L. and Collins, J. J., *Phys. Rev. E* 56 (**1997**) p. R3749

10 Bielawski, S., Derozier, D. and Glorieux, P., *Phys. Rev. E* 49 (**1994**) p. R971

11 Basso, M., Genesio, R. and Tesi, A., *Syst. Control Lett.* 31 (**1997**) p. 287

12 Lu, W., Yu, D. and Harrison, R. G., *Int. J. Bifurcation Chaos Appl. Sci. Eng.* 8 (**1998**) p. 1769

13 Pierre, T., Bonhomme, G. and Atipo, A., *Phys. Rev. Lett.* 76 (**1996**) p. 2290

14 Gravier, E., Caron, X., Bonhomme, G., Pierre, T. and Briancon, J. L., *Eur. J. Phys. D* 8 (**2000**) p. 451

15 Mausbach, Th., Klinger, Th., Piel, A., Atipo, A., Pierre, Th. and Bonhomme, G., *Phys. Lett. A* 228 (**1997**) p. 373

16 Fukuyama, T., Shirahama, H. and Kawai, Y., *Phys. Plasmas* 9 (**2002**) p. 4525

17 Lüthje, O., Wolff, S. and Pfister, G., *Phys. Rev. Lett.* 86 (**2001**) p. 1745

18 Parmananda, P., Madrigal, R., Rivera, M., Nyikos, L., Kiss, I. Z. and Gaspar, V., *Phys. Rev. E* 59 (**1999**) p. 5266

19 Guderian, A., Munster, A. F., Kraus, M., Schneider, F. W., *J. Phys. Chem. A* 102 (**1998**) p. 5059

20 Benner, H. and Just, W., *J. Korean Phys. Soc.* 40 (**2002**) p. 1046

21 Krodkiewski, J. M. and Faragher, J. S., *J. Sound Vib.* 234 (**2000**) p. 591

22 Hall, K., Christini, D. J., Tremblay, M., Collins, J. J., Glass, L. and Billette, J., *Phys. Rev. Lett.* 78 (**1997**) p. 4518

23 Simmendinger, C. and Hess, O., *Phys. Lett. A* 21 (**1996**) p. 97

24 Münkel, M., Kaiser, F. and Hess, O., *Phys. Rev. E* 56 (**1997**) p. 3868

25 Simmendinger, C., Münkel, M. and Hess, O., *Chaos, Solitons Fractals* 10 (**1999**) p. 851

26 Batlle, C., Fossas, E. and Olivar, G., *Int. J. Circuit Theory Appl.* 27 (**1999**) p. 617

27 Fronczak, P. and Holyst, J. A., *Phys. Rev. E* 65 (**2002**) p. 026219

28 Galvanetto, U., *Int. J. Bifurcation Chaos Appl. Sci. Eng.* 12 (**2002**) p. 1877

29 Bleich, M. E. and Socolar, J. E. S., *Int. J. Bifurcation Chaos Appl. Sci. Eng.* 10 (**2000**) p. 603

30 Rappel, W. J., Fenton, F. and Karma, A., *Phys. Rev. Lett.* 83 (**1999**) p. 456

31 Konishi, K., Kokame, H. and Hirata, H. K., *Phys. Rev. E* 60 (**1999**) p. 4000

32 Holyst, J. A. and Urbanowicz, K., *Physica A* 287 (**2000**) p. 587

33 Holyst, J. A., Zebrowska, M. and Urbanowicz, K., *Eur. Phys. J. B* 20 (**2001**) p. 531

34 Tsui, A. P. M. and Jones, A. J., *Physica D* 135 (**2000**) p. 41

35 Mensour, B. and Longtin, A., *Phys. Lett. A* 205 (**1995**) p. 18

36 Mitsubori, K. and Aihara, K. U., *Proc. R. Soc. A* 458 (**2002**) p. 2801

37 Rosenblum, M. and Pikovsky, A., *Phys. Rev. Lett.* 92 (**2004**) p. 114102

38 Rosenblum, M. and Pikovsky, A., *Phys. Rev. E* 70 (**2004**) p. 041904

39 Socolar, J. E. S., Sukow, D. W. and Gauthier, D. J., *Phys. Rev. E* 50 (**1994**) p. 3245

40 Pyragas, K., *Phys. Lett. A* 206 (**1995**) p. 323

41 Pyragas, K., *Phys. Rev. Lett*. 86 (**2001**) p. 2265

42 Pyragas, K., Pyragas, V. and Benner, H., *Phys. Rev. E* 70 (**2004**) p. 056222

43 Pyragas, V. and Pyragas, K., *Phys. Rev. E* 73 (**2006**) p. 036215

44 Just, W., Bernard, T., Ostheimer, M., Reibold, E. and Benner, H., *Phys. Rev. Lett*. 78 (**1997**) p. 203

45 Nakajima, H., *Phys. Lett. A* 232 (**1997**) p. 207

46 Nakajima, H. and Ueda, Y., *Physica D* 111 (**1998**) p. 143

47 Pyragas, K., *Phys. Rev. E* 66 (**2002**) p. 026207

48 Lathrop, D. P. and Kostelich, E. J., *Phys. Rev. A* 40 (**1989**) p. 4028

49 So, P., Ott, E., Schiff, S. J., Kaplan, D. T., Sauer, T. and Grebogi, C., *Phys. Rev. Lett*. 76 (**1996**) p. 4705

50 Rössler, O. E., *Phys. Lett. A* 57 (**1976**) p. 397

51 Pyragiene, T. and Pyragas, K., *Phys. Rev. E* 72 (**2005**) p. 026203

52 Ushio T., *IEEE Trans. Circuits Syst. I* 43 (**1996**) p. 815

53 Lorenz, E. N., *J. Atmos. Sci*. 20 (**1963**) p. 130

4

Beyond the Odd-Number Limitation
of Time Delayed Feedback Control

Bernold Fiedler, Valentin Flunkert, Marc Georgi, Philipp Hövel, and Eckehard Schöll

4.1
Introduction

The stabilization of unstable states is a central issue in applied nonlinear science. Starting with the work of Ott, Grebogi, and Yorke [1], a variety of methods have been developed in order to stabilize unstable periodic orbits (UPOs) embedded in a chaotic attractor by employing tiny control forces [2–4]. A particularly simple and efficient scheme is time delayed feedback as suggested by Pyragas [5], which uses the difference $z(t) - z(t - \tau)$ of a signal z at a time t and a delayed time $t - \tau$. It is an attempt to stabilize periodic orbits of (minimal) period T by a feedback control which involves a time delay $\tau = nT$, for a suitable positive integer n. A linear feedback example is

$$\dot{z}(t) = f(\lambda, z(t)) + B[z(t - \tau) - z(t)] \tag{4.1}$$

where $\dot{z}(t) = f(\lambda, z(t))$ describes a d-dimensional nonlinear dynamical system with bifurcation parameter λ and an unstable orbit of (minimal) period T. B is a suitably chosen constant feedback control matrix. Typical choices are multiples of the identity or of rotations, or matrices of low rank. More general nonlinear feedbacks are conceivable, of course. The main point, however, is that the Pyragas choice $\tau_P = nT$ of the delay time eliminates the feedback term on the orbit, and thus recovers the original T-periodic solution $z(t)$. In this sense the method is noninvasive.

Although time delayed feedback control has been widely used with great success in real-world problems in physics, chemistry, biology, and medicine, e.g. [6–18] (see Chapters 19–32 of this volume), severe limitations are imposed by the common belief that certain orbits cannot be stabilized for any strength of the control force. In fact, it has been contended that periodic orbits with an odd number of real Floquet multipliers greater than unity cannot be stabilized by the Pyragas method [19–24], even if the simple scheme (4.1) is extended by multiple delays in the form of an infinite series [25]. To circumvent this restriction

more complicated control schemes, like an oscillating feedback [26], half-period delays for special, symmetric orbits [27], or the introduction of an additional, unstable degree of freedom [24, 28], have been proposed. In this chapter, we claim, and show by example, that the general limitation for orbits with an odd number of real unstable Floquet multipliers greater than unity does not hold: stabilization may be possible for suitable choices of B [29]. Our example consists of an unstable periodic orbit generated by a subcritical Hopf bifurcation. In particular, this refutes the theorem in [20].

4.2
Mechanism of Stabilization

Consider the normal form of a subcritical Hopf bifurcation, extended by a time delayed feedback term

$$\dot{z}(t) = \left[\lambda + i + (1 + i\gamma)|z(t)|^2\right]z(t) + b[z(t - \tau) - z(t)] \tag{4.2}$$

with $z \in \mathbb{C}$ and real parameters λ and γ. Here the Hopf frequency is normalized to unity. The feedback matrix B is represented by multiplication with a complex number $b = b_R + ib_I = b_0 e^{i\beta}$ with real b_R, b_I, β, and positive b_0. Note that the nonlinearity $f(\lambda, z(t)) = [\lambda + i + (1 + i\gamma)|z(t)|^2]z(t)$ commutes with complex rotations. Therefore $\exp(i\vartheta)z(t)$ solves (4.2), for any fixed ϑ, whenever $z(t)$ does. In particular, nonresonant Hopf bifurcations from the trivial solution $z \equiv 0$ at simple imaginary eigenvalues $\eta = i\omega \neq 0$ produce rotating wave solutions $z(t) = z(0)\exp\left(i\dfrac{2\pi}{T}t\right)$ with period $T = 2\pi/\omega$ even in the nonlinear case and with delay terms. This follows from uniqueness of the emanating Hopf branches.

Transforming Eq. (4.2) to amplitude and phase variables r, θ using $z(t) = r(t)e^{i\theta(t)}$, we obtain at $b = 0$

$$\dot{r} = \left(\lambda + r^2\right)r \tag{4.3}$$

$$\dot{\theta} = 1 + \gamma r^2. \tag{4.4}$$

An unstable periodic orbit (UPO) with $r = \sqrt{-\lambda}$ and period $T = 2\pi/(1 - \gamma\lambda)$ exists for $\lambda < 0$. This is the orbit we will stabilize. We will call it the *Pyragas orbit*. At $\lambda = 0$ a subcritical Hopf bifurcation occurs, and the steady state $z = 0$ loses its stability. The Pyragas control method chooses delays as $\tau_P = nT$. This defines the local *Pyragas curve* in the (λ, τ)-plane for any $n \in \mathbb{N}$,

$$\tau_P(\lambda) = \frac{2\pi n}{1 - \gamma\lambda} = 2\pi n(1 + \gamma\lambda + \cdots), \tag{4.5}$$

which emanates from the Hopf bifurcation points $\lambda = 0$, $\tau = 2\pi n$.

Under further nondegeneracy conditions, the Hopf point $\lambda = 0$, $\tau = nT$ ($n \in \mathbb{N}_0$) continues to a Hopf bifurcation curve $\tau_H(\lambda)$ for $\lambda < 0$. We determine this *Hopf curve* next. It is characterized by purely imaginary eigenvalues $\eta = i\omega$ of the transcendental characteristic equation

$$\eta = \lambda + i + b(e^{-\eta\tau} - 1), \tag{4.6}$$

which results from the linearization at the steady state $z = 0$ of the delayed system (4.2). Separating Eq. (4.6) into real and imaginary parts

$$0 = \lambda + b_0[\cos(\beta - \omega\tau) - \cos\beta] \tag{4.7}$$
$$\omega - 1 = b_0[\sin(\beta - \omega\tau) - \sin\beta] \tag{4.8}$$

and using the trigonometric identity

$$[\cos(\beta - \omega\tau)]^2 + [\sin(\beta - \omega\tau)]^2 = 1 \tag{4.9}$$

to eliminate $\omega(\lambda)$ from Eqs. (4.7), (4.8) yields an explicit expression for the multivalued Hopf curve $\tau_H(\lambda)$ for a given control amplitude b_0 and phase β:

$$\tau_H = \frac{\pm \arccos\left(\frac{b_0 \cos\beta - \lambda}{b_0}\right) + \beta + 2\pi n}{1 - b_0 \sin\beta \mp \sqrt{\lambda(2b_0 \cos\beta - \lambda) + b_0^2 \sin^2\beta}}. \tag{4.10}$$

Note that τ_H is not defined in the case of $\beta = 0$ and $\lambda < 0$. Thus complex b is a necessary condition for the existence of the Hopf curve in the subcritical regime $\lambda < 0$. Figure 4.1 displays the family of Hopf curves $n = 0, 1, \ldots$ (solid), Eq. (4.10), and the Pyragas curve $n = 1$ (dashed), Eq. (4.5), in the (λ, τ) plane. In Fig. 4.1 (b) the domains of instability of the trivial steady state $z = 0$, bounded by the Hopf curves, are marked by light grey shading. The dimensions of the unstable manifold of $z = 0$ are given in parentheses along the τ-axis in Fig. 4.1 (b). By construction, the delay τ becomes a multiple of the minimal period T of the bifurcating Pyragas orbits along the Pyragas curve $\tau = \tau_P(\lambda) = nT$, and the time delayed feedback term vanishes on these periodic orbits. The inset of Fig. 4.2 displays the Hopf and Pyragas curves for different values of the feedback b_0. These choices of b_0 are displayed as full circles in the main figure, which shows the domain of control in the plane of the complex feedback gain b. For $b_0 > b_0^{\mathrm{crit}}$ (a) the Pyragas curve runs partly inside the Hopf curve. With decreasing magnitude of b_0 the Hopf curves pull back to the right in the (λ, τ)-plane until the Pyragas curves lie fully outside the instability regime of the trivial steady state (c). At the critical feedback value (b) the Pyragas and Hopf curves are tangent at $(\lambda = 0, \tau = 2\pi)$.

Standard exchange of stability results [30], which hold verbatim for delay equations, then assert that the bifurcating branch of periodic solutions locally inherits linear asymptotic (in)stability from the trivial steady state, i.e., it con-
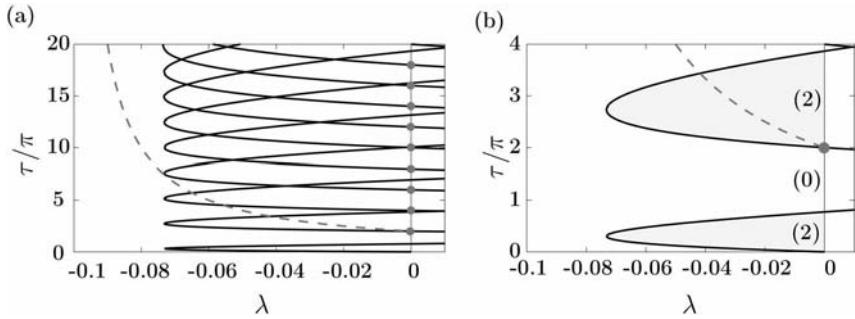
Fig. 4.1 Pyragas (dashed) and Hopf (solid) curves in the (λ, τ)-plane: (a) Hopf bifurcation curves $n = 0, ..., 10$, (b) Hopf bifurcation curves $n = 0, 1$ in an enlarged scale. Light grey shading marks the domains of unstable $z = 0$ and numbers in parentheses denote the dimension of the unstable manifold of $z = 0$ ($\gamma = -10$, $b_0 = 0.3$, and $\beta = \pi/4$).
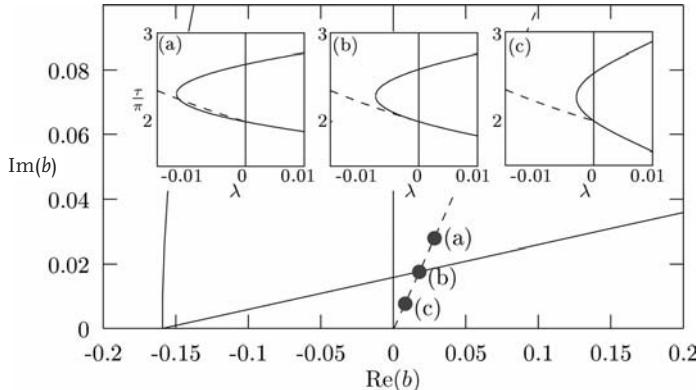
Fig. 4.2 Change of Hopf curves with varying control amplitude b_0. The main figure shows the complex plane of control gain b. The three values marked by full circles correspond to the insets (a), (b), (c), where the Hopf (solid) and Pyragas (dashed) curves are displayed for $\beta = \frac{\pi}{4}$ and three different choices of b_0: (a) $b_0 = 0.04 > b_0^{\text{crit}}$, (b) $b_0 = 0.025 \approx b_0^{\text{crit}}$, and (c) $b_0 = 0.01 < b_0^{\text{crit}}$ ($\lambda = -0.005$, $\gamma = -10$).

sists of stable periodic orbits on the Pyragas curve $\tau_P(\lambda)$ inside the shaded domains for small $|\lambda|$. We stress that an unstable trivial steady state is not a sufficient condition for stabilization of the Pyragas orbit. In fact, the stabilized Pyragas orbit can become unstable again if $\lambda < 0$ is further decreased, for instance in a torus bifurcation. However, there exists an interval for values of λ in our example for which Pyragas stabilization occurs. More precisely, for small $|\lambda|$ unstable periodic orbits possess a single Floquet multiplier $\mu = \exp(\Lambda\tau)$ with $1 < \mu < \infty$, near unity, which is simple. All other nontrivial Floquet multipliers lie strictly inside the complex unit circle. In particular, the (strong) unstable dimension of these periodic orbits is odd, here 1, and their unstable manifold is two dimensional. This is shown in Fig. 4.3 (a) (top), which depicts solutions Λ
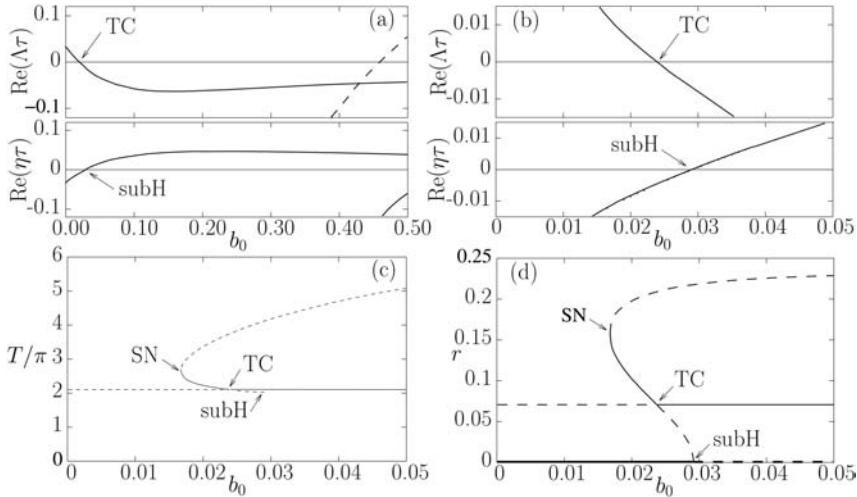
Fig. 4.3 (a) Top: Real part of Floquet exponents Λ of the periodic orbit vs. feedback amplitude b_0. Bottom: Real part of the eigenvalue η of the steady state vs. feedback amplitude b_0. (b) Blow-up of (a). (c) periods and (d) radii of the periodic orbits vs. b_0. The solid and dashed curves correspond to stable and unstable periodic orbits, respectively. Parameters in all panels: $\lambda = -0.005$, $\gamma = -10$, $\tau = \frac{2\pi}{1-\gamma\lambda}$, $\beta = \pi/4$.

of the characteristic equation of the periodic solution on the Pyragas curve (see the appendix).

The largest real part of Λ is positive for $b_0 = 0$. Thus the periodic orbit is unstable. As the amplitude of the feedback gain increases, the largest real part of the eigenvalue becomes smaller and eventually changes sign at a transcritical bifurcation (TC). Hence the periodic orbit is stabilized. Note that an infinite number of Floquet exponents are created by the control scheme; their real parts tend to $-\infty$ in the limit $b_0 \to 0$, and some of them may cross over to positive real parts for larger b_0 (dashed line in Fig. 4.3 (a)), terminating the stability of the periodic orbit.

Panel (a) (bottom) illustrates the stability of the steady state by displaying the largest real part of the eigenvalues η. The interesting region of the top and bottom panels where the periodic orbit becomes stable and the fixed point loses stability is magnified in panel (b).

Figure 4.4 shows the behavior of the Floquet multipliers $\mu = \exp(\Lambda\tau)$ of the Pyragas orbit in the complex plane with the increasing amplitude of the feedback gain b_0 as a parameter (marked by arrows). There is an isolated real multiplier crossing the unit circle at $\mu = 1$, in contrast to the result stated in [20]. This is caused by a transcritical bifurcation in which the Pyragas orbit collides with a delay-induced stable periodic orbit. In panels (c) and (d) of Fig. 4.3 the periods and radii of all circular periodic orbits ($r = \text{const}$) are plotted versus the feedback strength b_0. For small b_0 only the initial (unstable) Pyragas orbit (T and r independent of b_0) and the steady state $r = 0$ (stable) exist. With in-
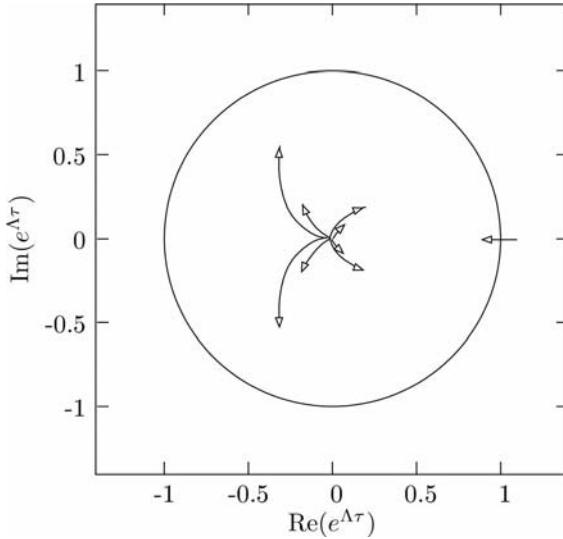
Fig. 4.4 Floquet multipliers $\mu = \exp(\Lambda\tau)$ in the complex plane with the feedback amplitude $b_0 \in [0, 0.3]$. Arrows indicate the direction of increasing b_0. Same parameters as in Fig. 4.3.

creasing b_0 a pair of unstable/stable periodic orbits is created in a saddle-node (SN) bifurcation. The stable one of the two orbits (solid) then exchanges stability with the Pyragas orbit in a transcritical bifurcation (TC), and finally ends in a subcritical Hopf bifurcation (subH), where the steady state $r = 0$ becomes unstable. The Pyragas orbit continues as a stable periodic orbit for larger b_0. Except at TC, the delay-induced orbit has a period $T \neq \tau$ (see Fig. 4.3 (c)). Note that the respective exchanges of stability of the Pyragas orbit (TC) and the steady state (subH) occur at slightly different values of b_0. This is also corroborated by Fig. 4.3 (b). The mechanism of stabilization of the Pyragas orbit by a transcritical bifurcation relies upon the possible existence of such delay-induced periodic orbits with $T \neq \tau$, which was overlooked, e.g., in [20]. Technically, the proof of the odd-number limitation theorem in [20] fails because the trivial Floquet multiplier $\mu = 1$ (Goldstone mode of the periodic orbit) was neglected there; $F(1)$ in equation (14) in [20] is thus zero and not less than zero, as assumed [31]. At TC, where a second Floquet multiplier crosses the unit circle, this results in a Floquet multiplier $\mu = 1$ of algebraic multiplicity 2.

4.3
Conditions on the Feedback Gain

Next we analyze the conditions under which stabilization of the subcritical periodic orbit is possible. From Fig. 4.1 (b) it is evident that the Pyragas curve must lie inside the yellow region, i.e., the Pyragas and Hopf curves emanating from

the point $(\lambda, \tau) = (0, 2\pi)$ must locally satisfy the inequality $\tau_H(\lambda) < \tau_P(\lambda)$ for $\lambda < 0$. More generally, let us investigate the eigenvalue crossings of the Hopf eigenvalues $\eta = i\omega$ along the τ-axis of Fig. 4.1. In particular, we derive conditions for the unstable dimensions of the trivial steady state near the Hopf bifurcation point $\lambda = 0$ in our model equation (4.2). On the τ-axis ($\lambda = 0$), the characteristic equation (4.6) for $\eta = i\omega$ is reduced to

$$\eta = i + b(e^{-\eta\tau} - 1), \tag{4.11}$$

and we obtain two series of Hopf points given by

$$0 \leq \tau_n^A = 2\pi n \tag{4.12}$$

$$0 < \tau_n^B = \frac{2\beta + 2\pi n}{1 - 2b_0 \sin\beta} \quad (n = 0, 1, 2, \ldots). \tag{4.13}$$

The corresponding Hopf frequencies are $\omega^A = 1$ and $\omega^B = 1 - 2b_0 \sin\beta$. Note that series A consists of all Pyragas points, since $\tau_n^A = nT = \frac{2\pi n}{\omega^A}$. In series B the integers n have to be chosen such that the delay $\tau_n^B \geq 0$. The case $b_0 \sin\beta = 1/2$, only, corresponds to $\omega^B = 0$ and does not occur for finite delays τ.

We evaluate the crossing directions of the critical Hopf eigenvalues next, along the positive τ-axis and for both series. Abbreviating $\frac{\partial}{\partial\tau}\eta$ by η_τ the crossing direction is given by $\text{sign}(\text{Re}\eta_\tau)$. Implicit differentiation of (4.1) with respect to τ at $\eta = i\omega$ implies

$$\text{sign}(\text{Re}\eta_\tau) = -\text{sign}(\omega)\,\text{sign}(\sin(\omega\tau - \beta)). \tag{4.14}$$

We are interested specifically in the Pyragas-Hopf points of series A (marked by dots in Fig. 4.1) where $\tau = \tau_n^A = 2\pi n$ and $\omega = \omega^A = 1$. Indeed $\text{sign}(\text{Re}\eta_\tau) = \text{sign}(\sin\beta) > 0$ holds, provided we assume $0 < \beta < \pi$, i.e., $b_I > 0$ for the feedback gain. This condition alone, however, is not sufficient to guarantee stability of the steady state for $\tau < 2n\pi$. We also have to consider the crossing direction $\text{sign}(\text{Re}\eta_\tau)$ along series B, $\omega^B = 1 - 2b_0 \sin\beta$, $\omega^B\tau_n^B = 2\beta + 2\pi n$, for $0 < \beta < \pi$. Equation (4.14) now implies $\text{sign}(\text{Re}\eta_\tau) = \text{sign}(2b_0 \sin\beta - 1))\sin\beta) = \text{sign}(2b_0 \sin\beta - 1)$.

To compensate for the destabilization of $z = 0$ upon each crossing of any point $\tau_n^A = 2\pi n$, we must require stabilization ($\text{sign}(\text{Re}\eta_\tau) < 0$) at each point τ_n^B of series B. If $b_0 \geq 1/2$, this requires $0 < \beta < \arcsin(1/(2b_0))$ or $\pi - \arcsin(1/(2b_0)) < \beta < \pi$. The distance between two successive points τ_n^B and τ_{n+1}^B is $2\pi/\omega^B > 2\pi$. Therefore, there is at most one τ_n^B between any two successive Hopf points of series A. Stabilization requires exactly one such τ_n^B, specifically: $\tau_{k-1}^A < \tau_{k-1}^B < \tau_k^A$ for all $k = 1, 2, \ldots, n$. This condition is satisfied if, and only if

$$0 < \beta < \beta_n^*, \tag{4.15}$$

where $0 < \beta_n^* < \pi$ is the unique solution of the transcendental equation

$$\frac{1}{\pi}\beta_n^* + 2nb_0 \sin\beta_n^* = 1. \tag{4.16}$$

This holds because the condition $\tau_{k-1}^A < \tau_{k-1}^B < \tau_k^A$ first fails when $\tau_{k-1}^B = \tau_k^A$. Equation (4.15) represents a necessary but not yet sufficient condition that the Pyragas choice $\tau_P = nT$ for the delay time will stabilize the periodic orbit.

To evaluate the remaining condition, $\tau_H < \tau_P$ near $(\lambda, \tau) = (0, 2\pi)$, we expand the exponential in the characteristic equation (4.6) for $\omega\tau \approx 2\pi n$, and obtain the approximate Hopf curve for small $|\lambda|$:

$$\tau_H(\lambda) \approx 2\pi n - \frac{1}{b_I}(2\pi n b_R + 1)\lambda. \tag{4.17}$$

Recalling (4.5), the Pyragas stabilization condition $\tau_H(\lambda) < \tau_P(\lambda)$ is therefore satisfied for $\lambda < 0$ if, and only if,

$$\frac{1}{b_I}\left(b_R + \frac{1}{2\pi n}\right) < -\gamma. \tag{4.18}$$

Equation (4.18) defines a domain in the plane of the complex feedback gain $b = b_R + ib_I = b_0 e^{i\beta}$ bounded from below (for $\gamma < 0 < b_I$) by the straight line

$$b_I = \frac{1}{-\gamma}\left(b_R + \frac{1}{2\pi n}\right). \tag{4.19}$$

Equation (4.16) represents a curve $b_0(\beta)$, i.e.,

$$b_0 = \frac{1}{2n\sin\beta}\left(1 - \frac{\beta}{\pi}\right), \tag{4.20}$$

which forms the upper boundary of a domain given by inequality (4.15). Thus Eqs. (4.19) and (4.20) describe the boundaries of the domain of control in the complex plane of the feedback gain b in the limit of small λ. Figure 4.5 depicts this domain of control for $n = 1$, i.e., a time delay $\tau = \frac{2\pi}{1 - \gamma\lambda}$. The lower and upper solid curves correspond to Eqs. (4.19) and (4.20), respectively. The grayscale displays the numerical result of the largest real part, wherever < 0, of the Floquet exponent, calculated from linearization of the amplitude and phase equations around the periodic orbit (see the appendix). Outside the shaded areas the periodic orbit is not stabilized. With increasing $|\lambda|$ the domain of stabilization shrinks, as the deviations from the linear approximation (4.17) become larger. For sufficiently large $|\lambda|$ stabilization is no longer possible, in agreement with Fig. 4.1 (b). Note that for real values of b, i.e., $\beta = 0$, no stabili-
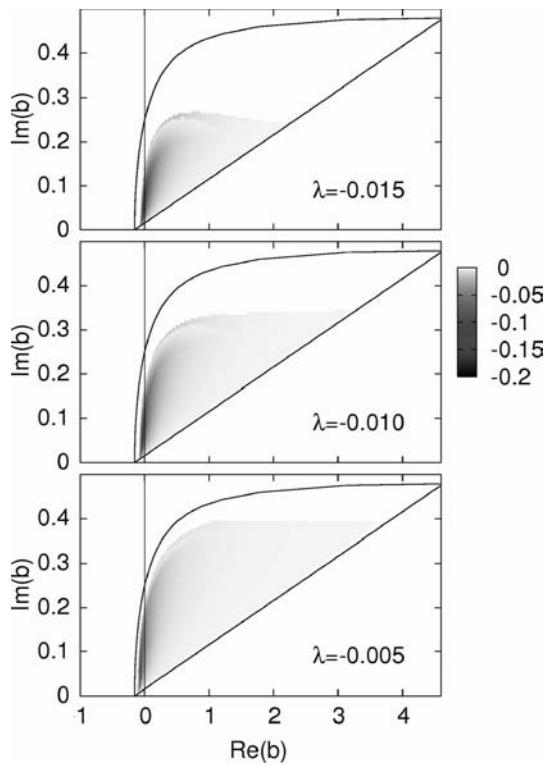
Fig. 4.5 Domain of control in the plane of the complex feedback gain $b = b_0 e^{i\beta}$ for three different values of the bifurcation parameter λ. The solid curves indicate the boundary of stability in the limit $\lambda \nearrow 0$, (see (4.19), (4.20)). The shading shows the magnitude of the largest (negative) real part of the Floquet exponents of the periodic orbit ($\gamma = -10$, $\tau = \frac{2\pi}{1-\gamma\lambda}$).
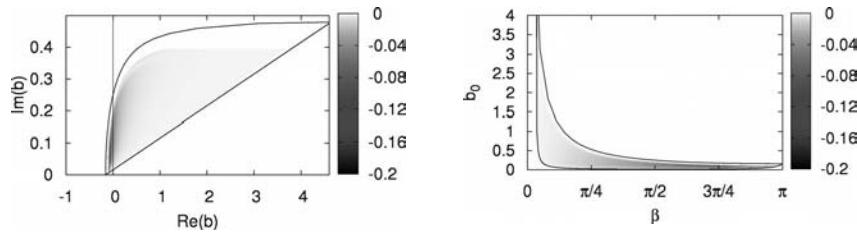
Fig. 4.6 Domain of control in the complex b-plane (left) and the β-b_0-plane (right) ($\lambda = -0.005$, $\gamma = -10$, $\tau = \frac{2\pi}{1-\gamma\lambda}$).

zation occurs at all. Hence, stabilization fails if the feedback matrix B is a multiple of the identity matrix. Figure 4.6 compares the control domain for the same value of $|\lambda|$ for the representation in the planes of complex feedback b (left), and amplitude b_0 and phase β (right).

4.4
Conclusion

In conclusion, we have refuted a theorem which claims that a periodic orbit with an odd number of real Floquet multipliers greater than unity can never be stabilized by time delayed feedback control. For this purpose we have analyzed the generic example of the normal form of a subcritical Hopf bifurcation, which is paradigmatic for a large class of nonlinear systems. We have worked out explicit analytical conditions for stabilization of the periodic orbit generated by a subcritical Hopf bifurcation in terms of the amplitude and the phase of the feedback control gain [32]. Our results underline the crucial role of a nonvanishing phase of the control signal for stabilization of periodic orbits violating the odd-number limitation. The feedback phase is readily accessible and can be adjusted, for instance, in laser systems, where subcritical Hopf bifurcation scenarios are abundant and Pyragas control can be realized via coupling to an external Fabry-Perot resonator [18]. The importance of the feedback phase for the stabilization of steady states in lasers [18] and neural systems [33], as well as for stabilization of periodic orbits by a time delayed feedback control scheme using spatio-temporal filtering [34], has been noted recently. Here, we have shown that the odd-number limitation does not hold in general, which opens up fundamental questions as well as a wide range of applications. The result will not only be important for practical applications in physical sciences, technology, and life sciences, where one might often desire to stabilize periodic orbits with an odd number of positive Floquet exponents, but also for tracking of unstable orbits and bifurcation analysis using time delayed feedback control [35].

Acknowledgments

Appendix: Calculation of Floquet Exponents

The Floquet exponents of the Pyragas orbit can be calculated explicitly by rewriting Eq. (4.2) in polar coordinates $z = r\,e^{i\theta}$

$$\dot{r} = (\lambda + r^2)\, r + b_0[\cos(\beta + \theta(t-\tau) - \theta)\, r(t-\tau) - \cos(\beta)\, r] \tag{4.21}$$

$$\dot{\theta} = 1 + \gamma r^2 + b_0[\sin(\beta + \theta(t-\tau) - \theta)\, \frac{r(t-\tau)}{r} - \sin(\beta)] \tag{4.22}$$

and linearizing around the periodic orbit according to $r(t) = r_0 + \delta r(t)$ and $\theta(t) = \Omega t + \delta\theta(t)$, with $r_0 = \sqrt{-\lambda}$ and $\Omega = 1 - \gamma\lambda$ (see Eq. (4.3)). This yields

$$\begin{pmatrix} \delta\dot{r}(t) \\ \delta\dot{\theta}(t) \end{pmatrix} = \begin{bmatrix} -2\lambda - b_0\cos\beta & b_0 r_0 \sin\beta \\ 2\gamma r_0 - b_0 \sin\beta\, r_0^{-1} & -b_0\cos\beta \end{bmatrix} \begin{pmatrix} \delta r(t) \\ \delta\theta(t) \end{pmatrix} \tag{4.23}$$

$$+ \begin{bmatrix} b_0\cos\beta & -b_0 r_0 \sin\beta \\ b_0\sin\beta r_0^{-1} & b_0\cos\beta \end{bmatrix} \begin{pmatrix} \delta r(t-\tau) \\ \delta\theta(t-\tau) \end{pmatrix}. \tag{4.24}$$

With the ansatz

$$\begin{pmatrix} \delta r(t) \\ \delta\theta(t) \end{pmatrix} = u\, \exp(\Lambda t), \tag{4.25}$$

where u is a two-dimensional vector, one obtains the autonomous linear equation

$$\begin{pmatrix} -2\lambda + b_0\cos\beta\,(e^{-\Lambda\tau} - 1) - \Lambda & -b_0 r_0 \sin\beta\,(e^{-\Lambda\tau} - 1) \\ 2\gamma r_0 + b_0 r_0^{-1}\sin\beta\,(e^{-\Lambda\tau} - 1) & b_0\cos\beta\,(e^{-\Lambda\tau} - 1) - \Lambda \end{pmatrix} u = 0. \tag{4.26}$$

The condition of vanishing determinant then gives the transcendental characteristic equation

$$\begin{aligned} 0 = &\left(-2\lambda + b_0\cos\beta\,(e^{-\Lambda\tau} - 1) - \Lambda\right)\left(b_0\cos\beta\,(e^{-\Lambda\tau} - 1) - \Lambda\right) \\ &- b_0 r_0 \sin\beta\,(e^{-\Lambda\tau} - 1)\left(2\gamma r_0 + b_0 r_0^{-1}\sin\beta\,(e^{-\Lambda\tau} - 1)\right) \end{aligned} \tag{4.27}$$

for the Floquet exponents Λ, which can be solved numerically.

References

1 E. Ott, C. Grebogi, and J. A. Yorke: *Controlling chaos*, Phys. Rev. Lett. **64**, 1196 (1990).

2 H. G. Schuster (ed.): *Handbook of Chaos Control*, 1st ed. (Wiley-VCH, Weinheim, 1999).

3 S. Boccaletti, C. Grebogi, Y. C. Lai, H. Mancini, and D. Maza: *The control of chaos: theory and applications*, Phys. Rep. **329**, 103 (2000).

4 D. J. Gauthier: *Resource letter: Controlling chaos*, Am. J. Phys. **71**, 750 (2003).

5 K. Pyragas: *Continuous control of chaos by self-controlling feedback*, Phys. Lett. A **170**, 421 (1992).

6 K. Pyragas and A. Tamaševičius: *Experimental control of chaos by delayed self-controlling feedback*, Phys. Lett. A **180**, 99 (1993).

7 S. Bielawski, D. Derozier, and P. Glorieux: *Controlling unstable periodic orbits by a delayed continuous feedback*, Phys. Rev. E **49**, R971 (1994).

8 T. Pierre, G. Bonhomme, and A. Atipo: *Controlling the chaotic regime of nonlinear ionization waves using time delay autosyn-*

chronisation method, Phys. Rev. Lett. **76**, 2290 (1996).

9 K. Hall, D.J. Christini, M. Tremblay, J.J. Collins, L. Glass, and J. Billette: *Dynamic control of cardiac alterans*, Phys. Rev. Lett. **78**, 4518 (1997).

10 D.W. Sukow, M.E. Bleich, D.J. Gauthier, and J.E.S. Socolar: *Controlling chaos in a fast diode resonator using time delay auto-synchronisation: Experimental observations and theoretical analysis*, Chaos **7**, 560 (1997).

11 O. Lüthje, S. Wolff, and G. Pfister: *Control of chaotic Taylor-Couette flow with time delayed feedback*, Phys. Rev. Lett. **86**, 1745 (2001).

12 P. Parmananda, R. Madrigal, M. Rivera, L. Nyikos, I.Z. Kiss, and V. Gáspár: *Stabilization of unstable steady states and periodic orbits in an electrochemical system using delayed-feedback control*, Phys. Rev. E **59**, 5266 (1999).

13 J.M. Krodkiewski and J.S. Faragher: *Stabilization of motion of helicopter rotor blades using delayed feedback-modelling, computer simulation and experimental verification*, J. Sound Vib. **234**, 591 (2000).

14 T. Fukuyama, H. Shirahama, and Y. Kawai: *Dynamical control of the chaotic state of the current-driven ion acoustic instability in a laboratory plasma using delayed feedback*, Phys. Plasmas **9**, 4525 (2002).

15 C. von Loewenich, H. Benner, and W. Just: *Experimental relevance of global properties of time delayed feedback control*, Phys. Rev. Lett. **93**, 174101 (2004).

16 M.G. Rosenblum and A.S. Pikovsky: Phys. Rev. Lett. **92**, 114102 (2004).

17 O.V. Popovych, C. Hauptmann, and P.A. Tass: *Effective desynchronization by nonlinear delayed feedback*, Phys. Rev. Lett. **94**, 164102 (2005).

18 S. Schikora, P. Hövel, H.-J. Wünsche, E. Schöll, and F. Henneberger: *All-optical noninvasive control of unstable steady states in a semiconductor laser*, Phys. Rev. Lett. **97**, 213902 (2006).

19 W. Just, T. Bernard, M. Ostheimer, E. Reibold, and H. Benner: *Mechanism of time delayed feedback control*, Phys. Rev. Lett. **78**, 203 (1997).

20 H. Nakajima: *On analytical properties of delayed feedback control of chaos*, Phys. Lett. A **232**, 207 (1997).

21 H. Nakajima and Y. Ueda: *Limitation of generalized delayed feedback control*, Physica D **111**, 143 (1998).

22 I. Harrington and J.E.S. Socolar: *Limitation on stabilizing plane waves via time delay feedback*, Phys. Rev. E **64**, 056206 (2001).

23 K. Pyragas, V. Pyragas, and H. Benner: *Delayed feedback control of dynamical systems at subcritical Hopf bifurcation*, Phys. Rev. E **70**, 056222 (2004).

24 V. Pyragas and K. Pyragas: *Delayed feedback control of the Lorentz system: An analytical treatment at a subcritical Hopf bifurcation*, Phys. Rev. E **73**, 036215 (2006).

25 J.E.S. Socolar, D.W. Sukow, and D.J. Gauthier: *Stabilizing unstable periodic orbits in fast dynamical systems*, Phys. Rev. E **50**, 3245 (1994).

26 H.G. Schuster and M.B. Stemmler: *Control of chaos by oscillating feedback*, Phys. Rev. E **56**, 6410 (1997).

27 H. Nakajima and Y. Ueda: *Half-period delayed feedback control for dynamical systems with symmetries*, Phys. Rev. E **58**, 1757 (1998).

28 K. Pyragas: *Control of chaos via an unstable delayed feedback controller*, Phys. Rev. Lett. **86**, 2265 (2001).

29 B. Fiedler, V. Flunkert, M. Georgi, P. Hövel, and E. Schöll: *Refuting the odd-number limitation of time delayed feedback control*, Phys. Rev. Lett. **98**, 114101 (2007).

30 O. Diekmann, S.A. van Gils, S.M.V. Lunel, and H.-O. Walther: *Delay Equations*. Springer, New York 1995.

31 A. Amann (private communication).

32 For the complex conjugate values of *b*, stabilization of the periodic orbit can be shown by analogous arguments.

33 M.G. Rosenblum and A.S. Pikovsky: *Delayed feedback control of collective synchrony: An approach to suppression of pathological brain rhythms*, Phys. Rev. E **70**, 041904 (2004).

34 N. Baba, A. Amann, E. Schöll, and W. Just: *Giant improvement of time delayed feedback control by spatio-temporal filtering*, Phys. Rev. Lett. **89**, 074101 (2002).

35 J. Sieber and B. Krauskopf: *Control based bifurcation analysis for experiments*, Nonlinear Dynamics, DOI: 10.1007/s11071-007-9217-2 (2007).

5
On Global Properties of Time Delayed Feedback Control

Wolfram Just

5.1
Introduction

Topics in control are a genuine subject in engineering and applied mathematics. Such a field was developed in the wake of the Second World War [1]. Although it is virtually not possible to give a comprehensive overview of the whole subject, it is often an essential feature of standard control approaches to use to some extent structural information about the underlying dynamics, the possibility of reconstructing dynamical equations of motion from measured signal, or focus on simple time independent target states. There exists a rather complete theory for linear systems. Furthermore, global aspects of the dynamics can be dealt with by Lyapunov techniques which are applicable when the underlying equations of motion are known. From such a perspective control theory provides a strong link to optimization problems.

Within control theory different types of methods have been classified. Actually, from the point of view of applications it usually does not matter whether the method is invasive, i.e., a finite control force has to be applied when the target state is reached, or noninvasive. The latter type, often called orbit control in the engineering context, stabilizes genuine unstable motion of the dynamical system and requires only small control forces. Such an idea was combined in the early 90s with properties of chaotic dynamical systems to solve the so-called pole placement problem for the stabilization of unstable periodic states by applying tiny control forces [2]. Dynamical system approaches, i.e., stable and unstable manifolds were employed to design suitable control algorithms for controlling the huge number of unstable states embedded in chaotic attractors by application of tiny control forces. Although such an idea was known to some extent by engineers it became quite popular among physicists [3].

On the other hand, stabilization of time-periodic states without any knowledge of the structure of the underlying dynamics still posed some challenge in particular when noninvasive methods are of interest, which can, e.g., be used for spectroscopic purposes as well. Control techniques based on suitable time

delayed feedback of measured signals have been proposed for such a purpose [4] and have been applied to a variety of experimental setups, e.g., for the control of laser systems [5], Taylor-Couette flows [6], in ferromagnetic resonance experiments [7], in electrochemical cells [8], and of course for demonstration purpose in elastomechanics [9] and electronic circuit experiments [10]. Even applications in biosystems have been reported [11], although some of the setups do not result in a completely noninvasive scheme.

Although motion with time delay results in dynamical systems with infinite-dimensional phase space, there exists a fairly comprehensive approach to solve linear equations of motion, in particular for the autonomous case [12]. Thus, most systematic theoretical investigations of time delayed feedback control have been based so far on linear stability analysis (cf. e.g. [13–15]). Several universal features of the control scheme were uncovered by such an approach. Periodic orbits with an odd number of positive unstable Floquet multipliers cannot be stabilized by plain time delayed feedback schemes [16], but such a constraint does not apply in general for autonomous systems (see chapter 4 for a detailed discussion of this case). In fact, most examples where time delayed feedback control has been applied successfully use unstable periodic orbits which were generated in a period doubling cascade where such an "odd-number limitation" does not apply. Furthermore, simple time delayed feedback control fails for systems with fast time scales [17], or systems with large Floquet exponents [18]. Modifications of plain time delayed feedback control were able to overcome such limitations. Application of an external periodic modulation, so-called rhythmic control [19–21], or an unstable control loop [22] can cope with the odd-number limitation while the application of multiple time delay, so-called extended time delayed feedback control [17], allows for the stabilization of periodic states in fast systems. Other important aspects have been addressed as well. Above all, methods for the adjustment of suitable delay times have been developed [23–25] and the influence of control loop latency has been analysed in some detail [26, 27]. Meanwhile even comprehensive overviews of approaches based on linear analysis are available in the literature (cf. e.g. [28, 29]).

Time-delayed feedback control aims at stabilization of time-periodic states when no information about the underlying dynamical system is available, apart from a measured signal $s(t)$. Thus analytical approaches should be based on general equations of motion which do not make reference to any particular model [14]. Time-delayed feedback control applies a control force $F(t) = K(s(t) - s(t - \tau))$ generated from a time delayed difference to a dynamical system so that the most general setup reads

$$\dot{\underline{x}}(t) = \underline{f}(\underline{x}(t), F(t)), \qquad (5.1)$$

where the measured signal is some, in general unknown, function of the internal degrees of freedom, $s(t) = g(\underline{x}(t))$. If the time delay τ is chosen such that it coincides with an integer multiple of the period of the target state, then the control force will vanish when the target state is reached and the control
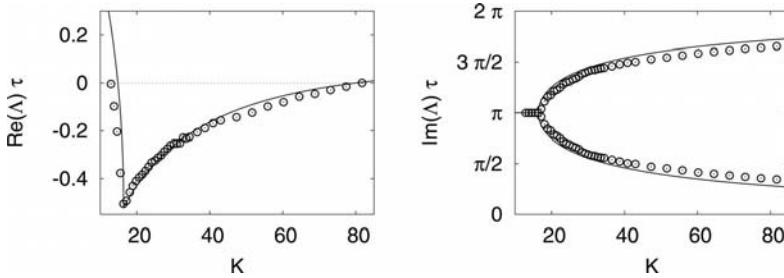
Fig. 5.1 Typical dependence of the leading Floquet exponent Λ on the control amplitude, for an unstable periodic orbit generated in a period doubling sequence. Symbols: experimental data from an electronic circuit experiment, line: analytical result according to a mean field like expansion (cf. [30] for details).

scheme is potentially noninvasive. Even within such a general setup one is able to discuss the linear stability of the target state and the performance of the control scheme [14]. Results for the stability exponents obtained in such a way are in agreement with measurements (cf. Fig. 5.1) and yield some of the universal features of time delayed feedback control. In particular, depending on the control amplitude K a domain, usually an interval, is obtained where the control signal $s(t) - s(t - \tau)$ tends to zero, all stability exponents develop a negative real part, and control is successful. The boundaries of this interval are the control thresholds. At the lower threshold usually a flip or period doubling bifurcation appears which is responsible for the onset of control. At the upper threshold an instability with nontrivial frequency, i.e., a Hopf bifurcation, occurs. This upper threshold is often less robust and more vulnerable with respect to external perturbations. It is this threshold which will be of interest within our investigations, although similar arguments can be applied to the lower control threshold as well.

Since time delayed feedback control results in a system of differential-difference equations the corresponding linear stability analysis yields infinitely many eigenvalue branches reflecting the infinite-dimensional phase space of the dynamical system. Such branches can be detected even in experiments and may change the simple scenario sketched in Fig. 5.1 (cf. e.g. [30, 31]). Nevertheless, at a qualitative level one often gets reasonable agreement with the simple theory just sketched.

The basin of attraction, i.e., the set of initial conditions for which control works successfully, is one of the essential objects that cannot be assessed by linear analysis. Such a global feature of the control system is of central interest and has rarely been addressed so far for time delayed feedback control. If one assumes that the underlying equations of motion are known one would be able to estimate such basins, e.g., by the famous Lyapunov functional method which is available as well for time delay dynamics (cf. e.g. [32]). In fact, such ideas are very powerful, e.g., when one designs numerical tools for root finding. But such a concept cannot be employed easily for time delayed feedback control. We will

discuss such a link in Section 5.2. Although global properties of particular model systems subjected to time delayed feedback control can be estimated by numerical means, e.g., by employing continuation techniques [33] such a strategy can hardly yield generic features of basins of attraction. Furthermore, numerical techniques can be used for the computation of low-dimensional manifolds but are still not able to determine, e.g., an infinite-dimensional basin boundary. To overcome such problems basins for time delayed feedback control have been probed along low-dimensional cross sections by applying well-defined perturbations to the system under considerations [34] and the method has been even implemented in experiments [35]. One discovers structures for the basins of attraction that are comparable to those found in low-dimensional dynamical systems. But such features may depend on the underlying equations of motion and do not seem to provide a universal mechanism. On the other hand, a closer look at the instabilities determining the control boundaries can reveal a mechanism for generating basins that just depend on the type of instability and that do not rely on the details of the equations of motion [36]. These ideas will be briefly outlined in Section 5.3. The corresponding analytical normal form analysis will be described in Section 5.4 and some consequences for time delayed feedback control will be mentioned. To keep this part less technical we present the analysis within the setup of time-discrete dynamics although similar, but much more involved, considerations can be carried out for the more realistic time-continuous setup as well.

5.2
A Comment on Control and Root Finding Algorithms

Noninvasive control aims at stabilizing unstable orbits of the underlying dynamical system by application of asymptotically small control forces. Thus, in some abstract setting the application of the control loop replaces the original dynamical system by a different one which possesses the former unstable orbit as a stable object. From that point of view such control schemes have something in common with numerical root finding algorithms.

To illustrate the principal aspect of such an idea let us consider for simplicity a time-discrete dynamical system $x_{n+1} = f(x_n)$. An unstable periodic orbit of period p, i.e., a periodic point of order p, $\xi_* = f^p(\xi_*)$, should be the desired target state. If the equations of motion are known then the determination of that object reduces to finding the roots of $f^p(\xi_*) - \xi_* = 0$. There are plenty of algorithms available to perform such a task, one of the most famous being the Newton-Raphson method. This method results in an iteration scheme $x_{m+1} = x_m - (f^p(x_m) - x_m)/((f^p)'(x_m) - 1)$ which converges to the periodic point ξ_* for appropriate initial conditions. Thus, the Newton-Raphson method replaces the original dynamics with unstable periodic point ξ_* by a fictitious dynamics with stable point ξ_*. The desired target state can be simply obtained by iteration. In such a sense the scheme could be viewed as a control algorithm.

While the Newton-Raphson method has excellent local convergence properties since the sequence converges faster than exponentially toward the target state it is one of the classical examples having often quite poor global properties as the choice of the initial condition is crucial for convergence. The basin of attraction of the target state ξ_* is usually a quite complicated set with fractal basin boundary.

Thus, even for the numerical determination of periodic states one relies on different methods. Again one replaces the original motion by a fictitious dynamics which preserves preferably all periodic points of, say, period p. Following an idea introduced in [37] which was further refined in [38] and [39] one introduces the differential equation

$$\frac{dx}{ds} = -\gamma(f^p(x) - x) \qquad (5.2)$$

such that the stationary states of the solution $x(s)$ yield the desired target states ξ_*. The main benefit of this approach comes from the observation that at least for one-dimensional maps f the global properties of Eq. (5.2) can be determined easily as the differential equation (5.2) can be derived from a potential $dx/ds = -\gamma U'(x)$, where $U(x) = \int (f^p(x) - x)\,dx$ denotes a Lyapunov function. For such type of system it is quite easy to show that the energy $U(x(s))$ decreases for $\gamma > 0$ and any solution apart from those which stay at maxima of the potential tends toward a minimum of the potential. The basin of attraction of such a minimum is bounded by the two neighboring maxima (cf. Fig. 5.2). Straightforward integration of Eq. (5.2) for a few initial conditions yields all the minima of the potential. Reverting the sign of γ interchanges the role of maxima and minima and the same integration procedure now yields the maxima as
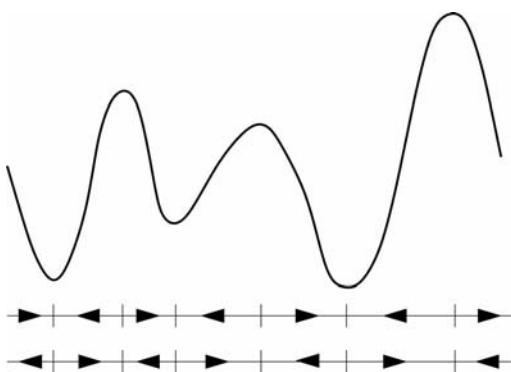
Fig. 5.2 Diagrammatic view of the potential $U(x) = \int (f^p(x) - x)\,dx$ governing the dynamics of Eq. (5.2). The critical points of the potential and the motion in the one-dimensional phase space for positive and negative values of γ are indicated as well.

well. Thus, all critical points of the potential, i.e., all the periodic points of the original dynamical system, can be obtained within a few steps.[1] These ideas can be generalized to higher dimensional maps [37–39] and it is possible to retain to some extent the potential structure which ensures the nice global properties, although it might be more difficult to obtain a priori estimates for the basins of attraction.

There is in fact no need to introduce a time-continuous fictitious dynamics. For instance, one may approximate the derivative by a finite stepsize estimate $(x_{m+1} - x_m)/\Delta s$ and thus obtains the fictitious map

$$x_{m+1} = x_m - \gamma \Delta s (f^p(x_m) - x_m). \tag{5.3}$$

As long as the stepsize Δs is sufficiently small so that the right-hand side is a monotonic function of x_m the good global properties of the time-continuous version are preserved due to the cobweb theorem. There are of course different ways to introduce a time-discrete version and the just mentioned Euler scheme is often not the most efficient way.

A superficial inspection of the scheme (5.3) suggests that a difference involving an iterated state plays a crucial role. From that perspective Eq. (5.3) seems to have something in common with time delayed feedback schemes. Actually, a simple time delayed feedback scheme for the stabilization of a period-p orbit reads

$$x_{n+1} = f(x_n) + K(x_n - x_{n-p}) \tag{5.4}$$

and it is tempting to discuss similarities and differences between Eqs. (5.3) and (5.4). First of all Eq. (5.3) has the same phase space dimension as the original one-dimensional map while the time delay dynamics (5.4) acts on a p-dimensional phase space. Such an increase of phase space dimension is a characteristic feature of any time delay system [32]. Thus, already the linear stability properties of both equations are different since the additional degrees of freedom inherent in the time delay may alter the stability properties of the target state [30]. It is now not surprising that time delayed feedback schemes do not share the nice global features of the Biham-Wenzel method since global dynamical features surely depend on the underlying phase space. Time-delayed feedback schemes, like Eq. (5.4), have of course the advantage to be based on the real-time dynamics so that their implementation in real applications is possible. It would be tempting to improve time delayed feedback control in such a way that it shares the nice potential properties of root finding algorithms, but no such improvement seems to be available at the moment. The study of global features of time delayed feedback control is nevertheless of great interest and nice global features like for the Biham-Wenzel scheme are surely the desired goal. Above

---

[1] The presentation used here differs from the original scheme proposed by Biham and Wenzel which is better adapted for numerical purposes. The approach used here is able to uncover the global properties of the root finding scheme.

all, a generic mechanism is needed which is independent of the underlying model, like the potential dynamics in the case of the Biham-Wenzel method, to determine the basins of attraction and the global performance of time delayed feedback schemes.

5.3
Codimension-Two Bifurcations and Basins of Attraction

Determination of basins of attraction is already a challenge for nonlinear ordinary differential equations and one cannot expect to give a full account for time delay dynamics. Here we will identify a simple mechanism based on local bifurcation theory which determines some basin of attraction in a generic way and which proves its relevance for time delayed feedback schemes.

5.3.1
The Transition from Super- to Subcritical Behavior

Let us just recall a few elementary features of Hopf bifurcations although such facts can be found in graduate textbooks (cf. e.g. [40]). When a system experiences a Hopf bifurcation an instability takes place where a fixed point becomes unstable with respect to two oscillating modes.[2] Thus the motion can be reduced to a two-dimensional coordinate, usually a complex number $z(t)$, which obeys the so-called normal form

$$\dot{z}(t) = \lambda z(t) + rz(t)|z(t)|^2. \tag{5.5}$$

Derivation of such an effective equation of motion can be found in textbooks (cf. Section 5.4.1 as well). The coefficient of the linear part coincides with the critical eigenvalue. $\text{Re}(\lambda) < 0$ yields a stable fixed point $z = 0$, a case which we will call the subthreshold regime, while $\text{Re}(\lambda) > 0$ yields an unstable fixed point, the superthreshold regime. The cubic coefficient r is essential for the nontrivial dynamics in the vicinity of the instability. Actually, from the very beginning one can confine to real-valued coefficients. Introducing polar coordinates $z = \rho \exp(i\phi)$ Eq. (5.5) is written as

$$\dot{\rho}(t) = \text{Re}(\lambda)\rho(t) + \text{Re}(r)\rho^3(t) \tag{5.6a}$$
$$\dot{\phi}(t) = \text{Im}(\lambda) + \text{Im}(r)\rho^2(t) \tag{5.6b}$$

---

2) Strictly speaking a Hopf bifurcation denotes an instability of a fixed point in a time-continuous system. Later on we will apply such a concept to the instability of periodic orbits as well, i.e., to fixed points in time-discrete maps. In such a case one often calls an instability caused by a complex conjugated pair of eigenvalues of a Neimark-Sacker bifurcation since some additional strong resonance conditions become important (cf. Appendix A). Here, in order to simplify the notation, we are a little by sloppy with the notation and call such an instability a Hopf bifurcation as well.

Fig. 5.3 Diagrammatic view of a supercritical (left: $\mathrm{Re}(r) < 0$) and subcritical (right: $\mathrm{Re}(r) > 0$) Hopf bifurcation (cf. Eq. (5.5)). Full line: stable fixed point/limit cycle, broken line: unstable fixed point/limit cycle. Bifurcation parameter $\mathrm{Re}\,\lambda$ increases from left to right.

so that imaginary parts of the coefficients just cause an amplitude-dependent oscillation. Equation (5.6a) obviously has a nontrivial stationary solution $\rho_\ell = (-\mathrm{Re}(\lambda)/\mathrm{Re}(r))^{1/2}$ whenever the square root is real valued. This nontrivial solution corresponds to a limit cycle of radius ρ_ℓ. Thus, if $\mathrm{Re}(r) < 0$ the limit cycle exists for $\mathrm{Re}(\lambda) > 0$, i.e., in the superthreshold regime where the trivial fixed point is unstable, while for $\mathrm{Re}(r) > 0$ the nontrivial solution exists in the region $\mathrm{Re}(\lambda) < 0$, i.e., the subthreshold regime (cf. Fig. 5.3). The stability of the resulting limit cycle can be easily evaluated from Eq. (5.6a) by computing the derivative of the right-hand side at ρ_ℓ, $-2\mathrm{Re}(\lambda)$. The limit cycle is stable for $\mathrm{Re}(r) < 0$, the so-called supercritical case, and unstable for $\mathrm{Re}(r) > 0$, the subcritical case.[3] The features are summarized in Fig. 5.3.

While a supercritical transition is continuous when changing the bifurcation parameter the subcritical transition is discontinuous showing hysteresis as well since a different dynamical state is attained in the superthreshold regime. In addition, in the subthreshold regime the unstable limit cycle which surrounds the stable fixed point yields the basin boundary (cf. Fig. 5.4). Thus subcritical behavior always suffers from small basins since the coexisting unstable limit cycle contracts toward the fixed point when the bifurcation point is approached. No such feature exists for the supercritical transition where the basin is determined by some global feature of the dynamics. Thus, basins remain large even close to the bifurcation point. This generic mechanism works in higher dimensional phase spaces as well where the stable manifold of the unstable limit cycle yields the basin boundary. Locally the basin has the topology of a higher dimensional cylinder (cf. Fig. 5.4).

When $\mathrm{Re}(\lambda)$ changes sign a Hopf bifurcation takes place which is either super- or subcritical depending on the sign of $\mathrm{Re}(r)$. If the latter quantity becomes small and changes sign as well then a codimension-two bifurcation takes place since two conditions $\mathrm{Re}(\lambda) = 0$ and $\mathrm{Re}(r) = 0$ have to be satisfied. Such a higher order instability governs the transition from super- to subcritical behavior. The universal features of such a transition depend on higher order terms in the normal form (5.5) and yield some information about the limit cycles in-

---

[3] Alternative notions for super-/subcritical bifurcations that can be found in the literature are continuous/discontinuous transitions or forward/inverse bifurcation.
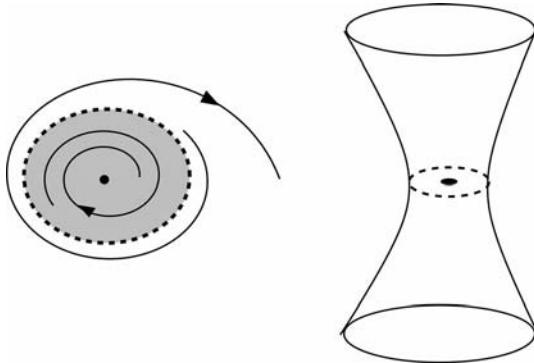
Fig. 5.4 Left: diagrammatic view of the two-dimensional phase space portrait close to a subcritical Hopf bifurcation in the subthreshold regime: unstable limit cycle (broken line) and basin of the stable fixed point (shaded).

Right: geometry of the stable manifold of the unstable limit cycle (broken line), i.e., the basin boundary of the stable fixed point, in a three-dimensional phase space.

volved in the Hopf bifurcation and the occurring hysteresis (cf. e.g. [40] for further details).

5.3.2
Probing Basins of Attraction in Experiments

As shown in the previous section subcritical bifurcations, i.e., discontinuous transitions and hysteresis, yield a limitation for the basin of the stable state at least when the bifurcation point is approached. This generic mechanism can also be relevant for time delayed feedback control, e.g., at the upper control threshold when a subcritical Hopf bifurcation occurs. The principal aspects of such a mechanism can be demonstrated by numerical simulations (cf. Section 5.4.2 or [36]) and it even proves its relevance in real experiments [35]. Here we just summarize the essential features. More details about the experiment can be found in chapter 26 of the book.

Detection of discontinuous transitions, e.g., at the upper control threshold, the corresponding bistability, and recording hysteresis, is easily accomplished by an adiabatic increase respectively decrease of the control amplitude. Discontinuity in the amplitude of the control signal $s(t) - s(t - \tau)$ shows up (cf. Fig. 5.5 for an experimental realization in an electronic circuit experiment). Thus, subcritical transitions are easily detected. Probing the basin of attraction of the stabilized periodic orbit in the subthreshold regime is a much more challenging task. The phase space of differential-difference equations is infinite-dimensional since the whole history enters the dynamics. The basin and the basin boundary are infinite-dimensional objects as well. Nevertheless, close to the bifurcation point the basin admits the geometry sketched in Fig. 5.4. Thus, if one applies a well-defined perturbation to the controlled system, e.g., a voltage pulse at a defi-
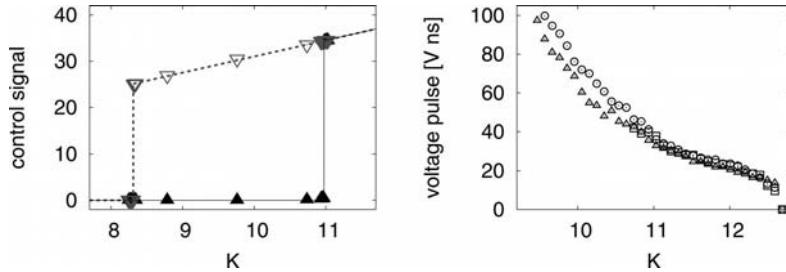
Fig. 5.5 Left: dependence of the amplitude of the control signal on the control amplitude K in an electronic circuit experiment: adiabatic increase (black, full symbols, line), adiabatic decrease (grey, open symbols, broken line) of K. Lines are a guide for the eye. Right: critical voltage pulse to destroy the controlled state, in dependence on the control amplitude. Different symbols correspond to different durations of the pulse.

nite value of the phase of the periodic orbit, then one probes the basin along a low-dimensional cross section in phase space, e.g., along a line or a two-dimensional surface. By monitoring the maximal strength of the pulse such that the system returns to the stabilized state one obtains an estimate for the diameter of the basin of attraction in this cross section. Experimental data displayed in Fig. 5.5 show indeed the characteristic S-shape for the diameter of the basin (cf. Fig. 5.3) when recorded in dependence on the control amplitude. Thus, subcritical bifurcations yield reduced basins of attraction and an enhanced sensitivity of the controlled systems with respect to external perturbations.

5.4
A Case Study of Global Features for Time-Delayed Feedback Control

Determination of the type of instability which limits control domains for time delayed feedback control is in principle quite straightforward [36]. But explicit computations of such normal forms become quite involved for time-continuous time delay equations [32] even when fairly simple model systems are considered (cf. e.g. [41, 42]). Here we want to illustrate the relevance of sub- and supercritical transitions for the formation of basins of attraction. For the purpose of visualization we even want to avoid the problems that are related to infinite-dimensional phase spaces. Since we are interested in the principal mechanism we focus on the simplest setup, namely the stabilization of fixed points in a one-dimensional map. In view of the previous remarks it is obvious that for such models there exist much more powerful tools for controlling unstable fixed points. But the case study presented here gives some insight into global features of time delayed feedback control and the results can be generalized to time-continuous systems as well. Moreover, the analysis presented here for the time-discrete setup is simpler from the technical point of view, although it has only relevance for real control experiments at a qualitative level.

5.4.1
Analytical Bifurcation Analysis of One-Dimensional Maps

Let us consider a one-dimensional map $x_{n+1} = f(x_n)$ with fixed point $\xi_* = f(\xi_*)$. To stabilize the fixed point a simple time delayed feedback scheme is applied,

$$x_{n+1} = f(x_n) + K(x_n - x_{n-1}). \tag{5.7}$$

Actually, the phase space dimension of Eq. (5.7) has increased just by 1 and it is for that reason why the analysis of this time delay system stays to be rather straightforward. In a neighborhood of the fixed point a Taylor series expansion of Eq. (5.7) up to third order yields, using the variable $\delta x_n = x_n - \xi_*$,

$$\delta x_{n+1} = f'(\xi_*)\delta x_n + K(\delta x_n - \delta x_{n-1}) + \frac{f''(\xi_*)}{2}(\delta x_n)^2 + \frac{f'''(\xi_*)}{3!}(\delta x_n)^3 + \cdots. \tag{5.8}$$

It is now the scope to transform such an equation of motion into the normal form (cf. Eq. (5.31)). Details of the formal calculation are summarized in Appendix A.

Using the state vector $\underline{y}_n = (y_n^{(1)}, y_n^{(2)}) = (\delta x_n, \delta x_{n-1})$, Eq. (5.8) can be cast into a nonlinear two-dimensional map (cf. Eq. (5.28)). The linear part of the motion is governed by the two-dimensional matrix

$$\underline{\underline{A}} = \begin{pmatrix} f'(\xi_*) + K & -K \\ 1 & 0 \end{pmatrix}. \tag{5.9}$$

Stability of the trivial solution is easily expressed in terms of the determinant and the trace of this matrix. Here we are interested in cases where we are close to a Hopf bifurcation, i.e., usually close to the upper control threshold. Then the matrix (5.9) admits a complex conjugated pair of eigenvalues μ_c, μ_c^* with modulus 1, $\mu_c = \exp(i\varphi_c)$. Thus

$$1 = \det(\underline{\underline{A}}) = K_c \tag{5.10}$$

and

$$\text{tr}(\underline{\underline{A}}) = f'(\xi_*) + K_c = \mu_c + \mu_c^* = 2\cos(\varphi_c) \in (-2, 2). \tag{5.11}$$

The eigenvector for the eigenvalue μ_c is obviously given by

$$\underline{u}_c = \begin{pmatrix} \mu_c \\ 1 \end{pmatrix} \tag{5.12}$$

while the eigenvector of the corresponding adjoint eigenvalue problem (cf. Eq. (5.29b)) reads

$$\underline{v}_c^{\dagger} = (-\mu_c, 1). \tag{5.13}$$

If the control amplitude K deviates from its critical value $K_c = 1$, then the linear part changes by the amount

$$\underline{\underline{\delta A}} = \delta K \begin{pmatrix} 1 & -1 \\ 0 & 0 \end{pmatrix} \tag{5.14}$$

when $\delta K = K - K_c$ denotes the distance of the control amplitude from the control boundary.

So far we have written down the linear terms of the equations of motion (5.8). In order to determine the normal form we have to consider quadratic and cubic nonlinearities as well. Using the notation introduced in Appendix A the quadratic and cubic terms can be expressed through bilinear and trilinear expressions, $B : \underline{y}_n : \underline{y}_n :$ and $C : \underline{y}_n : \underline{y}_n : \underline{y}_n :$ respectively, where

$$B : \underline{u} : \underline{v} := \frac{f''(\xi_*)}{2} \begin{pmatrix} u^{(1)} v^{(1)} \\ 0 \end{pmatrix} \tag{5.15 a}$$

$$C : \underline{u} : \underline{v} : \underline{w} := \frac{f'''(\xi_*)}{3!} \begin{pmatrix} u^{(1)} v^{(1)} w^{(1)} \\ 0 \end{pmatrix}. \tag{5.15 b}$$

The evolution equation (5.8) has been cast into the vector notation of Eq. (5.28) and for the coefficients of the normal form (5.31) the expressions (5.37) and (5.39) can be evaluated readily.

For the unfolding parameter (5.37) we obtain, using Eqs. (5.12), (5.13), and (5.14)

$$\varepsilon = \frac{\langle \underline{v}_c | \underline{\underline{\delta A}} \, \underline{u}_c \rangle}{\langle \underline{v}_c | \underline{u}_c \rangle} = \delta K \frac{\mu_c(1 - \mu_c)}{1 - \mu_c^2} = \mu_c \frac{\delta K \exp(-i\varphi_c/2)}{2 \cos(\varphi_c/2)}, \tag{5.16}$$

where we have used the polar representation of the critical eigenvalue as well, $\mu_c = \exp(i\varphi_c)$. Since

$$\mathrm{Re}(\varepsilon/\mu_c) = \delta K/2 \tag{5.17}$$

the trivial fixed point is stable if $\delta K < 0$, i.e., below the control threshold while control fails above that threshold, $\delta K > 0$ (cf. Appendix B for the linear stability criterion).

The nature of the Hopf bifurcation is determined by the cubic coefficient (5.39). The two auxiliary vectors (5.35) are just computed from Eqs. (5.9), (5.10), (5.12), and (5.15 a)

$$\underline{\alpha} = \frac{f''(\xi_*)}{2} \frac{1}{\det(\mu_c^2 \underline{\underline{1}} - \underline{\underline{A}})} \begin{pmatrix} \mu_c^2 & -1 \\ 1 & \mu_c^2 - f'(\xi_*) - 1 \end{pmatrix} \begin{pmatrix} \mu_c^2 \\ 0 \end{pmatrix}$$

$$= \frac{f''(\xi_*)/2}{(\mu_c^2 - \mu_c)(\mu_c^2 - 1/\mu_c)} \begin{pmatrix} \mu_c^4 \\ \mu_c^2 \end{pmatrix} \tag{5.18a}$$

$$\underline{\beta} = \frac{f''(\xi_*)}{2} \frac{1}{\det(\underline{\underline{1}} - \underline{\underline{A}})} \begin{pmatrix} 1 & -1 \\ 1 & -f'(\xi_*) \end{pmatrix} \begin{pmatrix} |\mu_c|^2 \\ 0 \end{pmatrix}$$

$$= \frac{f''(\xi_*)/2}{(1 - \mu_c)(1 - 1/\mu_c)} \begin{pmatrix} 1 \\ 1 \end{pmatrix}. \tag{5.18b}$$

Now the evaluation of the terms entering the coefficient (5.39) is straightforward, applying the definitions (5.15)

$$\frac{\langle \underline{v}_c | B : \underline{u}_c^* : \underline{\alpha} : \rangle}{\langle \underline{v}_c | \underline{u}_c \rangle} = -\left(\frac{f''(\xi_*)}{2}\right)^2 \frac{\mu_c^4}{(1 - \mu_c^2)(\mu_c^2 - \mu_c)(\mu_c^2 - 1/\mu_c)}$$

$$= \mu_c \left(\frac{f''(\xi_*)}{2}\right)^2 \frac{i}{8 \sin \varphi_c \sin(\varphi_c/2) \sin(3\varphi_c/2)} \tag{5.19a}$$

$$\frac{\langle \underline{v}_c | B : \underline{u}_c : \underline{\beta} : \rangle}{\langle \underline{v}_c | \underline{u}_c \rangle} = -\left(\frac{f''(\xi_*)}{2}\right)^2 \frac{\mu_c^2}{(1 - \mu_c^2)(1 - \mu_c)(1 - 1/\mu_c)}$$

$$= \mu_c \left(\frac{f''(\xi_*)}{2}\right)^2 \frac{-i}{8 \sin \varphi_c \sin^2(\varphi_c/2)} \tag{5.19b}$$

$$\frac{\langle \underline{v}_c | C : \underline{u}_c : \underline{u}_c : \underline{u}_c^* : \rangle}{\langle \underline{v}_c | \underline{u}_c \rangle} = -\left(\frac{f'''(\xi_*)}{3!}\right) \frac{\mu_c^2}{1 - \mu_c^2}$$

$$= \mu_c \left(\frac{f'''(\xi_*)}{3!}\right) \frac{-i}{2 \sin(\varphi_c)}. \tag{5.19c}$$

Thus

$$\mathrm{Re}(r/\mu_c) = 0 \tag{5.20}$$

since all contributions to the cubic coefficient are imaginary.[4] Hence the control law (5.7) just realizes the transition between sub- and supercritical behavior (cf. Appendix B for the conditions on super- and subcritical Hopf bifurcations for maps), no matter what the values of the second and third derivatives are, i.e., no matter what kind of one-dimensional map is considered. The result is in fact far from surprising since it is due to some hidden symmetry which is shared by the control law (5.7). If one considers the value of the critical coupling $K_c = 1$ then the Jacobian of the corresponding two-dimensional map is easily computed to be (cf. Eq. (5.9))

---

[4] The imaginary part diverges if $\varphi_c = 0, \pm\pi, \pm 2\pi/3$, i.e., in the case of a strong resonance.

$$\mathrm{Jac}_f(\underline{x}) = \begin{pmatrix} f'(x^{(1)}) + K_c & -K_c \\ 1 & 0 \end{pmatrix}. \tag{5.21}$$

The determinant of the Jacobian equals 1 and the two-dimensional map is area preserving. Hence, all the dissipative contributions to the normal form, i.e., the real parts of the coefficients, will vanish. This particular symmetry will be destroyed if a different type of coupling is considered, and a transition from sub- to supercritical behavior can be realized.

5.4.2
Dependence of Sub- and Supercritical Behavior on the Observable

The control scheme (5.7) can be modified in a simple way by altering the observable from which the time delayed control force is derived. If we keep for simplicity the additive coupling of the control force, then the dynamics is determined by

$$x_{n+1} = f(x_n) + K(g(x_n) - g(x_{n-1})), \tag{5.22}$$

where $g(x_n)$ denotes the measured signal which depends on the state x_n in general in a nonlinear way. With a suitable choice of the observable $g(x_n)$ it is possible to generate supercritical behavior at the upper control threshold. It is rather straightforward to apply the analytical perturbation scheme of the previous section to the current setup. But here we just illustrate the essential behavior in a phenomenological way by a simple numerical simulation.

For that purpose let us choose $g(x) = x + \lambda x^2$. The free parameter λ allows for tuning the nonlinearity of the measured signal. The choice $\lambda = 0$ corresponds to the setup of the previous section with degenerated bifurcations at the upper control threshold. For the underlying dynamical system we employ the logistic map $f(x) = 1 - ax^2$ at a parameter value $a = 1.6$ to ensure for chaotic motion. The control thresholds can be easily computed using linear stability analysis. Actually, comparing Eq. (5.7) with Eq. (5.22) it is obvious that the previous results can be used when K is replaced by $g'(\xi_*)K$. In particular, the upper control threshold is given by $g'(\xi_*)K_c = 1$. For a sensible comparison of results for different observables it is therefore appropriate to use the normalized control amplitude $g'(\xi_*)K$ since this quantity governs the linear stability properties.

Numerical simulations show that a supercritical Hopf bifurcation is found for $\lambda > 0$ while for $\lambda < 0$ subcritical behavior prevails (cf. Fig. 5.6). The supercritical transition is continuous and no hysteresis or bistability occurs when one compares results obtained from an adiabatic increase and decrease of the control amplitude. The subcritical transition for $\lambda < 0$ is discontinuous. Actually, phase space points escape to infinity in the superthreshold regime as a result of a lack of phase space contraction and dissipation in the model (cf. the previous section).
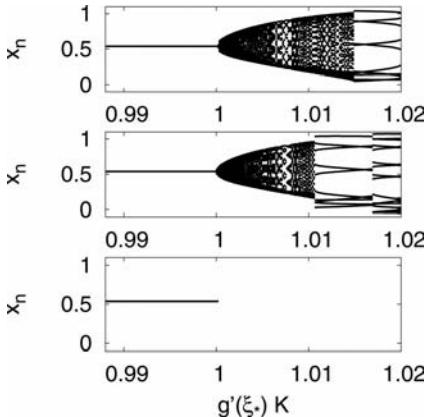
Fig. 5.6 Bifurcation diagrams of the model (5.22) with $f(x) = 1 - ax^2$, $g(x) = x + \lambda x^2$, and $a = 1.6$. Top: $\lambda = 0.2$ adiabatic increase of the control amplitude, middle: $\lambda = 0.2$ adiabatic decrease of the control amplitude, bottom: $\lambda = -0.2$ adiabatic increase of the control amplitude. Successful control for $g'(\xi_*)K < 1$. Continuous transition for $\lambda = 0.2$ with regions of additional bistability above the control threshold. Discontinuous transition for $\lambda = -0.2$ where the solution escapes to infinity for $K > K_c$.

The transition from super- to subcritical behavior which has been induced by the change of observable is accompanied by a corresponding change in the global dynamical features. Figure 5.7 shows the basins of attraction of the stabilized fixed point in the subthreshold regime, $K < K_c$, for positive and negative values of λ, i.e., for the super- and subcritical Hopf bifurcation, respectively. In the subcritical case, $\lambda < 0$, the basin of attraction is restricted to a small neighborhood of the target state, in particular when the control amplitude is close to the critical value K_c. No such constraint is observed in the supercritical case, $\lambda > 0$, where the basin of attraction remains large even when the boundary of the control interval is approached. Thus, the suitable choice of observable has a profound effect on the global properties of the control, as predicted by the previous analytical considerations.

5.4.3
Influence of the Coupling of the Control Force

As long as the desired unstable target state is embedded in a chaotic attractor one may improve the control performance by applying the control force only if the actual state is close to the target state. Such events happen because of the recurrence properties of chaotic motion. Within the context of time delayed feedback control such events can be identified easily since the control force becomes small when the system is close to the target state. Corresponding ideas have been proposed for time delayed feedback control from the very beginning [4]. Within the context of the previous example it means that one caps the con-
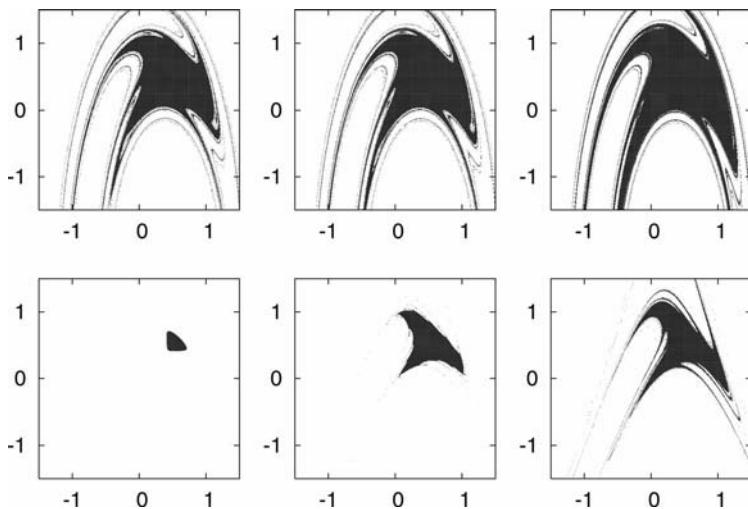
Fig. 5.7 Basin of attraction of the model (5.22) for supercritical (top: $\lambda = 0.2$) and subcritical (bottom: $\lambda = -0.2$) transitions, displayed in the $x_0 - x_{-1}$ plane of initial conditions and different values of the control amplitude: $g'(\xi_*)K = 0.999$ (left), 0.99 (middle), 0.95 (right). Black dots mark initial conditions resulting in successful stabilization of the target state $\xi_* = 0.537\ldots$. Basins are essentially independent of K in the supercritical case while a considerable reduction of the basin in the subcritical case occurs close to the control threshold.

trol force $x_n - x_{n-1}$ when its value becomes too large. In terms of a mathematical model that means

$$x_{n+1} = f(x_n) + Kh(x_n - x_{n-1}), \tag{5.23}$$

where the coupling function $h(x)$ is odd, $h(x) = h(-x)$, has slope 1 for small argument to keep the results comparable to the previous investigations, $h'(0) = 1$, and saturates or decays for large values of the argument. Indeed such a coupling function will enhance the control performance since it is able to induce supercritical Hopf bifurcations at the upper control threshold and thus enlarges basins of attraction even without chaotic recurrence to the target state.

It is quite straightforward to supply the details of the analytical perturbation expansion when we assume $h'(0) = 1$ and $h''(0) = 0$. Recall that with these assumptions the Taylor series expansion reads

$$h(x_n - x_{n-1}) = x_n - x_{n-1} + \frac{h'''(0)}{3!}(x_n - x_{n-1})^3 + \cdots. \tag{5.24}$$

It is obvious that the analysis of Section 5.4.1 still applies as far as linear and quadratic terms are concerned (cf. Eq. (5.8)). Just the cubic nonlinearity (cf.

Eq. (5.15 b)) changes since in view of Eq. (5.24) and $K_c = 1$ an additional additive contribution occurs

$$C : \underline{u} : \underline{v} : \underline{w} := \frac{f'''(\xi_*)}{3!} \begin{pmatrix} u^{(1)} v^{(1)} w^{(1)} \\ 0 \end{pmatrix}$$
$$+ \frac{h'''(0)}{3!} \begin{pmatrix} (u^{(1)} - u^{(2)})(v^{(1)} - v^{(2)})(w^{(1)} - w^{(2)}) \\ 0 \end{pmatrix}. \tag{5.25}$$

Thus, for the computation of the cubic coefficient of the normal form we just have to recalculate Eq. (5.19 c) which is pretty straightforward using the eigenvectors (5.12) and (5.13),

$$\frac{\langle \underline{v}_c | C : \underline{u}_c : \underline{u}_c : \underline{u}_c^* : \rangle}{\langle \underline{v}_c | \underline{u}_c \rangle}$$
$$= - \left(\frac{f'''(\xi_*)}{3!} \right) \frac{\mu_c^2}{1 - \mu_c^2} - \frac{h'''(0)}{3!} \frac{\mu_c(\mu_c - 1)(\mu_c - 1)(\mu_c^* - 1)}{1 - \mu_c^2}$$
$$= \mu_c \left(\frac{f'''(\xi_*)}{3!} \right) \frac{-i}{2 \sin(\varphi_c)} + \mu_c \frac{h'''(0)}{3!} \frac{2 \exp(-i\varphi_c/2) \sin^2(\varphi_c/2)}{\cos(\varphi_c/2)}. \tag{5.26}$$

Now Eqs. (5.19 a), (5.19 b), and (5.26) yield

$$\mathrm{Re}(r/\mu_c) = \frac{2h'''(0)}{3!} \sin^2(\varphi_c/2). \tag{5.27}$$

Supercritical behavior occurs if $h'''(0) < 0$ which corresponds locally to a saturation of the control force, while subcritical behavior and corresponding deterioration of the basins are caused for $h'''(0) > 0$. The local codimension-two analysis thus nicely complies with the observations described above and highlights the importance of the coupling scheme for global properties of time delayed feedback control.

5.5
Conclusion

Time-delayed feedback control has been developed to stabilize time-periodic states with tiny control forces when no detailed information about the underlying dynamics is available. Meanwhile properties of such control schemes are quite well understood as far as linear stability is concerned. But even from the linear perspective there are unsolved problems of experimental relevance. Apart from very preliminary numerical studies of model systems (cf. e.g. [13, 31]) it is rather unclear how properties of the measured signal and the coupling of the control force to the internal degrees of freedom affect the control properties in

detail. While such questions are addressed by standard control theory in great detail, comparable results are still missing for time delayed feedback control.

Apart from numerical simulations of model systems properties of time delayed feedback control are scarcely investigated beyond linear stability analysis. For instance, almost no analytical results are available concerning basins of attraction or the robustness of the control scheme with respect to external, e.g., stochastic, perturbations. While such results are delivered by standard control theory using Lyapunov functions such a strategy cannot be applied directly to time delayed feedback schemes unless the structure of the underlying equations of motion is known. In the near future one may hope that the application of numerical continuation schemes to particular models of time delayed feedback control may give some insight into global properties of the delay dynamics (cf. e.g. [43]). The ultimate goal, however, should be a modification of time delayed feedback schemes such that generic systems show good Lyapunov stability properties.

The case study presented here followed a different less ambitious route. Application of bifurcation theory to time delay dynamics may give some insight into generic features of time delayed feedback control. The analysis of local higher order codimension bifurcations related to the behavior at control thresholds is able to yield information about the global phase space structure. The analysis presented here for the time-discrete case can be performed in the more realistic time-continuous setup as well [36]. Such approaches are potentially able to yield universal global features of time delayed feedback control as demonstrated in the previous sections. It is furthermore tempting to apply such ideas for analyzing the influence of external perturbations beyond the linear response regime, to employ global phase space structures for implementing targeting procedures (cf. e.g. [3]) for time delayed feedback control, and to study the interrelation between spatial degrees of freedom and time delay. Thus, there are still plenty of interesting problems around which are of general interest for time delay dynamics and which are not restricted to the study of control problems.

Appendix A
Normal Form Reduction

Normal form calculations for Hopf bifurcations are a standard procedure. To keep the presentation self-contained and since appropriate closed expressions for the normal form parameters are rarely available in the literature we here just recall the computation. Suppose a system with a trivial fixed point $\underline{y} = 0$ experiences a Hopf bifurcation. Close to the critical point a Taylor series expansion of the d-dimensional map yields the expression

$$\underline{y}_{n+1} = \underline{\underline{A}}\,\underline{y}_n + \underline{\underline{\delta A}}\,\underline{y}_n + B : \underline{y}_n : \underline{y}_n : + C : \underline{y}_n : \underline{y}_n : \underline{y}_n : + \cdots. \tag{5.28}$$

The matrix $\underline{A}$ governs the linear part of the motion at the bifurcation point. Thus the corresponding eigenvalue problem

$$\underline{\underline{A}}\,\underline{u}_c = \mu_c \underline{u}_c \tag{5.29 a}$$

$$\underline{v}_c^\dagger \underline{\underline{A}} = \mu_c \underline{v}_c^\dagger \tag{5.29 b}$$

possesses a complex conjugated pair of eigenvalues μ_c, μ_c^*, where $|\mu_c| = 1$. Equation (5.29 b) just states the adjoint eigenvalue equation with $\underline{v}_c^\dagger$ denoting the Hermitian conjugate. Such an eigenvector will turn out to be quite useful for analytical calculations. The additional linear contribution to Eq. (5.28), $\underline{\delta A}$, is supposed to be small and takes the deviation from the bifurcation point into account. Furthermore, nonlinear quadratic and cubic contributions to the equations of motion are captured by the tensors B and C.[5]

We are looking for a two-dimensional surface in the full phase space being invariant with respect to the dynamics of Eq. (5.28), and tangent to the plane spanned by the two critical vectors $\underline{u}_c$ and $\underline{u}_c^*$ when a system at the bifurcation point is considered. Thus it captures the slow part of motion in the vicinity of the critical point. Such a manifold can be written in terms of a complex valued coordinate z_n as

$$\underline{y}_n = \underline{u}_c z_n + \underline{u}_c^* z_n^* + \underline{\delta} z_n + \underline{\delta}^* z_n^* + \underline{a} z_n^2 + \underline{a}^* (z_n^*)^2 + 2\underline{\beta}|z_n|^2 + \underline{\gamma} z_n |z_n|^2 + \cdots. \tag{5.30}$$

Here ... denotes the remaining cubic nonresonant contributions and terms of higher order. The additional linear term $\underline{\delta} z_n$ accounts for deviations from the bifurcation point and is therefore of the same small order as $\underline{\delta A}$. It is our goal to

---

5) The v-component of $B : \underline{u} : \underline{v} :$ is given by $\sum_{\mu\rho} B^{(\nu\mu\rho)} u^{(\mu)} v^{(\rho)}$. In view of Eq. (5.28) we assume a symmetric expression $B : \underline{u} : \underline{v} : = B : \underline{v} : \underline{u} :$ and employ homogeneity $B : a\underline{u} : \underline{v} : = a B : \underline{u} : \underline{v} :$ and additivity $B : \underline{u} + \underline{w} : \underline{v} : = B : \underline{u} : \underline{v} : + B : \underline{w} : \underline{v} :$. An analogous notation is used for the cubic nonlinearity $C : \underline{u} : \underline{v} : \underline{w} :$.

fix the parameters $\underline{a}$, $\underline{\beta}$, $\underline{\gamma}$, and $\underline{\delta}$ in such a way that the dynamics for the slow coordinate z_n obeys the so-called normal form

$$z_{n+1} = (\mu_c + \varepsilon)z_n + rz_n|z_n|^2 + \cdots, \tag{5.31}$$

where the small deviation from the critical point, ε, is assumed to be of the order $\mathcal{O}(z^2)$.

Employing the invariance of the surface (5.30) we can immediately obtain explicit expressions for the coefficients appearing in Eq. (5.31). On the one hand, Eq. (5.30) yields

$$
\begin{aligned}
&\underline{y}_{n+1} \\
&= \underline{u}_c z_{n+1} + \underline{u}_c^* z_{n+1}^* + \underline{\delta} z_{n+1} + \underline{\delta}^* z_{n+1}^* \\
&\quad + \underline{a} z_{n+1}^2 + \underline{a}^*(z_{n+1}^*)^2 + 2\underline{\beta}|z_{n+1}|^2 + \underline{\gamma} z_{n+1}|z_{n+1}|^2 + \cdots \\
&= \left(\mu_c z_n + \varepsilon z_n + rz_n|z_n|^2 + \ldots\right)\underline{u}_c + \left(\mu_c^* z_n^* + \varepsilon^* z_n^* + r^* z_n^*|z_n|^2 + \ldots\right)\underline{u}_c^* \\
&\quad + \mu_c \underline{\delta} z_n + \mu_c \underline{\delta}^* z_n^* + \mu_c^2 \underline{a} z_n^2 + (\mu_c^*)^2 \underline{a}^*(z_n^*)^2 + 2\underline{\beta}|z_n|^2 + \mu_c \underline{\gamma} z_n|z_n|^2 + \cdots, \tag{5.32}
\end{aligned}
$$

where for the last step Eq. (5.31) has been employed. On the other hand the same quantity is, according to Eq. (5.28), given by

$$
\begin{aligned}
\underline{y}_{n+1} &= \underline{\underline{A}}\,\underline{y}_n + \underline{\underline{\delta A}}\,\underline{y}_n + B : \underline{y}_n : \underline{y}_n : + C : \underline{y}_n : \underline{y}_n : \underline{y}_n : + \cdots \\
&= \underline{\underline{A}}\,\underline{u}_c z_n + \underline{\underline{A}}\,\underline{u}_c^* z_n^* + \underline{\underline{A}}\,\underline{a} z_n^2 + \underline{\underline{A}}\,\underline{a}^*(z_n^*)^2 + 2\underline{\underline{A}}\,\underline{\beta}|z_n|^2 + \underline{\underline{A}}\,\underline{\gamma} z_n|z_n|^2 \\
&\quad + \underline{\underline{A}}\,\underline{\delta} z_n + \underline{\underline{A}}\,\underline{\delta}^* z_n^* + \underline{\underline{\delta A}}\,\underline{u}_c z_n + \underline{\underline{\delta A}}\,\underline{u}_c^* z_n^* \\
&\quad + B : \underline{u}_c : \underline{u}_c : z_n^2 + B : \underline{u}_c^* : \underline{u}_c^* : (z_n^*)^2 + 2B : \underline{u}_c : \underline{u}_c^* : |z_n|^2 \\
&\quad + 2B : \underline{u}_c^* : \underline{a} : z_n|z_n|^2 + 4B : \underline{u}_c : \underline{\beta} : z_n|z_n|^2 \\
&\quad + 3C : \underline{u}_c : \underline{u}_c : \underline{u}_c^* : z_n|z_n|^2 + \cdots, \tag{5.33}
\end{aligned}
$$

where here for the last step Eq. (5.30) has been used. If we equate contributions of the same order in Eqs. (5.32) and (5.33) we obtain the desired coefficients for the normal form (5.31).

Contributions of order $\mathcal{O}(z)$ in Eqs. (5.32) and (5.33) match because of the eigenvalue equation (5.29). Matching the contributions of second order, $\mathcal{O}(z^2)$, we obtain, comparing the coefficients of z_n^2 and of $|z_n|^2$

$$\mu_c^2 \underline{a} = \underline{\underline{A}}\,\underline{a} + B : \underline{u}_c : \underline{u}_c : \tag{5.34a}$$
$$\underline{\beta} = \underline{\underline{A}}\,\underline{\beta} + B : \underline{u}_c : \underline{u}_c^* : . \tag{5.34b}$$

The second-order contribution associated with $(z_n^*)^2$ just yields the complex conjugate of Eq. (5.34a). If $\mu_c \neq 1$ and $\mu_c^2 \neq \mu_c^*$, one can solve Eqs. (5.34) since the coefficients appearing on the left-hand side are not contained in the spectrum of the matrix $\underline{\underline{A}}$. Thus, the parameters of the center manifold (5.30) are determined by

$$\underline{a} = (\mu_c^2 \underline{1} - \underline{\underline{A}})^{-1} B : \underline{u}_c : \underline{u}_c : \tag{5.35 a}$$

$$\underline{\beta} = (\underline{1} - \underline{\underline{A}})^{-1} B : \underline{u}_c : \underline{u}_c^* : . \tag{5.35 b}$$

We now proceed and equate coefficients of the order $\mathcal{O}(\varepsilon z)$ in Eqs. (5.32) and (5.33). For the coefficient of εz_n we get

$$\varepsilon \underline{u}_c + \mu_c \underline{\delta} = \underline{\underline{\delta A}} \, \underline{u}_c + \underline{\underline{A}} \, \underline{\delta}. \tag{5.36}$$

As μ_c is eigenvalue of the matrix $\underline{\underline{A}}$ a nontrivial condition, the so-called Fredholm condition, has to be imposed on ε in order that Eq. (5.36) can be solved for $\underline{\delta}$. In fact, if we multiply Eq. (5.36) from the left with the eigenvector $\underline{v}_c^\dagger$ of the adjoint eigenvalue equation (5.29 b) the contributions containing $\underline{\delta}$ cancel due to the eigenvalue condition and we are left with

$$\varepsilon \langle \underline{v}_c | \underline{u}_c \rangle = \langle \underline{v}_c | \underline{\underline{\delta A}} \, \underline{u}_c \rangle, \tag{5.37}$$

where we have introduced the usual inner product by $\langle \underline{v} | \underline{u} \rangle = \underline{v}^\dagger \underline{u}$. Equation (5.37) is nothing else but the well-known first-order perturbative result for the shift of eigenvalues.

If we finally equate the cubic terms, $z_n |z_n|^2$, in Eqs. (5.32) and (5.33) we obtain the condition

$$r\underline{u}_c + \mu_c \underline{\gamma} = 2B : \underline{u}_c^* : \underline{a} : +4B : \underline{u}_c : \underline{\beta} : +3C : \underline{u}_c : \underline{u}_c : \underline{u}_c^* : +\underline{\underline{A}} \, \underline{\gamma}. \tag{5.38}$$

Again application of the Fredholm condition, i.e., multiplication with the adjoint eigenvector, yields the expression for the coefficient of the cubic term

$$r\langle \underline{v}_c | \underline{u}_c \rangle = \langle \underline{v}_c | 2B : \underline{u}_c^* : \underline{a} : +4B : \underline{u}_c : \underline{\beta} : +3C : \underline{u}_c : \underline{u}_c : \underline{u}_c^* : \rangle. \tag{5.39}$$

Thus all coefficients of the normal form (5.31) have been expressed in terms of quantities of the underlying equation of motion (5.28).

In order to eliminate the other, nonresonant, cubic contributions in the normal form (5.31) which have not been written down explicitly, one requires the additional constraints $\mu_c^2 \neq 1$ and $\mu_c^4 \neq 1$ on the critical eigenvalue. When the so-called strong resonance conditions, $\mu_c^k = 1$, $k = 1, 2, 3, 4$, are avoided the motion is given in terms of the Hopf normal form.[6]

---

6) Unlike for differential equations higher order contributions to the normal form cannot be neglected when the dynamics on the resulting invariant circle is of interest (cf. e.g. [40]).

Appendix B
Super- and Subcritical Hopf Bifurcation for Maps

Conditions for super- and subcritical behavior of the time-discrete normal form (5.31) describing the Hopf instability are quite similar to the time-continuous case we dealt with in Section 5.3.1. There are, however, minor technical differences and for further reference we just recall the basic facts. A transformation to polar coordinates is in principle possible in the time-discrete setup, but less straightforward. We follow a different strategy and employ a transformation to a rotating frame using $\zeta_n = \mu_c^n z_n$. Then Eq. (5.31) reads

$$\zeta_{n+1} - \zeta_n = \frac{\varepsilon}{\mu_c} \zeta_n + \frac{r}{\mu_c} \zeta_n |\zeta_n|^2. \tag{5.40}$$

In a small neighborhood of the bifurcation point, i.e., $|\varepsilon| \ll |\mu_c| = 1$, the amplitude $|\zeta_n|$ becomes of order $\mathcal{O}(\sqrt{|\varepsilon|})$ and the rate of change $\zeta_{n+1} - \zeta_n$ turns out to be small as well. Capturing these features with the scaling $\zeta_n = \sqrt{|\varepsilon|}\zeta(|\varepsilon|n)$ one reduces the map (5.40) to the differential equation (5.5) and the conditions of Section 5.3.1 on the bifurcation apply. Thus $\text{Re}(\varepsilon/\mu_c) < 0$ yields subthreshold dynamics and $\text{Re}(\varepsilon/\mu_c) > 0$ corresponds to the behavior beyond the Hopf instability. A supercritical Hopf bifurcation occurs for $\text{Re}(r/\mu_c) < 0$ while $\text{Re}(r/\mu_c) > 0$ yields subcritical behavior.

References

1 R. Bellmann, *Dynamic Programming and Modern Control Theory* (Academic Press, New York 1965).

2 E. Ott, C. Grebogi, and Y. A. Yorke, *Controlling chaos*, Phys. Rev. Lett. **64**, 1196 (1990).

3 T. Shinbrot, *Progress in the control of chaos*, Adv. Phys. **44**, 73 (1995).

4 K. Pyragas, *Continuous control of chaos by self-controlling feedback*, Phys. Lett. A **170**, 421 (1992).

5 S. Bielawski, D. Derozier, and P. Glorieux, *Controlling unstable periodic orbits by a delayed continuous feedback*, Phys. Rev. E **49**, R971 (1994).

6 O. Lüthje, S. Wolff, and G. Pfister, *Control of chaotic Taylor-Couette flow with time delayed feedback*, Phys. Rev. Lett. **86**, 1745 (2001).

7 H. Benner and W. Just, *Control of chaos by time delayed feedback in high power ferromagnetic resonance experiments*, J. Kor. Phys. Soc. **40**, 1046 (2002).

8 P. Parmananda, R. Madrigal, M. Rivera, L. Nyikos, I. Z. Kiss, and V. Gáspár, *Stabilization of unstable steady states and periodic orbits in an electrochemical system using delayed-feedback control*, Phys. Rev. E **59**, 5266 (1999).

9 T. Hikihara and T. Kawagoshi, *An experimental study on stabilization of unstable periodic motion in magneto-elastic chaos*, Phys. Lett. A **211**, 29 (1996).

10 K. Pyragas and A. Tamasevicius, *Experimental control of chaos by delayed self-controlling feedback*, Phys. Lett. A **180**, 99 (1993).

11 K. Hall, D. J. Christini, M. Tremblay, J. J. Collins, L. Glass, and J. Billette, *Dynamic control of cardiac alternans*, Phys. Rev. Lett. **78**, 4518 (1997).

12 R. Bellmann and K. L. Cooke, *Differential-Difference Equations* (Academic Press, New York 1963).

13 M. E. Bleich and J. E. S. Socolar, *Controlling spatiotemporal dynamics with time de-*

layed feedback, Phys. Rev. E **54**, R17 (1996).

14 W. Just, T. Bernard, M. Ostheimer, E. Reibold, and H. Benner, *Mechanism of time delayed feedback control*, Phys. Rev. Lett. **78**, 203 (1997).

15 K. Pyragas, *Analytical properties and optimization of time delayed feedback control*, Phys. Rev. E **66**, 026207 (2002).

16 H. Nakajima, *On analytical properties of delayed feedback control of chaos*, Phys. Lett. A **232**, 207 (1997).

17 J. E. S. Socolar, D. W. Sukow, and D. J. Gauthier, *Stabilizing unstable periodic orbits in fast dynamical systems*, Phys. Rev. E **50**, 3245 (1994).

18 W. Just, E. Reibold, H. Benner, K. Kacperski, F. Fronczak, and J. Hołyst, *Limits of time delayed feedback control*, Phys. Lett. A **254**, 158 (1999).

19 S. Bielawski, D. Derozier, and P. Glorieux, *Experimental characterization of unstable periodic orbits by controlling chaos*, Phys. Rev. A **47**, R2492 (1993).

20 H. G. Schuster and M. B. Stemmler, *Control of chaos by oscillating feedback*, Phys. Rev. E **56**, 6410 (1997).

21 W. Just, *On the eigenvalue spectrum for time delayed Floquet problems*, Physica D **142**, 153 (2000).

22 K. Pyragas, *Control of chaos via an unstable delayed feedback controller*, Phys. Rev. Lett. **86**, 2265 (2001).

23 A. Kittel, J. Parisi, and K. Pyragas, *Delayed feedback control of chaos by self-adapted delay-time*, Phys. Lett. A **198**, 433 (1995).

24 H. Nakajima, H. Ito, and Y. Ueda, *Automatic adjustment of delay time and feedback gain in delayed feedback control of chaos*, IEICE Trans. Fund. Electr. **E80A**, 1554 (1997).

25 W. Just, J. Möckel, D. Reckwerth, E. Reibold, and H. Benner, *Delayed feedback control of periodic orbits in autonomous systems*, Phys. Rev. Lett. **81**, 562 (1998).

26 W. Just, D. Reckwerth, E. Reibold, and H. Benner, *Influence of control loop latency on time delayed feedback control*, Phys. Rev. E **59**, 2826 (1999).

27 P. Hövel and J. E. S. Socolar, *Stability domains for time delay feedback control with latency*, Phys. Rev. E **68**, 036206 (2003).

28 *Handbook of Chaos Control*, edited by H. G. Schuster (Wiley-VCH, Berlin 1999).

29 W. Just, H. Benner, and E. Schöll, in *Control of chaos by time delayed feedback: a survey of theoretical and experimental aspects*, Vol. 43 of *Advances in Solid State Physics*, edited by B. Kramer (Springer, Berlin 2003), p. 589.

30 W. Just, E. Reibold, K. Kacperski, P. Fronczak, J. Hołyst, and H. Benner, *Influence of stable Floquet exponents on time delayed feedback control*, Phys. Rev. E **61**, 5045 (2000).

31 O. Beck, A. Amann, E. Schöll, J. E. S. Socolar, and W. Just, *Comparison of time delayed feedback schemes for spatio-temporal control of chaos in a reaction-diffusion system with global coupling*, Phys. Rev. E **66**, 016213 (2002).

32 J. K. Hale and S. M. Verduyn Lunel, *Introduction to Functional Differential Equations* (Springer, New York 1993).

33 K. Engelborghs, T. Luzyanina, and D. Roose, *Numerical bifurcation analysis of delay differential equations*, J. Comput. Appl. Math. **125**, 265 (2000).

34 K. Yamasue and T. Hikihara, *Domain of attraction for stabilized orbits in time delayed feedback controlled Duffing systems*, Phys. Rev. E **69**, 056209 (2004).

35 C. v. Loewenich, H. Benner, and W. Just, *Experimental relevance of global properties of time delayed feedback control*, Phys. Rev. Lett. **93**, 174101 (2004).

36 W. Just, H. Benner, and C. v. Löwenich, *On global properties of time delayed feedback control: weakly nonlinear analysis*, Physica D **199**, 33 (2004).

37 O. Biham and W. Wenzel, *Characterization of unstable periodic orbits in chaotic attractors and repellers*, Phys. Rev. Lett. **63**, 819 (1989).

38 P. Schmelcher and F. K. Diakonos, *Detecting unstable periodic orbits of chaotic dynamical systems*, Phys. Rev. Lett. **78**, 4733 (1997).

39 R. L. Davidchack and Y.-C. Lai, *Efficient algorithm for detecting unstable periodic orbits in chaotic systems*, Phys. Rev. E **60**, 6172 (1999).

40 J. Guckenheimer and P. Holmes, *Nonlinear Oscillations, Dynamical Systems,*

and Bifurcations of Vector Fields (Springer, New York 1986).

41 F. Giannakopulos and A. Zapp, *Bifurcations in a planar system of differential delay equations modeling neural activity*, Physica D **159**, 215 (2001).

42 B. F. Redmond, V. G. LeBlanc, and A. Longtin, *Bifurcation analysis of a class of* *first-order nonlinear delay-differential equations with reflectional symmetry*, Physica D **166**, 131 (2002).

43 B. Krauskopf and K. Green, *Computing unstable manifolds of periodic orbits in delay differential equations*, J. Comput. Phys. **186**, 230 (2003).

6

Poincaré-Based Control of Delayed Measured Systems: Limitations and Improved Control

Jens Christian Claussen

6.1
Introduction

What is the effect of measurement delay on Ott, Grebogi, and Yorke (OGY) chaos control? Which possibilities exist for improved control? These questions are addressed within this chapter, and the OGY control case is considered as well as a related control scheme, difference control; both together form the two main Poincaré-based chaos control schemes, where the control amplitude is computed once during the orbit after crossing the Poincaré section.

If the stabilization of unstable periodic orbits or fixed points by the method given by Ott, Grebogi, Yorke [23] and Hübler [15] can only be based on a measurement delayed by τ orbit lengths, resulting in a control loop latency, the performance of unmodified OGY control is expected to decay. For experimental considerations, it is desired to know the range of stability with minimal knowledge of the system. In Section 6.3, the area of stability is investigated both for OGY control and for difference control, yielding a delay-dependent maximal Lyapunov number beyond which control fails. Sections 6.3.4 to 6.4.3 address the question how the control of delayed measured chaotic systems can be improved, i.e., what extensions must be considered if one wants to stabilize fixed points with a higher Lyapunov number. Fortunately, the limitation can be overcome most elegantly by linear control methods that employ memory terms, as linear predictive logging control (Section 6.4.1) and memory difference control (Section 6.4.3). In both cases, one is equipped with an explicit deadbeat control scheme that allows, within linear approximation, us to perform control without principal limitations in delay time, dimension, and Ljapunov numbers.

6.1.1
The Delay Problem–Time-Discrete Case

For fixed point stabilization in time-continuous control, the issue of delay has been investigated widely in control theory, dating back at least to the Smith pre-

dictor [31]. This approach mimics the, yet unknown, actual system state by a linear prediction based on the last measurement. Its time-discrete counterparts discussed in this chapter allow us to place all eigenvalues of the associated linear dynamics to zero, and always ensure stability. The (time continuous) Smith predictor with its infinite-dimensional initial condition had to be refined [12, 24], giving rise to the recently active fields of *model predictive control* [3]. For fixed point stabilization, an extension of permissible latency has been found for a modified proportional-plus-derivative controller [28].

Delay is also a generic problem in the control of chaotic systems. The effective delay time τ in any feedback loop is the sum of at least three delay times, the duration of measurement, the time needed to compute the appropriate control amplitude, and the response time of the system to the applied control. The latter effect appears especially when the applied control additionally has to propagate through the system. This response time may extend to one or more cycle lengths [21]. If one wants to stabilize the dynamics of a chaotic system onto an unstable periodic orbit, one is in a special situation. In principle, a proper engineering approach could be to use the concept of sliding mode control [10], i.e., to use a co-moving coordinate system and perform suitable control methods within it. However, this requires quite accurate knowledge of whole trajectory and stable manifold, with respective numerical or experimental costs.

Therefore, direct approaches have been developed by explicitly taking into account either a Poincaré surface of section [23] or the explicit periodic orbit length [26]. This field of *controlling chaos*, or stabilization of chaotic systems, by small perturbations, in system variables [15] or control parameters [23], has developed to a widely discussed topic with applications in a broad area from technical to biological systems. Especially in fast systems [2, 29] or for slow drift in parameters [4, 22], difference control methods have been successful, namely the time-continuous Pyragas scheme [26], ETDAS [29], and time-discrete difference control [1].

As for the control method itself, the discussion of the measurement delay problem in chaos control has to take into account the special issues of the situation: in classical control applications one always tries to keep the control loop latency as short as possible. In chaotic systems however, one wants to control a fixed point of the Poincaré iteration and thus has to wait until the next crossing of the Poincaré surface of section, where the system again is in vicinity of that fixed point.

The stability theory and the delay influence for time-continuous chaos control schemes has been studied extensively [11, 14, 17–19], and an improvement of control by periodic modulation has been proposed in [20]. For measurement delays that extend to a full period, however, no extension of the time-continuous Pyragas scheme is available.

This chapter discusses the major Poincaré-based control schemes OGY control [23] and difference feedback [1] in the presence of time delay, and addresses the question what strategies can be used to overcome the limitations due to the delay [8]. We show how the measurement delay problem can be solved systema-

tically for OGY control and difference control by rhythmic control and memory methods and give constructive direct and elegant formulas for the deadbeat control in the time-discrete Poincaré iteration. While the predictive control method LPLC presented below for OGY control has a direct correspondence with the Smith predictor and thus can be reviewed as its somehow straightforward implementation within the unstable subspace of the Poincaré iteration, this prediction approach does not guarantee a stable controller for difference control. However, within a class of feedback schemes linear in system parameters and the system variable, there is always a unique scheme where all eigenvalues are zero, i.e., the MDC scheme presented below. The method can be applied also for more than one positive Lyapunov exponent, and shows, within validity of the linearization in vicinity of the orbit, to be free of principal limitations in Lyapunov exponents or delay time. For zero delay (but the inherent period one delay of difference control), MDC has been demonstrated experimentally for a chaotic electronic circuit [4] and a thermionic plasma discharge diode [22], with excellent agreement, both of stability areas and transient Lyapunov exponents, with the theory presented here. This chapter is organized as follows. After introducing the notation within a recall of OGY control, we give a brief summary of limitations that occur for unmodified OGY control; details can be found in [8]. From Section 6.3.6 we introduce different memory methods to improve control, of which the LPLC approach appears to be superior as it allows stabilization of arbitrary fixed points for any given delay. The stabilization of unknown fixed points is discussed in Section 6.4.3, where we present a memory method (MDC) that again allows stabilization of arbitrary unstable fixed points. For all systems with only one instable Lyapunov number, the iterated dynamics can be transformed on an eigensystem which reduces to the one-dimensional case, and the generalization to the case of higher dimensional subspaces is straightforward [9].

6.1.2
Experimental Setups with Delay

Before discussing the time-discrete reduced dynamics in the Poincaré iteration, it should be clarified how this relates to an experimental control situation. On a first glance, the time-discrete viewpoint seems to correspond only to a case where the delay (plus waiting time to the next Poincaré section) exactly matches the orbit length, or a multiple of it. Generically, in the experiment one experiences a nonmatching delay. Application of all control methods discussed here requires introduction of an additional delay, usually by waiting for the next Poincaré crossing, so that measurement and control are applied without phase shift at the same position of the orbit. In this case the next Poincaré crossing position x_{t+1} is a function of the values of x and r at a finite number of previous Poincaré crossings only, i.e. it does not depend on intermediate positions. Therefore the (a priori infinite-dimensional) delay system reduces to a finite-dimensional iterated map. If the delay (plus the time of the waiting mechanism

to the next Poincaré crossing) does not match the orbit length, the control schemes may perform less efficiently. Even for larger deviations from the orbit, the time between the Poincaré crossings will vary only marginally; thus a control amplitude should be available in time. In practical situations therefore the delay should not exceed the orbit length minus the variance of the orbit length that appears in the respective system and control setup.

In a formal sense, the Poincaré approach ensures robustness with respect to uncertainties in the orbit length, as it always ensures a synchronized reset of both trajectories and control. Between the Poincaré crossings the control parameter is constant; the system is independent of everything *in advance of* the last Poincaré crossing. It is solely determined by the differential equation (or experimental dynamics). Thus the next crossing position is a well-defined iterated function of the previous one. This is quite in contrast to the situation of a delay-differential equation (as in Pyragas control), which has an infinite-dimensional initial condition it "never gets rid of." One may proceed to stability analysis via Floquet theory [13] as investigated for continuous [17] and impulse length issues in Poincaré-based [5–7] control schemes. Though a Poincaré crossing detection may be applied as well, the position will depend not only on the last crossing, but also on all values of the system variable within a time horizon defined by the maximum of the delay length and the (maximal) time difference between two Poincaré crossings (being nonstroboscopic). Thus the Poincaré iteration would be a function between two infinite-dynamical spaces. Contrary to a delay differential equation with *fixed* delay, a major advantage of a Poincaré map is to reduce the system dynamics to a low-dimensional system; therefore *for all control schemes discussed here,* the additional dimensionality is not a continuous horizon of states, but merely a finite set of values that were measured at the previous Poincaré crossings.

6.2
Ott-Grebogi-Yorke (OGY) Control

The method of Ott, Grebogi, and Yorke [23] stabilizes unstable fixed points, or unstable periodic orbits utilizing a Poincaré surface of section, by feedback that is applied in the vicinity of the fixed point x^* of a discrete dynamics $x_{t+1} = f(x_t, r)$. For a chaotic flow, or corresponding experiment, the system dynamics $\dot{\vec{x}} = \vec{F}(\vec{x}, r)$ reduces to the discrete dynamics between subsequent Poincaré sections at $t_0, t_1, \ldots, t_n$. This description is fundamentally different from a stroboscopic sampling as long as the system is not on a periodic orbit, where the sequence of differences $(t_i - t_{i-1})$ would show a periodic structure.

If there is only one positive Lyapunov exponent, we can proceed considering the motion in the unstable direction only. One can transform on the eigensystem of the Jacobi matrix $\dfrac{\partial f}{\partial r}$ and finds again the equations of the one-dimensional case, i.e., one only needs to apply control in the unstable direction (see

e.g. [5, 9]). Thus stability analysis and control schemes of the one-dimensional case holds also for higher dimensional systems provided there is only one unstable direction. For two or more positive Lyapunov exponents one can proceed in a similar fashion [5, 9].

In OGY control, the control parameter r_t is made time dependent. The amplitude of the feedback $r_t = r - r_0$ added to the control parameter r_0 is proportional by a constant ε to the distance $x - x^*$ from the fixed point, i.e., $r = r_0 + \varepsilon(x_t - x^*)$, and the feedback gain can be determined from a linearization around the fixed point, which reads, if we neglect higher order terms,

$$
\begin{aligned}
f(x_t, r_o + r_t) &= f(x^*, r_0) + (x_t - x^*) \cdot \left(\frac{\partial f}{\partial x}\right)_{x^*, r_0} \\
&\quad + r_t \cdot \left(\frac{\partial f}{\partial r}\right)_{x^*, r_0} \\
&= f(x^*, r_0) + \lambda(x_t - x^*) + \mu r_t \\
&= f(x^*, r_0) + (\lambda + \mu \varepsilon) \cdot (x_t - x^*).
\end{aligned}
\tag{6.1}
$$

The second expression vanishes for $\varepsilon = -\lambda/\mu$, that is, in linear approximation the system arrives at the fixed point at the next time step, $x_{t+1} = x^*$. The uncontrolled system is assumed to be unstable in the fixed point, i.e. $|\lambda| > 1$. The system with applied control is stable if the absolute value of the eigenvalues of the iterated map is smaller than 1,

$$
|x_{t+1} - x^*| = |(\lambda + \mu \varepsilon) \cdot (x_t - x^*)| < |x_t - x^*|
\tag{6.2}
$$

Therefore ε has to be chosen between $(-1 - \lambda)/\mu$ and $(+1 - \lambda)/\mu$, and this interval is of width $2/\mu$ and independent of λ, i.e., fixed points with arbitrary λ can be stabilized. This property however does not survive for delayed measurement [8], as surveyed below.

6.3
Limitations of Unmodified Control and Simple Improved Control Schemes

In this section the limitations of unmodified control are discussed, both for OGY control and for difference control. For completeness, rhythmic control and a state space memory control are discussed in Sections 6.3.4 and 6.3.6.

6.3.1
Limitations of Unmodified OGY Control in the Presence of Delay

We want to know what limitations occur if the OGY rule is applied without modification. Intuitively, one expects the possibility of unstable behavior of $(\tau + 1)$ control loops that mutually overlap in the course of time (see Fig. 6.1).
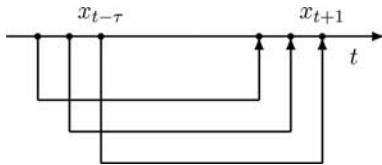
Fig. 6.1 Unmodified control in the presence of delay (schematically).

In OGY control, the control parameter r_t is time dependent, and without loss of generality we assume that $x^* = 0$ and that $r_t = 0$ if no control is applied. First we discuss the simplest relevant case $\tau = 1$ explicitly. For one time step delay, instead of $r_t = \varepsilon x_t$ we have the proportional feedback rule:

$$r_t = \varepsilon x_{t-1}. \tag{6.3}$$

Using the time delayed coordinates (x_t, x_{t-1}), the linearized dynamics of the system with applied control is given by $\begin{pmatrix} x_{t+1} \\ x_t \end{pmatrix} = \begin{pmatrix} \lambda & \mu\varepsilon \\ 1 & 0 \end{pmatrix} \begin{pmatrix} x_t \\ x_{t-1} \end{pmatrix}$. The eigenvalues of $\begin{pmatrix} \lambda & \mu\varepsilon \\ 1 & 0 \end{pmatrix}$ are given by $a_{1,2} = \frac{\lambda}{2} \pm \sqrt{\frac{\lambda^2}{4} + \varepsilon\mu}$. Control can be achieved with ε being in an interval $] -1/\mu, (1-\lambda)/\mu[$ with the width $(2-\lambda)/\mu$ (see Fig. 6.2).

In contrast to the nondelayed case, we have a requirement $\lambda < 2$ for the Lyapunov number: direct application of the OGY method fails for systems with a Lyapunov number of 2 and higher [4, 8]. This limitation is caused by the additional degree of freedom introduced in the system due to the time delay.

Now we consider the general case. If the system is measured delayed by τ steps, $r_t = \varepsilon x_{t-\tau}$, we can write the dynamics in time delayed coordinates $(x_t, x_{t-1}, x_{t-2}, \ldots x_{t-\tau})^\mathrm{T}$:
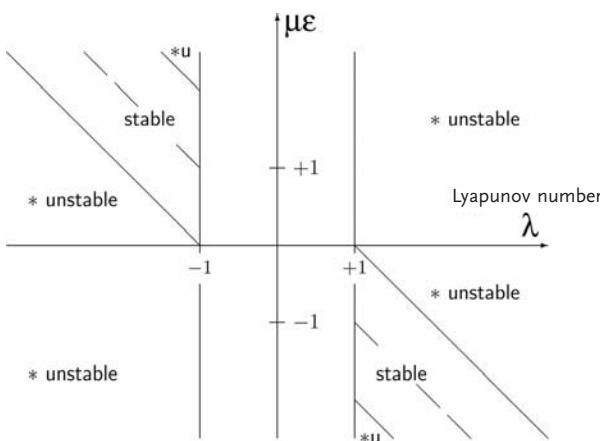
Fig. 6.2 Stability range of OGY control.

$$
\begin{pmatrix} x_{t+1} \\ \vdots \\ \\ \\ \vdots \\ x_{t-\tau+1} \end{pmatrix} = \begin{pmatrix} \lambda & 0 & \cdots & & \cdots & 0 & \varepsilon\mu \\ 1 & 0 & & & & & 0 \\ 0 & 1 & \ddots & & & & \vdots \\ \vdots & & \ddots & & & & \\ & & & \ddots & & & \\ \vdots & & & & \ddots & 0 & \vdots \\ 0 & \cdots & & \cdots & 0 & 1 & 0 \end{pmatrix} \begin{pmatrix} x_t \\ \vdots \\ \\ \\ \vdots \\ x_{t-\tau} \end{pmatrix}. \tag{6.4}
$$

The characteristic polynomial is given by (we define rescaled coordinates $\tilde{a} := a/\lambda$ and $\tilde{\varepsilon} = \varepsilon\mu/\lambda^{\tau+1}$)

$$
0 = P(a) = (a - \lambda)a^{\tau} - \varepsilon\mu
$$
$$
\text{or } 0 = P(\tilde{a}) = (\tilde{a} - 1)\tilde{a}^{\tau} - \tilde{\varepsilon}. \tag{6.5}
$$

Figure 6.3 shows the maximum of the absolute value of the eigenvalues.

In rescaled coordinates $\tilde{a} = 1/\lambda$ corresponds to a control interval $\tilde{\varepsilon}_{\pm}(\tau, \lambda)$. For

$$
\lambda_{\max} = 1 + \frac{1}{\tau} \tag{6.6}
$$

the control interval vanishes, and for $\lambda \geq \lambda_{\max}(\tau)$ no control is possible [4, 8]. If we look at the Lyapunov exponent $\Lambda := \ln\lambda$ instead of the Lyapunov number, we find with $\ln x < (x - 1)$ the inequality

$$
\Lambda_{\max} \cdot \tau < 1. \tag{6.7}
$$
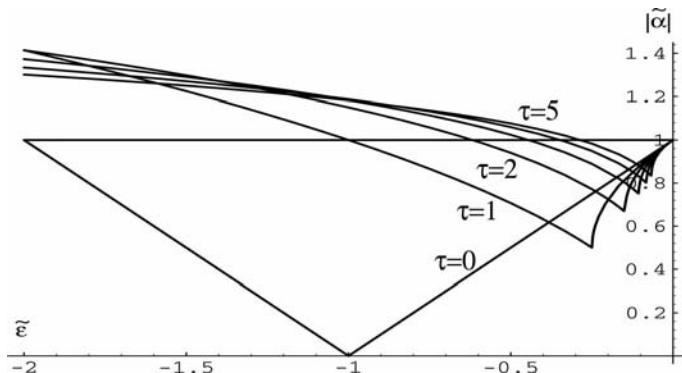
Fig. 6.3 Control intervals for several time delays $\tau = 0 \ldots 5$: The plots show the maximal absolute value of the eigenvalues as a function of the rescaled control gain $\tilde{\varepsilon}$. Values of $|\tilde{a}| = 1/\lambda$ correspond to $|a| = 1$ in (6.5) without rescaling, so one can obtain the range $]\varepsilon_-, \varepsilon_+[$ for which control is successfully achieved.

Therefore, delay time and Lyapunov exponent limit each other if the system is to be controlled. This is consistent with the loss of knowledge in the system by exponential separation of trajectories.

6.3.2
Stability Diagrams Derived by the Jury Criterion

For small τ one can derive easily the borders of the stability area with the help of the Jury criterion [5, 8]. The Jury criterion [16] gives a sufficient and necessary condition that all roots of a given polynomial are of modulus smaller than unity. Given a polynomial $P(x) = a_n x^n + a_{n-1} x^{n-1} + \cdots + a_1 x + a_0$, one applies the iterative *Jury table* scheme:

$$\forall_{0 \leq i \leq n} \quad b_i := a_{n-i}$$
$$a_n := b_n / a_n$$
$$\forall_{1 \leq i \leq n} \quad a_{i-1}^{\text{new}} := a_i - a_n b_i$$

giving a_n and coefficients $a_{n-1} \ldots a_0$ for the next iteration. The Jury criterion states that the eigenvalues are of modulus smaller than unity if and only if $\forall_{1 \leq i \leq n} |a_i| < 1$. The criterion gives $2n$ (usually partly redundant) inequalities that define hypersurfaces in coefficient space. The complete set of lines is shown in Fig. 6.4 for $\tau = 4$ to illustrate the redundancy of the inequalities generated by the Jury table. For $\tau = 1$, the Jury coefficients are given by $a_1 = -\lambda/(1 + \mu\varepsilon)$ and $a_2 = -\mu\varepsilon$. Control is only necessary for $|\lambda| > 1$, and by folding the relevant stability area into the same quadrant one obtains Fig. 6.5 showing how $\lambda_{\max}$ decreases for increasing τ.

6.3.3
Stabilizing Unknown Fixed Points: Limitations of Unmodified Difference Control

As the OGY approach discussed above requires the knowledge of the position of the fixed point, one may wish to stabilize purely by feeding back differences of the system variable at different times. This becomes relevant in the case of parameter drifts [4] which often can occur in experimental situations. A time-con-
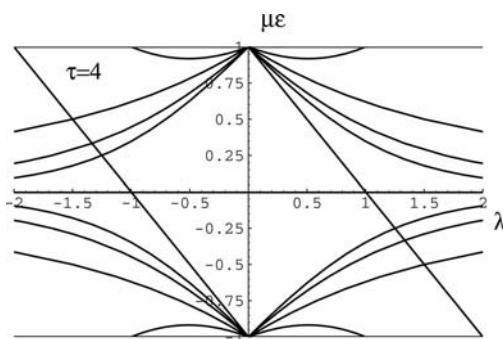
Fig. 6.4 Complete Jury diagram for $\tau = 4$.
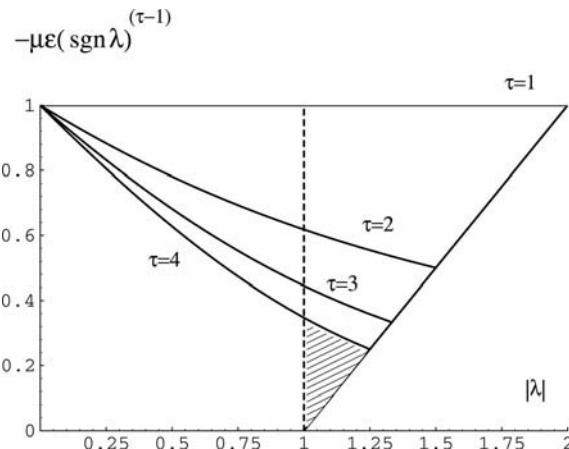
$$-\mu\varepsilon(\operatorname{sgn}\lambda)^{(\tau-1)}$$

Fig. 6.5 Stability areas for $\tau = 1, 2, 3, 4$, combined. Only for $|\lambda| > 1$ control is necessary (dashed line), and the stability area (shaded for $\tau = 4$) extends to $|\lambda_{\max}| = 2, 3/2, 4/3, 5/4$. Note that still both positive and negative λ can be controlled. The abscissa $-\mu\varepsilon(\operatorname{sgn}\lambda)^{(\tau-1)}$ takes into account that for odd τ a negative $\mu\varepsilon$ is required, independent of the sign of λ.

tinuous strategy $r(t) = \varepsilon(x(t) - x(t - \tau_{\mathrm{d}}))$ has been introduced by Pyragas [26], where $r(t)$ is updated continuously and τ_{d} matches the period of the unstable periodic orbit. The time-discrete counterpart (i.e., control amplitudes are calculated every Poincaré section) is the difference control scheme [1]: for control without delay, a simple difference control strategy

$$r_t = \varepsilon(x_{t-\tau} - x_{t-\tau-1}) \tag{6.8}$$

is possible for $\varepsilon\mu = -\lambda/3$, and eigenvalues of modulus smaller than unity of the matrix $\begin{pmatrix} \lambda + \varepsilon\mu & -\varepsilon\mu \\ 1 & 0 \end{pmatrix}$ are obtained only for $-3 < \lambda < +1$, so this method stabilizes only for oscillatory repulsive fixed points with $-3 < \lambda < -1$ [1] see the $\tau = 0$ case in Fig. 6.6).

We can proceed in a similar fashion as for OGY control. In the presence of τ steps delay the linearized dynamics of difference control is given by

$$
\begin{pmatrix} x_{t+1} \\ \vdots \\ \\ \\ \\ \vdots \\ x_{t-\tau} \end{pmatrix}
=
\begin{pmatrix}
\lambda & 0 & \cdots & & 0 & \varepsilon\mu & -\varepsilon\mu \\
1 & 0 & & & & & 0 \\
0 & 1 & \ddots & & & & \vdots \\
\vdots & & \ddots & & & & \\
& & & \ddots & & & \\
\vdots & & & & \ddots & 0 & \vdots \\
0 & \cdots & & \cdots & 0 & 1 & 0
\end{pmatrix}
\begin{pmatrix} x_t \\ \vdots \\ \\ \\ \\ \vdots \\ x_{t-\tau-1} \end{pmatrix}
$$
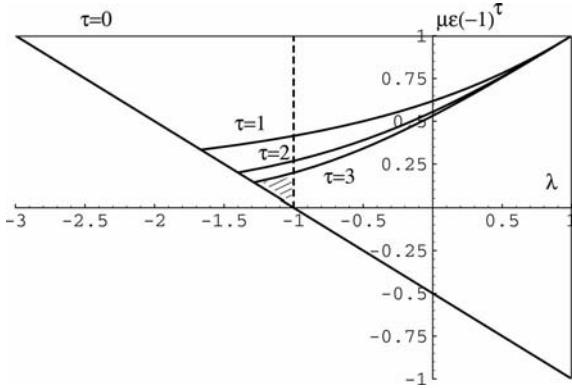
Fig. 6.6 Difference feedback for $\tau = 0, 1, 2, 3$: Stability borders derived by the Jury criterion [5, 8]. The stability diagram of the nondelayed case $\tau = 0$ has already been given in [1]. From $\lambda = -1$ (dashed line) to $\lambda = +1$ the system is stable without control. For each τ, control is effective only within the respective area (shaded for $\tau = 3$).

in delayed coordinates $(x_t, x_{t-1}, \ldots x_{t-\tau-1})$, and the characteristic polynomial is given by

$$0 = (a - \lambda)a^{\tau+1} + (1 - a)\varepsilon\mu. \tag{6.9}$$

As we have to use $x_{t-\tau-1}$ in addition to $x_{t-\tau}$, the system is of dimension $\tau + 2$, and the lower bound of Lyapunov numbers that can be controlled is found to be

$$\lambda_{\text{inf}} = -\frac{3 + 2\tau}{1 + 2\tau} = -\left(1 + \frac{1}{\tau + 1/2}\right) \tag{6.10}$$

and the asymptotic control amplitude at this point is

$$\varepsilon\mu = \frac{(-1)^\tau}{1 + 2\tau}. \tag{6.11}$$

The stability area in the $(\mu\varepsilon, \lambda)$ plane is bounded by the lines $a_i = \pm 1$ where a_i are the coefficients given by the Jury criterion [16] (see Fig. 6.6). For $\tau = 0$, the Jury coefficients are $a_1 = -\dfrac{\lambda + \varepsilon\mu}{1 + \varepsilon\mu}$ and $a_2 = \varepsilon\mu$. For $\tau = 1$ to $\tau = 3$, the Jury coefficients are given in [8].

The controllable range is smaller than for the unmodified OGY method, and is restricted to oscillatory repulsive fixed points with $\lambda_{\text{inf}} < \lambda \leq -1$. Thus, delay severely reduces the number of controllable fixed points, and one has to develop special control strategies for the control of delayed measured systems. A striking observation is that inserting $\tau + \frac{1}{2}$ for τ in Eq. (6.6) exactly leads to the expression in Eq. (6.10) which reflects the fact that the difference feedback control can be interpreted as a discrete first derivative, taken at time $t - (\tau + \frac{1}{2})$. Thus the controllability relation (6.7) holds again.

As λ^{-1} is implying a natural time scale (that of exponential separation) of an orbit, it is quite natural that control becomes limited by a border proportional to a product of λ and a feedback delay time. Already without the additional difficulty of a measurement delay this is expected to appear for any control scheme that itself is using time delayed feedback: e.g., the extensions of time-discrete control schemes discussed in [30] with an inherent Lyapunov number limitation due to memory terms, and the experimentally widely applied time-continuous schemes Pyragas and ETDAS [11, 17, 19]. Here Pyragas control has the Lyapunov exponent limitation $\Lambda\tau_p \leq 2$ together with the requirement of the Floquet multiplier of the uncontrolled orbit having an imaginary part of π, meaning that deviations from the orbit after one period experience to be flipped around the orbit by that angle, which is quite the generic case [18]. This nicely corresponds with the requirement of a negative Lyapunov number that appears in difference control. A positive Lyapunov number in the time-discrete picture corresponds to a zero flip of the time-continuous orbit, and is consistently uncontrollable in both schemes.

Recently, the influence of a control loop latency control loop latency has also been studied for continuous time delayed feedback [18] by Floquet analysis, obtaining a critical value for the measurement delay τ, that corresponds to a maximal Lyapunov exponent $\log|\lambda_{\text{inf}}| = \Lambda\tau_p = \dfrac{1}{1/2 + \tau/\tau_p}$, where τ_p is the orbit length and matched feedback delay. By the log inequality that again translates (for small Lyapunov exponents) to our result for the time-discrete difference control. An exact coincidence could not be expected, as in Pyragas control the feedback difference is computed continuously sliding with the motion along the orbit, where in difference control it is evaluated within each Poincaré section. For the ETDAS scheme with latency, a detailed analysis is performed in [14], showing that the range of stability can be extended compared to the Pyragas scheme. Although the time-continuous case (as an a priori infinite-dimensional delay-differential system) could exhibit much more complex behavior, it is however astonishing that for all three methods, OGY, difference, and Pyragas control, the influence of measurement delay mainly results in the same limitation of the controllable Lyapunov number.

6.3.4
Rhythmic Control Schemes: Rhythmic OGY Control

As pointed out for difference control in the case $\tau = 0$ in [1], one can eliminate the additional degrees of freedom caused by the delay term. One can restrict himself to applying control rhythmically only every $\tau + 1$ time steps ($\tau + 2$ for difference control), and then leaving the system uncontrolled for the remaining timesteps (see Fig. 6.7). Then $\varepsilon = \varepsilon(t)$ appears to be time dependent with

$$\varepsilon(t \bmod \tau) = (\varepsilon_0, 0, \ldots, 0) \tag{6.12}$$
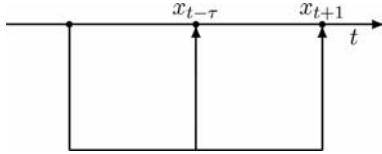
Fig. 6.7 Rhythmic control (schematically). Keeping control quiet for τ intermediate time steps avoids the additional degrees of freedom. However, the effective Lyapunov number to be controlled then is raised to $\lambda^{\tau+1}$.

and, after $(\tau + 1)$ iterations of (6.4), we again have a matrix as in (6.4), but with $\lambda^{\tau+1}$ instead of λ. Equivalently, we can write

$$x_{t+(\tau+1)} = \lambda^{\tau+1}x_t + \varepsilon_0\mu x_t. \tag{6.13}$$

What we have done here is controlling the $(\tau + 1)$-fold iterate of the original system. This appears to be formally elegant, but leads to practically uncontrollable high effective Lyapunov numbers $\lambda^{\tau+1}$ for both large λ and large τ.

Even if the rhythmic control method is of striking simplicity, it remains unsatisfying that control is kept quiet, or inactive, for τ time steps. Even if the state of the system x is known delayed by τ, one knows (in principle) the values of x_t for $t < \tau$, and one could (in principle) store the values $\delta r_{t-\tau}, \ldots, \delta r_t$ of the control amplitudes applied to the system. This can be done, depending on the timescale, by analog or digital delay lines, or by storing the values in a computer or signal processor (observe that there are some intermediate frequency ranges where an experimental setup is difficult).

Both methods, rhythmic control and simple feedback control in every time step, have their disadvantages: for rhythmic control it is necessary to use rather large control amplitudes, in average λ^{τ}/τ, and noise sums up to an amplitude increased by factor $\sqrt{\tau}$. For simple feedback control the dimension of the system is increased and the maximal controllable Lyapunov number is bounded by (6.6). One might wonder if there are control strategies that avoid these limitations. This has necessarily to be done by applying control in each time step, but with using knowledge what control has been applied between the last measured time steps $t - \tau$ and t. This concept can be implemented in at least two ways, by storing previous values of x_t (Section 6.3.6) or by storing previous values of δr_t (LPLC, Section 6.4.1 and MDC, Section 6.4.3).

6.3.5
Rhythmic Difference Control

To enlarge the range of controllable λ, one again has the possibility of reducing the dimension of the control process in linear approximation to 1 by applying control every $\tau + 2$ time steps.
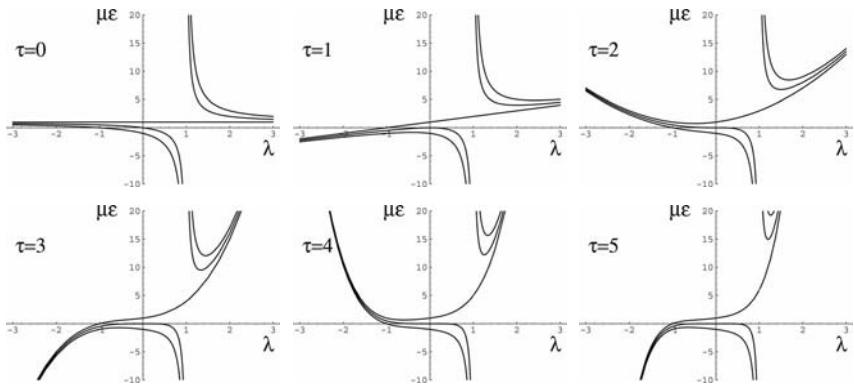
Fig. 6.8 Stability area of rhythmic difference control for $\tau = 0, 1, 2, 3, 4, 5$.

$$x_{t+1} = \lambda x_t + \mu\varepsilon(x_{t-\tau} - x_{t-\tau-1}) \tag{6.14}$$
$$= (\lambda^{\tau+1} + \mu\varepsilon\lambda - \mu\varepsilon)x_{t-\tau-1}$$

and the goal $x_{t+1} \stackrel{!}{=} 0$ can be fulfilled by

$$\mu\varepsilon = -\frac{\lambda^{\tau+1}}{1 - \lambda}. \tag{6.15}$$

One has to choose $\mu\varepsilon$ between $\mu\varepsilon_\pm = -\dfrac{\lambda^{\tau+1} \pm 1}{1 - \lambda}$ to achieve control as shown in Fig. 6.8. The case $\tau = 0$ has already been discussed in [1]. With rhythmic control, there is no range limit for λ, and even fixed points with positive λ can be stabilized by this method.

When using differences for periodic feedback, one still has the problem that the control gain increases by λ^τ, and noise sums up for $\tau + 1$ time steps before the next control signal is applied. Additionally, now there is a singularity for $\lambda = +1$ in the "optimal" control gain given by (6.14). This concerns fixed points where differences $x_t - x_{t-1}$ when escaping from the fixed point are naturally small due to a λ near to $+1$.

Here one has to decide between using a large control gain (but magnifying noise and finite precision effects) or using a small control gain of order $\mu\varepsilon_-(\lambda = +1) = \tau + 1$ (but having larger eigenvalues and therefore slow convergence).

Two other strategies that have been discussed by Socolar and Gauthier [30] are discretized versions of time-continuous methods. Control between $\lambda = -(3 + R)/(1 - R)$ and $\lambda = -1$ is possible with discrete ETDAS ($R < 1$) $r_t = \varepsilon \sum_{k=0}^{\infty} R^k(x_{t-k} - x_{t-k-1})$ and control between $\lambda = -(N + 1)$ and $\lambda = -1$ is achieved with discrete NTDAS (let N be a positive integer) which is defined by $r_t = \varepsilon\left(x_t - \frac{1}{N}\sum_{k=0}^{N} x_{t-k}\right)$. Both methods can be considered to be of advantage even in time-discrete control in the Poincaré section, e.g., if the number of ad-

justable parameters has to be kept small. Whereas these methods are mainly applied in time-continuous control, especially in analog or optical experiments, for time-discrete control the MDC strategy described below allows us to overcome the Lyapunov number limitations.

6.3.6
A Simple Memory Control Scheme: Using State Space Memory

We extend the single delay line by several artificial delay lines (see Fig. 6.9), each with an externally tuneable control gain coefficient [5, 9]:

$$r_t = \varepsilon_1 x_{t-1} + \varepsilon_2 x_{t-2} + \cdots + \varepsilon_{n+1} x_{t-n-1} \qquad (6.16)$$
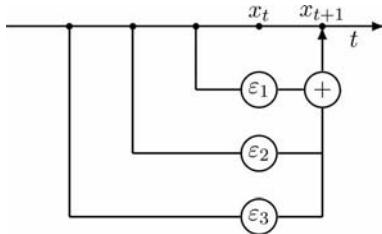
Fig. 6.9 A state space memory control (schematically). For electronic or optic analog circuits, the idea to use additional delay lines is appealing, though the applicability is restricted to the $\tau = 1$ OGY case (which will cover most experiments).

For n steps memory (and one step delay) the control matrix is

$$
\begin{pmatrix} x_{t+1} \\ \vdots \\ \\ \\ \vdots \\ x_{t-n} \end{pmatrix}
=
\begin{pmatrix}
\lambda & \varepsilon_1 & \cdots & & \varepsilon_n & \varepsilon_{n+1} \\
1 & 0 & & & & 0 \\
0 & 1 & \ddots & & & \vdots \\
\vdots & & \ddots & \ddots & & \\
& & & \ddots & 0 & \vdots \\
\vdots & & & \ddots & 1 & 0 \\
0 & \cdots & & \cdots & 0 &
\end{pmatrix}
\begin{pmatrix} x_t \\ \vdots \\ \\ \\ \vdots \\ x_{t-n-1} \end{pmatrix}
\qquad (6.17)
$$

with the characteristic polynomial $(a - \lambda)a^{n+1} + \sum_{i=1}^{n} \varepsilon_i a^{n-i}$. We can choose $a_1 = a_2 = \cdots = a_{n+2} = -\lambda/(n+2)$ and evaluate optimal values for all ε_i by comparing with the coefficients of the product $\prod_{i=1}^{n+2}(a - a_i)$. This method allows control up to $\lambda_{\max} = 2 + n$; thus arbitrary λ can be controlled if a memory length of $n > \lambda - 2$ and the optimal coefficients ε_i are used.

For more than one step delay, one has the situation $\varepsilon_1 = 0, \ldots, \varepsilon_{\tau-1} = 0$. This prohibits the "trivial pole placement" given above (choosing all a_i to the same value) and therefore reduces the maximal controllable λ and no general scheme

for optimal selection of the ε_i applies. One can alternatively use the LPLC method described below, which provides an optimal control scheme. One could wonder why to consider the previous state memory scheme at all when it does not allow us to make all eigenvalues zero in *any* case. First, the case of up to one orbit delay and moderately small λ already covers many low-period orbits. Second, there may be experimental setups where the feedback of previous states through additional delay elements and an analog circuit is experimentally more feasible than feedback of past control amplitudes.

6.4
Optimal Improved Control Schemes

6.4.1
Linear Predictive Logging Control (LPLC)

If it is possible to store the previously applied control amplitudes $r_t, r_{t-1}, \ldots$, then one can predict the actual state x_t of the system using the linear approximation around the fixed point (see Fig. 6.10). That is, from the last measured value $x_{t-\tau}$ and the control amplitudes we compute estimated values iteratively by

$$y_{t-i+1} = \lambda x_{t-i} + \mu r_{t-i} \tag{6.18}$$

leading to a *predicted* value y_t of the actual system state. Then the original OGY formula can be applied, i.e., $r_t = -\lambda/\mu y_t$. In this method the gain parameters are again linear in $x_{t-\tau}$ and all $\{r_{t'}\}$ with $t - \tau \le t' \le t$, and the optimal gain parameters can be expressed in terms of λ and μ.
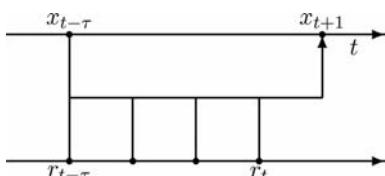
Fig. 6.10 Linear predictive logging control (schematically). In LPLC, all intermediately applied control amplitudes are employed for a linear prediction. A corresponding scheme (MDC, Section 6.4.3) exists also for difference control.

In contrast to the memory method presented in the previous subsection, the LPLC method directs the system (in linear approximation) in one time step onto the fixed point. However, when this control algorithm is switched on, one has no control applied between $t - \tau$ and $t - 1$, so the trajectory has to be fairly near to the orbit (in an interval with a length of order δ/λ^τ, where δ is the inter-

val halfwidth where control is switched on). Therefore the time one has to wait until the control can be successfully activated is of order $\lambda^{\tau-1}$ larger than that in the case of undelayed control.

The LPLC method can also be derived as a general linear feedback in the last measured system state and all applied control amplitudes since the system was measured by choosing the feedback gain parameters in a way that the linearized system has all eigenvalues zero. The linear ansatz

$$r_t = \varepsilon \cdot x_{t-\tau-i} + \eta_1 r_{t-1} + \cdots \eta_\tau r_{t-\tau} \tag{6.19}$$

leads to the dynamics in combined delayed coordinates $(x_t, x_{t-1}, \ldots, x_{t-\tau}, r_{t-1}, \ldots, r_{t-\tau})$

$$
\begin{pmatrix} x_{t+1} \\ x_t \\ \vdots \\ x_{t-\tau+1} \\ r_t \\ \vdots \\ r_{t-\tau+1} \end{pmatrix}
=
\begin{pmatrix}
\lambda & 0 & \cdots & \cdots & 0 & \varepsilon & \eta_1 & \eta_2 & \cdots & \cdots & \eta_\tau \\
 & 0 & & & & & & & & & \\
 & 1 & \ddots & & & & & & & & \\
 & & \ddots & \ddots & & & & & & & \\
 & & & \ddots & \ddots & & & & & & \\
 & & & & 1 & 0 & & & & & \\
0 & 0 & \cdots & \cdots & 0 & \varepsilon & \eta_1 & \eta_2 & \cdots & \cdots & \eta_\tau \\
 & & & & & 1 & 0 & & & & \\
 & & & & & & \ddots & \ddots & & & \\
 & & & & & & & \ddots & \ddots & & \\
 & & & & & & & & 1 & 0 &
\end{pmatrix}
\begin{pmatrix} x_t \\ x_{t-1} \\ \vdots \\ x_{t-\tau} \\ r_{t-1} \\ \vdots \\ r_{t-\tau} \end{pmatrix}
$$

giving the characteristic polynomial

$$
\begin{aligned}
0 = & -a^\tau (a^{\tau+1} + a^\tau(-\lambda - \eta_1) \\
& + a^{\tau-1}(\lambda \cdot \eta_1 - \eta_2) + a^{\tau-2}(\lambda \cdot \eta_2 - \eta_3) \\
& \ldots + a^1(\lambda \cdot \eta_{\tau-1} - \eta_\tau) + (\lambda \cdot \eta_\tau - \varepsilon)).
\end{aligned} \tag{6.20}
$$

All eigenvalues can be set to zero using $\varepsilon = -\lambda^{\tau+1}$ and $\eta_i = -\lambda^i$. A generalization to more than one positive Lyapunov exponent is given in [9].

6.4.2
Nonlinear Predictive Logging Control

One can also consider a nonlinear predictive logging control (NLPLC) strategy [9] as the straightforward extension to the LPLC method for nonlinear prediction. If the system has a delay of several time steps, the interval where control is achieved becomes too small. However, if it is possible to extract the first nonlinearities from the time series, prediction (and control) can be fundamentally improved. In NLPLC, the behavior of the system is predicted each time step by a truncated Taylor series

$$x_{t+1} = \lambda x_t + \frac{\lambda_2}{2} x_t^2 + \mu r_t + \frac{\mu_2}{2} r_t^2 + v x_t r_t + o(x_t^3, x_t^1 r_t, x_t r_t^2, r_t^3)$$

using applied control amplitudes $\{r_t\}$ for each time step. This equation has to be solved for r_t using $x_{t+1} \stackrel{!}{=} 0$. A similar nonlinear prediction method has been described by Petrov and Showalter [25]. They approximate the $x_{t+1}(x_t, r_t)$ surface directly from the time series and use it to direct the system to any desired point. Both Taylor approximation or Petrov and Showalter method can be used here iteratively, provided one knows the delay length. Both approaches could be regarded as a nonlinear method of model predictive control [3], applied to the Poincaré iteration dynamics.

From a practical point of view, it has to be mentioned that one has to know the fixed point x^* more accurately than in the linear case. Otherwise one experiences a smaller range of stability and additionally a permanent nonvanishing control amplitude will remain. This may be of disadvantage especially if the fixed point drifts in time (e.g. by other external parameters such as temperature) or if the time series used to determine the parameters is too short.

6.4.3
Stabilization of Unknown Fixed Points: Memory Difference Control (MDC)

As all methods mentioned above require the knowledge of the position of the fixed point, one may wish to stabilize purely by feeding back differences of the system variable at different times. Without delay, difference feedback can be used successfully for $\varepsilon\mu = -\lambda/3$, and eigenvalues of modulus smaller than unity of the matrix $\begin{pmatrix} \lambda + \varepsilon\mu & -\varepsilon\mu \\ 1 & 0 \end{pmatrix}$ are obtained only for $-3 < \lambda < +1$, so this method stabilizes only for oscillatory repulsive fixed points with $-3 < \lambda < -1$ [1].

Due to the inherent additional period one delay of difference control and MDC, the τ period delay case of MDC corresponds, in terms of the number of degrees of freedom, to the $\tau + 1$ period delay case of LPLC.

One may wish to generalize the linear predictive feedback to difference feedback. Here, caution is advised. In contrast to the LPLC case, the reconstruction of the state $x_{t-\tau}$ from differences $x_{t-\tau-i} - x_{t-\tau-i-1}$ and applied control amplitudes r_{t-j} is no longer unique. As a consequence, there are infinitely many ways to compute an estimate for the present state of the system, but only a subset of these leads to a controller design ensuring convergence to the fixed point. Among these there exists an optimal every-step control for difference feedback with minimal eigenvalues and in this sense optimal stability.

To derive the feedback rule for MDC [4, 5, 9], we directly make the linear ansatz

$$r_t = \varepsilon \cdot (x_{t-\tau-i} - x_{t-\tau-i-1}) + \eta_1 r_{t-1} + \cdots \eta_\tau r_{t-\tau}$$

with the dynamics in combined delayed coordinates

$$\begin{pmatrix} x_{t+1} \\ x_t \\ \vdots \\ x_{t-\tau+2} \\ x_{t-\tau+1} \\ r_t \\ r_{t-1} \\ \vdots \\ r_{t-\tau+1} \end{pmatrix} = \begin{pmatrix} \lambda & 0 & \cdots & 0 & \varepsilon & -\varepsilon & \eta_1 & \eta_2 - \eta_1 & \cdots & \cdots & \eta_\tau - \eta_{\tau+1} \\ 1 & 0 & & & & & & & & & \\ & 1 & \ddots & & & & & & & & \\ & & \ddots & \ddots & & & & & & & \\ & & & \ddots & \ddots & & & & & & \\ & & & & 1 & 0 & & & & & \\ 0 & 0 & \cdots & 0 & \varepsilon & -\varepsilon & \eta_1 & \eta_2 - \eta_1 & \cdots & \cdots & \eta_\tau - \eta_{\tau+1} \\ & & & & & & 1 & 0 & & & \\ & & & & & & & \ddots & \ddots & & \\ & & & & & & & & \ddots & \ddots & \\ & & & & & & & & & 1 & 0 \end{pmatrix} \begin{pmatrix} x_t \\ x_{t-1} \\ \vdots \\ x_{t-\tau+1} \\ x_{t-\tau} \\ r_{t-1} \\ r_{t-2} \\ \vdots \\ r_{t-\tau} \end{pmatrix}$$

giving the characteristic polynomial

$$\begin{aligned}
0 = & - a^\tau (a^{\tau+1} + a^\tau (-\lambda - \eta_1) \\
& + a^{\tau-1}(\lambda \cdot \eta_1 - \eta_2) + a^{\tau-2}(\lambda \cdot \eta_2 - \eta_3) \\
& \ldots + a^2(\lambda \cdot \eta_{\tau-2} - \eta_{\tau-1}) \\
& + a^1(\lambda \cdot \eta_{\tau-1} - \eta_\tau - \varepsilon) + (\lambda \cdot \eta_\tau + \varepsilon)).
\end{aligned} \tag{6.21}$$

All eigenvalues can be set to zero using $\varepsilon = -\lambda^{\tau+1}/(\lambda - 1)$, $\eta_\tau = +\lambda^\tau/(\lambda - 1)$ and $\eta_i = -\lambda^i$ for $1 \le i \le \tau - 1$. This defines the MDC method. For more than one positive Lyapunov exponent see [5, 9].

6.5 Summary

Delayed measurement is a generic problem that can appear in controlling chaos experiments. In some situations it may be technically impossible to extend the control method; then one wants to know the stability borders with minimal knowledge of the system.

We have shown that both OGY control and difference control cannot control orbits with an arbitrary Lyapunov number if there is only delayed knowledge of the system. The maximal Lyapunov number up to which an instable orbit can be controlled is given by $1 + \dfrac{1}{\tau}$ for OGY control and $1 + \dfrac{1}{\tau + 1/2}$ for difference control. For small τ the stability borders can be derived by the Jury criterion, so that the range of values for the control gain ε can be determined from the knowledge of the Taylor coefficients λ and μ. If one wants to overcome these limitations, one has to modify the control strategy.

We have presented methods to improve Poincaré-section-based chaos control for delayed measurement. For both classes of algorithms, OGY control and difference control, delay affects control, and improved control strategies have to be

applied. Improved strategies contain one of the following principle ideas: rhythmic control, control with memory for previous states, or control with memory for previously applied control amplitudes. In special cases the unmodified control, previous state memory control, or rhythmic control methods could be considered, especially when experimental conditions restrict the possibilities of designing the control strategy.

In general, the LPLC and MDC strategies allow a so-called deadbeat control with all eigenvalues zero; and they are in this sense optimal control methods. All parameters needed for controller design can be calculated from linearization parameters that can be fitted directly from experimental data. This approach has also been sucessfully applied in an electronic [4] and plasma [22] experiment.

References

1 Bielawski S., Derozier D. and Glorieux P. (1993) *Phys. Rev. A* **47** (4), 2492–2495.

2 Blakely J. N., Illing L. and Gauthier D. J. (2004) Controlling fast chaos in delay dynamical systems, *Phys. Rev. Lett.* **92**, 193901.

3 Carmacho E. F. and Bordons C. (1999) *Model Predictive Control*, Springer, London.

4 Claussen J. C., Mausbach T., Piel A. and Schuster H. G. (1998) *Phys. Rev. E* **58**, 7256.

5 Claussen J. C. (1998) *Stabilisierung zeitverzögert gemessener Systeme* (in German), PhD thesis, Kiel.

6 Claussen J. C. (2002) Floquet stability analysis of Ott-Grebogi-Yorke and difference control, *arXiv.org e-print* nlin.CD/0204060.

7 Claussen J. C. (2005) Influence of the impulse length in Poincare-based chaos control, Proc. ENOC 2005, Eindhoven, pp. 1100–1107.

8 Claussen J. C. (2004) *Phys. Rev. E* **70**, 046205.

9 Claussen J. C. and Schuster H. G. (2004) *Phys. Rev. E* **70**, 056225.

10 Edwards C. and Spurgeon S. K. (1998) *Sliding Mode Control: Theory and Applications*, Taylor & Francis, London.

11 Franceschini G., Bose S. and Schöll E. (1999) *Phys. Rev. E* **60**, 5426.

12 Hägglund T. (1996) An industrial deadtime compensating PI controller, *Control Eng. Practice* **4**, 749–756.

13 Hale J. K., Verduyn Lunel S. M. (1993) *Introduction to Functional Differential Equations*, Springer, New York.

14 Hövel P. and Socolar E. S. (2003) *Phys. Rev. E* **68**, 036206.

15 Hübler A. W. (1989) *Helv. Phys. Acta* **62**, 343–346.

16 Jury E. I. and Blanchard J. (1961) Proc. IRE **49**, 1947–1948; Jury E. I. and Blanchard J. (1961) Proc. IRE **49**, 1948–1949; Katsuhiko Ogata, *Discrete-Time Control Systems*, Prentice-Hall, Hertfordshire 1995; Martins de Carvalho J. L. (1993) *Dynamical Systems and Automatic Control*, Prentice Hall, Hertfordshire.

17 Just W., Bernard T., Ostheimer M., Reibold E. and Benner H. (1997) *Phys. Rev. Lett.* **78**, 203.

18 Just W., Reckwerth D, Reibold E. and Benner H. (1999) *Phys. Rev. E* **59**, 2826.

19 Just W., Reibold E., Kacperski K., Fronczak P. and Hołyst L. (1999) *Phys. Lett. A* **254**, 158.

20 Just W., Popovich S., Amann A., Baba N. and Schöll E. (2003) *Phys. Rev. E* **67**, 026222.

21 Mausbach T., Klinger T., Piel A., Atipo A., Pierre T. and Bonhomme G. (1997) *Phys. Lett. A* **228**, 373.

22 Mausbach T., Klinger T. and Piel A. (1999) Chaos and chaos control in a strongly driven thermionic plasma diode, *Phys. Plasmas* **6** (10), 3817–3823.

23 Ott E., Grebogi C. and Yorke J. A. (1990) *Phys. Rev. Lett.* **64**, 1196–1199.

24 Palmor Z. (1980) Stability properties of Smith dead-time compensator controllers, Int. J. Control **32** (4), 937–949.

25 Petrov V. and Showalter K. (1996) *Phys. Rev. Lett.* **76**, 3312–3315.

26 Pyragas K. (1992) *Phys. Lett. A* **170**, 421–428.

27 Schuster H. G. and Just W. (2005) *Deterministic Chaos: An Introduction*, 4th edn., Wiley-VCH, Weinheim.

28 Sieber J. and Krauskopf B. (2005) *Dyn. Sys.* **20**, 189–199; Sieber J. and Krauskopf B. (2004) *Nonlinearity* **17** (1), 85–103.

29 Socolar J. E. S., Sukow D. W. and Gauthier D. J. (1994) *Phys. Rev. E* **50** (6), 3245–3248.

30 Socolar J. E. S. and Gauthier D. J. (1998) *Phys. Rev. E* **57** (6), 6589–6595.

31 Smith O. J. M. (1953) Closed control of loops with dead time, *Chem. Eng. Prog.* **53**, 217–219.

7
Nonlinear and Adaptive Control of Chaos

Alexander Fradkov and Alexander Pogromsky

7.1
Introduction

For almost three decades after the term "chaos" was coined, chaotic phenomena and chaotic behavior have been observed in numerous natural and model systems in physics, chemistry, biology, ecology, and so on. Paradigm of chaos allows us to better understand inherent properties of natural systems. Engineering applications are rapidly developing in areas such as lasers and plasma technologies, mechanical and chemical engineering and telecommunications.

Chaotic systems are deterministic dynamical systems exhibiting irregular, seemingly random behavior. Two trajectories of a chaotic system starting close to each other will diverge after some time (so-called sensitive dependence on initial conditions). Mathematically, chaotic systems are characterized by local instability and global boundedness of the trajectories. Since local instability of a linear system implies unboundedness (infinite growth) of its solutions, a chaotic system should be necessarily nonlinear, i.e., should be described by a nonlinear mathematical model.

An important consequence of the system instability is high sensitivity with respect to changes of input (controlling action). It means that small changes of input may produce large variations in system behavior. Such a phenomenon and its implications in physics were described in the seminal paper [1] that triggered an explosion of activities and thousands of publications related to control of chaos.

Control of chaos, or control of chaotic systems, is the boundary field between control theory and dynamical systems theory studying when and how it is possible to control systems exhibiting irregular, chaotic behavior. Control of chaos is closely related to nonlinear control and many methods of nonlinear control are applicable to chaotic systems. However control of chaotic systems has some specific features. In the early 1990s when the first methods of controlling chaos were proposed, no systematic applications of nonlinear control machinery were made. At that time a number of new ideas in control were developed, such as

OGY and Pyragas methods [1, 2]. Later a systematic study and comparative analysis of different methods for control of chaos, including conventional methods of nonlinear control theory were carried out [3–8].

Methods of nonlinear control are well presented in a number of monographs and textbooks [17, 19, 20]. In order to facilitate their application a brief survey of main nonlinear control ideas will be given in this chapter. The chosen methods of gradient, speed gradient, and feedback linearization are simple yet general (applicable to the models of arbitrarily high order).

An important problem arising when dealing with real-world systems is uncertainty. Properties of both controlled systems and their environment are not known precisely and may change during experiment. A powerful way of coping with uncertainty is the usage of adaptive control methods. Even if a model of the system is known, it may be too complicated for effective control algorithm design and a suitable auxiliary model may be needed (for example, model of the controlled Poincaré map in the OGY method). Methods of adaptive control are also well presented in textbooks and monographs [16, 17, 21]. It is convenient to consider adaptive and nonlinear control in one package, since their design is often based on similar approaches. Indeed, even if the controlled system is described by a linear model, arranging feedback tuning of its parameters makes the overall system model linear. Because of place limitation only the main definitions and principles related to adaptive control and an example will be considered in this chapter.

Before exposition of the methods some preliminaries are given concerning system models, control goals, and properties of chaotic systems. After exposition of the methods some illustrating examples are presented.

7.2
Chaos and Control: Preliminaries

7.2.1
Definitions of Chaos

There exists different definitions of a chaotic system and chaotic behavior. The following quotation gives an idea of the situation.

> ■ *There are many possible definitions of chaos. In fact, there is no general agreement within the scientific community as to what constitutes a chaotic dynamical system. [12]*

In most of definitions chaotic processes are treated as solutions of nonlinear differential or difference equations, characterized by local instability and global boundedness. It means that solutions with close initial conditions will diverge to some finite distance after some time (so-called sensitive dependence on initial conditions). Below a typical definition and a typical criterion of chaos are introduced. For more details see, for example [9–11].

Consider the system of differential equations

$$\dot{x} = f(x), \tag{7.1}$$

where $x \in \mathbb{R}^n$ is the n-dimensional state vector, $\dot{x} = dx/dt$ stands for the time derivative of x. Let $A \subset \mathbb{R}^n$ be an *attracting set* of (7.1) (any solution of (7.1) starting from a vicinity of A approaches A as $t \to \infty$). The set A is called a *chaotic attractor* if it is minimal (does not contain other attracting sets), bounded and unstable (any solution starting from A is unstable in a certain sense, e.g. Lyapunov unstable). The system (7.1) is called *chaotic* if it possesses at least one chaotic attractor. Similarly for discrete-time system $x_{k+1} = f(x_k)$.

Although the above definition is used very often, some alternatives have been suggested in the literature. For example, the definition due to Devaney [12] requires additionally that periodic trajectories are dense in the attractor. Some authors prefer to use the term "strange attractor" instead of "chaotic attractor." The term "strange attractor" introduced by Ruelle and Takens [13] in 1971 means that the attractor is a porous (fractal) set that cannot be represented as a piece of manifold and therefore has a noninteger, fractional dimension. In fact in overwhelming part of applications the concepts of "strange attractor" and "chaotic attractor" are indistinguishable.

7.2.2
Models of Controlled Systems

A formal statement of a control problem typically begins with a model of the system to be controlled (*controlled system* or *controlled plant*) and a model of the control objective (*control goal*). If the plant model is not given *a priori* (as in many real life applications) some approximate model should be determined in some way. Several classes of models are considered in the literature related to control of chaos. The most common class consists of continuous systems with lumped parameters described in state space by differential or difference equations

$$\dot{x} = F(x, u), \qquad x_{k+1} = F(x_k, u_k) \tag{7.2}$$

where x is the n-dimensional vector of the state variables; u is the m-dimensional vector of inputs (control variables). For the continuous-time case the vector function $F(x, u)$ is usually assumed continuously differentiable, which guarantees local existence and uniqueness of solutions of (7.2). The model should also include the description of measurements, i.e., the l-dimensional vector of output variables y should be defined, for example

$$y = h(x). \tag{7.3}$$

If the outputs are not defined explicitly, it is assumed that all the state variables are available for measurement, i.e. $y = x$.

More details concerning different classes of controlled system models and their peculiarities can be found in [3].

7.2.3
Control Goals

The main classes of control goals are briefly described below.

Stabilization   A typical goal for control of chaotic systems is stabilization of an unstable periodic solution (orbit). Let $x_*(t)$ be the T-periodic solution of the free $(u(t) = 0)$ system (7.2) with the initial condition $x_*(0) = x_{*0}$, i.e. $x_*(t + T) = x_*(t)$ for all $t \geq 0$. If the solution $x_*(t)$ is unstable, a reasonable goal is stabilization or driving solutions $x(t)$ of (7.2) to $x_*(t)$ in the sense of fulfillment of the limit relation

$$\lim_{t \to \infty} [x(t) - x_*(t)] = 0 \tag{7.4}$$

or driving the output $y(t)$ to the desired output function $y_*(t)$, i.e.

$$\lim_{t \to \infty} [y(t) - y_*(t)] = 0 \tag{7.5}$$

for any solution $x(t)$ of (7.2) with initial conditions $x(0) = x_0 \in \Omega$, where Ω is a given set of initial conditions.

The problem is to find a control function either in the form of an open-loop (feedforward) control

$$u(t) = U(t, x_0) \tag{7.6}$$

or in the form of state feedback

$$u(t) = U(x(t)) \tag{7.7}$$

or output feedback

$$u(t) = U(y(t)) \tag{7.8}$$

to ensure the goal (7.4) or (7.5).

Such a problem is nothing but a tracking problem standard for control theory. However, the key feature of the control of chaotic systems is to achieve the goal by means of sufficiently small (ideally, arbitrarily small) control. Solvability of this task is not obvious since the trajectory $x_*(t)$ is unstable.

A special case of the above problem is stabilization of the unstable equilibrium x_{*0} of system (7.2) with $u = 0$, i.e. stabilization of x_{*0}, satisfying $F(x_{*0}, 0) = 0$. Again, this is just the standard regulation problem with an additional restriction that "small control" solutions are sought. Such a restriction makes the problem far from standard: even for a simple pendulum, nonlocal

solutions of the stabilization problem with small control are nontrivial. The class of admissible control laws can be extended by introducing dynamic feedback described by differential or time delayed models. Similar formulations hold for discrete and time delayed systems.

Chaotization   A second class of control goals corresponds to the problems of *excitation* or *generation* of chaotic oscillations (also called *chaotization, chaotification* or *anticontrol*). Sometimes these problems can be reduced to the form (7.5), but the goal trajectory $x_*(t)$ is no longer periodic, while the initial state is equilibrium. The goal trajectory may be specified only partially. Otherwise, the goal may be to meet some formal criterion of chaos, for example, positivity of the largest Lyapunov exponent.

Synchronization   Third important class of control goals corresponds to *synchronization* (more accurately, *controlled synchronization* as opposed to *autosynchronization* or *self-synchronization*). Generally speaking, synchronization is understood as concordance or concurrent change of the states of two or more systems or, perhaps, concurrent change of some quantities related to the systems, for example, alignment of oscillation frequencies. If the required relation is established only asymptotically, one may speak about *asymptotic synchronization*. If synchronization does not exist in the system without control ($u = 0$) the following *controlled synchronization* problem may be posed: find a control function $u(t)$ ensuring synchronization in the closed-loop system. In this case synchronization is the control goal. For example, the goal corresponding to asymptotic synchronization of the two system states x_1 and x_2 can be expressed as follows:

$$\lim_{t\to\infty}[x_1(t) - x_2(t)] = 0. \qquad (7.9)$$

In the extended state space $x = \{x_1, x_2\}$ of the overall system, relation (7.9) implies convergence of the solution $x(t)$ to the diagonal set $\{x : x_1 = x_2\}$.

Asymptotic identity of the values of some quantity $G(x)$ for two systems can be formulated as

$$\lim_{t\to\infty}[G(x_1(t)) - G(x_2(t))] = 0. \qquad (7.10)$$

Goal functions   To solve a control problem it is often convenient to rewrite the goals (7.4), (7.5), (7.9) or (7.10) in terms of an appropriate goal function $Q(x, t)$ as follows:

$$\lim_{t\to\infty} Q(x(t), t) = 0. \qquad (7.11)$$

For example, to reduce the goal (7.9) to the form (7.11) one may choose the squared Euclidean distance between state vectors of the subsystems as a goal function:

$$Q(x) = |x_1 - x_2|^2.$$

Instead of Euclidean norm other quadratic functions can also be used. For example, in the case of the goal (7.4) the goal function

$$Q(x,t) = [x - x_*(t)]^\top \Gamma [x - x_*(t)],$$

where Γ is a positive definite symmetric matrix can be used. The choice of the matrix Γ provides the possibility of weighting different components of the system state vector to take into account differences in their scale or importance.

In the case of chaotization problem, a goal function $G(x)$ may be introduced such that the goal is to achieve the limit inequality

$$\underline{\lim}_{t \to \infty} G(x(t)) \geq G_*. \tag{7.12}$$

Typical choice of the goal function for chaotization is the largest Lyapunov exponent: $G = \lambda_1$ with $G_* > 0$. In some cases the total energy of mechanical or electrical oscillations can serve as $G(x)$.

In terms of goal functions more subtle control goals can be specified, for example, the control goal may be to modify a chaotic attractor of the free system in the sense of changing some of its characteristics (Lyapunov exponents, entropy, fractal dimension, etc.). The freedom of choice of the goal function can be utilized for design purposes.

7.3
Methods of Nonlinear Control

Among numerous nonlinear control methods that may be used for chaos control we will briefly describe just two big classes: goal-oriented methods and geometrical methods.

Goal-oriented techniques A number of methods are based on reduction of the current value of some goal (objective) function $Q(x(t), t)$. The current value $Q(x(t), t)$ may reflect the distance between the current state $x(t)$ and the current point of the goal trajectory $x_*(t)$, such as $Q(x, t) = |x - x_*(t)|^2$, or a function of the distance between the current state and the goal surface $h(x) = 0$, such as $Q(x) = |h(x)|^2$. For discrete-time systems a reasonable direction to change the control variable is the direction of the gradient of $Q(x)$ at the next step with respect to control u. For continuous-time systems the value $Q(x)$ does not depend directly on control u and decreasing the value of the speed $\dot{Q}(x) = \partial Q / \partial x F(x, u)$ can be posed as immediate control goal instead of decreasing $Q(x)$. This is the basic idea of the *speed gradient* (SG) method, which was first used for control of chaotic systems in [33–35]. Both gradient and speed gradient methods are described below in Sections 7.3.1 and 7.3.2.

Geometrical methods   A number of methods are based upon ideas of differential geometry used for transformation of the system description to a simplified form. A typical geometrical method is feedback linearization. It will be described in Section 7.3.3.

7.3.1
Gradient Method

Numerous systems in physics, biology, economics, and other areas can be described by discrete-time dynamical models. Even if a natural system is functioning in continuous time, its variables are often available for measurement or control only at some discrete sampling time instants and, therefore, the system model can be presented in a discrete-time form. Consider a class of controlled systems described by the discrete-time state-space model:

$$x_{k+1} = F(x_k, u_k), \quad y_k = h(x_k, u_k), \tag{7.13}$$

where $x_k \in \mathbb{R}^n$ is the value of the state vector at the kth step of system functioning, $y_k \in \mathbb{R}^l$ is the corresponding value of the output, and $u_k \in \mathbb{R}^m$ is the kth value of the input (control) action. The vector functions F and h are assumed to be well defined for all values of states and inputs. In the case when the model (7.13) describes behavior of a continuous-time system measured at some sampling instants $k = 0, 1, 2, \ldots$, the variables can be interpreted as follows: $x_k \in \mathbb{R}^n$ is the value of the state vector $x(t)$ at the sampling instant t_k; $y_k \in \mathbb{R}^l$ is the value of the output measured at the sampling instant t_k, and $u_k \in \mathbb{R}^m$ is the value of the input (control) applied to the system at the sampling interval $t_k \leq t < t_{k+1}$, $k = 0, 1, 2, \ldots$.

Let the goal function $Q(x) \geq 0$ be given and the control goal be specified as

$$Q(x_{k+1}) \leq \Delta, \quad \text{when} \quad k > k_*, \tag{7.14}$$

where $\Delta > 0$ is the prespecified threshold value. The gradient method of control algorithm design consists of two stages. At the first stage the reduced goal function depending on the number of the step is calculated, substituting (7.13) into (7.14):

$$Q_k(u) = Q(F_k(x_k, u)). \tag{7.15}$$

The reduced goal function directly depends on u. At the second stage the gradient vector

$$\nabla_u Q_k(u) = \text{col}\left(\frac{\partial Q_k(u)}{\partial u^{(1)}}, \ldots, \frac{\partial Q_k(u)}{\partial u^{(m)}}\right)$$

({\ it col} stands for column vector) is calculated and the control algorithm

$$u_{k+1} = u_k - \gamma_k \nabla_u Q_k(u_k), \tag{7.16}$$

where $\gamma_k \geq 0$ is the algorithm parameter (step size), is derived.

The algorithm (7.16) makes the current control correction $\Delta u_k = u_{k+1} - u_k$ along the descent direction of the current goal function $Q_k(u)$. The idea of the gradient method comes from optimization theory. However, in optimization problems the objective function does not depend on k. It is worth noting that there is no reason to use more complicated algorithms for control of a dynamical system because at every step the goal function may change.

A simple algorithm does not necessarily have simple applicability conditions. To formulate such conditions we use the so-called method of the *recursive goal inequalities* proposed by Yakubovich in 1966 [15, 16]. The key point of the method is to introduce a deadzone into the algorithm, i.e. to choose $\gamma_k = 0$ if the goal inequality (7.14) is fulfilled. The precise formulation of the applicability conditions can be found in [3, 15]. Essentially, three main conditions should be fulfilled: (A) the function $Q_k(u)$ is convex in u; (B) there exists a common solution $u = u_*$ to the system of the goal inequalities $Q_k(u) < \Delta$, $k = 0, 1, 2, \ldots$; (C) the choice of the gain γ_k takes into account the deadzone: if the current inequality $Q_k(u_k) \leq \Delta$ holds, then $\gamma_k = 0$ is chosen.

Note that it often happens that the right-hand side of the algorithm (7.16) depends on the whole nonmeasurable state vector x_k. There are two standard ways to treat such problems. The first is to include an additional dynamical system (so-called *observer*), which performs an online estimation of the unknown state vector. The second is to replace the state space model (7.2) of the controlled system by the input–output model:

$$y_{k+1} = \Phi(y_k, \ldots, y_{k-n}, u_k, \ldots, u_{k-n+1}). \tag{7.17}$$

Then at the kth step one will need to evaluate control in the form $u_k = U(y_k, \ldots, y_{k-n}, u_{k-1}, \ldots, u_{k-n+1})$ which is easier to design.

7.3.2
Speed-Gradient Method

A continuous-time counterpart of the gradient method is the so-called *speed-gradient (SG) method*. Like the gradient method for discrete-time systems, SG-method is intended for control problems where control goal is specified by means of a goal function.

Consider a nonlinear time-varying system

$$\dot{x} = F(x, u, t) \tag{7.18}$$

and control goal

$$\lim_{t \to \infty} Q(x(t), t) = 0, \tag{7.19}$$

where $Q(x, t) \geq 0$ is a smooth goal function.

In order to design the control algorithm the scalar function $\dot{Q} = \omega(x, u, t)$ is calculated that is the speed (rate) of changing $Q_t = Q(x(t), t)$ along trajectories of (7.18): $\omega(x, u, t) = \partial Q(x, t)/\partial t + [\nabla_x Q(x, t)]^\top F(x, u, t)$. Then it is required to evaluate the gradient of $\omega(x, u, t)$ with respect to input variables: $\nabla_u \omega(x, u, t) = (\partial \omega/\partial u)^\top = (\partial F/\partial u)^\top \nabla_x Q(x, t)$. Finally, the algorithm of changing $u(t)$ is determined according to the differential equation

$$\frac{du}{dt} = -\Gamma \nabla_u \omega(x, u, t), \tag{7.20}$$

where $\Gamma = \Gamma^\top > 0$ is a positive definite gain matrix, for example, $\Gamma = \text{diag}\{\gamma_1, \ldots, \gamma_m\}$, $\gamma_i > 0$. The algorithm (7.20) is called the *speed-gradient (SG) algorithm*, since it suggests to change $u(t)$ proportionally to the gradient of the speed of changing Q_t.

The origin of the algorithm (7.20) can be explained as follows. In order to achieve the control goal (7.19) it is desirable to change $u(t)$ in the direction where $Q(x(t), t)$ decrease. However, it may be a problem since $Q(x(t), t)$ does not depend on $u(t)$ directly. Instead one may try to decrease $\dot{Q}$ in order to achieve the inequality $\dot{Q} < 0$, which implies the decrease of $Q(x(t), t)$. The speed $\dot{Q} = \omega(x, u, t)$ generically depends on u explicitly which allows us to write down (7.20). The speed-gradient algorithm can also be interpreted as a continuous-time counterpart of the gradient algorithm, since for small sampling step size the direction of the gradient is close to the direction of the speed gradient.

Let us illustrate speed-gradient design methodology for a class of tracking control problems for controlled systems linear in the inputs:

$$\dot{x} = A(x, t) + B(x, t)u, \tag{7.21}$$

where $x(t) \in \mathbb{R}^n$ is the state vector, $u(t) \in \mathbb{R}^m$ is the vector of controlling variables (inputs) which may be either physical quantities or adjustable parameters, $A(x, t)$ is the n-vector, and $B(x, t)$ is the $n \times m$-matrix. Let the control goal have the form

$$\lim_{t \to \infty} [y(t) - y_*(t)] = 0, \tag{7.22}$$

where $y(t) = h(x(t)) \in \mathbb{R}^l$ is the l-vector of regulated variables (outputs), and $y_*(t) \in \mathbb{R}^l$ is the goal trajectory (desired trajectory) of the outputs. It is clear that the goal (7.22) has the equivalent form (7.19) if the goal function $Q(x, t)$ is chosen as follows:

$$Q(x, t) = \frac{1}{2}[y - y_*(t)]^\top P[y - y_*(t)], \tag{7.23}$$

where P is the symmetric positive-definite $l \times l$-matrix.

For the purpose of control algorithm design rewrite equation (7.21) in the form

$$\dot{x} = A(x, t) + \sum_{i=1}^{m} B_i(x, t) u_i, \tag{7.24}$$

where u_i are components of the vector $u \in \mathbb{R}^m$ and $B_i(x, t) \in \mathbb{R}^n$ are columns of the matrix $B(x, t)$. Then the rate (speed) of changing $Q(x(t), t)$ along trajectories of the system (for constant u) is as follows:

$$\omega(x, u, t) = [y - y_*(t)]^\top P[CA(x, t) + CB(x, t)u - \dot{y}_*(t)], \tag{7.25}$$

where $C = C(x, t) = \partial G(x, t)/\partial x$. Taking the gradient of (7.25) in u we obtain the speed gradient and the speed-gradient algorithm in the following form:

$$\nabla_u \omega(x, u, t) = B(x, t)^\top C^\top P[y - y_*(t)], \tag{7.26}$$

$$\frac{du}{dt} = -\Gamma B(x, t)^\top C^\top P[y - y_*(t)]. \tag{7.27}$$

To simplify design, the gain matrix Γ is often chosen as the diagonal matrix ($\Gamma = \text{diag}\{\gamma_i\}$) or scalar matrix ($\Gamma = \gamma I$) where γ_i, γ are positive numbers. For a special case of the system linear in inputs the algorithm (7.27) is nothing but the classical *integral control law*.

In a similar way the so-called speed-gradient algorithm is designed in finite form

$$u(t) = u_0 - \Gamma \nabla_u \omega(x(t), u(t), t), \tag{7.28}$$

where u_0 is some initial value of a control variable, for example, $u_0 = 0$. Algorithm (7.28) is a generalization of the classical *proportional control law*.

The more general form of speed-gradient algorithms is sometimes useful:

$$u(t) = u_0 - \gamma \psi(x(t), t), \tag{7.29}$$

where $\gamma > 0$ is the scalar gain parameter and the vector function $\psi(x, t)$ satisfies the so-called *pseudogradient condition*

$$\psi(x, t)^\top \nabla_u \omega(x, u, t) \geq 0 \tag{7.30}$$

for all x, u, t. A special case of (7.29) is called the *sign-like* or *relay-like* algorithm:

$$u(t) = u_0 - \gamma \, \text{sign} \, \nabla_u \omega(x(t), u(t), t), \tag{7.31}$$

where sign of a vector is understood component wise: for a vector $z = \text{col}(z_1, \ldots, z_m)$ sign z is defined as $\text{sign} \, z = \text{col}(\text{sign} \, z_1, \ldots, \text{sign} \, z_m)$.

In order to make a reasonable choice of the control algorithm parameters the applicability conditions should be verified. Let us formulate applicability conditions for a combined finite-differential version of the SG-algorithm

$$\frac{d(u + \lambda \psi(x,t))}{dt} = -\Gamma \nabla_u \omega(x,u,t) \tag{7.32}$$

where $\Gamma = \Gamma^\top > 0, \quad \psi(x,t)^\top \nabla_u \omega(x,u,t) \geq 0.$

Theorem 7.1 *Let the following assumptions A1–A4 be satisfied.*

A1 *The functions F and $\nabla_u \omega$ are continuous in x and u, piecewise continuous in t and locally bounded uniformly in t, that is for any $\beta > 0$ there exists $C(\beta)$ such that*

$$|F(x,u,t)| + |\nabla_u(x,t)| \leq C(\beta)$$

holds if $|x| \leq \beta$ and $|u| \leq \beta$.

A2 *The function Q is nonnegative, uniformly continuous in any set of the form $\{(x,t) : |x| \leq \beta, t \geq 0\}$ and radially unbounded, that is*

$$\inf_{t \geq 0} Q(x,t) \to +\infty \quad \text{if} \quad |x| \to \infty.$$

A3 *The function ω is convex in u, that is the inequality*

$$\omega(x,u_*,t) - \omega(x,u,t) \geq (u_* - u)^\top \nabla_u \omega(x,u,t)$$

holds for all $u \in \mathbb{R}^m, u_* \in \mathbb{R}^m, x \in \mathbb{R}^n, t \geq 0$.

A4 *There exists a constant vector $u_* \in \mathbb{R}^m$ and a nonnegative continuous scalar function $\rho : \mathbb{R}^n \to \mathbb{R}_+$ such that for any solution $x(t)$ of (7.18) the following inequality*

$$\omega(x(t),u_*,t) \leq -\rho(x(t))$$

holds for all $t \geq 0$.
Then any solution $(x(t), u(t))$ of (7.18), (7.32) is bounded and

$$\lim_{t \to \infty} \rho(x(t)) = 0.$$

First let us discuss assumptions A1–A4. Condition A1 guarantees existence and uniqueness of solutions of the system (7.18), (7.32) at least on some finite time interval and from the practical point of view this assumption is not restrictive. Assumption A2 about radial unboundedness of $Q(x,t)$ helps us to establish glo-

bal properties of the overall system. This assumption is valid, for example, for the quadratic objective function

$$Q(x, t) = (x - \bar{x}(t))^\top H(t)(x - \bar{x}(t))$$

if the vector $\bar{x}(t)$ is bounded and the matrix $H(t)$ is positive definite uniformly in t: $H(t) \geq \delta I_n, \delta > 0$.

The main conditions are A3 – convexity of the function $\omega(x, u, t)$ in u and A4 – existence of "ideal" control u_* such that $\omega(x, u_*, t) \leq 0$ for all x (attainability condition). Convexity condition A3 holds, for example, if the function ω is linear in u. To check Assumption A3 for twice differentiable in u functions ω it is sufficient to verify the inequality $\nabla_u^2 \omega(x, u, t) \geq 0$. Assumption A4 is the most restrictive one. It requires the existence of the constant value of the control variable for which the control objective is achieved. Also this assumption gives a clue to how to choose the objective function Q – it must coincide with the Lyapunov function of the overall system which proves its stability for some fixed (perhaps, unknown) value of the input variable.

More results concerning applicability conditions of speed-gradient algorithms can be found in [3, 17].

The speed-gradient algorithms can be modified to take into account constraints. For example, let the equality constraint be given as

$$g(x(t), u(t), t) = 0, \tag{7.33}$$

where g is a smooth scalar function, and a scalar control function $u(t)$ is to be chosen such that (7.33) is satisfied for all $t \geq 0$. The modified (constrained) SG-algorithm in differential form is as follows:

$$\dot{u}(t) = -\gamma \nabla_u \omega(x(t), u(t), t) - \lambda(t) \nabla_u g(x(t), u(t), t), \tag{7.34}$$

where the Lagrange multiplier $\lambda(t)$ is chosen to satisfy the condition $\dot{g} = 0$, that is

$$\lambda(t) = \frac{-\gamma \nabla_u \omega(x(t), u(t), t) + \nabla_x g^\top F(x(t), u(t), t) + \partial g / \partial t}{|\nabla_u g(x(t), u(t), t)|^2}. \tag{7.35}$$

The initial condition $u(0)$ should satisfy constraint too: $g(x(0), u(0), t) = 0$. The case of SG-algorithms in finite form and the case of inequality constraints are considered in a similar way.

The speed-gradient algorithm is tightly associated with the concept of Lyapunov function $V(x)$ – a function of the system state nonincreasing along its trajectories. The Lyapunov function is an abstraction for such physical characteristics as energy and entropy. It is important that the Lyapunov function can be used not only for analysis but also for system design. In particular, for the speed-gradient algorithms in the finite form the goal function itself may serve as the Lyapunov function: $V(x) = Q(x)$. The Lyapunov function for differential

form of SG-algorithms is as follows: $V(x,u) = Q(x) + 0.5(u - u_*)^\top \Gamma^{-1}(u - u_*)$, where u_* is the desired "ideal" value of controlling variables. Note that in order to justify the discrete-time gradient algorithm one may use the Lyapunov function as the square distance between the current and the "ideal" controlling variables $V(u) = |u - u_*|^2$.

7.3.3
Feedback Linearization

The gradient and the speed-gradient methods represent a family of *goal-oriented methods* which allow the designer of control system to create the control algorithm for a nonlinear controlled system as soon as the control goal is formulated by means of a goal function. However, it is not a unique approach to control system design. A number of other more sophisticated approaches can be found in the control literature (see [3, 17–22]). Below one of most popular methods, *feedback linearization*, will be briefly presented.

Consider the systems affine in control:

$$\dot{x} = f(x) + g(x)u. \tag{7.36}$$

Definition 7.2 System (7.36) is called *feedback linearizable in the open domain* $\Omega \in \mathbb{R}^n$ if there exists a smooth coordinate change $z = \Phi(x), x \in \Omega$, and a feedback transformation

$$u = a(x) + \beta(x)v, \tag{7.37}$$

with smooth functions a, β such that Φ and β are smoothly invertible in Ω and the closed loop system (7.36) and (7.37) is linear, i.e. there exist constant matrices $A \in \mathbb{R}^{n \times n}$ and $B \in \mathbb{R}^{n \times m}$ so that

$$f(x) + g(x)a(x) = A, \quad g(x)\beta(x) = B, \quad x \in \Omega. \tag{7.38}$$

Feedback linearizability of the system means that it is equivalent to the system

$$\dot{z} = Az + Bv, \tag{7.39}$$

where $z(t) \in \mathbb{R}^n$ is the new state vector and $v(t) \in \mathbb{R}^m$ is the new input, which contains the nonlinearities.

Definition 7.3 System (7.36) is said to have *relative degree* $r, r \leq n$, *at point* $x_0 \in \mathbb{R}^n$ *with respect to the output*

$$y = h(x), \tag{7.40}$$

if for any $x \in \Omega$, where Ω is some neighborhood of x_0, the following conditions are valid:

$$L_g L_f^k h(x) = 0, \ k = 0, 1, \ldots, r - 2, \quad L_g L_f^{r-1} h(x) \neq 0.$$

Recall that $L_\psi \phi(x) = \sum_{i=1}^n \frac{\partial \phi}{\partial x_i} \psi_i(x)$ stands for the Lie derivative of the vector function ϕ along the vector field ψ. Relative degree r is exactly equal to the number of times one has to differentiate the output in order to have the input explicitly appearing in the equation which describes the evolution of $y^{(r)}(t)$ in the neighborhood of x_0.

Theorem 7.4 *(Criterion of feedback linearizability for single-input/single-output systems). System (7.36) is feedback linearizable in the neighborhood Ω of a point $x_0 \in \mathbb{R}^n$ if and only if there exists a smooth scalar function $h(x)$ defined in Ω such that the relative degree r of (7.36), (7.40) is equal to n.*

In the case $r = n$ the state transformation $z = \Phi(x)$ and the feedback law reducing (7.36) to the chain of integrators (so-called *Brunovsky form*) can be chosen as follows:

$$\Phi(x) = \mathrm{col}(h(x), L_f h(x), \ldots, L_f^{n-1} h(x)) \tag{7.41}$$

$$u = \frac{1}{L_g L_f^{n-1} h(x)} \left[-L_f^n h(x) + v \right]. \tag{7.42}$$

7.3.4
Other Methods

For stabilization of a goal point or manifold other methods of modern nonlinear control theory have been used, for example, center manifold theory; backstepping iterative design or the method of macrovariables; passivity based design; absolute stability theory; H_∞ control; combination of Lyapunov and feedback linearization methods (see surveys [5, 6, 8]).

A number of papers are devoted to application of variable structure systems (VSS) and sliding modes [23–25]. Switching makes the system hybrid that potentially improves its performance yet complicates its analysis. Note that VSS algorithms for the switching surface $h(x) = 0$ coincide with the speed-gradient algorithms for the goal function $Q(x) = |h(x)|$. A fruitful direction is the use of frequency-domain methods applied to nonlinear control. In particular, approximate methods of harmonic balance for evaluation and prediction of chaotic modes can be used together with rigorous absolute stability theory [26]. An interesting method within this framework employs a selective ("washout") filter which damps all signals with frequencies beyond some narrow range [27]. If such a filter is included in the feedback loop of a chaotic system and the base frequency of the filter coincides with the frequency of one of the existing unstable periodic solutions, then it is plausible that the system will be in a periodic motion rather than in chaotic. This approach was applied to control of lasers.

The majority of nonlinear control approaches can be grouped into two large classes: goal-oriented approaches (Lyapunov, speed-gradient, passivity-based methods) and compensation approaches (feedback linearization, geometric methods). The interrelation between these classes can be illustrated as follows. Let the control goal be stabilization of some output variable $y = h(x)$ of the affine system $\dot{x} = f(x) + g(x)u$, at zero level. Lyapunov (or speed-gradient) methods introduce a goal function $Q(x) = |h(x)|^2$ and gradually decrease its derivative $\dot{Q}$ according to the condition $h^\top \partial h / \partial x (f + gu) < 0$, for example, moving along the speed gradient (antigradient of $\dot{Q}$):

$$u = -\gamma g^\top (\nabla h) h.$$

To respect the "small control" requirement it is necessary to choose sufficiently small gain $\gamma > 0$.

On the other hand, the compensation approaches introduce an auxiliary macrovariable $a(x) = \dot{y} + \varrho y$ with some $\varrho > 0$ and immediately force it to zero with the control:

$$u = -\frac{f^\top (\nabla h) + \varrho h}{g^\top (\nabla h)} \, .$$

Note that $a = 0$ if and only if $\dot{Q} = -2\varrho Q$, i.e. compensation is equivalent to specifying a rate decrease of $Q(x)$. As a result, any desired "instantaneous" transient rate can be achieved at the cost of loss of flexibility and loss of the "small control" property.

Therefore using the well-developed machinery of modern linear and nonlinear control theories often does not take full account of the special aspects of chaotic motions. This often means that the "small control" requirement is violated. To respect the "small control" requirement the gain $\gamma > 0$ should be sufficiently small. An outer deadzone may be introduced in terms of the goal function, for example

$$u(t) = \begin{cases} -\gamma \nabla_u \dot{Q}(x, u), & \text{if} \quad |Q(x(t))| \leq \Delta, \\ 0, & \text{otherwise.} \end{cases} \tag{7.43}$$

Another peculiarity of chaotic systems is that the models of chaotic systems often do not satisfy the global Lipschitz condition owing to the presence of polynomial nonlinearities $x_1 x_2$, x^2, etc. Although trajectories of chaotic systems are bounded, it is not necessarily the case when the system is influenced by control. Therefore, a special attention should be paid to providing boundedness of the solutions by special choice of controls. Otherwise the solution may escape in finite time and it will not make sense to discuss stability and convergence issues.

Let us demonstrate usage of nonlinear control methods for chaos control by examples.

7.3.5
Gradient Control of the Hénon System

The Hénon map is a popular example of two-dimensional quadratic mapping which produces the discrete-time system with chaotic behavior. The Hénon system is described by the following difference equations

$$\begin{cases} x_{k+1} = 1 - ax_k^2 + by_k, \\ y_{k+1} = x_k, \end{cases} \tag{7.44}$$

where x_k, y_k are the scalar state variables, a, b are the scalar parameters. The dynamics of the Hénon system is well studied (see, for example, [12]) and this system also has become a benchmark example in the studies concerning oscillations and chaos. It is not difficult to obtain that the fixed point of the Hénon map if exists is given by

$$(x_*, y_*) = \left(-c + \sqrt{c^2 + a}, -c + \sqrt{c^2 + a} \right), \tag{7.45}$$

where $c = (1 - b)/2$ and calculating eigenvalues of the Jacobi matrix calculated at this point one may derive that it is unstable for the following values of the system parameters: $a = 1.4, b = 0.3$.

Suppose that the system (7.44) can be controlled:

$$\left. \begin{cases} x_{k+1} = a - x_k^2 + by_k + u_k, \\ y_{k+1} = x_k, \end{cases} \right\} \tag{7.46}$$

where $u_k \in \mathbb{R}^1$ is the control action which is to be designed to achieve the desired behavior of the controlled system. Following [3, 28], consider the problem of stabilization of the unstable equilibrium for the Hénon system.

In this case the control goal is as follows:

$$\lim_{k \to \infty} x_k = x_*, \quad \lim_{k \to \infty} y_k = y_*$$

where (x_*, y_*) is an (unstable) fixed point of (7.46). This control goal can be characterized by the following objective function:

$$Q(x_{k+1}) = \frac{1}{2} |x_{k+1} - x_*|^2 \tag{7.47}$$

Solving this control problem we will assume that the whole state vector is available for measurements and the values of parameters a, b are known to the system designer.

Substituting x_{k+1} from (7.46) into (7.47) we obtain the objective function explicitly depending on the control and therefore after some simple calculations (see Section 2.7) we can obtain the gradient control algorithm

$$u_k = -\gamma \nabla_{u_k} Q(x_k)$$
$$= -\frac{\gamma}{1+\gamma}(a - x_k^2 + by_k - x_*) \tag{7.48}$$

Stability properties of the algorithm (7.48) are established by the following results.

Proposition 7.1 *A sufficient condition for the local stability of the fixed point of the controlled Hénon system (7.46), (7.48) is*

$$\gamma > (b + 2x_* - 1) \equiv 2(b-1) + \sqrt{(b-1)^2 + 4a}. \tag{7.49}$$

Proof: Consider the Jacobi matrix of the controlled system

$$D\tilde{H} = \begin{bmatrix} -2x/(1+\gamma) & b/(1+\gamma) \\ 1 & 0 \end{bmatrix} \tag{7.50}$$

and suppose that all its eigenvalues are less than 1 in absolute value at the fixed point

$$|-x_*\delta \pm \sqrt{(x_*\delta)^2 + b\delta}| < 1, \qquad \text{where} \quad \delta = 1/(1+\gamma). \tag{7.51}$$

Then we immediately obtain the condition (7.49).

Proposition 7.2 *A sufficient condition for the global stability of the fixed point of the controlled Hénon system (7.46), (7.48) is*

$$\gamma > (b + x_* + 1) \equiv \frac{1}{2}(3b + 1 + \sqrt{(b-1)^2 + 4a}). \tag{7.52}$$

Proof: Consider the following chain of inequalities (we denote $Q_k = Q(x_k)$):

$$2Q_{k+1} = (1+\gamma)^{-2}[f(x_k, y_k) - x_*]^2$$
$$= (1+\gamma)^{-2}[f(x_k, y_k) - f(x_*, x_*) + f(x_k, x_*) - f(x_k, x_*)]^2$$
$$= (1+\gamma)^{-2}[b(y_k - x_*) - (x_k + x_*)(x_k - x_*)]^2$$
$$\leq (1+\gamma)^{-2}[b|y_k - y_*| + |x_k + x_*||x_k - x_*|]^2.$$

Here we denote $f(x, y) = a - x^2 + by$. Denoting $\delta_k = |x_k - x_*| \geq 0$ and noticing that $|y_k - y_*| = |x_{k-1} - x_*|$, we have the following recursive inequality:

$$\delta_{k+1} \leq (1+\gamma)^{-1}[b\delta_{k-1} + |x_k + x_*|\delta_k] \leq (1+\gamma)^{-1}[b\delta_{k-1} + |2 + x_*|\delta_k]. \tag{7.53}$$

It is easy to show that all positive solutions of (7.53) tend to zero (i.e. the control goal is achieved) if all the roots $\lambda_{1,2}$ of the equation $\lambda^2 - A\lambda - B = 0$, with

$A = |2 + x_*|(1 + \gamma)^{-1}, B = b(1 + \gamma)^{-1}$, are less than unity in absolute value. Then we immediately obtain the condition (7.52).

7.3.6
Feedback Linearization Control of the Lorenz System

Consider the controlled Lorenz system with control appearing in the third equation:

$$\dot{x}_1 = \sigma(x_2 - x_1),$$
$$\dot{x}_2 = rx_1 - x_2 - x_1x_3,$$
$$\dot{x}_3 = -\beta x_3 + x_1x_2 + u.$$

Let $y = x_1$. Then

$$L_f y = \dot{y} = \dot{x}_1 = \sigma(x_2 - x_1),$$
$$L_f^2 y = L_f(L_f y) = \ddot{x}_1 = \sigma(\dot{x}_2 - \dot{x}_1) = \sigma[(r+1)x_1 - 2x_2 + x_1x_3],$$

and, therefore, the relative degree is equal to 3 everywhere except the plane $x_1 = 0$. New coordinates can be chosen as follows:

$$z = \Phi(x) : z_1 = x_1,$$
$$z_2 = \sigma(x_2 - x_1),$$
$$z_3 = \sigma[(r+1)x_1 + 2x_2 + x_1x_3],$$
$$x = \Phi^{-1}(z) : x_1 = z_1,$$
$$x_2 = \frac{1}{\sigma}z_2 + z_1,$$
$$x_3 = \frac{1}{x_1}\left[\frac{1}{\sigma}z_3 - (r-1)z_1 - \frac{2}{\sigma}z_2\right].$$

It is seen that the system is feedback linearizable for $x_1 \neq 0$. Thus for the Lorenz system there is no globally defined smooth feedback linearizing transformation. Feedback linearization allows us to stabilize the system to any fixed point in any half-space $\{x_1 < 0\}$, and $\{x_1 > 0\}$ is not suitable for global stabilization of the Lorenz system. Another disadvantage is in that the approach ignores the internal dynamics of the system and formally allows us to achieve any desired dynamics of the closed loop system. In fact the achievement of arbitrary dynamical behavior may require significant power of control, for example, if the initial state is far from the desired one or the desired motion is rapidly changing. Such a drawback is typical for a number of works based on conventional control theory approaches.

Another problem is that of incomplete measurements. A standard approach to output feedback control is using an observer-based controller that allows for

systematic use of dynamic output feedback. Proportional feedback in the extended space (x, u) (i.e. dynamic feedback) aimed at achievement of the desired dynamics of the closed loop system was proposed and examined in [29, 30].

The potential of dynamic feedback can be better exploited using an observer-based framework that allows for systematic use of output feedback. A survey of nonlinear observer techniques can be found in [31] (see also Sec. 5.2). Linear high-gain observer-based control for globally Lipschitz nonlinearities was studied in [32].

Note that models of chaotic systems often do not satisfy a global Lipschitz condition owing to the presence of polynomial nonlinearities $x_1 x_2$, x^2, etc. Although trajectories of chaotic systems are bounded, this is not necessarily the case when the system is influenced by control. Therefore special attention should be paid to providing boundedness of the solutions by appropriate choice of controls. Otherwise the solution may escape in finite time and it does not make sense to discuss stability and convergence issues. The possibility of escape in nonlinear controlled systems is often overlooked in application papers.

7.3.7
Speed-Gradient Stabilization of the Equilibrium Point for the Thermal Convection Loop Model

One of the simplest experimental setups which can demonstrate complex oscillatory behavior is the chaotic thermal convection loop. In the literature the following controlled thermal convection loop model was considered [36]:

$$
\begin{aligned}
\dot{x} &= \sigma(y - x), \\
\dot{y} &= -y - xz, \\
\dot{z} &= -z + xy - r + u,
\end{aligned}
\tag{7.54}
$$

where u is the control variable which is a fluctuation in the heating rate superimposed on the nominal rate r, σ is the Prandtl number, and r is the Raleigh number. This model can be obtained from the Lorenz system by replacing $z - r$ with z and assuming that $r = \mathrm{const}$ and $b = 1$. For $u = 0$ and $0 < r < 1$ the system has one stable globally attracting equilibrium $(0, 0, -r)$ that corresponds to the no-motion state of the thermal convection. At $r = 1$ two additional equilibrium points C_+ and C_- emerge: $x = y = \pm\sqrt{r - 1}$, $z = -1$. The convection equilibria lose their stability in the Andronov-Hopf bifurcation at $r = \sigma(\sigma + 4)/(\sigma - 2)$. For larger values of the parameter r the system has no more equilibrium points.

In [36] the on–off controller was proposed to stabilize the inherent unstable equilibrium point of this system:

$$
u = -\gamma \mathrm{sgn}(z + 1).
\tag{7.55}
$$

Practical experimentation showed that the controller (7.55) stabilizes the thermal convection in either clockwise or counterclockwise direction that corresponds to the stabilization of one of the equilibria C_+ or C_-.

It was proved in [3] that the controller (7.55) is a special case of the speed-gradient algorithm in finite form (7.31) for the objective function

$$Q(x, y, z) = (x - \sqrt{r-1})^2/\sigma + (y - \sqrt{r-1})^2 + (z+1)^2.$$

It was shown that any trajectory of the overall system tends to some rest point contained in the set of points (x, y, z) such that

$$\left\{ x = y, \left| (x + \sqrt{r-1})(x - \sqrt{r-1}) \right| \leq \gamma, z = -1 \right\}. \tag{7.56}$$

It yields convergence of the solution to the neighborhood of one of the inherent equilibrium points C_+ or C_- for small γ.

7.4
Adaptive Control

7.4.1
General Definitions

In a variety of physical applications parameters of the system under control are unknown. Information about the structure of the model may also be incomplete. It makes adaptive control schemes very promising. Most methods belong to either direct or indirect (identification-based) parametric adaptive control schemes. In the direct case the model of the system is represented in a parametric form:

$$\dot{x} = F(x, \theta, u), y = h(x), \tag{7.57}$$

where θ is a vector of unknown parameters. Based on (7.57), a parametric representation of the controller is

$$u = \mathcal{U}(x, u, \hat{\theta}), \tag{7.58}$$

where $\hat{\theta}$ is a vector of adjustable parameters that are changed according to the adaptation law

$$\hat{\theta}(t) = \Theta'[x(s), u(s), \hat{\theta}(s), 0 \leq s \leq t]. \tag{7.59}$$

Most existing results are based on linearly parameterized models (7.57) or linearly parameterized controllers (7.58). If the initial model is not linearly parameterized, one may try to transform it to a linearly parameterized form. The

controller (7.58) is usually designed using model reference or feedback lineari-zation approaches. Proofs are typically based on Lyapunov functions, quadratic in original or in some transformed variables.

7.4.2
Adaptive Master-Slave Synchronization of Rössler Systems

Consider the Rössler system:

$$\begin{cases} \dot{\zeta}_1 = -\zeta_2 - \zeta_3 \\ \dot{\zeta}_2 = \zeta_1 + a\zeta_2 \\ \dot{\zeta}_3 = c + \zeta_3(\zeta_1 - b) \end{cases} \tag{7.60}$$

with output

$$\zeta_3 = (001)\zeta.$$

Assume that the coefficients a, b, c are positive. From (7.60) one can easily see that $\zeta_3 = 0$ implies $\dot{\zeta}_3 = c > 0$, from which it follows that whenever $\zeta_3(0) \geq 0$ then $\zeta_3(t) = y(t) > 0$ for all $t > 0$ (the graph of $\zeta_3(t)$ cannot intersect the line $\zeta_3 = 0$ since otherwise $\dot{\zeta}_3$ should be nonpositive for $\zeta_3 = 0$). Consider the comparison function $V = (\zeta_1^2 + \zeta_2^2)/2 + \zeta_3 > 0$. Taking the time deriva-tive of this function along the solutions of the Rössler system yields $\dot{V} = a\zeta_2^2 + c - b\zeta_3 \leq 2aV + c$, which implies that the solutions (with $\zeta_3(0) \geq 0$) are well defined on the infinite time interval $[0, \infty)$.

The problem we address is to design a dynamical system (slave) such that some functions of its state vector converge toward $\zeta_1(t), \zeta_2(t), \zeta_3(t)$. One diffi-culty of the design is that some parameters of the master system are unknown. Another problem is that the equations of the slave system can depend on the output of the master, rather than on its whole state vector of the master system. From a control theory point of view this problem is often referred to as adaptive observer design problem. Since unknown parameters enter the initial system model nonlinearly, we introduce the following change of coordinates

$$(x_1 x_2 x_3) = (\zeta_1 \zeta_2 \log \zeta_3), y = \log \zeta_3,$$

which is well defined as long as $\zeta_3(t) > 0$ for all $t > 0$.

$$\begin{pmatrix} \dot{x}_1 \\ \dot{x}_2 \\ \dot{x}_3 \end{pmatrix} = \underbrace{\begin{pmatrix} 0 & -1 & 0 \\ 1 & a & 0 \\ 1 & 0 & 0 \end{pmatrix}}_{A} \begin{pmatrix} x_1 \\ x_2 \\ x_3 \end{pmatrix} + \underbrace{\begin{pmatrix} -e^y \\ 0 \\ -b \end{pmatrix}}_{f_0(y)} + c \underbrace{\begin{pmatrix} 0 \\ 0 \\ e^{-y} \end{pmatrix}}_{f_1(y)}, \tag{7.61}$$

$$y = x_3 = Cx, \quad C = (001).$$

Suppose that the parameter c is unknown, $\theta = c$, and the problem is to design an adaptive observer to estimate the variables x_1 and x_2 and the value of the unknown parameter c. To do so, we first introduce a new variable $\xi \in \mathbb{R}^2$:

$$\begin{pmatrix} \dot{\xi}_1 \\ \dot{\xi}_2 \end{pmatrix} = \begin{pmatrix} k_1 & -1 \\ k_2 + 1 & a \end{pmatrix} \begin{pmatrix} \xi_1 \\ \xi_2 \end{pmatrix} + \begin{pmatrix} k_1 \\ k_2 \end{pmatrix} e^{-y}$$

where the constants k_1 and k_2 are chosen such that the matrix

$$\begin{pmatrix} k_1 & -1 \\ k_2 + 1 & a \end{pmatrix}$$

is Hurwitz. Introduce the variable $\eta \in \mathbb{R}^2$:

$$\begin{pmatrix} \eta_1 \\ \eta_2 \end{pmatrix} = \begin{pmatrix} x_1 \\ x_2 \end{pmatrix} - \theta \begin{pmatrix} \xi_1 \\ \xi_2 \end{pmatrix} + \begin{pmatrix} k_1 \\ k_2 \end{pmatrix} y$$

Now let us rewrite the system in the (η, y) coordinates:

$$\begin{pmatrix} \dot{\eta}_1 \\ \dot{\eta}_2 \\ \dot{y} \end{pmatrix} = \underbrace{\begin{pmatrix} k_1 & -1 & -k_1^2 + k_2 \\ k_2 + 1 & a & -(k_1 k_2 + k_1 + a k_2) \\ 1 & 0 & -k_1 \end{pmatrix}}_{\bar{A}} \begin{pmatrix} \eta_1 \\ \eta_2 \\ y \end{pmatrix}$$

$$+ \underbrace{\begin{pmatrix} -k_1 b - e^y \\ -k_2 b \\ -b \end{pmatrix}}_{\bar{f}_0} + \theta \underbrace{\begin{pmatrix} 0 \\ 0 \\ 1 \end{pmatrix}}_{B} \underbrace{(\xi_1 + e^{-y})}_{u}.$$

For the chosen values of k_1, k_2 it is possible to find a positive definite matrix $P = P^\top$ and a matrix $L = (l_1, l_2, l_3)^\top$ such that the matrix

$$(\bar{A} - LC)^\top P + P(\bar{A} - LC) \tag{7.62}$$

is negative definite and $P\bar{B} = C^\top$. Therefore, the adaptive observer equations with the speed-gradient adaptation law can be chosen as follows:

$$\begin{pmatrix} \dot{\hat{\eta}}_1 \\ \dot{\hat{\eta}}_2 \\ \dot{\hat{y}} \end{pmatrix} = \begin{pmatrix} k_1 & -1 & -k_1^2 + k_2 \\ k_2 + 1 & a & -(k_1 k_2 + k_1 + a k_2) \\ 1 & 0 & -k_1 \end{pmatrix} \begin{pmatrix} \hat{\eta}_1 \\ \hat{\eta}_2 \\ \hat{y} \end{pmatrix}$$

$$+ \begin{pmatrix} -k_1 b - e^y \\ -k_2 b \\ -b \end{pmatrix} + \hat{\theta} \begin{pmatrix} 0 \\ 0 \\ 1 \end{pmatrix} (\xi_1 + e^{-y}) + \begin{pmatrix} l_1 \\ l_2 \\ l_3 \end{pmatrix} (\hat{y} - y)$$

$$\dot{\hat{\theta}} = -\gamma (\xi_1 + e^{-y})(\hat{y} - y), \quad \gamma > 0.$$

If the signal $(\xi_1(t) + e^{-y(t)})$ satisfies the so-called Persistency of Excitation condition (see, for example, [17]) (this is the case if $y(t)$ is bounded) the estimate $\widehat{\theta}(t)$ converges to its true value c and therefore one can estimate the variables $x_1(t)$ and $x_2(t)$:

$$\begin{pmatrix} \widehat{x}_1(t) \\ \widehat{x}_2(t) \end{pmatrix} = \begin{pmatrix} \widehat{\eta}_1(t) \\ \widehat{\eta}_2(t) \end{pmatrix} + \widehat{\theta}(t) \begin{pmatrix} \xi_1(t) \\ \xi_2(t) \end{pmatrix} - \begin{pmatrix} k_1 \\ k_2 \end{pmatrix} y(t).$$

We carried out computer simulation to demonstrate the convergence property of the designed adaptive observer for the following values of system parameters: $a = 0.2, b = 5.7, c = 0.2$. For these values of parameters the system possesses chaotic attractor and the initial conditions of the system were chosen in its domain of attraction: $x_1(0) = 2, x_2(0) = 1, x_3(0) = 1$; the observer parameters were chosen as $k_1 = -5$, $k_2 = 30$, $l_1 = 0, l_2 = 0, l_3 = -100$, $\gamma = 8$. The initial conditions of the observer were $\widehat{\eta}_1(0) = 1, \widehat{\eta}_2(0) = 2, \widehat{y}(0) = -30, \xi_1(0) = 0$, $\xi_2(0) = 0, \widehat{\theta}(0) = 0$. Figure 7.1 (left) demonstrates the convergence of the adjustable parameter $\widehat{\theta}(t)$ to its true value, and the Fig. 7.1 (right) shows that the error between the variables $x_1(t)$ and $x_2(t)$ and their estimates decays with time.

As a simple exercise we propose the reader to design an adaptive observer for the Rössler system under the additional condition that the parameter b is unknown as well.

Let us design an adaptive observer for the Rössler system from the previous example, yet this time we assume that the parameter a is unknown. Let Q be the matrix

$$Q = \begin{pmatrix} -a & -1 & 1 \\ 1 & 0 & -a \\ 0 & 0 & 1 \end{pmatrix}, \quad Q^{-1} = \begin{pmatrix} 0 & 1 & a \\ -1 & -a & -(a^2 - 1) \\ 0 & 0 & 1 \end{pmatrix}.$$

Introduce a new variable $z \in \mathbb{R}^3$: $z = Qx$. Then the system (7.61) can be rewritten as follows:

$$\begin{pmatrix} \dot{z}_1 \\ \dot{z}_2 \\ \dot{z}_3 \end{pmatrix} = \underbrace{\begin{pmatrix} 0 & 0 & 0 \\ 1 & 0 & -1 \\ 0 & 1 & 0 \end{pmatrix}}_{A} \begin{pmatrix} z_1 \\ z_2 \\ z_3 \end{pmatrix} + \underbrace{\begin{pmatrix} ce^{-y} - b \\ -e^y \\ ce^{-y} - b \end{pmatrix}}_{f_0(y)} + a \underbrace{\begin{pmatrix} e^y \\ -ce^{-y} + b \\ y \end{pmatrix}}_{f_1(y)},$$

$$y = z_3 = Cz, \quad C = (001).$$

Suppose a is unknown, $\theta = a$. Introduce the variable $\xi \in \mathbb{R}^2$:

$$\begin{pmatrix} \dot{\xi}_1 \\ \dot{\xi}_2 \end{pmatrix} = \begin{pmatrix} 0 & k_1 \\ 1 & k_2 \end{pmatrix} \begin{pmatrix} \xi_1 \\ \xi_2 \end{pmatrix} + \begin{pmatrix} k_1 \\ k_2 \end{pmatrix} y + \begin{pmatrix} e^y \\ -ce^y + b \end{pmatrix},$$
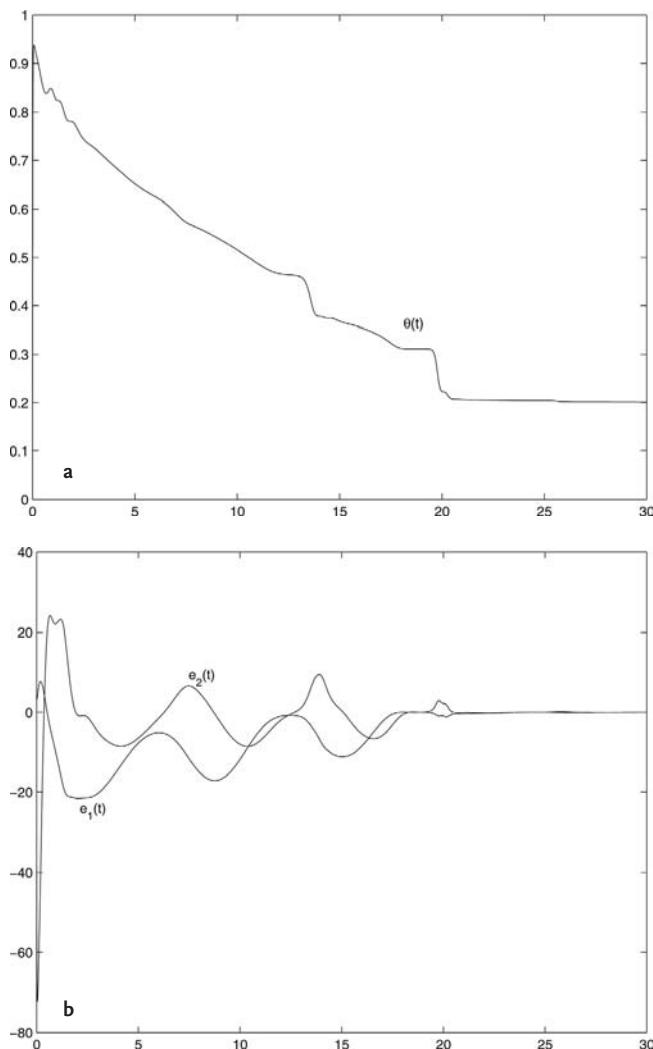
Fig. 7.1 a Convergence of the adjustable parameter to its true value. **b** Estimation error versus time.

where the constants k_1 and k_2 are negative, $k_1, k_2 < 0$. Introduce the variable $\eta \in \mathbb{R}^2$:

$$\begin{pmatrix} \eta_1 \\ \eta_2 \end{pmatrix} = \begin{pmatrix} z_1 \\ z_2 \end{pmatrix} - \theta \begin{pmatrix} \xi_1 \\ \xi_2 \end{pmatrix} + \begin{pmatrix} k_1 \\ k_2 \end{pmatrix} y$$

Then

$$
\begin{pmatrix} \dot{\eta}_1 \\ \dot{\eta}_2 \\ \dot{y} \end{pmatrix} = \underbrace{\begin{pmatrix} 0 & k_1 & -k_1 k_2 \\ 1 & k_2 & -(k_1 + k_2^2 + 1) \\ 0 & 1 & k_2 \end{pmatrix}}_{\bar{A}} \begin{pmatrix} \eta_1 \\ \eta_2 \\ y \end{pmatrix}
$$

$$
+ \underbrace{\begin{pmatrix} (k_1 + 1)(ce^{-y} - b) \\ k_2(ce^{-y} - b) - e^y \\ ce^{-y} - b \end{pmatrix}}_{\bar{f}_0} + \theta \underbrace{\begin{pmatrix} 0 \\ 0 \\ 1 \end{pmatrix}}_{\bar{B}} \underbrace{(\xi_2 + y)}_{u}.
$$

The triple $(\bar{A}, \bar{B}, C)$ is strictly passifiable via output injection provided $k_1, k_2 < 0$, that is, there is a positive definite $P = P^\top$ such that (7.62) is negative definite and $P\bar{B} = C^\top$ and the adaptive observer for this system can be designed according to the speed-gradient method as follows:

$$
\begin{pmatrix} \dot{\widehat{\eta}}_1 \\ \dot{\widehat{\eta}}_2 \\ \dot{\widehat{y}} \end{pmatrix} = \begin{pmatrix} 0 & k_1 & -k_1 k_2 \\ 1 & k_2 & -(k_1 + k_2^2 + 1) \\ 0 & 1 & k_2 \end{pmatrix} \begin{pmatrix} \widehat{\eta}_1 \\ \widehat{\eta}_2 \\ \widehat{y} \end{pmatrix}
$$

$$
+ \begin{pmatrix} (k_1 + 1)(ce^{-y} - b) \\ k_2(ce^{-y} - b) - e^y \\ ce^{-y} - b \end{pmatrix} + \widehat{\theta} \begin{pmatrix} 0 \\ 0 \\ 1 \end{pmatrix} (\xi_2 + y)
$$

$$
+ \begin{pmatrix} l_1 \\ l_2 \\ l_3 \end{pmatrix} (\widehat{y} - y)
$$

$$
\dot{\widehat{\theta}} = -\gamma(\xi_2 + y)(\widehat{y} - y), \quad \gamma > 0,
$$

where the gain $L = (l_1, l_2, l_3)^\top$ is chosen such that (7.62) is negative definite.

As before, if the function $\xi_2(t) + y(t)$ satisfies the Persistency of Excitation condition, the estimate $\widehat{\theta}(t)$ converges to its true value a and one can estimate the variables $x_1(t)$ and $x_2(t)$ as follows:

$$
\widehat{x}_1(t) = \widehat{\eta}_2(t) + \widehat{\theta}(t)(\xi_2(t) + y(t)) - k_2 y(t)
$$

$$
\widehat{x}_2(t) = -\widehat{\eta}_1(t) - \widehat{\theta}(t)\widehat{\eta}_2(t) - \widehat{\theta}(t)\xi_1(t) - \widehat{\theta}^2(t)\xi_2(t)
$$

$$
+ k_1 y(t) + k_2 \widehat{\theta}(t)y(t) - \widehat{\theta}^2(t)y(t) + y(t).
$$

To verify the theoretical results we performed a simulation with the following parameters: $a = 0.2, b = 5.7, c = 0.2, \ x_1(0) = 2, x_2(0) = 1, x_3(0) = 1, \ k_1 = -3,$ $k_2 = -3, \ l_1 = k_1 k_2, \ l_2 = k_1 + k_2^2 + 1, \ l_3 = -k_2 - 100, \ \gamma = 30.$ The initial conditions of the observer were taken as $\widehat{\eta}_1(0) = 1, \ \widehat{\eta}_2(0) = 2, \ \widehat{y}(0) = 0, \xi_1(0) = 0,$ $\xi_2(0) = 0, \ \widehat{\theta}(0) = 0.$ The results of simulation are presented jointly in Fig. 7.2.
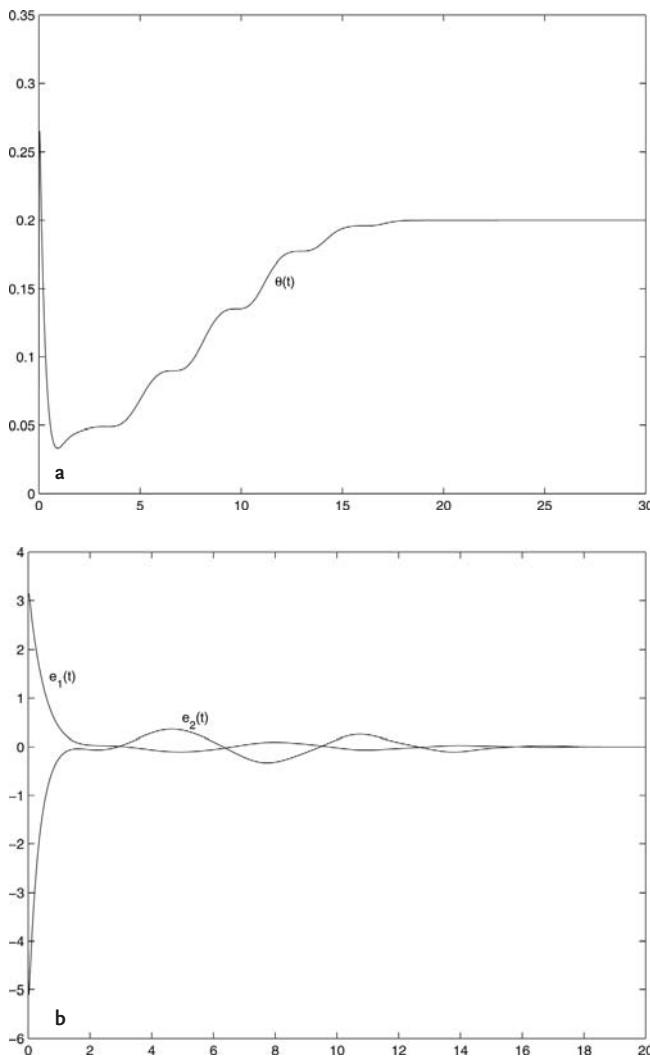
Fig. 7.2 a Convergence of the adjustable parameter to its true value. **b** Estimation error versus time.

7.5
Other Problems

Among other problems related to control of chaos the following ones are most important.

Controllability Although controllability of nonlinear systems is well studied, few results are available on reachability of typical control goals by small control. A general idea, illustrated by many case studies is that the more a system is

"unstable" (chaotic, turbulent) the "simpler," or the "cheaper," is to achieve exact or approximate controllability.

Other control goals Among alternative control goals achieving the desired period, desired process dimension, desired invariant measure, desired Kolmogorov entropy are studied in the literature. A method for the so-called *tracking chaos* problem, following a time-varying unstable orbit, was proposed by Schwartz and Triandaf in 1992 based on the continuation method for solving equations.

Identification A number of papers are devoted to identification of chaotic systems. In most of them conventional identification schemes are used. It has been demonstrated that the presence of chaos facilitates and improves parameter convergence.

Chaos in control systems *Control of chaos* should not be mixed up with *chaos in control systems*. In the latter field that has been developed since the late 1970s, conditions for chaotic behavior in conventional feedback control systems are under examination.

7.6
Conclusions

It is seen from the publication statistics that the field is rapidly developing in the beginning of the 21st century. Today, there are many efficient methods for control of chaos in the literature. Using the methods of nonlinear and adaptive control is very promising. However, special care should be taken to respect "small control" requirement. Among methods of nonlinear control feedback linearization and goal-oriented techniques are the most popular ones. They can also be used for adaptive control.

   Possibilities of controlling complex behavior by means of small control open new horizons both in science and in technology. Such methods may be efficient for solving problems where applying stronger control is not possible either because of lack of resources (as in many large scale systems: economies, energy systems, weather control and others) or because intervening natural dynamics is undesirable (for example, in biological and biomedical applications, environmental systems). Development of new methods for control of chaos or "control by tiny corrections" may be of utmost importance for sustained development of humanity.

Acknowledgment

References

1 Ott, T., Grebogi, C., Yorke, G. Controlling chaos, Phys. Rev. Lett. 1990, Vol. 64, No. 11, pp. 1196–1199.

2 Pyragas, K. Continuous control of chaos by self-controlling feedback, Phys. Lett. A 1992, Vol. 170, pp. 421–428.

3 Fradkov, A. L., Pogromsky, A. Yu. *Introduction to Control of Oscillations and Chaos.* World Scientific, Singapore, 1998.

4 Chen, G., Dong, X. *From chaos to order: perspectives, methodologies and applications.* World Scientific, Singapore, 1998.

5 Andrievsky, B. R., Fradkov, A. L. Control of chaos: I. Methods. Autom. Remote Control 2003, Vol. 64, No. 5, pp. 673–713.

6 Andrievsky, B. R., Fradkov, A. L. Control of chaos. II. Applications. Autom. Remote Control 2004, Vol. 65, No. 4, pp. 505–533.

7 Fradkov, A. L. Control of chaotic systems. In: *Encyclopedia of Life Support Systems (EOLSS)*, Developed under the auspices of the UNESCO, Eolss Publishers, Oxford, UK, 2003 [http://www.eolss.net].

8 Fradkov, A. L., Evans, R. J. Control of chaos: Methods and applications in engineering, Annu. Rev. Control 2005, Vol. 29, No. 1, pp. 33–56.

9 Moon, F. *Chaotic and Fractal Dynamics. An Introduction for Applied Scientists and Engineers.* Wiley, New York, 1992.

10 Neimark, Yu. I., Landa, P. S. *Stochastic and Chaotic Oscillations,* Kluwer, Dordrecht, 1987 (translated from the Russian edition).

11 Strogatz, S. *Nonlinear Dynamics and Chaos.* Addison-Wesley, Reading, MA, 1994.

12 Devaney, R. *A First Course in Chaotic Dynamical Systems.* Addison-Wesley, Reading, MA, 1992.

13 Ruelle, D., Takens, F. On the nature of turbulence, Comm. Math. Phys. 1971, Vol. 20, No. 2, pp. 167–192.

14 Katok, A., Hasselblat, B. *Introduction to the Modern Theory of Dynamical Systems. Encyclopedia of Mathematics and Its Applications*, No. 54, Cambridge University Press, London.

15 Bondarko, V. A., Yakubovich, V. A. The method of recursive goal inequalities in adaptive control theory, Int. J. Adaptive Control Sign. Proc. 1992, Vol. 6, No. 3, pp. 141–160.

16 Fomin, V., Fradkov, A., Yakubovich, A. *Adaptive Control of Dynamical Systems,* Nauka, Moscow, in Russian.

17 Fradkov, A. L., Miroshnik, I. V., Nikiforov, V. O. *Nonlinear and Adaptive Control of Complex Systems.* Kluwer, Dordrecht, 1999.

18 Nijmeijer, H., van der Schaft, A. J. *Nonlinear Dynamical Control Systems.* Springer, New York, 1990.

19 Isidori, A. *Nonlinear Control Systems.* 3rd edition. Springer, New York, 1995.

20 Khalil, H. K. *Nonlinear Systems.* 3rd edition. Prentice-Hall, Upper Saddle River, 2002.

21 Krstić, M., Kanellakopoulos, I., Kokotović, P. V. *Nonlinear and Adaptive Control Design.* Wiley, New York, 1995.

22 Zhou, K., Doyle, J. C., Glover, K. *Robust and Optimal Control.* Prentice-Hall, Englewood Cliffs, NJ, 1996.

23 Konishi, K., Hirai, M., Kokame, H. Sliding mode control for a class of chaotic systems, Phys. Lett. A 1998, Vol. 245, pp. 511–517.

24 Yau, H. T., Chen, C. K., Chen, C. L. Sliding mode control of chaotic systems with uncertainties, Int. J. Bifur. Chaos 2000, Vol. 10, pp. 1139–1147.

25 Yu, X. H. Variable structure control approach for controlling chaos. Chaos, Solitons, Fractals 1997, Vol. 8, pp. 1577–1586.

26 Basso, M., Genesio, R., Giovanardi, L., Tesi, A. Frequency domain methods for chaos control. In: *Controlling Chaos and Bifurcations in Engineering Systems.* Ed. G. Chen, CRC Press, Boca Raton, FL, 1999, pp. 179–204.

27 Meucci, R., Labate, A., Ciofini, M. Controlling chaos by negative feedback of subharmonic components, Phys. Rev. E 1997, Vol. 56, pp. 2829–2834.

28 Guzenko, P. Yu., Fradkov, A. L. Gradient control of Hénon map dynamics. Int. J.

Bifur. Chaos 1997, Vol. 7, No. 3, pp. 701–705.

29 Magnitskii, N. A., Sidorov, S. V. Control of chaos in nonlinear dynamical systems, Diff. Eq. 1998, Vol. 34, pp. 1501–1509.

30 Zhao, H., Wang, Y. H., Zhang, Z. B. Extended pole placement technique and its applications for targeting unstable periodic orbit. Phys. Rev. E 1998, Vol. 57, pp. 5358–5365.

31 Nijmeijer, H., Mareels, I. M. Y. An observer looks at synchronization, IEEE Trans. Circ. Syst. I 1997, Vol. 44, pp. 882–890.

32 Liao, T. L. Observer-based approach for controlling chaotic systems, Phys. Rev. E. 1998, Vol. 57, pp. 1604–1610.

33 Fradkov, A. L. Nonlinear adaptive control: regulation, tracking, oscillations. Proc.

1st IFAC Workshop "New trends in design of control systems", Smolenice, 1994, pp. 426–431.

34 Fradkov, A. L., Pogromsky, A. Yu. Methods of adaptive control of chaotic systems. Proc. of 12th IFAC World Congress, San Francisco, 1996, pp. 185–190.

35 Fradkov, A. L., Pogromsky, A. Yu. Speed gradient control of chaotic continuous-time systems. IEEE Trans. Circ. Syst. I 1996, Vol. 43, pp. 907–913.

36 Singer, J., Wang, Y. Z., Bau, H. H. Controlling a chaotic system. Phys. Rev. Lett. 1991, Vol. 66, pp. 1123–1125.

37 Guckenheimer, J., Holmes, P. *Nonlinear Oscillations, Dynamical Systems and Bifurcations of Vector Fields*. Springer, Berlin, 1983.

Part II
Controlling Space-Time Chaos

8
Localized Control of Spatiotemporal Chaos

Roman O. Grigoriev and Andreas Handel

8.1
Introduction

Many physical, chemical, and biological systems of interest evolve in a nonequilibrium environment. As these systems are driven further out of equilibrium, they tend to display progressively more complicated dynamics, with steady spatially uniform states replaced first by nonchaotic patterned states and eventually by spatiotemporal chaos. This complexity is often undesirable and considerable benefits could be derived by forcing the system toward a less complex (but usually unstable) steady or time-periodic state. In response to this challenge, control of spatiotemporal chaos has emerged in recent years as a problem of increasing fundamental and applied value.

Control of turbulent boundary flows [17], mechanical vibrations, and noise [37] is already an indispensable component of industrial design. Many other significant technological applications, such as mixing [62], optical fiber manufacture [70], coating [4, 39], wide aperture semiconductor lasers [56], inertial confinement [67], combustion [81], and chemical reactions [10], could crucially benefit from our ability to control (either suppress or enhance) the instabilities leading to complex spatiotemporal dynamics. Considerable effort is currently being invested in control of ventricular fibrillation [79] and epilepsy [23].

Besides these practical applications, the ability to control spatiotemporal dynamics opens up a whole new direction in fundamental research by providing a unique capability to study otherwise inaccessible unstable states of extended nonequilibrium systems. This capability can be used, for instance, to experimentally construct complete bifurcation diagrams [49], study the dynamics and stability of isolated modes [22], detect and study unstable recurrent patterns [5], or reproducibly impose initial conditions [74].

Although the first attempts to control spatiotemporally complex dynamics are centuries old, a scientific approach has not been employed until 1904, when boundary layer theory was developed by Prandtl [68]. Subsequent attempts to suppress turbulence, from either empirical or linear stability perspective, lead to

the creation of the field of flow control. More recently, control of low-dimensional chaos in nonlinear systems, that originated with the work of Ott, Grebogi, and Yorke [61] based on Floquet theory, has been extended to spatiotemporal dynamics. These two, originally independent, tracks have now merged, as recent studies (e.g., by Kawahara [47]) indicate.

The following classification [17] of various control approaches is helpful: By *passive* control we will understand applying any time-independent perturbation which tends to suppress the instability. *Predetermined active* control goes one step further by generalizing the class of perturbations to include time dependence. We will refer to these two approaches as *open-loop* control. In contrast, the *closed-loop* control is based on feedback: it aims to stabilize an unstable steady (or time periodic) state of the system by applying perturbations which depend on the deviation from that state.

Below, we will concentrate on closed-loop control as the most advanced way to influence the dynamics. Although it is more difficult to design and implement, closed-loop control offers a number of significant advantages over the open-loop variety. First, closed-loop control can be systematically designed by following a few rather general principles, while no systematic ways of designing open-loop control exist. Closed-loop control is substantially more energy efficient because the magnitude of feedback depends on the deviation from the target state: effectively the control is switched off in the absence of disturbances, while the open-loop control is always on. Equally important from the practical standpoint, closed-loop control is generally more flexible and robust: it can be designed to handle noise and uncertainties in the modeling and parameters. From the fundamental perspective, closed-loop control provides a unique capability to study unstable states inaccessible without control by changing their stability properties, in contrast to open-loop control which replaces the unstable states with *different* stable states.

Although the field of closed-loop control of complex systems is much younger than the field of flow control (its roots can be traced to work by Lions on optimal control of systems governed by PDEs [54] in early 1970s) it too has reached a certain level of maturity. This can be attested by a number of successful experimental implementations in systems such as vibrating beams [13], chemical reactions [65], patches of heart tissue [21], plasma drift waves [24], and fluid convection in confined geometries [66, 76], all of which, in the absence of control, display *temporal* instabilities, but have a rather regular *spatial* structure. Most of these examples use the technique of single-input single-output (SISO) control, which is based on reconstructing the state of the system by making repetitive measurements of a single variable and then stabilizing one of the originally unstable steady or time-periodic states using a sequence of perturbations of a single parameter of that system.

This approach aimed at low-dimensional (due to strong geometrical confinement) systems breaks down, partially or completely, when applied to weakly confined systems, whose dynamics is characterized by spatial disorder and is, therefore, high dimensional. The dynamics of such systems is rather weakly de-

pendent on the boundary conditions and, as a result, recovers the symmetries inherited from the translational and rotational invariance of the unbounded physical space. These symmetries lead to degeneracies in the evolution operators describing the dynamics near the target state, resulting in the failure of single-parameter control. As previous studies (e.g., [26]) have shown, these degeneracies require the use of multipoint, or distributed, measurements (sensing) and feedback (actuation), i.e., multiple-input multiple-output (MIMO) control.

8.1.1
Empirical Control

Several empirical methods have been developed to achieve control of weakly confined systems without relying on the knowledge on the evolution equations. Their complete description can be found elsewhere in this book. The simplest one is a generalization of Pyragas' time delay autosynchronization (TDAS) algorithm [69] and can be used to stabilize an unstable *time-periodic* orbit (e.g., a plane wave) with temporal period τ by applying feedback proportional to the difference in the state of the system at times t and $t - \tau$. The extended version of this algorithm (ETDAS) suggested by Bleich and Socolar [8], constructs the feedback as a weighted difference between the states of the system as times t, $t - \tau$, $t - 2\tau$, …. (E)TDAS was found to have a limitation when applied to spatially extended system in more than one spatial dimension, though: control fails for the target states with an odd number of unstable eigenvalues [46, 58], the origin of which can be traced to spatial symmetries [38]. The generalized version of ETDAS (GETDAS) [57] goes around this limitation by replacing scalar weights with matrices. Yet, even GETDAS fails if there are stationary modes in the uncontrolled system [80], as is the case in weakly confined systems with continuous translational and/or rotational symmetry, characterized by the existence of symmetry-related Goldstone modes with zero growth rates.

Other studies have shown the possibility to achieve control of unstable *steady* or *time-periodic* patterns by applying feedback proportional to the instantaneous local deviation of the system from the target state. This method is sometimes referred to as (local) proportional control (LPC) [40] or, in the context of fluid flows, opposition control [33]. Although this method is relatively simple and, like ETDAS, does not require the knowledge of the dynamical equations, it requires feedback to be applied to all degrees of freedom of the system (e.g., all components of the velocity vector at every point in space for fluid flows [31]) to be successful – a requirement that is essentially impossible to satisfy in practice. If LPC is applied only to selected degrees of freedom (e.g., to one component of the velocity everywhere in space [30] or to all components of the velocity along a boundary [11]) the spatiotemporal chaos cannot be completely suppressed.

8.1.2
Model-Based Control

If the equations governing the dynamics of the system are known, one can improve on these empirical control methods. In the model-based approach, the description of the system is usually simplified by collapsing it along the strongly confined spatial direction(s) [1] (say, z) using either mode truncation (e.g., as in the analysis of Rayleigh-Bénard convection (RBC) [41, 76] or wide aperture lasers [6]) or an approximation based on a perturbation expansion (e.g., as in the lubrication, or long wavelength, approximation for thin film flows [27, 60]), producing a reduced order model depending only on the extended (weakly confined) directions (say, x and y). It is then assumed that spatially distributed feedback is applied by perturbing the system at all points (x, y) in the extended directions by an amount proportional to the deviation of the system from the target state (either a uniform state or a plane wave) at the same location (x, y). As a result, a system

$$\partial_t \mathbf{v} = \mathbf{f}[\mathbf{v}, u], \tag{8.1 a}$$

$$u = kw, \qquad w = \mathbf{c} \cdot (\mathbf{v} - \mathbf{v}_0), \tag{8.1 b}$$

is obtained, where $\mathbf{f}[\cdot, \cdot]$ and $\mathbf{v}(x, y, t)$ are, respectively, the evolution operator and the state of the open-loop system, $u(x, y, t)$ is the feedback (i.e., the disturbance applied to one of the system parameters), $\mathbf{c}$ is a constant vector describing the relation between the system state and the measurement $w(x, y, t)$, and the feedback gain k is the proportionality constant between the deviation from the target state $\mathbf{v}_0(x, y, t)$ and the feedback signal.

In the physical system the deviation can often be measured at one (or both) of the boundaries, say $z = 0$ and $z = l_z$ (e.g., oxygen concentration on the surface of platinum catalyst in CO oxidation [63]), in a plane $z = z_0$ between the boundaries (e.g., velocity for a turbulent shear flow [51] or temperature for RBC [77]), or an integrated deviation for $0 < z < l_z$ can be used (e.g., shadowgraphic amplitude for RBC [42]). Similarly, feedback can be applied by changing the boundary conditions at one (or both) of the boundaries (e.g., heat flux through the boundary in RBC [42, 77]) or by applying an integrated disturbance (e.g., volumetric heating of the fluid in Marangoni-Bénard convection [74] or superimposition of the electromagnetic field with its filtered and time delayed version in a He–Ne laser [53]). Since the closed-loop system is translationally invariant in the extended directions, the eigenfunctions of the reduced order model are given by either Fourier modes (for spatially uniform) or by Bloch-Floquet waves

---

[1] In nonequilibrium systems, confined directions usually correspond to the direction of the flux driving the system out of equilibrium (e.g., momentum transport in shear fluid flows, heat flux in convection, etc.), while there is no flux, on average, in the extended directions [12]. Of course, it is possible that, in large aspect ratio systems, zero-mean-flux directions can effectively become confined as well.

(for plane wave target states). Hence the linearized evolution equations block diagonalize in the Fourier space, producing an infinite set of ODEs (state-space representation)

$$\dot{\bar{\mathbf{v}}} = A\bar{\mathbf{v}} + \mathbf{b}\bar{u},$$
$$\bar{u} = k\mathbf{c} \cdot \bar{\mathbf{v}}, \tag{8.2}$$

labeled by the wave number $\mathbf{q} = (q_x, q_y)$, where $\bar{\mathbf{v}}(\mathbf{q}, t) = \mathcal{F}_{\mathbf{q}}(\mathbf{v} - \mathbf{v}_0)$ and $\bar{u}(\mathbf{q}, t) = \mathcal{F}_{\mathbf{q}}u$ are the Fourier transformed state and feedback variables, $A(\mathbf{q}, t) = \mathcal{F}_{\mathbf{q}}(\partial \mathbf{f}/\partial \mathbf{v}|_{\mathbf{v}_0})\mathcal{F}_{\mathbf{q}}^{-1}$ is the Jacobian of the open-loop system and the vector $\mathbf{b}(\mathbf{q}, t) = \mathcal{F}_{\mathbf{q}}(\partial \mathbf{f}/\partial u|_{\mathbf{v}_0})\mathcal{F}_{\mathbf{q}}^{-1}$ describes how the feedback affects different degrees of freedom of the system. Finally, the feedback gain k is chosen to simultaneously stabilize all Fourier modes.

Although this physically motivated approach often works well, it too has limitations. For instance, a constant gain k stabilizing all Fourier modes might not exist, as, e.g., the analysis of the complex Ginzburg-Landau equation (CGLE) [7] and lubrication equations describing evaporating liquid films [27] shows. An improved version of this approach developed by one of us (RG) [27] and Bamieh et al. [3] uses the results of linear stability analysis to systematically design the feedback. The systematic approach shows that a stabilizing feedback can only be found when A, $\mathbf{b}$, and $\mathbf{c}$ satisfy certain restrictive conditions. These conditions are often (but certainly not always) satisfied for systems described by only a few coupled scalar fields. For instance, thin liquid films can be described by one variable (e.g., film height [60]), RBC requires two variables (e.g., temperature and vertical velocity [77]), while single mode wide-aperture laser models are three dimensional (e.g., complex amplitude of the electric field and carrier density [6]).

When a stabilizing feedback does exist, it often has to be wave number dependent (as well as time dependent for time-periodic target states). Furthermore, optimal (in the sense of time-averaged deviation of the system from the target state) feedback [3, 27] is generically wave number dependent and, therefore, nonlocal in the real space,

$$u = \int d\mathbf{q} \mathcal{F}_{\mathbf{q}}^{-1} k(\mathbf{q}) \mathcal{F}_{\mathbf{q}} w, \tag{8.3}$$

such that the feedback at a particular spatial location depends on the deviation from the target state at other locations. Several other theoretical [52] and experimental [43, 55] studies of nonlinear optical systems have also found that Fourier filtered feedback is required in order to stabilize unstable patterns.

The model-based approach becomes indispensable when A, $\mathbf{b}$, and $\mathbf{c}$ do not satisfy the restrictions alluded to above, which is the generic case. This requires modifications to (8.1 b) and (8.2) with the goal of reconstructing the deviation $\mathbf{v} - \mathbf{v}_0$ from the scalar measurement w (see e.g. [14] for details). Specifically, (8.2) is replaced with

$$\dot{\bar{\mathbf{v}}} = A\bar{\mathbf{v}} + \mathbf{b}\bar{u},$$
$$\dot{\hat{\mathbf{v}}} = A\hat{\mathbf{v}} + \mathbf{b}\bar{u} - \hat{\mathbf{k}}(\bar{w} - \mathbf{c} \cdot \hat{\mathbf{v}}),$$
$$\bar{u} = \mathbf{k} \cdot \hat{\mathbf{v}}, \tag{8.4}$$

where $\bar{w}(\mathbf{q}, t) = \mathcal{F}_{\mathbf{q}} w$, $\hat{\mathbf{k}}$ is the filter gain, and both it and the feedback gain $\mathbf{k}$ become vectors. Respectively, the first equation in (8.1 b) is replaced with $u = \mathcal{F}_{\mathbf{q}}^{-1}\bar{u}$. By subtracting the second equation in (8.4) from the first, one finds that $\hat{\mathbf{v}} \to \bar{\mathbf{v}}$ provided $A + \hat{\mathbf{k}}\mathbf{c}^{\dagger}$ (or $A^{\dagger} + \mathbf{c}\hat{\mathbf{k}}^{\dagger}$) is stable, while $\bar{\mathbf{v}} \to 0$ provided $A + \mathbf{b}\mathbf{k}^{\dagger}$ is stable. We find that mathematically the problem of finding $\hat{\mathbf{k}}$ given $\mathbf{c}$ is equivalent to that of finding $\mathbf{k}$ given $\mathbf{b}$. It is a standard control-theoretic result that the feedback gain $\mathbf{k}$ and the filter gain $\hat{\mathbf{k}}$ can be found provided A and $\mathbf{b}$ satisfy the *controllability* (or the weaker *stabilizability*) condition and A and $\mathbf{c}$ satisfy the *observability* (or the weaker *detectability*) condition [14, 26]. This duality between the feedback and sensing parts of the controller allows one to solve both the problem of state reconstruction and the problem of feedback control using the assumption that the complete knowledge about the state of the system is available (i.e., replacing $\mathbf{c}$ with a unit matrix in (8.1 b)). A review by Kim [48] discusses the application of this approach to control of turbulent boundary flows.

The model-based approach makes no assumptions regarding the number of unstable directions and access to all degrees of freedom (for sensing or actuation) is not required. This makes physical sense: for instance, in convective systems temperature perturbations also control the velocity, while in lasers the perturbations of the electric field also control the polarization and the population inversion. However, the crucial step in the analysis – block-diagonalization of the linearized evolution equations – hinges on the implicit assumption of translational (or rotational) invariance, which cannot always be justified.

For instance, the assumption that both sensing and feedback are spatially continuous (in other words, independent sensing is done, or feedback applied, at every point in the space of extended directions) is usually unrealistic, although the development of micro-electro-mechanical systems (MEMS) could change that. So far, systems for which both sensing and actuation can be done optically represent the only exception. For instance, all-optical analog feedback loops have proved effective for control of pattern formation in nonlinear optical systems [43, 53, 55, 64], while the applicability of thermalized optical perturbations for control of thin film flows has been demonstrated by Semwogerere and Schatz [74] and Garnier et al. [22].

More typically, both sensing and feedback have to be implemented using an array of discrete elements. Several theoretical studies of coupled ODEs [59], CGLE [9, 45], and two-dimensional turbulence [31, 75] suggest that it is possible to achieve control using LPC applied via an array of spatially localized sensors and actuators, but that array should be rather dense. The existing convection experiments achieved *partial* stabilization of the flow by using a large number of small heaters (15 in [41], 24 in [76] and [49]), but provided little information on the relation between spatial resolution and the degree of stabilization. This rela-

tion, especially in the limit of sparse sensor/actuator arrays, is of fundamental importance from both physical and control theoretic perspective. Several different conjectures have been made regarding the density of the sensor/actuator array necessary to achieve control. Some studies suggest that the distance between the closest elements is determined by the correlation length [9, 45], while others suggest that the number of elements in the array should equal the number of unstable modes [1, 32]. Other studies [15, 25, 28] have shown that, for an appropriately chosen feedback, a much smaller density (limited by noise) of sensors/ actuators can be achieved.

In the following sections we will discuss the conditions affecting the density and structure of the sensor/actuator array and describe how a stabilizing feedback gain can be computed. Although the generalization of our results to time-periodic target states is, in principle, straightforward, we will limit our discussion to steady states to make it more accessible. Furthermore, we will initially assume that complete information about the system state is available and then discuss how the results change if only partial information can be obtained using an array of sensors. Finally, we will assume that the system has only one extended direction (say, x) and is laterally bounded, $0 < x < l_x$ (we will drop the index of l_x below).

8.2
Symmetry and the Minimal Number of Sensors/Actuators

If feedback is applied via spatially localized actuators, how many such actuators, at a minimum, are needed to suppress chaos in favor of a particular target state? As the theory developed in [26] shows, the answer to this question depends on the symmetries of the system and the target state, but not on the system size or on how the feedback is computed. This is a fundamental issue that has to be understood before moving on.

In a laterally bounded system the wave numbers will be discrete rather than continuous, $q_x = \cdots, q_{-2}, q_{-1}, q_0, q_1, q_2, \cdots$. Defining the feedback signal applied by actuators $m = 1, 2, \ldots, M$ as $\mathbf{u} = (u_1, u_2, \ldots, u_M)$, we can write the evolution equations describing our system as

$$\dot{\mathbf{v}}_n = A_n \bar{\mathbf{v}}_n + B_n \mathbf{u}, \qquad n = \cdots, -2, -1, 0, 1, 2, \ldots, \tag{8.5}$$

where $B(q) = \mathcal{F}_q(\partial \mathbf{f} / \partial \mathbf{u}|_{\mathbf{v}_0})$, $B_n = B(q_n)$, $A_n = A(q_n)$ and $\bar{\mathbf{v}}_n(t) = \bar{\mathbf{v}}(q_n, t)$. If we denote the number of scalar fields describing the state of the system (i.e., the dimensionality of $\mathbf{v}$) as N, then A_n would be an $N \times N$ matrix and B_n would be an $N \times M$ matrix.

Let β_k be the eigenvalues of the full block-diagonal Jacobian of the system

$$\hat{A} = \text{diag}(\ldots, A_{-2}, A_{-1}, A_0, A_1, A_2, \ldots) \tag{8.6}$$

and let μ_k be the degeneracy of eigenvalue β_k. Further, let

$$\bar{A}_k = \begin{pmatrix} A_{n_1} & & \\ & \ddots & \\ & & A_{n_\mu} \end{pmatrix}, \quad \bar{B}_k = \begin{pmatrix} B_{n_1} \\ \vdots \\ B_{n_\mu} \end{pmatrix}, \tag{8.7}$$

where the indices run over the values of n for which β_k is an eigenvalue of A_n. It can be shown then [26], that the feedback $\mathbf{u}$ stabilizing the system (8.5) exists, provided (i) the number M of columns of B (and hence of actuators) is no less than the highest degeneracy of the unstable eigenvalues,

$$M \geq \max_{\mathrm{Re}(\beta_k)>0} \mu_k, \tag{8.8}$$

and (ii) at least one of the columns of $\bar{B}_k$ is nonorthogonal to the adjoint eigenvectors of $\bar{A}_k$ for all k with $\mathrm{Re}(\beta_k) > 0$.

The degeneracy is usually determined by the symmetries of the evolution equation and once these symmetries are identified, the situation usually simplifies considerably. Let us look at some examples. Consider the complex Ginzburg-Landau equation with δ-localized feedback

$$\partial_t v = \varepsilon v + (1 + ib)\partial_x^2 v - (1 + ic)|v|^2 v + (1 + id)\sum_{m=1}^{M}\delta(x - x_m)u_m \tag{8.9}$$

and periodic boundary conditions on a domain of length $l = 2\pi$ (such that $q_n = n$). Assuming u_m to be real, linearizing (8.9) about the steady state $v_0 = 0$ and Fourier transforming, we obtain the evolution equations for the real and imaginary parts of $\bar{v}_n = \bar{r}_n + i\bar{s}_n$:

$$\begin{pmatrix} \dot{\bar{r}}_n \\ \dot{\bar{s}}_n \end{pmatrix} = A_n \begin{pmatrix} \bar{r}_n \\ \bar{s}_n \end{pmatrix} + B_n\mathbf{u}, \qquad A_n = \begin{pmatrix} \varepsilon - n^2 & bn^2 \\ -bn^2 & \varepsilon - n^2 \end{pmatrix},$$
$$B_n = \begin{pmatrix} \cos(nx_1) - d\sin(nx_1) & \cdots & \cos(nx_M) - d\sin(nx_M) \\ d\cos(nx_1) + \sin(nx_1) & \cdots & d\cos(nx_M) + \sin(nx_M) \end{pmatrix}. \tag{8.10}$$

The reflection symmetry of the evolution equation (8.9) and the target state $v_0 = 0$ has transpired in the degeneracy of the eigenvalues of the linearized system, $\beta_{-n}^{\pm} = \beta_n^{\pm} = \varepsilon - n^2 \pm ibn^2$. We find that $\mu_n = 2$ for all $n \neq 0$ and, consequently, at least two actuators are needed to stabilize the chosen target state. This is a special case of the general result proved in [26]: the minimal number of independent feedback signals should be no less than the dimensionality of the largest irreducible representation of the isotropy subgroup $\mathcal{G}_{\bar{v}_0}$ of the system, which is defined as a set of all transformations with respect to which both the open-loop evolution equation (i.e., (8.9) with $\mathbf{u} = 0$) and the target state are invariant. In this particular case $\mathcal{G}_{\bar{v}_0} = O(2) \times U(1)$ (spatial translations and reflec-

tion plus the global phase symmetry $v \to e^{i\phi}v$) and its largest irreducible representation is two dimensional.

The second lesson can be learned by considering part (ii) of the stabilizability condition. Without loss of generality we can pick the origin of the coordinate system such that $x_1 = 0$, so that

$$\bar{A}_n = \begin{pmatrix} A_{-n} & 0 \\ 0 & A_n \end{pmatrix}, \qquad \bar{B}_n = \begin{pmatrix} 1 & \cos(nx_2) + d\sin(nx_2) \\ d & d\cos(nx_2) - \sin(nx_2) \\ 1 & \cos(nx_2) - d\sin(nx_2) \\ d & d\cos(nx_2) + \sin(nx_2) \end{pmatrix}. \tag{8.11}$$

It is easy to check that $\mathbf{e}^{\dagger} = (1, i, -1, -i)$ is an adjoint eigenvector of $\bar{A}_n$ and the condition (ii) is not satisfied whenever $e^{\dagger}\bar{B}_n = 0$ (or $x_2 = \pi/n$). In other words, stabilizability is lost whenever an unstable eigenfunction of the system, e.g., $v_n = \sin(nx)$, has nodes at the locations of both actuators.

Similar conclusions can be drawn for a laterally infinite system with nonlocal coupling defined by an integral, as opposed to a differential, equation. Consider, for instance, the following evolution equation:

$$\partial_t v(x, t) = \varepsilon v(x, t) + \int_{-\infty}^{\infty} e^{-\frac{(x-x')^2}{2\sigma^2}} v(x', t)dx - v^3(x, t) + \sum_{m=1}^{M} \delta(x - x_m)u_m(t). \tag{8.12}$$

After linearization about the trivial steady state $v_0 = 0$ and Fourier transformation (8.12) reduces to a set of ODEs

$$\dot{v}_q = \beta_q v_q + \sum_{m=1}^{M} e^{iqx_m} u_m, \tag{8.13}$$

with doubly degenerate eigenvalues

$$\beta_{\pm q} = \varepsilon + \sqrt{2\pi}\sigma e^{-\frac{\sigma^2 q^2}{2}}. \tag{8.14}$$

Consequently, at least a pair of actuators is needed, and the spacing should satisfy condition (ii) with

$$\bar{A}_q = \begin{pmatrix} \beta_q & 0 \\ 0 & \beta_q \end{pmatrix}, \qquad \bar{B}_q = \begin{pmatrix} 1 & e^{-iqx_2} \\ 1 & e^{iqx_2} \end{pmatrix}, \tag{8.15}$$

which requires $qx_2 \neq \pi n$ for all integer n and all q such that $\beta_q > 0$. Defining $\lambda_{\min}$ to be the smallest unstable wavelength, we can write the stabilizability conditions as $|x_1 - x_2| < \lambda_{\min}/2$.

Summing up, we can formulate the following rule of thumb for control of steady uniform states in translationally and reflectionally invariant one-dimensional systems: *At least a pair of actuators separated by less than half the wavelength*

of every unstable mode is necessary to achieve stabilization. In higher dimensions more actuators will be needed, as determined by the respective symmetry group.

Introduction of mean flux in any of the lateral directions changes these results dramatically. For instance, adding a reflection symmetry-breaking term $(1 + ia)\partial_x v$ to the right-hand side of (8.9) changes the eigenvalues to

$$\beta_n^\pm = \varepsilon - an - n^2 \pm i(bn^2 - n), \tag{8.16}$$

removing the reflection-related degeneracy for all n, $\beta_{-n}^\pm \neq \beta_n^\pm$. Since now all $\mu_n = 1$, just one actuator may be sufficient (in one dimension). This reduction in the minimal number of actuators provides, at least to some extent, the explanation for the observation that if either mean flux is introduced [18] or if the actuators are not stationary, but move through the system (regularly [75] or randomly [20]), fewer of them are needed to suppress chaos. Indeed, the introduction of a term such as $\mathbf{a} \cdot \nabla v$ into the right-hand side of the evolution equation (8.1a) is equivalent to changing the reference frame to the one moving with velocity $\mathbf{a}$, in which the actuators, previously stationary, move with velocity $-\mathbf{a}$.

We conclude this section with a few general remarks. The stricter controllability condition requires satisfaction of (i) and (ii) for all k, stable and unstable. We should note, however, that spatially extended systems with a continuous spatial variable cannot be made controllable as stable modes with arbitrarily small wavelengths exist, so condition (ii) is impossible to satisfy. Second, using the duality of feedback and sensing parts, we conclude that the same conditions (i) and (ii) apply to an array of sensors.

Needless to say, one should not expect the results for the minimal number of actuators (or sensors) to hold in practice for systems of arbitrary size. The main reason for this is that linear stability analysis only considers the dynamics of infinitesimal disturbances, while real disturbances always have a finite size. We will look at the effect of disturbances in the next sections.

8.3
Nonnormality and Noise Amplification

If the system can be made formally stabilizable, control can only fail as a result of failure of linear stability analysis when disturbances grow so large that nonlinear terms become nonnegligible. To determine the dynamics of disturbances, however, we do need to define how the feedback is computed.

Again, to illustrate the main idea we will restrict our attention to a narrower class of spatially extended systems, following our earlier study [35]. Specifically, we will consider scalar translationally and reflection symmetric versions of (8.1a) in one spatial dimension with periodic boundary conditions. Examples of this class of systems include such model equations as the real Ginzburg-Landau, Kuramoto-Sivashinsky, and Swift-Hohenberg equations. These model equa-

tions describe the dynamics of generic, spatially extended systems close to several common types of bifurcations [12] and thus are of particular importance in the studies of spatiotemporal dynamics.

As in the previous section, we will assume that the feedback is applied through an array of spatially localized actuators. Linearizing about a steady uniform state we obtain the following equation for the deviation from the target state

$$\partial_t v(x,t) = \hat{A}v(x,t) + \sum_{m=1}^{M} b_m(x)u_m(t), \tag{8.17}$$

where $\hat{A}$ is a linear operator and $b_m(x)$ are the influence functions describing the location and spatial extent of each of the M actuators. Assuming the state of the system can be obtained either by direct measurements or via a state reconstruction procedure described in Section 8.1.2 we can express the feedback signals $u_m(t)$ as linear functions of the deviation

$$u_m(t) = \int_0^l k_m(x)v(x,t)dx, \tag{8.18}$$

where $k_m(x)$ is the feedback gain that should be chosen such that the uniform state is stabilized. The nonlocality of this feedback law is the price one has to pay for the generality of this approach that will allow us to use a very sparse array of actuators. In contrast, local proportional control (e.g., $u_m(t) = kv(x_m,t)$ with $b_m(x) = \delta(x - x_m)$) generically breaks down as soon as the distance between actuators exceeds $\lambda_{\min}/2$ (see e.g. [19]).

To simplify the problem of computing M feedback gains we can use the symmetry of the problem by making the actuators identical (e.g., by setting $b_m(x) = b_0(x - x_m)$) and placing the controllers in a regular array, so the closed-loop system will retain a discrete translational symmetry (subgroup of continuous translational symmetry of the open-loop system). However, placing the actuators in a periodic array will make the Fourier mode with the period equal to twice the array spacing $s = l/M$ uncontrollable and lead to the loss of stabilizability as long as that mode is unstable. We thus find that in a periodic array one should choose $s < s_{\max} \equiv \lambda_{\min}/2$, so that the number of actuators scales with the system size, $M \geq 2l/\lambda_{\min}$.

A significantly smaller number of actuators will be needed, if a periodic array of *pairs* of actuators is used instead, with the spacing s_1 in the pair smaller than $s_{\max}$ and the spacing $s_2 = 2l/M$ between the pairs potentially much larger than $s_{\max}$. The resulting array will have a discrete translational symmetry $(x \rightarrow x + s_2)$ and a reflection symmetry about the midpoint between any neighboring actuators. These symmetries dictate the following choice of influence functions:

$$b_m(x) = \begin{cases} b_0\big(x - (m - \Delta)\frac{l}{M}\big), & m - \text{odd}, \\ b_0\big(x - (m - 1 + \Delta)\frac{l}{M}\big), & m - \text{even}, \end{cases} \tag{8.19}$$

where we have defined $\Delta = s_1/s_2$. For instance, four actuators would be placed as two pairs, one pair at $x = (1 \pm \Delta)l/4$ and the other at $x = (3 \pm \Delta)l/4$. To preserve the symmetries of the closed-loop system we also choose the gains $k_m(x)$ as translated and reflected versions of each other, mirroring the choice (8.19) we have made for the influence functions, so that only a single unknown weight function $k_0(x)$ needs to be determined (also see [3]).

Fourier transforming the linearized evolution equation (8.17) and the feedback law (8.18) we obtain the system

$$\dot{\bar{v}}_n = \beta_n \bar{v}_n + \sum_{m=1}^{M} B_n^m \sum_{p=-\infty}^{\infty} K_{-m}^p \bar{v}_p \equiv (M\bar{v})_n, \tag{8.20}$$

where $\bar{v}_n$, B_n^m, and K_n^m are the Fourier coefficients of $v(x,t)$, $b_m(x)$, and $k_m(x)$, respectively, $\beta_n = \beta(q_n)$ (with $q_n = 2\pi n/l$) are the eigenvalues of the linearized open-loop system, and M is the Jacobian of the closed-loop system.

At this point it is appropriate to mention that the choice of the influence function $b_0(x)$, which is determined by the physical construction of the actuators, plays an important role in the control problem. For instance, the Fourier spectrum of $b_0(x)$ should contain all unstable modes; modes missing in the spectrum will be uncontrollable. On the other hand, if the spectrum contains stable modes as well, the feedback stabilizing the unstable modes of the open-loop system can destabilize some of the stable modes. This problem is referred to as control spillover [32]. As a result, despite the block-diagonalization of the open-loop system, the calculation of feedback has to include all modes that appear in the spectrum of $b_0(x)$, both unstable and stable ones.

It turns out that the Fourier coefficients of $k_0(x)$ can be found analytically in the limit of singularly localized influence functions, $b_0(x) = \delta(x)$, as a function of the eigenvalues β'_n of the closed-loop system. This results in the so-called pole placement control. The details can be found in [35]. Here we will mention the main result: the largest Fourier coefficient, and with it the maximum of $k_0(x)$, scales exponentially with the length of the system divided by the number of controllers

$$k_{\max} \sim e^{\frac{l}{Ml_0}}, \tag{8.21}$$

where l_0 is a characteristic length which, to leading order in l, is given by

$$l_0 = \pi \left(\int_{-\infty}^{\infty} \ln \frac{|\beta_{\max} - \beta'(q)|}{|\beta_{\max} - \beta(q)|} \, dq \right)^{-1}, \qquad \beta_{\max} = \max_n \beta_n \tag{8.22}$$

(for large l the wave numbers q_n are dense, so we can parameterize new eigenvalues using a functional form $\beta'(q_n) = \beta'_n$).

This result shows that although in principle it is possible to find a stabilizing feedback for any system size l and number of actuators M, the price one pays

for making l large or M small is the exponential increase in the magnitude of the feedback signal applied by the actuators. It is not difficult to imagine the consequences of such a feedback: a small $O(\sigma)$ initial disturbance would generate an $O(k_{\max}\sigma)$ perturbation applied by the nearby actuators resulting, at least temporarily, in the amplification of that initial disturbance by roughly a factor of $k_{\max}$. Since the closed-loop system is linearly stable, all sufficiently small disturbances will eventually decay, making this feedback-generated disturbance amplification transient. Mathematically, transient growth of disturbances can be related to the nonnormality of the Jacobian M of the closed-loop system and is characterized by the transient amplification factor

$$\gamma \equiv \max_{t,\bar{\mathbf{v}}(0)} \frac{\|\bar{\mathbf{v}}(t)\|_2}{\|\bar{\mathbf{v}}(0)\|_2} = \max_t \left\|e^{Mt}\right\|_2 \equiv \left\|e^{Mt_{\max}}\right\|_2, \tag{8.23}$$

which measures the maximum amplitude of an evolved disturbance $\bar{\mathbf{v}}(t)$ (or $v(x,t)$) for all possible initial conditions $\bar{\mathbf{v}}(0)$ (or $v(x,0)$). The initial condition producing the maximal amplification at time $t_{\max}$ is often called the optimal disturbance $\bar{\mathbf{v}}_{\mathrm{opt}}$ and is given by the right singular vector corresponding to the largest singular value of $e^{Mt_{\max}}$ [16]. For normal operators $\gamma = 1$, but for nonnormal ones it can be arbitrarily large. Several authors have introduced quantities similar to (8.23) to characterize transient growth [16, 71–73]. We should point out that the transient amplification factor is analogous to transfer norms which arise in the input–output description commonly used in control theoretic analyses, including those concerning transient growth [2, 44, 50].

Under fairly general assumptions it can be shown [35] that transient amplification does indeed scale with $k_{\max}$:

$$\gamma \sim \frac{k_{\max}}{|\beta'_{\max}|} \propto e^{\frac{l}{M l_0}}, \qquad \beta'_{\max} = \max_n \beta'_n. \tag{8.24}$$

In case the full information about the system state is unavailable, one has to use an array of sensors to reconstruct it from the local measurements. The duality of this problem to the feedback problem allows us to immediately make a couple of conclusions. First, the array of sensors should be built according to the same principles as the array of actuators to ensure that the system state can be reconstructed. Second, the total transient amplification will be given by the product of those for each stage (sensing, feedback) [25, 34]. If the sensing stage mirrors the feedback stage (same number and arrangement of sensors and actuators and sensing gain equal to feedback gain), we obtain

$$\gamma_{\mathrm{total}} = \gamma^2 = e^{\frac{2l}{M l_0}}. \tag{8.25}$$

Summing up, we have found that regardless of how small the magnitude σ of initial disturbances is, the transient growth in the feedback loop will amplify them to an $O(\gamma\sigma)$ magnitude which, for sufficiently large spacing $s_2 = 2l/M$ be-
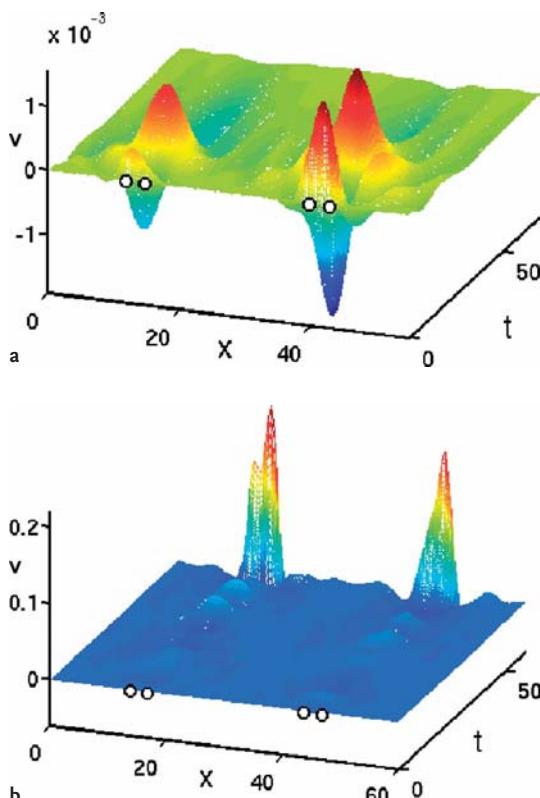
Fig. 8.1 Control of the Kuramoto-Sivashinsky equation (8.26) using localized feedback applied at the four points marked with circles. **a** Control succeeds for a system of size $l = 55$. Note the strong initial transient localized around the actuators and preceding the asymptotic decay. **b** Control fails for a system of larger size $l = 60$.

tween controller pairs, will be large enough for the linear stability analysis to break down and for control to fail. This is illustrated in Fig. 8.1 for the Kuramoto-Sivashinsky equation

$$\partial_t v = -\partial_x^2 v - \partial_x^4 v - v\partial_x v. \tag{8.26}$$

Exactly when the breakdown occurs depends on (i) the magnitude of noise σ, (ii) the placement of actuators and the choice of feedback gain which affect transient amplification factor γ, and (iii) the particular form of the nonlinear terms which determines the limits of the validity of the linear approximation. We address this last issue in the next section.

8.4
Nonlinearity and the Critical Noise Level

The effect of nonlinear terms can be considered from different perspectives. The simplest argument suggests that, as long as the evolution equations are nondimensionalized to get rid of very large or very small parameters, the importance of nonlinear terms can be judged based simply on their order of magnitude. We will limit our scope to the most common type of nonlinearities found in spatiotemporal dynamics, those having the form of a power of the disturbance, occasionally with a spatial derivative in the mix (e.g., quadratic nonlinearities in the logistic coupled map lattice [15, 28], Kuramoto-Sivashinsky equation [1], Navier-Stokes equation [48, 75] or Boussinesque equations [77], cubic nonlinearities in the CGLE [7] and Swift-Hohenberg equation [35], quartic nonlinearity in thin film equations [27, 60] and so on). An upper bound for the breakdown of the linear control approach is immediately obvious: If a disturbance σ is transiently amplified such that $\gamma\sigma = O(1)$, the nonlinear terms become important and the linear approach becomes invalid. This estimate gives the upper bound for the noise level

$$\sigma_{\max} \sim \gamma^{-1}. \tag{8.27}$$

Numerical integration performed for a generalized (real) Ginzburg-Landau equation with a custom nonlinear term $f(v)$,

$$\partial_t v = v + \partial_x^2 v + f(v), \tag{8.28}$$

and with feedback applied at one of the boundaries,

$$v(0, t) = 0, \qquad v'(l, t) = \int_0^l k(x)v(x, t)dx, \tag{8.29}$$

shows that for nonlinearities with an odd power p, e.g., $f(v) = v^3$ or v^5, one does indeed find the scaling (8.27) at large l [29]. For even powers, e.g., $f(v) = v^2$ or $v\partial_x v$, one instead finds a different scaling law

$$\sigma_{\max} \sim \gamma^a, \qquad a = -\frac{p}{p - 1}. \tag{8.30}$$

This scaling can also be understood using order of magnitude arguments and employing the idea of bootstrapping originally introduced by Trefethen et al. [78] in the context of shear flow (in)stability. The idea of the argument is that the purely linear growth leading to the estimate (8.27) is preempted by a positive-feedback loop involving transient amplification and nonlinearity. The critical noise level in this case can be found by equating the order of magnitude of the initial (primary) disturbance with the magnitude of the nonlinear terms acting on the amplified disturbance, which act as a secondary disturbance that is

further transiently amplified, $O(\sigma) = O((\gamma\sigma)^p)$. Solving for σ one immediately obtains (8.30). The justification of the scaling law for the model (8.28) and (8.29) with an arbitrary power p can be found in [29].

One could ask if the scaling exponents in (8.27) and (8.30) or even the power-law scaling itself obtained for a particular model equation are generic and hence our understanding of the effect of nonlinear terms complete. Unfortunately, the answer is negative on both counts. The situation is far more complicated even in the framework of the simple model considered here. One can see this by studying the limit of small, rather than large, system size, as was done in [36]. In this limit all calculations can be done analytically.

Without repeating the details of the analysis we will summarize the results. The system size l is chosen such that only one Fourier mode is unstable and one mode is very weakly stable. Feedback is chosen to make the stable mode weakly stable as well, so that the dynamics of the closed-loop system in the Fourier space is characterized by two slow, nearly degenerate, modes and an infinite number of fast (strongly) stable modes. Adiabatic elimination of the fast modes reduces the dynamics to the subspace spanned by the two slow modes. The analysis performed for the cubic and the quadratic nonlinearity then shows that the basin of attraction of the target state is bounded by the stable manifold of one (for quadratic) or two (for cubic nonlinearity) saddle-type steady states that emerge in the vicinity of the target state as a result of feedback (see Fig. 8.2). The shape and size of the stable manifold determine the critical noise level. Computing the amplification factor γ one can find that the power law scal-
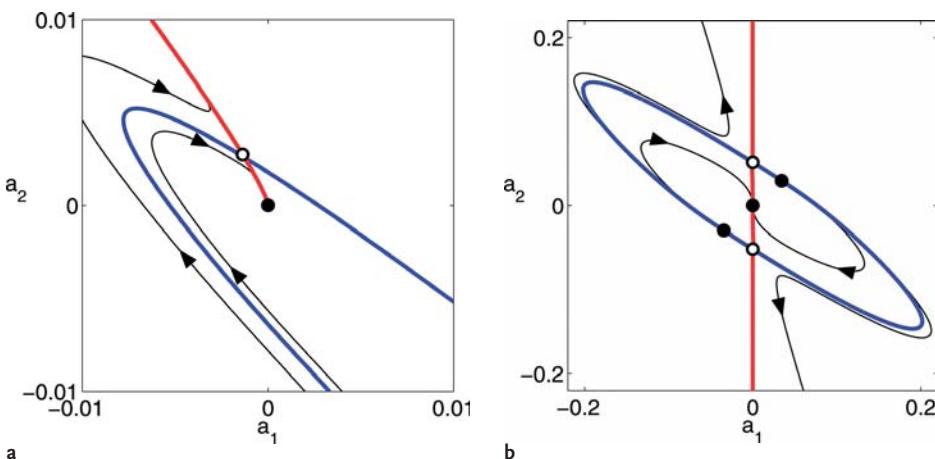
Fig. 8.2 The phase portrait of the model (8.28) with the quadratic **a** and the cubic **b** nonlinearity in the subspace parameterized by the amplitudes a_1 and a_2 of the two slow modes. The filled and the open black dots show the nodes and saddles, respectively. The blue and red curves show the stable and unstable manifolds, respectively, of the saddles. The black curves are the typical trajectories.

ing $\sigma_{\max} \sim \gamma^a$ is an exceptional case. More typically $\sigma_{\max}$ is not uniquely determined by γ, but also depends on the time $t_{\max}$ at which the maximal transient amplification is achieved.

The relation between $\sigma_{\max}$ and γ provides the last piece of the puzzle, relating the environmental noise, the symmetry of the system, the density of the sensor/actuator array, and the choice of the closed-loop eigenvalues through equations such as (8.22), (8.24), and (8.30).

8.5
Conclusions

The field of feedback control of nonlinear spatially extended systems has grown too large in the past ten or so years to give credit to all researchers who have contributed to its development. In this chapter, we discussed some of the recent results, concentrating mostly on localized feedback control. From the discussion presented in these pages it should be clear that our understanding has reached a level of maturity necessary to address real problems of interest.

On the other hand, many problems remain unresolved. For instance, the feedback control of spatially and temporally periodic states has received much less attention than control of uniform steady states, with numerical studies overwhelming analytical investigations. The nonlinear stability of closed-loop systems is another area where progress has been limited, with the majority of studies concentrating on low-dimensional models rather than true spatiotemporal dynamics. Another fundamental problem awaiting solution is the problem of ''targeting'', as it is referred to in the context of low-dimensional systems, which becomes progressively more challenging as the dimensionality of the system increases.

References

1 C. Antoniades and P. D. Christofides. Integrating nonlinear output feedback control and optimal actuator/sensor placement for transport-reaction processes. *Chem. Eng. Sci.*, 56:4517–4535, 2001.

2 B. Bamieh and M. Dahleh. Energy amplification in channel flows with stochastic excitation. *Phys. Fluids*, 13:3258, 2001.

3 B. Bamieh, F. Paganini, and M. Dahleh. Distributed control of spatially invariant systems. *IEEE Trans. Aut. Cont.*, 47:1092, 2002.

4 D. R. Bassett. Hydrophobic coatings from emulsion polymers. *J. Coat. Technol.*, 73:43, 2001.

5 M. Bertram and A. Mikhailov. Pattern formation in a surface chemical reaction with global delayed feedback. *Phys. Rev. E*, 63:0661021, 2001.

6 M. E. Bleich, D. Hochheiser, J. V. Moloney, and J. E. S. Socolar. Controlling extended systems with spatially filtered, time delayed feedback. *Phys. Rev. E*, 55:2119, 1997.

7 M. E. Bleich and J. E. S. Socolar. Controlling spatiotemporal dynamics with time delay feedback. *Phys. Rev. E*, 54:R17, 1996.

8 M. E. Bleich and J. E. S. Socolar. Stability of periodic orbits controlled by time de-

lay feedback. *Phys. Letters A*, 210:87–94, 1996.

9 S. Boccaletti, J. Bragard, and F.T. Arecchi. Controlling and synchronizing spacetime chaos. *Phys. Rev. E*, 59:6574–6578, 1999.

10 D. Bonvin, editor. *Advanced control of chemical processes*. Proc. IFAC Symposium, Kyoto, Japan, 1994.

11 H. Choi, P. Moin, and J. Kim. Active turbulence control for drag reduction in wall-bounded flows. *J. Fluid Mech.*, 262:75, 1994.

12 M.C. Cross and P.C. Hohenberg. Pattern formation outside of equilibrium. *Rev. Mod. Phys.*, 65:851, 1993.

13 W.L. Ditto and M.L. Spano. Mastering chaos. *Scientific American*, 269:78–84, 1993.

14 P. Dorato, C.T. Abdallah, and V. Cerone. *Linear quadratic control*. Krieger Publishing Company, Melbourne, 2000.

15 D.A. Egolf and J.E.S. Socolar. Failure of linear control in noisy coupled map lattices. *Phys. Rev. E*, 57:5721, 1998.

16 B.F. Farrell and P.J. Ioannou. Generalized stability theory, part I: Autonomous operators. *J. Atmos. Sci.*, 53:2025, 1996.

17 M. Gad-El-Hak. *Flow control: passive, active, and reactive flow management*. Cambridge University Press, Cambridge, 2000.

18 H. Gang, X. Jinghua, G. Jijua, L. Xiangming, Y. Yugui, and B. Hu. Analytical study of spatiotemporal chaos control by applying local injections. *Phys. Rev. E*, 62:R3043, 2000.

19 H. Gang and Q. Zhilin. Controlling spatiotemporal chaos in coupled map lattice systems. *Phys. Rev. Lett.*, 72:68–71, 1994.

20 J. Gao, X. Wang, G. Hu, and J. Xiao. Control of spatiotemporal chaos by using random itinerant feedback injections. *Phys. Letters A*, 283:342–348, 2001.

21 A. Garfinkel, M.L. Spano, W.L. Ditto, and J.N. Weiss. Controlling cardiac chaos. *Science*, 257:1230–1235, 1992.

22 N. Garnier, R.O. Grigoriev, and M.F. Schatz. Optical manipulation of microscale fluid flow. *Phys. Rev. Lett.*, 91:054501, 2004.

23 B.J. Gluckman, H. Nguyen, S.L. Weinstein, and S.J. Schiff. Adaptive electric field control of epileptic seizures. *J. Neuroscience*, 21:590–600, 2001.

24 E. Gravier, X. Caron, G. Bonhomme, T. Pierre, and J.L. Briançon. Dynamical study and control of drift waves in a magnetized laboratory plasma. *Eur. Phys. J. D*, 8:451–457, 2000.

25 R.O. Grigoriev. Control of spatially extended chaotic systems. In H.G. Schuster, editor, *Handbook of Chaos Control*. Wiley-VCH, New Jersey, 1998.

26 R.O. Grigoriev. Symmetry and control: spatially extended chaotic systems. *Physica D*, 140:171, 2000.

27 R.O. Grigoriev. Control of evaporatively driven instabilities of thin liquid films. *Phys. Fluids*, 14:1895, 2002.

28 R.O. Grigoriev, M.C. Cross, and H.G. Schuster. Pinning control of spatiotemporal chaos. *Phys. Rev. Lett.*, 79:2795, 1997.

29 R.O. Grigoriev and A. Handel. Spectral theory for the failure of linear control in a nonlinear stochastic system. *Phys. Rev. E*, 66:065301, 2002.

30 S. Guan, G.W. Wei, and C.-H. Lai. Controllability of flow turbulence. *Phys. Rev. E*, 69:066214, 2004.

31 S. Guan, Y.C. Zhou, G.W. Wei, and C.H. Lai. Controlling flow turbulence. *Chaos*, 13:64–70, 2003.

32 G. Hagen and I. Mezić. Control spillover in dissipative evolution equations. In *Proc. of the American Control Conference*, vol. 6, pp. 3783–3787, Chicago, Illinois, June 2000.

33 E.P. Hammond, T.R. Bewley, and P. Moin. Observed mechanisms for turbulence attenuation and enhancement in opposition-controlled wall-bounded flows. *Phys. Fluids*, 10:2421, 1998.

34 A. Handel. *Thesis: Limits of localized control in extended nonlinear systems*. Georgia Institute of Technology, 2004.

35 A. Handel and R.O. Grigoriev. Pattern selection and control via localized feedback. *Phys. Rev. E*, 72:066208, 2005.

36 A. Handel and R.O. Grigoriev. Transient dynamics and nonlinear stability of spatially extended systems. *Phys. Rev. E*, 74:036302, 2006.

37 C.H. Hansen and S.D. Snyder. *Active control of noise and vibration*. E & FN Spon, London, 1997.

38 I. Harrington and J. E. S. Socolar. Limitation on stabilizing plane waves via time-delay feedback. *Phys. Rev. E*, 64:056206, 2001.

39 P. Hinz and H. Dislich. Anti-reflecting light-scattering coatings via the sol–gel procedure. *J. Non. Cryst. Solids*, 82:411, 1986.

40 L. E. Howle. Control of Rayleigh-Bénard convection in a small aspect ratio container. *Int. J. Heat Mass Transfer*, 40:817–822, 1996.

41 L. E. Howle. Active control of Rayleigh-Bénard convection. *Phys. Fluids*, 9:1861–1863, 1997.

42 L. E. Howle. The effect of boundary properties on controlled Rayleigh-Bénard convection. *J. Fluid Mech.*, 411:3958, 2000.

43 S. J. Jense, M. Schwab, and C. Denz. Manipulation, stabilization, and control of pattern formation using fourier plane filtering. *Phys. Rev. Lett.*, 81:1614–1617, 1998.

44 M. R. Jovanović and B. Bamieh. Componentwise energy amplification in channel flows. *J. Fluid Mech. – to be published*, 2004.

45 L. Junge and U. Parlitz. Synchronization and control of coupled Ginzburg-Landau equations using local coupling. *Phys. Rev. E*, 61:3736–3742, 2000.

46 W. Just, T. Bernard, M. Ostheimer, E. Reibold, and H. Benner. Mechanism of time delayed feedback control. *Phys. Rev. Lett.*, 78:203–206, 1997.

47 G. Kawahara. Laminarization of minimal plane couette flow: Going beyond the basin of attraction of turbulence. *Phys. Fluids*, 17:041702, 2005.

48 J. Kim. Control of turbulent boundary layers. *Phys. Fluids*, 15:1093–1105, 2003.

49 P. Kolodner and G. Flätgen. Spatial-feedback control of dispersive chaos in binary-fluid convection. *Phys. Rev. E*, 61:2519, 2000.

50 E. Lauga and T. R. Bewley. Performance of a linear robust control strategy on a nonlinear model of spatially-developing flows. *J. Fluid Mech. – to be published*, 2004.

51 J. Lim and J. Kim. A singular value analysis of boundary layer control. *Phys. Fluids*, 16:1980–1988, 2004.

52 H. Lin. Suppression of transverse instabilities in a laser by use of a spatially filtered feedback. *J. Opt. Soc. Am. B*, 17:239–246, 2000.

53 H. Lin and S. Mahadoo. Control of beam patterns in a helium-neon laser using a spatially filtered feedback. *Optics Comm.*, 228:357–364, 2003.

54 J. L. Lions. *Optimal control of systems governed by partial differential equations*. Springer, New York, 1971.

55 A. V. Mamaev and M. Saffman. Selection of unstable patterns and control of optical turbulence by fourier plane filtering. *Phys. Rev. Lett.*, 80:3499–3502, 1998.

56 J. V. Moloney. Spontaneous generation of patterns and their control in nonlinear optical systems. *J. Opt. B: Quantum Semiclass. Opt.*, 1:183–190, 1999.

57 H. Nakajima. A generalization of the extended delayed feedback control for chaotic systems. In *Proc. of Control of Oscillations and Chaos*, vol. 2, pp. 209–212, Saint-Petersburg, Russia, July 2000.

58 H. Nakajima and Y. Ueda. Limitation of generalized delayed feedback control. *Physica D*, 111:143–150, 1998.

59 M. Núñez and G. Mato. Controlling chaos in systems of coupled oscillators. *Physica A*, 307:315–330, 2002.

60 A. C. Or, R. E. Kelly, L. Cortelezzi, and J. L. Speyer. Control of long-wavelength Marangoni-Bénard convection. *J. Fluid Mech.*, 387:321–341, 1999.

61 E. Ott, C. Grebogi, and J. A. Yorke. Controlling chaos. *Phys. Rev. Lett.*, 64:1196, 1990.

62 J. M. Ottino. *The kinematics of mixing: stretching, chaos, and transport*. Cambridge University Press, Cambridge, 1989.

63 R. Pandit, A. Pande, S. Sinha, and A. Sen. Spiral turbulence and spatiotemporal chaos: characterization and control in two excitable media. *Physica A*, 306:211–219, 2002.

64 L. Pastur, L. Gostiaux, U. Bortolozzo, S. Boccaletti, and P. L. Ramazza. Experimental targeting and control of spatiotemporal chaos in nonlinear optics. *Phys. Rev. Lett.*, 93:063902, 2004.

65 V. Petrov, V. Gaspar, J. Masere, and K. Showalter. Controlling chaos in the

Belousov-Zhabotinsky reaction. *Nature*, 361:240243, 1993.

66 V. Petrov, M. F. Schatz, K. A. Muehlner, S. J. Van Hook, W. D. McCormick, J. B. Swift, and H. L. Swinney. Nonlinear control of remote unstable states in a liquid bridge convection experiment. *Phys. Rev. Lett.*, 77:3779–3783, 1996.

67 A. R. Piriz. Hydrodynamic instability of ablation fronts in inertial confinement fusion. *Phys. Plasmas*, 8:997–1002, 2001.

68 L. Prandtl. Über Flüssigkeitsbewegung bei sehr kleiner Reibung. In *Proc. Third Int. Math. Cong.*, pp. 484–491, Heidelberg, Germany, 1904.

69 K. Pyragas. Continuous control of chaos by self-controlling feedback. *Phys. Lett. A*, 170:421–428, 1992.

70 D. Quéré. Fluid coating on a fiber. *Annu. Rev. Fluid Mech.*, 31:347, 1999.

71 S. C. Reddy, P. J. Schmid, and D. S. Henningson. Pseudospectra of the Orr-Sommerfeld operator. *SIAM J. on Appl. Math.*, 53:15, 1993.

72 P. J. Schmid. Linear stability theory and bypass transition in shear flows. *Phys. Plasmas*, 7:1788, 2000.

73 P. J. Schmid and D. S. Henningson. *Stability and transition in shear flows.* Springer, New York, 2001.

74 D. Semwogerere and M. F. Schatz. Evolution of hexagonal patterns from controlled initial conditions in a Bénard-Marangoni convection experiment. *Phys. Rev. Lett.*, 88:054501, 2002.

75 G. Tang, S. Guan, and G. Hu. Controlling flow turbulence with moving controllers. *Eur. Phys. J. B*, 48:259–264, 2005.

76 J. Tang and H. H. Bau. Experiments on the stabilization of the no-motion state of a fluid heated from below and cooled from above. *J. Fluid Mech.*, 363:153–171, 1998.

77 J. Tang and H. H. Bau. Numerical investigation of the stabilization of the no-motion state of a fluid layer heated from below and cooled from above. *Phys. Fluids*, 10:1597, 1998.

78 L. N. Trefethen, A. E. Trefethen, S. C. Reddy, and T. A. Driscoll. Hydrodynamic stability without eigenvalues. *Science*, 261:578, 1993.

79 J. N. Weiss, P.-S. Chen, Z. Qu, H. S. Karagueuzian, and A. Garfinkel. Ventricular fibrillation. How do we stop the waves from breaking? *Circ. Res.*, 87:1103–1107, 2000.

80 S. Yamamoto, T. Hino, and T. Ushio. Dynamic delayed feedback controllers for chaotic discrete-time systems. *IEEE T. Circuits I*, 48:785–789, 2001.

81 A. Yoshida. *Smart control of turbulent combustion.* Springer, New York, 2001.

9
Controlling Spatiotemporal Chaos:
The Paradigm of the Complex Ginzburg-Landau Equation

Stefano Boccaletti and Jean Bragard

We discuss some issues related with the control of space–time chaotic states in the framework of the one-dimensional complex Ginzburg-Landau equation (CGLE). We address the problem of control over turbulent regimes. In particular, we are interested in lowering the number of controllers which are spatial location where the perturbation is applied. We implement in parallel a local control technique for restoring an unstable plane wave solution. We show that the system extension does not influence the density of controllers needed in order to achieve control.

9.1
Introduction

At first glance, controlling chaos may sound counter intuitive: one can find it difficult to understand how the concept of control could be applied to the concept of chaos. In fact, a huge literature of the nineties in the physics community has proved that these two terms can be reconciled, by showing that tiny perturbations applied to a chaotic system are sufficient to control its dynamics, driving it toward a desired predetermined behavior.

The problem can be stated as follows: given a system (or a model equation representing to a good accuracy the dynamics of a specific process), how can one impose that such system performs a predetermined operation? When the dynamical system is inherently chaotic, two options are possible. One can select parameters so as to drive back the system to a region where the dynamics is restored to a regular dynamics, and this process is usually referred to as suppression of chaos [31]. Alternatively, one can take advantage of the great richness in the structure of the chaotic attractor, where infinite unstable periodic solutions are embedded. In this second case, usually referred to as control of chaos [12], one can properly select very tiny (in some cases vanishingly small) perturbations able to force the appearance of a specific periodic behavior or a desired portion of the chaotic trajectory. Historically, the control of chaos grew as a new

discipline as a consequence of the awareness of the omnipresence of chaos in dynamical systems.

The huge increase in the literature devoted to control of chaos traces back to the beginning of the nineties. After the seminal work by Ott-Grebogi-Yorke (OGY) [42], there has been a constant interest in the control of chaos, and many alternative approaches have been suggested, as the time delayed control method [49], and the adaptive method [8]. Furthermore, chaos control was theoretically proved in a large variety of time discrete, as well as time continuous systems [12] and even in the case of delayed dynamical systems [9].

The large body of literature devoted to this subject is rooted in the crucial role that chaos control can play in many practical applications, such as communications with chaos [25, 40], secure communication processes [4, 10, 18, 21, 33, 46]. Furthermore, experimental control of chaos has been achieved in many different areas such as chemistry [47], laser physics [38, 39, 51], electronic circuits [27], and mechanical systems [19].

In a second step, the interest switched to the application of control schemes in spatially extended systems. After some preliminary attempts [3] to control spatiotemporal chaos, attention has turned to the control of two-dimensional patterns [36, 37], or of coupled map lattices [23, 43], or of particular model equations, such as the complex Ginzburg-Landau equation (CGLE) [41] and the Swift–Hohenberg equation for lasers [7, 26].

While for time chaotic systems the different proposed schemes for chaos control have found several experimental verifications, in the extended case experimental realizations are so far limited in the field of nonlinear optics [6, 30, 44, 50] and also in the control of Kármán vortex street in two-dimensional simulations of fluid turbulence [24, 45]. The main reason for this substantial lack of experimental verifications is that not all the proposed schemes for control of spatiotemporal chaos are straightforwardly implementable. For instance, many methods use dense space-extended perturbations, i.e., perturbations that have to be applied at any point of the system, and this requirement represents a serious limitation for any experimental implementations. In coupled map lattices, few examples of global control [43], or control with a finite number of local perturbations [23] have been reported. Some relevant examples in the neural network control (modeled by coupled map lattices) have also been treated [22].

The most relevant question that arises when considering spatially extended systems is therefore to assess whether the perturbation has to be dense in space, i.e., it must be applied to all points of the considered system. In this paper, we review some results about conditions for controlling chaos in spatially extended systems [11], with reference to the complex Ginzburg-Landau equation (CGLE). In the first two sections, after recalling the basic properties of CGLE, we will show that it is not necessary to apply control to all points of the systems, but we can rely on a finite number of local controllers. We will answer the question about the time one has to wait in order to restore a regular dynamics from a chaotic one. Furthermore, we will address issues on the minimal number of local controllers that still provides control over the dynamics, and

how strong the applied forcing must be in order to drive the system to a regular behavior. In the third section, we will show the results of using a parallel extension of the Pyragas' technique [49]. The last section overviews some still open problems.

9.2
The Complex Ginzburg-Landau Equation

In the rest of this paper, we will test control schemes over the celebrated one-dimensional complex Ginzburg-Landau equation (CGLE). This equation has been extensively investigated in the context of space–time chaos, since it describes the universal dynamical features of an extended system close to a Hopf bifurcation [2, 17], and therefore it can be considered as a good model equation in many different physical situations, such as in laser physics [16], fluid dynamics [32], chemical turbulence [34], bluff body wakes [35], or ring of Josephson's junctions [29]. In fact, the importance of the CGL is well known in solid state physics since the pioneering work of Ginzburg and Landau [20], in the phenomenological description of the superconductivity transition. An interested reader will find an account of the GL theory in Abrikosov [1].

In CGLE, a complex field $A(x,t) = \rho(x,t)e^{i\phi(x,t)}$ of modulus $\rho(x,t)$ and phase $\phi(x,t)$ obeys

$$\dot{A} = A + (1 + ia)\partial_x^2 A - (1 + i\beta) \mid A \mid^2 A. \tag{9.1}$$

Here, dot denotes temporal derivative, ∂_x^2 stays for the second derivative with respect to the space variable $0 \leq x \leq L$ (L being the system extension), a and β are real coefficients characterizing linear and nonlinear dispersion. This model equation arises in physics as an "amplitude" equation, providing a reduced universal description of weakly nonlinear spatiotemporal phenomena in extended continuous media in the proximity of an Hopf bifurcation [2].

Different dynamical regimes occur in Eq. (9.1) for different choices of the parameters a, β [15, 53].

In particular, Eq. (9.1) admits plane wave solutions (PWS) of the form

$$A_q(x,t) = \sqrt{1-q^2}e^{i(qx+\omega t)} \qquad -1 \leq q \leq 1, \tag{9.2}$$

where q is the wavenumber in Fourier space, and the associated temporal frequency is given by

$$\omega = -\beta - (a - \beta)q^2. \tag{9.3}$$

The stability of such PWS can be analytically studied below the Benjamin-Feir-Newel (BFN) line (defined by $a\beta = -1$ in the parameter space). Namely, for $a\beta > -1$, one can define a critical wavenumber

$$q_c = \sqrt{\frac{1+\alpha\beta}{2(1+\beta^2)+1+\alpha\beta}} \tag{9.4}$$

such that all PWS are linearly stable in the range $-q_c \leq q \leq q_c$. Outside this range, PWS become unstable through the Eckhaus instability [28].

When crossing from below the BFN line in the parameter space, Eq. (9.4) shows that q_c vanishes and all PWS become unstable. Above this line, one can identify different turbulent regimes [15, 53], called respectively amplitude turbulence (AT) or defect turbulence, phase turbulence (PT), bi-chaos, and a spatiotemporal intermittent regime. The borders in parameter space for each one of these dynamical regimes are schematically drawn in Fig. 9.1, together with the BFN line. Along this review, we will concentrate on PT and AT, since they constitute the fundamental dynamical states of the fields, and their main properties have received considerable attention in recent years including the definition of suitable order parameters marking the transition between them [14, 54, 55].

Phase turbulence (PT) is a regime where the chaotic behavior of the field is dominated by the dynamics of $\phi(x,t)$. In PT the modulus $\rho(x,t)$ changes only smoothly, and is always bounded away from zero. At variance, AT is the dynamical regime wherein the fluctuations of $\rho(x,t)$ become dominant over the phase dynamics. The complex field experiences therefore large amplitude oscillations which can (locally and occasionally) cause $\rho(x,t)$ to vanish. As a consequence,
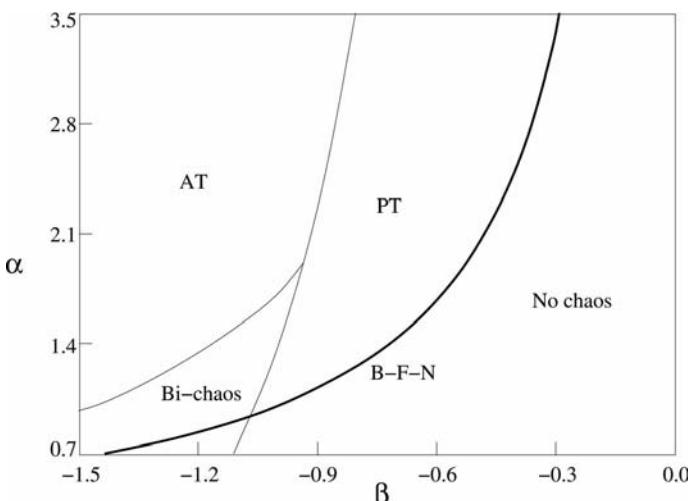
Fig. 9.1 (α,β) parameter space for Eq. (9.1). The lines delimit the borders for each one of the dynamical regimes produced by Eq. (9.1), and the Benjamin-Feir-Newel (B-F-N) line for stability of the plane wavesolutions. Amplitude turbulence (AT) and phase turbulence (PT) are the main dynamical regimes of the CGLE (see text for their detailed description).

at all those points (hereinafter called space–time defects or phase singularities) the global phase of the field $\Phi \equiv \arctan\left[\dfrac{\mathbf{Im}(A)}{\mathbf{Re}(A)}\right]$ shows a singularity.

All simulations presented here were performed with a Crank-Nicholson, Adams-Bashforth scheme which is the second order in space and time [48], with a time step $\delta t = 10^{-2}$ and a grid size $\delta x = 0.25$. Three system sizes $(L = 100, 10^3, 10^4)$ have been considered, and in all cases periodic boundary conditions $[A(0, t) = A(L, t)]$ have been imposed.

9.2.1
Dynamics Characterization

A first interesting parameter characterizing the CGLE dynamics is the defect density. By counting all defects appearing during a numerical simulation, one can define the defect density by

$$n_D = \frac{N_{\text{def}}}{LT}, \tag{9.5}$$

where L is the system size and T is the integration time during which the number of phase defects N_{def} is summed up. Numerically, phase defects at time t have been counted as those points x_i where the modulus $\rho(x_i, t)$ is smaller than a numerical threshold fixed to 2.5×10^{-2} and that are furthermore local minima for the function $\rho(x, t)$.

Figure 9.2 shows n_D versus the parameter β at $a = 2$ for different system sizes ranging over two orders of magnitude. The quantity n_D is clearly an intensive parameter (from a thermodynamic sense), and is a good indicator for differentiating between AT and PT regime. It is interesting to note, however, that the transition between AT and PT is not sharp and depends of the system
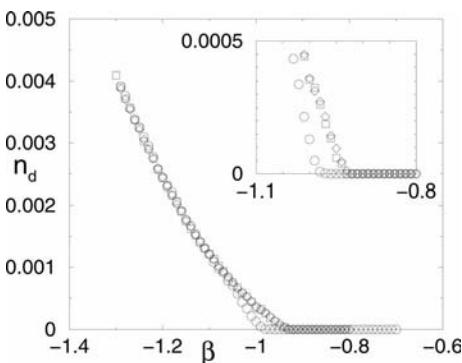
Fig. 9.2 Defect density as a function of β for different system sizes. Open circles, squares, and diamonds are for $L = 100, 10^3, 10^4$, respectively.

size. The complete characterization of this transition is still a question of debate [14].

A second important parameter in the characterization of the CGLE is the natural average frequency. Such a frequency is calculated from long numerical simulations of CGLE by averaging in space the unfolded phase ϕ defined in $\mathbb{R}$ rather than in $[0, 2\pi]$. We have

$$\Omega = \lim_{t \to \infty} \frac{\langle \phi(x,t) \rangle_x}{t} \tag{9.6}$$

where $\langle \cdots \rangle_x$ stands for spatial average.

Figure 9.3 reports Ω versus the parameter β at $a = 2$. In order to construct Fig. 9.3, we have integrated the CGLE for a very long simulation time (usually $t_s = 15,000$) after eliminating the transient behavior occurring in the first $t_t = 5,000$. We also have tested the sensibility of the results by choosing different initial random conditions.

It should be emphasized that all initial conditions were chosen to have a zero average phase gradient, because the frequency in the PT regime is highly sensitive to the average phase gradient [14].

A third classical indicator is the linear spatial auto-correlation function

$$C(\xi) = \langle \bar{A}(x,t) A(x + \xi, t) \rangle_t \tag{9.7}$$

where $\langle \cdots \rangle_t$ stands here for a time average. It has been theoretically predicted [16] that the defects have a dynamical role in mediating the shrinking process of ξ. Figure 9.4 strikingly illustrates this fact for the CGLE. The AT regime (solid line) is for parameters $a = 2$ and $\beta = -1.05$ and the parameters for the PT regime (dashed line) are $a = 2$ and $\beta = -0.87$. The decays to zero are not exponential but we can still define the correlation length as the value of ξ for which
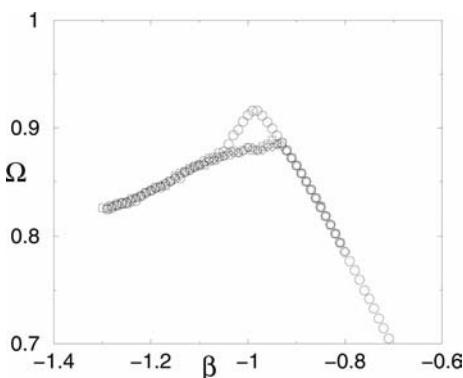
Fig. 9.3 Natural averaged frequency Ω (see text for definition) versus β for $a = 2$. The same symbol convention is used for the system size L as in Fig. 9.2.
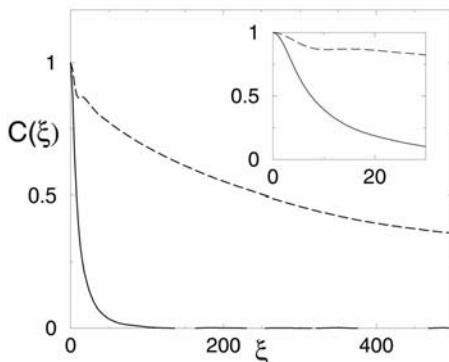
Fig. 9.4 Linear spatial auto-correlation lengths for the AT (solid line) and PT (dashed line) regime of the CGLE (see text for parameter values). The system size L is fixed to 10,000.

$C(\xi) = 1/e$, in doing so we get approximately $\xi = 10.8$ and $\xi = 470$ for the AT and PT regimes, respectively, and for the larger system size used, i.e., $L = 10,000$. Still it is important to note that in the insert of Fig. 9.4, the correlation for the PT regime (soft turbulence) does not follow a monotonic decay. In the following, we will show that this initial steep decay of the cross correlation function even for the PT regime debilitate the process of chaos control and it is presumably responsible for the low performance of the Pyragas control scheme (to be defined in the following section).

From this preliminary discussion, one learns that the CGLE dynamics can be characterized by some intensive indicators as the density of defects, the natural frequency or the correlation length. With increasing the system extension (L), the values of these three parameters stay roughly constant, for system sizes large enough to prevent the dynamics from being affected by any "finite size" effects.

9.3
Control of the CGLE

After having characterized the dynamics of the CGLE, we will tackle the problem of its control. In particular, we will address the issue of whether control can be achieved for a certain number of controllers (extensive case) or rather for a certain density of controllers (intensive case). In this section, we will finally point out that it is the density rather than the number of controllers that matters for the control of the spatiotemporal dynamics. For this purpose, we will test a control strategy for two system sizes ($L = 1,000$ and $L = 10,000$) that differ by a decade and that are both in the "large" system size limit.

Let us begin with the problem of controlling space–time chaos in the AT regime. For this purpose, we set $a = 2$ and $\beta = -1.05$. In a previous analysis [11]

we have used a system size of $L = 64$ which is more than two orders of magnitude smaller than the larger one reported here, and have demonstrated that the control of space–time chaos is doable. Control of space–time chaos here would imply stabilization of a given unstable periodic pattern out of the AT regime. We therefore select a goal pattern $g(x, t)$, represented by any of the plane wave solutions in Eq. (9.2), which are all unstable in the AT regime.

In order to drive the dynamics to the desired goal pattern we add to the right-hand side of Eq. (9.1) a perturbative term $U(x, t)$ of the type

$$
\begin{aligned}
U(x, t) &= 0, && \text{for } x \neq x_i, \\
U(x, t) &= U_i(t), && \text{for } x = x_i,
\end{aligned}
\tag{9.8}
$$

where $i = 1, \ldots, M$ and $x_i = 1 + (i - 1)v$ are the positions of M local equally spaced controllers, mutually separated by a distance v ($x_{i+1} - x_i = v$). The controller distance v will indeed be a crucial parameter in our studies. It indicates in some sense how dense the controllers must be in order to attain the goal dynamics, and we will show that (i) such density has to be relatively large for the control to be effective and (ii) such density is indeed independent of the system size L. In our previous analyses [11], the perturbations were selected by using the adaptive algorithm [8]. In such a case, however, a full control of the perturbation strength applied to the system is not always guaranteed, and, in some cases, the perturbation can occasionally reach unacceptably large values. This represents a limitation of our previous approach, especially if one wants to apply this scheme on a real experiment. We here will turn to the simpler Pyragas control scheme where the strength of the perturbation K_0 is fixed externally by the operator. The perturbation takes the form

$$
U_i(t) = K_0(g(x_i, t) - A(x_i, t)).
\tag{9.9}
$$

Figure 9.5 exemplifies the control task of one of the unstable plane wave for $K_0 = 0.125$ and $v = 0.25$ and a system size ($L = 1{,}000$). The control procedure is effective in the AT regime, and is associated with the suppression of all defects. The arrow indicates the time when the control is switched on.

The control process described above also works for the PT regime, as shown in Fig. 9.6. In the following, we move to compare quantitatively the difference between the two control processes in the AT and PT regimes and for two different system sizes. Our evidence will indicate that the PT regime is only slightly more easily controllable for the parameters selected in the present study which leads to the conclusion that the Pyragas control scheme does not fully exploit the large correlation length of the soft PT regime.

In order to make such quantitative comparison, we monitor the time evolution of the difference between the goal solution and the field A

$$
E(t) = \frac{1}{L} \int |A(x, t) - g(x, t)| \, dx,
\tag{9.10}
$$

a

b
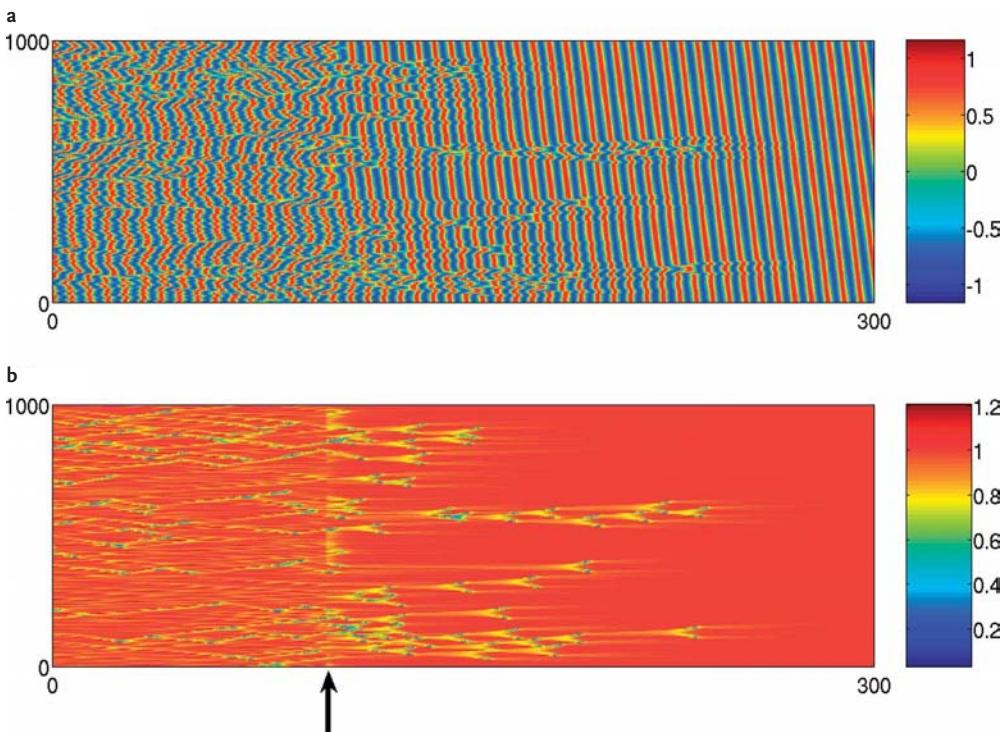
Fig. 9.5 Space (vertical)-time (horizontal)-plots of the real part of A (**a**) and modulus of A (**b**) in the AT regime ($\beta = -1.05$). Time is increasing from 0 to 300 and the control is switched on at $t = 100$. The parameters for the control are $K_0 = 0.125$ and $v = 0.25$.

The goal dynamics is chosen such that the system size $L = 1{,}000$ contains two wavelengths of the desired PWS. The associated frequency $\omega = 1.0495$ is calculated from the dispersion relation (9.3). The system size L is 1,000.

where the factor $1/L$ accounts for averaging over space. Figure 9.7 reports the time evolution of $E(t)$ for the AT (solid line) and PT (dashed line) regimes. It is apparent from the figure that the difference between controlling a PT or AT regime is not significant when selecting $K_0 = 0.5$ and $v = 0.5$. Similar results are found for $L = 1{,}000$ and $L = 10{,}000$.

In order to gather more information on the control process, we define the transient time τ needed for control as the time at which the error $E(t)$ becomes smaller than a given threshold (in what follows we set the threshold to be 10^{-2}).

This allows us to study the influence on control of the two main parameters used in our scheme, namely the fixed strength of the control K_0 and the distance between two adjacent controllers v, for the two chosen system sizes $L = 1{,}000$ and $L = 10{,}000$.

As one would expect, the transient time τ is an increasing function of v, at a fixed value of K_0. Furthermore, we observe that there is a threshold for control-

a

b
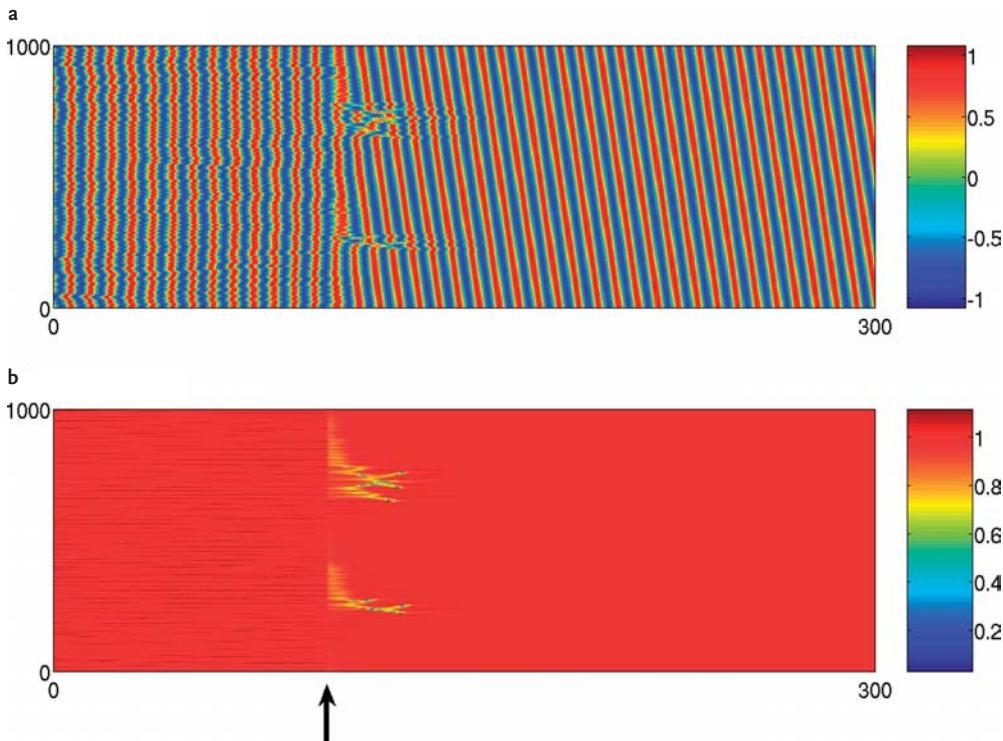
Fig. 9.6 Space (vertical)-time (horizontal)-plots of the real part of A (**a**) and modulus of A (**b**) in the PT regime ($\beta = -0.87$). Time is increasing from 0 to 300 and the control is switched on at $t = 100$. The parameters for the control are $K_0 = 0.125$ and $v = 0.25$. The goal dynamics is chosen such that the system size $L = 1,000$ contains two wavelengths of the desired PWS. The associated frequency $\omega = 0.8695$ is calculated from the dispersion relation Eq. (9.3). The system size L is 1,000. Note the appearance of few defects in the transient after the control is switched on.

ler density below which the control method fails in stabilizing the PWS for any value of the coupling strength K_0. An example of this behavior is reported in Fig. 9.8, which shows how τ increases with v for $K_0 = 4$, for both AT and PT regimes. Figure 9.8 confirms that the density of controllers is indeed the important quantity that enables control. The two system sizes $L = 1,000$ and $L = 10,000$ are represented by diamonds and squares symbols, respectively and the filled and open symbols are for the AT and PT regimes, respectively. From Fig. 9.8, one concludes that controlling a PT regime is only slightly easier than controlling the AT regime which indicates that the Pyragas method is presumably not the best in controlling the PT regime.

In addition, one would also intuitively expect τ to be a decreasing function of K_0 at fixed v, reflecting the fact that an initial choice of a larger control strength helps the system to attain more rapidly the desired goal behavior. Figure 9.9
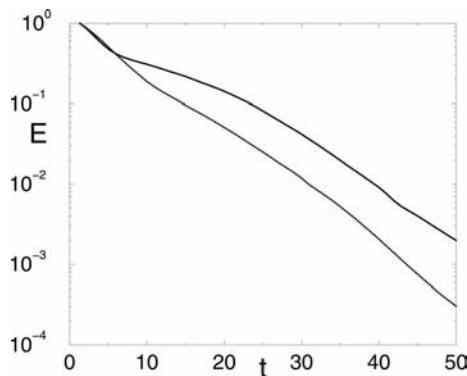
Fig. 9.7 Time evolution of the control error (see text for definition) for the AT (solid line) and PT (dotted line) regimes. The control parameters are $K_0 = 0.5$ and $v = 0.5$. The system size L is 10000.
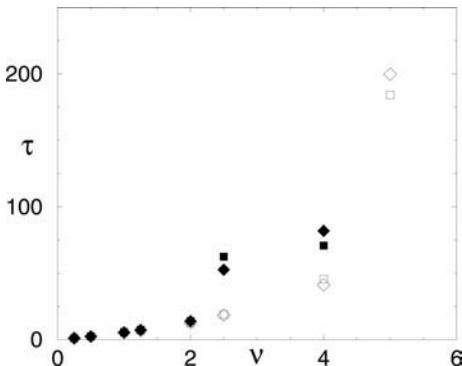
Fig. 9.8 Dependence of the control time τ with the separation of the controllers v for two different system sizes ($L = 1,000$ is represented with square symbols and $L = 10,000$ is represented with diamond symbols). Open and filled symbols are for the control of the PT and AT regimes, respectively. The control parameter $K_0 = 4$ is fixed in all the simulations.

confirms this fact by reporting the dependence of the control time τ with the control strength K_0 at two fixed density of controllers $v = 0.25$ and $v = 0.5$ (diamonds and triangles, respectively) and for the two cases AT and PT (filled and open symbols, respectively). The system size is fixed to $L = 10,000$.
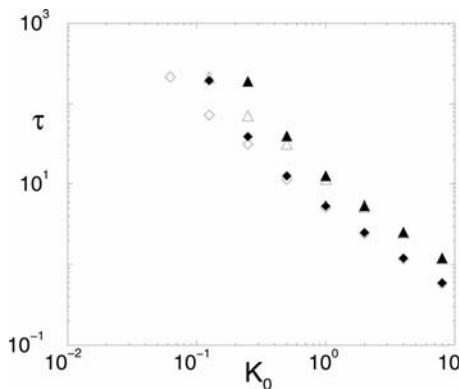
Fig. 9.9 Dependence of the control time τ with the control strength K_0. The separation between the controllers is fixed to $v = 0.25$ (diamonds) and $v = 0.5$ (triangles). AT and PT regimes are represented by filled and open symbols, respectively. Note the logarithmic scales for both axes.

9.4
Conclusions and Perspectives

In this article, we have reconsidered the problem of controlling a spatiotemporal state generated by a CGLE into an unstable plane wave solution. In the present study, we have considered two different system sizes ($L = 1,000$ and $L = 10,000$) shown to be in the large system size limit. Control of spatiotemporal chaos is achieved for sufficient large control strength and density of controllers. It is also interesting to note that the result of Bragard and Boccaletti [13] concerning the integral behavior of the synchronization is also valid in the case of chaos control in the limit of dense control spacing. Let us recall that it states that if the distance between the controllers is doubled the strength must be also doubled in order to achieve control in the same time.

The questions that we leave open for further studies are the following: will a further increase in the size of the system eventually compromising the ability of control? In the thermodynamic limit ($L \to \infty$), for instance, one would really need an infinite number of controllers. Apart of being very difficult to realize in practice, one may ask if control is still "stable" in this thermodynamic limit. Another relevant question concerns the selection of equally spaced controllers. We believe that it does not represent an optimal choice for achieving stabilization of PWS especially in the PT regime (soft turbulence). An answer to this question would result from comparatively testing the effectiveness of different controller positioning functions, or from giving analytical conditions for optimal controller placing. In this context, a promising approach has been proposed that connects control of spatiotemporal chaos with the Floquet control theory [5, 52].

Acknowledgment

References

1 Abrikosov, A. 1988. Fundamentals on the Theory of Metals, Elsevier, The Netherlands.

2 Aranson, I. & Kramer, L. 2002. The world of the complex Ginzburg-Landau equation. *Rev. Mod. Phys.* **74**, 99–143.

3 Aranson, I., Levine, H. & Tsimring, L. 1994. Controlling spatiotemporal chaos. *Phys. Rev. Lett.* **72**, 2561–2564.

4 Argyris, A., Syvridis, D., Larger, L., Annovazzi-Lodi, V., Colet, P., Fischer, I., Garcia-Ojalvo, J., Mirasso, C., Pesquera, L. & Shore, K. A. 2005. Chaos-based communications at high bit rates using commercial fibre-optic links. *Nature* **437**, 343–346.

5 Baba, N., Amann, A., Schöll, E. & Just, W. 2002. Giant improvement of time delayed feedback control by spatio-temporal filtering. *Phys. Rev. Lett.* **89**, 074101.

6 Benkler, E., Kreuzer, M., Neubecker, R. & Tschudi, T. 2000. Experimental control of unstable patterns and elimination of spatiotemporal disorder in nonlinear optics, *Phys. Rev. Lett.* **84**, 879–882.

7 Bleich, M., Hochheiser, D., Moloney, J. & Socolar, E. 1997. Controlling extended systems with spatially filtered, time delayed feedback. *Phys. Rev. E* **55**, 2119–2126.

8 Boccaletti, S. & Arecchi, F. T. 1995, Adaptive control of chaos. *Europhys. Lett.* **31**, 127–132.

9 Boccaletti, S., Maza, D., Mancini, H., Genesio, R. & Arecchi, F. T. 1997. Control of defects and space-like structures in delayed dynamical systems, *Phys. Rev. Lett.* **79**, 5246–5249.

10 Boccaletti, S., Farini, A. & Arecchi, F. T. 1997 b. Adaptive synchronization of chaos for secure communication, *Phys. Rev. E* **55**, 4979–4981.

11 Boccaletti, S., Bragard, J. & Arecchi, F. T. 1999. Controlling and synchronizing space time chaos. *Phys. Rev. E* **59**, 6574–6578.

12 Boccaletti, S., Grebogi, C., Lai, Y.-C., Mancini, H. & Maza, D. 2000. The control of chaos: theory and applications. *Physics Report* **329**, 103–197.

13 Bragard, J. & Boccaletti, S. 2000. Integral behavior for localized synchronization in nonidentical extended systems. *Phys. Rev. E* **62**, 6346–6351.

14 Brusch, L., Torcini, A., van Hecke, M., Zimmermann, M. & Bar, M. 2001. Modulated amplitude waves and defects formation in the one-dimensional complex Ginzburg-Landau equation. *Physica* **D160**, 127–151.

15 Chate, H. 1994. Spatiotemporal intermittency regimes of the one-dimensional complex Ginzburg-Landau equation. *Nonlinearity* **7**, 185–204.

16 Coullet, P., Gill, L. & Rocca, F. 1989. Optical vortices. *Opt. Commun.* **73**, 403–408.

17 Cross, M. & Hohenberg, P. 1993. Pattern formation out of equilibrium. *Rev. Mod. Phys.* **65**, 851–1112.

18 Cuomo, K. & Oppenheim, A. 1993. Circuit implementation of synchronized chaos with applications to communications. *Phys. Rev. Lett.* **71**, 65–68.

19 Ditto, W., Rauseo, S. & Spano, M. 1990. Experimental control of chaos. *Phys. Rev. Lett.* **65**, 3211–3214.

20 Ginzburg, V. & Landau, L. 1950. On the theory of superconductivity. *Zh. eksper. teor. fiz.* **20**, 1064–1082.

21 Gershenfeld, N. & Grinstein, G. 1995. Entrainment and communication with dissipative pseudorandom dynamics. *Phys. Rev. Lett.* **74**, 5024–5027.

22 Greilich, A., Markus, M. & Goles, E. 2005. Control of spatiotemporal chaos: dependence of the minimum pinning distance on the spatial measure entropy. *Eur. Phys. J. D.* **33**, 279–283.

23 Grigoriev, R., Cross, M. & Schuster, H. 1997. Pinning control of spatiotemporal chaos. *Phys. Rev. Lett.* **79**, 2795–2798.

24 Guan, S., Wei, G. & Lai, C. 2004. Controllability of flow turbulence. *Phys. Rev. E.* **69** (6), 6214.

25 Hayes, S., Grebogi, C., Ott, E. & Mark, A. 1994. Experimental control of chaos for communication. *Phys. Rev. Lett.* **73**, 1781–1784.

26 Hochheiser, D., Moloney, J. & Lega, J. 1997. Controlling optical turbulence. *Phys. Rev. A* **55**, R4011–R4014.

27 Hunt, E. 1991. Stabilizing high-period orbits in a chaotic system: The diode resonators. *Phys. Rev. Lett.* **67**, 1953–1955.

28 Janiaud, B., Pumir, A., Bensimon, D., Croquette, V., Richter, H. & Kramer, L. 1992. The Eckhaus instability for traveling waves. *Physica* **D55**, 269–286.

29 Josephson, B. 1962. Possible new effects in superconductive tunnelling. *Phys. Lett.* **1**, 251–253.

30 Juul Jensen, S., Schwab, M. & Denz, C. 1998. Manipulation, stabilization, and control of pattern formation using Fourier space filtering, *Phys. Rev. Lett.* **81**, 1614–1617.

31 Kivshar, Y., Rodelsperger, F. & Benner, H. 1994. Suppression of chaos by non-resonant parametric perturbations. *Phys. Rev. E* **49**, 319–324.

32 Kolodner, P., Slimani, S., Aubry, N. & Lima, R. 1995. Characterization of dispersive chaos and related states of binary-fluid convection. *Physica* **D85**, 165–224.

33 Kocarev, L. & Parlitz, U. 1995. General approach for chaotic synchronization with applications to communications. *Phys. Rev. Lett.* **74**, 5028–5031.

34 Kuramoto, Y. & Koga, S. 1981. Turbulized rotating chemical waves. *Prog. Theor. Phys. Suppl.* **66**, 1081–1085.

35 Leweke, T. & Provansal, M. 1994. Model for the transition in bluff body wakes. *Phys. Rev. Lett.* **72**, 3174–3177.

36 Lu, W., Yu, D. & Harrison, R. 1996. Control of patterns in spatiotemporal chaos in optics. *Phys. Rev. Lett.* **76**, 3316–3319.

37 Martin, R., Scroggie, A., Oppo, G.-L. & Firth, W. 1996. Stabilization, selection and tracking of unstable patterns by

Fourier space techniques. *Phys. Rev. Lett.* **77**, 4007–4010.

38 Meucci, R., Gadomski, W., Ciofini, M. & Arecchi, F. 1994. Experimental control of chaos by means of weak parametric perturbations. *Phys. Rev. E* **49**, R2528–R2531.

39 Meucci, R., Ciofini, M. & Abbate, R. 1996. Suppressing chaos in lasers by negative feedback. *Phys. Rev. E* **53**, R5537–R5540.

40 Minai, A. & Durai Pandian, T. 1998. Communicating with noise: How chaos and noise combine to generate secure encryption keys. *Chaos* **8**, 621–628.

41 Montagne, R. & Colet, P. 1997. Nonlinear diffusion control of spatiotemporal chaos in the complex Ginzburg-Landau equation. *Phys. Rev. E* **56**, 4017–4024.

42 Ott, E., Grebogi, C. & Yorke, J. A. 1990. Controlling chaos. *Phys. Rev. Lett.* **64**, 1196–1199.

43 Parmananda, P., Hildebrand, M. & Eiswirth, M. 1997. Controlling turbulence in coupled map lattice system using feedback techniques. *Phys. Rev. E* **56**, 239–244.

44 Pastur, L., Gostiaux, L., Bortolozzo, U., Boccaletti, S. & Ramazza, P.L. 2004. Experimental targeting and control of spatiotemporal chaos in nonlinear optics, *Phys. Rev. Lett.* **93**, 063902 (1–4).

45 Patnaik, B. & Wei, G. 2002. Controlling wake turbulence. *Phys. Rev. Lett.* **88**, 054502.

46 Peng, J., Ding, E., Ding, M. & Yang, W. 1996. Synchronizing hyperchaos with a scalar transmitted signal. *Phys. Rev. Lett.* **76**, 904–907.

47 Petrov, V., Gaspar, V., Masere, J. & Showalter, K. 1993. Controlling chaos in the Belousov-Zhabotinsky reaction. *Nature* **361**, 240–243.

48 Press, W., Teukolsky, S., Vetterling, W. & Flannery, B. 1992. Numerical Recipes in Fortran 90: The Art of Scientific Computing. Cambridge University Press, Cambridge.

49 Pyragas, K. 1992. Continuous control of chaos by self-controlling feedback. *Phys. Lett.* **A170**, 421–428.

50 Ramazza, P.-L., Bortolozzo, U. & Boccaletti S. 2006. Experimental synchronization of spatiotemporal chaos in nonlinear optics. *Phys. Rev. E* **73(3)**, 6213.

51 Roy, R., Murphy, T., Maier, T., Gills, Z. & Hunt, E. 1992. Dynamical control of chaotic laser: Experimental stabilization of globally coupled system. *Phys. Rev. Lett.* **68**, 1259–1262.

52 Sakamoto, N. 2006. Floquet-based chaos control for continuous-time systems with stability analysis. *Phys. Lett. A* **356**, 316–323.

53 Shraiman, B., Pumir, A., van Saarlos, W., Hohenberg, P., Chaté, H. & Holen, M. 1992. Spatiotemporal chaos in the one-dimensional complex Ginzburg-Landau equation. *Physica* **57**, 241–248.

54 Torcini, A. 1996. Order parameter for the transition from phase to amplitude turbulence. *Phys. Rev. Lett.* **77**, 1047–1050.

55 Torcini, A., Frauenkron, H. & Grassberger, P. 1997. Studies of phase turbulence in the one-dimensional complex Ginzburg-Landau equation. *Phys. Rev. E* **55**, 5073–5081.

10
Multiple Delay Feedback Control

Alexander Ahlborn and Ulrich Parlitz

10.1
Introduction

One of the first attempts to tame chaotic systems was proposed in 1989 by Hübler and Lüscher [1] who devised unidirectional control methods for driving nonlinear systems to some goal dynamics. At the same time Ott, Grebogi, and Yorke (OGY) developed a sophisticated control technique based on local approximations of the flow [2] that was published in 1990 and stimulated an avalanche of publications on applications and alternative chaos control methods [3–5]. One of these techniques is *time delay autosynchronization* (TDAS) first suggested by Pyragas [6]. Similar to OGY-control TDAS aims at stabilizing UPOs embedded in the chaotic attractor of the system to be controlled. From a practical point of view, however, TDAS is much easier to implement than OGY control, for example by means of analog electronic circuits. For a general system

$$\dot{\mathbf{x}} = \mathbf{f}(\mathbf{x}, \mathbf{u}) \tag{10.1}$$

with state vector $\mathbf{x}$ TDAS requires a time delayed value $\mathbf{g}[\mathbf{x}(t - \tau)]$ of some observable $\mathbf{g}[\mathbf{x}(t)]$ both entering the control signal

$$\mathbf{u}(t) = k\{\mathbf{g}[\mathbf{x}(t - \tau)] - \mathbf{g}[\mathbf{x}(t)]\}. \tag{10.2}$$

The parameter k is the gain of the feedback loop, $\mathbf{g}$ denotes a (suitable) measurement function, and τ is the delay time typically chosen to equal the period of the UPO to be stabilized. In this case, the control signal vanishes on the periodic orbit, i.e., the UPO is not distorted by TDAS but only its stability properties are changed. Therefore, this kind of stabilization is also called *noninvasive* control. In 1994, a generalization of TDAS was suggested called *extended TDAS* (ETDAS) [7, 8] where the feedback signal

$$\mathbf{u}(t) = k \left\{ (1 - R) \sum_{n=1}^{\infty} R^{n-1} \mathbf{g}[\mathbf{x}(t - n\tau)] - \mathbf{g}[\mathbf{x}(t)] \right\} \tag{10.3}$$

$$= k\{\mathbf{g}[\mathbf{x}(t - \tau)] - \mathbf{g}[\mathbf{x}(t)]\} + R\mathbf{u}(t - \tau) \tag{10.4}$$

with $R \in]-1, 1[$ is based on an infinite sequence of delayed observables $\mathbf{g}[\mathbf{x}(t - n\tau)]$ whose delay times $n\tau$ are integer multiples of some fundamental delay time τ. As can be seen from Eq. (10.4) the ETDAS-control signal can be generated using the TDAS scheme (10.2) with an additional delayed control signal $\mathbf{u}(t - \tau)$. Detailed investigations showed that ETDAS provides larger stability regions and periodic orbits with higher stability compared to TDAS. For stabilizing fixed points (steady states) Chang et al. [9, 10] suggested to consider the limit $\tau \to 0$ and $R \to 1$ in Eq. (10.4) resulting in a single pole high-pass filter

$$\dot{\mathbf{u}}(t) = -\omega_0 \mathbf{u}(t) - k\dot{\mathbf{g}}[\mathbf{x}(t)] \tag{10.5}$$

with cut-off frequency $\omega_0 = (1 - R)/\tau$.

10.2
Multiple Delay Feedback Control

(E)TDAS proved to be very useful for stabilizing UPOs but it is less efficient for steady states. This is partly due to the fact that the control signal vanishes for any τ-periodic solution. To impose a constraint that is fulfilled for constant solutions, only a second feedback term is necessary with a *different* delay time $\tilde{\tau}$ resulting in

$$\mathbf{u}(t) = k\{\mathbf{g}[\mathbf{x}(t - \tau)] - \mathbf{g}[\mathbf{x}(t)]\} + \tilde{k}\{\mathbf{g}[\mathbf{x}(t - \tilde{\tau})] - \mathbf{g}[\mathbf{x}(t)]\}. \tag{10.6}$$

If the ratio of delays $\tau/\tilde{\tau}$ is irrational, then there exists no periodic orbit on which the control signal vanishes. Only for fixed points $\mathbf{x}_0$ (with $\mathbf{g}[\mathbf{x}] = $ const.) the differences in Eq. (10.6) vanish and the control signal equals zero resulting in a noninvasive control. In general, more than two delay lines may exist and the gain factors of the delayed and the not delayed signals may be different. The control signal of such a *multiple delay feedback control* (MDFC) [11–13] is written as

$$\mathbf{u}(t) = k_0 + k_{1a}\mathbf{g}_1[\mathbf{x}(t - \tau_1)] - k_{1b}\mathbf{g}_1[\mathbf{x}(t)] + \cdots$$
$$+ k_{Ma}\mathbf{g_M}[\mathbf{x}(t - \tau_M)] - k_{Mb}\mathbf{g_M}[\mathbf{x}(t)] \tag{10.7}$$

with M different delay times $\tau_1, \ldots, \tau_M$ and M different observables $\mathbf{g_m}$. With asymmetrical gains ($k_{ma} \neq k_{mb}$) this control signal provides in general an *invasive* control scheme and if a solution of the original system is to be stabilized additional constraints have to be imposed on the gain factors k_{ma} and k_{mb} [13].

However, if a fixed point is to be stabilized noninvasive control can also be implemented by choosing the constant gain k_0 appropriately. This option can be used, for example, to overcome some limitations of delayed feedback due to controllability requirements as will be discussed in Section 10.4. Here, we shall first focus on *symmetric* MDFC ($k_{ma} = k_{mb} = k_m$) with vanishing bias k_0 and later discuss examples where asymmetric control is superior.

10.2.1
Linear Stability Analysis

For many experimental and theoretical systems it turned out that MDFC is more suitable for fixed point stabilization than (E)TDAS or single pole high pass filtering (10.5) [12, 13]. This can best be seen by a linear stability analysis of the vector field $\mathbf{f}$ in the vicinity of a fixed point $\mathbf{x}_0$.[1] For simplicity we shall consider the case of an additive control force

$$\dot{\mathbf{x}}(t) = \mathbf{f}[\mathbf{x}(t)] + \mathbf{u}(t). \tag{10.8}$$

Application of a delayed feedback in the form of Eq. (10.7) results in an infinite-dimensional control problem with an infinite number of eigenvalues to be calculated upon linear stability analysis. Fortunately, only a finite number of eigenvalues larger than some given constant (e.g., larger than zero) occur [14] facilitating the search for eigenvalues with positive real parts. Stabilization of the fixed point $\mathbf{x}_0$ is successful if all eigenvalues λ of the controlled system possess a negative real part $\mathrm{Re}(\lambda)$. Therefore, to decide whether the feedback is successful or not one has to calculate the eigenvalue λ with the largest real part of the transcendental characteristic equation $\det[\Delta(\lambda)] = 0$ based on the characteristic matrix

$$\Delta(\lambda) = \lambda I - D\mathbf{f}(\mathbf{x}_0) - U(\mathbf{x}_0, \lambda), \tag{10.9}$$

where I denotes the unit matrix, $D\mathbf{f}(\mathbf{x}_0)$ is the Jacobian of the unperturbed system at the fixed point $\mathbf{x}_0$ and

$$U(\mathbf{x}_0, \lambda) = \sum_{m=1}^{M} \left(k_{ma} e^{-\lambda \tau_m} - k_{mb} \right) D\mathbf{g_m}(\mathbf{x}_0) \tag{10.10}$$

is the feedback matrix based on the Jacobian matrices $D\mathbf{g_m}(\mathbf{x}_0)$ of the measurement functions.

---

[1] In the presence of coexisting fixed points, basins of attraction, initial conditions and the choice of control parameters decide to which fixed point the system dynamics converges in the end. Thus, for every fixed point an individual stability analysis has to be performed.

10.2.2
Example: Colpitts Oscillator

To give an illustration of MDFC we consider the electronic Colpitts oscillator [13, 15] shown in Fig. 10.1 that is described by a three-dimensional set of differential equations

$$C_1 \frac{dU_{C_1}}{dt} = -a_F f(-U_{C_2}) + I_L + \frac{C_1}{T} u(t)$$
$$C_2 \frac{dU_{C_2}}{dt} = (1 - a_F) f(-U_{C_2}) - G_0 U_{C_2} + I_L - I_0 \qquad (10.11)$$
$$L \frac{dI_L}{dt} = -U_{C_1} - U_{C_2} - R I_L + U_{cc},$$

where U_{C_1}, U_{C_2} are capacitor voltages, I_L is the current through the inductivity, $I_0 = (U_{C_2} + U_{cc})/R_1$, and

$$I_E = f(U_{BE}) = I_S \left[\exp\left(\frac{U_{BE}}{U_t}\right) - 1 \right] \qquad (10.12)$$

is the emitter current of the transistor. A typical time scale of oscillations for the system running without control is given by

$$T = \sqrt{L \frac{C_1 C_2}{C_1 + C_2}} \qquad (10.13)$$

resulting in a natural period of oscillations of $T_0 = 2\pi T$, if the control signal

$$u(t) = \sum_{m=1}^{M} k_{ma} U_{C_1}(t - \tau_m) - k_{mb} U_{C_1}(t) \qquad (10.14)$$

is switched off. Chaotic dynamics occurs for the free running case ($u(t) = 0$) if parameters are fixed to $L = 91 \,\mu\text{H}$, $R = 33 \,\Omega$, $R_1 = 242 \,\Omega$, $C_1 = 68 \,\text{nF}$, $C_2 = 68 \,\text{nF}$, $I_s = 14.34 \,\text{fA}$, $U_t = 0.027 \,\text{V}$, $a_F \approx 0.99$, $U_{cc} = 5 \,\text{V}$, $G_0 = 0$. The Col-
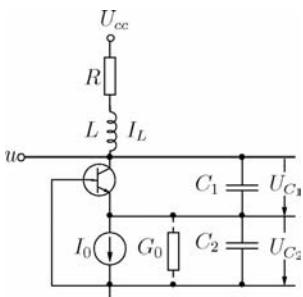
Fig. 10.1 Colpitts oscillator.

pitts oscillator possesses an unstable fixed point at $\mathbf{x}_0 = (U_{C_1}, U_{C_2}, I_L)$ $\approx (5.1759, -0.7502, 0.0174)$. For the calculation of the stability diagrams shown in Fig. 10.2 we started with a grid in the complex plane, computed $\det[\Delta(\lambda)]$ using Eqs. (10.9) and (10.10) and detected those λ values for which $\det[\Delta(\lambda)]$ is already close to zero. These λ values were then used as initial conditions for a damped Newton's algorithm to determine the exact roots of the characteristic equation $\det[\Delta(\lambda)] = 0$.
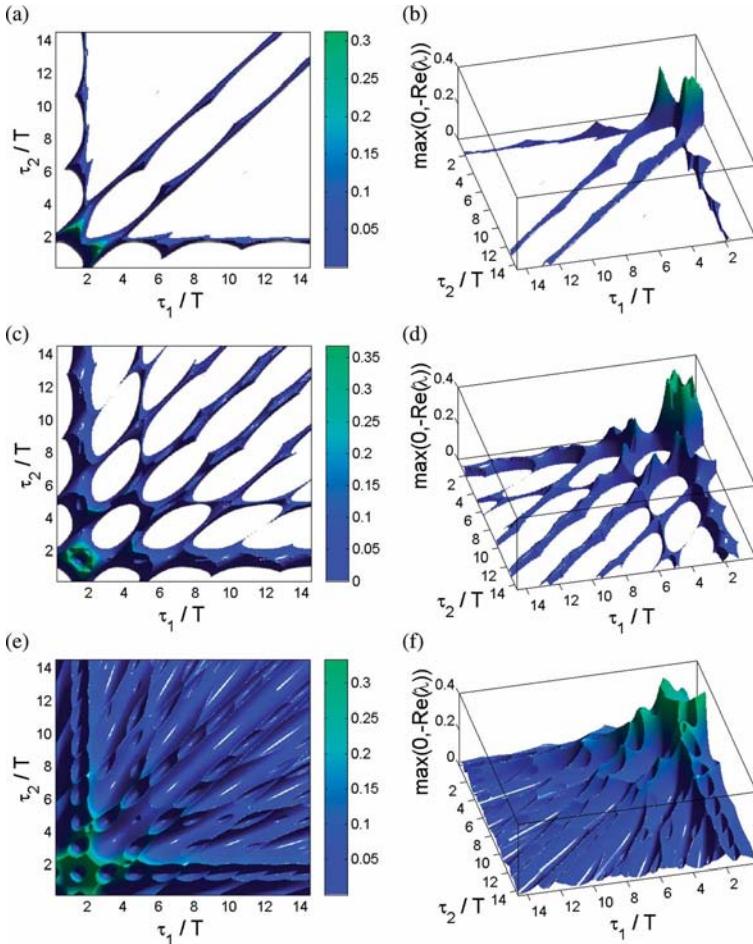
Fig. 10.2 Stability diagrams of the controlled Colpitts oscillator (10.11), using MDFC (10.14) with (a), (b) two, (c), (d) three and (e),(f) four delay times ($k_m = 1.35$, $\tau_3 = 3.1$, $\tau_4 = 1.32$). (a), (c), (e) Combinations of delay times τ_1/T and τ_2/T leading to fixed point stabilization are colored. The color scaling is given by the stability function $\max[0, -\mathrm{Re}(\lambda)]$ where λ denotes the eigenvalue with the largest real part $\mathrm{Re}(\lambda)$. (b), (d), (f) Stability function $\max[0, -\mathrm{Re}(\lambda)]$ versus τ_1/T and τ_2/T. Note that (b), (d), (f) are rotated compared to (a), (c), (e), respectively.

Figure 10.2 shows the resulting stability diagrams of the controlled Colpitts oscillator with identical symmetric gains $k_{ma} = k_{mb} = k_m = 1.35$ and $k_0 = 0$. The diagrams show the stability function $\max[0, -\text{Re}(\lambda)]$ color coded versus τ_1/T and τ_2/T where λ denotes the eigenvalue with the largest real part.

In the white areas fixed point stabilization fails and the diagonal in the τ_1/T–τ_2/T parameter plane in Fig. 10.2 (a) corresponds to TDAS control Eq. (10.2) with a single delay time $\tau_1/T = \tau_2/T = \tau/T$.[2]

As can be seen, with TDAS steady state stabilization is not possible for delay times τ larger than $\approx 2T$. In contrast, MDFC enables successful fixed point control for all delay times $\tau_m/T \in [0.2, 14]$ if delay combinations are chosen that lie within some stripes running in parallel to the diagonal. These stripes are separated by a horizontal distance corresponding to approximately one half of the natural period $T_0 = 2\pi T$ of the Colpitts oscillator. Highest stability for MDFC using two delay times is obtained for the two peaks in the upper right corner of the diagram (in parallel to the diagonal) in Fig. 10.2 (b) occurring for independent delay times $\tau_1/T \neq \tau_2/T$.

However, the use of different delay times can be further exploited. Application of a third delay time leads to a significant enlargement of stability regions shown in Fig. 10.2 (c) and (d) for $\tau_3/T = 3.1$ and fixed gains ($k_1 = k_2 = k_3 = 1.35$) resulting in even higher stability (≈ -0.37). In contrast to this the highest stability value of TDAS is ≈ -0.17 (ETDAS for $R = 0.7$: ≈ -0.3) [13]. Using additionally a forth delay time $\tau_4/T = 1.32$ steady state stabilization is possible for the whole parameter plane $\tau_1/T, \tau_2/T \in [0.2, 14]$ as shown in Fig. 10.2(e) and (f). The larger the delay times are chosen the lower is the achieved stability of
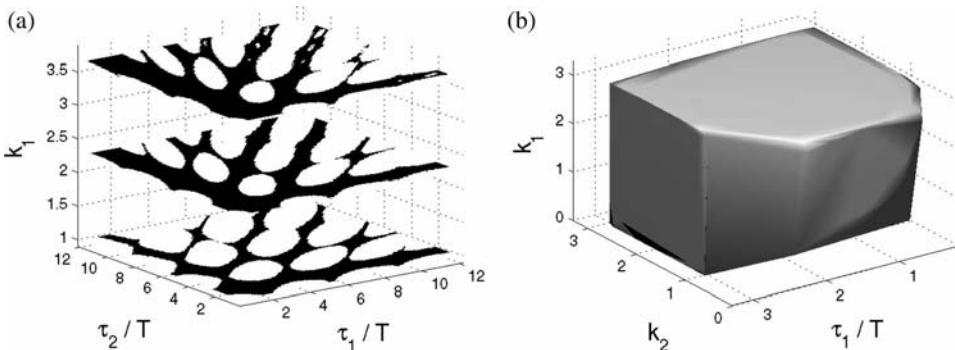
Fig. 10.3 MDFC fixed point stabilization of the Colpitts oscillator (10.11) using three delay times. (a) Three cross sections of the MDFC parameter space for fixed $\tau_3/T = 3.1$ and $k_2 = k_3 = 1.35$. Fixed point stabilization is successful in the parameter regions marked in black. (b) Stability region versus τ_1/T, k_1, and k_2 showing control parameter combinations leading to fixed point stabilization ($\tau_2/T = 1.8$, $\tau_3/T = 3.1$, and $k_3 = 1.35$).

2) All stability plots shown in Fig. 10.2 start with delay times $\tau_i > 0.2$ to make sure that at least two delay times are active for every τ_1–τ_2 combination.

the considered fixed point but in contrast to (E)TDAS stabilization is still possible. Figure 10.3 (a) shows the extended stability regions in parameter space obtained with MDFC based on three delay times. For this three-dimensional projection the gains of the second and third delay time are set to $k_2 = k_3 = 1.35$ and $\tau_3/T = 3.1$. Parameter combinations of τ_1/T, τ_2/T and k_1 resulting in fixed point stabilization are marked black to visualize how stability regions change for varying gain k_1.

10.2.3
Comparison with High-Pass Filter and PD Controller

We shall now compare the performance of MDFC with conventional control techniques like a single pole high-pass filter Eq. (10.5) or a PD controller

$$u(t) = k_p U_{C_1} + k_d \frac{dU_{C_1}}{dt}. \tag{10.15}$$

Figure 10.4 (a) shows the stability function $\max[0, -\mathrm{Re}(\lambda)]$ versus feedback gain k and cut-off frequency ω_0 of the high pass filter.

As can be seen, a maximum stability of ≈ 0.3 can be achieved. In comparison, MDFC with $k_1 = 0.27$, $k_2 = 1.56$, $k_3 = 0.28$, $\tau_1 = 3.613$, $\tau_2 = 2$, $\tau_3 = 3.111$ yields a stability of $\max[0, -\mathrm{Re}(\lambda)] \approx 0.4767$. Figure 10.4 (b) shows results for a conventional PD-controller. Here, the same stability function $\max[0, -\mathrm{Re}(\lambda)]$ is plotted (color scaled) versus the gains k_p and k_d exhibiting a maximum value of about 0.462. This is comparable to the stability achieved with MDFC but the gain factors k_p and k_d required (see Fig. 10.4 (b)) are much higher than the MDFC parameters given above.
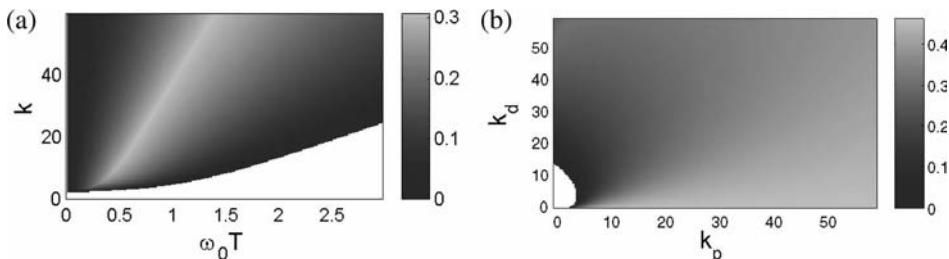
Fig. 10.4 Fixed point stabilization of the Colpitts oscillator using (a) a single pole high pass filter (10.5) and (b) a PD-controller (10.15). Stability function $\max[0, -\mathrm{Re}(\lambda)]$ (color scaled) versus (a) feedback gain k and cut-off frequency ω_0 and (b) proportional gain k_p and differential gain k_d.

10.2.4
Transfer Function of MDFC

To improve the intuitive understanding of the proposed MDFC scheme we shall now change to the frequency domain. Fourier transformation of the control signal Eq. (10.14) provides the transfer function

$$T(f) = \sum_{m=1}^{M} k_{ma} e^{-i2\pi f \tau_m} - k_{mb} = \frac{\hat{u}(f)}{\hat{U}_{C_1}(f)} \qquad (10.16)$$

linking the output $\hat{u}(f)$ linearly to the input signal $\hat{U}_{C_1}(f)$. Figure 10.5 (a) shows the Fourier spectrum of the unperturbed Colpitts system (10.11). Figure 10.5 (c) reveals the absolute value of the transfer function $|T(f)|$ for the case of a single delay time $(\tau_1/T = 10, k_{1a} = k_{1b} = 1$, solid line), two active delays $(\tau_1/T = 10, \tau_2/T = 5, k_{1a} = k_{1b} = k_{2a} = k_{2b} = 1$, dash-dotted line), three active time delays $(\tau_1/T = 10, \tau_2/T = 5, \tau_3/T = 3.1, k_{ma} = k_{mb} = 1, m = 1, 2, 3$, dotted line), and four individual delay times $(\tau_1/T = 10, \tau_2/T = 5, \tau_3/T = 3.1, \tau_4/T = 1.32, k_{ma} = k_{mb} = 1, m = 1, 2, 3, 4$, dashed line). The notch at $f = 0$ is necessary for fixed point stabilization guaranteeing a noninvasive feedback signal since a frequency lying in a notch is not fed back [9]. Consequently, the other notches for $f > 0$ have to be placed within the Fourier space such that all (main) frequencies (corresponding to dominant UPOs embedded in the chaotic attractor) are fed back by the control signal. Since τ_1 and τ_2 do not eliminate all frequencies (nonvanishing control signal) of the oscillator this holds for the Colpitts oscillator only after activation of the third and forth delay time. Corresponding phases are shown in Fig. 10.5 (d) providing for multiple delays a smoother shape than TDAS with a single delay time does.

An example for fixed point stabilization in the presence of only two delay times is shown in Fig. 10.5 (e) and (f) where the feedback is defined in a way avoiding any notches in the relevant part of the frequency domain. The additionally activated third and fourth time delay only shift the eigenvalues to more stable ones in terms of negative real parts. Delay times are set to $\tau_1/T = 7$ (solid line), $\tau_1/T = 7$, $\tau_2/T = 5$ (dash-dotted line, feeding back all main frequencies), $\tau_1/T = 7$, $\tau_2/T = 5$, $\tau_3/T = 3.1$ (dotted line) and $\tau_1/T = 7$, $\tau_2/T = 5$, $\tau_3/T = 3.1$, $\tau_4/T = 1.32$ (dashed line). Phases presented in Fig. 10.5(f) are more or less constant for $f \in [0.1, 0.35]$ in contrast to the phase jumps if only one delay time is switched on.

Until now all gain factors k_{ma}, k_{mb} have been chosen mutually equal (symmetric) to guarantee a vanishing control signal for each feedback term consisting of the difference of a single delayed signal and its undelayed counterpart. However, choosing the gains k_{ma}, k_{mb} individually it is possible to adjust the characteristics of the transfer function Eq. (10.16) to the investigated control problem in a more flexible way [13]. For example, Fig. 10.5 (g) and (h) show the filter characteristics with asymmetric gains $k_{1a} = 1.3$, $k_{1b} = 0.7$, $k_{2a} = 0.4$,
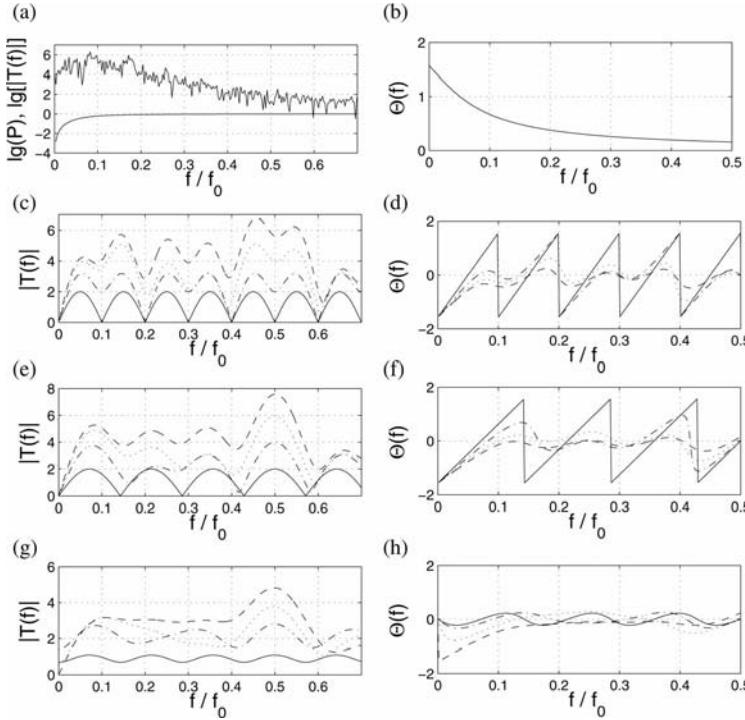
Fig. 10.5 (a) Fourier spectrum of the unperturbed Colpitts oscillator (10.11) and transfer function of a high-pass filter with cut-off frequency $f_0 = \omega_0/2\pi = 0.08$. (b) Corresponding phase of the high-pass filter. (c),(e),(g) Absolute value of the transfer function (10.16) for different choices of delay times and gain factors: (c) Symmetric gains $k_{ma} = k_{mb} = 1$, one delay time $\tau_1/T = 10$ (solid line), two delay times $\tau_1/T = 10$, $\tau_2/T = 5$ (dash-dotted line), three delay times $\tau_1/T = 10$, $\tau_2/T = 5$, $\tau_3/T = 3.1$ (dotted line), and four delay times $\tau_1/T = 10$, $\tau_2/T = 5$, $\tau_3/T = 3.1$ and $\tau_4/T = 1.32$ (dashed line). The fixed point is stabilized if three or four delay times are used, but control with one or two delays fails because the notches $[|T(f)| \approx 0]$ are

located in the range of main frequencies of the free running system (compare spectrum in Fig. 10.5 (a)). (e) For control parameters $k_{ma} = k_{mb} = 1$ and $\tau_1/T = 7$ (solid line), $\tau_1/T = 7$, $\tau_2/T = 5$ (dash-dotted line), $\tau_1/T = 7$, $\tau_2/T = 5$, $\tau_3/T = 3.1$ (dotted line), $\tau_1/T = 7$, $\tau_2/T = 5$, $\tau_3/T = 3.1$ and $\tau_4/T = 1.32$ (dashed line) no notches are located in the range of the main frequencies and fixed point stabilization is possible already with two or more delay loops. (g) Same delay times as in (e) but different asymmetric gains: $k_{1a} = 1.3$, $k_{1b} = 0.7$, $k_{2a} = 0.4$, $k_{2b} = 1$, $k_{3a} = 0.8$, $k_{3b} = 0.5$, $k_{4a} = 0.4$, $k_{4b} = 0.7$. (d),(f),(h) Corresponding phases marked the same way as in (c),(e),(g), respectively.

$k_{2b} = 1.0$, $k_{3a} = 0.8$, $k_{3b} = 0.5$, $k_{4a} = 0.4$, $k_{4b} = 0.7$ for the same delay times as in Fig. 10.5 (e) and (f) providing a noninvasive control signal if all delay times are switched on.

10.3
From Multiple Delay Feedback Control to Notch Filter Feedback

The investigation of transfer functions of MDFC showed that successful feedback is related to a smart placement of notches in the frequency domain to suppress specific frequencies. Therefore, as an alternative one can approximate the MDFC transfer function locally by linear notch filters. This leads to *notch filter feedback* (NFF) [16] showing similar behavior within the relevant part of the Fourier spectrum as MDFC does. For illustration we consider again the Colpitts oscillator exhibiting chaotic motion (Fig. 10.6 (b)) for the free running system ($u(t) = 0$) and the TDAS control signal

$$u(t) = k[U_{C_1}(t) - U_{C_1}(t - \tau)] \tag{10.17}$$
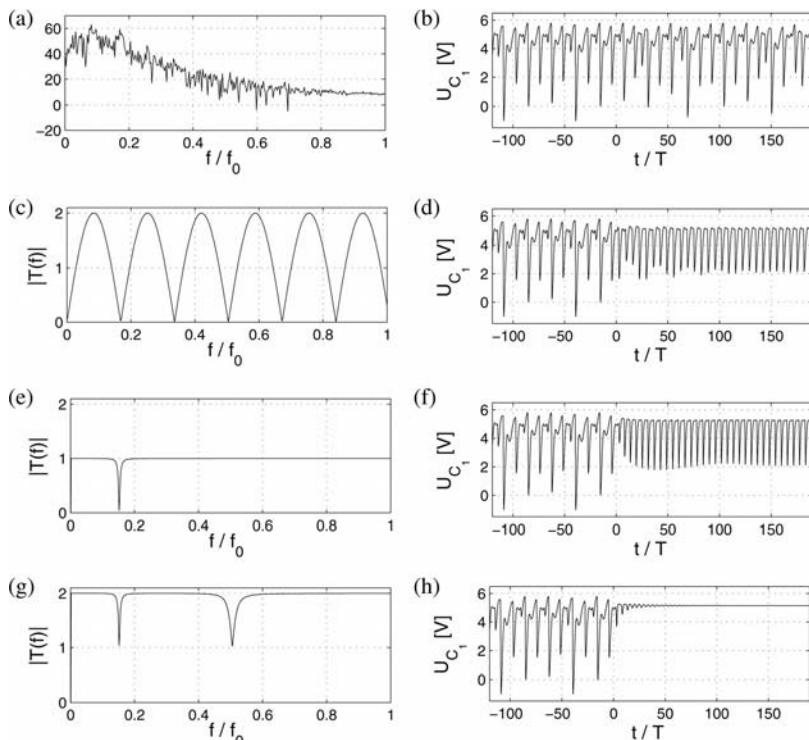
Fig. 10.6 Colpitts oscillator Eq. (10.11) controlled by different feedback schemes. (a),(b) Spectrum and time series of the free running system, respectively. Absolute value of the transfer function $|T(f)|$ and time series of the controlled system (feedback switched on at $t = 0$) for: (c), (d) TDAS control (10.17), (e), (f) single notch filter control (10.19), (g), (h) two notch filters control (10.20).

coupling to the first component of Eq. (10.11). Adjusting the control parameters to $k = -0.72$ and $\tau = 6.66$ stabilizes the period-one orbit visible in Fig. 10.6 (d). The placement of notches corresponds in Fig. 10.6 (c) to the fundamental frequency of the considered UPO and its harmonics. Thus, all troubling frequencies in the broad band spectrum (Fig. 10.6 (a)) not belonging to the UPO are suppressed. Nearly the same result can be obtained, if a suitable notch filter replaces Eq. (10.17) neglecting the higher harmonic notches of the TDAS scheme. Suitable notch filters can, for example, be implemented by the well-known Wien filter

$$
\begin{aligned}
\dot{V}_{C_1} &= \frac{1}{RC}\left(V_{\text{in}} + \frac{2Q-1}{Q} V_{C_2} - V_{C_1} \right) \\
\dot{V}_{C_2} &= \frac{1}{RC}\left(V_{\text{in}} + \frac{Q-1}{Q} V_{C_2} - V_{C_1} \right) \\
V_{\text{out}} &= \frac{1}{Q} V_{C_2}
\end{aligned}
\tag{10.18}
$$

with filter resonance frequency $f = (2\pi RC)^{-1}$ and filter quality Q responsible for the filter steepness. The feedback signal is given by

$$
u(t) = k[V_{\text{in}}(t) - V_{\text{out}}(t)].
\tag{10.19}
$$

V_{C_1} and V_{C_2} correspond to capacitor voltages in the electronic realization of the Wien filter, V_{in} and V_{out} denote the filter's input and output signal, respectively. In this special case U_{C_1} of Eq. (10.11) is used as input signal leading to the result shown in Fig. 10.6 (f). The feedback is based on a single notch filter Eq. (10.18) using the parameters $R = 10460\,\Omega$, $C = 0.1\,\text{mF}$, $Q = 16.9$, $k = 0.75$. As can be seen in Fig. 10.6 (e) the corresponding transfer function has no notch for $f = 0$ and thus describes an invasive control scheme. One may, however, use a high-pass filter for the input signals or subtract a fixed value to eliminate these offsets and render the control scheme noninvasive.

Similar to MDFC, stabilization of fixed points by NFF requires two or more notch filters connected in parallel. For the control signal

$$
u(t) = k_1\left[V_{\text{in}}^{(1)} - V_{\text{out}}^{(1)} \right] + k_2\left[V_{\text{in}}^{(2)} - V_{\text{out}}^{(2)} \right]
\tag{10.20}
$$

all spectral components are eliminated and the steady state is reached after transients if resonance frequencies $f_{1,2}$ and qualities $Q_{1,2}$ are suitably chosen. Using the filter transfer function of Fig. 10.6 (g) leads to fixed point stabilization presented in Fig. 10.6 (h). Parameters are $k_1 = k_2 = 0.75$, $Q_1 = 16.9$, $Q_2 = 14.9$, $C_1 = C_2 = 0.1\,\text{mF}$, and $R_1 = 10460\,\Omega$, $R_2 = 3150\,\Omega$.

To compare NFF based on two notch filters with MDFC a linear stability analysis is performed in the vicinity of the fixed point of the Colpitts oscillator Eq. (10.11). In contrast to MDFC the NFF stability analysis yields a characteristic
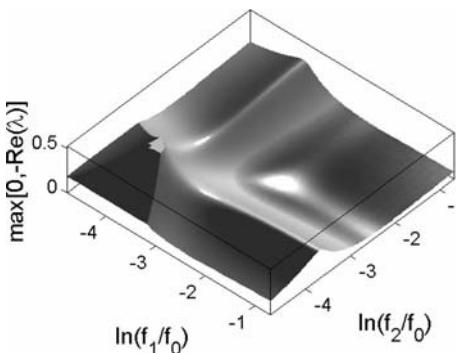
Fig. 10.7 Fixed point stabilization for the Colpitts oscillator Eq. (10.11) using NFF with two notch filters. Stability function $\max[0, -\mathrm{Re}(\lambda)]$ versus resonance frequencies f_1 and f_2 ($k_1 = k_2 = 1.5, Q_1 = Q_2 = 0.8$).

The system is stabilized, if the eigenvalue λ with the largest real part $\mathrm{Re}(\lambda)$ possesses negative sign. Thus, the larger the peaks the more stable is the feedback.

polynomial with a finite number of roots whose real part has to be analyzed. Figure 10.7 shows the resulting stability function $\max[0, -\mathrm{Re}(\lambda)]$ versus filter resonance frequencies $f_{1,2} = (2\pi R_{1,2} C)^{-1}$ if the ac coupled component of U_{C_1} is used as input signal for the notch filters. The fixed point is stabilized, if all eigenvalues possess negative real parts. Thus, the larger the stability values in Fig. 10.7 the more stable is the applied feedback. The maximum stability is ≈ -0.4 which is in the range of MDFC and more stable than (E)TDAS as well as its limit case of a single pole high-pass filter. Highest performance is achieved, if the filter resonance frequencies do not coincide with the oscillator's main frequencies $\approx 0.15\, f_0$ and $\approx 0.09\, f_0$ (minimum visible as a white spot in Fig. 10.7) and are chosen mutually different from each other. This is clear since frequencies lying in a notch are not fed back and steady state stabilization is not possible. The main advantage of NFF is its easy implementation in analog hardware to control, for example, very fast dynamical systems.

10.4
Controllability Criteria

Similar to some limitations of delay control of UPOs [17, 18] there also exist restrictions for fixed point stabilization using (E)TDAS. Chang et al. [9] showed that a single pole high-pass filter cannot stabilize steady states with an odd number of real positive eigenvalues. In the following we shall demonstrate that for fixed point stabilization the odd number problem can be overcome by using MDFC with asymmetrical gains or using NFF without ac-coupling.

10.4.1
Multiple Delay Feedback Control

For simplicity we consider an MDFC scheme where a variable of the state vector is observed and where the control signal is added to the differential equation describing the dynamics of this variable.[3)] The stability of the controlled system is determined by the characteristic function

$$S(\lambda) = \det[\Delta(\lambda)] = \det[\lambda I - D\mathbf{f}(\mathbf{x}_0) - U(\mathbf{x}_0, \lambda)] \tag{10.21}$$

$$= \lambda^n + \sum_{j=0}^{n-1} c_j \lambda^j + \bar{u}(\lambda) \sum_{j=0}^{n-1} d_j \lambda^j, \tag{10.22}$$

where $\bar{u}(\lambda)$ denotes the Laplace transform of the control signal. The characteristic function $S(\lambda)$ is composed of a purely polynomial part with parameters c_j (resulting from the free running system) and a polynomial-transcendental part with parameters d_j (resulting from the feedback). For finite control gains and coefficients c_j and d_j the limit $\lim_{\lambda \to \infty} S(\lambda) = \infty$ holds. Stabilization is possible if the control parameters can be chosen in a way such that the function $S(\lambda)$ possesses no roots in the right half of the complex plane (i.e., no roots with positive real parts).

To show that this goal cannot always be achieved let us first consider (E)TDAS control (10.4) with

$$\bar{u}(\lambda) = k \frac{e^{-\lambda\tau} - 1}{1 - \mathrm{Re}^{-\lambda\tau}}. \tag{10.23}$$

Here $\bar{u}(\lambda)$ vanishes at the origin $\lambda = 0$ and the characteristic function at $\lambda = 0$

$$S(0) = \det[-D\mathbf{f}(\mathbf{x}_0)] = (-1)^n \det[D\mathbf{f}(\mathbf{x}_0)] = \prod_{j=1}^{n}(-e_j) = c_0 \tag{10.24}$$

depends only on the Jacobian matrix $D\mathbf{f}(\mathbf{x}_0)$ of the n-dimensional free running system and its eigenvalues e_j, and *not* on the control parameters. For an odd number of real positive eigenvalues an odd number of negative factors occurs in the product in Eq. (10.24) and $S(0) < 0$. Since $S(\lambda)$ restricted to the real axis is a continuous function the boundary conditions $S(0) < 0$ and $\lim_{\lambda \to \infty} S(\lambda) = \infty$ imply the existence of at least one unstable eigenvalue in the right half plane – independently of the feedback gains. Therefore, using (E)TDAS it is not possible to remove this instability.

If we apply MDFC instead of (E)TDAS the Laplace transform Eq. (10.23) is replaced by

$$\bar{u}(\lambda) = \sum_{m=1}^{M} k_{ma} e^{-\lambda\tau_m} - k_{mb} \tag{10.25}$$

---

3) The same arguments also hold for more general cases not presented here for better readability.

which (in contrast to Eq. (10.23)) does not vanish for $\lambda = 0$. Thus the characteristic function at the origin

$$S(0) = c_0 + \left(\sum_{m=1}^{M} k_{ma} - k_{mb} \right) d_0 \tag{10.26}$$

depends on the (differences of the) gain factors $k_{ma} - k_{mb}$. This dependence can be exploited to shift $S(0)$ to positive values. Since the limit $\lim_{\lambda \to \infty} S(\lambda) = \infty$ is still valid the characteristic function possesses now an even number of roots on the positive real axis whose number depends on the control scheme and the underlying dynamical system. In contrast to the (E)TDAS case discussed above there exists at least no fundamental obstacle to stabilize the fixed point with properly chosen control parameters. Therefore, in general, two delay terms are required to control a fixed point with an odd number of positive eigenvalues: one delay term (with asymmetric gains) to construct an extended system with $S(0) > 0$ and a second delay term to stabilize this extended system using (E)TDAS. Using appropriate values for the gain constant k_0 in Eq. (10.7) (that does not enter the characteristic function (10.26)) this control scheme can be made noninvasive for any given (unstable) fixed point.

10.4.2
Notch Filter Feedback and High-Pass Filter

The same problem to stabilize fixed points with an odd number of positive eigenvalues occurs for a single pole high-pass filter and for NFF with ac coupled input. In the case of a single pole high-pass filter [9] the value of the characteristic function at zero is given by

$$S(0) = \omega_0 \det \left[-D\mathbf{f}(\mathbf{x}_0) \right] = \omega_0 \prod_{j=1}^{n} (-e_j), \tag{10.27}$$

where e_j are the eigenvalues of the Jacobian matrix $D\mathbf{f}(\mathbf{x}_0)$ at the fixed point $\mathbf{x}_0$ and $\omega_0 > 0$ is the cut-off frequency (see (10.5)). Similar to the (E)TDAS case $S(0)$ is negative if an odd number of positive eigenvalues exists and this implies the existence of a root of $S(\lambda)$ on the positive real axis that cannot be removed by any choice of the control parameters ω_0 and k.

For NFF the characteristic function reads

$$S(\lambda) = \det \left[\lambda I - A \right] = \lambda^N + \sum_{j=0}^{N-1} a_j \lambda^j, \tag{10.28}$$

where A denotes the Jacobian matrix of the full N-dimensional system consisting of the dynamical system and the feedback controller (e.g., a Wien filter implementation of NFF). For $\lambda = 0$ we obtain

$$S(0) = \omega_0^M \prod_{m=1}^{M} \omega_m^2 \prod_{j=1}^{n} (-e_j) \tag{10.29}$$

if M notch filters are applied with resonance frequencies $\omega_m = 2\pi f_m > 0$. To guarantee a noninvasive feedback input signals are ac coupled with cut-off frequency $\omega_0 > 0$. Again $S(0) < 0$ if an odd number of positive eigenvalues exists resulting in at least one root within the interval $[0, \infty[$ for any choice of the control parameters. Without ac coupled input signals the proof given above does not hold any longer and it is possible to stabilize unstable fixed points with odd numbers of positive eigenvalues using NFF. In this case one may subtract a suitable constant from the control signal to obtain a noninvasive control scheme for a given fixed point.

10.5
Laser Stabilization Using MDFC and NFF

A challenging task for all chaos control methods is the stabilization of steady states of intracavity frequency doubled solid state lasers generating blue and green light. With this type of lasers chaotic intensity fluctuations occur if the pump rate exceeds some critical threshold [19]. During the past 20 years, various attempts have been made to solve or at least to reduce these fluctuations using optical solutions or feedback control applied to an appropriate system parameter (e.g., the laser's pump current). However, most control methods failed for medium or higher pump rates, in particular for so-called type II chaos with active modes in two orthogonally polarized directions [20, 21].

Our own experiments confirmed the observation that it is nearly impossible to stabilize a compact frequency doubled laser (type II chaos, main frequencies between 1 and 1.5 MHz, system latency $\approx 0.5\,\mu s$) using conventional P-controllers, TDAS, or a single pole highpass filter in the feedback loop. On the other hand, both MDFC [12, 22] and NFF [16] have been applied successfully in experiments and simulations to stabilize the steady state of this chaotic laser exhibiting high frequency intensity fluctuations.

The experimental setup is shown in Fig. 10.8 (a), where the laser's pump current w_0 provided by a current source is influenced by the feedback signal via a bias-T. The laser emits infrared radiation of wavelength 1064 nm as well as frequency doubled green laser light with a wavelength of 532 nm. Both light emissions are separated from each other by a frequency selective beam splitter. Input signals for MDFC and NFF are optionally the two ac coupled orthogonally polarized infrared intensities $\tilde{I}_x$ and $\tilde{I}_y$ or the ac component of the green intensity $\tilde{G}$. Using the infrared signals the pump current modulation for MDFC may be written as

$$\Delta w(t) = a_x \tilde{I}_x(t - \tau_x) - b_x \tilde{I}_x(t) + a_y \tilde{I}_y(t - \tau_y) - b_y \tilde{I}_y(t) \tag{10.30}$$

(a)

(b)
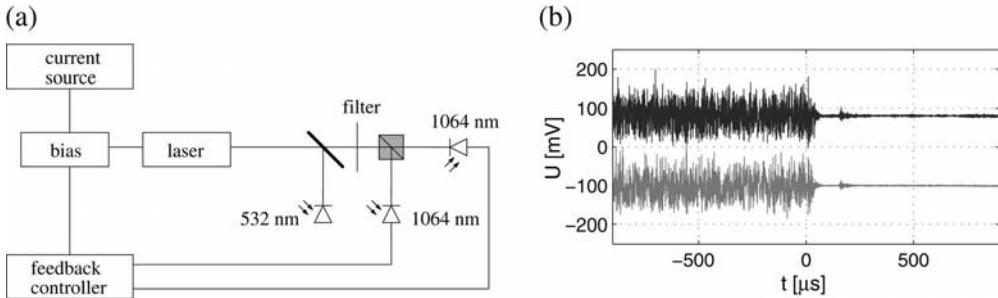
Fig. 10.8 Suppression of chaotic intensity fluctuations of a frequency doubled Nd:YAG laser using MDFC as defined in Eq. (10.30). (a) Experimental setup. (b) Time series showing the orthogonally polarized ac coupled infrared signals $\tilde{I}_x$ (upper trace) and $\tilde{I}_y$ (lower trace). After activation of feedback control at $t = 0$ the chaotic fluctuations are suppressed. Similar results have been obtained with NFF control [16].

and with the green laser light intensity

$$\Delta w(t) = a_x \tilde{G}(t - \tau_x) - b_x \tilde{G}(t) + a_y \tilde{G}(t - \tau_y) - b_y \tilde{G}(t). \qquad (10.31)$$

In both cases, two delay times, τ_x and τ_y, are typically in the range of $\tau_x \approx 0.6\,\mu s$ and $\tau_y \approx 2.8\,\mu s$. All control parameters $a_x, b_x, a_y, b_y, \tau_x, \tau_y$ are chosen experimentally to achieve fixed point stabilization. Figure 10.8 (b) shows a successful laser stabilization using MDFC. Before the control signal is switched on at $t = 0\,s$ intensity fluctuations are visible which are then damped out by the feedback until the noise level is reached. In this laser experiment three to four lasing modes are active. This case was also simulated [22] with an extended (multimode) laser model describing an inhomogeneous end-pumped YAG crystal. MDFC provides stability for the whole range of three mode operation including additional slow sinusoidal modulation of the pump current without any uprising chaotic dynamics (occurring without control).

The fact that asymmetrical gains turned out to be more efficient for stabilization than symmetrical ones [22] was also confirmed experimentally [12] where asymmetric MDFC was superior to symmetric MDFC and TDAS.

For NFF using two notch filters according to Eqs. (10.18) and (10.19) the pump current modulation is given by the difference

$$\Delta w(t) = k_1 \left[V_{\text{in}}^{(1)} - V_{\text{out}}^{(1)} \right] + k_2 \left[V_{\text{in}}^{(2)} - V_{\text{out}}^{(2)} \right] \qquad (10.32)$$

of the filtered output V_{out} and the filter input signals $V_{\text{in}}^{(1)}$ and $V_{\text{in}}^{(2)}$. Here the two ac coupled orthogonally polarized infrared intensities $\tilde{I}_x$ and $\tilde{I}_y$ or the ac component of the green intensity $\tilde{G}$ can be used as input to implement a non-invasive stabilization of the laser [16]. The experimental adjustment of the filter resonance frequencies is relatively easy for a suitably chosen filter quality Q. Simulations at a fixed pump rate $w_0 = 1.247$ [16] reveal that stability regions are

most enlarged if the quality Q is not chosen too high and feedback gains k_1 and k_2 are chosen different (asymmetric).

10.6
Controlling Spatiotemporal Chaos

Feedback control can also be applied to extended spatiotemporal (chaotic) systems [23]. In particular, (E)TDAS has been used to control a large number of spatially extended systems to achieve various goal dynamics [24–32]. Furthermore, efficiency of the delayed feedback methods can significantly be improved by spatially filtering the applied control signal [33].

10.6.1
The Ginzburg-Landau Equation

As prototypical example of a spatiotemporal chaotic system we shall employ the two-dimensional complex *Ginzburg-Landau equation* (GLE)

$$\partial_t f = (1 + ia)\nabla^2 f + f - (1 + ib)f|f|^2 + u \qquad (10.33)$$

with periodic boundary conditions and an external control signal $u(\mathbf{x}, t)$ that will be used to stabilize and manipulate the occurring spatiotemporal chaos. ∂_t and ∇ denote the temporal and the spatial derivatives, respectively. For numerical integration of Eq. (10.33) a fourth order Runge-Kutta scheme in time is combined with a spectral method in space based on a spatial grid of 90×90 elements. Depending on the parameter values a and b the complex solution $f = f(\mathbf{x}, t)$ of the free running GLE (10.33) exhibits different types of spatiotemporal chaos.

The GLE (10.33) possesses an unstable steady state solution $f(\mathbf{x}, t) = 0$ which can be stabilized by means of a P-controller or (delayed) feedback control. Furthermore, traveling plane waves

$$f(\mathbf{x}, t) = f_0 e^{i(\mathbf{k_0} \cdot \mathbf{x} - \omega_0 t)} \qquad (10.34)$$

with wave vector $\mathbf{k_0}$, frequency ω_0 and amplitude f_0 comprise unstable solutions of the GLE (see stability analysis in [36]). Substituting (10.34) into the GLE (10.33) one obtains the relations $\omega_0 = k_0^2(a - b) + b$ and $f_0 = \sqrt{1 - k_0^2}$ where $k_0^2 = \mathbf{k_0} \cdot \mathbf{k_0} \leq 1$. In the one-dimensional case this kind of UPOs embedded in the chaotic attractor of the system can be stabilized by means of TDAS [34, 35]. For higher dimensional systems, however, the torsion [17, 18] required for (E)TDAS to work is not guaranteed any more and (E)TDAS fails if $ab < -1$ [36].

We shall now show that this limit can be overcome by using asymmetric delayed feedback and the stability range can be extended by using several independent delay times.

10.6.2
Controlling Traveling Plane Waves

To stabilize unstable plane waves (10.34) we use a control signal

$$u(\mathbf{x}, t) = \sum_{m=1}^{M} k_{ma} f(\mathbf{x}, t - \tau_m) - k_{mb} f(\mathbf{x}, t) \tag{10.35}$$

and assume that the controlled plane wave is given as

$$f(\mathbf{x}, t) = f_c e^{i(\mathbf{k_c} \cdot \mathbf{x} - \omega_0 t)}. \tag{10.36}$$

If this plane wave is substituted in (10.35) one obtains

$$u(\mathbf{x}, t) = \left(\sum_{m=1}^{M} k_{ma} e^{-i\omega_0 \tau_m} - k_{mb} \right) f(\mathbf{x}, t) = T(\omega_0) f(\mathbf{x}, t) \tag{10.37}$$

with transfer function $T(\omega_0)$. Inserting the plane wave solution (10.36) and the corresponding control term (10.37) into the GLE (10.33) results in

$$1 - k_c^2 - f_c^2 + \text{Re}[T(\omega_0)] = 0$$
$$\omega_0 - ak_c^2 - bf_c^2 + \text{Im}[T(\omega_0)] = 0 \tag{10.38}$$

where $k_c^2 = \mathbf{k_c} \cdot \mathbf{k_c}$. $\text{Im}[T(\omega_0)]$ and $\text{Re}[T(\omega_0)]$ denote the imaginary and real part of the feedback's transfer function $T(\omega_0)$, respectively. Combining both constraints of Eq. (10.38) we can eliminate the amplitude f_c and obtain the dispersion relation

$$k_c^2 = k_0^2 + \Delta k^2 \tag{10.39}$$

where

$$\Delta k^2 = \frac{b\text{Re}[T(\omega_0)] - \text{Im}[T(\omega_0)]}{b - a} \tag{10.40}$$

describes the wavenumber shift due to the feedback control. Since $k_0^2 \leq 1$ the relation $k_c^2 \geq 0$ is fulfilled if $\Delta k^2 \geq -1$. If the condition

$$b\text{Re}[T(\omega_0)] = \text{Im}[T(\omega_0)] \tag{10.41}$$

holds Δk^2 vanishes and control results in a traveling plane wave with same wavenumber $k_c = k_0$ as the free running system but different amplitude $f_c = \sqrt{f_0^2 + \text{Re}[T(\omega_0)]}$.

The magnitude of the wavenumber shift depends on the shape of the transfer function $T(\omega)$ that can be adjusted with the parameters of the control loop. To
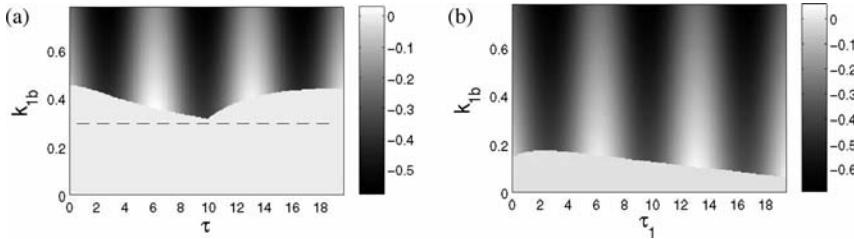
Fig. 10.9 Stabilization of plane wave solutions (10.34) of the GLE (10.33) with $a = 1.1$ and $b = -1$ using the delayed feedback signal (10.35). In the gray-shaded regions of the control parameter space τ_1–k_{1b} stabilization is successful and results in a gray-scaled wavenumber shift Δk^2 (10.40).

(a) Single delay feedback with $k_{1a} = 0.3$. The dashed line denotes the particular case of symmetric feedback ($k_{1a} = k_{1b}$) that fails to stabilize the plane waves. (b) MDFC with two delay times and fixed control parameters $k_{1a} = 0.3, k_{2a} = 0.1, k_{2b} = 0.3, \tau_2 = 7.2$.

illustrate this dependence we show in Fig. 10.9 (a) and (b) the value of Δk^2 (gray scaled) in the control parameter plane τ_1–k_{1b} for MDFC with one and two delay times, respectively. Below some critical values of the gain k_{1b} control fails and the plane wave remains unstable (light gray shading in Fig. 10.9). Control with $\Delta k = 0$ occurs for specific values of τ_1 and k_{1b}. Since the parameter values of the GLE are in this case $a = 1.1$ and $b = -1$ the TDAS controllability criterion $ab > -1$ derived in [36] is *not* fulfilled. Therefore, symmetric delayed feedback control with $k_{1a} = k_{1b}$ fails as can also be seen in Fig. 10.9 (a), where the dashed line at $k_{1b} = 0.3 = k_{1a}$ lies in the unstable region. In contrast, asymmetric delayed feedback enables stabilization if the gain k_{1b} is sufficiently high, including parameter combinations where Δk^2 vanishes (see Fig. 10.9 (a)).

Similar to the results obtained with the Colpitts oscillator and several other dynamical systems application of an additional feedback loop with a different delay time $\tau_2 = 7.2$ results in increasing stability, here visible as a reduced size of the unstable region shown in Fig. 10.9 (b).

10.6.3
Local Feedback Control

The kind of homogeneous feedback control of the GLE considered so far is interesting from a theoretical point of view because it allows some analytical treatment. Practically, however, it is very difficult to implement a delayed feedback where signals are homogeneously measured and applied at all points in space. In contrast to the idealized case described by Eqs. (10.33) and (10.35) any experimental sensor of finite size will measure the activity of the process of interest in terms of spatial averages in some sensor region. Furthermore, control signals may be applied at some specific locations, only. Therefore, we shall introduce now *control cells* describing small spatial areas where spatially averaged observations are measured and/or where the control signal is applied [37].

For many experiments or practical applications it is desirable to use only a small number of control cells. We will present in the following different examples of manipulated Ginzburg-Landau dynamics where only very few control cells are employed.

In the first example, turbulent dynamics (Fig. 10.10 (a)) occurring with Eq. (10.33) for $a = 1.1$ and $b = -1$ is locally turned into traveling waves. Here MDFC as illustrated in Fig. 10.10 (g) is applied to selected control cells shown as white rectangles in Fig. 10.10. Figure 10.10 (b) shows the control transient and Fig. 10.10 (c) the resulting plane waves between the two rows of controllers. Delay times and gain factors equal $\tau_1 = 25$, $\tau_2 = 62$, $\tau_3 = 94$ and $k_{1a} = 0.33$, $k_{1b} = 0.67$, $k_{2a} = 0.365$, $k_{2b} = 0.68$, $k_{3a} = 0.405$, $k_{3b} = 0$, respectively. Note that since $ab < -1$ control using homogeneous (E)TDAS would fail in this case [36].
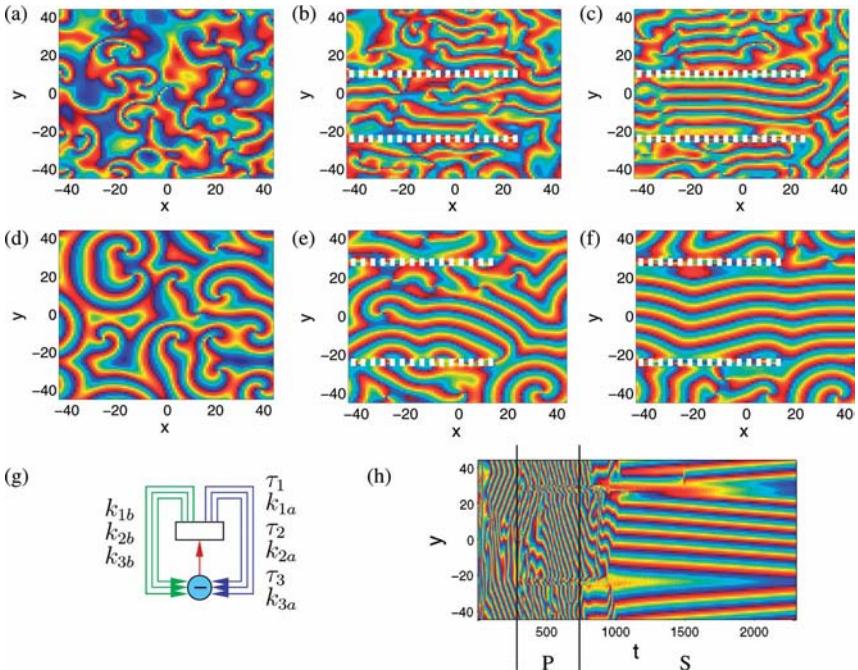
Fig. 10.10 Color-coded phase of the complex solution of the two-dimensional Ginzburg-Landau equation (10.33) for ($a = 1.1$, $b = -1$) (a–c) and ($a = -1.45, b = 0.34$) (d–h). Without feedback turbulent dynamics (a) or spiral waves (d) occur. With MDFC applied at some control cells (marked in white), a control transient is observed (b), (e) and the complex dynamics is converted to plane waves (c),(f) traveling with constant velocity. Here, signals from each control cell are fed back with and without delay as illustrated in (g) for a single control cell. (h) Spatiotemporal evolution of dynamics in a vertical section of Fig. 10.3 (e) located at $x = -20$. Feedback with parameter set P is activated at $t = 300$. For $t > 700$ feedback parameters are changed from set P to parameter set S resulting in slower traveling plane waves. The values of both control parameter sets P and S are given in the text.

Figure 10.10 (d)–(f) shows how chaotic spiral dynamics occurring for $a = -1.45$ and $b = 0.34$ can also be converted to plane waves using local MDFC. Here again MDFC sketched in Fig. 10.10 (g) is used with control parameters $\tau_1 = 20$, $\tau_2 = 59$, $\tau_3 = 89$, $k_{1a} = 0.13$, $k_{2a} = 0.4$, $k_{3a} = 0$, $k_{1b} = 0.43$, $k_{2b} = 0.49$, and $k_{3b} = 0$. To visualize the temporal dynamics, Fig. 10.10 (h) shows the phase values in a vertical section of the x–y plane at $x = -20$ as a function of time t. First feedback control is activated at $t = 300$ using the parameter set $P = (\tau_1 = 20, \tau_2 = 59, \tau_3 = 104$, $k_{1a} = 0.13, k_{2a} = 0.4, k_{3a} = 0, k_{1b} = 0.43, k_{2b} = 0.49, k_{3b} = 0)$. Spiral waves occurring between the two rows of control cells are converted into plane wave fronts that are accelerated until they reach their (constant) maximum speed. For $t > 700$ the feedback parameters are changed to set $S = (\tau_1 = 20, \tau_2 = 59, \tau_3 = 104$, $k_{1a} = 0.23, k_{2a} = 0.32, k_{3a} = 0.1, k_{1b} = 0.43, k_{2b} = 0.21, k_{3b} = 0)$. As can be seen in Fig. 10.10 (h) this control parameter set results in plane waves traveling with a lower velocity. In this way time scales (e.g., periods of oscillations) of local activity can be modified in a wide range. If only very few and therefore spatially widely separated control cells are used a phenomenon similar to diffraction occurs where spiral waves wriggle around the control cells without being influenced substantially. Thus the more control cells are used the more stable are the results. Simulations show that, for a small number of activated control cells their distance should not exceed the spatial correlation length. Best performance is achieved for control cells in a horizontal distance of one half of the spatial correlation length, and gains that have been adjusted experimentally.

For the previous examples we used individual MDFC at each cell, i.e., signals from a given cell were used to control the same cell (see Fig. 10.10 (g)). This is of course not the only way how feedback can be applied to a spatially extended system. In general, (delayed) signals from different control cells can be combined and the resulting signal can be applied to some other control cell. Two examples for such more sophisticated MDFC strategies are presented in Fig. 10.11. The parameters $a = -1.45$ and $b = 0.34$ of the GLE (10.33) are the same as for Figs. 10.10 (d)–(h) resulting in chaotic spiral waves if no control is applied (Fig. 10.11 (a) and (d)). The control cells are grouped in small line segments and their wiring (including three delays τ_1, τ_2 and τ_3) is given in Fig. 10.11 (g) and (h) for the top and bottom row, respectively. With the configuration in the top row a spiral wave is generated (Fig. 10.11 (b)) and trapped (Fig. 10.11 (c)) in the center. Control parameters chosen for this case are $k_{1a} = 0.22$, $k_{2a} = 0.1$, $k_{3a} = 0.35$, $k_{1b} = 0.3$, $k_{2b} = 0.5$, $k_{3b} = 0.0$ with delay times $\tau_1 = 41$, $\tau_2 = 27$, $\tau_3 = 49$. The rotation direction of the spiral wave can be manipulated by changing the feedback parameters. Furthermore, it is important to choose the spatial distance of complementary control cells within a certain range, such that spiral waves have enough space to develop. If the controlled region is chosen too small or too large several spiral waves or other turbulent structures occur.

With the geometry of control cells used in the bottom row of Fig. 10.11, two spiral waves rotating in opposite direction occur during transient (Fig. 10.11 (e)) once feedback is switched on. These two spirals, however, are unstable and only
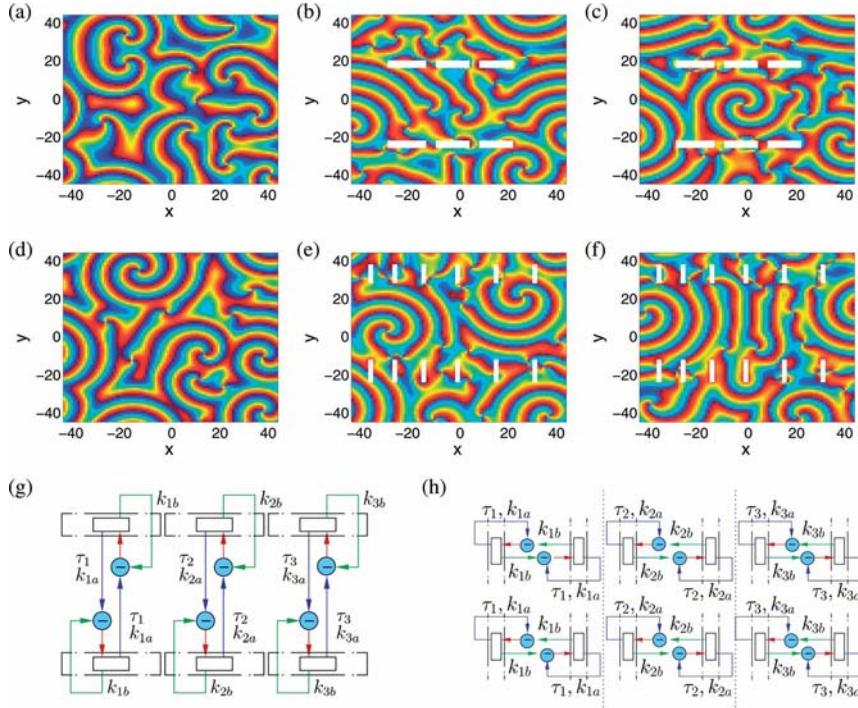
Fig. 10.11 Color-coded phase dynamics of the Ginzburg-Landau equation (10.33) for $a = -1.45$ and $b = 0.34$. First row: trapping of a rotating spiral wave using control scheme (g). Second row: generation and annihilation of plane waves using control scheme (h). (a),(d) Chaotic spiral waves without control, (b),(e) control transient, (c),(f) final, controlled dynamics. Parameters of the control schemes are given in the text.

one spiral survives due to competing dynamics. In the long time evolution bent wave fronts emitted by one spiral are straightened under the influence of the feedback control and then caught up again by the next spiral wave located at the opposite side of the controlled region (Fig. 10.11 (f)). The whole dynamics is thus some sort of wave-baseball with one spiral acting as a pitcher and the other one as the catcher. For this example the coupling scheme shown in Fig. 10.11 (h) was used with parameters $k_{1a} = 0.11$, $k_{2a} = 0.25$, $k_{3a} = 0.32$, $k_{1b} = 0.27$, $k_{2b} = 0.2$, $k_{3b} = 0.39$, $\tau_1 = 57$, $\tau_2 = 29$, and $\tau_3 = 79$.

10.7
Conclusion

Multiple delay feedback control (MDFC) is an efficient method for stabilizing (unknown) steady states and provides new options for controlling and manipulating complex spatiotemporal dynamics. The main difference compared to

Pyragas' delayed feedback (TDAS) and its extensions (ETDAS) is the use of several independent delay times and asymmetric gains factors. In this way more specific control transfer functions can be implemented and one can bypass some fundamental obstacles when trying to stabilize fixed points with an odd number of positive eigenvalues. Furthermore, MDFC control can be to some extent approximated by notch filter feedback (NFF). Both, MDFC and NFF are well suited for practical applications because they can easily be implemented in electronic hardware. As an example, we presented experimental results where a chaotic frequency doubled Nd:YAG laser was stabilized by MDFC as well as NFF. The full potential of MDFC applied to a spatiotemporal system still has to be explored. The examples given here indicate that it not only offers new means for suppressing chaotic fluctuations but more interestingly provides a large toolbox for specific and sophisticated manipulations of complex spatiotemporal structures, such as (guided) plane waves, and trapped or interacting spiral waves.

References

1 Hübler, A. and Lüscher, E., *Naturwissenschaften 76* (1989), p. 67

2 Ott, E., Grebogi, C., and Yorke, J., *Phys. Rev. Lett. 64* (1990), p. 1196

3 Kapitaniak, T., *Controlling Chaos*, Academic Press, New York, 1996

4 Schuster, H. G. (Ed.), *Handbook of Chaos Control*, Wiley-VCH, Weinheim 1999

5 Boccaletti, S., Grebogi, C., Lai, Y. C., Mancini, H., Maza, D., *Phys. Rep. 329* (2000), p. 103

6 Pyragas, K., *Phys. Lett. A 170* (1992), p. 421

7 Socolar, J. E. S., Sukow, D. W., and Gauthier, D. J., *Phys. Rev. E 50* (1994), p. 3245

8 Sukow, D. W., Bleich, M. E., Gauthier, D. J., and Socolar, J. E. S., *Chaos 7* (1997), p. 560

9 Chang, A., Bienfang, J. C., Hall, G. M., Gardner, J. R., and Gauthier, D. J., *Chaos 8* (1998), p. 782

10 Gauthier, D. J., *Opt. Lett. 23* (1998), p. 703

11 Ahlborn, A. and Parlitz, U., *AIP Conf. Proc. 742* (2004), p. 241

12 Ahlborn, A. and Parlitz, U., *Phys. Rev. Lett. 93* (2004), p. 264101

13 Ahlborn, A. and Parlitz, U., *Phys. Rev. E 72* (2005), p. 016206

14 Hale, J. K., *Appl. Math. Sci.* Vol. 3, Springer, Berlin 1977

15 de Feo, O., Maggio, G. M., and Kennedy, M. P., *Int. J. Bif. Chaos 10(5)* (2000), p. 935

16 Ahlborn, A. and Parlitz, U., *Phys. Rev. Lett. 96(3)* (2006), p. 034102

17 Nakajima, H., *Phys. Lett. A 232* (1997), p. 207

18 Just, W., Bernard, T., Ostheimer, M., Reibold, E., and Benner, H., *Phys. Rev. Lett. 78(2)* (1997), p. 203

19 Baer, T., *J. Opt. Soc. Am. B 3* (1986), p. 1175

20 Risk, W. P., Gosnell, T. R., Nurmikko, A. V., *Compact blue-green lasers*, Cambridge University Press, New York, 2003.

21 Abarbanel, H. D. I., Gills, Z., Liu, C., Roy, R., *Phys. Rev. A 53* (1996), p. 440

22 Ahlborn, A. and Parlitz, U., *Opt. Lett. 31* (2006), p. 465

23 Mikhailov, A. S. and Showalter, K., *Phys. Rep. 425* (2006), p. 79

24 Beck, O. et al., *Phys. Rev. E 66* (2002), p. 016213

25 Münkel, M., Kaiser, F., and Hess, O., *Phys. Rev. E 56* (1997), p. 3868

26 Zykov, V. S., Mikhailov, A. S., and Müller, S. C., *Phys. Rev. Lett. 78* (1997), p. 3398

27 Rappel, W. J., Fenton, F., and Karma, A., *Phys. Rev. Lett. 83* (1999), p. 456

28 Franceschini, G., Bose, S., and Schöll, E., *Phys. Rev. E 60* (1999), p. 5426

29 Tung, C. and Chan, C. K., *Phys. Rev. Lett. 89* (2002), p. 248302

30 Beta, C. and Mikhailov, A. S., *Physica D 199* (2004), p. 173

31 Zykov, V. S. and Engel, H., *Physica D 199* (2004), p. 243

32 Zykov, V. S., Bordiougov, G., Brandtstädter, H., Gerdes, I., and Engel, H., *Phys. Rev. Lett. 92* (2004), p. 018304

33 Baba, N., Amann, A., Schöll, E., Just, W., *Phys. Rev. Lett. 89* (2002), p. 074101

34 Bleich, M. E. and Socolar, J. E. S., *Phys. Rev. E 54* (1996), p. R17

35 Battogtokh, D. and Mikhailov, A., *Physica D 90* (1996), p. 84

36 Harrington, I. and Socolar, J. E. S., *Phys. Rev. E 64* (2001), p. 056206

37 Junge, L. and Parlitz, U., *Phys. Rev. E 61(4)* (2000), p. 3736

Part III
Controlling Noisy Motion

11
Control of Noise-Induced Dynamics

Natalia B. Janson, Alexander G. Balanov, and Eckehard Schöll

11.1
Introduction

In Part I of this book the fundamental principles of control of irregular oscillations are discussed. Irregularity of motion generally means its unpredictability, which, when it comes to engineering applications, one is usually keen to avoid or at least to minimize. In contrast, when it comes to biological systems, too much regularity might be regarded as a sign of a certain disfunction. For example, the normal heart rhythm of a healthy human at rest is not periodic, but is moderately irregular [1], while the perfect periodicity can be life threatening. Also, epileptic seizure or Parkinsons' disease are accompanied by the unusually regular activity of big clusters of neurons in brain [2, 3]. Hence, in some situations one needs to make the motion in the system more disordered.

Also, the need might arise to speed up or to slow down the motion, or to change the shape of oscillations or waves in the system or medium under study. Finally, one might be interested in suppressing the unwanted oscillations or waves altogether.

Most generally, we define control as the adjustment of the properties of the motion in the system in a desired way by applying some external perturbation.

Irregularity can arise from two main sources. First, the dynamics of the system where the motion occurs can be deterministically chaotic, which would generally imply sensitivity to the choice of initial conditions: the negligibly small error in the initial conditions grows exponentially with time, and this makes forecasts of the future trajectories impossible. The phase space of such systems contains a countable set of unstable periodic orbits with different periods. If for the purposes of control one needs to turn chaotic motion into a periodic one, this could be achieved by applying a small force to the system in an intelligent way, so that one of the unstable orbits becomes stable [4–6]. There are at least three general approaches that realize this idea: a continuous external perturbation [7], a time-discrete conditioned perturbation [8], and a feedback

loop in the form of the difference between the current state of the system and its state some τ time units ago [9].

The second source of irregularity in the motion occurs due to the inevitable presence of random fluctuations, or noise, in any real macroscopic system. Even if without these fluctuations the system would have behaved in an ordered predictable way, e.g., performing periodic motion, the presence of noise makes the behavior of such a system irregular and hence unpredictable. Obviously, the situation becomes even more complicated if without noise the system was already in the state of deterministic chaos: noise just adds to the complexity of its motion.

In [10] the systems were considered that without noise performed periodic or deterministically chaotic oscillations. These systems were subjected to the external noise that made their oscillations less regular. Delayed feedback in Pyragas form was shown to be capable of manipulating the regularity, or coherence, within certain ranges.

There is a separate class of motion that is fundamentally different from that described above: it occurs only due to the external fluctuations that are applied to the system. If these fluctuations are removed (even hypothetically), the motion will cease altogether. A famous example of such motion occurs in a bistable potential with a particle, to which a weak external periodic forcing is applied. Without noise, because the forcing is weak, the particle oscillates within the same well only and cannot reach the neighbouring well. However, as external noise is applied, the particle can occasionally jump between the wells. This situation is associated with the well-known *stochastic resonance* (SR) phenomenon [11, 12]. In [13, 14] the methods for the control of SR were introduced.

Finally, it might be that without noise, the system demonstrates no motion at all, and only application of noise initiates some oscillations. A famous example of such systems are excitable neurons, in which random fluctuations arise due to the conducting ion channels, synaptic noise, and noise resulting from the coupling to a large number of other neurons emitting signals [15].

In nonlinear systems, the noise-induced motion can be quite irregular at small noise, but, counterintuitively, its regularity can grow with the increase of noise strength, reaching the maximum at some moderate noise. After that maximum, the further increase of noise makes the motion less regular. This is the renowned phenomenon of *coherence resonance* (CR) [16–18]. The systems that demonstrate noise-induced oscillations and CR are sometimes called *CR oscillators*. The noise-induced phenomena are prominent in many areas of science, e.g., physics, biology, chemistry, etc. [19–25].

It should be noted that the properties of noise-induced oscillations, like timescales, shape, coherence (regularity), are defined jointly by the structure of the phase space of the system, and by the statistical properties of the applied noise. The obvious ways to achieve the desired kind of motion could be to change either the system structure, or the statistical properties of noise, or both. However, in applications to real-life systems, and especially in biological ones, the detailed structure of the system under study is often unknown, and even if it

were known, one would not want to intrude in an invasive way that could change it. At the same time, noise is defined by the environment and is also not subject to manipulation. The method capable of amending the features of noise-induced behavior should be noninvasive, i.e., not interfering with the system structure, and ideally not requiring the knowledge of it. It should also be sufficiently simple for realization.

In [26] the modified method of [8] was used to control noise-induced motion in FitzHugh-Nagumo system in an excitable regime. In [27] an external periodic force was proposed for the control of noise-induced oscillations in a pendulum with a randomly vibrating suspension axis.

In this chapter we will describe a more general and universal control method: the delayed feedback control proposed by Pyragas [9] for the control of deterministic chaos, which the author considers in more detail in Chapter 3. The idea of the method is as follows: it is known that deterministically chaotic motion is due to the existence of a chaotic attractor, whose skeleton in the phase space is formed by a countable set of unstable periodic orbits with different periods. We want to make the system oscillate periodically. Assume that the only information known about the system comes in the form of its experimental realization $s(t)$, that is formally expressed as some generally nonlinear scalar function, or functional, of its dynamical variables. Assume in addition that we know the period T_0 of one of the unstable periodic orbits. Then application of a feedback force $F(t)$ constructed as

$$F(t) = K(s(t - \tau) - s(t)), \tag{11.1}$$

where K is the feedback strength, and τ is time delay being equal to the orbit period T_0, can make this orbit stable [9], provided the value of K lies within a certain range. A remarkable feature of this method is that once the control is achieved, i.e., the system starts to oscillate periodically with period T_0, the control force $F(t)$ vanishes completely, i.e., this kind of control is noninvasive. The conditions for K for successful control have been thoroughly studied in [28–32].

One might ask "What happens if we do not know the period of the orbit?". One can guess the approximate value of this period by observing realizations $s(t)$ of the system, or by examining the peaks of the Fourier power spectrum. Another merely experimental approach is to apply feedback $F(t)$ as in Eq. (11.1) with different values of τ and to monitor the values of $F(t)$: once τ achieves T_0, the system oscillates periodically with period T_0, and $F(t)$ becomes zero at all times [9]. Note that this happens only if the value of K is chosen (guessed) correctly. Also, note that if τ is not exactly T_0, but close to it, the system might still oscillate periodically, but with period slightly different from T_0, in which case the control force $F(t)$ will not be zero. The full diagram of possible regimes in the (τ, K) plane for a paradigmatic example of a chaotic system was revealed in [33].

Pyragas's control method is perhaps the most universal at the moment, since it does not require the knowledge of the evolution equations of the system un-

der study, or of the phase space structure, or even the location of the unstable periodic orbit. It has also the advantage of being noninvasive in the sense that the control force vanishes as soon as the desired periodic regime is achieved. Finally, its experimental implementation is quite simple: one only needs to record the signal $s(t)$ of the system and to feedback the force $F(t)$ as in Eq. (11.1).

The idea to apply the Pyragas method for the control of noise-induced motion [34, 35] has arisen from the observation that such motion is in some respect similar to deterministic chaos. Although no deterministic periodic orbits are involved in the formation of noise-induced trajectories in the phase space, the phase portrait itself may look like a smeared-out limit cycle. Moreover, the notion of a "stochastic limit cycle" was proposed in [36]. A stochastic limit cycle can be formally introduced if one considers an appropriate projection of the phase portrait on some manifold (plane or surface), and calculates a two-dimensional probability distribution density on this manifold. If this distribution has a shape reminiscent of a crater, at least qualitatively, one can define a closed curve through its edges (highest points), and call this a stochastic limit cycle.

One can also introduce an average period for such a limit cycle. Of course, both the shape and the period of a stochastic limit cycle will be defined only in a statistical, averaged, sense. In addition, the motion around the stochastic limit cycle can be smeared out to a smaller or larger extent, and also the instantaneous periods of oscillations can deviate from the average period more or less. This means that the noise-induced motion can have different degrees of regularity.

Hence, noise-induced motion does possess a characteristic shape and time-scale of its oscillations. The idea is to try to apply the Pyragas delayed feedback in order to adjust the average period, the regularity, and perhaps the shape of noise-induced oscillations, by analogy with the deterministically chaotic ones.

11.2
Noise-Induced Oscillations Below Andronov-Hopf Bifurcation and their Control

As an example, consider the van der Pol system which is a famous paradigm for a nonlinear oscillator, under the influence of noise and delayed feedback

$$
\begin{aligned}
\dot{x} &= y, \\
\dot{y} &= (\varepsilon - x^2)y - \omega_0^2 x + K(y(t-\tau) - y) + D\eta(t).
\end{aligned}
\tag{11.2}
$$

Here, ε is the bifurcation parameter: in the absence of noise ($D = 0$), if ε is positive, the system demonstrates self-sustained limit-cycle oscillations, and if it is negative, the attractor is a stable fixed point. At $\varepsilon = 0$, a supercritical Andronov-Hopf (AH) bifurcation occurs. $\omega_0 > 0$ defines the frequency of self-sustained oscillations that occur just after the bifurcation, i.e., at $0 < \varepsilon \ll 1$. $\eta(t)$ is Gaussian white noise with zero mean and unity variance,
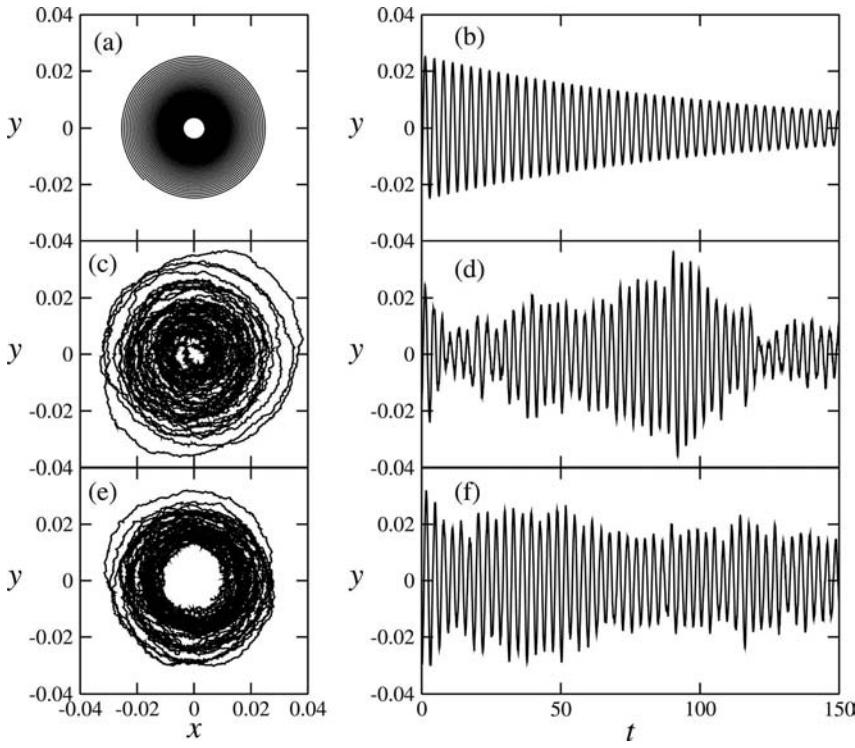
Fig. 11.1 Phase portraits and realizations of oscillations in the van der Pol system (11.2) at $\omega_0 = 1$, $\varepsilon = -0.01$. (a) and (b) No noise, no feedback; (c) and (d) noise-induced oscillations at $D = 0.003$ without feedback; (e) and (f) noise-induced oscillations at $D = 0.003$ with feedback $K = 0.2$ and $\tau = 6.28 \approx T_0^e$.

$$\langle \eta(t) \rangle = 0,$$
$$\langle \eta(t)\eta(t') \rangle = \delta(t - t'). \tag{11.3}$$

D is the strength of noise, τ is the delay, and $K > 0$ is the delayed feedback strength. The term $K(y(t - \tau) - y(t))$ represents the feedback force $F(t)$ as in Eq. (11.1), where the system observable is taken to be the variable y of Eqs. (11.2).

If ε satisfies $-2\omega_0 < \varepsilon < 0$, without noise and feedback ($D = 0$, $K = 0$), the system exhibits only damped oscillations that are illustrated by the phase portrait and realization in Fig. 11.1 (a) and (b). They effectively die out after some sufficiently long time interval. However, inclusion of noise ($D > 0$) induces oscillations that are not damped. In Fig. 11.1 (c) and (d) the phase portrait and realization are shown for Eqs. (11.2) at small noise $D = 0.003$. For this and all other illustrations we fix $\omega_0 = 1$.

11.2.1
Weak Noise and Control: Correlation Function

Consider Eqs. (11.2) at small negative ε ($\varepsilon < 0; |\varepsilon| \ll 1$), i.e., just below the Andronov-Hopf bifurcation, and at small $D \ll 1$. Since noise is weak, oscillations occur mostly in the close vicinity of the origin and rarely leave it (see Fig. 11.1 (c) and (d)). In this case, Eqs. (11.2) linearized around the fixed point can serve as a good approximation

$$\dot{x} = y,$$
$$\dot{y} = \varepsilon y - \omega_0^2 x + K(y(t-\tau) - y(t)) + D\eta(t). \tag{11.4}$$

Equations (11.4) can be rewritten in the matrix form as

$$d\mathbf{x} = (\widehat{A}\mathbf{x} + \widehat{B}\mathbf{x}(t-\tau))dt + \widehat{D}\mathbf{N}dt, \tag{11.5}$$

where

$$\mathbf{x} = \begin{pmatrix} x \\ y \end{pmatrix}, \quad \widehat{A} = \begin{pmatrix} 0 & 1 \\ -\omega_0^2 & \varepsilon - K \end{pmatrix}, \quad \widehat{B} = \begin{pmatrix} 0 & 0 \\ 0 & K \end{pmatrix},$$
$$\widehat{D} = \begin{pmatrix} 0 & 0 \\ 0 & D \end{pmatrix}, \quad \mathbf{N} = \begin{pmatrix} 0 \\ \eta \end{pmatrix}. \tag{11.6}$$

It is easy to show that $\langle x \rangle = \langle y \rangle = 0$, where $\langle \rangle$ denotes averaging over the ensemble of realizations of the random process.

Assume that at the time t_0 the state vector was $\mathbf{x}(t_0)$, and we know the values of $\mathbf{x}(t)$ in the interval $t \in [t_0 - \tau; t_0)$. Then for $t > t_0$, the solution of Eq. (11.5) is

$$\mathbf{x}(t) = \exp\left[(t-t_0)\widehat{A}\right]\mathbf{x}(t_0) + \int_{t_0}^{t} \exp\left[(t-s)\widehat{A}\right]\left(\widehat{B}\mathbf{x}(s-\tau) + \widehat{D}\mathbf{N}(s)\right)ds. \tag{11.7}$$

Multiply Eq. (11.7) by $\mathbf{x}^T(t_0)$ (superscript T means transpose), average over the ensemble of realizations, and take into account that $\langle \widehat{D}\mathbf{N}\mathbf{x}^T \rangle = \widehat{0}$ ($\widehat{0}$ is the 2×2 matrix with all zero components), to obtain the correlation matrix $\widehat{R}(t_0, t)$

$$\widehat{R}(t_0, t) = \begin{pmatrix} \Psi_{xx}(t_0, t) & \Psi_{xy}(t_0, t) \\ \Psi_{xy}(t_0, t) & \Psi_{yy}(t_0, t) \end{pmatrix} = \begin{pmatrix} \langle x(t_0)x(t) \rangle & \langle x(t_0)y(t) \rangle \\ \langle x(t_0)y(t) \rangle & \langle y(t_0)y(t) \rangle \end{pmatrix}$$

of the random process in Eqs. (11.4) [37]. Namely,

$$\widehat{R}(t_0, t) = \exp\left[(t-t_0)\widehat{A}\right]\widehat{R}(t_0, t_0) + \int_{t_0}^{t} \exp\left[(t-s)\widehat{A}\right]\widehat{B}\widehat{R}(t_0, s-\tau)ds. \tag{11.8}$$

Assigning $t_0 = t - \Theta$ we can rewrite

$$\widehat{R}(t - \Theta, t) = \exp\left[\Theta\widehat{A}\right]\widehat{R}(t - \Theta, t - \Theta)$$

$$+ \int_0^\Theta \exp\left[(\Theta - s)\widehat{A}\right]\widehat{B}\widehat{R}(t - \Theta, s + t - \Theta - \tau)\mathrm{d}s.$$

If we consider a stationary process in Eqs. (11.4), its correlation matrix will not depend on the time t, but only on the argument Θ. Hence, we can choose any convenient value of t which in our case would be $t = \Theta$. This gives us

$$\widehat{R}(\Theta) = \exp\left[\Theta\widehat{A}\right]\widehat{R}(0) + \int_0^\Theta \exp\left[(\Theta - s)\widehat{A}\right]\widehat{B}\widehat{R}(s - \tau)\mathrm{d}s.$$

By differentiating the above equation with respect to Θ, we obtain the following linear delay-differential equation for $\widehat{R}$:

$$\frac{\mathrm{d}\widehat{R}}{\mathrm{d}\Theta} = \widehat{A}\widehat{R} + \widehat{B}\widehat{R}(\Theta - \tau), \qquad \widehat{R}(-\Theta) = \widehat{R}(\Theta), \tag{11.9}$$

where the expression on the right-hand side describes the fact that the correlation and cross-correlation functions Ψ_{xx}, Ψ_{xy}, and Ψ_{yy} of the stationary processes $x(t)$ and $y(t)$ are even. A full analytical solution of this equation is available in [38, 39]. It can also be shown [37] that

$$\widehat{A}\widehat{R}(0) + \widehat{R}(0)\widehat{A}^T + \widehat{R}(\tau)\widehat{B}^T + \widehat{B}\widehat{R}^T(\tau) + \widehat{D}\widehat{D}^T = \widehat{0}. \tag{11.10}$$

The characteristic equation of (11.9) is

$$\lambda^2 = -\omega_0^2 + (\varepsilon - K)\lambda + K\lambda e^{-\lambda\tau}. \tag{11.11}$$

The eigenvalue λ is generally a complex number $\lambda = p + iq$, and separating Eq. (11.11) into real and imaginary parts gives the following equations for p and q:

$$p^2 - q^2 + \omega_0^2 - p\varepsilon + K(p - pe^{-p\tau}\cos q\tau - qe^{-p\tau}\sin q\tau) = 0, \tag{11.12}$$

$$2pq - q\varepsilon + K(q + pe^{-p\tau}\sin q\tau - qe^{-p\tau}\cos q\tau) = 0. \tag{11.13}$$

11.2.2
Weak Noise and No Control: Correlation Time and Spectrum

For the uncontrolled case $K = 0$, Eqs. (11.12) and (11.13) have two roots $\lambda_{1,2} = p_0 \pm iq_0$, where

$$p_0 = \frac{\varepsilon}{2}, \qquad q_0 = \sqrt{\omega_0^2 - \frac{\varepsilon^2}{4}} \approx \omega_0. \tag{11.14}$$

Now, let us assess quantitatively the effect of delayed feedback on the regularity of noise-induced oscillations of the observed variable $y(t)$. Regularity can be most universally characterized by the correlation function $\Psi_{yy}(\Theta)$: the faster it decays, the more disordered the process is. However, in order to assess how quickly the given function decays, it is convenient to introduce the correlation time t_{cor}, e.g., as [40, 42]

$$t_{\text{cor}} = \frac{1}{\Psi_{yy}(0)} \int_0^\infty |\Psi_{yy}(\Theta)| d\Theta. \tag{11.15}$$

Smaller t_{cor} means faster decay and a less regular process. The solution of Eq. (11.9) for $\Psi_{yy}(\Theta)$ at $K = 0$ is

$$\Psi_{yy}(\Theta) = C \exp(p_0 \Theta) \cos(q_0 \Theta), \tag{11.16}$$

where C is a constant of integration. Using the definition (11.15) and the fact that $\Psi_{yy}(0) = C$, the correlation time is

$$t_{\text{cor}} = \int_0^\infty \exp(p_0 \Theta) \big| \cos(q_0 \Theta) \big| d\Theta = \frac{|p_0| \left(\exp\dfrac{|p_0|\pi}{q_0} - 1 \right) + 2q_0 \exp\dfrac{|p_0|\pi}{2q_0}}{\left(\exp\dfrac{|p_0|\pi}{q_0} - 1 \right) (p_0^2 + q_0^2)}. \tag{11.17}$$

If $|p_0| \ll 1$, then $\exp\dfrac{|p_0|\pi}{q_0} \simeq 1 + \dfrac{\pi|p_0|}{\omega_0}$, and the expression above is approximately equal to

$$t_{\text{cor}} \simeq \frac{|p_0|\dfrac{\pi|p_0|}{q_0} + 2q_0 \left(1 + \dfrac{\pi|p_0|}{2q_0} \right)}{\dfrac{\pi|p_0|}{q_0} (p_0^2 + q_0^2)} = \frac{\dfrac{\pi p_0^2}{q_0} + 2q_0 + \pi|p_0|}{\dfrac{\pi|p_0|^3}{q_0} + \pi|p_0|q_0} \simeq \frac{2}{\pi|p_0|}. \tag{11.18}$$

The same approximate result can be obtained more easily [41] without evaluating the integral in Eq. (11.17). One can take into account that $p_0 < 0$ and $|p_0| \ll 1$, and note that the envelope $C \exp(p_0 \Theta)$ of Ψ_{yy} decreases slowly, as compared to $\cos(q_0 \Theta)$, i.e., during one full period of cosine $C \exp(p_0 \Theta)$ hardly changes. Then the integral on the left-hand side of Eq. (11.17) can be approximated by the average of cosine over its period $2\pi/q_0$, multiplied by the integral of the exponential term, i.e.,

$$t_{\text{cor}} \approx \frac{q_0}{2\pi} \int_0^{2\pi/q_0} \big| \cos(q_0 \Theta) \big| d\Theta \int_0^\infty \exp(p_0 \Theta) d\Theta = \frac{2}{\pi|p_0|}. \tag{11.19}$$

However, one should remember that if $|p_0| \ll 1$ does not hold, this approximation becomes inaccurate, and one should use the full expression in Eq. (11.17).

Now, let us consider the characteristic quantity that is associated with the timescales of the random process, namely, the Fourier power spectral density, which in the following will be referred to as *spectrum* for brevity. The spectrum of random oscillations is introduced via the Wiener-Khintchine theorem as the Fourier transform of the correlation function. The spectrum arising from Ψ_{yy} defined by Eq. (11.16) is

$$S_{yy} \sim \frac{\omega^2}{(\omega^2 - q_0^2)^2 + \omega^2 p_0^2},$$

which is a Lorentzian with the central frequency $q_0 \approx \omega_0$ (see Eq. (11.14)) and the width $|p_0| = \dfrac{|\varepsilon|}{2}$.

11.2.3
Weak Noise and Control: Correlation Time

At $K \neq 0$, Eqs. (11.12) and (11.13) have an infinite number of characteristic roots $\lambda_j = p_j \pm iq_j, j = 1, 2, \ldots,$. Hence, the solution of Eq. (11.9) is

$$\Psi_{yy}(\Theta) = \sum_{j=1}^{\infty} C_j e^{p_j \Theta} \cos q_j \Theta. \qquad (11.20)$$

Here, the constants C_j should be defined using the prescribed initial conditions which we do not discuss here (for more details see [37–39]).

The numerical solutions for p_j and eigenperiods $T_j^e = 2\pi/q_j$ are shown in Fig. 11.2 (a) and (b) for $\omega_0 = 1, \varepsilon = -0.01$ and $K = 0.2$ depending on τ. One can see that as τ grows, all p_j tend to approach the τ-axis from below. Branches with different p_j are oscillating and crossing each other, but at any τ there exists a largest $p_j = p^{\max}$, which is always negative. The period of the highest spectral peak (grey circles in Fig. 11.2 (b)) always coincides with the eigenperiod T_j^e of the least stable eigenmode, i.e., the one with the largest real part p_j. Hence, whenever two branches of p_j cross over with increasing τ, the dominant eigenperiod jumps to the next branch. This provides an explanation of the strongly nonmonotonic, discontinuous evolution of the dominant spectral peak of the noise-induced motion under delayed feedback.

We note here that the same characteristic equation (11.11), and as a consequence Eqs. (11.12) and (11.13), arise if one analyzes the stability of the fixed point of Eqs. (11.2) without the account of stochastic input ($D = 0$). It is easy to show that the delayed feedback in the form used does not change the number or the position of the fixed points existing in the uncontrolled system. Hence, the fixed point of the van der Pol equation remains the only fixed point when the feedback is applied. The analysis of its stability will lead us to Eq. (11.11).

A natural question to ask here would be whether the feedback is capable of inducing any bifurcation of the fixed point in the system that could change its
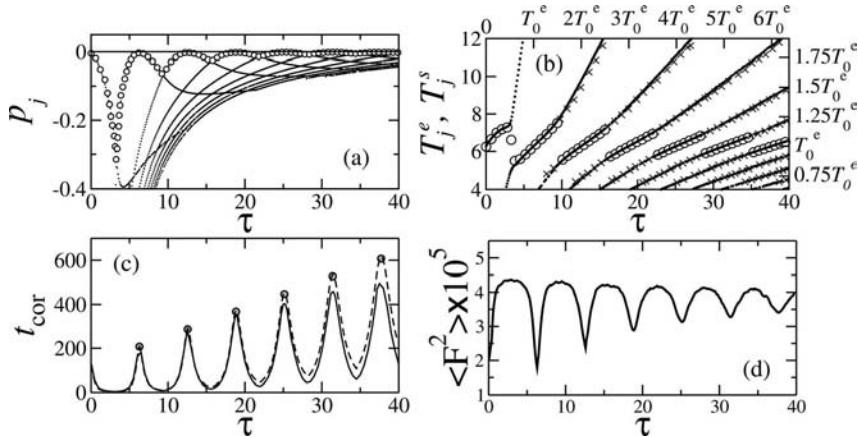
Fig. 11.2 Eigenvalues and correlation time of the van der Pol system at $\omega_0 = 1$, $\varepsilon = -0.01$, $D = 0.003$ and $K = 0.2$, as functions of τ. (a) Dots: real parts p_j of the eigenvalues λ_j found from Eqs. (11.12) to (11.13). Grey circles: p^{max}. (b) Dots: eigenperiods $T_j^e = 2\pi/q_j$, where q_j are the imaginary parts of the eigenvalues from Eqs. (11.12) to (11.13). Grey circles: periods T_j^s of the highest spectral peaks obtained by numerical simulation. Crosses: periods T_j^s of other spectral peaks. $T_0^e = 2\pi/q_0 \approx 2\pi/\omega_0$ is the eigenperiod without feedback $K = 0$. (c) Correlation time estimated numerically (solid line), analytically using Eq. (11.26) (dashed line), and the maxima $t_{cor,n}^{max}$ estimated with Eq. (11.28) (circles). (d) Variance of control force Eq. (11.29) versus τ.

stability properties and give rise to a different stable solution. For example, can the feedback induce an Andronov-Hopf bifurcation and result in the appearance of a stable periodic solution, which would turn the oscillations in Eqs. (11.2) from *noise-induced* to *noise-influenced* ones? A bifurcation would occur if at least one p_j crosses zero. Figure 11.2 (a) shows the typical behavior of p_j which does not suggest such a possibility. But this should be checked rigorously.

The condition for bifurcation is $p = 0$. We substitute this into Eq. (11.13) and find

$$\frac{K - \varepsilon}{K} = \cos q\tau. \tag{11.21}$$

Since $\varepsilon < 0$, and we consider $K > 0$, this condition is never fulfilled, and we can conclude that the delayed feedback used does not lead to bifurcation.

From Eq. (11.21) it follows that if p is close to 0, and $|\varepsilon| \ll K$, then $\cos q\tau \simeq 1$, i.e.,

$$q = \frac{2\pi n}{\tau} \tag{11.22}$$

and the respective eigenperiod T^e is

$$T^e = \frac{2\pi}{|q|} = \frac{\tau}{n}. \tag{11.23}$$

Thus, for the values of τ at which p^{max} is close to 0, the eigenperiods T^e depend linearly upon τ [34].

Finally, let us investigate at which values of τ the largest $p_j = p^{max}$ approaches zero most closely. Substitute Eq. (11.22) into Eq. (11.12) to find

$$\tau = \frac{2\pi n}{\omega_0} = nT_0^e. \tag{11.24}$$

Hence, the largest p_j is closest to zero at the values of delay τ that are multiples of the eigenperiods T_0^e of the uncontrolled system. In Fig. 11.2 (b) black dots show the eigenperiods T_j^e versus τ obtained by numerically solving Eqs. (11.12) and (11.13). Indeed, in agreement with Eq. (11.23), around $\tau = nT_0^e$, the T_j^e whose corresponding real part p_j is the largest, behaves almost piecewise linearly.

The numerically simulated phase trajectory and realization of Eq. (11.2) with control applied at $K = 0.2$ and $\tau = T_0^e$ are shown in Fig. 11.1 (e) and (f). One can see that at least during the given observation time the oscillations look more regular.

Equation (11.18) establishes that the correlation time t_{cor} in the absence of control is approximately inversely proportional to the value of the real part p of the eigenvalue λ of characteristic equations (11.12) and (11.13) at $K = 0$, if the absolute value of p is sufficiently small. The closer p is to zero, the larger the correlation time, and the more regular the system behavior is.

Looking at Fig. 11.2 (a), we observe that in the presence of control, when the largest $p_j = p^{max}$ approaches zero, it is quite well separated from all other p_j. Hence, we can speak of the dominating eigenmode, and the correlation function in Eq. (11.20) can be approximated by

$$\Psi_{\gamma\gamma}(\Theta) \approx \sigma_\gamma^2(\tau, K)e^{p^{max}\Theta}\cos(q^{max}\Theta), \tag{11.25}$$

where $\sigma_\gamma^2(\tau, K) = \Psi_{\gamma\gamma}(0)$ is the variance of γ that depends on the parameters of the feedback. By analogy with Eq. (11.18), we infer that the correlation time t_{cor} with control should be inversely proportional to the value of p^{max} corresponding to this dominant eigenmode, i.e.,

$$t_{cor} = \frac{2}{\pi p^{max}}, \tag{11.26}$$

and it achieves its maxima as p^{max} becomes closest to zero, i.e., at $\tau = nT_0^e$. In Fig. 11.2 (c) the estimate of t_{cor} according to Eq. (11.26) is shown by the dashed line, while p^{max} was taken from Fig. 11.2 (a). The "true" t_{cor} estimated from the numerical simulation of the realizations of Eqs. (11.2) is given in Fig. 11.2 (c) by

the solid line. One can see that the two curves agree quite well for small τ, but they start to diverge at τ larger than roughly three T_0^e. The approximate and the exact value of t_{cor} differ if the largest p_j is not well separated from the other p_j's.

Let us now determine t_{cor} at the optimum values $\tau = nT_0^e$. In the following we will omit the superscript max for brevity. Note that at $|p| \ll 1$, we can approximately use the Taylor expansion $\exp(-p\tau) \simeq 1 - p\tau$. Substituting this into Eq. (11.13) we obtain

$$2p - \varepsilon + K - K + Kp\tau = 0,$$

or

$$p = \frac{\varepsilon}{2 + K\tau}. \tag{11.27}$$

Then the maxima $t_{cor,n}^{max}$, $n = 0, 1, 2, \ldots$, of the correlation time t_{cor} with the delayed feedback control, taking account of Eq. (11.24), are given by [41, 43]

$$t_{cor,n}^{max} \approx \frac{2}{\pi|p|} \approx \frac{4}{\pi|\varepsilon|} \left(1 + \frac{K\tau}{2}\right)\bigg|_{\tau = nT_0^e} = \frac{4}{\pi|\varepsilon|} \left(1 + \frac{\pi Kn}{\omega_0}\right). \tag{11.28}$$

In Fig. 11.2 (c) the $t_{cor,n}^{max}$ are shown by circles. In agreement with Eq. (11.28), the maxima of the numerical t_{cor} indeed lie approximately on the straight line, at least for smaller τ.

A quantity immediately relevant when one considers control, is the force required to produce the observed change. Consider the normalized control force $\tilde{F}$, which is the control force F divided by the feedback strength K, namely

$$\tilde{F}(t) = y(t - \tau) - y(t). \tag{11.29}$$

Since $\langle y \rangle = 0$, the time average of $\tilde{F}$ is zero. Hence, the convenient quantity that would characterize the applied effort is the variance $\langle \tilde{F}^2 \rangle$, which can be expressed as [41]

$$\langle \tilde{F}^2 \rangle = 2\left(\langle y^2 \rangle - \langle y(t)y(t - \tau) \rangle\right) = 2\sigma_y^2(\tau, K) - 2\Psi_{yy}(\tau) \tag{11.30}$$
$$\approx 2\sigma_y^2(\tau, K)\left(1 - e^{p_j\tau} \cos q_j\tau\right)$$

where the approximation (11.25) for the correlation function $\Psi_{yy}(\tau)$ is used. Note that σ_y^2 is the variance, or total power, of the process, that can be calculated, e.g., through the power spectral densities (spectrum) as

$$\sigma_y^2 = \int_{-\infty}^{\infty} S(\omega)d\omega$$

For the estimates of spectrum see Section 11.2.4–11.2.6.

In Fig. 11.2 (d) the numerical estimate of $\langle \tilde{F}^2 \rangle$ is given as a function of τ for $K = 0.2$. It is interesting that the minima of $\langle \tilde{F}^2 \rangle$ correspond to the maxima of t_{cor}. That means that less force is required to control more regular behavior. However, as we expected, in contrast to the deterministic case, this force never vanishes.

11.2.4
Weak Noise and Control: Spectrum

In order to characterize the timescales of noise-induced oscillations, it is convenient to consider the spectrum of the process, which in principle can be obtained as a Fourier transform (FT) of the correlation function Ψ_{yy} given by Eq. (11.20). Since the FT is a linear operation, the full spectrum will be the sum of FTs of all components of Ψ_{yy}, i.e., the superposition of Lorentzians with different widths p_j and different central frequencies q_j (e.g., [39]) [1]. We can test this inference by comparing the spectral peak periods T_j^s obtained by numerical simulation and the eigenperiods $T_j^e = 2\pi/q_j$ obtained by solving numerically Eqs. (11.12) and (11.13). The respective graphs are given in Fig. 11.2 (b): eigenperiods T_j^e are shown by dots, while circles and crosses show the periods of the spectral peaks T_j^s, and they coincide remarkably. Also, the highest spectral peak has the period (circles) that coincides with the eigenperiod of the least stable eigenmode and changes almost piecewise linearly with τ.

However, in [41] a more direct method to obtain the spectrum of the process described by Eq. (11.4) is used. The linearized van der Pol equations (11.4) can be written as a single stochastic delay differential equation (SDDE) of the second order:

$$\ddot{x} - \varepsilon \dot{x} + \omega_0^2 x - K(\dot{x}(t-\tau) - \dot{x}(t)) = D\eta(t). \tag{11.31}$$

Consider the Fourier transform of Eq. (11.31) which can be expressed as

$$\hat{x}(\omega) = \frac{D\hat{\eta}(\omega)}{\omega_0^2 - \omega^2 + i\omega\varepsilon + i\omega K(e^{i\omega\tau} - 1)}, \tag{11.32}$$

where $\hat{x}(\omega)$ and $\hat{\eta}(\omega)$ denote the Fourier transforms of $x(t)$ and $\eta(t)$, respectively. Since $y(t) = \dot{x}(t)$, the FTs of x and y are related as

$$\hat{y}(\omega) = -i\omega\hat{x}(\omega). \tag{11.33}$$

By applying the Wiener-Khintchine theorem [40], we can derive the spectra of the processes $\eta(t)$ and $y(t)$. We use Eq. (11.3) for η [42]

$$\langle \hat{\eta}(\omega)\hat{\eta}^*(\omega') \rangle = \delta(\omega - \omega')/(2\pi). \tag{11.34}$$

---

[1] In order to obtain the spectrum this way, one has to find the coefficients C_j: this can be done, but will involve some further calculations using the approach of e.g. [38, 39].
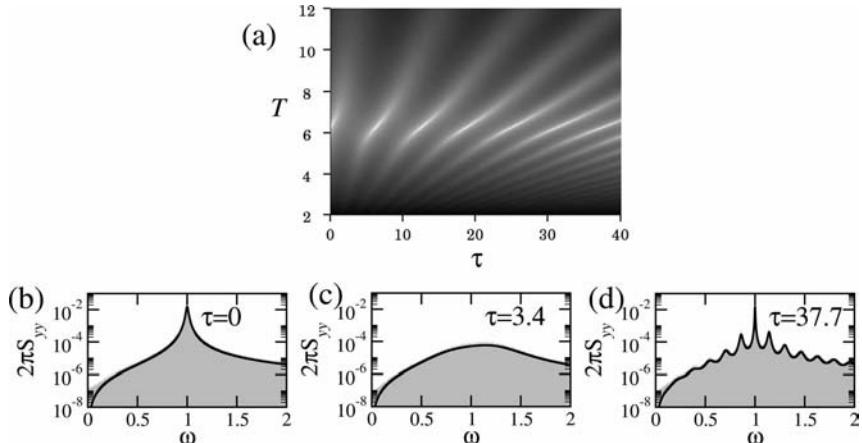
Fig. 11.3 Spectra of oscillations in the van der Pol system (11.2) at $\omega_0 = 1$, $\varepsilon = -0.01$, $D = 0.003$, $K = 0.2$, and different values of τ. (a) Density plot of the analytical spectrum from Eq. (11.36) in the (τ, T) plane with $T = 2\pi/\omega$, where ω is the spectral frequency. The spectral power is indicated by grey-shading: bright shading corresponds to large power. (b)–(d) Spectra from numerical simulation (black line) and from Eq. (11.36) (shaded). (b) $\tau = 0$ (no control), (c) $\tau = 3.4$ (minimal regularity), (d) $\tau = 37.7$ (maximal regularity).

We can also obtain the power spectral density $S(\omega)$ of y via

$$\langle \hat{y}(\omega)\hat{y}^*(\omega') \rangle = \delta(\omega - \omega') S(\omega). \tag{11.35}$$

It yields

$$S(\omega) = \frac{D^2}{2\pi} \frac{\omega^2}{(\omega^2 - \omega_0^2 + \omega K \sin(\omega\tau))^2 + \omega^2(\varepsilon - K(1 - \cos(\omega\tau)))^2}. \tag{11.36}$$

In Fig. 11.3 a series of power spectral densities at small $D = 0.003$ is shown for $K = 0.2$ and three different values of τ: (b) $\tau = 0$ (no control), (c) $\tau = 3.4$ (minimal regularity), and (d) $\tau = 37.7$ (maximal regularity) (see Fig. 11.2 (c) for reference). Shaded grey areas depict numerically obtained spectra, and black lines show the analytical approximation (11.36). One can see that the analytical spectra match the numerical ones with quite good accuracy.

11.2.5
Any Noise and No Control: Correlation Time

In the previous section we used a linear approximation (11.4) of Eqs. (11.2), which was valid under the assumption that the noise intensity D is small. However, as the noise in the system grows, the effect of the nonlinearity becomes more and more pronounced, and the simple linearization, Eq. (11.4), is no long-

er valid. To take into account the strength of noise, one can use the *mean field approximation* [43] which extends standard mean field approaches [44] by a self-consistency condition. Consider the coefficient $(\varepsilon - x^2(t))$ in the second equation (11.2). This coefficient obviously depends on the current value of x at each time t. However, it might be reasonable to consider its value on average, namely

$$\left(\varepsilon - x^2(t)\right) \approx \left(\varepsilon - \langle x^2 \rangle\right) = \varepsilon - R_{xx}(0) = \tilde{\varepsilon}. \tag{11.37}$$

For a stationary process in Eqs. (11.2), $\langle x \rangle = 0$, so $R_{xx}(0)$ is in fact the variance which also does not depend on time. Hence, $\tilde{\varepsilon}$ is a constant, and Eq. (11.37) simply leads to an effective rescaling of the bifurcation parameter of Eq. (11.4). For the uncontrolled case $K = 0$, we have a 2D Ornstein-Uhlenbeck process $\mathbf{x}(t)$

$$\mathbf{dx} = \hat{A}\mathbf{x}dt + \hat{D}\mathbf{N}dt, \quad \hat{A} = \begin{pmatrix} 0 & 1 \\ -\omega_0^2 & \tilde{\varepsilon} \end{pmatrix}, \quad \hat{D} = \begin{pmatrix} 0 & 0 \\ 0 & D \end{pmatrix}, \quad \mathbf{N} = \begin{pmatrix} 0 \\ \eta \end{pmatrix}, \tag{11.38}$$

with the effective parameter $\tilde{\varepsilon}$ (cf. with Eqs. (11.5) and (11.6)). For $\tilde{\varepsilon} < 0$, the variance matrix $\hat{R}(0)$ obeys the following equation [40]:

$$\hat{A}\hat{R}(0) + \hat{R}(0)\hat{A}^T + \hat{D}\hat{D}^T = \hat{0} \tag{11.39}$$

or

$$\begin{pmatrix} 0 & 1 \\ -\omega_0^2 & \tilde{\varepsilon} \end{pmatrix} \begin{pmatrix} R_{xx}(0) & R_{xy}(0) \\ R_{xy}(0) & R_{yy}(0) \end{pmatrix} +$$

$$\begin{pmatrix} R_{xx}(0) & R_{xy}(0) \\ R_{xy}(0) & R_{yy}(0) \end{pmatrix} \begin{pmatrix} 0 & -\omega_0^2 \\ 1 & \tilde{\varepsilon} \end{pmatrix} = \begin{pmatrix} 0 & 0 \\ 0 & D \end{pmatrix} \begin{pmatrix} 0 & 0 \\ 0 & D \end{pmatrix}. \tag{11.40}$$

This matrix equation can be rewritten as a set of linear algebraic equations

$$2R_{xy}(0) = 0,$$
$$R_{yy}(0) - \omega_0^2 R_{xx}(0) + \tilde{\varepsilon}R_{xy}(0) = 0,$$
$$-\omega_0^2 R_{xx}(0) + \tilde{\varepsilon}R_{xy}(0) + R_{yy}(0) = 0,$$
$$-\omega_0^2 R_{xy}(0) + \tilde{\varepsilon}R_{yy}(0) - \omega_0^2 R_{xy}(0) + \tilde{\varepsilon}R_{yy}(0) = -D^2,$$

whose solution is

$$R_{yy}(0) = -\frac{D^2}{2\tilde{\varepsilon}}$$
$$R_{xy}(0) = 0$$
$$R_{xx}(0) = \frac{D^2}{-2\tilde{\varepsilon}\omega_0^2}.$$

The last expression can be substituted into Eq. (11.37) to obtain

$$\tilde{\varepsilon} = \varepsilon + \frac{D^2}{2\tilde{\varepsilon}\omega_0^2}, \tag{11.41}$$

$$2\tilde{\varepsilon}^2\omega_0^2 - 2\tilde{\varepsilon}\varepsilon\omega_0^2 - D^2 = 0,$$

$$\tilde{\varepsilon} = \frac{\varepsilon}{2} \pm \sqrt{\left(\frac{\varepsilon}{2}\right)^2 + \frac{D^2}{2\omega_0^2}}.$$

The root with a "minus" sign has no physical meaning, since it gives a zero value for $\tilde{\varepsilon}$ in the limit $D \to 0$. The final expression is

$$\tilde{\varepsilon} = \frac{\varepsilon}{2} + \sqrt{\left(\frac{\varepsilon}{2}\right)^2 + \frac{D^2}{2\omega_0^2}}. \tag{11.42}$$

This approach, that was used in [43] for determining $\tilde{\varepsilon}$, is self-consistent, since the mean-field approximation $\langle x^2 \rangle$ of the nonlinearity is calculated self-consistently as the variance of the resulting effective Ornstein-Uhlenbeck process. It shows that the effect of noise in the nonlinear system is to shift the effective bifurcation parameter further away from the Hopf bifurcation. Now we are able to find an analytical expression for the correlation time t_{cor}, which extends the result of Eq. (11.19) beyond the limit of weak noise and gives the explicit dependence of t_{cor} upon the noise intensity D:

$$t_{\text{cor}} \approx \frac{2}{\pi|p_0|} = \frac{4}{\pi|\tilde{\varepsilon}|}. \tag{11.43}$$

It is in excellent agreement with numerical simulations of the nonlinear van der Pol system over a large range of noise intensities [43].

11.2.6
Any Noise and Control: Correlation Time and Spectrum

The use of the mean field approximation (11.37) for the uncontrolled case has resulted in a renormalized bifurcation parameter due to noise, i.e., substitution of ε by $\tilde{\varepsilon}$, Eq. (11.42). In analogy with Section 11.2.3, one can extend the use of this approximation to the controlled case. Namely, the estimates (11.26) and (11.28) for the correlation time can be turned into

$$t_{\text{cor}} = \frac{2}{\pi|p^{\max}|} \tag{11.44}$$

$$t_{\text{cor},n}^{\max} \simeq \frac{4}{\pi|\tilde{\varepsilon}|}\left(1 + \frac{\pi Kn}{\omega_0}\right). \tag{11.45}$$
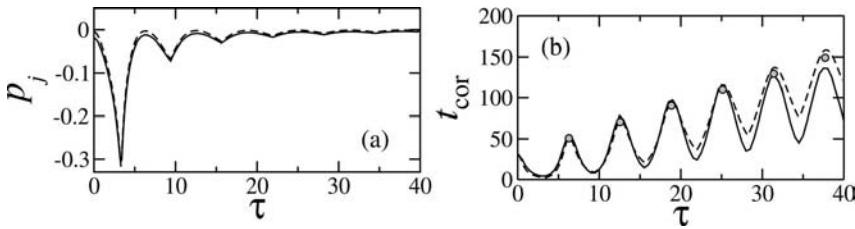
Fig. 11.4 Characteristics of the random process in the van der Pol system with control equation (11.2) for moderate noise as a function of τ. $\omega_0 = 1$, $\varepsilon = -0.01$, $D = 0.1$, and $K = 0.2$. (a) The largest real part of the eigenvalue $p^{\max}$ obtained by solving numerically Eqs. (11.12)–(11.13); dashed line: with ε, black line: mean field approximation $\tilde{\varepsilon}$ Eq. (11.42). (b) Correlation time t_{cor}: numerical estimate (solid line), mean field approximation using Eq. (11.44) (dashed line) and using Eq. (11.45) for maxima (grey circles).
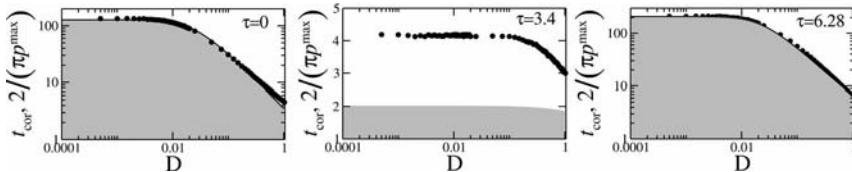
Fig. 11.5 Correlation time of the van der Pol system (11.2) oscillations as a function of noise intensity D at $\omega_0 = 1$, $\varepsilon = -0.01$, $K = 0.2$ and different values of τ. Circles show the estimates from numerical simulation, shaded grey shows the mean field approximation using Eq. (11.44), and the solid black line using Eq. (11.45). The values of τ indicated in the figures correspond to: no control ($\tau = 0$), control with the minimal regularity ($\tau = 3.4$), and control with the first maximum of regularity ($\tau = 6.28$).

The values of t_{cor} obtained by numerical simulation for moderate noise intensity $D = 0.1$ is shown in Fig. 11.4 (b) as a function of τ. One can see that the values of t_{cor} at the maxima are considerably smaller that those for small noise in Fig. 11.2 (c), as expected. The approximation of t_{cor} by Eq. (11.44) is shown by the dashed line, and of $t_{\mathrm{cor},n}^{\max}$ by Eq. (11.45) by grey circles.

It is interesting to check how the regularity of noise-induced oscillations depends upon the noise intensity D, and also how good the analytical mean field approximations Eqs. (11.44), (11.45) and Eq. (11.42) are. Figure 11.5 depicts the correlation time at $K = 0.2$ as a function of noise intensity D at three different values of τ: 0 (no control), 3.4 (the first minimum of t_{cor}) and 6.28 (the first maximum of t_{cor}). Maxima and minima are taken from Figs. 11.2 (c) and 11.4 (b), and they approximately coincide for different D. Circles show the results of numerical simulation, shaded grey are approximations using Eq. (11.44), and the black solid line shows the estimate using Eq. (11.45) which is available only for optimal $\tau \approx 2\pi n/\omega_0$ and hence cannot be used for $\tau = 3.4$. Black lines and circles are in an impressive agreement, which matches the results of [43]. Approximation (11.44) matches the numerics slightly better than
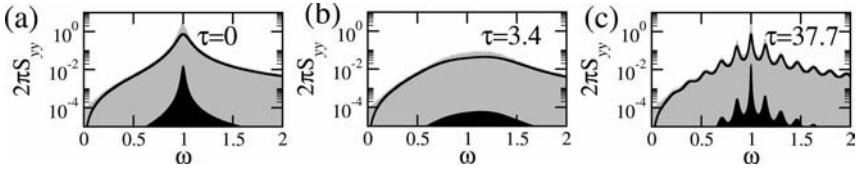
Fig. 11.6 Spectra of oscillations in the van der Pol system (11.2) at $\omega_0 = 1$, $\varepsilon = -0.01$, $D = 0.1$, $K = 0.2$, and different values of τ: S_{yy} obtained by numerical simulation (shaded grey), estimated analytically with mean field approximation (11.46) (black line), and estimated analytically without mean field approximation (11.36) (shaded black). (b) $\tau = 0$ (no control), (c) $\tau = 3.4$ (minimal regularity), (d) $\tau = 37.7$ (maximal regularity).

Eq. (11.45) for the optimal τ, but from the figures the difference is hardly visible. For the nonoptimal $\tau = 3.4$, Eq. (11.44) becomes inaccurate, as expected.

The spectrum can also be estimated analytically in the framework of the self-consistent mean field approximation by replacing ε with $\tilde{\varepsilon}$ in Eqs. (11.31) and (11.36):

$$S(\omega) = \frac{D^2}{2\pi} \frac{\omega^2}{(\omega^2 - \omega_0^2 + \omega K \sin(\omega\tau))^2 + \omega^2(\tilde{\varepsilon} - K(1 - \cos(\omega\tau)))^2}. \tag{11.46}$$

The spectra for moderate noise intensity $D = 0.1$ are shown in Fig. 11.6: numerical (shaded grey), analytic using Eq. (11.46) (black lines), and for comparison analytic estimates for small noise (shaded black). The same values of τ are used as in Fig. 11.3. One can compare the deviations of the two different analytical estimates from the numerical data and make sure that the rescaled bifurcation parameter $\tilde{\varepsilon}$ indeed provides more accurate estimates for larger noise.

11.2.7
So, What Can We Control?

The above sections have described the effects of the delayed feedback added to the van der Pol equation below the Andronov-Hopf bifurcation with noise. One might ask "What is the relevance of these results to control?" Remember that we were aiming at adjusting the properties of noise-induced oscillations by suitably choosing the parameters of the control scheme. Let us summarize our observations.

Note that the introduction of the feedback is strongly influencing the appearance of the spectra (Figs. 11.3 and 11.6). First, in addition to the main spectral peak that exists without the feedback, new peaks appear. Second, the central frequencies, heights, and widths of these peaks move with τ. For a better illustration of spectral properties, it is convenient to extract all spectral peaks and to introduce their periods $T_j^s = 2\pi/\omega_j$, $j = 1, 2, \ldots$, where ω_j are the central peak frequencies.

In Fig. 11.2 (b), the basic period T_{bas}^s [2] is shown by light-grey circles, while other T_j^s are denoted by crosses, all depending on τ. If the spectrum normalized by the total power of oscillations can be interpreted as the distribution of power over frequencies, then the basic period can be understood as the most probable period of oscillations. Notably, each peak period T_j^s coincides to a good accuracy with the respective eigenperiod T_j^e, and T_{bas}^s coincides with T_j^e for which $|p_j|$ is the smallest (not obvious from the figure, but verified). This can be interpreted as follows: noise excites various eigenmodes in the system; the less stable the mode is (the smaller its $|p_j|$), the higher the respective spectral peak.

We observe that the evolution of T_{bas}^s depends in an almost piecewise linear way upon τ. This means that the most probable period of oscillations can be adjusted by the feedback in a desirable way, which effects the control of time-scales. Also, the heights and the widths of spectral peaks vary with τ. The shape of the peaks defines the shape of the autocorrelation function, and consequently the correlation time. This means that by changing τ one is able to control the regularity of noise-induced oscillations.

11.3
Noise-Induced Oscillations in an Excitable System and their Control

Consider a very different kind of noise-induced motion: oscillations in excitable systems [45]. An excitable system remains in the rest state if it is not perturbed externally. It responds to an external perturbation in a selective way: if the perturbation is below a certain threshold, the system returns to its rest state, and if it exceeds this threshold, the system performs an excursion in the phase space [16, 17]. Excitability is an inherent property of certain neurons [46], as well as some chemical reactions [47] and semiconductor nanostructures [48].

A paradigmatic example of an excitable system is a simplified FitzHugh-Nagumo system

$$\mu \frac{\mathrm{d}x}{\mathrm{d}t} = x - \frac{x^3}{3} - y,$$
$$\frac{\mathrm{d}y}{\mathrm{d}t} = x + a + K(y(t-\tau) - y) + D\eta(t). \tag{11.47}$$

We choose the parameters $\mu = 0.01$ and $a = 1.1$ such that in the absence of feedback the only attractor of the system is a stable node. Here, as in Eq. (11.2), τ is a time delay, $K > 0$ is the feedback strength, and D is the intensity of Gaussian white noise η with zero mean.

---

2) By basic period we mean the inverse of the frequency of the highest peak in the Fourier power spectrum of oscillations. By mean period we mean the average time of phase trajec- tory return to some secant surface. These two periods coincide only in purely periodic oscillations.
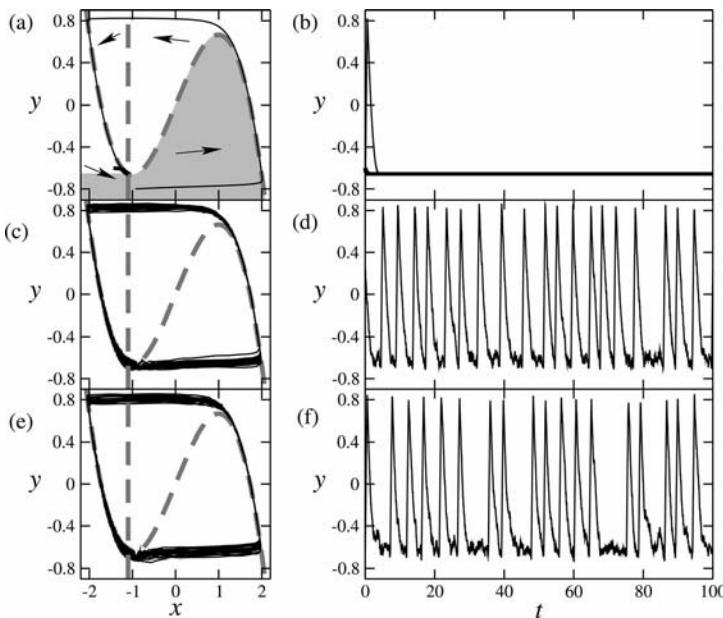
Fig. 11.7 Phase portraits and realizations of the FitzHugh-Nagumo system (11.47) at $\mu = 0.01$, $a = 1.1$. (a) and (b) No noise, no feedback; (c) and (d) noise-induced oscillations at $D = 0.09$ without feedback; (e) and (f) noise-induced oscillations at $D = 0.09$ with feedback $K = 0.2$ and $\tau = 5$ (maximal regularity, see Fig. 11.9 (b)). In (a) dashed lines show the nullclines, and arrows show schematically the directions of the phase flow, and the shaded area outlines the set of initial conditions from which the system would perform a big excursion.

First, we illustrate the behavior of system (11.47) by phase portraits and realizations (see Fig. 11.7). It is convenient to characterize the motion of an excitable system in the phase plane with the help of nullclines, which are the lines defined by $\dot{x} = 0$ and $\dot{y} = 0$: they separate different directions of motion in the phase space and intersect at the fixed point.

In Fig. 11.7 (a), (c), and (e) the nullclines are shown by grey dashed lines, and the directions of the phase flow are very roughly indicated by the arrows. Because μ is chosen to be small, the motion between the fixed point and the right-hand branch of the cubic parabola, and between the right-hand maximum of the parabola and left-hand branch, occurs almost instantly, and the respective parts of trajectories are almost parallel to the x-axis.

Figure 11.7 (a) and (b) illustrates the behavior of the system without random fluctuations ($D = 0$). If the initial conditions are set above the grey shaded area, the system follows the phase flow and comes back to the fixed point (thick lines). If the initial conditions are set inside the grey shaded area, the phase point being carried by the phase flow, performs a large excursion in the phase plane and only after that settles down at the fixed point (thin line).

Figure 11.7 (c) and (d) illustrates Eq. (11.47) with noise $D = 0.09$ but without control $K = 0$. If the current value of $D\eta(t)$ is small, the system stays in the vicinity of the fixed point, but if the fluctuation is such that the phase point is thrown into the shaded area, the system performs the large excursion in the phase plane before returning to the fixed point. The instantaneous period of oscillations contains two components: time of escape from the vicinity of the fixed point (activation time) and time of travel along the branches of the parabola (excursion time) [49]. Figure 11.7 (e) and (f) illustrates Eq. (11.47) with noise $D = 0.09$ and with control $K = 0.2$ and $\tau = 5$.

The stability of the fixed point can be checked analytically using the standard approach. It has been shown that delayed feedback does not induce Andronov-Hopf bifurcations in Eqs. (11.47). The global character of oscillations renders the local approach used for the van der Pol system in Section 11.2 inappropriate. Therefore, in this section we present only the results of numerical simulation. As an observable of random processes in the FitzHugh-Nagumo system we choose the variable y.

11.3.1
Coherence Resonance in the FitzHugh-Nagumo System

The FitzHugh-Nagumo system (11.47) is a well-known example of a system demonstrating coherence resonance (CR). The correlation time estimated from numerical realizations of Eq. (11.47) is shown in Fig. 11.8 (a) by grey circles as a function of noise intensity D. One can see that at small D, t_{cor} is small, which means small regularity of oscillations. As D increases from zero, the oscillations remarkably become more ordered which is manifested in the growth of their correlation time. t_{cor} achieves a maximum at $D \approx 0.09$, and then starts to decay. Note that noise-induced oscillations in the van der Pol system do not have this property (see Fig. 11.5): with increasing noise their correlation time decreases monotonically.
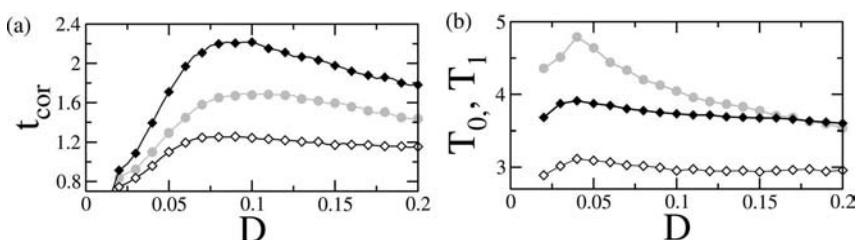
Fig. 11.8 (a) Correlation time and (b) basic periods of oscillation versus D of the realizations of the FitzHugh-Nagumo system (11.47) at $a = 1.1$, $\mu = 0.01$, with $K = 0$ (grey circles), with $K = 0.2$ at $\tau = 4.12$ (black diamonds), and $\tau = 2.9$ (white diamonds), obtained by numerical simulation.

Here, it is interesting to reveal how the timescales of noise-induced oscillations depend on D. We calculate the spectrum of oscillations for each value of D, extract the highest spectral peak and estimate its period T_{bas}^s. In Fig. 11.8 (b) grey circles show the basic period T_{bas}^s of noise-induced oscillations versus noise intensity D without feedback. One can see that this period changes with noise quite substantially. Hence, the system is not robust with regard to noise, which might be viewed as a disadvantage in certain situations.

11.3.2
Correlation Time and Spectrum when Feedback is Applied

By analogy with our studies of the van der Pol system, we will be interested in the regularity and the timescales of oscillations depending on the parameters of the delayed feedback, when the control with the above parameters is applied.

Let us choose a noise intensity at which the system demonstrates most regular oscillations without feedback, $D = 0.09$. The correlation time of noise-induced oscillations for fixed $K = 0.2$ is shown in Fig. 11.9 (b) in dependence on τ. As with the van der Pol system (Fig. 11.2 (c)), it oscillates with τ, and on average grows. However, the maxima of regularity are observed not almost exactly at the multiples of the basic period without control $T_{bas}^s = 4.12$ as in the van der Pol system, but first at some value close to $\tau = 5$, and then at some values that can be regarded as its multiples only very roughly.

At the same time, the timescales change with τ as well: in Fig. 11.9 (a) the spectral periods T_i^s are shown as black dots, while the basic period T_{bas}^s is denoted by grey circles. Again, like in the van der Pol system, the periods behave almost piecewise linearly. The maximal regularity is observed when T_{bas}^s becomes close to its value 4.12 without the feedback, which happens at $\tau \approx 5$.

The spectra of noise-induced oscillations for fixed $K = 0.2$ and different τ are shown in Fig. 11.10. In (a) the general view of the spectrum in dependence on τ is shown by grey shading, where brighter regions correspond to larger power. One observes the same qualitative appearance of this plot as with the van der Pol system: the spectrum changes with τ quite substantially: the number of
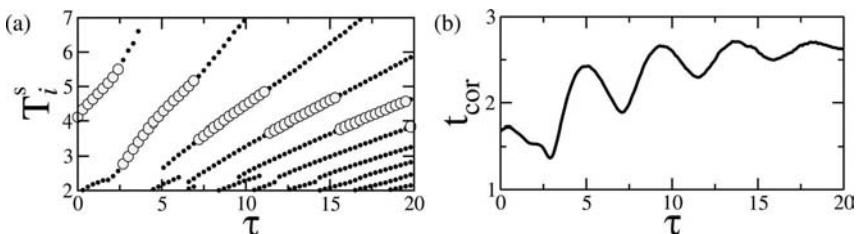
Fig. 11.9 (a) Spectral peak periods T_i^s and (b) correlation time versus τ from the realizations of the FitzHugh-Nagumo system (11.47) at $a = 1.1$, $\mu = 0.01$, $D = 0.09$, and $K = 0.2$, obtained by numerical simulation.
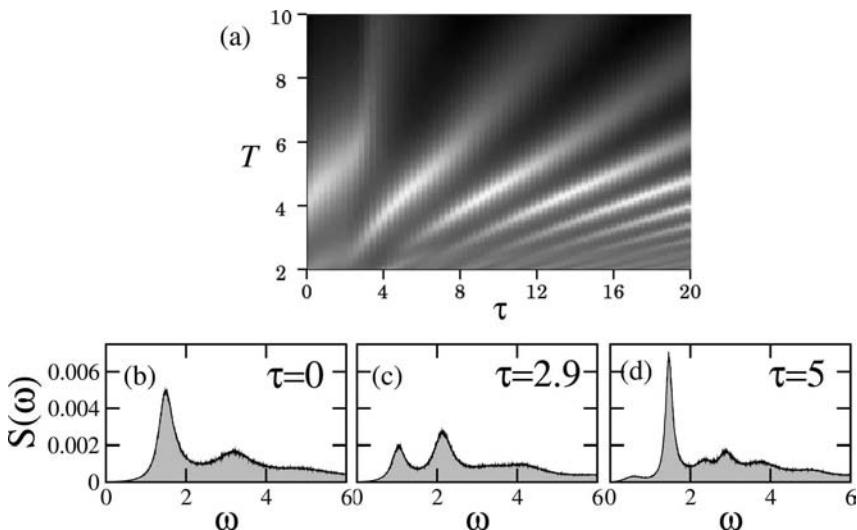
Fig. 11.10 Spectra of oscillations in the Fitz-Hugh-Nagumo systems (11.47) at $a = 1.1$, $\mu = 0.01$, $D = 0.09$, $K = 0.2$, at different values of τ, obtained from numerical simulations. (a) Density plot of the spectrum. (b) $\tau = 0$ (no control), (c) $\tau = 2.9$ (minimal regularity), (d) $\tau = 5$ (maximal regularity) (cf. Fig. 11.9 (b))

peaks changes, the peaks move, and their heights and widths vary. In Fig. 11.10 (b)–(d) several cross sections of this picture are shown with τ set equal to: (b) 0 (no control), (c) 2.9 (most irregular oscillations), (d) 5 (the first maximum of t_{cor}).

Finally, let us consider whether the feedback can make the system more robust with respect to changes in the noise intensity. We fix $K = 0.2$ and fix τ at two values: $\tau = 2.9$ with minimal regularity, and $\tau = 4.12$ at which regularity is larger than without feedback. The basic peak periods T^s_{bas} are shown in Fig. 11.8 (b) as white and black diamonds, respectively. In both cases, the delayed feedback reduces the range of variation of T^s_{bas} under a change in noise intensity. At the same time, the correlation time (Fig. 11.8 (a)) behaves in qualitatively the same way as without feedback, namely, it becomes maximal at approximately the same noise intensity. However, the quantitative value of t_{cor} is substantially lower at $\tau = 2.9$, and substantially higher at $\tau = 4.12$ for the whole range of D.

11.3.3
Control of Synchronization in Coupled FitzHugh-Nagumo Systems

The effect of time delayed feedback control upon noise-induced oscillations in two linearly coupled FitzHugh-Nagumo systems as a simple model of two interacting neurons has also been investigated [50]. Application of delayed feedback to only one of two subsystems can be shown to be able to change coherence

and timescales of noise-induced oscillations either in the given subsystem, or globally. It is also able to induce or to suppress stochastic synchronization under certain conditions. The coupled system without control displays a 1:1 synchronization tongue in the (D_1, C) parameter plane, given by the noise strength D_1 in the first subsystem and the coupling strength C. Frequency and phase synchronization occurs in the same area of the parameter plane. If the first of the two interacting subsystems is subjected to local delayed feedback, it is possible to manipulate the global dynamics of the system of interacting oscillators.

The delayed feedback can be applied to the system in different states of synchrony, e.g., moderately synchronized, weakly synchronized, and strongly synchronized. In all three cases, 1:1 synchronization can be either improved or weakened, depending upon the choice of τ and K. Like the correlation times, the synchronization index is modulated nonmonotonically as a function of the delay time τ, indicating that there is resonance-like behavior for certain values of τ. Perfect synchronization can only be achieved if the uncontrolled state is already sufficiently synchronized. The mechanism behind the action of the delayed feedback can be understood on the basis of the discussion in the previous subsection. The feedback applied to a single excitable system is able to change the timescales and coherence of noise-induced oscillations. When the system subjected to the feedback is coupled to another system, the shift of the timescale of the former will lead to a proportional shift of the timescale of the latter. The exact magnitude of the shift in the second subsystem will depend on the closeness of the two subsystems to the state of synchronization. Only if the two subsystems are sufficiently 1:1 synchronized from the beginning, the shift in the second system can be expected to match the shift in the first system.

An important observation is that the delay-induced increase of coherence of the global dynamics is most frequently accompanied by the growth of the degree of synchronization. However, a large synchronization index does not always mean high coherence: delayed feedback can induce, or make stronger, the synchronization between the two subsystems, but the state of each subsystem, and their global dynamics, can become more disordered at the same time. The converse is also true.

It is remarkable that delayed feedback control can influence global characteristics of the two coupled systems although the control is only applied locally to a subsystem. It is thus possible to enhance or destroy the regularity of oscillations and the stochastic synchronization of the two systems by choosing appropriate control parameters, in particular a suitable delay time.

11.3.4
What can We Control in an Excitable System?

We have revealed that in analogy with a system below an Andronov-Hopf bifurcation, as considered in the previous section, the properties of oscillations in an excitable system can be changed by means of delayed feedback control. One can change the most probable periods and the regularity of oscillations. In addition,

delayed feedback makes the system more robust with regard to the strength of noise and stabilizes both the basic period and the regularity of its oscillations.

Recently, an experimental work [51] has confirmed that the delayed feedback can enhance the regularity of the noise-induced motion in an excitable system represented by an electrochemical cell, for the appropriate values of time delay τ.

11.4
Delayed Feedback Control of Noise-Induced Pulses in a Model of an Excitable Medium

In Section 11.3 we have considered the noise-induced oscillations in a single excitable system. However, the excitability can be the property of the spatially extended medium, in which each point can be perceived as an excitable unit, and all points are coupled to their neighbours. In excitable media, noise can induce waves and lead to the formation of quite coherent spatiotemporal patterns [52, 53], to maintain the existing patterns [47], and even to support wave propagation [54]. This phenomenon has been attracting increasing attention, also for its potential importance for, and applicability in, neuroscience [55, 56] and cardiac dynamics [45, 57].

In this section the effect of the delayed feedback on the noise-induced spatiotemporal patterns in an excitable medium is assessed. As a model a famous paradigm for an excitable medium was chosen: the Oregonator equations that describe the Belousov-Zhabotinsky (BZ) chemical reaction. This reaction can be relatively easily implemented in an experiment, so a realistic situation was simulated that reproduced the conditions of a real experiment.

11.4.1
Model Description

The photosensitive version of the BZ reaction has become a prototype system for experimental studies of noise-induced phenomena in spatially extended excitable media [53, 54, 58]. It can be described by the modified Oregonator equations having the following form [59]:

$$
\begin{aligned}
\partial_t u &= \frac{1}{\varepsilon}\left(u - u^2 - w(u - q)\right) + D_u \partial_x^2 u, \\
\partial_t v &= u - v, \\
\partial_t w &= \frac{1}{\varepsilon'}\left(fv + \phi - w(u + q)\right) + D_w \partial_x^2 w.
\end{aligned}
\tag{11.48}
$$

Here, the variables u, v, w are concentrations of bromous acid, the oxidized form of the catalyst, and bromide, respectively. D_u and D_v are the constants of spatial diffusion for the variables u and v. In what follows the following parameters will be fixed as in [60]: $q = 0.002$, $f = 1.4$, $1/\varepsilon = 11.7$, $1/\varepsilon' = 1059$, and

$D_u = 1$, $D_w = 1.12$. Note that Eqs. (11.48) is a one-dimensional approximation of a medium that is effectively two-dimensional (if the thickness can be neglected). The length of the medium is set $L = 19.2$, and periodic boundary conditions are used.

The intensity of light applied to the medium is linked to the parameter ϕ in Eqs. (11.48), which is the principal control parameter for this study. If there were no spatial diffusion ($D_u = D_w = 0$), the dynamics of the system (kinetics) would have been qualitatively similar to the one in a single FitzHugh-Nagumo system (11.47). For $\phi > 4.24 \times 10^{-3}$ the system is excitable, and the kinetics has a single stable steady state. If ϕ is less than 4.24×10^{-3}, the kinetics demonstrates self-sustained oscillations.

Noise has to be introduced in the model, and the most natural and simple way to do this from the viewpoint of an experiment would be to make ϕ vary randomly in time around some mean value ϕ_0

$$\phi(x,t) = \phi_0(1 + \eta(x,t)). \tag{11.49}$$

ϕ_0 was fixed at 0.005 for which the system is excitable. In a real experiment with a photosensitive BZ medium, the applied fluctuations of light are essentially the same within a certain small portion of the medium. Also, the light fluctuations are never infinitely fast, i.e., never delta correlated. To simulate this, the spatial domain was divided into N cells of equal size $\lambda = L/N$. To each cell number i, $i = 1, 2, ..., N$, correlated noise $\hat{\eta}_i(t)$ with zero mean is applied according to

$$\frac{\mathrm{d}}{\mathrm{d}t}\eta(x,t)\big|_{x \in [(i-1)\lambda, i\lambda]} \equiv \frac{\mathrm{d}}{\mathrm{d}t}\hat{\eta}_i(t) = \frac{1}{\tau_{\mathrm{ou}}}(-\hat{\eta}_i + \xi_i(t)), \tag{11.50}$$

where $\xi_i(t)$ is Gaussian white noise. The correlation function of $\hat{\eta}_i(t)$ is

$$\langle \hat{\eta}_i(t)\hat{\eta}_j(s) \rangle = \delta_{ij}\sigma^2 \exp(-|t - s|/\tau_{\mathrm{ou}}). \tag{11.51}$$

Here δ_{ij} denotes the Kronecker delta (0 if $i \neq j$ and 1 if $i = j$), τ_{ou} is the correlation time of the Ornstein-Uhlenbeck (OU) process described by Eq. (11.50) and $\sigma^2 = \langle \eta^2 \rangle$ is its intensity which is chosen same for all cells. The parameters of noise were fixed at the values that provided a maximally coherent spatiotemporal dynamics: $\sigma = 0.5$, $\tau_{\mathrm{ou}} = 0.5$ and $\lambda = 1.2$ [61].

An important factor that has to be taken into account is that ϕ cannot be negative, since it is proportional to the applied illumination. Therefore, in the simulations the values of ϕ were eliminated that were less than zero, and also larger than $2\phi_0$ in order to preserve symmetry in the noise distribution. The following procedure was adopted: Eq. (11.50) was integrated, and at each time step it was checked whether for all i the values of $\hat{\eta}_i(t)$ fell within the interval $[-1, 1]$. If for some i this condition was not satisfied, the integration of Eq. (11.50) was continued for the given i only, until a suitable value of $\hat{\eta}_i(t)$ emerged. When all $\hat{\eta}_i(t)$
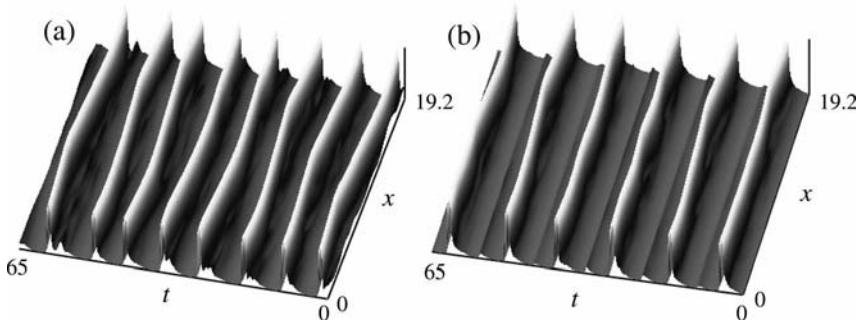
Fig. 11.11 Noise-induced spatiotemporal patterns in the Oregonator model (11.48). $u(x,t)$ is shown in logarithmic scale (a) without control, (b) with control at $K = 0.3$ and $\tau = 5.25$. Small steps parallel to the x-axis in (b) manifest application of control force.

were as required, they were fed into Eqs. (11.48). Obviously, the stochastic process obtained in this way was no longer of OU type. However, its correlation time and noise intensity deviated by less than 10% from the respective values of an OU process.

As noise is applied to the given point x, it takes on average t_a time units to excite ("activate") the medium locally. At the chosen parameters of noise activation time t_a is negligibly small. After the point x of the medium achieves its excited state, it returns to its rest state during a "refractory period" t_r. During t_r, at the given position x the medium cannot be excited again.

In the presence of spatial diffusion ($D_u \neq 0$, $D_w \neq 0$), at the excited point x a pair of pulses nucleate and then propagate in opposite directions with the same constant velocity. In order to prevent nucleations on the border of the medium, for this study periodic boundary conditions were adopted. As a result, each pulse from the simultaneously nucleated pair inevitably meets another pulse from the same pair, or from another pair, and they both annihilate (see Fig. 11.14).

This mechanism leads to the formation of quite distinct patterns in space-time, a typical example being shown in Fig. 11.11 (a). Here, the values of $u(x,t)$ are plotted in logarithmic scale.

11.4.2
Characteristics of Noise-Induced Patterns

Before assessing the effect of delayed feedback on Eqs. (11.48), we need to introduce convenient parameters characterizing the whole medium, since it would be cumbersome to describe each point of it. The simplest way to overcome this problem is to introduce the space-averaged activator concentration of $u(x,t)$ [62, 63]
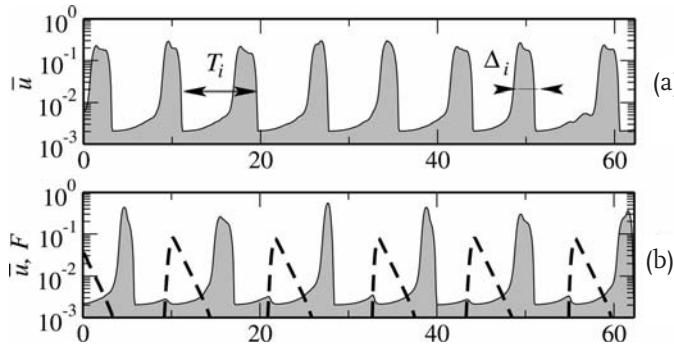
Fig. 11.12 Space-average activator concentration $\bar{u}(t)$ in the Oregonator model (11.48) (a) without control and (b) with control at $K = 0.3$ and $\tau = 5.25$. The dashed line shows the control force $F(t)$.

$$\bar{u}(t) = \frac{1}{L} \int_0^L u(x', t) \mathrm{d}x' \qquad (11.52)$$

and hence to deal with the description of a one-dimensional realization instead of a function of two variables. Figure 11.12 (a) shows $\bar{u}$ corresponding to the space–time plot in Fig. 11.11 (a). The realization exhibits pronounced spikes, so interspike intervals T_i can be introduced as the intervals between the successive crossings by the variable $\bar{u}(t)$ of a threshold 0.03 from above to below (see Fig. 11.12 (a)). The basic timescale of the noise-induced pattern can be characterized by the mean interspike interval $\langle T_i \rangle$, where $\langle \rangle$ denotes the average over all spikes.

Also, a sequence of T_i's contains information on the temporal regularity of the pattern: the more regular the pattern is in time, the more periodically $\bar{u}$ spikes, i.e., the less the T_i's change from one spike to another and the less their variance is [64]. The temporal coherence can be measured as the normalized variance R_T of T_i

$$R_T = \sqrt{\langle (T_i - \langle T_i \rangle)^2 \rangle} / \langle T_i \rangle. \qquad (11.53)$$

The smaller the R_T, the more regular the oscillations are in time.

However, one also needs to characterize how regular the pattern is in space. Note that one spike in $\bar{u}(t)$ persists while the medium still propagates the initial perturbation generated by noise. If more than one pair of pulses are nucleated almost simultaneously, the total propagation time for all these pairs is less than for one pair (see third and fourth stripes from the left in Fig. 11.14 (b)), and the respective spike will be narrower. We can introduce the ith spike duration Δ_i as the time during which $\bar{u} \geq 0.03$, and the average spike duration $\langle \Delta_i \rangle$ as a measure of spatial regularity (homogeneity) [61].

11.4.3
Control of Noise-Induced Patterns

In experiments with the photosensitive BZ medium the feedback can be most easily realized via the applied illumination, hence here it was introduced into the parameter ϕ as follows [64]

$$\phi(x, t) = \phi_0(1 + \eta(x, t)) + F(t), \tag{11.54}$$

where

$$F(t) = KsH(s), \quad s = v(x_0, t - \tau) - v(x_0, t). \tag{11.55}$$

Here $H(s)$ is the Heaviside function (0 for $s < 0$ and 1 for $s \geq 0$), K is the feedback strength, τ is the time delay, and $x_0 = L/2 = 9.6$ is the detection point chosen arbitrarily. Note that delayed feedback is nonlinear here, and the reason behind the choice of this particular form of it is that ϕ should take only positive values. Since feedback can only increase the value of ϕ, this means that the control force can only suppress the activity in the system. This is a crucial difference from the control scheme used in Sections 11.2 and 11.3.

Also, it is important to note that in a real experiment the monitored variable is the v-field. That is why the feedback signal had to be formed from the observations of this variable at point x_0.

The effect of delayed feedback with $\tau = 5.25$ and $K = 0.3$ on the noise-induced patterns is illustrated in Fig. 11.11 (b), where $u(x, t)$ is shown in logarithmic scale. Small steps parallel to the x-axis in (b) manifest the application of the control force, when the activity in the system is being suppressed. Already from the space–time plots it is clear that the feedback can produce a remarkable effect on the system: the pulses arrive at more equal time intervals, and each stripe of activity is narrower, since more than one pair of pulses are more likely to be initiated almost simultaneously.

In order to gain deeper insight into the effect of the feedback, we fix the feedback strength $K = 0.2$ and study how the variation of the time delay τ influences the properties of noise-induced motion.

The three characteristics $\langle T_i \rangle$, R_T, and $\langle \Delta_i \rangle$ of this motion depending on τ are given in Fig. 11.13. All the quantities oscillate with a characteristic timescale close to the mean interspike interval $\langle T_i^0 \rangle \simeq 8$ without feedback [64].

Mean interspike interval $\langle T_i \rangle$ The plot contains almost linear segments (Fig. 11.13 (a)), which can be associated with the entrainment of timescales by delayed feedback as in Sections 11.2 and 11.3. The principal difference from the above results is that $\langle T_i \rangle$ is always larger than $\langle T_i^0 \rangle$ because the feedback force in the form (11.55) can only postpone the nucleation of the new pulse pairs.

Temporal regularity R_T Delayed feedback increases R_T for τ less but close to 5, at which it has a global minimum (Fig. 11.13 (b)). Note that this minimum occurs at a value of τ close to the refractory period t_r (see Fig. 11.14).
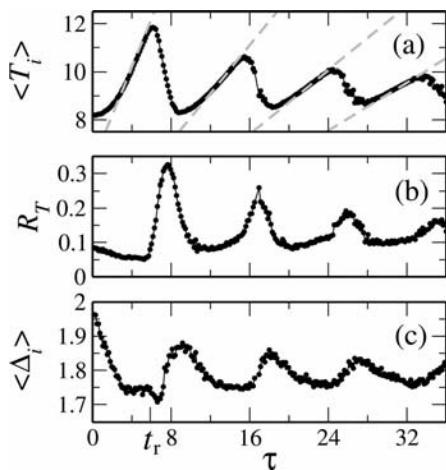
Fig. 11.13 Mean interspike interval $\langle T \rangle$, temporal coherence R_T and spatial coherence Δ versus τ at $K = 0.3$, for Oregonator model (11.48) [64].
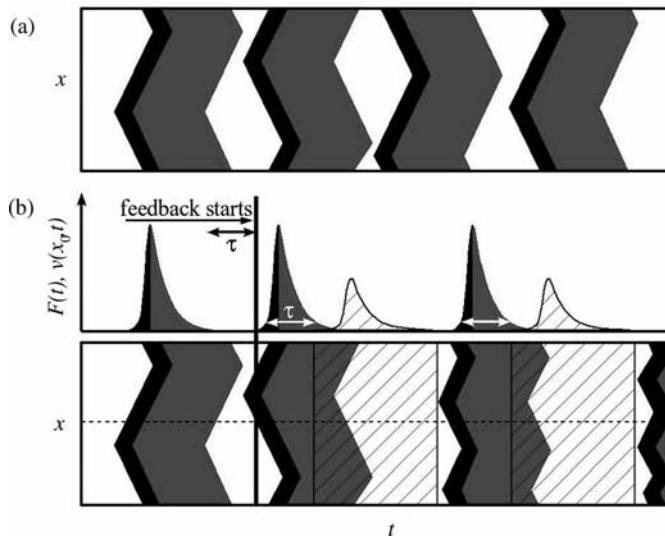
Fig. 11.14 Schematic illustration of the noise-induced pattern formation in Oregonator model equations (11.48), and of its delayed feedback control, provided the noise is strong, i.e., activation time is negligible. Black areas indicate the excited state, grey areas the refractory state, and hatched areas indicate where the positive feedback is applied. (a) No feedback. (b) Feedback is applied, with the top graph indicating the respective profiles of $v(x_0)$ and of the feedback force F.

Spatial regularity $\langle \Delta_i \rangle$ is less than $\langle \Delta_i^0 \rangle$, the latter being the value without feedback control, for all the values of time delay τ studied (Fig. 11.13 (c)). The feedback increases the number of simultaneous nucleations of pulse pairs, and hence increases spatial regularity (homogeneity) of the pattern.

Note that the effect of the delayed feedback in the excitable medium is somewhat similar to the one in a single excitable unit (Section 11.3), and is different from that in the system below an Andronov-Hopf bifurcation (Section 11.2), where maximal improvement of coherence was obtained for τ close to the mean period $\langle T_i^0 \rangle$ of oscillations without feedback. The effect is also markedly different from the linear delayed feedback control of noise-induced patterns in a globally coupled reaction–diffusion system used to model a semiconductor nanostructure [65] described in Section 11.5.

11.4.4
Mechanisms of Delayed Feedback Control of the Excitable Medium

Here we consider the mechanisms underlying the behavior of the system subjected to delayed feedback control.

Figure 11.14 sketches the patterns shown in Fig. 11.11. In (a) the situation without control is illustrated: from the steady state (white areas) an excitation starts (black stripes), followed by a refractory state (grey areas) which lasts time t_r for each element of the medium. After this time has elapsed, each element recovers its steady state and can get excited again. The probability of a new nucleation is then proportional to the portion of the medium that has recovered the steady state. With the chosen noise parameters, a new nucleation occurs with probability close to 1 immediately after the whole medium has passed the refractory period, but often this happens even before that.

In Fig. 11.14 (b) the medium in the presence of feedback force is illustrated. The upper panel shows the value of $v(x_0, t)$, and the feedback force (hatched area) starts only after the moment indicated by the vertical bar. A positive force is applied to the whole medium, τ time units after the element at x_0 gets excited, and its duration is marked by hatched area in the lower panel. This force inhibits activity in the medium resulting in an effective increase of the refractory period of the medium and thus of T_i. From this it follows directly that $\langle T_i \rangle$ depends linearly on τ when $\tau \leq t_r$. When the force vanishes, all elements of the medium recover the steady state simultaneously, unlike the case without forcing illustrated in (a), and any element can get excited. This maximizes the probability of a nucleation, and even of more than one nucleation almost at the same time. Hence, the patterns become more homogeneous in space and $\langle \Delta_i \rangle$ decreases.

Notably, if τ is less but close to t_r, the moment when the whole medium recovers the steady state does not depend on the shape of the fronts of the spatiotemporal pattern. Therefore, the larger the τ, the stronger the positive feedback force is that suppresses the nucleation, the more effectively the pulse nucleation

is inhibited before the force disappears. Therefore, the maximal temporal and spatial regularity are achieved at τ close to t_r, which is confirmed by the positions of the first minima of $R_T(\tau)$ and of $\langle \Delta_i \rangle$ in Fig. 11.13 (b) and (c), respectively.

As τ gets closer to the mean period $\langle T_i^0 \rangle$ without control, the feedback is applied when, or after, the medium nucleates. So the force can suppress the pulses even before they meet and annihilate, which breaks the pattern quite badly. This corresponds to the worst temporal and spatial regularity (see Fig. 11.13 (a)) [64]. As τ starts to exceed $\langle T_i^0 \rangle$, the situation described for $\tau \leq t_r$ is repeated, the regularity slightly improves and $\langle T_i \rangle$ increases. Moreover, it can be expected that for each successive linear segment in the dependence of $\langle T_i \rangle$ on τ the relationship

$$\langle T_i \rangle \approx (\tau + t_p)/n \qquad (11.56)$$

holds, where n is integer and $t_p \approx 6.2$ is the average duration of the pulse $v(x_0, t)$ (excited state duration plus refractory period, see Fig. 11.14). As seen from Fig. 11.13 (a), this expression can be used for quite an accurate estimate of $\langle T_i \rangle$ (grey dashed lines).

Finally, the effect of feedback was studied as a function of its strength K, as τ was fixed at two characteristic values corresponding to the maximum and to the minimum of regularity. In both cases, as K grows, the action of the feedback becomes more prominent, which is probably expected. Namely, if at the given value of τ the feedback increases (decreases) some characteristic quantity, the increase of K leads to the larger increase (decrease) of it.

11.4.5
What Can Be Controlled in an Excitable Medium?

Modeling of a real experiment with a photosensitive BZ medium has allowed us to predict that a nonlinear time delayed feedback will be able to manipulate the temporal and spatial regularity of noise-induced spatiotemporal patterns in a full-scale experiment as well. In the model, by choosing the appropriate time delay, one can deliberately increase or decrease both spatial and temporal regularity and adjust the timescales of the medium dynamics. The same study was done with the system using Neumann boundary conditions, under which the pulses are absorbed by the boundary. The dependences for $\langle T_i \rangle$, R_T, and $\langle \Delta_i \rangle$ match those in Fig. 11.13 with high accuracy. An experimental verification of the predicted effect of delayed feedback control remains a challenge for future work.

11.5
**Delayed Feedback Control of Noise-Induced Patterns
in a Globally Coupled Reaction–Diffusion Model**

In this section, we consider a reaction–diffusion model which exhibits a different kind of spatiotemporal patterns, namely localized breathing and spiking oscillations. It has been used to describe current density patterns in a semiconductor nanostructure, a double-barrier resonant tunneling diode (DBRT). More generally, it describes an extended medium of activator–inhibitor type with a global coupling [66]. We will study the effects of noise in this system and investigate whether we can control noise-induced spatiotemporal oscillations by the method of time delayed feedback [65, 67]. The model equations are given in dimensionless form by

$$\frac{\partial a}{\partial t} = f(a, u) + \frac{\partial}{\partial x}\left(D(a)\frac{\partial a}{\partial x}\right) + D_a \xi(x, t), \tag{11.57}$$

$$\frac{du}{dt} = \frac{1}{\varepsilon}(U_0 - u - rJ) + D_u \eta(t) - K[u(t) - u(t - \tau)]. \tag{11.58}$$

Here $u(t)$ is the inhibitor, and $a(x, t)$ is the activator variable. In the semiconductor context, $u(t)$ denotes the voltage drop across the nanostructure, which consists of two barriers and a quantum well embedded in between, and $a(x, t)$ is the electron density in the quantum well. The x coordinate describes the lateral re-distribution of electrons in the quantum well plane perpendicular to the current flow, giving rise to filamentary current densities. The nonlinear, nonmonotonic function $f(a, u)$ describes the balance of the incoming and outgoing current densities of the quantum well [66, 68, 69]

$$
\begin{aligned}
f(a, u) = &\left[\frac{1}{2} + \frac{1}{\pi}\arctan\left(\frac{2}{\gamma}\left(x_0 - \frac{u}{2} + \frac{d}{r_B}a\right)\right)\right] \\
&\times \left[\ln\left(1 + \exp\left(\eta_e - x_0 + \frac{u}{2} - \frac{d}{r_B}a\right)\right) - a\right] - a,
\end{aligned} \tag{11.59}
$$

and $D(a)$ is an effective diffusion coefficient, which is dependent on electron density [70]:

$$D(a) = a\left(\frac{d}{r_B} + \frac{1}{1 - \exp(-a)}\right). \tag{11.60}$$

In Eqs. (11.59) and (11.60) the parameters were set as $\gamma = 6$, $x_0 = 114$, $d/r_B = 2$, $\eta_e = 28$, and their physical meaning can be found, e.g., in [65]. The local current density in the device is $j(a, u) = \frac{1}{2}(f(a, u) + 2a)$, and $J = \frac{1}{L}\int_0^L jdx$ is associated with the global current. Equation (11.58) represents Kirchhoff's law of the circuit in which the device is operated, i.e., the total current J is the sum of the capacitive and the conductive currents. The external bias voltage U_0, the

dimensionless load resistance $r \sim R_L$, and the time-scale ratio $\varepsilon = R_L C/\tau_a$ (where C is the capacitance of the circuit and τ_a is the tunneling time) act as bifurcation parameters. We consider a system of width $L = 30$ with Neumann boundary conditions $\partial_x a = 0$ at $x = 0$ and $x = L$, corresponding to no charge transfer through the lateral boundaries.

The noise sources $\xi(x, t)$ and $\eta(t)$ represent uncorrelated Gaussian white noise of intensities D_a and D_u, respectively:

$$
\begin{aligned}
\langle \xi(x, t) \rangle = \langle \eta(t) \rangle &= 0 \qquad (x \in [0, L]), \\
\langle \xi(x, t) \xi(x', t') \rangle &= \delta(x - x') \delta(t - t'), \\
\langle \eta(t) \eta(t') \rangle &= \delta(t - t').
\end{aligned}
\tag{11.61}
$$

Here we concentrate on the effects of *external* noise modeled by the additional noise voltage $D_u \eta(t)$ in the current equation. This term is easily accessible in a real circuit and the noise intensity D_u can be adjusted in a large parameter range using a noise generator in parallel with the supply bias, as realized experimentally, e.g., in [24]. *Internal* fluctuations of the local current density on the other hand, e.g., shot noise [71], cannot be tuned from the outside. Therefore in the following we keep this value fixed at a small noise intensity of $D_a = 10^{-4}$, corresponding to a noise current density of the order of $50 \, \text{mA/cm}^2$, which is within the range of Poissonian shot noise currents. Time-delayed feedback is applied to the voltage variable u in Eq. (11.58), since the voltage is easily accessible in a real experiment. By varying the control amplitude K, we can adjust the strength of the control force; τ is the time delay of the feedback loop.

11.5.1
Spatiotemporal Dynamics in the Uncontrolled Deterministic System

In the noise-free, uncontrolled case, $D_u = D_a = K = 0$, one can calculate the nullclines of the system. These are plotted in Fig. 11.15 using the current–voltage projection of the originally infinite-dimensional phase space. There are three curves, the nullcline $\dot{u} = 0$ (i.e., the *load line*) and two nullclines $\dot{a} = 0$, one for a reduced system, including only spatially homogeneous states, and one for the full system. We call the system *spatially homogeneous* if the space dependent variable $a(x, t)$ is uniformly distributed over the whole width of the device, i.e., $a(x, t) = a(t)$ for all $x \in [0, L]$, otherwise it is called *spatially inhomogeneous*.

In Fig. 11.15 one can see the Z-shaped current–voltage characteristic of the DBRT (solid curve), and the inset represents our special regime of interest for the following investigations. We fix $\varepsilon = 6.2$ slightly below the Andronov-Hopf bifurcation, which occurs at $\varepsilon_{\text{Hopf}} \approx 6.469$. In this regime we have a stable, spatially inhomogeneous fixed point marked "I" in Fig. 11.15, which is determined by the intersection of the load line with the nullcline $\dot{a} = 0$ for inhomogeneous $a(x, t)$. The neighboring intersection of the load line with the homogeneous nullcline (marked "H") defines another, spatially homogeneous fixed point
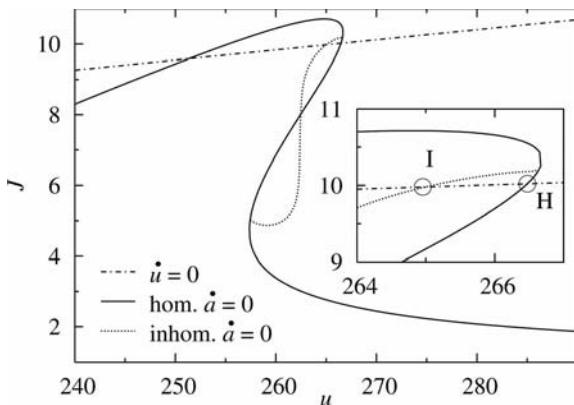
Fig. 11.15 Current–voltage characteristic of the DBRT model (11.57) and (11.58). The nullclines for the dynamical variables u (which is the load line, dash-dotted) and a in the case of a homogeneous $a(x)$ (solid) and in the case of inhomogeneous $a(x)$ (dotted) are shown. The inset shows an enlargement, where I and H mark the inhomogeneous and the homogeneous fixed points of the system, respectively. $U_0 = -84.2895$, $r = -35$. Other parameters are as in [67, 72].

which is a saddle-point. It is stable with respect to completely homogeneous perturbations but generally unstable against spatially inhomogeneous fluctuations.

Finally, the system (11.57) and (11.58) has a stable homogeneous fixed point which is characterized by negative voltage u and almost zero current density J. This point corresponds to the nonconducting regime of the DBRT, which is beyond the scope of the present study.

In Fig. 11.16 one can see a rather rapid transition of the deterministic system from the slightly perturbed homogeneous fixed point (H) to the inhomogeneous filamentary one (I). This illustrates that for the given parameters, the only stable solution, apart from a trivial, nonconducting fixed point, is an inhomogeneous steady state.
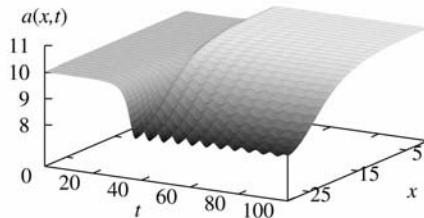
To quantify the degree of (in)homogeneity we use the measure of the *absolute spatial variation* $v(t)$ of $a(x, t)$ defined by

$$v(t) \equiv \int_0^L \left| \frac{\partial a(x, t)}{\partial x} \right| \mathrm{d}x. \tag{11.62}$$

For completely homogeneous states $a(x, t) = a(t)$ the absolute spatial variation equals zero and the larger $v(t)$ grows, the more inhomogeneous the spatial charge carrier density distribution $a(x, t)$ appears. In Fig. 11.16 (b) the spatial variation of $v(t)$ tends toward a fixed value of approximately 2.6, indicating the inhomogeneity of the corresponding fixed point.

Note that beyond the Andronov-Hopf bifurcation of the spatially inhomogeneous fixed point, complex chaotic scenarios including spatiotemporal breathing

a)

b)
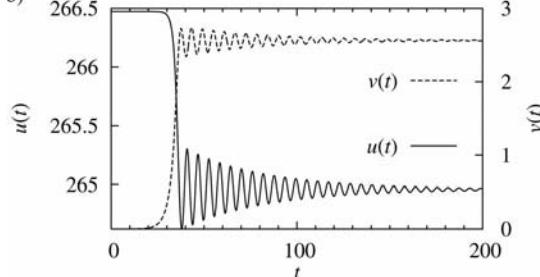
Fig. 11.16 Transition from the homogeneous initial state to the spatially inhomogeneous fixed point due to a small spatially inhomogeneous perturbation in Eqs. (11.57) and (11.58) in the noise-free case. (a) Charge carrier density distribution $a(x, t)$. (b) Time series $v(t)$ (dashed) and $u(t)$ (solid). At $t = 0$ the system is prepared in the homogeneous fixed point $u(0) = 266.47$, $a(x, 0) = 10.02$ with a very small initial random perturbation. System parameters: $U_0 = -84.2895$, $r = -35$, $\varepsilon = 6.2$, $D_a = D_u = 0$ [67].

and spiking oscillations occur [69]. These deterministic space–time patterns can also be stabilized by time delayed feedback control, as discussed in Chapter 24 of this book. However, here we confine our attention to a different parameter regime, where the inhomogeneous fixed point is stable.

11.5.2
Noise-Induced Patterns in the Uncontrolled System

In the following, we will investigate the behavior of the uncontrolled system under variation of the noise intensity D_u. Note that this noise term does not have any space-dependent influence upon a. Now we initialize the system at the inhomogeneous fixed point and simulate it with different noise intensities D_u. The results can be seen in Fig. 11.18. While for small noise the system exhibits rather small oscillations around the inhomogeneous fixed point (topmost panel), with increasing noise intensity a transition to completely homogeneous oscillations occurs (bottom panel). For intermediate values of D_u one can see the competition between the inhomogeneous and the spatially homogeneous modes (middle panel). Let us now quantify the spatial and the temporal ordering of the system. We call the system spatially coherent if the space-dependent variable

$a(x, t)$ is uniformly distributed over the whole length of the device. In order to reveal whether a particular state of the system is spatially homogeneous or not we use the simple measure of the *absolute spatial variation* defined in Eq. (11.62). The temporal ordering of the system, on the other hand, can be measured by the correlation time [42]

$$t_{\text{cor}} \equiv \frac{1}{\sigma^2} \int_0^\infty |\Psi(s)| ds, \qquad (11.63)$$

where $\Psi(s) \equiv \langle (u(t) - \langle u \rangle)(u(t - s) - \langle u \rangle) \rangle$ is the autocorrelation function of the variable $u(t)$, and $\sigma_u^2 = \Psi(0)$ is its variance. By calculating the temporal mean values $\langle v \rangle$ of $v(t)$ for different D_u, we can characterize the degree of spatial homogeneity of the dynamics in dependence on the noise intensity. In Fig. 11.17 (a) these values are plotted versus the noise intensity, and one can see that the mean value of v monotonically tends toward zero with increasing noise, indicating an increase in spatial coherence. The error bars in this plot show the standard deviation. In fact, they reflect an essential feature of this transition; namely the competition between spatially inhomogeneous and homogeneous modes for intermediate values of D_u. The larger the standard deviation of v is, the more "mixed" the dynamics appears. Figure 11.17 (b) offers the same information showing the variance σ_v^2 of v versus D_u. For noise close to zero only, slight oscillations around the inhomogeneous fixed point with almost fixed spa-
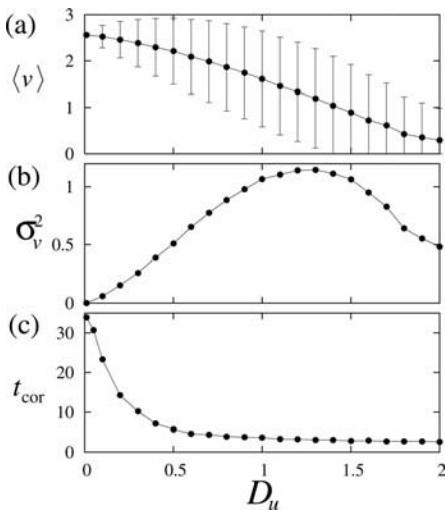
Fig. 11.17 Spatial and temporal ordering of the dynamics in Eqs. (11.57) and (11.58) in dependence of noise intensity D_u for $D_a = 0.001$. (a) Time-average $\langle v \rangle$ of the order parameter $v(t)$ defined by Eq. (11.62), error bars correspond to the standard deviation of v. (b) Variance σ_v^2 of the parameter v (corresponding to the square of the error bars from (a)). (c) Correlation time of the variable $u(t)$ as in Eq. (11.63) [67].

tial profile of $a(x, t)$ lead to a vanishingly small variance of v. With increasing noise, more and more frequently the system tends to a homogeneous state. The variance exhibits a maximum around $D_u = 1.3$, indicating maximal fluctuations of the system between homogeneous and inhomogeneous modes. Thus, this value could be treated as a boundary between predominantly filamentary and predominantly homogeneous behavior. For even larger noise intensity, the homogeneous mode is getting more and more dominant, and therefore the variance of v again falls off toward zero.

On the other hand, the correlation time versus noise intensity in Fig. 11.17 (c) shows that the temporal coherence of the system in contrast to the spatial ordering decreases rapidly with increasing noise.

In summary, noise induces oscillations in the system, which would otherwise rest in its inhomogeneous fixed point. With growing noise intensity, the dynamics changes from small inhomogeneous oscillations, which are quite coherent in time, to spatially homogenous oscillations, which on the other hand appear very irregular in time.

11.5.3
Time-Delayed Feedback Control of Noise-Induced Patterns

In order to control the noise-induced patterns, we will now use the method of time delayed feedback which was previously applied successfully in deterministic chaos control of this particular system [72].
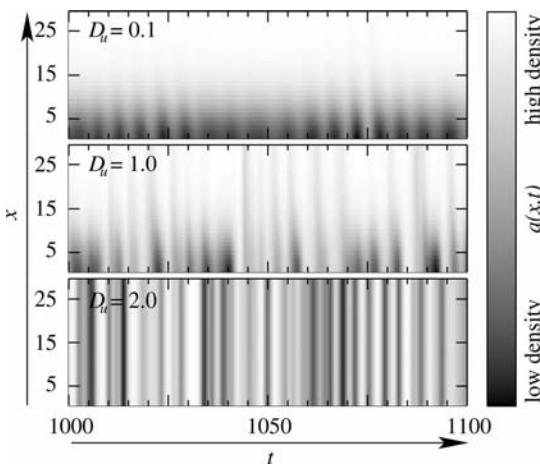
Fig. 11.18 Spatiotemporal patterns $a(x, t)$ in Eqs. (11.57) and (11.58), induced by noise with different intensities $D_u = 0.1, 1.0, 2.0$. At $t = 0$, the system is prepared in the spatially inhomogeneous steady state 'I' and with the parameters of Fig. 11.15. The system is then simulated with $D_a = 10^{-4}$ and D_u as indicated. $U_0 = -84.2895$, $r = -35$, $\varepsilon = 6.2$. Time t and space x are measured in units of the tunneling time τ_a and the diffusion length l_a, respectively. Typical values at 4 K are $\tau_a = 3.3$ ps and $l_a = 100$ nm [65].
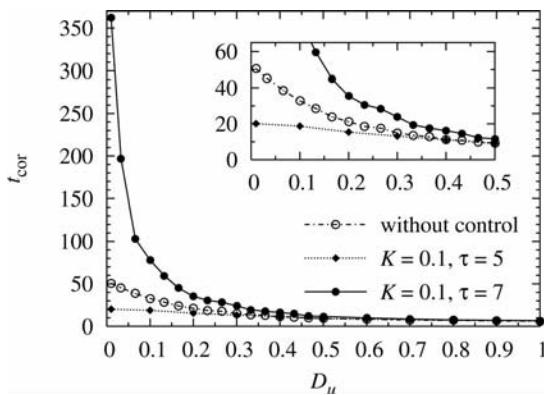
Fig. 11.19 Correlation time vs noise intensity D_u of oscillations in Eqs. (11.57) and (11.58), without control ($K = 0$) and with control and two different values of τ as indicated. Averages from 100 time series of length $T = 10000$, parameters as in Fig. 11.18. The inset shows a blow-up [65].
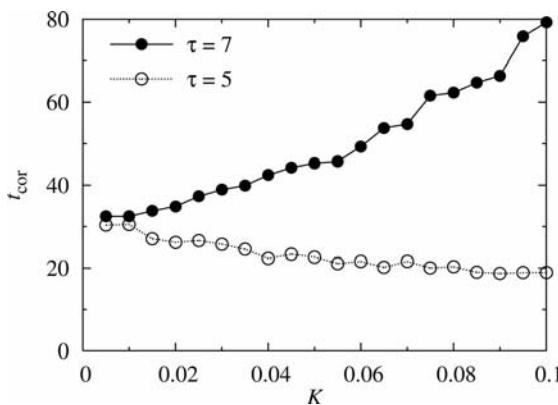
Fig. 11.20 Correlation time of oscillations in Eqs. (11.57) and (11.58) vs feedback strength K for $\tau = 5$ and $\tau = 7$. $D_u = 0.1$, $D_a = 10^{-4}$. Averages from 100 time series of length $T = 10\,000$, parameters as in Fig. 11.18 [65].

In order to get a first impression whether or not this control force is able to change the temporal regularity of the noise-induced oscillations, we fix $D_u = 0.1$, $D_a = 10^{-4}$, as in the upper panel of Fig. 11.18, and calculate the correlation time t_{cor} in dependence of the feedback strength K for two different delay times τ. From Fig. 11.20 one can see that the qualitative result depends strongly upon the choice of the delay time. While for $\tau = 7$ the control loop strongly increases the correlation time with increasing K, it is on the other hand able to decrease it significantly for $\tau = 5$. The same can be seen from

a)

b)
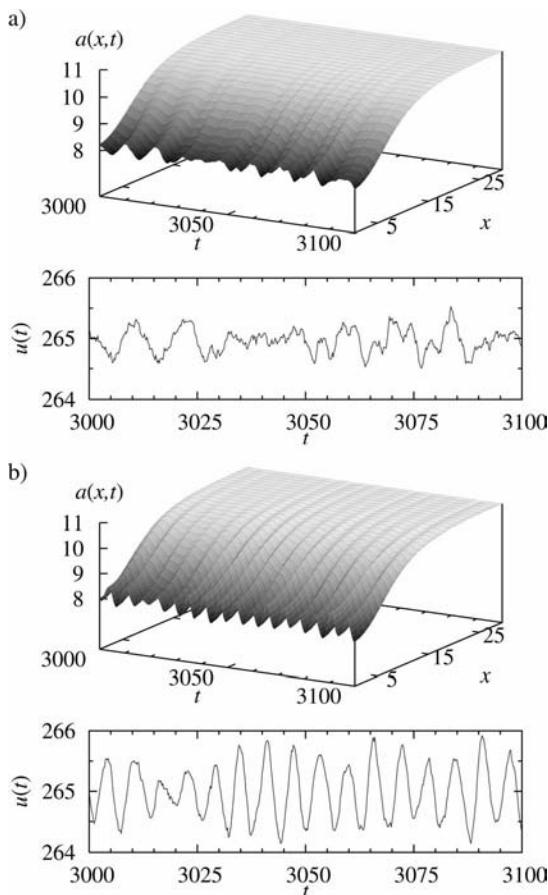
Fig. 11.21 Spatiotemporal patterns $a(x,t)$ and voltage time series $u(t)$ in Eqs. (11.57) and (11.58), for different values of the control strength K and delay time τ: (a) $\tau = 4.0$, $K = 0.4$, (b) $\tau = 13.4$, $K = 0.1$. $D_u = 0.1$, $D_a = 10^{-4}$ and other parameters as in Fig. 11.18 [65].

Fig. 11.19. Here, the control with $K = 0.1$ and $\tau = 7$ enhances t_{cor}, as compared with the uncontrolled case, over a relatively wide range of the noise intensity up to $D_u \approx 0.5$, whereas $\tau = 5$ decreases it within the same range. This behavior is very similar to that found for the van der Pol system in Section 11.2. The difference in regularity for different values of τ and K also shows up in the corresponding spatiotemporal patterns and voltage time series (Fig. 11.21), where (b) is clearly more regular than (a).

The role of the appropriate choice of the control delay τ becomes even clearer if we keep K fixed and calculate the correlation time in dependence of τ. The result is plotted in Fig. 11.22 (a), where one can clearly see the oscillatory charac-
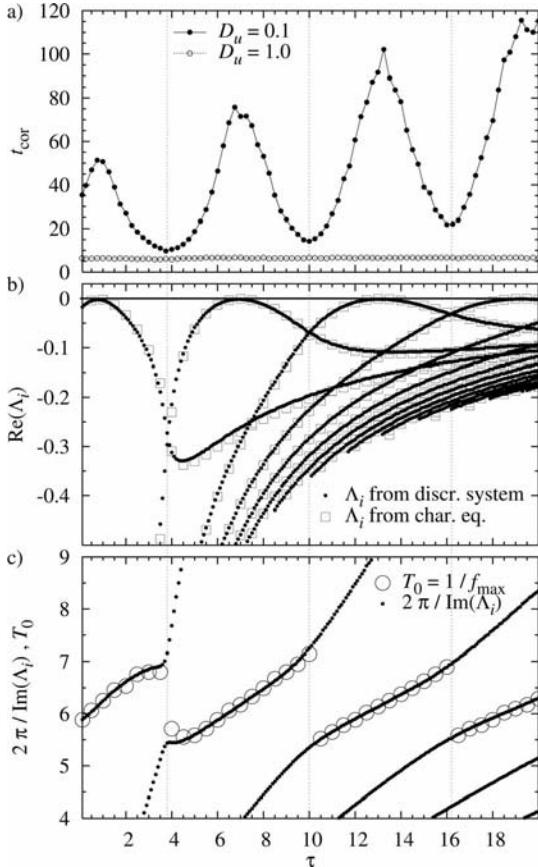
Fig. 11.22 Characteristics of noise-induced oscillations in Eqs. (11.57) and (11.58) under delayed feedback. (a) Correlation time (Eq. (11.63)) for two different noise intensities in dependence of the feedback delay τ. (b) Real parts of the eigenvalues Λ_i of the linearized deterministic system ($D_a = D_u = 0$) calculated at the spatially inhomogeneous fixed point for $K = 0.1$. The black dots are calculated from the spatially discretized system (set of ODEs) whereas the squares are calculated from Eq. (11.75) (see text). The vertical dotted lines mark values of τ at which the *leading* eigenvalue (i.e. the one with the largest real part) changes. (c) Eigenperiods $2\pi/\text{Im}(\Lambda_i)$ of the deterministic system and basic periods $T_0 := 1/f_{max}$ of the noise-induced oscillations, where f_{max} denotes the frequency of the highest peak in the Fourier power spectral density of the noisy system with $D_u = 0.1$, $K = 0.1$ [65].

ter of the correlation time under variation of τ, which is characterized by the presence of "optimal" values of τ, corresponding to the maximal regularity, and "worst" values of τ which are related to the minimal regularity of the noise-induced dynamics. At the same time, it is shown that the control with $K = 0.1$ produces no effect at all upon the correlation time if the noise is too large (lower curve for $D_u = 1.0$).

11.5.4
Linear Modes of the Inhomogeneous Fixed Point

The fact that noise-induced oscillations take place in the vicinity of the spatially inhomogeneous fixed point gives us a hint that some properties of these oscillations could relate to the stability of the above mentioned fixed point. In order to gain some insight into how the control actually affects the system dynamics around the spatially inhomogeneous fixed point, we linearize the system (11.57) and (11.58) for $D_u = D_a = 0$ and calculate the complex eigenvalues Λ_i at the fixed point. First, we calculate these eigenvalues from the spatially discretized system which we use for the numerical simulation. This discretized version is just a set of ordinary differential equations (ODEs), and the linearization and the eigenvalues can be computed easily.

In Fig. 11.22 (b) one can see that the control with $K = 0.1$ does not change the stability of the inhomogenous fixed point, since the real parts of all eigenvalues do not become positive within the given range of τ. Nevertheless, with increasing τ the real parts of the eigenvalues intersect at particular values of τ (vertical dotted lines) and therefore the *leading* eigenvalue, i.e., the *least stable* one, or the one with the largest real part, changes at these values of τ. As one can see, these crossover points correspond to the minima of the correlation time in Fig. 11.22 (a), whereas the local maxima of the real parts correspond to the maxima of the correlation time. This gives rise to a rather intuitive explanation for the behavior of the correlation time: The closer to zero the real part of an eigenvalue is, the weaker is the attracting stability of the fixed point and the easier it is for the noise to excite exactly the oscillating mode corresponding to this particular eigenvalue. On the other hand, at the intersection points of the real parts of the leading eigenvalue, these values have the largest distance from zero, meaning that the attracting stability of the fixed point is stronger and in addition there are two different corresponding oscillating modes which are excited by the noise. Thus the control cannot reach its optimal effect.

As a direct consequence, the main frequency which is activated by the noise, switches exactly at these values of τ to the eigenfrequency of the corresponding leading eigenvalue. In Fig. 11.22 (c) the eigenperiods are plotted as black dots in dependence of τ. The circles mark the positions of the highest peak in the Fourier power spectrum for the corresponding noisy system with $D_u = 0.1$. One can clearly see that these main periods switch from one branch to another exactly at the positions where the real parts of two different eigenvalues cross over. As we have already noted, the eigenvalues for the linearized deterministic system at the inhomogeneous fixed point, plotted as black dots in Fig. 11.22 (b) and (c), are computed numerically for the system (11.57) in the deterministic case by using the spatially discretized set of ordinary differential equations.

In order to achieve a deeper understanding of the stability properties of the inhomogeneous fixed point under the influence of the control force, and to obtain the general form of the characteristic equation which determines the eigenvalues of this linearized system, we perform the linearization of the original

continuous system (11.57) and (11.58) at the spatially inhomogeneous fixed point $(a_0(x), u_0)$. Introducing

$$a_x \equiv \frac{\partial a}{\partial x}, \qquad a_{xx} \equiv \frac{\partial^2 a}{\partial x^2}, \qquad b(a, a_x, a_{xx}) \equiv \frac{\partial}{\partial x}(D(a)a_x), \tag{11.64}$$

and a linear operator

$$\mathcal{L} \equiv \left. \frac{\partial f}{\partial a} \right|_{a_0, u_0} + \left. \frac{\partial b}{\partial a} \right|_{a_0} + \left. \frac{\partial b}{\partial a_x} \right|_{a_0} \frac{\partial}{\partial x} + \left. \frac{\partial b}{\partial a_{xx}} \right|_{a_0} \frac{\partial^2}{\partial x^2}, \tag{11.65}$$

and using the ansatz $\delta a(x, t) = e^{\Lambda t} \tilde{a}(x)$, $\delta u(t) = e^{\Lambda t} \tilde{u}$ for the deviations from the fixed point, we can write down the coupled eigenvalue problem:

$$\Lambda \tilde{a}(x) = \mathcal{L}\tilde{a}(x) + f_u(x)\tilde{u}, \tag{11.66}$$

$$\Lambda \tilde{u} = -\frac{r}{\varepsilon L} \int_0^L j_a(x)\tilde{a}(x)\mathrm{d}x + \left[-\frac{1 + rJ_u}{\varepsilon} + K\left(e^{-\Lambda \tau} - 1\right) \right] \tilde{u}, \tag{11.67}$$

$$\text{with} \quad f_u \equiv \left. \frac{\partial f}{\partial u} \right|_{a_0, u_0}, \quad j_a \equiv \left. \frac{\partial j}{\partial a} \right|_{a_0, u_0}, \quad J_u \equiv \frac{1}{L}\int_0^L \left. \frac{\partial j}{\partial u} \right|_{a_0, u_0} \mathrm{d}x.$$

For the case $K = 0$ this eigenvalue problem of the inhomogeneous filamentary fixed point has been analyzed generally [73]. In the voltage-clamped case ($\delta u = 0$), the Sturmian eigenvalue equation $\lambda \tilde{a} = \mathcal{L}\tilde{a}$ with Neumann boundary conditions (which can be shown to be self-adjoint) has solutions $\lambda_0 > \lambda_1 > \lambda_2 > \cdots$ where the corresponding eigenmode $\psi_n(x)$ has n nodes, and $\lambda_0 > 0$, while for $n \geq 1$ all other eigenvalues are negative, $\lambda_n < 0$. The eigenmodes $\tilde{a}(x)$ of the full Eqs. (11.66) and (11.67) can be expanded in terms of the voltage-clamped eigenmodes $\psi_n(x)$

$$\tilde{a}(x) = \sum_n (\tilde{a}, \psi_n)\psi_n(x), \tag{11.68}$$

where $(\tilde{a}, \psi_n) \equiv \frac{1}{L}\int_0^L \tilde{a}(x)\psi_n(x)\mathrm{d}x$ denotes the usual scalar product in Hilbert space. Inserting this into Eq. (11.66) yields

$$\Lambda \sum_n (\tilde{a}, \psi_n)\psi_n(x) = \sum_n \lambda_n(\tilde{a}, \psi_n)\psi_n(x) + f_u(x)\tilde{u}. \tag{11.69}$$

Forming the scalar product with ψ_m and using orthonormality gives the expansion coefficients

$$(\tilde{a}, \psi_m) = \frac{(f_u, \psi_m)}{\Lambda - \lambda_m}\tilde{u}. \tag{11.70}$$

The expansion (11.68) can be inserted into Eq. (11.67):

$$\Lambda \tilde{u} = \left[-\frac{r}{\varepsilon} \sum_n \frac{(f_u, \psi_n)(j_a, \psi_n)}{\Lambda - \lambda_m} - \frac{1 + rJ_u}{\varepsilon} + K\left(e^{-\Lambda\tau} - 1\right) \right] \tilde{u}. \tag{11.71}$$

We will now neglect the higher modes ψ_n because they oscillate fast whereas $a_0(x)$ varies slowly in space, and approximate the sum in Eq. (11.68) by the dominant first term ψ_0 with $\lambda_0 > 0$. We obtain the characteristic equation for the eigenvalue Λ:

$$\Lambda^2 + \left(\frac{1 + rJ_u}{\varepsilon} - \lambda_0 \right)\Lambda + (\lambda_0 - \Lambda)K\left(e^{-\Lambda\tau} - 1\right) - \frac{\lambda_0}{\varepsilon}(1 + r\sigma_d) = 0, \tag{11.72}$$

where the static differential conductance σ_d at the inhomogeneous fixed point

$$\sigma_d \equiv \left. \frac{dJ}{du} \right|_{a_0, u_0} = J_u + \left(j_a, \frac{da}{du} \right) = J_u - (j_a, \psi_0)\frac{(f_u, \psi_0)}{\lambda_0} \tag{11.73}$$

has been introduced using Eqs. (11.68)–(11.70) in the static case $\Lambda = 0$ [66]. Without control, $K = 0$, Eq. (11.72) reduces to a characteristic polynomial of the second order, which gives the well-known conditions for the stability of a filament [73]:

$$A \equiv \frac{1 + rJ_u}{\varepsilon} - \lambda_0 > 0,$$
$$C \equiv -\frac{\lambda_0}{\varepsilon}(1 + r\sigma_d) > 0. \tag{11.74}$$

Without control, an Andronov-Hopf bifurcation on the two-dimensional center manifold occurs if $A = 0$. With control, Eq. (11.72) can be expressed as

$$\Lambda^2 + A\Lambda + (B - \Lambda)K\left(e^{-\Lambda\tau} - 1\right) + C = 0 \tag{11.75}$$

with $B \equiv \lambda_0 > 0$. The parameters A, B, C can be calculated directly from Eq. (11.74). For the inhomogeneous fixed point, $\lambda_0 = 1.0281$ has been calculated in [74]; $J_u = -0.1615$ can be obtained by using the condition for an Andronov-Hopf bifurcation ($A = 0$) in Eq. (11.74); $\sigma_d = 0.226$ can be estimated from the current-voltage characteristic shown in Fig. 11.15.

This yields $A = 0.0447$, $B = 1.0281$, and $C = 1.1458$. Note that in dimensional units the unstable eigenvalue of the voltage-clamped system $\lambda_0 = B$ is approximately equal to the inverse tunneling time $1/\tau_a$. With these values, we can solve Eq. (11.75). For $K = 0.1$ the real parts of this solution in dependence of τ are also shown in Fig. 11.22 (b) as squares. They coincide with very good accuracy.

In order to estimate the maxima of $p = \text{Re}(\Lambda)$ in dependence of the control delay τ (to find the "optimal" delay), we assume $p \approx 0$ (but $p \neq 0$!), $K \ll 1$ and

separate Eq. (11.75) into real and imaginary parts. A straightforward calculation yields that p has a maximum if $q\tau - \arctan\left(\dfrac{B}{q}\right) = 2\pi n$, n is integer. Since $q = \text{Im}(\Lambda) \approx 1$ in the vicinity of the maxima of p (cf. Fig. 11.22 (c)) and also $B \approx 1$, we get

$$\tau = 2\pi n + \frac{\pi}{4}. \tag{11.76}$$

According to this simple formula, the first four maxima of $p = \text{Re}(\Lambda)$ appear at $\tau \approx 0.8$, 7.1, 13.4, and 19.6, which is in very good agreement with Fig. 11.22 (b). Next, we consider the eigenvalues at larger values of τ, i.e., $\tau \gg 1$, $p \approx 0$, $q \neq 0$, in Eq. (11.75):

$$\cos\left(q\tau - \arctan\left(\frac{B}{q}\right)\right)\sqrt{\left(\frac{B}{q}\right)^2 + 1} = \frac{A + K}{K}. \tag{11.77}$$

This, with $A \approx 0$ and again $B/q \approx 1$, yields

$$\cos\left(q\tau - \frac{\pi}{4}\right) = \frac{1}{\sqrt{2}} \tag{11.78}$$

$$\Leftrightarrow q\tau - \frac{\pi}{4} = \frac{\pi}{4} + 2\pi n, \qquad n \in \mathbb{Z}. \tag{11.79}$$

Hence, we arrive at an estimate for the period $T = 2\pi/q$,

$$T = \frac{4\tau}{1 + 4n} \tag{11.80}$$

which describes the piecewise linear behavior of the eigenperiods for larger τ with again very good agreement.

Finally, we investigate the condition for an Andronov-Hopf bifurcation (i.e., $p = 0$, $q \neq 0$) in dependence of K. Equation (11.77) together with $B/q \approx 1$ yields

$$\cos\left(q\tau - \frac{\pi}{4}\right) = \frac{A + K}{K\sqrt{2}}. \tag{11.81}$$

If the right-hand side is larger than unity, no solution exists and thus no an Andronov-Hopf bifurcation and no instability of the fixed point can occur:

$$\frac{A + K}{K\sqrt{2}} > 1 \quad \Leftrightarrow \quad K < \frac{A}{\sqrt{2} - 1} \approx 0.1. \tag{11.82}$$

This determines a lower bound for the maximal control strength which we are not allowed to exceed, as long as we do not want to lose the original stability of the fixed point. This maximum is perfectly confirmed by Fig. 11.23 where the region is outlined, in which the inhomogeneous fixed point remains stable un-
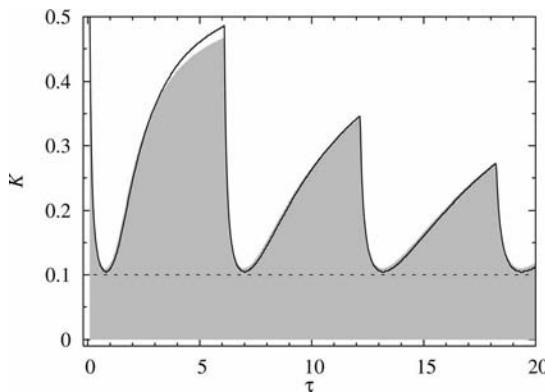
Fig. 11.23 Region of stability in the τ–K-plane of the deterministic system (11.57) and (11.58), $D_u = D_a = 0$. The area below the curve marks the region within which the inhomogeneous fixed point is still stable under the influence of the control loop. Within the upper region, the fixed point is unstable. The shaded area is calculated from the space discretized system of ODEs, whereas the black curve is calculated from Eq. (11.75). The dotted line corresponds to the upper bound of K given in Eq. 11.82) [65].

der the influence of the control term. Here, one can see the very good match between the stability region estimated from the space-discretized system of ODEs on the one hand (shaded area), and from the general characteristic equation (11.75) on the other hand (black curve).

11.5.5
Delay-Induced Oscillatory Patterns

So far, we have kept the control amplitude fixed and varied the control delay τ. But as we have already seen in Fig. 11.23, the control force can in principle change the deterministic behavior of the system. For a given τ and sufficiently large K, the control loop changes the deterministic dynamics of our system: The previously stable fixed point exhibits an Andronov-Hopf bifurcation, becomes unstable, and a stable periodic spatiotemporal pattern is induced in the system by the control loop. With increasing K, the shape of this induced periodic breathing pattern changes from small spatially inhomogeneous oscillations around the previously stable fixed point into a spatiotemporal spiking pattern and further into a completely spatially homogeneous oscillation. In order to see whether or not the deterministic spiking behavior still persists under the influence of noise, we have added different noise intensities to the system at $K = 1$. The result is shown in Fig. 11.24, and one can see that again increasing noise renders the dynamics more and more spatially homogeneous, even though there exists a deterministic stable limit cycle corresponding to a spiking pattern.
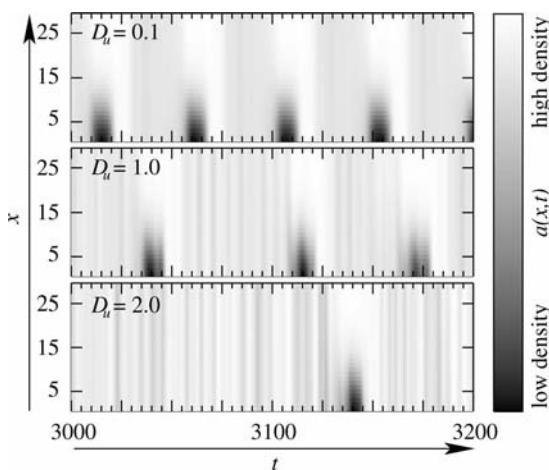
Fig. 11.24 Spatiotemporal patterns $a(x,t)$ of system (11.57) and (11.58) with noise and control, $K = 1.0$, $\tau = 7.0$, $D_a = 10^{-4}$, D_u as indicated, other parameters as in Fig. 11.18 [65].

11.5.6
What Can Be Controlled in a Globally Coupled Reaction–Diffusion System?

We have investigated the complex spatiotemporal behavior of a reaction–diffusion system of activator–inhibitor type with a global coupling due to the attached electrical circuit. Unlike the locally coupled reaction–diffusion system (Oregonator model) studied in the previous section, this model does not exhibit pulse or wave propagation for the parameters chosen. Rather, it exhibits noise-induced localized space–time patterns of breathing or spiking type if it is operated below the Andronov-Hopf bifurcation of the spatially inhomogeneous fixed point. In this respect, it generalizes the van der Pol system to a class of spatially extended systems, which show similar features of the correlation time and the spectrum of space-time patterns under the influence of time delayed feedback control. An important new aspect is, however, the spatial degree of freedom. The noise which is applied globally to a space-independent variable determines the type of the spatiotemporal pattern of these oscillations. While for small noise intensity the system demonstrates oscillations which are quite correlated in time, but spatially inhomogeneous, with increasing noise intensity the shape of the spatiotemporal pattern changes qualitatively until the system reaches a highly homogeneous state. Thus, the increase of spatial coherence is accompanied by the decrease of temporal correlation of the observed oscillations. In between these two situations, for intermediate noise strength one can observe complex spatiotemporal behavior resulting from the competition between homogeneous and inhomogeneous oscillations. Delayed feedback is an efficient method for the manipulation of essential characteristics of noise-induced spatiotem-

poral dynamics, i.e., timescales, temporal regularity, and spatial homogeneity. The model can be used to describe the spatiotemporal current density patterns in a semiconductor nanostructure, namely, the double barrier resonant tunneling diode (DBRT). Noise-induced space-time patterns and their control by time delayed feedback have also been investigated for a different semiconductor nanostructure consisting of a periodic sequence of barriers and quantum wells, i.e., a superlattice [48, 75]. It exhibits complex nonlinear dynamics of interacting charge fronts, and demonstrates coherence resonance of noise-induced moving front patterns. It is an excitable medium, and the coherence and timescales of noise-induced oscillations in this nanostructure can also be manipulated by time delayed feedback.

11.6
Summary and Conclusions

The present work is devoted to the review of the existing methods of control of noise-induced dynamics. Several paradigmatic models demonstrating different types of this dynamics are considered: a system below an Andronov-Hopf bifurcation, a single excitable system, an excitable spatially extended medium, and a globally coupled reaction–diffusion system. Although these systems are very different in their structure, application of the delayed feedback to them has remarkably revealed some universal features, like the ability to adjust timescales and regularity of the motion that was induced merely by external random fluctuations, by choosing the appropriate values of the feedback parameters K and τ. Moreover, increase of τ causes an approximately piecewise linear increase of the basic timescales of this motion, although the proportionality coefficient is different for different ranges of τ. This phenomenon can be associated with the phenomenon of autosynchronization that was earlier discovered in purely deterministic systems.

Acknowledgments

References

1 *Task Force of the European Society of Cardiology and the North American Society of Pacing and Electrophysiology. Heart rate variability: standards of measurement, phys-iological interpretation and clinical use*, Circulation **93**, 1043 (1996).

2 J. Bancaud, O. Henriksen, F. Rubio-Donnadieu, M. Seino, F. E. Dreifuss, and J. K. Penry: *Proposal for revised clinical*

and electroencephalographic classification of epileptic seizures, Epilepsia **22**, 489 (1981).

3 F. A. Lenz, H. C. Kwan, R. L. Martin, R. R. Tasker, J. O. Dostrovsky, and Y. E. Lenz: *Single unit analysis of the human ventral thalamic nuclear group: Tremor-related activity in functionally identified cells*, Brain **117**, 531 (1994).

4 T. Kapitaniak: *Controlling Chaos: Theoretical and Practical Methods in Non-Linear Dynamics*, Academic Press, New York, London, 1996.

5 H. G. Schuster (Ed.): *Handbook of Chaos Control: Foundations and Applications*, first edn, Wiley-VCH, Weinheim, 1999.

6 S. Boccaletti, C. Grebogi, Y.-C. Lai, H. Mancini, and D. Maza: *The control of chaos: theory and applications*, Phys. Rep. **329**, 103–197 (2000).

7 R. Lima and M. Pettini: *Suppression of chaos by resonant parametric perturbations*, Phys. Rev. A **41**, 726–733 (1990).

8 E. Ott, C. Grebogi, and J. A. Yorke: *Controlling chaos*, Phys. Rev. Lett. **64**, 1196–1199 (1990).

9 K. Pyragas: *Continuous control of chaos by self-controlling feedback*, Phys. Lett. A **170**, 421–428 (1992).

10 D. Goldobin, M. Rosenblum, and A. Pikovsky: *Controlling oscillator coherence by delayed feedback*, Phys. Rev. E **67**, 061119 (2003).

11 R. Benzi, A. Sutera, and A. Vulpiani: *The mechanism of stochastic resonance*, J. Phys. A **14**, L453–L458 (1981).

12 P. Jung: *Periodically driven stochastic systems*, Phys. Rep. **234**, 175–295 (1993).

13 L. Gammaitoni, M. Locher, A. Bulsara, P. Hanggi, J. Neff, K. Wiesenfeld, W. Ditto, and M.E. Inchiosa: *Controlling stochastic resonance*, Phys. Rev. Lett. **82**, 4574–4577 (1999).

14 J. F. Lindner, J. Mason, J. Neff, B. J. Breen, W. L. Ditto, and A. R. Bulsara: *Noninvasive control of stochastic resonance*, Phys. Rev. E **63**, 041107 (2001).

15 S. Zeng and P. Jung: *Mechanism for neuronal spike generation by small and large ion channel cluster*, Phys. Rev. E **70**, 011903 (2004).

16 Hu Gang, T. Ditzinger, C. Z. Ning, and H. Haken: *Stochastic resonance without external periodic force*, Phys. Rev. Lett. **71**, 807–810 (1993).

17 A. S. Pikovsky and J. Kurths: *Coherence resonance in a noise-driven excitable system*, Phys. Rev. Lett. **78**, 775–778 (1997).

18 A. Neiman, P. I. Saparin, and L. Stone: *Coherence resonance at noisy precursors of bifurcations in nonlinear dynamical systems*, Phys. Rev. E **56**, 270 (1997).

19 K. Wiesenfeld and F. Moss: *Stochastic resonance and the benefits of noise: from ice ages to crayfish and SQUID*, Nature (London) **373**, 33–36 (1995).

20 V. S. Anishchenko, A. B. Neiman, F. Moss, and L. Schimansky-Geier: *Stochastic resonance: noise enhanced order*, Physics-Uspekhi **42**, 7–39 (1999).

21 G. Giacomelli, M. Giudici, S. Balle, and J. R. Tredicce: *Experimental evidence of coherence resonance in an optical system*, Phys. Rev. Lett. **84**, 3298–3301 (2000).

22 K. Miyakawa and H. Ishikawa: *Experimental observation of coherence resonance in an excitable chemical reaction system*, Phys. Rev. E **66**, 046204 (2002).

23 G. Schmidt, I. Goychuk, and P. Hänggi: *Channel noise and synchronization in excitable membranes*, Physica A **325**, 165–175 (2003).

24 V. V. Sherstnev, A. Krier, A. G. Balanov, N. B. Janson, A. N. Silchenko, and P. V. E. McClintock: *The stochastic laser: mid-infrared lasing induced by noise*, Fluct. Noise Lett. **3**, L91–L95 (2003).

25 O. V. Ushakov, H.-J. Wünsche, F. Henneberger, I. A. Khovanov, L. Schimansky-Geier, and M. A. Zaks: *Coherence resonance near a Hopf bifurcation*, Phys. Rev. Lett. **95**, 123903 (2005).

26 D. J. Christini and J. J. Collins: *Controlling nonchaotic neuronal noise using chaos control techniques*, Phys. Rev. Lett. **75**, 2782–2785 (1995).

27 P. S. Landa, A. A. Zaikin, M. G. Rosenblum, and J. Kurths: *Control of noise-induced oscillations of a pendulum with a randomly vibrating suspension axis*, Phys. Rev. E **56**, 1465–1470 (1997).

28 M. E. Bleich and J. E. S. Socolar: *Stability of periodic orbits controlled by time-delay feedback*, Phys. Lett. A **210**, 87 (1996).

29 W. Just, T. Bernard, M. Ostheimer, E. Reibold, and H. Benner: *Mechanism of*

time delayed feedback control, Phys. Rev. Lett. **78**, 203 (1997).

30 H. Nakajima: *On analytical properties of delayed feedback control of chaos*, Phys. Lett. A **232**, 207 (1997).

31 W. Just, E. Reibold, H. Benner, K. Kacperski, P. Fronczak, and J. Holyst: *Limits of time delayed feedback control*, Phys. Lett. A **254**, 158 (1999).

32 B. Fiedler, V. Flunkert, M. Georgi, P. Hövel, and E. Schöll: *Refuting the odd number limitation of time delayed feedback control*, Phys. Rev. Lett. **98**, 114101 (2007).

33 A. G. Balanov, N. B. Janson, and E. Schöll: *Delayed feedback control of chaos: Bifurcation analysis*, Phys. Rev. E **71**, 016222 (2005).

34 N. B. Janson, A. G. Balanov, and E. Schöll: *Delayed feedback as a means of control of noise-induced motion*, Phys. Rev. Lett. **93**, 010601 (2004).

35 A. G. Balanov, N. B. Janson, and E. Schöll: *Control of noise-induced oscillations by delayed feedback*, Physica D **199**, 1–12 (2004).

36 H. Treutlein and K. Schulten: *Noise-induced neural impulses*, Eur. Biophys. J. **13**, 355–365 (1986); *Noise induced limit cycles of the Bonhoeffer-van der Pol model of neural pulses*, Ber. Bunsenges. Phys. Chem. **89**, 710 (1985).

37 E. I. Verriest and P. Florchinger: *Stability of stochastic systems with uncertain time delays*, System & Control Lett. **24**, 41–47 (1995).

38 F. M. Asl and A. G. Ulsoy: *Analysis of a system of linear delay differential equations*, J. Dynamic Sys., Meas. Control **125**, 215–223 (2003).

39 A. Amann, E. Schöll, and W. Just: *Some basic remarks on eigenmode expansions of time delay dynamics*, Physica A **373**, 191 (2007).

40 C. W. Gardiner: *Handbook of Stochastic Methods*, Springer, Berlin, Heidelberg, 2004.

41 E. Schöll, A. Balanov, N. B. Janson, and A. Neiman: *Controlling stochastic oscillations close to a Hopf bifurcation by time delayed feedback*, Stoch. Dyn. **5**, 281 (2005).

42 R. L. Stratonovich: *Topics in the Theory of Random Noise*, Vol. 1, Gordon and Breach, New York, 1963.

43 J. Pomplun, A. Amann, and E. Schöll: *Mean field approximation of time delayed feedback control of noise-induced oscillations in the van der Pol system*, Europhys. Lett. **71**, 366 (2005).

44 N. G. van Kampen: *Stochastic Processes in Physics and Chemistry*, North-Holland, Amsterdam, 1992.

45 B. Lindner, J. García-Ojalvo, A. Neiman, and L. Schimansky-Geier: *Effects of noise in excitable systems*, Phys. Rep. **392**, 321 (2004).

46 H. Tuckwell: *Introduction to Theoretical Neurobiology*, Vol. 1, Cambridge University Press, Cambridge, 1988.

47 S. Alonso, I. Sendiña-Nadal, V. Pérez-Muñuzuri, J. M. Sancho, and F. Sagués: *Regular wave propagation out of noise in chemical active media*, Phys. Rev. Lett. **87**, 078302 (2001).

48 J. Hizanidis, A. G. Balanov, A. Amann, and E. Schöll: *Noise-induced front motion: signature of a global bifurcation*, Phys. Rev. Lett. **96**, 244104 (2006).

49 B. Lindner and L. Schimansky-Geier: *Analytical approach to the stochastic Fitz-Hugh-Nagumo system and coherence resonance*, Phys. Rev. E **60**, 7270–7276 (1999).

50 B. Hauschildt, N. B. Janson, A. G. Balanov, and E. Schöll: *Noise-induced cooperative dynamics and its control in coupled neural models*, Phys. Rev. E **74**, 051906 (2006).

51 G. J. Escalera Santos, J. Escalona, and P. Parmananda: *Regulating noise-induced spiking using feedback*, Phys. Rev. E **73**, 042102 (2006).

52 J. García-Ojalvo, A. Hernández-Machado, and J. M. Sancho: *Effect of external noise on the Swift-Hohenberg equation*, Phys. Rev. Lett. **71**, 1542–1545 (1993).

53 V. Beato, I. Sendiña-Nadal, I. Gerdes, and H. Engel: *Noise-induced wave nucleations in an excitable chemical reaction*, Phys. Rev. E **71**, 035204(R) (2005).

54 S. Kádár, J. Wang, and K. Showalter: *Noise-supported travelling waves in subexcitable media*, Nature **391**, 770 (1998).

55 P. Jung, A. Cornell-Bell, K. S. Madden, and F. Moss: *Noise-induced spiral waves in Astrocyte Syncytia show evidence of self-organized criticality*, J. Neurophysiol. **79**, 1098 (1998).

56 S. Coombes and Y. Timofeeva: *Sparks and waves in a stochastic fire-diffuse-fire model of* Ca^{2+} *release*, Phys. Rev. E **68**, 021915 (2003).

57 Y. Zhou and P. Jung: *Noise and complexity in three-dimensional excitable media*, Europhys. Lett. **49**, 695 (2000).

58 I. Sendiña-Nadal, S. Alonso, V. Perez-Munuzuri, M. Gomez-Gesteira, V. Perez-Villar, L. Ramirez-Piscina, J. Casademunt, J. M. Sancho, and S. Sagues: *Brownian Motion of Spiral Waves Driven by Spatiotemporal Structured Noise*, Phys. Rev. Lett. **84**, 2734 (2000).

59 H. J. Krug, L. Pohlmann, and L. Kuhnert: *Analysis of the Modified Complete Oregonator Accounting for Oxygen Sensitivity and Photosensitivity of Belousov-Zhabotinsky Systems*, J. Phys. Chem. **94**, 4862 (1990).

60 J. Bragard and S. Boccaletti: *Integral behavior for localized synchronization in non-identical extended systems*, Phys. Rev. E **62**, 6346 (2000).

61 V. Beato and H. Engel: *Coherence resonance phenomena in an excitable system driven by colored noise*, Noise Fluct. Lett. **6**, L85–L94 (2006).

62 V. Beato and H. Engel: *Pulse propagation in a model for photosensitive Belousov-Zhabotinsky reaction with external noise*, SPIE Proceedings **5114**, 353 (2003).

63 L. Q. Zhou, X. Jia and Q. Ouyang: *Experimental and numerical studies of noise-induced coherent patterns in a subexcitable system*, Phys. Rev. E **88**, 138301 (2002).

64 A. G. Balanov, V. Beato, N. B. Janson, H. Engel, and E. Schöll: *Delayed feedback control of noise-induced patterns in excitable media*, Phys. Rev. E **74**, 016214 (2006).

65 G. Stegemann, A. G. Balanov, and E. Schöll: *Delayed feedback control of stochastic spatiotemporal dynamics in a*

resonant tunneling diode, Phys. Rev. E **73**, 016203 (2006).

66 E. Schöll: *Nonlinear spatio-temporal dynamics and chaos in semiconductors*, Cambridge University Press, Cambridge, 2001.

67 G. Stegemann, A. G. Balanov, and E. Schöll: *Noise-induced pattern formation in a semiconductor nanostructure*, Phys. Rev. E **71**, 016221 (2005).

68 M. Meixner, P. Rodin, E. Schöll, and A. Wacker: *Lateral current density fronts in globally coupled bistable semiconductors with S- or Z-shaped current voltage characteristic*, Eur. Phys. J. B **13**, 157 (2000).

69 E. Schöll, A. Amann, M. Rudolf, and J. Unkelbach: *Transverse spatio-temporal instabilities in the double barrier resonant tunneling diode*, Physica B **314**, 113 (2002).

70 V. Cheianov, P. Rodin, and E. Schöll: *Transverse coupling in bistable resonant-tunneling structures*, Phys. Rev. B **62**, 9966 (2000).

71 Y. M. Blanter and M. Büttiker: *Shot noise in mesoscopic conductors*, Phys. Rep. **336**, 1 (2000).

72 J. Unkelbach, A. Amann, W. Just, and E. Schöll: *Time-delay autosynchronization of the spatio-temporal dynamics in resonant tunneling diodes*, Phys. Rev. E **68**, 026204 (2003).

73 A. Alekseev, S. Bose, P. Rodin, and E. Schöll: *Stability of current filaments in a bistable semiconductor system with global coupling*, Phys. Rev. E **57**, 2640 (1998).

74 J. Unkelbach: *Rückkopplungsgesteuerte transversale Dynamik der resonanten Tunneldiode*, Master's thesis, TU Berlin (2002).

75 J. Hizanidis, A. G. Balanov, A. Amann, and E. Schöll: *Noise-induced oscillations and their control in semiconductor superlattices*, Int. J. Bifur. Chaos **16**, 1701 (2006).

12
Controlling Coherence of Noisy and Chaotic Oscillators by Delayed Feedback

Denis Goldobin, Michael Rosenblum, and Arkady Pikovsky

We describe a method to control the coherence of oscillations by a delayed feedback. It can be applied to noisy periodic as well as to chaotic autonomous oscillations and allows one to modify the diffusion constant of the phase. Particularly, coherence can be improved what makes oscillations easier to synchronize. A multiple delay control shows better performance than the single-delay one. We present the theory of the delayed feedback control based on the Gaussian approximation of the noisy phase dynamics.

Coherence is one of the main characteristics of self-oscillating systems. For periodic oscillators it determines their quality as clocks, and usually the improvement of the coherence is one of the major goals in the construction of such oscillators. In terms of the phase dynamics, the coherence is quantitatively measured by the phase diffusion constant. It is proportional to the width of the spectral peak of oscillations. Many chaotic oscillators can also be described in the framework of the phase dynamics, thus allowing one to characterize their coherence by virtue of the phase diffusion constant as well [1].

In this chapter we describe how the coherence of oscillations is influenced by external delayed feedback. Application of a delayed feedback is widely used to control different properties of the dynamical systems: to make chaotic oscillators operate periodically (Pyragas' control method [2]), to control space–time chaos [3, 4], to suppress collective synchrony in oscillator populations [5–8] (see also the contribution of Tass et al. in this book). In this chapter we are not considering such delay-induced qualitative changes in the dynamics, but focus on the quantitative effect of a delayed feedback on the phase diffusion properties. This chapter is based on recent publications [9–11].

12.1
Control of Coherence: Numerical Results

12.1.1
Noisy Oscillator

In this section we present a numerical evidence for a possibility to control the phase coherence by a delayed feedback. We begin by presenting the results of numerical simulation for noisy van der Pol oscillator:

$$\ddot{x} - \mu(1 - x^2)\dot{x} + \Omega_0^2 x = k(\dot{x}(t - \tau) - \dot{x}(t)) + \zeta(t)$$
$$\langle \zeta(t)\zeta(t')\rangle = 2d^2\delta(t - t')\,. \tag{12.1}$$

The left-hand side represents the van der Pol equation; in the absence of noise and delay ($k = d = 0$) and for small nonlinearity μ this model has a limit cycle solution $x_0 \approx 2\cos\phi$, $\dot{x}_0 \approx -2\Omega_0\sin\phi$ with a uniformly growing phase $\phi(t) \approx \Omega_0 t + \phi_0$ [12]. Under the influence of noise and in the absence of feedback ($k = 0$, $d > 0$), $\phi(t)$ diffuses according to $\left\langle(\phi(t) - \langle\phi(t)\rangle)^2\right\rangle \propto D_0 t$; the diffusion constant D_0 is proportional to the intensity of noise d^2.

We expect that in the presence of feedback the diffusion constant D generally differs from D_0; this is confirmed by the numerical results, shown in Fig. 12.1 for $\Omega_0 = 1$, $d = 0.1$, and $\mu = 0.7$. One can see that diffusion can be suppressed or enhanced, depending on the feedback strength k and the delay time τ.
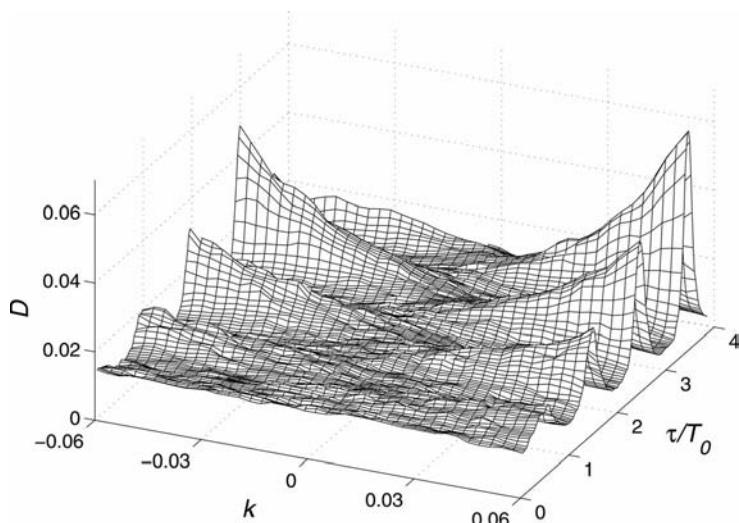
Fig. 12.1 Diffusion constant D for the phase of the noise-driven van der Pol oscillator with delayed feedback (12.1) as a function of τ/T_0 and k; $T_0 = 2\pi/\Omega_0 \approx 6.61$ is the oscillation period without delay.

12.1.2
Chaotic Oscillator

Another numerical example demonstrates the effect of delayed feedback on phase diffusion in the chaotic Lorenz model

$$\dot{x} = \sigma(y - x),$$
$$\dot{y} = rx - y - xz,$$
$$\dot{z} = -bz + xy + k(z(t - \tau) - z(t)),$$
(12.2)

where $\sigma = 10$, $r = 32$, and $b = 8/3$. The phase of the Lorenz system is well-defined if one uses a projection of the phase space on the plane $(u = \sqrt{x^2 + y^2}, z)$ (see [1] and Fig. 12.3). Note that there is no noise term in Eqs. (12.2): because of chaos the phase of the autonomous system grows nonuniformly, with a nonzero diffusion constant.

The dependence of the diffusion constant D of the phase on the feedback parameters k and τ is shown in Fig. 12.2. Qualitatively this dependence is similar to that for the van der Pol model. However, there is an important distinction: the diffusion has a very deep minimum for positive feedback constant k and the delay time close to the mean oscillation period; here the rotation of the phase point along the trajectory of the Lorenz system becomes highly coherent.
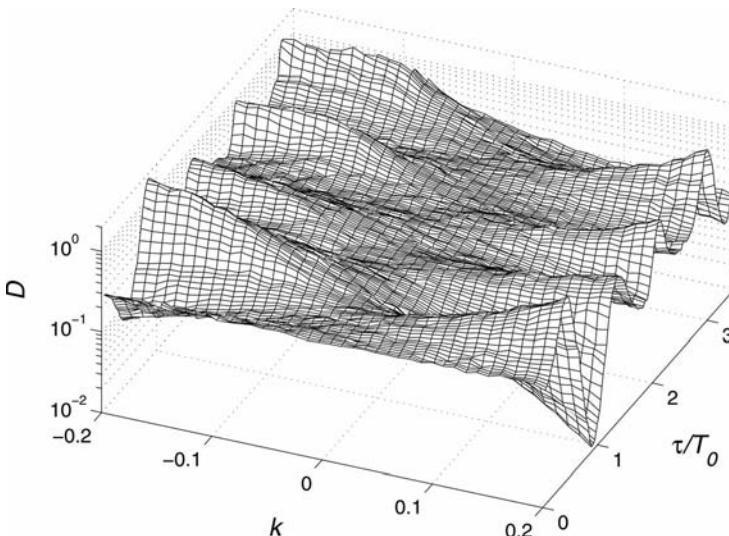
Fig. 12.2 Diffusion constant D for the Lorenz system (12.2) as the function of τ/T_0 and k. $T_0 \approx 0.69$ is the average oscillation period without delay. Note the logarithmic scale of the D-axis.

Another representation of the effect of the delayed feedback on the coherence of the process is given by the power spectrum. Indeed, the power spectrum of an oscillatory observable has a peak at frequency Ω_0, and the width of the peak is proportional to the diffusion constant D. In Fig. 12.3 we show how the feedback changes the spectrum of the Lorenz system for the cases of maximal enhancement and maximal suppression of the diffusion constant. In this figure we also demonstrate that the effect is not related to suppression of chaos: large variations of the diffusion constant (up to factor 10) are not reflected in the topology of the strange attractor; also the calculated Lyapunov exponents are very close to those without feedback. This suggests that the effect of feedback on the coherence can be described in the framework of phase approximation to the dy-
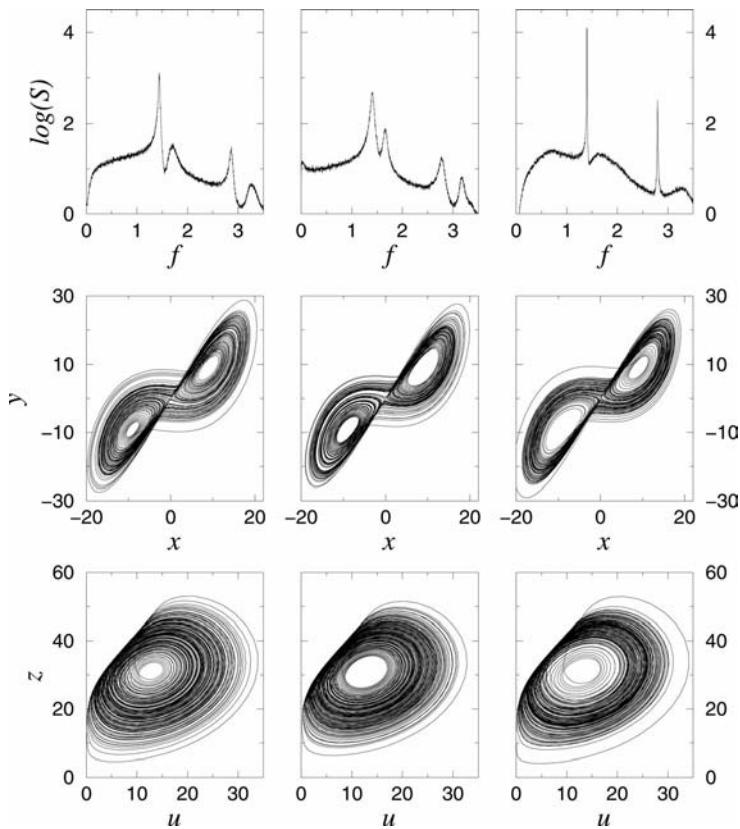
Fig. 12.3 Spectra of the *z* component of the Lorenz system and projections of the phase portrait for the system in the absence of delayed feedback (left column) and in the presence of feedback with delay $\tau = 0.3$ (middle column) and $\tau = 0.65$ (right column); feedback strength $k = 0.2$. Note that feedback makes the spectral peak essentially more broad (enhanced diffusion, middle column) or more narrow (suppressed diffusion, right column), whereas practically no changes can be seen in the phase portraits.
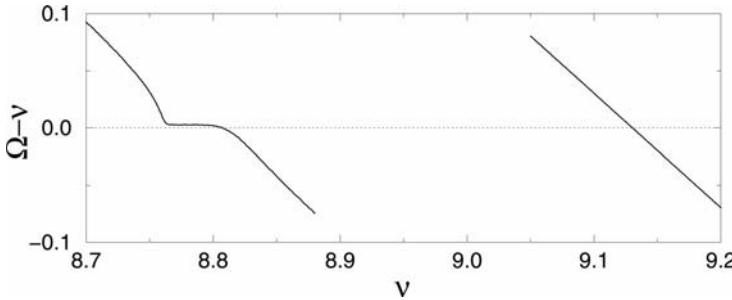
Fig. 12.4 Entrainment of the Lorenz system by a harmonic force with $E = 2$. Right graph: without feedback the mean oscillator frequency Ω is not locked to the driving frequency v. Left graph: the feedback with $k = 0.2$, $\tau = 0.65$ makes the oscillator coher- ent, what results in the appearance of the synchronization region $\Omega \approx v$ (cf. [14, 15]). Note also that the mean frequency is shifted by the feedback; this effect is theoretically explained below.

namics (this approximation has been used in [13] to describe phase synchroni- zation of chaotic oscillators).

12.1.3
Enhancing Phase Synchronization

One of the implications of the coherence control is a possibility to govern syn- chronization properties of an oscillator. Indeed, the ability of an oscillator to be entrained directly depends on the phase diffusion constant, thus improving co- herence means improving of the ability to synchronize [1]. We illustrate this by consideration of the phase synchronization of the Lorenz system by a periodic force $E \sin vt$ added to the equation for the variable z (Fig. 12.4). In the absence of the feedback the force is too weak to entrain the system, while the coherent oscillator demonstrates synchronization.

12.2
Theory of Coherence Control

12.2.1
Basic Phase Model

The basic model we study in this chapter is the equation describing the dy- namics of the phase under influence of noise and delay:

$$\dot{\phi} = \Omega_0 + \xi(t) + a \sin(\phi(t - \tau) - \phi(t)), \tag{12.3}$$

where the noisy term $\xi(t)$ is assumed to be Gaussian. Equation (12.3) has been used in [16] to describe evolution of the phase of an optical field in a laser with

weak optical feedback. Of our main interest are the diffusion properties of the phase $\phi(t)$. Under influence of the noise, in the absence of feedback, it diffuses $\langle(\phi(t) - \langle\phi(t)\rangle)^2\rangle \propto D_0 t$ with the diffusion constant $D_0 = \int_{-\infty}^{\infty} \langle\xi(t')\xi(t'+t)\rangle dt$. This constant determines the coherence of oscillations, as the power spectrum of an observable $x = \cos(\phi)$ has a peak at frequency Ω_0, whose width is D. The feedback changes the diffusion constant, and the main goal of our investigation is to find dependence of D on the parameters a, τ.

12.2.2
Noise-Free Case

We start our theoretical consideration with the noise-free case, when Eq. (12.3) reduces to $\dot{\phi} = \Omega_0 + a\sin(\phi(t-\tau) - \phi(t))$. If we seek for a solution with a uniformly rotating phase $\phi(t) = \Omega t$, we obtain

$$\Omega + a\sin\Omega\tau = \Omega_0 \,. \tag{12.4}$$

This equation has a unique solution for any Ω_0 if $|a\tau| < 1$, otherwise multiple solutions are possible. The latter case is especially difficult and will be considered elsewhere (see numerical simulations of effect of noise on the multistable states in (12.3) in [16]). Below we will consider a situation with small delayed feedback only, where no multistability occurs. We will also show that noise can destroy multistability, so that in its presence the condition $|a\tau| < 1$ can be weakened.

12.2.3
Gaussian Approximation

Our main statistical approach in studying Eq. (12.3) is based on the Gaussian approximation for $\phi(t)$. First, we separate the average rotation and the fluctuations according to $\phi = \Omega t + \psi$. For the fluctuating instantaneous frequency (which is also Gaussian) $v(t) = \dot{\psi}$ we get from (12.3)

$$v(t) = \Omega_0 - \Omega + \xi(t) - a\sin\Omega\tau\cos\eta + a\cos\Omega\tau\sin\eta \,. \tag{12.5}$$

The equation for the mean frequency Ω results from the averaging of (12.5): $0 = \Omega_0 - \Omega - a\sin\Omega\tau\langle\cos\eta\rangle$. The phase difference $\eta = \psi(t-\tau) - \psi(t) = -\int_{t-\tau}^{t} v(s)ds$ is Gaussian with zero average, thus

$$\langle\cos\eta\rangle = \exp\left[-\frac{\langle\eta^2\rangle}{2}\right], \quad \langle\eta^2\rangle = 2\int_0^{\tau}(\tau-s)V(s)ds \equiv 2R \,. \tag{12.6}$$

Here, we have introduced the autocorrelation function of the instantaneous frequency $V(s) = \langle v(t)v(t+s)\rangle$. In the introduced notations, the equation for the average frequency can be rewritten as

$$\Omega = \Omega_0 - ae^{-R}\sin\Omega\tau\,. \tag{12.7}$$

One can note that it is analogous to Eq. (12.4), but has an additional factor e^{-R}, which describes a reduction of the influence of the delayed feedback due to phase diffusion.

To obtain equations for the autocorrelation function $V(s)$ we also introduce the autocorrelation function of noise C and the cross-correlation function S, defined according to $C(s) = \langle \xi(t)\xi(t+s)\rangle$, $S(s) = \langle \xi(t)v(t+s)\rangle$. Equations for V and S are obtained via multiplication of Eq. (12.5) by $v(t+u)$ and $\xi(t+u)$ and averaging:

$$\langle v(t)v(t+u)\rangle = \langle \xi(t)v(t+u)\rangle - a\sin\Omega\tau\left\langle v(t+u)\cos\left(\int_{t-\tau}^{t}v(s)\mathrm{d}s\right)\right\rangle$$
$$- a\cos\Omega\tau\left\langle v(t+u)\sin\left(\int_{t-\tau}^{t}v(s)\mathrm{d}s\right)\right\rangle,$$

and similar for $\langle v(t)\xi(t+u)\rangle$. To accomplish the averaging we use the Furutsu–Novikov formula, valid for Gaussian variables x, y having zero averages: $\langle xF(y)\rangle = \langle xy\rangle\langle F'(y)\rangle$. With application to our averaging procedure this means that all averaged terms of the form $\langle x\cos y\rangle$ vanish and other give

$$\left\langle v(t+u)\sin\left(\int_{t-\tau}^{t}v(s)\mathrm{d}s\right)\right\rangle = e^{-R}\int_{-\tau}^{0}V(s-u)\mathrm{d}s\,,$$
$$\left\langle \xi(t+u)\sin\left(\int_{t-\tau}^{t}v(s)\mathrm{d}s\right)\right\rangle = e^{-R}\int_{-\tau}^{0}S(s-u)\mathrm{d}s\,.$$

As a result we obtain

$$V(u) = S(u) - ae^{-R}\cos\Omega\tau\int_{0}^{\tau}V(s+u)\mathrm{d}s\,, \tag{12.8}$$

$$S(u) = C(u) - ae^{-R}\cos\Omega\tau\int_{0}^{\tau}S(u-s)\mathrm{d}s\,. \tag{12.9}$$

Together with Eq. (12.7) and the definition of quantity R given by (12.6) they constitute a closed system.

To proceed further it is convenient to consider the spectra, according to

$$\mathcal{V}(\omega) = \frac{1}{2\pi}\int_{-\infty}^{\infty}\mathrm{d}u\,V(u)e^{-i\omega u}$$

and similar expressions for $\mathcal{S}, \mathcal{C}$ which are Fourier transforms of S and C, respectively. Then Eqs. (12.8) and (12.9) yield

$$\mathcal{V}(\omega) = \mathcal{S}(\omega) - ae^{-R}\cos\Omega\tau\frac{e^{i\omega\tau} - 1}{i\omega} \,,$$

$$\mathcal{S}(\omega) = \mathcal{C}(\omega) - ae^{-R}\cos\Omega\tau\mathcal{S}(\omega)\frac{1 - e^{-i\omega\tau}}{i\omega} \,,$$

what allows us to exclude $\mathcal{S}(\omega)$ and to obtain

$$\mathcal{V}(\omega) = \mathcal{C}(\omega)\left[1 + 2a\tau e^{-R}\cos\Omega\tau\frac{\sin\omega\tau}{\omega\tau} + a^2\tau^2 e^{-2R}\cos^2\Omega\tau\frac{2 - 2\cos\omega\tau}{\omega^2}\right]^{-1} \,.$$

Equation (12.7) in the spectral form reads (here we use that $\mathcal{V}(\omega)$ is an even function)

$$R = \int_{-\infty}^{\infty}(1 - \cos\omega\tau)\omega^{-2}\mathcal{V}(\omega)\mathrm{d}\omega \,.$$

This system is still hard to solve in a general form, due to integration in the expression for R.

12.2.4
Self-Consistent Equation for Diffusion Constant

The quantity of main interest for us is the diffusion constant of the phase ψ, it is related to the spectral density of the frequency fluctuations at zero frequency: $D = 2\pi\mathcal{V}(0)$. For this quantity we obtain: $D = D_0(1 + a\tau e^{-R}\cos\Omega\tau)^{-2}$, where $D_0 = 2\pi\mathcal{C}(0)$ is the diffusion constant in the absence of the feedback. To obtain a closed system for determining D we assume further that the spectrum of the frequency fluctuations $\mathcal{V}(\omega)$ is very broad. One can expect this for broad spectrum of noise $\mathcal{C}(\omega)$, i.e., if the noise is nearly delta correlated. More precisely, we need to assume that the correlation time of frequency is much smaller than the delay time τ, so that the integral can be approximated as $R \approx \int_{-\infty}^{\infty}(1 - \cos\omega\tau)\omega^{-2}\mathcal{V}(0)\mathrm{d}\omega = \tau D/2$. As a result, we obtain a closed system of equations – the main result of our analysis –

$$D = \frac{D_0}{(1 + a\tau e^{\frac{-\tau D}{2}}\cos\Omega\tau)^2} \,, \quad \Omega = \Omega_0 - ae^{\frac{-\tau D}{2}}\sin\Omega\tau \,, \tag{12.10}$$

relating the diffusion constant D in the presence of the feedback to the "bare" diffusion constant D_0 and to the parameters of the feedback τ and a, as well to the "bare" frequency Ω_0. This is a nonlinear system of two equations for two variables D and Ω, which can be solved numerically for a given set of parameters.
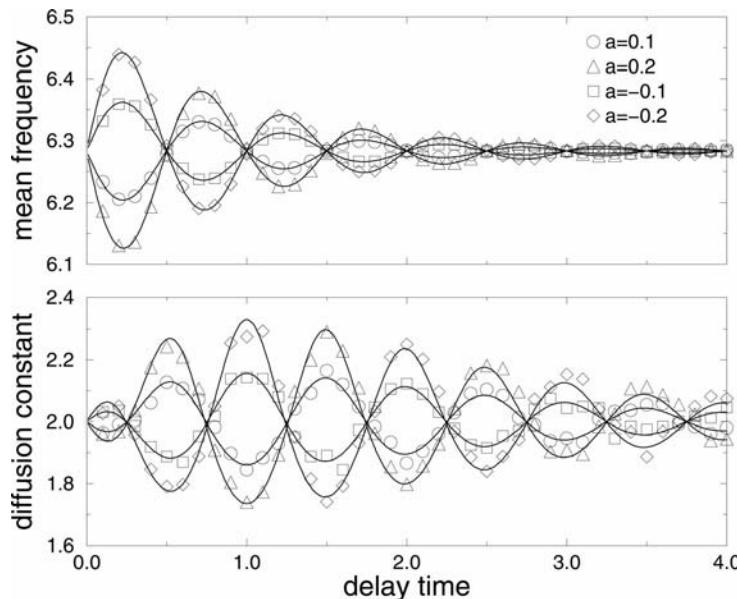
Fig. 12.5 Diffusion constant and mean frequency as functions of delay τ for $\sigma^2 = 1$ and $\Omega_0 = 2\pi$, and different values of feedback. Symbols: direct numerical simulation of model (12.3); solid lines: theory (12.10).

12.2.5
Comparison of Theory and Numerics

In Fig. 12.5 we compare the results of direct numerical simulation of the phase model (12.3) with theoretical predictions (12.10). In this case of relatively strong noise the correspondence is rather good.

Figure 12.6 demonstrates the results for the van der Pol model (12.1). The only parameter we have fitted here is the "no control" frequency $\Omega_0 \approx 0.95$. Here the correspondence with theory is good for small τ, but fails for large τ. The reason is that in this case the effective noise is small and therefore the feedback control is effective even for large delays. However, for large $a\tau$ Eq. (12.10) exhibits multistability, which results in an enhancement of the diffusion; here the Gaussian approximation used in derivation of (12.10) is not valid.

12.3
Control of Coherence by Multiple Delayed Feedback

Here we describe how the oscillation coherence can be controlled by a multiple delayed feedback. For the van der Pol model (Eq. (12.1)) such a feedback is written as
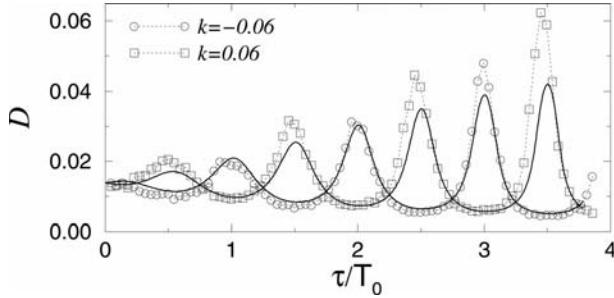
Fig. 12.6 Diffusion constant D of the van der Pol model with delayed feedback (parameters are the same as in Fig. 12.1). Symbols present the results of the direct numerical simulation; solid lines show the corresponding theoretical results according to Eqs. (12.10). The delay time is normalized by the average period $T_0 = 2\pi/0.95$.

$$\ddot{x} - \mu(1 - x^2)\dot{x} + \omega_0^2 x = k \sum_{v=0}^{\infty} R^v [\dot{x}(t - (v+1)\tau) - \dot{x}(t - v\tau)] + \zeta(t),$$

$$\langle \zeta(t)\zeta(t') \rangle = 2d^2\delta(t - t'). \tag{12.11}$$

A similar feedback has been suggested by Socolar et al. [17] in the context of chaos control. Despite the infinite sum of delays, it can be quite easily realized in experiments [18] (roughly speaking, one has to send the signal $\dot{x}(t)$ to a Fabry-Perot resonator with reflection coefficient at the 'mirrors' R). For convergence reasons we confine R to the range $(-1, 1)$. Noteworthy, that setting $R = 0$ we recover model (12.1) with just one feedback term.

Similar to the basic phase model (12.3) above, the equation for the phase can be written as

$$\dot{\phi} = \omega_0 + \frac{k}{2} \sum_{v=0}^{\infty} R^v \{ \sin[\phi(t - (v+1)\tau) - \phi] - \sin[\phi(t - v\tau) - \phi] \} + \xi(t), \tag{12.12}$$

with the effective noise $\xi(t)$. Again, our main goal is to investigate the diffusion properties of the phase. To this end we separate the phase into an average growth and fluctuations, $\phi(t) = \Omega t + \psi(t)$. We then obtain for the fluctuating instantaneous frequency $\dot{\psi}$ by substituting into Eq. (12.12) the following equation

$$\begin{aligned}
\dot{\psi} = \omega_0 - \Omega + \xi \\
+ \frac{k}{2} \sum_{v=0}^{\infty} R^v \{ \cos[\Omega(v+1)\tau] \sin[\psi(t - (v+1)\tau) - \psi] \\
- \cos[\Omega v\tau] \sin[\psi(t - v\tau) - \psi] - \sin[\Omega(v+1)\tau] \cos[\psi(t - (v+1)\tau) - \psi] \\
+ \sin[\Omega v\tau] \cos[\psi(t - v\tau) - \psi] \}.
\end{aligned} \tag{12.13}$$

Without noise, $\xi = \psi = \dot{\psi} = 0$, Eq. (12.13) simplifies to

$$0 = \omega_0 - \Omega - \frac{k}{2} \sum_{v=0}^{\infty} R^v \{ \sin[\Omega(v+1)\tau] - \sin[\Omega v \tau] \} . \tag{12.14}$$

The main effect is that the delayed feedback changes the frequency of the oscillator. Furthermore, the implicit equation (12.14) provides either a unique or multiple solutions for Ω. Here we choose the model parameters in the domain where no multistability occurs.

Our main assumption allowing to perform statistical analysis of the basic model analytically is that the phase fluctuations ψ are Gaussian. However, we do not *a priori* confine the Gaussian noise ξ to be white. After averaging Eq. (12.13) over the fluctuations of $\dot{\psi}$ (which are Gaussian distributed, too), we obtain for the mean frequency Ω:

$$\Omega = \omega_0 + \frac{k}{2} \sum_{v=0}^{\infty} R^v \left\{ \sin[\Omega v \tau] \varepsilon^{-\frac{\langle \eta_v^2 \rangle}{2}} - \sin[\Omega(v+1)\tau] \varepsilon^{-\frac{\langle \eta_{v+1}^2 \rangle}{2}} \right\} . \tag{12.15}$$

Here we have used the fact that the phase difference $\eta_v \equiv \psi(t - v\tau) - \psi(t)$ has Gaussian distribution with zero mean and therefore $\langle \cos \eta_v \rangle = \exp[-\langle \eta_v^2 \rangle / 2]$ and $\langle \sin \eta_v \rangle = 0$. With $\eta_v = -\int_{t-v\tau}^{t} \dot{\psi}(s) ds$ we obtain for the variance of η_v

$$\langle \eta_v^2 \rangle = 2 \int_0^{v\tau} (v\tau - u) C_{\dot{\psi}}(u) du \equiv 2T_v , \tag{12.16}$$

where $C_{\dot{\psi}}(u) \equiv \langle \dot{\psi}(t) \dot{\psi}(t+u) \rangle$ is the autocorrelation of the fluctuating part of the frequency. In order to obtain equations for $C_{\dot{\psi}}(u)$, we introduce the autocorrelation of the noise $C_{\xi}(u) \equiv \langle \xi(t)\xi(t+u) \rangle$ and the cross-correlation $C_{\xi\dot{\psi}}(u) \equiv \langle \xi(t) \dot{\psi}(t+u) \rangle$. After multiplying Eq. (12.13) with $\dot{\psi}(t+u)$ or $\xi(t+u)$ and averaging, we obtain

$$C_{\dot{\psi}}(u) = C_{\xi\dot{\psi}}(u) + \frac{k}{2} \sum_{v=0}^{\infty} R^v \left\{ \cos[\Omega v \tau] \varepsilon^{-T_v} \int_0^{v\tau} C_{\dot{\psi}}(s+u) ds \right.$$
$$\left. - \cos[\Omega(v+1)\tau] \varepsilon^{-T_{v+1}} \int_0^{(v+1)\tau} C_{\dot{\psi}}(s+u) ds \right\} , \tag{12.17}$$

$$C_{\xi\dot{\psi}}(u) = C_{\xi}(u) + \frac{k}{2} \sum_{v+0}^{\infty} R^v \left\{ \cos[\Omega v \tau] \varepsilon^{-T_v} \int_0^{v\tau} C_{\xi\dot{\psi}}(u-s) ds \right.$$
$$\left. - \cos[\Omega(v+1)\tau] \varepsilon^{-T_{v+1}} \int_0^{(v+1)\tau} C_{\xi\dot{\psi}}(u-s) ds \right\} . \tag{12.18}$$

Together with the definition of T_v (12.16), Eqs. (12.15), (12.17), and (12.18) constitute a closed system. To exclude the crosscorrelations, we look at the power spectra $S_{\dot{\psi}}(\omega) = \frac{1}{2\pi} \int_{-\infty}^{\infty} C_{\dot{\psi}}(u) \varepsilon^{-i\omega u} du$ and similar expressions for S_{ξ} and $S_{\xi\dot{\psi}}$. This leads to

$$S_{\dot\psi}(\omega) = S_{\xi\dot\psi}(\omega) + \frac{k}{2}\sum_{v=0}^{\infty} R^v\left\{\cos[\Omega v\tau]\varepsilon^{-T_v}S_{\dot\psi}(\omega)\frac{\varepsilon^{i\omega v\tau}-1}{i\omega}\right.$$
$$\left. - \cos[\Omega(v+1)\tau]\varepsilon^{-T_{v+1}}S_{\dot\psi}(\omega)\frac{\varepsilon^{i\omega(v+1)\tau}-1}{i\omega}\right\},$$

$$S_{\xi\dot\psi}(\omega) = S_{\xi}(\omega) + \frac{k}{2}\sum_{v=0}^{\infty} R^v\left\{\cos[\Omega v\tau]\varepsilon^{-T_v}S_{\xi\dot\psi}(\omega)\frac{1-\varepsilon^{-i\omega v\tau}}{i\omega}\right.$$
$$\left. - \cos[\Omega(v+1)\tau]\varepsilon^{-T_{v+1}}S_{\xi\dot\psi}(\omega)\frac{1-\varepsilon^{-i\omega(v+1)\tau}}{i\omega}\right\}.$$

This system of equations can be solved for $S_{\dot\psi}$:

$$S_{\dot\psi}(\omega) = S_{\xi}(\omega)\left[1 - \frac{k}{2i\omega}\sum_{v=0}^{\infty} R^v S_v\right]^{-1}\left[1 + \frac{k}{2i\omega}\sum_{v=0}^{\infty} R^v S_v^*\right]^{-1}. \tag{12.19}$$

Here, the star denotes complex conjugation and

$$S_v \equiv \cos[\Omega v\tau]\varepsilon^{-T_v}(1-\varepsilon^{-i\omega v\tau}) - \cos[\Omega(v+1)\tau]\varepsilon^{-T_{v+1}}(1-\varepsilon^{-i\omega(v+1)\tau}).$$

The spectral form of Eq. (12.16) reads

$$T_v = \int_{-\infty}^{\infty} S_{\dot\psi}(\omega)\frac{1-\cos[\omega v\tau]}{\omega^2}\,d\omega. \tag{12.20}$$

Now we make one further approximation: we assume that the spectrum of fluctuations of frequency $\dot\psi$ is very broad, almost white, and replace in (12.20) the spectrum $S_{\dot\psi}(\omega)$ by its value at zero frequency:

$$T_v \approx \int_{-\infty}^{\infty} S_{\dot\psi}(0)\frac{1-\cos[\omega v\tau]}{\omega^2}\,d\omega = \frac{v\tau D}{2}. \tag{12.21}$$

In writing the last term we use the Green-Kubo formula $D = 2\pi S_{\dot\psi}(0)$, which relates the diffusion constant D of the phase with the power spectrum of the frequency fluctuations at zero frequency. Thus, finally from Eq. (12.19) we obtain the equation for the diffusion constant

$$D = D_0\frac{4(1 + R^2E^2 - 2RE\cos[\Omega\tau])^4}{A^2(\Omega, \tau, k, R, E)}. \tag{12.22}$$

Here $D_0 = 2\pi S_{\xi}(0)$, $E \equiv \varepsilon^{-\tau D/2}$, and

$$A(\Omega, \tau, k, R, E) \equiv E(1+R^2E^2)(8R+k(R-1)\tau)\cos[\Omega\tau]$$
$$-2(1+4R^2E^2+R^4E^4+k(R-1)RE^2\tau+2R^2E^2\cos[2\Omega\tau]).$$

We also substitute (12.21) in Eq. (12.15) which after summation yields

$$\Omega = \omega_0 + \frac{k}{2} \left\{ \frac{\varepsilon^{-\frac{\tau D}{2}} \sin \Omega \tau (R-1)}{1 - 2R\varepsilon^{-\frac{\tau D}{2}} \cos \Omega \tau + R^2 \varepsilon^{-\tau D}} \right\}. \tag{12.23}$$

Equations (12.22) and (12.23) constitute a closed system for the simultaneous determination of the mean frequency and diffusion. Below we compare numerical solutions of these implicit equations with direct numerical simulations.

The validity of the analysis above, including that of Gaussian approximation, is now checked by direct simulations of the phase equation (12.12) assuming the noise $\xi(t)$ to be Gaussian. Clearly, one has to approximate the infinite sum of delay terms. Instead of just truncating this sum at some fixed $v < \infty$, we rather mimic the behavior of real physical systems, starting at $t = t_0$ with given initial condition $\phi(t) \equiv \phi_0(t)$ for $t \in [t_0 - \tau, t_0)$ by observing the equality:

$$\sum_{v=0}^{\infty} R^v \{ \sin[\phi_{(v+1)\tau} - \phi] - \sin[\phi_{v\tau} - \phi] \} = (1 - R)(X \cos \phi - Y \sin \phi),$$

where

$$X(t) \equiv \sum_{v=1}^{\infty} R^{v-1} \sin \phi(t - v\tau) = \sin \phi(t - \tau) + R\, X(t - \tau),$$

$$Y(t) \equiv \sum_{v=1}^{\infty} R^{v-1} \cos \phi(t - v\tau) = \cos \phi(t - \tau) + R\, Y(t - \tau).$$

Note that in order to compute the infinite sum in Eq. (12.12) now it is only necessary to store the phase and related quantities X, Y over a duration of just one delay period. This successive construction of the infinite sum is completely analogous to the behavior of a signal in a Fabry-Perot interferometer.

In Figs. 12.7 and 12.8 we compare the results of the numerical simulations with the analytical predictions according to Eqs. (12.22) and (12.23). Obviously, both in the case of strong and small noise the correspondence between the numerics and analytical results is good. Clearly, in comparison to the single delayed feedback scheme of [9], the introduction of the multiple delayed feedback parameter R can lead to a larger variety of phase dynamics and hence of the system behavior. For example, for the same value of the feedback strength k, with increasing R the suppression of diffusion is stronger.
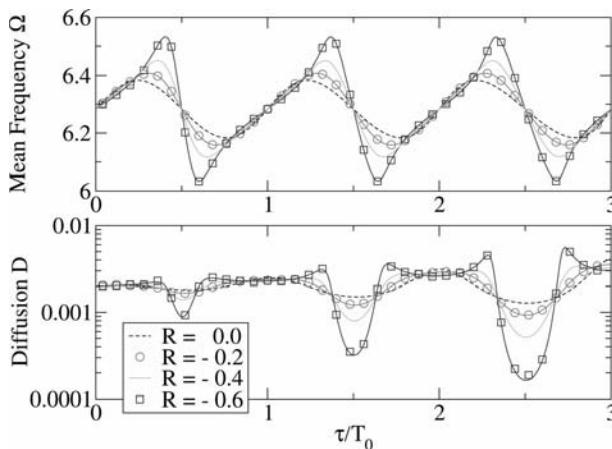
Fig. 12.7 Diffusion constant D and mean frequency Ω for small noise $d^2 = 2 \times 10^{-3}$ and $\omega_0 = 2\pi$ and $k = -0.2$.
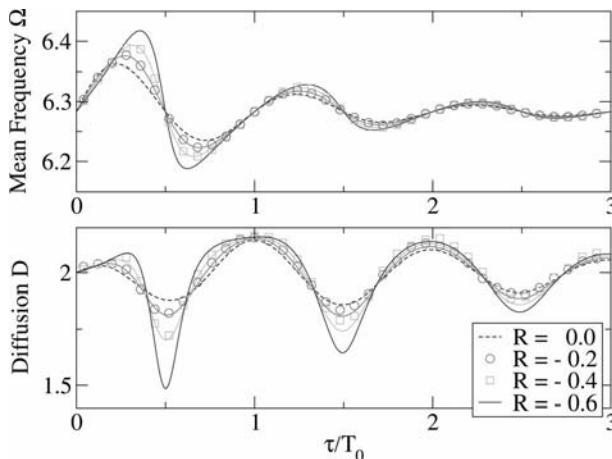
Fig. 12.8 Diffusion constant D and mean frequency Ω for large noise $d^2 = 2.0$ and $\omega_0 = 2\pi$ and $k = -0.2$.

12.4
Conclusion

In this chapter we have summarized theoretical and numerical results on the delay feedback control of coherence of oscillations (for a possible experimental realization see [19]). Our consideration has been restricted to the cases of weak feedback only. For large feedback several novel features appear due to possible multistability of the phase dynamics. A detailed study of these effects in presence of noise remains a challenging problem.

References

1 A. Pikovsky, M. Rosenblum, J. Kurths, Synchronization. A Universal Concept in Nonlinear Sciences, Cambridge University Press, Cambridge, 2001.

2 K. Pyragas, Continuous control of chaos by self-controlling feedback, Phys. Lett. A 170 (1992) 421–428.

3 G. Franceschini, S. Bose, E. Schöll, Control of chaotic spatiotemporal spiking by time delay autosynchronization, Phys. Rev. E 60 (5) (1999) 5426–5434.

4 P. Parmananda, J.L. Hudson, Controlling spatiotemporal chemical chaos using delayed feedback, Phys. Rev. E 64 (3) (2001) 037201.

5 M. Rosenblum, A. Pikovsky, Controlling synchronization in an ensemble of globally coupled oscillators, Phys. Rev. Lett. 92 (11) (2004) 114102.

6 M. Rosenblum, A. Pikovsky, Delayed feedback control of collective synchrony: An approach to suppression of pathological brain rhythms, Phys. Rev. E 70 (2004) 041904.

7 M. Rosenblum, N. Tukhlina, A. Pikovsky, L. Cimponeriu, Delayed feedback suppression of collective rhythmic activity in a neuronal ensemble, Int. J. Bif. Chaos 16 (7) (2006) 1989–1999.

8 M. Rosenblum, N. Tukhlina, A. Pikovsky, L. Cimponeriu, Feedback suppression of neural synchrony by vanishing stimulation, Phys. Rev. E 75 (2007) 011918.

9 D. Goldobin, M. Rosenblum, A. Pikovsky, Controlling oscillator coherence by delayed feedback, Phys. Rev. E 67 (6) (2003) 061119.

10 D. Goldobin, M. Rosenblum, A. Pikovsky, Coherence of noisy oscillators with delayed feedback, Physica A 327 (2003) 124–128.

11 A.H. Pawlik, A. Pikovsky, Control of oscillators coherence by multiple delayed feedback, Physics Letters A 358 (3) (2006) 181–185.

12 N.N. Bogoliubov, Y.A. Mitropolsky, Asymptotic Methods in the Theory of Nonlinear Oscillations, Gordon and Breach, New York, 1961.

13 M. Rosenblum, A. Pikovsky, J. Kurths, From phase to lag synchronization in coupled chaotic oscillators, Phys. Rev. Lett. 78 (1997) 4193–4196.

14 M. Zaks, E.-H. Park, M. Rosenblum, J. Kurths, Alternating locking ratios in imperfect phase synchronization, Phys. Rev. Lett. 82 (1999) 4228–4231.

15 E.-H. Park, M.A. Zaks, J. Kurths, Phase synchronization in the forced Lorenz system, Phys. Rev. E 60 (6) (1999) 6627–6638.

16 C. Masoller, Noise-induced resonance in delayed feedback systems, Phys. Rev. Lett. 88 (3) (2002) 034102.

17 J.E.S. Socolar, D.W. Sukow, D.J. Gauthier, Stabilizing unstable periodic orbits in fast dynamical systems, Phys. Rev. E 50 (4) (1994) 3245–3248.

18 D.W. Sukow, M.E. Bleich, D.J. Gauthier, J.E.S. Socolar, Controlling chaos in a fast diode resonator using extended time delay autosynchronization: Experimental observations and theoretical analysis, CHAOS 7 (4) (1997) 560–576.

19 S. Boccaletti, E. Allaria, R. Meucci, Experimental control of coherence of a chaotic oscillator, Phys. Rev. E 69 (6) (2004) 066211.

13
Resonances Induced by the Delay Time
in Nonlinear Autonomous Oscillators with Feedback

Cristina Masoller

The dynamics of nonlinear oscillators which are weakly perturbed by loops is studied as a function of the time of the feedback. By using as numerical examples with recurrent synaptic connections and with feedback, it is shown that the delay induces resonant features in the natural frequency and in the amplitude of the oscillations. These features can be understood in terms of a simple linear equation, in spite of the particular nonlinearities of each system. Consequences for the dynamics of delayed, such as networks of oscillatory neurons, are also discussed. Feedback loops are relevant for the control of human balance [1, 2], for generating persistent memory in neuronal systems [3, 4], for cellular differentiation in genetic circuits [5], etc. Time delays, arising from the fact that signal propagation realistically occurs at a finite velocity, are often a source of instabilities, multistability, chaotic behavior and oscillation death. On the other hand, since the pioneer work of Pyragas [6] it is well known that time delayed feedback can stabilize periodic orbits embedded in chaotic attractors. Recently, novel applications of delayed feedback have been proposed, including the control of the noise induced motion [7, 8], the control of the coherence of noisy and/or chaotic autonomous oscillators [9–11], the control of synchrony in coupled neurons [12], the stabilization of unstable fixed points by random coupling delays [13] or by using multiple feedback loops [14, 15], the control of space–time patterns occurring in extended systems [16–19], the control of collective synchrony in coupled oscillators [20–22], etc.

   In this contribution we study the interplay between the intrinsic dynamics of a nonlinear oscillator and a weak time delayed feedback loop. Specifically, we study the dependence of the natural frequency and amplitude of the oscillations on the delay time, τ, of the feedback loop. We consider autonomous systems that have a well-defined natural oscillation period, T_0 (the oscillations can be relaxation oscillations, self-sustained, chaotic or stochastic). Using a laser model and a neuron model as numerical examples we show that a weak time delayed feedback loop induces two main features: a piecewise linear variation of the oscillation frequency with τ and an enhancement (or suppression) of the oscillations for values of τ related to T_0. We also show that a good understanding of

these feedback-induced features can be developed in terms of a simple linear equation. Consequences for the dynamics of delayed-coupled oscillators, such as laser arrays and networks of oscillatory neurons, are also discussed. We show that delay-induced resonances manifest themselves in the collective mean-field, and are often more pronounced when an oscillator is coupled to other similar units.

We start by considering the simplest possible model describing an oscillator with a delayed feedback loop:

$$\dot{z} = -\lambda z(t) + \eta z(t - \tau), \tag{13.1}$$

where $z = x + iy$ and $\lambda = a + i\Omega_0$ are complex and η is real. This linear equation has a fixed point at $z = 0$ whose stability can be analyzed with the ansatz $z = z_0 \exp(-st)$ where $s = \beta + i\Omega$. This gives the characteristic equation $s = \lambda - \eta \exp(s\tau)$ that has to be solved numerically. There are an infinite number of eigenvalues and the stability of the fixed point will be enhanced (diminished) by the feedback if $\beta > a$ ($\beta < a$) for all s.

The real part of the eigenvalues as a function of τ is displayed in Fig. 13.1 (a) for $\eta > 0$, and in Fig. 13.1 (b) for $\eta < 0$. Enhanced stability occurs at $\tau \sim (n + 1/2) T_0$ for $\eta > 0$ (at $\tau \sim n T_0$ for $\eta < 0$), where $T_0 = 2\pi/|\Omega_0|$. The imaginary part of the eigenvalue with largest real part, displayed in Fig. 13.1 (c), is a
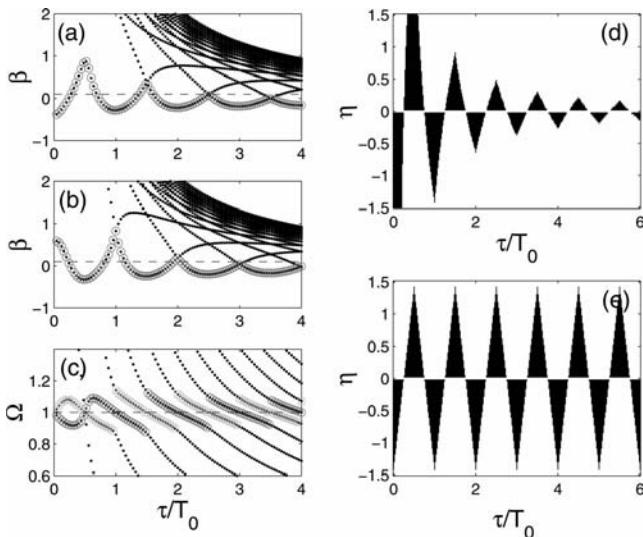
Fig. 13.1 Real part of the eigenvalues of Eq. (13.1) for $a = 0.1$, $T_0 = 1$, (a) $\eta = 0.5$, (b) $\eta = -0.5$. The circles indicate the largest eigenvalue and the dashed line gives the value of a. (c) Imaginary part of the eigenvalues. The largest eigenvalue is indicated with circles for $\eta = 0.5$ (with squares for $\eta = -0.5$). (d) Enhanced stability regions in the $(\tau/T_0, \eta)$ parameter space with $T_0 = 1$ fixed. (e) Enhanced stability regions in the $(\tau/T_0, \eta)$ parameter space with $\tau = 1$ fixed.

piecewise linear function of τ, and changes suddenly at $\tau \sim (n + 1/2)T_0$ for $\eta > 0$ (at $\tau \sim nT_0$ for $\eta < 0$). The regions of enhanced stability, obtained varying τ and η (for fixed Ω_0), are displayed in black in Fig. 13.3 (d). Let me remark that these resonances have different features from the well-known resonances that depend only on the phase difference between the oscillator and the re-injected signal (see Fig. 13.3 (e), where the enhanced stability regions were calculated varying the natural frequency Ω_0 and η while keeping τ fixed). Recently, similar results have been found in time delayed feedback control of steady states: in a generic linear normal form model, equivalent to Eq. (13.1) [23, 24], and experimentally, in a multisection semiconductor laser, with time delayed feedback from an external Fabry-Perot cavity [25].

Next, let us show that in spite of its simplicity, Eq. (13.1) provides a good qualitative description of delay-induced features in oscillatory feedback systems. First, we consider the equations for a single-mode semiconductor laser with optical feedback [26]:

$$\dot{E} = k(1 + ia)(N - 1)E + \eta E(t - \tau)e^{-i\omega_0\tau} + \sqrt{D}\xi, \tag{13.2}$$

$$\tau_N \dot{N} = j - N - NI, \tag{13.3}$$

where E is the slowly varying complex amplitude, $I = |E|^2$ is the laser intensity, N is the carrier density, k is the cavity losses, a is the linewidth enhancement factor, $\omega_0\tau$ is the feedback phase, D is the spontaneous emission strength, ξ is a Gaussian white noise with zero mean, j is the injection current, and τ_N is the carrier lifetime.

In the absence of feedback, Eqs. (13.2) and (13.3) have a single fixed point ($I_s = j - 1$, $N_s = 1$) which is a stable focus if $j > 1$ and is approached with transient relaxation oscillations of period $T_0 = 2\pi\sqrt{\tau_n/[2k(j - 1)]}$. In the presence of feedback, if $\eta\tau\sqrt{1 + a^2} > 1$ there is of fixed points (the so-called external-cavity modes) that become unstable as the feedback strength η or delay time τ increase, leading to periodic, quasiperiodic and chaotic oscillations [27, 28]. The amplitude, $A = [\max(I) - \min(I)]/2$, and the frequency of the main peak in the intensity power spectrum vs. τ (for fixed η) are displayed in Fig. 13.2(a) and (b) respectively. For small τ the fixed points are stable and the laser intensity is constant ($A = 0$). For longer τ the amplitude of the intensity oscillations increases nonmonotonically with τ: is maximum for $\tau \sim (n + 1/2)T_0$ (where n is an integer) and is minimum for $\tau \sim nT_0$. The width of the stability regions decreases with η, τ, and for large η, τ no resonances are observed. The frequency of the intensity oscillations varies in a piecewise linear relation with τ and changes abruptly at $\tau \sim nT_0$. Weak optoelectronic feedback, where the injection current depends on the delayed laser output, $j = j_0[1 + \gamma(I(t - \tau) - I_s)]$ [29, 30], has similar effects. In Fig. 13.2 (c) there are stability regions where the intensity is constant and regions where it exhibits large oscillations; in addition, the frequency of the intensity oscillations (Fig. 13.2 (d)) changes suddenly at certain values of τ and is a piecewise linear function of τ for τ larger than a few intrinsic oscillation periods.
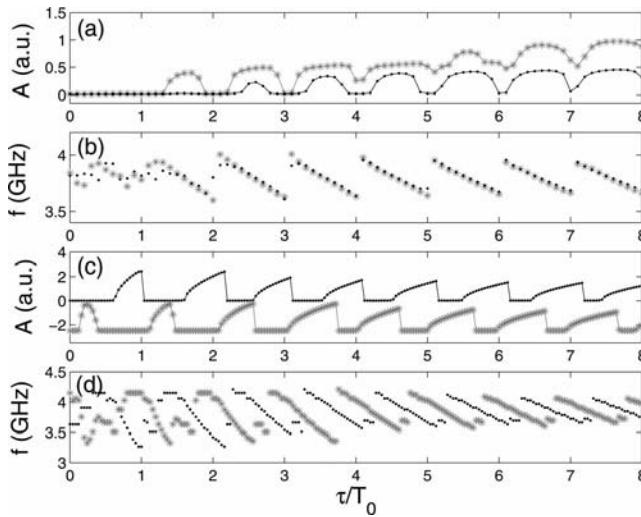
Fig. 13.2 Amplitude (a) and frequency (b) of the oscillations of the output intensity of a laser with optical feedback vs. the delay time. $\eta = 0.8$ ns^{-1} (.) and 1.2 ns^{-1} (*, red online). Amplitude (c) and frequency (d) of the intensity oscillations for optoelectronic feedback: $\gamma = 0.05$ (.), $\gamma = -0.05$ (*, red online, displaced vertically by -2.5). Parameters are: $k = 300$ ns^{-1}, $a = 3$, $\omega_0 \tau = 0$ rad, $D = 10^{-5}$ ns^{-1}, $j = 2$ and $\tau_N = 1$ ns.

As a second example we consider a type model of an oscillatory neuron [31–33], extended to account for a recurrent synaptic connection [34]:

$$C_M \dot{V} = I_l - I_d - I_r - I_{sd} - I_{sr} + \eta V(t - \tau), \tag{13.4}$$

where V is the voltage, I_d and I_r are de- and re-polarization currents and I_{sd} and I_{sr} are slow currents (for details of the model equations see [31]). We choose parameters such that the neuron in the absence of feedback displays of period T_0. Due to the excitable nature of the dynamics it can be expected that even weak feedback strengths can be a strong perturbation to the intrinsic sub-threshold oscillations. The feedback may amplify the oscillation amplitude, inducing threshold-crossings and giving rise to firing activity that can be self-regularized by the delay time. This is indeed observed in Fig. 13.3: for weak negative feedback the oscillation amplitude is enhanced and the neuron fires spikes; however, the feedback is not strong enough to induce firings for all delay values: there are feedback-induced spikes only in windows of the delay centered at $\tau \sim (n + 1/2)T_0$ with n integer. Moreover, in these windows the firing dynamics are regularized by the delay: for short delays the neuron fires tonic spikes (Fig. 13.3 (d)), while for longer delays it fires spikes-with-skippings (Fig. 13.3 (e)). For weak positive feedback the oscillation amplitude is diminished and there is also a nonmonotonic relationship with τ: the amplitude is maximum (minimum) for $\tau \sim nT_0$ ($\tau \sim (n + 1/2)T_0$). For both, positive and negative feedback,
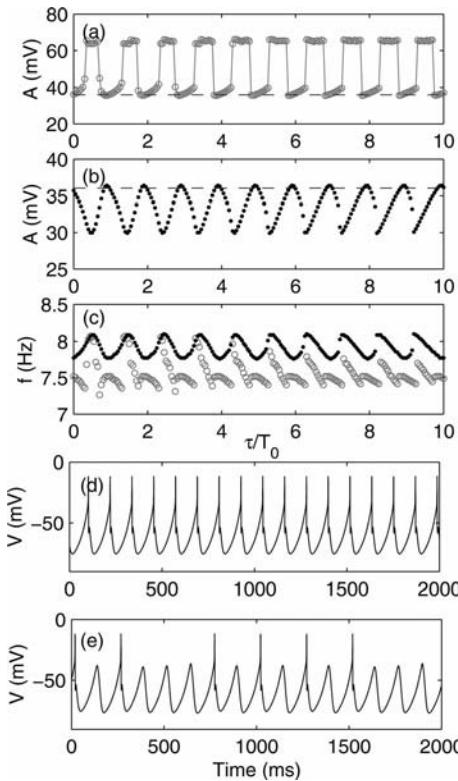
Fig. 13.3 Amplitude of the neuron oscillations vs. τ for (a) $\eta = -0.001$, (b) $\eta = 0.001$. The dashed line indicates the amplitude of the subthreshold oscillations for $\eta = 0$. (c) Frequency of the oscillations vs. τ (dots: $\eta = 0.001$, circles: $\eta = -0.001$). Firing dynamics for $\eta = -0.001$ and $\tau = 0.5\, T_0$ (d), $\tau = 8.5\, T_0$ (e). Parameters are as in [25] with $T = 35°C$.

the frequency of the neuronal oscillations is a piecewise linear function of τ for τ larger than a few T_0.

Let me remark that Eq. (13.1) provides a simple explanation for the feedback-induced features seen in the laser and in the neuron model and gives a deeper understanding of their universality. Similar effects have been reported in other autonomous systems presenting an intrinsic oscillation period. For example, for Rössler and Lorenz oscillators, in [35] stability islands were found analytically and confirmed numerically, when the delay time is about $(n + 1/2)T$, where n is an integer and T is the average intrinsic period of the chaotic oscillator. While these effects were explained in terms of a stability analysis of the solutions of the specific models, we have shown that Eq. (13.1) offers a simple paradigm for a qualitative understanding.

Moreover, the enhanced stability regions in Fig. 13.1 (d) are remarkably similar to the stability regions of the incoherent state of an ensemble of delayed-

coupled studied by Yeung and Strogatz [36]. To investigate the relationship between the dynamics of a single oscillator with a weak feedback loop and that of an ensemble of weakly coupled oscillators, we consider N identical oscillators with delayed mean field coupling:

$$\dot{\mathbf{x}}_i(t) = \mathbf{f}(\mathbf{x}_i) + \frac{\eta}{N}\sum_{j=1}^{N} \mathbf{x}_j(t - \tau). \tag{13.5}$$

The dynamics of the synchronized state, $\mathbf{x}_i(t) = \mathbf{x}_j(t) = \mathbf{x}(t)\ \forall\ i, j$, is governed by $\dot{\mathbf{x}} = \mathbf{f}(\mathbf{x}) + \eta\mathbf{x}(t - \tau)$. Therefore, for parameters (η, τ) such that the synchronized state is stable, the array oscillations can be either enhanced or suppressed by tuning the delay time. Let us first show how this applies to an array of semiconductor lasers coupled through an external mirror [37–40]:

$$\dot{E}_i = k(1 + ia)(N_i - 1)E_i$$
$$+ \frac{\eta}{N}\sum_{j} E_j(t - \tau)\exp\left(-i\omega_0\tau\right) + \sqrt{D}\xi(t), \tag{13.6}$$

$$\tau_N \dot{N}_i = j - N_i - N_i I_i, \tag{13.7}$$

where E_i and N_i are the complex field and carrier density of the ith laser, respectively, and the parameters have the same meaning as in Eqs. (13.2) and (13.3). Figure 13.4 (a) displays the amplitude of the oscillations of the incoherent intensity, $I = 1/N\sum_j |E_j|^2$, vs. the delay time. An array of $N = 5$ lasers is considered but similar results are found for other values of N. For comparison, the
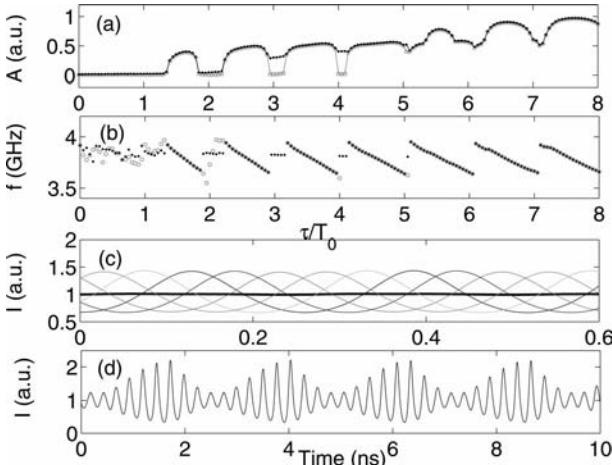

Fig. 13.4 Laser array: amplitude (a) and frequency (b) of the oscillations of the output of one laser (.) and of the output of the array (o, red online) vs. τ. (c) Out-of-phase oscillations for $\tau = 4T_0$. Thin lines: individual intensities, thick line: incoherent intensity. (d) In-phase oscillations for $\tau = 7.5T_0$. Parameters as in Fig. 13.2.

amplitude of the oscillations of a single laser is also displayed. The resonances observed previously in one laser are clearly present in the output of the array. Enhanced (suppressed) oscillations occur for $\tau \sim (n + 1/2)T_0$ ($\tau \sim nT_0$). For most values of the delay the lasers synchronize in-phase ($I_j = I \; \forall \; j$). In the enhanced stability islands ($\tau \sim nT_0$) the individual intensities can be either in-phase or out-of-phase (in agreement with the results of [38]). As in the case of a single laser, for large (η, τ) the resonances are washed out. The frequency of the collective oscillations also exhibits a piecewise linear relation with τ (Fig. 13.4 (b)); however, in the regions of enhanced stability there is a locking behavior such that the frequency of the collective oscillations is an integer multiple of $1/T_0$ (not shown), while the frequency of the oscillations of a single laser is nearly independent of τ (black dots in Fig. 13.4 (b)).

Similar results are found in networks of oscillatory neurons coupled through the delayed mean-field:

$$C_M \dot{V}_i = I_{l,i} - I_{d,i} - I_{r,i} - I_{sd,i} - I_{sr,i} + \eta V(t - \tau). \tag{13.8}$$

Here V_i is the membrane potential of the ith neuron, $V = \frac{1}{N}\sum_{j=1}^{N} V_j$ is the collective mean field and the other variables have the same meaning as in Eq. (13.4). Figure 13.5 displays the amplitude of the oscillations of the mean
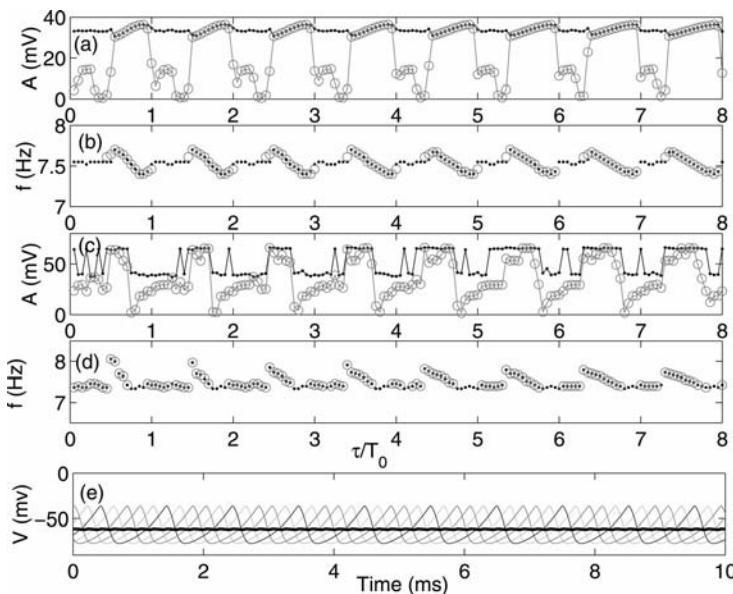

Fig. 13.5 Neuron ensemble: amplitude (a), (c) and frequency (b), (d) of the mean field oscillations (circles, red online) vs. τ for $\eta = 0.001$ (a), (b); $\eta = -0.001$ (c),(d). The dots display the amplitude and frequency of the oscillations of a single neuron. (e) Sub-threshold oscillations in antiphase (the thick line indicates the mean field). Parameters as in Fig. 13.2.

field vs. τ for fixed η. For comparison, the amplitude of the oscillations of a single neuron is also displayed (an array of $N = 5$ neurons is considered but similar results are found for other values of N). For both, positive and negative feedback, the mean field exhibits periodic features at delay times separated by T_0. For $\eta > 0$ (Fig. 13.5 (a)) the individual neurons display only, which can be either in-phase, out-of-phase, or in perfect antiphase depending on τ. In the latter case the mean field is constant and $A = 0$. For $\eta < 0$ (Fig. 13.5 (c)) the array displays even more complex behavior: depending on τ either all the neurons fire spikes, or they all display subthreshold oscillations, or some neurons display subthreshold oscillations while the others display spiking behavior (i.e., the ensemble divides into clusters). The neuronal oscillations can be either in-phase or out-of-phase depending on the delay. It can be observed that there are periodic windows of τ where the neurons display antiphased subthreshold oscillations which result in a nearly constant mean field ($A = 0$). There is also of solutions with the coexistence for certain parameters of in-phase and out-of-phase behavior. For positive and negative feedback the frequency of both, the mean field and a single neuron has a piecewise linear dependence with τ (Fig. 13.5 (b) and (d)). Also resembling the behavior of the laser array, in the regions of out-of-phase behavior the frequency of the mean field is nT_0^{-1} (not shown) while the frequency of the individual neurons is nearly constant, independent of τ.

Mutual coupling can lead to an enhancement of the resonances with respect of the case of a single oscillator with feedback. By comparing the amplitude of the oscillations of a single neuron (Fig. 13.3 (a) and (b)) with the amplitude of the mean-field of N coupled neurons (Fig. 13.5 (a) and (c)) it can be observed that in spite of the fact that the strength of the signal re-injected into a neuron is the same, the coupling with other units enhances the delay-induced resonances with respect to the case of a self-feedback loop.

Concluding, we have shown that a weak delayed feedback loop induces universal resonant features as a function of the delay time that are common to autonomous nonlinear oscillators and that can be understood in terms of the simple linear equation (13.1). We have also shown that these resonant features manifest themselves in the collective behavior of delayed-coupled oscillators.

References

1 G. Stepan and L. Kollar, "Balancing with reflex delay", Math. Comp. Modelling **31**, 199 (2000).

2 J. L. Cabrera and J. G. Milton, "On-off intermittency in a human balancing task", Phys. Rev. Lett. **89**, 158702 (2002).

3 J. Foss, A. Longtin, B. Mensour, and J. Milton, "Multistability and delayed recurrent loops", Phys. Rev. Lett. **76**, 708 (1996).

4 J. Foss and J. Milton, "Multistability in recurrent neural loops arising from delay", J. Neurophysiology **84**, 975 (2000).

5 G. M. Suel, J. Garcia-Ojalvo, L. M. Liberman, and M. B. Elowitz, "An excitable gene regulatory circuit induces transient cellular differentiation", Nature **440**, 545 (2006).

6 K. Pyragas, "Continuous control of chaos by self-controlling feedback", Phys. Lett. A **170**, 421 (1992).

7 N. B. Janson, A. G. Balanov, and E. Schöll, "Delayed feedback as a means of control of noise-induced motion", Phys. Rev. Lett. **93**, 010601 (2004).

8 A. G. Balanov, N. B. Janson, and E. Schöll, "Control of noise-induced oscillations by delayed feedback", Physica D **199**, 1 (2004).

9 D. Goldobin, M. Rosenblum and A. Pikovsky, "Controlling oscillator coherence by delayed feedback", Phys. Rev. E **67**, 061119 (2003).

10 S. Boccaletti, E. Allaria, and R. Meucci, "Experimental control of coherence of a chaotic oscillator", Phys. Rev. E **69**, 066211 (2004).

11 A. H. Pawlik and A. Pikovsky, "Control of oscillators coherence by multiple delayed feedback", Phys. Lett. A **358**, 181 (2006).

12 B. Hauschildt, N. B. Janson, A. Balanov, and E. Schöll, "Noise-induced cooperative dynamics and its control in coupled neuron models", Phys. Rev. E **74**, 051906 (2006).

13 C. Masoller and A. C. Marti, "Random delays and the synchronization of chaotic maps", Phys. Rev. Lett. **94**, 134102 (2005).

14 A. Ahlborn and U. Parlitz, "Stabilizing unstable steady states using multiple delay feedback control", Phys. Rev. Lett. **93**, 264101 (2004).

15 A. Ahlborn and U. Parlitz, "Laser stabilization with multiple-delay feedback control", Opt. Lett. **31**, 465 (2006).

16 L. Pastur, L. Gostiaux, U. Bortolozzi, S. Boccaletti, and P. L. Ramazza, "Experimental targeting and control of spatiotemporal chaos in nonlinear optics", Phys. Rev. Lett. **93**, 063902 (2004).

17 C. Beta and A. S. Mikhailov, "Controlling spatiotemporal chaos in oscillatory reaction–diffusion systems by time delay auto synchronization", Physica D **199**, 173 (2004).

18 O. Beck, A. Amann, E. Schöll, J. E. S. Socolar, and W. Just, "Comparison of time delayed feedback schemes for spatiotemporal control of chaos in a reaction–diffusion system with global coupling", Phys. Rev. E **66**, 016213 (2002).

19 N. Baba, A. Amann, E. Schöll and W. Just, "Giant improvement of time delayed feedback control by spatio-temporal filtering", Phys. Rev. Lett. **89**, 074101 (2002).

20 M. Rosenblum and A. Pikovsky, "Controlling synchronization in an ensemble of globally coupled oscillators", Phys. Rev. Lett. **92**, 114102 (2004).

21 M. Rosenblum and A. Pikovsky, "Delayed feedback control of collective synchrony: an approach to suppression of pathological brain rhythms", Phys. Rev. E **70**, 041904 (2004).

22 M. Rosenblum, N. Tukhlina, A. Pikovsky, and L. Cimponeriu, "Delayed feedback suppression of collective rhythmic activity in a neuronal ensemble", Int. J. Bif. Chaos **16**, 1989 (2006).

23 P. Hövel and E. Schöll, "Control of unstable steady states by time delayed feedback methods", Phys. Rev. E **72**, 046203 (2005).

24 S. Yanchuk, M. Wolfrum, P. Hövel, and E. Schöll, "Control of unstable steady states by long delay feedback", Phys. Rev. E **74**, 026201 (2006).

25 S. Schikora, P. Hövel, H.-J. Wünsche, E. Schöll, and F. Henneberger, "All-optical noninvasive control of unstable steady states in a semiconductor laser", Phys. Rev. Lett. **97**, 213902 (2006).

26 J. Ohtsubo, Progress in Optics, edited by E. Wolf (North-Holland, Amsterdam, 2002), Vol. 44, Chapter 1.

27 D. Lenstra, B. H. Verbeek, and A. J. Denboef, "Coherence collapse in single-mode semiconductor-lasers due to optical feedback", IEEE J. Quantum Electron. **21**, 674 (1985).

28 J. Mork, B. Tromborg and J. Mark, "Chaos in semiconductor lasers with optical feedback – theory and experiment", IEEE J. Quantum Electron. **28**, 93 (1999).

29 D. Pieroux and T. Erneux, "Strongly pulsating lasers with delay", Phys. Rev. A **53**, 2765 (1996).

30 S. Tang and J. M. Liu, "Chaotic pulsing and quasi-periodic route to chaos in a semiconductor laser with delayed optoelectronic feedback", IEEE J. Quantum Electron. **37**, 329 (2001).

31 H. A. Braun, M. T. Huber, M. Dewald, K. Schafer, and K. Voigt, "Computer simulations of neuronal signal transduction: The role of nonlinear dynamics and noise", Int. J. Bifurc. Chaos **8**, 881 (1998).

32 U. Feudel, A. Neiman, X. Pei, W. Wojtenek, H. A. Braun, M. T. Huber, and F. Moss, "Homoclinic bifurcation in a Hodgkin-Huxley model of thermally sensitive neurons", Chaos **10**, 231 (2000).

33 A. Neiman, X. Pei, D. Russell, W. Wojtenek, L. Wilkens, F. Moss, H. A. Braun, M. T. Huber, and K. Voigt, "Synchronization of the noisy electrosensitive cells in the paddlefish", Phys. Rev. Lett. **82**, 660 (1999).

34 M. Sainz-Trapaga, C. Masoller, H. A. Braun, and M. T. Huber, "Influence of time delayed feedback in the firing pattern of thermally sensitive neurons", Phys. Rev. E **70**, 031904 (2004).

35 J. W. Ryu, W. H. Kye, S. Y. Lee, M. W. Kim, M. Choi, S. Rim, Y. J. Park, and C. M. Kim, "Effects of time delayed feedback on chaotic oscillators", Phys. Rev. E **70**, 036220 (2004).

36 M. K. S. Yeung and S. H. Strogatz, "Time delay in the Kuramoto model of coupled oscillators", Phys. Rev. Lett. **82**, 648 (1999).

37 J. Garcia-Ojalvo, J. Casademont, M. C. Torrent, C. R. Mirasso, and J. M. Sancho, "Coherence and synchronization in diode-laser arrays with delayed global coupling", Int. J. Bifurc. Chaos **9**, 2225 (1999).

38 G. Kozyreff, A. G. Vladimirov, and P. Mandel, "Global coupling with time delay in an array of semiconductor lasers", Phys. Rev. Lett. **85**, 3809 (2000).

39 G. Kozyreff, A. G. Vladimirov, and P. Mandel, "Dynamics of a semiconductor laser array with delayed global coupling", Phys. Rev. E **64**, 016613 (2001).

40 A. G. Vladimirov, G. Kozyreff, and P. Mandel, "Synchronization of weakly stable oscillators and semiconductor laser arrays", Europhys. Lett. **61**, 613 (2003).

Part IV
Communicating with Chaos, Chaos Synchronization

14
Secure Communication with Chaos Synchronization

Wolfgang Kinzel and Ido Kanter

14.1
Introduction

Chaos synchronization is a counterintuitive phenomenon. A chaotic system moves irregularly and unpredictably, and two chaotic systems, starting from almost identical initial states, end in completely uncorrelated trajectories [1]. Hence it came as a surprise when Pecora and Carroll showed in 1990 that two chaotic systems which are coupled by some of their internal variables can synchronize to a common identical chaotic motion [2]. The dynamics is still irregular and unpredictable, but both sides have identical trajectories.

The combination of synchronization and unpredictability leads to an interesting application for secure communication: A secret message which is to be sent from Alice to Bob is encoded in the chaotic signal which is exchanged between these two partners. Since the signal is chaotic it is difficult – if not impossible – to extract the message from the irregular signal. This signal, however, synchronizes the dynamical system of Alice with the one of Bob who can immediately decode the message. It is not obvious how to implement this idea, but in fact communication by synchronized chaotic electronic circuits was demonstrated in 1992 by Cuomo and Oppenheim [3] and by Parlitz et al. [4].

These pioneering papers stimulated intensive research on communication with synchronized chaos which is still ongoing. One fascinating realization of this concept are systems of chaotic lasers. Lasers are a paradigm for coherent oscillations of the electromagnetic field of light waves. However, if a small fraction of the beam is re-injected into the cavity the laser can change to a state of chaotic motion, where the intensity of its beam is modulated on a sub-nanosecond time scale.

Communication with synchronized chaotic lasers has been demonstrated by Van Wiggeren and Roy in 1998 [5]. In principle, it is possible to transmit secret messages by chaotic laser beams with a rate of larger than 10^9 bits per second on a broadband carrier. Recently, synchronization of chaotic semiconductor lasers and transmission of secret messages encoded in the laser beams has been

demonstrated over a large distance in the public fiber network of Greece [6]. This research opens promising directions for future technological applications.

On the other side, synchronization of chaotic lasers has fascinating fundamental aspects. The lasers are driven by time delayed couplings and feedback, and the system is well described by a set of ordinary difference-differential equations [7]. The delay terms generate high-dimensional chaos which is still a challenge to mathematical research [8]. In addition, various kinds of synchronization have been observed and analyzed for such chaotic systems, like complete, generalized, anticipated, lag and phase synchronization [9]. Spontaneous symmetry breaking and sub-lattice synchronization have recently been reported [10, 11].

Secret communication relies on the fact that an attacker (Eve) is not able to decode the message from the exchanged signal. If Eve does not know anything about the chaotic systems of Alice and Bob she still can try to analyze the exchanged signal using the tools of nonlinear dynamics [12]. If Eve, however, knows the chaotic equations used by Alice and Bob but not their secret parameters, Eve may try to estimate the parameters from the recorded signal.

If, in addition, Eve knows the parameters as well, then Eve knows everything which Alice and Bob know from each other. In this case one might guess that it is impossible to send secret messages. However, this is not true. Modern cryptographic methods generate a secret key over a public channel. These methods, which were pioneered by Diffie and Hellmann in 1976, are based on the number theory [13]. Recently, it has been suggested that public channel cryptography may be possible using synchronization of chaotic systems [14–16]. This novel promising aspect of nonlinear dynamics will be emphasized in this overview.

14.2
Synchronization of Chaotic Systems

Let us consider two dynamical systems x and y which are driven by a time-dependent signal s, as sketched in Fig. 14.1. These systems may be ordinary differential equation for high-dimensional variables $x(t)$ and $y(t)$,

$$\dot{x} = f(x, s), \quad \dot{y} = f(y, s) \tag{14.1}$$
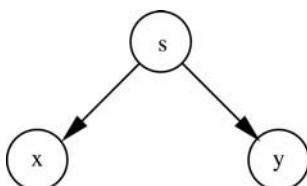
Fig. 14.1 A chaotic signal $s(t)$ drives two identical nonlinear systems x and y. The synchronous solution $x(t) = y(t)$ is stable if all conditional Lyapunov exponents are negative.

with some vector function f and some signal $s(t)$. For instructive simplicity we will demonstrate the principles of synchronization and communication with the simplest chaotic system, the iterated Bernoulli map [1, 9],

$$x_t = f(x_{t-1}), \quad f(x) = (ax) \mod 1. \tag{14.2}$$

For $a > 1$ the trajectories x_t are chaotic with a flat density on the unit interval $[0, 1]$. In the following we consider $a > 1$, only. Using the Bernoulli map, the scenario of Fig. 14.1 may be realized as

$$\begin{aligned} x_t &= (1 - \varepsilon)f(x_{t-1}) + \varepsilon f(s_{t-1}) \\ y_t &= (1 - \varepsilon)f(y_{t-1}) + \varepsilon f(s_{t-1}). \end{aligned} \tag{14.3}$$

The parameter $\varepsilon \in [0, 1]$ controls the strength of the drive s. The sequence s_t may be generated from any mechanism like noise or an independent chaotic equation. Obviously, the synchronous trajectory $x_t^0 = y_t^0$ is a solution of Eq. (14.3). However, this solution may be unstable to tiny perturbations. Hence we consider small deviations from the synchronous state,

$$\delta x_t = x_t - x_t^0, \quad \delta y_t = y_t - y_t^0. \tag{14.4}$$

Expanding Eq. (14.3) yields

$$\delta x_t = (1 - \varepsilon)a \, \delta x_{t-1}, \quad \delta y_t = (1 - \varepsilon)a \, \delta y_{t-1}. \tag{14.5}$$

These equations show that the synchronous solution is stable if the Lyapunov exponent λ of the subsystem is negative,

$$(1 - \varepsilon)a < 1 \quad \text{or} \quad \lambda = \ln|(1 - \varepsilon)a| < 0. \tag{14.6}$$

Switching off the drive, the subsystems must not be chaotic, otherwise the synchronous trajectory is unstable [9].

Note that in this simple model the driving signal s_t does not appear in the stability analysis, since the derivative $f'(x_{t-1}^0) = a$ does not depend on the trajectory x_t^0.

Pecora and Carroll [2] realized that the drive s may be a part of the chaotic system x, as indicated in Fig. 14.2. The left side represents the transmitter of Alice who sends the signal s to the receiver Bob. Bob is using s as a part of his dynamic equations, which are identical to those of Alice. Again we demonstrate this principle with the Bernoulli iteration:

$$\begin{aligned} s_t &= (1 - \varepsilon)f(s_{t-1}) + \varepsilon f(x_{t-1}), \\ x_t &= (1 - \varepsilon)f(x_{t-1}) + \varepsilon f(s_{t-1}), \\ y_t &= (1 - \varepsilon)f(y_{t-1}) + \varepsilon f(s_{t-1}). \end{aligned} \tag{14.7}$$
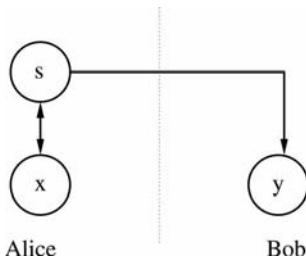
Fig. 14.2 The chaotic system of Alice is decomposed into a
signal variable $s(t)$ and several passive variables $x(t)$. The
signal $s(t)$ synchronizes the passive variables $y(t)$ of the
identical nonlinear system of Bob.

The dynamics of Alice is chaotic since the stability matrix of the (s, x) system,

$$\begin{pmatrix} (1 - \varepsilon)a & \varepsilon a \\ \varepsilon a & (1 - \varepsilon)a \end{pmatrix} \tag{14.8}$$

always gives one positive Lyapunov exponent $\lambda = \ln a > 0$, independent of the
strength ε of the drive. However, the stability of the synchronous solution
$x_t = y_t$ is determined, as before, by Eq. (14.6). The total dynamic system of Alice
is chaotic but the subsystems x and y are synchronous provided the conditional
Lyapunov exponents are negative.

This is a general result which holds for iterated maps as well as for any
chaotic system. Alice has to decouple her dynamic system into active and pas-
sive variables s and x. The active variables are inserted into the system of Bob.
Bob's system can synchronize to Alice's provided the conditional Lyapunov expo-
nents of the passive variables are negative.

To apply this scenario to communication one would like to send a scalar sig-
nal s which is part of a high-dimensional phase space (s, x). Can a scalar signal
synchronize high-dimensional chaos? The answer is positive. On the synchroni-
zation manifold $x_t = y_t$ there may exist a spectrum of positive Lyapunov expo-
nents whereas perpendicular to this manifold any perturbation will relax back
to the manifold, i.e., all conditional Lyapunov exponents are negative. This has
been shown for Lorenz and Rössler equations and coupled map lattices [17]. In
addition, this holds for dynamical systems with delay [8].

As mentioned before, the synchronization mechanism of Fig. 14.2 can be im-
plemented by ordinary differential equations for $x(t), y(t)$ and $s(t)$. Such equa-
tions have been realized with electronic circuits of nonlinear elements [3, 18,
19]. Another fascinating possibility to realize communication by synchronization
of chaotic systems are lasers. Applying a feedback to the laser cavity by injecting
another beam – either from the laser itself or from another laser – the laser can
be driven to a state of chaotic modulation of its intensity and phase [5, 8, 20,
21]. The time the light wave needs to go from Alice to Bob usually exceeds the
time scales which determine the dynamics of a laser. Therefore, the two chaotic
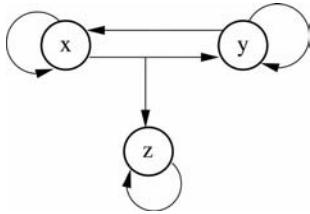
Fig. 14.3 Two dynamical systems x and y with delayed feedback are interacting by mutual delayed signals. An eavesdropper with an identical dynamical system z is driven by the signal from x, but cannot interact with the two partners.

systems of Alice and Bob are coupled by a time delayed signal with a delay time τ. This delay time just shifts the chaotic trajectories $y(t) = x(t - \tau)$. However, if additional delay times enter by self-feedback and if there is a bidirectional coupling between the lasers of Alice and Bob, the synchronization may become more complex, for example, anticipated chaos is possible [22].

Let us consider the configuration sketched in Fig. 14.3. Here three chaotic units are involved in the synchronization process: Alice and Bob are interacting by mutual coupling and Eve is driven by the signal of Alice. All three units have a self-feedback, and all exchanged signals – mutual, directed and self-feedback – are transmitted with an identical delay time τ. For simplicity, we again illustrate this mechanism with the Bernoulli map [1],

$$
\begin{aligned}
x_t &= (1 - \varepsilon)f(x_{t-1}) + \varepsilon\kappa f(x_{t-\tau}) + \varepsilon(1 - \kappa)f(y_{t-\tau}), \\
y_t &= (1 - \varepsilon)f(y_{t-1}) + \varepsilon\kappa f(y_{t-\tau}) + \varepsilon(1 - \kappa)f(x_{t-\tau}), \\
z_t &= (1 - \varepsilon)f(z_{t-1}) + \varepsilon\kappa f(z_{t-\tau}) + \varepsilon(1 - \kappa)f(x_{t-\tau}).
\end{aligned}
\tag{14.9}
$$

Since feedback and exchange delay times are identical, the synchronous trajectory $x_t = y_t = z_t = x_t^0$ is a solution of these equations, with

$$
x_t^0 = (1 - \varepsilon)f(x_{t-1}^0) + \varepsilon f(x_{t-\tau}^0).
\tag{14.10}
$$

The spectrum of Lyapunov exponents can be calculated exactly, using the method developed in [23]. In particular, in the limit of infinitely large delay times, $\tau \to \infty$, the equations have been solved analytically [11]. Here we consider this limit, only. For $\varepsilon > 0$ the system is in a state of high dimensional chaos, the Kaplan-Yorke dimension increases proportional to the delay time τ. For $\kappa = 0.5$ the two systems x and y receive an identical feedback, which in the limit of large delay time may be considered as noise. Hence, according to Eq. (14.6), x and y are synchronal for $\varepsilon > (a - 1)/a$.

If the two delay terms have different strength, $\kappa \neq 0.5$, the synchronal trajectory is stable for

$$\frac{a-1}{2a\varepsilon} < \kappa < \frac{2a\varepsilon - a + 1}{2a\varepsilon}, \quad \varepsilon > (a-1)/a. \tag{14.11}$$

Eve is not interacting with Alice and Bob. We assume that she is recording only the signal of Alice. Therefore, the area of stable synchronization is different from the one of Alice and Bob. If $x_t = y_t$ one finds for Eve

$$\kappa < \frac{a(\varepsilon - 1) + 1}{a\varepsilon}, \quad \varepsilon > (a-1)/a. \tag{14.12}$$

The phase diagram is shown in Fig. 14.4. There is no overlap between the range of parameters where Alice and Bob synchronize and where Eve is able to follow the trajectories of Alice and Bob. In particular, if in addition the exchanged signals are nonlinear functions of x_t and y_t, respectively, then Eve cannot adjust her parameters to synchronize with Alice and Bob.

This phenomenon is not specific to these simple maps, but it has also been found in corresponding experiments on chaotic semiconductor lasers [16]. Feedback with delay generates high-dimensional chaos which can be synchronized by exchanged laser beams. The experimental and corresponding numerical phase diagrams show different areas of synchronization between mutually coupled and directionally coupled lasers. If the self-feedback is absent, $\kappa = 0$ in Fig. 14.4, the iterated maps are not synchronized. For the semiconductor lasers, however, a symmetry breaking has been reported for this case: One laser takes the role of a leader which drives the opposite laser which follows with the delay time τ [10]. Since the time-shifted trajectories are not a solution of the corresponding Eqs. (14.9), the laser intensities do not completely coincide, they have a large overlap only.
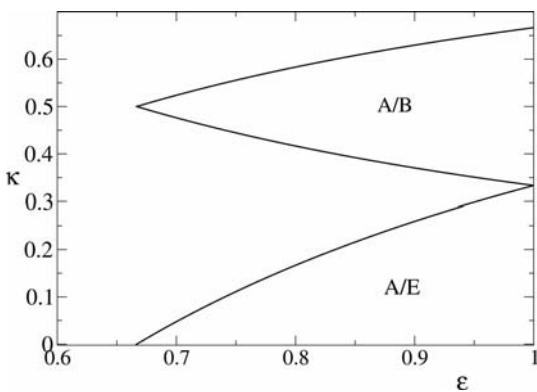
**Fig. 14.4** Phase diagram of configuration of Fig. 14.3 where the three systems are Bernoulli maps with parameter $a = 3$ and infinite delay times. ε is the strength of the total time-delayed couplings, and $\kappa\varepsilon$ is the strength of the self-feedback. In the upper region the two partners x and y synchronize, whereas only in the lower region the eavesdropper z can synchronize with y.

Note, however, in the case where Eve is recording both of the signals from Alice as well as Bob, she is able to synchronize her system. In this case one needs an asymmetry between self- and mutual feedback to prevent Eve from adjusting her parameters.

Two-way is different from one-way, interaction is more than drive, this principle promises novel methods of public channel cryptography which are explained in Sections 14.6–14.8. In the following section we will discuss how to encode a message $m(t)$ into the exchanged signal $s(t)$.

14.3
Coding and Decoding Secret Messages in Chaotic Signals

In the previous section we have seen that two systems which are in a state of high-dimensional chaos can be synchronized by a scalar signal $s(t)$ being exchanged between the two systems. For communication, a master/slave configuration is usually considered: Alice is transmitting a signal $s(t)$ to Bob which synchronizes his chaotic equations. Now Alice wants to use this mechanism to send a secret message to Bob. How can she encode the message $m(t)$ into the transmitted signal $s(t)$ such that an eavesdropper Eve recording the signal is not able to extract the message from the signal?

There are two ways to encode and decode a message into the chaotic system of Alice and Bob: 1. to modulate the transmitted signal $s(t)$ by the message $m(t)$, and 2. to modulate the dynamics of Alice's system $x(t)$ by the message. The first method is often called *chaos masking* while the second method has the names *chaos modulation* or *chaos shift keying*.

Let us demonstrate these two principles with the Bernoulli maps. In the simplest case of Fig. 14.1 the two systems x_t and y_t are driven by an external random signal s_t. Now Alice is sending an additional signal $\tilde{s}_t = x_t + m_t$ to Bob. Since Bob is synchronal to Alice, he just can subtract his own variable from this signal to recover the message,

$$m_t = \tilde{s}_t - y_t. \tag{14.13}$$

If the dynamics is complex enough, and if the message has a small amplitude compared to the carrier x_t, then it is not easy to extract the message from the transmitted signal s_t without knowing the dynamical equations of Alice and Bob.

In this simple example of chaos masking, however, one has to transmit two signals s_t and $\tilde{s}_t$. But it is possible to transmit a secret message by a single scalar signal s_t, only. In the simplest case, the message is just added to one of the internal variables, $s_t = x_t + m_t$. Now there are two possibilities, illustrated in Fig. 14.5: The signal influences the dynamics of the transmitter (chaos modulation, left side) or the signal is immediately transmitted to the receiver (chaos masking, right). In the first case, it is possible, in principle, to decode the mes-
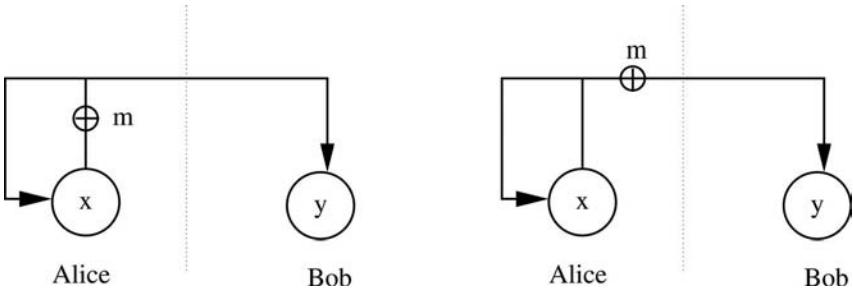
Fig. 14.5 Encoding a secret message m. Left: Chaos modulation. The message modulates the dynamics of Alice's equations, and Bob can extract the message without errors. Right: Chaos masking. The message is added to the exchanged signal and extracted by the mechanism of chaos pass filter.

sage without any error. In the second case, decoding relies on a phenomenon which has been named *chaos-pass filter* [20]. Let us illustrate these two cases with the iterated maps with delay. The equations for chaos modulation are

$$
\begin{aligned}
s_t &= x_t + m_t, \\
x_t &= (1 - \varepsilon) f(x_{t-1}) + \varepsilon f(s_{t-\tau}), \\
y_t &= (1 - \varepsilon) f(y_{t-1}) + \varepsilon f(s_{t-\tau}).
\end{aligned}
\tag{14.14}
$$

The dynamics of the receiver y_t is identical to the one of the transmitter x_t, thus the system synchronizes, $x_t = y_t$, if the subsystem has negative Lyapunov exponents, i.e., for $\varepsilon > (a-1)/a$ [11]. The receiver is recording the transmitted signal s_t, hence he can immediately decode the message, $m_t = s_t - y_t$.

For the other case, the equations for chaos masking are

$$
\begin{aligned}
s_t &= x_t + m_t, \\
x_t &= (1 - \varepsilon) f(x_{t-1}) + \varepsilon f(x_{t-\tau}), \\
y_t &= (1 - \varepsilon) f(y_{t-1}) + \varepsilon f(s_{t-\tau}).
\end{aligned}
\tag{14.15}
$$

The receiver has a different dynamics than the transmitter, thus they do not synchronize perfectly. However, they still have a large overlap with each other and the message can also be decoded with the difference $m_t = s_t - y_t$. But there is an error, the recovered message has only some overlap to the original one.

It is not obvious why chaos masking is working. The dynamical system y_t is driven by the sum $x_t + m_t$. Nevertheless, it follows a trajectory which is close to the dynamics of the transmitter, $x_t \simeq y_t$. The chaotic system filters the message out of the drive. It functions as a *chaos-pass filter*. This phenomenon is not well understood, yet, although it seems reasonable that perturbations perpendicular to a stable synchronization manifold are damped [24].

Both of the encoding/decoding methods, chaos modulation as well as chaos-pass filter, have been implemented in electronic circuits as well as in chaotic lasers [3, 5, 19, 25, 26]. In most cases a directed coupling – a master/slave configuration – has been used. Only recently, a chaos-pass filter has applied to mutual couplings in the context of public key cryptography [16]. This method will be introduced in Section 14.8.

There are other possibilities to encode a message into a chaotic system. For instance, the parameters of the transmitter can be modulated with the message. In particular, if the message is binary, $m_t \in \{0, 1\}$, the receiver may be synchronal for $m_t = 0$ and detuned for $m_t = 1$. If one of the transmitter variables is transmitted, then the receiver knows whether the corresponding variable of his dynamical system can follow ($m_t = 0$) or not ($m_t = 1$). For chaotic lasers, these parameters which are modulated by the message may be the pump current or the phase shift. Modulating the phase shift corresponds to modulating the delay time τ [25].

14.4
Analysis of the Exchanged Signal

The secret message which Alice sends to Bob is encoded in a chaotic signal on the transmission line. An eavesdropper Eve is recording this signal. If Eve does not know the dynamics which generates the signal, is she still able to recover the message from the transmitted signal?

In fact, nonlinear dynamics offers many powerful tools to analyze data produced by deterministic chaos [12]. Chaotic trajectories of dissipative system usually move on low-dimensional manifolds which may be reconstructed from partial information on the trajectories. Accordingly, from the transmitted signal $s(t)$ a low-dimensional manifold can be constructed, and an additional encoded message may be extracted from deviations from this manifold.

Consequently, for the early implementations of chaos-based communication by Lorenz equations, the encoded message was extracted by the technique of return maps [27]. The maxima and minima of the transmitted signal were recorded and consecutive differences and sums of these data were plotted. This return map clearly showed almost one-dimensional segments. A message encoded either by chaos modulation or by chaos masking generated points away from these segments. Hence this message could easily be extracted, at least for low frequencies. For high frequencies, however, the message could be directly reconstructed from the power spectrum of the transmitted signal.

Chaotic lasers offer additional structures which can be used to extract messages by the technique of return maps. The output intensity of chaotic lasers consists of a series of irregularly spaced pulses. The sequence of intensity maxima and time intervals of these spikes was plotted as return maps. The relation between intensity maxima and interspike intervals allowed to extract a message encoded in the transmitted laser beam [28].

For low-dimensional chaotic manifolds, simple return maps yield an effective tool to extract the message from the chaotic signal. However, is this approach still feasible for high-dimensional chaos, for hyper-chaotic communication schemes?

Even in such a case it is possible to reconstruct the high-dimensional attractor. After the transmitted signal $s(t)$ has been recorded, a sequence of vectors is constructed with a time delay τ, $x_t = (s_t, s_{t-\tau}, s_{t-2\tau}, \ldots, s_{t-(n-1)\tau})$. If n is large enough, a sequence of these n-dimensional vectors moves on a manifold which is smaller than n. Locally, this manifold can be fitted by smooth functions with a few parameters. Then the message is visible, as before, from deviations from this manifold. Using this method, it was possible to extract a message from a signal of a six-dimensional hyper-chaotic system, a combination of Lorenz and Rössler equations [29].

Chaotic systems with time delay, like lasers with external feedback, offer another possibility to use high-dimensional chaos for communication. However, also for this case tools to reconstruct the chaotic attractor have been developed [30]. For simple systems like the Mackey-Glass equation, the encoded message was successfully extracted by these embedding methods [31].

To demonstrate the principle of reconstructing hyper-chaotic attractors, let us consider again the Bernoulli iteration with time delay, Eq. (14.9). For this simple case it is immediately obvious that the three-dimensional vectors $(x_t, x_{t-1}, x_{t-\tau})$ are iterated on a two-dimensional manifold. But the dimension of the chaotic attractor is very large, of the order of τ. Hence a low-dimensional embedding technique is able to extract a message from high-dimensional hyper-chaos.

Chaotic lasers with feedback allow another method to decode a message from the chaotic beam. For chaos modulation a small message is like a perturbation of the dynamics of the transmitter which is described by a response function. The structure of this response function is determined by the feedback loop, it can be modeled by a few parameters. These parameters can be estimated from the exchanged signal, at least for a fiber-ring laser [32].

Up to this point, we have assumed that an eavesdropper Eve has no information on the dynamical equations of Alice and Bob. If, however, Eve knows the equations but does not know their parameters, she has more information for a successful attack. In this case, there exist methods to estimate the parameters of chaotic equations from the transmitted signals [33].

In summary, there exists a toolbox of nonlinear dynamics to analyze the transmitted signal and to estimate the encoded message. For simple systems, these tools could be successfully applied, even in the case of hyper-chaos. For more complex systems, these methods did not work, yet. Consequently, the security of chaos-based cryptography depends on the fact that it is computationally infeasible to extract the message from the transmitted signal. The system has to be complex enough to increase the amount of computational effort to an extent which is not available to an eavesdropper. Note that modern cryptographic methods, based on number theory, also depend on the computational infeasibility to break the code [13].

14.5
Neural Cryptography

In the previous sections, we have seen how secret messages can be encoded in a chaotic system. Alice and Bob have to use an identical dynamical system with identical parameters. If an attacker Eve knows these equations as well as their parameters she should be able to extract the message, too.

However, this is only true for directed couplings. In this case Alice and Bob have to use a secure private channel to agree on a common encryption key, namely the secret parameters of their equations. In the following sections we show how Alice and Bob can send secret messages over a public channel without previous agreements over secure private channels. Eve knows all the details about the system, equations, parameters as well as any exchanged information; nevertheless she is not able to decode the secret message which Alice is transmitting to Bob.

The first dynamical system which was developed for public key exchange is based on the synchronization of artificial neural networks which are trained on their mutual outputs [14]. This method has been named neural cryptography. It consists of a simple algorithm for discrete variables which can easily be implemented on small integrated circuits. And it allows new kinds of cryptographic protocols, since the algorithm is continuously generating new encryption keys. From the point of nonlinear dynamics, neural cryptography may be considered as an ensemble of random walks with reflecting boundaries which is synchronized by public chaotic (random) signals. This random walk is controlled by binary signals transmitted between the two partners over the public channel [34].

For neural cryptography, each partner has a multilayer neural network, a tree parity machine, as shown in Fig. 14.6. Each network consists of KN input units $x_{k,i}$, K hidden units σ_k and one output unit τ. There is a layer of synaptic weights $w_{k,i}$ between the input and hidden units. These weights are discrete variables with a depth L,
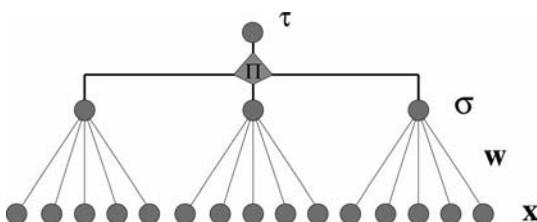
**Fig. 14.6** Multilayer neural network (tree parity machine) used for neural cryptography. $\mathbf{x}_k$: Public random input vectors. $\mathbf{w}_k$: Synaptic weights with discrete components. σ: Hidden units. τ: Output bit, the product of the hidden units. Alice and Bob are transmitting their output bits and train their synaptic weights according to the configuration of their hidden units.

$$w_{k,i} \in \{-L, -L+1, ..., L-1, L\}, \quad k = 1, 2, .., K; \; i = 1, ..., N. \tag{14.16}$$

Typical values of these parameters are $K = 3, L = 3, N = 1000$. Given $K = 3$ input vectors $\mathbf{x}_k$, the hidden units and the output of the network are calculated from

$$\sigma_k = \text{sign}(\mathbf{w}_k \cdot \mathbf{x}_k), \quad \tau = \sigma_1 \sigma_2 \sigma_3. \tag{14.17}$$

Hence the value of a hidden unit is just the sign of the vector product of the corresponding N-dimensional input and weight vectors. The output bit of the network is given by the product of the hidden units.

The dynamics of the two networks of Alice and Bob is defined by the following algorithm: At each time step K new common random input vectors $\mathbf{x}_k$ are generated. Alice and Bob calculate their hidden units and output units. If the two output bits are different, they start with a new common input vector. If the two output bits are identical, $\tau^A = \tau^B$, they change their synaptic weights in the direction of the input vectors, but only for these hidden units, which agree with the two output bits.

Each component of the weight vectors $\mathbf{w}_k$ is driven by the corresponding component of the input vector $\mathbf{x}_k$. Since Alice and Bob are driven by the same input vectors, their components are performing almost identical random walks and synchronize due to the reflecting boundaries. The updates of the components are controlled by the internal state of the system; the output and hidden units are functioning like on/off signals. This leads to attractive as well as repulsive steps for the weight vectors of Alice and Bob, and the synchronization process is a competition between these two kinds of steps. Finally Alice and Bob synchronize completely, and the common synchronized weight vectors perform an identical random walk in the KN-dimensional hypercube.

The generation of the secret key is defined as follows: Alice and Bob are starting from private random weight vectors $\mathbf{w}_k^A$ and $\mathbf{w}_k^B$, respectively. At each time step they receive K public input vectors $\mathbf{x}_k$, exchange their output bits τ^A and τ^B and update their synaptic weights. As soon as they are synchronized, they use their identical synaptic weights as a common secret key. This secret key may either be used for standard encryption networks, or Alice and Bob continue the dynamics without exchanging bits but using them as one-time pad for encryption.

An eavesdropper Eve knows all the details of the algorithm and records all the transmitted bits. She knows the sequence of input vectors, as well. Hence she uses an identical neural network and trains it using the same rules. However, there is an important difference: Alice and Bob are reacting to their mutual output bits, they are interacting. Eve, on the other hand, can only listen to the communication, but she cannot interact. It turns out that Alice and Bob have a higher probability for attractive steps than Eve [35]. That leads to a short synchronization time for Alice and Bob while Eve needs a very long time to synchronize [40]. Since the dynamics is stopped when Alice and Bob have identical weight vectors, the probability of a successful attack of Eve is very low.

In the limit of large keys, $N \rightarrow \infty$, scaling laws could be derived, which quantitatively define the level of security of neural cryptography [14, 34]. It turns out that the synaptic depth L, i.e., the number of possible states of each component $w_{k,i}$ of the weight vectors, is the essential parameter which controls the security. The probability of a successful attack of Eve decays exponentially with L

$$P_E \propto e^{-\gamma L}. \tag{14.18}$$

Increasing the value of L increases the synchronization time t_{syn} of Alice and Bob. But this time increases only polynomially with L,

$$t_{\mathrm{syn}} \propto L^2. \tag{14.19}$$

Consequently, the security of neural cryptography can be increased to any desired level without increasing the effort for synchronization too much.

Of course, there may exist many extensions of this method to improve either the security or the success of attacks. The security could be improved by combining neural networks with chaotic maps or by selecting appropriate input vectors (queries). The eavesdropper could make use of an ensemble of networks in genetic or majority attacks. But after all these investigations, the scaling laws, Eqs. (14.18) and (14.19), could be recovered. Neural cryptography appears to be secure.

Recently, this method has been implemented in integrated circuits [36]. It promises novel cryptographic protocols and applications.

14.6
Public Key Exchange by Mutual Synchronization

Neural cryptography, discussed in Section 14.5, has shown that it is possible to generate a secret key over a public channel key by a stochastic process. An eavesdropper Eve may know all the details of the communication process, nevertheless Eve is not able to synchronize with Alice and Bob and extract the secret message from the transmitted signals. In neural cryptography, the random or chaotic drive is generated by an external mechanism. In this section, we report on investigations to extend the idea of public key exchange to mutual synchronization to chaotic differential equations without an external drive [37].

Each of the two partners Alice and Bob is using a set of Lorenz equations with identical public parameters in the chaotic regime. The two Lorenz systems are coupled by a function $s(t)$ of their variables. The equation of Alice is, for example,

$$\frac{dx^A}{dt} = 10(y^A - x^A) + K[s^B(t) - s^A(t)],$$

$$\frac{dy^A}{dt} = 28x^A - y^A - x^A z^A, \tag{14.20}$$

$$\frac{dz^A}{dt} = x^A y^A - \frac{8}{3} z^A.$$

Bob has the identical equations for his variables, and since Eve knows these equations she will use corresponding equations for her variables, too. The signals $s^A(t)$ and $s^B(t)$ are transmitted between Alice and Bob, and Eve is recording them.

The main problem is to find signals $s^A(t), s^B(t)$, which first synchronize Alice with Bob, second, do not synchronize Eve with Alice, and third, do not allow to extract the variables of Alice using the tools of nonlinear dynamics discussed in Section 14.4. Given such signals, Alice and Bob can use some digits of their synchronized variables $x^A(t)$ and $x^B(t)$ for a secret key.

To meet the conditions 1 and 2, [37] suggests to take a nonlinear function $s(t)$ of the variable $x(t)$ with two time delays,

$$s^A(t) = x^A(t - \tau_1) + \text{sign}(x^A(t - \tau_1)) A (x^A(t - \tau_1) - x^A(t - \tau_2))^2. \tag{14.21}$$

It turns out that the coupling values K, where Alice and Bob synchronize but Eve does not, are limited to an interval, only. Figure 14.7 shows the largest con-
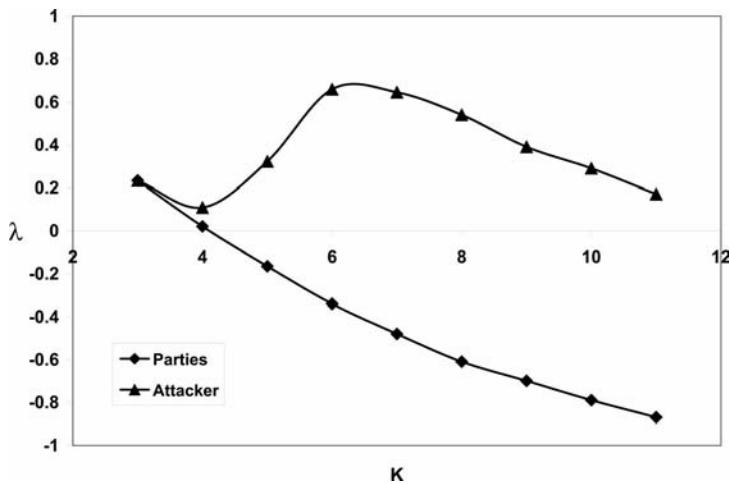

Fig. 14.7 Largest conditional Lyapunov exponents of three Lorenz systems coupled by nonlinear time-delayed signals with strength K. The lower curve is the result for the two partners interacting by mutual signals while the upper curve is the result for an eavesdropper using the signal of one partner.

ditional Lyapunov exponent of the A/B and A/E systems. Only for Alice and Bob there is a range of negative exponents. For large values of K the systems diverge. Hence, even if Eve tries to adjust her parameter K she will not be able to synchronize with Alice and Bob.

Subsequent calculations, however, have shown that the function of Eq. (14.21) can be analyzed with the tools of Section 14.4. The variable $x(t)$ can be estimated by embedding $s(t)$ in a three-dimensional phase space. But the function $s(t)$ of Eq. (14.21) can be extended such that the tools of nonlinear dynamics do not work, at least with a feasible computational effort. In [37] the amplitude A of Eq. (14.21) was replaced by a nonlinear function of $s^A(t)$ and $s^B(t)$ and a common public noise was added. Embedding techniques were not successful for those signals.

Although the system of Eve does not synchronize with the ones of Alice and Bob, its trajectory may stay in the vicinity of the synchronization manifold. Hence one has to consider – as in neural cryptography – the probability that Eve recovers the first a digits of the variable $x^A(t)$. Figure 14.8 shows that this success probability decreases exponentially with the number a, whereas the synchronization time increase linear with a. The security of the method is even stronger if Alice, Bob, and Eve are using a ring of N Lorenz equations instead of a single Lorenz triplet. The ring has internal couplings as well as mutual ones as in Eq. (14.21). Numerical simulations showed that the success probability decreases exponentially with the number N of Lorenz triplets, whereas the
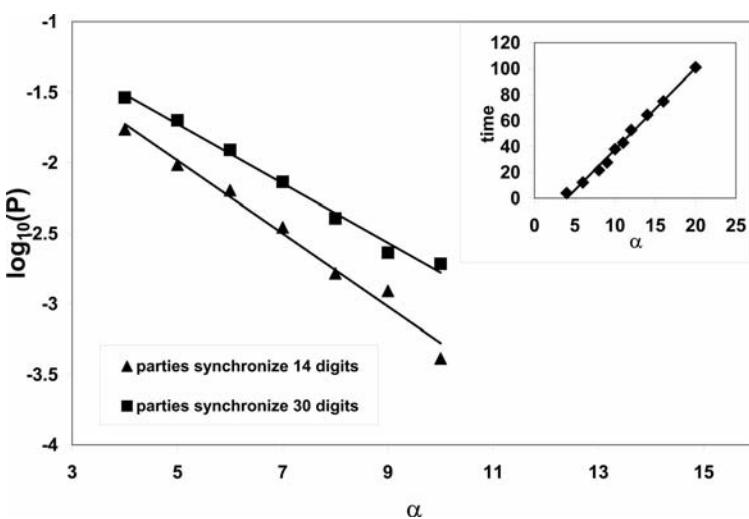

Fig. 14.8 Probability that an eavesdropper can extract the first a digits of the key variable x^A, after the two partners have synchronized their key variables to 14 or 30 digits, respectively. Inset: Synchronization time of the partners as a function of precision a.

synchronization time increases linearly with *N*, only. Similar to neural cryptography, public key exchange by chaos synchronization can be adjusted to any level of security.

14.7
Public Keys by Asymmetric Attractors

In the two previous sections, the methods of nonlinear dynamics have been used to construct a public key exchange protocol. A secret key could be generated between two partners although the exchange of the information as well as any details of the algorithm are known to any attacker who is recording the communication between the two partners.

The two previous methods were based on complete synchronization of two chaotic systems. Consequently, both partners used identical dynamical systems; these key exchange protocols were symmetric. Asymmetric protocols, on the other hand, may offer some advantages with respect to security and authorization. Thus it is interesting to look for asymmetric encryption protocols based on nonlinear dynamics.

Such an asymmetric method has been suggested by Tenny et al. [15]. The transmitter T and the receiver R are using different dynamical systems. The one of the transmitter is public whereas the receiver uses a private system which is unknown to the transmitter and any eavesdropper. Both sides are sending signals $s_T(t)$ and $s_R(t)$ which drive the whole dynamical system.

The message $m(t)$ is included into the signal $s_T(t)$ sent by the transmitter T. Let us consider the case where the message consists of bits, $m = 0, 1$. The system of the transmitter depends on the value of $m(t)$. The complete system, transmitter as well as receiver, has two attractors, one for $m = 0$ and one for $m = 1$. Since the receiver knows the complete dynamical system he can simulate it for $m = 0$ as well as for $m = 1$, and he finally can decide to which of the two attractors the exchanged signal $s_T(t)$ comes closest. Hence the receiver recovers the transmitted bit m with some error rate which depends on the mutual overlap between the two attractors.

An eavesdropper may record the two signals $s_T(t)$ and $s_R(t)$. But she does not know the dynamical system of R. Thus she cannot simulate the complete system and cannot determine the two attractors for $m = 0$ and $m = 1$. Of course, if the process is repeated many times, the eavesdropper can distinguish between two attractors, using the embedding methods for $s_T(t)$ of the tool box of nonlinear dynamics [12]. Consequently, the receiver has to use a new dynamical system for each single received bit.

Similar to the methods of the two previous sections, this algorithm is based on mutual interaction: The transmitter is sending the message encoded into its dynamical variables while the receiver drives the systems of the transmitter by some of his own variables. In principle, this method opens the possibility to construct asymmetric public encryption protocols based on nonlinear dynamics.

In practice, its first version is still inconvenient since the dynamics has to be changed after each bit, and its security against advanced attacks has still to be investigated.

14.8
Mutual Chaos Pass Filter

In Section 14.2 we have seen that a bidirectional coupling may lead to synchronization whereas, using identical parameters, a system driven by only one of the partners does not synchronize. If, however, the driven system receives the signals from both of the two partners it is not so easy to prevent synchronization of the eavesdropper. But also in this case bidirectional coupling is different from unidirectional one, and one may try to use this difference for secure communication.

In fact, recently a mechanism has been suggested which has the potential of secure public channel communication. This mechanism was named *mutual chaos-pass filter* [16]. It allows the two partners to transmit bits on top of a chaotic signal with a very low bit error rate. The transmission is bidirectional, both partners are sending secret messages to each other. An eavesdropper recording the bidirectional chaotic signal can recover the messages only with a high bit error rate. The difference of bit error rates between the partners and the attacker can be amplified using repetition codes, and finally a secure communication can be realized by transmission of compressed blocks of bits of suitable lengths. Consequently, a quantitative difference of bit error rates between partners and for the attacker is sufficient to realize a secure public channel communication.

Let us demonstrate the principle of mutual chaos-pass filter with chaotic maps as in Section 14.2. The only difference to Fig. 14.3 and Eq. (14.9) is that now Alice is adding a message m_t and Bob is adding noise n_t to their transmitted signals. Hence Eq. (14.9) has to be extended to

$$s_t^x = x_t + m_t, \quad s_t^y = y_t + n_t. \tag{14.22}$$

$$A : x_t = (1 - \varepsilon)f(x_{t-1}) + \varepsilon \kappa f(x_{t-\tau}) + \varepsilon(1 - \kappa)f(s_{t-\tau}^y). \tag{14.23}$$

$$B : y_t = (1 - \varepsilon)f(y_{t-1}) + \varepsilon \kappa f(y_{t-\tau}) + \varepsilon(1 - \kappa)f(s_{t-\tau}^x). \tag{14.24}$$

$$E : z_t = (1 - \varepsilon)f(z_{t-1}) + \varepsilon \kappa f(s_{t-\tau}^y) + \varepsilon(1 - \kappa)f(s_{t-\tau}^x). \tag{14.25}$$

In the following we show results for the logistic map $f(x) = |4x(1 - x)|$, for a binary message $m_t \in \pm m$ and for a uniform distribution of noise $n_t \in [-r, r]$. The system of Bob is driven by the signal $x_t + m_t$, he is responding with y_t and sending $y_t + n_t$. It turns out that Bob's response is almost identical to the state of x_t of Alice, thus Bob can recover the message from

$$m_t^B = \text{sign}(s_t^x - y_t). \tag{14.26}$$

The eavesdropper Eve tries to recover the message from

$$m_t^E = \text{sign}(s_t^x - z_t). \tag{14.27}$$

The fraction of wrong bits is the bit error rate. Figure 14.9 shows the bit error rates of Bob and Eve as a function of the strength of the noise which Bob is sending to Alice. Without noise, Eve has identical equations as Bob, hence she has identical bit error rates. However, if Bob is sending noise, one can find parameters such that Bob has a lower bit error rate than Eve. Figure 14.10 shows that for strong self-feedback there is a range of κ values for which an eavesdropper has a disadvantage.

As mentioned before, in principle a quantitative difference of bit error rates can be used for secure communication. Of course, in the case of simple maps this difference appears to be rather small. But in the case of semiconductor lasers, the corresponding equations show a much larger difference of bit error rates. For realistic values of the laser parameters, [16] reports bit error rates of 10^{-4} for the partners and 10^{-2} for an eavesdropper (see Fig. 14.11).

Such a large difference in bit error rates promises to realize an effective secure communication by chaotic laser beams. Even if an eavesdropper knows all the parameter values of the laser system she is not able to extract the message from the transmitted signals. It is interesting that security relies on the mechanism that Bob has is sending noise or an additional message to Alice. Security is induced by noise.
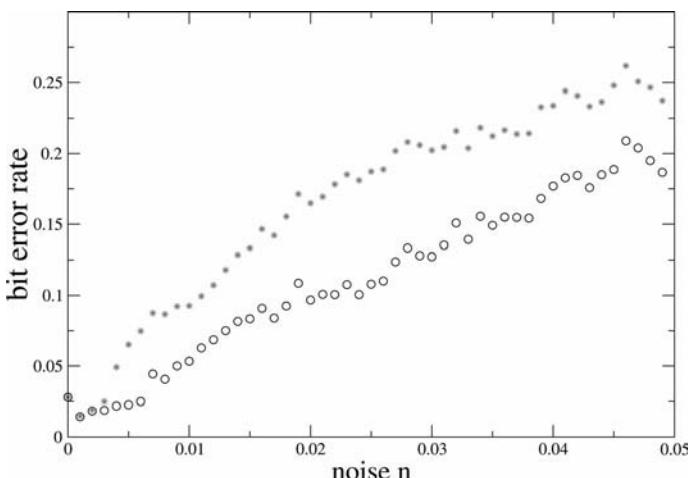

Fig. 14.9 Bit error rates as a function of noise level r/m. The partners (circles) as well as the eavesdropper (stars) are using logistic maps with delay with parameters $\varepsilon = 0.8$ and $\kappa = 0.76$.
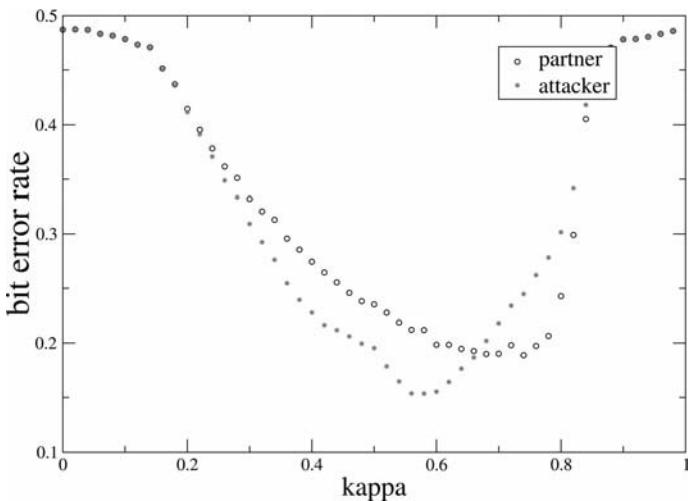
Fig. 14.10 As in Fig. 14.9, for parameters $\varepsilon = 0.8$ and noise level $r/m = 2.5$.
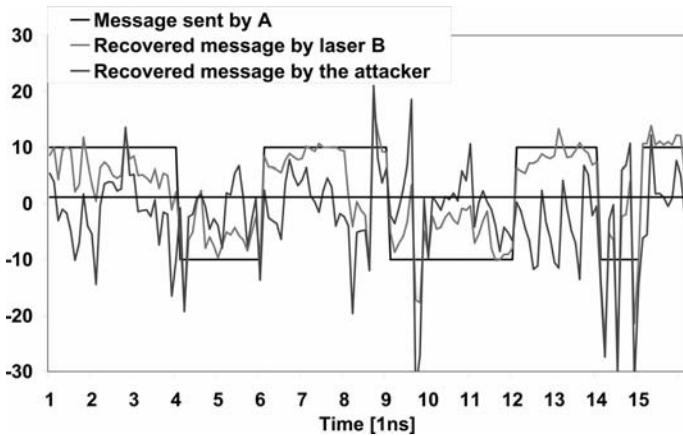
Fig. 14.11 Transmitted and recovered messages for the laser equations, from [16].

14.9
Discussion

The synchronization of chaotic systems offers an interesting possibility to send secure information via chaotic signals, generated either by electronic circuits or by laser systems with feedback. Since the pioneering work of Pecora and Carroll in 1990, intensive research on coupled chaotic systems has explored possibilities, limitations and hardware realizations of secure communication with chaos synchronization.

Most investigations assumed private keys, i.e., before communication, the partners have agreed on common secret parameters of their chaotic systems. In this overview we emphasize a new aspect of chaos synchronization, namely public key exchange. A secret key is generated via a public channel; an eavesdropper recording the exchanged information may know all the parameters of the system. Recent investigations suggest that such a protocol may be realized by two chaotic systems with a bidirectional coupling instead of a unidirectional one. In particular, first experiments on chaotic semiconductor lasers support this possibility. However, more work is needed, experimentally as well as theoretically, to understand the phenomena and their mechanisms and limitations before successful applications can be realized.

All types of synchronization found for chaotic lasers during the last decade can also be found for unidirectionally and mutually coupled chaotic maps, among them: identical/anticipated synchronizations and the chaos-pass filter mechanism for unidirectional coupling, and achronal/isochronal synchronizations and the mutual chaos-pass filter mechanism for mutual coupling.

A major conclusion of this paper is that there is a window in the parameter space for which the mutual coupled chaotic maps synchronize very well, yet a unidirectionally coupled map does not: both ways is more advantageous than one way. This feature is also common for coupled chaotic lasers. However, an analytical examination of quantities such as Lyapunov and conditional Lyapunov exponents is much simpler for chaotic maps than for chaotic lasers. These results suggest, similar to neural cryptography, an alternative method for public channel cryptography that does not rely on traditional number theoretical methods.

This prognosis provokes the following two principle questions: The first is whether mutually chaotic lasers are more secure than mutually coupled chaotic maps. On one hand it is clear that the implementation of chaotic maps or even Lorenz systems, for instance, in integrated electronic circuits is much simpler than the implementation of chaotic lasers. On the other hand, the implementation of advanced attacks based on an ensemble of interacting attackers or reliance upon record and play scenarios are possible for maps but are in question for chaotic lasers.

The second question is whether one can formulate dynamical protocols such as synchronization of neural networks, chaotic maps, and chaotic lasers in the traditional language of information and complexity theory.

Synchronization of time delayed chaotic systems is characterized by the language of Lyapunov exponents, but is that the appropriate language to analyze notions such as security and capacity of the communication channel? Can we find suitable quantitative analytical methods to estimate, for instance, version space or information gain during the unidirectional/mutual learning or synchronization processes? With respect to the complexity theory, an established bridge between chaotic and stochastic processes and NPC problems is absent, and only recently was a small preliminary step in this direction accomplished [38, 39].

Progress in these two directions and the emergence of new concepts, new theoretical techniques and methods are required in order to bridge between chaos synchronization and information and complexity theory. Chaos synchronization stands alone as an independent field of research, but as soon as we enter the field of advanced communication protocols an adaptation of new concepts will inevitably emerge.

References

1 H. G. Schuster and W. Just. *Deterministic Chaos.* Wiley-VCH, Weinheim, 2005.

2 L. M. Pecora and T. L. Carroll. Synchronization in chaotic systems. *Phys. Rev. Lett.*, 64(8):821–824, 1990.

3 K. M. Cuomo and A. V. Oppenheim. Circuit implementation of synchronized chaos with applications to communications. *Phys. Rev. Lett.*, 71(1):65–68, 1993.

4 U. Parlitz, L. Chua, L. Kocarev, K. Halle, and A. Shang. aha. *Int. J. Bif. Chaos*, 2:973, 1992.

5 G. D. VanWiggeren and R. Roy. Communication with chaotic lasers. *Science*, 279:1198–1200, 1998.

6 A. Argyris, D. Syvridis, L. Larger, V. Annovazzi-Lodi, P. Colet, I. Fischer, J. García-Ojalvo, C. R. Mirasso, L. Pesquera, and K. A. Shore. Chaos-based communications at high bit rates using commercial fibre-optic links. *Nature*, 438:343, 2005.

7 R. Lang and K. Kobayashi. External optical feedback effects on semiconductor injection laser properties. *IEEE J. Quant. Electr.*, 16(3):347–355, 1980.

8 V. Ahlers, U. Parlitz, and W. Lauterborn. Hyperchaotic dynamics and synchronization of external-cavity semiconductor lasers. *Phys. Rev. E*, 58(6):7208–7213, 1998.

9 A. Pikovsky, M. Rosenblum, and J. Kurths. *Synchronization, a universal concept in nonlinear sciences.* Cambridge University Press, Cambridge, 2001.

10 T. Heil, I. Fischer, W. Elsässer, J. Mulet, and C. R. Mirasso. Chaos synchronization and spontaneous symmetry-breaking in symmetrically delay-coupled semiconductor lasers. *Phys. Rev. Lett.*, 86(5):795–798, 2001.

11 J. Kestler, W. Kinzel, and I. Kanter. *To be published*, 2007.

12 H. Kantz and T. Schreiber. *Nonlinear Time Series Analysis.* Cambridge University Press, Cambridge, 2004.

13 D. R. Stinson. *Cryptography: Theory and Practice.* CRC Press, Boca Raton, FL, 1995.

14 I. Kanter, W. Kinzel, and E. Kanter. Secure exchange of information by synchronization of neural networks. *Europhys. Lett.*, 57(1):141–147, 2002.

15 R. Tenny, L. S. Tsimring, L. Larson, and H. D. I. Abarbanel. Using distributed nonlinear dynamics for public key encryption. *Phys. Rev. Lett.*, 90(4):047903, 2003.

16 E. Klein, N. Gross, E. Kopelowitz, M. Rosenbluh, L. Khaykovich, W. Kinzel, and I. Kanter. Public-channel cryptography based on mutual chaos pass filters. *Phys. Rev. E*, 1–4, 2006.

17 J. H. Peng, E. J. Ding, M. Ding, and W. Yang. Synchronizing hyperchaos with a scalar transmitted signal. *Phys. Rev. Lett.*, 76(6):904–907, 1996.

18 K. M. Cuomo, A. V. Oppenheim, and S. H. Strogatz. Synchronization of Lorenz-based chaotic circuits with applications to communications. *IEEE Trans. Circ. Syst.*, 40(10):626–633, 1993.

19 L. Kocarev and U. Parlitz. General approach for chaotic synchronization with applications to communication. *Phys. Rev. Lett.*, 74(25):5028–5031, 1995.

20 I. Fischer, Y. Liu, and P. Davis. Synchronization of chaotic semiconductor laser dynamics on subnanosecond time scales and its potential for chaos communication. *Phys. Rev. A*, 62:011801, 2000.

21 R. Vicente, T. Pérez, and C. R. Mirasso. Open- versus closed-loop performance of synchronized chaotic external-cavity

semiconductor lasers. *IEEE J. Quant. Electr.*, 38(9):1197–1204, 2002.

22 H. U. Voss. Anticipating chaotic synchronization. *Phys. Rev. E*, 61(5):5115–5119, 2000.

23 S. Lepri, G. Giacomelli, A. Politi, and F. T. Arecchi. High-dimensional chaos in delayed dynamical systems. *Physica D*, 235–249, 1993.

24 A. Murakami and K. A. Shore. Chaos-pass filtering in injection-locked semiconductor lasers. *Phys. Rev. A*, 72:053810, 2005.

25 T. Heil, J. Mulet, I. Fischer, C. R. Mirasso, M. Peil, P. Colet, and W. Elsässer. On/off phase shift keying for chaos-encrypted communication using external-cavity semiconductor lasers. *IEEE J. Quant. Electr.*, 38(9):1162–1170, 2002.

26 C. R. Mirasso, R. Vicente, P. Colet, J. Mulet, and T. Pérez. Synchronization properties of chaotic semiconductor lasers and applications to encryption. *Compt. Rend. Phys.*, 5:613–622, 2004.

27 G. Pérez and H. A. Cerdeira. Extracting messages masked by chaos. *Phys. Rev. Lett.*, 74(11):1970–1973, 1995.

28 P. M. Alsing, A. Gavrielides, V. Kovanis, R. Roy, and K. S. Thornburg Jr. Encoding and decoding messages with chaotic lasers. *Phys. Rev. E*, 56(6):6302–6310, 1997.

29 K. M. Short and A. T. Parker. Unmasking a hyperchaotic communication scheme. *Phys. Rev. E*, 58(1):1159–1162, 1998.

30 R. Hegger, M. J. Bünner, and H. Kantz. Identifying and modeling delay feedback

systems. *Phys. Rev. Lett.*, 81(3):558–561, 1998.

31 C. Zhou and C.-H. Lai. Extracting messages masked by chaotic signals of time-delay systems. *Phys. Rev. E*, 60(1):320–323, 1999.

32 J. B. Geddes, K. M. Short, and K. Black. Extraction of signals from chaotic laser data. *Phys. Rev. Lett.*, 83(25):5389–5392, 1999.

33 U. Parlitz. Estimating model parameters from time series by autosynchronization. *Phys. Rev. Lett.*, 76(8):1232–1235, 1996.

34 A. Ruttor, W. Kinzel, and I. Kanter. Neural cryptography with queries. *J. Stat. Mech.*, 2005(01):P01009, 2005.

35 M. Rosen-Zvi, E. Klein, I. Kanter, and W. Kinzel. Mutual learning in a tree parity machine and its application to cryptography. *Phys. Rev. E*, 66:066135, 2003.

36 M. Volkmer and S. Wallner. Tree parity machine rekeying architectures. *IEEE Trans. Comput.*, 54(4):421–427, 2005.

37 E. Klein, R. Mislovaty, I. Kanter, and W. Kinzel. Public-channel cryptography using chaos synchronization. *Phys. Rev. E*, 72:016214, 2005.

38 J. N. Tsitsiklis and V. D. Blondel. Lyapunov exponents of pairs of matrices. *Math. Control, Signals Syst.*, 10(1):31–40, 1997.

39 P. Jacquet, G. Seroussi, and W. Szpankowski. *Data Compression Conference*. DCC 2004, 2004.

40 A. Ruttor, W. Kinzel and I. Kanter. Dynamics of neural cryptography. *Phys. Rev. E*, 75:056104, 2007.

15
Noise Robust Chaotic Systems

Thomas L. Carroll

15.1
Introduction

When the first papers on chaotic synchronization were published [1], many believed that self-synchronizing chaotic systems would find use in communication [2–9]. Later, as engineers with more background in communication entered the field, it was realized that because self-synchronizing chaotic systems are stored reference systems, they could not compete in terms of efficiency with more conventional communication techniques such as code division multiple access (CDMA) systems, which had the benefit of a stored reference signal. There may still be some potential for self-synchronized chaotic systems in niche applications, such as military uses, where power efficiency is not the only factor limiting application. In some cases, for example, speed of synchronization or simplicity may be more important than overall power efficiency. CDMA systems require power management techniques which may not be compatible with use in combat. There may also be interest in combining communication signals with radar signals, but the desirable properties for a radar signal may not be the same as desirable properties for a communication signal. Radar signals must also be robust to Doppler shifts, caused by relative motion of the transmitter and the target, but Doppler shifts complicate synchronization of conventional communication systems.

Many of the early examples of self-synchronizing chaotic systems were severely affected by noise in the communication channel [10, 11]. As little as 10% noise added to the driving signal could destroy all evidence of synchronization. The two main reasons of this sensitivity were that the synchronized response systems were nonlinear, causing mixing of the noise and the signal, and the response systems did not include any form of time integration to reduce the effects of noise. Some form of time integration is essential in all forms of noise reduction, whether the noise reduction technique is simple signal averaging, a phase sensitive detector such as a phase locked loop, a correlation detector such as a matched filter used in radar, or a CDMA system which completes a digital

XOR operation between a stored code sequence and an incoming signal. One method to accomplish time integration in a self-synchronized chaotic system is to use a chaotic system with multiple time scales; multiple time scale chaotic systems will be described in this chapter.

15.2
Chaotic Synchronization

There have been many different demonstrations of synchronized chaotic systems: in essence, all of the demonstrations begin with a chaotic drive system:

$$\frac{d\vec{x}}{dt} = f(\vec{x}), \tag{15.1}$$

and a response system that is coupled in some way to the drive system:

$$\frac{d\vec{y}}{dt} = g(\vec{y}) + h(\vec{x}). \tag{15.2}$$

The coupling function h is chosen so that all of the Lyapunov exponents of the response system are negative. If the g and h functions are chosen so that $\vec{y}$ converges to $\vec{x}$, then the synchronization is identical; otherwise, the synchronization is said to be generalized if there is a continuous function between $\vec{y}$ and $\vec{x}$. There are situations where the response system of Eq. (15.2) has all negative Lyapunov exponents and there is no function between $\vec{y}$ and $\vec{x}$, but this situation will not be addressed here.

15.3
2-Frequency Self-Synchronizing Chaotic Systems

15.3.1
Simple Maps

In order to illustrate the principles of multiple time scale chaotic systems, an example using a simple map is developed [12]. This map is not suitable for practical applications because noise robustness is lost when the noise amplitude exceeds a certain threshold, but it does serve to illustrate the basic principles. The example uses a coupled pair of 1d maps, where one of the maps consists of a multiplication by a constant and a modulus, while the other map acts as a low-pass filter. The coupled maps are given by

$$x_1(n+1) = 1.5x_1(n) - 0.1\tau x_2(n) \mod 1,$$
$$x_2(n+1) = \left(\frac{4}{\tau}\right)x_1(n) + \left(1 - \frac{1}{\tau}\right)x_2(n). \tag{15.3}$$

Looking at the x_2 map alone, it can be seen that the term multiplying x_2 will approach 1 as τ increases, while the x_1 term driving the map will decrease, so as τ increases the x_2 part of the map will change more and more slowly in response to the x_1 driving term, acting as a low-pass filter. As long as $\tau > 1$ and $< \infty$, the x_2 map acts as a low-pass filter. From digital filter theory [13], the absolute magnitude of the gain of the x_2 map is $A(f) = 1/\sqrt{1 + \beta^2 - 2\beta \cos(2\pi f)}$ where f is the frequency (ranging from 0 to 0.5) and $\beta = (1 - 1/\tau)$. For $\tau = 1$ ($\beta = 0$) the magnitude of the gain is 1.0 for all frequencies, while $A(f)$ decreases with f for $\tau > 1$. As τ becomes very large, β approaches a limiting value of 1.0, causing the cutoff frequency f_c (defined as the frequency where the amplitude response is down by a factor of 2 from its maximum) to approach a limiting value, meaning that little additional filtering effect is gained for values of $\tau \gg 10$. The factors of τ in the x_1 equation and $4/\tau$ in the x_2 equation are present simply to scale the map values into a convenient range. It should be noted that the x_2 map does not contain a modulus operator. For $\tau = 10$, the eigenvalues of the map are $1.2 \pm 0.56i$. The factor of τ in the x_1 map is used to influence the stability properties of the response system.

Figure 15.1 shows the power spectra of the signals from the map for $\tau = 10.0$. Figure 15.1 (a) is a power spectrum of $x_1(n)$, while 15.1(b) is a power spectrum of $x_2(n)$.

The response system is

$$x_t(n) = x_1(n) + \eta,$$

$$y_1(n + 1) = 1.5y_1(n) - 0.1\tau y_2(n) + 1.5(x_t(n) - y_1(n)) \mod 1, \tag{15.4}$$

$$y_2(n + 1) = \left(\frac{4}{\tau}\right)y_1(n) + \left(1 - \frac{1}{\tau}\right)y_2(n).$$

The term η represents a Gaussian white noise signal. Variations in the stability of the response system may change its synchronization behavior in the presence of noise, so this coupling configuration was chosen so that the eigenvalue of the response map with the largest absolute magnitude was independent of τ, with a value of 0.63.
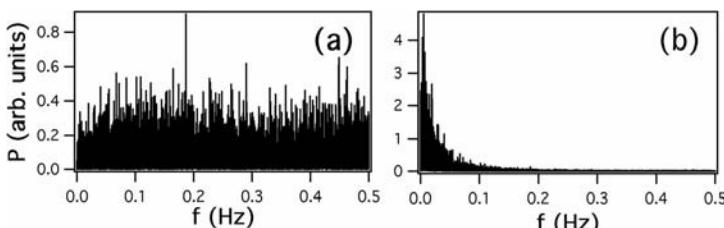

Fig. 15.1 (a) Power spectrum of the transmitted signal x_t from the map of Eqs. (15.3). (b) Power spectrum of the signal x_2 from the map of Eqs. (15.3).

When even a small amount of noise is added to the transmitted signal x_t, large errors in synchronization may result because of the sensitive nature of the modulus function. With even a very small amount of noise, the value of $y_1(n)$ might be altered by the modulus function while $x_1(n)$ has not been changed. Sterling [14] has developed a technique to correct for this problem: the feedback signal at the next iteration is computed and compared to the same signal when y_1 differs by the amount of the modulus:

$$y_f = \min_{\{j=-1,0,1\}} \{x_t(n+1) - [y_1(n+1) + j]\},$$

$$y_1(n+1) \rightarrow y_1(n+1) + j_{\min}. \tag{15.5}$$

The next value of $y_1(n)$ is corrected by adding the value of j that minimizes y_f.

Figure 15.2 shows the rms synchronization error δ when the noise signal η had a rms amplitude of 0.05 and τ was varied (the standard deviation of $x_1(n)$ was 0.28). The synchronization error δ was the rms value of $x_2(n) - y_2(n)$ divided by the rms value of $x_2(n)$. The dark circles in Fig. 15.2 show that the synchronization error decreases as τ increases. The synchronization error approaches a lower bound as τ increases because the filter cutoff frequency does not change much for $\tau \gg 10$, as explained above. The noise level of 0.18 (noise rms/signal rms) is shown as a horizontal line in Fig. 15.2.

Since the y_2 map is the low-pass filter in the response system, it is legitimate to ask if the y_1 part of the response system is necessary at all. As an alternative, the driving signal was input directly into the y_2 map:

$$y_2(n+1) = \left(\frac{4}{\tau}\right)x_t + \left(1 - \frac{1}{\tau}\right)y_2(n) \tag{15.6}$$
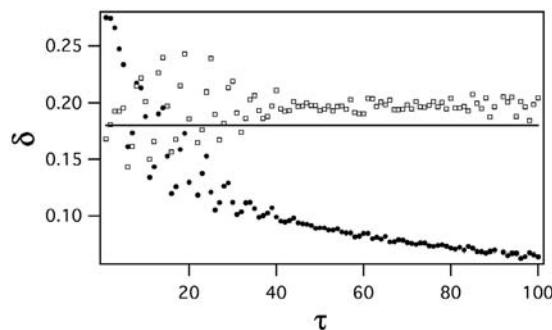

Fig. 15.2 Dark circles show synchronization error as a function of time constant τ for the response system of Eqs. (15.4) when the added noise is about 18% of the transmitted signal.
The open squares show the synchronization error when only a simple filter (as in Eq. (15.6)) is used for the response system.

This response system was stable. The synchronization error for this configuration is shown in Fig. 15.2 as open squares. The synchronization error in this case does not decrease as τ increases, but rather stays close to the noise level of x_t.

15.4
2-Frequency Synchronization in Flows

Noise robust chaotic systems based on chaotic flows are more practical, but the first flow example is used because it is easy to analyze [15]. The power spectrum of the output signal of the additive 2-frequency Rössler system is too broad to be transmitted, but the additive system is easy to analyze. It can be seen from this example that when the additive 2-frequency Rössler system is in its noise robust state, the low frequency part of this coupled nonlinear system looks mathematically very similar to a linear resonant system with a very narrow bandwidth, which accounts for the relative insensitivity to noise.

15.4.1
2-Frequency Additive Rössler

The 2-frequency Rössler chaotic system is described by [16, 17]

$$\frac{dx_1}{dt} = -a_0(\gamma_{11}x_1 + \gamma_{12}x_2 + x_3 + \beta x_4),$$

$$\frac{dx_2}{dt} = -a_0(x_1 - \gamma_{22}x_2),$$

$$\frac{dx_3}{dt} = -a_0(g(x_1) + x_3),$$

$$\frac{dx_4}{dt} = -a(\gamma_{44}x_4 + \gamma_{45}x_5 + x_6 + \gamma_{41}|x_1|),$$

$$\frac{dx_5}{dt} = -a(-x_4 + \gamma_{55}x_5 + x_3),$$

$$\frac{dx_6}{dt} = -a(-g(x_4) + x_6),$$

$$g(x) = \begin{Bmatrix} 0 & x < b_1 \\ m_1(x - b_1) & x \ge b_1 \end{Bmatrix}, \tag{15.7}$$

where $a_0 = 1$, $m_1 = 15$, $b_1 = 3$, $\gamma_{11} = \gamma_{44} = 0.02$, $\gamma_{12} = \gamma_{45} = 0.5$, $\gamma_{22} = 0.11$, $\gamma_{45} = 0.5$ and $\gamma_{55} = 0.02$. Equation (15.7) contains a fast system and a slow system. The x_1–x_3 equations describe a chaotic Rössler-like [18] system. The x_4–x_6 equations are a damped nonlinear system coupled to the Rössler system. The frequency band of the damped nonlinear system is determined by the time constant a, which is between 0 and 1. If $a_0 = 1$ and $a = 0.1$, for example, the frequency band of the x_4–x_6 system is 1/10th of the frequency band of the Rössler system of the x_1–x_3 equations. The parameter β could also vary between 0 and 1.
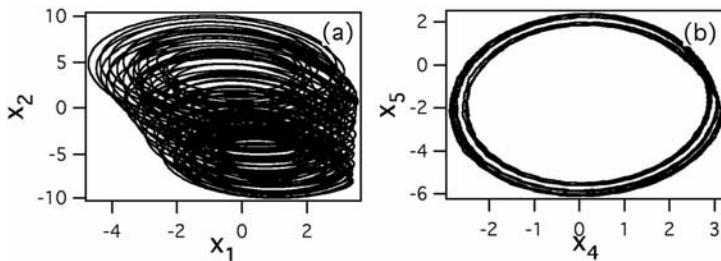
Fig. 15.3 Attractors for Eqs. (15.7).
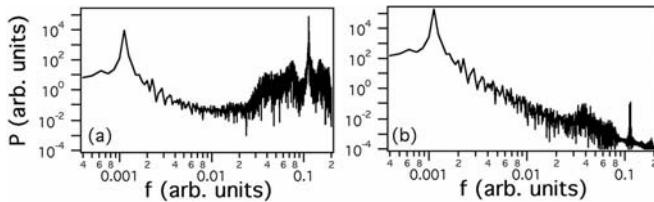
Fig. 15.4 (a) Power spectrum of x_1 from Eqs. (15.7) (peak frequency=0.113). (b) Power spectrum of x_4 from Eq. (15.7) (peak frequency=0.00113).

The 6d noise robust system was numerically integrated with a 4th order Runge–Kutta integration routine with a time step of 0.04 s. Figure 15.3 shows x_2 versus x_1 for $a_0 = 1$, $a = 0.01$, and $\beta = 1.0$, while 15.3(b) shows x_5 versus x_4 for these same parameters. Figure 15.4(a) is a power spectrum of x_1, while 15.4(b) is a power spectrum of x_4, showing the difference in frequencies.

A synchronous response system matching the drive system of Eqs. (15.7) was also built. The signal x_2 from Eqs. (15.7) was used as a drive signal. The response system was described by

$$x_d = x_2 + \eta\,,$$
$$\frac{dy_1}{dt} = -a_0(\gamma_{11}y_1 + \gamma_{12}y_2 + y_3 + \beta y_4)\,,$$
$$\frac{dy_2}{dt} = -a_0(y_1 - \gamma_{22}x_d)\,,$$
$$\frac{dy_3}{dt} = -a_0(g(y_1) + y_3)\,,$$
$$\frac{dy_4}{dt} = -a(\gamma_{44}y_4 + \gamma_{45}y_5 + y_6 + \gamma_{41}|y_1|)\,,$$
$$\frac{dy_5}{dt} = -a(-y_4 + \gamma_{55}y_5 + y_3)\,,$$
$$\frac{dy_6}{dt} = -a(-g(y_4) + y_6)\,. \tag{15.8}$$
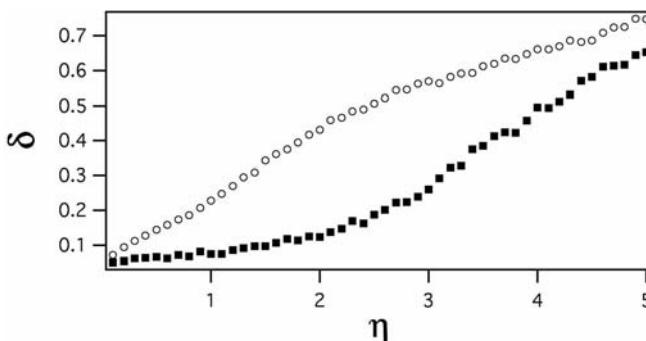
Fig. 15.5 Synchronization error δ as a function of normalized noise rms amplitude η for $a_0 = 1$ and slow time constant $a = 0.1$ (open circles) or 0.01 (filled in squares).
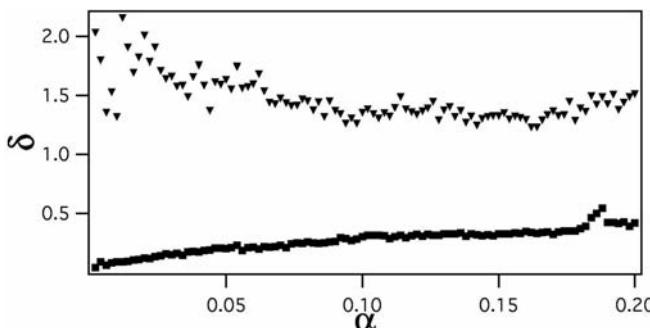

Fig. 15.6 Syn error δ as a function of slow time constant a. The squares are for $\beta = 1.0$, while the triangles are for $\beta = 0.0$.

The parameters in Eqs. (15.8) were chosen to match the parameters in Eqs. (15.7). The term η in Eqs. (15.8) was an additive white noise term.

When $\eta = 0$ (no noise), the 6d response system of Eqs. (15.8) synchronized to the 6d drive system of Eqs. (15.7) (after an initial transient). Additive noise caused a synchronization error. The error in synchronization δ was measured by calculating the rms value of $x_4 - y_4$ when Gaussian white noise was added to the driving signal x_d.

Figure 15.5 shows the synchronization error δ as a function of the noise rms amplitude η for $a_0 = 1$ and two different values of a, $a = 0.1$, and $a = 0.01$ (with $\beta = 1$). The noise rms amplitude was normalized by the transmitted signal rms amplitude. While the increase in synchronization error with noise was not linear, it was monotonic. There was no threshold effect as seen in [19, 20]. For the smaller value of a, corresponding to a greater difference in time scales between fast and slow systems, noise caused a smaller synchronization error.

Figure 15.6 shows the synchronization error δ as a function of the slow time constant a for two different values of β, $\beta = 1.0$ and $\beta = 0$. The rms amplitude

of the added noise was four times the rms amplitude of the driving signal x_2. When $\beta = 1.0$, the synchronization error decreases as the slow time constant a decreases, so in an applied setting, synchronization quality in the presence of noise could be adjusted to an arbitrary precision by adjusting the value of a. The practical result is that adequate synchronization may be maintained for any noise level by properly adjusting the relative time scales of the fast and slow systems.

Also shown in Fig. 15.6 is the synchronization error as a function of a when $\beta = 0$. Not only the synchronization error decrease with a, but also the error actually appears to increase for the lowest values of a. Changing the value of β has destroyed the noise robust property of this chaotic system.

15.4.2
Parameter Variation and Periodic Orbits

In order to understand the origin of the noise robustness, it is useful to find out what changes in the chaotic system as the parameter β is varied. From Fig. 15.3(b), the slow part of this chaotic system looks nearly periodic, so it should be useful to study the long period unstable periodic orbits (UPOs) for this system. The Newton-Raphson method is commonly applied to find UPOs [21].

There is a major numerical problem with finding UPOs with periods on the slow time scale of this system. The largest Lyapunov exponent for this system was 0.14 bits/s, while the long UPOs had periods on the order of 1720 s. By the time one slow orbit has been completed, most of the information about the initial conditions of the system will have been erased by the exponential growth of errors caused by the finite precision of the computer. As a result, when the Newton-Raphson method is applied, the range of initial conditions over which it converges is very small.

Because the separation between slow and fast time scales is large for this system, it is possible to approximately separate the 2-frequency Rössler system into a fast system and a slow system using the quasi steady state approximation from singular perturbation theory [22]. We may then apply the Newton-Raphson technique to the slow system only, leading to much better convergence.

Equation (15.8) for the synchronized response system (with $a_0 = 1$) may be rewritten as

$$a\frac{d\gamma_1}{d\tau} = -(\gamma_{11}\gamma_1 + \gamma_{12}\gamma_2 + \gamma_3 + \beta\gamma_4)\,,$$

$$a\frac{d\gamma_2}{d\tau} = -(\gamma_1 - \gamma_{22}x_d)\,,$$

$$a\frac{d\gamma_3}{d\tau} = -(g(\gamma_1) + \gamma_3)\,,$$

$$\frac{d\gamma_4}{d\tau} = -(\gamma_{44}\gamma_4 + \gamma_{45}\gamma_5 + \gamma_6 + \gamma_{41}|\gamma_1|)\,,$$

$$\frac{d\gamma_5}{d\tau} = -(-\gamma_4 + \gamma_{55}\gamma_5 + \gamma_3)\,,$$

$$\frac{d\gamma_6}{d\tau} = -(-g(\gamma_4) + \gamma_6)\,, \tag{15.9}$$

where $\tau = at$ represents a slow time scale. In the approximation $a \to 0$, the γ_1–γ_3 part of Eqs. (15.8) becomes a set of algebraic equations, which may be solved for the variables $\bar{y}_1$, $\bar{y}_2$, and $\bar{y}_3$, the quasi steady state approximations. Substituting these values into the slow equations yields

$$
\begin{aligned}
\frac{dy_4}{d\tau} &= -(\gamma_{41}\gamma_{22}|x_d| + \gamma_{44}y_4 + \gamma_{45}y_5 + y_6)\,, \\
\frac{dy_5}{d\tau} &= -(-b_1(\bar{y}_1)m_1(\bar{y}_1) - \gamma_{22}m_1(\bar{y}_1)x_d - y_4 + \gamma_{55}y_5)\,, \\
\frac{dy_6}{d\tau} &= -(-g(y_4) + y_6)\,.
\end{aligned}
\tag{15.10}
$$

The constants m_1 and b_1 from the function $g(y)$ have been written as functions of $\bar{y}_1$ because their presence depends on the value of $\bar{y}_1$. Because the function $g(y)$ is piecewise linear, it is not possible to find actual algebraic solutions for $\bar{y}_1$, $\bar{y}_2$ and $\bar{y}_3$, but for the purpose of this paper it does not matter. The approximate relations of Eqs. (15.10) will be used only to find a Jacobian for use with the Newton-Raphson method for finding UPOs of the low frequency system, so terms not explicitly dependent on the slow variables will drop out. In the quasi steady state approximation, the Jacobian for the slow system is

$$
J = \begin{pmatrix} -\gamma_{44} & \gamma_{45} & -1, \\ 1 & \gamma_{55} & 0, \\ \frac{\partial g(y_4)}{\partial y_4} & 0 & -1 \end{pmatrix}.
\tag{15.11}
$$

In this approximation, the values of the fast variables do not appear in the slow Jacobian. The value of y_4 was determined by numerically integrating the full set of equations (without the quasi steady state approximation) in the synchronized state.

15.4.3
Unstable Periodic Orbits

There may have been more than one period 1 UPO for the slow system for a given set of parameters, so the following numerical calculations do show some fluctuations. It would have been desirable to follow one distinct UPO as the parameters changed and calculate its properties, but the poor convergence of the Newton-Raphson algorithm for these long periods made tracking of an individual orbit impossible. Normally, one could track a UPO with parameter changes by finding the initial conditions for a UPO, making a small change in a parameter, and using the previous initial conditions as the starting point for a new UPO search, but for these long orbits, the search failed to converge for parameter changes as small as 0.1%.

Because tracking UPOs was not possible, for each new set of parameters, the equations of motion (Eqs. (15.7)) were started with random initial conditions.
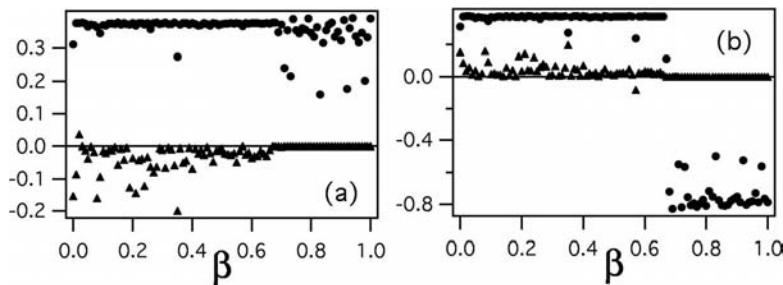
Fig. 15.7 (a) and (b) Nonzero Floquet multipliers for the slow UPO as β is changed. The circles are the real parts of the Floquet multipliers, while the triangles are the imaginary parts. There is a bifurcation at $\beta = 0.68$.

After initial transients died off, the values of the variables in Eqs. (15.7) were used as initial conditions in the UPO search. The approximate UPO period was also estimated from Eqs. (15.7) and used as an initial condition. The resulting UPO search converged for about 25% of the initial conditions.

15.4.4
Floquet Multipliers

It was believed that the noise robust properties of the system of Eqs. (17.7) were related to the stability of the slow system, so the slow Jacobian of Eqs. (15.1) was used to calculate the Floquet multipliers for the slow orbit. Figure 15.7 shows the Floquet multipliers for the slow orbit as the variable β is changed. For $\beta > 0.68$, the Floquet spectrum consists of two purely real values (with magnitude <1) and one 0 value. This is the same type of Floquet spectrum one would see for a linear oscillator driven at its resonant frequency [23]. Although
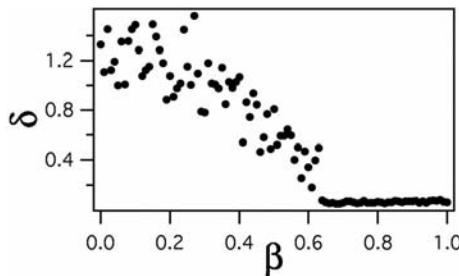

Fig. 15.8 Synchronization error δ as a function of β. The rms amplitude of the added Gaussian white noise is twice the rms amplitude of the driving signal. The noise robustness property appears to be lost for $\beta < 0.68$, corresponding to the bifurcation in the Floquet spectrum.

this orbit for the entire 6d system is unstable, the slow part of the system by it-self does not contain any instabilities, so there are no Floquet multipliers >1 for the slow part of the orbit.

The bifurcation seen in the Floquet spectrum for the slow orbit corresponds to a loss of the noise robustness spectrum for this system. Figure 15.8 shows the synchronization error δ for the response system of Eqs. (15.8) as β is varied. The rms value of the added noise in this example was twice the rms value of the driving signal. For $\beta > 0.68$, the synchronization error is small, and is unaf-fected by changes in β. For $\beta < 0.68$, the synchronization error is larger, and in-creases as β decreases.

15.4.5
Linewidths

Another way to confirm that the slow part of this Rössler system acts like a res-onant system is to measure the width of the largest peak in the power spectrum of the x_4 signal. One way to measure the linewidth is by measuring the Q fac-tor, the ratio of the center frequency of the main peak in the power spectrum to the width of this peak. The width of the peak is the width for which the power is half of the power at the maximum. A larger Q factor corresponds to a nar-rower linewidth, meaning that the low frequency part of the Rössler system acts like a narrowly tuned filter. Figure 15.9 shows the Q factor as a function of β. Note that the vertical axis in Fig. 15.9 is logarithmic.

The Q factor undergoes a large increase between $\beta = 0.4$ and 0.6. Above $\beta = 0.6$, the low frequency part of the Rössler system acts like a narrow band-fil-ter below this point, the low frequency part has a much broader bandwidth. Be-cause the bandwidth of the low frequency part is so small $\beta > 0.6$, it will not be as strongly affected by additive noise as it will be for $\beta < 0.6$.

The dependence of synchronization error on α, as shown in Figs. 15.5 and 15.6, fits with this narrow band filter picture. The Q factor for a filter is the ra-
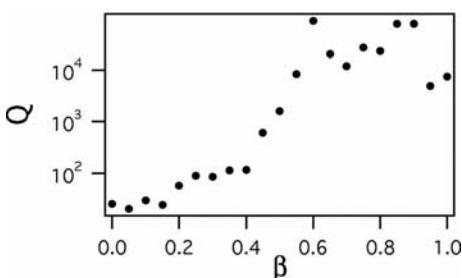

Fig. 15.9 Q factor for the low frequency part of the Rössler system as a function of β. Note that the vertical axis is logarithmic.

tio of center frequency to bandwidth, so if a constant Q is maintained, filter bandwidth will decrease as the center frequency of the filter decreases. The center frequency of the low frequency part of the chaotic system is dependent on the time constant a. As the filter bandwidth decreases, less of the noise will fall within the filter pass band, so the effect of noise on the slow part of the system should decrease.

15.5
Circuit Experiments

The synchronization properties of the 2-frequency additive Rössler system were also tested in a circuit experiment. The drive circuit was described by Eqs. (15.7), with the parameters $m_1 = 15$, $b_1 = 3$, $\gamma_{11} = 1$, $\gamma_{44} = 0.05$, $\gamma_{12} = \gamma_{45} = 0.5$, $\gamma_{22} = 0.11$, $\gamma_{55} = 0.05$, and $\beta = 1$. The time constants a_0 and a were set by changing the capacitors in the circuit. The circuit schematic is shown in Fig. 15.11.

When the circuit parameters were chosen so that $a_0 = 10^4$, $a = 10^3$, $\gamma_{44} = 0.05$, and $\gamma_{45} = 0.02$, the time scales were separated by a factor of 10, so the higher frequency peak in the power spectrum was at 1110 Hz and lower frequency peak in the power spectrum was at 111 Hz. Choosing different parameters altered the relative frequencies of the main peaks in the power spectrum of the circuit. If $a_0 = 10^4$, $a = 10^2$, $\gamma_{44} = 0.02$, and $\gamma_{45} = 0.02$, then the peak frequency in x_1 is still at 1110 Hz, but the peak frequency in x_4 is now at 11.1 Hz.

The response circuit was coupled to the drive in a different fashion than the response system of Fig. 15.8. Adding extra parameters to the coupling terms allowed for the Lyapunov exponents of the response system to be minimized, increasing the speed with which the response synchronized to the drive. The response circuit was described by

$$x_t = \sum_{i=1}^{6} k_i x_i \qquad y_r = \sum_{i=1}^{6} k_i y_i \,,$$

$$\frac{dy_1}{dt} = -a_0(\gamma_{11}y_1 + \gamma_{12}y_2 + y_3 + \beta y_4 + b_1(x_t - y_r)) \,,$$

$$\frac{dy_2}{dt} = -a_0(-y_1 + \gamma_{22}y_2 + b_2(x_t - y_r)) \,,$$

$$\frac{dy_3}{dt} = -a_0(-g(y_1) + y_3 + b_3(x_t - y_r)) \,,$$

$$\frac{dy_4}{dt} = -a(\gamma_{44}y_4 + \gamma_{45}y_5 + y_6 + \gamma_{41}|y_1|) \,,$$

$$\frac{dy_5}{dt} = -a(-y_4 + \gamma_{55}y_5 + y_3) \,,$$

$$\frac{dy_6}{dt} = -a(-g(y_4) + y_6) \tag{15.12}$$

i	k_i	b_i
1	5.34	−0.53
2	−2.58	0.34
3	−3.10	−0.23
4	1.60	0
5	−0.89	0
6	−1.61	0

Fig. 15.10 Values of k_i and b_i parameters in Eqs. (15.12).
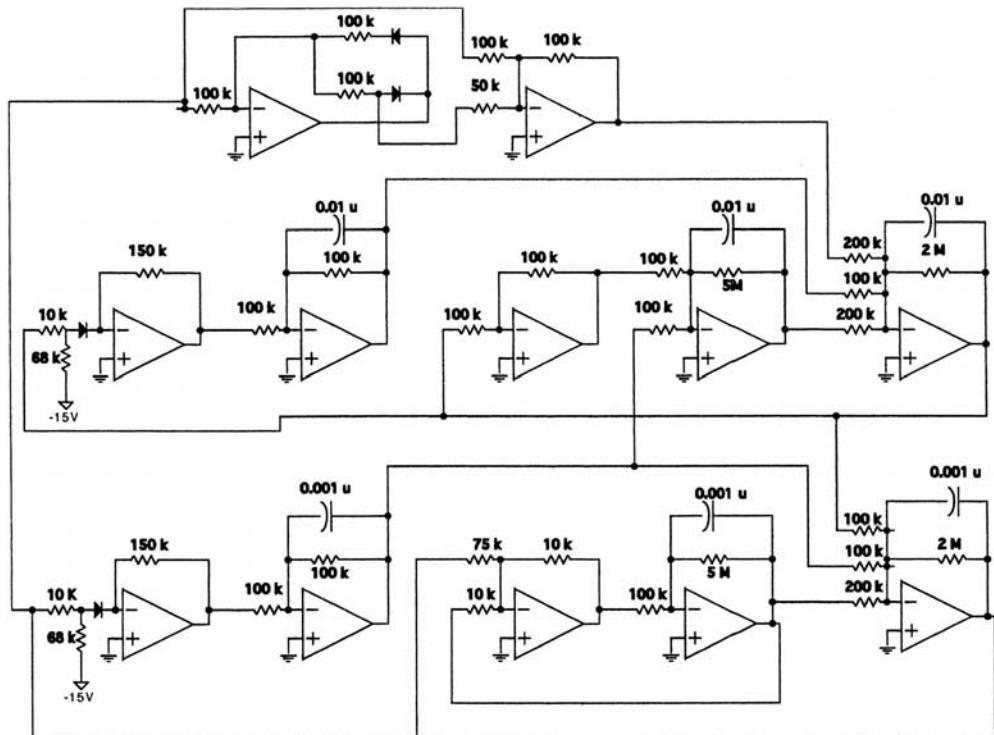

Fig. 15.11 Schematic for 2-frequency additive Rössler circuit.

with parameters $\gamma_{11} = 1$, $\gamma_{44} = 0.05$, $\gamma_{12} = \gamma_{45} = 0.5$, $\gamma_{22} = 0.11$, $\gamma_{55} = 0.05$, and $\beta = 1$. Note that the error signal $x_t - y_r$ is fed back only into the high frequency part of the circuit, y_1 to y_3.

The parameters k_i and b_i are set to minimize the largest Lyapunov exponent for the response circuit corresponding to Eqs. (15.12) [24, 25]. The k_i's and b_i's are varied by a linear optimization routine in order to minimize the largest Lyapunov exponent for the response circuit. For the parameters listed in Fig. 15.10, the largest Lyapunov exponent for the response circuit was $-1160\ \text{s}^{-1}$ ($a_0 = 10^4$, $a = 10^3$). There are many other possible combinations of the k's and b's that give similar Lyapunov exponents.
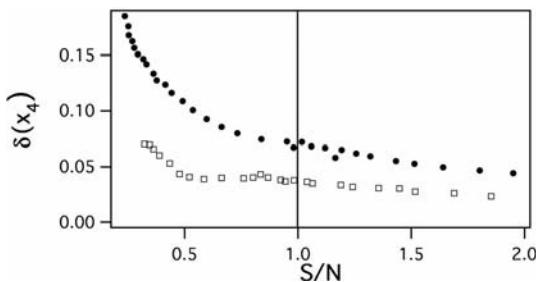
Fig. 15.12 RMS synchronization error $\delta(x_4)$ from the circuit as a function of RMS signal-to-noise ratio S/N. (a) Frequency ratio of 10. (b) Frequency ratio of 100.

15.5.1
Noise Effects

By varying the ratio between the frequencies of the two parts of the circuit, the amount of synchronization error caused by noise could be varied. To test this feature, white noise was added to the transmitted signal x_t (defined in Eqs. (15.1)). The signal-to-noise ratio (S/N) was calculated by dividing the RMS amplitude of x_t by the RMS amplitude of the white noise. The synchronization error for the low frequency part of the circuit, $\delta(x_4)$, was calculated by dividing the RMS amplitude of x_4-y_4 by the RMS amplitude of x_4.

Figure 15.12 shows the synchronization error as a function of S/N for two different ratios of a_0 and a. The filled-in circles show the synchronization error for a frequency ratio of 10. The synchronization error at a S/N of 1 (0 dB) is about 0.07, climbing to about 0.14 at a S/N of 0.33 (−4.8 dB). The minimum synchronization error at high S/N is about 0.02 because of mismatch between the circuits.

The open squares in Fig. 15.12 show the synchronization error for a frequency ratio of 100. For this larger frequency ratio, the synchronization error at a S/N of 1 is about 0.035, while at a S/N of 0.33 the error is about 0.07.

15.6
Communication Simulations

Probably a better practical measure of noise robustness than simple synchronization error is the bit error rate (BER) (BER for information transmitted by means of a chaotic carrier. The information transmission simulation described here is far from optimal (a method based on symbolic dynamics would probably be superior), but the simple communication simulation described here does illustrate a necessary principle for a noise robust communication system: as the noise level increases, it should be possible to increase bit length to maintain a constant BER, even when the signal-to-noise ratio is below 0 dB.

For this particular communication scheme, the transmitter is modified by weakly coupling a periodic signal to the low frequency part of the transmitter in order to synchronize its phase to a reference signal.

$$\frac{d\theta}{dt} = \omega,$$
$$\frac{dx_4}{dt} = -a(\gamma_{44}x_4 + \gamma_{45}x_5 + x_6 + \gamma_{41}|x_1| - k(s_1\sin(\theta) - \beta x_1)). \quad (15.13)$$

The signal θ is the phase control signal, used to modulate the phase of the low frequency part of the oscillator in order to communicate. The frequency ω is set equal to the peak frequency of the low frequency part of the oscillator, and the signal θ is coupled into the low frequency part in order to phase synchronize the oscillator [26]. The information signal, s_1, is set equal to ±1, while the coupling constant $k = 0.2$, and $\beta = 0.37$. The response system was described by Eq. (15.12).

The information signal s_1 in Eqs. (15.13) was set to ±1 to simulate a binary signal. The value of s_1 determined the phase of the low frequency part of Eqs. 15.13.

The response system of Eqs. (15.12) synchronizes to the transmitter, so the phase of the low frequency part of the response system reveals the phase of the corresponding part of the drive system, so that we can find the value of the information signal s_1 in Eqs. (15.13). A phase detector was used to accomplish this phase measurement:

$$\frac{d\theta}{dt} = \omega,$$
$$\frac{du}{dt} = \frac{dy_4}{dt} - \frac{a}{100.0}u,$$
$$v = \text{sgn}[\sin(\theta)]u$$
$$\frac{dw}{dt} = \frac{a}{10.0}(v - 0.1w). \quad (15.14)$$

The frequency ω, the frequency of the local reference oscillator in the response system, was the same frequency as in Eq. (15.13). As long as the phase of the local reference oscillator does not drift by much over one cycle, exact phase synchronization between the local oscillator and the chaotic response system is not necessary. The signal u was a high-pass filtered version of y_4, high-pass filtered because the absolute value function in Eqs. (15.12) produced a DC offset in y_4 when the noise signal was large. The "sgn" function is the signum function (+1 for the argument >0, -1 for the argument <0). The variable w in Eqs. (15.14) is set to zero at the start of each bit interval, and w is measured at the end of each bit interval to determine the value of the received bit. The measured value of w will be >0 or <0, depending on the bit value. For the simulations described here, it will be assumed that the local periodic oscillators have been synchronized.

The necessary bandwidth for the chaotic signal is found by measuring the BER. A low-pass filtered noise signal is added to a low-pass filtered version of the signal x_t and the resulting BER is measured at the receiver as the filter breakpoint is lowered. At some given breakpoint, the BER is seen to increase, so the filter breakpoint is set larger than this value. For the system in this paper, the minimum filter breakpoint was 7.5.

Figure 15.13 shows the probability of bit error P_b for the system of Eqs. (15.12)–(15.14). The dark circles show P_b for a bit length of $L = 653.9$, in which case a_0 was set to 10 and a was set to 0.2. The open circles show P_b for a bit length of $L = 1307.84$ (twice as long), with $a_0 = 10$ and $a = 0.1$. The open squares show P_b for $L = 20{,}924.8$, with $a_0 = 10.0$ and $a = 6.25 \times 10^{-3}$. The actual bit rates depend on the overall scale of the a values. The energy per bit/(noise power spectral density) (E_b/N_0) is calculated for a 2-sided noise power spectrum. The three sets of data lie along the same curve, demonstrating that the curve of P_b versus E_b/N_0 does not depend on bit length, a property not yet seen in other transmitted reference chaotic communication systems. The solid line in Fig. 15.14 shows the probability of bit error for binary phase shift keying (BPSK) [13] for comparison.

The noise robustness of this system may be further explored by changing the bit length L and finding the probability of bit error at a constant value of E_b/N_0. In Fig. 15.14, E_b/N_0 is held constant at 14.3 dB while the bit length L is varied by a factor of 32, from 653.9 to 20,924.8. The slow time constant a is varied at the same time the bit length is varied, so a varies from 0.2 to $0.2/32 = 0.00625$, while a_0 is held constant at 10.0. The upper scale in Fig. 15.14 shows the signal-to-noise ratio in decibels. The probability of bit error is seen to be roughly constant when the bit length L varies by a factor of 32, demonstrating that this
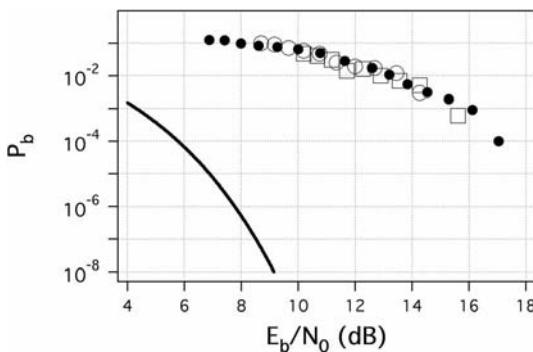
**Fig. 15.13** Probability of bit error P_b as a function of (energy per bit)/(2 sided noise power spectral density) (E_b/N_0) for the communication system described by Eqs. (15.12)–(15.14). The filled in circles are for a bit length of $L = 653.9$ s, while the open circles are for L twice as long, and the open squares are for L 32 times as long. The solid line is for binary phase shift keying (BPSK).
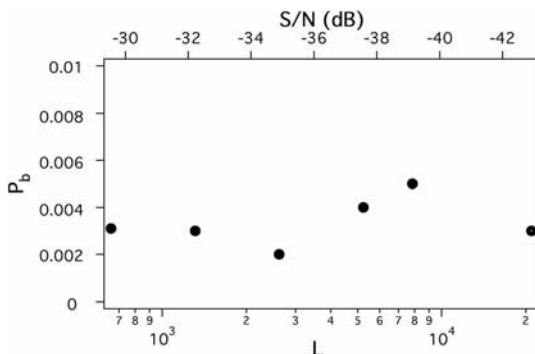
Fig. 15.14 Probability of bit error P_b for different bit lengths L at a constant E_b/N_0 of 14.3 dB. L varies by a factor of 32. The top axis is the corresponding signal-to-noise ratio.

self-synchronizing chaotic system is noise robust for added Gaussian noise. In addition, the performance of this communication system does not degrade when the signal-to-noise ratio is below 0 dB.

15.7
Multiplicative Two-Frequency Rössler Circuit

The final example of this chapter is a version of the Rössler system that is more practical for actual applications, and the final communication example is also more practical. The multiplicative version of the 2-frequency Rössler system is more useful because the required bandwidth is less, although it is harder to understand theoretically than the additive version.

The multiplicative 2-frequency Rössler circuit is described by [29]

$$\frac{dx_1}{dt} = -a_0 f(x_4)(0.02x_1 + 0.5x_2 + x_3 + 0.1x_4),$$

$$\frac{dx_2}{dt} = -a_0 f(x_4)(-x_1 - 0.13x_2),$$

$$\frac{dx_3}{dt} = -a_0 f(x_4)(-g(x_1) + x_3),$$

$$\frac{dx_4}{dt} = -a(0.02x_4 + 0.5x_5 + 0.5|x_1|),$$

$$\frac{dx_5}{dt} = -a(-x_4 + 0.02x_5),$$

$$g(x) = \begin{Bmatrix} 0 & x < 3 \\ 15(x-3) & x \geq 3 \end{Bmatrix}$$

$$f(x) = 1 + 0.2(x + 1.75), \tag{15.15}$$
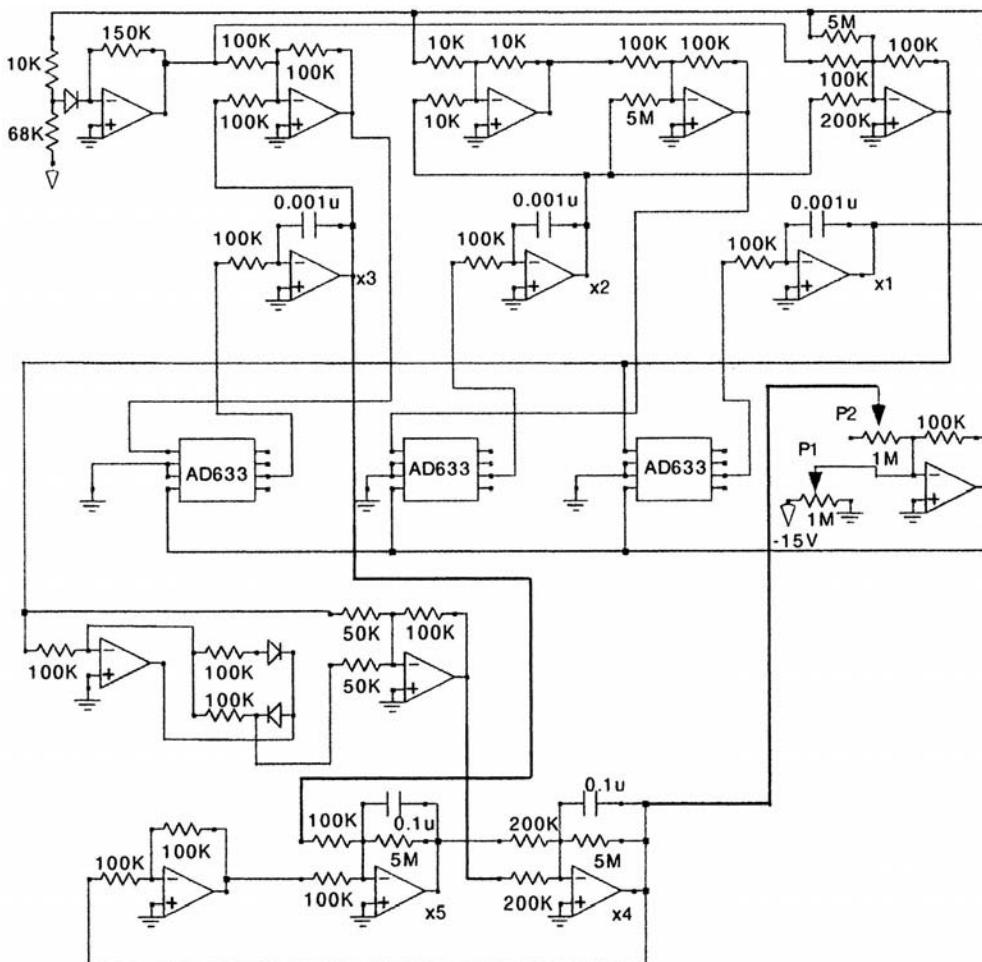
Fig. 15.15 Schematic of the 2-frequency multiplicative Rössler circuit described in Eqs. (15.15).

where $a_0 = 10^4$ and $a = 100$. For these parameters, the signal x_1 has a frequency of approximately 10.5 Hz, while x_3 has a frequency of about 946 Hz. The function $f(x)$ serves to broaden the spectrum of the fast signals (x_1 through x_3). Figure 15.15 is a schematic of the circuit described by Eqs. (15.15).

In many applications of radar or sonar, the power amplifier used to transmit the signal is most efficient for a signal with a constant envelope. In order to have a constant envelope transmitted signal, the signal that is actually transmitted is

$$\frac{dx_t}{dt} = -a_0 \left(sq\left(\frac{x_2}{x_1^2 + x_2^2} \right) + x_t \right), \tag{15.16}$$
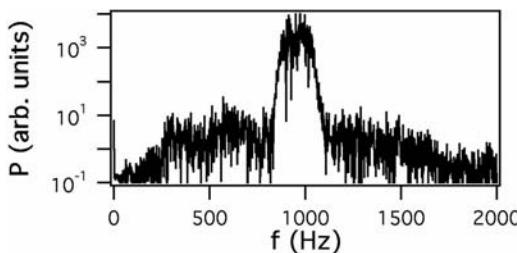
Fig. 15.16 Power spectrum of the signal x_t described in Eqs. (15.16).

where the $sq(x)$ function means that $sq(x) = 15$ V if $x>0$ and $sq(x) = -15$ V if $x<0$. The $sq(x)$ function was executed by an operational amp with a very large gain. The integral was used as a low-pass filter so that x_t was not a square wave. Figure 15.16 shows the power spectrum of x_t.

The response circuit may be described by the equations

$$\frac{dy_1}{dt} = -a_0(0.02y_1 + 0.5y_2 + 0.1y_4),$$

$$\frac{dy_2}{dt} = -a_0(-y_1 - kx_t),$$

$$\frac{dy_3}{dt} = -a(0.1y_3 + 0.5y_4 + 0.5|y_1|),$$

$$\frac{dy_4}{dt} = -a(-y_3 + 0.1y_4). \tag{15.17}$$

The response circuit does not match the drive circuit, which means that exact synchronization is not possible. In order to determine when generalized synchronization took place, the auxiliary system approach was used [27]. A second response circuit that was identical (within experimental error) was built. In order to improve the matching between circuits, resistors with a 1% tolerance were used, and a 20 turn potentiometer was used in the integrator for the y_1 signal to correct the time constant a for error in the capacitor value. The y_3 signals from the two response circuits were compared to determine if generalized synchronization was occurring.

Probably the most efficient way to communicate with chaotic systems is to use chaos control techniques to choose different symbolic dynamics [10, 28]. For the 2-frequency multiplicative Rössler circuit, chaos control may also be used to differentiate between different transmitter–receiver pairs. One could try to create different chaotic transmitter–receiver pairs by designing completely different chaotic circuits, but design of chaotic systems is difficult, so it is easier to use one chaotic system and create different transmitter–receiver pairs by choosing different dynamics.

The basic method for creating drive-response pairs is this:

1. Allow the chaotic drive system to follow a chaotic trajectory of finite length *L*, and store control information about this trajectory.
2. Control the drive system to always follow this finite length chaotic trajectory. Since the trajectory is finite length, it must be repeated, so the system is actually periodic with period *L*.
3. While the drive system follows a designated trajectory, use a signal from the drive system to drive a response system. The response system need not be identical to the drive system, as generalized synchronization can be useful for some applications.
4. While this response system is being driven, store control information about it.
5. Use the stored control information to control the driven response system. The response system trajectory will be the same as it was without control if the same drive signal is being used.
6. If the drive signal is now switched to a different signal, then the response system trajectory will be different.

The drive system can be controlled to follow different trajectories. Each different drive system trajectory has a corresponding response system trajectory when the response is uncontrolled. Using the matching response control sequence will not alter the response trajectory, but using a nonmatching response control sequence will alter the response from the uncontrolled trajectory.

For this experiment, rather than try to control the drive circuit, a 10,000 point signal x_t from the drive circuit was digitized at 20,000 points/s and played back through an arbitrary waveform generator. The playback rate was chosen so that the frequency of the signal from the arbitrary waveform generator matched the frequency of the original drive signal. Chaotic signals were recorded at two different times, resulting in two different chaotic sequences, labeled as *chaos1* and *chaos2*. The chaotic signals were played back with a peak-to-peak amplitude of 1.98 V, and the drive constant *k* in Eqs. (15.17) was set to 1.0.

For the control of the response circuit, the γ_3 signal was first passed through a 1 μF capacitor to remove the DC component. This signal was then integrated by an operational amp integrator to smooth out any residual ripple in γ_3, producing the signal ψ:

$$\frac{\mathrm{d}\psi}{\mathrm{d}t} = -a(\gamma_3 + 0.1\psi)\,, \tag{15.18}$$

where *R* and C_1 were previously defined. Several logic circuits were then used to give a short +5 V pulse when ψ crossed 0 in the negative direction.

In order to record the necessary control information, the response circuits were driven by the recorded x_t signal from the drive circuit, which had been controlled by the sequences *chaos1* or *chaos2*. When ψ crossed 0 in the negative direction, the value of γ_1 was stored for the response control sequence. The response control sequence when the drive circuit was controlled by *chaos1* was
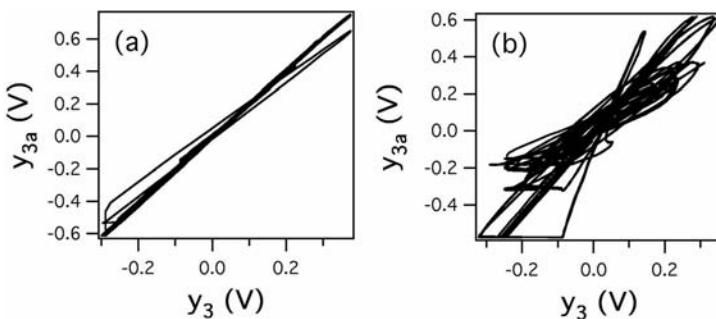
Fig. 15.17 (a) Plot showing synchronization of the response circuit (y_3) and the auxiliary response circuit (y_{3a}), confirming generalized synchronization when the correct response control sequence for a particular drive signal is used. (b) Plot showing a lack of general-ized synchronization between the response circuit (y_3) and the auxiliary response circuit (y_{3a}) when a response control sequence that does not correspond to the drive signal is used.

response1, and when the drive was controlled by *chaos2*, the response control sequence was *response2*.

During control, the response circuits were driven by the recorded x_t signal from the drive circuit, which had been controlled by the sequences *chaos1* or *chaos2*. When ψ crossed 0 in the negative direction, the difference between y_3 and the corresponding signal from the matching auxiliary circuit, y_{3a}, was compared to a fixed threshold in the computer. If $|y_3 - y_{3a}| > 0.3$, it was assumed that the response circuits were not synchronized, and the phase of the response control sequence was advanced by 1. If the difference was less than the threshold, the control phase was not advanced. For either result, the computer then set y_3 for the circuit to the next value in the response control sequence, after which the response control sequence phase was advanced. The sequences *chaos1* and *chaos2* corresponded to five cycles of the slow part of the circuit, so each control sequence had a length of five.

Figure 15.17 (a) is a plot of y_{3a} versus y_3 when the arbitrary waveform generator is playing back the drive signal x_t from a drive circuit controlled by *chaos1* and the response circuit is being controlled by the control sequence *response1*. There are some occasional small departures from synchronization, but most of the time the two auxiliary systems are synchronized. Figure 15.17(b) is the same plot when the drive circuit was controlled by *chaos2* but the response control sequence was still *response1*. There is a definite loss of synchronization, so the pair of response circuits are able to recognize the difference between *chaos1* and *chaos2*.

The effect of interference from another chaotic signal on the response circuits was also tested. A second arbitrary waveform generator was used to play back the transmitted signal from a drive circuit controlled by *chaos2*. This second transmitted signal, x_{t2}, was added to the x_t signal from a drive circuit controlled by *chaos1*. When both x_t and x_{t2} had the same amplitude, the cross correlation

between γ_3 and γ_{3a} was 0.96. When the x_{t2} signal amplitude was 1.5 times the amplitude of the x_t signal, the cross correlation dropped to 0.91, lower than the value when the wrong drive signal was used. The response circuits can reject some interference, but they have trouble if the interference is too similar to the driving signal.

15.8
Conclusions

Synchronous chaotic systems need not be sensitive to added noise. In this chapter, we have presented one way to construct self-synchronizing chaotic systems that are robust to added noise, that is by adding a second oscillator at a lower frequency. We have shown above that for the correct parameters, this lower frequency nonlinear oscillator has some of the same properties as a linear resonant oscillator, which allows it to filter out noise and interference. Elsewhere, we have speculated that this same mechanism may be at work in biological systems [15]. We have also demonstrated some simple communication schemes that use the 2-frequency circuits. While these communication ideas are not as efficient as standard digital communication methods, their simplicity and fast synchronization may make them useful for niche applications.

Noise robust chaotic systems are not limited to having only 2 frequencies. More low frequency oscillators may be added if necessary to produce other desirable properties, such as a better autocorrelation function for radar applications [30]. The multifrequency method is a useful design tool for chaotic systems.

References

1 L. M. Pecora and T. L. Carroll, Physical Review Letters 64 (1990), p. 821–824.

2 L. O. Chua, T. Yang, G.-Q. Zhong and C. W. Wu, IEEE Transactions on Circuits and Systems Part I 43 (1996), p. 862–868.

3 K. M. Cuomo and A. V. Oppenheim, Physical Review Letters 71 (1993), p. 65–68.

4 L. Kocarev and U. Parlitz, Physical Review Letters 74 (1995), p. 5028–5031.

5 G. Kolumban, M. P. Kennedy and L. O. Chua, IEEE Transactions on Circuits and Systems – Part I: Fundamental Theory and Applications 44 (1997), p. 927–935.

6 K. Murali and M. Lakshmanan, Physical Review E 48 (1993), p. 1624–1626.

7 A. V. Oppenheim, K. M. Cuomo, R. J. Barron and A. E. Freedman, in 3rd Technical Conference on Nonlinear Dynamics and Full Spectrum Processing, 1995, AIP, New York, 1995.

8 U. Parlitz, L. Kocarev, T. Stojanovski and H. Preckel, Physical Review E 53 (1996), p. 4351–4361.

9 N. F. Rulkov and L. Tsimring, International Journal of Circuit Theory and Applications 27 (1999), p. 555–567.

10 C. Williams, IEEE Transactions on Circuits and Systems Part I: Fundamental Theory and Applications 48 (2001), p. 1394–1404.

11 A. Abel, W. Schwartz and M. Goetz, IEEE Transactions on Circuits and Systems Part I 47 (2000), p. 1726–1732.

12 T. L. Carroll, Chaos 12 (2002), p. 275–278.

13 B. Sklar, Digital Communications, Fundamentals and Applications, Prentice-Hall, Englewood Cliffs, NJ, 1988.

14 D. G. Sterling, Chaos 11 (2001), p. 29–46.

15 T. L. Carroll, Chaos 15 (2005), p. 013109.

16 T. L. Carroll, IEEE Transactions on Circuits and Systems Part I: Fundamental Theory and Applications 48 (2001), p. 1519–1522.

17 T. L. Carroll, Physical Review E 64 (2001), p. 015201(R).

18 O. E. Rössler, Z. Naturforsch. 38 a (1983), p. 788–801.

19 C. Zhou, J. Kurths, I. Z. Kiss and J. L. Hudson, Physical Review Letters 89 (2002), p. 014101.

20 C. Zhou and J. Kurths, Physical Review Letters 88 (2002), p. 230602.

21 T. S. Parker and L. O. Chua, Practical Numerical Algorithms for Chaotic Systems, Springer, Berlin 1989.

22 P. Kokotovic, H. Khalil and J. O'Reilly, Singular Perturbation Methods in Control: Analysis and Design, SIAM, Philadelphia, 1999.

23 J. Guckenheimer and P. Holmes, Nonlinear Oscillations, Dynamical Systems, and Bifurcations of Vector Fields, Springer, Berlin, 1990.

24 J. H. Peng, E. J. Ding, M. Ding and W. Yang, Physical Review Letters 76 (1996), p. 904–907.

25 G. A. Johnson, D. J. Mar, T. L. Carroll and L. M. Pecora, Physical Review Letters 80 (1998), p. 3956–3959.

26 A. S. Pikovsky, M. G. Rosenblum, G. V. Osipov and J. Kurths, Physica D 104 (1997), p. 219–238.

27 H. D. I. Abarbanel, N. F. Rulkov and M. M. Sushchik, Physical Review E 53 (1996), p. 4528–4535.

28 S. Hayes, C. Grebogi, E. Ott and A. Mark, Physical Review Letters 73 (1994), p. 1781–1784.

29 T. L. Carroll, Physical Review E 69 (2004), p. 046202

30 T. L. Carroll, Chaos 15 (2005), p. 013109.

16
Nonlinear Communication Strategies

Henry D. I. Abarbanel
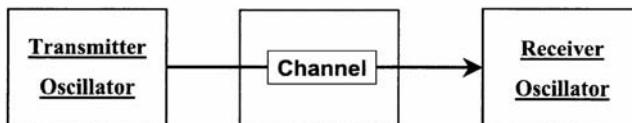
16.1
### Introduction

Many communication schemes using linear or nonlinear transmitters and receivers utilize synchronization between those elements to provide the framework for the modulation of information onto the transmitter waveform and the demodulation of that information at the receiver. Figure 16.1 presents a block diagram overview of this, and is hardly original to this discussion [1]. If the transmitter produces chaotic waveforms, then the channel must provide capacity beyond that to carry the information in a transmitted message as the entropy of the transmitter is

$$-\sum_{\text{symbols}} P(\text{symbols}) \log\left(P(\text{symbols}) > 0\right),$$

and the "state" of the transmitter must be sent along with the message so that the receiver can reconstruct that state. The receiver must recognize the transmitter signal and must determine whether or not the transmitter waveform is modulated. There are "chaotic communication" strategies which do not utilize synchronization. They rely on "on/off" methods where some aspect of the attractor, perhaps some phase space region, is assigned to a particular symbol, and the receiver need not know anything about the transmitter but needs only a lookup table to determine which symbol has been sent [1, 2]. No particular nonlinear aspects of the signal generation are used. Who really cares about using chaotic signals as carriers of information? In a sense the key property of the chaotic carrier is that it is naturally broadband and rather simple to generate. Chaotic transmitter receiver pairs can be autosynchronizing as well. My personal best guess for how all this work on chaotic communication will be useful in real-world communication is this: *knowing it can be done, people will devise communication strategies which use the method in order to save power, to reduce the cost of design, to achieve robust transmitters or receivers, and to achieve better signal-to-*

Communicating with Oscillators

Synchronize Oscillators

Put message on at Transmitter ⟶ Take message off at Receiver

Nonlinear Transmitter   Nonlinear Channel---Equalization

Distortion Noise

Fig. 16.1 Overview of a communication system based on synchronizing the transmitter and receiver oscillators.

noise characteristics – all these are interesting things the present discussion does not address.

16.1.1
Secrecy, Encryption, and Security?

In evaluating encryption systems one must assume the adversary has total knowledge of your communication system, transmitter, and receiver. If you do not share it with them, they will steal it. Think about how the allies broke the WWII German Enigma system; they had a copy.

Realistic security of communication then means it takes so long for the adversary to determine which parameters you used in your transmission at a given moment that the importance of the message is zero when it is finally de-crypted long after the transmission occurs. This is accomplished by algorithms that are very difficult to reverse-engineer and/or require very lengthy computa-tions, such as PGP or other schemes.

Chaos-based communication methods add little or nothing to strong security, and discussing them as if they were somehow more secure is misleading. Even referring to chaotic communication schemes as "secure" is a misnomer as a general rule.

The topics in this chapter will cover:
- the previous general discussion,
- synchronization: when is it possible? How to test for it?
- communication schemes without nonlinear channel distortion,
- communication by pulses in a nonlinear channel that disperses, attenuates, and distorts, and
- undoing the nonlinear channel, undistortion or equalization.

16.2
Synchronization

The general problem of synchronization is shown in Fig. 16.2 [3–6]. A transmitter with multidimensional state $\mathbf{x}(t)$ sends a scalar signal $s(t) = h(\mathbf{x}(t))$ to a receiver which has a state $\mathbf{y}(t)$. If there is a function determining the connection between the transmitter state and the receiver state at time t, $\mathbf{y}(t) = q(\mathbf{x}(t))$, then we say the transmitter and the receiver are in a state of generalized synchronization [7]. Identity synchronization, $\mathbf{x}(t) = \mathbf{y}(t)$, can occur when $G(\mathbf{y} = \mathbf{x}, s = 0) = F(\mathbf{x})$. The important thing about generalized synchronization is that since the state of the receiver is determined by the state of the transmitter, modulation of the transmitter signal is detectable at the receiver.
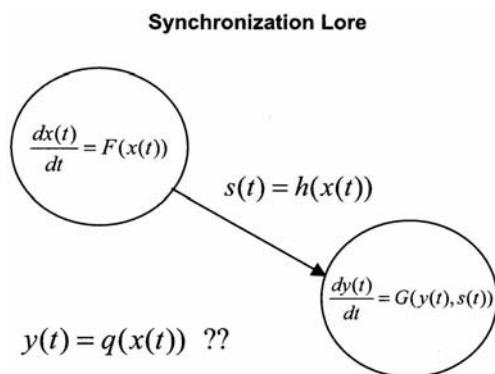

Fig. 16.2 Basic scheme for synchronization. When the transmitter $\mathbf{x}(t)$ is synchronized with the receiver $\mathbf{y}(t)$, $\mathbf{y}(t) = q(\mathbf{x}(t))$, and the measurement of the receiver state tells us the transmitter state. Identity synchronization is $q(\mathbf{x}(t)) = \mathbf{x}(t)$; $\mathbf{y}(t) = \mathbf{x}(t)$.


Fig. 16.3 Layout of the auxiliary system method for determining generalized synchronization between a transmitter with dynamical variables $\mathbf{x}(t)$ and a receiver with dynamical variables $\mathbf{y}(t)$.

How can we tell whether a transmitter and a receiver can be in generalized synchronization? One useful method is the "auxiliary system method" shown in Fig. 16.3 [8].

Using two identical copies of the receiver, present the same output $\mathbf{x}(t)$ to the receiver via $s(t)$. After some transient, if the output of the two receivers is the same $\mathbf{y}_1(t) = \mathbf{y}_2(t)$, then there is generalized synchronization. This is actually clear as both outputs are equal to $q(\mathbf{x}(t))$. The main caveat on this statement is that the systems could be multistable; namely, they might have several attractors with complicated basins of attraction. The result here requires that the two receiver systems start within the same basin of attraction.

It is usually quite difficult, perhaps impossible, to build two *identical* receivers, however, a clever method developed by Tang et al. in 1997 [9] neatly skirts
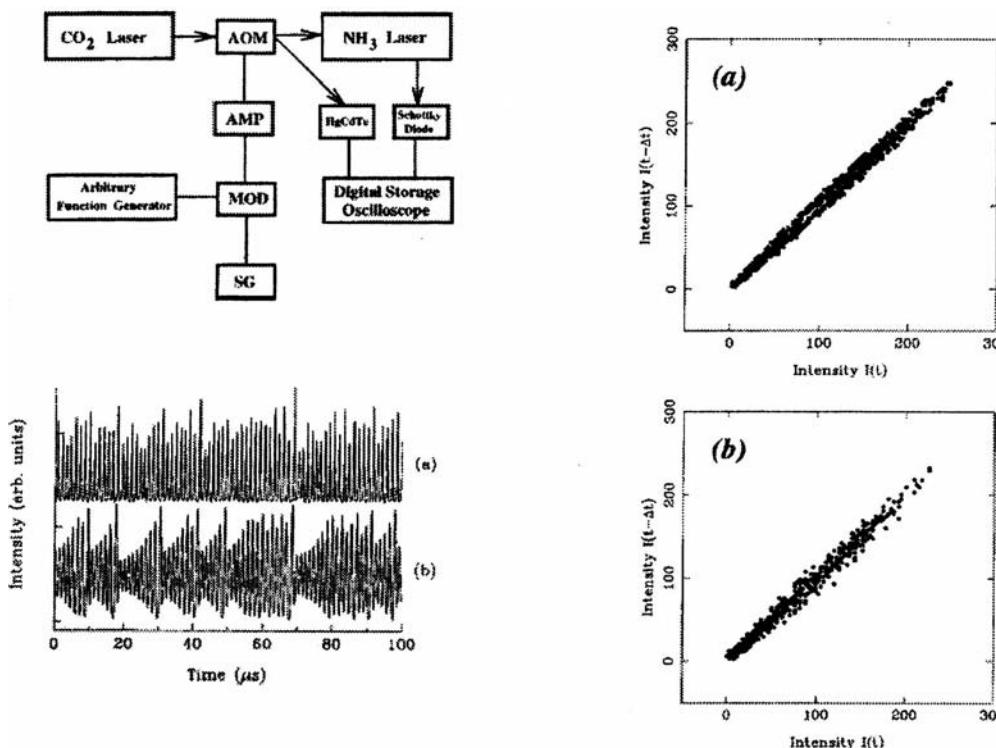

Fig. 16.4 (Upper left) Layout of the Tang et al. [9] experiments. A signal generator produces output from the three-dimensional Lorenz system. This modulates the output intensity of a CO_2 laser which is injected into an NH_3 laser. The output of the CO_2 laser is measured by a HgCdTe device to be $\approx 1 \frac{W}{cm^2}$, and the output of the NH_3 laser is measured by a Schottky diode. The NH_3 output is recorded every $\Delta t = 150$ μs and plotted against itself. (Lower left) (a) The output of the NH_3 laser; (b) the output of the CO_2 laser. The two signals are not identical. (Right panels) (a) The CO_2 laser intensity plotted against itself with a 150 μs delay; (b) the NH_3 laser intensity plotted against itself recorded 150 μs earlier. This demonstrates generalized synchronization of the lasers. For lower CO_2 laser intensity, this does not occur.

this issue. Tang et al. record the input signal $s(t)$ from a transmitter and then present the same signal to the same receiver at different times with intervals between the presentations large enough that the receiver oscillator is in a different state each time the transmitter signal is presented. Tang et al. presented their recorded transmitter signal to the receiver periodically with a separation Δt between the presentations. This results in outputs $o_n(t) = o(t + (n - 1)\Delta t)$. One then plots $o_n(t)$ versus $o_{n-1}(t)$ and looks for a straight line at 45° in the plot.

Tang et al. drove a CO_2 laser with output from a Lorenz attractor and then used the light from the CO_2 laser to drive an NH_3 laser. They examined the generalized synchronization of the two lasers as a function of the intensity of the CO_2 laser beam. They used $\Delta t = 150$ µs. The general outline of the experiment is shown in Fig. 16.4. Not shown are results with lower CO_2 laser intensity where generalized synchronization does not occur.

The real message here, besides the nice formulation of the auxiliary system method, is that one can test in practice for generalized synchronization between a chosen transmitter and a selected receiver. When one finds it is present for some range of couplings, then we have identified a useful pair of devices that could possibly be used for communication. We highly recommend this as a first step in determining whether a selected transmitter and receiver will be a good match for nonlinear communication.

16.3
Communicating Using Chaotic Carriers

In Fig. 16.5 we show the general scheme for communicating between two oscillators. This works for linear and for nonlinear systems. A fraction $cV_T(t)$ of the
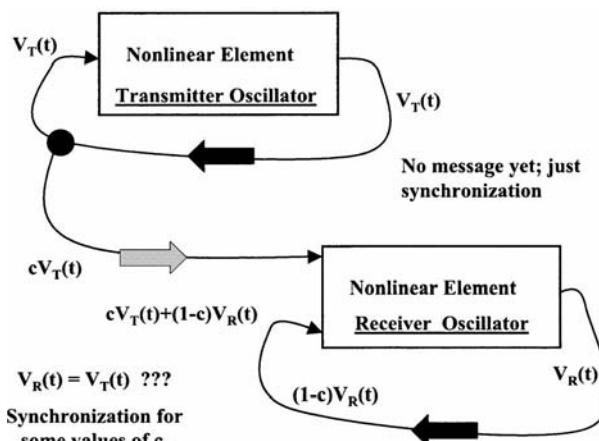

Fig. 16.5 General scheme for transmitting signals between two nonlinear oscillators. A fraction c is taken from the circulating signal in the transmitter and sent to the receiver. If $V_R(t) = V_T(t)$ for some values of c, synchronization occurs. There is no message being sent at this stage.

circulating signal in the transmitter is sent to the receiver and a fraction of the receiver signal $(1 - c)V_R(t)$ is added to this at the input to the receiver. For some values of c we may have $cV_T(t) + (1 - c)V_R(t) = V_T(t) = V_R(t)$, so synchronization is a possible solution to this system. The state of the transmitter is determined by $V_T(t)$ and other internal, possibly unmeasured dynamical variables $\mathbf{u}_T(t)$. The same is true for the receiver which is described by $V_R(t)$ and $\mathbf{u}_R(t)$. The dynamical equations associated with Fig. 16.5 are

$$\frac{dV_T(t)}{dt} = F(V_T(t), \mathbf{u}_T(t)),$$

$$\frac{d\mathbf{u}_T(t)}{dt} = \mathbf{G}(V_T(t), \mathbf{u}_T(t)),$$

$$\frac{dV_R(t)}{dt} = F(cV_T(t) + (1 - c)V_R(t), \mathbf{u}_R(t)),$$

$$\frac{d\mathbf{u}_R(t)}{dt} = \mathbf{G}(cV_T(t) + (1 - c)V_R(t), \mathbf{u}_R(t)). \tag{16.1}$$

A very useful special case of this is for $c = 1$, which makes the receiver open loop while the transmitter is unaffected. The signal coming into the nonlinear element of the transmitter is $V_T(t)$ whatever the value of c, but when $c = 1$ the value of the signal into the receiver nonlinear element is also $V_T(t)$. This means the output from the receiver dynamics must also be $V_T(t)$, and the receiver and transmitter are synchronized. This idea requires the receiver nonlinear element to be identical to the transmitter nonlinear element, but as we shall see in an experimental result below, even though one can never attain this identity of transmitter and receiver, the scheme works rather well. The $c = 1$ strategy expressed in equations is this:

$$\frac{dV_T(t)}{dt} = F(V_T(t), \mathbf{u}_T(t)),$$

$$\frac{d\mathbf{u}_T(t)}{dt} = \mathbf{G}(V_T(t), \mathbf{u}_T(t)),$$

$$\frac{dV_R(t)}{dt} = F(V_T(t), \mathbf{u}_R(t)),$$

$$\frac{d\mathbf{u}_R(t)}{dt} = \mathbf{G}(V_T(t), \mathbf{u}_R(t)). \tag{16.2}$$

Except for the equation for $V_R(t)$ this is essentially the synchronization idea of Pecora and Carroll [4]. The first discussion of the $c = 1$ idea was by Volkovskii and Rulkov in 1993 [10].

One introduces a message $M(t)$ into this $c = 1$ idea as shown in Fig. 16.6. The symbol ⓒ is meant to be any invertible operation. The modulated carrier $M(t) ⓒ V_T(t)$ is received, and the receiver produces $V_R(t) = V_T(t)$. Now using $V_T(t)$ and $M(t) ⓒ V_T(t)$, one can invert the received signal to recover $M(t)$.
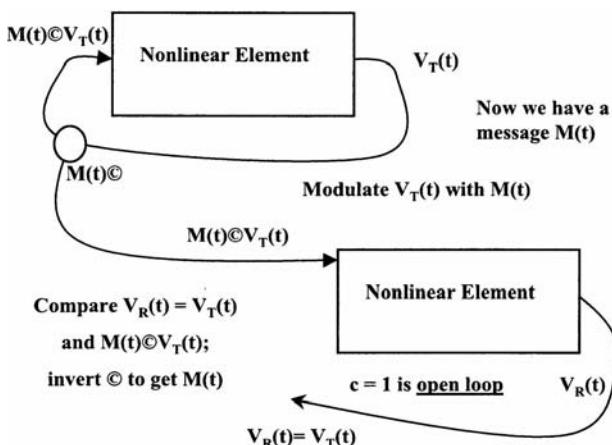
Fig. 16.6 General scheme for transmitting signals between two nonlinear oscillators with $c = 1$ compared to Fig. 16.5. This is a closed loop transmitter and an open loop receiver. Experimental examples of this setup are discussed in the text.

16.4
Two Examples from Optical Communication

16.4.1
Rare-Earth-Doped Fiber Amplifier Laser

Rare earth elements, erbium is especially widely used, have a strong transition line in the wavelength range where conventional, off-the-shelf optical fibers have either a minimum of dispersion or absorption, namely between about 1300 nm and 1550 nm. If one dopes the glass of an optical fiber with erbium with a concentration of a few hundred parts per million, the lasing amplification of light input to about 10 m of doped fiber can be as large as 30 dB. This makes such fiber amplifiers very attractive commercially as inserts into long distance fiber lines.

If one takes a commercially available amplifier with a doped fiber such as this as the active element, one can make an oscillating laser by reinserting the amplifier output back into the amplifier input. Figure 16.7 shows this in graphic form and indicates how such a laser might be used for communicating using the methods just discussed. In the laser system one dynamical variable is the complex electric field amplitude in the transmitter $E_T(t)$ and the other is the population inversion $w_T(t)$ in the erbium active element. One can measure the electric field $E_T(t)$ but not the population inversion $w_T(t)$.

The dynamical description of this system involves a time delay τ associated with the propagation of the electric field from the output of the amplifier back into the input. The $c = 1$ equations for the system involve a time-τ map of the electric field through the fiber connecting the amplifier exit to its input and dif-
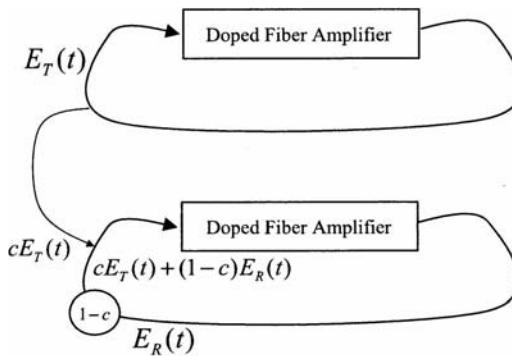
Fig. 16.7 Use of the two rare-earth-doped fiber amplifiers as transmitter and receiver in communication. Chaotic oscillations of the electric field circulating in the fiber connecting the output to the input of the doped-fiber amplifier are to be used as the carrier of information.

ferential equations describing the population inversion being pumped, by a drive Q, attenuating with a time constant $\frac{1}{T_1}$, and being driven by the electric field with a gain G and a phenomenological induced emission strength A:

$$E_T(t + \tau) = M_E(w_T(t), E_T(t)) ,$$
$$\frac{dw_T(t)}{dt} = Q - \frac{1}{T_1} \left\{ w_T(t) + 1 + \frac{A}{G} |E_T(t)|^2 (e^{Gw_T(t)} - 1) \right\} ,$$
$$E_R(t + \tau) = M_E(w_R(t), E_T(t)) ,$$
$$\frac{dw_R(t)}{dt} = Q - \frac{1}{T_1} \left\{ w_R(t) + 1 + \frac{A}{G} |E_T(t)|^2 (e^{Gw_R(t)} - 1) \right\} , \tag{16.3}$$

and M_E is the solution to the propagation equations for the electric field around the optical fiber.

This system is attractive since one can actually prove that it synchronizes [13]. Note that

$$\frac{d(w_T(t) - w_R(t))}{dt} = \frac{-1}{T_1} \left\{ w_T(t) - w_R(t) + \frac{A}{G} |E_T(t)|^2 e^{Gw_R(t)} (e^{G(w_T(t) - w_R(t))} - 1) \right\} , \tag{16.4}$$

and using the fact that $e^x - 1 \geq x$ to show

$$\frac{d(w_T(t) - w_R(t))}{dt} \leq - \frac{(w_T(t) - w_R(t))}{T_1} \left\{ 1 + \frac{A}{G} |E_T(t)|^2 e^{Gw_R(t)} \right\} , \tag{16.5}$$

we see that $w_T(t) - w_R(t) \to 0$ for large times.

This result agrees both with the experiments of Raj Roy and his students [11, 12] who used rare-earth-doped fiber amplifiers for communication and with numerical simulations of the closed-loop system of the fiber amplifier coupled to itself.

The rare earth doped fiber laser communication method has been shown to work by Raj Roy and his students. It suffers a serious drawback as an interesting practical system arising from the very long lifetime of the metastable atomic state of erbium at the upper level of the lasing transition. This lifetime is nearly 10 ms which is orders of magnitude larger than typical atomic transition lifetimes, and it effectively limits the communication bandwidth of such a scheme to 100 Hz which is not very attractive.

However, the ideas can be explored in another optical system where the bandwidth for communication is hundreds of megahertz or even a few gigahertz. We turn to that now.

16.4.2
Time Delay Optoelectronic Feedback Semiconductor Laser

The semiconductor optoelectronic feedback laser consists of a standard laser diode with another diode reading the intensity of the output light and feeding the output current of that diode into the bias current of the original laser. Figure 16.8 shows the setup used by J.-M. Liu at UCLA and his students. The equations for the complex amplitude of the electric field in the laser diode $E(t)$ and the population inversion $N(t)$ read

$$\frac{dE(t)}{dt} = -\frac{\gamma E(t)}{2} + i(\omega_0 - \omega_c) + \frac{\Gamma}{2}(1 - ib)g(N(t))E(t)$$

$$\frac{dN(t)}{dt} = \frac{J(t)}{ed}\left(1 + a\frac{|E(t-\tau)|^2}{|E_0|^2}\right) - \frac{N(t)}{\tau_s} - \frac{2\varepsilon_0 n^2}{\hbar\omega_0}g(N(t))|E(t)|^2 . \qquad (16.6)$$

As a function of the delay τ around the optoelectronic feedback loop the system undergoes bifurcations from fixed points (constant intensity output) for $\tau \leq 3$ ns to low-dimensional chaos near $\tau \approx 4$ ns and to higher dimensional chaotic behavior (dimension about 11.5) near $\tau \approx 10$ ns.

In Fig. 16.9 we have the results of a series of experiments carried out at $c = 0.8$; near, but below, the condition $c = 1$ for an open loop receiver [14]. In
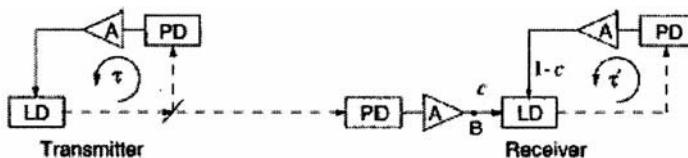

Fig. 16.8 Experimental setup of the optoelectronic feedback semiconductor laser used by J.-M. Liu and his students at UCLA.
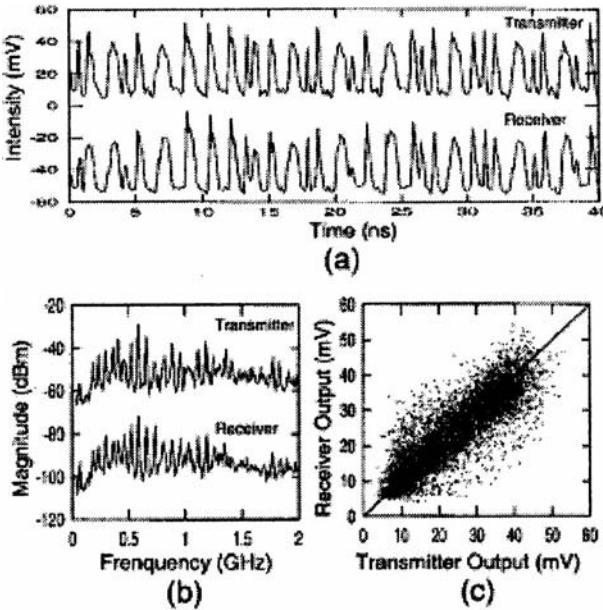
Fig. 16.9 Experimental results for chaotic synchronization using the setup in Fig. 16.8 and $c = 0.8$. In (a) is shown the time series of the transmitter and the receiver. In (b) are the Fourier spectra of the transmitter and the receiver. In (c) the outputs of diodes (in mV) proportional to the transmitter and receiver intensities are plotted against one another.

this circumstance we see that the time series of intensity for the transmitter and receiver and the Fourier power spectrum (panels (a) and (b) in Fig. 16.9) are rather similar to the eye, and in panel (c) where the transmitter and receiver intensities are plotted against one another, we see that the synchronization is rather good.

In Fig. 16.10 this similarity is explored quantitatively. We define the cross-correlation coefficient

$$\rho = \frac{\langle (I_T(t) - \langle I_T(t)\rangle)(I_R(t) - \langle I_R(t)\rangle)\rangle}{\sqrt{\langle (I_T(t) - \langle I_T(t)\rangle)^2\rangle \langle (I_R(t) - \langle I_R(t)\rangle)^2\rangle}} \,, \tag{16.7}$$

where $I_T(t) = |E_T(t)|^2$ is the transmitter intensity and $I_R(t) = |E_R(t)|^2$, the receiver intensity, and the time average $\langle f(t)\rangle$ is

$$\langle f(t)\rangle = \frac{1}{T}\int_{-\frac{T}{2}}^{\frac{T}{2}} f(t)\,\mathrm{d}t \,. \tag{16.8}$$

In Fig. 16.10 we see a plot of ρ versus c for this transmitter/receiver laser setup as well as ρ at $c = 0.8$ as a function of the fractional time delay mismatch $\frac{\Delta\tau}{\tau}$ be-
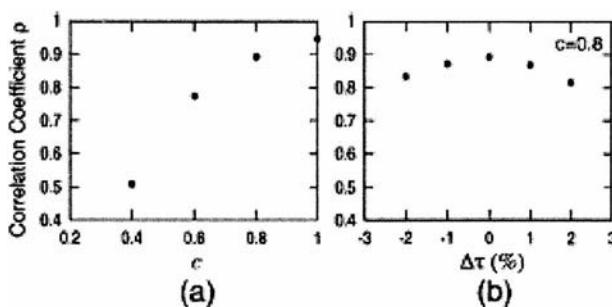
Fig. 16.10 Experimental results from J.-M. Liu, UCLA. (Left-hand panel (a)) The cross-correlation coefficient between the transmitter output and the receiver output as a function of c. The quality of the syn- chronization improves as $c \rightarrow 1$. (Right-hand-panel (b)) The quality of synchronization at $c = 0.8$ as a function of the mismatch $\frac{\Delta \tau}{\tau}$ between the time delays in the transmitter and receiver.

tween the transmitter and receiver. As expected the synchronization is better (indicated by large ρ) as c increases toward $c = 1$ and when the fractional time delay mismatch is zero. The sensitivity on c is quite strong while the sensitivity of synchronization to time delay mismatch is rather small. Possibly this is due to near generalized synchronization between the lasers, but this has not been tested quantitatively.

With this synchronization demonstrated between chaotic semiconductor lasers, we can ask about their use and accuracy in transmitting information bearing signals modulated onto the chaotic waveforms as carriers. J.-M. Liu and students have demonstrated that communication bandwidths of several hundreds of MHz can be achieved in the laboratory using these devices [14–16].

16.5
Chaotic Pulse Position Communication

The chaotic synchronization desired for communication is thwarted by several common features of communication channels:

- Attenuation of the transmitted signal means that amplitudes at the transmitter are not matched by amplitudes at the transmitter; this leads to $V_T(t) \neq V_R(t)$.
- Dispersion in the channel can lead to distortion of waveforms; this leads to $V_T(t) \neq V_R(t)$.
- Distortion of the transmitted signal by nonlinear properties of the channel itself changes the waveform departing the transmitter when it arrives at the receiver; this leads to $V_T(t) \neq V_R(t)$.

A solution to this problem was implemented long ago by a channel which is noisy, leaky, unreliable in its transmission characteristics, and generally a very
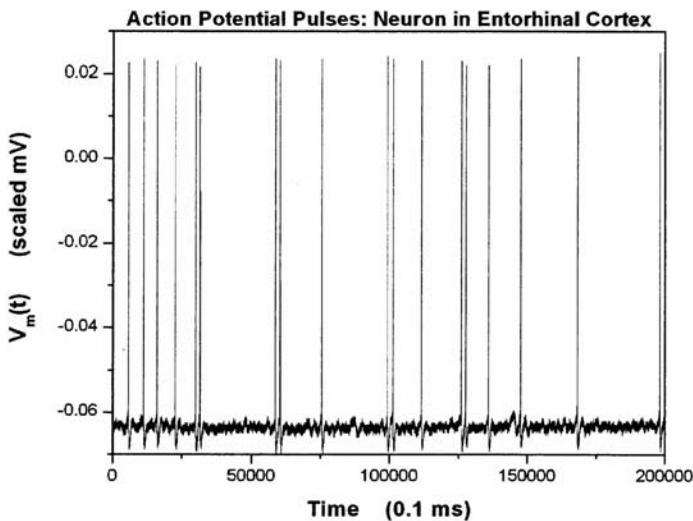
Fig. 16.11 Pulses used in a lossy, noisy, strongly dispersing, generally quite lousy communication channel – the axon connecting neurons in a biological network. This is a recording of action potentials, called spikes or pulses, from a chaotically oscillating stellate cell in the entorhinal cortex of rat. Data courtesy of J. Haas, UCSD.

lousy communication medium. We refer to the axons that connect neurons in biological circuits. Yet despite these inherent flaws, these channels are used by us for important functions of life.

These transmitters and receivers and the connections among them "solved" the communication problem by sending signals that do not rely on amplitude or precise wave shape. These systems transmit pulses of voltage known as action potentials. The waveforms sent in this manner are all nearly identical, and thus all information is located in the time intervals between the pulses. Figure 16.11 shows an observed chaotic pulse train as measured from a stellate cell in the entorhinal cortex of a rat.

Inspired by this apparently robust way of modulating information onto a carrier, we developed a transmitter receiver pair with $c = 1$ which sent sequences of pulses through the atmosphere using pulses of electromagnetic radiation [17]. Information was modulated onto these pulse sequences by assigning a "zero" to a pulse left unchanged and a "one" to a pulse that was delayed within a certain fixed window in time. The receiver autosynchronized to the transmitter because of the $c = 1$ open-loop configuration, so the receiver knew when a pulse should arrive, and it was thus sensitive to the time delay of a pulse.

Figure 16.12 is a block diagram for choatic pulse position modulation. This was built in an analogue electronic circuit and used to transmit music as we

Putting Information on Pulse Trains

o For a binary code:

[**Leave pulse alone for a "0"**

[**Delay pulse by fixed time for a "1"**
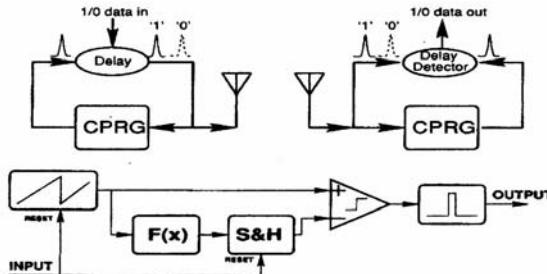
Fig. 16.12 Schematic of chaotic pulse position modulation (CPPM) as a communication methodology. A binary code is established by recording a "zero" at the receiver when the transmitted pulse arrives "on time" at the receiver. Since the receiver is synchronized to the transmitter by choosing $c = 1$ (an open-loop receiver configuration), it "knows" when pulses are supposed to arrive. If the pulse is delayed with a small window at the transmitter, the receiver registers a "one."

now describe. Figure 16.13 displays the waveform (upper left) of a cut from a song by the group "Chicago" which was recorded as an ASCII "wav" file and used to drive a chaotic pulse generator producing the transmitted signal shown in the upper right of the figure. The reconstructed or demodulated waveform is shown in the lower left panel. The transmitted pulse sequence signal arriving at the receiver is distorted in amplitude and shape by the atmospheric transmission channel, but the timing of the pulses is preserved well enough to allow accurate, robust reconstruction of the original waveform by interpreting (demodulating) the 0 s and 1s. Each pulse is spectrally wideband and the chaotic interval between pulses and a further wideband characteristic to the transmitted signal, so this may be the ultimate wideband communication device.

Finally, but not displayed here, CPPM has a bit error rate versus signal-to-noise ratio characteristic rather close to that of the best linear communication methods. As noted several times here, it can never achieve as good a BER versus $\frac{S}{N}$ characteristic as linear methods since some of the channel bandwidth must be used to reconstruct the transmitter state at the receiver.

Original Signal

Transmitted Signal using Chaotic Pulse Modulation

Recovered Signal

Original, transmitted, and recovered signal using chaotic pulse communication

Communications bandwidth 100kHz
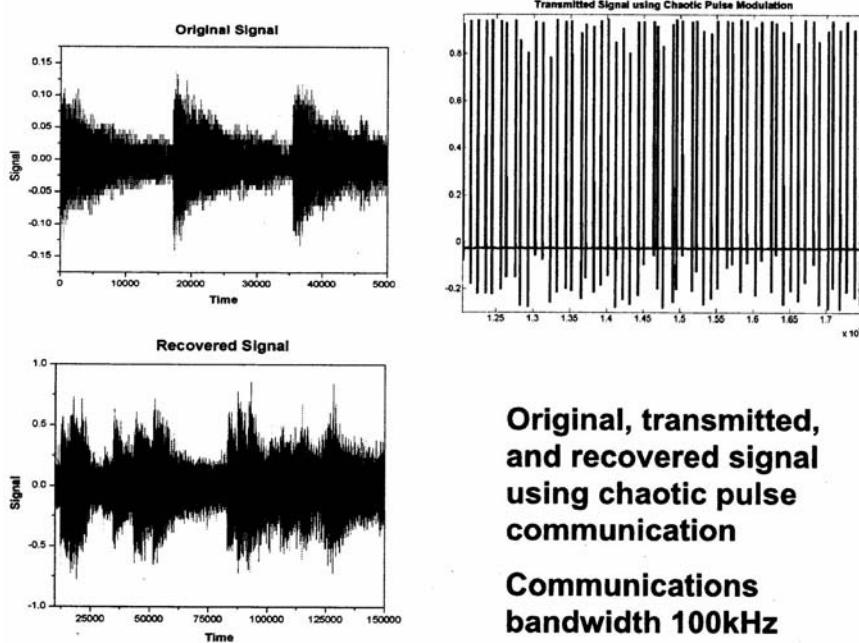
Fig. 16.13 A song from the band "Chicago" transmitted using chaotic pulse modulation and demodulated at the receiver. Shown are the original recorded file (upper left), the transmitted file comprised of pulses with chaotic interpulse intervals (upper right), and the final demodulated signal at the receiver (lower left). The chaotic pulse modulation device had a communication bandwidth of about 80 kHz.

16.6
Why Use Chaotic Signals at All?

With these optical physics and chaotic pulse position modulation examples we have demonstrated that one can use chaotic carriers to transmit information. Many other examples can be given and may be found in the growing literature on this subject [18, 19]. One may then ask why would we wish to do this? Not the least of the issues is that, as noted in Section 16.1, one must reserve some of the channel capacity available for reconstructing the full state of the transmitter at the receiver. So this communication method can never be as good in terms of the usual bit-error rate versus signal-to-noise ratio criterion used in evaluating communication systems.

Here are some ideas to think about in this regard:

• Chaotic systems, especially in the $c = 1$ open-loop receiver configuration, autosynchronize. Along with the positive Lyapunov exponents of the transmitter or receiver which lead to the chaos in the first place, there are negative Lyapunov exponents which are used in the autosynchronization of the trans-

mitter and receiver. This means no additional circuitry may be required for synchronization of chaotic carriers.

- Connected with the autosynchronization is the fact that nonlinear oscillators, because a stiff requirement of strict linearity is not imposed on their circuitry, may be very simple and inexpensive to design and build. The chaotic pulse position modulation described before used "Radio Shack" quality analog circuitry and costs only 10 s of dollars to construct.

- Although we noted that chaotic signals provide no special cryptographic security in the formal sense, the fact that one may design and utilize a large repertory of chaotic waveforms that are unknown to eavesdroppers means simple electronic designs may be good enough for law enforcement level security even though the higher standards of, say, NSA requirements are not met. Of course, using serious encryption technology before transmitting a signal addresses the security issue in a familiar manner.

- In particular, pulse communication have a low multipath interference and low interference with existing communication strategies. Of course, they are inherently broadband as noted earlier.

- In linear systems one often uses "white noise" as a way to probe the response of a system to a broad range of frequencies. In probing a nonlinear system, one may wish to use a low dimensional, say $D = 3$, signal as a way to examine a broad range of frequencies without introducing the very large (in principle, infinite) number of degrees of freedom associated with "white noise."
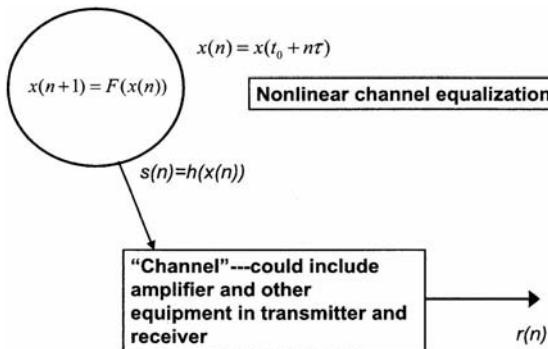
16.7
Undistorting the Nonlinear Effects of the Communication Channel

In sending a signal from a transmitter, we sample the output signal every τ_s or at sampling frequency $\frac{1}{\tau_s}$. The transmitter is in state $\mathbf{x}(n) = \mathbf{x}(n) = \mathbf{x}(t_0 + n\tau_s)$ with t_0 an initial time, and we wish to send the scalar signal $s(n) = h(\mathbf{x}(n))$ to the receiver. However, if the channel is not linear, the signal $r(n)$ arrives at the transmitter instead of $s(n)$. By observing $r(n)$ can we reconstruct $s(n)$ at the receiver, and thus "undistort" or equalize the effects of the channel?

This answer is known in linear systems, and we give here a quite thoroughly tested answer [20, 21] that works for nonlinear systems (see Fig. 16.14).

The way to consider the answer is to recognize that the full information about the state of the transmitter $\mathbf{x}(n)$ is, via the state-space reconstruction theorem or "embedding" theorem [5, 22], in the sequence $s(n)$ or equivalently in the sequence $r(n)$. Each sequence allows us to build reconstructed phase space vectors that capture the properties of the state of the transmitter. If we reconstruct the state space of the transmitter using $s(n)$, then $r(n)$ must be predicted by this as there is nothing more about the transmitter state left to reconstruct. Similarly, if we reconstruct the state space of the transmitter using $r(n)$, then $s(n)$ must be predicted by this as there is nothing more about the transmitter state left to reconstruct.

Fig. 16.14 A graphic depicting the basic question associated with removing nonlinear distortion of a signal due to channel characteristics. A transmitter with state $\mathbf{x}(t)$ is sampled at time intervals τ_s; therefore, we know $\mathbf{x}(n) = \mathbf{x}(t_0 + n\tau_s)$, where t_0 is some initial time. We wish to send a scalar function $s(n) = h(\mathbf{x}(n))$ from the transmitter to the receiver, perhaps modulated by an information bearing message. Because of distortion in the channel, a signal $r(n)$ arrives instead. Can we recover $s(n)$ from observations of $r(n)$?

Start by selecting a training set of simultaneously measured transmitter outputs $s(n)$ and channel outputs $r(n)$. From observations of the output of the channel, namely, the $r(n)$, $n = 0, 1, \dots, N$ form the D-dimensional received signal vectors [5, 22]

$$\mathbf{R}(n) = [r(n), r(n - T), \dots, r(n - D - 1)T],\tag{16.9}$$

where T is an integer determining the number of time delays to use in constructing the components of $\mathbf{R}(n)$, and D is an integer telling us the dimension of the reconstructed receiver space. We choose T using average mutual information between entries of $\mathbf{R}(n)$, and we select D using false nearest neighbors [5]. You may use your own preferred methods for this, if you wish.

For every D-dimensional vector $\mathbf{R}(n)$, we have a connection $s(n) = G(\mathbf{R}(n))$, where $G()$ is a scalar function in the D-dimensional space. If we can represent $G()$ accurately, we can use channel output to recover the transmitted signal $s(n)$ – the channel input. To this end, represent the function $G(\mathbf{X})$ acting on vectors $\mathbf{X}$ in the reconstructed D-dimensional space as a series in some selected basis functions $\phi_m(\mathbf{X})$ in that space; namely,

$$G(\mathbf{X}) = \sum_{m=1}^{M} c_m \phi_m(\mathbf{X}).\tag{16.10}$$

In our training sequence we now have many receiver vectors $\mathbf{R}(n)$ associated with many transmitter scalars $s(n)$. In the D-dimensional space, each $\mathbf{R}(n)$ has N_B near-

est neighbors which we call $\mathbf{R}^{(l)}(n)$, $l = 0, 1, 2, ..., N_B$, $\mathbf{R}^{(l=0)}(n) = \mathbf{R}(n)$. These nearest neighbors are associated with scalar channel inputs $s^{(l)}(n)$ via

$$s^{(l)}(n) = G(\mathbf{R}^{(l)}(n)) = \sum_{m=1}^{M} c_m(n)\phi_m(\mathbf{R}^{(l)}(n)),\qquad (16.11)$$

and the coefficients in the sum $c_m(n)$ are now recognized as being connected with a local region of the state space near $\mathbf{R}(n)$.

To determine the coefficients $c_m(n)$ connecting the $\mathbf{R}^{(l)}(n)$ to the $s^{(l)}(n)$ in the neighborhood of $\mathbf{R}(n)$ we minimize the least squares cost function

$$\sum_{l=0}^{N_B}\left(s^{(l)}(n) - \sum_{m=1}^{M} c_m(n)\phi_m(\mathbf{R}^{(l)}(n))\right)^2.\qquad (16.12)$$

When we know the $c_m(n)$ for each region of state space where an observed vector $\mathbf{R}(n)$ and its neighbors lie, we have characterized the transformation from that region of state space to the scalar input $s(n)$.

$G(\mathbf{X})$ is represented by a piecewise local set of sums over our selected basis functions $\phi_m(\mathbf{X})$. Since we will want to use the functions locally in the D-dimensional space, polynomials are a fine choice for $\phi_m(\mathbf{X})$. Many other functions will work as well.

Now we are ready for new channel output $r_{\text{new}}(t_0 + k\tau_s) = r_{\text{new}}(k)$. We measure a new value of the channel output, $r_{\text{new}}(k)$. What is the value of $s_{\text{new}}(k)$ associated with this? To answer this question we form the new data vector

$$\mathbf{R}_{\text{new}}(k) = [r_{\text{new}}(k), r_{\text{new}}(k - T), ..., r_{\text{new}}(k - D - 1)T],\qquad (16.13)$$

and ask which among all the data vectors in the training set is closest in D-dimensional state space to $\mathbf{R}_{\text{new}}(k)$? "Close" can be in any metric, but we suggest use of the usual Euclidian metric as that was employed in determining coefficients in the training set.

Suppose the training set data vector $\mathbf{R}(j)$ is closest to $\mathbf{R}_{\text{new}}(k)$. That suggests that vectors in the neighborhood of $\mathbf{R}(j)$ will tell us with what input the new data vector $\mathbf{R}_{\text{new}}(k)$ should be associated. Using the coefficients $c_m(j)$ we have a map adjusted to be accurate, in a least squares sense, to the relationship $s(j) = G(\mathbf{R}(j))$ in the neighborhood of $\mathbf{R}(j)$, so we expect

$$G_j(\mathbf{X}) = \sum_{m=1}^{M} c_m(j)\phi_m(\mathbf{X}),\qquad (16.14)$$

to provide the map from $\mathbf{R}$ space to s space we need. This suggests that we use the rule

$$s_{\text{new}}(k) = \sum_{m=1}^{M} c_m(j)\phi_m(\mathbf{R}_{\text{new}}(k)),\qquad (16.15)$$

to estimate the new input to the channel that results in the observed channel output $r_{new}(k)$ and the associated data vector $\mathbf{R}_{new}(k)$. The only way information from the training set and from the region of D-dimensional receiver vector space near $\mathbf{R}_{new}(k)$ enters the determination of $s_{new}(j)$ is via the coefficients $c_m(j)$ in the $\mathbf{R}$ space $\rightarrow s$ map.

For each new observation we do the same thing: form the new data vector $\mathbf{R}_{new}$; locate the closest member of the D-dimensional training set; use the local map for that region of state space to map the new vector $\mathbf{R}_{new}$ to the estimated input s_{new}. This process is quite efficient as one needs to find a nearest neighbor to a D-dimensional vector among N such vectors, and that can be done in order $N\log(N)$ operations. Then one has the associated coefficients $c_m(j)$ and needs only evaluate a finite weighted sum over known functions.

The UCSD group of nonlinear scientists has applied this to two communication channels. The first was magnetic recording on tape. Here the writing process on the magnetic medium is nonlinear while the readout is linear. We were able to record at six times the bit density on the tape achieved by previous methods and read back the recorded message without distortion. The second channel was the commercial DSL transmission channel available to many subscribers worldwide over their existing telephone lines. Impressive results were achieved in that case as well.

16.8
Conclusions

This has been an overview of methods in communicating with chaotic waveforms or chaotic pulse sequences that in laboratory or field demonstrations have proven quite successful. In the case of chaotic pulse position modulation (CPPM) the bit-error rate as a function of the signal-to-noise ratio is very close to the best linear methods.

We went over quite a few general statements in our introduction, many without any demonstration, and we encourage the reader, especially new students to this subject, to peruse the literature to satisfy themselves that statements appearing to be our opinion alone might nonetheless be accurate.

Overall by reviewing methods that work within the context of the general closed loop transmitter–open loop receiver paradigm, we hope we have provided a rich testbed for new ideas on how to use the methods discussed in many innovative contexts. Indeed, although there are applications of the nonlinear channel equalization (or nonlinear undistortion) methods [20], there is ample room for improvement on the basic algorithm we presented.

After quite a bit of research into the use of chaotic waveforms for communication, some summary might be possible.

• First, it is clear that many methods for communication long used but employing linear carriers have proven, perhaps not surprisingly, to work when chaotic carriers are substituted. The paper by Lau and Kolumban [2] is a good

exploration of those issues. Also Kolumban's paper at the 2006 Bristol Workshop [19] explores this issue in detail.

- Second, it has become clear that security, in the rigorous sense used by cryptographers, is not a special or even plausible feature of communication using chaotic waveforms. Perhaps some kind of barrier to the uninitiated comes from using chaotic waveforms, but not "secure" communication as used widely.

- Third, it seems there are many interesting opportunities to explore new strategies for communication where inexpensive, simple circuitry is at the heart of the implementation. This might include using chaotic waveforms in radar applications – a form of communication [19] – or other applications where the structure in state space associated with the broad spectral content of simple nonlinear chaotic oscillators might be a valuable combination. Using such signals as probes of unknown "black box" dynamical systems whose structure one wishes to uncover was mentioned above as a possible use of this.

- Finally, using nonlinear dynamical techniques, chaotic or not, to undo the unwanted distortion of a nonlinear channel may prove very helpful in extending the range and usefulness of linear communication methods impaired by their encounter with nonlinearity.

References

1 Van Trees, H. L., *Detection, Estimation, and Modulation Theory, Part I*, Wiley, New York (1968).

2 Lau, F. C. M. and Geza Kolumban, "Performance limit of chaotic digital waveform communication systems: approach of maximizing a posteriori probability," *Circuits, Syst., Signal Process.* 24, 639–655 (2005).

3 Afraimovich, V. S., N. N. Verichev, and M. I. Rabinovich, "Stochastic synchronization of oscillation in dissipative systems," *Izvestiya Vysshikh Uchebnykh Zavedenii, Radiofizika* 29, 1050–1060 (1986).

4 Pecora, L. M. and T. C. Carroll, "Synchronization in chaotic systems," *Phys. Rev. Lett.* 64, 821–824 (1990).

5 Abarbanel, H. D. I., *Analysis of Observed Chaotic Data*, Springer, New York (1996).

6 Pikovsky, A., M. Rosenblum, and J. Kurths, *Synchronization: A Universal Concept in Nonlinear Sciences,* Cambridge University Press, Cambridge (2003).

7 Rulkov, N. F., M. M. Sushchik, L. S. Tsimring, and H. D. I. Abarbanel, "Generalized synchronization of chaos in directionally coupled chaotic systems," *Phys. Rev. E* 51, 980–994 (1995).

8 Abarbanel, H. D. I., N. F. Rulkov, and M. M. Sushchik, "Generalized synchronization of chaos: The auxiliary system approach," *Phys. Rev. E* 53, 4528–4535 (1996).

9 Tang, D. Y., R. Dykstra, M. W. Hamilton, and N. R. Heckenberg, "Observation of generalized synchronization of chaos in a driven chaotic system," *Phys. Rev. E* 57, 5247–5251 (1998).

10 Volkovskii, A. R. and N. F. Rulkov, "Synchronous chaotic behavior of nonlinear oscillating system as the principle of the detection of signals," *Tech. Phys. Lett.* 19, 97 (1993).

11 VanWiggeren, G. D. and Rajarshi Roy, "Communication with chaotic lasers," *Science* 279, 1198–1200 (1998).

12 VanWiggeren, G. D. and Rajarshi Roy, "Chaotic communication using time delayed optical systems," *Int. J. Bifurcation Chaos* 9, 2129–2156 (1999).

13 Abarbanel, H.D.I. and M.B. Kennel, "Synchronizing high-dimensional chaotic optical ring dynamics," *Phys. Rev. Lett.* 80, 3153–3156 (1998).

14 Chen, H.F. and J.-M. Liu, "Open-loop chaotic synchronization of injection-locked semiconductor lasers with gigahertz range modulation," *IEEE J. Quantum Electron.* 36, 27–34 (2000).

15 Abarbanel, H.D.I., M.B. Kennel, L. Illing, S. Tang, H.F. Chen, and J.-M. Liu, "Synchronization and communication using semiconductor lasers with optoelectronic feedback," *IEEE J. Quantum Electron.* 37, 1301–1311 (2001).

16 Tang, S. and J.-M. Liu, "Synchronization of high-frequency chaotic optical pulses," *Opt. Lett.* 26, 596–598 (2001).

17 Sushchik, M. Jr., N.F. Rulkov, L. Larson, L.S. Tsimring, H.D.I. Abarbanel, K. Yao, and A. Volkovskii, "Chaotic pulse position modulation: a robust method of communicating with chaos," *IEEE Commun. Lett.* 4, 128–130 (2000).

18 Homer, M.E., S.J. Hogan, M. di Bernardo, and C. Williams, "The importance of choosing attractors for optimizing chaotic communication," *IEEE Trans. Circuits Syst. II: Express Briefs* 51, 511–516 (2004).

19 Many excellent contemporary contributions to this subject are found in the on line listings from the August 2006 workshop on "Transmission of Chaotic Signals", Bristol, England; http://www.enm.bris.ac.uk/workshop/chaotic-signals/.

20 Abarbanel, H.D.I. and E.C. Tumer, "Reading Neural Encodings using Phase Space Methods," Springer Applied Mathematical Sciences Series Celebratory Volume for the Occasion of the 70th birthday of Larry Sirovich Subj-class: Biological Physics; Neurons and Cognition; Quantitative Methods; "Perspectives and Problems in Nonlinear Science," eds. E. Kaplan, J. Marsden and K Sreenivasan, Springer, New York (2003).

21 Abarbanel, H.D.I., T.A. Carroll, L.M. Pecora, J.J. Sidorowich, and L.S. Tsimring, "Predicting physical variables in time delay embedding," *Phys. Rev. E* 49, 1840–1853 (1994).

22 Kantz, H. and T. Schreiber, "Nonlinear time series analysis," 2nd ed., Cambridge University Press, Cambridge (2003).

17
Synchronization and Message Transmission for Networked Chaotic Optical Communications

K. Alan Shore, Paul S. Spencer, and Ilestyn Pierce

17.1
Introduction

This chapter provides an overview of experimental and theoretical work directed at the exploitation of optical chaos in networked communication. Several approaches have been adopted for the practical implementation of the concept of performing digital communication using synchronized chaotic lasers [1]. Due to their direct compatibility with existing optical fiber communication technology, semiconductor lasers (laser diodes) have attracted the attention of many workers seeking to exploit optical chaos in communication [2]. The specific focus of the present chapter is the use of external cavity semiconductor lasers for this purpose. In this configuration the laser source is subject to optical feedback from an external mirror. Despite the simplicity of the configuration the behavior of the semiconductor laser in this case is extremely complex and has remained a topic of detailed investigation for several decades. An indication of the rich dynamical behavior of external cavity semiconductor lasers is provided in a recent research monograph [3].

The emphasis of this chapter is on experimental work performed in the authors' experimental laboratory providing realizations of key functionalities for optical chaos communication. Appropriate theoretical analysis underpinning the experimental work is also included. It is remarked in this respect that the experimental work has provided a number of interesting challenges for theoretical exposition. Although several of those challenges have now been met, a number of key issues continue to provide fertile areas for theoretical activity.

In the following sections attention is given to the key functionalities which enable networked optical communication using external cavity laser diodes. The most fundamental requirement for effecting communication using a chaotic carrier is that of chaos synchronization. The counter-intuitive proposal of Ott, Grebogi, and Yorke [4] that such synchronization could be effected stimulated the pioneering experimental activity of Roy et al. [5] and led to subsequent experimental realizations in a number of laser systems and, in particular, the first

demonstration of chaos synchronization in external cavity laser diodes by Sivaprakasam et al. [6]. A striking feature of that experimental demonstration is the remarkable robustness of the chaos synchronization – its persistence over a long period of time in a laboratory lacking environmental controls offered powerful support to prospects for subsequent practical deployment.

This chapter establishes the framework for networked communication using chaotic external cavity laser diodes. A number of outstanding challenges remain to be met in relation to practical implementations. Specific attention is drawn here to the need to devise robust means for quantifying the security of chaos-based communication. A particular requirement in this respect is to engender a dialog with workers in relevant communities – and specifically classical cryptography – who may be able to assist in further progressing the significant achievements already made in the use of chaotic external cavity laser diodes.

17.2
Synchronization and Message Transmission

The general concept of synchronization has a long historical tradition and its modern manifestations have been summarized in a major work [7]. The general context for chaos synchronization in external cavity semiconductor lasers has been delineated by Sivaprakasam and Masoller [8] (chapter 6) to which attention is directed for further references. The generic experimental configuration includes a transmitter or master laser and a receiver or slave laser. Unidirectional optical coupling between the transmitter and slave laser enables synchronization of the dynamics of the two lasers.

Mirasso et al. [9] showed theoretically that coupled chaotic semiconductor lasers with optical feedback can be synchronized and used in encoded communication systems which was subsequently demonstrated experimentally by Sivaprakasam and Shore [6]. Synchronization is dependent upon a number of controllable experimental parameters including the strength of the optical coupling between the transmitter and receiver lasers [10]. Frequency detuning between the lasers also affects the achieved quality of synchronization. Earlier theoretical studies show that synchronization is best achieved when the detuning between two diode lasers is zero [11]. For negative detuning a negative gradient dominates and the branch with a positive gradient disappears. The appearance of a negative gradient in the synchronization diagram is termed *inverse synchronization*. Inverse synchronization occurs due to nonresonant coupling between the master and slave lasers and synchronization is due to resonant coupling between the two lasers [12, 13]. A synchronization regime similar to this, which was termed 'antisynchronization', was found by Wedekind and Parlitz [14].

In the synchronization of *identical* lasers, in closed-loop configuration two qualitatively different synchronization regimes can occur [15, 16]. When both lasers are subjected to the same feedback strength and the slave laser is subjected to an appropriate optical coupling the slave laser output at a given time syn-

chronizes with the master laser output taking account of a lag time arising by the time of flight between the lasers, i.e., $I_s(t) = I_m(t - \tau_c)$, where τ_c is the time of flight between the lasers. This regime is called isochronous or generalized synchronization and corresponds to the synchronization found numerically in [9] and experimentally in [6].

A different regime was found numerically by Ahlers et al. [17], which occurs when the master and slave lasers have the same amount of external injection, i.e., when the master laser feedback strength is equal to the sum of the slave laser feedback strength and the optical coupling strength. In this case the slave laser output synchronizes with the master laser output according to $I_s(t) = I_m(t - \Delta\tau)$, where the lag time is given by $\Delta\tau = \tau_c - \tau$, where τ is the external cavity round trip time. This is termed complete synchronization. A qualitative verification of the condition for this latter case was undertaken experimentally in [18].

If the lasers are sufficiently close to each other, such that $\tau_c < \tau$ then $\Delta\tau < 0$ and the slave laser output anticipates the master laser output. Masoller [19] showed that this is a particular case of the *anticipating synchronization* regime discovered by Voss [20]. The dependence of the lag time on the delay time was verified experimentally by Liu et al. [21].

Synchronizing a series of chaotic lasers becomes essential when the chaotic lasers are put to use in practical communication systems such as for use in message relay as described in Section 17.3.2. An experimental demonstration has been made of the synchronization of three chaotic diode lasers [22].

As may be expected in such an arrangement, time of flight lag times appear in the synchronization. Building on a demonstration of anticipated synchronization in mutually coupled lasers [23] it was shown that it is possible to nullify the time of flight lag time [24]. This phenomenon has also been observed in the case that all lasers are mutually coupled [25]. Furthermore, it has also been possible to obtain complete synchronization with zero-time lag [26]. Frequency detuning can be utilized to effect synchronization switching [27].

The foregoing work has considered synchronization in edge-emitting semiconductor lasers. In respect of vertical cavity surface emitting lasers (VCSELs), Spencer et al. [28] investigated theoretically the synchronization of chaotic VCSELs. Later Ohtsubo et al. [29] reported an experimental observation of chaotic synchronization in mutually coupled stand-alone VCSELs. Exploiting the polarization properties of VCSELs experimental demonstrations of regular and inverse synchronization in VCSELs have been performed [30]. In addition to VCSELs, recently synchronization of chaotic self-pulsing lasers has been achieved [31].

Having established the capability of effecting chaos synchronization using external cavity lasers attention is turned to the use of such a chaotic carrier for the transmission of messages. Attention has been given to the relative merits of using open- and closed-loop configurations [32]; the vital issue of message bandwidth has been addressed [33] and message transmission using chaotic VCSELs has been achieved [34].
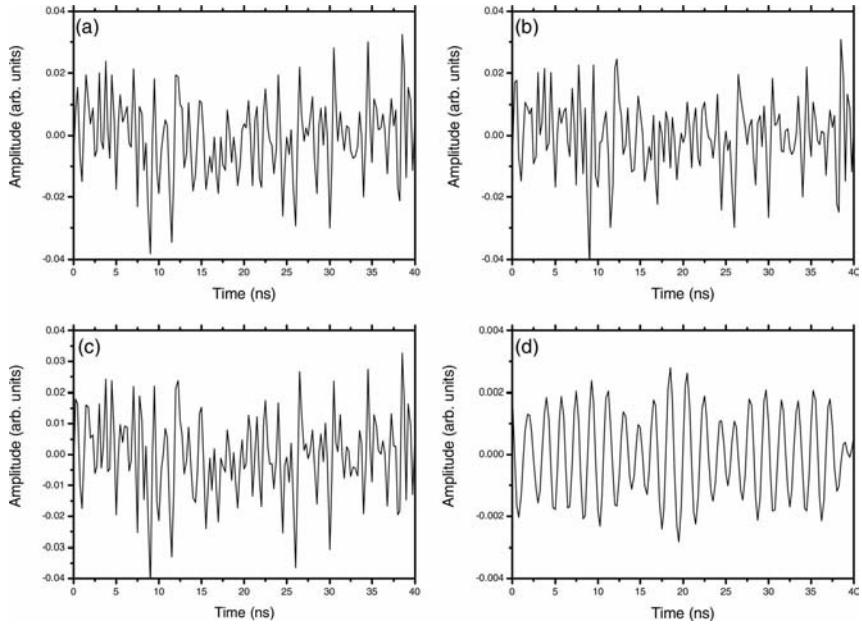
Fig. 17.1 Chaos synchronization and message recovery:
(a) transmitter laser time trace, (b) receiver laser time trace,
(c) decoder laser time trace, (d) recovered message [37].

Although the foregoing demonstrate the efficacy with which message extraction can be achieved using chaotic semiconductor lasers it remains of practical importance to illuminate the physical mechanism which allows message extraction. This has been achieved in recent detailed theoretical work [35, 36].

Figure 17.1 shows the time traces of the transmitter laser (Fig. 17.1 (a)), receiver laser (Fig. 17.1 (b)), decoder laser (Fig. 17.1 (c)) and recovered message (Fig. 17.1 (d)). It is observed that the three lasers are well synchronized and the message (which is the difference between the time traces shown in Figs. 17.1 (c) and 17.1 (b) is recovered.

17.3
Networked Chaotic Optical Communication

Here attention is given to experimental demonstrations of the functionalities required to achieve networked communication systems: chaos message multiplexing, chaos message broadcasting and message relay (to allow extension of the reach of the chaos communication link).

17.3.1
Chaos Multiplexing

It has been demonstrated experimentally [37] that two chaotic optical communication channels can be configured over a single transmission path using two external-cavity laser diodes as transmitter lasers, and a single stand-alone receiver laser. The two chaotic communication channels were shown to operate independently: two messages, at different modulation frequencies, generated via direct current modulation of the transmitter lasers, can be masked by the chaos and recovered at the receiver laser by the use of a decoder laser as illustrated in Fig. 17.1. The decoder laser is used to select the channel to be utilized. The channels operate at different laser wavelengths and thus constitute a wavelength division multiplexing (WDM) scheme [37]. Attention has also been given to two mode synchronization [38] as a basis for chaos wavelength division multiplexed operation.

17.3.2
Message Relay

In conventional communication systems, network operations are often performed with the assistance of relay stations which provide the opportunity to enhance the distance over which information can be transmitted. A similar functionality would be extremely attractive in chaotic optical communication. In order to implement such a system, the requirement is to couple three or more chaotic transmitters and receivers in cascade configuration and then successfully extract a message at the terminal receiver. A basic requirement for success-
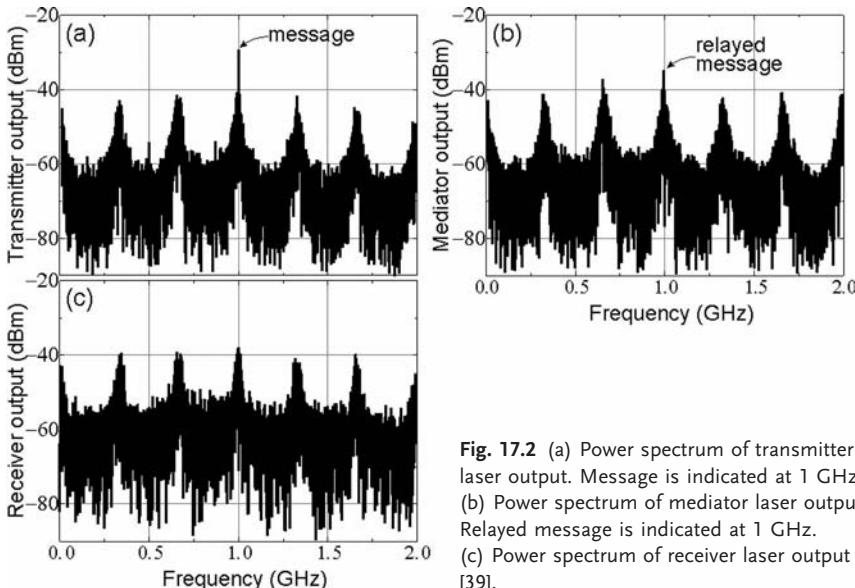

Fig. 17.2 (a) Power spectrum of transmitter laser output. Message is indicated at 1 GHz. (b) Power spectrum of mediator laser output. Relayed message is indicated at 1 GHz. (c) Power spectrum of receiver laser output [39].
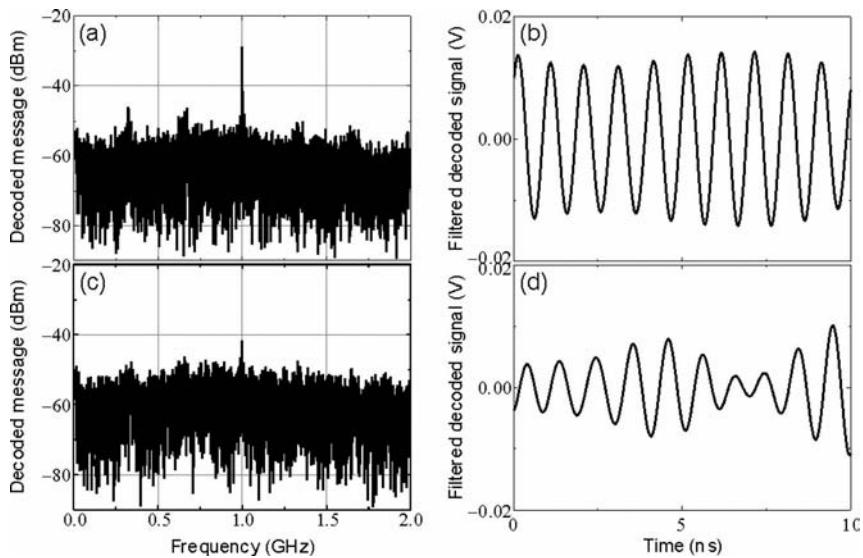
Fig. 17.3 (a) Power spectrum of message decoded in mediator side. Presence of message is clearly revealed at 1 GHz. (b) Filtered decoded message. (c) Power spectrum of message decoded from relayed chaotic message in receiver side. Presence of message is clearly revealed at 1 GHz. (d) Filtered decoded message [39].

ful message transmission in such a configuration is the achievement of robust chaos synchronization between the cascaded transmitters and receivers. Based on such cascade synchronization, we illustrate here the successful relay of a 1 GHz chaotic message using three cascade-coupled distributed feedback (DFB) laser diodes, termed here the transmitter, mediator, and receiver lasers. In the arrangement used here, the transmitter laser is rendered chaotic due to the application of optical feedback in an external cavity. A 1 GHz message is encoded using the chaotic carrier [39]. The mediator laser performs as a chaotic relay. Figure 17.2 shows that message recovery in both the mediator and receiver lasers has been achieved. It is apparent from Fig. 17.3 that some distortion occurs in the relay process and hence multiple-repetition will require optimization of the synchronization [39].

17.3.3
Message Broadcasting

In order to implement a chaotic communication network it is highly attractive to have the capability of broadcasting a message from one transmitter to several receivers. In this section a discussion is offered of an experimental demonstration of GHz message broadcasting at telecommunication wavelengths using a chaotic ex-
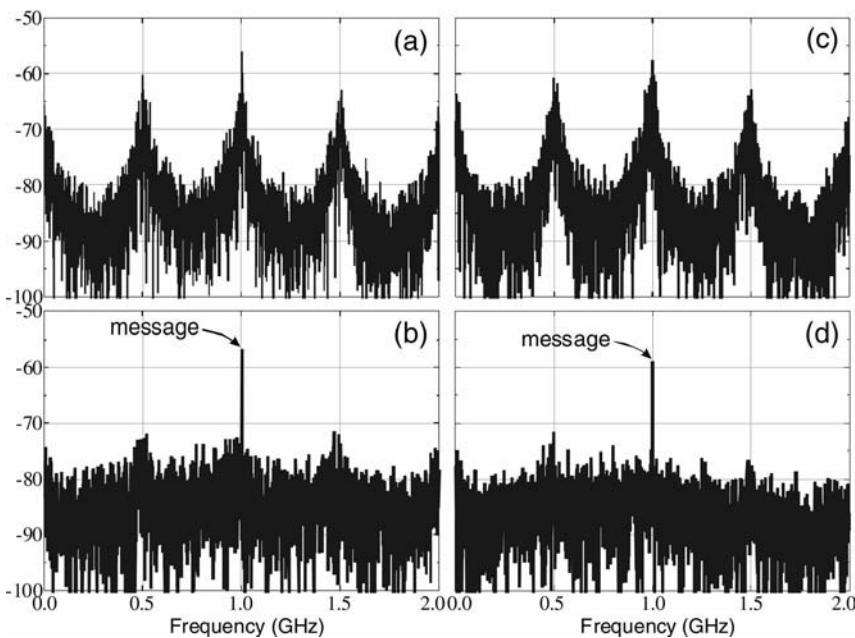
Fig. 17.4 Power spectra of the encoded and decoded message. (a) the transmitted signal from PD1. (b) The recovered message in the receiver laser 1. (c) The transmitted signal from PD3. (d) The recovered message in the receiver laser 2 [40].

ternal-cavity DFB laser transmitter and two DFB laser receivers. The experimental setup is described fully in [40]. Because of their relevance to conventional optical fiber communication systems, three single-mode DFB laser diodes emitting at 1550 nm are used, as the transmitter laser (TL), receiver laser 1 (RL1), and receiver laser 2 (RL2), respectively.

Varying the optical feedback level of the TL, several dynamical regimes, including chaotic regimes, are obtained in the transmitter. Among them, the low frequency fluctuation (LFF) regime is used here for message encoding. The bandwidth of the chaotic outputs is more than 4 GHz which is adequate to encode the 1 GHz message. The technique used for message encoding is that of chaotic modulation where the TL is directly modulated. The 1 GHz message masked by the chaotic signal is transmitted to both the receiver lasers. Figure 17.4 (a) shows the power spectrum as the result of message encoding and decoding. Since the dominant LFF peak appears at 1 GHz, the 1 GHz message cannot be noticed in the figure demonstrating that the message encoding is effective. Figure 17.4 (b) displays the power spectrum of the message recovered from RL1, where the message is clearly visible at 1 GHz. The extracted message has a 14.7 dB signal-to-noise ratio which indicates efficient message recovery. Figure 17.4 (c) shows the power spectrum of the signal broadcast to RL2. As in

Fig. 17.4 (a), the figure displays an effective message encoding. Figure 17.4 (d) shows the power spectrum of the recovered message from RL2. These results provide an experimental demonstration of broadcasting of a high frequency message to two receiver lasers using a chaotic optical carrier generated in a DFB laser subject to optical feedback.

17.4
Summary

This chapter has summarized experimental and theoretical work concerned with the use of external cavity semiconductor lasers in optical chaos communication. The versatility of this configuration has been illustrated by its use in delivering networking functionalities. The chapter has also sought to point out some of the rather subtle dynamical behavior, which underpins the experimentally observed behavior. Further opportunities for development of this activity have been indicated in respect of recent experiments performed using chaotic self-pulsing laser diodes.

Acknowledgments

References

1 P. Colet and R. Roy, 'Digital communication with synchronized lasers', *Opt. Letts.*, 19, 2056–2058, 1996.

2 *See* 'Feature section on optical chaos and applications in cryptography', *IEEE J. Quantum Electron.*, 38 (9) 2002.

3 D.M. Kane and K.A. Shore (Editors), *Unlocking Dynamical Diversity*, Wiley, New York, pp. 1–339, 2005.

4 E. Ott, C. Grebogi and J.A. Yorke, 'Controlling chaos', *Phys. Rev. Lett.*, 64, 1196–1199, 1990.

5 R. Roy, T.W. Murphy, T.D. Maiter, Z. Gills and E.R. Hunter, 'Dynamic control of chaotic laser-experimental stabilisation of globally coupled system', *Phys. Rev. Lett.*, 68, 1259–1262, 1992.

6 S. Sivaprakasam and K.A. Shore, 'Demonstration of optical synchronization of chaotic external-cavity laser diodes', *Optics Lett.*, 24, 466–468, 1999.

7 A. Pikovsky, M. Rosenblum and J. Kurths, *Synchronization: A Universal*

Concept in Nonlinear Sciences, Cambridge University Press, Cambridge, 2001.

8 S. Sivaparakasam and C. Masoller Ottieri, 'Chaos Synchronization', Chapter 6 in D. M. Kane and K. A. Shore (Editors), *Unlocking Dynamical Diversity*, Wiley, New York, 2005.

9 C. R. Mirasso, P. Colet and P. Garcia Fernandez, 'Synchronization of chaotic semiconductor lasers: Application to encoded communications', *IEEE Photonics Technol. Lett.*, 8, 299–301, 1996.

10 S. Sivaprakasam and K. A. Shore, 'Message encoding and decoding using chaotic external-cavity diode lasers', *IEEE J. Quantum Electron.*, 36, 35–39, 2000.

11 P. S. Spencer and C. R. Mirasso, 'Analysis of optical chaos synchronization in frequency-detuned external-cavity VCSEL's', *IEEE J. Quantum Electron.*, 35, 803–809, 1999.

12 S. Sivaprakasam, P. S. Spencer, P. Rees and K. A. Shore, 'Regimes of chaotic synchronization in external cavity laser diodes', *IEEE J. Quantum Electron.*, 38, 1155–1161, 2002.

13 S. Sivaprakasam, I. Pierce, P. Rees, P. S. Spencer, K. A. Shore and A. Valle, 'Inverse synchronization in semiconductor laser diodes', *Phys. Rev. A.*, 64, 013805, 2001.

14 I. Wedekind and U. Parlitz, 'Experimental observation of synchronization and anti-synchronization of chaotic low-frequency-fluctuations in external cavity semiconductor lasers', *Int. J. Bifurc. Chaos*, 11, 1141–1147, 2001.

15 A. Locquet, F. Rogister, M. Sciamanna and M. Blondel, 'Two types of synchronization in unidirectionally coupled chaotic external-cavity semiconductor lasers', *Phys. Rev. E.*, 64, 04520 (R), 2001.

16 A. Locquet, C. Masoller, P. Megret and M. Blondel, 'Comparison of two types of synchronization of external cavity semiconductor lasers', *Opt. Lett.* 27, 31–33, 2002.

17 V. Ahlers, U. Parlitz, W. Lauterborn, 'Hyperchaotic dynamics and synchronization of external-cavity semiconductor lasers', *Phys. Rev. E*, 58, 7208–7213, 1998.

18 S. Sivaprakasam, E. M. Shahverdiev and K. A. Shore, 'Experimental verification of the synchronization condition for chaotic external cavity laser diodes', *Phys. Rev. E*, 62, 2000.

19 C. Masoller, 'Anticipation in synchronization of chaotic semiconductor lasers with optical feedback', *Phys. Rev. Lett.*, 86, 2782–2785, 2001.

20 H. U. Voss, 'Anticipating chaotic synchronization', *Phys. Rev. E*, 61, 5115–5119, 2000.

21 Y. Liu, Y. Takiguchi, P. Davis, T. Aida, S. Saito and J. M. Liu, 'Experimental observation of complete chaos synchronization in semiconductor lasers', *Appl. Phys. Lett.*, 80, 4306–4308, 2002.

22 S. Sivaprakasam and K. A. Shore, 'Cascaded synchronization in external-cavity laser diodes', *Opt. Lett.*, 26, 253–255, 2001.

23 S. Sivaprakasam, E. M. Shahverdiev, P. S. Spencer and K. A. Shore, 'Experimental demonstration of anticipating synchronization in chaotic semiconductor lasers with optical feedback', *Phys. Rev. Lett.*, 87, 154101, 2001.

24 S. Sivaprakasam, J. Paul, P. S. Spencer, P. Rees and K. A. Shore, 'Nullified time-of-flight lead-lag in synchronization of chaotic external-cavity laser diodes', *Opt. Lett.*, 28, 1397–1399, 2003.

25 I. Fischer, R. Vicente, J. M. Buldu, M. Peil, C. R. Mirasso, M. C. Torrent and J. Garcia-Ojalvo, 'Zero-lag long-range synchronization via dynamical relaying', *Phys. Rev. Lett.*, 97, 123902, 2006.

26 M. W. Lee, J. Paul, C. Masoller and K. A. Shore, 'Observation of cascade complete chaos synchronization with zero time lag in laser diodes', *J. Opt. Soc. America B*, 23, 846–851, 2006.

27 M. W. Lee, J. Paul, I. Pierce and K. A. Shore, 'Frequency detuned synchronization switching in chaotic DFB laser diodes', *IEEE J. Quantum Electron.*, 41, 302–307, 2005.

28 P. S. Spencer, C. R. Mirasso, P. Colet and K. A. Shore, 'Modeling of optical synchronization of chaotic external-cavity VCSELs', *IEEE J. Quantum Electron.*, 34, 1673–1679, 1998.

29 N. Fujiwara, Y. Takiguchi and J. Ohtsubo, 'Observation of the synchronization of chaos in mutually injected vertical-cavity surface-emitting semiconductor lasers', *Opt. Lett.*, 28, 18, 1677–1679, 2003.

30 Y. Hong, M. W. Lee, P. S. Spencer and K. A. Shore, 'Synchronization of chaos in unidirectionally coupled VCSELs', *Opt. Lett.*, 29, 1215–1217, 2004.

31 M. W. Lee, I. Pierce and K. A. Shore, 'Synchronisation of chaotic pulse-sequences in self-pulsating laser diodes', *Workshop on the Transmission of Chaotic Signals*, Centre for Communications Research, University of Bristol, Bristol, 1–3 August 2006.

32 M. W. Lee, J. Paul, S. Sivaprakasam and K. A. Shore, 'Comparison of closed-loop and open-loop feedback schemes of message decoding using chaotic laser diodes', *Opt. Lett.*, 28, 2168–2170, 2003.

33 J. Paul, S. Sivaprakasam, P. S. Spencer, P. Rees and K. A. Shore, 'GHz bandwidth message transmission using chaotic diode lasers', *Elec. Lett.*, 38, 28–29, 2002.

34 M. W. Lee, Y. Hong and K. A. Shore, 'Experimental demonstration of VCSEL-based chaotic optical communications', *IEEE Photon. Technol. Lett.*, 16, 10, 2392–2394, 2004.

35 A. Murakami and K. A. Shore, 'Chaos-pass filtering in injection-locked semiconductor lasers', *Phys. Rev. A*, 72, 053810, p. 8, 2005.

36 A. Murakami and K. A. Shore, 'Analogy between optically driven injection-locked laser diodes and driven damped linear oscillators', *Phys. Rev. A*, 73, 043804, p. 9, 2006.

37 J. Paul, S. Sivaprakasam and K. A. Shore, 'Dual-channel chaotic optical communications using external-cavity semiconductor lasers', *J. Opt. Soc. Am. B*, 21, 514–521, 2004.

38 M. W. Lee and K. A. Shore, 'Two-mode chaos synchronization using a multi-mode external-cavity laser diode and two single-mode laser diodes', *J. Lightwave Technol.*, 23, 1068–1073, 2005.

39 M. W. Lee and K. A. Shore, 'Demonstration of a chaotic optical message relay using DFB laser diodes', *IEEE Photon. Tech. Letts.*, 18, 169–171, 2006.

40 M. W. Lee and K. A. Shore, 'Chaotic message broadcasting using DFB laser diodes', *Electron. Lett.*, 40, 614–615, 2004.

18
Feedback Control Principles for Phase Synchronization

Vladimir N. Belykh, Grigory V. Osipov, and Jürgen Kurths

18.1
Introduction

Synchronization is an important phenomenon observed in nature and science [1]. Synchronization in a dynamical system is the phenomenon of the onset of *balance* between the phases of the subsystems' state variables' oscillations, which is caused by an onset of the energy balance. This phenomenon is called phase synchronization (PS). Especially, PS is typical for many systems in biology and neuroscience [2–6] and physics [7–11]. The balance of the phases of oscillations can be accompanied with a balance of the corresponding amplitudes. In this case generalized synchronization (GS) can be observed in dynamical systems and in the case of the full coincidence of synchronized variables the complete (full) synchronization sets in [12–15]. Depending on the type of coupling two main classical cases of synchronization can be distinguished: external and mutual. In the former case a freely evolving master system, acting as an external force, drives the slave system. Often, the increase of the external force leads to locking in, and synchronization occurs. Note that such a drive-response (or master slave) configuration is frequently commonly used in chaotic communication [16, 17, 18]. Mutual synchronization can be observed in the case of bidirectional coupling and is commonly accompanied by the hysteresis phenomenon [19].

We propose an automatic control method of phase locking of regular and chaotic nonidentical oscillations, when all subsystems interact via a feedback [20]. This method is based on the well-known principle of feedback control which takes place in nature and is successfully used in engineering. Considering the models of coupled systems in biology, neuroscience, and ecology one can see that in many of them the coupling between interacting elements is *nonlinear*, and usually has the form of quadratic functions of the subsystem variables. Such a coupling serves as the basis of an internal self-organization mechanism leading to a balanced motion in these systems. Synaptically coupled neurons [31, 32], phase transitions in human hand movement [33], ecological systems [28], or spinal generators of locomotion [34] are only some well-known

examples of balanced cooperative oscillatory motion, caused by a nonlinear coupling. In engineering, nonlinear coupling, is used, for example, in coupled lasers [22, 23] or phase-locked loops (PLL) [21].

Different methods for controlling the behavior of dynamical systems have been used for chaos control [35, 36, 37, 38, 39]. An adaptation of these methods for the stabilization of a chaotic trajectory of one system to a chaotic trajectory of another *identical* system, i.e., for a *control of complete synchronization*, is presented in [40–44]. In [45, 46] it was shown that the main problems of *complete* synchronization being regarded as a control problem can be solved on the basis of control theory methods. On the other hand, the problem of *phase* synchronization has not been formulated and hence considered before as a control theory problem. In contrast to the mentioned methods, our novel approach is directed at controlling the phases via characteristic time scales (CTS) of two (or many) different interacting oscillators.

In contrast to unidirectional (Fig. 18.1 (a)) and bidirectional (Fig. 18.1 (b)) coupling, the approach presented here supposes the existence of a special controller, which allows to change the parameters of the controlled systems
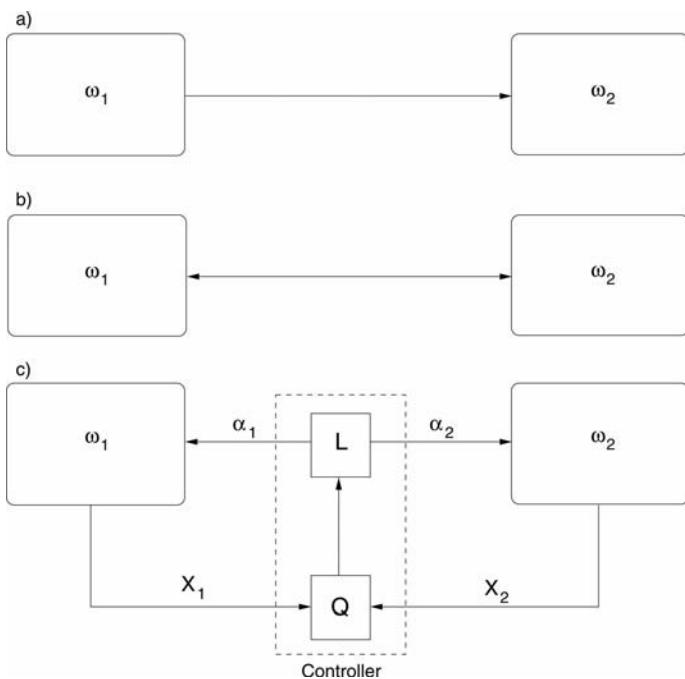

Fig. 18.1 Three main schemes of inter-element coupling between two oscillators having natural frequencies ω_1 and ω_2: (a) unidirectional, (b) bidirectional , and (c) coupling via feedback loop with controller composed of quadratic form (18.6) and linear operator (18.5).

(Fig. 18.1 (c)). For this purpose we extract first the mutual correlation between the CTS, then filter the obtained signal, and finally change the systems' parameters which govern the CTS.

This chapter is structured as follows: First we discuss general principles of automatic PS for arbitrary coupled systems with a controller whose input is given by a special quadratic form of coordinates of the individual systems and its output is a result of the application of a linear differential operator. Second, we demonstrate the effectiveness of our approach for controlled PS on several examples: (i) two coupled regular oscillators, (ii) coupled regular and chaotic oscillators, (iii) two coupled chaotic Rössler oscillators, (iv) coupled chaotic Rössler and Lorenz oscillators, (v) ensembles of locally coupled regular oscillators, (vi) ensembles of locally coupled chaotic oscillators, and (vii) ensembles of globally coupled chaotic oscillators.

18.2
General Principles of Automatic Synchronization

To begin with, we describe the automatic phase locking for two *arbitrary different* regular or chaotic oscillators given by

$$\frac{dx_{1,2}}{d\phi_{1,2}} = F_{1,2}(x_{1,2}) , \tag{18.1}$$

where $x_{1,2}$ and $F_{1,2}$ are $n_{1,2}$-dimensional vectors, $\phi_{1,2}$ are time-dependent variables, e.g., in the simplest case $\phi_{1,2} = \omega_{1,2}t$, where $\omega_{1,2}$ are parameters defining the time-dependence rate (in some cases, frequencies) of oscillations $x_{1,2}(t)$. Let us suppose that both systems have regular or chaotic attractors given by solutions $x_1^*(\phi_1)$ and $x_2^*(\phi_2)$, where $\phi_{1,2}$ stand for independent variables. Our purpose is to synchronize the oscillations using a feedback control of CTS of coupled oscillators in such a way that the new CTS $\Omega_{1,2}^{-1}$ become equal. Here $\Omega_{1,2}$ are the mean observed frequencies of the oscillators being controlled.

In order to synchronize the subsystems (18.1), we apply a feedback control of the following form:

$$\frac{dx_{1,2}}{dt} = \omega_{1,2}(1 + a_{1,2}u)F_{1,2}(x_{1,2}) , \tag{18.2}$$

$$\frac{d\phi_{1,2}}{dt} = \omega_{1,2}(1 + a_{1,2}u)) , \tag{18.3}$$

$$Lu = Q(x_1, x_2), \tag{18.4}$$

where L is a *linear stable operator*:

$$L = \gamma_k \frac{d^k}{dt^k} + \gamma_{k-1} \frac{d^{k-1}}{dt^{k-1}} + \cdots + \gamma_1 \frac{d}{dt} + \gamma_0 \tag{18.5}$$

acting as a low-pass filter, all γ_k are nonnegative constants. $Q(x_1, x_2)$ is a quadratic form:

$$Q(x_1, x_2) = \sum_{l=1}^{n_s} q_l x_1^{(l)} x_2^{(l)}, \tag{18.6}$$

where $n_s \leq \min(n_1, n_2)$, $q_l = \text{const} \geq 0$, is weighted scalar product of vectors x_1 and x_2; $a_{1,2}$ are control parameters, $u \in R^1$ is a control variable.

Statement. Systems 2–4 have the attractor

$$A = \{x_i = x_i^*(\phi_i), u = u^*(t),$$

$$\phi_i = \phi i^*(t) = \omega_i t + a_i \omega_i \int_{t_0}^{t} u^*(\tau) d\tau\}, \tag{18.7}$$

$$i = 1, 2.$$

Indeed, Eqs. (18.2) and (18.3), being equivalent to Eqs. (18.1), give $x_{1,2} = x_{1,2}^*(\phi_{1,2})$. Equation (18.4) at $x_{1,2}^*(\phi_{1,2})$ has a bonded set of solutions $S = \{\|u\| < K\}$, where $K = \text{const}$, due to the boundedness of $Q(x_1^*, x_2^*)$ and the stability of the operator L. Therefore, the solution $u^*(t) \in S$. Note that for the equivalence of Eqs. (18.2) and (18.3) to Eqs. (18.1) we have to assume the condition $1 + a_{1,2} u^*(t) > 0$, which is valid when $1 - a_{1,2} K > 0$.

Using the substitutions $\theta = \phi_2 - \phi_1$ and $\psi = \phi_2 + \phi_1$ we transform Eqs. (18.3) and (18.4) at $x_{1,2}^*$ into the system:

$$\frac{d\theta}{dt} = \omega_2 - \omega_1 + \beta u, \tag{18.8}$$

$$\frac{d\psi}{dt} = \omega_1 + \omega_2 + \gamma u, \tag{18.9}$$

$$\beta^{-1} L \left(\frac{d\theta}{dt} - (\omega_2 - \omega_1) \right) = Q(x_1^*(\psi - \theta), x_2^*(\psi + \theta)), \tag{18.10}$$

where $\beta = \omega_2 a_2 - \omega_1 a_1$ and $\gamma = \omega_1 a_1 + \omega_2 a_2$. ψ is the fast variable if $\omega_1 + \omega_2 >> \gamma^{-1} K$. Assuming the latter and averaging (18.10) we obtain the equation for the phase difference θ:

$$a_k \frac{d^{k+1}\theta}{dt^{k+1}} + \cdots + a_1 \frac{d^2\theta}{dt^2} + a_0 \frac{d\theta}{dt} = a_0(\omega_2 - \omega_1) + \beta G(\theta), \tag{18.11}$$

where

$$G(\theta) = \sum_{l=1}^{n_s} q_l \overline{x_1^{(l)} x_2^{(l)}} \tag{18.12}$$

is the average with respect to the fast variable ψ, and has a form of a correlation function. Then the stable either steady state(s) $(G(\theta) = a_0(\omega_2 - \omega_1)$ or another attractor(s) of oscillatory type in Eqs. (18.11) define the successful PS.

The described principle of synchronization is effectively used in applications of PLL in a large number of radio- and telecommunication devices, radio-location, etc. It can also be identified in a huge variety of examples in nature, where the interaction of some *oscillatory* objects leads to their *balanced* behavior. This behavior is mainly achieved by a *nonlinear interaction* of the elements [24–30]. Coupled lasers [23], synaptically coupled neurons [31], phase transitions in human hand movement [33], ecological systems [6], and spinal generators of locomotion [34] are only some well-known examples of balanced cooperative oscillatory motion, caused by a nonlinear coupling. Usually this coupling has the form of a quadratic function of variables of the interacting elements [47]. This type of coupling is able to minimize the oscillators' phase difference and therefore it causes synchronization.

Moreover, another control principle very similar to Eqs. (18.2)–(18.4) can be used for system (18.1), when the variable $x_1(x_2)$ is increasing (decreasing) with some characteristic exponent $\omega_1(\omega_2)$ for some bounded interval. Then, the system (18.1) describes a *growth-decay* process. In order to manage this process we apply the same type of feedback control, i.e., we use the quadratic form, but, here we add our control variable u directly to the process velocities:

$$
\begin{aligned}
\dot{x}_{1,2} &= F_{1,2}(x_{1,2}, \omega_{1,2}) + a_{1,2}u\,, \\
Lu &= Q(x_1, x_2)\,,
\end{aligned}
\tag{18.13}
$$

where we state that some chosen (L, Q)-pair in Eqs. (18.13) leads to the emergence of balanced (synchronized) oscillations of x_1 and x_2. As an example let us consider a *"predator-prey" system* [48]:

$$
\begin{aligned}
\dot{x}_1 &= \omega_1 x_1(1 - x_1) + a_1 u\,, \\
\dot{x}_2 &= -\omega_2 x_2 + a_2 u\,, \\
\tau \dot{u} &= -u + \beta x_1 x_2\,.
\end{aligned}
\tag{18.14}
$$

This system has a globally stable limit cycle, i.e., variables x_1 and x_2 become balanced. For $\tau = 0$ the system (18.14) is the Lotka-Volterra-type equations from mathematical ecology. They demonstrate the role of a hidden self-control interaction $\beta x_1 x_2$, causing the self-organization between predator's growth and prey's decay.

In the proposed control schemes the control in the form of some quadratic form is applied multiplicatively in order to achieve the PS and additively in order to achieve the growth-decay rates balance.

It appears that our proposed feedback principle of PS as well as amplitudes balance for synchronization is general and is realized in nature. We confirm this statement via two model systems which are paradigmatic in nonlinear dy-

namics. First, we show the *error* control system, where feedback control for PS is applied to the linear system (a "predator-prey" system in eigenspace) with a saddle steady state:

$$\dot{x} = -\sigma(x - y),$$
$$\dot{y} = (r - u)x - y,$$
$$\dot{u} = -bu + xy.$$
(18.15)

It is easy to see that this is the Lorenz system [50] having a strange attractor. We conclude that here an error in the control leads to the emergence of chaos.

The Rössler oscillator [51]

$$\dot{x} = -y - u,$$
$$\dot{y} = x + ay,$$
$$\dot{u} = -b - cu + xu,$$
(18.16)

is an example where the *error* control scheme of additive balance is applied to an oscillatory system. The chaotic behavior is again a result of the *error* control.

We have performed many analytical and numerical investigations which show successful application of proposed control scheme. Here, we shall present only three examples.

18.3
Two Coupled Poincaré Systems

As the simplest case, we consider feedback control of PS in two coupled Poincaré systems:

$$\dot{x}_1 = -\omega_1(1 + a_1 u)y_1 - \lambda(x_1^2 + y_1^2 - p^2)x_1,$$
$$\dot{y}_1 = \omega_1(1 + a_1 u)x_1 - \lambda(x_1^2 + y_1^2 - p^2)y_1,$$
$$\dot{x}_2 = -\omega_2(1 + a_2 u)y_2 - \lambda(x_2^2 + y_2^2 - p^2)x_2,$$
$$\dot{y}_2 = \omega_2(1 + a_2 u)x_2 - \lambda(x_2^2 + y_2^2 - p^2)y_2,$$
$$\dot{u} = -\gamma u + \beta x_1 x_2.$$
(18.17)

Here, (x_i, y_i) describe the two Poincaré systems and u is the control variable. $\omega_{1,2}$ are the frequencies, p is the amplitude of oscillations and $\lambda > 0$ determines the relaxation to the limit cycle. $\beta_{1,2}$ and γ are the parameters of the controller. The constants $a_{1,2}$ determine the coupling scheme. By simple modification of a_i it is possible to realize both bidirectional ($a_i \neq 0$, $i \in \{1, 2\}$) or unidirectional ($a_i = 0$, $a_j \neq 0$) coupling. Note that in this scheme the coupling strength a_i may as well take negative numbers. In (18.17) we have taken very simple forms for the quadratic form $Q(x_1, x_2) = \beta x_1 x_2$ and the linear operator $L = \frac{d}{dt} + \gamma$. How-

ever, we note that also different, more sophisticated, functions may be used with similar results. For example, we have checked that synchronization indeed occurs with different quadratic forms such as $Q(x_1, x_2) = (x_1 - x_2)^2$, or $Q(x_1, y_2) = (x_1 - y_2)^2$.

Using polar coordinates $x_i = \rho_i \cos \phi_i, y_i = \rho_i \sin \phi_i$, we rewrite system (18.17) in the form

$$
\begin{aligned}
\dot{\rho}_{1,2} &= \lambda \rho_{1,2}(p^2 - \rho_{1,2}^2), \\
\dot{\phi}_{1,2} &= \omega_{1,2}(1 + a_{1,2}u), \\
\dot{u} &= -\gamma u + \beta \rho_1 \rho_2 \cos(\phi_1)\cos(\phi_2).
\end{aligned}
\tag{18.18}
$$

The product of cosine functions in (18.18) can be decomposed into a slow and a rapidly oscillating term. In the limit $\omega_1 + \omega_2 > \gamma$ the low-pass filter L is damping out the 'high' frequencies, which further simplifies the dynamics. Let $\omega_2 = \omega_1 + \Delta\omega$. After relaxation of the radial equation, $\dot{\rho}_i = 0$, the radius of each oscillator is fixed to $\rho_i = p$. Thus, after averaging we arrive at the following simplified equations for the control variable u and the phase difference $\theta = \phi_2 - \phi_1$:

$$
\begin{aligned}
\dot{\theta} &= \Delta\omega + (a_2\omega_2 - a_1\omega_1)u, \\
\dot{u} &= -\gamma u + \frac{\beta p^2}{2}\cos\theta.
\end{aligned}
\tag{18.19}
$$

Rewritten as a second-order differential equation this leads to

$$
\ddot{\theta} + \gamma\dot{\theta} - \gamma\Delta\omega - \frac{\beta}{2}p^2(a_2\omega_2 - a_1\omega_1)\cos\theta = 0.
\tag{18.20}
$$

This pendulum-like equation for the evolution of the phase difference describes the synchronization regime of the two oscillators interacting via feedback control. The existence of this regime is defined by a stable steady state in (18.20) with the coordinates

$$
\cos\theta^* = \frac{2\gamma}{\beta p^2}u^*, \qquad u^* = \frac{\Delta\omega}{a_1\omega_1 - a_2\omega_2},
\tag{18.21}
$$

which does exist in the range

$$
\frac{\beta p^2}{2\gamma} > \left| \frac{\Delta\omega}{a_2\omega_2 - a_1\omega_1} \right|.
\tag{18.22}
$$

Synchronization is achieved when the effective coupling strength, here $\varepsilon_{\text{eff}} = \beta p^2/(2\gamma)$, is larger than a function of the frequencies, i.e., $\varepsilon_{\text{eff}} > f(\omega_i, a_i)$. In the contrast to the linear diffusive coupling, for example by terms $\beta(x_{2,1} - x_{1,2})$, the condition (18.22) depends on the values of the amplitudes of

oscillations p. Larger p provides the appearance of synchronization at smaller values of coupling β.

18.4
Coupled van der Pol and Rössler Oscillators

Now two structurally different oscillators are coupled: regular – van der Pol – oscillator and chaotic – Rössler – oscillator [51]. The equations describing the control scheme (same L and Q as in the previous section) for PS of such oscillators are

$$
\begin{aligned}
\dot{x}_1 &= -\omega_1(1 + a_1 u)\gamma_1 - z_1\,, \\
\dot{\gamma}_1 &= \omega_1(1 + a_1 u)x_1 + a\gamma_1\,, \\
\dot{z}_1 &= b - cz_1 + x_1 z_1\,, \\
\dot{x}_2 &= \gamma_2\,, \\
\dot{\gamma}_2 &= -(\omega_2(1 + a_2 u))^2 x_2 + \varepsilon(p^2 - x_2^2)\gamma_2\,, \\
\dot{u} &= -\gamma u + \beta x_1 x_2\,,
\end{aligned}
\tag{18.23}
$$

where x_1, γ_1, z_1 are the variables of the Rössler oscillator, and x_2, γ_2 are the variables of the van der Pol oscillator. u is again the control variable added in both subsystems, $a_{1,2}, \beta$ and γ are control parameters. We set $\beta = \gamma = 1$. For the van der Pol oscillator we choose the following set of parameters: $\omega_2 = 1$, $\varepsilon = 0.01$, and $p = 4$. The parameters of the Rössler oscillator will be chosen as: $a \in [0.15 : 0.2]$, $b = 0.1$, $c = 8.5$, and $\omega_1 = 1$. For these values the topology of the chaotic Rössler attractor is rather simple, i.e., phase-coherent, and one can introduce the phase in the form

$$
\phi_1 = \arctan(\gamma_1/x_1)\,.
\tag{18.24}
$$

For chosen ε the phase trajectory of the van der Pol oscillator regularly monotonously oscillates around the origin, so we can use a similar definition of the phase

$$
\phi_2 = -\arctan(\gamma_2/x_2)\,.
\tag{18.25}
$$

In order to test the existence of PS between Rössler and van der Pol oscillators, we use as in the previous chapters two criteria: PS sets in
(i) if the mean frequencies of both coupled subsystems become equal (frequency locking)

$$
\Omega_2 = \Omega_1\,,
\tag{18.26}
$$

where the frequencies are defined as

$$\Omega_{1,2} = \lim_{T \to \infty} \frac{\phi_{1,2}(T) - \phi_{1,2}(0)}{T} \; ; \tag{18.27}$$

(ii) and if the phase difference is bounded

$$|\phi_2 - \phi_1| \le \text{const.} \tag{18.28}$$

We consider two types of unidirectional (drive–response) feedback coupling:
(a) we control the characteristic time of the Rössler oscillator ($a_2 = 0$ in (18.23)) (Fig. 18.2), or
(b) we control the characteristic time of the van der Pol oscillator ($a_1 = 0$ in (18.23)) (Fig. 18.3). In both the cases there are critical values of the feedback control parameters $a_{1,2}^*$ corresponding to the onset of synchronization.

First, we study the case where the van der Pol oscillator is the drive system and the Rössler oscillator is the controlled response system. We set $a = 0.15$, so that the chaotic attractor of the Rössler oscillator is phase coherent. To illustrate the transition to PS, we plot the mean frequency difference and the three largest Lyapunov exponents versus the control parameter a_1 (Fig. 18.2 (a)), as well as a
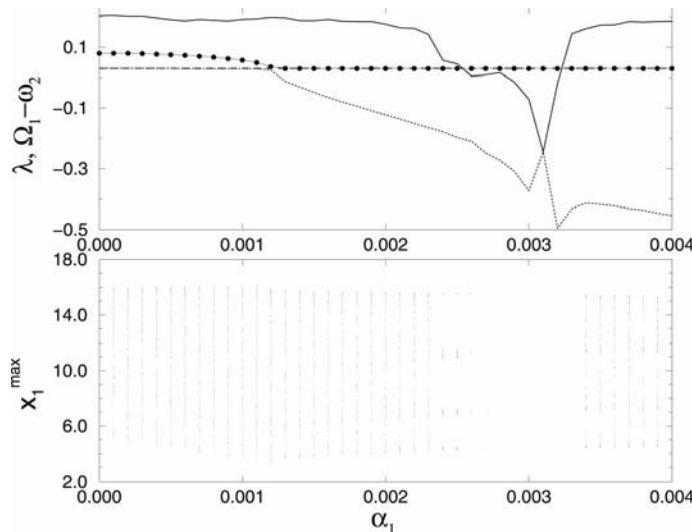

Fig. 18.2 Transition to PS for the unidirectionally ($a_1 = 0$ in (18.23)) feedback coupled Rössler and van der Pol oscillators. The van der Pol oscillator is the drive system and the Rössler oscillator is the controlled response system. The mean observed frequency of the Rössler oscillator Ω_1 at $a_1^* = 0.00123$ becomes equal to the frequency of the van der Pol oscillator ω_2. (a) The three largest Lyapunov exponents, one of which is always zero, and the difference of the mean observed frequencies $\Omega_1 - \omega_2$ (circles) versus the control parameter a_1. (b) Maxima of x_1 versus a_1.
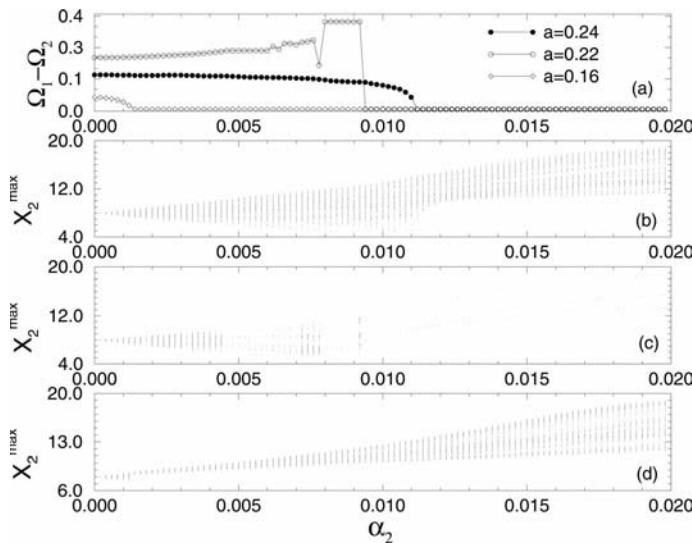
Fig. 18.3 Transition to PS for the unidirectionally ($a_2 = 0$ in (18.23)) feedback coupled Rössler and van der Pol oscillators. The Rössler oscillator is the drive system and the van der Pol oscillator is the controlled response system. The observed frequency of the van der Pol oscillator Ω_2 after some a_2^* becomes equal to the mean frequency of the Rössler oscillator Ω_1. (a) The difference of the mean observed frequencies $\Omega_1 - \Omega_2$ (circles) versus control parameter a_2. (b)–(d) Maximal values of x_2 versus a_2. The parameters are: (b) $a = 0.24$, (c) $a = 0.22$ (for $a = 0.22$ attractor in Rössler oscillator is periodic), and (d) $a = 0.16$.

bifurcation diagram (Fig. 18.2(b)). We find that PS occurs at $a_1^* = 0.00123$. There the behavior of the Rössler oscillator remains chaotic but with the mean observed frequency Ω_1 equal to the frequency ω_2 of the van der Pol oscillator. A similar situation of chaotic frequency locking was observed in [52, 53], where effects of PS were observed in a chaotic system forced by an external periodic signal. In contrast to this, our interacting subsystems are autonomous and therefore without coupling two zero Lyapunov exponents exist. In this case the transition to PS can be analyzed by means of the Lyapunov exponents spectrum. As it can be seen from Fig. 18.2(a) the frequency locking occurs approximately (shortly after) at the same value of a_1 for which one of the zero Lyapunov exponents becomes negative. Our numerical experiments (for other values of a) show that usually the behavior of the controlled Rössler oscillator remains chaotic. But there are also intervals of a_1 where the behavior of the Rössler oscillator becomes periodic (Fig. 18.2). Thus, very small coupling allows to control chaotic systems in such a way that (i) we can govern the mean frequency of oscillations and (ii) we can get periodic oscillations too.

In the second case of unidirectional feedback coupling, the Rössler oscillator is the drive system and the van der Pol oscillator is the controlled response system. Here we analyze not only the phase-coherent chaotic attractor ($a = 0.16$)

but also the funnel attractor ($a = 0.24$). In the latter case the topology of the attractor is rather complicated and the phase can not be defined as in (18.24). Thus, we introduce another phase definition [49]

$$\phi_1 = \arctan(\dot{y}_1/\dot{x}_1), \tag{18.29}$$

and use the same two criteria (18.26) and (18.28) as in the previous case. We plot in Fig. 18.3(a) the difference of the mean observed frequencies $\Omega_1 - \Omega_2$ versus the feedback control parameter a_1 for different values of a. In all cases PS occurs at some critical values a_2^*, but with increasing a a larger value a_2^* is needed to achieve the locking. The onset of PS is well manifested in the bifurcation diagrams (Figs. 18.3(b)–(d)). One can see that with increasing a_2 the interval l of possible maximum values of x_2 becomes larger at first. But at the transition point to synchronization a strong shrinking of the interval l is observed. It means that the variables x_2 and y_2 become localized in a relatively small area.

We have also performed numerical simulations where the van der Pol and the Rössler oscillator are mutually coupled by feedback ($a_{1,2} \neq 0$). The effect of both regular and chaotic PS has been observed there as well.

18.5
Two Coupled Rössler Oscillators

In this section we will demonstrate feedback control of chaotic PS for two coupled Rössler oscillators:

$$
\begin{aligned}
\dot{x}_{1,2} &= -\omega_{1,2}(1 + a_{1,2}u)y_{1,2} - z_{1,2}, \\
\dot{y}_{1,2} &= \omega_{1,2}(1 + a_{1,2}u)x_{1,2} + ay_{1,2}, \\
\dot{z}_{1,2} &= b - cz_{1,2} + x_{1,2}z_{1,2}, \\
\dot{u} &= -\gamma u + \beta x_1 x_2,
\end{aligned}
\tag{18.30}
$$

where $x_{1,2}, y_{1,2}, z_{1,2}$ are the variables of the first and second Rössler oscillator respectively. We set: $\beta = \gamma = 1$, $a = 0.15$, $b = 0.1$, $c = 8.5$, $\omega_1 = 0.98$, and $\omega_2 = 1.02$. Hence, for both oscillators the phase definitions (18.24) can be used. The existence of PS between Rössler oscillators is tested again by the criteria (18.26) and (18.28).

We computed the Lyapunov exponents spectrum (Fig. 18.4(a)), the mean frequency difference (Fig. 18.4(a)), and the evolution of the phase difference (Fig. 18.4(b)). PS sets in at the essentially small coupling $a_1^* = -a_2^* \approx 0.000415$. Note that shortly before PS one of the zero Lyapunov exponents becomes negative. With increasing a_1, the frequency difference decreases smoothly (without jump), i.e., a soft transition to PS takes place. This is manifested in the evolution of the phase difference, namely for the control parameters close to the critical value a_1^* phase locking at large time intervals is observed (Fig. 18.4(b)).
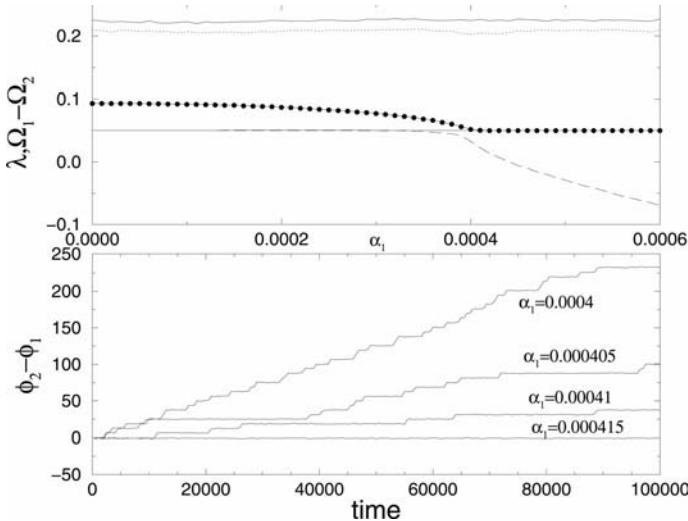
Fig. 18.4 Synchronization of two coupled Rössler oscillators (18.30). The parameters are: $a = 0.15, b = 0.1, c = 8.5, \omega_1 = 0.98$, $\omega_2 = 1.02, a_1 = -a_2$, and $\beta = \gamma = 1$. (a) The four largest Lyapunov exponents and the difference of the mean observed frequencies $\Omega_1 - \Omega_2$ (circles) versus the control parameter a_1. (b) Difference of the phases $\phi_2 - \phi_1$ for nonsynchronous ($a_1 = 0.0004; 0.000405; 0.00041$) and synchronous ($a = 0.000415$) regimes.

Let us compare the effectiveness of the proposed coupling scheme with respect to the diffusive coupling usually considered. In the latter case the equations of motions for two diffusively coupled Rössler oscillators are (see [55]):

$$\begin{aligned}
\dot{x}_{1,2} &= -\omega_{1,2} y_{1,2} - z_{1,2} + \beta(x_{2,1} - x_{1,2}), \\
\dot{y}_{1,2} &= \omega_{1,2} x_{1,2} + a y_{1,2}, \\
\dot{z}_{1,2} &= b - c z_{1,2} + x_{1,2} z_{1,2}.
\end{aligned} \tag{18.31}$$

In order to estimate the critical coupling strength corresponding to the appearance of synchronization, we make a transformation to cylindrical coordinates: $x_{1,2} = \rho_{1,2} \cos\phi_{1,2}$ and $y_{1,2} = \rho_{1,2} \sin\phi_{1,2}$. Then for the feedback-coupled oscillators (18.30), the averaged equation for the difference $\theta = \psi_2 - \psi_1$ of slow phases $\psi_{1,2} = \phi_{1,2} - \omega_0 t$ reads as

$$\ddot{\theta} + a\dot{\theta} - a\beta\rho_1\rho_2 \sin\theta = a\Delta. \tag{18.32}$$

If we neglect the fluctuations of the amplitude, Eq. (18.32) has the stationary solution:

$$\bar{\theta} = -\arcsin(\Delta/(\beta\rho_1\rho_2)). \tag{18.33}$$

This state exists and is stable if

$$\left|\frac{\Delta}{\rho_1\rho_2}\right| < \beta. \tag{18.34}$$

The equation for the phase difference of (18.31) can be recast in the form:

$$\dot{\theta} - \frac{\beta}{2}\frac{\rho_1^2 + \rho_2^2}{\rho_1\rho_2}\sin\theta = \Delta. \tag{18.35}$$

The stable stationary state

$$\bar{\theta} = \arcsin(2\Delta\rho_1\rho_2)/(\beta(\rho_1^2 + \rho_2^2)) \tag{18.36}$$

exists in the range

$$\beta > (|2\Delta\rho_1\rho_2|)/(\rho_1^2 + \rho_2^2). \tag{18.37}$$

If we take not strongly different oscillators (i.e., $\rho_1 \approx \rho_2$) this range is reduced to

$$\beta > |\Delta|. \tag{18.38}$$

Therefore, by equivalent parameters of the interacting oscillators the synchronization range for the feedback coupling (Eq. (18.30)) is $p^2 = \rho_1\rho_2$ times larger than for the diffusive coupling (Eq. (18.31)). This estimation is in very good agreement with our numerical results.

We have also analyzed the synchronization transitions for the simplest case of a linear operator L. For $a \gg 1$ the filtered control variable u can be expressed by $\sin(\phi_2 - \phi_1)$, where the phases $\phi_{1,2}$ are introduced by (18.24). Then the Eqs. (18.30) can be rewritten as

$$\begin{aligned}
\dot{x}_{1,2} &= -\omega_{1,2}[1 + a_{1,2}\sin(\phi_{2,1} - \phi_{1,2})]y_{1,2} - z_{1,2}, \\
\dot{y}_{1,2} &= \omega_{1,2}[1 + a_{1,2}\sin(\phi_{2,1} - \phi_{1,2})]x_{1,2} + ay_{1,2}, \\
\dot{z}_{1,2} &= b - cz_{1,2} + x_{1,2}z_{1,2}.
\end{aligned} \tag{18.39}$$

The dependence of the mean frequency ratio Ω_2/Ω_1 on the parameter $a_1 = -a_2$ for different a shows the onset of PS again for a very small coupling strength (Figs. 18.5 and 18.6).

18.6
Coupled Rössler and Lorenz Oscillators

Now we will apply the automatic PS to the coupled Rössler and Lorenz oscillators, i.e., chaotic oscillators with a well-pronounced difference in topology (see Sections 18.4 and 18.5). The model is (Fig. 18.7)

$$\dot{x}_1 = \tau(-\omega(1 + a_1 u)y_1 - z_1),$$
$$\dot{y}_1 = \tau(\omega(1 + a_1 u)x_1 + ay_1),$$
$$\dot{z}_1 = b - cz_1 + x_1 z_1,$$
$$\dot{x}_2 = \sigma(y_2 - x_2),$$
$$\dot{y}_2 = rx_2 - y_2 - x_2 z_2,$$
$$\dot{z}_2 = (1 + a_2 u)(-bz_2 + x_2 y_2),$$
$$\dot{u} = -\gamma u + x_1 z_2,$$

(18.40)
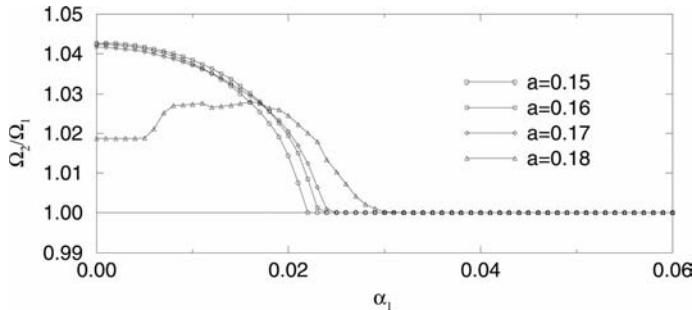
Fig. 18.5 Synchronization of two coupled Rössler oscillators (18.39). The ratio of the mean observed frequencies Ω_2/Ω_1 versus the control parameter a_1. The parameters of the individual oscillators are the same as in Fig.18.4.
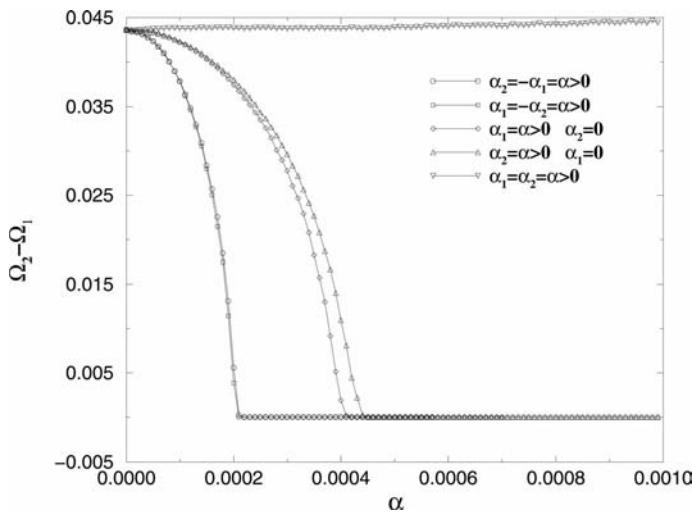

Fig. 18.6 Synchronization of two coupled Rössler oscillators (18.39) for different coupling schemes. Plotted is the frequency of the mean observed frequencies $\Omega_2 - \Omega_1$ versus the control parameter α. The coupling parameters a_1 and a_2 are taken as explained in the figure. The parameters of the individual oscillators are the same as in Fig. 18.4.
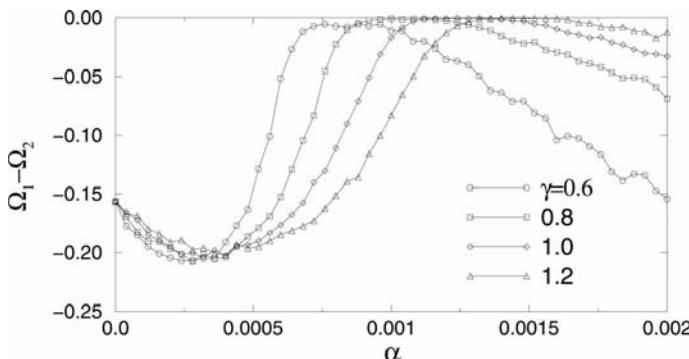
Fig. 18.7 Synchronization of coupled Rössler and Lorenz oscillators (18.40). The parameters are: $a = 0.15, b = 0.1$, $c = 8.5, \omega = 0.98, \sigma = 10, r = 28, b = 8/3, a_1 = -a_2 = a$, and $\beta = \gamma = 1$. The difference of the mean observed frequencies $\Omega_1 - \Omega_2$ versus the control parameter α.

where $x_{1,2}, y_{1,2}, z_{1,2}$ are the variables of the Rössler and Lorenz oscillators, respectively. The parameters a, b, c and the phase of the Rössler oscillator are the same as in the previous case; $\omega = 0.98$, $\tau = 8.3$, $\sigma = 10$, $r = 28$, and $b = 8/3$ and the phase of the Rössler oscillator is measured as before. The phase of the Lorenz oscillator is calculated as $\theta = \arctan((z_2 - 27)/(\sqrt{x_2^2 + y_2^2} - 12))$. In Fig. 18.7 we present results of the transition to chaotic PS between Rössler and Lorenz oscillators. One can see an interval of α where PS occurs. Therefore, using the proposed scheme we are able to achieve chaotic PS between oscillators with a strong difference in their topology.

18.7
Principles of Automatic Synchronization in Networks of Coupled Oscillators

The formation of collective behavior in large ensembles or networks of coupled oscillatory elements is one of the oldest problem in the study of dynamical systems. Nevertheless, it is an actually challenging field for a theoretical understanding as well as for applications in various disciplines, ranging from physics, chemistry, earth sciences via biology and neuroscience to engineering, business and social sciences. Due to the large number of effective degrees of freedom in spatially extended systems, a rich variety of spatiotemporal regimes is observed. Three main types of collective behavior are distinguished: (i) a fully incoherent state or highly developed spatiotemporal disorder; (ii) partially coherent states, where some of the participants in the network behave in some common rhythm; (iii) a fully coherent state or a regime of globally synchronized elements. The basic phenomenon of these structure formations is synchronization, i.e., regime of coherent activity, which is universal in many dynamical systems

and can be understood from the analysis of common models of oscillatory networks.

Oscillatory arrays can have regular arrangement (1D arrays or 2D lattices) with the coupling extended to the nearest neighbors (local coupling), or global coupling among all the oscillators. Such simple coupling topology of the oscillators is relevant to many experimental and natural situations.

The locally or globally coupled networks can be considered as *regular networks*. However, there are many real-world systems which are neither locally nor globally coupled, but often display a much more complicated coupling topology. Examples include Internet and world wide web in communication systems, neural system or genetic regulation in biology, epidemic spreading and synchronization in social and ecological systems, etc. [57–59].

Let us consider an ensemble of arbitrary regular or chaotic oscillators given by the system

$$\dot{x}_j = F_j(x_j, \omega_j), \qquad j = 1, \ldots, N \qquad (18.41)$$

where x_j and F_j are n-vectors, ω_j are parameters defining the time dependence rate of oscillations $x_j(t)$ and N is the number of oscillators.

In order to synchronize these systems, we apply a feedback control between all of them in the following form:

$$\dot{x}_j = F_j(x_j, \omega_j + a_j u_j),$$
$$Lu_j = Q_j(x_1, \ldots, x_N), \qquad j = 1, \ldots, N, \qquad (18.42)$$

where L is again a linear operator acting as a low-pass filter; the function $Q_j(x_1, \ldots, x_N)$ is:

$$Q_j(x_1, \ldots, x_N) = \sum_{k=1, k \neq j}^{N} Q_k(x_j, x_k), \qquad (18.43)$$

where Q_k is a quadratic form $Q_k = x_j^T H x_k$ which characterizes the coupling between the jth and the kth oscillators.
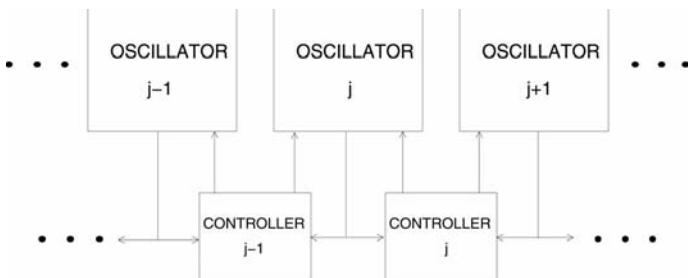

Fig. 18.8 Local feedback coupling in a chain of oscillators.

Now we study whether the control variable $u_j(t)$ added to each oscillator can provide a synchronous behavior between interacting elements. Figure 18.8 presents a simple scheme which roughly describes the proposed coupling technique.

We demonstrate the method of feedback control for PS for ensembles of (i) locally coupled regular oscillators (Section 18.8), (ii) locally coupled chaotic oscillators (Section 18.9), and (iii) globally coupled chaotic oscillators (Section 18.10).

18.8
Synchronization of Locally Coupled Regular Oscillators

As the simplest case, we consider feedback control of PS in an ensemble of *locally* mutually coupled Poincaré systems:

$$
\begin{aligned}
\dot{x}_j &= -(a_j u_j + \omega_j) y_j - \lambda(x_j^2 + y_j^2 - p^2) x_j\,, \\
\dot{y}_j &= (a_j u_j + \omega_j) x_j - \lambda(x_j^2 + y_j^2 - p^2) y_j\,, \\
\dot{u}_j &= -u_j + \beta_{j+1} x_j y_{j+1} + \beta_{j-1} x_j y_{j-1}\,,
\end{aligned}
\tag{18.44}
$$

where $j = 1, \ldots, N$, ω_j are the frequencies, p is the amplitude of oscillations, and $\lambda > 0$ is a damping parameter of the oscillators, u_j is the control variable, a_j and β_j are the parameters of the jth controller. We assume free-end boundary conditions: $\beta_0 = \beta_{N+1} = 0$. For the quadratic form Q_j we take the simplest form of coupling with nearest neighbors

$$
Q_j = \beta_{j+1} x_j y_{j+1} + \beta_{j-1} x_j y_{j-1}\,.
\tag{18.45}
$$

In this example we take the linear operator L in the form $L = \frac{d}{dt} + 1$. Using polar coordinates $x_j = \rho_j \cos\phi_j$, $y_j = \rho_j \sin\phi_j$, we rewrite (66) in the following form:

$$
\begin{aligned}
\dot{\rho}_j &= \lambda \rho_j (p^2 - \rho_j^2)\,, \\
\dot{\phi}_j &= a_j u_j + \omega_j\,, \\
\dot{u}_j &= -u_j + \beta_{j+1} \rho_j \rho_{j+1} \cos\phi_j \sin\phi_{j+1} + \\
&\quad + \beta_{j-1} \rho_j \rho_{j-1} \cos\phi_j \sin\phi_{j-1}\,, \qquad j = 1, \ldots, N\,.
\end{aligned}
\tag{18.46}
$$

We take a linear increasing distribution of individual frequencies $\omega_j = \omega_1 + \Delta(j - 1)$, and $a_j = a$, $\beta_j = \beta$. Then by introducing the phase difference variable $\theta_j = \phi_j - \phi_{j+1}$, $\hat{a} = a\beta/2$ and averaging the system (18.46), we obtain:

$$
\ddot{\phi}_1 + \dot{\phi}_1 = \omega_1 + \hat{a}p \sin\theta_1\,,
\tag{18.47}
$$

$$
\ddot{\theta}_j + \dot{\theta}_j = \Delta + \hat{a}p(\sin\theta_{j+1} - 2\sin\theta_j + \sin\theta_{j-1})\,, \qquad j = 1, \ldots, N-1\,.
\tag{18.48}
$$

with the boundary conditions: $\theta_0 = \theta_N = 0$. These equations describe the synchronization regime in an ensemble of coupled Poincaré systems. The existence of a PS regime is defined by a stable steady state in (18.48). This state $(\bar{\theta}_1, \dots, \bar{\theta}_j, \dots, \bar{\theta}_{N-1})$ in system (18.48) corresponds to a regime of global synchronization in the chain. Hence, the system of equations for the stationary phase differences $\bar{\theta}_n$ can be written as

$$\Delta + \hat{a}p\left(\sin\bar{\theta}_2 - 2\sin\bar{\theta}_1\right) = 0,$$

$$\Delta + \hat{a}p\left(\sin\bar{\theta}_{j+1} - 2\sin\bar{\theta}_j + \sin\bar{\theta}_{j-1}\right) = 0, \qquad j = 2, \dots, N-2, \qquad (18.49)$$

$$\Delta + \hat{a}p\left(\sin\bar{\theta}_N - 2\sin\bar{\theta}_{N-1}\right) = 0.$$

The distribution of $\bar{\theta}_j$ is [54]:

$$\sin\bar{\theta}_j = \frac{\Delta}{2\hat{a}p}\left(Nj - j^2\right). \qquad (18.50)$$

It follows from (18.50) that the system (18.48) can have 2^{N-1} steady states. But only one of them ($\bar{\theta}_j \in [-\pi/2; \pi/2]$ for all $j = 1, \dots, N-1$) can be stable. As the frequency mismatch Δ is increased, the condition for the existence of steady states

$$\left|\frac{\Delta}{2\hat{a}p}\left(Nj - j^2\right)\right| < 1. \qquad (18.51)$$

is violated first for $j = N/2$ at even N, i.e., for the middle element in the chain. Thus, the condition for the existence of a stable steady state in the N-element chain is given by the inequality

$$\left|\frac{\Delta N^2}{8\hat{a}p}\right| < 1. \qquad (18.52)$$

The frequency of global synchronization Ω_s may be determined from Eqs. (18.48), such that

$$\Omega_s = \omega_1 + \frac{\Delta}{2}\left(N - 1\right). \qquad (18.53)$$

Then the frequencies for all elements are equal to the mean frequency of the elements in the ensemble. With an increase of the frequency mismatch Δ (or decrease of the coupling a), a loss of global synchronization takes place. For a long chain two synchronization clusters occur, i.e., the chain is divided into two clusters each of size $N/2$, both consisting of mutually synchronized oscillators. Further increase of Δ (decrease of a) leads to a sequence of destruction of the one cluster structure of the synchronized elements and to the appearance of another structure. This sequence obtained in numerical experiments is presented

in Fig. 18.9. From this figure, we recognize two types of transitions between cluster structures. In the first type, a "hard" transition without intermediate structures occurs from the state with n ($n + 1$) clusters to the state with $n + 1$ (n) clusters (see, for example, the interval $[0.019 : 0.023]$). In the second type, a "soft" transition happens with a smooth transition of intermediate structures one into the other. As follows from Fig. 18.9, the theoretically and numerically obtained condition of global synchronization and the global synchronization frequency are in very good agreement.

18.9
Synchronization of Locally Coupled Chaotic Oscillators

Now we will demonstrate feedback control of chaotic PS in ensembles of *locally* coupled Rössler oscillators (Fig. 18.10)

$$
\begin{aligned}
\dot{x}_j &= -(\omega_j + a_j u_j)y_j - z_j\,, \\
\dot{y}_j &= (\omega_j + a_j u_j)x_j + ay_j\,, \\
\dot{z}_j &= b - cz_j + x_j z_j\,, \\
\dot{u}_j &= -\gamma_j u_j + \beta_{j+1} x_j y_{j+1} + \beta_{j-1} x_j y_{j-1}, \qquad j = 1, \ldots, N\,.
\end{aligned}
\tag{18.54}
$$

We set: $a = 0.15$, $b = 0.1$, $c = 8.5$, $a_j = a$, $\gamma_j = \beta_j = 1$. Like in the Poincaré systems, we introduce a gradient distribution of natural frequencies
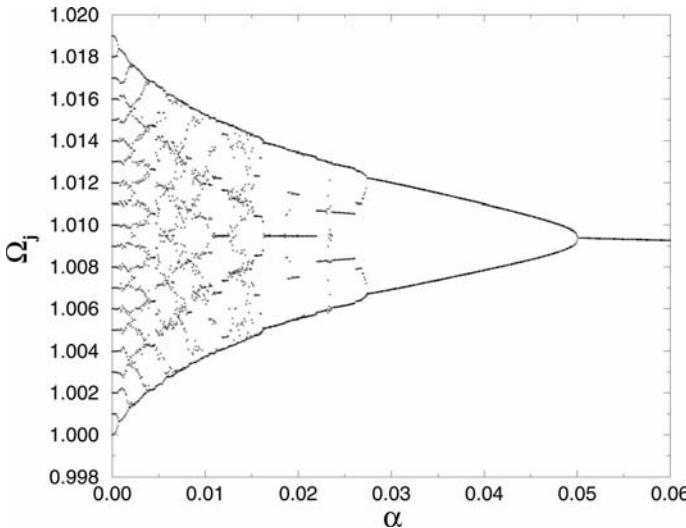

Fig. 18.9 Observed frequencies Ω_j in a chain of Poincaré systems (Eqs. (18.44)) with linear distribution of individual frequencies versus a. $N = 20$, $p = 1$, $\omega_1 = 0.98$, $\Delta = 0.001$.

$\omega_j = \omega_1 + \Delta(j-1)$ with $\omega_1 = 0.98$, and $\Delta = 0.0001$. Another variant considered below is a random distribution of natural frequencies in the range $[\omega_1, \omega_1 + \Delta(N-1)]$. We again assume free-end boundary conditions: $\beta_0 = \beta_{N+1} = 0$. The control scheme Q_j is the same as in the previous section and $L = \frac{d}{dt} + \gamma_j$. As a condition of synchronization we again consider the coincidence of the observed partial frequencies defined in (18.27).

We have performed numerical simulations with a chain of 100 elements with a linear and a random distribution of the individual frequencies. For each element for different a the frequency Ω_j has been calculated. We find that in both the cases by increasing the coupling a all frequencies Ω_j become equal, which means global chaotic PS sets in.

We have also analyzed synchronization transitions in the simplest case of a linear operator L. For $\gamma_j \gg 1$ the filtered control variable u_j can be expressed as

$$u_j = \sin(\phi_{j+1} - \phi_j) + \sin(\phi_{j-1} - \phi_j)\,, \tag{18.55}$$

where the phases ϕ_j are introduced via (18.24). Then Eqs. (18.54) can be rewritten as

$$\begin{aligned}
\dot{x}_j &= -\omega_j y_j - z_j + \\
&\quad - \omega_j a(\sin(\phi_{j+1} - \phi_j) + \sin(\phi_{j-1} - \phi_j))y_j\,, \\
\dot{y}_j &= \omega_j x_j + a y_j + \\
&\quad + \omega_j a(\sin(\phi_{j+1} - \phi_j) + \sin(\phi_{j-1} - \phi_j))x_j\,, \\
\dot{z}_j &= b - c z_j + x_j z_j\,, \qquad j = 1, \ldots, N\,.
\end{aligned} \tag{18.56}$$
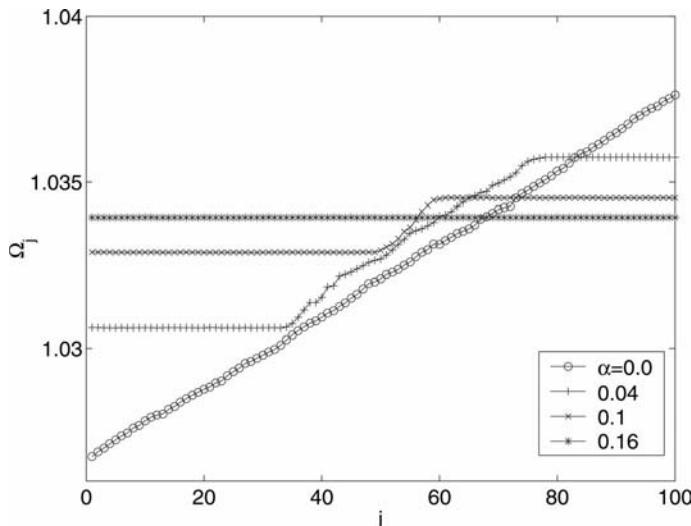
Fig. 18.10 Mean frequencies Ω_j in a chain of Rössler oscillators with a linear distribution of individual frequencies for different a. The number of elements $N = 100$, $\omega_1 = 0.98$, $\Delta = 0.0001$.
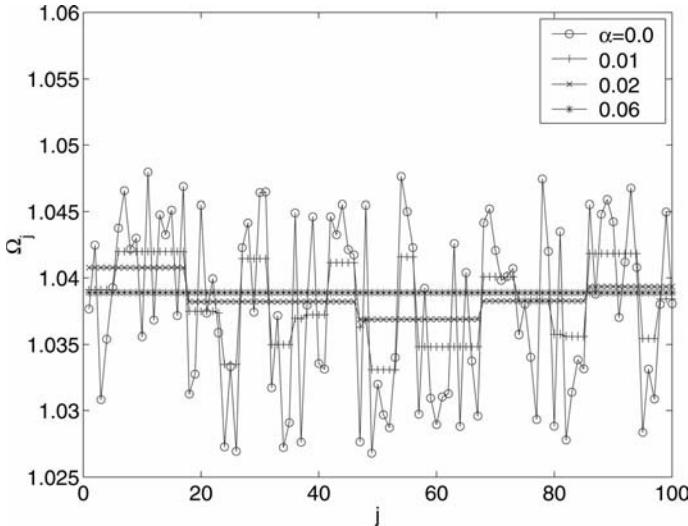
Fig. 18.11 Mean frequencies Ω_j in a chain of Rössler oscillators with randomly distributed frequencies in the interval [0.98,1] for different a. The number of elements $N = 100$.

The dependence of the mean frequencies Ω_j on the parameter a with linear (Fig. 18.10) respectively random (Fig. 18.11) distributions of the individual frequencies exhibit the onset of PS for a very small coupling term.

18.10
Synchronization of Globally Coupled Chaotic Oscillators

Finally we study the potential of the presented method for *globally* coupled Rössler oscillators:

$$
\begin{aligned}
\dot{x}_j &= -(\omega_j + a_j u_j)y_j - z_j \\
\dot{y}_j &= (\omega_j + a_j u_j)x_j + ay_j\,, \\
\dot{z}_j &= b - cz_j + x_j z_j\,, \\
\dot{u}_j &= -\gamma_j u_j + x_j \sum_{k=1,k\neq j}^{N} \beta_k y_k, \qquad j = 1,\dots, N\,.
\end{aligned}
\tag{18.57}
$$

We take the same parameters of individual elements as in the previous section and randomly distributed frequencies ω_j. Let us choose again all $\gamma_j \gg 1$. Then the filtered control variable u_j can be described in the form

$$
u_j = \sum_{k=1,k\neq j}^{N} \sin(\phi_j - \phi_k)
\tag{18.58}
$$

and (18.57) can be rewritten as

$$\dot{x}_j = -\omega_j y_j - z_j +$$
$$- \omega_j a \sum_{k=1,k\neq j}^{N} \sin(\phi_j - \phi_k))y_j \,,$$
$$\dot{y}_j = \omega_j x_j + a y_j + \tag{18.59}$$
$$+ \omega_j a \sum_{k=1,k\neq j}^{N} \sin(\phi_j - \phi_k))x_j \,,$$
$$\dot{z}_j = b - c z_j + x_j z_j, \qquad j = 1,\ldots,N \,.$$

Following [30], we characterize the degree of synchronization by means of the *order parameter*.

$$R = \lim_{N\to\infty} \frac{N_l}{N} \,, \tag{18.60}$$

where N_l is the size of the largest cluster of synchronized oscillators. This frequency order parameter is for fully incoherent oscillators $R = 0$, and reaches for globally synchronized behavior the maximum $R = 1$. The order parameter R averaged over 10 samples of randomly distributed frequencies ω_j is presented in Fig. 18.12. We see that there exists a critical value a^* when all oscillators be-
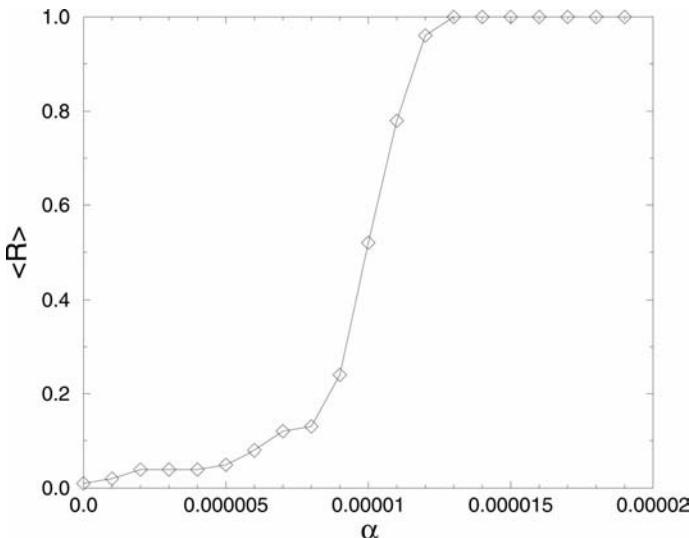

Fig. 18.12 Frequency entrainment in the ensemble of globally feedback coupled Rössler oscillators with randomly distributed frequencies in the interval [0.98,1] versus a. The number of elements is $N = 100$.

come synchronized. This transition from a fully incoherent behavior to a fully coherent (synchronized one) has been typically observed in ensembles of globally coupled elements.

18.11
Conclusions

In this chapter we have presented a feedback control method for automatic phase locking of regular and chaotic oscillators.

The main advantages of this method are the following:

- *The effect of the amplitudes* of the interacting subsystems on the difference of their phases provides a high efficiency of this approach; large amplitudes lead to a small phase difference.
- The proposed method can be used for automatic synchronization of oscillators of different nature (regular and chaotic), and different topology (e.g., coupled Rössler and Lorenz oscillators) and complexity (e.g., chaotic and hyperchaotic Rössler oscillators).
- Phase synchronization already sets in at very small values of control parameters, which is very important from an energetical point of view.
- The method can be used to synchronize elements coupled in small (two units) and large (chains and lattices) ensembles. In the latter case the coupling can be local or global.
- Synchronization can be obtained for very small coupling values. On the other hand, sometimes synchronization cannot be obtained at all. This seems to be a trade-off.

This presented approach can be helpful (i) for the understanding of self-organization mechanisms in many systems in the nature with regular and complex structure and (ii) for the design of different schemes of automatic synchronization in communication and engineering (phase antenna arrays [60, 61], and PLL [62–64]) and could be applied to ecology and medicine.

References

1 Pikovsky P. S., Rosenblum M. G., J. Kurths J. *Synchronization – A Universal Concept in Nonlinear Sciences, Cambridge University Press, Cambridge,* **2001**.

2 Elson R. C. et al. *Phys. Rev. Lett. 81* **(1998)**, p. 5692.

3 Schäfer C. et al. *Nature 392* **(1998)**, p. 239.

4 Tass P. et al. *Phys. Rev. Lett. 81* **(1998)**, p. 3291.

5 Belykh V., Belykh I., Hasler M. *Phys. Rev. E 62* **(2000)**, p. 6332.

6 Blasius B., Huppert A., Stone L. *Nature 399* **(1999)**, p. 354.

7 Fabiny L., Colet P., Roy R. *Phys. Rev. A 47* **(1993)**, p. 4287.

8 Roy R., Thornburg K. S. Jr. *Phys. Rev. Lett. 72* **(1994)**, p. 2009.

9 Anishchenko V. S., Vadivasova T. E., Postnov D. E., Safonova M. A., *Int. J.*

Bifurc. Chaos Appl. Sci. Eng. 2 **(1992)**, p. 633.

10 DeShazer D. et al. *Phys. Rev. Lett. 87* **(2001)**, p. 044101.

11 Belykh V., Belykh I., Mosekilde E. *Phys. Rev. E 63* **(2001)**, p. 036216.

12 A special issue on phase synchronization in chaotic systems, edited by J. Kurths, *Int. J. Bifurc. Chaos 11* **(2000)**.

13 Boccaletti S., Kurths J., Osipov G., Valladares D. L., Zhou C. *Phys. Rep. 366* **(2002)**, p. 1.

14 A special isssue on control and synchronization in chaotic dynamical systems. J. Kurths et al. *Chaos 13* **(2003)**.

15 Osipov G. V., Kurths J., Zhou C. *Synchronization in Oscillatory Networks*, Springer, Berlin **(2007)**.

16 Pecora L. M., Carroll T. L. *Phys. Rev. Lett. 64* **(1990)**, p. 821.

17 Dedieu H., Kennedy M. P., Hasler M., *IEEE Trans. Circuits Syst. II 40* **(1993)**, p. 634.

18 Kocarev L., Parlitz U., *Phys. Rev. Lett. 74* **(1995)**, p. 5028.

19 Van der Pol B., *Phil. Mag. 6 ser. 43* **(1992)**, p. 700.

20 Belykh V. N., Osipov G. V., Kuckländer N., Blasius B., Kurths J., *Physica D 200* **(2005)**, p. 81.

21 Lindsey W. C., *Synchronization Systems in Communication and Control*, Prentice-Hall, Englewood Cliffs, NJ, **1972**.

22 Fabiny L. et al., *Phys. Rev. A 47* **(1993)**, p. 4287.

23 Oliva R. A., Strogatz S. H., *Int. J. Bifurc. Chaos Appl. Sci. Eng. 11* **(2001)**, p. 2359.

24 Aizawa Y., *Prog. Theor. Phys. 56* **(1976)**, p. 703.

25 Christiansen D., Alstrom P., Levinsen M. T., *Physica D 56* **(1992)**, p. 23.

26 Eckhorn R., *Biol. Cybern. 60* **(1987)**, p. 121.

27 Guckenheimer J., Holmes P., *Nonlinear Oscillations, Dynamical Systems, and Bifurcations of Vector Fields*, Springer, Berlin, Heidelberg, **1990**.

28 Murray J. D., *Mathematical Biology*, Springer, Berlin, Heidelberg, **1989**.

29 Haken, H., *Synergetics. An Introduction*, Springer, Berlin, Heidelberg, **1977**.

30 Kuramoto, Y., *Chemical Oscillations, Waves, and Turbulence*, Springer, Berlin, Heidelberg, **1984**.

31 Rabinovich, M., et al., *Phys. Rev. Lett. 87* **(2001)**, p. 068102.

32 Karbowski, J., Ermentrout, G. B., *Phys. Rev. E 65* **(2002)**, p. 031902.

33 Haken, H., Kelso, J. A. S., Bunz, H., *Biol. Cybern. 51* **(1985)**, p. 347.

34 Cohen, A. H., Holmes, P. J, Rand, R. H., *J. Math. Biol. 13* **(1982)**, p. 345.

35 Ott, E., Grebogy, C., Yorke, J. A., *Phys. Rev. Lett. 64* **(1990)**, p. 1196.

36 Pyragas, K., *Phys. Lett. A 170* **(1992)**, p. 421.

37 Boccaletti, S., Grebogi, C., Lai, Y.-C., Mancini, H., Maza, D., *Phys. Rep. 329* **(2000)**, p. 103.

38 Schikora, S., Hövel, P., Wunsche, H. J., Schöll, E., Hennenberger, F., *Phys. Rev. Lett. 97* **(2006)**, p. 213902.

39 Schuster, H. G., *Handbook of Chaos Control, Wiley-VCH, Weinheim,* **(1999)**.

40 Mehta, N. J., Hendersen, R. M., *Phys. Rev. A 44* **(1991)**, p. 4861.

41 Lai, Y. C., Grebogi, C., *Phys. Rev. E 47* **(1993)**, p. 2357.

42 Newell, T. C., et al., *Phys. Rev. E 49* **(1994)**, p. 313.

43 Konnur, R., *Phys. Rev. Lett., 77* **(1996)**, p. 2937.

44 Ho, M. Ch., Hung, Y. Ch., Chou, Ch. H., *Phys. Lett. A 296* **(2002)**, p. 43.

45 Pogromsky, A., Nijmeijer, H., *IEEE Trans. Circuit Syst. I 48* **(2001)**, p. 152.

46 Pogromsky, A. Yu., Santoboni, G., Nijmeijer, H., *Physica D 172* **(2002)**, p. 65.

47 Tass, P., Haken, H., *Z. Phys. B 100* **(1996)**, p. 303.

48 Kolmogorov, A., *G. Inst. Ital. Attuari 7* **(1936)**, p. 74.

49 Osipov, G. V., Hu, B., Zhou, Ch., Ivanchenko, M. V., Kurths, J., *Phys. Rev. Lett. 91* **(2003)**, p. 24101.

50 Sparrow, C., *The Lorenz Equations: Bifurcations, Chaos, and Strange Attractors* Springer, Berlin, **1982**.

51 Rössler, O. E., *Phys. Lett. A 57* **(1976)**, p. 397.

52 Stone, E. F., *Phys. Lett. A 163* **(1992)**, p. 367.

53 Pikovsky, A. S., Rosenblum, M. G., Osipov, G. V., Kurths, J., *Physica D 104* **(1997)**, p. 219.

54 Afraimovich, V. S., Nekorkin, V. I., Osipov, G. V., Shalfeev, V. D., *Stability,*

Structures and Chaos in Nonlinear Synchronization Networks, World Scientific, Singapore, **1994**.

55 Rosenblum, M. G., Pikovsky, A. S., Kurths, J., *Phys. Rev. Lett. 76* **(1996)**, p. 1804.

56 Aronson, D. G., Ermentrout, G. B., Kopell, N., *Physica D 41* **(1990)**, p. 403.

57 Albert, R., Barabási, A. L., *Rev. Mod. Phys. 74* **(2002)**, p. 47.

58 Zhou, C., Motter, A., Kurths, J., *Phys. Rev. Lett. 96* **(2006)**, p. 034101.

59 Zhou, C., Kurths, J., *Phys. Rev. Lett. 96* **(2006)**, p. 164102.

60 York, R. A., Itoh, T., *IEEE Trans. Microwave Theory Tech. 46* **(1998)**, p. 1920.

61 Chang, K., York, R. A., Hall, P. S., Itoh, T. *IEEE Trans. Microwave Theory Tech. 50* **(2002)**, p. 937.

62 Buckwalter, J. F., Heath, T H., York, R. A., *IEEE Trans. Microwave Theory Tech. 51* **(2003)**, p. 952.

63 Maccarini, P. F., Buckwalter, J. F., York, R. A., *IEEE MTT-S Digest* **(2003)**, p. 1689.

64 Mishagin, K. G., Shalfeev, V. D., *Tech. Phys. Lett. 32* **(2006)**, p. 1014.

Part V
Applications to Optics

19
Controlling Fast Chaos in Optoelectronic Delay Dynamical Systems

Lucas Illing, Daniel J. Gauthier, and Jonathan N. Blakely

19.1
Introduction

Recent studies have shown that fast chaotic dynamics can be used for a variety of applications such as information transmission with high power efficiency [1], generating truly random numbers [2, 3], radar [4–8], as well as novel spread spectrum [9], ultrawide bandwidth [10, 11], and optical [12, 13] communication schemes. In these applications, it is desirable to generate chaos in the fast regime where the typical time scale of the fluctuations is on the order of 1 ns or less [12, 14]. The ability to control the chaotic trajectory to specific regions in phase space is also desirable [1, 15, 16].

For applications requiring controlled trajectories, it is possible to use recently developed chaos-control methods. The key idea underlying these techniques is to stabilize a desired dynamical behavior by applying feedback through minute perturbations to an accessible parameter when the system is in a neighborhood of the desired trajectory in state-space [17–19].

In particular, many of the control protocols attempt to stabilize one of the unstable periodic orbits (UPOs) that are embedded in the chaotic attractor (although the control of unstable steady state has also been investigated, see, for example, [20–23]). While the control of UPOs has been very successful for slow systems (characteristic time scale > 1 µs) [24–27], applying feedback control to fast chaotic systems is challenging because the controller requires a finite time to sense the current state of the system, determine the appropriate perturbation, and apply it to the system. This finite time interval, often called the control-loop latency τ_l, can be problematic if the state of the system is no longer correlated with its measured state at the time when the perturbation is applied. Typically, chaos control fails when the latency is on the order of the period of the UPO to be stabilized [28–30].

Another difficulty faced in controlling fast chaos is the fact that many high-speed chaos generators are delay dynamical systems. Time-delayed feedback occurs naturally in high-speed systems, where the time it takes signals to propa-

gate through the device components is comparable to the time scale of the fluctuations. Hence many fast systems are most accurately described by time delay differential equations. In fact, most fast chaos generators reported in the literature make explicit use of the propagation delay through components to generate delay-induced chaotic oscillations. Such systems evolve in an infinite-dimensional phase space and can display very high-dimensional chaotic attractors [31]. Examples of fast broadband chaotic oscillators that are modeled as time delay systems include electronic [32], optoelectronic [14, 33], and microwave oscillators [1], as well as lasers with delayed optical feedback [12], and nonlinear optical resonators [34].

One approach to avoid the failure of chaos control due to latency is to simplify the controller as much as possible in order to minimize τ_l. An example of this approach are methods that apply perturbations of a predetermined strength when the system crosses some threshold in phase space [35, 36]. Using these methods, successful control of fast but low-dimensional chaos was demonstrated. As an example, an UPO with period $T_{PO} = 23$ ns was stabilized [35]. A drawback of these methods is that they rely on the ability to easily define windows and walls in phase space. This task is conceptually much more difficult in the case of delay systems where the phase space is infinite dimensional. Perhaps for this reason, these methods have not yet been applied successfully to delay systems.

The control of very fast chaotic delay dynamical systems is an outstanding problem because of two challenges that arise: control-loop latencies are unavoidable, and complex high-dimensional behavior of systems is common due to inherent time delays. The primary purpose of this chapter is to explain, by means of a simple example, why latency can be a significant problem adversely affecting control and to describe an approach for controlling time delay systems even in the presence of substantial control-loop latency. This is a general approach that can be applied to any of the fast time delay systems described above. As a specific example, we demonstrate this general approach by using time delay autosynchronization control [37] to stabilize fast periodic oscillations ($T_{PO} \sim 12$ ns) in an optoelectronic device. In principle, much faster oscillations can be controlled using, for example, high-speed electronic or all-optical control components, paving the way to using controlled chaotic devices in high-bandwidth applications.

19.2
Control-Loop Latency: A Simple Example

To get an idea of why latency poses a practical problem, we consider in this section the control of a first-order linear dynamical system by a simple but commonly used control method known as proportional feedback [38]. In this method, the controller produces a perturbation proportional to the difference between a measurement of the state of the system and a reference value. An anal-

ysis of this system provides a simple demonstration of how control fails due to latency.

Consider the linear differential equation

$$\dot{x} = ax \qquad \text{with} \quad a > 0 \tag{19.1}$$

and suppose it is our goal to stabilize the unstable fixed point x_* of this system, that is to stabilize $x_* = 0$.

Note that a is the exponential growth rate of perturbations and therefore a^{-1} is the natural time scale of the dynamical system. When control is added to the system, it is reasonable to expect that latency will degrade the performance of the controller when it is of the order of or greater than a^{-1}. In this case, the perturbation can grow significantly before the controller can respond. Before demonstrating this formally, let us examine the case of instantaneous feedback.

To apply proportional closed-loop feedback, the system's state is compared to a reference state (the fixed point in this case) and a signal proportional to the difference is fed back to the system affecting its future evolution. When the feedback is instantaneous, the dynamical system in the presence of the controller is described by the differential equation

$$\dot{x} = ax - \gamma(x - x_*) = (a - \gamma)x, \tag{19.2}$$

where γ denotes the strength of the feedback or control gain.

From Eq. (19.2), the effect of the controller is clear. If $\gamma > a$, the perturbation decays and the fixed point is stable. A useful method for visualizing the effect of a controller is to plot the control gain γ versus the parameter a, as is shown in Fig. 19.1(a). The region in this plot where the unstable state is stabilized by the controller is referred to as the domain of control.

The effect of latency on the controller can be quantified by determining how the domain of control changes as latency becomes significant. Suppose the control signal is applied at a time τ_l later than it would be if it were instantaneous. The evolution of the dynamical system is then given by
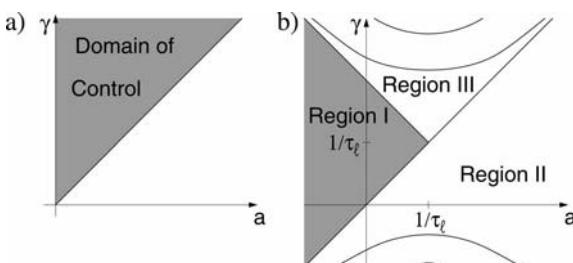

Fig. 19.1 Schematic depiction of the domain of control for the linear system with (a) instantaneous control feedback (Eq. (19.2)) and with (b) latency (Eq. (19.3)).

$$\dot{x}(t) = ax(t) - \gamma\{x(t - \tau_l) - x_*\},$$
$$= ax(t) - \gamma x(t - \tau_l). \tag{19.3}$$

The controller's effect on the stability of the fixed point is determined by examining the evolution of a small perturbation $\delta = x - x_*$ of the form

$$\delta(t) = \delta_0 e^{\lambda t}. \tag{19.4}$$

Substituting Eq. (19.4) into Eq. (19.3) yields the characteristic equation

$$\lambda - a + \gamma e^{-\lambda \tau_l} = 0. \tag{19.5}$$

The left-hand side of Eq. (19.5) is known as the characteristic quasipolynomial and will be denoted by $\Phi(\lambda)$. If the fixed point is stable, that is the perturbation decays, then $\Phi(\lambda)$ must have no roots with positive real parts. The region in the $a\gamma$ parameter space where this condition is satisfied is the domain of control.

Although the roots λ of Eq. (19.5) can be written in closed form in terms of the Lambert W function [39] in this simple example, it is instructive to determine the domain of control by the method of D-partition [40]. In this method, one divides the $a\gamma$ plane into distinct regions separated by curves on which $\Phi(\lambda)$ has at least one root with real part equal to zero. At all points within one such region of the plane, $\Phi(\lambda)$ has the same number of roots with a positive real part. To locate the domain of control, one has to identify the particular region in which that number is zero.

The first boundary is found by setting λ equal to zero to obtain the line

$$a = \gamma. \tag{19.6}$$

To obtain the rest, assume $\lambda = i\gamma$ so that Eq. (19.5) becomes

$$i\gamma - a + \gamma e^{-i\gamma \tau_l} = 0. \tag{19.7}$$

Separating the real and imaginary parts gives the parametric form of the infinite set of curves that make up the remaining boundaries

$$a\tau_l = \frac{\gamma \tau_l}{\sin(\gamma \tau_l)}\cos(\gamma \tau_l), \qquad \gamma \tau_l = \frac{\gamma \tau_l}{\sin(\gamma \tau_l)}. \tag{19.8}$$

One curve defined by these equations meets the line $a = \gamma$ at a cusp point $(a, \gamma) = (1/\tau_l, 1/\tau_l)$ and defines Region I, as is shown schematically in Fig. 19.1 (b). The remaining infinite set of curves have an approximately hyperbolic shape and the curves' location is also indicated in Fig. 19.1 (b).

In the case where $a < 0$ and no control is applied ($\gamma = 0$), the fixed point is stable so that no solutions to Eq. (19.5) have positive real parts. Therefore, for all points in Region I of Fig. 19.1 (b), there are no solutions to Eq. (19.5) with

positive real parts. To determine the number of roots with positive real part in Region II, note that the characteristic equation reduces to the simple form

$$\lambda = a \tag{19.9}$$

along the line $\gamma = 0$, and therefore there is clearly only one root with a positive real part.

To determine the number of roots with positive real part in Region III, consider the sign of the differential of the root of $\Phi(\lambda)$ with zero real part as a boundary is crossed. Specifically, if

$$\Phi(\lambda, a, \gamma) = 0, \tag{19.10}$$

then

$$\frac{\partial \Phi}{\partial \lambda} d\lambda + \frac{\partial \Phi}{\partial a} da + \frac{\partial \Phi}{\partial \gamma} d\gamma = 0. \tag{19.11}$$

The differential of the real part of the root is

$$\text{Re}(d\lambda) = \text{Re} \left(\frac{-\frac{\partial \Phi}{\partial a} da - \frac{\partial \Phi}{\partial \gamma} d\gamma}{\frac{\partial \Phi}{\partial \lambda}} \right). \tag{19.12}$$

Moving from Region II to III across the line $a = \gamma$, assuming $da < 0$, $d\gamma = 0$, and $\gamma > 1/\tau_l$, Eq. (19.12) becomes

$$\text{Re}(d\lambda) = \frac{da}{1 - \gamma\tau_l} > 0. \tag{19.13}$$

The real part receives a positive increment, implying that points in Region III have at least one more root with positive real part than in Region II. A similar analysis of the other boundaries shows that further roots with positive real parts appear as each boundary is crossed on the line $a = 0$ moving away from Region I. Therefore, Region I is the only region with no unstable roots. The domain of control is simply the section of Region I to the right of the line $a = 0$ as shown in Fig. 19.1(b).

In contrast to the latency-free case, no control is possible when $\tau_l > a^{-1}$. Control can only be achieved if the latency is shorter than the characteristic timescale of the system. This result is consistent with the intuitive argument presented above that perturbations to the system may grow too rapidly for the control response to be effective. Figure 19.1(b) also shows that the domain of control is of finite extent even when $\tau_l < a^{-1}$, whereas it extends to arbitrarily large values of feedback gain γ when latency is not present. Thus, large feedback gain tends to enhance the destabilizing effect of latency. Analogous effects of control-loop latency have been found in chaos-control schemes. Some examples are cited in the following section.

19.3
Controlling Fast Systems

Proportional feedback and related approaches have been very successful in controlling chaos in slow systems (characteristic time scale >1 μs), but scaling these schemes to significantly higher frequencies, such as those encountered in high-speed electronic or optical systems, for example, is challenging for several reasons. One important issue in high-speed feedback control of chaotic systems is the latency through the control loop, as we have discussed in Section 19.2. An additional important issue is that it is difficult to accurately determine, store, and regenerate the reference state. The reference state in the example that is discussed in Section 19.2 is the fixed point $x_* = 0$. For the case where the stabilization of an UPO is the control aim, the reference state is the phase space trajectory of the UPO, denoted by $x_*(t)$.

As first suggested by Pyragas [37], the UPOs of a dynamical system can be controlled using continuous feedback that does not require knowledge of $x_*(t)$. In this scheme, which we refer to as "time delay autosynchronization" (TDAS), the control perturbations are designed to synchronize the current state of the system to a time delayed version of itself, with the time delay equal to one period of the desired orbit. Specifically, UPOs of period T_{PO} can be stabilized by continuous adjustment of an accessible parameter by an amount

$$\varepsilon(t) = -\gamma \left[s(t) - s(t - \tau) \right], \tag{19.14}$$

where τ is the delay with $\tau = T_{PO}$, γ is the control gain, and s is the measured signal, that is a function of the system's internal degrees of freedom. Note that $\varepsilon(t)$ vanishes when the system is on the UPO since $s(t) = s(t - \tau)$ for all t. This control scheme has been successfully applied to diverse experimental systems such as electronic circuits [28, 30, 41–43], Taylor-Couette fluid flow [44], an ^{15}NH$_3$ laser [45], a strongly driven magnetic system [46], plasma instabilities [47, 48], and a chemical reaction [49, 50] (see also other chapters of this book). The simplicity of TDAS allows it to be implemented with much less latency than most control schemes. However, some finite latency is always present and, if large enough, can lead to failure as shown below. However, the main drawback to TDAS is that it is not effective at controlling highly unstable orbits.

Socolar et al. [51] introduced a generalization of TDAS, called "extended time delay autosynchronization" (ETDAS), that is capable of extending the domain of effective control significantly [30, 52] and is easy to implement in high-speed systems. Stabilizing UPOs is achieved by feedback of an error signal that is proportional to the difference between the value of a state variable and an infinite series of values of the state variable delayed in time by integral multiples of τ. Specifically, ETDAS prescribes the continuous adjustment of the system parameter by

$$\varepsilon(t) = -\gamma \left[s(t) - (1 - R) \sum_{k=1}^{\infty} R^{k-1} s(t - k\tau) \right], \tag{19.15}$$
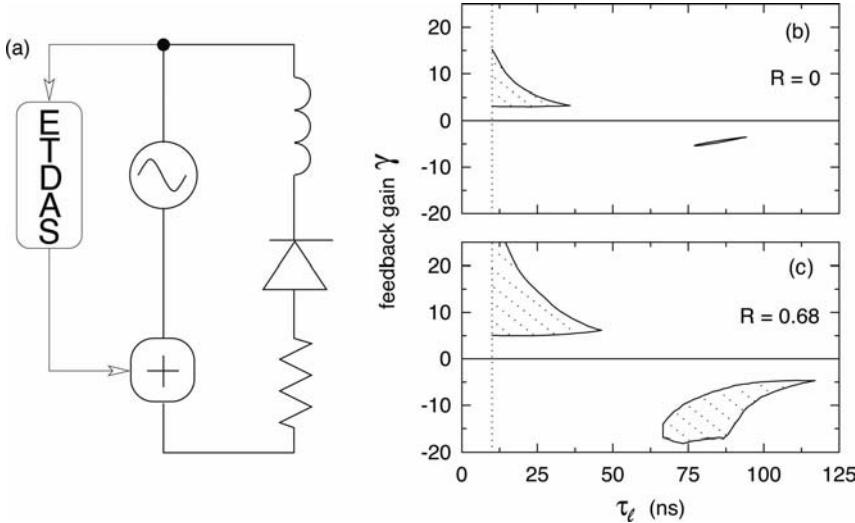
Fig. 19.2 Diode resonator. (a) Schematic of circuit: It consists of a rectifier diode, an inductor and a resistor, which is driven by a leveled sinusoidal voltage (10.1 MHz) that passes through a high-speed signal conditioner where it is combined with the controller signal. (b) Effects of control-loop latency τ_l on the domain of control for the period-1 UPO. Controlled regions are shown for $R = 0$ and $R = 0.68$. The dashed vertical line at $\tau_l = 10$ ns indicates the minimum latency attainable with our implementation of ETDAS.

where $-1 \leq R < 1$ regulates the weight of information from the past. Highly unstable orbits can be stabilized as $R \rightarrow 1$. The case $R = 0$ corresponds to TDAS. We emphasize that, for any R, $\varepsilon(t)$ vanishes when the UPO is stabilized since $s(t - k\tau) = s(t)$ for all t and k, and therefore there is no power dissipated in the feedback loop whenever ETDAS is successful. Note that no property of the UPO must be known in advance except its period. In periodically driven systems, where the period of the orbit is determined from the driving, no features of the UPO need ever be determined explicitly. The control parameters γ and R can be determined empirically in an experiment or by performing a linear stability analysis of the system in the presence of ETDAS feedback control [53, 54].

TDAS and ETDAS are often the control method of choice in high-speed chaotic systems because they are continuous feedback controllers that do not require knowledge of a reference state. Nevertheless, deleterious effects of control-loop latency have also been found in these chaos-control schemes. For example, Sukow et al. [30] investigated the effect of latency on control of a fast chaotic electronic circuit using ETDAS. The electronic circuit was a diode resonator and is shown schematically in Fig. 19.2 (a). In both the cases, the domain of control decreased in size as the latency increases, until control is finally lost.

As can be seen in Fig. 19.2 (b), the maximum latency at which control was attained was as much as four times larger with ETDAS than TDAS, but ETDAS

control failed when the latency reached $\sim 86\%$ of the correlation time of the uncontrolled orbit even in the best case observed. Just et al. [28] developed an approximate prediction for the critical latency at which TDAS control fails. They predict that TDAS control can be achieved when

$$\tau_l < T_{PO} \frac{(1 - \nu T_{PO}/2)}{\nu T_{PO}}, \tag{19.16}$$

where T_{PO} and ν are the period and Floquet exponent (or average growth rate of perturbations) of the UPO to be stabilized, respectively. This prediction was tested in experiments on a nonlinear electronic circuit with Rössler type behavior. Control failed experimentally when the latency reached a value $\sim 11\%$ of the period of the UPO. Equation (19.16) predicted failure at $\sim 12.5\%$ of the period, in reasonable agreement with the experimental results [28].

We have discovered that the effects of control-loop latency can be mitigated when controlling chaotic systems involving a nonlinear element and an inherent time delay T_D, as shown schematically in Fig. 19.3 (a). Chaos can be con-
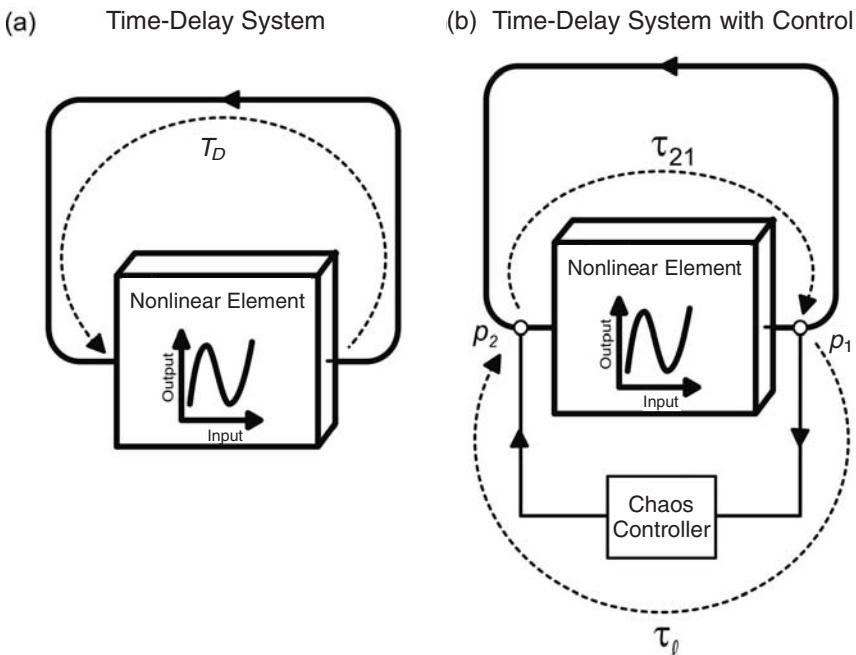
Fig. 19.3 (a) Schematic of a typical topology of a time-delay system consisting of a nonlinear element and a long loop connecting the output to the input of the element, introducing a total time-delay T_D. (b) Schematic of feedback control that measures the state at point p_1 and perturbs the system at p_2. The propagation time through the controller (control-loop latency) is denoted by τ_ℓ and τ_{21} is the propagation time from p_2 to p_1. Note that the signal takes a time $T_D - \tau_{21}$ to get from p_1 to p_2.

trolled in time delay systems by taking advantage of the fact that it is often possible to measure the state of the system at one point in the time delay loop (p_1) and to apply perturbations at a different point (p_2), as shown in Fig. 19.3 (b). Such distributed feedback is effective because the state of the system at p_2 is just equal to its state p_1 delayed by the propagation time $T_D - \tau_{21}$ through the loop between the points. The arrival of the control perturbations at p_2 is timed correctly if

$$\tau_l + \tau_{21} = T_D. \tag{19.17}$$

Hence, it is possible to compensate for a reasonable amount of control-loop latency τ_l by appropriate choice of p_1 and p_2. The advantage of this approach is that the propagation time through the controller does not have to be faster than the controlled dynamics. In contrast, the conventional approach for controlling chaos is to perform the measurement and apply the perturbations instantaneously ($\tau_l \to 0$), which requires controller components that are much faster than the components of the chaotic device to approximate instantaneous feedback. Note that we have not specified a method of computing the control perturbations. In principle, any of the existing methods [18] may be used as long as they can be implemented with latency satisfying Eq. (19.17).

19.4
A Fast Optoelectronic Chaos Generator

To demonstrate the feasibility of controlling fast chaos using this general concept, we apply it to a chaotic optoelectronic device. The device consists of the laser, which acts as a current-controlled source, the interferometer, which constitutes the passive nonlinearity in the system, and the feedback loop with bandpass characteristics. A schematic of the experimental setup is shown in Fig. 19.4, where the labels A–M correspond to components that we refer to and describe below.

The light source is an AlGaInP diode laser (A – Hitachi HL6501MG, wavelength 0.65 μm) with a multiquantum well structure. The diode is housed in a commercial mount (B – Thorlabs TCLDM9) equipped with a bias-T for adding an RF component to the injection current. Thermoelectric coolers in the mount are connected to a proportional-integral-derivative feedback controller (Thorlabs TEC2000) to provide 1 mK temperature stability thereby minimizing frequency and power drift. The output light of the laser is collimated by a lens (D – Thorlabs C230TM-B, $f = 4.5$ mm) producing an elliptical beam (1 mm × 5 mm) with a maximum output power of 35 mW.

The passive nonlinearity in the experiment consists of a Mach-Zehnder interferometer with unequal path lengths (path difference 45 cm) into which the laser beam is directed. A silicon photodetector (E – Hammamatsu S4751, DC-750 MHz bandwidth, 15 V reverse bias) measures the intensity of light emitted
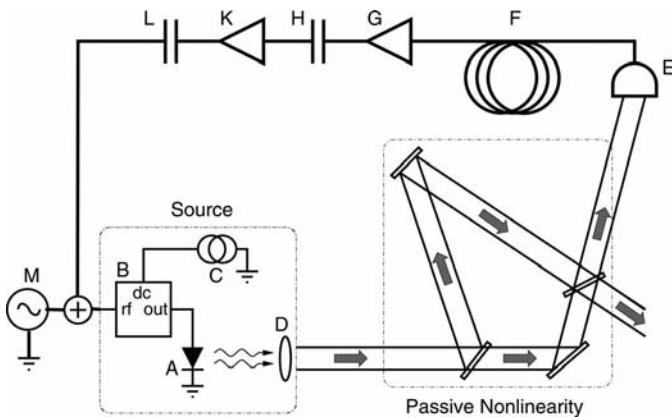
Fig. 19.4 Experimental setup of a chaotic time-delay device of the type shown in Fig. 19.3(a). The device consists of a voltage-controlled source, a passive nonlinearity, and a feedback loop with bandpass characteristics. The components labeled A–M and details of the setup are explained in the text.

from one output port of the interferometer. The size of the photodiode is much smaller than the width of the laser beam so only a fraction of the interferometer's output is detected. The small detector size ensures that only one fringe appears within the beam cross section thus compensating for wavefront aberrations and slight laser beam misalignment and improving the fringe visibility. A neutral density filter is fixed to the front of the laser mount limiting the optical power reaching the photodiode to prevent saturation.

The feedback-loop photodiode produces a current proportional to the optical power falling on its surface. The current flows through a 50-Ω resistor. The voltage across that resistor is transmitted down a coaxial cable (F – RU 58, total length $\sim$ 327 cm). The signal emanating from the cable passes through a low-noise, fixed-gain, AC-coupled amplifier (G – MiniCircuits ZFL-1000LN, bandwidth 0.1–1000 MHz), a DC-blocking chip capacitor (H – 220 pF), an AC-coupled amplifier (K – Mini-Circuits ZFL-1000GH, bandwidth 10–1200 MHz), and a second DC-blocking chip capacitor (L – 470 pF). The capacitors reduce the loop gain at frequencies below $\sim$ 7 MHz, where a thermal effect enhances the laser's sensitivity to frequency modulation [55, 56]. The system is subject to an external driving force provided by adding an RF voltage to the feedback signal (M). (The driven system has more prominent bifurcations than the undriven device.) The resulting voltage is applied to the bias-T (B) in the laser mount. The bias-T converts the signal into a current and adds it to a DC injection current from a commercial laser driver (C – Thorlabs LDC500). The length of the coaxial cable can be adjusted to obtain values of the time delay T_D in the range 11–20 ns.

This optoelectronic device displays a range of periodic, quasiperiodic, and chaotic behavior [57] that is set by the amplifier gain and the ratio of the time
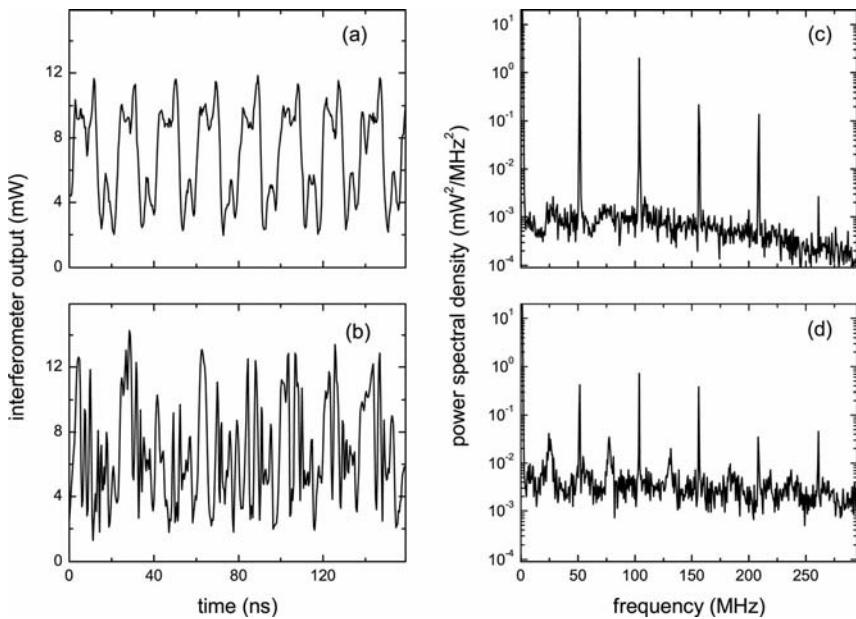
Fig. 19.5 Experimentally measured time series and power spectra of the output power at the second port of the active interferometer with external modulation showing route to chaos as Γ is increased. The loop gain Γ is (a), (c) 2.2 mV/mW and (b), (d) 15.4 mV/mW.

delay to the characteristic response time of the system (typically set to a large value). As an example, we show, in Fig. 19.5, experimental time series and power spectra of the optical power at the second interferometer port with $V_m = 225$ mV and $\Omega_m/2\pi = 51.7$ MHz. With the feedback gain below $\Gamma = 6.7 \pm 0.4$ mV/mW, the system displays a periodic oscillation at the external modulation frequency (to within the 300 kHz resolution bandwidth of the spectrum analyzer) as shown in Fig. 19.5 (a) and (c). As the gain increases, a peak appears in the power spectrum at about half the fundamental frequency. As the gain is increased further, the broad background rises and the tall peaks at the fundamental frequency and its harmonics weaken. The power spectrum for $\Gamma = 15.0 \pm 0.5$ mV/mW, shown in Fig. 19.5 (d), is quite broad and the peaks have nearly dropped to the level of background which has risen significantly above the noise floor. This is indicative of high-dimensional chaos in the system.

A theoretical model for the optoelectronic device is given by [57]

$$\tau_l \dot{V}(t) = -V(t) + \Gamma P(t - T_D)\{1 + b\sin[a(P(t - T_D) - P_0)]\}, \qquad (19.18)$$

$$\dot{P}(t) = -\frac{1}{\tau_h}(P(t) - P_0) + \kappa\left[\dot{V}(t) + \Omega_m V_m \cos(\Omega_m t)\right]. \qquad (19.19)$$

Table 19.1 Definition of symbols and measured values of the model parameters.

Symbol	Value	Description
τ_ℓ	0.66 ± 0.05 ns	Low-pass filter time constant
τ_h	22 ± 0.5 ns	High-pass filter time constant
T_D	19.1 ± 0.1 ns	Device delay-time
κ	$(4.8 \pm 0.1)\ \mu$W/mV	Modulation sensitivity
a	1.89 ± 0.05 mW^{-1}	Interferometer sensitivity
b	0.8 ± 0.02	Fringe visibility
P_0	26 ± 0.5 mW	Operating point optical power
Γ	0–18 mV/mW	Feedback gain
V_m	225 mV	External drive amplitude
Ω_m	3.25×10^8 rad/s	External drive frequency
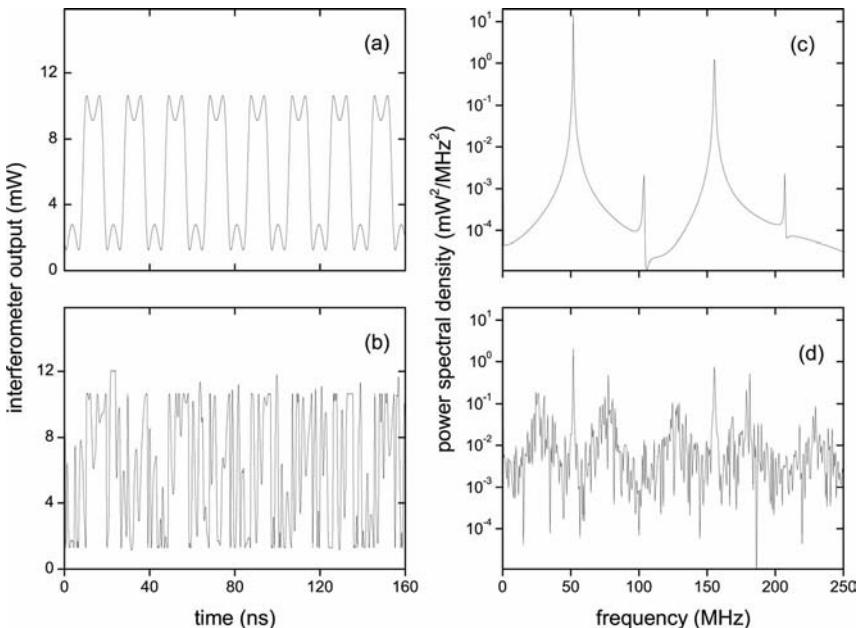
Fig. 19.6 Time series and power spectra from the numerically integrated model of the modulated system showing the route to chaos. The gain Γ is (a, c) 2.2 mV/mW and (b, d) 15.4 mV/mW.

All parameters in this model can be measured and are displayed in Table 19.1.

Using the same gain values as in the experiment, very similar time series and power spectra are produced by the model, as shown in Fig. 19.6. With $\Gamma = 2.2$ mV/mW, as shown in Fig. 19.5 (a), the model displays a period-1 orbit. In Fig. 19.6 (d), where $\Gamma = 15.4$ mV/mW, the power spectrum is considerably

flattened and the system is clearly chaotic. High-dimensional chaos is also confirmed in numeric simulations that determine the Lyapunov spectrum and find positive Lyapunov exponents and attractor Lyapunov dimension $D_L \gg 5$ [57].

19.5
Controlling the Fast Optoelectronic Device

We apply our control method to the optoelectronic device using the setup shown in Fig. 19.7 by measuring the state of the system (denoted by $s(t)$) at point p_1 and injecting continuously a control signal $\varepsilon(t + \tau_l)$ at point p_2. For a given device time delay T_D, coaxial cable can be added or removed from the con-
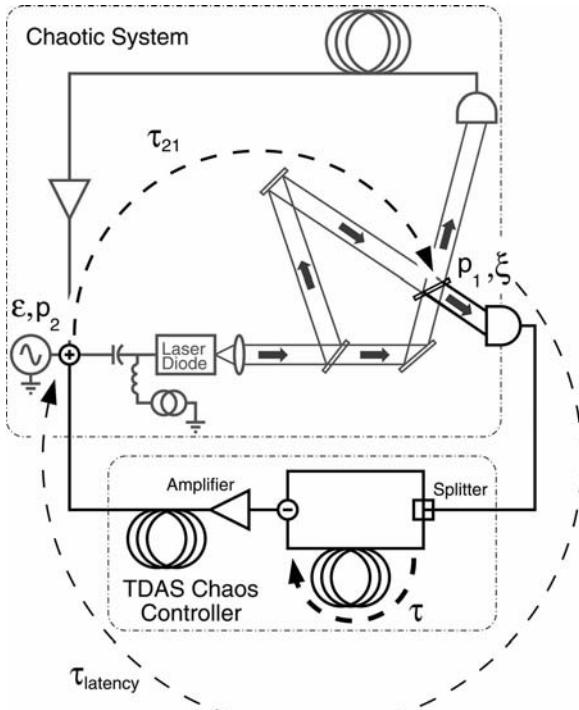
Fig. 19.7 Experimental system with controller. The measurement point p_1 is the second beam splitter of the interferometer. Perturbations are applied at p_2, an RF-power combiner. The time τ_{21} for a signal to propagate from point p_2 to p_1 is ~ 3 ns. The controller contains two delay lines, the first sets τ, the period of the orbit to be controlled, and the second is used to adjust the latency τ_l to properly time the arrival of perturbations at p_2. The state of the system is monitored through a directional coupler positioned directly after the photodiode in the delay loop of the optoelectronic device. The control signal is measured through a directional coupler at the output of the controller.

trol loop to obtain a value of $\tau_l + \tau_{21}$ satisfying Eq. (19.17). To compute the control perturbations ε, we use TDAS, that is the controller synchronizes the system to its state one orbital period in the past by setting $\varepsilon(t) = -\gamma[s(t) - s(t - \tau)]$, where τ is a control-loop delay that is set equal to the period T_{PO} of the desired orbit, and γ is the control gain [37, 42]. When synchronization with the delayed state is successful, the trajectory of the controlled system is precisely on the UPO and the control signal is comparable to the noise level in the system. We emphasize that this modified TDAS control was chosen for ease of implementation in this proof-of-concept experiment but that our approach is consistent with other control methods applicable to delay systems (e.g., [51, 58]).

Controlling the fast optoelectronic device is initiated by setting the various control-loop time delays ($\tau_l + \tau_{21}$ and τ) and applying the output of the TDAS controller to point p_2 with γ set to a low value ($\gamma = 0.1$ mV/mW). Upon increasing γ to 10.3 mV/mW, we observe that $\varepsilon(t)$ decreases, which we further minimize by making fine adjustments to τ and $\tau_l + \tau_{21}$. Successful control is indicated when $\varepsilon(t)$ drops to the noise level of the device. Figure 19.8 (c) shows the periodic temporal evolution of the controlled orbit with a period of $T_{PO} \sim 12$ ns. The corresponding power spectrum, shown in Fig. 19.8 (d), is dominated by a single fundamental frequency of 81 MHz and its harmonics. The observation of successful stabilization of one of the UPOs embedded in the chaos of the uncontrolled optoelectronic device is consistent with the theoretical prediction of a mathematical model describing the optoelectronic device in the presence of control, as shown in Fig. 19.8 (g) and (h), where the simulated time series and power spectrum, respectively, indicate periodic oscillations.

The data shown in Fig. 19.8 are the primary result of this experiment, demonstrating the feasibility of controlling chaos in high-bandwidth systems even when the latency is comparable to the characteristic time scales of the chaotic device (compare $T_{PO} \sim 12$ ns and $\tau_l \sim 8$ ns).

To control this fast UPO, we used the smallest value of $\tau_l + \tau_{21}$ attainable with our current experimental apparatus. Hence, it is not possible to fully explore the effects on control when we change τ_{21}. Therefore, we slowed down the chaotic optoelectronic device by increasing the device delay-time T_D. In this way, we can explore ($\tau_l + \tau_{21}$) over a range including values that are shorter than T_D. Figure 19.9 shows the size of the measured (circles) and predicted (line) control perturbations as a function of $\tau_l + \tau_{21}$. It is seen that control is possible over a reasonably large range of time delays (~ 0.5 ns) centered on T_D so that it is not necessary to set precisely the control-loop delay, a practical benefit of this scheme.

From the data shown in Fig. 19.9, we can infer what would happen if $p_1 = p_2$ (the conventional method of implementing chaos control with nearly instantaneous feedback). In this case, $\tau_{21} = T_D$ and hence control would only be effective when $\tau_l < 0.5$ ns, which is not possible using our implementation of TDAS.

Increasing the feedback gain Γ of the chaotic optoelectronic device increases the complexity of the dynamics, that is the dimension of the chaotic attractor
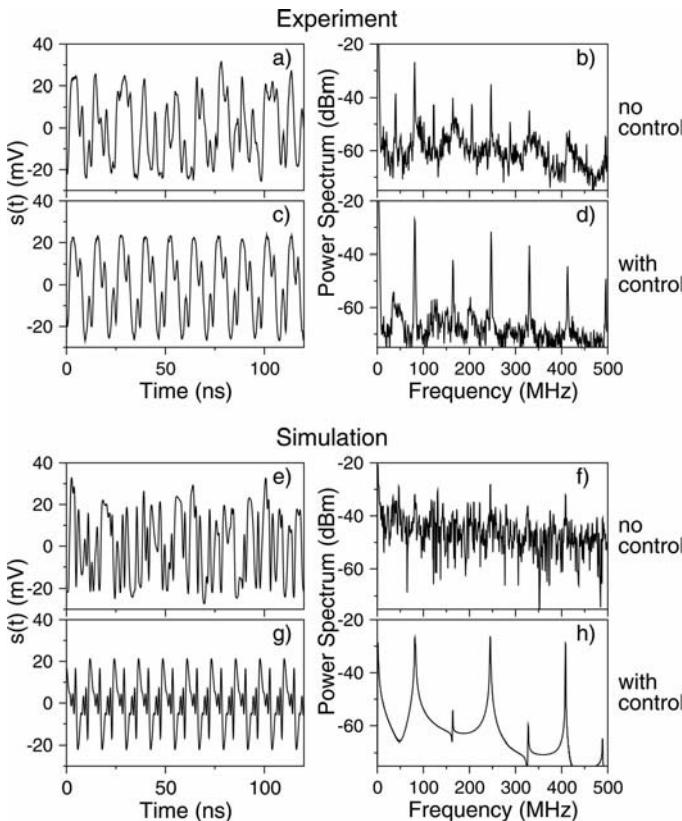
Fig. 19.8 Experimental (a)–(d) and simulated (e)–(h) data showing control of fast chaos. The state of the system is monitored by measuring the voltage in the delay loop before the amplifier (see Fig. 19.7). The device delay-time is $T_D \sim 11$ ns. (a) The chaotic time series of the monitored voltage in the absence of control, (b) the corresponding broad power spectrum, (c) the periodic time series of the stabilized orbit with control on, and (d) the corresponding power spectrum. The effect of control in simulations is consistent with our experimental results, as shown by the simulated time series of the monitor voltage without (e) and with (g) control and the corresponding power spectra (f) and (h).

grows [31, 57]. In Fig. 19.10 we show that the domain of control shrinks as Γ is increased and that control fails for large values of Γ ($\Gamma > 14$ mV/mW). This demonstrates that the modified TDAS control fails to stabilize UPOs when the optoelectronic device operates in a regime of high-dimensional chaos in the absence of control. The domain of control could be increased by using ETDAS. However, experimental implementation of ETDAS is likely to be more challenging than the modified TDAS method because, in many cases, it can require a predistortion stage in the controller [30]. Thus, the modified TDAS method provides a balance of design simplicity and tolerance to latency.
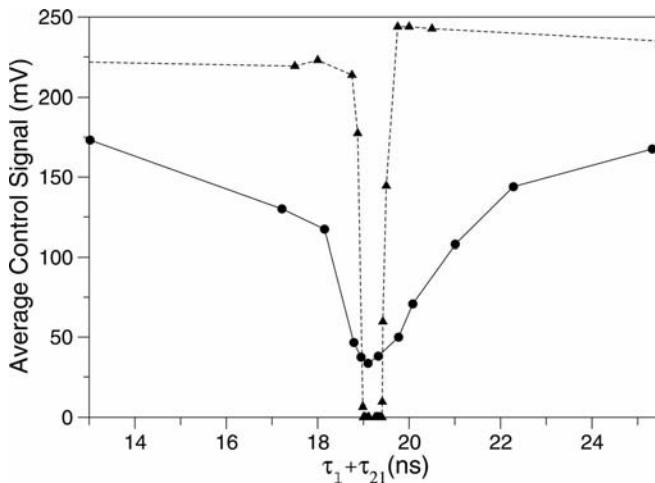
Fig. 19.9 Time-averaged control signal in the experiment (circles) and simulation (triangles). The minimum centered around $T_D = 19.1$ ns is the region of successful control, where $\langle \varepsilon(t) \rangle$ is at the noise level (~ 30 mV, estimated by breaking the control loop and measuring the control signal when the optoelectronic device is in a periodic regime). The width of the minimum (~ 0.5 ns) indicates that control succeeds despite small errors in $\tau_l + \tau_{21}$. Noise in the experiment smooths out the sharp transition from controlled to uncontrolled behavior observed in simulation.
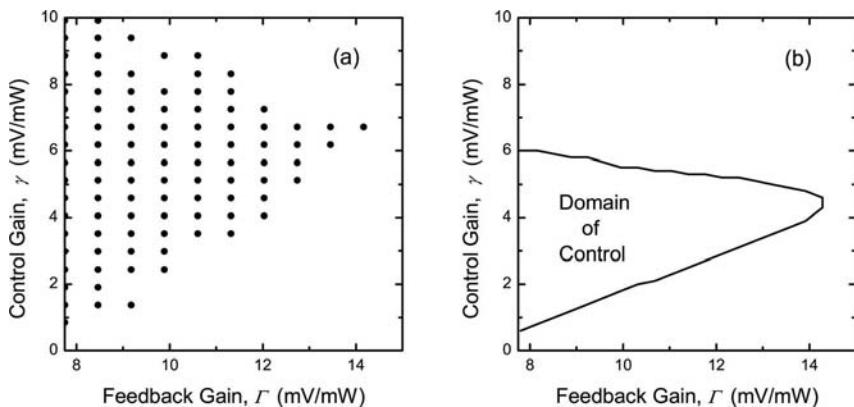
Fig. 19.10 (a) Experimental and (b) theoretical domains of control in the parameter plane spanned by feedback gain Γ of the chaotic optoelectronic device and the control gain γ. The device delay-time was $T_D = 19.1$ ns.

19.6
Outlook

In this chapter, we have demonstrated control of a fast delay dynamical system using a controller with substantial control-loop latency. For comparison, we list in Table 19.2 the period of the stabilized UPO and the estimated controller latency for a few experiments that have been reported in the literature. Note that the modified TDAS controller discussed in this chapter not only controls fast systems, that is, stabilizes the UPO with the shortest period, but the latency of the modified TDAS controller is also nearly equal to the period of the stabilized orbit. This tolerance to latency is in contradistinction to other methods such as limiter control but is shared by ETDAS, which also has demonstrated a similar tolerance to latency.

In principle, faster time delay chaotic systems can be controlled using our approach as long as the controller uses technology (e.g., integrated circuits, all-optical) that is as fast as the system to be controlled so that τ_l is comparable to T_D. Traditional chaos-control schemes require that τ_l be much shorter than T_D, increasing substantially the cost and complexity of the controller. With regard to potential applications, we note that adjustments to our controller allows for controlling different UPOs embedded in the chaotic system, which could be used for symbolic-dynamic-based communication schemes. Overall, our research points out the importance of using time delay dynamical systems combined with distributed control for applications requiring fast controlled chaos.

Finally, our approach of control in the presence of control-loop latency is equally useful for nonchaotic fast and ultrafast time delay devices, where the fast time scale makes the suppression of undesired instabilities challenging (e.g., the double-pulsing instability in femtosecond fiber lasers [60]).

Table 19.2 Period of some experimentally stabilized UPOs and latency of the controller. The modified TDAS method described in this chapter is used to stabilize the UPO with the highest frequency reported to date. Note that with this method the latency need not be small compared to the period of the orbit.

Chaos control method	Orbit period, T_{PO}	Control-loop latency, τ_l
TDAS [30, 51]	99 ns	< 30 ns
ETDAS [30, 51]	99 ns	< 120 ns
Pulsewidth modulation [35]	52 ns	4.4 ns
Limiter control [36]	23 ns	$\lesssim$ 1 ns [a]
Modified TDAS [59]	12 ns	8 ns

a   N. Corron, private communication.

Acknowledgement

References

1 V. Dronov, M. Hendrey, T. Antonsen, and E. Ott, Chaos **14**, 30 (2004).

2 J. Gleeson, Appl. Phys. Lett. **81**, 1949 (2002).

3 T. Stojanovski, J. Pihl, and L. Kocarev, IEEE Trans. Circuits Syst. I, Fundam. Theory Appl. **48**, 382 (2001).

4 F. Y. Lin and J. M. Liu, IEEE J. Quantum Electron. **40**, 1732 (2004).

5 B. C. Flores, E. A. Solis, and G. Thomas, IEE Proc.-Radar Sonar Navig. **150**, 313 (2003).

6 V. Venkatasubramanian and H. Leung, IEEE Signal Processing Lett. **12**, 528 (2005).

7 K. Myneni, T. A. Barr, B. R. Reed, S. D. Pethel, and N. J. Corron, Appl. Phys. Lett. **78**, 1496 (2001).

8 T. Carroll, Chaos **15**, 013109 (2005).

9 M. Kennedy, G. Kolumban, G. Kis, and Z. Jako, IEEE Trans. Circuits Syst. I, Fundam. Theory Appl. **47**, 1702 (2000).

10 N. F. Rulkov, M. M. Sushchik, L. S. Tsimring, and A. R. Volkovskii, IEEE Trans. Circuits Syst. I, Fundam. Theory Appl. **48**, 1436 (2001).

11 G. M. Maggio, N. Rulkov, and L. Reggiani, IEEE Trans. Circuits Syst. I, Fundam. Theory Appl. **48**, 1424 (2001).

12 G. VanWiggeren and R. Roy, Science **279**, 1198 (1998).

13 A. Argyris, D. Syvridis, L. Larger, V. Annovazzi-Lodi, P. Colet, I. Fischer, J. García-Ojalvo, C. R. Mirasso, L. Pesquera, and K. A. Shore, Nature **437**, 343 (2005).

14 H. D. I. Abarbanel, M. B. Kennel, L. Illing, S. Tang, H. F. Chen, and J. M. Liu, IEEE J. Quantum Electron. **37**, 1301 (2001).

15 S. Hayes, C. Grebogi, and E. Ott, Phys. Rev. Lett. **70**, 3031 (1993).

16 H. D. I. Abarbanel and P. S. Lindsay, IEEE Trans. Circuits Syst. II **40**, 643 (1993).

17 E. Ott, C. Grebogi, and J. A. Yorke, Phys. Rev. Lett. **64**, 1196 (1990).

18 D. J. Gauthier, Am. J. Phys. **71**, 750 (2003).

19 L. Illing, D. J. Gauthier, and R. Roy, *Controlling Optical Chaos, Spatio-Temporal Dynamics, and Patterns* (Academic Press, New York, 2006), vol. 54 of *Advances In Atomic, Molecular, and Optical Physics*.

20 A. Chang, J. Bienfang, G. Hall, J. Gardner, and D. Gauthier, Chaos **8**, 782 (1998).

21 D. Gauthier, Opt. Lett. **23**, 703 (1998).

22 A. Ahlborn and U. Parlitz, Phys. Rev. Lett. **93**, 264101 (2004).

23 S. Yanchuk, M. Wolfrum, P. Hövel, and E. Schöll, Phys. Rev. E **74**, 026201 (2006).

24 R. Roy, T. W. Murphy Jr., T. D. Maier, Z. Gills, and E. R. Hunt, Phys. Rev. Lett. **68**, 1259 (1992).

25 E. R. Hunt, Phys. Rev. Lett. **67**, 1953 (1991).

26 V. Petrov, V. Gaspar, J. Masere, and K. Showalter, Nature **361**, 240 (1993).

27 A. Garfinkel, M. L. Spano, W. L. Ditto, and J. N. Weiss, Science **257**, 1230 (1992).

28 W. Just, D. Reckwerth, E. Reibold, and H. Benner, Phys. Rev. E **59**, 2826 (1999).

29 P. Hövel and J. Socolar, Phys. Rev. E **68**, 36206 (2003).

30 D. W. Sukow, M. E. Bleich, D. J. Gauthier, and J. E. S. Socolar, Chaos **7**, 560 (1997).

31 J. Farmer, Physica D **4D**, 366 (1982).

32 G. Mykolaitis, A. Tamasevicius, A. Cenys, S. Bumeliene, A. N. Anagnostopoulos, and N. Kalkan, Chaos, Solitons Fractals **17**, 343 (2003).

33 J. P. Goedgebuer, L. Larger, and H. Porte, Phys. Rev. Lett. **80**, 2249 (1998).

34 K. Ikeda, K. Kondo, and O. Akimoto, Phys. Rev. Lett. **49**, 1467 (1982).

35 K. Myneni, T. A. Barr, N. J. Corron, and S. D. Pethel, Phys. Rev. Lett. **83**, 2175 (1999).

36 N. Corron, B. Hopper, and S. Pethel, Int. J. Bifurcation and Chaos **13**, 957 (2003).

37 K. Pyragas, Phys. Lett. A **170**, 421 (1992).

38 K. Ogata, *Modern Control Engineering, 2nd edition* (Prentice-Hall, Englewood Cliffs, NJ, 1990).

39 R. M. Corless, G. H. Gonnet, D. E. G. Hare, D. J. Jeffry, and D. E. Knuth, Adv. Comput. Math. **5**, 329 (1996).

40 L. E. El'sgol'ts and S. B. Norkin, *Introduction to the Theory and Application of Differential Equations with Deviating Arguments* (Academic Press, New York, 1973).

41 K. Pyragas and A. Tamasevicius, Phys. Lett. A **180**, 99 (1993).

42 D. Gauthier, D. Sukow, H. Concannon, and J. Socolar, Phys. Rev. E **50**, 2343 (1994).

43 C. von Loewenich, H. Benner, and W. Just, Phys. Rev. Lett. **93**, 174101 (2004).

44 O. Lüthje, S. Wolff, and G. Pfister, Phys. Rev. Lett. **86**, 1745 (2001).

45 R. Dykstra, D. Y. Tang, and N. R. Heckenberg, Phys. Rev. E **57**, 6596 (1998).

46 H. Benner and W. Just, J. Kor. Phys. Soc. **40**, 1046 (2002).

47 T. Pierre, G. Bonhomme, and A. Atipo, Phys. Rev. Lett. **76**, 2290 (1996).

48 E. Gravier, X. Caron, G. Bonhomme, and T. Pierre, Phys. Plasmas **6**, 1670 (1999).

49 C. Beta, M. Bertram, A. S. Mikhailov, H. H. Rotermund, and G. Ertl, Phys. Rev. E **67**, 046224 (2003).

50 I. Z. Kiss, Z. Kazsu, and V. Gaspar, Chaos **16**, 033109 (2006).

51 J. Socolar, D. Sukow, and D. Gauthier, Phys. Rev. E **50**, 3245 (1994).

52 K. Pyragas, Phys. Lett. A **206**, 323 (1995).

53 M. E. Bleich and J. E. S. Socolar, Phys. Lett. A **210**, 87 (1996).

54 W. Just, T. Bernard, M. Ostheimer, E. Reibold, and H. Benner, Phys. Rev. Lett. **78**, 203 (1997).

55 S. Kobayashi, Y. Yamamoto, M. Ito, and T. Kimura, IEEE J. Quantum Electron. **18**, 582 (1982).

56 C.-Y. Tsai, C.-H. Chen, T.-L. Sung, C.-Y. Tsai, and J. M. Rorison, Appl. Phys. Lett. **74**, 917 (1999).

57 J. N. Blakely, L. Illing, and D. J. Gauthier, IEEE J. Quantum Electron. **40**, 299 (2004a).

58 W. Michiels, K. Engelborghs, P. Vansevenant, and D. Roose, Automatica **38**, 747 (2002).

59 J. N. Blakely, L. Illing, and D. J. Gauthier, Phys. Rev. Lett. **92**, 193901 (2004b).

60 F. O. Ilday, J. Buckley, H. Lim, F. Wise, and W. Clark, Opt. Lett. **28**, 1365 (2003).

20
Control of Broad-Area Laser Dynamics
with Delayed Optical Feedback

Nicoleta Gaciu, Edeltraud Gehrig, and Ortwin Hess

The light emitted by a broad-area semiconductor laser is spectacularly bright but at the same time generally displays vivid spatiotemporal and even chaotic dynamics. This very "un-laser-like" feature is a footprint of the complex interplay of ultrafast carrier and light-field dynamics within the laser leading to spatiospectral hole burning, light diffraction and self-focusing. From the viewpoint of application, the stabilization and control of the chaotic dynamics of semiconductor lasers clearly is most important. However, this task is here particularly challenging since the large cavity width needed for achieving the high output signal leads to a complex spatiospectral mode dynamics. One thus has to find ways to control a continuum of spatial, temporal, and even spectrally dependent processes.

This chapter presents modeling results of the complex spatiotemporal and spatiospectral dynamics of large-area lasers controlled by delayed optical feedback. Our theory is based on a Maxwell-Bloch approach taking into account the transverse and longitudinal dependence of the light fields and the charge carriers. Results of the spatially and temporally resolved simulations open a way to an identification of parameter regimes – such as length of the delay line and feedback strength – where an optimum control can be achieved and show the importance of a fundamental analysis for the understanding of the physical processes within the laser structure. This may pave the way for the development and design of novel control schemes for semiconductor lasers with optimized spatial and spectral emission characteristics.

20.1
Introduction: Spatiotemporally Chaotic Semiconductor Lasers

Due to their high output power, broad-area semiconductor lasers (BALs) are widely used in different applications such as environmental sensing, telecommunications and printing technologies. This generation of (for semiconductor lasers) exceptionally high output powers of up to several Watts is achieved by in-

creasing the laser stripe width of typically a few microns up to a few hundred microns (50 µm to 500 µm [1]). However, the large transverse stripe width also leads to the coexistence and interplay of a multitude of longitudinal and transverse modes. This complex mode dynamics and the interplay of spatial with temporal degrees of freedom are responsible for the formation of dynamic filamentation and chaotic spatiotemporal dynamics on nano- and picosecond time scales [2–4]. These processes affect the spectral and spatial coherence and finally limit the laser performance.

The destabilizing mechanism in BALs is, in particular, closely related to the nonlinear dynamics and interplay of multiple transverse modes. For practical reasons, it is thus desired to stabilize the emission dynamics by reducing the number of excited transverse modes. Several concepts have been proposed and applied aiming to control and stabilize the spatiotemporal instabilities. In optics and laser science a common route of applying control is based on external feedback components such as conventional mirrors. Configurations with so-called delayed optical feedback use the light fields emitted by the laser itself to stabilize the dynamics (after the roundtrip in an external resonator). An early attempt to control complex semiconductor laser dynamics based on this principle is described in [5] for a diode laser array.

If we consider BALs with delayed optical feedback (BALDOFs), the action of the external cavity may be characterized by two parameters: the reflectivity of the external mirror and the external round-trip time. If we recall the complexity of the spatiotemporal dynamics of broad-area lasers it is not surprising that in various experiments [6–8] and numerical studies [4, 9, 10] the application of delayed optical feedback was shown to lead to both, controlled dynamics or instabilities depending on the particular value of the reflectivity of the external mirror or on its distance from the laser. While this demonstrated a strong dependence of the overall behavior on these parameters few systematic tendencies emerged. It has become clear that the key to achieving a successful and, in particular, robust control is to explore the nature of the underlying physical processes and including them in schemes that may allow us to set up suitable control scenarios.

Although having been studied for some time, semiconductor lasers with delayed optical feedback have recently generated considerable renewed interest [8, 11–17]. In the short-cavity regime (i.e., external cavities with a few cm length) the formation of regular pulse packaging forming a low-frequency state combined with fast regular intensity pulsations has been found [18]. This could be explained by the characteristic dynamics of the system around the steady state solution in the phase space. Theoretical studies [19] have discussed the role of low-frequency fluctuations (LFFs) in semiconductor lasers and the influence of coexisting modes has been highlighted in [20]. Experiments have shown [21–23] that the multimode dynamics is of particular importance in the regime where LFFs occur (i.e., dropouts arising at injection currents close to threshold and moderate feedback levels). It was demonstrated that in the LFF regime an excitation of longitudinal side modes can occur near power dropouts for both fre-

quency-selective [24] and non-selective optical feedback [21, 23]. Further computational studies [7, 25] have shown that external optical frequency filters may allow the control over several dynamical attractors and to stabilize the modes [26]. Recent works also explore the influence of electrooptical feedback on the dynamics of semiconductor lasers [27, 28].

With improvements in semiconductor material technology and the growing sophistication of the laser devices themselves the derivation of suitable theoretical models that realistically take into account the respective material properties and cavity design is thus still an issue of high importance.

The time-honored theoretical basis for the study of delay-induced temporal instabilities in semiconductor lasers are the Lang-Kobayashi rate equations [29], disregarding any direct influence of spatial effects. More recent extensions that explicitly take into account the spatiotemporal nature of the light-field and charge carrier dynamics are based on the Maxwell-Bloch approach [4, 30–32].

In the following we discuss the application of delayed optical feedback in various modifications to achieve suppression of spatiotemporal instabilities in BALs. Our comprehensive modeling approach for large-area semiconductor lasers (such as laser arrays or broad-area lasers) is based on an extended system of Maxwell-Bloch equations [4, 30–32]. This framework allows us to study the influence of delayed optical feedback on the spatiotemporal dynamics of large-area semiconductor lasers and eventually enables us to demonstrate the successful stabilization of coherent single-mode emission.

The next section (20.2) gives a summary of the Maxwell-Bloch theory. We will discuss the model equations that combine a multimode and transversely resolved description of the dynamic optical fields with delayed optical feedback with a spatially and temporally resolved model of the active medium. This will allow us to visualize the mode spectrum of the free-running laser (Section 20.3) and monitor the complex spatiotemporal dynamics (Section 20.4). Section 20.5 presents modeling results on delayed optical feedback configurations highlighting regimes where a suppression of higher order transverse modes can be obtained. A particular focus lies in the influence of external cavity length and external mirror reflectivity on spatiotemporal dynamics and emission properties of BALDOFs. Section 20.6 concludes this chapter.

20.2
Theory: Two-Level Maxwell-Bloch Equations

The structure of a typical broad-area laser is illustrated in Fig. 20.1. The pump current is injected via a contact stripe. The current density is $J(x)$ above the active stripe and zero in the regions surrounding the active region. The injected carriers pass the cladding layers and lead to stimulated emission, spontaneous emission, and nonradiative recombination processes. Our theoretical description is based on a spatially resolved Maxwell-Bloch approach [4] and describes the

spatiotemporal light field and carrier dynamics in spatially extended semiconductor lasers. Here we use an effective two-level multimode Maxwell-Bloch approach. The system of coupled nonlinear and stiff partial differential equations consists of spatiotemporally resolved wave equations for the counter-propagating light fields (including the full longitudinal mode dynamics) and two-level Bloch equations for the dynamics of the charge carriers and dipoles. The theory includes, in particular, (multimode) counter-propagating light waves, light diffraction, polarization dynamics, dynamic self-focusing, carrier diffusion, and scattering.

To model the laser dynamics the equations of motion are integrated by fully resolving the lateral (i.e., over the whole width of the laser) and longitudinal (i.e., propagation) direction thereby taking into account the spatially and temporally varying light-matter coupling. The dynamic spatiotemporal interplay of longitudinal modes that typically affects the emission dynamics of broad-area lasers is included via a multimode expansion of the fields. These spatially dependent multimode wave equations for the dynamics of the light fields propagating in the forward ('+') and backward ('−') direction thus read

$$\frac{\partial}{\partial t}E^{\pm} + \frac{\partial}{\partial z}E^{\pm} = iD_p \frac{\partial^2}{\partial x^2}E^{\pm} - i\eta E^{\pm} + \frac{ik_0}{2\varepsilon_0 n_l}\Gamma P_{(0)}^{\pm}. \tag{20.1}$$

The diffraction coefficient is $D_p = (2n_l k_0)^{-1}$ with the vacuum wavenumber $k_0 = 2\pi/\lambda$. The waveguiding properties derived from effective index approximation are included in the parameter η, Γ is the confinement factor. Via the polarization the light fields are locally coupled to carriers within the active medium. Its materials' properties are represented in terms of the following Bloch equations for the spatiotemporally varying carrier density and the polarization:

$$\frac{\partial}{\partial t}P_{(0)}^{\pm} = -\gamma_p \left[\left(1 + i\frac{\bar{\omega}}{\gamma_p}\right) + (\rho + i\sigma)N\right]P_{(0)}^{\pm}$$
$$+ \beta\left((N_{(0)} + ia)E^{\pm} + N_{(1)}E^{\mp}\right)$$
$$\frac{\partial}{\partial t}P_{(1)}^{\pm} = -\gamma_p \left[\left(1 + i\frac{\bar{\omega}}{\gamma_p}\right) + (\rho + i\sigma)N\right]P_{(1)}^{\pm} + \beta N_{(1)}E^{\pm}$$
$$\frac{\partial}{\partial t}N_{(0)} = \Lambda + D_f \nabla^2 N_{(0)} - \gamma_{nr}N_{(0)}$$
$$- 2\left(E^{+}\left(P_{(0)}^{+} - \Lambda_0 E^{+}\right)^{*} + E^{-}\left(P_{(0)}^{-} - \Lambda_0 E^{-}\right)^{*} + c.c.\right)$$
$$\frac{\partial}{\partial t}N_{(1)} = -4D_f k_z^2 N_{(1)} - \gamma_{nr}N_{(1)}$$
$$- 2\left(E^{+}\left(P_{(0)}^{-} - \Lambda_0 E^{-}\right)^{*} + E^{-*}\left(P_{(0)}^{+} - \Lambda_0 E^{+}\right)\right.$$
$$\left. + E^{+*}P_{(1)}^{+} + E^{-}P_{(1)}^{-*}\right). \tag{20.2}$$
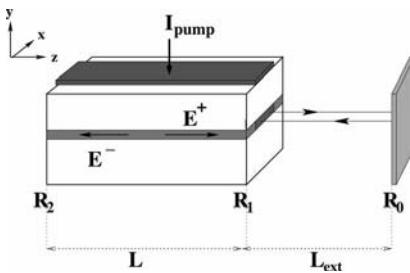
Fig. 20.1 Schematic figure of a broad-area semiconductor laser with delayed optical feedback.

Table 20.1 Parameters of the broad area semiconductor laser used in the numerical simulations

L (cavity length)	1000 μm
w (stripe width)	100 μm
d (thickness of active layer)	0.15 μm
n_c (refractive index of the cladding layers)	3.35
n_a (refractive index of the active layer)	3.59
λ (laser wavelength)	807 nm
R_2 (front facet mirror reflectivity)	0.05
R_1 (back facet mirror reflectivity)	0.95
R_0 (external mirror reflectivity)	From 0.01 to 0.30
I_{pump} (injection current)	From 300 mA to 1050 mA
I_{th} (threshold current)	295 mA
τ_{in} (internal round-trip time)	24 ps
τ_{ext} (external round-trip time)	From 0.6 ps to 666 ps

In Eqs. (20.1) and (20.2) the quantities $P_{(0)}^{\pm}$, $P_{(1)}^{\pm}$, $N_{(0)}$ and $N_{(1)}$ are the (lowest and first order) coefficients of the mode expansion. Λ describes carrier injection via the contact stripe, D_f is the carrier diffusion constant and k_z denotes the wave number of the propagating light fields. $\bar{\omega}$ is the frequency detuning between the frequency of the electron–hole pair and the light frequency. γ_{nr} describes the rate of nonradiative recombination and γ_p is the dephasing of the dipole. The dimensionless constant β determines the maximum gain. The material parameters ρ and σ consider the increase in the polarization decay rate and the drift of the gain maximum with increasing carrier density, respectively. The α-factor describes the amplitude phase coupling. The parameter Λ_0 guarantees a vanishing gain at transparency.

These multimode Maxwell-Bloch equations will in the following be the basis for our studies of the spatiotemporal dynamics of broad-area lasers with coherent external injection in external cavity configuration with the aim of a control and/or stabilization of the spatiotemporal dynamics. We focus on a specific but representative model system of a BAL with a GaAs active layer sandwiched between cladding layers of $Al_xGa_{1-x}As$. The devices have a cavity length of 1–2 mm and a stripe width of 100 μm. The material parameters used in the simulations are summarized in Table 20.1.

20.3
Dynamics of the Solitary Laser

In the first step, we will analyze the solitary BAL (i.e., without feedback or injection). In this context, it is particularly instructive to discuss optical spectra that have been calculated from the time-dependent light-field dynamics (as obtained from the multimode Maxwell-Bloch equation) using a Fourier analysis. Figure 20.2 shows the optical spectra of a free-running broad-area laser for three different values of the injection current. The horizontal axis depicts the frequency and the vertical axis the position on the laser facet.

The multimode structure of a free-running BAL is a direct consequence of the large stripe width and lack of a lateral confinement of the diffusing charge carriers. The nonlinear interaction of the optical fields and the semiconductor active medium thereby leads to an additional complexity and determines the number and intensity of the various modes. Each mode group is associated with a particular longitudinal mode of the laser. The longitudinal modes are separated by $\Delta\lambda = 0.09$ nm ($\Delta\omega = 41.78$ GHz). Within each longitudinal mode "family" higher order transverse modes can be easily identified by their shorter wavelength and their multilobed spatial intensity distribution. The number of supported transverse modes is given by the Fresnel number $F = w^2/\lambda L$, where w is the stripe width, λ is the wavelength of transmitted light, and L is the cavity length. In the given example, the calculated maximum number of transverse modes is 12. The dependence of the number of longitudinal and transverse modes on current is further visualized in Fig. 20.3. When the injection current reaches a value of about two times the threshold current, the number of transverse modes doubles (compared to the number at threshold) within each group of longitudinal modes. A further increase in injection current leads to a further and fast increase in the number of transverse modes. This effect originates from the increased importance of carrier dynamics: with increasing current the nonlinear spatial and spectral dynamics leads to an increased rise in the gain. Moreover, the carrier-induced refractive index induces dynamic filamentation in the gain medium which is a principal cause of multimode dynamics. In the
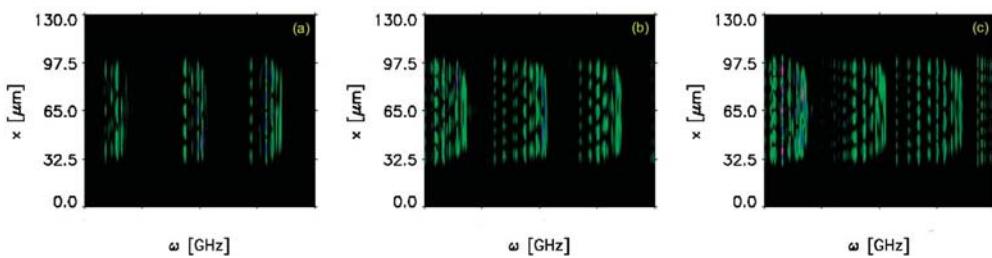
Fig. 20.2 Optical spectra of a solitary BAL in dependence on injection currents: (a) $I_{pump} = 1.2\,I_{th}$, (b) $I_{pump} = 2\,I_{th}$, (c) $I_{pump} = 2.8\,I_{th}$.
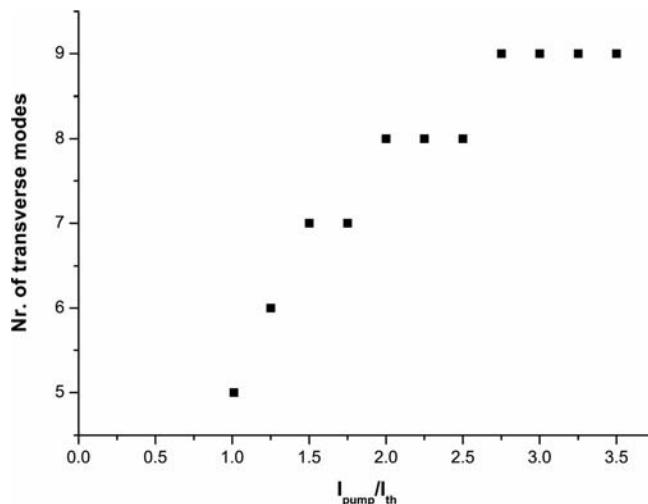
Fig. 20.3 The number of transverse modes of a free-running BAL as a function of injection current.

next section, we will discuss the control in the mode dynamics via a coherent external light field.

20.4
Detection of Spatiotemporal Complexity

In order to reveal the ultrafast emission dynamics of a large-area laser we will in the following simulate the injection of a coherent light field into the active area. This allows us to investigate the spatiotemporal light-field and carrier dynamics within the active area of the laser. Thereby, we will concentrate on the following situations:

- A *continuous wave* optical injection reveals a significant reduction of the number of coexisting transverse modes of the free-running laser. Thereby, the selection and stabilization of individual transverse modes can be controlled by the amplitude and the lateral profile of the injected light field.
- The injection of a single optical *pulse* demonstrates the possibility of an efficient coupling and synchronization of the longitudinal modes of the laser leading to the emission of short regular pulse sequences [33].

20.4.1
Reduction of the Number of Modes by Coherent Injection

In order to investigate the fundamental interaction processes within the active area of a BAL we can detect parts of the laser-internal dynamics by injecting a coherent light beam of an external laser into the resonator of the BAL. The output
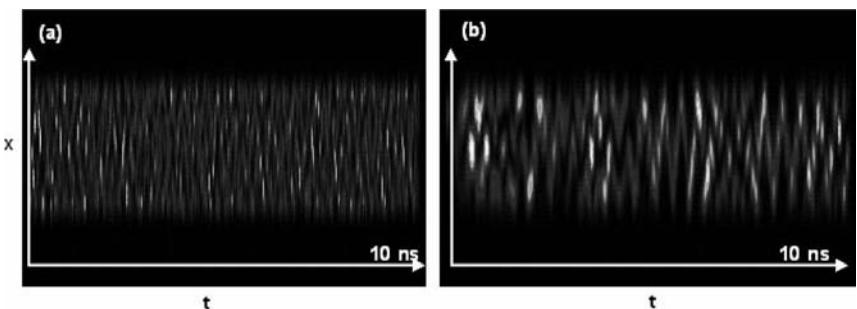
Fig. 20.4 Near-field dynamics of (a) the free-running and of (b) the optically injected large-area laser.

signal emitted by the BAL then visualizes the response to such an additional coherent optical injection (next to the normal electrical pumping). In the first example we monitor the near-field dynamics with and without (optical) injection of a continuous single-mode light beam on the basis of the multimode Maxwell-Bloch equations. The results are summarized in Fig. 20.4 for a time window of 10 ns. Without injection (Fig. 20.4 (a)) the nonlinear interaction between diffraction and propagation on the one hand and carrier diffusion and scattering on the other hand lead to a complex dynamics of the light fields. The light-field dynamics shows the influence of both, the ultrafast spatiotemporal dynamics (corresponding to the longitudinal mode dynamics) and the slow transverse dynamics (corresponding to the transverse modes). The injection of a coherent resonant light beam (Fig. 20.4 (b)) can – depending on the power and spatial profile of the injected light field – lead to the excitation and selection of a specific transverse mode. As an example, Fig. 20.4 (b) shows the near-field dynamics of a BAL (width 100 μm, length 2 mm) into which we have injected a Gaussian light beam (full width at half maximum 15 μm). Clearly, one can see a regular, slow transverse dynamics. The fast dynamics originating from the existence and interplay of longitudinal modes, on the other hand, is clearly reduced (Fig. 20.4 (b)).

The selection of a transverse mode can be further studied on the basis of the spatially resolved emission spectra (Fig. 20.5). The spectra have been calculated from the light fields at the output facet. They show that the injection of an external laser leads to a reduction of the number of coexisting modes. The efficiency of the mode-selection process as well as the order of the chosen mode thereby strongly depends on the injection current and properties of the input beam (power, beam waist, angle of incidence). In the given example, the input power was in the order of magnitude of the free-running laser and the beam waist has been varied in the regime 10–50 μm. In the next example, Fig. 20.6 shows the near-field dynamics of a large-area laser for a width of the injected field of (a) 20 μm and (b) 10 μm, respectively. The model results clearly reveal that a reduction of the beam waist lead to the selection of another mode (in the example: a mode of higher order).
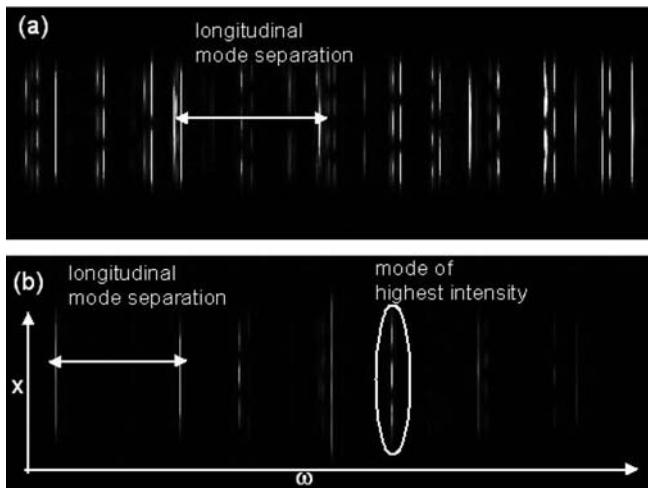
Fig. 20.5 Spatially resolved emission spectrum at the output facet (x) of a large-area laser without (a) and with (b) continuous light injection.
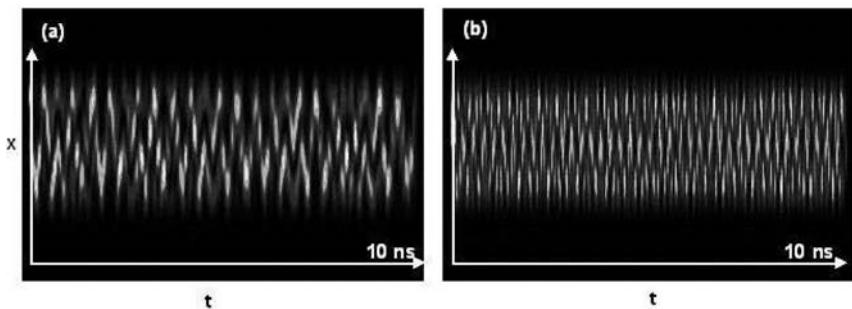

Fig. 20.6 Near-field dynamics of the optically injected BAL for a beam waist of (a) 20 μm and (b) 10 μm.

20.4.2
Pulse-Induced Mode Synchronization

In the final step (considering external optical injection) we investigate the possibility to monitor the ultrashort emission dynamic with an injected light pulse. As we have seen, the emission of a free-running large-area laser is typically characterized by transverse filaments and the formation of fast intensity pulsation as consequence of light fields counter propagating in the laser-active media thereby interacting with the spatially inhomogeneous active laser medium. To enhance and to detect the formation of this intensity pulsation, we now inject an optical ps-pulse into the (running) laser and investigate its propagation and
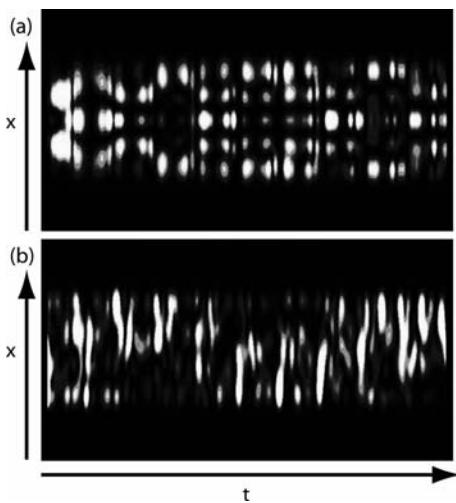
Fig. 20.7 Emission dynamics of a large-area laser triggered by a light pulse. The horizontal axis shows time and the vertical axis the lateral position on the laser facet. Displayed is the dynamics in a time window of 1000 ps, starting at (a) 200 ps and (b) 3200 ps after pulse injection.

its impact on the emission. The peak power of the injected pulse is slightly larger than the power emitted by the free-running laser. The results are summarized in Fig. 20.7. The figure shows the near-field dynamics of the optically injected large-area laser for two time windows of 1000 ps, starting (a) 200 ps and (b) 3200 ps after the optical injection, respectively. In the simulations the injection of the light pulse (without chirp, pulse duration 50 ps) has been realized via the boundary conditions of the light fields in the wave equation.

The plots reveal the buildup and decay of a coherent enhancement and stabilization of dynamic longitudinal mode coupling: in the first time-trace (Fig. 20.7 (a)), 200 ps after the injection, the injected light pulse starts its dynamic interaction with the laser-internal light field. After a few round-trips in the active area the pulse has established a synchronization of the complex transverse light-field dynamics of the free-running laser leading to the formation of regular pulses with a homogeneous lateral light field distribution that extends over the whole width of the laser. After the pulse injection the emission of the BAL thus changes into an almost completely pulsed output synchronized across the laser stripe resulting in high output peaks that can be seen in the figure. The periodicity of the emitted light pulses thereby corresponds to the round-trip time in the large-area laser. The periodic intensity modulations that can be seen in the free-running laser (see Fig. 20.4 (a)) thus are triggered by the propagating light pulse leading to a dynamic mode-locking of the longitudinal modes.

In the second time window, starting 3200 ps after the injection of the light pulse, the transverse light pattern has changed significantly. A complex trans-
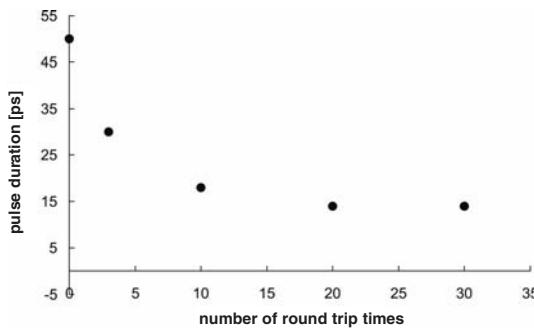
Fig. 20.8 Evolution of the pulse duration as function of the number of cavity roundtrips. The value of 13 ps is the finally stable pulse duration which persists for several nanoseconds.

verse light-field dynamics arises leading to asymmetric intensity patterns. This behavior originates from the dynamic wave mixing caused by the dynamic non-linear interaction of the injected light pulse and the laser-internal light fields within the active charge carrier plasma inside the laser medium. The nonlinear light-matter coupling then leads to a decrease in the influence of the controlling light pulse and to a reduction of the pulse amplitude. Instead, the transverse degree of freedom gains more and more importance leading to characteristic transverse dynamics that is typical for the free-running laser: the light fields migrate from one side to the other on slower timescales of several hundreds of picoseconds. The coupling of the longitudinal modes of the large-are laser has finally diminished. The laser emission then is again characterized by a complex spatiotemporal light-field dynamics given by the mutual interplay of light diffraction, hole burning and carrier scattering leading to a complex longitudinal and transverse light-field dynamics.

The complex spatiospectral modes existing in a large-area laser thus play an ambivalent role in the dynamics: On the one hand, they support the buildup of a mode locking realized by an external signal leading to a pulsed emission across the entire laser stripe. On the other hand, the lateral extension is finally responsible for a decay of the mode locking generated by an injected light pulse due to chaotic dynamics and lateral instabilities.

Integration of the light fields at the output facet in transverse direction allows the calculation of the duration of the emitted pulses in dependence of the number of round trips. The computational results summarized in Fig. 20.8 clearly reveal a reduction in pulse duration from 50 ps to 13 ps indicating the occurrence of longitudinal mode locking. This behavior could also be seen in experiments [33]. The spectral width of the injected unchirped pulse is less than the longitudinal mode separation and thus cannot simultaneously couple to the numerous longitudinal modes coexisting in the semiconductor gain spectrum. This clearly proofs that the observed mode locking is a dynamic effect originating from dynamic interplay between pulse propagation and spatiospectral mode dynamics.

Our space–time modeling illustrates how the dynamic interaction of the injected pulse with the internal laser field efficiently couples the longitudinal modes and synchronizes the output across the laser stripe. However, we have to conclude that the control of the light emission by an injected light pulse as in the shown mode-locking example typically persists for only several nanoseconds, i.e., in the order of 50–100 round trips. On the one hand, this indicates the potential of semiconductor lasers for short optical pulse generation. On the other hand, this clearly demonstrates that more complex schemes are required to control the radiation on longer time scales. This can be obtained by using delayed optical feedback as realized in an external cavity configuration. This will be shown in the next section.

20.5
Self-Induced Stabilization and Control with Delayed Optical Feedback

In many applications semiconductor lasers subject to back reflections of their own emitted light field exhibit a complex dynamics such as low-frequency fluctuations or coherence collapse [23]. However, the main goals as required for and in applications are, in particular, high output power in few modes, good spatial and temporal coherence as well as stable emission. It is highly remarkable that in spite of a considerable number of scientific studies and resulting publications having focused on the influence of external optical feedback on (semiconductor) lasers, there still remain many unanswered questions.

The operation of BALs with delayed optical feedback is strongly dependent on two control parameters: the external mirror reflectivity R_0 (i.e., feedback strength, spatial structure or frequency selectivity) and the external cavity length L_{ext} (delay of the feedback). For a BALDOF, the equations describing the dynamics of the light fields propagating in forward and backward directions within the laser read

$$\frac{n_l}{c}\frac{\partial}{\partial t}E^{\pm} \pm \frac{\partial}{\partial z}E^{\pm} = iD_p\frac{\partial^2}{\partial x^2}E^{\pm} - i\eta E^{\pm} + \Gamma\frac{ik_o}{2\varepsilon_0 n_l}P^{\pm}_{(0)} + \frac{k}{\tau_{\text{in}}}E^{\pm}(t - \tau_{\text{ext}}). \quad (20.3)$$

The last term in Eq. (20.3) is the time delayed term describing the field reflected from the external mirror. $\tau_{\text{in}} = 2n_a L/c$ and $\tau_{\text{ext}} = 2L_{\text{ext}}/c$ are the internal round-trip time and external round-trip time, respectively. c is the speed of light, n_a is the refractive index of the active medium, and L is the laser cavity length. The dimensionless parameter k takes into account the reflectivity of the external mirror (R_0) and the laser facet mirror reflectivity (R_1).

$$k = (1 - R_1)\sqrt{\frac{R_0}{R_1}}. \quad (20.4)$$

Thus, the external cavity is described by two parameters: the strength of the feedback and the external delay time.

20.5.1
Influence of Delayed Optical Feedback

The application of a delayed optical feedback may have a significant influence on the transverse mode dynamics. As we will show it is, in particular, possible to influence the number of modes. Indeed, experiments have demonstrated [6] that an optical feedback with low feedback strength may stabilize the emission dynamics and reduce the number of modes drastically.

In the first step, we will focus on the conventional feedback setup (i.e., plane external mirror) described in Fig. 20.1. To characterize the behavior of the delay-system we have calculated the optical spectrum for various external mirror reflectivities (from 1% to 10%) and injection currents $I_{th} \leq I_{pump} \leq 3.5 \ I_{th}$ for a
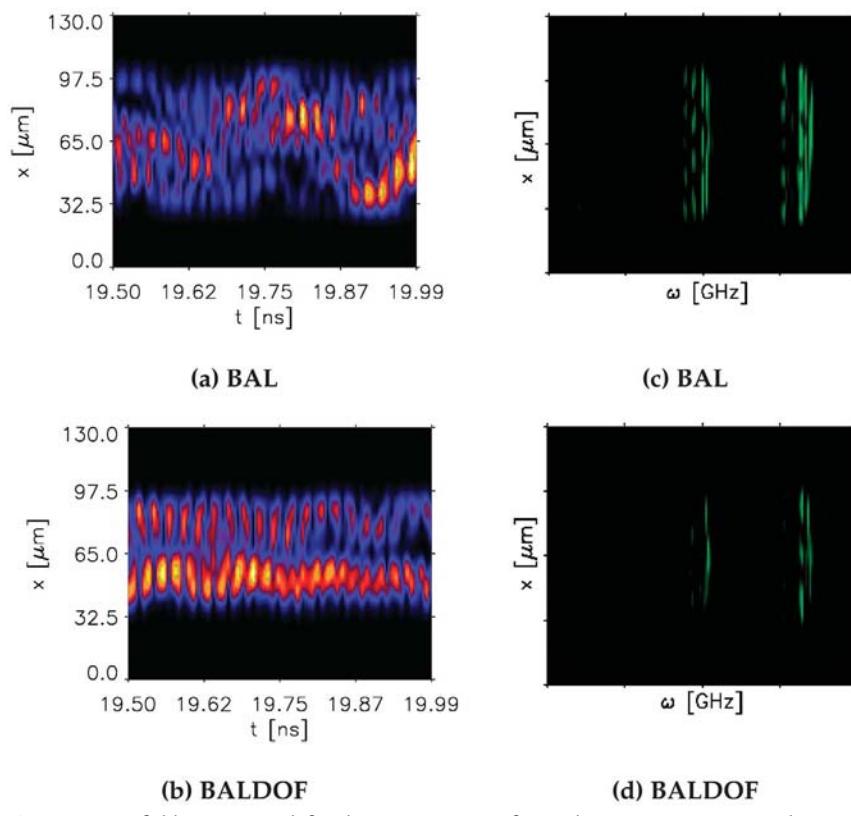
Fig. 20.9 Near-field intensities (left column) and optical spectrum (right column) of a free-running BAL ((a) and (c)) and of BALDOF ((b) and (d)) with an external mirror reflec-tivity of 2%. The injection current is close to threshold, the external cavity length is $L_{ext} = 3$ cm.
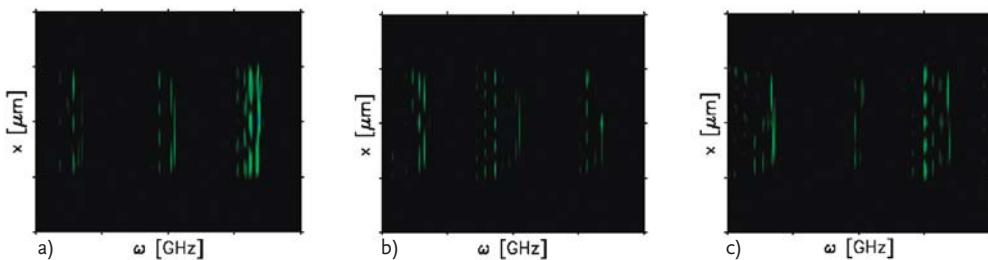
Fig. 20.10 Optical spectra of a BALDOF subject to delayed optical feedback ($R_0 = 2\%$ and $L_{ext} = 3$ cm) and different injection currents: (a) $I_{pump} = 1.2\, I_{th}$, (b) $I_{pump} = 2\, I_{th}$, (c) $I_{pump} = 2.8\, I_{th}$.

fixed value of external cavity length ($L_{ext} = 3$ cm). The partial reinjection of the light emission (after the passage in the external cavity) into the active area leads to a broadening of the spectrum and to a reduction of the number of longitudinal and transverse modes. This effect originates from the dynamic gain competition generated by the interaction of the multimode BALDOFs emission and the external cavity. This phenomenon is associated with the spatiotemporal dynamics of the filaments. Generally, the local gain is depressed in regions of high optical intensity leading to a local increase in refractive index, which further confines the light and increases the local field intensity. The superposition of internal cavity modes with the external cavity modes as realized by the reinjection of the emitted light fields lead to self-stabilization and spatiospectral condensation of the laser emission. Optical feedback thus can be seen as the basis of a regenerative self-focusing feedback. This effect is visualized in Fig. 20.9. Shown are the dynamics of the intensity at the output facet (left column) and optical spectra (right column) for a free-running BAL (a) and (c), and a BALDOF (b) and (d) with an external mirror reflectivity of 2%. The emitted near-field intensity is coded via colored scale, such that the red to yellow shading corresponds to high intensities and blue shading corresponds to low intensities. The migrating filaments manifest themselves in spots of high to low intensity which change their position in space and time.

Corresponding simulation results showing the result of an increase in the injection current are summarized in Fig. 20.10. As shown in this figure, the same tendency, namely the reduction of the number of transverse and longitudinal modes, can be seen for all current values. This highlights the large potential of the feedback-induced mode selection.

20.5.2
Influence of the Delay Time

It is well known that the delay time (determined by the length of the external cavity) has a strong influence on the spatiotemporal dynamics of BALDOF. This is due to the fact that the optical field that is fed back into the laser cavity
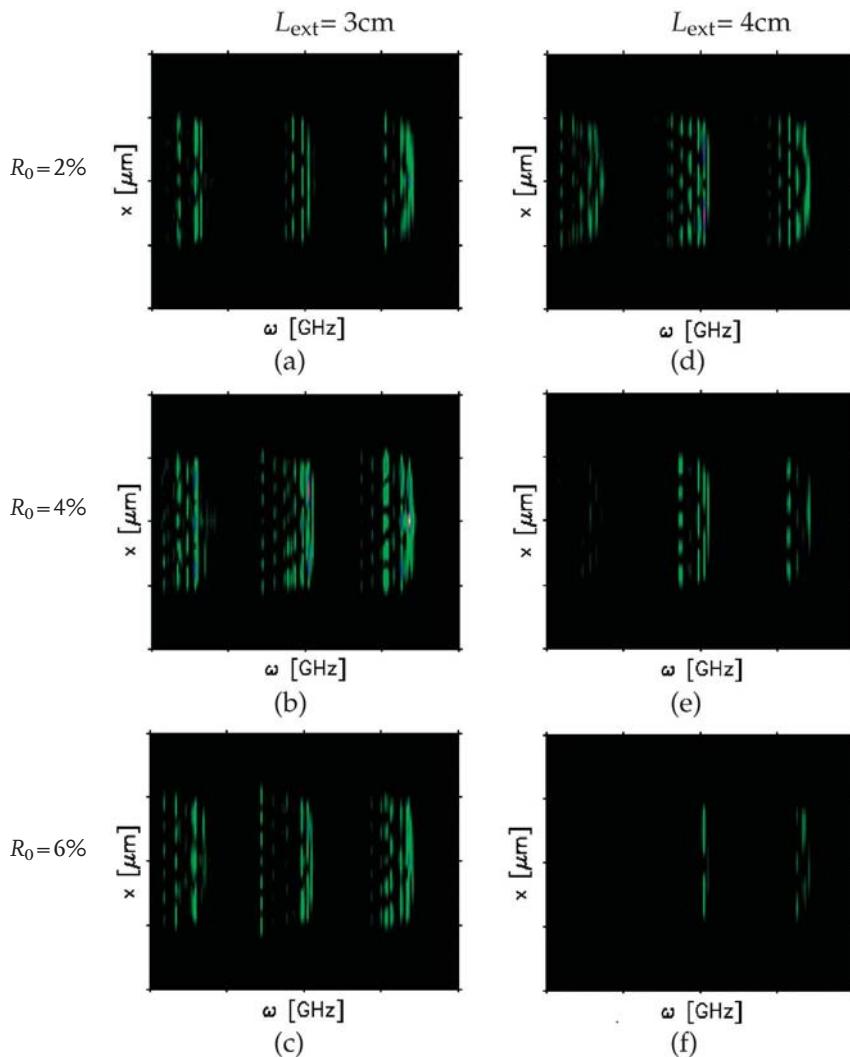
Fig. 20.11 Optical spectra of a BALDOF with external mirror reflectivities of $R_0 = 2\%$ (first row), $R_0 = 4\%$ (second row) and $R_0 = 6\%$ (third row). The external cavity length is $L_{ext} = 3$ cm (first column) and $L_{ext} = 4$ cm (second column). The injection current was set to $I_{pump} = 1.5 I_{th}$.

strongly interacts with the different intercavity modes. The coupling between these modes is, in turn, influenced by the length of the external cavity and thus determines the spatiotemporal dynamics of the system. As a consequence, very different operation regimes may be obtained, ranging from stable emission to

coherence collapse. It has been demonstrated in experiments [34] that there is a resonant coupling between these modes if the ratio between the length of the external cavity and the optical length of the semiconductor laser cavity is a multiple integer or half integer within the interval 2 and 5. This corresponds to an external cavity length between 1.18 cm and 2.96 cm.

In the following we will discuss, in particular, the influence of the delay time on the spatiotemporal dynamics of the semiconductor laser by varying the external cavity length between 1 cm and 10 cm (in steps of 0.5 cm), without being restricted by the condition mentioned above. In the numerical simulations, the external mirror reflectivity was varied between 1% and 10%. The optical spectra shown in Fig. 20.11 visualize the change in number of transverse and longitudinal modes in dependence on the feedback regime. The injection current was set to 1.5 I_{th}. For values of the external cavity length of less than 3 cm a strong reduction in the number of transverse modes could only be obtained for comparatively moderate feedback strength (2% reflectivity of the external mirror, Fig. 20.11 (a)).

Increasing the external cavity length to 4 cm leads to a much stronger reduction in transverse and longitudinal modes. This stabilization of emission dynamics not only occurs at low value of the external reflectivity (4%) but also for higher values (between 4% and 9%).
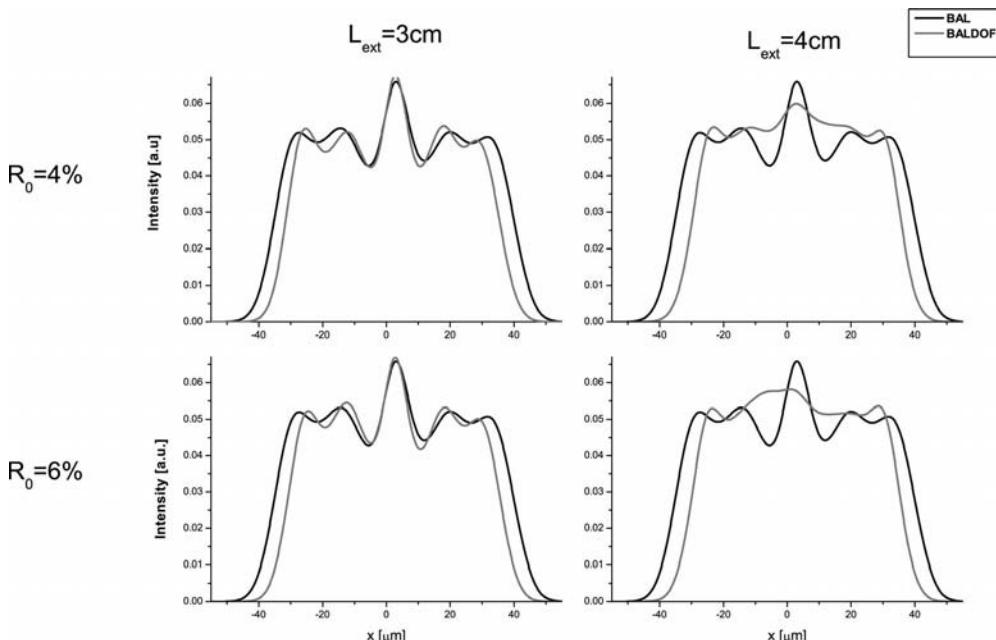
Fig. 20.12 Comparison of averaged near-field intensities between BAL and BALDOF.

In order to gain further insight into the mode competition we will in the following cast a closer look on the time-averaged near-field intensity. The results summarized in Fig. 20.12 clearly indicate the correlation between spatial and spectral dynamics. For a length of the external cavity of 3 cm (left column in Fig. 20.12) only few differences can be seen between the free-running laser and the BALDOF: as a general tendency the external mirror reflectivity slightly narrows the near-field intensity profile. This is due to a reduction of the transverse modes. If the external cavity length reaches a value of 4 cm, a strong mode competition arises leading to a considerable reduction of the modes (Fig. 20.12 (right column)).

Thus we may conclude that the number of transverse modes can be significantly reduced if the external cavity length is set to proper values (above 3 cm). For a sufficiently high delay time it is possible to significantly reduce the number of transverse and longitudinal modes in a large range of values of external mirror reflectivities. Of particular interest are the BALDOFs with an external mirror reflectivity between 2% and 10% and external cavity length between 4 cm and 9 cm. In this regime the number of transverse modes decreases dramatically (Fig. 20.13) for all injection currents (here: varied between threshold and three time threshold current).
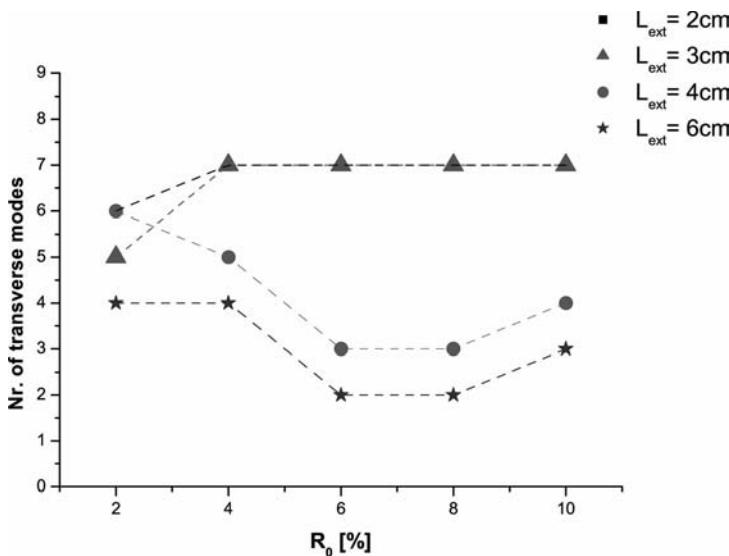
Fig. 20.13 Number of transverse modes as function of external mirror reflectivity and external cavity length. The injection current is $1.5 I_{th}$.

20.5.3
Spatially Structured Delayed Optical Feedback Control

With our space–time modeling of the multimode dynamics of large-area lasers with delayed optical feedback from a distant plane mirror we have so far demonstrated that the reinjection of parts of the emitted light into the active area can – for appropriate parameters corresponding to an appropriate setup – lead to a partial stabilization of the light-field dynamics and to a reduction of the number of modes. However, the results have also shown that a complete suppression of all modes except the fundamental mode still seems to be out of reach with a simple setup involving delayed-feedback from a flat reflector. Furthermore, the selection of suitable parameters seems to be particularly crucial. On the one hand, a careful choice of the feedback parameters may lead to a successful stabilization of the spatiotemporal chaos in semiconductor lasers. On the other hand, a naive application of a delayed optical feedback with an arbitrary choice in the feedback parameters may even increase the spatiotemporal complexity of the system [32, 38].

For an improved control over the interplay of spatial and spectral degrees of freedom one thus has to consider more complex control setups. A straightforward method is the application of a spatially structured delayed optical feedback (SDOF). This can easily be incorporated in the delay equations

$$
\frac{n_l}{c}\frac{\partial}{\partial t}\boldsymbol{E}^{\pm} \pm \frac{\partial}{\partial z}\boldsymbol{E}^{\pm} = iD_p\frac{\partial^2}{\partial x^2}\boldsymbol{E}^{\pm} - i\eta\boldsymbol{E}^{\pm} + \Gamma\frac{ik_o}{2\varepsilon_0 n_l}\boldsymbol{P}_{(0)}^{\pm} + \frac{k}{\tau_{\rm in}}\boldsymbol{E}^{\pm}(\sigma x, z, t - \tau_{\rm ext}) .
$$

(20.5)

The feedback term now depends on the curvature of the radius R of the external convex mirror:

$$
\sigma = \frac{R}{\sqrt{\left(\frac{w}{2}\right)^2 + (L_{\rm ext} + R)^2}}
$$

(20.6)

In this section we will thus discuss the influence of SDOF on the emission dynamics of BALs. In particular, we will vary the radius and reflectivity of the external curved mirror and the length of the external cavity. The results will be compared to the system with unstructured (flat) delayed optical feedback. Earlier results [35] had demonstrated that it should be possible to coherently couple the chaotic filaments and to obtain a narrow far-field for a suitable choice of the control parameters. Experimental investigations have been performed on configurations where the radius of the convex mirror was $R = 1$ mm and the external cavity length was varied between 1.2 mm and 1.6 mm [36] or set to 3 cm [37]. In order to get a full overview on the influence of all parameters on the spatiotemporal dynamics we here vary the radius of external mirror in the range
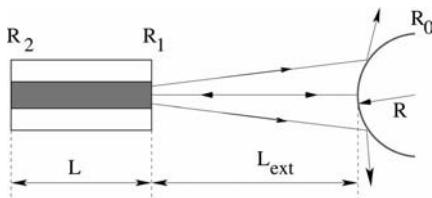
Fig. 20.14 Schematic figure of a broad-area laser with structured delayed optical feedback (SDOF). The radius of the curve mirror is denoted by R.

1 mm ... 9 cm, the external mirror reflectivity between 2% and 20% and the external cavity length between 3 cm and 9 cm.

The schematic drawing of the setup for the structured delayed optical feedback is shown in Fig. 20.14. The external length for the curved mirror is set to $L_{ext} = 3$ cm to comply with the regime where a controlled reduction of modes has been obtained.

The radius of the external mirror determines the spatial fraction of the radiation that is fed back: For sufficiently small values of the radius only light near the transverse center of the active area is fed back whereas radiation coming from parts near the lateral edges is – due to the curvature – reflected to the sides and thus does not reenter the active area. We thus expect a strong influence of a variation in the radius of the external mirror on the emission dynamics.

As an example, Fig. 20.15 presents numerical results on the optical spectra. The radius of the curved mirror was varied between 1 mm and 9 cm. The numerical results reveal a very strong dependence of the number of modes on the radius of the external mirror. A small value ($R = 3$ mm) of the radius does indeed, as expected, lead to a spectral condensation and stabilization of lower order transverse modes. Larger values, however, may even increase the chaotic spatiospectral dynamics: In this case, a larger spatial fraction of the light at the external mirror is reflected back into the active area thereby inducing – due to the curvature of the mirror – an additional mixing of transverse modes. For values of the radius of less than $R = 3$ mm the fraction of the reflected light is too small to have a significant influence on the internal light-field dynamics.

Please note that the small value of $R = 3$ mm not only stabilizes low-order transverse modes but additionally reduces the number of longitudinal modes. In order to gain further insight into this effect we visualize in Fig. 20.16 two snapshots of the spatial distribution of the intracavity intensity for (a) a free-running BAL and (b) one for a system with SDOF where the radius of the curved mirror has been set to 3 mm and the external mirror reflectivity to 2%. As can be seen in Fig. 20.16, smaller intensity variations in propagation direction can be seen in the system with SDOF revealing a reduced number of participating longitudinal modes. Our numerical results thus clearly demonstrate
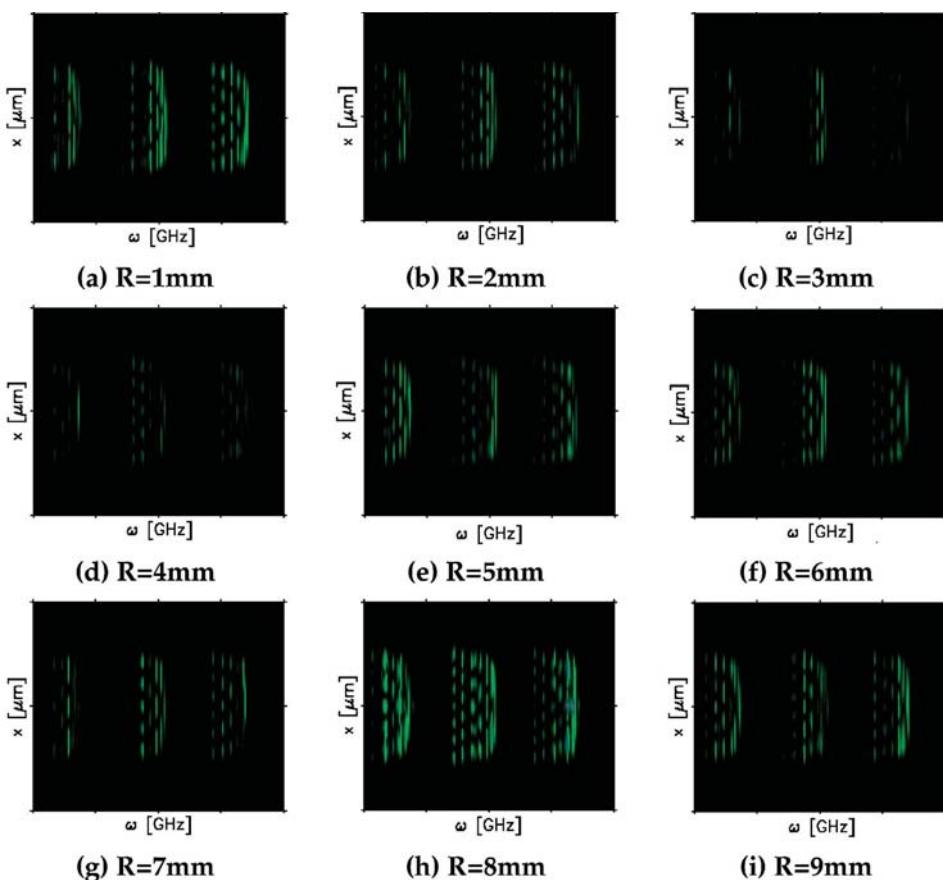
Fig. 20.15 Optical spectra of a BAL with SDOF for different values of the radius of the external curved mirror. The reflectivity of the curved mirror is 2%.

that a thorough choice in the parameter of the radius of the external mirror is crucial for the behavior of the system.

We will now vary the reflectivity of the external mirror between 2% and 20% and investigate its influence on the spectral emission properties. The parameter of the radius will remain constant ($R = 3$ mm). Figure 20.17 summarizes results of our modeling of the optical spectra in dependence of the external mirror reflectivity. The figure illustrates the strong effect of the reflectivity on the higher order transverse modes and longitudinal modes: Compared to the low mirror reflectivity ($R_0 = 2\%$) the introduction of a stronger feedback (i.e., larger mirror reflectivities) leads to a less efficient mode reduction. The moderate feedback level with $R_0 = 2\%$ thus represents the optimum for the stabilization of the light-field dynamics. In that regime, the zigzag moment that is typical for

(a) BAL

(b) SDOF
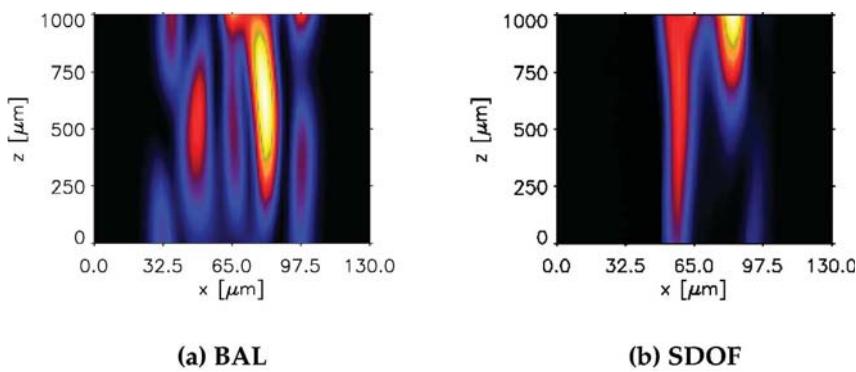
Fig. 20.16 Snapshots of the spatial distribution of the intra-cavity intensity in (a) free-running BAL and (b) a BAL with SDOF ($R_0=2\%$, $L_{ext}=3$ cm, $R=3$ mm) . The injection current is $I_{pump}=1.5\,I_{th}$ in both cases. The snapshots were taken 19 ns after the start-up.

(a) $R_0 = 2\%$

(b) $R_0 = 4\%$

(c) $R_0 = 6\%$

(d) $R_0 = 8\%$

(e) $R_0 = 10\%$

(f) $R_0 = 20\%$
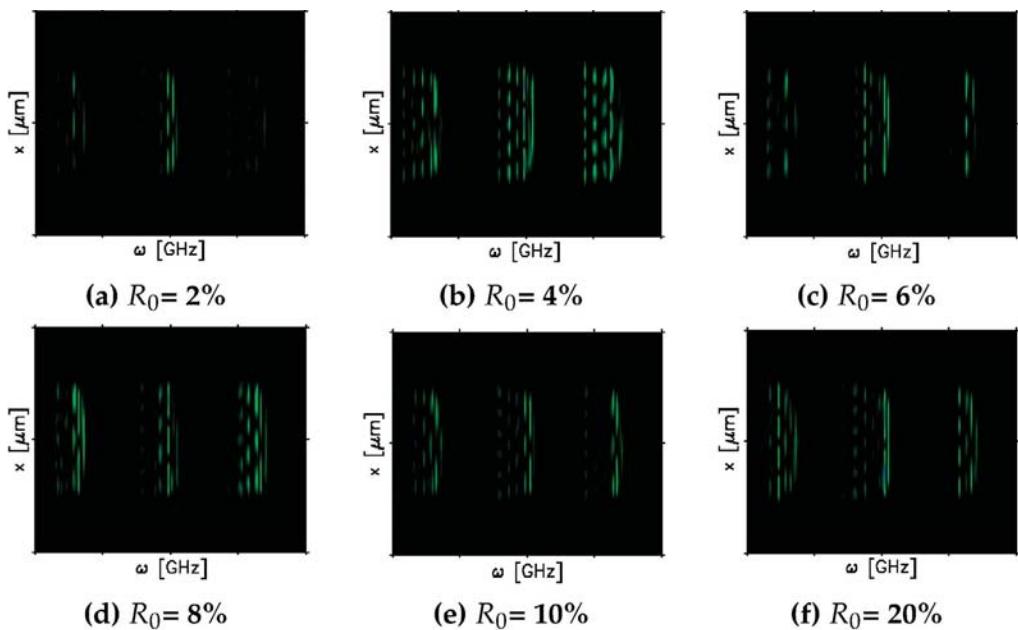
Fig. 20.17 Optical spectra of a BAL with SDOF in dependence on the reflectivity of the external curved mirror. The radius of curved mirror was set to 3 mm.

the transverse light-field dynamics does not extend over the full lateral width. Instead, the emitted intensity is to a higher degree concentrated in the center of the laser. In combination with the curvature of the external mirror the moderate

feedback level thus leads to a better transverse modes control and longitudinal side mode suppression.

In a next step of our analysis of the broad-area laser with SDOF setup, we will investigate the influence of the external cavity length on the optical spectra. For this purpose, this control parameter was varied in the same regime as in the case of the system with plane external mirror (see Section 20.5.2). The systematic calculation of optical spectra has shown that an external cavity length of $L_{ext} = 3$ cm leads to an analogue tendency as in the case of the plane mirror. Similarly, setting the external mirror reflectivity of the system with SDOF to 2% leads to a strong influence on the higher transverse mode dynamics and to a reduction of mode number. The results are summarized in Fig. 20.18. If the distance is increased to 4 cm, the minimum number of transverse modes is obtained for an external mirror reflectivity of $R_0 = 6\%$. It is important to note that generally the feedback strength and delay line represent coupled parameters in their influence on the dynamics of the laser. A change in one of the two parameters implies also a corresponding shift in the second parameter if one wants to bring the system back to optimized behavior. Nevertheless, our modeling shows that the delay line and thus the external cavity length play the major role (compared to the influence of the reflectivity of the external mirror) in the control of mode dynamics. For a given resonator length, the external mirror reflectivity then can be used for a "fine-tuning" of the dynamics control. Our numerical re-
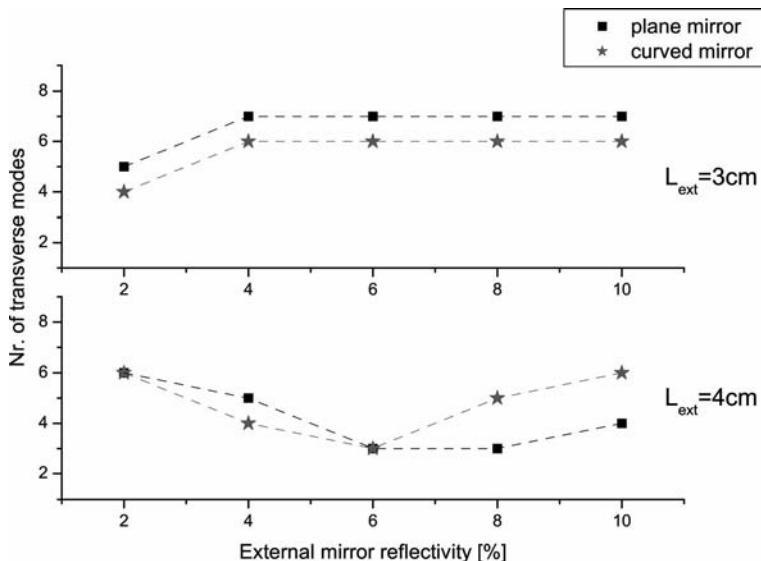

Fig. 20.18 Number of transverse modes versus external mirror reflectivity for a plane mirror (black square points) and curved mirror (red star points). The top graphic is for a 3 cm external cavity length and bottom graphic is for 4 cm.

sults clearly reveal the influence of SDOF on the spatiotemporal and spatiospec-
tral dynamics. A curvature in the mirror leads to a reduction of the modes and
to a stabilization of the light-field dynamics: the filaments in the near field are
pinned and a spectral condensation of the modes occurs. This clearly demon-
strates the positive influence of appropriately tailored SDOF on the spatiotem-
poral dynamics of BALs.

20.5.4
Filtered Spatially Structured Delayed Optical Feedback

The high complexity of the spatiotemporal light dynamics in a BAL involving
and coupling longitudinal "modes" with transverse "modes" immediately leads
to the question whether it is possible at all to obtain a full mode control, i.e.,
the reduction to single-mode operation. Recent studies [7, 25, 26, 39] have dem-
onstrated that a spectrally filtered optical feedback (e.g., a Fabry-Perot interfe-
rometer) can lead to a further control and mode selection.

Filtered delayed optical feedback may, in general, be classified into different
regimes with respect to the filter bandwidth relative to the external-cavity mode
spacing and the relaxation oscillation frequency of the laser: large, intermediate,
and narrow filter situations. Here, we concentrate on a system with a narrow fil-
ter (10 MHz, ..., 1 GHz). We will show that such a system may lead to a
further reduction in mode number.

In order to include the spectral lineshape of the filter, we include in our mod-
el an additional equation describing the dynamics of the feedback amplitude [7,
25, 26]. Assuming a Lorentzian lineshape of the filter one obtains the following
equations:

$$\frac{\partial}{\partial t}E^{\pm} \pm \frac{\partial}{\partial z}E^{\pm} = iD_p\frac{\partial^2}{\partial x^2}E^{\pm} - i\eta E^{\pm} + \Gamma P_{(0)}^{\pm} + \frac{k}{\tau_{\text{in}}}E_{bf}^{\pm}(\sigma x, z, t - \tau_{\text{ext}})$$

$$\frac{\partial}{\partial t}E_{bf}^{\pm} = \frac{1}{2}\Delta\omega E(t - \tau)\exp(-i\omega_0\tau) + (i\omega_f - \frac{1}{2}\Delta\omega)E_{bf}^{\pm}, \qquad (20.7)$$

where ω_f is the center frequency of the filter relative to the frequency of the so-
litary laser (ω_0), $\Delta\omega$ is the full width at half maximum of the filter.

In the following we will show selective results of the modeling of a system
with *spectrally filtered and spatially structured delayed optical feedback*. In a first
step we have varied the linewidth of the spectral filter in a range 10 MHz ... 1
GHz. The results are summarized in Fig. 20.19 (for a current of $1.5I_{\text{th}}$ and a
length of 4 cm of the external cavity). Generally, the application of a narrow-fil-
tered feedback enables the reduction of mode number. In our example the par-
ticular values of the linewidth in the order of a few hundred MHz allowed for
both, the reduction of the spectra to a longitudinal mode group and the selec-
tion of a single transverse mode (the fundamental mode) of this group. With in-
creasing linewidth (approaching the GHz regime) more modes can coexist lead-
ing to a more complex multimode behavior.
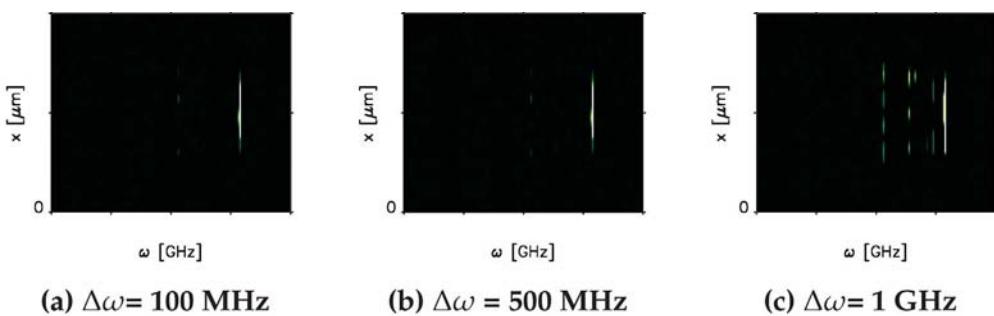
Fig. 20.19 Optical spectra of the BAL with spectrally filtered feedback: dependence on the linewidth (FWHM) of the filter.
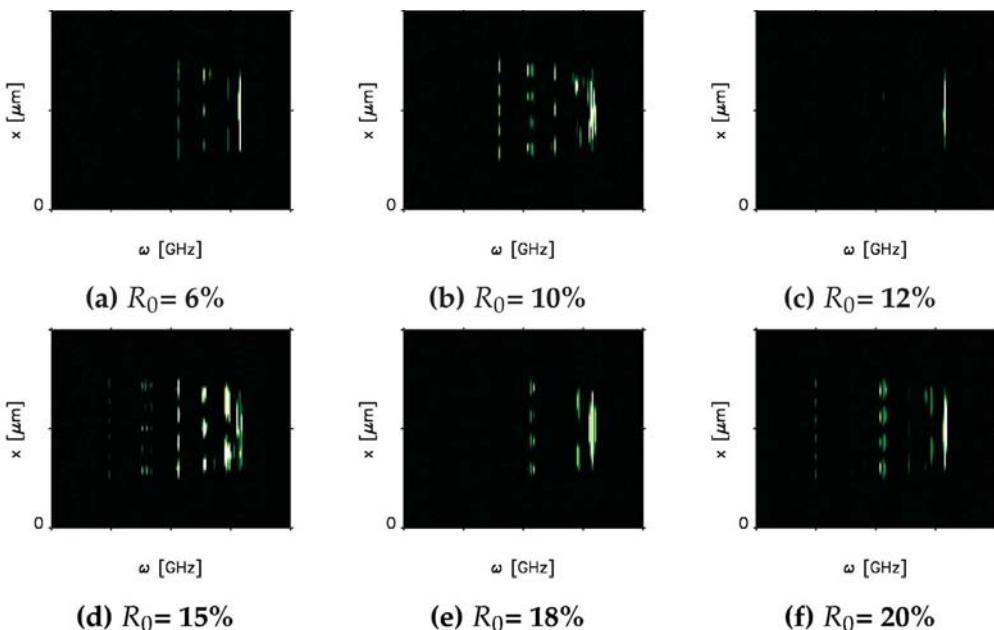

Fig. 20.20 Optical spectra of the BAL with spectrally filtered feedback: Dependence on feedback strength.

The investigations on the system with a curved external mirror have revealed that feedback systems may exhibit a strong dependence on the reflectivity of the external mirror. In a second step, we thus vary the feedback strength (i.e., the reflectivity of the external mirror) and analyze the influence on the emission spectra. Figure 20.20 summarizes the results. Similar to the situation without filter one can recognize a strong dependence on the feedback strength. In particular, the optimum value of the external reflectivity of the system with spec-

trally filtered feedback is not necessarily identical to the value of the BAL system with only spatially selective feedback. In the given example, we can obtain an almost single-mode emission for $R = 12\%$, whereas the optimum reflectivity of the respective system without filter was $R = 6\%$.

20.6
Conclusions

We have investigated the influence of delayed optical feedback on the (coupled transverse and longitudinal) multimode dynamics of broad-area semiconductor lasers. Our study was performed on the basis of spatially resolved multimode Maxwell-Bloch equations that allow us to analyze the correlation between external mirror reflectivity, delay time and emission characteristics aiding in the interpretation of experimental results and allowing the prediction of regimes where a controlled reduction of modes can be obtained.

In particular, it has been shown that the external round-trip time and the reflectivity of external mirror strongly determine the behavior of the laser. Extensive numerical simulations allowed us to confirm the external cavity length as a major control parameter: small modification of the external delay time leads to large changes in the spatiotemporal dynamics. This clearly highlights the complexity and nonlinearity of dynamic coupling of light fields and carriers in BALDOFs. Furthermore, application of spatially structured feedback by using a curved external mirror can improve the stabilization of the mode dynamics.

At the same time, the results of our systematic study presented here in this chapter demonstrate the high complexity of the spatiotemporal dynamics of delayed optical feedback systems. They reveal, in particular, that an efficient emission control requires the systematic control of *all* degrees of freedom.

Figure 20.21 summarizes the schematic setup and resulting emission characteristics (as represented by the spatially resolved emission spectra) of the broad-area laser systems considered in this chapter:

- The plane-mirror setup (*top*) represents the easiest configuration. The feedback is defined via the feedback strength and the round-trip time in the external resonator. However, the complex interplay of spatial, spectral, and temporal degrees of freedom may – depending on delay time and feedback strength lead to both, a partial emission control (with a reduced mode number) or chaotic lasing. A thorough control thus is difficult to achieve.
- Spatially structured delayed optical feedback (*middle row*) realized by, e.g., a curved external mirror allows a much higher emission control. Due to the control of spatial (via the x-dependence of the feedback) and temporal (via the delay time) degrees of freedom this system allows an improved control of the spatiotemporal dynamics. Furthermore, a feedback-induced genesis of a chaotic behavior is less probable compared to the plane-mirror configuration. Depending on chosen parameters such as, e.g., curvature and reflectivity of the
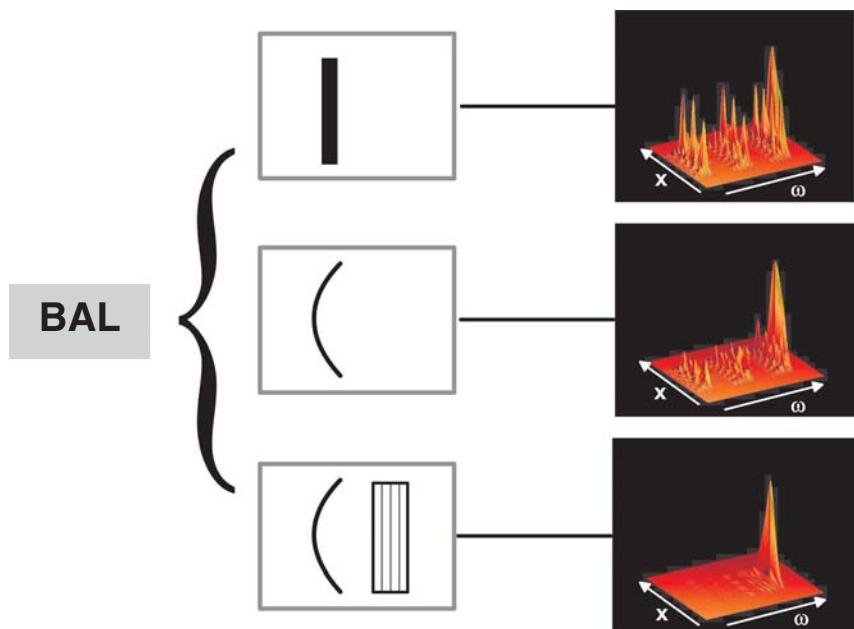
Fig. 20.21 Schematic overview of setup (left) and characteristic spatially resolved spectra (right) of a broad-area semiconductor laser with delayed optical feedback. Top: plane-mirror setup. Middle: spatially SDOF. Bottom: spectrally filtered SDOF.

external mirror the spatially structured feedback configuration allows a significant reduction in mode number.

- Spectrally *filtered* spatially structured optical feedback as realized by combining spatially structured feedback with a spectral filter eventually leads to the over-all control of spatial, spectral and temporal degrees of freedom and to single-mode operation.

In future work, we will more systematically simulate the influence of filtered optical feedback on the spatiotemporal dynamics of BALs. The influence of this configuration on the spectral degree of freedom will further improve the mode reduction process and allow to derive further conditions for both, single-mode emission characteristics and controlled spatiotemporal dynamics as desired in advanced applications such as, for example, complex spatiotemporal encryption schemes.

References

1 Fischer, I., Hess, O., Elsässer, W., Göbel, E., *Europhys. Lett.* 35, (**1996**), p. 579.

2 Marciante, J.R., Agrawal, G.P., *IEEE J. Quantum Electron.* 33, (**1997**), p. 1174.

3 Burkhard, T., Ziegler, M.O., Fischer, I., Elsässer, W., *Chaos Solitons Fractals* 10, (**1999**), p. 845.

4 Gehrig, E., Hess, O., Springer, Berlin, **2003**.

5 Chang-Hasnain, C.J., Welch, D.F., Scifres, D.R., Whinnery, J.R., Dienes, A., Burnham, R., *Appl. Phys. Lett.* 49, (**1980**), p. 680.

6 Mandre, S., Fischer, I., and Elsässer, W., *Opt. Comm.* 244, (**2005**), p. 355.

7 Fisher, A.P.A., Andersen, O.K., Yousefi, M., Stolte, S., Lenstra, D., *IEEE J. Quantum Electron.* 36, (**2000**), p. 375.

8 Heil, T., Fischer, I., Elsässer, W., *Phys. Rev. Lett.* 87, (**2001**), p. 243901.

9 Simmendinger, C., Preisser, D., Hess, O., *Opt. Express* 5, (**1999**), p. 48.

10 Carr, T., Pieroux, D., Mandel, P., *Phys. Rev. A* 63, (**2001**), p. 033817.

11 Abdulrhaman, S.G., Ahmed, M., Okamoto, T., Ishimori, W., Yamada, M., *IEEE J. Select. Topics Quantum Electron.,* 9, (**2003**), p. 1265.

12 Masoller, C., *Physica D,* 168/169, (**2002**), p. 171.

13 Verheyden, K., Green, K., Roose, D., *Phys. Rev. E* 69, (**2004**), p. 036702.

14 Schikora, S., Hövel, P., Wünsche, H.-J., Schöll, E., and Henneberger, F., *Phys. Rev. Lett.* 97, (**2006**), p. 213902.

15 Fischer, A.P.A., Yousefi, M., Lenstra, D., Carter, M.W., Vemuri, G., *Phys. Rev. Lett.* 92, (**2004**), p. 23901.

16 Erzgräber, H., Krauskopf, B., Lenstra, D., Fischer, A.P.A., Vemuri, G., *Phys. Rev. E* 73, (**2006**), p. 055201(R).

17 Mandre, S.K., Fischer, I., Elsässer, W., *Opt. Lett.* 28, (**2003**), p. 1135.

18 Heil, T., Fischer, I., Elsässer, W., Gavrielides, A., *Phys. Rev. Lett.* 87, (**2001**), p. 243901.

19 Huyet, G., Porta, P.A., Hegarty, A.P., McInerney, J.G., Holland, F., *Opt. Commun.* 180, (**2000**), p. 339.

20 Buldu, J.M., Rogister, F., Trull, J., Serrat, C., Torrent, M.C., Garcia-Ojalvo, J., Mirasso, C.R., *J. Opt. B: Quantum Semiclass. Opt.* 4, (**2002**), p. 415.

21 Huyet, G., Balle, A., Giudici, M., Green, C., Giacomelli, G., Tredicce, J.R., *Opt. Commun.* 149, (**1998**), p. 341.

22 Wallace, I., Yu, D., Harrison, R.G., Gavrielides, A., *J. Opt. B: Quantum Semiclass. Opt.* 2, (**2000**), p. 447.

23 Vaschenko, G., Giudici, M., Rocca, J., Menoni, C., Tredicce, J., Balle, S., *Phys. Rev. Lett.* 81, (**1998**), p. 5536.

24 Giudici, M., Giuggioli, L., Green, C., Tredicce, J.R., *Chaos Solitons Fractals* 10, (**1999**), p. 811.

25 Yousefi, M., Lenstra, D., Vemuri, G., Fischer, A., *IEE Proc.-Optoelectron.* 148, (**2001**), p. 233.

26 Green, K., Krauskopf, B., *Opt. Commun.* 258, (**2006**), p. 243.

27 Vicente, R., Dauden, J., Colet, P., Toral, R., *IEEE J. Quant. Electron.,* 41, (**2005**), p. 541.

28 Rajesh, S., Nandakumaran, V.M., *Physica D* 213, (**2006**), p. 113.

29 Lang, R., Kobayashi, K., *IEEE J. Quantum Electron.* 16, (**1980**), p. 347.

30 Aachihara, H., Hess, O., Indik, R., Moloney, J.V., *J. Opt. Soc. Am. B* 10, (**1993**), p. 496.

31 Fischer, I., Hess, O., Elsässer, E., Göbel, E., *Europhys. Lett.* 35, (**1996**), p. 579.

32 Münkel, M., Kaiser, F., Hess, O., *Physics Lett. A* 222, (**1996**), p. 67.

33 Kaiser, J., Fischer, I., Elsässer, W., Gehrig, E., Hess, O., *J. Select. Topics Quantum Electron.* 10, (**2004**), p. 968.

34 Peil, M., Fischer, I., Elsässer, W., *Phys. Rev. A 73,* (**2006**), p. 023805.

35 Simmendinger, C., Preisser, D., Hess, O., *Opt. Express* 5, (**1999**), p. 48.

36 Wolff, S., Fouckhardt, H., *Opt. Express* 7, (**2000**), p. 222.

37 Mandre, S.K., PhD thesis, Logos, Berlin, (**2006**).

38 Simmendinger, C., Hess, O., *Phys. Lett. A* 216, (**1997**), p. 97.

39 Fischer, A.P.A., Andersen, O.K., Yousefi, M., Stolte, S., Lenstra, D., *IEEE J. Quantum Electron.* 36, (**2000**), p. 375.

21
Noninvasive Control of Semiconductor Lasers by Delayed Optical Feedback

Hans-Jürgen Wünsche, Sylvia Schikora, and Fritz Henneberger

Semiconductor lasers are key components of modern optical information technologies. Due to inherent nonlinearities, they can emit not only continuous light but also periodic pulse trains or even chaotic output. The role of chaos is two edged. For many purposes, it has to be avoided in order to maintain stable operation of the laser. On the other hand, secure communication by using chaotic light has become an issue of growing interest [1–3].

In this context, methods of chaos control become important [4]. Among them, the Pyragas schema has attracted particular attention, as detailed knowledge of the target state is not required here [5]. The control signal is built from the difference $s(t) - s(t - \tau)$ between the present and an earlier value of an appropriate system variable s. We denote this control schema and variations of it (e.g. [6–12]) as differential delayed feedback control (DDFC).[1] DDFC primarily aims at the stabilization of an unstable periodic orbit embedded in a chaotic attractor. It is noninvasive if the delay τ equals the period T of the orbit. Noninvasive control stabilizes unstable states but does not change the states themselves, since the control force acts only if the system deviates from the state to be stabilized. This property entails a further aspect of DDFC. Unstable states frequently interconnect attractors in phase space and form thus the skeleton of the nonlinear dynamics. Bifurcation analysis uncovers mathematically also the unstable objects of the phase portrait. Their experimental study is, however, difficult, because they are visited for short times only. DDFC overcomes this difficulty and provides direct access to unstable orbits and equilibria in the experiment.

Involving no numerically expensive computations, DDFC is capable of controlling systems with fast dynamics still in real-time mode. This feature is particularly important for semiconductor lasers. Technical progress goes toward increasingly higher speed of operation. Multisection semiconductor lasers, as being used in this study, have been operated at tens of GHz [13, 14] and the THz range is in view. These picosecond timescales are too short even for fast electronic control circuits. Therefore, it is desirable to perform the control en-

---

1) The Pyragas schema is also known as time delayed feedback control (TDFC) or as time delayed autosynchronization (TDAS).
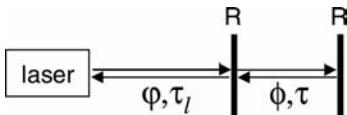
Fig. 21.1 Scheme of the FP configuration for all-optical DDFC of a laser. R: mirror reflectivity, τ, ϕ: round-trip time and phase shift in the cavity, respectively, τ_l, φ: the same for the latency between laser and cavity.

tirely in the optical domain where the velocity of light sets the ultimate speed limit.

Two configurations for all-optical DDFC have been proposed already a decade ago: optical feedback from a Michelson interferometer [15] and optical feedback from a Fabry-Pérot (FP) cavity [7, 16]. The Michelson configuration is the optical version of the original Pyragas method [5], whereas the FP setup corresponds to the extended version introduced by Socolar et al. [16]. In both cases, the variable s is given by the optical field amplitude E emitted by the device. We will explicitly consider the FP configuration of Fig. 21.1. The laser emission is forwarded into the cavity and a part reinjected into the device by the reflections at the cavity mirrors. In this way, a control signal of the form $E(t) - E(t - \tau)$ can indeed be constructed under appropriate conditions. Compared to DDFC in the electrical domain, the optical phase becomes important and its role must be thoroughly analyzed [32, 34, 43].

Although being conceptually evident and despite a numerical proof-of-concept study [15, 17], optical DDFC has not yet been implemented experimentally. The difficulty lies in the relatively long timescales on which the chaotic behavior of most lasers proceeds. They translate in cavity lengths that are either completely impractical or where the efforts to stabilize the cavity are so extensive that methods relying on optoelectronic feedback are much better suited. For multisection semiconductor lasers, the situation is just reversed: optoelectronic control, as mentioned already above, is no longer practical, while external cavities in the few-millimeter range can be easily combined with the laser in a robust setup. A future option is even integration of laser and FP cavity in a single device.

This chapter describes the first step toward all-optical DDFC, namely noninvasive stabilization of unstable steady states. This approach should not be confused with long-established methods for stabilizing laser emission by external cavities like the powerful Pound-Drever–Hall technique [18] or the use of filtered feedback [19–22]. Those methods are either not all-optical or invasive.

21.1
The Role of the Optical Phase

Before considering specific models, we discuss general features of optical DDFC. Each component of the electromagnetic field emitted by a laser varies as
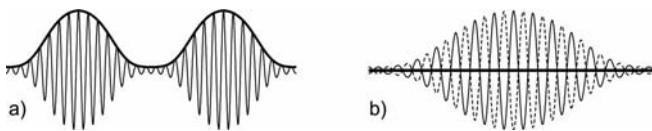
Fig. 21.2 Scheme of modulated optical waves. Thin: total field
$\mathcal{E}(t)$. Bold: slow amplitude $|E(t)|$. (a) Periodic pulsation. (b)
Subtractive superposition of two identical pulses with carrier
waves phase-shifted by an odd multiple of π.

$$\mathcal{E}(t) = \mathrm{Re}\left\{ E(t)e^{-i\overline{\omega}t} \right\}. \tag{21.1}$$

The exponential factor represents the carrier wave. Its period $2\pi/\overline{\omega}$ is in the femtosecond range and thus much shorter than any other time constant involved in the laser dynamics. The complex amplitude $E(t)$ varies orders of magnitude slower in time, even much slower as in the illustrations of Fig. 21.2. The control scenario considered in what follows relates to this slowly varying part of the electromagnetic field. The modulus of $E(t)$ determines the optical power

$$P(t) = |E(t)|^2, \tag{21.2}$$

that is measured, e.g., by a photodiode. The optical phase is lost in such a measurement. It plays, however, a central role in the interferometric control setup of Fig. 21.1. If the phase shift between the partial waves is π, the fields cancel each other and the total power fed back to the laser becomes zero (cf. Fig. 21.2 (b)). This cancellation is the basis for noninvasive all-optical control. Let us consider a periodic orbit. In the optical domain, such an orbit corresponds to a power-pulsation, while the total field $\mathcal{E}(t)$ represents a torus of two frequencies, $\overline{\omega}$ and the frequency of $|E(t)|$. Control of a torus is a complicated goal. However, as the two frequencies are so extremely different and as the laser equations are invariant under multiplication of the field with a constant phase factor, the torus is merely a modulated wave without any coupling between the two frequencies [23].

In order to calculate the field sent back from the interferometer to the laser, one has to sum up over all partial waves created by the reflectivities of the setup. Assuming plane-waves, this procedure yields [24, 25]

$$E_b(t) = Ke^{i\varphi} \sum_{n=0}^{\infty} (\mathcal{R}e^{i\phi})^n \left[\mathcal{F}e^{i\phi} E(t_{n+1}) - E(t_n) \right] \qquad \text{with } t_n = t - \tau_l - n\tau. \tag{21.3}$$

We have arranged the terms in such a way that the equivalence with the control signal needed in DDFC becomes obvious. For the Michelson configuration, only the term with $n = 0$ is present. τ and ϕ are the cavity round-trip time and phase shift, respectively. Note that the amplitude propagation and hence τ are determined by the group velocity, while the phase velocity enters ϕ. The quantities

$\mathcal{R} = R e^{-\gamma_r L_r}$, and $\mathcal{F} = \mathcal{R} + \mathcal{T}$ combine the other cavity parameters (R: mirror power reflectivity, $\mathcal{T}$: transmittance, L_r: resonator length, γ_r: absorption coefficient). The round-trip between the laser and the cavity is associated with a control latency τ_l [26, 27] and an extra phase shift φ. K characterizes the strength of the control signal and includes the reflection at the front mirror ($\sqrt{R}$) as well as all propagation losses.

Noninvasive control demands $E_b = 0$. If $E(t)$ is a periodic function, this is obviously fulfilled if τ is an integer multiple of the period T and $\mathcal{F}e^{i\phi} = 1$. The Fourier transform of Eq. (21.3),

$$E_b(\omega) = -K e^{i\varphi} \frac{1 - \mathcal{F}e^{i(\phi+\omega\tau)}}{1 - \mathcal{R}e^{i(\phi+\omega\tau)}} E(\omega), \tag{21.4}$$

provides another view on these conditions. The prefactor of $E(\omega)$ is the amplitude reflectivity of the interferometer. Its modulus exhibits distinct minima at the resonance frequencies $\omega_m^{\mathrm{FP}} = -\phi + 2\pi m/\tau$ (m integer) which tend to zero for $\mathcal{F} \to 1$ (cf. Fig. 21.3). Hence, the control signal can vanish only if the laser emits a periodic pulsation with spectral components exactly at these resonances. Such a match by proper choice of ϕ can be achieved, if the ratio of the pulsation frequency $2\pi/T$ and the round-trip frequency of the cavity $2\pi/\tau$ is integer.

The latency round-trip enters the control signal of Eq. (21.3) twofold: First, via the phase φ and, second, directly by τ_l in the slowly varying field amplitudes. The dynamics of the latter is governed by the timescales of the internal laser dynamics. τ_l itself becomes thus important, if it approaches these timescales. In many practical setups and, in particular, in the experiments presented below, this is indeed the case. Too large latency times generally decrease the ability of control as they reduce the role of the cavity. The latency phase φ is tunable by subwavelength changes of the optical path which has no effect on the slow amplitudes. Therefore, while the cavity phase ϕ is fixed by the resonance condition, φ is an additional free parameter that makes the control phase-sensitive. Conventional DDFC corresponds to $\varphi = 0$. When changing φ by π, the control force just reverses sign and, by this, the direction into which the system is driven: toward or away from the target state. Consequently, control can be only achieved in one half of a 2π phase period.
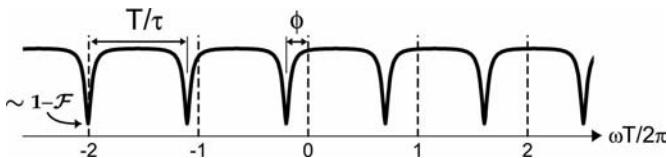

Fig. 21.3 Spectrum of the control signal according to Eq. (21.4). Thick solid: modulus $|E_b(\omega)/E(\omega)|$ of the interferometer reflectivity. Dashed: line positions of a pulsation with period T. Parameter: $\mathcal{R} = 0.7, \mathcal{F} = 0.95, T/\tau = 0.903$.

Experimentally, it is quite challenging to meet both the two cavity conditions, $e^{i\varphi} = 1$ and $\tau/T \in$ integer, as well as to adjust a sufficiently short latency time. In the remainder, we concentrate on the control of continuous-wave (*cw*) states. Stabilization of steady state operation of lasers is of high practical relevance [28, 29]. In the spectral domain, a *cw* state is a special case of a periodic orbit where the frequency spectrum is shrunk to a single line. The specific topology we consider is a focus point – the *cw* emission – that becomes unstable in a Hopf bifurcation where a periodic orbit corresponding to a power self-pulsation is born. Though the τ/T-condition is relaxed here, we shall see that even this case is far from being simple.

21.2
Generic Linear Model

In this subsection, basic features of phase-dependent optical DDFC are discussed in the framework of a simple but generic model. We consider a nonlinear system with a focus point E_0, the stability of which is governed by the complex eigenvalues $\lambda \pm i\omega$. The system is located closely beyond a Hopf bifurcation. Here, the focus is unstable, i.e., it holds $\lambda > 0$ for the damping term. Adding a control force and linearizing around the fixed point provides the generic equation [30–32]

$$\dot{E}(t) = (\lambda - i\omega)(E(t) - E_0) + Ke^{i\varphi}[E(t - \tau_l - \tau) - E(t - \tau_l)]. \qquad (21.5)$$

The second term on the right-hand side is identical to the control signal of Eq. (21.3) assuming resonance and neglecting multiple round-trips ($n = 0$). At a Hopf bifurcation, a pair of complex eigenvalues crosses the imaginary axis. The location of the bifurcation in the parameter space in the presence of the control signal is thus obtained by seeking solutions $E(t) - E_0 \sim \exp(-i\Omega t)$ of Eq. (21.5) with real Ω. This ansatz yields the algebraic equation

$$Ke^{i\varphi} = i\frac{\lambda + i(\Omega - \omega)}{2\sin(\Omega\tau/2)}e^{-i\Omega(\tau_l + \tau/2)}. \qquad (21.6)$$

Variation of Ω defines a curve in the (φ, K)-plane where the number N_u of eigenvalue pairs with positive real part changes by one. Such a Hopf curve is depicted in Fig. 21.4 (a) for given τ and τ_l. It consists of several branches which even cross each other. We are interested in the domain $N_u = 0$ enclosed by the lowest branch as it represents the domain of control. There is a minimum value $K_{\min} = \lambda/2$ of the strength parameter below which no control is possible. The existence of such a minimum is reasonable as the focus must be triggered sufficiently much by the control force within the destabilization time λ^{-1}. It is reached for $\Omega = \omega$ at a latency phase $\varphi = -\omega\tau_l$ (modulo 2π) and under the condition $\tau = (m + 1/2)T_0$ (*m*: integer). The latter relates the intrinsic period of the
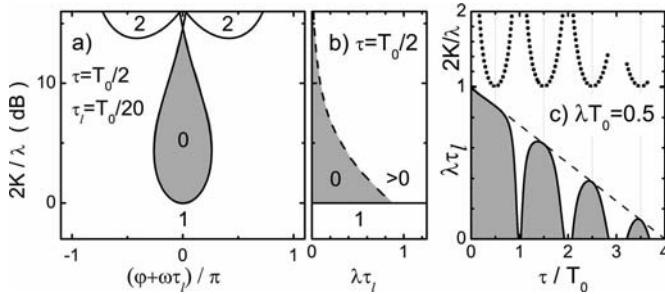
Fig. 21.4 Stabilization of an unstable focus by optical DDFC according to Eq. (21.6). (a) Solid: Hopf bifurcations in the (φ, K) plane (note the logarithmic vertical scale). Domain labels: number N_u of eigenvalue pairs with positive real part. (b) Lowest Hopf bifurcation (solid) and maximum of the control domain (dashed) versus latency time τ_l for optimum latency phase φ. (c) Largest allowed latency τ_l (solid) and the corresponding K (dotted) required for noninvasive control versus cavity round-trip time τ. Dashed: limit (21.7). The focus can be stabilized only in the gray regions. Focus parameters: $\lambda T_0 = 0.5$.

unstable focus $T_0 = 2\pi/\omega$ to the round-trip time in the cavity: spiral motion out of focus and control signal are in anti-phase and the system thus stabilized. For larger K, control becomes possible in a continuous band of φ. However, the band width behaves nonmonotonic and, eventually, the ability of control is lost again at certain maximum value $K_{\max}$ where the Hopf curve crosses itself. Delay-induced oscillations with frequencies Ω far from the intrinsic frequency ω are responsible for this limitation. As a function of the latency time τ_l, $K_{\min}$ is a constant, while $K_{\max}$ decreases rapidly and monotonic (Fig. 21.4(b)). At the point where the maximum reaches the minimum, the derivative of Eq. (21.6) with respect to Ω vanishes. A plot of this double root as a function of τ is shown in panel (c) of Fig. 21.4. For half-integer τ/T_0, the latency time is restricted by

$$\tau_l < \frac{1}{\lambda} - \frac{\tau}{2}. \tag{21.7}$$

Such a condition holds also for other classes of systems [26, 27]. The reduction by τ is plausible because a larger τ gives the focus more time to destabilize. When detuning τ/T_0 from the optimum half-integer resonances, the control range decreases rapidly and the required K increases. Reaching integer τ/T_0, control is ultimately lost. This is intuitively clear because the control force is always zero at these points.

In the context of laser emission, the above model supposes that the plane of the optical amplitudes represents the center manifold of the unstable focus. This is strictly not correct, because the occupation inversion is an extra degree-of-freedom of the laser. In fact, its dynamics comes into play by distinct relaxation oscillations when approaching the focus. Furthermore, the model is only valid in direct vicinity of the focus point, while the real dynamics in the laser is

essentially determined also by the phase space topology in the farer distance. Nevertheless, we shall see that features of the generic model indeed occur in more elaborated models and in the experiment.

21.3
Generalized Lang-Kobayashi Model

In this subsection, we consider the most simple nonlinear model of optical DDFC of a semiconductor laser. Although limited to lasers with stable single-mode emission, it reveals new generic effects of optical DDFC beyond the linear approximation. It generalizes the paradigmatic Lang-Kobayashi (LK) equations [33] to the control configuration of the previous subsection. Details can be found in [34]. The optical field and the occupation inversion in the laser are represented by a mean amplitude $E(t)$ and a mean carrier density $N(t)$, respectively, obeying the equations of motion

$$\frac{\mathrm{d}E}{\mathrm{d}t} = (1 - ia)NE + Ke^{i\varphi}[E(t - \tau_l - \tau) - E(t - \tau_l)], \tag{21.8}$$

$$\frac{\mathrm{d}N}{\mathrm{d}t} = \varepsilon(J - N - (2N + 1)|E|^2). \tag{21.9}$$

J is the excess pump current, $\varepsilon \ll 1$ is the ratio between photon and carrier lifetimes, and a is the linewidth enhancement factor governing the amplitude-phase coupling. All times are measured in units of the photon lifetime.

Independent of K and φ, this system has always the particular solution [2]

$$N = 0, \qquad E = \sqrt{J}e^{i\psi} \qquad (\psi: \text{arbitrary phase}), \tag{21.10}$$

the so-called solitary laser mode (SLM). For the solitary laser ($K = 0$) above threshold ($J > 0$), this solution is a stable focus and represents the only attractor. The impact of control ($K > 0$) is illustrated in Fig. 21.5. The SLM can change its stability in a local Hopf bifurcation (see panel (b)). This behavior is in qualitative agreement with the linear model. In addition, however, new solutions of the type $E \sim e^{-i\omega t}$ can appear in pairs at saddle-node (SN) bifurcations. Because of constant power $|E|^2$ and constant carrier density N, these external cavity modes (ECM) also represent steady laser states with *cw*-emission. The ECMs are situated on a figure eight in the (ω, N) plane, the crossing point of which is given by the SLM. Changing φ, they move along the eight and meet the SLM at transcritical bifurcations (cf. panel (a)). Bistability between ECM and SLM can occur too.

The creation of feedback-induced steady states is a general consequence of the invariance of the laser equations against multiplication of E with a phase

---

2) Strictly speaking, the family of solutions with different phases ψ.
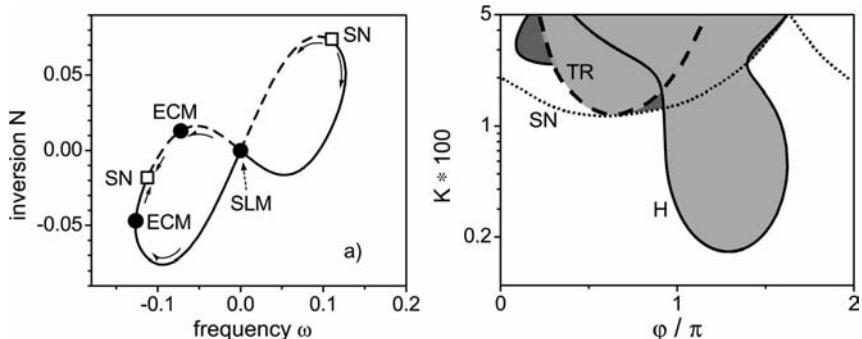
Fig. 21.5 Optical DDFC within the generalized LK model. Parameter: $a = 2$, $J = 0.3$, $\varepsilon = \tau_l = 0.001$, $\tau = 40$. (a) Curves of feedback induced modes in the (ω, N) plane for $K = 0.05$. SN: saddle-node bifurcation. ECM: external cavity mode at a particular latency phase. SLM: solitary laser mode. Solid line: node. Dashed: saddle. Arrows indicate how the ECM moves with increasing latency phase. SLM keeps its position independent of phase. (b) Bifurcations in the (φ, K) plane. Solid (H): Hopf of a stable mode. Dashed (TR): transcritical. Dotted (SN): saddle-node. Stability of the central mode. White area: stable *cw* operation. Light-gray region: unstable regime of SLM. Dark-gray regions: bistability between SLM and ECM.

factor (rotational invariance). Therefore, the related instabilities set a general limitation of optical DDFC, which does not occur in systems without rotational symmetry. Their influence on the control domains cannot be obtained within the LK model which produces always a stable *cw* state for $K \rightarrow 0$. A more realistic laser model is thus considered in Section 21.5 in conjunction with the experiment.

21.4
Experiment

The device utilized in the experiment is an integrated tandem laser (ITL). A schematics of the experimental setup combining the ITL with a properly designed FP cavity is depicted in Fig. 21.6.

The emission from one of the ITL facets is collimated by a spherical ball lens and sent under normal incidence through a neutral density filter to the cavity. The reflected light is fed back to the ITL along the same path. The power spectrum is measured by coupling the emission from the opposite device facet into a fiber and recording it by a 40 GHz electrical spectrum analyzer (ESA) after amplification and optoelectronic conversion by a 50 GHz photodiode. Optical spectra are measured with a resolution of 0.01 nm. The average power transmitted through the etalon is determined with a large area IR photo diode. For reasons of stability, the whole setup is installed on a vibration-damped table.
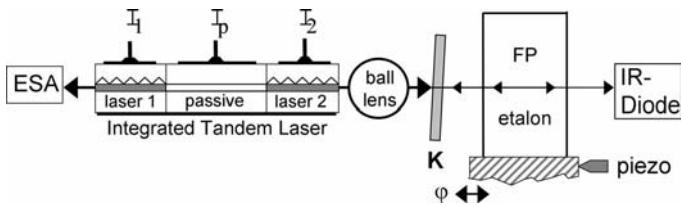
Fig. 21.6 Schematics of the experimental control configuration. In the ITL, two distributed feedback (DFB) lasers are connected via a passive waveguide section. Amplitude K and latency phase φ of the control signal from the FP are defined by a variable neutral density filter and a piezo positioning, respectively. ESA: electrical spectrum analyzer. IR-Diode: power measurement.

21.4.1
The Integrated Tandem Laser

The ITL chip has a design similar to [35]. It consists of two DFB lasers, each 220 μm long, separated by a 500 μm wide passive waveguide section. The coupling of the two lasers in the ITL is comparatively strong, as about 50% of the optical power passes the passive section. Nevertheless, owing to a specific grating design, both lasers of the tandem operate always single-mode. Current induced heating changes the refractive index in the active sections. The associated wavelength shift of about 20 nm/A enables us to tune separately the emission wavelengths of the lasers by asymmetric current pumping. An important internal parameter is the phase shift in the passive section. Current injection in this section modifies the refractive index via free-carrier transitions, by which this phase shift can be adjusted. The device is mounted on a copper heat sink and the temperature is controlled by a Peltier cooler with an accuracy of 0.01 K.

In the parameter space of the three injection currents I_1, I_2, and I_p, the ITL exhibits a rich variety of operational modes [35]. Among them are the regions of *cw* operation, regular power pulsation, and also chaotic emission. Representative examples of optical and power spectra of the solitary device in these regimes are shown in Fig. 21.7. The RO pulsations with lower frequencies are due to undamped relaxation oscillations, while those in the few-10 GHz range denoted by MB result from beating between competing optical modes [35, 36]. The transitions between these dynamical regimes take place through certain bifurcations. Here, we focus on the Hopf bifurcation in which the laser output changes from steady state to a RO-type self-pulsation when the phase current I_p is tuned through a critical value. The bifurcation is experimentally identified by the emergence of a respective peak in the power spectrum [37]. A noisy precursor of the pulsation is already present before the bifurcation and its width Δv decreases dramatically when approaching the bifurcation point (Fig. 21.8). Beyond this point, the peak height grows strongly, while the width stays small, indicating a well-developed self-pulsation.
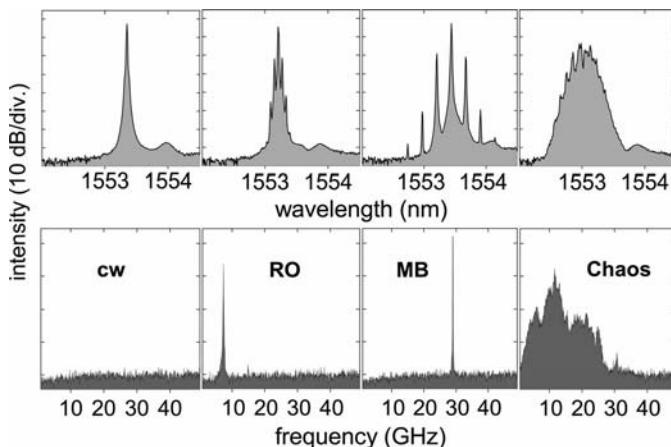
Fig. 21.7 Main types of dynamical regimes of the ITL. From left to right: *cw* emission, relaxation oscillations (RO), mode beating pulsations (MB), chaos. Upper row: optical spectra, lower row: power spectra.
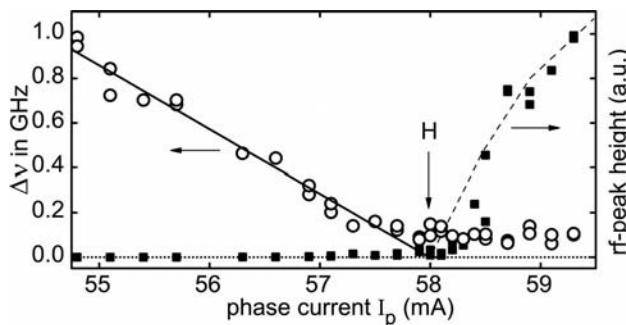

Fig. 21.8 Width (circles) and height (squares) of the dominant peak in the power spectrum of the solitary ITL versus phase current. Dashed: guide for the eye. Solid: linear fit for determining the Hopf bifurcation (H). DFB currents: $I_1 = 30$ mA, $I_2 = 45$ mA.

21.4.2
Design of the Control Cavity

Parallelism and stability of the FP mirrors on a subwavelength scale are paramount for generating a well-defined control signal. Both requirements are fulfilled by a block of quartz glass with a dielectric coating of 76% reflectivity. Figure 21.9 displays the transmission and reflection spectrum of the $L_r = 4$ mm thick etalon. The distance between adjacent resonances corresponds to a free spectral range of $1/\tau \approx 26$ GHz. The pulsation frequency of the ITL at the
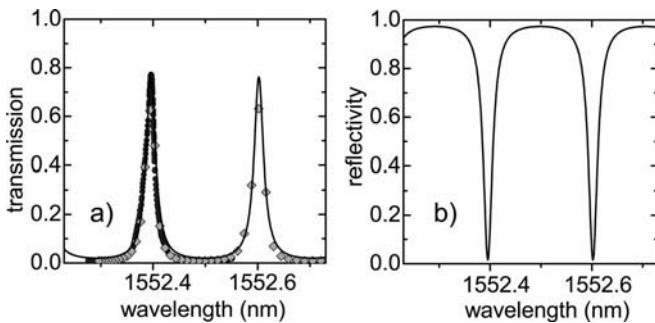
Fig. 21.9 Transmission (a) and reflectivity (b) spectra of the FP quartz-glass etalon. Symbols: measured data. Line: theoretical fit with the parameters given in the text.

Hopf bifurcation is $1/T_0 \approx 12$ GHz. The round-trip time in the FP cavity is thus close to the optimum $\tau = T_0/2$ found in Section 21.2. The further parameters of the etalon are obtained from a fit of the standard FP formulas to the experimental data. The refractive index is $\bar{n} = 1.43$, the absorption coefficient is $\gamma_r = 0.05$ cm^{-1}, and the mirror reflectivity and absorbance are $R = 0.76$ and $A = 0.005$, respectively. These values yield $\mathcal{F} = 0.98$, i.e., a reflectivity as small as 4×10^{-4} at the FP resonances.

21.4.3
Maintaining Resonance

The second requirement for noninvasive control is resonance between the FP cavity and the device emission. When moving the device through the Hopf bifurcation by tuning the phase current, the emission wavelength changes in general too. Therefore, to maintain resonance, the laser wavelength has to be readjusted. This is accomplished as follows: After setting a certain value of I_p, the device temperature is accommodated until a maximum of the power transmitted through the cavity indicates resonance. In this way, the bifurcation is traversed along a line of constant wavelength in the current-temperature plane. The temperature change involved in the accommodation is far below 1 K. The essential characteristics of the Hopf bifurcation in the solitary ITL device like the frequency of RO pulsations and their damping are unaffected under such small temperature variations.

21.4.4
Latency and Coupling Strength

As pointed out in Section 21.2 (Fig. 21.4 (b)), the ability of control rapidly declines for increasing latency time. The minimum separation between ITL and FP cavity, given by the space required for filter and lens, sets a lower limit of

$\tau_l = 60$ ps for the present experimental arrangement. According to Eq. (21.7), the critical value beyond which control is ultimately lost is $\tau_l = \lambda^{-1} - \tau/2$. The order of the damping λ can be estimated from the width Δv of the self-pulsation precursor in the power spectrum (cf. Fig. 21.8). This yields $|\lambda| = \pi\Delta v \approx 3$ ns^{-1} and, in view of the short cavity round-trip of $\tau = 40$ ps, an upper boundary for the latency time of about 300 ps. The experimental setup is thus capable of DDFC.

The phase shift φ associated with the latency is an extra parameter. Depending on its value, stabilization or destabilization occurs. φ can be tuned over several periods of 2π by translating the whole cavity on a subwavelength scale with the aid of a piezo-actor. The change of the latency time in this range is of no influence on the ITL dynamics.

The strength K of the control signal is adjusted by the density gradient of the filter. If K becomes too large, instabilities due to feedback-induced modes disturb the control experiment, as predicted by the LK model of Section 21.3. On the other hand, K has to overcome a certain level in order to affect markedly the ITL. We have found that $K \approx 5\%$ is an appropriate compromise in this trade-off.

21.4.5
Results of the Control Experiment

The power spectra measured in the presence of the FP cavity clearly demonstrate successful stabilization of the steady state emission beyond the Hopf bifurcation. Typical results are summarized in Fig. 21.10. The narrow peak associated with the well-developed self-pulsation of the solitary ITL collapses by nearly two orders of magnitude (Fig. 21.10 (a)). The frequency shift under control is indicative of the fact that the stabilized state is different from the stable state of the solitary ITL before the bifurcation. Plotting width and height of the peak as a function of the phase current, a distinct shift of the bifurcation point becomes evident (Figs. 21.10 (b) and (c)). The feedback from the cavity generates a significant damping ($\lambda < 0$) of the relaxation oscillations. At the solitary bifurcation current, a value of $|\lambda| = 1$ ns^{-1} is found.

Periodicity with respect to the latency phase φ is demonstrated in Fig. 21.11. The experimental data are in very good agreement with numerical simulations presented in detail in Section 21.5.

The spectrally integrated power transmitted through the FP cavity undergoes the same cyclic variation as the peak height of the self-pulsations. Outside the control domains, nonresonant Fourier components arise which reduce the transmission signal. In the domains, high transmission indicates low reflectivity of the FP cavity. In the calculations, the reflected power is indeed many orders of magnitude below the significance level. From the experimental signal at the transmission plateaus, it can be estimated that much less than 1 per mille of the intensity is fed back into the device. These findings clearly signify noninvasive character of the control.
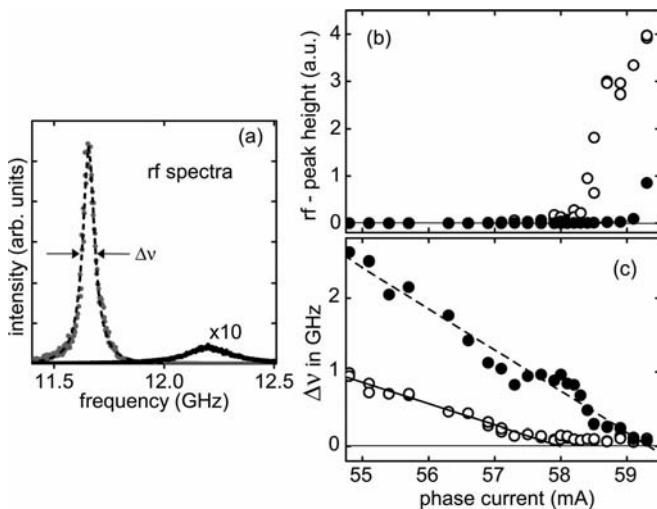
Fig. 21.10 Stabilizing a steady state through a Hopf bifurcation. (a) Typical power spectra beyond the bifurcation. Gray dots: measured for the solitary ITL. Dashed: Lorentzian fit. Solid black: with external FP cavity. (b) and (c) Height and width, respectively, of the spectral peak versus phase current I_P. Open circles: solitary ITL. Full circles: with control by the FP. Solid and dashed lines in panel (c): linear fits for determining the bifurcation points.
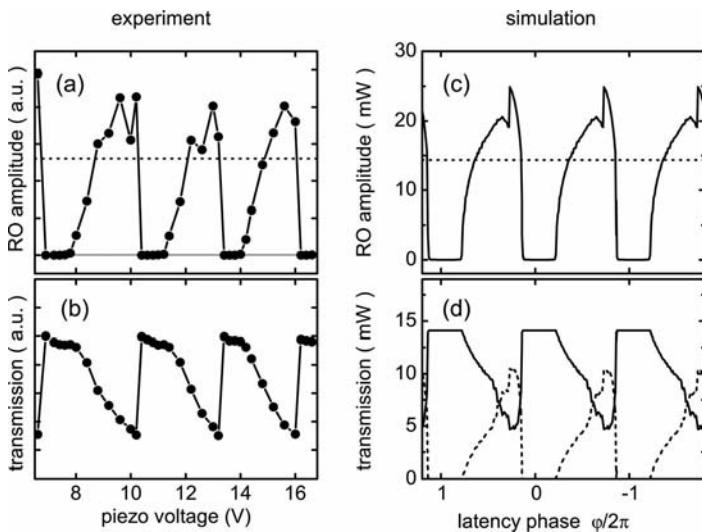

Fig. 21.11 Control of unstable steady states in dependence on the latency phase. The point of operation is $I_p = 58.5$ mA. Left column: experiment, $\tau_l = 3\tau \approx 120$ ps, the latency phase decreases proportional to the voltage at the piezo actor (cf. Fig. 21.6). Right column: simu-lation, $K = 4\%$, $\tau_l = \tau \approx 45$ ps, the phaseshift is varied via δ_l (see Section 21.5). Upper row: amplitude of the RO self-pulsations. Dotted: without control. Lower row: power transmitted through the FP (solid) and reflected power (dashed) in the case of simulation.
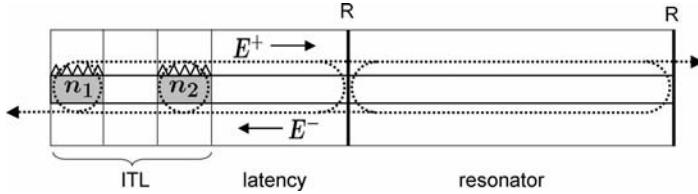
Fig. 21.12 Scheme of the simulated waveguide setup of the control configuration. Parameters are chosen according to the experiment.

21.5
Numerical Simulation

In this subsection, we present a device-specific numerical simulation which confirms the experimental results and yields a deeper understanding of the conditions for optical DDFC of semiconductor lasers.

The waveguide geometry under consideration is sketched in Fig. 21.12. The laser tandem is extended by two additional passive sections. The lossless FP section with identical reflectivities $R = 0.7$ is connected to the ITL by a latency section with variable coupling strength K and phase shift φ. Round trip times $\tau = \tau_l \approx 44.6$ ps are used unless noted otherwise. Transverse effects like diffraction or collimation are ignored in the model.

21.5.1
Traveling-Wave Model

In the framework of the Maxwell-Bloch equations [38], the field-carrier dynamics in multisection DFB lasers can be described by a well-established traveling-wave (TW) model [39–42]. The extension of the TW model to the control configuration of Fig. 21.12 is straightforward. We consider the case where the medium polarization can be adiabatically eliminated. We also use a mean-field-type approximation assuming that the occupation inversion in the DFB laser sections can be described by spatially averaged carrier densities [32]. The total optical field along the whole compound cavity is expressed by a superposition of forward and backward traveling waves

$$\mathcal{E}(z,t) \sim \mathrm{Re}\left\{ E^+(z,t)e^{-i(\overline{\omega}t - \overline{k}z)} + E^-(z,t)e^{-i(\overline{\omega}t + \overline{k}z)} \right\}, \tag{21.11}$$

of central frequency $\overline{\omega}$ and wavenumber $\overline{k}$. By normalization, $|E^\pm(z,t)|^2$ represents the guided optical power.

The equations of motion of the field-carrier dynamics are [35, 36]

$$\left[\frac{1}{c_g} \frac{\partial}{\partial t} \pm \frac{\partial}{\partial z} \right] \begin{pmatrix} E^+ \\ E^- \end{pmatrix} = i \begin{pmatrix} \beta & \kappa \\ \kappa & \beta \end{pmatrix} \begin{pmatrix} E^+ \\ E^- \end{pmatrix}, \tag{21.12}$$

$$\frac{dn_s}{dt} = \frac{I_s}{eV} - \frac{n_s}{\tau_n} - \frac{c_g g_s S_s}{1 + \varepsilon S_s} \quad (s = 1, 2) \tag{21.13}$$

(c_g: group velocity, I_s: injection current, e: elementary charge, V: volume of active zone, τ_n: carrier life time, ε: coefficient of nonlinear gain saturation). The index s numbers the sections of the setup. The complex DFB coupling constant κ and the carrier density n_s are nonzero only in the DFB sections $s = 1, 2$. The propagation parameter β is given by

$$\beta = \delta_s + i\frac{\gamma_s}{2} + \frac{g_s}{2}\left(a - \frac{i}{1 + \varepsilon S_s}\right) \tag{21.14}$$

(a: linewidth enhancement factor, δ_s and γ_s: constant background contributions from refraction and absorption, respectively, at the central frequency $\overline{\omega}$ of the guided wave). The unsaturated optical gain in the active sections is approximated by a linear relation

$$g_s = g' \cdot (n_s - n^{\text{tr}}) \tag{21.15}$$

(g': differential gain, n^{tr}: transparency concentration, $g_s = 0$ for $s \neq 1, 2$).

$$S_s = (c_g \hbar \overline{\omega} V)^{-1} \int_s dz(|E^+|^2 + |E^-|^2) \tag{21.16}$$

denotes the effective photon number. The TW model is completed by linear boundary conditions

$$\begin{pmatrix} E^+(+,t) \\ E^-(-,t) \end{pmatrix} = \begin{pmatrix} t_+ & r_- \\ r_+ & t_- \end{pmatrix}\begin{pmatrix} E^+(-,t) \\ E^-(+,t) \end{pmatrix} \tag{21.17}$$

at all interfaces. Arguments and subscripts $\mp$ refer to incidence from left- or right-hand sight, with $E^+(-,t) = 0$ and $E^-(+,t) = 0$ at the front and end facet, respectively. The transmission ($t_\pm$) and reflection ($r_\pm$) coefficients are interrelated by power-conservation conditions. Neglecting interface absorbance, it holds $t_\pm = \sqrt{1 - |r_\pm|^2}$.

The FP etalon is loss-free ($\gamma_r = 0$) and has external and internal mirror reflectivities $-\sqrt{R}$ and $+\sqrt{R}$, respectively, with $R = 0.7$. All other reflectivities are $r_\pm = 0$. Values for further parameters can be found in [32]. Variable losses γ_l and wavenumbers δ_l in the latency section with length $L_l = 1.76$ mm are used to tune the control parameters $K = \exp(-\gamma_l L_l)$ and $\varphi = 2\delta_l L_l$.
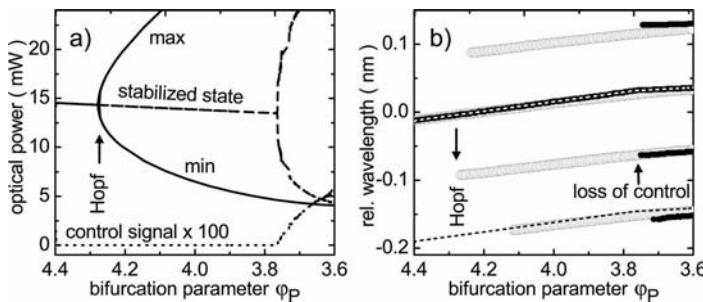
Fig. 21.13 (a) Maximum and minimum of the laser emission vs. internal phase shift φ_p. Solid: Solitary ITL. Dashed: ITL with lossless FP ($\varphi = 0, K = 0.1, e^{i\phi} = 1$). Dotted: Time averaged control signal E_b. (b) Main peaks in the optical spectrum (within 20 dB below maximum). Gray circles: Solitary ITL, thick black: ITL with lossless FP, dashed: resonances of the FP. DFB currents: $I_1 = 8$ mA, $I_2 = 80$ mA.

21.5.2
Noninvasive Control Beyond a Hopf Bifurcation

Instead of the current I_p, the internal phase shift $\varphi_p = 2L_p\delta_p$ in the passive section is used as a bifurcation parameter. It is tuned via the static wavenumber δ_p. Note that increasing I_p means decreasing δ_p. Figure 21.13(a) shows the minimum and maximum value of the emitted power taken from transients calculated over a time interval of 8 ns. Equal values mean *cw* output. The solitary ITL undergoes the Hopf bifurcation under study at $\varphi_p = 4.277$. In full analogy to the experiment, relaxation oscillations with a period of $T_0 \approx 87$ ps become undamped here. The bifurcation is also evidenced by the optical spectrum where extra peaks equidistantly separated by the frequency of the self-pulsations emerge (Fig. 21.13(b)).

With latency and resonant FP section added, *cw* operation is maintained beyond the solitary bifurcation point. The feedback signal practically disappears in the whole stabilization range, confirming the noninvasive character of the control. Only a single peak is present in the optical spectrum. Like in the measurements, the peak shifts under variation of the bifurcation parameter. Thus, also in the computations, the resonance frequencies of the FP cavity have to be readjusted. An iteration procedure is applied that stops when at least one spectral line coincides with a FP resonance. Control is lost at $\varphi_p = 3.765$ where again a self-pulsation appears. In what follows, the ITL is set well beyond the solitary bifurcation point ($\varphi_p = 4.15$).

21.5.3
Control Dynamics

The simulation provides insight into the dynamics of the control force that is hardly obtainable experimentally. Switching suddenly K from zero to a value of
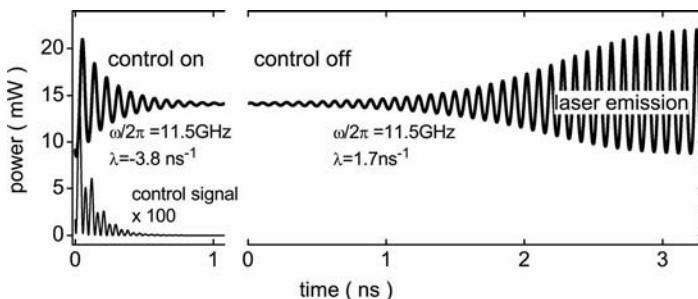
Fig. 21.14 Output transients after switching control on (left) and off (right), lower left: control signal. Parameters of Fig. 21.13 and $\varphi_p = 4.15$.

5% (left panel of Fig. 21.14), the ITL turns from a free-running stable self-pulsation into steady state mode. The control signal returned from the FP section is initially about 1% of the 15 mW device output, but it drops dramatically down. The steady state is approached with an exponential time constant of $\tau_{con} \approx 260$ ps. This time is a quantitative measure of the control efficiency and is investigated below as a function of the control parameters. Under the reverse switch of K, the self-pulsation recovers (right panel of Fig. 21.14). The rise time 0.59 ns and frequency 11.5 GHz of the small-amplitude oscillations arising at the initial stage represent the complex eigenvalue $\lambda - i\omega$ of the unstable focus. The frequency 11.2 GHz of the fully developed pulsation is only slightly slower because the point of operation is still close to the Hopf bifurcation.

21.5.4
Variation of the Control Parameters

The specific photon–gain coupling of the ITL also determines essentially the domain of control. In what follows, the initial state of the device is always set to a self-pulsation of the uncontrolled ITL. The criterion of noninvasive control is that the emitted power and wavelength asymptotically approach those of the unstable focus for $K = 0$.

For given K, the phase range of control is bordered by different bifurcations. At the right border in Fig. 21.15(a), a self-pulsation is born in a Hopf bifurcation. When decreasing φ, stability is first transferred through a transcritical bifurcation to a cw state that is nonresonant to the FP cavity, as already predicted by the LK model of Section 21.3. Here, the character of the control changes from noninvasive to invasive. The nonresonant cw emission ends eventually with the birth of a nonresonant self-pulsation in another Hopf bifurcation. The plot in Fig. 21.15(b) changing K for fixed φ is reminiscent of Fig. 21.4(a) for the linear model. However, the loss of control at large K is now specifically related to a jump to another cavity mode where a self-pulsation is stable at the given value of φ. The control time diverges at the borders of the control do-
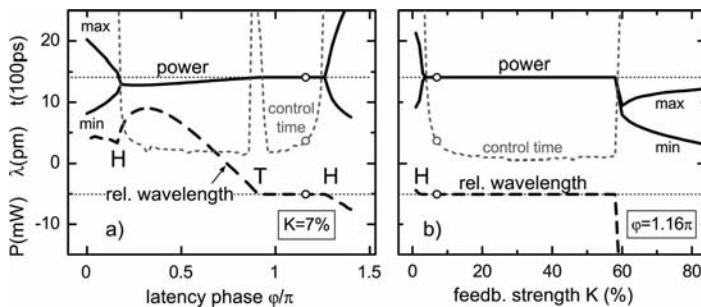
Fig. 21.15 Control properties vs. latency phase φ (a) and strength (b). Solid: minimum and maximum of the emitted power, dashed: mean wavelength relative to $2\pi c/\overline{\omega}$, thin dashed: control time τ_{con}, thin dotted: wavelength and power of the unstable *cw* emission. Symbols mark the bifurcations as follows: H – Hopf bifurcation, T – transcritical bifurcation. Circles: $\varphi/\pi = 1.16$ and $K = 7\%$.
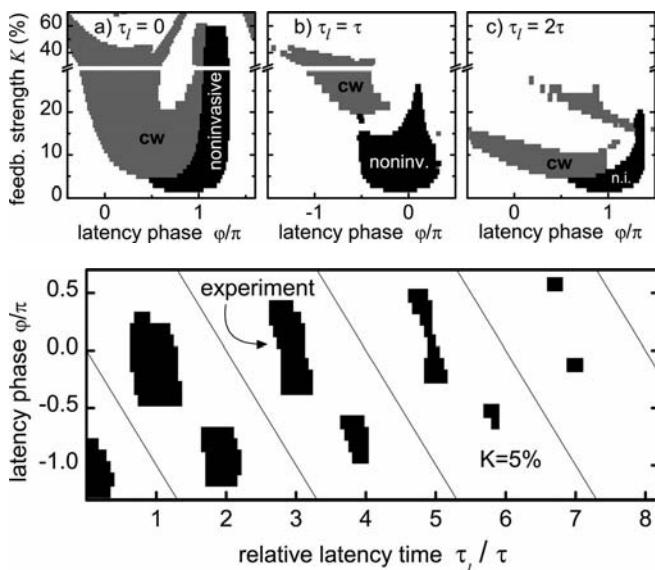

Fig. 21.16 Two-parameter control domains. Black: noninvasive, gray: invasive, white: no *cw* emission achieved. Upper panels: (φ, K) domains for different latency times τ_l. Lower panel: (φ, τ_l) domains for $K = 5\%$ and $\tau = T_0/2$. Thin solid: $\varphi = -\omega\tau_l$.

mains as well as at the transcritical bifurcation. In the range of robust control, this time becomes as short as $\tau_{con} = 50$ ps.

The control islands in the (φ, K) plane are depicted in Fig. 21.16. In addition, the role of the latency time τ_l is demonstrated. A plot in the (τ_l, φ) plane reveals cyclic behavior. The size of the control domains shrinks with increasing τ_l, con-

trol is lost for the present device beyond $\tau_l/\tau \approx 7$. These findings disagree with the predictions of the linear generic model of Section 21.2 in two regards. First, the control domains are shifted by about π from the line $\varphi = -\omega\tau_l$. This shift is related to the phase difference between the counter-propagation waves in the laser. Such a difference is ignored in the generic model but has to be additionally provided by the control loop in the real device. Second, the control islands break up for half integer τ_l/τ in contrast to the generic model (cf. Fig. 21.4 (b)). The experiments described above are performed in the large control island at $\tau_l/\tau = 3$. A direct experimental verification of the $\tau_l - \varphi$ relation was not possible because the absolute value of φ is unknown after having readjusted τ_l. However, the measurements confirm optimum control near to integer τ_l/τ and loss of control for large τ_l.

21.6
Conclusions

In a proof-of-concept experiment, the noninvasive all-optical control of the stable state of a semiconductor laser close to a Hopf bifurcation is demonstrated by using an external FP cavity. Both the experiments as well as a theoretical in depth analysis, reaching from a generic model up to a device specific numerical simulation, uncovers a quite complex control scenario which is produced by the latency phase in conjunction with the other control parameters. In practical devices, extra bifurcations come into play that determine the domain of control. In a more mathematical context, we have investigated the control of a modulated wave where, unlike other systems, the phase is an inherent parameter generating a complex-valued control gain. The experimental access to such a gain configuration offers the possibility of studying many other interesting questions, e.g., under what conditions periodic orbits of a modulated-wave state can be stabilized.

Acknowledgment

References

1 Feature Section on Optical Chaos and Applications to Cryptography, *IEEE J. Quantum Electron*. 38, no. 9 (**2002**) pp. 1138–1204.

2 Argyris, A., et al., *IEEE J. Quantum Electron.* 41, no. 6 (**2005**) pp. 892–897.

3 Pérez, T., et al., *IEEE Photon. Technol. Lett.* 18, no. 20 (**2006**) pp. 2135–2137.

4 Schuster, H.G., *Handbook of Chaos Control*, Wiley-VCH, Weinheim (**1999**).

5 Pyragas, K., *Phys. Lett. A 170* (**1992**) p. 421.

6 Kittel, A., Parisi, J., and Pyragas, K., *Phys. Lett. A* 198 (**1995**) p. 433.

7 Sukow, D.W., et al., *Chaos 7* (**1997**), p. 560.

8 Pyragas, K., *Phys. Rev. Lett.* 86 (**2001**) p. 2265.

9 Baba, N., et al., *Phys. Rev. Lett.* 89 (**2002**) 074101.

10 Beck, O., et al., *Phys. Rev. E* 66 (**2002**) 016213.

11 Harrington, I., and Socolar, J.E.S., *Phys. Rev. E* 69 (**2004**) 056207.

12 Ahlborn, A., and Parlitz, U., *Phys. Rev. E* 72 (**2005**) 016206.

13 Bornholdt, C., Slovak, J., and Sartorius, B., *Electron. Lett.* 40 (**2004**) p. 192.

14 Slovak, J., et al., *Proc. 31th Europ. Conf. on Optical Communication (ECOC)* (**2005**) Glasgow (UK).

15 Lu, W., and Harrison, R.G., *Opt. Commun.* 109 (**1994**) p. 457.

16 Socolar, J.E.S., Sukow, D.W., and Gauthier, D.J., *Phys. Rev. E* 50 (**1994**) p. 3245.

17 Simmendinger, C., and Hess, O., *Phys. Lett. A* 216 (**1996**) p. 97.

18 Drever, R.W.P. et al., *Appl. Phys. B* 31, no. 2 (**1983**) pp. 97–105.

19 Dahmani, B., Hollberg, L., and Drullinger, R., *Opt. Lett.* 12, no. 11 (**1987**) pp. 876–878.

20 Kazarinov, R.F., and Henry, Ch.H., *IEEE J. Quantum Electron.* 23, no. 9 (**1987**) pp. 1401–1409.

21 Wieman, C.E., and Hollberg, L., *Rev. Sci. Instrum.* 62, no. 1 (**1991**) pp. 1–20.

22 Erzgräber, H., et al., *Phys. Rev. E* 73 (**2006**) 055201 (R).

23 Rand, D., *Arch. Rat. Mech. Anal.* 79 (**1982**) pp. 1–38.

24 Born, M., and Wolf, E., *Principles of Optics*, 6th edition, Pergamon Press, Oxford, **1984**.

25 Hernandez, G., *Fabry-Pérot interferometers*, Cambridge University Press, Cambridge, **1986**.

26 Just, W., Reckwerth, D., Reibold, E., and Benner, H., *Phys. Rev. E* 59 (**1999**) p. 2826.

27 Hövel, P., and Socolar, J.E.S., *Phys. Rev. E* 68 (**2003**) 036206.

28 Gills et al., *Phys. Rev. Lett.* 69 (**1992**) 3169.

29 Ahlborn, A., and Parlitz, U., *Phys. Rev. Lett.* 96 (**2006**) 034102.

30 Rosenblum, M., and Pikovsky, A., *Phys. Rev. E* 70 (**2004**) 041904.

31 Hövel, P., and Schöll, E., *Phys. Rev. E* 72 (**2005**) 046203.

32 Schikora, S., et al., *Phys. Rev. Lett.* 97 (**2006**) 213902.

33 Lang, R., and Kobayashi, K., *IEEE J. Quantum Electron.* 16 (**1980**) pp. 347–355.

34 Tronciu, V.Z., et al., *Phys. Rev. E* 73 (**2006**) 046205.

35 Wünsche, H.-J., et al., *Phys. Rev. Lett.* 94 (**2005**) 163901.

36 Bauer, S., et al., *Phys. Rev. E* 69 (**2004**) 016206.

37 Ushakov, O., et al., *Phys. Rev. Lett.* 92 (**2004**) 043902.

38 Arecchi, F.T., and Bonifaci, R., *IEEE J. Quantum Electron.* 1 (**1965**) p. 169.

39 Zhang, L.M., et al. *IEEE J. Quantum Electron.* 30 (**1994**) pp. 1389–1395.

40 Homar, M., Moloney, J.V., and San Miguel, M., *IEEE J. Quantum Electron.* 32 (**1996**) pp. 553–566.

41 Serrat, C., and Masoller, C., *Phys. Rev. A* 73 (**2006**) 043812.

42 M. Radziunas, *Physica D* 213 (**2006**) p. 98.

43 Fiedler B., et al., *Phys. Rev. Lett.* 98 (**2007**) 114101

22
Chaos and Control in Semiconductor Lasers

Junji Ohtsubo

Chaos is controllable although we cannot foresee the future of chaotic evolutions due to the sensitivity of the initial condition of a nonlinear system. A chaotic system may be controlled by a small perturbation for the accessible parameters even when the system originally outputs irregular chaotic oscillations. The minute perturbation required for chaos control is extracted by the examination from the chaotic attractor of the system. The idea of chaos control is completely different from ordinary control methods. The perturbation for a nonlinear system is very small and little affects the state of the system. The method is also applicable in nonlinear chaotic optical systems. Here we discuss chaos control methods in chaotic semiconductor laser systems. The idea of chaos control gives rise to good indications for the development of new stable laser devices.

22.1
Introduction

A semiconductor laser is an intrinsically stable laser which is categorized into class B. Indeed, a semiconductor laser does not show any instability as far as it is operated at solitary mode. However, a semiconductor laser that is theoretically described by the field and carrier density equations can be easily destabilized by the introduction of external perturbations (additional degrees-of-freedom) such as external optical feedback, optical injection, or modulation. A variety of dynamics has been studied by many researchers for the past two decades [1, 2]. Recently, semiconductor lasers, which have new device structures, have been developed, for example, vertical-cavity semiconductor lasers, which has a vertical cavity against for the semiconductor substrate, and broad area laser (BAL), which has a broad stripe width of the active area. These lasers have quite different structures of cavities from those of ordinary edge-emitting semiconductor lasers. They originally have extra degrees-of-freedom compared with ordinary edge-emitting lasers and are essentially unstable chaotic lasers even in their solitary oscillations

[2, 3]. For semiconductor lasers destabilized by external perturbations and for newly developed semiconductor lasers, controls of laser oscillations are very important issues in practical applications [1].

We cannot foresee the future of chaotic evolutions, since a small deviation from the initial condition in a nonlinear system results in a completely different solution of the system output. However, chaos can be controllable [4]. Of course, a nonlinear system does not always show unstable oscillations. Indeed, the system can be controlled and stabilized to one of steady states by appropriately shifting the parameters even when the system originally outputs irregular chaotic oscillations. In such control, the perturbations for the system may be large and the system is switched to another state from the original oscillation by the parameter shifts. But, the idea of chaos control is completely different from ordinary control methods. The perturbation for a nonlinear system is very small and affects the state of the system only little. In chaos control, the system is controlled to nearby unstable periodic or fixed orbit (saddle node point of the system). In this chapter, we discuss the method of chaos control and give some applications in semiconductor laser systems. We demonstrate suppression of unstable oscillations in semiconductor lasers. Also some examples for laser controls in newly developed lasers as device structures are presented [2].

22.2
Chaos in Semiconductor Lasers

22.2.1
Laser Chaos

A laser is defined by three variables, the complex field E in the laser medium, the macroscopic polarization P of matter, and the population inversion W to attain the laser oscillation. The dynamic properties of a laser can be described by these three variables. A laser is usually modeled by three-level or four-level atoms with a Fabry–Perot-type resonator. However, we here assume a model of two-level atoms with unidirectional ring resonator, which is a good approximation for actual laser oscillations [1, 2, 5–7]. Starting from the Maxwell equation of a complex field with polarization of matter in a laser medium and applying the slowly varying-envelope approximation (SVEA) we obtain the rate equation for the laser oscillations. Also from the coupled Bloch equations for the transitions between the two-level atoms, we obtain the population inversion equation. In actual lasers, we require pumping for the laser oscillations, so that the pumping term should be added to the population inversion equation. Further the phenomenological terms for the damping oscillations are added to each term. Then we finally obtain the Maxwell-Bloch equations for the scaled three variables of the laser oscillations as follows [2]:

$$\frac{\mathrm{d}\bar{E}}{\mathrm{d}t} = i\frac{c}{2\eta}\bar{P} - \frac{1}{2T_{\mathrm{ph}}}\bar{E},$$

$$T_2\frac{\mathrm{d}\bar{P}}{\mathrm{d}t} = -(1 - i\delta)\bar{P} - i\bar{E}\bar{W}, \tag{22.3}$$

$$T_1\frac{\mathrm{d}\bar{W}}{\mathrm{d}t} = \bar{W}_0 - \bar{W} + \frac{\mathrm{Im}\left[\bar{E}^*\bar{P}\right]}{I_{\mathrm{sat}}},$$

where $\bar{E}$ is the complex field, $\bar{P}$ is the polarization of matter, and $\bar{W}$ is the population inversion. Here c is the velocity of light, η is the reflectivity of the medium, δ is the atomic detuning, $\bar{W}_0$ is the population inversion due to pumping at the threshold, and I_{sat} is the saturation intensity. T_{ph}, T_2, and T_1 are the relaxation times of the photon, the polarization, and the population inversion, which play crucial roles for the dynamics of the laser oscillations. Equations (22.1)–(22.3) are known as the Lorenz-Haken equations, since the three equations are almost the same as the Lorenz equations, which describe convective fluids as a model for the atmospheric turbulence, and the laser rate equations are derived by Haken [5]. Therefore, a laser is intrinsically a chaotic system.

Taking into consideration the rate equations (22.1)–(22.3), the laser first shows stable intensity oscillation above the first threshold with the increase in the pump. Then, far above the first threshold, the laser reaches the second threshold where it exhibits chaotic dynamics [7]. From a dynamical point of view, lasers can be categorized into three different classes depending on the typical timescales of the relaxations [8]. However, lasers do not always show instabilities and chaotic behaviors, and most lasers are actually stable. Indeed, chaotic dynamics are only observed for a laser when all the relaxation times are compatible. In some lasers, the timescales of these three relaxations are the same, such as infrared-gas lasers. These lasers are called class C lasers and show chaotic instabilities far above the first laser threshold, usually at or above ten times the pump current of the first laser threshold [9, 10]. In some lasers one of the time scales is much faster than the others. Such lasers are essentially stable lasers. In these lasers, the relaxation time is much faster than those of the photon decay time and the relaxation time of the population inversion, and the two rate equations, the complex field and population inversion equations, are enough to describe the laser operations. These lasers are called class B lasers, which are commercially available and very important in applications. Examples are solid-state lasers, fiber lasers, CO_2 lasers, and semiconductor lasers. The other lasers are categorized into class A, in which the laser is described only by the field equation. These lasers are mostly stable lasers. Examples for this class are visible gas lasers. So lasers which are commercially available and under practical applications are stable in their solitary oscillations.

In spite of such stable lasers of classes A and B, the lasers can still exhibit chaotic dynamics with the introduction of extra degrees-of-freedom, such as gain modulation, external optical feedback, and optical injection. Semiconductor lasers are easily destabilized by external perturbations [2]. Since a semiconductor

laser is modulated through the injection current and it has a low internal reflectivity in the case of edge-emitting semiconductor laser, the laser parameters are easily accessible. For examples, semiconductor lasers indeed show chaotic dynamics when subject to injection current modulation, self-optical feedback from an external reflector, and optical injection from a different laser. Another example of the introduction of extra degrees-of-freedom is the installation of additional laser structures to ordinary edge-emitting laser [2]. Vertical-cavity surface-emitting lasers (VCSEL) are promising candidates for future optical communications and optical data storage systems [11]. But VCSELs have quite a different spatial structure with circular aperture compared to ordinary edge-emitting laser, then we must consider the spatial dependence of the radial direction in the laser oscillation, namely we must take into consideration the spatial-dependent terms in the laser rate equations. This spatial dependence means an additional degree-of-freedom and the laser exhibits unstable oscillations without external perturbations to the laser.

Another example of unstable laser oscillations under solitary laser mode are BALs [3]. The structure of a BAL is almost the same as that of an edge-emitting laser except for the large stripe width along the active layer. The stripe width of an ordinary edge-emitting laser is only a few micron meter; on the other hand, a BAL has a stripe width of several tens to hundred micron meters. Therefore, we must consider the spatial dependence along the stripe width and this introduces the extra degree-of-freedom to the laser which leads to chaotic dynamics in its solitary oscillations. In the following, we focus on chaotic dynamics of optical feedback effects in ordinary edge-emitting lasers and also some newly developed semiconductor lasers.

22.2.2
Optical Feedback Effects in Semiconductor Lasers

Instability in semiconductor lasers is much enhanced by optical feedback from an external reflector [2]. Figure 22.1 shows a geometry for optical feedback in a semiconductor laser. Depending on the feedback fraction, the external cavity length, and also the operating conditions of a semiconductor laser, the laser ex-
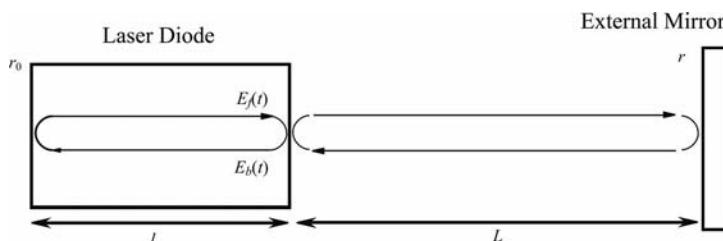
Fig. 22.1 Model of semiconductor laser with optical feedback.

hibits various stable and unstable oscillations. The important parameter is the optical feedback fraction and the dynamics are roughly categorized into five regimes [12]. With moderate optical feedback around 1% of the optical amplitude feedback from an external reflector (regime IV), the instabilities are much enhanced in semiconductor lasers, and strong chaotic oscillations are observed in the laser output power. The amount of optical feedback is moderate in a sense of optical amplitude; however, the optical feedback counted in intensity is only 10^{-4}%. It is surprising that, even for such small optical feedback intensity, the laser is destabilized and shows irregular intensity fluctuations which do not come from a statistical origin but from a deterministic way. The amount of optical feedback in this regime is not only important for fundamental chaotic dynamics but also for practical applications. In optical data storage systems, the returned light from a disk surface to the laser corresponds to this level. Also the optical feedback from optical fiber is the same order as this amount in optical fiber communications. For weaker optical feedback, the feedback introduces small effects to the laser and the laser shows either stable or slight unstable oscillations. On the other hand, the laser oscillation is stabilized at higher feedback fraction. We are here interested in this moderate optical feedback where the laser exhibits chaotic oscillations.

The rate equations for the complex field E and the carrier density n (which corresponds to the population inversion) in the presence of optical feedback are described by Lang-Kobayashi equations [13].

$$
\begin{aligned}
\frac{\mathrm{d}E(t)}{\mathrm{d}t} = {} & \frac{1}{2}(1 - ia)G_n\{n(t) - n_{\mathrm{th}}\}E(t) \\
& + \frac{\kappa}{\tau_{\mathrm{in}}}E(t - \tau)\exp(i\omega_0\tau)
\end{aligned}
\tag{22.4}
$$

$$
\frac{\mathrm{d}n(t)}{\mathrm{d}t} = \frac{J}{ed} - \frac{n(t)}{n_s} - \{G_s(t) - n_0\}|E(t)|^2 .
\tag{22.5}
$$

In the field equation, a is the linewidth enhancement factor, κ is the feedback coefficient due the external optical feedback, G_n is the gain, n_{th} is the carrier density at the threshold, $\tau = 2L/c$ is the round trip time of light within the external cavity, τ_{in} is the round trip time of light in the internal cavity, ω_0 is the angular oscillation frequency of the laser. The extra term has a delay time τ and the complex field is described by a delay differential equation. This is the origin of instability and chaotic dynamics in semiconductor lasers. In the carrier equation, e is the elemental charge, J is the injection current density, d is the thickness of the active layer, n_0 is the carrier density at transparency, and τ_s is the carrier relaxation time. We assume regime IV where optical feedback is not so high, so that the multiple optical feedback effect within the external reflector can be neglected.

Figure 22.2 is an examples of chaotic oscillations in semiconductor laser with optical feedback. Figure 22.2 (a) shows chaotic laser output and its power spec-
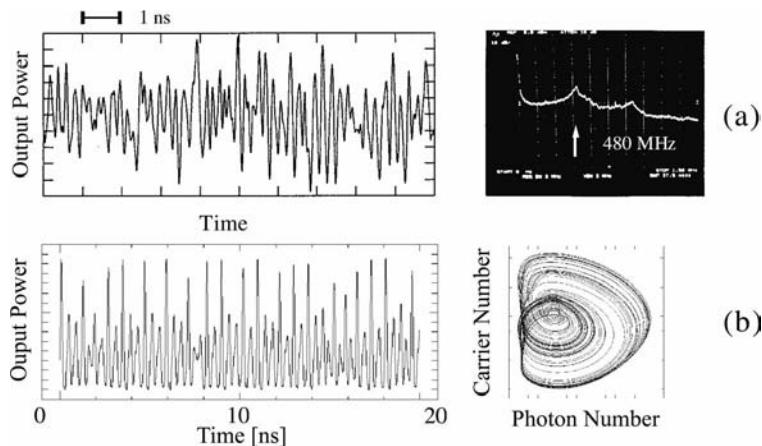
Fig. 22.2 (a) Chaotic oscillation (left) and its rf spectrum
(right) with strong optical feedback in semiconductor laser
(experiment). (b) Numerical simulations of chaotic waveform
(left) and its chaotic attractor (right).

trum obtained from experiments. The chaotic fluctuation has mainly two spectral components; one is a chaotic fluctuation related to the laser relaxation oscillation and the other is a frequency corresponding to the external cavity length. In this waveform, the external cavity frequency of 480 MHz, which is related to the external cavity length, is observable. Figure 22.2(b) shows the calculated chaotic output using Eqs. (22.4) and (22.5). The right is the chaotic attractor calculated from the waveform. The chaotic oscillation is well reproduced by the numerical simulation (note that the experimental signal is DC cut one). But, of course, we could not exactly trace the chaotic waveform due to the dependence of the various parameters and also the initial condition of the system. Chaotic oscillations are also observed by optical injection and injection current modulation. Similar dynamic characteristics are observed depending on the variations of perturbation parameters. Thus chaos is common in perturbed semiconductor lasers.

22.2.3
Chaotic Effects in Newly Developed Semiconductor Lasers

At present, edge-emitting semiconductor lasers are commonly used as light sources in a wide range of applications in optical communications, optical data storage systems, and so on. Those narrow stripe Fabry-Pérot lasers, multi quantum well lasers, and distributed feedback lasers are essentially stable in their solitary oscillations. Recently, a variety of laser structures are proposed to fabricate coherent light sources, such as functional light oscillations, high power operations, low threshold operations, etc. Those lasers usually have additional struc-
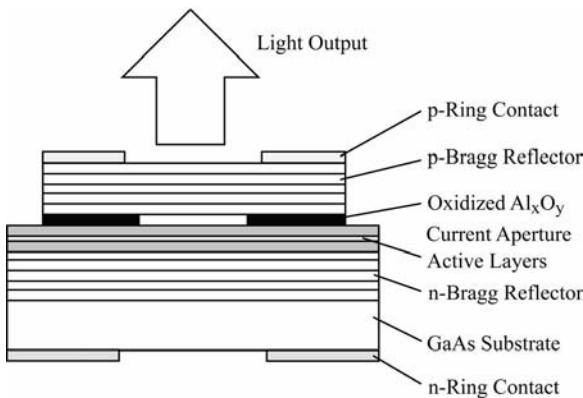
Fig. 22.3 Schematics of a selectively oxidized VCSEL structure.

tures on top of ordinary laser configuration. One of the promising lasers of newly developed structures are vertical-cavity surface-emitting lasers (VCSELs) [11]. Figure 22.3 is a schematic geometry of a selective oxidized VCSEL. A VCSEL emits light vertical to its substrate surface and usually has circular disk aperture, while edge-emitting laser emits light along the substrate surface and the laser beam is usually an elliptic form. Due to their circular beam VCSELs could be used in various applications. However, a VCSEL involves instability in its solitary operation, since it has a spatial dependence due to a disk diameter larger than the optical wavelength and it has a polarization ambiguity. Furthermore, a VCSEL oscillates at higher spatial modes at a high bias injection current and the modes sometimes compete with each other for the same reason (large disk diameter). Therefore, a VCSEL itself is an unstable laser even without external perturbations [2].

Here, we briefly discuss VCSEL operations and some examples of unstable oscillations. As already discussed, the spatial dependence must be included to explain the dynamics of VCSELs. The total complex field of VCSEL oscillations is expanded by spatial modes as follows [14, 15]:

$$\mathbf{E}_{\text{total}}(r, \phi, z, t) = \frac{1}{2} \sum_{j=1}^{M} \hat{\mathbf{e}}_j E_j(t) \psi_j(r, \phi) A_0 \sin(\beta_z z) \exp(-i\omega_{th,j} t) + c.c., \qquad (22.6)$$

where M is the total number of the spatial modes, $\hat{\mathbf{e}}_j$ is the polarization vector for the Jth mode, ψ_j is the eigenfunction for the Jth mode, β_z is the propagation constant for the z direction, and A_0 is the normalization coefficient. The rate equation for the field E has the same form as that of edge-emitting laser. Since the carrier diffusion in the radial direction must be taken into account for the VCSEL dynamics, the rate equation for the carrier density is written by

$$\frac{d}{dt}n(r,\phi,t) = D\nabla_T^2 n(r,\phi,t) + \frac{J(r,\phi)}{ed} - \frac{n(r,\phi,t)}{\tau_s}$$

$$- \frac{\Gamma_d}{d}\sum_{j=1}^{M}G_{n,j}\{n(r,\phi,t) - n_0\}\big|E_j(t)\psi_j(r,\phi)\big|^2,\qquad(22.7)$$

where D is the coefficient for the carrier diffusion, the subscript T denotes the operation for the transverse coordinates, and Γ_d is the confinement factor for the longitudinal direction in the active layer. The spin–flip model for the carrier density is sometimes used to describe the dynamics of VCSELs [16, 17]. The rate equations are convenient to analyze simply the polarization dynamics of VCSELs. However, the model is limited only to the analysis of the dynamics for the fundamental spatial mode oscillations.

Figure 22.4 shows examples of instability observed in solitary VCSELs. Figure 22.4 (a) is the light–injection current (*L–I*) characteristics of a VCSEL experimentally obtained for a disk diameter of 6 μm [18]. In this experiment, clear switching of the polarization modes from *y*-mode (dominant polarization mode) to *x*-mode (perpendicular to the *y*-mode) is visible at the bias injection current of 9.5 mA. The device characteristics including polarization switching strongly depend on the properties of the laser materials. We can observe clear polarization switches for the increase of the bias injection current for some VCSELs, while we cannot see clear switching for others. The total output power at certain bias injection current is simply the addition of the outputs of the *y*- and *x*-polarization modes. Even in solitary oscillations, VCSELs exhibit dynamic characteristics. One of such dynamics is an antiphase irregular oscillation of the optical output powers between the two crossed polarization modes. Figure 22.4 (b) shows an experimental example of antiphase oscillations of the *y*- and *x*-polarization modes in a VCSEL. Unstable pulsations and bistability are sometimes observed at the switching point of the two polarization modes without any external disturbances. In this figure, when the output power of the *y*-polarization modes
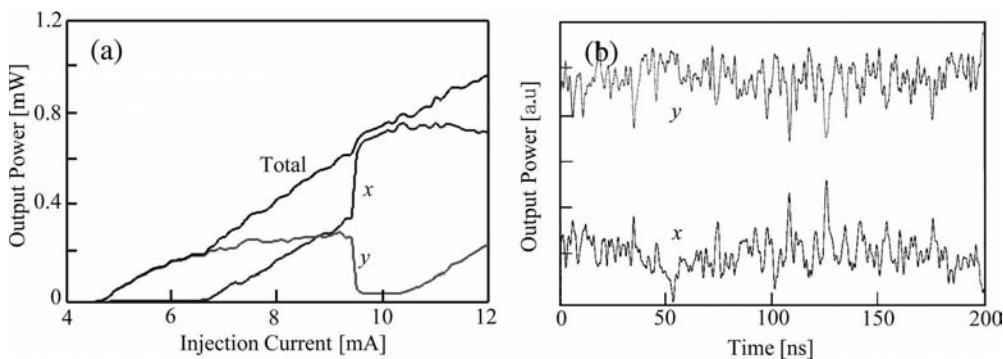
Fig. 22.4 (a) *L–I* characteristics of VCSEL. (b) Unstable antiphase oscillations of crossed polarization components.
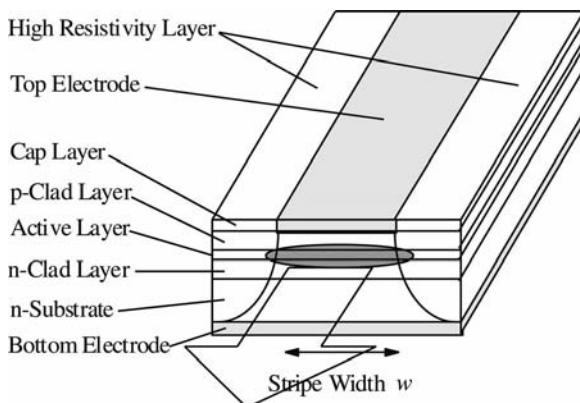
Fig. 22.5 BAL structure.

goes down, the output power of the x-mode grows up, and vice versa. This is the well-defined anticorrelation phenomenon of the polarization modes in the laser output power in VCSELs.

High-power semiconductor lasers are one of the promising light sources for industrial applications, since the power conversion efficiency from electricity to light in those semiconductor lasers is much higher than in other lasers. One of the technologies for high-power semiconductor lasers is a broad area laser that has a broad stripe width ($\sim$100 μm that is about 20 times larger than those of ordinary edge-emitting semiconductor lasers). Broad area semiconductor lasers have a broad stripe width of the active region, hence the name. The effects of the carrier diffusion and the diffraction of light in the active region are essential for the dynamics in such a structure. Broad area semiconductor lasers have a similar structure as ordinary edge-emitting semiconductor lasers except for the broad stripe width. Figure 22.5 is an example of the device structures [19]. Although BALs can emit high optical power, the qualities of the laser beam show rather poor performances. For example, BALs usually operate at multimode both for the longitudinal and transverse modes. A broad area laser typically shows twin-peak or multiple-peak pattern in the far field. There exists carrier hole burning effects in the active region along the stripe width at high bias injection current [20]. The positions of the hole burning change and fluctuate with time. This gives rise to pulsating oscillations with picosecond and fast spatiotemporal filamentations. Filamentation of BALs, which shows zigzag motions of high intensity peaks along the internal cavity, is one of the typical features of BALs and it deteriorates much the laser performance [21].

A broad-area semiconductor laser itself is also an unstable device due to the spatial dependence in the laser oscillations. Broad area lasers usually oscillate with multiple modes. However, in the following considerations we assume a single longitudinal mode operation for the simplicity. Starting from the Helmholtz equation for the complex laser field $E(x, t)$ (x is the coordinate perpendi-

cular to the emitting direction fo the laser in the active layer, i.e. the direction along the laser stripe width), the rate equation is written as [2, 22]

$$\frac{\partial E(x,t)}{\partial t} = i D_e \frac{\partial^2 E(x,t)}{\partial x^2} + \frac{1}{2}(1 - ia)G_n\{n(x,t) - n_{\text{th}}\}E(x,t), \qquad (22.8)$$

where $D_e = d/2k_0\eta^2$ is the diffraction coefficient of the light (k_0 being the wavenumber in vacuum). The first term on the right-hand side of the equation is the diffraction effect due to the broad active area. The diffusion effect must also be included in the rate equation for the carrier density and it is given by

$$\begin{aligned}\frac{\partial n(x,t)}{\partial t} &= D_n \frac{\partial^2 n(x,t)}{\partial x^2} + \frac{J}{ed} - \frac{n(x,t)}{\tau_s} \\ &\quad - G_n\{n(x,t) - n_0\}|E(x,t)|^2,\end{aligned} \qquad (22.9)$$

where D_n is the diffusion coefficient of the carrier and it is defined by $D_n = l_d^2/\tau_s$ (l_d is the diffusion length). In reality, the injection current is a function not only of time but also of the x coordinate.

A BAL shows spatiotemporal instabilities without any external perturbations. Figure 22.6 is a filamentation observed in a near-field output of a BAL [21]. We can see that bright spot particles move back and forth with a zigzag manner along the stripe width. This coil-like pattern is called filamentation and it is a typical structure of the output power in BALs. The width of migrating filaments is typically around 10 μm and it takes them about several picoseconds to migrate from one edge of the active region to the other one. Figure 22.6 (a) is the numerical simulation for the experiment for Fig. 22.6 (b). Filamentation is universally observed not only for wide strip lasers but also for semiconductor laser arrays [23].
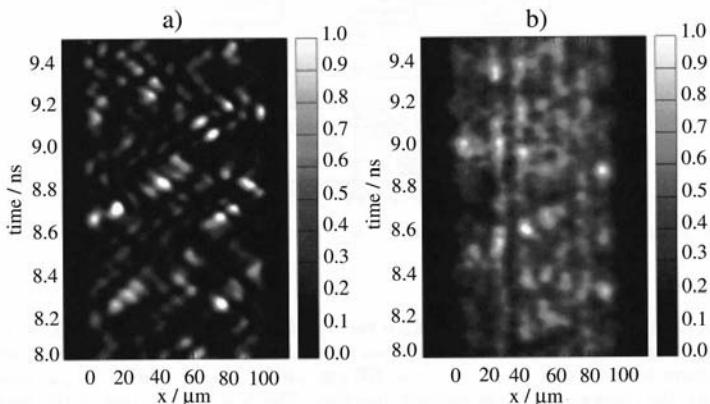
Fig. 22.6 Filamentation in BAL. (a) Numerical simulation.
(b) Filamentation experimentally observed by a streak camera
(©1996 EDP Science).

The origin for dynamic filamentation in BALs is not fully understood yet. However, the phenomena can be related to the effects of self-focusing, diffraction, and spatial hole-burning, which depend on spatial carrier diffusion as the relevant physical mechanisms [20, 24]. The self-focusing tends to guide high intensity regions resulting in a decrease of the optical gain. Thus, in the neighboring regions, the gain is higher. In addition, diffraction couples light into this neighboring region so that the spot of high intensity starts to migrate. At the edges of the active area, coupling via diffraction occurs only to one side, leading to the change of direction of migration. To control and reduce the effect of filamentation, a flared laser having a tapered cavity has been used [3]. In such lasers, the filamentation have been reduced but different complex spatiotemporal dynamics have been encountered.

22.3
Chaos Control in Semiconductor Lasers

Chaos induced by nonlinear effects is usually an unfavorable phenomena and we keep away from such irregular oscillations in practical applications. However, chaos is controllable. In 1990, the algorithm of chaos control OGY method was proposed in which the method applies appropriately estimated minute perturbations to an accessible system parameter to select and stabilize a certain periodic orbit (unstable periodic orbit: UPO) [4, 25]. The idea indicates that a chaotic system can be turned into a system with multipurpose flexibility in the meaning that one can obtain various desired orbits from only a simple system without dramatically modifying the configurations of the system. The method is called chaos control. The application of the OGY method requires the full mathematical description of a nonlinear model. We need the attractors or the Poincaré map in advance to analyze and control the system. Based on this information, the parameter is perturbed by the mathematical method and the system is forced to fall down onto an unstable periodic orbit. Therefore, the OGY algorithm is difficult to apply to real experimental systems. The method comes from a rather mathematical basis and can only be applicable for experimental situations where one knows explicitly the exact parameter values in the dynamical system, since the parameter values are important for the calculations of unstable periodic orbits. Although the method is difficult to apply to actual situations of chaos control, it has been modified and new techniques applicable to actual experimental systems have been proposed by taking over the essence of the OGY method.

As an alternative method of the OGY algorithm in practical applications, the method of continuous control algorithm which is suitable for control of practical nonlinear systems has been proposed. The continuous control method is applicable to a system with fast chaotic oscillations such as semiconductor lasers [26, 27]. In the following, we show an example of stabilization of chaotic oscillations induced by optical feedback in semiconductor lasers based on the continuous control method. Figure 22.7 shows an example of the continuous control
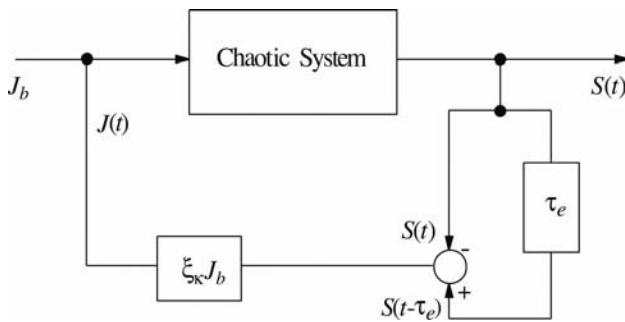
Fig. 22.7 Block diagram of continuous chaos control system.

systems in chaotic semiconductor lasers induced by optical feedback. The chaotic output from a semiconductor laser is once detected by a photodetector and electronically fed back into the bias injection current of the laser. The control signal is the difference between the detected intensities from the laser at present and before the time τ_e. Using the feedback gain ξ_K, the term for the injection current in the carrier density equation in Eq. (22.5) is replaced by

$$J = J_b[1 + \xi_K\{S(t - \tau_e) - S(t)\}], \tag{22.10}$$

where J_b is the bias injection current without control. The second term of the parenthesis on the right-hand side equation is the control signal. The delay time τ_e for the control is usually chosen to be the same as the optical feedback time. But, there is an optimum time delay for the control depending on the parameter conditions and it is not always the same value as the optical feedback time τ. After the continuous control is succeeded and the output of the laser is forced to a periodic or fixed oscillation, the control signal vanishes ($S(t - \tau_e) = S(t)$) and the original state is little affected by the control.

The continuous control method has been applied to suppress irregular oscillations in chaotic semiconductor laser systems and a number of studies for the numerical simulations have been published [28]. However, little experimental work has been reported for the implementation of the continuous chaos control. In actual, the delay τ_e is electronically generated by an analogue circuit and the control signal is fed back into the bias injection current of the laser. Therefore, we must design a fast response circuit for fast laser oscillations. The finite response of the electronic circuits, including photodetector and amplifier, always encounters beside of the setting of the delay τ_e. For real systems, we must take these effects into account. It is noted that a perturbation for the chaos control must be very small and the system is scarcely affected by the control. Therefore, it is not easy to realize laser stabilization in a strict sense of chaos control. Nevertheless, the analysis of finding stable points in the bifurcation diagram gives rise to good indication for the control of irregular oscillations of the sys-

tem even if the control signal does not have small value and the residual of the control is not small.

Another powerful method for the application in experimental systems is the occasional proportional feedback (OPF) method [29–31]. The OPF method modifies the OGY algorithm. The OPF method also perturbs one of the system control parameters by carefully feeding back a part of the output signal. It creates only small alterations of the attractor and pushes the system so as to stabilize to the periodic orbit. Digital and analogue electronic circuits, such as comparator and sample/hold circuits, are required for the implementation of the method and periodic components of the attractor are extracted from the chaotic output of the system. Then, the system is stabilized to a periodic orbit by appropriately setting a synchronous signal. The seeding synchronous signal is estimated from the system parameters. Therefore, we require the information only for the characteristic time of the system such as the delay time in advance. However, we do not need the exact characteristic time but only a rough estimate of it. When the parameters are set within certain ranges of the appropriate values, a signal for the chaos control is autonomously output. The control signal is pulse-like and much smaller than the chaotic oscillations and the level is also small enough for the assumption of minute perturbation for the system in chaos control. It is noted that the control signal is continuously generated in the OPF method even after the control is succeeded. This is different from the continuous control in which the control signal vanishes after the success of the control.

Figure 22.8 shows an example of an OPF control system for stabilization of chaotic laser output induced by optical feedback in a semiconductor laser. Since
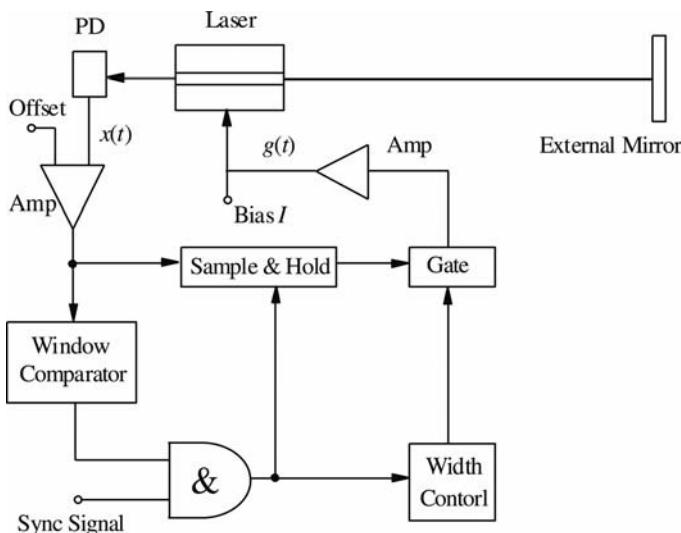
Fig. 22.8 Control of chaotic oscillation induced by optical feedback in semiconductor laser based on the OPF method.

the OPF technique is implemented using analogue and digital electronic circuits, the control can be performed very fast and is applicable to a variety of nonlinear systems. Different from the continuous control method, the electronic circuits used in the OPF method are not simple and the implementation may not be easy for a nonlinear system with fast response over nanosecond oscillations. It should be pointed out that the OPF method is essentially a limited case of the OGY algorithm, when the contracting direction of the chaos attractor is infinite in strength. In laser systems, the controls of chaotic oscillations have been successfully performed based on the OPF method. The OPF method has been applied for stabilization and control of class B lasers with slow relaxation oscillations, such as solid-state lasers, fiber lasers, and CO_2 lasers. In semiconductor lasers, the method is also applied to the control in optoelectronic hybrid systems.

The chaos control methods discussed above more or less require the detection of chaotic signal, the processing of the post-detection signal, and feedback of it to the laser. Therefore, it is sometimes difficult to implement the methods for fast response nonlinear laser systems in practical applications. There is a simple way to realize chaos control suitable for systems with fast chaotic oscillations. Based on the linear stability analysis for the steady states in chaotic semiconductor laser systems, we can derive the characteristic equation related to stable and unstable states of the system output [32, 33]. The real parts of the solutions for the characteristic equation derived from the linear stability analysis represent the damping rate of the oscillations and the imaginary parts denote the accompanying frequencies. The obtained frequencies are the candidates for periodic oscillations of unstable saddle node points which are embedded into the system close to the initial operating point. In accordance with this fact, the chaotic system can be controlled to a periodic or fixed state by modulating the accessible parameter with one of the frequencies obtained by the linear stability analysis. The control method works indeed as far as unstable periodic orbits are not far away from the operating point. In a semiconductor laser with optical feedback, a sinusoidal injection current modulation is the easiest way to perform the control. The modulation is applied to the bias injection current in Eq. (22.5) as

$$J = J_b \{ 1 + m \sin(2\pi f_0 t) \} , \tag{22.11}$$

where f_0 is the modulation frequency calculated from the linear stability analysis and m is the modulation index with small amplitude. There is an allowable range for the parameter values of f_0 and m for successful control. The robustness for the control depends on the extent of the attractor and the basin of each possible linear mode.

In the following, an example for the sinusoidal modulation control to the injection current in semiconductor lasers with optical feedback is given. Figure 22.9 is the plot of mode distribution calculated from the linear stability analysis for the system [32, 33]. Under the operating condition, the laser shows chaotic
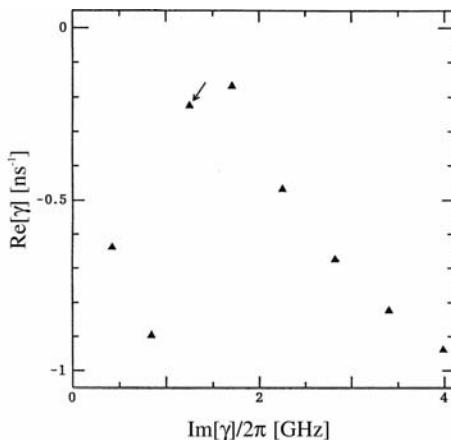
Fig. 22.9 Mode distributions calculated from linear stability analysis.

oscillations. All the calculated modes within this region have negative real values; therefore, the calculated modes are candidates for unstable periodic solutions. But, the stability of the modes and the robustness for the control are different from one mode to the others and must be investigated by using bifurcation diagrams for the control parameters. We focus on the mode indicated by the arrow in the figure and use this mode as the sinusoidal modulation control.

Figure 22.10 (a) shows an example of chaos control using a sinusoidal modulation to the injection current in a semiconductor laser with optical feedback. The sinusoidal modulation control is performed by modulating the injection current with the modulation frequency of $f_0 = 1.251$ GHz and the modulation index of $m = 0.021$ of the bias injection current. The modulation index is sufficiently small for satisfying the assumption of little effect for the original chaotic state to the system. A chaotic waveform in Fig. 22.10 (a) is controlled to a period-1 oscillation by the modulation of one of the mode frequencies as shown in Fig. 22.10 (b). Figures 22.10 (c) and (d) are the attractors for Fig. 22.10 (a) and (b), respectively, in the phase space of the laser output power and the carrier density. The chaotic attractor in Fig. 22.10 (c) is controlled to the periodic state in Fig. 22.10 (d). The robustness of the method with respect to parameter variations is an important issue. In this method, there is a finite modulation range of the parameters for effective control; for example, successful control is achieved within the range of several tens to a hundred MHz centered at the exact mode frequency. However, the extent of the attractor after the control is slightly deformed by the modulation. One important issue of chaos control is the response time after the control signal is switched on. The time required for successful control using sinusoidal modulation has been studied by Uchida et al. [34]. According to their results, the time required for reaching the stabilization has statistical distributions for each trial, but the characteristic time is
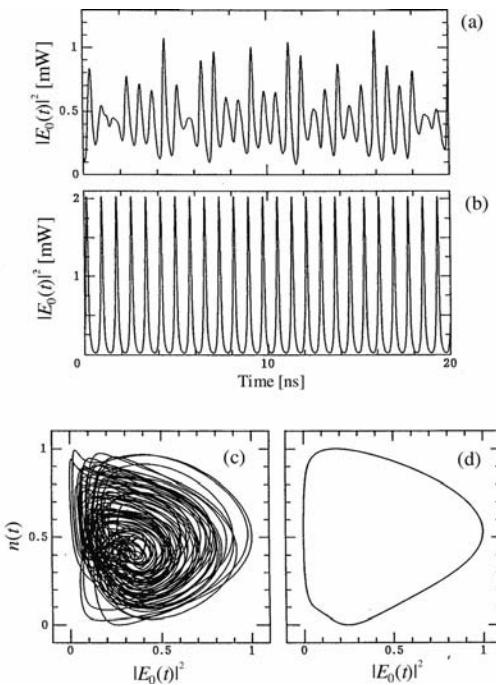
Fig. 22.10 Sinusoidal modulation control in semiconductor lasers with optical feedback. (a) Chaotic oscillation before control. (b) Controlled period-1 oscillation by a targeted mode modulation. (c) and (d) Attractors corresponding to (a) and (b).

roughly ten times of the laser relaxation oscillation time of the laser (equivalently ten times of the typical timescale of chaotic oscillations).

The main noise source in free-running semiconductor lasers is the spontaneous emission of photons in laser mediums. Noises in semiconductor lasers are greatly enhanced by optical feedback. The detailed definition and descriptions for the noise characteristics in semiconductor lasers can be found in the book by Pertermann [35]. In relation to the noise of the optical power δS to the mean power $\langle S \rangle$, the relative intensity noise (RIN) in semiconductor lasers is defined by

$$\text{RIN} = \frac{\langle \delta S^2 \rangle}{\langle S \rangle^2} , \tag{22.12}$$

where the optical output power from the laser is defined by $S(t) = \langle S \rangle + \delta S(t)$. Actually, the feedback induced irregular intensity fluctuation is not a noise but a chaotic fluctuation. However, the effects of the phenomena are similar to

noises in free-running semiconductor lasers. Therefore, we use the same notation for the feedback-induced irregular fluctuations.

The RIN induced by optical feedback form an external reflector is strongly dependent on the feedback level. At external reflectivity around 0.001% in intensity, the RIN has almost the same level as the solitary oscillation. Above this level, the RIN abruptly increases and reaches the maximum value at the external reflectivity of 0.1 to 0.01%. Without optical feedback, RIN for ordinary edge-emitting semiconductor lasers under solitary oscillations is less than −140 dB/Hz. However, in the presence of optical feedback, the RIN increases much higher than −125 dB/Hz in the feedback regions of chaotic and coherence collapse regimes. In the regions, we can observe the broadening of the oscillation linewidth, chaotic behaviors of the laser output, and the coherence collapse state of the laser [2]. A laser with a RIN above −125 dB/Hz cannot be used as a light source for optical data storage systems because of the increase of bit-rate errors. Even though the feedback level in this regime is very small, it affects much of the performance of the laser operation. To know the dynamics in this, feedback regions is also very important from a viewpoint of practical applications, such as the use for optical data storage systems, since the returned light from the disk surface in those systems is almost the same order. On the other hand, the RIN decreases with further increase in the feedback level. The noise characteristics are dependent not only on the reflectivity of the external mirror, but also on other system parameters such as the bias injection current and the external mirror position.

Unstable oscillation of semiconductor lasers subjected to optical feedback was stabilized by the introduction of a sinusoidal modulation to the injection current as shown in the previous section. Figure 22.11 shows the numerical result of
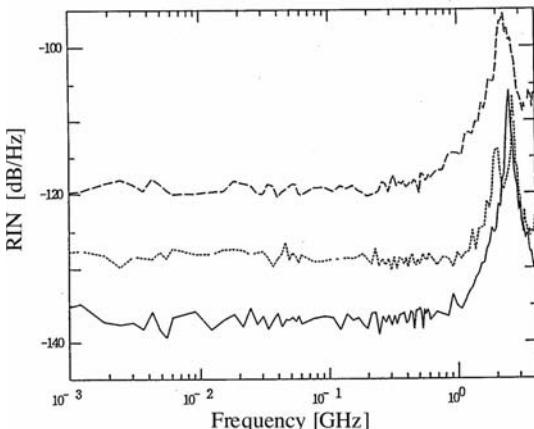
Fig. 22.11 RIN for sinusoidal modulation control. Solid line: RIN of solitary oscillation. Broken line: RIN for optical feedback without control. Dotted line: RIN for sinusoidal control.

the noise suppression by the sinusoidal modulation method [33]. The RIN of the solitary laser is ~ -140 dB/Hz in the lower frequency region (solid line). A frequency peak at about 3 GHz is the relaxation oscillation component. In the presence of optical feedback, the noise is extremely enhanced and it is about -120 dB/Hz in the lower frequency region as shown as the broken line in the figure. The noise level exceeds the allowed criterion for a light source of optical data storage systems. The dotted line shows the result of the control. One of the mode frequencies (in this case, it is 2.38 GHz) is chosen as a control frequency and the laser is modulated by this frequency through the injection current modulation. By the modulation, the laser shows synchronous oscillation (period-1) and the RIN in the lower frequency region is reduced to -130 dB/ Hz. The modulation amplitude is small, $m = 0.15$. The noise level attained by the control is enough for the requirement of a light source for the optical data storage system.

The modulation index of $m = 0.15$ used in Fig. 22.11 may be still larger from the viewpoint of chaos control. The modulation more or less affects the laser oscillation and closer investigation shows deviations of the chaos attractor from the original one. The modulation index must be less than about 0.01 for the ideal chaos control. Nevertheless, the laser is stabilized by rather a small signal compared with ordinary forced sinusoidal control without optimized frequency. In optical data storage systems, the suppression of optical feedback noise is the important issue. The light is reflected from a disk surface and is returned into the laser active layer. The feedback light induces much noise in the laser and causes serious problems for the performance of the data readout. In actual optical data storage systems, a high-frequency injection current modulation on the order of several hundreds MHz to one GHz has been employed to suppress feedback-induced noises [36, 37]. In such optical data storage systems, the modulation index over $m = 1.0$ was frequently used. The modulation depth is much larger than that of the chaos control and a laser is sometimes brought below the threshold by the modulation.

It was known on an empirical basis that there is a best modulation frequency for each optical data storage system. From the viewpoint of chaos control in semiconductor laser systems, the high-frequency modulation technique is closely related to the sinusoidal modulation control in chaos control in which the chaotic orbit is stabilized to a periodic oscillation, though the modulation depth is much larger than the expected chaos control. Strong modulation technique used for optical compact disk systems is considered as a forced oscillation to the light source. But, the method does not always work for every selected modulation frequency. Strong modulation to a semiconductor laser sometimes gives rise to unstable chaotic oscillations. Therefore, the optimized modulation frequency has some relation to the sinusoidal modulation control of chaos, even though the modulation frequency is selected on the empirical basis. Recently, a self-pulsating laser has been used for light sources of DVD in optical data storage systems. The chaos control algorithm introduced here may give us important information for the design of such devices and systems. The essence of

chaos control is that the control does not change the original dynamics of the nonlinear system. However, the original dynamics may be changed due to a very small but a nonnegligible modulation amplitude. In that case, the idea of chaos control is still effective for the control of an existing unstable periodic orbit as long as the modulation is small.

To decide the optimum frequency in the sinusoidal modulation control, we must establish a model for a real system and estimate the frequency. However, it is not easy to obtain all the parameter values of the system in advance. Nevertheless, we can guess the frequencies. The relaxation oscillation frequency of the laser is one of the candidates for the optimum frequency. Another one is the external cavity frequency and its higher harmonics. From the linear stability analysis, the mode frequencies of the optical feedback system are not always equal to the exact external cavity frequencies, but there exist mode frequencies close to the external cavity frequencies. As already discussed, there is a certain extent for the tolerance of the modulation frequency for a successful chaos control. In reality, which frequency is best for the control and suppression of noises, must be examined and tested by using each possible frequency. Noise induced by optical feedback is much suppressed by the best selection of the modulation frequency and, thus, the laser is stabilized with a small modulation power.

As an alternative modulation method for chaos control, we here show an example of the introduction of an extra mirror in the feedback loop to control chaotic oscillations in a semiconductor laser [38, 39]. Figure 22.12 shows the optical chaos control system using double external mirrors. One of the mirrors is the external mirror which gives rise to chaotic oscillations in the semiconductor laser and the second mirror is used for the control. In this system, a beat signal induced by the mixing of lights from the two mirrors plays the same role for a sinusoidal modulation as the bias injection current modulation. In the same manner as for the single mirror case with the bias injection current modulation, the linear stability analysis is applied to the rate equations with double external mirrors. However, the system is usually affected much by the second feedback mirror and the system might not fall into a nearby unstable periodic orbit by
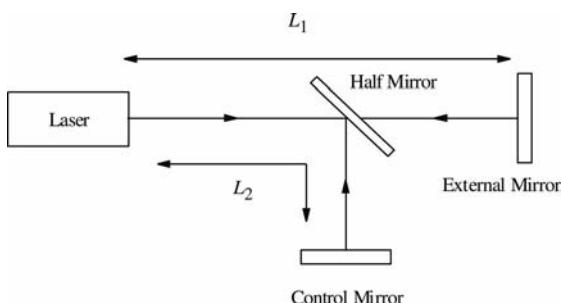
Fig. 22.12 Schematic diagram of optical chaos control system.

the control, but it is pulled apart from an accompanying antimode by the interference and is forced to another periodic or fixed state far from the original state. The system after the control may have a different attractor than the original one and, therefore, such a control is not categorized into chaos control with a small perturbation in the sense of OGY control. But, the technique is sometimes effective for stabilizing chaotic irregular oscillations. Rogister et al. experimentally controlled irregular oscillations of low-frequency fluctuations (LFFs) in semiconductor lasers induced by an external mirror using the second control mirror [40]. Without the second mirror in Fig. 22.10, the laser shows LFF oscillations within a certain range of the feedback of the external mirror. At this state, the laser is controlled to periodic or fixed state by appropriately choosing the feedback strength of the second mirror. The feedback level of the second mirror is estimated by the linear stability analysis as mentioned.

22.4
Control in Newly Developed Semiconductor Lasers

A semiconductor laser is essentially a stable class B laser; however, it is only true for edge-emitting lasers without any external perturbations which are described by simple rate equations with time development. Newly developed semiconductor lasers have additional degree-of-freedom compared with ordinary edge-emitting semiconductor lasers and they are no longer stable lasers. They show unstable chaotic oscillations without any external perturbations as discussed in Section 22.3. Therefore, the control of unstable oscillations in those lasers is an important issue in practical applications. Those lasers are either stabilized by external control or by installation of some control structures inside the device. To reduce unstable oscillations, the idea of chaos control is still effective for controls of those lasers.

In VCSELs, unstable oscillations such as polarization-mode switching, higher spatial mode excitations, and mode competitions have been reduced by introducing physical distortions to the laser materials. The polarization mode of VCSEL is also stabilized to a single mode by embedding quantum dots into the active layer. However, it is difficult to settle the problems only by such techniques. As an alternative method of VCSEL controls, optical injection from a different laser and optical feedback are used to stabilize the laser oscillations [41]. As a third technique, the excitation of higher spatial modes is suppressed and the laser is forced to stay to a single mode by a photonic structure installed at the top of the exit surface of the laser cavity [42, 43]. Here we briefly discuss the spatial mode stabilization of VCSELs by a photonic structure. Figure 22.13 shows an example of photonic structures and the controlled beam to the fundamental spatial mode [42]. A photonic structure in Fig. 22.13 (a) is installed at the top of the DBR reflector of the VCSEL cavity. Then only the fundamental spatial mode is excitable due to the limited band of the laser modes for a wide range of the bias injection current.
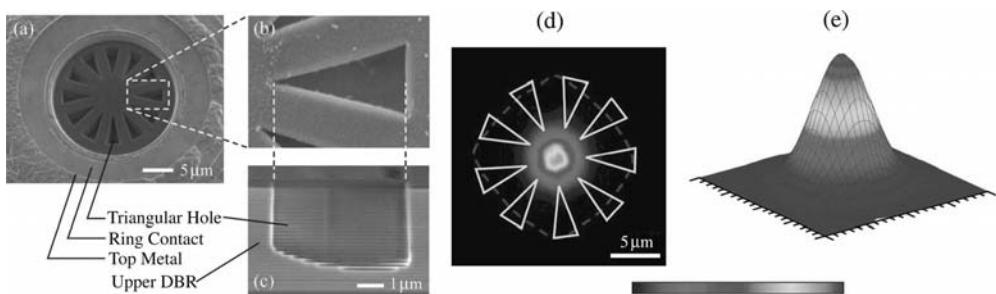
Fig. 22.13 VCSEL control by a photonic structure on the top of the exit facet. (a) Top view of photonic VCSEL. (b) Magnified top view and (c) its cross-section. (d) Near field pattern and (e) far field pattern of the VCSEL emission (©2004 AIP).

In BALs, filamentation discussed in Section 22.3 is one of the main instabilities to deteriorate strongly the performance of the laser oscillations. The quantum-dot structure is also effective to reduce filamentations of broad area laser oscillations. Quantum dots at an appropriate density are embedded into the active region of the laser cavity. In the presence of quantum dots, the dynamic motions of filaments are greatly suppressed and the laser can emit fairly stable beam compared with such as quantum-well semiconductor lasers. Figure 22.14 shows the comparisons of the beam qualities between quantum-dot and quantum-well lasers obtained by numerical simulations and experiments [19, 44]. The laser is a InGaAs quantum-dot laser (dot density 10^{11} cm^{-2}) of the strip width of 10 μm at the wavelength of 1.1 μm. As easily seen from Fig. 22.14 (a), the quantum-well laser has strong filamentations, while the quantum-dot laser is well-stabilized enough after the switch-on relaxation oscillation. The averaged beam profiles both for the simulations and the experiments are shown in Fig. 22.14 (b) and (c). The averaged beam profiles for quantum-well laser contain irregular peaks in their envelopes, which is the effect of filamentations on the order of picosecond. On the other hand, the good quality beam profiles are obtained for the quantum-dot lasers. The beam quality factor M^2 ($M^2 = (D/d)^2$: D and d being the observed and ideal Gaussian beam diameters), which is the measure of the beam quality compared to the ideal Gaussian beam, is much reduced in comparison with that of quantum-well lasers.

Another method of suppressing filamentations in BALs has been developed based on external control techniques. In the same manner as those in VCSELs, BAL can be stabilized by optical injection from a different laser or optical feedback. Here we discuss the control method based on optical feedback effects. Figure 22.15 is an experimental example of chaos control of BAL by optical feedback [45, 46]. The laser is a BAL with a stripe width of 100 μm and the output power of 1 W operating at pulse mode. The output power is once spatially filtered and is fed back to the active region by an external mirror with a spatial filter. Depending on the shape of the spatial filter, the filamentation can be con-
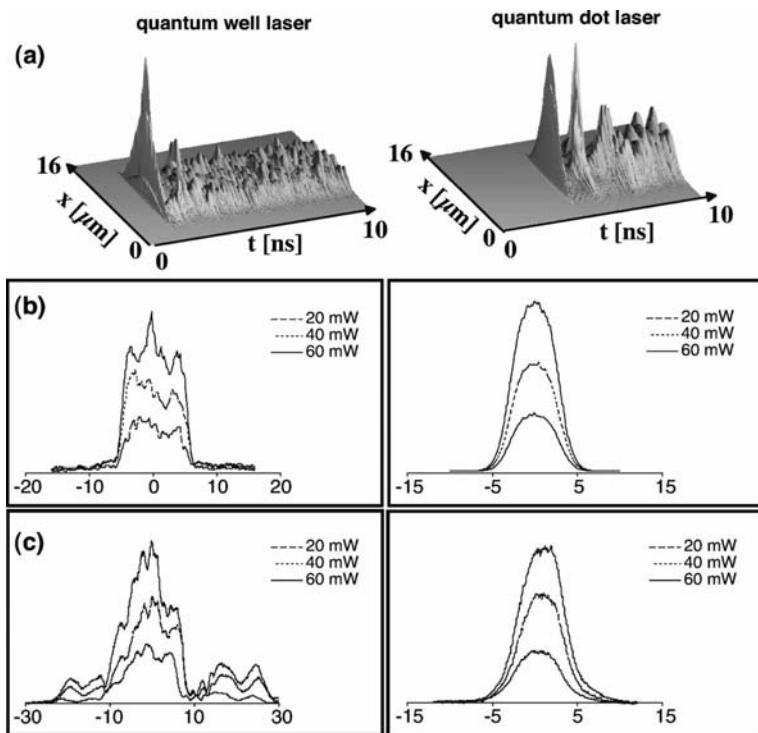
Fig. 22.14 Filamentation control by quantum-dot structure
in BAL. Left: quantum-well laser. Right: quantum-dot laser.
(a) Time resolved dynamic behaviors after laser switch-on
(numerical simulation). Averaged near-field patterns for
(b) theory and (c) experiments (©2004 AIP).

trolled and even eliminated under a certain condition of the filter configuration.
The length of the external mirror is 10 mm and the reflectivity of the mirror is
about 50% in intensity. The figure is a plot of near-field patterns at the laser exit
face observed by a streak camera. The horizontal axis is the position of the laser
exit face and the vertical axis is the time development for the laser oscillation.
The optical feedback is switched on at time $t = 0$ ns. Figure 22.15 (a) is a plot of
filamentation for a lower bias injection current at $I = 1.75 I_{th}$, while Fig. 22.15 (b)
is for a higher injection at $I = 3.0 I_{th}$. For the lower bias injection current, filamen-
tation is greatly suppressed by the feedback after a certain time lapse from the
switch-on (around 8 ns) and the averaged spatial beam profile becomes almost sin-
gle. For higher bias injection current, the filamentation is not completely elimi-
nated; however, it is still strongly suppressed compared to filamentations under
no control in Fig. 22.15. Usually, thermal lensing due to the high carrier density
concentration in the active layer may increasingly affect the beam characteristics
at high pump current, thus leading the degradation of the beam quality. Neverthe-
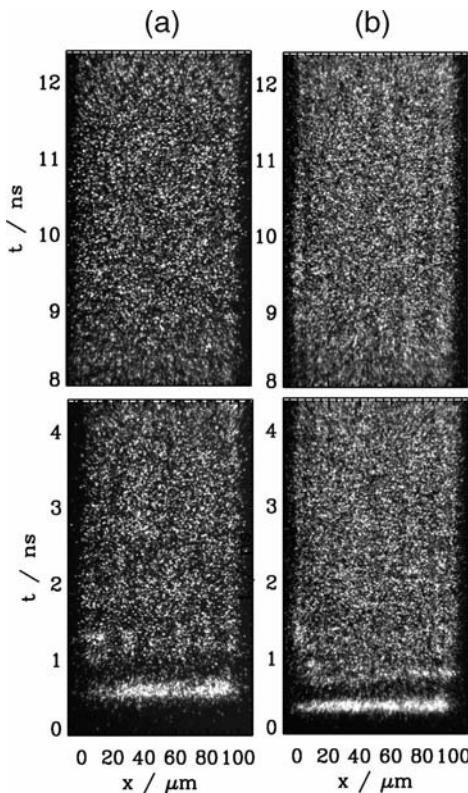
Fig. 22.15 Experimentally controlled filamentations in BAL by spatially filtered optical feedback. Near field patterns observed by a streak camera at the bias injection currents of (a) $I = 1.75I_{th}$ and (b) $I = 3.0I_{th}$ (©2003 OSA).

less, stabilization of the emission dynamics is still achieved by the scheme even at high operation currents. Fujita and Ohtsubo demonstrated chaos control in BALs based on the fact of coexistent states of chaos with optical feedback [47]. In their method, the laser is under chaotic oscillations by optical feedback at the initial state and the laser is controlled to another coexistent periodic or fixed state without changing the essential condition of the nonlinear system. By the control, the laser shows completely single states both for the transverse and longitudinal modes.

22.5
Conclusions

This chapter provided chaotic characteristics and controls in semiconductor lasers. Semiconductor lasers are categorized into stable class-B lasers, while they are very sensitive to the external perturbations such as optical feedback and opti-

cal injection. A rich variety of dynamics are observed in the laser output powers. Newly developed semiconductor lasers, which have different device structures than ordinary edge-emitting semiconductor lasers, originally have extra degrees-of-freedom and they are essentially unstable chaotic lasers even in their solitary oscillations. The dynamic is not only important from the basic studies in nonlinear optical systems, but it is also very important in terms of applications. The control of instabilities in semiconductor lasers, such as noise suppressions (actually suppressing chaotic irregular oscillations), are still important issues. Also unstable oscillations of newly developed semiconductor lasers are reduced or even stably controlled by introducing additional device structures. The essence of chaos control is that the control does not change the original dynamics of the nonlinear system. The discussions introduced here may not be necessarily based on the methods of chaos control in strict sense. However, the idea of chaos controls in this chapter may give us useful indications for the designs of such devices.

References

1 J. Ohtsubo, Chaotic dynamics in semiconductor lasers with optical feedback, In E. Wolf, editor, *Progress in Optics*, pages 1–84. North-Holland, Amsterdam **2002**.

2 J. Ohtsubo, *Semiconductor Lasers: Stability, Instability and Chaos*. Springer, Berlin **2005**.

3 E. Gehrig and O. Hess, *Spatio-Temporal Dynamics and Quantum Fluctuations in Semiconductor Lasers*. Springer, Heidelberg **2003**.

4 E. Ott, *Chaos in Dynamical Systems, second edition*. Cambridge University Press, Cambridge **2002**.

5 H. Haken, *Phys. Lett. A 53* (**1975**) p. 77.

6 H. Haken, *Light Volume* 2. North-Holland, Amsterdam **1985**.

7 G. H. M. van Tartwijk and G. P. Agrawal, *Prog. Quantum Electron.* 22 (**1998**) p. 43.

8 F. T. Arecchi, G. L. Lippi, G. P. Puccioni, and J. R. Tredicce, *Opt. Commun.* 51 (**1984**) p. 308.

9 L. W. Casperson, *IEEE J. Quantum Electron.* 14 (**1978**) p. 756.

10 *Special Issue, Instability in Active Optical Media. J. Opt. Soc. Am. B* 2 no. 1 (**1985**).

11 H. Li and K. Iga, *Vertical-Cavity Surface-Emitting Laser Devices*. Springer, Berlin **2002**.

12 R. W. Tkach and A. R. Chraplyvy, *J. Lightwave Technol.* 4 (**1986**) p. 1655.

13 R. Lang and K. Kobayashi, *IEEE J. Quantum Electron.* 16 (**1980**) p. 347.

14 A. Valle, J. Sarma, and K. A. Shore, *IEEE J. Quantum Electron.* 31 (**1995**) p. 1423.

15 J. Y. Law and G. P. Agrawal, *IEEE J. Quantum Electron.* 33 (**1997**) p. 462.

16 M. San Miguel, Q. Feng, and J. V. Moloney, *Phys. Rev. A* 52 (**1995**) p. 1728.

17 J. Martin-Regalado, F. Prati, M. San Miguel, and N. B. Abraham, *IEEE J. Quantum Electron.* 33 (**1997**) p. 765.

18 N. Fujiwara and J. Ohtsubo, *SPIE Proc.* 5349 (**2004**) p. 282.

19 E. Gehrig and O. Hess, *Phys. Rev. A* 65 (**2002**) 033804.

20 O. Hess and T. Kuhn, *Phys. Rev. A* 54 (**1996**) p. 3360.

21 I. Fischer, O. Hess, W. Elsässer, and E. Göbel, *EuroPhys. Lett.* 35 (**1996**) p. 579.

22 L. Rahman and H. Winful, *IEEE J. Quantum Electron.* 30 (**1994**) p. 1405.

23 D. Merbach, O. Hess, H. Herzel, and E. Schöll, *Phys. Rev. E* 52 (**1995**) p. 1571.

24 O. Hess, S. W. Koch, and J. V. Moloney, *IEEE J. Quantum Electron.* 31 (**1995**) p. 35.

25 E. Ott, C. Grebogi, and J. A. Yorke, *Phys. Rev. Lett.* 64 (**1990**) p. 1196.

26 K. Pyragas, *Phys. Lett. A* 170 (**1992**) p. 421.

27 K. Pyragas, *Phys. Lett. A* 181 (**1993**) p. 203.

28 A. V. Naumenko, N. A. Loiko, S. I. Turovets, P. S. Spencer, and K. A. Shore, *J. Opt. Soc. Am. B* 15 (**1998**) p. 551.

29 E. R. Hunt, *Phys. Rev. Lett.* 67 (**1991**) p. 1953.

30 R. Roy, T. W. Murphy, T. D. Maier, Z. Gills, and E. R. Hunt, *Phys. Rev. Lett.* 68 (**1992**) p. 1259.

31 Y. Liu and J. Ohtsubo, *Opt. Lett.* 19 (**1994**) p. 448.

32 Y. Liu, N. Kikuchi, and J. Ohtsubo, *Phys. Rev. E* 51 (**1995**) p. R2697.

33 N. Kikuchi, Y. Liu, and J. Ohtsubo, *IEEE J. Quantum Electron.* 33 (**1997**) p. 56.

34 A. Uchida, T. Sato, T. Ogawa, and F. Kannari, *IEEE J. Quantum Electron.* 35 (**1999**) p. 1374.

35 K. Petermann, *Laser Diode Modulation and Noise.* Kluwer Academic, Dordrecht **1988**.

36 A. Arimoto, M. Ojima, N. Chinone, A. Oishi, T. Gotoh, and N. Ohnuki, *Appl. Opt.* 25 (**1986**) p. 1398.

37 G. R. Gray, A. T. Ryan, G. P. Agrawal, and E. C. Gage, *Opt. Eng.* 32 (**1993**) p. 739.

38 Y. Liu, J. Ohtsubo, and S. Y. Ye, *Proc. SPIE* 2886 (**1996**) p. 120.

39 Y. Liu and J. Ohtsubo, *IEEE J. Quantum Electron.* 33 (**1997**) p. 1163.

40 F. Rosigter, P. Mégret, O. Deparis, M. Blondel, and T. Erneux, *Opt. Lett.* 24 (**1986**) p. 1218.

41 J. B. Altés, I. Gatare, K. Panajotov, H. Thienpont, and M. Sciamanna, *IEEE J. Quantum Electron.* 42 (**2006**) p. 198.

42 A. Furukawa, S. Sasaki, M. Hoshi, A. Matsuzono, K. Moritoh, and T. Baba, *Appl. Phys. Lett.* 85 (**2004**) p. 5161.

43 K. H. Lee, J. H. Back, I. K. Hwang, and Y. H. Lee, *Opt. Exp.* 12 (**2004**) p. 4136.

44 E. Gehrig, O. Hess, C. Ribbat, R. L. Sellin, and D. Bimberg, *Appl. Phys. Lett.* 84 (**2004**) p. 1650.

45 S. K. Mandre, I. Fischer, and W. Elsässer, *Opt. Lett.* 28 (**2003**) p. 1135.

46 S. K. Mandre, I. Fischer, and W. Elsässer, *Opt. Commun.* 244 (**2005**) p. 355.

47 Y. Fujita and J. Ohtsubo, *Appl. Phys. Lett.* 87 (**2005**) 031112.

23

From Pattern Control to Synchronization:
Control Techniques in Nonlinear Optical Feedback Systems

Björn Gütlich and Cornelia Denz

Historically interest in the control of nonlinear optical systems dates back to the discovery of the laser. The laser itself may be considered as a prototype of a nonlinear optical system. It consists of a nonlinear optical material placed into an optical cavity, which provides a feedback mechanism. The nonlinear nature of the laser, e.g., reveals itself in the transcritical bifurcation of the laser emission. Most often however, the nonlinear dynamics occurring in lasers are restricted to longitudinal modes in order to meet the demands of applications – namely high output power and uniform beam profiles. The whole range of complex nonlinear dynamics resulting in temporal and spatial instabilities, which come into play, if the laser dimensions are extended allowing for transverse modes, are generally considered as unacceptable for application. The suppression of nonlinear characteristics to create a well-defined laser output is no longer feasible in a spatially extended device such as vertical cavity surface emitting lasers (VCSELs). Therefore, control methods for such nonlinear spatial optical systems are required. Meanwhile, it is widely discussed not only to consider optical nonlinearity as harmful, but to use it for the implementation of all optical concepts for information processing. Suggestions for potential applications range from all optical routing and switching of optical information to optical data storage, methods of image recognition, and data encryption. For these applications, the control of nonlinear optical system and their spatiotemporal complex dynamics becomes even more obviously indispensable for it will not be sufficient to only suppress unwanted temporal or spatial complexity, but to realize control schemes, which allow us to address and select a certain target state, are required. Thus, the output needs not only be predictable, but control moreover must define the system output at a given input to the nonlinear system in a reliable manner according to the intention of the user.

Differently from time-dependent one-dimensional systems or coupled networks of one-dimensional constituents, the evolution of spatially extended continuous systems is often dominated by nonlocal effects such as diffraction or diffusion, which cause a continuous nonlocal spatial coupling. At the same time these nonlocal effects create the richness of the observed transverse structures

as well as they make the categorizing of the observed spatiotemporal dynamics and in consequence also its control more complicated. Therefore, in spatially extended and continuous systems often the simultaneous control of the complete transverse space is necessary for the implementation of control. Thus, optical experiments posses several fundamental advantages for implementing spatiotemporal control. Differently from other physical systems the dominant system parameter – the optical field – is directly observable in its amplitude and phase and both quantities can easily be manipulated. Therefore, a direct control of the complete optical field is feasible. Furthermore, optical fields have the inherent advantage that transverse control operations can be processed in parallel as opposed to sequentially. In particular the Fourier transformation is performed all optically and in parallel at the speed of light by a simple lens. Consequently, the realization of different operations such as convolutions or calculations of correlations can also be accomplished with plain all-optical schemes. Therefore, the demand for simultaneous control of the complete transverse space can easily be met in an optical system.

23.1
Control Methods for Spatiotemporal Systems

At this point, we will refrain form categorizing potential control schemes for spatiotemporal optical systems, which likely are as diverse as the rich spatiotemporal phenomena observed in these systems, instead we refer the reader to Part II on the control of space time chaos, which gives a more general description. Nonetheless we will here define some basic concepts on control, which will be used in context of this contribution. Spatiotemporal control can be *open loop* or *closed loop*. Concepts using open-loop schemes work without a feedback mechanism of the control and the control consist of a predefined signal, which is imposed onto the nonlinear system. In closed-loop schemes a feedback of the control signal to the actual system state exists. The control signal is derived from a comparison of the actual system state with the intended target state.

In the control schemes, either an approach of positive or negative control can be taken. In a *positive control* scheme the control signal, which often will be the target state, is added to the system; thus, the target state is amplified in the system. In a *negative control* scheme, the control signal is subtracted from the uncontrolled signal; thus, the deviations from the target state must be subtracted from the system to reach a target state.

An important difference between the persistent control (open-loop) and negative closed-loop control schemes is the vanishing of the control signals, when the target state is reached, for the latter case. If the control signal vanishes at the target state, the control can also be called *noninvasive*. This term reflects the fact that application of control in principle does not change the nonlinear system itself. The control only serves to select a certain solution from the manifold of system attractors and stabilizes the system at one specific target attractor. As

the selected solution already is a stationary solution of the system further control in principle will not be necessary, when the target state is reached. A remanent level of control however will always be present in real experimental situations due to the presence of noise.

Other control methods such as positive closed-loop control, persistent control and methods, which manipulate the potential system states, e.g., in restricting the possible system modes, in consequence must be called *invasive* methods as the control signal cannot vanish. Persistent external control will additionally modify the properties of the uncontrolled system in any case. In order to emphasize this conceptual difference between the closed-loop method of positive feedback and the open-loop method of persistent control, we will also refer to persistent external control as *forcing* in the following. Due to the fact that forcing is an open-loop method in this case not only the system inherent 'natural' solutions of the system can be studied, but also other external states can be applied as forcing. It can be expected that the system follows the forcing input, if it is a solution of the unforced system, while it remains open how the system responds to other forcing inputs.

A completely different approach to controlling spatiotemporal complexity is the fascinating phenomenon of *synchronization*. The term synchronization derives from the locking of the temporal behavior of two coupled pendulum clocks. Meanwhile the term has also been extended to the spatiotemporal domain. Therefore, one defines spatiotemporal synchronization as the locking of the spatiotemporal dynamics of coupled (nonlinear) spatiotemporal systems. Induced by the coupling, which can be small in comparison to the amplitude of the synchronized systems, the nonlinear spatiotemporal dynamics thus becomes completely or partially entrained by the spatiotemporal dynamics of another system. Therefore the complex dynamics of spatiotemporal chaos can control another complex spatiotemporal chaotic system enabling the implementation of encryption schemes in data communication via synchronized spatiotemporal chaos.

23.2
Optical Single-Feedback Systems

Here we will report on the progress, which has been made in controlling spatially extended nonlinear optical systems. At this, we will restrict ourselves to a model system of nonlinear optics the so-called class of single-feedback systems [1–22]. A single-feedback system consists of a nonlinear optical material and a single mirror, instead of two mirrors needed for the construction of a resonant cavity. Therefore, one can casually denote a single-feedback system as a semicavity. While these systems allow for a simplified theoretical and experimental treatment, they show at the same time a rich variety of self-organized and spontaneous formation of spatiotemporal complex structures ranging from well ordered pattern, solitary solutions to turbulent chaotic states [16–22]. The model

character of single-feedback systems stems from this combination of rich nonlinear effects and simplicity of numerical simulations. Since the nonlinear behavior is well known for many single-feedback systems [5, 12–15], they are also ideal for investigations on the control of spontaneous optical pattern and spatiotemporal complexity. The methods presented here are generic for many spatial optical systems and therefore can be adopted to other nonlinear optical systems, if system specifics are disregarded. Particularly, we will treat the control of spatiotemporal structures at two experimental model configurations here. In the first configuration, which uses a photorefractive nonlinearity, the feedback acts coherently at the nonlinear medium. The single-feedback scheme of the second model system, which uses a liquid crystal light valve (LCLV) as nonlinearity, is based on an incoherent mechanism. Both systems exhibit high nonlinear sensitivities, and thus investigation of spontaneous pattern formation and its control can be investigated at comparatively moderate laser powers. At the model system with the photorefractive nonlinearity, we will study invasive and noninvasive control methods, which operate in the Fourier space. At the second example of incoherent feedback, we will introduce an invasive control method acting in real space. Furthermore, we will demonstrate that this invasive control method can be interpreted as the spatial counterpart of synchronization, and we will then lead on to discuss first evidence of spatiotemporal synchronization of an optically turbulent state.

23.2.1
A Simplified Single-Feedback Model System

If we consider the self-organized formation of spatiotemporal structures [23], single-feedback systems can be regarded as the most basic nonlinear optical configuration which supports such spontaneously formed structures. First theoretical evidence on spontaneous pattern formation in optical single-feedback systems has been obtained by Firth et al. in the nineties [1].

In an idealization we will consider a single-feedback configuration with the simplest nonlinearity – a Kerr nonlinearity:

$$n = n_1 + n_2 I, \tag{23.1}$$

where the refractive index of the nonlinear optical material depends linearly on the intensity of the light field. The main ingredients for constructing a single-feedback system are a nonlinear optical medium, a feedback mirror and diffraction which is induced by a distance $L/2$ of free-space propagation between a mirror and a nonlinear medium (a schematic setup is depicted in Fig. 23.1).

A spatially extended planar electromagnetic wave E_{in} propagates in the forward direction through the nonlinear optical material in the setup. According to the refractive index of the nonlinear optical medium, the optical wave is modulated in its phase profile. The modulated wave reflects at the feedback mirror and passes the nonlinear medium again in the backward direction. After inter-
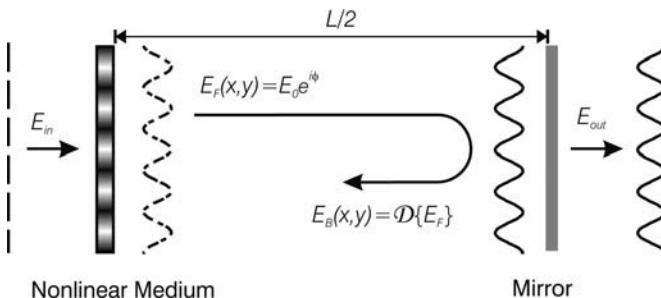
Fig. 23.1 Scheme of optical single feedback: A planar light wave E_{in} is modulated in its phase by a nonlinear optical medium E_F. E_F diffracts ($\mathcal{D}$) and is reflected at a mirror. After propagation the intensity of the field E_B is modulated. Interaction with the non-linear medium modifies the initial phase modulation of E_{in}. The feedback results in spontaneous formation of spatial optical structures, which are also observed in the optical field E_{out}.

action with the nonlinear medium, the waves leave the system. Thus, the optical beam interacts with the system once only and does not pass the system multiple times like in a resonant optical cavity. From this the expression *single feedback* is derived.

On its path from a nonlinear medium back to the nonlinear medium the optical wave experiences diffraction, while it propagates freely over the distance L. Mathematically diffraction is taken into account by the propagation operator

$$\mathcal{D}(E_F) = \exp\left(\frac{-iL}{2k_\lambda}\nabla_\perp^2\right)E_F, \qquad (23.2)$$

which can be derived from the optical wave equation applying the slowly varying envelope (SVE) approximation. The propagation distance L is scaled to the wavenumber k_λ of the light field. The transverse Laplacian $\nabla_\perp^2$ of the propagation operator acts at the modulated forward propagating wave E_F and transforms the induced phase profile into an amplitude modulation of the backward-propagating field E_B. The occurrence of this amplitude modulation can also be explained in terms of the so-called Talbot effect. Talbot discovered that a phase profile with a given spatial wavenumber transforms itself into the identical amplitude modulation, if the light wave propagates freely over a characteristic length, the Talbot length [24, 25].

Forward and backward-propagating light fields superimpose within the nonlinear medium. The resulting light field interacts with the nonlinear medium and changes its refractive index depending on the intensity distribution of the light field. If we assume the nonlinear medium to be optically thin, the nonlinear optical response and diffraction occur spatially well separated, and therefore both effects can also be treated separately in the experimental setup and the theoretical model. The evolution of the transverse optical field is observed

by extracting a fraction of the feedback wave E_{out} at the feedback mirror. Commonly the equivalent of light field's intensity distribution at the reentrance face of the nonlinear medium (near field), which propagates in the backward direction, or its spatial Fourier transform (far field) is observed.

Increasing the control parameter of the system, which is the light intensity in our introductory example, up to a threshold, the primarily stable homogeneous planar wave solution becomes modulationally unstable against spatial noise at a critical spatial wavenumber k_c [1]. Typically the critical wavenumber k_c is the same which appears in the Talbot effect-related self-imaging [4]. In the Fourier space, the critical wavenumber k_c represents a ring structure centered around the zero-order plane wave solution. Generally, distinct spatial modes start to grow from noise at the critical k_c ring and thus not the whole k_c ring becomes exited at the threshold. As a consequence, different spatial pattern and structures evolve spontaneously in the transverse plane of the light field. Most commonly hexagonal patterns are observed just above the threshold.

Inspired by Firth's pioneer work the spontaneous formation of transverse pattern has been studied experimentally and theoretically in many different configurations in the following decade [1–22]. Among the nonlinear materials investigated are atomic vapors [9, 12], organic materials [26], liquid crystals [4, 27], photorefractive crystals [13, 15], and so-called LCLVs [5, 8]. Meanwhile, these systems are well studied, models for the systems exist and the patterns which evolve in certain parameter regimes are quite well known. Here, we will restrict ourselves to the discussion of two distinct model systems at which we will exemplary demonstrate different control methods for spatially extended systems. The first model system uses a photorefractive crystal and the second a LCLV as nonlinearity. Besides the high nonlinearities observed in both systems, the photorefractive system has been chosen as an example for a nonlinearity which is based on a coherent mechanism and because of the high diversity of observed periodic patterns. The photorefractive effect is a bulk effect and thus propagation must be included in the theoretical description. The LCLV nonlinearity of the second model system can in contrast be considered as optically thin and its nonlinearity is based on an incoherent mechanism. The advantages of the LCLV model system are the high aspect ratios of the observed patterns, which also allow for the observation of disordered pattern domains and defects. In LCLV systems thus optical turbulence can easily be induced and furthermore a bistability allows for the observation of solitary structures.

23.2.2
The Photorefractive Single-Feedback System – Coherent Nonlinearity

Spontaneous formation of optical pattern in a single-feedback experiment with the coherent photorefractive nonlinearity has been first reported by Honda in 1993 [13]. In contrast to the Kerr-slice medium considered in Section 23.2.1, a photorefractive crystal cannot be assumed to be optically thin, but must be treated as a bulk medium. Therefore, nonlinear wave propagation within the
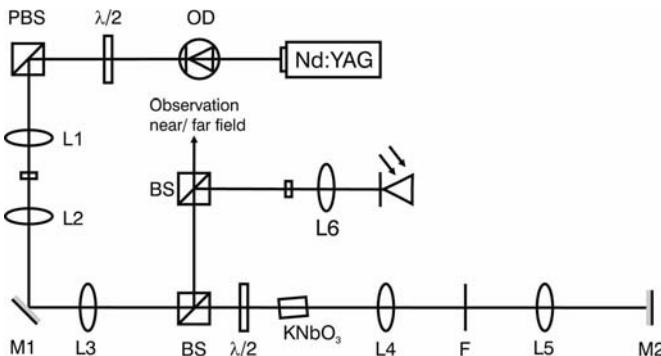
Fig. 23.2 Experimental setup of the photorefractive single-feedback system. The 4f-feedback arm projects a virtual mirror (M2) in a distance $d/2$ of the crystal exit face. Additionally the Fourier plane is accessible in the feedback arm (F). OD: optical diode; M: mirrors; L: lenses; BS: beam splitter; $\lambda/2$: half-wave plate.

nonlinear medium has to be taken into account in our consideration, which causes additional nonlocal effects and likely contributes to the richness of optical structures observed in this system [15]. In experiment iron-doped $KNbO_3$, crystals are used most commonly as photorefractive material, but spontaneous pattern formation in single-feedback configuration has also been observed in $BaTiO_3$ and $LiNbO_3$ [28, 29].

The experimental setup of the photorefractive single-feedback system, which is depicted in Fig. 23.2, follows along the line of the principle described in the previous section. The iron-doped photorefractive crystal is illuminated by a focused laser beam. After the crystal, a feedback assembly with a moveable mirror (M2) follows. Between the feedback mirror and photorefractive crystal, an optical 4f-configuration consisting of the lenses (L4) and (L5), which all-optically performs a spatial Fourier transformation and its reverse operation at the speed of light, is inserted. Besides providing a Fourier plane (F) at the focal point between both the lenses allowing for operations in the Fourier space, this configuration creates a virtual feedback mirror. Thus the configuration allows to position the image of the feedback mirror inside the crystal, which would be impossible if the mirror (M2) was placed directly behind the crystal. A frequency-doubled $Nd:YAG$ laser operating at 532 nm cw (output power: 100 mW) is used as a light source. A half-wave-retardation plate in combination with a polarizing beam splitter allows the variation of the input intensity, while an optical diode (OD) prevents back reflections into the laser. The optical beam is spatially high pass filtered between the lenses (L1 and L2), thus creating a uniform Gaussian beam profile. The lens L3 focuses the Gaussian beam into the photorefractive crystal which is tilted by approximately 5° to avoid parasitic reflections at the crystal faces. After passage of the feedback system, the evolution of the trans-

verse intensity distribution is analyzed using a fraction of the beam, which is reflected at BS1. For the purpose of beam analysis, the near field (beam profile at the exit face of the crystal) and the far field (Fourier transform) can be imaged to a CCD camera. The intensity of the backward-propagating light field can be measured with a photodiode.

23.2.3
Theoretical Description of the Photorefractive Single-Feedback System

Within the photorefractive crystal, the forward- and backward-propagating light fields interfere coherently. The resulting spatially inhomogeneous intensity distribution induces the excitation of charge carriers into the conduction band of the photorefractive crystal. These charge carriers are internally redistributed by different mechanisms such as drift and diffusion. The redistribution in turn results in the creation of a space charge electrical field, which is transformed into a modulation of the refractive index via the linear electrooptic effect [30]. Thus, the interference of the light fields results in a modulated refractive index due to the photorefractive effect, which actually behaves like a saturable Kerr nonlinearity. The intensity dependence of the refractive index modulation derives itself from the light-induced excitation of charge carriers, while the saturability of the nonlinearity is caused by the restricted number of excitable charge carriers. The action of the photorefractive effect can be interpreted in terms of a wave mixing process, which allows for energy exchange between the incident beams mediated by the refractive index grating due to a phase shift between the interference and the refractive index grating. This wave-mixing process can be described by two differential equations for the light fields A_1, A_2 in SVE approximation. A third equation describing the temporal evolution of the complex amplitude of the refractive index grating Q completes the model of the photorefractive system [31, 32].

$$
\begin{aligned}
&\partial_z A_1 + if \triangle_\perp A_1 = -Q A_2, \\
&\partial_z A_2 + if \triangle_\perp A_2 = Q^* A_1, \\
&\tau(I) \partial_t Q + Q = \gamma \frac{A_1 A_2^*}{|A_1|^2 + |A_2|^2}.
\end{aligned}
\tag{23.3}
$$

In these equations, the propagation coordinate z is scaled by the crystal length l, and the transverse Laplacian $\triangle_\perp$ is scaled by the beam waist w_0. τ accounts for the intensity-dependent relaxation time of the photorefractive effect. γ is the photorefractive coupling constant, which takes the role of the control parameter in the system. Experimentally, the coupling γ is modified by rotating the angle of the linear polarization of the incident beam. Therefore, the projection of the light field onto the c-axis of the photorefractive crystal and, i.e., the effective linear electrooptic coefficient is modified. According to the effective electrooptic

coefficient, the coupling between light field and refractive index modulation changes.

23.2.4
Linear Stability Analysis

A linear stability analysis of the system, which was performed by Honda and Banerjee [14] and extended by Schwab [15], yields the threshold condition for the spatial modulational instability:

$$\cos(wl)\cos(k_dl) + \frac{k_dl}{wl}\sin(wl)\sin(k_dl) + \frac{\gamma l}{2wl}\sin(wl)\cos(k_dl(1+2d)) = 0, \quad (23.4)$$

with the normalized wavenumber $k_d = k_x^2/(2k_0n_0)$, and the normalized position of the virtual mirror $d = n_0l/l$ and $wl = \sqrt{(k_dl)^2 - (\frac{1}{2}\gamma l)^2}$, respectively. The experimental determination of the curve of marginal instability for a fixed propagation distance d and the scaling of the critical wavenumber under variation of d are discussed in Section 23.3.1. In Fig. 23.6 of this section, the theoretical curve can also be found.

The most dominant pattern, which spontaneously evolves in experiment due to the spatial modulational instability, is a hexagonal pattern. However, more complex patterns can also be observed, if the virtual image plane is moved inside the crystal ($-0.8 < d < -0.3$). Typical near and far field images of the experimentally observed patterns are shown in Fig. 23.3. From the viewpoint of application it would now be interesting to access the whole range of system inherent pattern so-

a   b   c   d
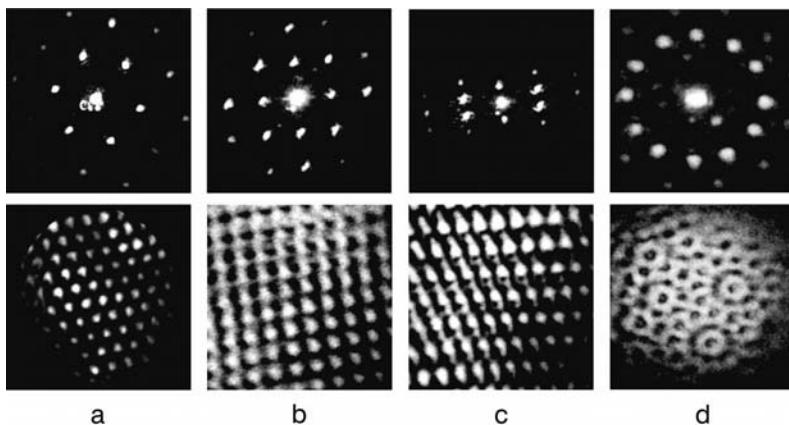
Fig. 23.3 Pictures of spontaneous patterns in the photorefractive single-feedback system: (a) hexagonal pattern, (b) square pattern, (c) squeezed hexagonal pattern, and (d) dodecagonal pattern. The upper row shows the far field and the lower row shows the near field of the patterns. Images (b)–(d) are taken in the multiple pattern region ($-0.8 < d < -0.3$). Pictures courtesy of M. Schwab.

lutions. Thus, suppressing the predominant pattern solutions in favor of stabilizing other unstable system inherent pattern solution is of interest. In a more fundamental approach control can also serve to investigate the nonlinear process responsible for self-organized pattern formation in experiment. But before we go on to discuss application of such control methods at spatially periodic pattern by using Fourier techniques, we will first introduce the second model system.

23.2.5
The LCLV Single-Feedback System – Incoherent Nonlinearity

The second single-feedback model system, at which we will study spatiotemporal optical control techniques, uses a so-called LCLV as nonlinearity [5–8]. In contrast to the previously discussed system, the feedback mechanism in this system acts incoherently. A LCLV is a hybrid device and functions as an optically-addressable spatial light modulator (OASLM). It consists of two functional layers – namely a readout and a writing side – and provides a saturable Kerr nonlinearity. The LCLV transforms an intensity distribution $I_w(x, y)$ incident onto its writing side, which consists of a photoconductive layer, into a modulation of the extraordinary polarization of the refractive index $n(x, y)$ of the readout side, which consists of a liquid crystal layer [33]. Both functional layers of the device are separated by a dielectric mirror. Thus, a planar wave incident onto the readout side of the LCLV is reflected at the internal mirror and leaves the LCLV in the backward direction, while its phase distribution $\phi(x, y)$ is modulated in dependence on the writing intensity I_w according to

$$\tau \partial_t \phi - l^2 \nabla_\perp^2 \phi + \phi = \phi_{\max} \left\{ 1 - \tanh^2(S(I_w, U_{\text{ext}})) \right\}$$
$$S(I_w, U_{\text{ext}}) = S_0 \frac{\kappa_1 I_w + 1}{\kappa_2 I_w + 1} \frac{U_{\text{ext}} - U_{\text{th}}}{U_0}. \tag{23.5}$$

This model equation for the nonlinear response of the LCLV reproduces the Kerr like behavior of the nonlinearity [5, 34]. A restricted spatial resolution of the device has been taken into account as an effective diffusion length l, while the dynamic behavior of the nonlinearity is included in the first temporal derivative of the phase as an effective response time τ. U_{ext} is an AC bias voltage, which is applied at the LCLV over transparent electrodes. $\phi_{\max}$, S_0, κ_1, κ_2, U_{th} and U_0 are device-specific fit parameters.

Due to the internal reflection of the planar readout wave, the experimental realization of the LCLV single-feedback scheme, which is depicted in Fig. 23.4, is not as straightforward as in the previously discussed experiment.

A planar input wave (E_p) from a cw Nd:YAG laser (output power 100 W) is expanded. It enters the LCLV, where it experiences a phase modulation $\phi(x, y)$ according to Eq. (23.6) and leaves the device after reflection at the internal mirror in the backward direction. A fraction of the phase-modulated pump wave is then reflected into the feedback loop by beam splitter (BS1), where the optical wave propagates freely over a distance L and i.e. experiences diffraction. Similar
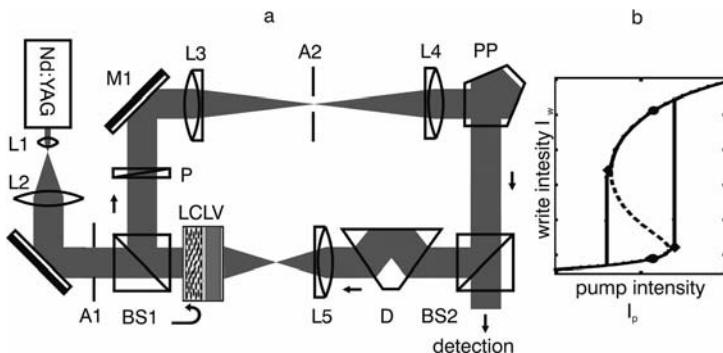
Fig. 23.4 (a) Schematic setup of the LCLV single-feedback system. Please refer to the text for a detailed description. (b) In polarization mode ($C \neq 0$) a bistability between a dark uniform and a pattern bright solution is observed, which enables the formation of solitary structures.

to the description in Section 23.2 the free-space propagation can be modeled according to

$$I_w = \left| \exp\left(\frac{-iL}{2k_\lambda}\nabla_\perp^2\right)\left(Be^{-i\phi} + C\right)E_p \right|^2 . \tag{23.6}$$

In addition to the propagation operator ($\exp\left(\frac{-iL}{2k_\lambda}\nabla_\perp^2\right)$) modulations of the polarization state of the feedback wave induced by the birefringent liquid crystal layer and a polarizer (P) in the feedback loop (B, C) as well as the nonlinear phase modulation $e^{(-i\phi)}$ must also be included [5]. B and C are amplitude factors, which account for the polarization effects and are derived from a Jones formalism [5]. The intensity distribution $I_w(x, y)$ resulting from free-space propagation is imaged to the photoconductive writing layer of the LCLV by different optical components like lenses (L), mirrors (M), a dove prism (D), and a penta prism (PP). In rotating the dove prism (D) a rotation of the intensity distribution $I_w(x, y)$ with respect to the phase modulation $\phi(x, y)$ induced by misaligned mirrors can be balanced. The penta prism serves to create an even number of reflections. At the photoconductive writing layer of the LCLV the intensity distribution incoherently induces the modulation of the liquid crystal's refractive index, thus closing the feedback loop. A fraction of the feedback beam is extracted at a beam splitter (BS2) for the detection of near and far field.

23.2.6
Phase-Only Mode

Like in the example of the Kerr nonlinearity in Section 23.2.1, the control parameter of the LCLV system is the input intensity. Analytic solutions for the system do

not exist. The linear stability analysis for phase-only modulation (i.e., if $C = 0$ and $B = 1$ in Eq. (23.6)) however yields for the curve of marginal instability:

$$\sigma \sin\left(\frac{L}{2k_\lambda} k^2\right) - l^2 k^2 - 1 = 0, \tag{23.7}$$

with k being the spatial wavenumber of the noise, and σ the sign of the nonlinearity. A positive sign of σ indicates that the nonlinearity acts self-focusing, while a negative sign indicates a self-defocusing nonlinearity. A symmetry in the model equation allows us to switch the character of the nonlinearity by using either positive or negative propagation lengths L. Similarly to the photorefractive experiment, a negative propagation L can experimentally be realized by projecting a virtual image plane to the writing side of the LCLV. At threshold of the modulational instability, hexagonal patterns are generally observed in phase-only ($C = 0$) mode (Fig. 23.5 (a)). Even though numerical analysis also predicts the presence of other pattern solutions like squares and stripes, these solutions are experimentally less stable in comparison to hexagons and thus are typically not observed [5, 7]. If the pump intensity is raised, the patterns become increasingly disordered (Fig. 23.5 (b)), as the whole critical k_c wave vector ring becomes excited instead of the distinct angular modes of a single hexagon orientation. Consequently, higher order wavenumbers $k_c^{(n)}$ become modulationally unstable. Finally, if the laser intensity is increased further additionally a dynamic instabili-
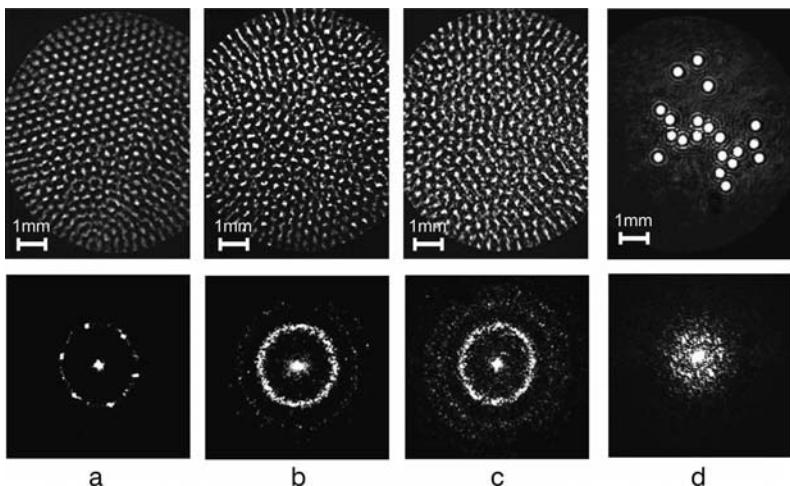
Fig. 23.5 Spontaneous pattern in the LCLV system: (a) hexagonal pattern ($I_{in} = 2\,I_{thr} = 200\,\mu W/cm^2$), (b) disordered static hexagonal pattern ($I_{in} = 4\,I_{thr}$), (c) spatiotemporally chaotic state ($I_{in} = 6\,I_{thr}$), and (d) interacting solitary structures. Images in the upper row depict the near field; the lower row shows the far field). Images (a)–(c) have been taken in the pure phase modulation mode ($C = 0$) and with defocusing nonlinearity ($L = 30$ cm). Image (d) is taken in polarization mode ($C \neq 0$) with a focusing nonlinearity ($L = -10$ cm) (images (a)–(c) printed with kind permission of E. Benkler, R Neubecker, © Tectum Verlag [7]).

ty of the structures sets in, which results in spatiotemporally complex patterns (Fig. 23.5 (c)). Even though yet no rigid theoretical definition for spatiotemporal chaos exists to our knowledge, in the literature these system states have been denoted as spatiotemporal chaos or optical turbulence [35–37].

23.2.7
Polarization Mode

If $C \neq 0$, a modulation of the polarization state is induced on top of the modulation resulting from the nonlinear phase shift ϕ. In combination with a polarizer in the feedback loop, the modulation of polarization state results in an additional modulation of the feedback intensity I_w. In a space-independent notation, Eq. (23.6) can be rewritten as

$$I_w = a\left(1 + \beta \cos \phi^0\right) I_p)$$
$$\phi^0 = \phi_{\max}\left\{1 - \tanh^2(S(I_w, U_{\text{ext}}))\right\}, \tag{23.8}$$

where $a = B^2 + C^2$ and $\beta = \frac{2B^2}{a}$. Induced by the cos-term in Eq. (23.9), which depends on the external bias voltage, a bistability of the writing intensity $I_w(I_p)$ can be observed in the system (see Fig. 23.4 (b)). Spontaneous formation of localized structures is observed [5, 6] at parameters where the system shows bistability. An example of these spontaneously forming bright localized structures is depicted in Fig. 23.5 (d). Commonly these spatially localized objects are also referred to as solitary structures or dissipative feedback solitons [38].

23.2.8
Dissipative Solitons in the LCLV Feedback System

In the most rigid definition a soliton is the solution of an integrable nonlinear wave equation. Due to the fact that these analytic solutions can interpreted as nonlinear objects, which obey to a law of conservation, the shape of these objects is preserved during propagation and even when they interact. However, the two-dimensional nonlinear optical wave equation is not integrable and thus analytic solutions do not exist. None the less spatial optical solitary solutions are observed, which form due to a balance between diffraction and nonlinear self-focusing. Thus their shape is preserved during propagation. Due to the non-integrability of the wave equation generally spatial optical solitons can interact with each other and do not obey to a law of conservation. These so-called spatial optical solitons either form, when light propagates in single pass configuration through a saturable nonlinear optical bulk medium [15, 39–41], or alternatively they can form in nonlinear optical resonators [42, 43] or single-feedback systems [5, 44–46], which is the case in the LCLV system discussed here. The single-feedback solitons and cavity solitons [38] possess similar features, because besides of the balance between nonlinear self-focusing and diffraction also a bistability is commonly necessary for their formation. Bright solitary structures in

cavities or single-feedback configuration are solutions of the systems, which establish an interconnection between a uniform dark stationary solution and a modulationally unstable bright solution. Due to their binary features and their robustness against perturbations solitary structures are often viewed as the natural information bit of nonlinear optical systems.

Without control, however, these localized states experience mutual interactions, drift spontaneously and due to the lack of a law of number conservation, they also can spontaneously merge and disappear. The mutual interactions of neighboring solitary structures induce a locking of the spots at characteristic interaction distances [45] and instead of formation at random positions in the transverse plane trapping of solitary structures to favorite pinning positions induced by system inhomogeneities has been reported [47]. These spontaneous effects can be explained by phase gradients of the feedback wave, as theory predicts a movement of localized states toward local extrema of these phase gradients [38]. In any case these interactions are hindering for the application of localized states in application and thus demand for methods of control. Since the main ideas, important for understanding the spontaneous formation of spatiotemporal structures in the model systems, have been treated we now turn to the discussion of control schemes for spatiotemporal structures.

As we have pointed out in the introduction the motivation for implementing control ranges from suppression of spatiotemporal dynamics to the addressing of a predefined target state, while ideas for potential applications have been the driving force for research. Without the intention of completeness we will in the following discuss the use of several exemplary control methods at the model single-feedback system with the photorefractive and the LCLV nonlinearity, which we have introduced above.

23.3
Spatial Fourier Control

Starting point for our discussion of controlling spatiotemporal pattern will be the application of invasive and noninvasive Fourier control methods, which have been obtained at the photorefractive model system. Fourier control will be used in the photorefractive experiment to experimentally analyze general properties of the nonlinear system behavior such as the curve of marginal instability and to stabilize other unstable periodic pattern solutions. Then we will introduce a persistent invasive forcing method applied in real space, which was used at the LCLV model system to control solitary solutions and periodic pattern. Finally controlling spatiotemporal chaotic states in terms of spatiotemporal synchronization will be introduced.

Pioneer work in controlling nonlinear spatially-extended optical systems has been accomplished by Fourier control methods [7, 15, 48–63]. In particular, the application of Fourier methods is excellently suited for controlling periodic pattern, because periodic patterns consist of specific spatial modes in the Fourier

space. A hexagonal pattern for example may consist of only six excited angular modes located at the critical k_c-ring. As Fourier control can be considered as the simplest method for controlling spatially periodic pattern and thus will be our starting point for discussing different control methods. The basic idea of spatial Fourier filtering has been proposed first in theoretical paper by Martin et al. [48, 49]. A control arm is added to the single-feedback scheme for the implementation of the suggested control. A fraction of the signal of the feedback experiment is coupled into the control arm, where a $4f$-configuration performs a Fourier transformation $\mathcal{FT}$ and its reverse operation $\mathcal{FT}^{-1}$. A filter mask, which defines a target state, is placed at the Fourier plane between the two lenses. The resulting control signal is superposed to the undisturbed single-feedback wave. Depending on the phase relation between the control wave and the feedback wave the superposition acts additive or subtractive. Both in-phase (positive) superposition, which induces an invasive control, and out-of-phase (negative) superposition, which acts as a noninvasive control, create a control, which suppresses solutions deviating from the target state and thus enhances the wanted spectral components of the target geometry. Mathematically the action of the Fourier control can be written in terms of the backward-propagating light field E_B as

$$E'_B = (1 \pm s\mathcal{FT}^{-1}\mathcal{M}\mathcal{FT})E_B, \tag{23.9}$$

where $\mathcal{M}$ represents the spatial Fourier control mask and s the strength of control. Most often the Fourier masks are amplitude masks, which block or transmit certain spectral components in space, depending on the realization of either positive or negative control. If the control scheme is switched from positive to negative control also the design of the Fourier filters must be inverted in order to address identical target states. Experimentally the absolute value of the control strength s can experimentally defined as the intensity of the control signal I_c divided by the intensity in the feedback arm I_f ($|s| = \frac{I_c}{I_f}$).

In selecting certain target states Fourier control can now serve to stabilize otherwise unstable or noisy pattern solutions. By addressing otherwise not accessible system states Fourier control can also contribute to a more detailed understanding for general processes involved in the spontaneous formation of spatial pattern. By this means Fourier control helps in gaining information about otherwise inaccessible or noisy system states. At the model system of the photorefractive single-feedback experiment we will now discuss at the experimental measurement of the curve of marginal instability and at the stabilization of unstable pattern solution how these aims can be achieved by means of such Fourier methods.

23.3.1
Experimental Determination of Marginal Instability

The determination of the curve of marginal instability by application of a Fourier control method has first been suggested by Pesch et al. for a sodium vapor single-feedback experiment [62], and a similar method was then realized in the photorefractive system [63]. The prediction for the onset of modulational instability of the photorefractive system, which has been derived from a linear stability analysis (see Eq. (23.5)) can thus be experimentally verified [63]. For this purpose, a Fourier filter was inserted in the feedback arm at the Fourier plane (F) (see Fig. 23.1). The control scheme thus modifies the backward-propagating light field E_B according to

$$E_B' = (\mathcal{FT}^{-1}\mathcal{M}\mathcal{FT})E_B, \tag{23.10}$$

with the Fourier mask $\mathcal{M}$ depicted in the insertion of Fig. 23.6 (b). Thus, the control invasively restricts the feedback signal to the modes transmitted by the Fourier mask and the control strength s is fixed to unity.

The Fourier filter fulfils two tasks: Firstly, the slit mask filter confines the system to one dimension. Secondly, a specific wavenumber, at which the threshold of marginal instability is to be measured, is selected by a second filter. The selected wavenumber can be altered by laterally shifting both filters in respect to each other. The intensity of the selected sideband can now be monitored by a photodiode, while the stress parameter of the system, the photorefractive coupling parameter γl, is gradually increased. As soon as the coupling parameter
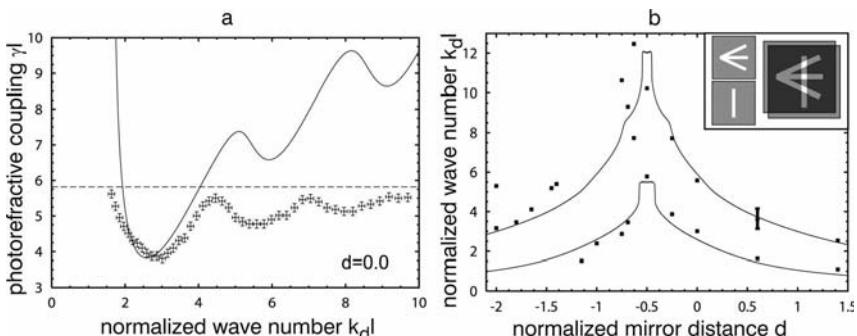
Fig. 23.6 (a) Experimental measurements of the threshold of modulational instability superposed to analytical values in the photorefractive system. The mirror position at the back face of the crystal (outside multiple pattern region). Theoretical prediction and experimental shape of the LSA curve qualitatively agree (for a detailed discussion see the text). (b) Wavenumbers of the threshold minima plotted over the mirror distance d. Disagreements between theory and experiment are found mainly in the multiple pattern region ($-1.5 < d < 0$) [63]. Reprinted with permission from O. Kamps, P. Jander, C. Denz, Phys Rev. E, 72, 016215 (2005). © 2005 by the American Physical Society.

reaches the threshold of modulation instability the intensity of the particular side band will start to grow. In order to track the whole curve of marginal instability, the procedure must be repeated at all available wavenumbers. An example of the obtained thresholds in dependence of the normalized transverse wavenumber at a distance of the virtual feedback mirror of $d = 0$ is shown in Fig. 23.6 (a). The horizontal line in the plot denotes the maximum coupling strength γl, which was provided by the photorefractive crystal. As the absolute value of γl_0 cannot be determined, the experimental data are calibrated to the absolute minimum of the numerical data, to allow comparison between numerical and experimental results. Qualitatively the shape of the LSA curve is confirmed in the experiment. However, compared to the maximum photorefractive coupling strength many detected modes should not have been excitable. The reason for this observation is not yet clear.

To clarify the influence of the virtual mirror position, also the first two wavenumber minima of the threshold have been plotted against the mirror position d (see Fig. 23.6 (b)). The black squares indicate the measured values while the lines represent the theoretical curves derived from Eq. (23.5). This plot also reveals that the symmetry of the curves in respect to the center of the crystal is broken in the experimental data. While the analytical threshold decreases from the crystal center toward the back face, the measured values increase. Wavenumbers larger than $k_d l = 13$ were experimentally not accessible. The measured values near the lower curve for $d \geq -0.6$ belong to a new minimum that appears in this parameter region. At growing distance from the crystal, the experimental data approach the theoretical curves. In these regions, the observed pattern sizes match the predictions from the linear stability analysis. Thus the method enables to compare theoretical prediction to the actual experimental behavior. Deviations between theory and experiment, e.g., the asymmetric behavior near the crystal center, are topics for ongoing research and are investigated in respect of their consequences for the formation of nonhexagonal patterns in this system [63]. The use of Fourier methods not only allows for the measurement of the onset of modulation instability, which we have shown here, but also the bifurcation diagram of unstable solutions such as square and roll solution has been tracked experimentally by monitoring the amplitude of the evolving pattern versus the increased control parameter pump intensity by using a non-invasive control scheme [59].

23.3.2
Stabilization of Unstable Pattern

Control in the Fourier space cannot only be used to track the curve of marginal instability but also enables the stabilization of otherwise unstable pattern solutions [7, 15, 53–61]. Fourier control, in intention of stabilizing optical pattern, can easily be implemented with a scheme similar to the method for determining the curve of marginal instability.
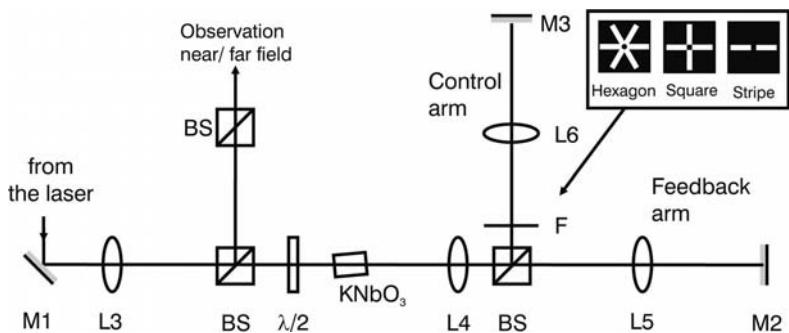
Fig. 23.7 Setup of the photorefractive system with Fourier control. To the single-feedback arm a control arm is added (M3). At the Fourier plane (F) Fourier filters are placed. The design of filters is depicted in the insertion. The Fourier filter define a target state. Control arm and feedback arm in combination form an optical Michelson interferometer. Depending on the phase relation between both arms positive ($s > 0$) or negative control ($s < 0$) can be realized. Thus, the Fourier modes transmitted by the Fourier filter are either amplified or suppressed in the feedback system [15].

23.3.3
Direct Fourier Filtering

Instead of the Fourier filter shown in Fig. 23.5 different Fourier masks, which select target geometries like a hexagon, a square or a stripe pattern, are directly placed into the feedback loop at the position of the Fourier plane (F) for this purpose. Examples of the filter design are shown in Fig. 23.7. As before the nonlinear system thus is restricted to the modes defined by the target state and therefore the control method acts invasively. The blocking of deviations from the target state can be rewritten in terms of a control strength of $s = 1$, and thus must be considered as a comparatively rigorous approach. Applying control directly in the feedback arm, it was possible to stabilize the hexagon, the square, and the stripe solution in the system [53, 54].

23.3.4
Positive Fourier Control

However, the stabilization of such unstable pattern geometries can also be achieved, if the proposed scheme [48, 49] with separate control and feedback arms (Eq. (23.9)) is implemented. Experimentally this can be realized, if a control arm is added to the feedback arm (see Fig. 23.7). In combination the control arm and the feedback arm form a Michelson interferometer. Depending on the path difference between both arms the phase difference between both optical waves varies from in-phase superposition to out-of-phase subtraction and thus also the character of the control method changes from positive invasive closed-loop control (Fourier control) ($s > 0$) for in-phase superposition to negative noninvasive closed-loop control ($s < 0$) for out-of-phase superposition. The separation of control from the sin-
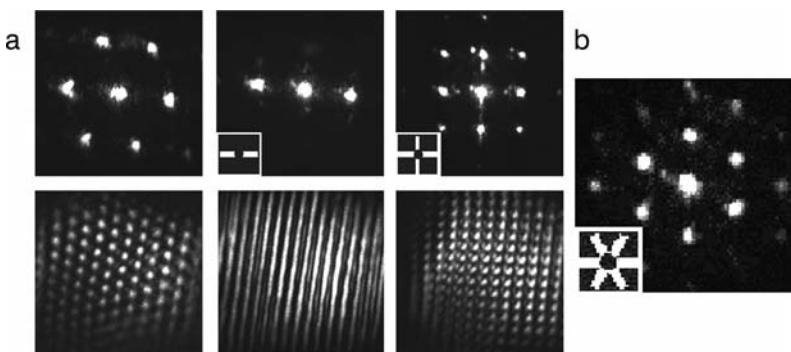
Fig. 23.8 Experimental results of Fourier control in the Michelson scheme. (a) Positive control ($s > 0$); right: near and far field of a hexagonal pattern without control; center: a slit mask establishes a pattern with stripe geometry; left: control stabilizes a square pattern. (b) Negative control ($s < 0$); selection of the azimuthal orientation of the hexagon. Originally the uncontrolled hexagon was rotated by $30°$. The control destabilizes the modes at $30°$ and the hexagon reorients in accordance with the orientation preferred by the control. (Reprinted from Fig. 10.15 in [15]). © 2003 Springer, Heidelberg, with kind permission of Springer Science and Business Media.)

gle-feedback system in this setup also allows us to monitor strength and spatial distribution of the activated control independently from the feedback.

The positive Fourier control scheme ($s > 0$) was implemented at a system state where only hexagonal pattern was observed in the uncontrolled system to stabilize unstable pattern solutions. Like in the control method applied directly in the control arm, patterns with otherwise unstable square and stripe geometry have successfully been stabilized with positive Fourier control [15, 60], even though positive control does not restrict the system to the target modes, but only amplifies the modes of the target modes in respect to other possible modes. Experimental results are shown in Fig. 23.8(a). In the case of the control of a hexagonal pattern, the action of control can be observed in the rotation of the hexagonal pattern with respect to the uncontrolled hexagons. If one uses the Fourier masks used for positive control (see insertion in Fig. 23.7) in the noninvasive negative control scheme ($s < 0$), it will not be possible to modify the stable pattern symmetry.

23.3.5
Noninvasive Fourier Control

The hexagonal mask used before for positive control has however been implemented in a negative control scheme. The application of the control results in the suppression of the hexagon modes in the white areas of the mask. The spontaneously forming hexagonal pattern was oriented at $30°$. Application of noninvasive Fourier control reorients the orientation of the hexagons and thus a hexagon pattern at an azimuthal orientation of $0°$ evolve (see Fig. 23.8(b)).

The Michelson-type control scheme constitutes a smaller intrusion into the single-feedback system compared to the direct Fourier control method described above, because control strengths ($|s| < 1$) can be chosen. If the Fourier filters used for positive control are inverted, i.e., if the black areas, which block the light, are made transparent and vice versa, the same result in stabilizing unstable pattern can also be obtained with the noninvasive Michelson-type control experiment. This has, e.g., been successfully demonstrated in the LCLV experiment [7, 56–59]. The noninvasive character of the control scheme has been proven by monitoring the amplitude of the control signal, while different unstable pattern solutions were stabilized [57]. The experiments show the predicted vanishing of the control signal on reaching the target state, if one neglects a remanent noise level control signal. The remanent noise level was depending on the controlled pattern symmetry between 1% and 8% of the original level of the control signal. Remarkably, the control strength needs to be in the order of $s \approx 0.4$ only [57]. The negative control can be used to annihilate defects in the spontaneous pattern geometry and even spatiotemporal chaos can be eliminated [58]. Fourier methods even allow for the control of the interactions between solitary structures [47, 64]. Therefore, Fourier control demonstrates to be a powerful tool that enables addressing and experimental analysis of otherwise not accessible states of a nonlinear optical system.

23.4
Real-Space Control

Another possibility for controlling spatial structures is the implementation of real-space control schemes. Real-space control is particularly useful, if a simple representation of the target state in the Fourier space is not available. If the target state thus does not consist of a few characteristic modes in the Fourier space or if the exact transverse position of the target state is of importance, real-space control will be more advisable. In principle, real-space control can be implemented easily in the same way as described above for Fourier control, if the appropriate plane in real space is chosen for the position of a control mask and if the design of the masks is suitably altered [65].

23.4.1
Invasive Forcing

For implementing control in real space, we will however take another approach to control. For this purpose, we will realize a persistent external control. Yet, such an external forcing has been mainly investigated in nonoptical context such as convection pattern and in chemical reaction diffusion systems [66–74]. One and two dimensional as well as static and dynamic forcing schemes have been applied to these systems. The real-space forcing here will be applied to the LCLV system. This system is particularly well suited for the application of real-
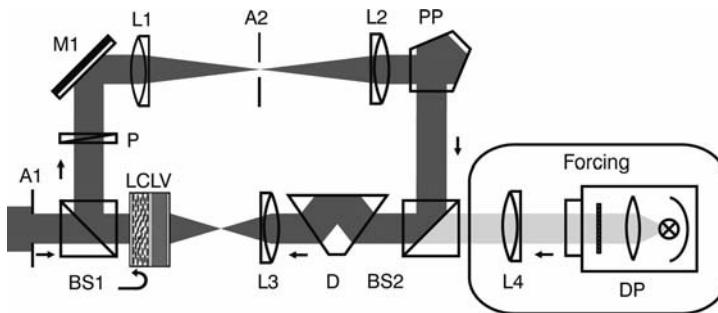
Fig. 23.9 Scheme of the experimental setup with forcing. A forcing input is created with a data projector (DP) as an incoherent white light intensity distribution. The forcing input is added to the feedback signal by projecting it to the photo-conductive side of the LCLV with a lens (L4).

space forcing, because solutions, such as solitary structures and periodic patterns with defects, which demand for absolute position control and which cannot represented in simple Fourier modes, exist in these systems. In the LCLV single-feedback experiment such a forcing scheme can be either realized by adding an offset intensity distribution to the feedback or by inducing a prephase modulation in the pump beam [75–77]. In more detail, we will here refer to results obtained with the amplitude method.

The forcing scheme used in the LCLV experiment is shown in Fig. 23.9. As the nonlinearity LCLV responds to an incoherent intensity distribution, plain white light can simply be used for this purpose. The spatial distribution of forcing is designed at a computer and a LCD-data projector (DP) accordingly generates the white light intensity distribution $I_{\text{forcing}}(x, y, t)$. At the beam splitter (BS2) the forcing intensity distribution is incoherently added to the signal of the single-feedback system. The projecting system, which images the intensity distribution to the photoconductive layer of the LCLV, consists of the lenses L3 and L4. At the LCLV's writing side the forcing signal acts as an offset of the writing intensity I_w. To model the forcing I_w in Eq. (23.6) thus simply must be replaced by the total intensity

$$I_{\text{tot}}(x, y, t) = I_w(x, y, t) + I_{\text{forcing}}(x, y, t). \tag{23.11}$$

The effect of the forcing onto the feedback system is twofold. Firstly the offset intensity acts similarly to the external bias voltage (U_{ext} in Eq. (23.6)) and i.e. the operation point of the nonlinearity is shifted locally [5]. Secondly, the additional intensity distribution I_{forcing} induces an offset in the nonlinearly induced phase distribution ϕ of the feedback wave. Thus, a similar effect like a phase modulation of the pump beam can be achieved [77]. Different spatial intensity distributions of the forcing have been used in the LCLV experiment. In more

detail, we will now discuss how the forcing can control the interaction and spatial position of localized structures.

23.4.2
Positioning of Localized States

As we have pointed out in Section 23.2.5, the behavior of dissipative solitons is determined by mutual interactions. For potential application of these binary nonlinear states a control must be implemented, which allows for the addressing and positioning of these solitary states. The control i.e. must be able to control the particular position of the solitary structures and at the same time both writing and erasure of individual solitary states must be feasible. Since the absolute position of a solitary structure needs to be controllable for application a real-space method is necessary. Using incoherent amplitude forcing promising results have recently been achieved [76].

An image of uncontrolled localized structures can be seen on the right-hand side of Fig. 23.10.

23.4.3
System Homogenization

In a first step toward controlling localized states the forcing with incoherent intensity distributions has been used to balance experimental imperfections in the spatial homogeneity of the LCLV's nonlinear response. For this purpose, the spatial distribution of the LCLV's nonlinear sensitivity has been determined by locally measuring the switching point of the bistability hysteresis. From this measurement, a normalized spatial function of the sensitivity has been calculated. The inverted sensitivity function has been used as forcing. Thus, the bias of the LCLV shifts the operation point of the nonlinearity in areas, which are less sensitive, toward a higher sensitivity, such a homogenized spatial sensitivity function of the nonlinear response is achieved. As a consequence, it has been observed that at otherwise constant parameters (i.e., I_{in}, U_{ext} constant), larger
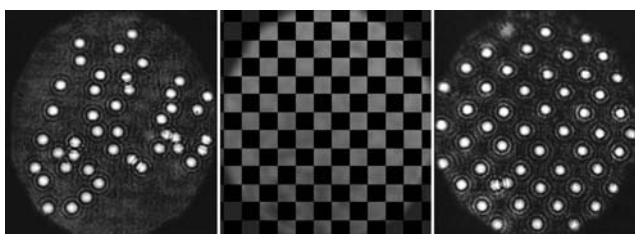
Fig. 23.10 Static forcing acting at localized states. Left: system without forcing; the localized structures interact and form at arbitrary favorite pinning positions; center: intensity distribution of the forcing input; right: the solitary structures are positioned by the persistent external control (reprinted from Fig. 8 in [76]). © 2005 Springer, Heidelberg, with kind permission of Springer Science and Business Media.

areas of the LCLV show bistability. Thus the formation of bistable localized states was observed in a larger area than in the uncontrolled case [76].

23.4.4
Static Positioning

The aim however not only is to homogenize the spatial sensitivity function of the nonlinearity but to achieve a control of the absolute position of localized structures, of their interaction behavior and their movements. Also a robust method for writing and erasing individual solitary structure is needed. Thus the forcing method was extended in order to achieve a control of the absolute positioning of localized structures by introducing a periodic structure into the forcing. For this purpose, a chessboard pattern, which varies from zero in black areas to one in its bright fields, was multiplied used as forcing input. The experimental image (see right-hand side of Fig. 23.10) shows that the localized structures now form in accordance with the chessboard matrix defined by the forcing input. Remaining inhomogeneities reveal themselves for example in two closely neighboring solitary structures in an area near the lower left hand corner of the image. The solitary structures also do not perfectly align to the grid, because the individual chessboard compartments leave some degree of freedom for the position of solitary structures due to their size. Note that the strength of the forcing in the image remains below the switching threshold for the ignition of the solitary structures. The existence of localized states thus is enabled, but they do not ignite spontaneously, instead they have been addressed by shining a broad addressing light pulse onto the photoconductive writing side of the LCLV. Thus, the action of persistent control can be interpreted as an artificial selection of favorite trapping positions for the formation of the spatial solitary structures, while in the uncontrolled system trapping spontaneous pinning positions has been observed [47].

23.4.5
Addressing and Dynamic Positioning

If the pump intensity level from the laser is chosen just below the parameter region of bistability, in contrast to the previous experiment localized states cannot exist due to the lack of bistability. The addition of the spatial forcing distribution at an appropriate strength can in this case shift the system's local operation point into the bistability region, while still localized states cannot form spontaneously. If another local or nonlocal intensity distribution is added, we only observe ignition of solitary spots at positions where the forcing input and additional switching intensity add up. Solitary states do not form at the dark areas of the forcing input and at positions not illuminated by the additional addressing intensity distribution. Thus, this situation can be interpreted as the realization of an all optical logical and operation. Furthermore, if we locally decrease the intensity in the bright regions of the forcing input, we observe that individ-

ual localized structures can also be switched off. In the LCLV setup yet erasing of localized structures has only been demonstrated by superposing an coherent addressing beam, which was π out of phase with the feedback [78, 79]. Therefore, in the specific setup a previously not accessible incoherent erasure method has been demonstrated. A complete addressing scheme using incoherent beams, which allow for writing and deletion of solitary structures in a robust manner, can be implemented with this method. In the same setup also a movie, which shows a moving chessboard pattern, has been used as a dynamic forcing signal.

The dynamic persistent control results in the movement of the solitary structures in the direction according to movement of the chessboard. The phase gradient of the chessboard domain walls thus pushes the solitary structures into the direction defined by the forcing movie [76]. The forcing method described above thus allows for the static and dynamic control of absolute positions of solitary structures as well as for the implementation of a robust and complete addressing scheme for localized states. The invasive forcing scheme is a very general method, which in principle also can be extended for the control of dissipative solitons in other nonlinear optical systems as for example optical cavities.

23.5
Spatiotemporal Synchronization

The fascinating phenomenon of synchronization is a completely different approach of controlling spatiotemporal complexity [80]. The investigations on chaos synchronization are also motivated in terms of potential applications because chaos synchronization can be used for chaos encrypted transmission of data. A detailed introduction to the field and how synchronization can be utilized for encrypted data communication can be found in Part IV on chaos synchronization. While the synchronization of one-dimensional chaotic oscillators [81] or networks of such oscillators [80] has been an emphasis of research activities, investigations on synchronization of spatially extended systems are still comparatively rare. In optical system, however, the synchronization of spatiotemporal chaos and the possibility for encrypted data transmission, besides one-dimensional chaotic laser oscillators [82–84], has also been demonstrated in a spatially extended ring cavity [85]. Also in LCLV systems first experimental investigations on synchronization of spatiotemporal chaos have been successfully performed [75, 86–88].

23.5.1
Spatial Synchronization of Periodic Pattern

In the first approach to synchronization static spatial hexagonal pattern has been used as forcing input to the LCLV single-feedback in the manner described in the previous section. While the system was operated in phase-only mode at

parameters where hexagonal patterns form spontaneously the wavelength of a hexagonal forcing input was altered. The nonlinear system response to the hexagonal forcing was either a locking in orientation and symmetry or the creation of a spatiotemporally turbulent state [75]. This behavior was interpreted as the spatial counterpart of temporal synchronization, since the locking appeared only at distinct resonant modes of the spatial wavenumber, such as $k_c, k_c/\sqrt{7}, k_c/\sqrt{3}$ and or higher order critical wavenumbers $k_c^{(n)}$. Also, when the stress parameter and forcing strength were varied, the formation of Arnold tongues typical for synchronization to external forcing signals in temporal nonlinear systems has been reported [75]. As a measure of synchronization the temporal autocorrelation of the optical and the symmetry of the hexagonal pattern have been taken. Both measures are well suited to determine the degree of spatial synchronization in the system.

23.5.2
Unidirectional Synchronization of Two LCLV Systems

Encouraged by the findings on static forcing, in the following also synchronization of the full spatiotemporal dynamical systems has been investigated in pioneering experiments [86]. The single-feedback system is split into two separate systems, (A) and (B), by introducing a mask with two apertures into the single-feedback for this purpose. The scheme of the synchronization setup is depicted in Fig. 23.11. Both systems run independently from each other, which has been demonstrated in calculating their mutual correlation. Now the system A was unidirectionally coupled to the system B. A fraction of the system A is imaged into the system B using beamsplitters and a mirror. A combination of $\lambda/2$-phase retarder and a polarizing filter enables the modulation of the coupling strength
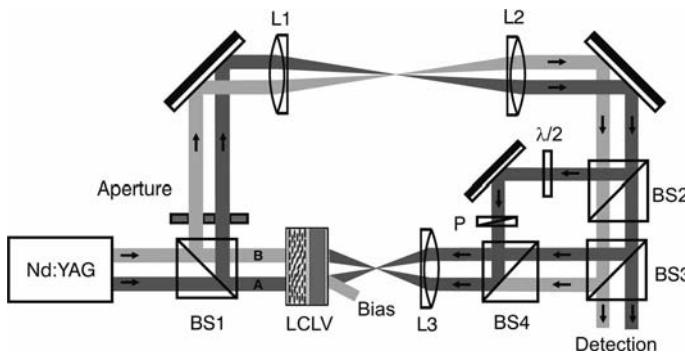
Fig. 23.11 Experimental scheme for spatiotemporal synchronization of separate LCLV systems. Two aperture splits the single-feedback system into two independent systems: (A) and Bob (B). A is unidirectionally coupled to B by two beam splitters (BS) and a mirror. The coupling strength can be adjusted by a combination of a $\lambda/2$-plate and a polarizer. The orientation of the polarizer ensures incoherent coupling. A uniform bias intensity is added to A to operate A and B at equal system states.

γ between the systems. The polarizer transmits the polarization which is perpendicular to the polarization state of the feedback wave in the system B. Thus the coupling superposes incoherently to system B ($I_{B'} = I_B + \gamma I_A$). To operate the system at equal system states a uniform bias intensity, which had an intensity equivalent to the intensity level of the coupling ($I_{A'} = I_A + I_{Bias}$, $I_{Bias} = \gamma \langle I_A \rangle_x$), has been incoherently added to system A. In experiment, the coupling strength has been increased at different input intensities, which were fixed during the increase of coupling.

The degrees of synchronization has been measured by calculating the spatial correlation function $\langle C_{AB} \rangle$ and the mutual information M_{AB} of both system states.

$$C_{AB}(\Delta x, \Delta t, t) = \frac{\langle \tilde{I}_A(x,t) \rangle \cdot \langle \tilde{I}_B(x - \Delta x, t - \Delta t) \rangle}{\sqrt{\langle \tilde{I}_A^2(x,t) \rangle_x \langle \tilde{I}_B^2(x,t) \rangle_x}}, \tag{23.12}$$

$$M_{AB} = H_A + H_{AB} \qquad \text{with} \qquad H = \sum p \log_2 p, \tag{23.13}$$

where the entropies H depend on the (joint) probability distributions p of the intensities I_A and I_B.

23.5.3
Synchronization of Spatiotemporal Complexity

The uncoupled systems do not show indications of synchronization. When the coupling is increased, a significant rise in correlation (Fig. 23.12 (a)) and mutual information (Fig. 23.12 (b)) functions are observed.

Due to experimental imperfections and remaining differences between systems A and B, the correlation coefficient does not reach unity. Later on at higher coupling strength the correlation on the mutual information even drops. We assume the bias intensity for system A to be the reason for the drop, because it likely does not perfectly balance the unidirectional coupling. The experiments have been performed at pump intensities of $I_{in} = 1.5 I_{thr}$ ($\square$), $I_{in} = 3 I_{thr}$ ($\bigcirc$)
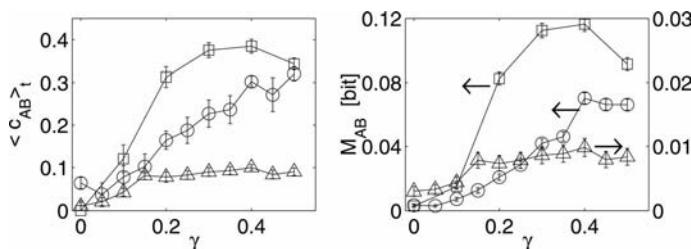
Fig. 23.12 Degree of spatiotemporal synchronization. (a) Time averaged correlation coefficient $\langle C_{AB} \rangle$; (b) mutual information M_{AB}. For details see the text. Reprinted with permission from R. Neubecker, B. Gütlich, Phys. Rev. Lett., 82, 154101-3. © 2004 by the American Physical society [86].

with a low-pass filter cutting wavenumbers just above k_c and at $I_{in} = 1.5I_{thr}$ ($\triangle$) with an open low-pass filter. The complexity of the system states in these measurements increases from hexagons with disorder at $I_{in} = 1.5I_{thr}$ (low-pass filtered) over strongly disorder hexagons at $I_{in} = 3I_{thr}$ (low-pass filtered) to optical turbulence at $I_{in} = 1.5I_{thr}$ (open low pass). In the same order also the maximum value of the correlation function and mutual information decrease. However, in every case a rise in correlation and mutual information indicating synchronization are observable. Thus, even though experimental imperfections are reported, nevertheless it can be concluded that to our knowledge first evidence for spatiotemporal synchronization of spatiotemporally complex system states in a nonlinear optical system has been found. After the achievement of the first experimental evidence on spatiotemporal synchronization, the current efforts aim at improvement of the experimental conditions to reach higher degrees of spatiotemporal synchronization. Particularly, the encryption method described in [85] yet cannot be implemented due to the comparatively small level of synchronization reported in the first experiment [86]. Since the primary results reported here are only a starting point for investigations on spatiotemporal synchronization rising levels of the synchronization degree needed for data encryption can be excepted for the near future.

23.6
Conclusions and Outlook

In conclusion, we have demonstrated how different control techniques allow for the control of the rich spatiotemporal structures observed in nonlinear optical experiments. In detail we have shown the experimental analysis of a spatially extended nonlinear system by means of Fourier control. Invasive and noninvasive control schemes have been presented, which enable the stabilization and addressing of otherwise unstable pattern solutions, such even stabilization of spatiotemporal chaos has been possible. Furthermore, we have shown a real-space forcing method, which enables the position control as well as an complete and robust addressing scheme for solitary structures, which allows for writing and deleting of individual localized states. Applied to static periodic patterns, the results on real-space forcing can be interpreted as spatial counterpart of synchronization. In an extension of this method, we have also presented the first experimental evidence on spatiotemporal synchronization of spatiotemporal chaos in an optical system. The methods presented here surely contribute greatly to the realization of the conceptual dream of "light guiding light". Currently, this conceptual dream is also actively pursued in context of investigations on periodically structured optical materials and in the field of photonic crystals. At present, first investigations on the control of nonlinear optical systems by using such periodically structured optical materials are under way and will in the near future explicitly extend the capabilities of the already excellent control methods presented here. However, the examples throughout this chapter show

impressively how spatially extended systems have become a fascinating field of nonlinear science with an overwhelming richness of phenomena, especially extended spatiotemporal patterns and localized states. In order to understand and to influence these states, we have shown that a number of powerful novel tools exists which pushes this area actively forward.

References

1 W. J. Firth. *J. Mod. Opt.,* 37(3):151, 1990.

2 G. D'Alessandro and W. J. Firth. *Phys. Rev. Lett.,* 66(20):2597–2600, 1991.

3 G. D'Alessandro and W. J. Firth. *Phys. Rev. A,* 46(1):537–548, 1992.

4 E. Ciaramella, M. Tamburrini and E. Santamato. *Appl. Phys. Lett.,* 63(12):1604–1606, 1993.

5 R. Neubecker, G.-L. Oppo, B. Thüring and T. Tschudi. *Phys. Ref. A,* 52(1):791–808, 1995.

6 B. Thüring, R. Neubecker, M. Kreuzer, E. Benkler, and T. Tschudi. *Asian J. Phys.,* 7(3):453, 1998.

7 R. Neubecker. *Pattern formation in an optical experiment. From fundametals to applications,* vol. 115 of *Reihe Physik.* Tectum, Marburg, 2004.

8 F. T. Arecchi, S. Boccaletti, S. Ducci, E. Pampaloni, P. L. Ramazza and S. Residori. *J. Non. Opt. Phys. & Mat.,* 9:183, 2000.

9 G. Giusfredi, J. F. Valley, R. Pon, G. Khitrova and H. M. Gibbs. *J. Opt. Soc. Am. B,* 5: 1181, 1988.

10 T. Ackemann, Yu. A. Logvin, A. Heuer and W. Lange. *Phys. Rev. Lett.,* 75(19):3450–3453, 1995.

11 A. Aumann, T. Ackemann, E. Große Westhoff, and W. Lange. *Phys. Rev. E,* 66:046220, 2002.

12 T. Ackemann and W. Lange. *Appl. Phys. B,* 72:21, 2001.

13 T. Honda. *Opt. Lett.,* 18(8):598, 1993.

14 T. Honda and P. Banerjee. *Opt. Lett.,* 21:778, 1996.

15 C. Denz, M. Schwab and C. Weilnau. *Transverse-Pattern Formation in Photorefractive Optics,* vol. 188. Springer Tracts in Modern Physics, 2003.

16 F. T. Arecchi. *Physica D,* 51: 450, 1991.

17 C. Denz, M. Schwab, M. Sedlatschek, T. Tschudi and T. Honda. *J. Opt. Soc. Am B,* 15:2057, 1998.

18 M. Schwab, C. Denz, and M. Saffman. *Appl. Phys. B,* 69:429, 1999.

19 F. Huneus, B. Schäpers, T. Ackemann, and W. Lange. *Appl. Phys. B,* 76:191–197, 2003.

20 A. J. Scroggie, W. J. Firth, G. S. McDonald, M. Tlidi, R. Lefever, and L. A. Lugiato. *Chaos, Solitons and Fractals,* 4(8/9):1323, 1994.

21 G. S. McDonald, W. J. Firth. *J. Mod. Opt.,* 37:613, 1990.

22 N. N. Rosanov, G. V. Khodova. *J. Opt. Soc. Am. B,* 7:1057, 1990.

23 M. C. Cross and D. Hohenberg. "Pattern formation outside equilibrium". *Mod. Phys.,* 65(3):851, 1993.

24 H. F. Talbot. 'Facts relating to optical science IV'. *Philos. Mag.,* 9:401, 1936.

25 K. Patorski. *Prog. Opt.,* 27:3, 1989.

26 J. Glückstad and M. Saffman. *Opt. Lett.,* 20(6):551, 1995.

27 R. Macdonald and H. J. Eichler. *Opt. Comm.,* 89(2–4):289, 1992.

28 T. Honda and H. Matsumoto. *Opt. Lett.,* 20(17):1755, 1995.

29 S. Odoulov, B. Sturman, and E. Krätzig. *Appl. Phys. B,* 70:645, 2000.

30 N. V. Kukhtarev, V. B. Markov, S. G. Odoulov, M. S. Soskin, and V. L. Vinetskii. *Ferroelectrics,* 22:949, 1979.

31 O. Sandfuchs, F. Kaiser, and M. R. Belic. *Phys. Rev. A,* 64:063809, 2001.

32 O. Sandfuchs. *Self-Organization, Amplitude Equations and Fourier Control in a Nonlinear Optical Feedback System.* Shaker, Aachen, 2001.

33 U. Efron (Editor). *Spatial light modulator technology: materials, devices and applications.* Marcel Dekker, Inc., 1995.

34 K. Lu, B. E. A. Saleh. *Appl. Opt.,* 30(17):2354–2362, 1991.

35 G. Schliecker, and R. Neubecker. *Phys. Rev. E,* 61(2):R997, 2000.

36 R. Neubecker, B. Thüring, M. Kreuzer, and T. Tschudi. *Chaos, Solitions & Fractals,* 10(4/5):681, 1999.

37 L. Pastur, U. Bortolozzo, and P. L. Ramazza. *Phys. Rev. E,* 69(1):016210–1, 2004.

38 N. Akhmediev and A. Ankiewicz (Eds.). *Dissipative solitons.* Springer, 2005.

39 M. Segev, B. Crosignani, A. Yariv, and B. Fischer. *Phys. Rev. Lett.,* 68(7):923–926, 1992.

40 M. Peccianti, G. Assanto. *Optics Lett.,* 26(21):1690, 2001.

41 M. Warengham, J. F. Hanninot, G. Abbate. *Optics Express,* 2(12):483, 1998.

42 V. B. Taranenko, K. Staliunas and C. O. Weiss. *Phys. Rev. A,* 56(2):1582, 1997.

43 M. Brambrilla, L. A. Lugiato, F. Prati, L. Spinelli and W. J. Firth. *Phys. Rev. Lett.,* 79(11):2042–2045, 1997.

44 A. Schreiber, B. Thüring, M. Kreuzer. *Opt. Commun.,* 136:415, 1997.

45 B. Schäpers, T. Ackemann and W. Lange. *J. Opt. Soc. Am. B,* 19(4):707, 2002.

46 P. L. Ramazza, S. Ducci, S. Boccaletti, and F. T. Arecchi. *J. Opt. B.: Quantum Semiclass. Opt.,* 2:399, 2000.

47 B. Gütlich, R. Neubecker, M. Kreuzer, and T. Tschudi. *Chaos,* 13(1):239, 2003.

48 R. Martin, A. J. Scroggie, G.-L. Oppo, and W. J. Firth. *Phys. Ref. Lett.,* 77(19):4007–4010, 1996.

49 G. K. Harkness, G.-L. Oppo, R. Martin, A. J. Scroggie and W. J. Firth. *Phys. Rev. A,* 58(3):2577, 1998.

50 Y. Hayasaki, H. Yamamoto, and N. Nishida. *Opt. Commun.,* 187:49, 2001.

51 E. V. Degtiarev and M. A. Vorontsov. *J. Opt. Soc. Am. B,* 12:1238, 1995.

52 T. Ackemann, B. Giese, B. Schäpers and W. Lange. *J. Opt. B: Quant. Semiclass. Opt.,* 1:70, 1999.

53 A. V. Mamaev and M. Saffman. *Phys. Rev. Lett.,* 16:3499, 1998.

54 S. J. Jensen, M. Schwab, C. Denz. *Phys. Rev. Lett.,* 81:1614, 1998.

55 C. Denz, P. Jander, M. Schwab, O. Sandfuchs, M. Belic, and F. Kaiser. *Ann. Phys.,* 13(7):391, 2004.

56 G. K. Harkness, G.-L. Oppo, E. Benkler, M. Kreuzer, R. Neubecker, and T. Tschudi. *J. Opt. B,* 1:177–182, 1999.

57 E. Benkler, M. Kreuzer, R. Neubecker, and T. Tschudi. *Phys. Rev. Lett.,* 84(5):879–882, 2000.

58 R. Neubecker, E. Benkler, R. Martin, and G.-L. Oppo. *Phys. Rev. Lett.,* 91(11):113903, 2003.

59 R. Neubecker and E. Benkler. *Phys. Rev. E,* 65:066206, 2002.

60 M. Schwab, M. Saffman, C. Denz, and T. Tschudi. *Opt. Commun.,* 170:129, 1999.

61 C. Denz, S. J. Jensen, M. Schwab, and T. Tschudi. *J. Opt. B,* 1:114, 1999.

62 M. Pesch, E. Große Westhoff, T. Ackemann, and W. Lange. *Phys. Rev. E,* 68:016209, 2003.

63 O. Kamps, P. Jander, and C. Denz. *Phys. Rev. E,* 72:016215, 2005.

64 P. L. Ramazza, E. Benkler, U. Bortolozzo, S. Boccaletti, S. Ducci, and F. T. Arecchi. *Phys. Rev. E,* 65:066204, 2002.

65 P. Wang and M. Saffman. *Opt. Lett.,* 24(16):1118, 1999.

66 H. R. Brandt. *Phys. Rev. A,* 32:3551, 1985.

67 C. Elphick. *J. Phys. A: Math. Gen.,* 19:1877, 1986.

68 R. Schmitz and W. Zimmermann. *Phys. Rev. E,* 53:5993, 1996.

69 L. M. Pismen. *Phys. Rev. Lett.,* 59:2740, 1987.

70 P. Coullet and D. Walgraef. *Europhys. Lett.,* 10:525, 1989.

71 O. Steinbock, V. Zykov, and S. C. Müller. *Nature (London),* 366:322, 1993.

72 V. Petrov, Q. Oyang, and H. L. Swinney. *Nature,* 388:655, 1997.

73 M. Dolnik, A. M. Zhabotinsky, and I. R. Epstein. *Phys. Rev. E,* 63:026101, 2001.

74 J. Wolff et al. *Science,* 294:134, 2001.

75 R. Neubecker and O. Jakoby. *Phys. Rev. E,* 67:066221, 2003.

76 B. Gütlich, H. Zimmermann, C. Denz, R. Neubecker, M. Kreuzer, and T. Tschudi. *Appl. Phys. B,* 81(7):927, 2005.

77 U. Bortolozzo and S. Residori. *Phys. Rev. Lett.,* 96(3):037801, 2006.

78 M. Brambrilla, L. A. Lugiato, and M. Stefani. *Europhys. Lett.,* 34:109, 1996.

79 M. Kreuzer, B. Thüring and T. Tschudi. *Asian J. Phys.,* 7(3):678, 1999.

80 A. Pikovsky, M. Rosenblum, and J. Kurths. *Synchronization.* Cambridge University Press, Cambridge, 2001.

81 E. Ott, C. Grebogi, and J. A. Yorke. Controlling chaos. *Phys. Rev. Lett.,* 64(11):1196, 1990.

82 R. Roy, T. W. Murphy, T. D. Maier, Z. Gills, and E. R. Hunter. *Phys. Rev. Lett.,* 68(9):1259, 1992.

83 P. Colet and R. Roy. *Optics Lett.,* 19(24):2056–2058, 1994.

84 I. Fischer, Y. Liu, and P. Davis. *Phys. Rev. A,* 62(1):011801, 2000.

85 J. Garcia-Ojalvo and Rajarshi Roy. *Phys. Rev. Lett.,* 86(22):5204, 2000.

86 R. Neubecker and B. Gütlich. *Phys. Rev. Lett.,* 92(15):154101, 2004.

87 E. A. Rogers, R. Kalra, R. D. Schroll, A. Uchida, D. P. Lathrop, and R. Roy. *Phys. Rev. Lett.,* 93:84101, 2004.

88 P. L. Ramazza, U. Bortolozzo, and S. Boccaletti. *Phys. Rev. E,* 73(3):036213, 2006.

Part VI
Applications to Electronic Systems

24
Delayed-Feedback Control of Chaotic Spatiotemporal Patterns in Semiconductor Nanostructures

Eckehard Schöll

24.1
Introduction

In this chapter, we apply chaos control to modern semiconductor structures whose structural and electronic properties vary on a nanometer scale. They provide an abundance of examples for nonlinear and chaotic dynamics and self-organized spatiotemporal patterns [1–3]. In these nanostructures nonlinear charge transport mechanisms are given, for instance, by quantum-mechanical tunneling through potential barriers, or by thermionic emission of hot electrons which have enough kinetic energy to overcome the barrier. A further important feature connected with potential barriers and quantum wells in such semiconductor structures is the ubiquitous presence of space charges. This, according to Poisson's equation, induces a further feedback between the charge carrier distribution and the electric potential distribution governing the transport. This mutual nonlinear interdependence is particularly pronounced in the cases of semiconductor heterostructures (consisting of layers of different materials) and low-dimensional nanostructures where abrupt junctions between different materials on an atomic length scale cause conduction band discontinuities resulting in potential barriers and wells. The local charge accumulation in these potential wells, together with nonlinear transport processes across the barriers have been found to provide a number of nonlinearities and instabilities in the current–voltage characteristics.

In particular, instabilities are very likely to occur in the case of negative differential conductance, i.e., if the current I decreases with increasing voltage U, and vice versa. The actual electric response depends upon the attached circuit which in general contains – even in the absence of external load resistors – unavoidable resistive and reactive components such as lead resistances, lead inductances, package inductances, and package capacitances. These reactive components give rise to additional degrees of freedom which are described by Kirchhoff's equations of the circuit. If, for instance, a circuit is considered which contains a capacitance C parallel to the semiconductor device, and a load resistance
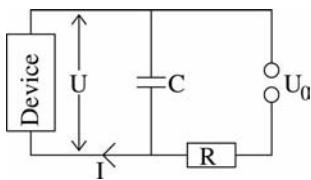
Fig. 24.1 A semiconductor device operated in a circuit with
load resistor R and capacitor C, and applied bias voltage U_0.

R_L and a bias voltage U_0 in series with the device (Fig. 24.1), then Kirchhoff's
laws lead to

$$U_0 = R_L I_0(t) + U(t),$$
(24.1)

$$I_0(t) = I(t) + C \frac{dU}{dt}.$$
(24.2)

Hence the temporal behavior of the voltage is determined by the circuit equation

$$\frac{dU(t)}{dt} = \frac{1}{C} \left(\frac{U_0 - U}{R_L} - I \right).$$
(24.3)

If a semiconductor element with negative differential conductance is operated
in a reactive circuit, oscillatory instabilities may be induced by these reactive
components, even if the relaxation time of the semiconductor is much smaller
than that of the external circuit so that the semiconductor can be described by
its stationary $I(U)$ characteristic and simply acts as a nonlinear resistor. Self-
sustained semiconductor oscillations, where the semiconductor itself introduces
an internal unstable temporal degree of freedom, must be distinguished from
those circuit-induced oscillations. The self-sustained oscillations under time-in-
dependent external bias will be discussed in the following. Examples for inter-
nal degrees of freedom are the charge carrier density, or the electron tempera-
ture, or a junction capacitance within the device. Equation (24.3) is then supple-
mented by a dynamic equation for this internal variable. It should be noted that
the same class of models is also applicable to describe neural dynamics in the
framework of the Hodgkin-Huxley equations [4].

The global $I(U)$ characteristic must be distinguished from the local current
density j versus electric field F. Two important cases of *negative differential con-
ductivity* (NDC) are described by an N-shaped or an S-shaped $j(F)$ characteris-
tic, and denoted by *NNDC* and *SNDC*, respectively. However, more complicated
forms like Z-shaped, loop-shaped, or disconnected characteristics are also possi-
ble [3]. NNDC and SNDC are associated with voltage- or current-controlled in-
stabilities, respectively. In the NNDC case the current density is a single-valued
function of the field, but the field is multivalued: the $F(j)$ relation has three

branches in a certain range of j. The SNDC case is complementary in the sense that F and j are interchanged. In the case of *NNDC*, the NDC branch is often but not always – depending upon external circuit and boundary conditions – unstable against the formation of nonuniform field profiles along the charge transport direction (*electric field domains*), while in the *SNDC* case *current filamentation* generally occurs, i.e., the current density becomes nonuniform over the cross-section of the current flow and forms a conducting channel, a current filament. The elementary structures which make up these self-organized patterns are stationary or moving *fronts* representing the boundaries of the high-field domain or high-current filament.

These primary self-organized spatial patterns may themselves become unstable in secondary bifurcation leading to periodically or chaotically breathing, rocking, moving, or spiking filaments or domains, or even solid-state turbulence and spatiotemporal chaos [1–3, 5–7].

Chaotic oscillations should be avoided for a reliable operation of semiconductor devices. Therefore, there is need for control of those. The important aspect of chaos control is the emphasis of noninvasive control methods together with the observation that chaos supplies a huge number of unstable states that can be stabilized with tiny control power [8]. A particularly simple and efficient scheme uses time delayed signals to generate control forces for stabilizing time periodic states [9] (*time delay autosynchronization*, TDAS, or *Pyragas control*), see Chapter 3. Within this approach, an intrinsically unstable periodic orbit is stabilized using a feedback loop which couples back the difference of an output variable at the actual time t and the same variable at a delayed time $t - \tau$. This scheme is simple to implement, quite robust, and has been applied successfully in real experiments, e.g., [10–20], see Chapters 19, 21, 25–31, 36. An extension to multiple time delays (*extended time delay autosynchronization*, ETDAS) has been proposed by Socolar et al. [21], and analytical insight into those schemes has been gained by several theoretical studies, e.g., [22–30], see Chapters 2–5, as well as by numerical bifurcation analysis, e.g. [31, 32]. Such self-stabilizing feedback control schemes (time delay autosynchronization) with different couplings of the control force have also been applied to spatiotemporal patterns resulting from various models of semiconductor oscillators [33–41]. This is the topic of the present chapter. We restrict ourselves to the stabilization of deterministic chaotic spatiotemporal patterns. It should, however, be noted that time delayed feedback control can also be applied to purely noise-induced oscillations and patterns in a regime where the deterministic system rests in a steady state, and in this way both the coherence and the mean frequency of the oscillations can be controlled in various nonlinear systems [42–49], including semiconductor nanostructures [50, 51], see Chapter 11 of this book.

In the following, we use two paradigmatic models of state-of-the-art semiconductor nanostructures (Fig. 24.2) where time delayed feedback control should be easy to implement experimentally by a feedback loop in the electronic circuit:

(i) Electron transport in semiconductor superlattices shows strongly nonlinear spatiotemporal dynamics. Complex scenarios including chaotic motion of
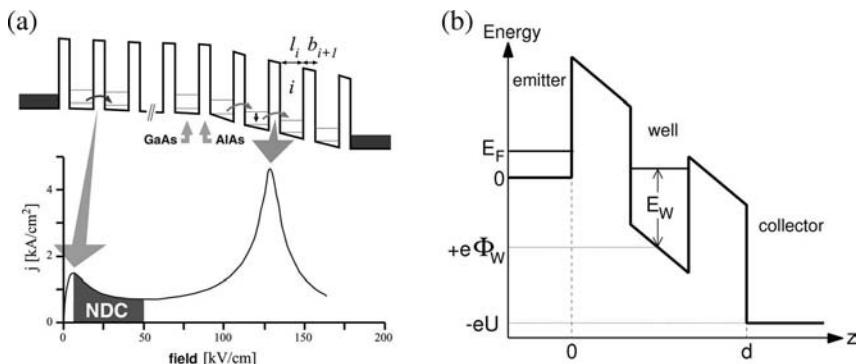
Fig. 24.2 Schematic energy profiles of two nanostructures. (a) Superlattice exhibiting domain formation. The associated current density (*j*) versus field (*F*) characteristic shows negative differential conductivity (NDC). The low-field domain corresponds to sequential tunneling between equivalent levels of adjacent quantum wells (low-field peak of the *j*(*F*) characteristic), while the high-field domain corresponds to resonant tunneling between different levels of adjacent wells (high-field peak). (b) Schematic potential profile of the double barrier resonant tunneling structure (DBRT). E_F and E_w denote the Fermi level in the emitter, and the energy level in the quantum well, respectively. *U* is the voltage applied across the structure.

multiple fronts and domains have been found under time-independent bias conditions [52], showing signs of universal front dynamics [53, 54]. Unstable periodic orbits corresponding to traveling field domain modes can be stabilized by time delayed feedback control. A novel control scheme using low-pass filtering and allowing for control loop latency has been developed [41].

(ii) Charge accumulation in the quantum-well of a double-barrier resonant-tunneling diode (DBRT) may result in lateral spatiotemporal patterns of the current density and chaos [55]. Unstable current density patterns, e.g., periodic breathing or spiking modes, can be stabilized in a wide parameter range by a delayed feedback loop. The control domains of different control schemes and the related Floquet spectrum are compared [40].

24.2
Control of Chaotic Domain and Front Patterns in Superlattices

Semiconductor superlattices [56] have been demonstrated to give rise to self-sustained current oscillations ranging from several hundred MHz [57, 58] to 150 GHz at room temperature [59]. In any case, a superlattice constitutes a highly nonlinear system [3, 60–62], and instabilities are likely to occur. Indeed, chaotic scenarios have been found experimentally [63–65] and described theoretically in periodically driven [66] as well as in undriven systems [52]. For a reliable operation

of a superlattice as an ultrahigh frequency oscillator such unpredictable and irregular conditions should be avoided, which might not be easy in practice.

Here we focus on simulations of dynamic scenarios for superlattices under fixed time-independent external voltage in the regime where self-sustained dipole waves are spontaneously generated at the emitter. The dipole waves are associated with traveling field domains, and consist of electron accumulation and depletion fronts which in general travel at different velocities and may merge and annihilate. Depending on the applied voltage and the contact conductivity, this gives rise to various oscillations modes as well as different routes to chaotic behavior [52, 54].

We use a model of a superlattice based on sequential tunneling of electrons. In the framework of this model, electrons are assumed to be localized at one particular well and only weakly coupled to the neighboring wells. The tunneling rate to the next well is lower than the typical relaxation rate between the different energy levels within one well. The electrons within one well are then in quasiequilibrium and transport through the barrier is incoherent. The resulting tunneling current density $J_{m\to m+1}(F_m, n_m, n_{m+1})$ from well m to well $m+1$ depends only on the electric field F_m between both wells and the electron densities n_m and n_{m+1} in the wells (in units of cm^{-2}). A detailed microscopic derivation of the model has been given elsewhere [60]. A typical result for the current density versus electric field characteristic is depicted in Fig. 24.2 (a) in the spatially homogeneous case, i.e., $n_m = n_{m+1} = N_D$, with donor density N_D.

In the following, we will adopt the total number of electrons in each well as the dynamic variables of the system. The dynamic equations are then given by the continuity equation

$$e\frac{\mathrm{d}n_m}{\mathrm{d}t} = J_{m-1\to m} - J_{m\to m+1}, \quad \text{for} \ \ m = 1, \ldots, N, \tag{24.4}$$

where N is the number of wells in the superlattice, and $e < 0$ is the electron charge.

The electron densities and the electric fields are coupled by the following discrete version of Gauss's law:

$$\varepsilon_r\varepsilon_0(F_m - F_{m-1}) = e(n_m - N_D), \quad \text{for} \ \ m = 1, \ldots, N, \tag{24.5}$$

where ε_r and ε_0 are the relative and absolute permittivities, and F_0 and F_N are the fields at the emitter and collector barrier, respectively.

The applied voltage between emitter and collector gives rise to a global constraint

$$U = -\sum_{m=0}^{N} F_m d, \tag{24.6}$$

where d is the superlattice period.

The current densities at the contacts are chosen such that dipole waves are generated at the emitter. For this purpose it is sufficient to choose Ohmic boundary conditions:

$$J_{0\rightarrow1} = \sigma F_0 \,, \tag{24.7}$$

$$J_{N\rightarrow N+1} = \sigma F_N \frac{n_N}{N_D} \,, \tag{24.8}$$

where σ is the Ohmic contact conductivity, and the factor n_N/N_D is introduced in order to avoid negative electron densities at the collector. Here we make the physical assumption that the current from the last well to the collector is proportional to the electron density in the last well. It is in principle possible to use a more realistic exponential emitter characteristic [67] or calculate the boundary conditions using microscopic considerations, but the qualitative behavior is not changed.

In our computer simulations we use a superlattice with $N = 100$ periods, $\text{Al}_{0.3}\,\text{Ga}_{0.7}\text{As}$ barriers of width $b = 5$ nm and GaAs quantum wells of width $w = 8\ nm$, doping density $N_D = 1.0 \times 10^{11}\ cm^{-2}$ and scattering induced broadening $\Gamma = 8\ meV$ at $T = 20\ K$. If the contact conductivity σ is chosen such that the intersection point with the homogeneous N-shaped current density versus field characteristic is at a sufficiently low current value, accumulation and depletion fronts are generated at the emitter. Those fronts form a traveling high-field domain, with leading electron depletion front and trailing accumulation front. For fixed voltage U Eq. (24.6) imposes constraints on the lengths of the high-field domains and thus on the front velocities. If N_a accumulations fronts and N_d depletion fronts are present, the respective front velocities v_a and v_d must obey $v_d/v_a = N_a/N_d$. Since the front velocities are monotonic functions of the current density [68], this also fixes the current. If the accumulation and depletion fronts have different velocities, they may collide in pairs and annihilate. With decreasing contact conductivity, or increasing voltage, chaotic scenarios arise, where the annihilation of fronts of opposite polarity occurs at irregular positions within the superlattice [52], leading to complex bifurcation diagrams.

In Fig. 24.3 (a) a density plot of the positions (well numbers) at which two fronts annihilate is shown as a function of the voltage. We see that for low voltage the annihilation takes place at a definite position in the superlattice with a variation of only a few wells. This distribution broadens for increasing voltage in characteristic bifurcation scenarios reminiscent of period doubling, leading to chaotic regimes. We note that in the chaotic regime periodic windows exist. A one-parameter bifurcation diagram is given in Fig. 24.3 (b), obtained by plotting the time difference Δt between two consecutive maxima of the electron density in a specific well. Chaotic bands and periodic windows can be clearly seen.

The transition from periodic to chaotic oscillations is enlightened by considering the space–time plot for the evolution of the electron densities (Fig. 24.4 (a)).
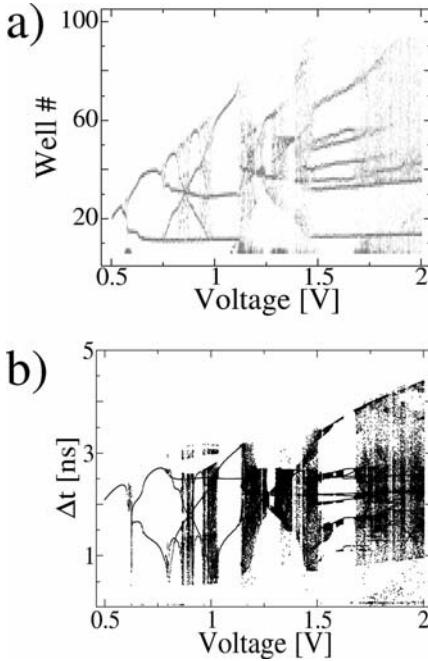
Fig. 24.3 (a) Positions where accumulation and depletion fronts annihilate vs. voltage at $\sigma = 0.5$ $\Omega^{-1}m^{-1}$. The grayscale indicates high (black) and low (white) numbers of annihilations at a given well. (b) Time differ-ences between consecutive maxima of the electron density in well no. 20 vs. voltage. Time series of length 600 ns have been used for each value of the voltage [52].

At $U = 1.15$ V chaotic front patterns with irregular sequences of annihilation of front pairs occur.

We shall now introduce a time delayed feedback loop to control the chaotic front motion and stabilize a periodic oscillation mode which is inherent in the chaotic attractor [41, 69]. As a global output signal which is coupled back in the feedback loop, it is natural to use the total current density $J = \frac{1}{N+1}\sum_{m=0}^{N} J_{m \to m+1}$. For the uncontrolled chaotic oscillations, J versus time (gray trace in Fig. 24.4 (a)) shows irregular spikes at those times when two fronts annihilate. Note that the gray current time trace is modulated by fast small-amplitude oscillations (due to well-to-well hopping of depletion and accumulation fronts in our discrete model) which are not resolved temporally in the plot. They can be averaged out by considering an exponentially weighted current density (black curve in Fig. 24.4 (b)), which corresponds to a low-pass filter:

$$\bar{J}(t) = a \int_0^t J(t')e^{-a(t-t')}dt' \tag{24.9}$$

with a cut-off frequency a.
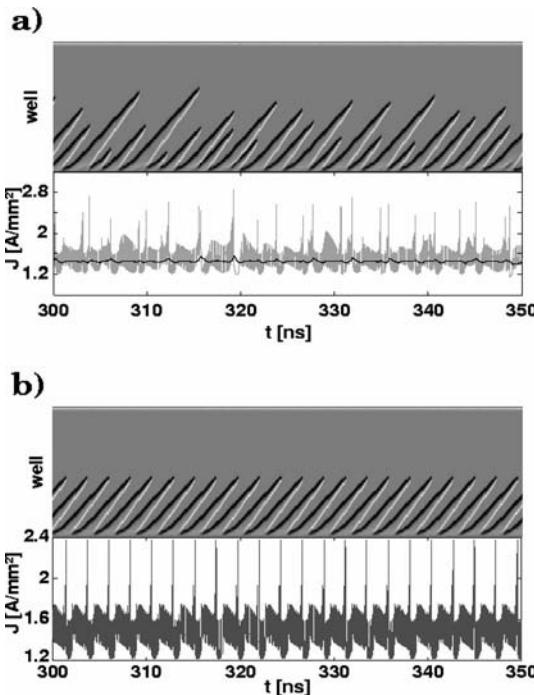
Fig. 24.4 Control of chaotic front dynamics by extended time-delay autosynchronization. (a) Space-time plot of the uncontrolled charge density, and current density J vs. time. (b) Same with global voltage control with exponentially weighted current density (denoted by the black curve). Parameters as in Fig. 24.3, $U = 1.15$ V, $\tau = 2.29$ ns, $K = 3 \times 10^{-6}$ V mm^2/A, $R = 0.2$, $a = 10^9$ s^{-1} [41].

The information contained in the low-frequency part of the current (Fig. 24.4 (a), black curve) is then used as input in the extended multiple-time autosynchronization scheme. The voltage U across the superlattice is modulated by multiple differences of the filtered signal at time t and at delayed times $t - \tau$

$$U(t) = U_0 + U_c(t),\tag{24.10}$$

$$\begin{aligned} U_c(t) &= -K\left[\bar{J}(t) - \bar{J}(t-\tau)\right] + RU_c(t-\tau) \\ &= -K\sum_{v=0}^{\infty} R^v\left[\bar{J}(t-v\tau) - \bar{J}(t-(v+1)\tau)\right] \\ &= -K\left[\bar{J}(t) - (1-R)\sum_{k=1}^{\infty} R^{k-1}\bar{J}(t-k\tau)\right], \end{aligned}\tag{24.11}$$

where U_0 is a time-independent external bias, and U_c is the control voltage. K is the amplitude of the control force, τ is the delay time, and R is a memory
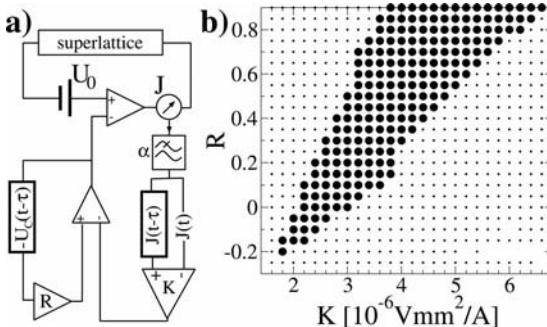
Fig. 24.5 (a) Control circuit including the low-pass filter with cut-off frequency a and the time-delayed feedback loop (K) and its extension to multiple time delays (R). (b) Control domain for global voltage control. Full circles denote successful control, small dots denote no control. Parameters as in Fig. 24.4 [41].

parameter. A sketch of the whole control circuit is displayed in Fig. 24.5 (a). Such a global control scheme is easy to implement experimentally. It is noninvasive in the sense that the control force vanishes when the target state of period τ has been reached. This target state is an unstable periodic orbit of the uncontrolled system. The period τ can be determined *a priori* by observing the resonance-like behavior of the mean control force versus τ. The result of the control is shown in Fig. 24.4 (b). The front dynamics exhibits annihilation of front pairs at fixed positions in the superlattice, and stable periodic oscillations of the current are obtained.

In Fig. 24.5 (b) the control domain is depicted in the parameter plane of R and K. A typical horn-like control domain similar to those known from other coupling schemes [37] is found. Control is achieved in a range of values of the control amplitude K, which is widened and shifted to larger K with increasing memory parameter R. Typically, the left-hand control boundary corresponds to a period-doubling bifurcation leading to chaos for smaller K, while the right-hand boundary is associated with a Hopf bifurcation. The shape of our control domain and its size resemble the results obtained analytically for diagonal control schemes where observables are measured and controlled locally. In particular, we do not observe the influence of other branches of the Floquet eigenvalue problem, which might reduce the size of the control domain severely [70]. Thus our control scheme is of similar control performance as local control.

In order to investigate the effect of the low-pass filtering on the frequency spectrum of the system, it is helpful to consider the transfer function formalism in the frequency domain for the ETDAS control scheme both with and without an additional low-pass filter [71].

In the frequency domain Eq. (24.11) reads

$$U_c(\omega) = -KT(\omega)J(\omega) \,, \tag{24.12}$$

where $T(\omega)$ denotes the transfer function which can be calculated as

$$T(\omega) = T_{\text{ETDAS}}(\omega) T_{\text{low-pass}}(\omega) . \tag{24.13}$$

$T_{\text{ETDAS}}(\omega)$ is the transfer function of the ETDAS control scheme [13] given by

$$T_{\text{ETDAS}}(\omega) = \frac{1 - e^{-i\omega\tau}}{1 - Re^{-i\omega\tau}} \tag{24.14}$$

and $T_{\text{low-pass}}(\omega)$ is the transfer function of the low-pass filter:

$$T_{\text{low-pass}}(\omega) = \frac{1}{1 + i\frac{\omega}{a}} . \tag{24.15}$$

The shape of $|T_{\text{ETDAS}}(\omega)|$ is displayed in Fig. 24.6 (a) for different values of R. As discussed by Sukow et al. [13], the transfer function drops to zero at multiples of the frequency of the unstable periodic orbit (UPO), i.e., τ^{-1}. The notches at these frequencies become narrower for larger R. Due to the notches, the frequency of the UPO does not contribute to the control signal, so that the control force vanishes if stabilization is successful. The steeper notches for larger R indicate that the ETDAS feedback is more sensitive to frequencies different from the one to be controlled, so that more feedback is produced for these unwanted frequencies, which makes the control scheme more efficient.
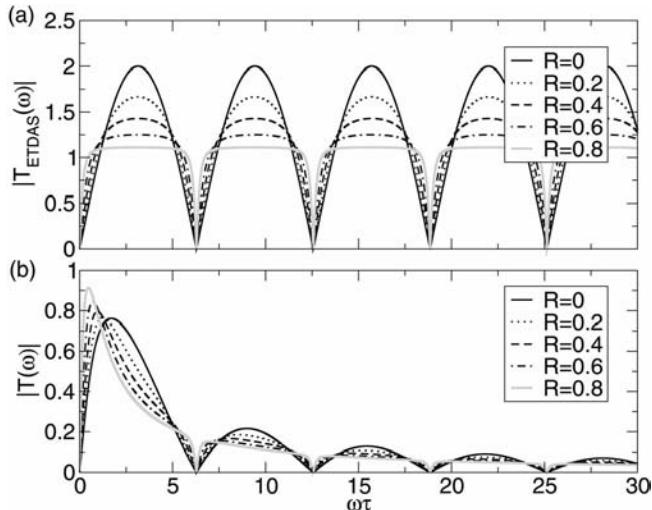
Fig. 24.6 (a) Absolute value of the ETDAS transfer function for different values of $R = 0$ (TDAS), 0.2, 0.4, 0.6, 0.8. (b) absolute value of the ETDAS transfer function including a low-pass filter with fixed $a\tau = 1$ for the same values of R as in (a) [71].

The maximum value of $|T_{\text{ETDAS}}(\omega)|$ approaches unity for R close to 1 and the plateaus become flatter. Therefore, intermediate frequencies generate a smaller response for larger R and thus are less likely to destabilize the system.

The combined transfer function $|T(\omega)|$ for ETDAS and low-pass filtering is displayed in Fig. 24.6(b). As in Fig. 24.6(a), there are notches at multiples of the frequency of the UPO, which become narrower for increasing R. The amplitudes of frequencies larger than the cut-off frequency a are reduced and thus are only minor contributions to the feedback response. This is important to notice in order to understand how the low-pass filter improves the controllability of the system.

Consider a control signal that inhibits frequency components above the frequency of the unstable periodic orbit, $\omega_0 = 2\pi/\tau$. As discussed above, the ETDAS transfer function becomes zero at multiples of ω_0 so that these frequencies are stabilized since no feedback is generated. The harmonics of a small deviation from ω_0 are given by $m(\omega_0 + \varepsilon) = m\omega_0 + m\varepsilon$ with an integer number m. It is likely that special harmonics of the deviation coincide with one of the notches. In this case, ETDAS would generate a control force that stabilizes $\omega_0 + \varepsilon$ and not only the desired frequency of the UPO ω_0. Inserting a low-pass filter overcomes this effect because higher frequency components are suppressed in the control signal.

Another way to understand the influence of the low-pass filter is to take a look at frequencies which should be destabilized, i.e., suppressed by the control scheme. For this discussion see Fig. 24.7, which depicts the transfer function of the ETDAS method for $R = 0.2$ with and without a low-pass filter ($a\tau = 1$) as the dashed and solid line, respectively. The circles and dots indicate an unwanted frequency ω_1 and its first three harmonics. Let us discuss first the case without a low-pass filter (solid line and black dots). Here we find that the third
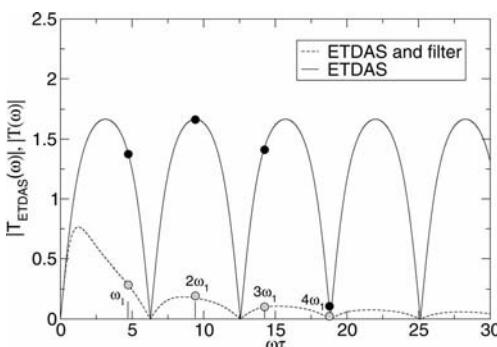
Fig. 24.7 Absolute value of the transfer function of the ETDAS method with and without low-pass filtering for $R = 0.2$: The solid line and black dots correspond to the case without a low-pass filter, the dashed line and the circles to the case with a low-pass filter ($a\tau = 1$). The leftmost dot and circle depict an unwanted frequency ω_1, the three rightmost dots and circles at $2\omega_1$, $3\omega_1$, and $4\omega_1$ the first three harmonics [71].

harmonic ($4\omega_1$) is almost located in the middle of a notch of the transfer function. Thus it will enter the generation of the control force with a high spectral weight so that the control scheme accidentally stabilizes its fundamental frequency ω_1. This effect can be overcome by an additional low-pass filter as shown by the dashed curve and the circles. Again the third harmonic is located near a minimum of the transfer function, but since the notch is not so steep due to the low-pass filter, the spectral weight of the harmonic is smaller. Therefore, the component of the control force that supports the fundamental frequency ω_1 is reduced.

In conclusion, time delay autosynchronization represents a convenient and simple scheme for the self-stabilization of high-frequency current oscillations due to moving domains in superlattices under dc bias. This approach lacks the drawback of synchronization by an external ultrahigh-frequency forcing, since it requires nothing but delaying of the global electrical system output by the specified time lag.

24.3
Control of Chaotic Spatiotemporal Oscillations in Resonant Tunneling Diodes

Next we consider a double-barrier resonant tunneling diode (DBRT), which exhibits a Z-shaped (bistable) current–voltage characteristic [3]. We include the lateral redistribution of electrons in the quantum well plane (coordinates x, y) giving rise to filamentary current flow [72, 73]. Complex chaotic scenarios including spatiotemporal breathing and spiking oscillations have been found in a simple deterministic reaction-diffusion model with one lateral dimension x [55] as well as with two lateral dimensions x, y [74]. We extend this model (in the one-dimensional case) to include control terms, and obtain the following equations [40] where we use dimensionless variables throughout:

$$\frac{\partial a}{\partial t} = f(a, u) + \frac{\partial}{\partial x}\left(D(a)\frac{\partial a}{\partial x}\right) - KF_a(x, t), \tag{24.16}$$

$$\frac{du}{dt} = \frac{1}{\varepsilon}(U_0 - u - rJ) - KF_u(t). \tag{24.17}$$

Here $u(t)$ is the inhibitor and $a(x, t)$ is the activator variable. In the semiconductor context $u(t)$ denotes the voltage drop across the device and $a(x, t)$ is the electron density in the quantum well. The nonlinear, nonmonotonic function $f(a, u)$ describes the balance of the incoming and outgoing current densities of the quantum well and is given explicitly in [40], and $D(a)$ is an effective, electron density dependent transverse diffusion coefficient [73]. The local current density in the device is $j(a, u) = \frac{1}{2}(f(a, u) + 2a)$, and $J = \frac{1}{L}\int_0^L j\,dx$ is associated with the global current. Eq. (24.17) represents Kirchhoff's law of the circuit (24.3) in which the device is operated. The external bias voltage U_0, the dimen-

sionless load resistance $r \sim R_L$, and the time-scale ratio $\varepsilon = R_L C / \tau_a$ (where C is the capacitance of the circuit and τ_a is the tunneling time) act as control parameters. The one-dimensional spatial coordinate x corresponds to the direction transverse to the current flow. We consider a system of width $L = 30$ with Neumann boundary conditions $\partial_x a = 0$ at $x = 0, L$ corresponding to no charge transfer through the lateral boundaries.

Equations (24.16) and (24.17) contain control forces F_a and F_u for stabilizing time periodic patterns. The strength of the control terms is proportional to the control amplitude K, which gives one important parameter of each control scheme. In the semiconductor context these forces can be implemented by appropriate electronic feedback circuits [36].

Without control, $K = 0$, one can calculate the null isoclines of the system. These are plotted in Fig. 24.8 using the current-voltage projection of the originally infinite-dimensional phase space. There are three curves, the null isocline $\dot{u} = 0$ (i.e., the *load line*, dash-dotted) and two null isoclines $\dot{a} = 0$, one for a reduced system, including only spatially homogeneous states (solid), and one for the full system (dotted). We call the system spatially homogeneous if the space-dependent variable $a(x, t)$ is uniformly distributed over the whole width of the device, i.e., $a(x, t) = a(t)$ for all $x \in [0, L]$ otherwise it is called *spatially inhomogeneous*. Figure 24.8 shows the Z-shaped homogeneous current-voltage characteristic of the DBRT (solid curve), and the branch of inhomogeneous, filamentary states (dotted). The inset represents our special regime of interest for the following investigations. With increasing ε, a supercritical Hopf bifurcation of the inhomogeneous steady state occurs at $\varepsilon_{\text{Hopf}} \approx 6.469$ (cf. Fig. 24.9). Below this we have a stable, spatially inhomogeneous fixed point marked 'I' in Fig. 24.8, which is deter-
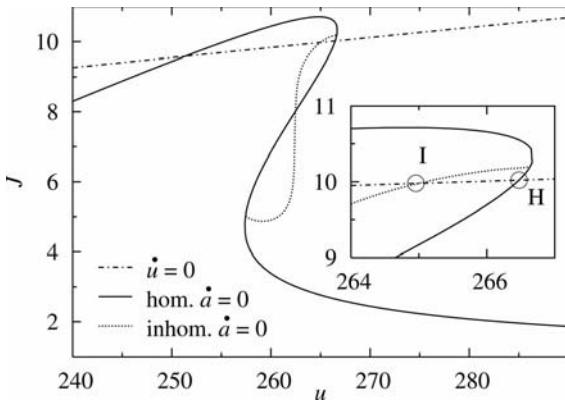
Fig. 24.8 Current-voltage characteristic of the DBRT model. The null isoclines for the dynamical variables u (which is the load line, dash-dotted) and a in the case of a homogeneous $a(x)$ (solid) and in the case of inhomogeneous $a(x)$ (dotted) are shown. The inset shows an enlargement, where I and H mark the inhomogeneous and the homogeneous fixed points of the system, respectively. $U_0 = -84.2895$, $r = -35$. Other parameters as in [40, 51, 75].
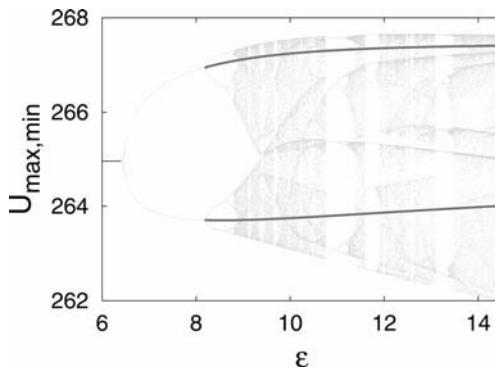
Fig. 24.9 Chaotic bifurcation diagram of the resonant tunneling diode. The maxima and minima of the voltage oscillations are plotted versus the time-scale parameter ε ($r = -35$, $U_0 = -84.2895$, $K = 0$).

mined by the intersection of the load line with the nullcline $\dot{a} = 0$ for inhomogeneous $a(x, t)$. The neighboring intersection of the load line with the homogeneous nullcline (marked 'H') defines another, spatially homogeneous fixed point which is a saddle-point. It is stable with respect to completely homogeneous perturbations but generally unstable against spatially inhomogenous fluctuations.

The dynamics of the free system, i.e., $K = 0$ develops temporally chaotic and spatially nonuniform states (spatiotemporal breathing or spiking) in appropriate parameter regimes [55], which can be corroborated by calculating the Lyapunov exponents [40]. A characteristic bifurcation diagram exhibiting a period-doubling route to chaos is shown in Fig. 24.9. Figure 24.10 shows two examples of periodically (a) and chaotically (b) breathing current filaments. Note that the current density distribution is qualitatively similar to the electron density distribution in the quantum well. For any value of L the system, due to the global coupling, allows only monotonic spatial profiles, i.e., current filaments located at the boundary of the spatial domain [76]. In the semiconductor context the time and length scales of our dimensionless variables are typically given by 3.3 ps (tunneling time) and 100 nm (diffusion length), respectively. Typical units of the electron density, the current density, and the voltage are 10^{10}cm^{-2}, $500\,\text{A/cm}^2$, and $0.35\,\text{mV}$, respectively.

We are concerned with controlling unstable time periodic patterns $u_p(t) = u_p(t + \tau)$, $a_p(x, t) = a_p(x, t + \tau)$ which are embedded in a chaotic attractor. For that purpose we apply control forces F_a and F_u which are derived from time delayed differences of the voltage and the charge density. For example, we may choose $F_u = F_{\text{vf}}$ with the voltage feedback force

$$F_{\text{vf}}(t) = u(t) - u(t - \tau) + RF_{\text{vf}}(t - \tau) \qquad (24.18)$$

(extended time delay autosynchronization).
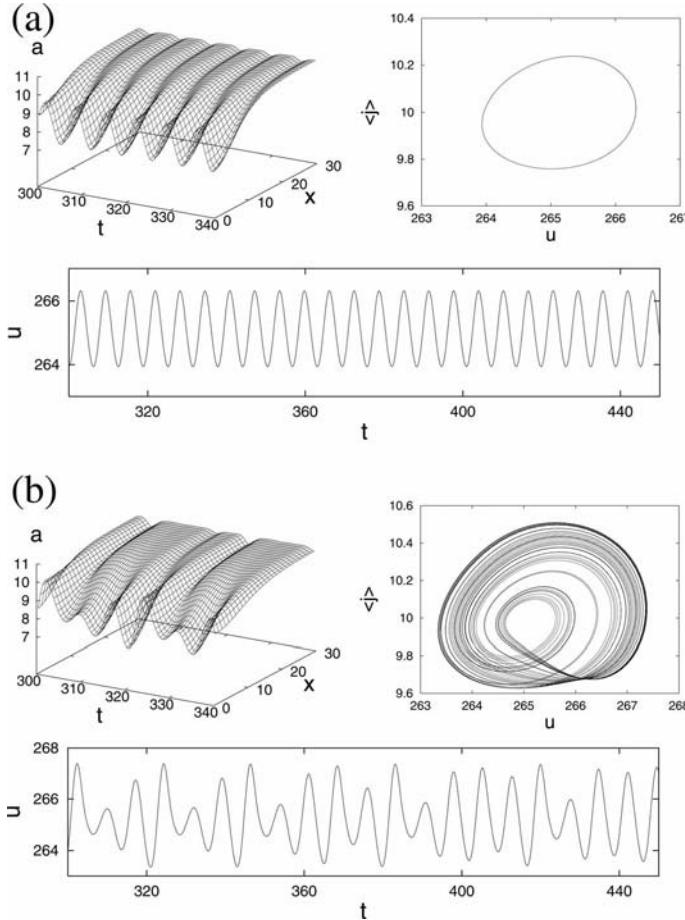
Fig. 24.10 Spatiotemporal breathing patterns of the DBRT: electron density evolution $a(x, t)$, phase portrait J vs. u, and voltage evolution $u(t)$ for (a) $\varepsilon = 7.0$: periodic breathing, (b) $\varepsilon = 9.1$: chaotic breathing ($r = -35$, $U_0 = -84.2895$, $K = 0$). Time t and space x are measured in units of the tunneling time τ_a and the diffusion length l_a, respectively. Typical values at 4 K are $\tau_a = 3.3$ ps and $l_a = 100$ nm [40].

Here we concentrate on the question how the coupling of the control forces to the internal degrees of freedom influences the performance of the control. For our model we consider five different choices for the control force F_a. On the one hand, we use a force which is based on the local charge density according to

$$F_{\text{loc}}(x, t) = a(x, t) - a(x, t - \tau) + RF_{\text{loc}}(x, t - \tau), \tag{24.19}$$

whereas on the other hand we propose a construction which is only based on its spatial average
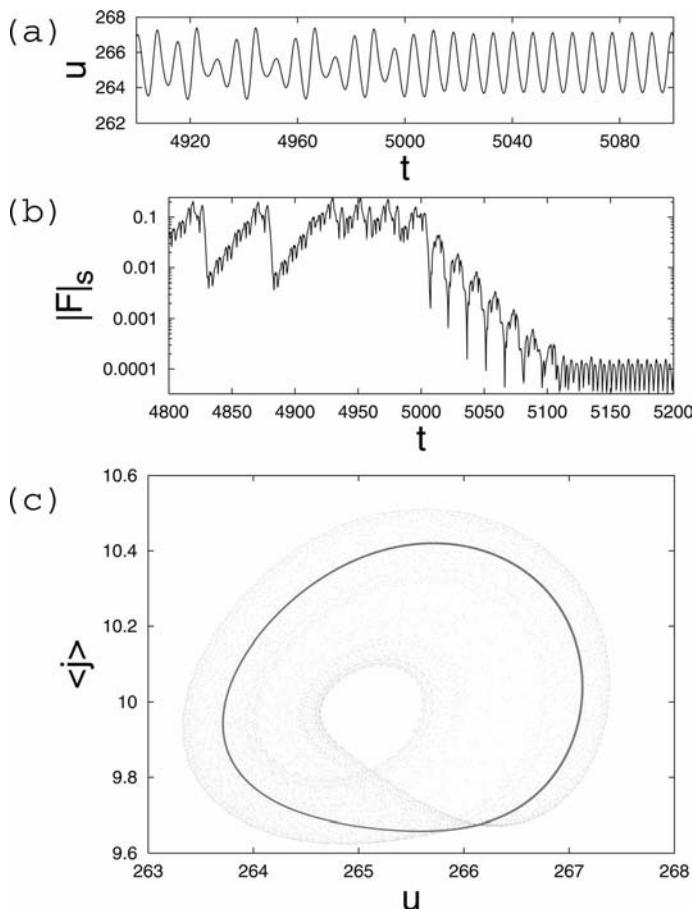
Fig. 24.11 Diagonal control in the DBRT, where the control force is switched on at $t = 5000$. (a) Voltage u vs. time, (b) supremum of the control force vs. time, (b) phase portrait (global current vs. volt- age) showing the chaotic breathing attractor and the embedded stabilized periodic orbit (black cycle). Parameters: $r = -35$, $\varepsilon = 9.1$, $\tau = 7.389$, $K = 0.137$, $R = 0$ [40].

$$F_{\mathrm{glo}}(t) = \frac{1}{L} \int_0^L [a(x,t) - a(x, t - \tau)]\mathrm{d}x + R F_{\mathrm{glo}}(t - \tau). \qquad (24.20)$$

We call the choice $F_a = F_{\mathrm{loc}}$ a *local* control scheme in contrast to the *global* control scheme $F_a = F_{\mathrm{glo}}$ which requires only the global average and does not depend explicitly on the spatial variable. The second option has considerable experimental advantages since the spatial average is related to the total charge in the quantum well and does not require a spatially resolved measurement.

In general, the analysis of the control performance of time delayed feedback methods results in differential-difference equations which are hard to tackle.
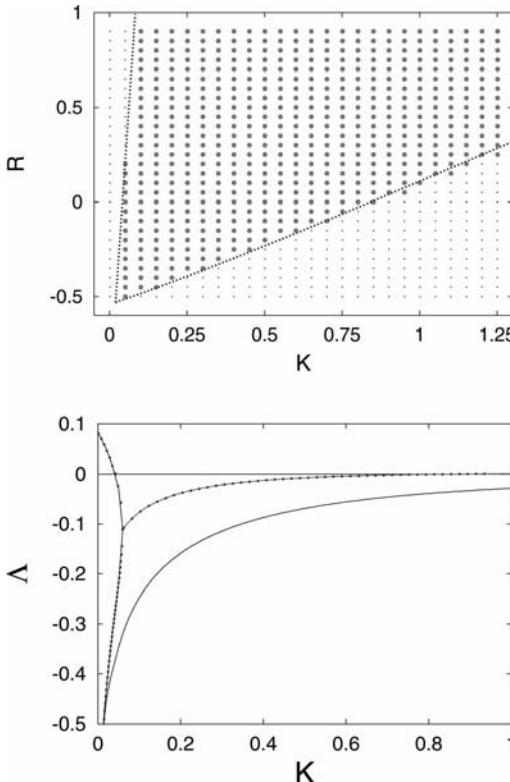
Fig. 24.12 Top: control domains in the (K, R) parameter plane for diagonal control of the unstable periodic orbit with period $\tau = 7.389$. Large dots: successful control in the numerical simulation, small gray dots: no control, dotted lines: analytical result for the boundary of the control domain according to [77]. Bottom: leading real parts Λ of the Floquet spectrum for diagonal control in dependence on K ($R = 0$) [40].

Stability of the orbit is governed by eigenmodes and the corresponding complex valued growth rates (Floquet exponents). There exists a simple case (which we call *diagonal* control) where analytical results are available [23, 77], namely for $F_a = F_{\text{loc}}$ and $F_u = F_{\text{vf}}$. It is a straightforward extension to a spatially extended system of an identity matrix for the control of discrete systems of ordinary differential equations (cf. [22]). Figure 24.11 shows successful control of a chaotic breathing oscillation after the control force is switched on.

In Fig. 24.12, the regime of successful control in the (K, R) parameter plane and the real part of the Floquet spectrum $\Lambda(K)$ for $R = 0$ is depicted. The control domain has a typical triangular shape bounded by a flip instability (period-doubling, $\Lambda = 0$, Imaginary part $\Omega = \pi/\tau$) to its left and by a Hopf (Neimark–Sacker) bifurcation to its right. Inclusion of the memory parameter R increases the range of K over which control is achieved. We observe that the numerical result fits very well with the analytical prediction.
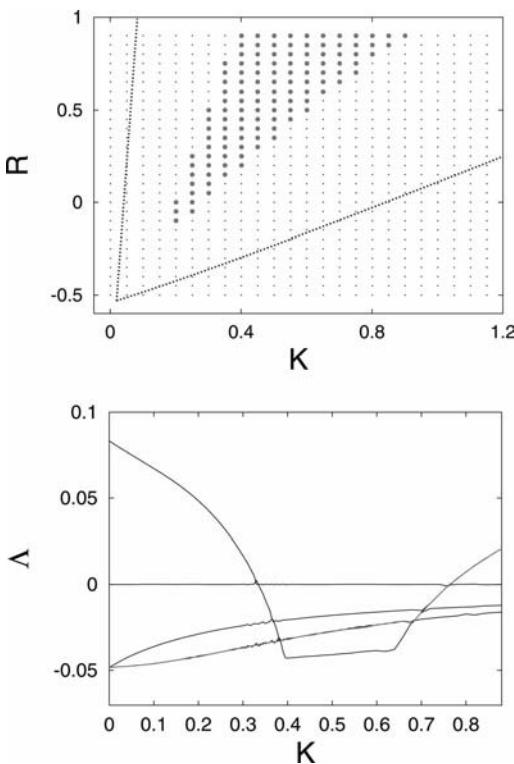
Fig. 24.13 Same as Fig. 24.12 for global control with voltage feedback (Bottom: $R = 0.7$) [40].

To confirm the bifurcations at the boundaries we consider the real part of the Floquet spectrum of the orbit subjected to control. Complex conjugate Floquet exponents show up as doubly degenerate pairs. The largest nontrivial exponent decreases with increasing K and collides at negative values with a branch coming from negative infinity. As a result a complex-conjugate pair develops and the real parts increase again. The real part of the exponent finally crosses the zero axis giving rise to a Hopf bifurcation. Our numerical simulations are in agreement with the analytical result.

Let us now replace the local control force $F_a = F_{loc}$ by the global control $F_a = F_{glo}$. Figure 24.13 shows the corresponding control regime and Floquet spectrum. The control domain looks similar in shape as for diagonal control, although the domain for the global scheme is drastically reduced. The shift in the control boundaries is due to different branches of the Floquet spectrum crossing the ($\Lambda = 0$)-axis.

It is now interesting to note that if we keep $F_a = F_{glo}$ as before but remove the voltage feedback completely, the control domain is shifted to higher K values and at the same time is dramatically increased (Fig. 24.14 (a)). From the
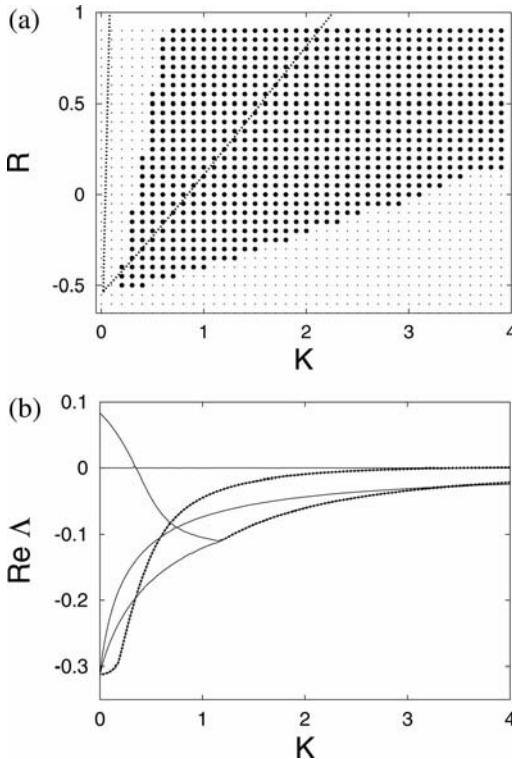
Fig. 24.14 The same as Fig. 24.12 for global control without voltage feedback ((b): $R = 0.1$). Note that the scale of the K-axis is changed [40].

Floquet spectrum we see that after the flip bifurcation the largest Floquet exponent does not immediately hybridize into a complex-conjugate pair, but the Hopf bifurcation is caused by another complex-conjugate pair which is not connected to the largest Floquet exponent. Thereby the Hopf bifurcation is suppressed and the control regime is increased. This behavior is very similar to that observed in a different reaction-diffusion model (modeling a heterostructure hot electron diode, HHED) [37], where it was found that additional control of the global variable u may gradually reduce the control regime to zero.

From the practical point of view the most relevant control scheme is the pure voltage control, i.e., $F_u = F_{vf}$, $F_a = 0$, since the voltage variable may be conveniently measured and manipulated by an external electronic device. The corresponding control domain and Floquet exponents are shown in Fig. 24.15. Here the control regime is even somewhat smaller than in the case of global control with voltage feedback but the shape of the control regime and the Floquet spectrum are qualitatively very similar. This opens up the opportunity to conveniently study chaos control in a real world device.
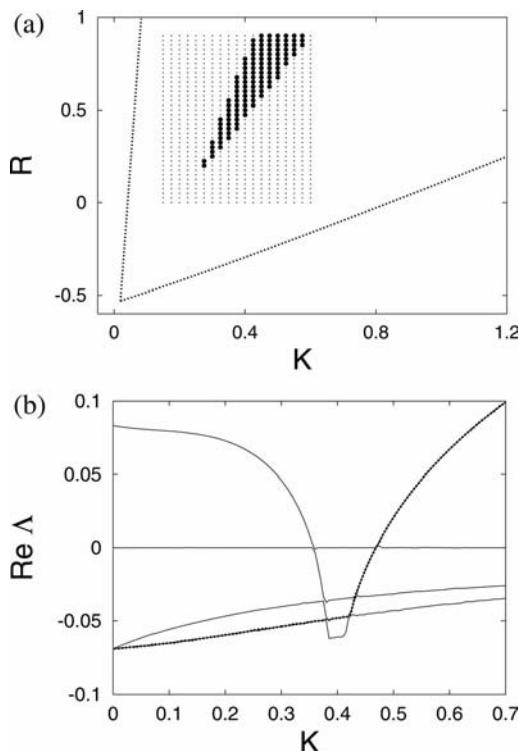
Fig. 24.15 The same as Fig. 24.12 for pure voltage control
((b): $R = 0.6$) [40].

We finally consider the case of local control without voltage feedback (Fig. 24.16). Here the control regime is, surprisingly, even larger than for diagonal control. The shape of the control regime is not triangular any more as before, but has an additional edge at low K and R values. The reason for this edge can be explained from the Floquet diagram. Here a Floquet exponent from below collides with the largest Floquet exponent at positive real values before the flip bifurcation occurs. This complex-conjugate pair then crosses the zero axes from above and undergoes an inverse Hopf bifurcation. For larger values of K another complex-conjugate pair performs a second Hopf bifurcation seemingly unrelated to the first one.

Finally, we note that the period-one orbit can be stabilized by our control scheme throughout the whole bifurcation diagram including chaotic bands and windows of higher periodicity, as marked by two solid lines in Fig. 24.9 for diagonal control. Thus our method represents a way of obtaining stable self-sustained voltage oscillations in a whole range of operating conditions, independently of parameter fluctuations.
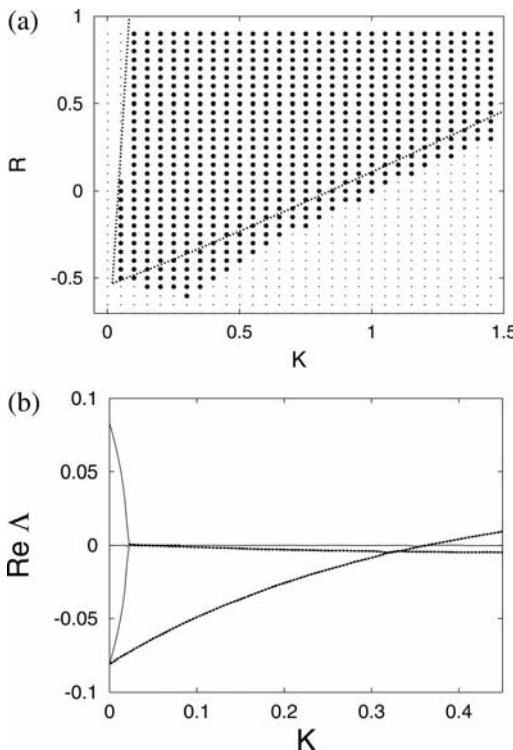
Fig. 24.16 The same as Fig. 24.12 for local control without voltage feedback ((b): $R = -0.55$) [40].

24.4
Conclusions

We have investigated the complex spatiotemporal behavior of two semiconductor nanostructures, viz. a superlattice and a double barrier resonant tunneling diode (DBRT). The first exhibits nonlinear dynamics of interacting fronts, while the second demonstrates breathing and spiking of filamentary current density patterns characteristic of globally coupled reaction-diffusion systems. Applying time delayed feedback control of the Pyragas type, we have been able to suppress deterministic chaos and stabilize periodic current oscillations corresponding to regular space-time patterns.

We have seen that delayed feedback can be an efficient method for manipulation of essential characteristics of chaotic spatiotemporal dynamics in a spatially discrete front system and in a continuous reaction-diffusion system. By variation of the time delay one can stabilize particular unstable periodic orbits associated with space–time patterns through a wide range of parameters, and thus adjust and stabilize the frequency of the electronic device.

The effects of the delayed feedback can be explained in terms of a Floquet mode analysis of the periodic orbits.

While these investigations have enlightened our basic understanding of nonlinear, spatially extended systems under the influence of time delayed feedback, they may also open up relevant applications as nanoelectronic devices like tunable oscillators and sensors.

Acknowledgments

References

1 E. Schöll: *Nonequilibrium Phase Transitions in Semiconductors* (Springer, Berlin, 1987).

2 M. P. Shaw, V. V. Mitin, E. Schöll, and H. L. Grubin: *The Physics of Instabilities in Solid State Electron Devices* (Plenum Press, New York, 1992).

3 E. Schöll: *Nonlinear Spatio-Temporal Dynamics and Chaos in Semiconductors* (Cambridge University Press, Cambridge, 2001).

4 A. L. Hodgkin and A. F. Huxley: *A quantitative description of membrane current and its application to conduction and excitation in nerve*, J. Physiol. **117**, 500 (1952).

5 J. Peinke, J. Parisi, O. E. Rössler, and R. Stoop: *Encounter with Chaos* (Springer, Berlin Heidelberg, 1992).

6 F. J. Niedernostheide (Editor): *Nonlinear Dynamics and Pattern Formation in Semiconductors and Devices* (Springer, Berlin, 1995).

7 K. Aoki: *Nonlinear Dynamics and Chaos in Semiconductors* (Institute of Physics Publishing, Bristol, 2000).

8 E. Ott, C. Grebogi, and J. A. Yorke: *Controlling chaos*, Phys. Rev. Lett. **64**, 1196 (1990).

9 K. Pyragas: *Continuous control of chaos by self-controlling feedback*, Phys. Lett. A **170**, 421 (1992).

10 S. Bielawski, D. Derozier, and P. Glorieux: *Controlling unstable periodic orbits by a delayed continuous feedback*, Phys. Rev. E **49**, R971 (1994).

11 T. Pierre, G. Bonhomme, and A. Atipo: *Controlling the chaotic regime of nonlinear ionization waves using time delay autsynchronisation method*, Phys. Rev. Lett. **76**, 2290 (1996).

12 K. Hall, D. J. Christini, M. Tremblay, J. J. Collins, L. Glass, and J. Billette: *Dynamic control of cardiac alterans*, Phys. Rev. Lett. **78**, 4518 (1997).

13 D. W. Sukow, M. E. Bleich, D. J. Gauthier, and J. E. S. Socolar: *Controlling chaos in a fast diode resonator using time delay autosynchronisation: Experimental observations and theoretical analysis*, Chaos **7**, 560 (1997).

14 O. Lüthje, S. Wolff, and G. Pfister: *Control of chaotic Taylor–Couette flow with time delayed feedback*, Phys. Rev. Lett. **86**, 1745 (2001).

15 P. Parmananda, R. Madrigal, M. Rivera, L. Nyikos, I. Z. Kiss, and V. Gáspár: *Stabilization of unstable steady states and periodic orbits in an electrochemical system using delayed-feedback control*, Phys. Rev. E **59**, 5266 (1999).

16 H. Benner and W. Just: *Control of chaos by time delayed feedback in high power ferromagnetic resonance experiments*, J. Kor. Phys. Soc. **40**, 1046 (2002).

17 C. Beta, M. Bertram, A. S. Mikhailov, H. H. Rotermund, and G. Ertl: *Controlling turbulence in a surface*

chemical reaction by time delay autosyn-chronization, Phys. Rev. E **67**, 046224 (2003).

18 C. von Loewenich, H. Benner, and W. Just: *Experimental relevance of global properties of time delayed feedback control*, Phys. Rev. Lett. **93**, 174101 (2004).

19 J. Schlesner, V. Zykov, H. Engel, and E. Schöll: *Stabilization of unstable rigid rotation of spiral waves in excitable media*, Phys. Rev. E **74**, 046215 (2006).

20 S. Schikora, P. Hövel, H. J. Wünsche, E. Schöll, and F. Henneberger: *All-optical noninvasive control of unstable steady states in a semiconductor laser*, Phys. Rev. Lett. **97**, 213902 (2006).

21 J. E. S. Socolar, D. W. Sukow, and D. J. Gauthier: *Stabilizing unstable periodic orbits in fast dynamical systems*, Phys. Rev. E **50**, 3245 (1994).

22 M. E. Bleich and J. E. S. Socolar: *Stability of periodic orbits controlled by time delay feedback*, Phys. Lett. A **210**, 87 (1996).

23 W. Just, T. Bernard, M. Ostheimer, E. Reibold, and H. Benner: *Mechanism of time delayed feedback control*, Phys. Rev. Lett. **78**, 203 (1997).

24 H. Nakajima: *On analytical properties of delayed feedback control of chaos*, Phys. Lett. A **232**, 207 (1997).

25 K. Pyragas: *Analytical properties and optimization of time delayed feedback control*, Phys. Rev. E **66**, 26207 (2002).

26 W. Just, H. Benner, and E. Schöll: *Control of chaos by time delayed feedback: A survey of theoretical and experimental aspects*, in *Advances in Solid State Phyics*, edited by B. Kramer (Springer, Berlin, 2003), vol. 43, pp. 589–603.

27 P. Hövel and J. E. S. Socolar: *Stability domains for time delay feedback control with latency*, Phys. Rev. E **68**, 036206 (2003).

28 P. Hövel and E. Schöll: *Control of unstable steady states by time delayed feedback methods*, Phys. Rev. E **72**, 046203 (2005).

29 S. Yanchuk, M. Wolfrum, P. Hövel, and E. Schöll: *Control of unstable steady states by long delay feedback*, Phys. Rev. E **74**, 026201 (2006).

30 B. Fiedler, V. Flunkert, M. Georgi, P. Hövel, and E. Schöll: *Refuting the odd number limitation of time delayed feedback control*, Phys. Rev. Lett. **98**, 114101 (2007).

31 A. G. Balanov, N. B. Janson, and E. Schöll: *Delayed feedback control of chaos: Bifurcation analysis*, Phys. Rev. E **71**, 016222 (2005).

32 J. Hizanidis, R. Aust, and E. Schöll: *Delay-induced multistability near a global bifurcation*, Int. J. Bifur. Chaos (2008), in press.

33 E. Schöll and K. Pyragas: *Tunable semiconductor oscillator based on self-control of chaos in the dynamic Hall effect*, Europhys. Lett. **24**, 159 (1993).

34 D. Reznik and E. Schöll: *Oscillation modes, transient chaos and its control in a modulation-doped semiconductor double-heterostructure*, Z. Phys. B **91**, 309 (1993).

35 D. P. Cooper and E. Schöll: *Tunable real space transfer oscillator by delayed feedback control of chaos*, Z. f. Naturforsch. **50 a**, 117 (1995).

36 G. Franceschini, S. Bose, and E. Schöll: *Control of chaotic spatiotemporal spiking by time delay autosynchronisation*, Phys. Rev. E **60**, 5426 (1999).

37 O. Beck, A. Amann, E. Schöll, J. E. S. Socolar, and W. Just: *Comparison of time delayed feedback schemes for spatio-temporal control of chaos in a reaction-diffusion system with global coupling*, Phys. Rev. E **66**, 016213 (2002).

38 N. Baba, A. Amann, E. Schöll, and W. Just: *Giant improvement of time delayed feedback control by spatiotemporal filtering*, Phys. Rev. Lett. **89**, 074101 (2002).

39 W. Just, S. Popovich, A. Amann, N. Baba, and E. Schöll: *Improvement of time-delayed feedback control by periodic modulation: Analytical theory of Floquet mode control scheme*, Phys. Rev. E **67**, 026222 (2003).

40 J. Unkelbach, A. Amann, W. Just, and E. Schöll: *Time-delay autosynchronization of the spatiotemporal dynamics in resonant tunneling diodes*, Phys. Rev. E **68**, 026204 (2003).

41 J. Schlesner, A. Amann, N. B. Janson, W. Just, and E. Schöll: *Self-stabilization of high frequency oscillations in semiconductor superlattices by time delay autosynchronization*, Phys. Rev. E **68**, 066208 (2003).

42 N. B. Janson, A. G. Balanov, and E. Schöll: *Delayed feedback as a means of*

control of noise-induced motion, Phys. Rev. Lett. **93**, 010601 (2004).

43 A. G. Balanov, N. B. Janson, and E. Schöll: *Control of noise-induced oscillations by delayed feedback*, Physica D **199**, 1 (2004).

44 E. Schöll, A. G. Balanov, N. B. Janson, and A. Neiman: *Controlling stochastic oscillations close to a Hopf bifurcation by time delayed feedback*, Stoch. Dyn. **5**, 281 (2005).

45 J. Pomplun, A. Amann, and E. Schöll: *Mean field approximation of time delayed feedback control of noise-induced oscillations in the Van der Pol system*, Europhys. Lett. **71**, 366 (2005).

46 B. Hauschildt, N. B. Janson, A. G. Balanov, and E. Schöll: *Noise-induced cooperative dynamics and its control in coupled neuron models*, Phys. Rev. E **74**, 051906 (2006).

47 A. G. Balanov, V. Beato, N. B. Janson, H. Engel, and E. Schöll: *Delayed feedback control of noise-induced patterns in excitable media*, Phys. Rev. E **74**, 016214 (2006).

48 J. Pomplun, A. G. Balanov, and E. Schöll: *Long-term correlations in stochastic systems with extended time delayed feedback*, Phys. Rev. E **75**, 040101 (2007).

49 T. Prager, H. P. Lerch, L. Schimansky-Geier, and E. Schöll: *Increase of coherence in excitable systems by delayed feedback*, J. Phys. A (2007) in press.

50 J. Hizanidis, A. G. Balanov, A. Amann, and E. Schöll: *Noise-induced oscillations and their control in semiconductor superlattices*, Int. J. Bifur. Chaos **16**, 1701 (2006).

51 G. Stegemann, A. G. Balanov, and E. Schöll: *Delayed feedback control of stochastic spatiotemporal dynamics in a resonant tunneling diode*, Phys. Rev. E **73**, 016203 (2006).

52 A. Amann, J. Schlesner, A. Wacker, and E. Schöll: *Chaotic front dynamics in semiconductor superlattices*, Phys. Rev. B **65**, 193313 (2002).

53 A. Amann, K. Peters, U. Parlitz, A. Wacker, and E. Schöll: *Hybrid model for chaotic front dynamics: From semiconductors to water tanks*, Phys. Rev. Lett. **91**, 066601 (2003).

54 A. Amann and E. Schöll: *Bifurcations in a system of interacting fronts*, J. Stat. Phys. **119**, 1069 (2005).

55 E. Schöll, A. Amann, M. Rudolf, and J. Unkelbach: *Transverse spatio-temporal instabilities in the double barrier resonant tunneling diode*, Physica B **314**, 113 (2002).

56 L. Esaki and R. Tsu: *Superlattice and negative differential conductivity in semiconductors*, IBM J. Res. Develop. **14**, 61 (1970).

57 J. Kastrup, R. Klann, H. T. Grahn, K. Ploog, L. L. Bonilla, J. Galán, M. Kindelan, M. Moscoso, and R. Merlin: *Self-oscillations of domains in doped GaAs–AlAs superlattices*, Phys. Rev. B **52**, 13761 (1995).

58 K. Hofbeck, J. Grenzer, E. Schomburg, A. A. Ignatov, K. F. Renk, D. G. Pavel'ev, Y. Koschurinov, B. Melzer, S. Ivanov, S. Schaposchnikov, and P. S. Kop'ev: *High-frequency self-sustained current oscillation in an Esaki–Tsu superlattice monitored via microwave emission*, Phys. Lett. A **218**, 349 (1996).

59 E. Schomburg, R. Scheuerer, S. Brandl, K. F. Renk, D. G. Pavel'ev, Y. Koschurinov, V. M. Ustinov, A. E. Zhukov, A. R. Kovsh, and P. S. Kop'ev: *InGaAs/InAlAs superlattice oscillator at 147 GHz*, Electron. Lett. **35**, 1491 (1999).

60 A. Wacker: *Semiconductor superlattices: A model system for nonlinear transport*, Phys. Rep. **357**, 1 (2002).

61 L. L. Bonilla: *Theory of nonlinear charge transport, wave propagation, and self-oscillations in semiconductor superlattices*, J. Phys.: Condens. Matter **14**, R341 (2002).

62 L. L. Bonilla and H. T. Grahn: *Non-linear dynamics of semiconductor superlattices*, Rep. Prog. Phys. **68**, 577 (2005).

63 Y. Zhang, J. Kastrup, R. Klann, K. H. Ploog, and H. T. Grahn: *Synchronization and chaos induced by resonant tunneling in GaAs/AlAs superlattices*, Phys. Rev. Lett. **77**, 3001 (1996).

64 K. J. Luo, H. T. Grahn, K. H. Ploog, and L. L. Bonilla: *Explosive bifurcation to chaos in weakly coupled semiconductor superlattices*, Phys. Rev. Lett. **81**, 1290 (1998).

65 O. M. Bulashenko, K. J. Luo, H. T. Grahn, K. H. Ploog, and L. L. Bonilla: *Multifractal dimension of chaotic attractors in a driven semiconductor superlattice*, Phys. Rev. B **60**, 5694 (1999).

66 O. M. Bulashenko and L. L. Bonilla: *Chaos in resonant-tunneling superlattices*, Phys. Rev. B **52**, 7849 (1995).

67 A. Amann, J. Schlesner, A. Wacker, and E. Schöll: *Self-generated chaotic dynamics of field domains in superlattices*, in *Proc. 26th International Conference on the Physics of Semiconductors (ICPS-26), Edinburgh 2002*, edited by J. H. Davies and A. R. Long (2003).

68 A. Amann, A. Wacker, L. L. Bonilla, and E. Schöll: *Dynamic scenarios of multi-stable switching in semiconductor superlattices*, Phys. Rev. E **63**, 066207 (2001).

69 J. Schlesner, A. Amann, N. B. Janson, W. Just, and E. Schöll: *Self-stabilization of chaotic domain oscillations in superlattices by time delayed feedback control*, Semicond. Sci. Technol. **19**, S34 (2004).

70 W. Just, E. Reibold, K. Kacperski, P. Fronczak, J. A. Holyst, and H. Benner: *Influence of stable Floquet exponents on time delayed feedback control*, Phys. Rev. E **61**, 5045 (2000).

71 P. Hövel: *Effects of chaos control and latency in time delay feedback methods*, Master's thesis, Technische Universität Berlin (2004).

72 M. Meixner, P. Rodin, E. Schöll, and A. Wacker: *Lateral current density fronts in globally coupled bistable semiconductors with S- or Z-shaped current voltage characteristic*, Eur. Phys. J. B **13**, 157 (2000).

73 V. Cheianov, P. Rodin, and E. Schöll: *Transverse coupling in bistable resonant-tunneling structures*, Phys. Rev. B **62**, 9966 (2000).

74 G. Stegemann and E. Schöll: *Two-dimensional spatiotemporal pattern formation in the double-barrier resonant tunneling diode*, New J. Phys. **9**, 55 (2007).

75 G. Stegemann, A. G. Balanov, and E. Schöll: *Noise-induced pattern formation in a semiconductor nanostructure*, Phys. Rev. E **71**, 016221 (2005).

76 A. Alekseev, S. Bose, P. Rodin, and E. Schöll: *Stability of current filaments in a bistable semiconductor system with global coupling*, Phys. Rev. E **57**, 2640 (1998).

77 W. Just, E. Reibold, H. Benner, K. Kacperski, P. Fronczak, and J. Holyst: *Limits of time delayed feedback control*, Phys. Lett. A **254**, 158 (1999).

25
Observing Global Properties of Time Delayed Feedback Control in Electronic Circuits

Hartmut Benner, Chol-Ung Choe, Klaus Höhne, Clemens von Loewenich,
Hiroyuki Shirahama, and Wolfram Just

25.1
Introduction

Control of complex and chaotic behavior has been one of the most rapidly developing topics in applied nonlinear science for more than one decade (cf. [1] and references therein). Contrary to traditional control schemes which have been developed by engineers and applied mathematicians for more than half a century, the emphasis of noninvasive methods has lead to new concepts such as time delayed feedback techniques [2]. Such a method has proven to be very useful in applications, in experimental TDF particular in experiments in physics, chemistry, or bioscience. Meanwhile the control mechanism has been understood from the theoretical point of view, as far as linear aspects of the control scheme are concerned (cf. e.g. [3]). But there is still considerable lack of knowledge from the global point of view, e.g., with respect to stability of the control scheme under external perturbations or the structure of basins of attraction of the controlled state. Such basins are of utmost importance in experimental realizations since their size determines the accessibility of the target state. Unfortunately, time delayed feedback control turns the dynamical system of interest into a differential-difference system and thus changes the structure of the underlying phase space considerably. Even if the original system has a quite simple structure, e.g., a low-dimensional phase space where only a few degrees of freedom are relevant, the phase space becomes infinite-dimensional by the application of time delayed feedback since the whole history of the state enters the dynamics as well [4]. Such a feature makes the investigation of global phase-space properties a difficult task even if one just wants to visualize high-dimensional basins of attraction, not to mention a systematic theoretical study.

Here we are going to study global features of time delayed feedback control for two different setups using electronic circuit experiments. In Section 25.2, extended time delayed feedback control is investigated [5]. We focus in particular on the reduction of basins of attraction which is related to discontinuous transi-

tions at the control boundaries, a phenomenon which is already predicted by general bifurcation theory. Consequences of such a phenomenon for experiments is illustrated. Section 25.3 deals with an extension of time delayed feedback control employing an unstable control loop to improve the control performance of time delayed feedback control [6]. We investigate how different types of coupling of the control force affects the basins of attraction and thus may improve the control performance from a global perspective.

25.2
Discontinuous Transitions for Extended Time Delayed Feedback Control

Time delayed feedback methods are based on the measurement of a signal $s(t)$. The control force is generated from a time delayed difference $s(t) - s(t - \tau)$. In order to keep such a scheme noninvasive the delay time τ is typically chosen to be the period of the target state. In order to improve the control performance filtering techniques in the frequency domain may be applied [5] so that the actual generation of the control force F reads

$$F(t) = K[s(t) - s(t - \tau)] + RF(t - \tau). \tag{25.1}$$

For filter parameter $R = 0$ the original Pyragas scheme is recovered where the control amplitude K yields one control parameter. The additional filter parameter R improves the control performance, in particular, when systems with fast time scales are considered. The control force is used to modulate an accessible parameter of the system. By adjustment of the two control parameters, K and R, successful stabilization of the target state may be achieved. Of particular interest for our purpose will be the set of initial conditions for which control works successfully.

25.2.1
Theoretical Considerations

Control performance of the extended scheme, Eq. (25.1), can be evaluated for quite general systems based on a linear stability analysis (cf. e.g. [7]). In particular, the control domain, i.e., the set of parameter values in the K–R control parameter plane for which control works successfully, shows generically a characteristic V-shape (cf. Fig. 25.1) when target states with an unstable negative Floquet multiplier are considered, e.g., unstable periodic orbits that have been generated via a period doubling cascade. The left-hand border of the control domain, the so-called lower control threshold, is connected with a period doubling bifurcation while the right-hand border of the domain is usually caused by a Hopf instability. While details of the control domain may depend on the particular system the overall picture coincides with the scenario just sketched (cf. e.g. [8–10] for further details).
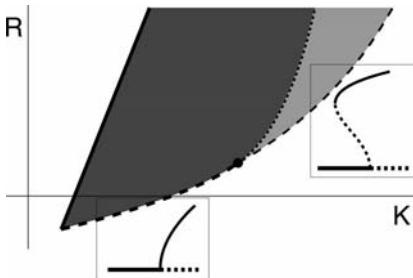
Fig. 25.1 Diagrammatic view of the control domain (dark and light gray-shaded) for extended time delayed feedback control. Lower control threshold (solid line), upper control threshold (broken line), saddle node bifurcation of the delay-induced orbit (dotted line). The dot indicates a transition from continuous to discontinuous bifurcation (cf. insets for the bifurcation diagram). The corresponding region of bistability between the controlled orbit and the delay-induced motion is light gray-shaded.

The upper control threshold, i.e., the right-hand border of the control domain will be of interest for our purpose as Hopf bifurcations yield a generic mechanism to determine basin boundaries [11]. If the transition at the control boundary is continuous then a stable oscillating, quasiperiodic solution is generated beyond the upper control threshold. But for discontinuous transitions a completely different dynamical state is reached when leaving the control domain. Furthermore, the Hopf bifurcation is caused in such a case by a collision with a formerly unstable limit cycle (cf. insets in Fig. 25.1) which exists throughout the control domain. Within the control domain, this unstable object gives rise to a finite basin of attraction. Furthermore, bistability and hysteresis are hysteresis observed. In particular, the basin of attraction becomes small when the control boundary is approached. Thus a discontinuous transition is an indicator for small basins of attraction and the character of the instability is crucial for the global properties of the control system.

25.2.2
Experimental Setup

We are going to demonstrate the relevance of such a mechanism by an electronic circuit experiment which has been performed recently [12]. A simple nonautonomous system is the nonlinear diode resonator sketched in Fig. 25.2. The circuit, which consists of an inductor (470 µH), a resistor (51 Ω), and three parallel diodes (1N4006) acting together as a nonlinear capacitor, is sinusoidally driven at fixed frequency (340 kHz), $U(t) = U_a \sin(2\pi\nu t)$. Without control the system undergoes a period doubling cascade to chaos on variation of the driving amplitude U_a. This scenario ensures for unstable periodic orbits with finite torsion so that these states are accessible to time delayed feedback control [3]. We performed our experiments at $U_a = 4.5$ V and choose the unstable period-one orbit as our target state. We measured the voltage at the resistor R and gener-
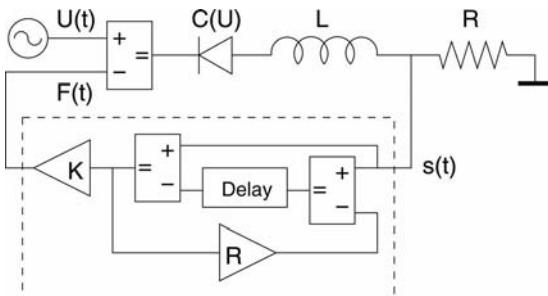
Fig. 25.2 Experimental setup of the nonlinear diode resonator
with extended time delayed feedback control device.

ated from this signal $s(t)$ our control force. The control loop employs multiple
delay terms which exactly emulate the recursive form of Eq. (25.1). Finally the
output of the control device was fed back to the driving voltage $U(t)$.

Having fixed the filter parameter R there exists a lower and an upper control
threshold for successful control. At the lower threshold the unstable orbit be-
comes stable through an inverse period doubling cascade and the output signal
$s(t)$ becomes finally periodic. At the upper control threshold the power spec-
trum develops side-bands. A Hopf bifurcation takes place which leads to a qua-
siperiodic state. Thus the scenario is in full accordance with the general theoret-
ical considerations of the previous section.

25.2.3
Observation of Bistability

Experimentally the Hopf bifurcation shows up most clearly in the frequency
spectrum of the signal $s(t)$. Inside the control domain we observe one sharp
line indicating the frequency of the controlled orbit. On increasing K a side-
band frequency together with its harmonics occurs directly at the Hopf bifurca-
tion (cf. Fig. 25.3). But this change happens discontinuously. When decreasing
K this spectrum is maintained for a larger range until the system finally jumps
back to the controlled state. This kind of hysteresis indicates that the observed
Hopf bifurcation is subcritical and that a region of bistability between the con-
trolled periodic orbit and a delay-induced quasiperiodic state occurs.

For the quantitative evaluation of the bistability we took the amplitude of the
first side-band peak at about 290 kHz. Figure 25.4 shows the dependence on
the control amplitude when K is adiabatically increased, respectively decreased.
Hysteresis and bistability is clearly visible with extremely sharp thresholds in K.
At the right-hand threshold a subcritical Hopf instability takes place, i.e., a qua-
siperiodic peak with finite amplitude occurs in the spectrum. The left-hand
threshold, i.e., the discontinuous breakdown of the quasiperiodic state, is caused
by a saddle node bifurcation (cf. e.g. [11]).
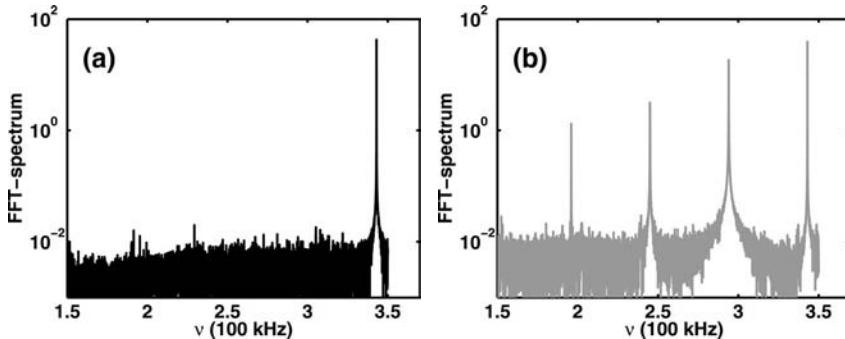
Fig. 25.3 Fourier spectrum of the measured signal at $K = 9.76$ and $R = 0.12$ for two different initial conditions: (a) controlled periodic orbit (adiabatic increase of the control amplitude), (b) delay-induced quasiperiodic state (adiabatic decrease of the control amplitude).
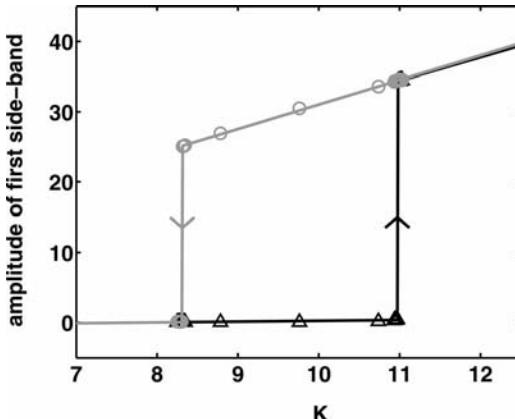
Fig. 25.4 Amplitude of the first side-band at 290 kHz vs. control amplitude K for $R = 0.12$. Triangles: increasing K, circles: decreasing K (cf. Fig. 25.3 for corresponding Fourier spectra).

Since the control domain and the just mentioned threshold values strongly depend on the filter parameter R we have probed the hysteresis for an accessible range $-0.25 < R < 0.25$. Figure 25.5 shows the corresponding thresholds in the K–R parameter plane. The lower threshold where control sets in and which is caused by the inverse flip period doubling yields a straight line, in accordance with the theoretical prediction. No hysteresis was observed at this lower threshold. Thus the bifurcation is supercritical. At the upper control threshold we observe a subcritical Hopf bifurcation for all R values. The region of bistability which is bounded by the saddle node instability of the delay-induced quasiperiodic state accounts for about 30% of the whole control domain. Within the whole range of investigated parameter values the Hopf bifurcation at the upper
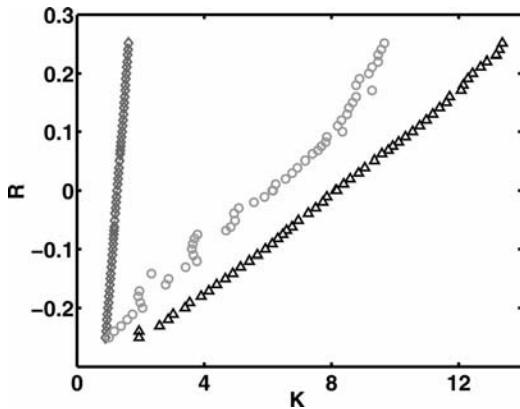
Fig. 25.5 Experimental results for the control thresholds in the *K–R* parameter plane. Diamonds: lower control threshold (supercritical flip bifurcation), triangles: upper control threshold (subcritical Hopf bifurcation), circles: collapse of the delay-induced quasiperiodic state (saddle node bifurcation).

boundary remained subcritical. No transition to supercritical behavior was observed. Apart from this feature the results are in full accordance with the theoretical expectation described above (cf. Fig. 25.1).

25.2.4
Basin of Attraction

As stated previously subcritical bifurcations pose severe constraints on the basin of attraction. We have analyzed such a property by probing the corresponding basin of attraction directly in our experiment. Our setup was modified in a way that a short pulse could be added to the driving voltage causing a perturbation to the stabilized orbit. A very short but strong pulse was applied at a fixed phase of the external periodic drive. Starting from the controlled state inside the bistable regime, we observed whether the system returned back to the controlled orbit or escaped to the quasiperiodic state. We made repeated experiments by varying systematically the control parameters as well as the width and the amplitude of the voltage pulse. As long as the strength of the pulse, i.e., the product of amplitude and width of the pulse does not exceed a critical value we find relaxation toward the periodic orbit. This critical strength gives a measure for the size of the basin of attraction. Results are shown in Fig. 25.6.

First, we find that the critical pulse strength does not depend on the precise form of the pulse. On variation of the pulse width (2.5%, 3.3%, and 5% of the period) the critical voltage amplitudes indicating the boundary of the basin of attraction scaled in the reciprocal way. Thus we obtained a nice data collapse and our experiment really probes for the basin of attraction. The size of the basin may be read off from the data displayed in Fig. 25.6.
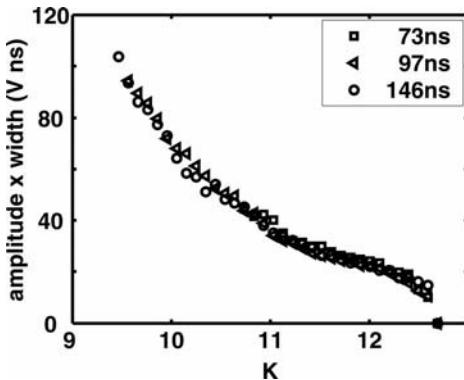
Fig. 25.6 Critical pulse strength in dependence on the control amplitude for different width of pulses at $R = 0.12$. Note that the modification of the experimental setup has slightly changed the system increasing the control thresholds by about 15%.

Second, the critical pulse strength tends toward zero when the upper control threshold is approached. That property is in full accordance with the scenario of the subcritical Hopf bifurcation since the basin of attraction becomes small as well in that limit. Furthermore, the dependence of the pulse strength on K shows an S-shape characteristics which is expected for the size of the basin according to the theoretical prediction (cf. the upper inset in Fig. 25.1 and the corresponding normal form analysis, e.g. [13]). Thus we have striking experimental evidence that subcritical behavior is a universal mechanism which determines global features of time delayed feedback control. Last but not least the data displayed in Fig. 25.6 indicate the sensitivity of the controlled system with respect to external perturbations and thus quantifies the degree of structural stability of the control scheme.

25.3
Controlling Torsion-Free Unstable Orbits

The second experimental example we are going to present refers to a control concept which is less straightforward than that in the previous case. It has been shown [3, 14] that only a certain class of periodic orbits characterized by a finite torsion can be stabilized by time delayed feedback control. Such a topological constraint means that any unstable periodic orbit with an odd number of real Floquet multipliers larger than unity can never be stabilized by this method[1].

---

1) In a recent reprint (arXiv:nlin.CD/0609056) Fiedler et al. have pointed out that such a constraint does not apply for limit cycles in autonomous systems because time translation invariance allows for the occurrence of transcritical bifurcations. Actually, the proofs of the odd number limitation implicitly use the assumption that the underlying dynamics is subjected to a periodic drive.
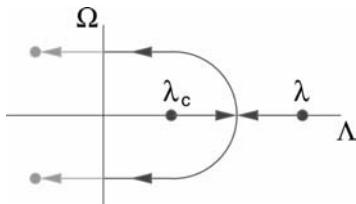
Fig. 25.7 Mechanism of time delayed feedback control by means of an unstable controller. Λ and Ω are the real and imaginary parts of the Floquet exponent of the controlled system. The real Floquet exponents of the unstable system, λ, and of the unstable controller, λ_c, collide under the influence of the control force, and a Hopf bifurcation occurs.

Different strategies have been suggested to overcome this constraint. For instance, the so-called rhythmic control [15] is based on the periodic modulation of the control signal with a period different from that of the orbit. This way the effect of torsion will be introduced artificially. Another way suggested recently [6] is based on the counter-intuitive concept to introduce an unstable degree of freedom into the control device. The key idea is to provide an even number of real Floquet multipliers by including an additional unstable degree of freedom in the feedback loop to overcome the limitation mentioned above. Bifurcation theory tells us that an even number of real unstable Floquet multipliers offer the possibility that, on variation of some bifurcation parameter, the corresponding Floquet branches may collide and undergo a Hopf bifurcation. This results in a complex conjugate pair of Floquet exponents (see Fig. 25.7). This way the missing torsion can be introduced via the additional unstable degree of freedom offered by the controller, and then the system becomes accessible again to time delayed feedback control. A detailed discussion of this idea can be found in a previous chapter of the handbook. Both methods were successfully applied to control torsion-free unstable periodic orbits in numerical simulations, but real experimental applications have been missing so far.

A prominent paradigmatic system showing such torsion-free unstable orbits is the unstable van der Pol oscillator which is described by the following equations of motion

$$\dot{x}(t) = -y(t) + \varepsilon x(t) + x^3(t)/3, \qquad (25.2\,\mathrm{a})$$
$$\dot{y}(t) = x(t). \qquad (25.2\,\mathrm{b})$$

Here, ε is the bifurcation parameter of system, and the time scale is normalized to the inverse oscillator frequency. Equation (25.2) differs from that for the conventional van der Pol oscillator merely by the sign of the nonlinear coefficient. For $\varepsilon < 0$, this equation has two coexisting solutions, a stable fixed point at the origin $x = y = 0$, and an unstable limit cycle with the period $\tau = 2\pi + \mathcal{O}(\varepsilon)$, amplitude $2\sqrt{-\varepsilon} + \mathcal{O}(\varepsilon)$, and a real positive Floquet exponent $\lambda = -\varepsilon + \mathcal{O}(\varepsilon^{3/2})$.

For $\varepsilon > 0$ the limit cycle disappears, and the fixed point at the origin becomes unstable. Thus at $\varepsilon = 0$ we have a subcritical Hopf bifurcation. The real positive Floquet exponent indicates that the limit cycle is unstable and shows no torsion.

25.3.1
Applying the Concept of an Unstable Controller

We assume that x is an observable accessible in experiment. To stabilize the unstable periodic orbit appearing for $\varepsilon < 0$ we consider the following control algorithm:

$$\dot{x}(t) = -y(t) + \varepsilon x(t) + x^3(t)/3 + w(t)f(x(t)) \tag{25.3a}$$
$$\dot{y}(t) = x(t) \tag{25.3b}$$
$$\dot{w}(t) = \lambda_c w(t) - K(x(t) - x(t - \tau))f(x(t)). \tag{25.3c}$$

The term $wf(x)$ in Eq. (25.3a) is the control signal perturbing the x-variable. The specific form of this coupling is given by the function $f(x)$ and will be specified later. Equation (25.3c) describes an unstable delayed feedback controller with $\lambda_c > 0$. Here w is the dynamical variable of the controller and K determines the feedback strength. Note that the control scheme does not change the solution of the free system corresponding to the unstable orbit of period τ, since for $x(t) = x(t - \tau)$ Eq. (25.3c) is satisfied by $w = 0$ and the control signal $w(t)f(x(t))$ in Eq. (25.3a) vanishes.

We just mention that in a recent article [16] Eq. (25.3) has been considered as a paradigm of a subcritical Hopf bifurcation showing an unstable torsion-free limit cycle. The possibility of stabilizing such an orbit was explored both analytically and by means of numerical simulations, and successful control was achieved.

25.3.2
Experimental Design of an Unstable van der Pol Oscillator

In order to probe the concept of an unstable controller in experiment we designed autonomous electronic circuits which could be mapped to Eq. (25.3). We first considered a serial LC oscillator with a cubic nonlinearity as had been suggested in [16]. The obvious idea to approximate the nonlinearity by a conventional Chua diode failed, because in such a circuit current and voltage were just interchanged with respect to the diode characteristics. However, a circuit with inductance, capacity, and nonlinearity in parallel connection (cf. Fig. 25.8) should overcome this problem and seemed to give a proper realization of our model Eq. (25.2). By means of a so-called negative resistor the unstable controller was designed in a straightforward way choosing for the coupling function $f(x)$ a simple linear one, $f(x) = x$. Nevertheless, our attempts to control such
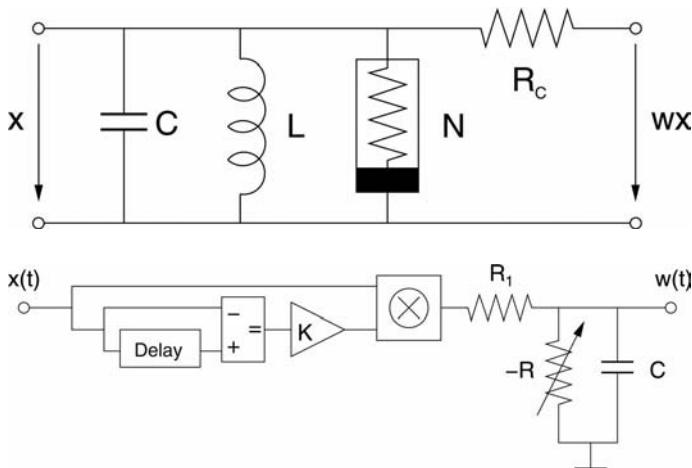
Fig. 25.8 Top: experimental implementation of unstable van der Pol oscillator by means of a parallel CLN resonator. The nonlinearity N is provided by a Chua diode. Bottom: design of the unstable controller described by Eq. (25.3).

an electronic realization of the unstable van der Pol oscillator were not successful. Failure was obviously caused by parasitic properties of the components. For instance, we found that the internal resistance of the inductor L gave rise to a rather strong symmetry-breaking term which spoiled the model properties. Moreover, this type of setup did not yet allow us to define the initial conditions of the system with sufficient accuracy.

In order to overcome these problems we finally decided to construct our model circuit merely from active components. So, Eq. (25.3) was designed step by step using operational amplifiers and integrated circuits. A block diagram of this setup is presented in Fig. 25.9. It includes the unstable controller as well as elements for defining the experimental initial conditions. The components at the top of Fig. 25.9 maps the relation $\dot{y} = x$. Then, by integrating x the variable y is obtained. The adder comprehends all terms contributing to $\dot{x}$, and x is again obtained by integration. The controller variable w is coupled to the x-component, so the product of w and $f(x)$ is also included in the adder inputs, while the delay term and the intrinsic instability of w are generated by the loops at the bottom. The bifurcation parameter ε, the control amplitude K, and the positive exponent λ_c are simply determined by the gain of electronic amplifiers. For defining the initial conditions, we introduced switches parallel to each of the integrator outputs which generate the variables $x(t), y(t)$, and $w(t)$. These switches allowed us to apply adjustable constant voltages x_0, y_0, and w_0, respectively. Thus, when switching on the system at $t = 0$, the variables $x(t)$ and $y(t)$ started from a well-defined state. At about one cycle later the feedback loop generating the control signal was switched on, simultaneously with the controller variable $w(t)$. Such a time-lag was necessary to obtain an appropriate delayed signal re-
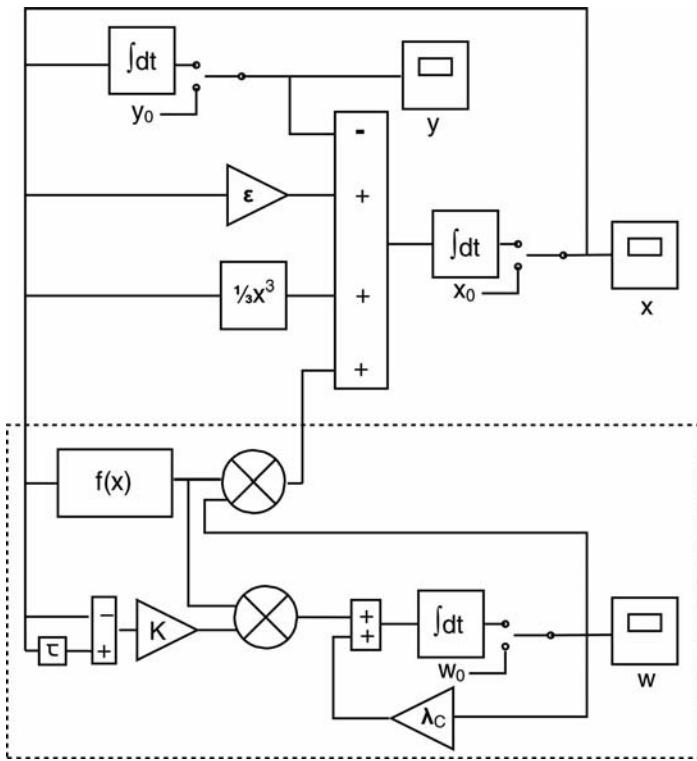
Fig. 25.9 Block diagram of the van der Pol oscillator with control loop (setup built from active components).

flecting the dynamics of the uncontrolled system close to the initial state. Note that the control generally failed when the feedback is switched on earlier than one cycle or later than seven or eight cycles. This is understandable since in the former case a proper delay signal has not yet developed while in the latter case the unstable system has already escaped too far away from the target state.

25.3.3
Control Coupling and Basin of Attraction

An essential result of our investigations was that the success of the unstable controller concept depends sensitively on the specific form of the coupling function $f(x)$. Our first choice for $f(x)$ followed the coupling suggested in [16]. The unstable degree of freedom, w, was coupled to the x-variable and, in turn, the delay term was coupled to the unstable controller w via a linear coupling $f(x) = x$ (cf. Eq. (25.3c)). In numerical simulations such a coupling had turned out to be essential for the control performance [16]. When applying this coupling scheme to our experiment, however, it failed for a large range of initial
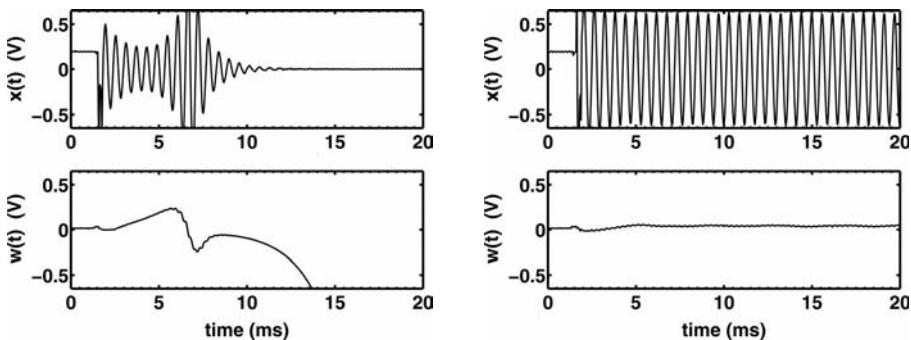
Fig. 25.10 Two attempts to control a torsion-free unstable orbit with linear coupling $f(x) = x$. Time series of $x(t)$ and $w(t)$ for the same set of initial conditions: $\varepsilon = -0.1$, $K = 0.3$, $x(0) = 0.2$ V, $y(0) = w(0) = 0$ V.

Left: relaxation toward the trivial fixed point with divergent control variable $w(t)$. Right: successful noninvasive stabilization of the unstable periodic orbit.

conditions. Figure 25.10 reflects a typical experimental situation. We chose the bifurcation parameter $\varepsilon = -0.1$, the control amplitude $K = 0.3$, and $y(0)$ and $w(0)$ were set to zero, while $x(0)$ was set to 0.2 V. We repeated the control experiment several times with the same set of parameters. In most cases the controller variable $w(t)$ immediately escaped to infinity while $x(t)$, after some irregular transients, settled either in the stable fixed point (cf. Fig. 25.10, l.h.s. column) or ended up in a high amplitude oscillatory state which meets the saturation limits of the operational amplifiers. In some cases, however, for the very same set of parameters we also achieved successful control (cf. Fig. 25.10, r.h.s. column), which, in fact, represents the first experimental evidence approving the concept of an unstable controller. The low success rate indicated that the method is rather sensitive to perturbations introduced by noise and by the irregular motion of the uncontrolled system during the starting phase. Such missing robustness is generally considered a serious drawback for practical applications.

However, it turned out that the low success rate could be improved considerably by changing the control function. When replacing the linear coupling $f(x) = x$ by a sigmoidal one, e.g., $f(x) = \text{sign}(x)$ or $f(x) = \tanh(\beta x)$, $\beta \gg 1$, the situation changed dramatically. Technically such a modification of the coupling could be easily implemented by means of an operational amplifier acting as a comparator. After such an implementation successful control could be achieved for a larger range of initial conditions with a success rate of almost 100% (cf. Fig. 25.11).

A quantitative estimate of the success of control was obtained by varying both control amplitude and initial conditions. For the case of linear coupling optimal control performance (for $\varepsilon = -0.1$) was obtained at $K = 0.4$. We set $x(0)$ and $w(0)$ to zero and increased $y(0)$ from 0 to 1 V in steps of 0.01 V. For each set of initial values we repeated the control experiment about 100 times. The part of successful attempts is shown in a histogram (cf. Fig. 25.12). For linear coupling
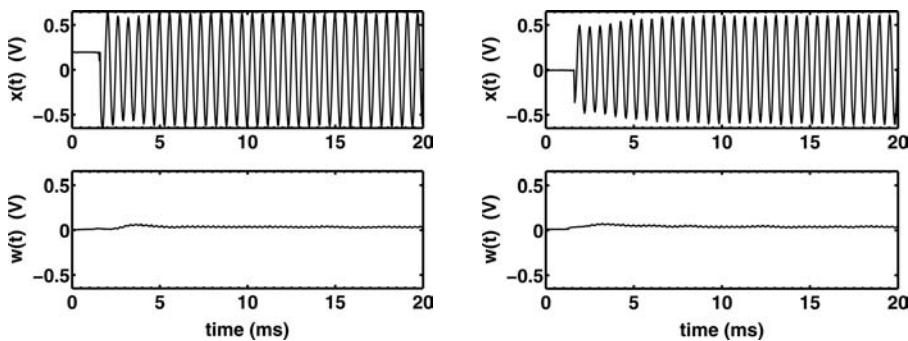
Fig. 25.11 Successful control of torsion-free unstable orbits with $f(x) = \mathrm{sign}(x)$, $\varepsilon = -0.1$, $K = 0.3$ and $y(0) = w(0) = 0$ V for different initial conditions: $x(0) = 0.2$ V (left) and $x(0) = 0$ V (right).
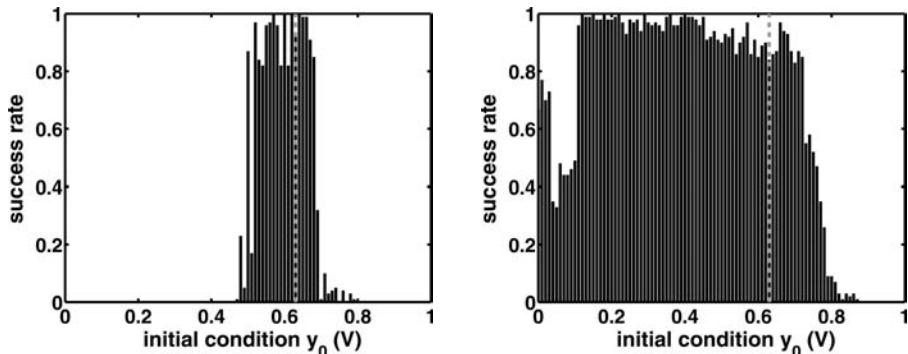
Fig. 25.12 "Basins of attraction" for different control couplings. L.h.s.: linear coupling $f(x) = x$, $K = 0.35$ (while $\varepsilon = -0.1$, $x(0) = w(0) = 0$ V). R.h.s.: sigmoidal coupling $f(x) = \mathrm{sign}(x)$, $K = 0.15$. Location of the unstable orbit is indicated by dashed line.

successful control was only achieved for $y(0)$ values from the neighborhood of the unstable orbit which is indicated by the dashed line at 0.63 V. For the case of a sigmoidal coupling optimal control was observed at $K = 0.15$, and the control regime was much larger than in the linear case. Accordingly we also obtained a much larger "basin of attraction" for the controlled orbit which now covers the full $y(0)$ range from 0 to 0.8 V yielding a success rate of almost 100%. At present we may only speculate about the mechanism for such a strong improvement. It is probably related to the limitation of the control force for strongly fluctuating x-transients during the onset of control. Without such a limitation large x-fluctuations might destroy the control by "overshooting."

25.4
Conclusions

Time delayed feedback control has been investigated for two different setups with regards to the global control performance. In particular, basins of attraction have been probed in electronic circuit experiments. Extended time delayed feedback control schemes were investigated in Section 25.2. Reduced basins of attraction and reduced structural stability have been measured which were caused by discontinuous transitions at control thresholds. Thus, a universal mechanism, well known in bifurcation theory, has shown its relevance in electronic circuit experiments. Section 25.3 dealt with the implementation of an unstable controller to stabilize torsion-free unstable periodic orbits that were generated in a subcritical Hopf bifurcation. The improvement of the control performance by changing the coupling scheme of the control force was demonstrated and a considerable enlargement of basins of attraction has been observed.

Some caution should be in place when using the term "basin of attraction". Since we were dealing with delay systems their dynamics is determined by previous states as well. Accordingly, the proper basin of attraction does not only depend on the actual values of the degrees of freedom, e.g., on initial conditions when the control is switched on, but also on the recorded delay states which determine the control force. When probing the basin of attraction in our experiment on the diode resonator in Section 25.2.4 the initial state was just the controlled orbit. The stability of this state in some neighborhood was probed by application of small perturbations which had even been synchronized with the phase of the external drive. Thus, all perturbations started from a state with a common history. Such a procedure may be considered as a finite-dimensional cross section in the infinite-dimensional phase space of the delay system. In practical applications, however, one is often less interested in the stability of the controlled state against perturbations once the system has settled on it. The problem how to reach the controlled state in the most efficient way is usually of more interest. Therefore, we have chosen in Section 25.3.3 a different type of approach to probe the global control performance. Here, control was switched on skipping a transient and the history of the dynamics was taken from the uncontrolled motion. Tiny fluctuations may amplify during the transient and we ended up with a probability distribution for successful control. Thus, the distributions reflect implicitly the size of the basin in a rather intricate way. Above all, such an approach seems to have a more direct relevance for real control experiments, although a direct link to theoretical considerations is more difficult to establish.

The experimental study is still in progress, and further systematic investigations on global properties are necessary. In particular, the effect of the specific form of control coupling on the control performance will be of major importance from the viewpoint of practical applications. Even now it is already clear that in systems without torsion the idea of the unstable controller does work and – for an appropriate type of coupling – results in robust time delayed feedback control suitable for practical applications.

References

1 *Handbook of Chaos Control,* edited by H. G. Schuster (Wiley-VCH, Berlin, 1999).

2 K. Pyragas, *Continuous control of chaos by self-controlling feedback,* Phys. Lett. A **170**, 421 (1992).

3 W. Just, T. Bernard, M. Ostheimer, E. Reibold, and H. Benner, *Mechanism of time delayed feedback control,* Phys. Rev. Lett. **78**, 203 (1997).

4 J. K. Hale and S. M. Verduyn Lunel, *Introduction to Functional Differential Equations* (Springer, New York, 1993).

5 J. E. S. Socolar, D. W. Sukow, and D. J. Gauthier, *Stabilizing unstable periodic orbits in fast dynamical systems,* Phys. Rev. E **50**, 3245 (1994).

6 K. Pyragas, *Control of chaos via an unstable delayed feedback controller,* Phys. Rev. Lett. **86**, 2265 (2001).

7 W. Just, E. Reibold, H. Benner, K. Kacperski, F. Fronczak, and J. Hołyst, *Limits of time delayed feedback control,* Phys. Lett. A **254**, 158 (1999).

8 J. E. S. Socolar and D. J. Gauthier, *Analysis and comparison of multiple-delay schemes for controlling unstable fixed points of discrete maps,* Phys. Rev. E **57**, 6589 (1998).

9 W. Just, E. Reibold, K. Kacperski, P. Fronczak, J. Hołyst, and H. Benner, *Influence of stable Floquet exponents on time delayed feedback control,* Phys. Rev. E **61**, 5045 (2000).

10 O. Beck, A. Amann, E. Schöll, J. E. S. Socolar, and W. Just, *Comparison of time delayed feedback schemes for spatio-temporal control of chaos in a reaction–diffusion system with global coupling,* Phys. Rev. E **66**, 016213 (2002).

11 J. Guckenheimer and P. Holmes, *Nonlinear Oscillations, Dynamical Systems, and Bifurcations of Vector Fields* (Springer, New York, 1986).

12 C. v. Loewenich, H. Benner, and W. Just, *Experimental relevance of global properties of time delayed feedback control,* Phys. Rev. Lett. **93**, 174101 (2004).

13 W. Just, H. Benner, and C. v. Loewenich, *On global properties of time delayed feedback control: weakly nonlinear analysis,* Physica D **199**, 33 (2004).

14 H. Nakajima, *On analytical properties of delayed feedback control of chaos,* Phys. Lett. A **232**, 207 (1997).

15 H. G. Schuster and M. B. Stemmler, *Control of chaos by oscillating feedback,* Phys. Rev. E **56**, 6410 (1997).

16 K. Pyragas, V. Pyragas, and H. Benner, *Delayed feedback control of dynamical systems at a subcritical Hopf bifurcation,* Phys. Rev. E **70**, 056222 (2004).

26
Application of a Black Box Strategy to Control Chaos

Achim Kittel and Martin Popp

26.1
Introduction

In this chapter a strategy of a user-friendly chaos controller for general purpose applications is discussed. The basic idea is to use the knowledge gained in recent years from nonlinear dynamics to set up a black box which can be used as easily as the well-known proportional-integral-differential controller (PID controller) in many problems [1–6].

Earlier in the field of chaos control the system under consideration had to be investigated in advance [7–11] to design a control strategy. But today different methods are developed to treat certain classes with the same strategy. This gives the opportunity to set up a controller able to stabilize different unstable nonlinear systems. In the following a possible realization of such a controller is introduced, the possibilities for the control of nonlinear chaotic systems are demonstrated, and are illustrated as a tool to investigate unknown nonlinear chaotic systems.

26.2
The Model Systems

In order to demonstrate the capabilities and the features of the controller it is applied to very different systems from the mathematical point of view. One of them is an oscillator obeying a set of ordinary differential equations (ODE) and the other is an oscillator which has to be described by delay-differential equations (DDE). The first oscillator is called the *Shinriki oscillator* and the second a *Mackey-Glass oscillator*.

26.2.1
Shinriki Oscillator

This type of nonlinear oscillator was introduced by the Japanese engineer Shinriki in 1981 [12]. The oscillator is a model system for a three-dimensional chaotic system. It serves here as a representative of autonomous systems which can be described by a system of ordinary differential equations and which exhibit a period-doubling sequence as a route to chaos [13].

The schematic of the circuit is shown in Fig. 26.1. The three system variables are the two voltages across the capacitors C_1 and C_2 and the current I_3 through the inductor L_1. The capacitor C_2 together with the inductor L_1 represent a parallel oscillator which is excited by the negative impedance converter (NIC) via the nonlinear element. The nonlinear element is formed by the two oppositely directed zener diodes D_1 and D_2 and the potentiometer P_2 in parallel. The NIC (marked in Fig. 26.1 by a dashed box) is compound of the operational amplifier (OPA) TL071 and three resistors. It has a feature that the characteristics of the resistor R_4 is inverted, i.e., if a positive voltage is applied to the NIC a negative current $I_{NIC} = -V/R_4$ is delivered by the NIC. This effect drives the capacitor C_1 and the parallel oscillator formed by C_2 and L_1 via the nonlinear element D_1 and D_2. The potentiometer P_1 reduces the effective current from the NIC and serves, therefore, as a handle to adjust the degree of excitation of the system. The system dynamics can be modeled by the three phase space variables: the voltage V_1 across the capacitor C_1, the voltage V_2 across the capacitor C_2, and the current I_3 through the inductor L_1 which is measured as the voltage drop across the resistor R_1.

The system of differential equations can be easily derived by means of the Kirchhoffs laws. They read
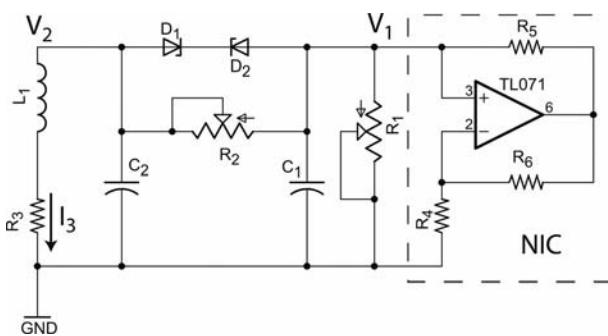
Fig. 26.1 The Shinriki oscillator. The oscillator generates chaotic oscillations similar to the one generated by the Rössler system and can be described well with a three-dimensional system of ordinary differential equations. For further details see the text.

$$C_1 \frac{dV_1}{dt} = -V_1 \left(\frac{1}{R_{\mathrm{NIC}}} + \frac{1}{R_1} \right) f(V_1 - V_2) \tag{26.1}$$

$$C_2 \frac{dV_2}{dt} = f(V_1 - V_2) - I_3 \tag{26.2}$$

$$L_1 \frac{dI_3}{dt} = -I_3 R_3 + V_2 \tag{26.3}$$

with $R_{\mathrm{NIC}} = -R_4$. $f(V_1 - V_2)$ denotes the $I-V$ characteristics of the nonlinear element and can be approximated by a polynomial. The dominant frequency of the oscillator is $f_0 = 1/(2\pi\sqrt{LC_2})$. For the given values of the devices[1] the frequency is about 900 Hz which is very convenient to investigate the system. On one hand the frequency is fast enough that one can observe long time series spanning over many periods of the characteristic frequency without having problems with drifting parameters. On the other hand the frequency is not too high to be digitized with a high over-sampling rate to grasp higher harmonics.

26.2.2
Mackey-Glass Type Oscillator

The second oscillator we will use as a model system represents a different class of systems. Mathematically, these systems are described by a system of DDE. We will restrict ourself to the one-dimensional system which was introduced by Mackey and Glass [14]. They modeled the concentration of the red blood cells for certain blood diseases by a delay-differential equation (DDE). This type of differential equation is a lot more complicated than a ODE because it is not necessary to know just one initial value but an interval of values.

Mackey and Glass used the following equation to describe the concentration of red blood cells:

$$\frac{dx}{dt} = \frac{ax(t - \tau)}{1 + x^n(t - \tau)} - cx \tag{26.4}$$

The first term on the right-hand side is the nonlinear term which represents the production rate of red blood cells. Because the production takes several days the system reacts to a certain concentration of red blood cells with this delay. It starts at zero at the concentration x of zero (clearly, x has to be positive), has a maximum at finite values of the concentration x and falls off to zero for larger concentrations. The second term of the right-hand side represents the decay rate of dying red blood cells.

The system was realized with an analog delay line a *buckle brigade delay line* (BBD), which shifts charge representing a certain voltage through a chain of capacitors. At the end of the chain the charge is converted back to a voltage. The

---

[1] $R_1 = 99.4\ \Omega$; $R_2 = 4.7\ \mathrm{k}\Omega$; $R_3 = 4.7\ \mathrm{k}\Omega$; $R_4 = 6.8\ \mathrm{k}\Omega$;
$C_1 = 10\ \mathrm{nF}$; $C_2 = 101\ \mathrm{nF}$; $L_1 = 323\ \mathrm{mH}$; $D_1 = D_2 = \mathrm{ZPD3.7}$.
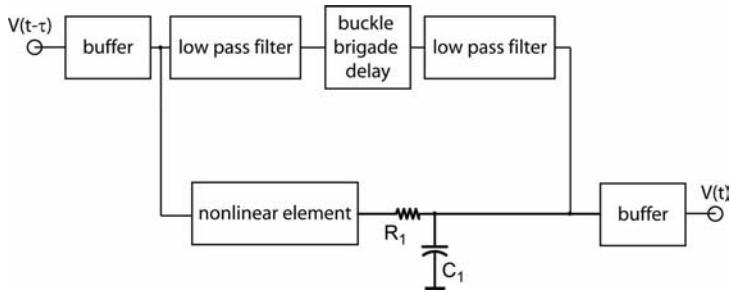
Fig. 26.2 Block diagram of the Mackey-Glass oscillator. The product of the resistance R_1 and the capacitance C_1 define the rate of change in the differential equation (26.4), i.e., a factor on the left-hand side ($R_1 = 11$ kΩ and $C_1 = 220$ nF; $R_1C_1 = 2.4$ ms). (b) Schematic of the nonlinear element used in the Mackey-Glass oscillator.
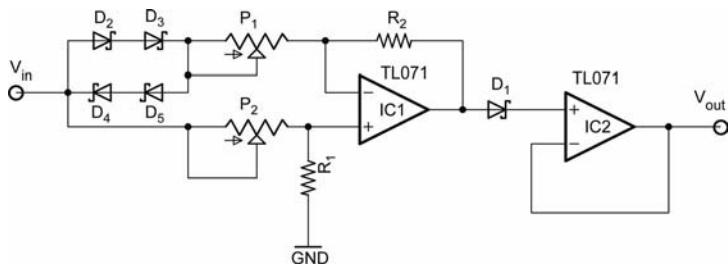
Fig. 26.3 Schematic of the nonlinear element used in the Mackey-Glass oscillator.

delay is determined by the number of capacitors and by the clock signal which clocks shifting of the charge from one capacitor to another. It can be varied by varying this clock frequency. A block diagram of the oscillator is shown in Fig. 26.2. The schematic of the used nonlinear element is shown in Fig. 26.3. It represents a single humped function at positive values. The capacitor C_1 and the resistor R_1 define the rate of change in the oscillator and the product C_1R_1 emerges in Eq. (26.4) as a factor on the left-hand side in front of the time derivative. Resistor R_1 and capacitor determine an upper cutoff frequency of the system. To characterize the electronic circuit it is helpful to use the dimensionless, reduced delay time which corresponds to the delay time in the Mackey-Glass system $\tau = \tau_{\text{BBD}}/C_1R_1$.

The measured characteristics are depicted in Fig. 26.4. In the figure the solid squares represent the measured characteristics from the electronic circuit and the open circles represent a curve fit of the equation:

$$\frac{\mathrm{d}x}{\mathrm{d}t} = \frac{ax(t-\tau)}{1+x^{10}(t-\tau)} \tag{26.5}$$
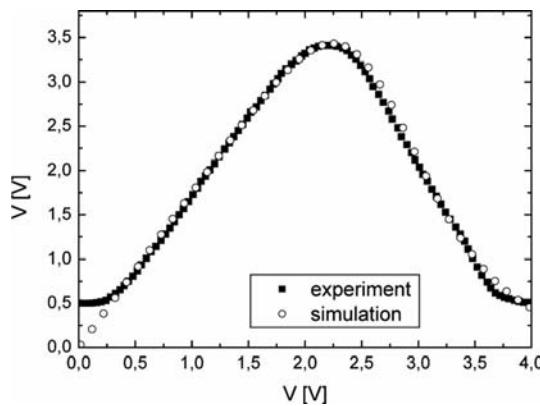
Fig. 26.4 Comparison of the experimental characteristics of the nonlinear element used in the Mackey-Glass oscillator and the fitted curve to these data.
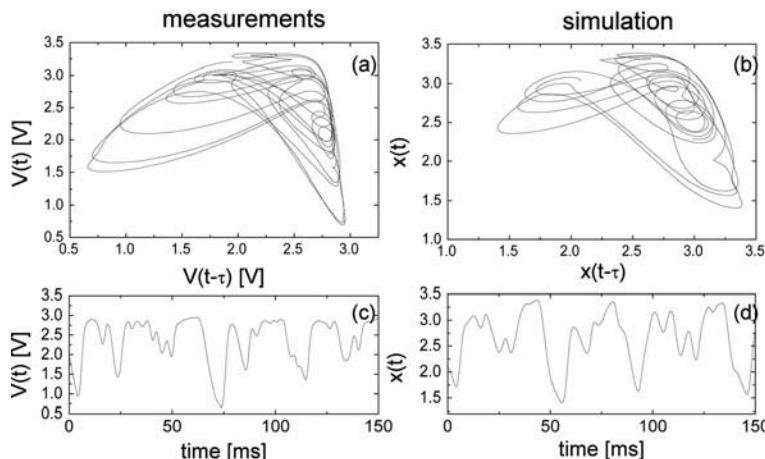
Fig. 26.5 (a) Phase portrait of a measured time series with $\tau = 4.06$. (b) Numerically simulated phase portrait. (c) Time series of the measured data depicted in (a). (d) Time series of the simulated data.

we achieve a $\chi^2 \approx 0.014$. With the appropriate parameters we are able to numerically integrate the system to compare it to the results from the electronic circuit.

Examples of a measured and a simulated time series are plotted in Fig. 26.5. It can be seen that the agreement is acceptable, i.e., tolerances of the devices, noise in the system, and parasitic inductances, and capacitances are small enough to be neglected.
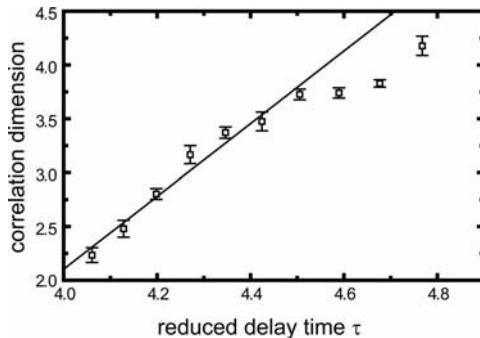
Fig. 26.6 Dependence of the correlation dimension on the reduced delay time τ. The line in the graph is only a guide for the eye and does not represent a fit.

One special feature of the delay-differential equations is depicted by the following. If we search for a solution for a system of ordinary differential equations we need to specify the initial values. To characterize a certain system state we have to know the same number of values as the number of first-order equations we have. In the case of a DDE the situation is completely different. Even if we are able to describe the dynamics by only one single equation, like in the case of the Mackey-Glass system, it is nevertheless necessary to know the values on the interval $[-\tau, 0]$. In principle this means an infinite number of values. As a consequence the complexity of the system increases with increasing delay time τ even if the system is described by a single equation. This feature can also be observed in the case of our Mackey-Glass oscillator. To characterize the complexity of the signals delivered by the oscillator we calculated the correlation dimension of the signals. The dependence of the correlation dimension on the reduced delay time is plotted in Fig. 26.6. It can be seen that the dimension of the system increases monotonously with increasing delay time as it is usual for this type of system. For these time delay systems it is often not possible to find unstable periodic orbits and, therefore, they do not allow for an analysis to find a tailored control strategy. The oscillator represents a second class of autonomous systems which will serve here as model system.

26.3
The Controller

The controller discussed here is based on the control strategy of the delayed-feedback control with self-adapted delay time [15]. To demonstrate that the control of chaotic systems does not need complex algorithms and electronics, the controller electronics is constructed mainly by means of transistor logic (TTL), i.e., a fixed wired circuit and not a fancy program which is running on a power-
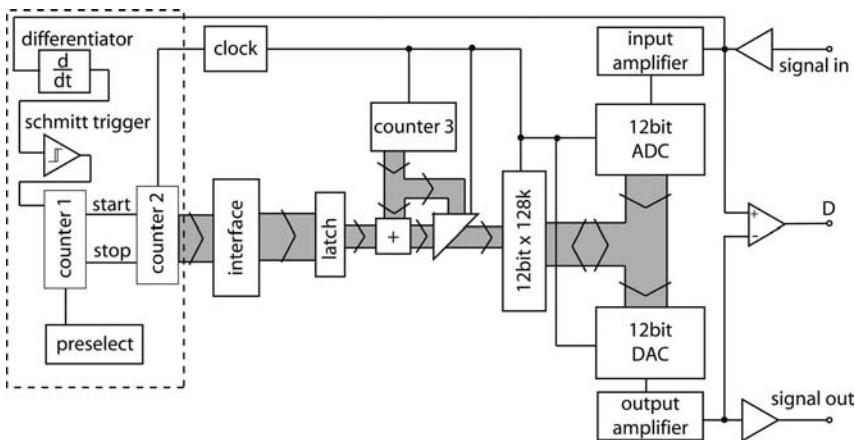
Fig. 26.7 Block diagram of the controller. The controller consists mainly of two parts. On the left-hand side marked by a dashed box the part which determines the current length of the period. The part on the right-hand side represents a delay line made of a ring memory of 128 thousand words length. For a detailed explanation see the text.

ful computer. The controller is applied to the two oscillators introduced above to analyze, e.g., detection of periodic orbits, and control these onto different periodic orbits.

A block diagram with different components of the controller is shown in Fig. 26.7. The left-hand side of the diagram, marked by the dashed box, represents the signal condition part of the circuit, which measures the time lag between different maxima. The part on the right-hand side is the delay line, which delays the signal by a certain amount of time and feeds it back into the system under control.

After the amplification of the signal at the input at the upper right corner it becomes electronically differentiated on the left side. A Schmitt trigger forms a square-wave signal out of the differentiated signal which switches at each maximum and then back at each minimum. The square-wave signal clocks a reverse counter (counter 1) which counts from a preselected value back to zero. By means of this preselected value it is possible to adjust the delay time of the lag between two, three, etc. maxima, i.e., different orders of periodic orbits can be stabilized. The counter starts and stops another counter (counter 2) which acts as a stop watch by using the clock signal generated by a quartz oscillator. The counter reading is transferred to the interface after the stop signal has arrived.

The delay line operates as a ring storage for the input signal. The delay time of the line is given by an increment between the current storage address and the current reading address. The time lag between the maxima is taken from the interface and stored in a latch. A free running counter (counter 3) is used to generate the addresses of the random access memory (RAM) which stores

the digital values of the input signal. The signal applied to the input is amplified and then digitized by a 12-bit A/D-converter at a rate of 500 kSamples/s. The digital value is stored in the RAM at an address calculated by adding the current counter reading of counter 3 and the value stored in the latch. During the second half of a clock cycle the digital value at the address of the counter reading of counter 3 is converted in the D/A-converter and provided at the output. The signal which is fed back into the system under control is calculated by the difference between the delayed signal and the current signal of the system $D = V(t) - V(t - \tau)$. The coupling constant K of the control signal can be adjusted by the amplification or attenuation of this difference.

26.4
Results of the Application of the Controller to the Shinriki Oscillator

First, we will discuss the results when the controller is connected to the Shinriki oscillator. As already mentioned the oscillator serves as a model system for systems which can be described by an ordinary differential equation. The controller can serve two different purposes. Firstly, the control of the system by stabilizing periodic orbits and, secondly, the investigation of an unknown system by *delay-time spectroscopy*. In the latter case the *control signal*, i.e., the time averaged square of the current delivered by the output buffer is recorded in dependence of the delay time. If the delay time of the controller corresponds to a integer multiple of an unstable periodic orbit of the system, the control signal decreases by several orders of magnitude.

The controller is connected to the system in the following way. The input of the controller is coupled directly to the point in the circuit diagram which is labeled by V_1. The output of the controller is realized by means of a buffer to ensure that it is only a one-way coupling. The output of the buffer is coupled via a resistor R_c to the same point. By selecting different values of the preselect of the controller we are able to control the Shinriki oscillator to periodic orbits of different orders.

Figure 26.8 gives a good overview of the system under control. Bifurcation diagrams are recorded for different situations and plotted together in one diagram to be able to compare the changes. To follow different bifurcation diagrams they are increasingly shifted against each other by a successive offset of 0.2. The resistor R_1 was varied as the bifurcation parameter and the resistor R_2 was kept constant at a value of 12.68 kΩ.

The diagram for the uncontrolled situation (marked with tiny filled squares) is plotted for the original values of the voltage oscillations. The results measured with a preselect of one, i.e., a period-1 orbit is stabilized, are represented by the hollow squares. It can be seen that the bifurcation diagram follows the same behavior as that of the unperturbed system until the branching of to the period-2 occurs. From this point the bifurcation diagram follows the unstable period-1 orbit until it becomes chaotic at high values of the bifurcation parame-
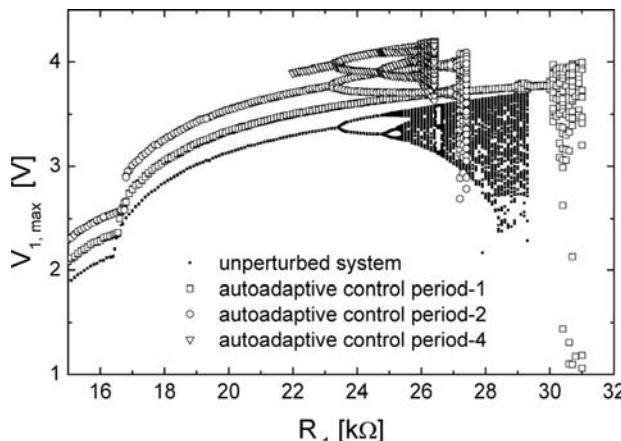
Fig. 26.8 Bifurcation diagram of the Shinriki oscillator. The tiny black squares represent the unperturbed system and the light squares, light circles, and light triangles result from the influence of the control to the period-1, period-2, and the period-4 orbit, respectively. For clarity the curves of the period-1, period-2, and period-4 are shifted by 0.2 V increasing offset against the unperturbed case and against each other.

ter ($R_1 = 30$ kΩ). If the preselect is changed to the value of two, the bifurcation changes as shown in Fig. 26.8 marked by hollow circles. The oscillator behavior is not changed until the bifurcation to the period-4 occurs. Here the period-2 orbit is stable until a value of the bifurcation parameter $R_1 \approx 27$ kΩ is reached. Here again, a chaotic oscillation starts. The situation for a preselect of four is depicted in Fig. 26.8 marked by hollow triangles. Here the period-4 orbit is stabilized until $R_1 \approx 26$ kΩ. From these findings we can conclude that higher periodic orbits are more sensitive to noise than the shorter ones.

In the following the influence of the control resistor R_c is discussed. It is not at all the case that a small control resistor which corresponds to a strong coupling will lead to stabilization of the system. In contrast depending on the limitation of the controller it is possible that the control resistor has to be of a value within a certain interval. This behavior is depicted exemplarily in Fig. 26.9. The involved parameter has been chosen as follows: $R_1 = 26.2$ kΩ and $R_2 = 12.68$ kΩ for the Shinriki oscillator and $T_1 = 1.41$ ms, $T_2 = 2.79$ ms, and $T_4 = 5.59$ ms for the delay times of the controller for the period-1, period-2, and period-4 orbit, respectively. It is not surprising that the larger interval of a possible stabilization is observed for the period-1 orbit. The interval for the period-2 orbit is drastically reduced and is located in the upper half of the interval for the period-1 interval. The situation is not simple as this can be seen from the fact that the interval for the period-4 orbit is shifted to higher control resistor values, i.e., reduced control coupling strength.
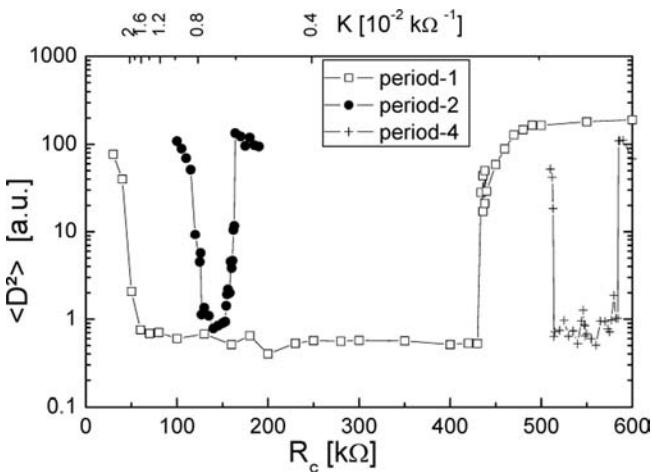
Fig. 26.9 The dependence of the averaged control signal on the control resistor for different values of the preselect and, therefore, different orders of the periodic orbits. The different periodic orbits are stabilized at different intervals of control resistor values.

26.4.1
Spectroscopy of Unstable Periodic Orbits

At the end of the presentation of the results gained from the Shinriki oscillator the *periodic orbit spectroscopy* (POS) is discussed. Here a fixed control resistor is chosen by which the controller is coupled to the system. The delay-time adaptor is switched off and the delay time is systematically varied over a range of differ-
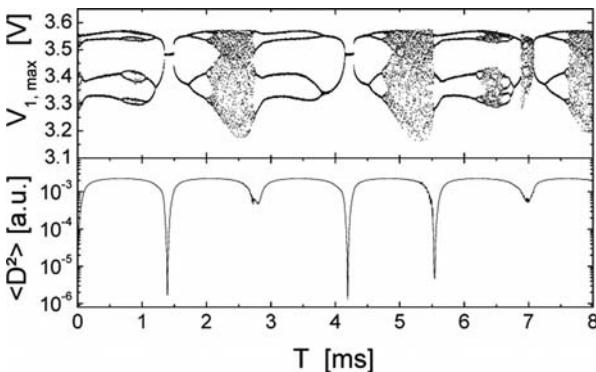
Fig. 26.10 Spectroscopy of periodic orbits of the Shinriki oscillator. Here the time delay of the controller is varied from 0 to 8 ms in steps of 4 μs. Period-1 orbits can be stabilized at 1.40 ms and 4.19 ms. At a value of 5.54 ms a period-4 orbit is stabilized as it can be seen in the upper part of the figure.

ent values. The averaged value of the resulting control signal $\langle D^2 \rangle$ is measured at each individual value of the delay time. $\langle D^2 \rangle$ is reaching a local minimum if the system under control is stabilized to periodic orbit of the length of the delay time of the controller. This can be utilized to find periodic orbits and, therefore, analyze an unknown system.

The results depicted in Fig. 26.10 show that the Shinriki oscillator possess a period-1 orbit at 1.40 ms and 4.19 ms and a period-4 orbit at 5.54 ms in the case $R_1 = 2.59$ kΩ and $R_2 = 12.68$ kΩ. The control resistor was chosen to be $R_c = 160$ kΩ. The control signal $\langle D^2 \rangle$ drops about three orders of magnitude which is a little less compared to the theoretical expectable maximum value in the case of a 12-bit converter.

26.5
Results of the Application of the Controller to the Mackey-Glass Oscillator

In this section the results will be discussed in a similar way as in the previous section. The difference is the type of oscillator which represents another class of systems. The Mackey-Glass system is described by integro-differential equations. This makes the analysis of the system more complicated. The fractal dimension of the attractor of such a system increases by changing a system parameter to a very high dimension. An analysis of such a high-dimensional system is complicated and it is not possible to distinguish the system from a noisy, i.e., stochastic system. There is no algorithm to determine the unstable periodic orbits from time series as is the case for systems described by ODEs.

In Fig. 26.11, a phase portrait of a chaotic and a stabilized unstable orbit of the Mackey-Glass oscillator is plotted. The parameters of the system are the in-
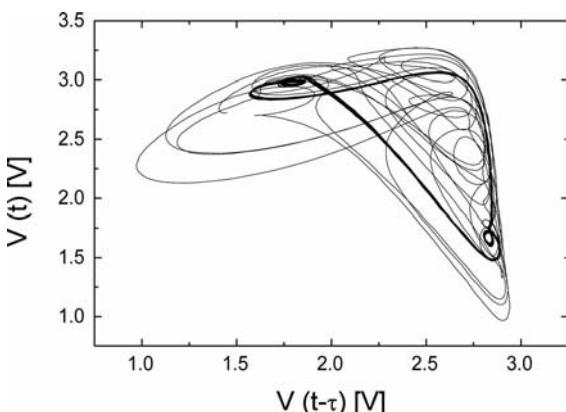
Fig. 26.11 Two-dimensional phase portrait of a chaotic oscillation of the Mackey-Glass oscillator (thin line) and the stabilized period-1 orbit applying the delayed-feedback controller (thick line).
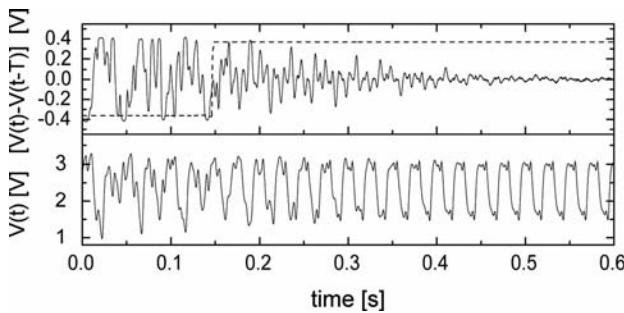
Fig. 26.12 Above: Transient of voltage drop across the control resistor $[V(t) - V(t - \tau)]$; below: of the voltage across the capacitor C_1 of the Mackey-Glass oscillator after the controller was switched on (step in the dashed line in the upper part).

ternal delay time of the Mackey-Glass oscillator 11.056 ms and $R_c = 15$ kΩ. The resulting delay time of the controller is $T = 25.2$ ms. The orbit which was originally an unstable periodic is embedded within the chaotic attractor but cannot be determined from the time series.

It is essential for the success of the control of an unstable periodic orbit that it does not disturb the system very much. During the transition (see Fig. 26.12) from the chaotic to the stable state it is crucial to not disturb too heavily. Therefore, it is necessary to use a limiter as described in Section 26.3. A too large feedback signal will change the system and can result in a new dynamic of the system under control and the controller itself. This kind of new dynamic is often undesired and the control signal $\langle D^2 \rangle$ is not vanishing even if the periodic state is reached, but this state is not a solution of the dynamic system alone.

The bifurcation for the chaotic system is depicted in Fig. 26.13 (a). For a proper determination of the bifurcation diagram it was necessary to use a linear combination of the voltages $V(t)$ and $V(t + \tau)$ because both voltages exhibit more than one maximum even in the case of the period-1 orbit. This can be seen in Figs. 26.11 and 26.12. In the diagram $V(t) - V(t - \tau)$ is plotted over the bifurcation parameter τ. Up to $\tau = 8.26$ the system possess a stable fixed point. A period doubling scenario can be seen which ends in a chaotic state above a $\tau = 9.51$ ms.

If the controller is applied to the Mackey-Glass oscillator and the preselect is set to one ($R_c = 20$ kΩ) the bifurcation changes as shown in Fig. 26.13 (b). The bifurcation diagram exhibits a hysteresis. If the bifurcation parameter is increased continuously the system exhibits a period-1 orbit which corresponds to the unstable period-1 orbit after the bifurcation to the period-2 state at $\tau = 9.05$ ms has taken place. The bifurcation as well as the chaotic state are completely suppressed over a large interval of the bifurcation parameter (marked in Fig. 26.13 (b) by an arrow pointing to the right). Above a value $\tau = 11.55$ ms the orbit changes drastically as depicted in Fig. 26.13 (c) without changes to the controller (marked in Fig. 26.13 (b) by an arrow pointing down).
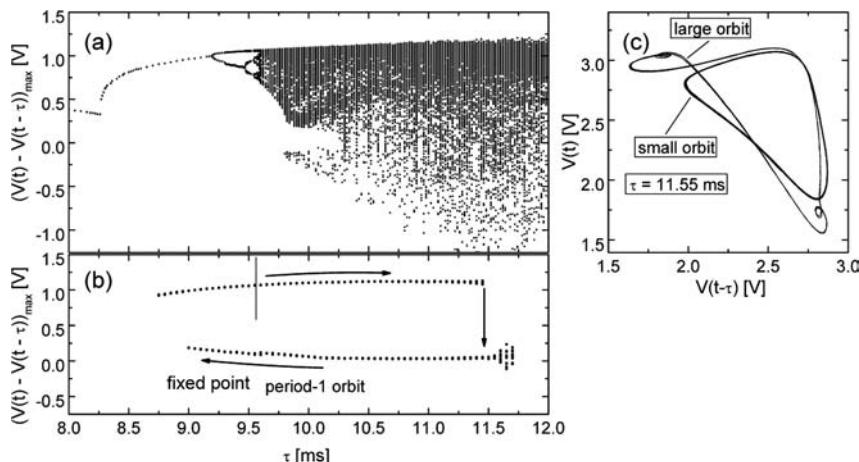
Fig. 26.13 (a) The bifurcation diagram of the Mackey-Glass oscillator without a control. (b) The bifurcation diagram with active control of the system. (c) The hysteretic behavior can be observed if the bifurcation parameter τ is firstly increased above a certain value and then decreased. The two branches of the hysteresis correspond to two limit cycles of different sizes.

The large orbit is now changed to a smaller one corresponding to an oscillation with a smaller amplitude. This transition is not reversible nor intermittent. Only if τ is lowered to 8.5 ms the system changes back to the larger orbit (marked in Fig. 26.13 (b) by an arrow pointing up). For larger values of $\tau > 11.6$ ms the small orbit cannot be stabilized any more. The small orbit changes continuously if parameter τ is decreased until an unstable fixed point is stabilized below $\tau \approx 9.6$ ms (marked by a vertical line in Fig. 26.13 (b)). Below $\tau = 8.25$ ms the fixed point is the stable one of the original Mackey-Glass oscillator.

Although the Mackey-Glass system is a lot more complicated than a low-dimensional ODE system the dependence on the coupling strength, i.e., the control resistor R_c in the present case, is simpler than in the case of the Shinriki oscillator. Figure 26.14 shows the dependence of the averaged control signal on the control resistor. In contrast to the Shinriki oscillator we observe only a minimal coupling strength as a condition for control for a stable periodic orbit.

26.5.1
Spectroscopy of Unstable Periodic Orbits

As already mentioned it is not possible to determine the unstable periodic orbits from measured time series, therefore, one has to rely on a control algorithm which is able to find the periodic orbits itself. To determine the unstable periodic orbits one can make use of the POS to perform a spectroscopy on these unstable orbits. Figure 26.15 shows the result of such a spectroscopy. The control signal shows six
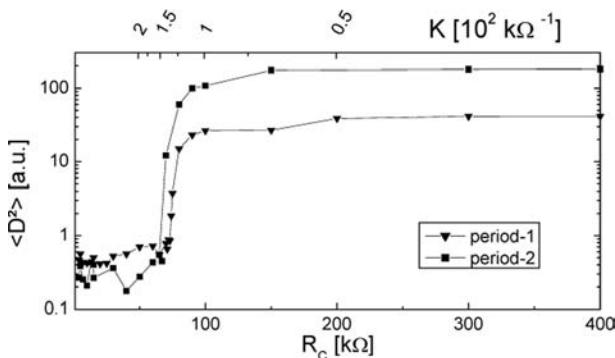
Fig. 26.14 Dependence of the control signal ΔV on the value of the control resistor, i.e., the coupling strength for the Mackey-Glass oscillator. The two curves correspond to a stabilization of the period-1 and period-2 orbit. In both the cases the system cannot be stabilized if the coupling strength is too small, i.e., the coupling resistor is larger than 80 kΩ.
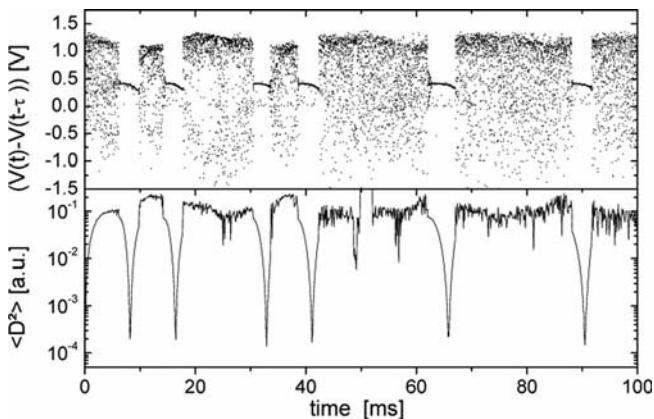
Fig. 26.15 Delay-time spectroscopy on the Mackey-Glass oscillator. In the upper part of the figure different local maxima of the voltage across the capacitor are plotted. In the lower part the control signal $\langle D^2 \rangle$ is plotted on a semilogarithmic scale. The delay time of the oscillator was $\tau = 10.056$ ms and the control resistor was chosen to be $R_c = 20$ kΩ. The delay-time interval reaching from 0 to 100 ms was scanned with 0.1 ms steps.

pronounced minima. If one examines the phase portrait it turns out that in all cases the same periodic orbit is stabilized even in cases if the delay time of the control is equivalent to multiples of the periodic time of the period orbit. This seems to be caused by the fact that control remained switched on during the scanning procedure. Under the influence of the control the system stays in the vicinity of this periodic orbit. If the control was switched off before the new delay time was

set the system can evolve freely and a lot of other more complex orbits could be stabilized. These orbits have a periodic time of up to the fourth of the internal delay time of the Mackey-Glass oscillator. The complex orbits were not caught after every switch to the control state but only with a certain probability. This fact can be understood in that the basin of attraction of the controlled orbit is restricted to a certain fraction of the visited phase space.

26.6
Further Improvements

The results discussed here were gained with a delay-feedback controller which was built from logic devices with low degree of integration. The intension was to demonstrate that no fancy controllers are needed, in principle, and this should be seen as a proof of concept. If a real application is planned a better choice would be to use a microcontroller-based system with an integrated AD- and DA-converter. Only if the requirements concerning resolution or speed of conversion cannot be fulfilled by a microcontroller should one use an external converter controlled by a microcontroller. Modern converters possess a conversion speed of about 80 MSamples/s at a resolution of 12 bit. This should be sufficient for many technical applications.

Here only delayed-feedback control is discussed. Extended feedback delay control [16–18] improves the performance of the controller in such a way that the parameter regions of possible control are enlarged. This can be incorporated very easily and would be advantageous.

As different as the two oscillators are they have one thing in common. They possess a torsion around the unstable periodic orbits and, therefore, the delayed-feedback control will work (see [19–21]). But there exists a class of systems without this torsion. It has been believed for a long time that such type of system cannot be stabilized by means of the continuous time-delay controller.

Different control schemes have been devised to overcome that limitation [22–24]. However, recently it was shown that this limitation does actually not hold [25], see Chapter 4.

26.7
Conclusions

It was demonstrated that it is possible to set up a black box controller with a control strategy which is applicable to different systems without redesigning the controller. It has to be stressed that the strategy is not applicable to any kind of system but to a large variety of different systems. Further improvements of the controller have been given. It was also shown that the controller can be used to analyze unknown systems in the sense that it is possible to find unstable periodic orbits hidden in the complex dynamics of these systems. Therefore, it also serves as a measurement tool.

References

1 S. Barnett. *Introduction to Mathematical Control Theory*. Clarendon Press, Oxford, 1975.

2 K. Zhou, J. C. Doyle and K. Glover. *Robust and Optimal Control*. Prentice-Hall, Upper Saddle River, NJ, USA, 1996.

3 W. L. Brogan. *Modern Control Theory*. Prentice-Hall, Upper Saddle River, NJ, USA, 1991.

4 J. C. Doyle, B. A. Francis and A. R. Tannenbaum. *Feedback Control Theory*. Macmillan, Englewood Cliffs, NJ, 1992.

5 M. Krstic, P. V. Kokotovic and I. Kanellakopoulos. *Nonlinear and Adaptive Control Design*. Wiley, New York, NY, USA, 1995.

6 B. C. Kuo. *Automatic Control Systems*. Prentice-Hall, Upper Saddle River, NJ, USA, 1987.

7 A. Hübler and E. Lüscher. Resonant stimulation and control of nonlinear oscillators. *Naturwissenschaften*, 76:67–69, 1989.

8 B. B. Plapp and A. W. Hübler. Nonlinear resonances and suppression of chaos in the rf-biased Josephson junction. *Phys. Rev. Lett.*, 65(18):2302–2305, 1990.

9 E. Ott, C. Grebogi and J. A. Yorke. Controlling chaos. *Phys. Rev. Lett.*, 64(11):1196–1199, 1990.

10 W. L. Ditto, S. N. Rauseo and M. L. Spano. Experimental control of chaos. *Phys. Rev. Lett.*, 65(26):3211–3214, 1990.

11 E. Atlee Jackson. Controls of dynamic flows with attractors. *Phys. Rev. A*, 44(8):4839–4853, 1991.

12 M. Shinriki, M. Yamamoto and S. Mori. Multimode oscillations in a modified Van Der Pol oscillator containing a positive nonlinear conductance. *Proc. IEEE*, 69(3):394–395, 1981.

13 A. Kittel, K. Pyragas and R. Richter. Prerecorded history of a system as an experimental tool to control chaos. *Phys. Rev. E*, 50(1):262–268, 1994.

14 M. C. Mackey and L. Glass. Oscillation and chaos in physiological control systems. *Science*, 197(4300):287, 1977.

15 A. Kittel, J. Parisi and K. Pyragas. Delayed feedback control of chaos by self-adapted delay time. *Phys. Lett. A*, 198 (5/6):433–436, 1995.

16 J. E. S. Socolar, D. W. Sukow and D. J. Gauthier. Stabilizing unstable periodic orbits in fast dynamical systems. *Phys. Rev. E*, 50(4):3245–3248, 1994.

17 K. Pyragas. Control of chaos via extended delay feedback. *Phys. Lett. A*, 206(5/6):323–330, 1995.

18 M. E. Bleich and J. E. S. Socolar. *Phys. Lett. A*, 210:87, 1996.

19 T. Ushio. *IEEE Trans. Circuits Syst. I, Fundam. Theory Appl.*, 43:815, 1996.

20 W. Just, T. Bernard, M. Ostheimer, E. Reibold and H. Benner. Mechanism of time delayed feedback control. *Phys. Rev. Lett.*, 78(2):203–206, 1997.

21 Hiroyuki Nakajima. On analytical properties of delayed feedback control of chaos. *Phys. Lett. A*, 232(3/4):207–210, 1997.

22 K. Pyragas. Control of chaos via an unstable delayed feedback controller. *Phys. Rev. Lett.*, 86(11):2265–2268, 2001.

23 K. Pyragas, V. Pyragas and H. Benner. Delayed feedback control of dynamical systems at a subcritical hopf bifurcation. *Phys. Rev. E (Stat., Nonlinear, Soft Matter Phys.)*, 70(5):056222, 2004.

24 K. Pyragas, V. Pyragas, I. Z. Kiss and J. L. Hudson. Adaptive control of unknown unstable steady states of dynamical systems. *Phys. Rev. E*, 70(2):026215, 2004.

25 B. Fiedler, V. Flunkert, M. Georgi, P. Hövel and E. Schöll. Refuting the odd-number limitation of time delayed feedback control. *Phys. Rev. Lett.*, 98(11):114101, 2007.

Part VII
Applications to Chemical Reaction Systems

27
Feedback-Mediated Control of Hypermeandering Spiral Waves

Jan Schlesner, Vladimir Zykov, and Harald Engel

27.1
Introduction

Two-dimensional rotating excitation waves are observed in a variety of quite different physical, chemical, and biological media. The well-known examples include cardiac muscle tissue [1, 2], aggregating slime-mould cells [3], catalytic surface reactions as the oxidation of carbon monoxide on a platinum single crystal surface [4], or concentration waves in the Belousov-Zhabotinsky (BZ) reaction [5–12]. From a theoretical point of view, all these experimentally available systems belong to a single broad class known as excitable media [10, 13–15].

Excitable media are essentially nonlinear dissipative dynamical systems with energy sources distributed in space. Wave processes in excitable media differ strongly from those in optics or acoustics. Due to a balance between energy influx and dissipation, the undamped propagation of a solitary wave is possible. Usually, a solitary wave includes a rapid transition from a stable rest state to an excited state followed by a slow recovery transition back to the rest state. During this phase, the medium is refractory, and only gradually recovers excitability. Due to the finite duration of the refractory phase, there is a minimal wavelength of a periodic wave train. Moreover, two propagating waves annihilate after a collision in contrast to an interference of waves in linear systems.

Spiral waves can be created using special initial conditions, or they evolve from a disruption in a propagating excitation wave caused by a heterogeneity of the medium. Although heterogeneities can facilitate their formation, spiral waves exist in completely homogeneous, spatially uniform excitable media. The influence of the boundary conditions decreases very fast with the distance from the boundary and practically vanishes if this distance exceeds the spiral wavelength. Thus, once created spiral waves represent very robust sources of wave activity in an excitable medium.

Sometimes, such self-sustained activity destroys normal functions of biological media and is undesirable. Certain cardiac arrhythmias as ventricular fibrillations, for example, are believed to be related to spiral wave dynamics and spiral

instabilities. The role of spiral waves of electric activity in cardiac arrhythmias is one motivation to elaborate efficient and gentle methods for the control of spiral waves.

A spiral wave induces temporal oscillations with space-dependent amplitude and phase in all sites of the medium. Different regimes of rotation have been observed for spiral waves which can be characterized by the trajectory described by the spiral tip [9, 11]. The simplest case is a periodic regime called rigid rotation with a tip moving along a circle. Rigidly rotating spiral waves have constant shape and rotate uniformly. Under certain conditions, a transition from one-frequency periodic to two-frequency quasiperiodic motion occurs where the spiral tip meanders rather than follows a circular orbit. Meandering spiral waves are of two types called outward and inward meandering depending on whether their tip trajectory forms a flower-like orbit with loops pointing outward or inward, respectively. Finally, more complicated hypermeandering motion has been reported that includes at least three incommensurate frequencies [16] or even chaotic dynamics [17, 18].

The theory of spiral waves has been intensively elaborated during the last years [19–30]. But despite great progress in the understanding of dynamics, stability and interaction of spiral waves, there are still many unsolved problems. One important issue is the control of spiral wave dynamics. Here we focus on the control of hypermeandering spiral waves which can be considered as an example of chaos control in spatially extended two-dimensional nonlinear dynamical system.

Two control strategies for hypermeandering spiral waves are discussed below. Firstly, we describe the feedback-mediated stabilization of rigidly rotating spiral waves in a parameter regime where they are unstable in the absence of feedback, and meandering or hypermeandering spiral waves are observed instead. Secondly, a feedback-mediated parametric modulation is applied to the medium that induces a displacement of the spiral core based on the phenomenon of resonant drift.

27.2
The FitzHugh-Nagumo Model

A prominent example for the study of wave propagation in excitable media is the FitzHugh-Nagumo model [17, 31, 32] given by the equations

$$\frac{\partial u}{\partial t} = \frac{1}{\varepsilon}[u - u^3/3 - v - F(t)] + D_u \Delta u, \tag{27.1}$$

$$\frac{\partial v}{\partial t} = \varepsilon(u + \beta - \chi v). \tag{27.2}$$

Here, $u(x, y, t)$ and $v(x, y, t)$ represent the dimensionless concentrations of the activator and the inhibitor, respectively, β, χ, and $\varepsilon \ll 1$ are given parameters,
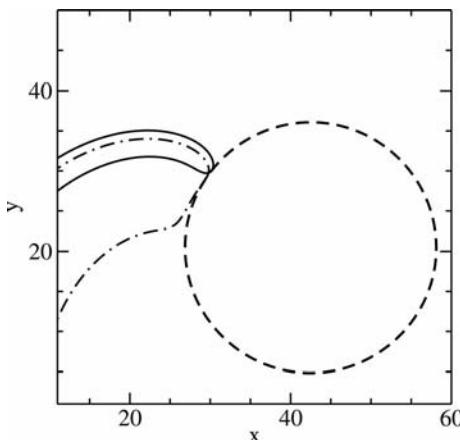
Fig. 27.1 Isoconcentration lines of the u – (solid line) and v – field (dash-dotted line) of a rigidly rotating spiral wave. The tip follows the dashed circular trajectory.

and D_u denotes the diffusion constant of the activator. The term $F(t)$ specifies a parametric forcing applied to the medium. Below, ε will be considered as the main bifurcation parameter that governs the transition from rigidly rotating to meandering and to hypermeandering spiral waves.

To obtain spiral wave solutions of the FitzHugh-Nagumo model, appropriate initial conditions have to be chosen for the numerical integration of Eqs. (27.1) and (27.2) as described in [17], for example. Figure 27.1 shows isoconcentration lines of a rigidly rotating spiral wave computed with parameters $\beta = 1.2$, $\chi = 0.5$, $\varepsilon = 0.14$, and $D_u = 1.0$. Except for ε, these parameters are kept fixed throughout the paper. Simulations were performed by the forward Euler method using the five-point finite-difference representation of the Laplacian with a spacing $\Delta x = \Delta y = 0.1$ and a time step $\Delta t = 0.002$.

Solid and dash-dotted lines in Fig. 27.1 represent a snapshot of the isoconcentration lines of the u-field at $u_c = 0.2$ and of the v-field at $v_c = -0.12$, respectively. The spiral wave rotates clockwise, and the spiral wave tip moves with a constant velocity along the boundary of the circular core shown by the dashed line. As the velocity of the tip in the normal direction to the core boundary is equal to zero, we can define the tip coordinates from the intersection between isoconcentration lines corresponding to two neighboring time instants t and $t + \Delta t$. We use this definition of the spiral tip in our computations below.

Different parameters in the FitzHugh-Nagumo model (27.1) and (27.2) result in rigidly rotating, meandering or hypermeandering spiral wave solutions [17]. For fixed values of χ, β, and D_u, the regime of rotation is uniquely defined by the parameter ε. The bifurcation scenario obtained under variation of ε is shown in Fig. 27.2. At $\varepsilon = 0.14$, the spiral is in the regime of rigid rotation. Decreasing ε, at a certain threshold a supercritical Hopf bifurcation occurs and rigid rota-
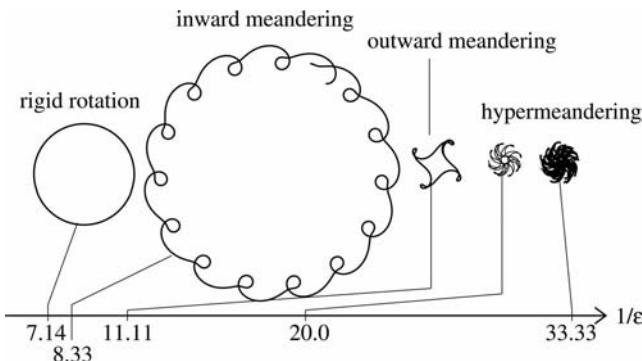
Fig. 27.2 Tip path patterns obtained under variation of the bifurcation parameter ε.

tion is replaced by outward meandering. When ε decreases further, outward meandering transforms to inward meandering. Finally, after crossing a second threshold the hypermeandering regime is established.

27.3
Stabilization of Rigidly Rotating Spirals in the Hypermeandering Regime

There are at least two approaches to stabilize an unstable rigidly rotating spiral wave: proportional feedback control and time delay autosynchronization [33]. Both are noninvasive meaning that the control force vanishes in the stabilized state, and that the control does not change the intrinsic dynamics.

Proportional feedback control (PFC) has been successfully applied to stabilize wave segments propagating in a two-dimensional excitable medium [34]. In a circular domain, PFC can force a rigidly rotating spiral wave to move toward the domain center [35]. Recently, rigid rotation of spiral waves was stabilized by PFC in a parameter range where it performs meandering motion in the absence of feedback [33].

On the other hand, the instability of rigid rotation can be viewed as a transition from a stable to an unstable periodic orbit (UPO) [20, 24–28]. Time delay autosynchronization (TDAS) [36, 37] has been successfully employed to stabilize UPOs in dynamical systems [38–40]. TDAS is especially efficient when all dynamical variables can be measured and controlled simultaneously [41].

In spatially extended media, either the system variables can be monitored only at a finite number of points, or spatially or temporally averaged variables are measured. Usually, the control signal is applied locally at a limited number of points or globally. In spite of these restrictions, there are many examples of successful control by TDAS in one-dimensional media [42–46]. In two- or three-dimensional systems, only few examples for the stabilization of spatiotemporal patterns by TDAS are known [33, 47].

Let us now analyze the applicability of PFC to suppress hypermeandering of spiral waves.

Characteristic for a rigidly rotating spiral wave is a constant distance r_0 between the tip and the core center. We propose to apply a control force $F(t)$ that is proportional to the difference between the actual distance from an arbitrarily chosen reference point, $r(t)$, and the desired core radius r_0

$$F(t) = K[r_0 - r(t)]. \tag{27.3}$$

Here, K denotes the feedback strength. Before we can apply PFC, the reference radius r_0 must be known. To determine r_0, simultaneously with Eqs. (27.1)–(27.3) we solve a simple relaxation dynamics according to

$$\frac{dr_0}{dt} = \frac{1}{\varepsilon'}[r(t) - r_0]. \tag{27.4}$$

Provided r_0 changes on a characteristic time scale much larger than the rotation period of the spiral wave, i.e., $\varepsilon' \gg T$, this additional equation ensures that r_0 is adapted automatically during feedback-mediated stabilization. In the limit $t \to \infty$, $r_0(t)$ approaches the previously unknown value r_0. Figure 27.3 (a) displays the tip trajectory calculated from Eqs. (27.1) and (27.2) in the presence of PFC according to Eq. (27.3). The cross marks the reference point. Under feedback the spiral tip becomes attracted to a circular orbit of radius r_0 centered at the reference point (red line in Fig. 27.3(a)). When the feedback is switched off the tip leaves the circular orbit. After a short transient it follows a path characteristic for a hypermeandering spiral wave (black line in Fig. 27.3 (a)). In the stabilized regime the control force vanishes, since $r(t) = r_0$. Therefore, the proposed control method stabilizes an existing UPO and does not induce a new periodic solution.

We have calculated numerically the dependence of the core radius and the rotation frequency of stabilized rigid rotation on the bifurcation parameter ε. In the absence of feedback, the considered range of ε-values corresponds to meandering and hypermeandering spiral waves. In the meandering regime, the Fourier spectra of the tip coordinates contain two basic frequencies. Under feedback control, the motion of the tip becomes periodic. The amplitude $r_0(\varepsilon)$ and the frequency $\omega(\varepsilon)$ of the remaining basic Fourier component are plotted in Fig. 27.4 (a) and (b), respectively. The same procedure has been applied in the hypermeandering regime. Here, the Fourier spectrum of the unperturbed spiral tip displays more than two basic frequencies on a continuous background. Under feedback, this complicated motion is replaced by the stabilized periodic orbit with a characteristic one-frequency spectrum, from which radius $r_0(\varepsilon)$ and frequency $\omega(\varepsilon)$ of the stabilized rigid rotation have been taken. To speed up, the numerical calculations, activator, and inhibitor field of a rigidly rotating spiral wave stabilized at a certain ε value can be used as an initial condition for feedback-mediated stabilization at a slightly changed value $\varepsilon + \delta\varepsilon$.
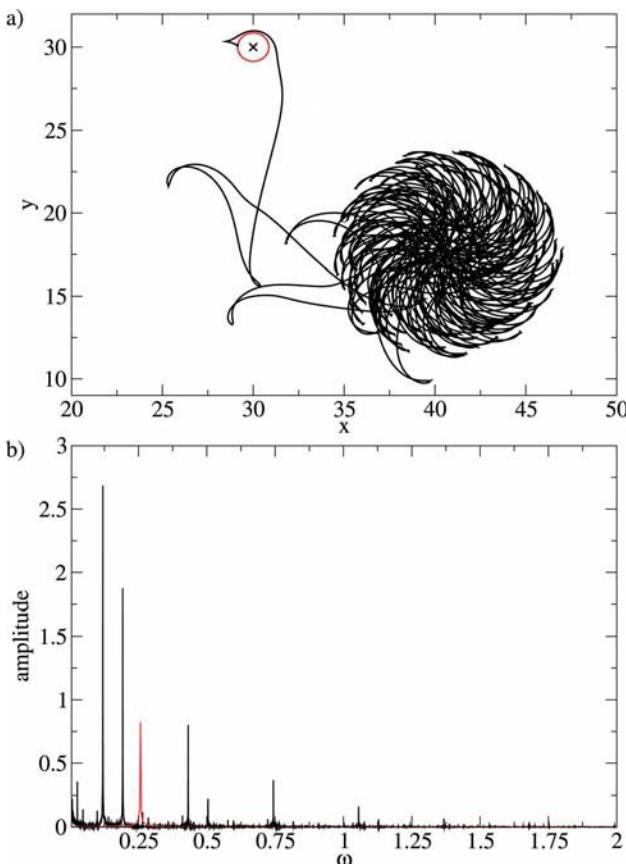
Fig. 27.3 (a) Rigid rotation of a spiral wave in the hypermeandering regime stabilized by PFC (red line). At time $t = 2000$, the feedback force is switched off, and the spiral tip moves along the black line characteristic for hypermeandering. Parameter values: $u_c = 0.2$, $\varepsilon = 0.03$, $\varepsilon' = 200$. (b) Fourier spectra of controlled (red) and uncontrolled (black) tip motion.

The results in Fig. 27.4 demonstrate that it is possible to suppress both the transition to meandering as well as to hypermeandering noninvasively by means of global PFC. In the stabilized regime, the whole medium oscillates periodically at the rotation frequency of the spiral wave. Finally, we emphasize again that application of noninvasive PFC can stabilize a periodic two-dimensional wave pattern in a broad parameter range with quite irregular autonomous spatiotemporal dynamics.
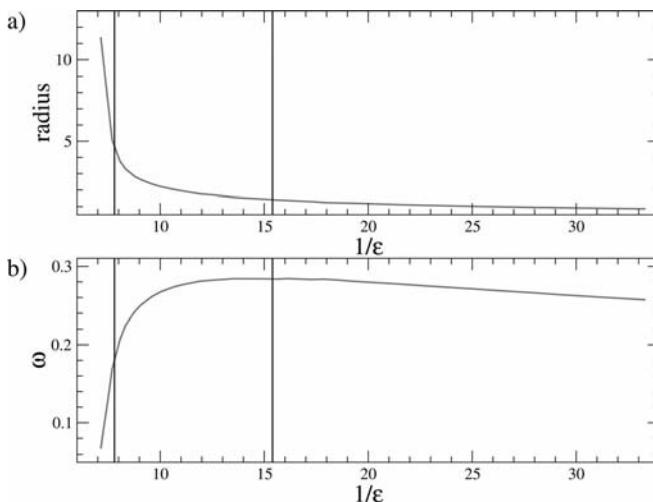
Fig. 27.4 Core radius (a) and rotation frequency (b) of feedback-stabilized rigid rotation vs. the control parameter ε. Left and right vertical lines mark the transition to meandering respectively hypermeandering in the absence of feedback.

27.4
Control of Spiral Wave Location in the Hypermeandering Regime

Sometimes the purpose of spiral wave control is to suppress irregular wave activity in the medium completely, rather than to replace it by unstable rigid rotation. In this situation, one possibility is the application of a large-amplitude excitability perturbation to the whole medium after which it will be recovered into the rest state. Such a huge external perturbation, called defibrillation shock in cardiology, can be rather dangerous as it can damage important living functions of biological systems.

Alternatively, a sequence of relatively weak perturbations can be applied to the system. Crucial for this control of spiral dynamics is the resonant drift of spiral waves in response to a periodic change in the excitability of the medium exactly at the rotation period of a *rigidly* rotating spiral wave. Resonant drift has been predicted for weakly excitable media within a kinematical description [48], confirmed in numerous computations and experiments [21, 49–52], and explained as a generic property of an excitable medium [53, 54]. Due to resonant drift, the spiral wave can be shifted to the boundary of the medium, where it hopefully should disappear. Below we demonstrate that under an appropriate feedback-mediated parameter modulation not only rigidly rotating, but also meandering and hypermeandering spiral waves can be moved along a pregiven direction through the medium.

Up to now there is no general theory which allows us to predict the rotation frequency ω the wavelength and the shape of a rotating spiral wave starting

from an underlying reaction–diffusion model like (27.1) and (27.2), though this problem has been the subject of numerous studies [21, 48, 53, 55–57]. A. Winfree was the first who suggested to approximate the wave front by an Archimedean spiral [6]

$$\Theta(r, t) = \Theta_0 - \frac{2\pi}{\lambda} r + \omega t, \tag{27.5}$$

where Θ and r denote polar coordinates with the origin at the rotation center. Rigidly rotating spiral wave solutions of Eqs. (27.1) and (27.2) outside a relatively small circle of radius $r_A \ll \lambda$ practically coincide with an Archimedean spiral. Recent extensive numerical simulations of spiral waves in the Oregonator model [58], and experiments with the light-sensitive BZ reaction [59] have confirmed the validity of the Archimedean approximation except of a small region of radius r_A. Note that (27.5) gives the asymptotic form of spiral wave solutions to the complex Ginzburg-Landau equation [60, 61]. The shape of weakly meandering spiral waves exhibits only small oscillations around an Archimedean shape, and the amplitude of these oscillations vanishes very quickly with increasing distance from the spiral center [24]. Below, we will use the Archimedean approximation to study the feedback-mediated resonant drift of meandering and hypermeandering spiral waves. The obtained results agree well with those from direct numerical simulations, and thus justify our simplified approach.

Now, we derive an iterative map that describes the effect of pulse-like excitability perturbations on spiral waves as outlined previously in [62]. Let us assume an unperturbed spiral wave that is rotating rigidly at a frequency ω_0 around a core center located at a site $z_0 = x_0 + i y_0$. One has to approximate the shape of this spiral by expression (27.5) to determine the spiral phase Θ_0. After a short perturbation, modeled as $F(t) = A_I \delta(t)$ in Eqs. (27.1) and (27.2), the rotation center, is shifted to a new site

$$z_1 = z_0 + h \exp(i\Theta_0 + i\varphi), \tag{27.6}$$

where h is the magnitude of this displacement whose direction is determined by the spiral phase Θ_0 and a constant φ characterizing the excitable medium. Additionally, the applied perturbation changes the rotation phase of the spiral by $\delta\Theta$. Changes in the spiral shape induced by the perturbation are assumed to relax on a time scale T_{rel} much smaller than the rotation period $T_0 = 2\pi/\omega_0$.

A second perturbation applied after the time interval T_m should produce a similar displacement. For $T_{\mathrm{rel}} \ll T_m$ the location of the spiral center after the second perturbation can be written as

$$z_2 = z_1 + h \exp(i\Theta_1 + i\varphi), \tag{27.7}$$

where

$$\Theta_1 = \Theta_0 + \delta\Theta + \omega_0 T_m. \tag{27.8}$$

Since the direction of the displacement remains the same after subtracting 2π from the right-hand side of Eq. (27.8), the last expression can be rewritten as

$$\Theta_1 = \Theta_0 + \left(\omega_0 + \frac{\delta\Theta}{T_m} - \omega_m \right) T_m. \tag{27.9}$$

Consequently, after k similar perturbations according to $F(t) = A_I \sum_{l=0}^{k-1} \delta(t - lT_m)$ the spiral displacement is

$$z_k = z_{k-1} + h \exp(i\Theta_{k-1} + i\varphi), \tag{27.10}$$

$$\Theta_{k-1} = \Theta_{k-2} + (\bar{\omega} - \omega_m)T_m, \tag{27.11}$$

where $k \geq 2$, and

$$\bar{\omega} = \omega_0 + \delta\Theta/T_m \tag{27.12}$$

denotes the averaged rotation frequency of the spiral wave perturbed by the applied modulation.

The phenomenon of resonant drift is induced under modulation with frequency $\omega_m = \bar{\omega}$. In this case, from Eq. (27.11) it follows $\Theta_k = \Theta_{k-1} = \cdots = \Theta_0$. All particular displacements occur in the same direction and the total shift of the spiral location after k perturbations is given by

$$z_k = z_0 + kh \exp(i\Theta_0 + i\varphi). \tag{27.13}$$

It is important to stress that if $\omega_m = n\bar{\omega}$, where n is an integer, $n > 1$, the result of n subsequent displacements, i.e., after one rotation period of the spiral wave, is equal to zero, because $z_{k+n} = z_k$. A long term drift is absent in this case.

Another interesting consequence from Eqs. (27.10)–(27.12) can be obtained in the case when ω_m is close to the averaged frequency of the perturbed spiral wave, $|\omega_m/\bar{\omega} - 1| \ll 1$. Under the assumption that the displacement h is small, the discrete maps (27.10) and (27.11) can be transformed into an ordinary differential equation for the spiral location $z(t)$:

$$\dot{z} = \frac{h}{T_m} \exp[i((\bar{\omega} - \omega_m)t + \Theta_0 + \varphi)]. \tag{27.14}$$

Thus, the velocity of the resonant drift induced by the periodic modulation is determined by the ratio h/T_m. Under resonant forcing, $\omega_m = \bar{\omega}$, the drift occurs along a straight line whose direction depends on the initial orientation Θ_0 of the spiral wave, and on the constant φ. More generally, if the parameter modulation is given by

$$F(t) = A_I \sum_{l=0}^{k} \delta(t - lT_m - t_0) \tag{27.15}$$

with arbitrary $t_0 \geq 0$, the drift direction γ should depend on the modulation phase $\phi_{\mathrm{mod}} = \bar{\omega}t_0 = \omega_m t_0$ as well yielding

$$\gamma = \varphi + \Theta_0 + \phi_{\mathrm{mod}}. \tag{27.16}$$

In summary, with $\omega_m = \bar{\omega}$ from Eq. (27.1) follows for the resonant drift

$$\dot{z} = \frac{h}{T_m}\exp(i\gamma) \tag{27.17}$$

with γ defined by Eq. (27.16).

Note that Eq. (27.14) obtained for the discrete modulation (27.15) practically coincides with induced drift equations known for a continuous periodic modulation [21, 48, 53]. The only difference is that the constant φ in (27.14) specifies a displacement direction induced by a sequence of δ-perturbations, but not by a harmonic perturbation $F(t) = A\cos(\bar{\omega}t)$. In both cases, this angle, which determines the drift direction for $\Theta_0 = \phi_{\mathrm{mod}} = 0$, is a characteristic parameter that depends on the properties of the excitable medium, and on the applied modulation method.

Assume now that we are able to monitor the wave activity along a straight line in the medium. Then, we can use this information to set up the following feedback loop. Each time a wave front becomes tangent to a virtual detector line, a short excitability perturbation is applied to the whole medium immediately or with some time delay τ. Without loss of generality, the detector line is given by $x = 0$, and the spiral wave is centered at coordinates (x, y) with $x > 0$. Within the Archimedean approximation for the spiral wave given by Eq. (27.5), straightforward geometrical considerations show that the wave front touches the detector each time t_k satisfying the equation

$$\bar{\omega}t_k + \Theta_0 - \frac{2\pi}{\lambda}r = \pi - \arctan\left(\frac{\sigma}{x}\right) + 2\pi k, \tag{27.18}$$

where

$$r(x) = x\sqrt{0.5 + \sqrt{0.25 + \left(\frac{\lambda}{2\pi x}\right)^2}}, \tag{27.19}$$

and

$$\sigma = \sqrt{r^2 - x^2} = \frac{\lambda x}{2\pi r}. \tag{27.20}$$

For the definition of $r(x)$ and σ compare Fig. 27.5. Equation (27.18) determines a modulating sequence similar to Eq. (27.15) with a phase shift

$$\phi_{\mathrm{mod}} = \pi - \Theta_0 + \frac{2\pi}{\lambda}r - \arctan\left(\frac{\sigma}{x}\right) + \bar{\omega}\tau, \tag{27.21}$$
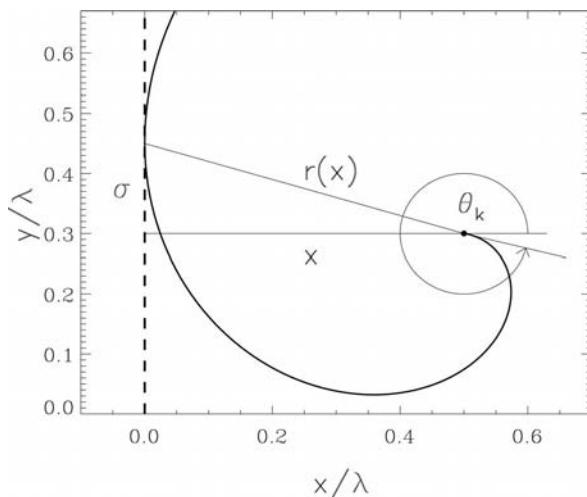
Fig. 27.5 An Archimedean spiral (solid curve) touches a line
detector (dashed).

where the time delay τ is taken into account. Substituting Eq. (27.21) into
Eq. (27.16), we obtain the direction γ of the induced drift as a function of the
coordinate $x > 0$.

$$\gamma(x) = \varphi + \pi + \frac{2\pi}{\lambda} r(x) - \arctan\left(\frac{\sigma}{x}\right) + \bar{\omega}\tau. \tag{27.22}$$

On the left-hand side of the line detector, the drift direction is determined by a
similar expression, however, an additional rotation by the angle π should be in-
cluded. This gives for $x < 0$

$$\gamma(x) = \varphi + \frac{2\pi}{\lambda} r(x) + \arctan\left(\frac{\sigma}{x}\right) + \bar{\omega}\tau. \tag{27.23}$$

Finally, the drift of the spiral center can be obtained by Eq. (27.17) with γ deter-
mined by Eqs. (27.22) and (27.23). The obtained drift velocity field is shown in
Fig. 27.6. There is a set of stationary trajectories given by the condition

$$\gamma(x) = \pi/2 + \pi n, \tag{27.24}$$

where n is an arbitrary integer. A stable stationary trajectory corresponds to an
even number $n = 2m$, while an odd number $n = 2m + 1$ characterizes an un-
stable one. Solid lines in Fig. 27.6 show three trajectories of spiral wave centers
placed initially at different distances from the line detector. Asymptotically they
are attracted by stable stationary trajectories with basins of attraction separated
by unstable stationary trajectories.
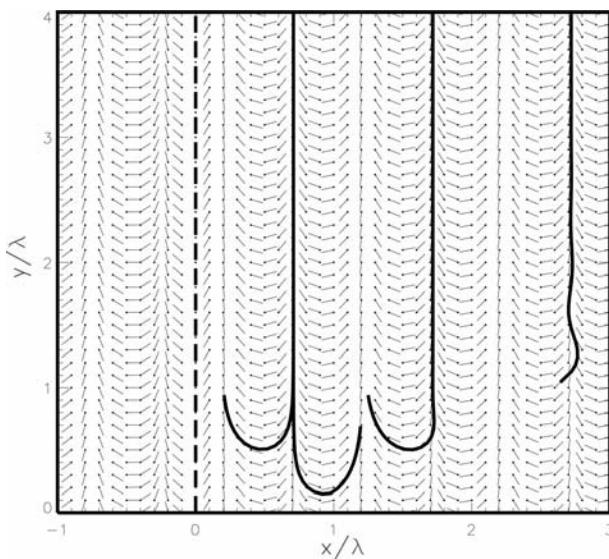
Fig. 27.6 Velocity field for spiral wave drift induced near a line detector. Solid lines show numerically obtained trajectories of the spiral center.
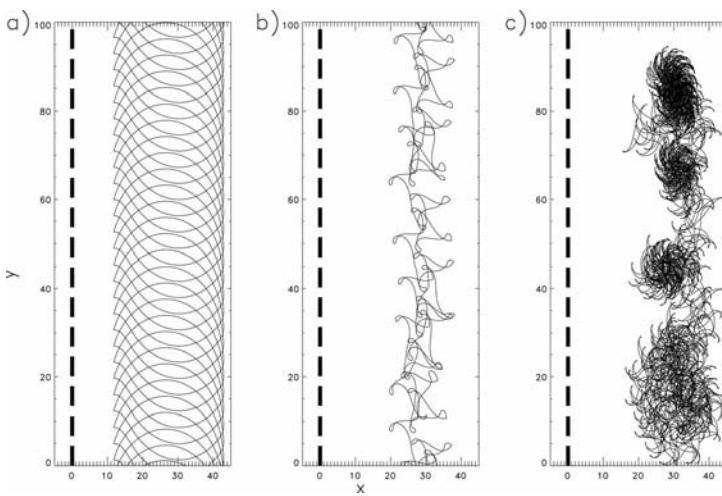
Fig. 27.7 Feedback-mediated resonant drift of (a) rigidly, (b) meandering, and (c) hypermeandering spiral waves in parallel to a line detector. The dashed line marks the detector. Parameter values: (a) $\varepsilon = 0.14$, $A_l = 0.1$, (b) $\varepsilon = 0.09$, $A_l = 0.05$, and (c) $\varepsilon = 0.03$, $A_l = 0.05$.

To check the predictions of the iterated-map approach we have performed direct numerical simulations of the FitzHugh-Nagumo equations. The results, shown in Fig. 27.7, clearly demonstrate that the proposed control algorithm works for rigidly rotating, meandering, and even hypermeandering spiral waves.

27.5
Discussion

We have presented two methods suitable to remove irregular wave activity in a bounded domain of an excitable medium that results from a hypermeandering spiral wave. The first method substitutes the irregular regime by a periodic one, forcing the spiral wave into the regime of rigid rotation. The second method causes a resonant drift of the hypermeandering spiral wave. In both cases we set up a feedback control to suppress the undesired wave activity.

In the meandering and hypermeandering regime rigidly rotating spiral waves are still a solution of the underlying reaction–diffusion equations which, however, is unstable. We have shown that this unstable solution can be stabilized applying a noninvasive proportional feedback control. After successful stabilization, the whole medium is excited periodically.

As rigid rotation is stabilized for values of the control parameter ε where it is unstable in the absence of feedback, our results are an example for a feedback-mediated impact on the selection of a two-dimensional spatiotemporal pattern.

Although this issue is not in our focus here, the proposed PFC allows us to determine the core radius and the rotation frequency of unstable rigidly rotating spiral waves numerically irrespectively of whether underlying model equations are known or not. Other characteristics, as the spatial profile of the unstable spiral wave or the spatial gradient close to the spiral core, in principle can be obtained too. This information could be very helpful in testing the validity of various theoretical approaches to spiral wave dynamics [21, 22, 29].

In the second part of the paper, we apply a variant of feedback-mediated resonant drift to shift a hypermeandering spiral wave to the boundary of the medium. The drift direction is in parallel to an arbitrarily oriented straight line detector along which the wave activity is monitored. This might be important for such possible applications as the low-voltage defibrillation of cardiac tissue, for example.

Because the phase of the feedback signal depends on the orientation of the spiral wave, the feedback-induced drift direction is uniquely determined by the position of the spiral center (in Archimedean approximation). Thus, under feedback control the dynamics of spiral wave can be described by a drift velocity field, and does not depend on the initial orientation of the spiral wave.

We find good agreement between the theoretically calculated velocity field of resonant drift and the numerically obtained drift trajectories of the spiral center. This is quite surprising, as the theoretical approach is based on an Archimedean approximation for the wave front which we not expected to hold for hyper-

meandering spiral waves. With respect to the studied feedback algorithm this approximation has been proven to be justified.

The theoretical approach presented in Section 27.4 is based on a very general description of excitable media and does not use specific features of particular systems. Therefore, the obtained results are of general value and can be applied to spiral wave dynamics in quite different excitable media.

References

1 M. A. Allessie, F. I. M. Bonke, and F. J. G. Schopman, Cric. Res. **33**, 54 (1973).

2 J. M. Davidenko, A. M. Pertsov, R. Salomonsz, W. Baxter, and J. Jalife, Nature **355**, 349 (1992).

3 G. Gerisch, Naturwissenschaften **58**, 430 (1971).

4 S. Jakubith, H. H. Rotermund, W. Engel, A. von Oertzen, and G. Ertl, Phys. Rev. Lett. **65**, 3013 (1990).

5 A. N. Zaikin and A. M. Zhabotinsky, Nature **225**, 535 (1970).

6 A. T. Winfree, Science **175**, 634 (1972).

7 R. J. Field, E. Körös, and R. M. Noyes, J. Am. Chem. Soc. **94**, 8649 (1972).

8 R. J. Field and M. Burger, Oscillations and Traveling Waves in Chemical Systems (Wiley, New York, 1985).

9 W. Jahnke, W. E. Skaggs, and A. T. Winfree, J. Phys. Chem. **93**, 740 (1989).

10 R. Kapral and K. Showalter (Eds.), Chemical Waves and Patterns (Kluwer, Dordrecht, 1995).

11 G. Li, Q. Ouyang, V. Petrov, and H. L. Swinney, Phys. Rev. Lett. **77**, 2105 (1996).

12 W. Jahnke and A. T. Winfree, Int. J. Bifurc. Chaos **1**, 455 (1991).

13 A. T. Winfree, The Geometry of Biological Time (Springer, Berlin, Heidelberg, 2000).

14 Y. Kuramoto, Chemical Oscillations, Waves and Turbulence (Springer, Berlin, Heidelberg, 1984).

15 V. Krinsky and H. Swinney (Eds), Wave and Patterns in Biological and Chemical Excitable Media (North-Holland, Amsterdam, 1991).

16 T. Plesser and K.-H. Müller, Int. J. Bifurc. Chaos **5**, 1071 (1995).

17 A. T. Winfree, Chaos **1**, 303 (1991).

18 H. Zhang and A. V. Holden, Chaos, Solitons Fractals **5**, 635 (1995).

19 A. S. Mikhailov, V. A. Davydov, and V. S. Zykov, Physica D **70**, 1 (1994).

20 D. Barkley, Phys. Rev. Lett. **68**, 2090 (1992).

21 V. Hakim and A. Karma, Phys. Rev. E **60**, 5073 (1999).

22 D. A. Kessler, H. Levine, and W. N. Reynolds, Physica D **70**, 115 (1994).

23 I. S. Aranson, L. Aranson, L. Kramer, and A. Weber, Phys. Rev. A **46**, R2992 (1992).

24 D. Barkley, M. Kness, and L. S. Tuckerman, Phys. Rev. A **42**, 2489 (1990).

25 D. Barkley, Phys. Rev. Lett. **72**, 164 (1994).

26 B. Fiedler, B. Sandstede, A. Scheel, and C. Wulff, Doc. Math. J. DMV **1**, 479 (1996).

27 M. Golubitsky, V. G. LeBlanc, and I. Melbourne, J. Nonlinear Sci. **7**, 557 (1997).

28 B. Sandstede, A. Scheel, and C. Wulff, J. Differ. Equ. **141**, 122 (1997).

29 D. Margerit and D. Barkley, Chaos **12**, 636 (2002).

30 P. Wheeler and D. Barkley, SIAM J. Appl. Dyn. Sys. **5**, 157 (2006).

31 R. FitzHugh, Biophys. **1**, 445 (1961).

32 J. Nagumo, S. Arimoto, and S. Yoshizawa, Proc. IRE **50**, 2061 (1962).

33 J. Schlesner, V. Zykov, H. Engel, and E. Schöll, Phys. Rev. E **74**, 046215 (2006).

34 E. Mihaliuk, T. Sakurai, F. Chirila, and K. Showalter, Phys. Rev. E **65**, 65602 (2002).

35 V. S. Zykov, A. S. Mikhailov, and S. C. Müller, Phys. Rev. Lett. **78**, 3398 (1997).

36 K. Pyragas, Phys. Lett. A **170**, 421 (1992).

37 J. E. S. Socolar, D. W. Sukow, and D. J. Gauthier, Phys. Rev. E **50**, 3245 (1994).

38 W. Just, D. Reckwerth, J. Möckel, E. Reibold, and H. Benner, Phys. Rev. Lett. **81**, 562 (1998).

39 D. J. Gauthier, D. W. Sukow, H. M. Concannon, and J. E. S. Socolar, Phys. Rev. E **50**, 2343 (1994).

40 A. Kittel, J. Parisi, and K. Pyragas, Phys. Lett. A **198**, 433 (1995).

41 W. Just, T. Bernard, M. Ostheimer, E. Reibold, and H. Benner, Phys. Rev. Lett. **78**, 203 (1997).

42 M. E. Bleich and J. E. S. Socolar, Phys. Rev. E **54**, R17 (1996).

43 G. Franceschini, S. Bose, and E. Schöll, Phys. Rev. E **60**, 5426 (1999).

44 N. Baba, A. Amann, E. Schöll, and W. Just, Phys. Rev. Lett. **89**, 074101 (2002).

45 O. Beck, A. Amann, E. Schöll, J. E. S. Socolar, and W. Just, Phys. Rev. E **66**, 016213 (2002).

46 J. Schlesner, A. Amann, N. B. Janson, W. Just, and E. Schöll, Phys. Rev. E **68**, 066208 (2003).

47 O. Lüthje, S. Wolff, and G. Pfister, Phys. Rev. Lett. **86**, 1745 (2001).

48 V. A. Davydov, V. S. Zykov, and A. S. Mikhailov, Usp. Fiz. Nauk **161**, 45 (1991) [Sov. Phys. Usp. **34**, 665 (1991)].

49 K. I. Agladze, V. A. Davydov, and A. S. Mikhailov, JETP Lett. **45**, 767 (1987).

50 S. Grill, V. S. Zykov, and S. C. Müller, J. Phys. Chem. **100**, 19082 (1996).

51 V. N. Biktashev and A. Holden, J. Theor. Biol. **169**, 101 (1994).

52 S. Nettesheim, A. von Oertzen, H. H. Rotermund, and G. Ertl, J. Chem. Phys. **98**, 9977 (1993).

53 R. M. Mantel and D. Barkley, Phys. Rev. E **54**, 4791 (1996).

54 B. Sandstede, A. Scheel, and C. Wulff, J. Nonlinear Sci. **9**, 439 (1999).

55 N. Wiener and A. Rosenblueth, Arch. Inst. Cardiol. Mex. **16**, 205 (1946).

56 V. S. Zykov, Simulation of Wave Processes in Excitable Media (Manchester University Press, Manchester, 1987).

57 J. J. Tyson and J. P. Keener, Physica **D 32**, 327 (1988).

58 A. Karma and V. S. Zykov, Phys. Rev. Lett. A **83**, 2453 (1999).

59 V. S. Zykov, O. Kheowan, O. Rangsiman, and S. C. Müller, Phys. Rev. E **65**, 026206 (2002).

60 P. S. Hagan, SIAM J. Appl. Math. **42**, 762 (1982).

61 I. S. Aranson and L. Kramer, Rev. Mod. Phys. **74**, 99 (2002).

62 V. S. Zykov and H. Engel, Unified approach to feedback-mediated control of spiral waves in excitable media. In L. Schimansky-Geier, B. Fiedler, J. Kurths, and E. Schöll (Eds.) Analysis and Control of Complex Nonlinear Processes in Physics, Chemistry and Biology, pages 243–272 (World Scientific, Singapore, 2007).

28
Control of Spatiotemporal Chaos
in Surface Chemical Reactions

Carsten Beta and Alexander S. Mikhailov

28.1
Introduction

Along with the chemical Belousov-Zhabotinsky system, catalytic surface reactions provide a classical example of a medium with a rich potential of nonequilibrium pattern formation. In such reactions, reacting molecules come by adsorption from the gas phase to the metal surface, diffuse on it and undergo reactions. By changing the rates of supply of the gaseous reactants, reaction conditions can easily be controlled. Because the reaction is confined to a catalytic metal surface, its process can readily be monitored by optical and electron microscopy methods. All basic kinds of nonequilibrium behavior, characteristic for bistable, excitable or oscillatory media, can be observed in surface chemical reactions. In the context of the present volume, it is important that spatiotemporal chaos (i.e., chemical turbulence) is also possible on catalytic surfaces. Both theoretical and experimental studies reveal that, in the oscillatory regime, the chaos is spontaneously developing via an instability of uniform oscillations leading to phase and amplitude turbulence.

Qualitatively, the behavior of real chemical systems near the onset of chaos is often in good agreement with the predictions of the complex Ginzburg-Landau (CGLE) equation that is valid for reaction–diffusion systems in the vicinity of a supercritical Hopf bifurcation. Therefore, surface chemical reactions provide a good opportunity to experimentally verify general predictions based on this equation. On the other hand, advanced realistic models of some surface reactions and, in particular, of the CO oxidation reaction on platinum are available. While remaining simple, these models reproduce, with a satisfactory quantitative agreement, the actually observed behavior.

To control spatiotemporal pattern formation and turbulence in surface reactions, various methods can be used. The control can be, for example, implemented by using narrowly focused laser light that locally heats the metal surface. In this chapter, only global-control methods are however considered, where the reaction is steered by varying the supply rates of reactants into the reaction cham-

ber and thus controlling partial pressures of these gaseous reactants. Not only external periodic forcing, but also various global-feedback schemes can be implemented by making the rates of reactants supply dependent on selected global properties of monitored adsorbate coverage distributions on a catalytic surface. Using the CO oxidation on platinum, first experiments on control of spatiotemporal chaos in chemical reactions have been performed.

28.2
The Catalytic CO Oxidation on Pt(110)

28.2.1
Mechanism

The catalytic oxidation of CO on platinum proceeds via a Langmuir-Hinshelwood mechanism [16], i.e., both CO and oxygen have to adsorb on the catalytic surface before the reaction to carbon dioxide can take place, which is immediately released into the gas phase. While CO adsorbs as a molecule, oxygen dissociates upon adsorption. At the temperatures considered here, only desorption of CO has to be taken into account, whereas oxygen desorption can be neglected. Similarly, only CO is diffusively mobile along the platinum surface, providing local coupling between neighboring sites on the crystal. The reaction can be summarized in the following scheme:

$$\begin{aligned} 2\,CO + 2\otimes &\rightleftharpoons 2\,CO_{ad} \\ O_2 + 2\otimes &\rightarrow 2\,O_{ad} \\ 2\,CO_{ad} + 2\,O_{ad} &\rightarrow 2\,CO_2\uparrow + 4\otimes, \end{aligned}$$ (28.1)

where $\otimes$ stands for a free adsorption site and the index "ad" denotes adsorbed species. Since the dissociative adsorption of oxygen requires two adjacent free sites on the surface, a high CO coverage asymmetrically inhibits the adsorption of oxygen. This induces bistable dynamics in a wide range of parameters, where a mainly oxygen covered reactive state coexists with a CO covered non-reactive state. Furthermore, the Pt(110) facet exhibits adsorbate dependent transitions in surface structure. The empty and oxygen covered surface reconstructs in a (1×2) missing row phase, whereas for sufficiently high CO coverages the reconstruction is lifed to the (1×1) bulk terminated structure. However, the sticking coefficient of oxygen is higher on the (1×1) structure as compared to the (1×2) surface, inducing an inherent negative feedback loop that can lead to excitable and oscillatory dynamics in this system [25]. In combination with lateral CO diffusion along the surface, a two-dimensional reaction–diffusion system is established that can exhibit a wealth of complex spatiotemporal concentration patterns. Note that the shape of concentration patterns on the Pt(110) surface is affected by anisotropy of CO surface diffusion [44]. Diffusion of CO is

faster in the $[1\bar{1}0]$ direction than in the perpendicular $[001]$ direction causing an elongated, or, in the case of curved fragments, elliptical shape of the pattern.

Further features like surface microfaceting, the formation of subsurface oxygen, and global coupling through the gas phase are only of secondary importance for the results presented in the following sections and will be neglected here.

28.2.2
Modeling

A mathematical model for the catalytic oxidation of CO on Pt(110) has been developed by Krischer, Eiswirth, and Ertl (KEE model) [15, 29]. Depending on the choice of external parameters, the model not only shows monostable and bistable behavior but also excitable and oscillatory dynamics. The KEE model is well established and has been successfully used for over a decade to study the dynamics of catalytic CO oxidation on Pt(110) numerically. It consists of three coupled differential equations, taking into account the most significant physical processes described in the previous section,

$$\partial_t u = k_1 p_{CO} s_{CO} (1 - u^3) - k_2 u - k_3 u v + D \nabla^2 u, \tag{28.2}$$

$$\partial_t v = k_4 p_{O_2} [s_{O,1\times1} w + s_{O,1\times2}(1 - w)](1 - u - v)^2 - k_3 u v, \tag{28.3}$$

$$\partial_t w = k_5 \left[\frac{1}{1 + \exp\left(\frac{u_0 - u}{\delta u}\right)} - w \right]. \tag{28.4}$$

The three variables u, v, and w are normalized between zero and one. They denote the CO coverage, the oxygen coverage, and the local fraction of the surface found in the nonreconstructed (1×1) structure, respectively. In Eqs. (28.2)–(28.4), adsorption of CO and oxygen is taken into account, k_1 and k_4 denoting the corresponding rate constants. In addition, adsorption depends on the respective sticking coefficients s_i, Eq. (28.3) taking different sticking probabilities of oxygen on the (1×1) and (1×2) facets into account. Desorption of CO is governed by the rate constant k_2, and reaction between the two adsorbed species proceeds with a rate constant k_3. The partial pressures of the reactants p_{CO} and p_{O_2} are global parameters that can be chosen externally.

Equation (28.4) describes the coverage dependent transition between the (1×2) missing row structure and the (1×1) bulk terminated surface taking place with a rate constant of k_5. The function f, describing the equilibrium value of w in Eq. (28.4), is exclusively determined by u and can be approximated by an exponential ansatz [42].

The KEE model has been modified and extended in many ways. A reduced two-variable version of the model was derived that gives qualitatively similar results for many aspects of the spatiotemporal dynamics [2, 17]. Also, global cou-

pling through the gas phase [18], faceting of the single crystal surface [29], and the formation of subsurface oxygen [43] have been taken into account.

28.2.3
Experimental Setup

Experiments are commonly performed under low pressure conditions in a stainless steel ultrahigh vacuum (UHV) vessel that is operated as a continuous flow reactor. The Pt(110) single crystal of about 10 mm in diameter is mounted inside the vacuum chamber and prepared, before each experiment, by repeated cycles of argon ion sputtering, and annealing up to 750 K. In many experiments, approximately 80% of the sample surface were covered by microlithographically deposited Ti, which is easily oxidized to catalytically inert TiO_2. Thus, only a few reactive compartments are left on the surface to reduce effects of global coupling through the gas phase.

Adsorbate patterns on the platinum surface are imaged using a photoemission electron microscope (PEEM). The PEEM yields spatially resolved real time images of the local work function across the sample surface. Due to the adsorbate dependence of the work function, different values of local work function can be translated into adsorbate coverages so that images of lateral concentration distributions on the catalyst surface become accessible in real time [39, 41]. According to the difference in work function between CO and O covered Pt, CO covered areas appear bright in the PEEM image, whereas O covered regions are dark. Besides PEEM, also optical methods are available to image the adsorbate patterns on a catalyst surface [39]. Ellipsomicroscopy for surface imaging (EMSI) and reflection anisotropy microscopy (RAM) allow the observation of self-organization on the catalyst surface even at high pressures [21, 40].

A schematic experimental setup for catalytic CO oxidation is shown in Fig. 28.1. It can be extended to incorporate various control schemes. In all cases discussed here, the control force acts on the partial pressure of CO in the reactor. Since changes in the pressure are experienced equally at all locations on the catalyst surface, the control is acting globally. In the continuously pumped reaction chamber, the dosing rate of CO gas determines the CO partial pressure
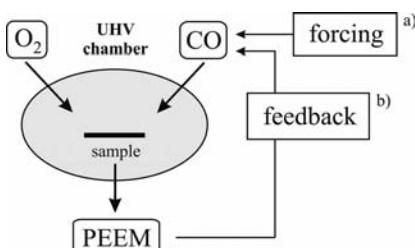
Fig. 28.1 Schematic setup with external forcing (a) and feedback (b) (from [9]).

p_{CO} and is controlled by an automated gas inlet system. In the following sections, both external forcing (a) and feedback (b) are implemented to change the electronic input signal of the inlet system. The CO partial pressure inside the chamber follows modulations in the inlet system with an intrinsic delay of $\tau_i \approx 0.6$ s determined by the residence time of gases in the pumped chamber.

28.3
Spatiotemporal Chaos in Catalytic CO Oxidation on Pt(110)

In his seminal book, Kuramoto has coined the term chemical turbulence for spatiotemporally chaotic dynamical states in chemical reaction diffusion systems [30]. Catalytic CO oxidation on Pt(110) is one of the few experimental systems that shows, besides a wealth of regular wave patterns, spatiotemporally disordered, irregular behavior of this type. Although observed already a long time ago [27], a detailed statistical analysis of its dynamics has been performed only recently [12] and will be summarized in this section.

In Fig. 28.2 (a), a snapshot from a spatiotemporally disordered, turbulent time series is shown. An irregular fine texture can be seen that is composed of randomly traveling and constantly reshaping structures. We apply a two-dimensional variant of the *analytic signal approach* to transform the series of PEEM images into time-dependent spatial distributions of phase and amplitude [6, 36, 37]. From the image intensity $I(\vec{x}, t)$, the analytic signal $\zeta(\vec{x}, t) = I(\vec{x}, t) + i\tilde{I}(\vec{x}, t)$ is generated, where $\tilde{I}(\vec{x}, t)$ is the Hilbert transform of $I(\vec{x}, t)$. The phase and amplitude variables are defined as $\phi = \arg\zeta$ and $R = \rho/\rho_{ref}(\phi)$ with $\rho = |\zeta|$ and $\rho_{ref}(\phi)$ a reference amplitude that compensates for deviations from harmonic oscillations [6].
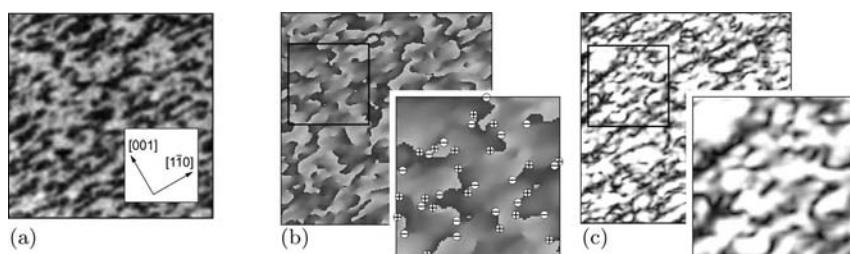
Fig. 28.2 Chemical turbulence in catalytic CO oxidation on Pt(110). (a) PEEM image of size $275 \times 275\,\mu m^2$. The parameters are $T = 502$ K, $p_{O_2} = 40.0 \times 10^{-5}$ mbar, and $p_{CO} = 13.1 \times 10^{-5}$ mbar. The inset shows the directions of fast and slow CO diffusion, $[1\bar{1}0]$ and $[001]$, respectively. (b) Phase and (c) amplitude representations of (a) with zooms of selected regions indicated by rectangular boxes. The images are coded in a linear gray scale color table, where white (black) denotes high (low) values of the respective quantity. In the zoom in (b), the locations of topological defects are marked with the symbols $\oplus$ and $\ominus$, according to their topological charge (from [12]).
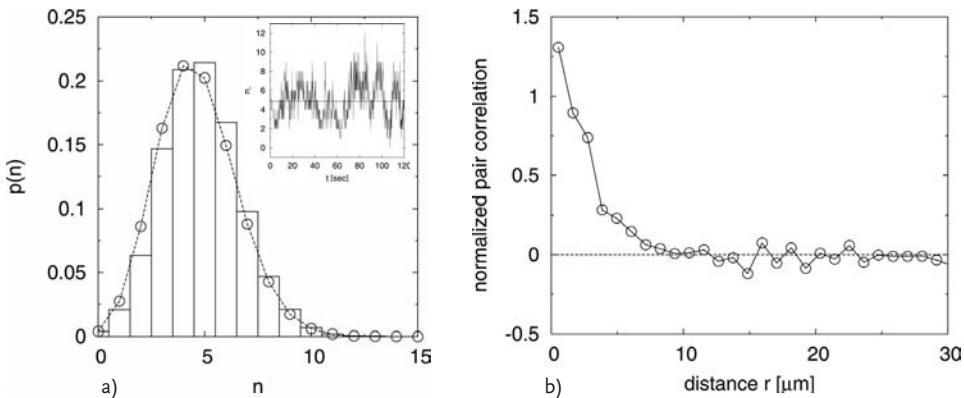
Fig. 28.3 (a) PDF of the number of defects n (bars) and modified Poisson distribution (open circles), determined from the gain and loss rates $c = 1.04$, $d = 0.02\,n^2 + 0.11\,n$, $e = 0.17$, and $l = 0.04\,n$. (a, inset) Number of negatively charged defects n_- as a function of time in an area of $50 \times 50\,\mu m$ in size. The dashed line at 4.84 denotes the mean value. (b) Normalized pair correlation function (from [12]).

In Fig. 28.2 (b) and (c), the phase and amplitude representations of the PEEM image in (a) are shown. In the phase image (b), topological defects can be characterized by an integer topological charge $m_{top} = \frac{1}{2\pi} \oint \nabla \phi(\vec{r}, t) \cdot d\vec{s}$, i.e., along any closed contour surrounding a defect, the phase changes by an amount of $2\pi\,m_{top}$. At a defect, the local amplitude drops to zero, the phase is not defined, and the phase gradient diverges. The number of defects was counted inside a region of $50 \times 50\,\mu m$ in size. In the inset of Fig. 28.3 (a), the number n_- of negative defects is shown as an example in the course of time. Figure 28.3 (a) displays the corresponding probability distribution function (PDF) for the number of defects n.

Assuming that the defects are statistically independent, the shape of the PDF can be explained in terms of a simple probabilistic model, based on the gain and loss rates of defects in the observed area [20]. The gain (creation and entering) and loss (decay and leaving) rates are determined from the experimental data. In first approximation, creation and entering of defects are independent of the number of defects n in the observed area, $c(n) = c_0$ and $e(n) = e_0$. The decay shows a combined quadratic and linear dependence on n, $d(n) = d_{01}\,n^2 + d_{02}\,n$, whereas the leaving rate grows linearly with n, $l(n) = l_0\,n$.

In the statistically stationary state, the master equation for the probability $p(n)$ of finding a number of n defects in the observed area reduces to a simple recursive relation for the PDF. With the above expressions for the rate constants, the recursion leads to a modified Poisson distribution [13, 46],

$$p(n) = \frac{1}{I_v(2\sqrt{\gamma})} \frac{\gamma^{(v/2)+n}}{\Gamma(v+1+n)n!}, \tag{28.5}$$

where I_v is the modified Bessel function, $\gamma = (c_0 + e_0)/d_{01}$ and $v = (d_{02} + l_0)/d_{01}$. The PDF is shown in Fig. 28.3 (a, open circles) for the values of $\gamma = 60.60$ and $v = 7.68$ determined from the gain and loss rates.

In Fig. 28.3 (b), the normalized pair correlation function is displayed (see [14, 24]) for definition). It shows that in the immediate vicinity of a defect, the probability of finding an oppositely charged defect is strongly increased. Gil et al. derived the first probabilistic description of defect turbulence in the framework of the CGLE [20]. Their analysis is based on the assumption that defects are well mixed and move independently of each other, i.e., that correlations between defects can be neglected.

Here, this is clearly not the case. The shape of the normalized pair correlation function can be understood by the presence of short-range correlations between oppositely charged defects. The peak at small distances indicates that a large number of defect pairs self-annihilate shortly after being created. Only to a lesser extent, the oppositely charged defects detach and travel independently through the system. In the latter case, defects mix and annihilation occurs proportional to n^2 as prediced by Gil et al. On the other hand, in the case of self-annihilation events, the oppositely charged defects are not statistically independent and annihilation will occur proportional to n. The sharp drop in the pair correlation function at intermediate distances suggests that annihilation events can be mostly attributed to these two scenarios, which leads to a combined quadratic and linear dependence of the effective annihilation rate on n.

28.4
Control of Spatiotemporal Chaos by Global Delayed Feedback

Global delayed feedback can be applied to control spatiotemporal chaos and pattern formation in extended dynamical systems. In this section, we present experimental [6, 10, 28] and numerical results [8, 28] from oscillatory catalytic CO oxidation on Pt(110) under global-delayed feedback. We review control of chemical turbulence in this system discussing both the formation of novel feedback-induced patterns and aspects of the invasiveness of the control scheme (for a review see also [34]).

Global feedback is implemented into the CO oxidation system as follows. The integral intensity $I(t)$ of the PEEM image is continuously recorded, normalized between zero and unity for the completely O and CO covered surface, respectively. From this quantity, a feedback signal is computed by taking the difference between the intensity delayed by a fixed time lag τ, $I(t - \tau)$, and either (a) a constant reference intensity I_{ref} or (b) the instantaneous image intensity $I(t)$. Case (b) is commonly referred to as time delay autosynchronization (TDAS) [38]. The resulting signal, multiplied by an additional intensity factor μ, is used as input for the electronically operated dosing system of CO gas into the reaction chamber,

(a) $p_{CO}(t) = p_{CO}^0 + \mu \left(I(t - \tau) - I_{ref} \right),$ (28.6)

(b) $p_{CO}(t) = p_{CO}^0 + \mu(I(t - \tau) - I(t)).$ (28.7)

The constant reference value I_{ref} was determined prior to each series of experiments as the time average of the global-PEEM intensity $I(t)$ in the initially developing state of spiral-wave turbulence. Note that an additional control loop latency τ_i is present, due to the finite pumping rate of the chamber. It was shown that for $\tau_i \ll \tau$ there is no significant qualitative difference to the results without control loop latency and, therefore, the effect of an intrinsic delay can be neglected in the discussion of the present results [10].

28.4.1
Control of Turbulence in Catalytic CO Oxidation – Experimental

Temperature and partial pressures of the reactants are chosen such that uniform oscillations are unstable in absence of feedback. The system spontaneously
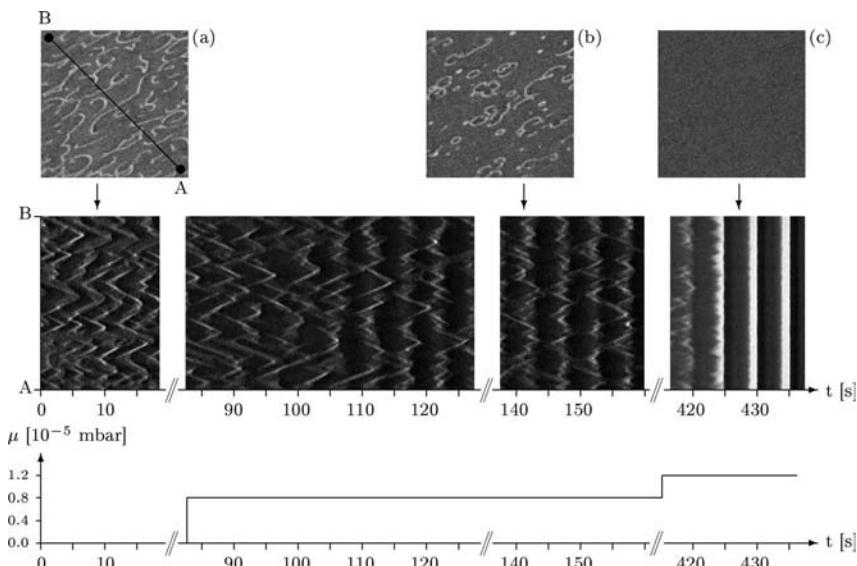
Fig. 28.4 Feedback-induced transition from chemical turbulence to homogeneous oscillations. (top) PEEM images of freely developing chemical turbulence in absence of feedback (a), intermittent turbulence for small values of feedback intensity (b), and homogeneous oscillations for higher values of feedback intensity (c). (middle) Space–time plot for the transition from turbulence to homogeneous oscillations along the line AB indicated in image (a). From left to right, the plot shows, with increasing time, turbulence for $\mu = 0.0$, transition to intermittent turbulence and the persistent state of intermittent turbulence for $\mu = 0.77 \times 10^{-5}$ mbar, and the transition to homogeneous oscillations for $\mu = 1.2 \times 10^{-5}$ mbar. Below the space–time diagram, the feedback intensity is plotted as a function of time. The parameters are $T = 505$ K, $p_{O_2} = 4 \times 10^{-4}$ mbar, $p_{CO}^0 = 9.5 \times 10^{-5}$ mbar, and $\tau = 3$ s (from [10]).

develops disordered, highly irregular spiral-wave turbulence. A snapshot of this dynamical state is shown in Fig. 28.4 (a). For sufficiently strong feedback intensities μ chemical turbulence can be suppressed with both feedback schemes (28.6) and (28.7) introduced above. We present a series of experiments, where both the feedback intensity μ and the delay time τ in (28.7) are systematically varied.

28.4.1.1 Control of Turbulence

In the presence of feedback, the system gradually synchronizes with increasing feedback intensity μ. An example of the feedback-induced transition from turbulence to homogeneous oscillations is shown in Fig. 28.4. For zero feedback intensity, the system is in a state of fully developed spiral-wave turbulence as displayed in Fig. 28.4 (a). Oscillations are already synchronized to a certain extent for intermediate values of μ resulting in a state of intermittent turbulence, Fig. 28.4 (b). Finally, for higher feedback intensities, complete synchronization is reached and the system performs homogeneous oscillations, see Fig. 28.4 (c). A space–time plot along the diagonal of the PEEM image further illustrates the process of synchronization as shown in the lower part of Fig. 28.4. Note that for synchronization of the system in dependence on the feedback intensity μ, strong hysteresis effects are observed.

In the state of control, the period T of homogeneous oscillations depends on the choice of the delay time τ in the feedback scheme. For $T = \tau$ the optimal case of a noninvasive feedback would be established. Figure 28.5 shows that the period approaches the line for which T equals τ with increasing delay (black squares). However, the actual intersection point for which $T = \tau$ is not reached and a jump occurs instead around the line given by $T = \tau$. As the value of T ap-
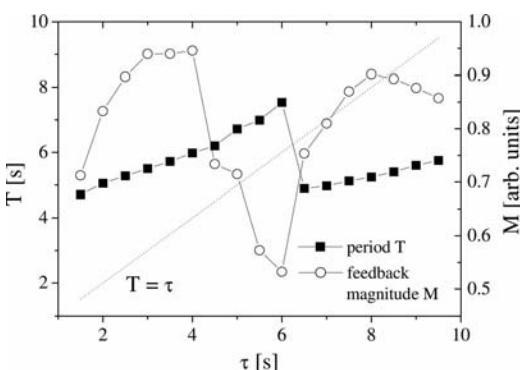
Fig. 28.5 Period T of homogeneous oscillations (black squares) and feedback magnitude $M = \langle |I(t - \tau) - I(t)| \rangle$ (open circles) as function of the delay time τ. The parameters are $T = 515$ K, $p_{O_2} = 4 \times 10^{-4}$ mbar, $p_{CO}^0 = 10.0 \times 10^{-5}$ mbar, and $\mu/p_{CO}^0 = 0.32$ (from [10]).

proaches τ, the feedback magnitude M (open circles) can be decreased by about 50%, indicating that the invasiveness of the feedback is reduced considerably by optimizing the choice of the delay time in the feedback scheme. However, the limit case of a completely noninvasive control could not be established in the experiments.

28.4.1.2 Spatiotemporal Pattern Formation

In a narrow interval of intermediate feedback intensities close to the transition from turbulence to uniform oscillations, different spatiotemporal patterns can be stabilized [6, 10, 28]. Here, we present an overview of the experimentally observed feedback induced space–time patterns that are obtained by application of the global-feedback scheme (28.6) (see Fig. 28.6). A large number of experi-
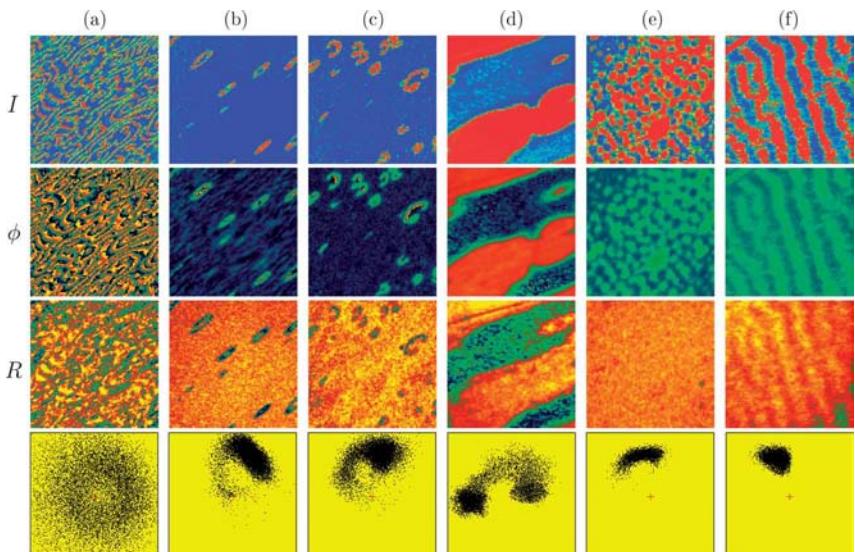
Fig. 28.6 (a)–(f) PEEM images (top row), distributions of phase (second row), amplitude (third row), and phase portraits (bottom row) for several typical patterns observed in CO oxidation experiments. In the PEEM images, blue (dark gray) color denotes surface areas predominantly covered by oxygen, and red (light gray) regions are mainly CO covered. Green (bright) color denotes intermediate values of intensity. In the phase and amplitude representations, yellow (bright) color denotes high, and blue (dark) color denotes low values. Green and red (gray) areas denote intermediate phase and amplitude values. The parameter values of temperature (K), oxygen partial pressure (10^{-5} mbar), base CO pressure p_0 (10^{-5} mbar), feedback intensity μ (10^{-5} mbar) and delay time τ (s) are, respectively: (a) 529, 40.0, 12.3, 0, 0; (b) 540, 40.0, 13.1, 1.7, 0.7; (c) 537, 40.0, 11.4, 3.0, 0.7; (d) 500, 10.0, 3.1, 0.6, 0.8; (e) 535, 40.0, 12.2, 4.0, 0.6; and (f) 505, 10.0, 3.3, 1.6, 0.8. The side length of images is (a), (c), (d) 330 μm, (b) 360 μm, (e) 210 μm, and (f) 270 μm (from [6]).

ments was conducted to study the spatiotemporal dynamics of the system under systematic variation of the feedback parameters μ and τ. In absence of feedback, the system displays *chemical turbulence* (Fig. 28.6 (a)).

As the feedback intensity is increased, intermittent turbulence can be observed. It is characterized by irregular cascades of localized patterns on a uniformly oscillating background. In particular, two types of localized objects can be identified, namely bubble-shaped structures and localized spiral-wave fragments, see Figs. 28.6(b) and (c).

Besides, several regular space–time patterns can be stabilized for delays in the interval $0.6\,\text{s} < \tau < 1.0$ s. The precise stability regions of these patterns depend sensitively on the choice of temperature and partial pressures. In the state of oscillatory phase clusters, the surface is divided into large domains ("clusters") of synchronous oscillations (Fig. 28.6 (d)). Two oscillatory states can be distinguished that show the same period (twice the period of the feedback signal) and identical amplitude while their phases are shifted by half a period with respect to each other. No intrinsic spatial wavelength is found in such a pattern. Note that oscillatory phase clusters under global-delayed feedback fulfill the condition of phase balance. This means that the total areas occupied by the two anti-phase domains within the imaged part of the surface are approximately equal. In Fig. 28.6 (e), oscillatory arrays of cells are shown that occupy the entire imaged surface area and are visible only during short intervals within each oscillation period when the surface switches between the uniformly CO and O covered states. Typically, the cellular arrays have an irregular structure with an average cell size of approximately $20\,\mu\text{m}$. No unambiguously regular, hexagonal arrays have been observed. Oscillatory standing waves are characterized by the repeated appearance of alternating bright and dark stripes from a uniform state. They form a spatially periodic array and have a wavelength of roughly 20–$50\,\mu\text{m}$ depending on the choice of parameters. A typical example of oscillatory standing waves is displayed in Fig. 28.6 (f).

The observed patterns can be further characterized by a decomposition of the experimental space–time data into phase and amplitude variables. This decomposition was performed using a variant of the analytic signal approach (see Section 28.3 and [6] for an explanation). The resulting phase and amplitude patterns are shown in the second and third row of Fig. 28.6, the phase portrait being displayed in the bottom row.

28.4.2
Control of Turbulence in Catalytic CO Oxidation – Numerical Simulations

Control of turbulence by global-delayed feedback was studied in numerical simulations of the model (28.2)–(28.4) [8, 28]. Global delayed feedback was introduced, similar to relation (28.6) in the experiment, through a dependence of the CO partial pressure on the average CO coverage $\bar{u}(t)$,

$$p_{\text{CO}}(t) = p_{\text{CO}}^0 + \mu\,(\bar{u}(t - \tau) - \bar{u}_{\text{ref}}). \tag{28.8}$$
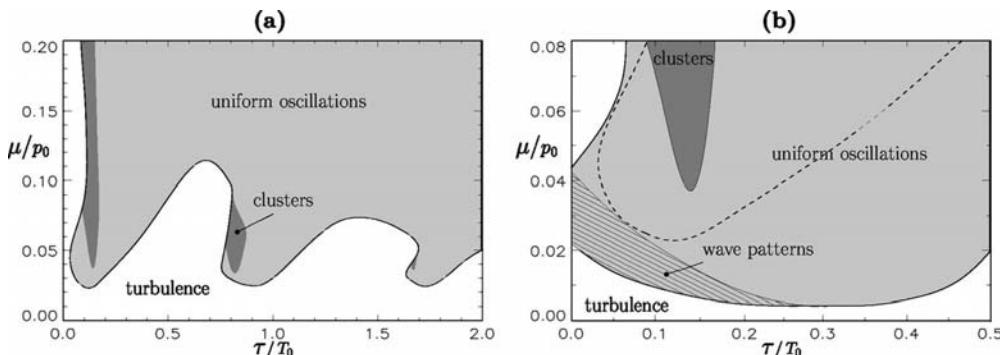
Fig. 28.7 Synchronization diagrams for the one-dimensional system in the presence of global-delayed feedback, starting from (a) developed turbulence and (b) the uniform initial state. The dashed line in (b) additionally shows the synchronization boundary, when starting from the turbulent state (from [8]).

The model parameters were chosen such that, in absence of feedback, an isolated system element performed nonharmonic stable oscillations of period $T_0 = 2.73$ s, but the system with diffusion showed spatiotemporal chaos characteristic for amplitude turbulence. The synchronization diagram, based on the simulations of the one-dimensional system, is displayed in Fig. 28.7.

For sufficiently large feedback intensity, global-delayed feedback allows to suppress amplitude turbulence and induces uniform oscillations in a wide range of delays (light gray-shaded regions). The minimal value of μ needed to stabilize uniform oscillations, i.e., the efficiency of the feedback, strongly depends on the choice of τ. At very small delays, $\tau/T_0 < 0.03$, the suppression of turbulence is impossible for realistic values of μ.

Close to the border of synchronization (the boundary between the white and the gray-shaded regions in Fig. 28.7 (a)), intermittent turbulence can be found. Here, a large part of the system is already synchronized, while a few amplitude defects persist and initiate cascades of defect reproduction that lead to random bursts of localized structures on a uniformly oscillating background. Defects reproduce until nearly the entire system is turbulent. Then, they simultaneously annihilate and only a few of them survive to initiate another turbulent cascade. In two space dimensions, this process is reflected by irregular cascades of circular structures on the background of uniform oscillations.

In the dark gray regions of Fig. 28.7, turbulence is suppressed and the formation of oscillatory cluster patterns can be observed. They consist of large, homogeneously oscillating domains that are separated by narrow domain interfaces. No intrinsic spatial wavelength is present in such patterns. Two different types of stable clusters are observed. Phase clusters are characterized by different domains that follow the same limit cycle but oscillate with opposite phase. Similar to the experiment, they show the property of phase balance (see above). Ampli-

tude clusters exist at $\tau/T_0 \approx 0.15$ for high feedback intensities, $\mu/p_0 > 0.17$. They are characterized by the coexistence of two stable limit cycles and do not show phase balance. The domain interfaces are stationary in time for both cluster types.

Figure 28.7 (b) shows the synchronization diagram as it is obtained when a uniform state with small superimposed random perturbations is taken as initial condition. In a wide range of delays, strong hysteresis is found for the transition between turbulence and uniform oscillations (compare the dashed line in Fig. 28.7 (b) denoting the former border of synchronization).

Inside the hatched region in Fig. 28.7 (b), standing waves develop from small random perturbations. These patterns consist of stationary periodic modulations of both the oscillation phase and amplitude (a local increase in R corresponding to a decrease in ϕ). They show an intrinsic wavelength that is a characteristic property of the pattern for a given set of system parameters. For decreasing feedback intensity, standing waves become unstable. They first give way to a pattern of breathing waves and, under a further decrease of feedback intensity, the pattern breaks down and phase turbulence develops in the system. In the two-dimensional system, this region approximately coincides with the range of parameters where *oscillatory cellular structures* are found. Like wave patterns, such structures represent small-amplitude modulations of uniform oscillations. Close to the border to uniform oscillations, the arrays of cells are regular and show a hexagonal symmetry.

Figure 28.8 presents a summary of different patterns in a two-dimensional system. CO coverage, phase distribution, amplitude distribution, and phase protrait are displayed from top to bottom. The unperturbed turbulent state (Fig. 28.8 (a)) is characterized by strong amplitude and phase fluctuations. Intermittent turbulence (Fig. 28.8 (b)) is observed close to the synchronization border under increasing feedback intensity. Stationary two-phase clusters (Fig. 28.8 (c)) were found for further increasing feedback intensity in narrow intervals of the delay time. Because the local oscillations inside the cluster domains exhibit period-two behavior, oscillations within different cluster domains at a given time differ also in amplitude; nonetheless, they correspond to the same limit cycle. Hexagonal cell arrays arising from a finite wavelength instability are shown in Fig. 28.8 (d). Secondary instabilities lead to breathing cellular structures (not shown in this figure), and to phase turbulence (Fig. 28.8 (e)).

28.4.3
Control of Turbulence in Oscillatory Media – Theory

A feedback scheme of type (28.6) was initially proposed by Battogtokh and Mikhailov [3] to control spatiotemporal chaos in reaction–diffusion systems. They demonstrated this in the framework of the complex Ginzburg-Landau equation that allows to study general aspects of turbulence in oscillatory media near a supercritical Hopf bifurcation. Their extensive investigation will be reviewed below (see also [34] and references therein). It served as a motivation and theoreti-
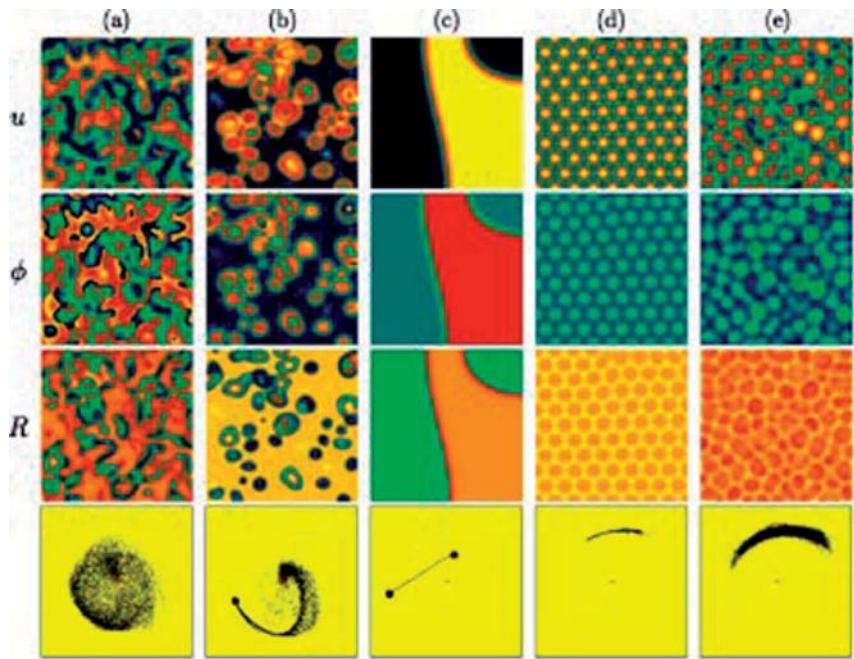
Fig. 28.8 Distributions of CO coverage (top row), oscillation phase (second row), amplitude (third row), and phase portraits (bottom) for (a) unforced turbulence and (b)–(e) several typical feedback-induced two-dimensional patterns. In the images, yellow color denotes high, green and red color intermediate, and blue color low values of displayed variables. In phase portraits (b) and (c), bold dots are added to indicate the uniform states (from [8]).

cal basis for the experimental and numerical work on catalytic CO oxidation that was presented in the earlier sections above.

For a general oscillatory reaction–diffusion system with an additional feedback term of type (28.6) the following amplitude equation can be derived close to the soft onset of oscillations,

$$\dot{\eta} = \eta - (1 + i\beta)|\eta|^2\eta + (1 + i\varepsilon)\nabla^2\eta + \mu e^{i\chi}\bar{\eta}(t)\,, \tag{28.9}$$

where

$$\bar{\eta}(t) = \frac{1}{S}\int\limits_{(S)} \eta(\vec{r}, t)\mathrm{d}\vec{r} \tag{28.10}$$

is the global average of the complex oscillation amplitude $\eta(\vec{r}, t)$. This equation was originally proposed in [45] (see also [3, 4, 32, 33]). Here, we choose the case where uniform oscillations are modulationally unstable in absence of feedback

and turbulence spontaneously develops. This situation is realized when $1 + \varepsilon\beta < 0$, i.e., uniform oscillations are Benjamin-Feir unstable.

Equation (28.9) admits a simple solution corresponding to bulk oscillations, $\eta(t) = \rho_0 e^{-i\Omega_0 t}$ with $\rho_0 = (1 + \mu\cos\chi)^{1/2}$ and $\Omega_0 = \beta + \mu(\beta\cos\chi - \sin\chi)$. As the feedback intensity μ is decreased, patterns characterized by spatial modulation of the oscillation phase can develop. To study the behavior of the globally coupled system near this first desynchronization transition [3, 19, 31, 33], one can write $\eta(\vec{r}, t)$ as a superposition of active modes. In one dimension, we have

$$\eta(x, t) = e^{-i\Omega t}\left[H + A_+ e^{i\kappa x} + A_- e^{-i\kappa x}\right]. \tag{28.11}$$

If ansatz (28.11) is substituted into Eq. (28.9), a pair of coupled equations for the complex amplitudes H and $A_\pm$ is obtained. Linear stability analysis [4, 31] allows to determine the threshold μ_c and the critical wave number κ_c of this instability (as the wave number of the modulation mode that first begins to grow).

Figure 28.9 shows the stability diagram of uniform oscillations. When the curve AB is crossed with decreasing feedback intensity μ, spatial modulations of the oscillation phase with wavelength $\lambda = 2\pi/\kappa_c$ develop. In two dimensions, such standing waves correspond to oscillating stripes. Additionally, resonant patterns of hexagonal symmetry can occur. If μ is further decreased, the mixed-mode states undergo subharmonic instabilities giving rise to breathing standing waves of cellular patterns, respectively [4].

Along the curve BC, bulk oscillations become unstable with respect to a long-wavelength spatial modulation with $\kappa_c \to 0$. Numerical simulations show [4] that here the medium breaks into large phase domain clusters with a size on the order of the dimension of the medium. The boundaries AD and CE are given by the condition $\mu = -1/\cos\chi$. On these lines, the amplitude $\rho_0 = (1 + \mu\cos\chi)^{1/2}$ of bulk synchronized oscillations should vanish. However, oscillations in the system cannot disappear (indeed, the steady state $\eta = 0$ is al-
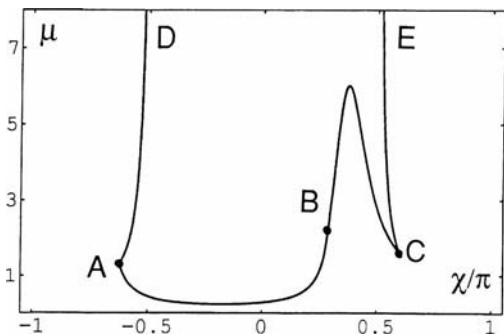
Fig. 28.9 Synchronization diagram for $\varepsilon = 2$ and $\beta = -1.4$. Bulk oscillations are linearly stable above the curve DABCE (from [4]).

ways unstable). Upon crossing of these boundaries, long-wavelength periodic modulation of the uniform oscillatory state develops as well. Note that suppression of turbulence is possible only inside a window of phase shifts χ.

In a two-dimensional system, different transition scenarios from defect mediated turbulence to uniform oscillations can be observed depending on the value of the phase shift χ. In absence of feedback, amplitude turbulence prevails. It is characterized by the presence of amplitude defects that occupy irregular cells formed by so-called shocks, lines of increased oscillation amplitude. Generally, regimes of intermittent turbulence are observed for small feedback intensities.

At intermediate values of μ, different regular patterns can be stabilized and give way to uniform oscillations for increasing μ. For $\chi = -0.2\pi$ hexagonal cellular patterns can be observed. If the phase shift is increased to $\chi = 0$, the transition to uniform oscillations occurs via the development of localized turbulent spots that emerge from the initial irregular cells of amplitude turbulence. For χ approaching 0.275π (point B in the synchronization diagram, Fig. 28.9), the cells get larger and, in the interval $0.275 < \chi/\pi < 0.599$ (corresponding to the segment BC in Fig. 28.9), they are replaced by large phase domains (clusters).
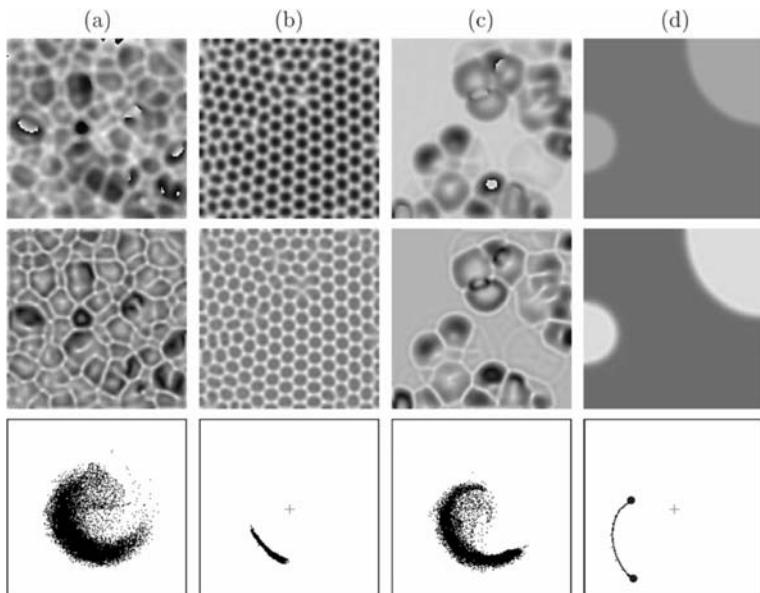
Fig. 28.10 Different two-dimensional patterns in the CGLE with global feedback ($\varepsilon = 2, \beta = -1.4$). For each pattern, the distributions of phase (top row), amplitude modulus (middle) and the phase portraits (bottom row) are shown. (a) Amplitude turbulence on background of an irregular cellular structure ($\mu = 0.18, \chi = -0.2$), (b) a cellular structure ($\mu = 0.26, \chi = -0.2$), (c) localized turbulence ($\mu = 0.55, \chi = 0$), and (d) amplitude clusters ($\mu = 4, \chi = 0.4$) (from [5]).

Inside the clusters, not only the phase, but also the amplitude of oscillations is changed. They result from a long-wavelength instability of the uniform mode and were first considered by Falcke et al. [19]. It can be shown [1] that the conditions for this instability are the same as those determining clustering in populations of globally coupled oscillators [22].

Figure 28.10 presents a summary of typical patterns found in numerical simulations of the complex Ginzburg-Landau equation with global feedback. For each pattern, the distributions of phase φ and amplitude ρ are shown. Additionally, the bottom row displays phase portraits of these patterns, constructed by plotting the states of all elements in the plane spanned by the polar coordinates (ρ, φ).

Note that the model (28.9) considered above was obtained by a reduction that is valid only for short delay times $\tau \ll 1$. Since time is measured in units of the relaxation time for the oscillation amplitude, which diverges near a supercritical Hopf bifurcation, this assumption always holds sufficiently close to the Hopf bifurcation point. Nonetheless, it may be also interesting to consider the global-control problem without assuming that the delay time is short.

28.4.4
Time Delay Autosynchronization

The control scheme implemented in the reduced model (28.9) is invasive. This means that when turbulence is suppressed and uniform oscillations are stabilized, the control signal does not vanish and, effectively, the system is then under the action of a uniform periodic driving force. It is known that for chaotic dynamical systems, described by a small number of variables, stabilization of unstable periodic orbits can be achieved in a non-invasive way by using *time delay autosynchronization* (TDAS) proposed by Pyragas [38]. Applications of this method to stabilize traveling waves in the CGLE using a local feedback scheme (where the control signal was separately generated for each point of the medium) have been studied [23, 35].

We have extended the investigations of Battogtokh and Mikhailov to study the effect of a global-TDAS scheme on the dynamics of the complex Ginzburg-Landau equation [10, 11]. This analysis complements the experimental studies performed with a feedback of type (28.7) that were presented above. For weak feedback a separation of time scales between amplitude and phase variables allows adiabatic elimination of the amplitude variable. If uniform oscillations are established in the system, the dynamics can be approximated by the phase equation for a single oscillator under the effect of weak TDAS,

$$\dot{\phi} = \omega + \mu f(\phi(t) - \phi(t - \tau)) \tag{28.12}$$

(see also [26]). Here, ω is the oscillation frequency in absence of feedback, τ is the delay time, and $\mu \ll 1$ the feedback intensity. The function f is generally
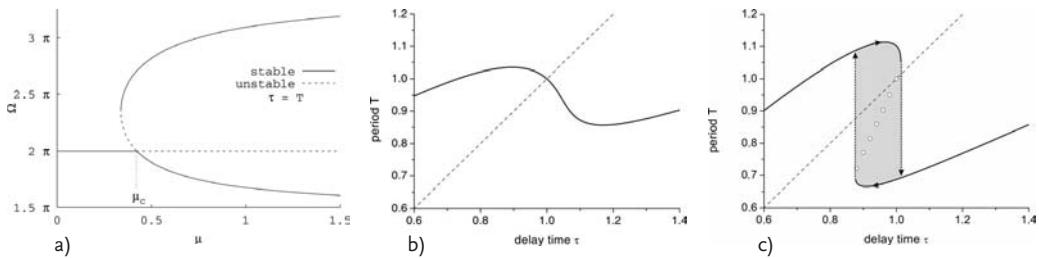
Fig. 28.11 (a) Oscillation frequency as function of the feedback intensity for $\tau = 1$ in the case of a Stuart-Landau oscillator, where $f(\Delta\phi) = a\sin(\Delta\phi) + b\cos(\Delta\phi) - b$, $\Delta\phi = \phi(t) - \phi(t - \tau)$, $a = \cos\chi + \beta\sin\chi$, and $b = \sin\chi - \beta\cos\chi$. The parameters are $\omega = 2\pi$, $\beta = 3$, and $\chi = \pi/6$. (b) and (c) Os-cillation period as function of delay time with (a) $\mu = 0.2$ and (b) $\mu = 0.6$. Hysteresis effects are found in the gray shaded region in (b). Open circles indicate unstable solutions yielded by Eq. (28.13). The time step for integration was $\Delta t = 0.0001$ (from [10]).

2π-periodic and satisfies the conditions $f(0) = f(2\pi) = 0$. See [10] for the derivation of Eq. (28.12) for a Stuart–Landau oscillator under TDAS feedback.

Uniform oscillations in the experimental system correspond to harmonic solutions $\phi(t) = \Omega t$ of the phase equation (28.12). Their oscillation frequency $\dot{\phi} = \Omega$ should satisfy

$$\Omega = \omega + \mu f(\Omega\tau) \quad \text{or} \quad \mu = \frac{\Omega - \omega}{f(\Omega\tau)}. \tag{28.13}$$

Figure 28.11 (a) shows different solutions Ω of Eq. (28.13) as a function of the feedback intensity for $\tau = T_0 = 2\pi/\omega$. Besides a solution $\Omega = \omega$ with vanishing feedback signal, other solutions with non-zero feedback emerge at higher feedback intensities via a saddle-node bifurcation. Solid (dotted) lines indicate linearly stable (unstable) solutions [10].

Tracing the dependence of T on the delay time τ in numerical simulations of Eq. (28.12), it was shown that the solution with $\Omega = \omega$ is indeed stable at $\tau = T_0$ for feedback intensities below a critical value $\mu < \mu_c$ (Fig. 28.11 (b)). For $\mu > \mu_c$ the $\Omega = \omega$ solution is unstable and a state with vanishing feedback signal cannot be established. Instead, a discontinuity occurs and hysteresis can be observed (see Fig. 28.11 (c)). This behavior is qualitatively similar to the experimental result displayed in Fig. 28.5. Similar results were obtained in numerical simulations of the realistic three variable reaction model for catalytic CO oxidation that was introduced in Section 28.2 [10].

To investigate control of turbulence in a spatially extended system, again the complex Ginzburg-Landau equation in the Benjamin-Feir unstable regime is considered,

$$\dot{\eta} = (1 - i\omega)\eta - (1 + i\beta)|\eta|^2\eta + (1 + i\varepsilon)\nabla^2\eta + F(t), \tag{28.14}$$

where, in this case, $F(t)$ is given by a global-TDAS term, $F(t) = \mu\,e^{i\chi}(\bar{\eta}(t - \tau)$ $-\bar{\eta}(t))$ with $\bar{\eta}(t) = \frac{1}{L}\int_0^L \eta(\vec{x}, t)\,d\vec{x}$. The parameters μ, τ, and χ denote the feedback intensity, the delay time, and a phase shift in the application of the control force, respectively. For sufficiently large μ, turbulence can be suppressed and uniform oscillations are stabilized. Based on the ansatz (28.11), we analyzed the linear stability of uniform oscillations in the presence of TDAS. For small amplitudes $A_\pm$ homogeneous contributions can be separated from spatially inhomogeneous terms, yielding a Stuart-Landau-type equation for H and a pair of coupled equations for A_+ and A_-.

The stability of the uniform system H corresponds to the case of the phase oscillator described above. Stability of uniform oscillations with respect to spatially inhomogeneous perturbations can be determined by solving the eigenvalue problem of the pair of linearized coupled equations for A_+ and A_-, yielding conditions for the critical feedback intensity and wavenumber. Based on these conditions, the stability boundary in the (τ, μ)-plane can be determined numerically. The resulting synchronization diagram is displayed in Fig. 28.12. Uniform oscillations are linearly stable (unstable) inside the gray shaded (white) regions. Repeated cusps are observed in the synchronization border whenever τ becomes equal to an integer multiple of the period of the unperturbed uniform system, $\tau = k\,2\pi/(\omega + \beta), k = 1, 2, 3, \dots$. For a discussion of the behavior at large delay time, see [11]. Numerical simulations indicate that regular spatiotemporal patterns like breathing and standing waves can be expected for μ-values close to the border of complete synchrony.

It was shown that for the choice of $\tau = 2\pi/\Omega_0$ a solution $\Omega = \Omega_0 = \omega + \beta$ exists for which the feedback signal is vanishing so that noninvasive control would be established. However, it can be demonstrated that in this case, the expression for the largest eigenvalue λ does not depend on μ, so that in the Benja-
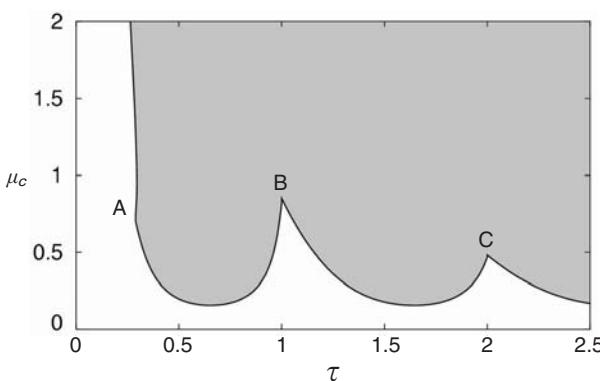
Fig. 28.12 Synchronization diagram. Uniform oscillations are stable inside the shaded region. The parameters are $\varepsilon = 2$, $\beta = -1.4$, $\omega = 2\pi - \beta \approx 7.68$, and $\chi = \pi/2$ (from [11]).

min-Feir unstable case, all inhomogeneous modes with a wave number less than $\kappa = \sqrt{-2(1 + \varepsilon\beta)/1 + \varepsilon^2}$ are growing independently of μ. Thus, for $1 + \varepsilon\beta < 0$ the solution with $\Omega = \omega + \beta$ is always unstable so that a noninvasive stabilization of uniform oscillations with TDAS is not possible in this type of system. This yields an explanation of the experimental findings summarized in Fig. 28.5.

28.5
Control of Spatiotemporal Chaos by Periodic Forcing

Spatiotemporal chaos in catalytic CO oxidation on Pt(110) can be also controlled by the application of an external periodic force [7, 34]. For an introduction to the experimental system and the laboratory setup, see Section 28.2. Again, temperature and partial pressures are chosen such that the unperturbed system spontaneously develops chemical turbulence. External periodic forcing is implemented via the gas phase by periodic modulation of the CO partial pressure in the reaction chamber,

$$p_{CO}(t) = p_{CO}^0 + \gamma \cos(2\pi\nu_f t)\,, \tag{28.15}$$

where the forcing amplitude and frequency γ and ν_f are independently chosen, external parameters. For large forcing amplitudes turbulence can be suppressed and uniform oscillations are established in the system. For intermediate forcing amplitudes, however, a rich variety of spatiotemporal patterns can be induced in this surface catalytic reaction.

Forcing frequencies in the range of $0.20\,\text{Hz} \leq \nu_f \leq 0.67\,\text{Hz}$ were applied, with modulations in CO partial pressure of a relative amplitude between 10% and 20%. Various nonresonant and resonant spatiotemporal patterns can be observed depending on the choice of the forcing parameters. For increasing forcing amplitude, freely evolving chemical turbulence is first replaced by intermittent turbulence. On the other hand, starting from frequency locked uniform oscillations, cellular structures can emerge upon a decrease of the forcing strength. Both patterns resemble intermittent turbulence and cellular structures observed in the presence of global-delayed feedback as described in Section 28.4.

Besides nonresonant structures, additional resonant patterns can be found at higher forcing frequency, $\nu_f \geq 0.5\,\text{Hz}$, due to 2:1 subharmonic entrainment of local oscillations. In particular, oscillatory phase clusters are observed. Similar to cluster states that emerge under global feedback, the surface splits into large domains belonging to either of two oscillatory states. Within both cluster states, local oscillations are entrained at half the frequency of the driving force, $\nu = \nu_f/2$, and locked to the external stimulus with a phase shift of one forcing period between the two clusters. At the low frequency edge of the 2:1 resonance, oscillatory stripe patterns occur, forming a labyrinthine structure. The growth mecha-
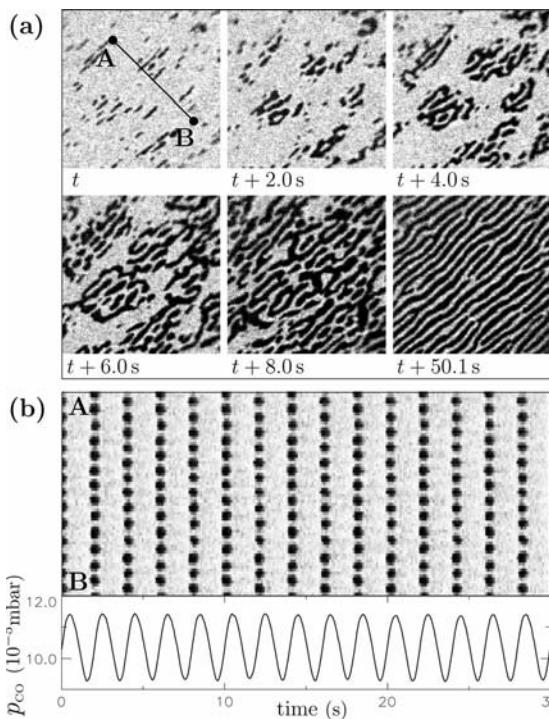
Fig. 28.13 Irregular oscillatory stripes under periodic forcing. (a) PEEM images $(240 \times 240\,\mu m^2)$ showing the initial development of the pattern at time intervals of one forcing period between subsequent snapshots (first five frames) and the fully developed structure (sixth frame). (b) Space–time diagram for the fully developed pattern, taken along the line *AB* indicated in the first image in (a). The curve below shows the corresponding temporal variation of CO partial pressure. The forcing frequency and amplitude are $v_f = 0.50\,Hz$ and $\gamma = 20.2\,\%$, respectively. The parameters are $T = 531\,K$, $p_{O_2} = 40.0 \times 10^{-5}$ mbar, and $p_{CO}^0 = 10.4 \times 10^{-5}$ mbar (from[7]).

nism of this pattern is illustrated in Fig. 28.13 (a). Starting from an initial state of uniform small-amplitude oscillations around a mainly CO covered state, the pattern grows stripe by stripe until it occupies the entire imaged surface area. Due to anisotropy of CO diffusion on the Pt(110) single crystal surface, the stripes are mainly oriented along the direction of fast CO diffusion (the $[1\bar{1}0]$ direction). The space–time diagram in Fig. 28.13 (b) shows that stripes occur only during short intervals of each oscillation cycle. After one forcing period, the locations of stripes are shifted, so that the initial pattern is repeated for every second forcing cycle.

References

1 M. Bär, M. Hildebrand, M. Eiswirth, M. Falcke, H. Engel, and M. Neufeld. Chemical turbulence and standing waves in a surface reaction model: The influence of global coupling and wave instabilities. *Chaos*, 4:499, 1994.

2 M. Bär, C. Zülicke, M. Eiswirth, and G. Ertl. Theoretical modeling of spatiotemporal self-organization in a surface catalyzed reaction exhibiting bistable kinetics. *J. Chem. Phys.*, 96:8595–8604, 1992.

3 D. Battogtokh and A. S. Mikhailov. Controlling turbulence in the complex Ginzburg-Landau equation. *Physica D*, 90:84–95, 1996.

4 D. Battogtokh, A. Preusser, and A. S. Mikhailov. Controlling turbulence in the complex Ginzburg-Landau equation II. Two-dimensional systems. *Physica D*, 106:327–362, 1997.

5 M. Bertram. *Controlling turbulence and pattern formation in chemical reactions*. PhD thesis, Technische Universität Berlin, 2002.

6 M. Bertram, C. Beta, M. Pollmann, A. S. Mikhailov, H. H. Rotermund, and G. Ertl. Pattern formation on the edge of chaos: Experiments with CO oxidation on a Pt(110) surface under global-delayed feedback. *Phys. Rev. E*, 67:036208, 2003.

7 M. Bertram, C. Beta, H. H. Rotermund, and G. Ertl. Complex patterns in a periodically forced surface reaction. *J. Phys. Chem. B*, 107:9610–9615, 2003.

8 M. Bertram and A. S. Mikhailov. Pattern formation on the edge of chaos: Mathematical modeling of CO oxidation on a Pt(110) surface under global-delayed feedback. *Phys. Rev. E*, 67:036207, 2003.

9 C. Beta. *Controlling Chemical Turbulence in Surface Reactions*. PhD thesis, Freie Universität Berlin, 2004.

10 C. Beta, M. Bertram, A. S. Mikhailov, H. H. Rotermund, and G. Ertl. Controlling turbulence in a surface chemical reaction by time delay autosynchronization. *Phys. Rev. E*, 67:046224, 2003.

11 C. Beta and A. S. Mikhailov. Controlling spatiotemporal chaos in oscillatory reaction–diffusion systems by time delay autosynchronization. *Physica D*, 199:173–184, 2004.

12 C. Beta, A. S. Mikhailov, H. H. Rotermund, and G. Ertl. Defect-mediated turbulence in a catalytic surface reaction. *Europhys. Lett.*, 75:868–874, 2006.

13 K. E. Daniels and E. Bodenschatz. Defect turbulence in inclined layer convection. *Phys. Rev. Lett.*, 88:034501, 2002.

14 J. Davidsen and R. Kapral. Defect-mediated turbulence in systems with local deterministic chaos. *Phys. Rev. Lett.*, 91:058303, 2003.

15 M. Eiswirth, K. Krischer, and G. Ertl. Nonlinear dynamics in the CO oxidation on Pt single crystal surfaces. *Appl. Phys. A*, 51:79–90, 1990.

16 T. Engel and G. Ertl. Elementary steps in the catalytic oxidation of carbon monoxide on platinum metals. *Adv. Catal.*, 28:1–77, 1979.

17 M. Falcke, M. Bär, H. Engel, and M. Eiswirth. Traveling waves in the CO oxidation on Pt(110): Theory. *J. Chem. Phys.*, 97:4555–4563, 1992.

18 M. Falcke and H. Engel. Pattern formation during the CO oxidation on Pt(110) surfaces under global coupling. *J. Chem. Phys.*, 101(7):6255–6263, 1994.

19 M. Falcke, H. Engel, and M. Neufeld. Cluster formation, standing waves, and

stripe patterns in oscillatory active media with local and global coupling. *Phys. Rev. E*, 52(1):763–771, 1995.

20 L. Gil, J. Lega, and J. L. Meunier. Statistical properties of defect-mediated turbulence. *Phys. Rev. A*, 41:1138–1141, 1990.

21 H. H. Rotermund, G. Haas, R. U. Franz, R. M. Tromp, and G. Ertl. Imaging pattern formation in surface reactions from ultrahigh vacuum up to atmospheric pressures. *Science*, 270:608–610, 1995.

22 V. Hakim and W. J. Rappel. Dynamics of the globally coupled Ginzburg-Landau equation. *Phys. Rev. A*, 46:R7437, 1992.

23 I. Harrington and J. E. S. Socolar. Limitation on stabilizing plane waves via time delay feedback. *Phys. Rev. E*, 64:056206, 2001.

24 M. Hildebrand, M. Bär, and M. Eiswirth. Statistics of topological defects and spatiotemporal chaos in a reaction–diffusion system. *Phys. Rev. Lett.*, 75:1503–1506, 1995.

25 R. Imbihl and G. Ertl. Oscillatory kinetics in heterogeneous catalysis. *Chem. Rev.*, 95:697–733, 1995.

26 E. M. Izhikevich. Phase models with explicit time delays. *Phys. Rev. E*, 58(1): 905–908, 1998.

27 S. Jakubith, H. H. Rotermund, W. Engel, A. v. Oertzen, and G. Ertl. Spatiotemporal concentration patterns in a surface reaction: Propagating and standing waves, rotating spirals, and turbulence. *Phys. Rev. Lett.*, 65(24):3013–3016, 1990.

28 M. Kim, M. Bertram, M. Pollmann, A. v. Oertzen, A. S. Mikhailov, H. H. Rotermund, and G. Ertl. Controlling chemical turbulence by global-delayed feedback: Pattern formation in catalytic CO oxidation on Pt(110). *Science*, 292:1357–1360, 2001.

29 K. Krischer, M. Eiswirth, and G. Ertl. Oscillatory CO oxidation on Pt(110): Modeling of temporal self-organization. *J. Chem. Phys.*, 96(12):9161–9172, 1992.

30 Y. Kuramoto. *Chemical Oscillations, Waves, and Turbulence*. Springer, Berlin, 1984.

31 D. Lima, D. Battogtokh, A. S. Mikhailov, P. Borckmans, and G. Dewel. Pattern selection in oscillatory media with global coupling. *Europhys. Lett.*, 42:631, 1998.

32 F. Mertens, R. Imbihl, and A. S. Mikhailov. Breakdown of global coupling in oscillatory chemical reactions. *J. Chem. Phys.*, 99:8668–8671, 1993.

33 F. Mertens, R. Imbihl, and A. S. Mikhailov. Turbulence and standing waves in oscillatory chemical reactions with global coupling. *J. Chem. Phys.*, 101:9903–9908, 1994.

34 A. S. Mikhailov and K. Showalter. Control of waves, patterns and turbulence in chemical systems. *Phys. Rep.*, 425:79–194, 2006.

35 K. A. Montgomery and M. Silber. Feedback control of traveling wave solutions of the complex Ginzburg-Landau equation. *Nonlinearity*, 17:2225–2248, 2004.

36 P. Panter. *Modulation, Noise, and Spectral Analysis*. McGraw-Hill, New York, 1965.

37 A. Pikovsky, M. Rosenblum, and J. Kurths. *Synchronization*. Cambridge University Press, Cambridge, 2001.

38 K. Pyragas. Continuous control of chaos by self-controlling feedback. *Phys. Lett. A*, 170:421–428, 1992.

39 H. H. Rotermund. Imaging of dynamic processes on surfaces by light. *Surf. Sci. Rep.*, 29:265–364, 1997.

40 H. H. Rotermund. Imaging pattern formation in surface reactions from ultrahigh vacuum up to atmospheric pressures. *Surf. Sci.*, 386:10–23, 1997.

41 H. H. Rotermund. Imaging surface reactions with a photoemission electron microscope. *J. Electron. Spectrosc.*, 98/99:41–54, 1999.

42 A. v. Oertzen, A. S. Mikhailov, H. H. Rotermund, and G. Ertl. Subsurface oxygen formation on the Pt(110) surface: Experiment and mathematical modeling. *Surf. Sci.*, 350:259–270, 1996.

43 A. v. Oertzen, H. H. Rotermund, A. S. Mikhailov, and G. Ertl. Standing wave patterns in the CO oxidation reaction on a Pt(110) surface: Experiments and modeling. *J. Phys. Chem. B*, 104(14):3155–3178, 2000.

44 A. v. Oertzen, H. H. Rotermund, and S. Nettesheim. Diffusion of carbon monoxide and oxygen on Pt(110): experiments performed with the PEEM. *Surf. Sci.*, 311:322–330, 1994.

45 G. Veser, F. Mertens, A. S. Mikhailov, and R. Imbihl. Global coupling in the presence of defects: synchronization in an oscillatory surface reaction. *Phys. Rev. Lett.*, 71:935–938, 1993.

46 H. Wang. Statistics of defect-mediated turbulence influenced by noise. *Phys. Rev. Lett.*, 93:154101, 2004.

29

Forcing and Feedback Control of Arrays
of Chaotic Electrochemical Oscillators

István Z. Kiss and John L. Hudson

29.1
Introduction

Several electrochemical systems give rise to chaotic current oscillations under potentiostatic control [1]. Low-dimensional chaos occurs, for example, during electrodissolution of copper (in phosphoric acid [2, 3] or acetate buffer [4]), nickel (in sulfuric acid [5–7]), and the electrocatalytic reduction of indium ions [8]. Complex chaotic behavior including chaotic bursting [9] and non-phase coherent [10] and high dimensional chaos [11] has been found during the electrodissolution of iron in sulfuric acid. These chaotic electrochemical systems are good testbeds for experimental verification of chaos control techniques since the current (proportional to the rate of reaction) can be conveniently measured and the circuit potential can be used as a control parameter.

Electrochemical experiments can be carried out on either a single electrode or on electrode arrays. Single electrodes can be used for a control of a single oscillator. In the experiments on electrode arrays the interactions among the elements must be considered as well as feedback and/or forcing. Both perturbations of global parameters (such as the circuit potential) and local parameters (through perturbation of resistors connected to the electrodes) are possible that enable testing various control techniques.

The control of chaotic behavior encompasses both the destruction of chaotic attractor by the stabilization of unstable periodic orbits (UPOs) and the control of coherence through, for example, phase synchronization [12, 13]. The control of chaotic behavior is typically achieved through resonant control (periodic perturbation of a system parameter [14, 15]), and discrete [16] or continuous [17] feedback. These standards methods have been successfully applied to low-dimensional chaotic electrochemical systems: the chaotic electrodissolution of copper was suppressed by periodic modulation of the circuit potential and period-1 and period-2 oscillations were observed [18]; simple proportional [3] and recursive [19] feedback, delayed feedback [20], and an artificial neural network method [21] were used to stabilize unstable periodic orbits.

Here we review some of our recent experimental results on the mechanisms of resonant and feedback techniques with a single oscillator, and their extensions to small assemblies and larger populations of chaotic oscillators. Since for sets and populations the interactions play important roles, we put special emphasis on the interaction of coupling and forcing and feedback, respectively. Finally, we discuss control of chaos on a collective level when the goal is the regularization of the mean field without a major change of the chaotic behavior on a local level.

29.2
Control of Single Chaotic Oscillator

29.2.1
Experimental Setup

A standard electrochemical cell consisting of a nickel working electrode, a $Hg/Hg_2SO_4/K_2SO_4$ reference electrode, and a platinum mesh counter electrode was used. Experiments were carried out in 4.5 M H_2SO_4 solution at a temperature of 11 °C. A schematic of the apparatus is shown in Fig. 29.1.

The 64 electrode array in an 8×8 geometry is shown; for experiments with a single oscillator the array is replaced with one electrode. The working electrodes are embedded in epoxy and reaction takes place only at the ends. The diameter of the electrode in the experiments on forcing of one oscillator is 2 mm and those of the 64 elements in the array are 1 mm. The currents of the electrodes are measured independently at a sampling rate of 100 Hz and thus the rate of reaction as a function of position and time is obtained. In some of the experiments global coupling is added to the array with the use of resistors. The exter-
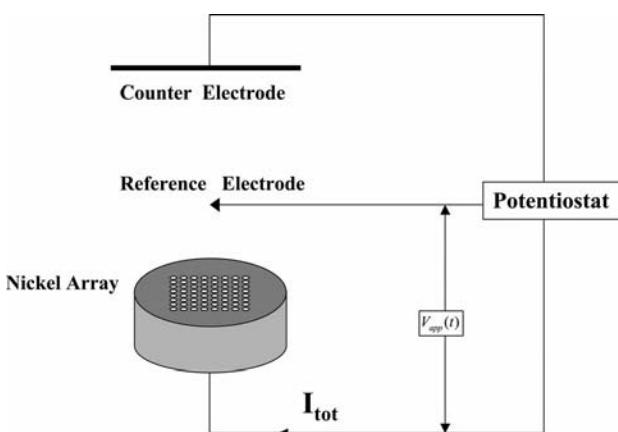
Fig. 29.1 Experimental setup.

nal resistors are added individually (R_{ind}) or collectively (R_{coll}). The collective resistor couples the electrodes globally and the strength of this coupling is characterized by a parameter ε, which is the ratio of collective to total resistance: $\varepsilon = R_{coll}/R_{tot}$. This value takes on values from zero to one as the global coupling increases. Additional details on the experiments can be found in the original papers [22–24].

The electrode is held at the applied potential ($V_{app}(t)$) with a potentiostat. The applied potential is the sum of a constant potential (V_0) and a perturbation $\delta V(t)$. The perturbation depends on the specific chaos control procedure and the following techniques are applied:

In the *forcing* experiments of both a single electrode and the array a sinusoidal signal with frequency Ω and amplitude A is superimposed on the applied potential: $\delta V(t) = A \sin 2\pi\Omega t$.

In the *feedback* experiments a feedback signal is generated with gain (K) and delay (τ). Two types of feedbacks are discussed.

In the direct delayed feedback the perturbation of output voltage is proportional to the difference of the delayed total current $I_{tot}(t - \tau)$ and the precalculated mean total current, $\langle I_{tot} \rangle$; the applied potential perturbation is then:

$$\delta V(t) = K[I_{tot}(t - \tau) - \langle I_{tot} \rangle]. \tag{29.1}$$

Since the feedback is a small amplitude perturbation of the applied potential, we assume that the mean total current does not change significantly after the feedback is imposed. The mean total current is used as the offset of the feedback signal to maintain the applied potential in the chaotic region.

In the differential-delayed feedback [17] the difference between the delayed and the actual value of the total current is used:

$$\delta V(t) = K[I_{tot}(t) - I_{tot}(t - \tau)]. \tag{29.2}$$

29.2.2
Chaotic Ni Dissolution: Low-Dimensional, Phase Coherent Attractor

29.2.2.1 Unforced Chaotic Oscillator
As reported in previous studies [7, 25], the potentiostatic dissolution of Ni exhibits chaotic dynamics if an appropriate series resistance (R_s) is added to the circuit. The reconstructed chaotic attractor from the current time series data, along with the corresponding power spectrum of the unforced system with $R_s = 170\,\Omega$, is shown in Fig. 29.2 (a) and (b), respectively. The chaotic attractor is low dimensional with an information dimension of approximately 2.2 [7]. The presence of a sharp peak at $f = 1.323$ Hz in the power spectrum implies strong phase coherence.
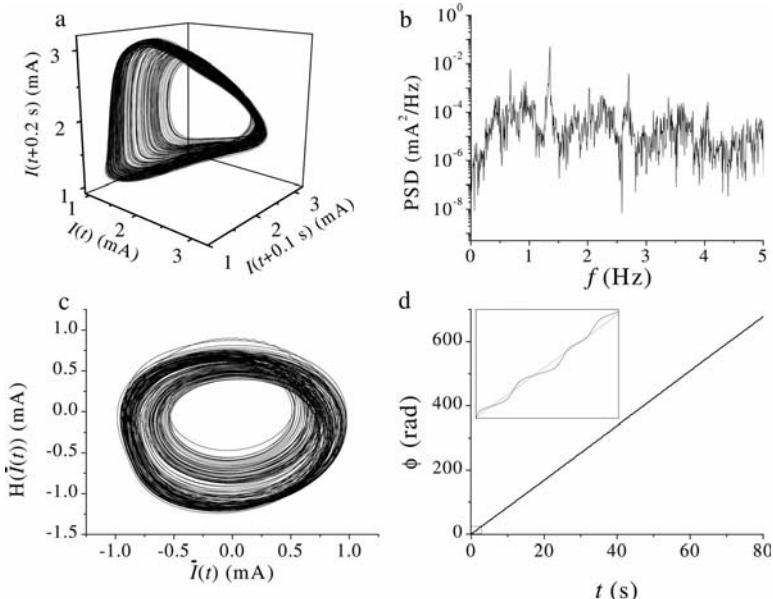
Fig. 29.2 Phase coherent chaotic oscillator [26]. (a) Reconstructed attractor using time delay coordinates. (b) Power spectrum. (c) Hilbert transform of the current, $H(\bar{I}(t))$, vs. current, $\bar{I}(t)$. (d) Phase $\phi(t)$ (solid) as a function of t. The linear least-squares fit (dotted in the inset, enlarged by a factor of 32) gives the frequency of the chaotic oscillation, $\omega_0 = 1.325$ Hz.

29.2.2.2 **Phase of the Unforced System**

In order to characterize the response of the chaotic system to a periodic forcing it is useful to compare the phases of the chaotic and forcing signals. We applied the Hilbert transform approach [27, 28] to obtain the phase $\phi(t)$ from the angle of a two-dimensional embedding in the Hilbert transform vs. signal phase space (see Fig. 29.2 (c)), where

$$H(I(t)) = \pi^{-1} \int_{-\infty}^{\infty} \frac{I(\tau)}{t - \tau} \mathrm{d}\tau \qquad (29.3)$$

is the Hilbert transform of $I(t)$. The frequency of the chaotic oscillations (ω_0), obtained from the linear least-squares fit to $\phi(t)$, is $\omega_0 = 1.325$ Hz (see Fig. 29.2 (d)). Note that although ϕ is monotonically increasing there are some slight deviations from the fitted line (Fig. 29.2 (d), inset). The deviations arise because the instantaneous frequency ($\mathrm{d}\phi(t)/\mathrm{d}t$) depends in general on the amplitude.

29.2.3
Forcing: Phase Synchronization and Intermittency

29.2.3.1 Forcing with $\Omega = \omega_0$

For forcing experiments [26] the phases of the chaotic ($\phi(t)$) and the periodic driving ($\psi(t)$) signals were determined.

Results are first presented with a forcing frequency of $\Omega = 1.32\,\text{Hz}$, which is within the experimental error of ω_0. A diagram showing the minima of the oscillations as a function of the forcing amplitude is presented in Fig. 29.3. At small amplitude the frequency of the oscillations locks on Ω although the chaotic dynamics are only affected slightly. Even at small amplitudes the small variation of ω ($\pm 0.015\,\text{Hz}$) that had been observed in the unforced system diminishes to $\pm 0.001\,\text{Hz}$. Therefore all the dynamical states shown in Fig. 29.3 have the same frequency regardless of the characteristics of the state. With increasing forcing amplitude, chaos→P4→P2→P1 transitions are observed. Note that the lowest branch of the P4 oscillations is actually two points; the values of those two minima are almost indistinguishable because of noise. The P4→P2 and P2→P1 transitions are inverse period-doubling bifurcations. [The experimental data cannot reveal the nature of chaos→P4 transition. One possible scenario can be an experimentally not resolvable period-doubling sequence. However, we cannot exclude the possibility of intermittency, which was observed with $\Omega \neq \omega_0$ (see later)].
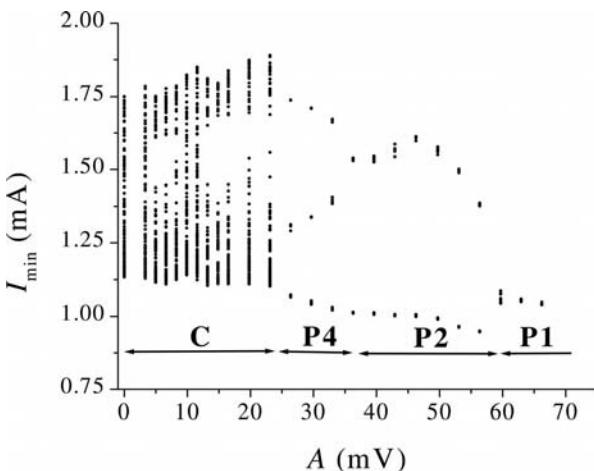
Fig. 29.3 Forcing a single oscillator with $\Omega = \omega_0$ [26]. The minima of the oscillations (I_{min}) as a function of the amplitude of the forcing (A) are shown. The forcing frequency $\Omega = 1.32\,\text{Hz}$ is within the experimental error of ω_0. The chaotic (C), period-4 (P4), period-2 (P2), and period-1 (P1) regions are also shown.
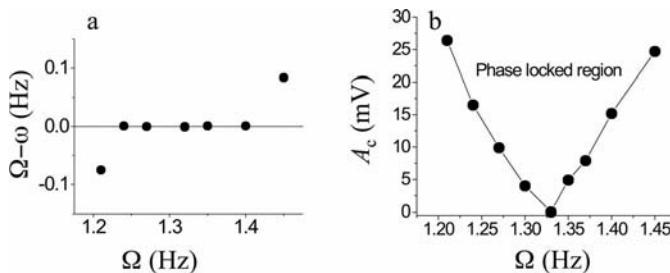
Fig. 29.4 Forcing a single oscillator with $\Omega \neq \omega_0$ [26]. (a) The frequency difference $(\Omega - \omega)$ as a function of the forcing frequency (Ω) for $A = 16.5$ mV. (b) The phase locked region in $A - \Omega$ parameter space.

29.2.3.2 Forcing with $\Omega \neq \omega_0$

Forcing experiments have been carried out for a range of forcing frequencies between 1.21 Hz and 1.45 Hz [26]. For a given amplitude ($A = 6.6$ mV, Fig. 29.4 (a)) phase synchronization occurs only for frequency region around ω_0. As the amplitude is made larger, the phase synchronized frequency region increases. Figure 29.4 shows the critical forcing amplitude A_c at which phase synchronization is observed. The experimentally determined synchronization tongue is approximately symmetric around ω_0.

The bifurcation diagrams at different frequencies were found to be similar to that presented in Fig. 29.3 for 1.21 Hz $\leq \Omega \leq$ 1.40 Hz. For larger forcing frequencies ($\Omega \geq 1.40$ Hz) the transition into the phase-locked region was qualitatively different; instead of a chaotic phase synchronization there is an intermittent transition from chaos to a periodic state; the periodic state is P2 for $\Omega = 1.45$ Hz, and P4 for $\Omega = 1.40$ Hz. The time series of the current and the phase difference are shown in Fig. 29.5 for $\Omega = 1.45$ Hz. Figures 29.5 (a) and (b) are for a forcing amplitude ($A = 23.1$ mV) just below critical.

The long P2 sequence is interrupted by a short chaotic series. The periodic region is phase synchronized, while during the chaotic region there is a phase slip. The current and phase difference are shown for amplitude close to the critical in Fig. 29.5 (c) and (d) ($A = 24.7$ mV); phase synchronization and period-2 oscillations are seen. For $\Omega = 1.40$ Hz, i.e., closer to ω_0 a similar intermittent transition was observed; however, the chaotic (not phase synchronized) state was transformed to a P4 (phase synchronized) state.

29.2.4
Delayed Feedback: Tracking

It is often possible to stabilize a UPO with a differential delayed feedback technique with appropriate control gain and delay set to the period of the UPO. Moreover, tracking of unstable orbits can be achieved by continuously updating K and τ. Among the control parameters, τ is of greatest importance since usually the gain
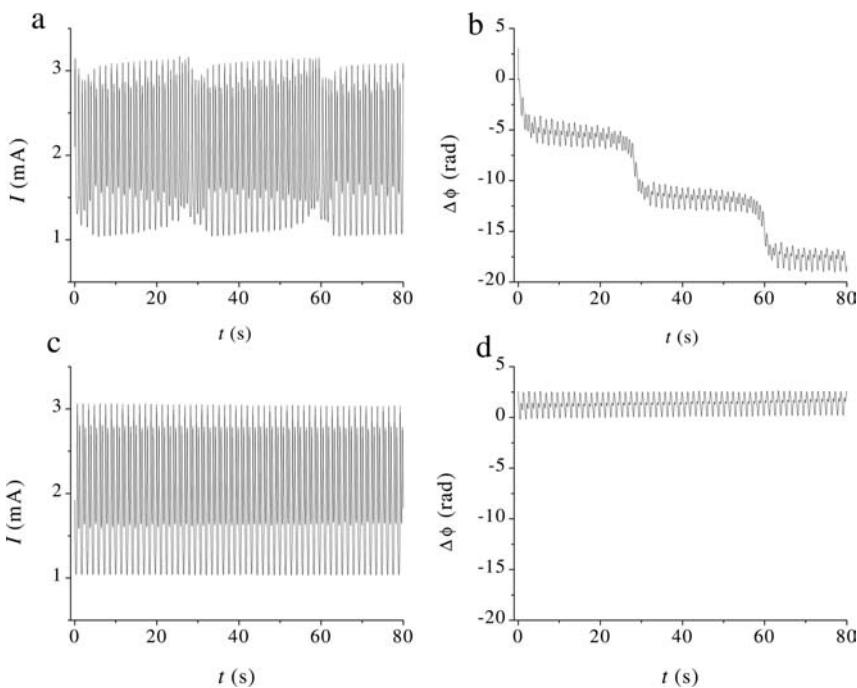
Fig. 29.5 Forcing a single oscillator: intermittency [26]. Current time series and phase differences, $\Omega = 1.45$ Hz (a), (b). Intermittent periodic and chaotic oscillations with phase slips. $A = 23.1$ mV, $A < A_{crit}$. (c), (d). Phase synchronized period state, $A = 24.7$.

can be set to a value that ensures successful control [29–31]. An analytical approximation for τ was suggested based on the calculation of the frequency of the control perturbation signal [32]. An even simpler method uses gradient descent for optimization with error function as the magnitude of control perturbations [33, 34]. Such a method is demonstrated in Fig. 29.6 with the low-dimensional chaotic anodic electrodissolution of copper in phosphoric acid [2, 3].

A successful control of a period-1 unstable orbit is shown in Fig. 29.6 (a) [35]; before the control is switched on ($t < 30$ s) the system exhibits low-dimensional chaotic current oscillations. After the control is turned on (i.e., the circuit potential is perturbed according to Eq. (29.2), periodic oscillations are observed. The initial value of the control constant τ was chosen to be the approximate period of the oscillations ($\tau = 0.85$ s) while the control gain K was adjusted to achieve best performance. The control perturbations do not vanish completely and an improvement of τ is automatically calculated with the gradient descent method. As τ increases to a limiting value of 0.980 s (not shown) the control perturbations decrease (Fig. 29.6 (a)). The control becomes more robust as well since stabilized oscillations show less variations in its amplitudes.
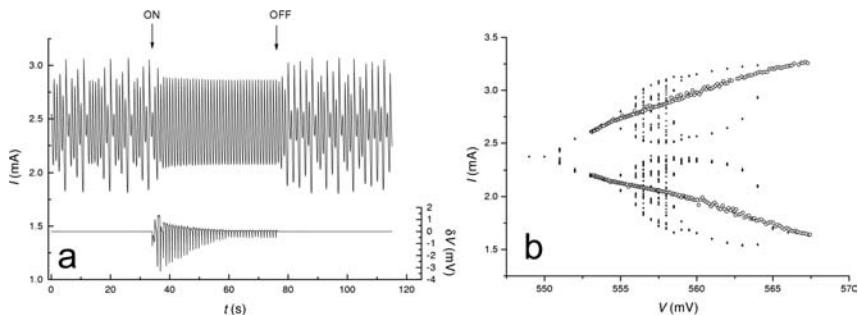
Fig. 29.6 Delayed-feedback control and tracking of a single chaotic oscillator [35]. (a) Stabilizing the unstable period-1 orbit using the delayed-feedback algorithm (Eq. (8.2)) $K = 4\,\mathrm{mV/mA}$ with corrections to the period, τ. The time series of the current (top, left axis) and the potential perturba- tions (bottom, right axis) as the period τ is adjusted every 2 s. (b) Tracking unstable peri- od-1 orbit. Diagram showing the maxima and minima of the stable (solid circle) and tracked unstable period-1 (open circle) oscil- lations.

In the chaotic copper dissolution without control a (steady state − period-1 − period-2 − period-4 − chaos − period-4 − period-2 − period-1) bifurcation struc- ture can be observed as the potential is varied as shown in Fig. 29.6 (b). Using the delayed-feedback control with autosetting time delay, the unstable period-1 orbit can traced through a period-doubling cascade [35]. The determined period (not shown) strongly depends on the bifurcation parameter, the circuit potential; it in- creases from about 0.8 s to 1.7 s. Note that the period-1 orbit was successfully traced in the entire bifurcation diagram covering the stability loss of the period-1 orbit.

29.3
Control of Small Assemblies of Chaotic Oscillators

The chaotic behavior of small assemblies (two to four elements) of chaotic oscil- lators represents a degree of complexity between those of a single, low-dimen- sional chaotic system and those of the fully developed spatiotemporal chaotic system [7, 22]. In these small assemblies the number of elements and the de- gree of their interactions determine the complexity of the collective signal; an example is shown in Table 29.1, where it is seen that the dimension of the mean signal increases from 2.8 to 4.8 as the number of elements is increased from two to four and as the coupling strength decreased.

The overall control of such assemblies has been successfully achieved by a combined control-synchronization procedure [22]. The spatial variations are re- moved by synchronization with local, simultaneous perturbations of the individ- ual resistors (δr_k) connected to the electrodes

$$\delta r_k(t) = C[i_k(t) - I_{\mathrm{tot}}/n],$$

Table 29.1 Control of small sets of oscillators: Procedures to stabilize a uniform periodic state for four system of different (overall) complexities [22].

			Procedures to stabilize the unstable P2 orbit [b]		
n [a]	ε [a]	D_2 [a]	synchronization for targeting	synchronization for control	delayed feedback method
4	0	4.8	+	+	+
2	0	3.5	+	+	+
4	0.4	2.9	+	−	+
2	0.2	2.8	−	−	+

a n = no. of electrodes. ε = global coupling. D_2 = correlation dimension.

b + required, − not required.
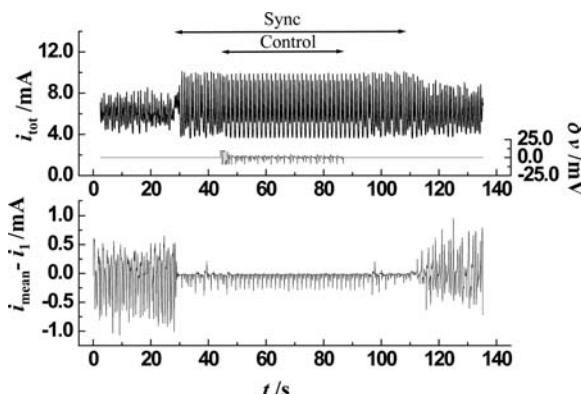
Fig. 29.7 Control of four-oscillator assembly with a combined control-synchronization procedure. Top figure: time series total current (left axis) and perturbations of the circuit potential (right axis) during stabilization of period-2 oscillations. Bottom: the difference between the current of one of the oscillators and the mean current. The local perturbations are applied during a period of length "Sync" while the global delayed feedback is applied during a period of "Control" [22].

where n is the number of electrodes, $i_k(t)$ is the current of the kth electrode, and C is a control constant. When the system is synchronized, the uniform periodic orbits are stabilized by a differential global delayed feedback of the (common) circuit potential of the array using the mean current.

Figure 29.7 shows the stabilization of the uniform period-2 oscillations of the most complex, uncoupled four oscillator system; during the local perturbations the individual oscillators become synchronized after which the "standard" delayed-feedback technique is capable of stabilizing the uniform period-2 oscillations.

Results of control experiments of assemblies with various complexities are summarized in Table 29.1. The simplest system, composed of two coupled

chaotic oscillators ($D_2 = 2.8$) was successfully controlled with the delayed feedback only. For a somewhat more complex coupled system with four coupled electrodes ($D_2 = 2.9$), the local perturbations need to be applied as a targeting procedure only to initiate the control; after successful control it could be switched off (i.e., the control is not globally stable). For the most complex systems with two and four uncoupled electrodes both local and global perturbations were required for successful chaos control.

29.4
Control of Oscillator Populations

We now turn to an array of 64 electrodes. Forcing and feedback were applied to a globally coupled electrode array. Therefore, we compare the effects of global coupling, forcing, and feedback [23, 36].

29.4.1
Global Coupling

As global coupling strength is increased, a population of 64 chaotic oscillators has been seen to undergo the sequence: Very weakly coupled chaos → Intermittent chaotic clusters → Stable chaotic clusters → Intermittent chaotic clusters → Chaotic synchronized state [6, 36]. These transitions are depicted schematically in the middle row of Fig. 29.8; representative cluster configurations are also shown in Fig. 29.8. In the 64 electrode system many stable cluster configurations are possible. We have observed clusters with as few as 18 elements so that the observed range is (18, 46) to (32, 32). A finite range of stable two-cluster configurations has also been observed in theoretical studies with coupled maps [37, 38]. Two of the cluster configurations obtained in the nickel experiments are shown in Fig. 29.8; one of these is a fairly balanced configuration (30, 34) whereas in the other there are 19 and 45 elements in each cluster, respectively. Note in both configurations of Fig. 29.8 that the edge elements have a tendency to be in the same cluster. There is a relatively small (but not zero) coupling that is inherent in the system [24, 39] and that exists even without the added coupling; coupling among the edge regions is somewhat stronger than it is among elements in the interior of the array. Although the stable cluster configurations are unaffected by small perturbations, a sufficiently large disturbance can move an element or elements from one cluster to another. In the intermittent cluster regions on either side of the stable cluster region, clusters form and break up. Sometimes two clusters form and at other times almost complete synchronization occurs; however, neither the cluster formation nor the synchronization is stable and both break up after a short time.
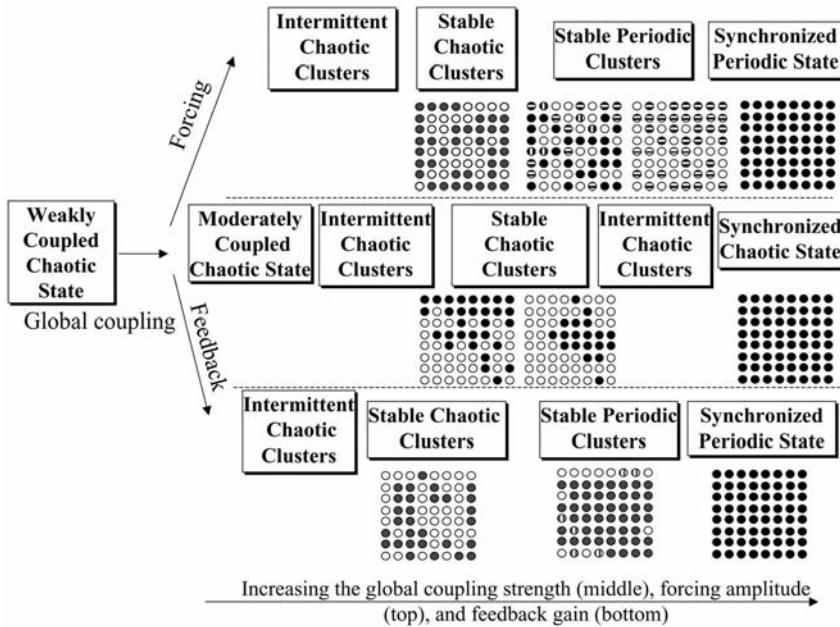
Fig. 29.8 The collective behavior of an array of 64 Ni electrodes with global coupling, forcing, and feedback. Top: with increasing the amplitude of the forcing. Middle: with in- creasing global coupling strength. Bottom: with increasing the gain of the feedback. In the stable clustering region some represen- tative cluster configurations are shown [23].

29.4.2
Periodic Forcing of Arrays of Chaotic Oscillators

The forcing is applied to a base state in which some global coupling is present, that is, to a state with a global coupling strength of $\varepsilon = 0.56$ [23, 36, 40]. We use this base state, rather than the very weakly coupled state because the forcing is not strong enough to synchronize the state at $\varepsilon = 0.0$ under the conditions of these experiments and because we wish to compare the transitions into and through the cluster states of forcing (and the feedback in the next section) with the globally coupled case; we thus start the sets of experiments at a state just below the stable cluster region. The forcing frequency is chosen to be near the dominant frequency of the unforced chaotic signal, $\omega_0 = 1.3$ Hz. With variations in the forcing amplitude over the range 0 to 50 mV the system, as shown in Fig. 29.8, goes through the following sequence: Unsynchronized chaos → Intermittent chaotic clusters → Stable chaotic clusters → Stable periodic clusters → Periodic synchronized state [23, 36, 40]. At 5 mV forcing amplitude the tendency of clustering and synchronization can be already seen but the clustered states are not stable and exist for short times. As the forcing amplitude is increased to 25 mV intermittent clustering can be more clearly seen; clusters form more often and remain intact for longer times before breaking up. The

clusters are still unstable but can hold together for times up to approximately 15 oscillation cycles. The clusters became stable as the forcing amplitude was increased to 30 mV. In the stable chaotic cluster region two clusters are always seen. The arrangement seen in Fig. 29.8 is (26, 38), i.e., the two clusters contain 26 and 38 elements, respectively. As the amplitude is increased further from the stable chaotic cluster region, stable periodic clusters form. Two to four stable clusters are seen, depending on conditions. Representative cluster arrangements are shown in Fig. 29.8. The four-cluster periodic configuration obtained at $A = 35$ mV is (5, 11, 23, 25). The sizes of the groups differ. When four clusters are formed there is a tendency for the clusters to group, that is, for two of the clusters to have similar time series but with a phase lag; the other two clusters then have a different time series. Thus two of the clusters are approximately on the same (periodic) attractor and the other two have a different cycle. When only two clusters exist, the limit cycles of the two clusters differ and thus the two do not just differ by a phase lag. The four-cluster state gives way to a two-cluster state as the forcing amplitude is increased. Although we do not have a sufficiently high resolution in the parameter (amplitude of forcing), it appears that the transition from a state with four clusters to one with two clusters may occur by a mechanism in which the sets of clusters with the same time series (but different phases) merge through a loss of the phase difference. Additional increase to a forcing amplitude of 50 mV results in a period-1, synchronized state.

29.4.3
Feedback on Arrays of Chaotic Oscillators

Direct delay feedback (Eq. (29.1)) was added to the chaotic oscillators using the same base state as that used in the forcing studies described in the section above [23, 36, 41]. The behavior was studied as a function of the feedback gain. The results presented here will all be for a zero time delay in the feedback. The dependence on feedback gain is also shown in Fig. 29.8, i.e., with increasing feedback gain we see: Unsynchronized chaos → Intermittent chaotic clusters → Stable chaotic clusters → Stable periodic clusters → Periodic synchronized state → Stable steady state. Representative cluster arrangements are shown in Fig. 29.8 for three values of the feedback gain. In the chaotic region two clusters are always obtained and the numbers of elements in the two clusters are approximately evenly balanced. The distribution ranged from (32, 32) to (28, 36); one of the (29, 35) configurations is shown in Fig. 29.8. As the feedback gain is increased and the behavior becomes periodic, two trends are noticed in the configurations: an imbalance in cluster sizes occurs and a third cluster arises. As the feedback gain is further increased, one of the clusters begins to dominate as seen in Fig. 29.8 and with further increase this cluster encompasses the entire array and synchronization is obtained.

29.4.4
Feedback, Forcing, and Global Coupling: Order Parameter

One measure of order/disorder in the coupled oscillator systems is an order parameter [36, 42] obtained from pair distances in three-dimensional reconstructed state space. The order parameter, $r(t)$, is defined as a fraction of the number of pairs whose distance in the three-dimensional state space is less than some value, here taken to be 0.06 mA. A mean order parameter is calculated by taking mean pair distances. The mean order parameter has a value approximately zero for uncoupled chaotic oscillators and one in the identically synchronized state. We show this mean order parameter as a function of feedback gain (K), forcing amplitude (A), and global coupling strength (ε) for the three types of coupling, respectively, in Fig. 29.9 [23, 36]. The order parameter for feedback is shown at the top of the figure. As the feedback gain is increased, the order parameter rises somewhat during the transition from the intermittent
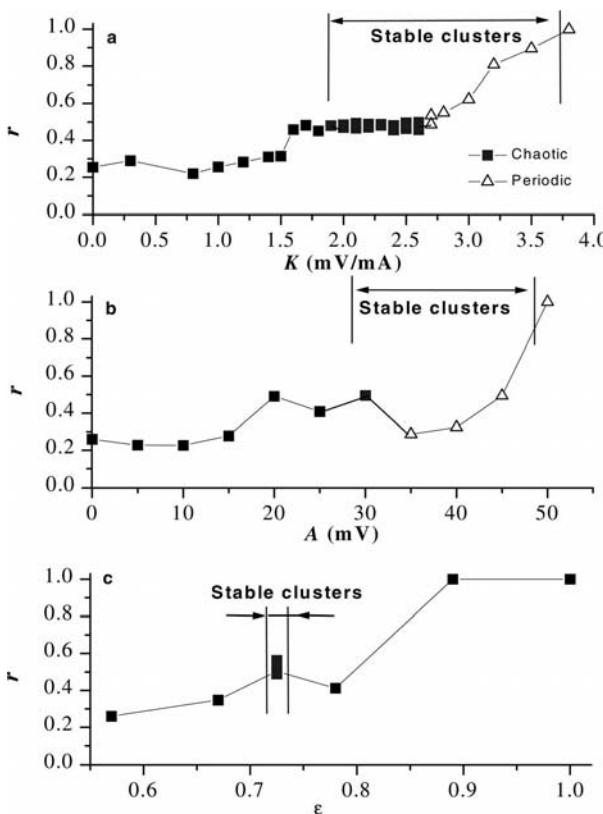
Fig. 29.9 Mean order parameter r based on mean distance as a function of global coupling strength. (a) Feedback. (b) Forcing. (c) Global coupling [36].

cluster to the stable cluster region; it then reaches a plateau (somewhat above 0.5) in the stable chaotic cluster region in which the two clusters are approximately the same size. The order parameter continues to increase in the stable periodic cluster region in which three clusters exist and finally increases to 1.0 with further increase in the gain since one of the clusters grows and dominates the system. In the case of external forcing shown in the center panel, the order parameter again increases with transition from intermittent clusters to stable chaotic clusters as the forcing amplitude is made larger. However, the order parameter drops during the transition from stable chaotic clusters ($A = 30$ mV) to stable periodic clusters (35 mV $\leq A \leq 45$ mV). This decrease in the order parameter occurs with the emergence of three- and four-cluster configurations for which the order is lower than the two cluster chaotic configuration. Additional increases in the forcing amplitude lead to a synchronized state with order parameter of one. The globally coupled case is shown at the bottom. The stable chaotic cluster region is also at a maximum of the order parameter; the stable clusters are bordered on both sides by regions of intermittent clusters that are less ordered.

The order parameter as a function of time (not shown) was also obtained [23, 41]. For low coupling strength the order parameter is near zero at all times. In the stable cluster regions, both chaotic and periodic, the order parameter varies only slightly from the mean value shown in Fig. 29.9. There are occasional peaks to values well above the base line. This is not caused by experimental error but rather by the close approach of the clusters. The variation in the order parameter with time results in chaotic itinerancy [37, 38, 43]: the variation in the number of precision-dependent clusters. In these experiments the order parameter varies with time from approximately one (one precision-dependent cluster) to low values (large number of clusters) [43].

29.4.5
Control of Complexity of a Collective Signal

In populations of chaotic oscillators the collective behavior can differ qualitatively from the local behavior because of the interactions among the oscillators [7, 24, 39, 44]. An example is shown in Fig. 29.10 where global coupling produces regular collective behavior as phase synchronization among the oscillators sets in [24, 39]. Without any added interactions the collective behavior (mean current, h, see Fig. 29.10 (a)) exhibits statistical fluctuations expected from the law of large numbers. However, at weak added coupling near where phase synchronization sets in (Fig. 29.10 (b)) the collective behavior is nearly periodic while the local behavior is nearly chaotic. At strong global coupling (Fig. 29.10 (c)) when identical synchronization occurs the local and global chaotic behaviors are identical. Figure 29.10 (d) shows that with increasing the interaction between the oscillators there is an optimal interaction strength at which the coherence of the collective signal is maximal and, therefore, with optimizing interactions among the oscillators the collective behavior can be made nearly periodic while the local oscillators are chaotic [24, 39].
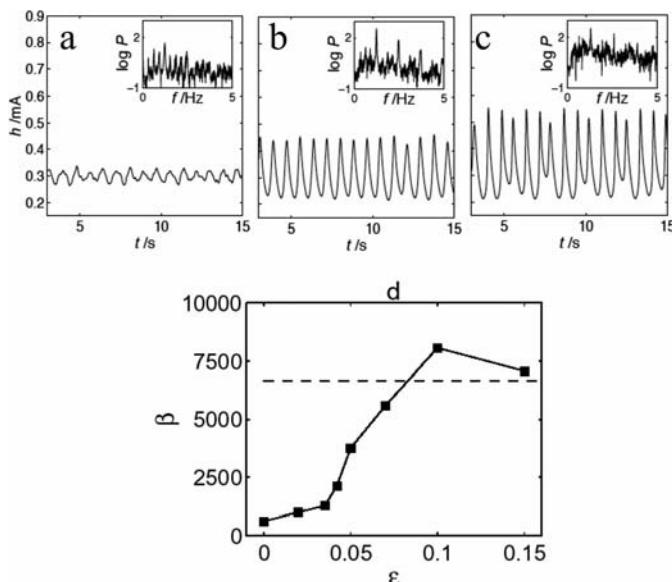
Fig. 29.10 Control of collective motion through global coupling of 64 chaotic oscillators. Top row: time series of mean current and the power spectrum (inset). (a) No added coupling ($\varepsilon = 0$). (b) Weak coupling ($\varepsilon = 0.1$). (c) Strong coupling ($\varepsilon = 1$). Bottom row: coherence factor (FFT peak divided by the width) as a function of coupling strength [24, 39].

29.5
Concluding Remarks

We have reviewed some chaos control studies with an experimental system of metal electrodissolution on single, small sets, and larger populations of electrodes. Phase synchronization, i.e., control of the phases of the oscillations during periodic forcing of a single chaotic oscillator, was first discussed. Chaotic phase synchronization, in general, can take place through three routes [45]; (i) phase synchronization through statistical phase locking with the amplitudes remaining uncorrelated, (ii) through intermittent destruction of the chaotic attractor, or (iii) through the parallel appearance of phase and generalized [46] synchronization. In the forcing experiments type (i) transition occurred when the forcing frequency was close to the inherent frequency of the chaotic behavior, and type (ii) occurred when the forcing frequency was far away from the inherent frequency. We note that the third route to chaotic phase synchronization was also observed in an electrochemical system, non-phase coherent chaotic iron electrodissolution on two electrodes; with increasing the coupling strength, phase and generalized synchronization occur in parallel [10].

A delayed-feedback technique can be used for tracking unstable periodic orbits while a system parameter, the circuit potential, was varied. The method is simpler than the OGY based methods and thus provides a versatile tool for con-

structing experimental bifurcation diagrams where both the stable and unstable phase objects are determined. Such bifurcation diagrams can be applied to gain insight into the dynamics of complex chemical reactions [47].

We also investigated populations of oscillators using electrode arrays to which global coupling, periodic forcing, and feedback were applied. The three types of experiments all produce intermittent and stable chaotic cluster states and synchronization with sufficiently large values of global coupling, feedback gain, and forcing amplitude, respectively. The three cases differ, however, in other details. With global coupling the stable chaotic cluster region is bounded on both sides by less ordered regions of intermittent clusters. With feedback, increases in gain past the stable chaotic cluster region yield periodic clusters, first two, and then three. As the gain becomes larger one of the three clusters grows and the array is synchronized. With the imposition of periodic forcing as many as four periodic stable clusters emerge. The imposed coupling differs in the three types of experiments. Global coupling produces direct interactions among the elements. The external forcing has a different role. There is some very weak inherent local and long-range coupling (through the electrolyte) and also moderate global coupling (controlled by system electronics) in the system to which the forcing is applied. This intrinsic coupling was too weak to produce clustering or synchronization but it did furnish interactions among the elements and contributed to the collective dynamics of the system. The application of the periodic forcing changes the dynamics of the individual elements and clustering and synchronization become possible with the same strength of intrinsic coupling. The feedback influences the dynamics of the individual oscillators and adds an additional global coupling. Although many theoretical studies of collective dynamics have been carried out with examples in biology, physics, and chemistry, far fewer experimental studies are known. The electrochemical arrays are ideal for such experiments since the dynamics can be measured at each site and the coupling can be carefully controlled.

Acknowledgment

References

1 J. L. Hudson and T. T. Tsotsis, Chem. Eng. Sci. **49**, 1493 (1994).

2 F. N. Albahadily and M. Schell, J. Chem. Phys. **88**, 4312 (1988).

3 I. Z. Kiss, V. Gáspár, L. Nyikos, and P. Parmananda, J. Phys. Chem. A **101**, 8668 (1997).

4 H. D. Dewald, P. Parmananda, and R. W. Rollins, J. Electrochem. Soc. **140**, 1969 (1993).

5 O. Lev, A. Wolffberg, M. Sheintuch, and L. M. Pismen, Chem. Eng. Sci. **43**, 1339 (1988).

6 W. Wang, I. Z. Kiss, and J. L. Hudson, Chaos **10**, 248 (2000).

7 I. Z. Kiss, W. Wang, and J. L. Hudson, Phys. Chem. Chem. Phys. **2**, 3847 (2000).

8 M. T. M. Koper and J. H. Sluyters, J. Electroanal. Chem. **303**, 65 (1991).

9 I. Z. Kiss, Q. Lv, L. Organ, and J. L. Hudson, Phys. Chem. Chem. Phys. **8**, 2707 (2006).

10 I. Z. Kiss, Q. Lv, and J. L. Hudson, Phys. Rev. E **71**, 035201 (2005).

11 C. B. Diem and J. L. Hudson, AIChE J. **33**, 218 (1987).

12 E. F. Stone, Phys. Lett. A **163**, 367 (1992).

13 M. G. Rosenblum, A. S. Pikovsky, and J. Kurths, Phys. Rev. Lett. **76**, 1804 (1996).

14 R. Lima and M. Pettini, Phys. Rev. A **41**, 726 (1990).

15 A. Y. Loskutov, J. Phys. A-Math. Gen. **26**, 4581 (1993).

16 E. Ott, C. Grebogi, and J. A. Yorke, Phys. Rev. Lett. **64**, 1196 (1990).

17 K. Pyragas, Phys. Lett. A **170**, 421 (1992).

18 P. Parmananda et al., J. Phys. Chem. B **104**, 11748 (2000).

19 P. Parmananda, P. Sherard, R. W. Rollins, and H. D. Dewald, Phys. Rev. E **47**, R3003 (1993).

20 P. Parmananda et al., Phys. Rev. E **59**, 5266 (1999).

21 I. Z. Kiss and V. Gáspár, J. Phys. Chem. A **104**, 8033 (2000).

22 I. Z. Kiss, V. Gáspár, and J. L. Hudson, J. Phys. Chem. B **104**, 7554 (2000).

23 I. Z. Kiss, W. Wang, and J. L. Hudson, Chaos **12**, 252 (2002).

24 I. Z. Kiss, Y. Zhai, and J. L. Hudson, Ind. Eng. Chem. Res. **41**, 6363 (2002).

25 O. Lev, A. Wolffberg, M. Sheintuch, and L. M. Pismen, Chem. Eng. Sci. **43**, 1339 (1988).

26 I. Z. Kiss and J. L. Hudson, Phys. Rev. E **64**, 046215 (2001).

27 D. Gábor, J. IEE London **93**, 429 (1946).

28 A. S. Pikovsky, M. G. Rosenblum, G. V. Osipov, and J. Kurths, Physica D **104**, 219 (1997).

29 A. G. Balanov, N. B. Janson, and E. Scholl, Phys. Rev. E **71**, 016222 (2005).

30 W. Just, H. Benner, and C. von Loewenich, Physica D **199**, 33 (2004).

31 O. Morgul, Phys. Lett. A **314**, 278 (2003).

32 W. Just et al., Phys. Rev. Lett. **78**, 203 (1997).

33 X. Yu, in Proceedings of the IEEE Int. Conf. on Decision and Control (IEEE, San Diego, CA, USA, 1997), pp. 401–405.

34 K. Pyragas and T. Tamasevicius, Phys. Lett. A **180**, 99 (1993).

35 I. Z. Kiss, Z. Kazsu, and V. Gáspár, Chaos **16**, 033109 (2006).

36 W. Wang, I. Z. Kiss, and J. L. Hudson, Phys. Rev. Lett. **86**, 4954 (2001).

37 K. Kaneko, Physica D **54**, 5 (1991).

38 K. Kaneko, Physica D **41**, 137 (1990).

39 I. Z. Kiss, Y. Zhai, and J. L. Hudson, Phys. Rev. Lett. **88**, 238301 (2002).

40 W. Wang, B. Green, and J. L. Hudson, J. Phys. Chem. B **105**, 7336 (2001).

41 W. Wang, I. Z. Kiss, and J. L. Hudson, Ind. Eng. Chem. Res. **41**, 330 (2002).

42 D. H. Zanette and A. S. Mikhailov, Phys. Rev. E **57**, 276 (1998).

43 I. Z. Kiss and J. L. Hudson, Chaos **13**, 999 (2003).

44 I. Z. Kiss, Y. M. Zhai, and J. L. Hudson, Science **296**, 1676 (2002).

45 G. V. Osipov et al., Phys. Rev. Lett. **91**, 024101 (2003).

46 N. F. Rulkov, M. M. Sushchik, L. S. Tsimring, and H. D. I. Abarbanel, Phys. Rev. E **51**, 980 (1995).

47 I. Schreiber and J. Ross, J. Phys. Chem. A **107**, 9846 (2003).

Part VIII
Applications to Biology

30
Control of Synchronization in Oscillatory Neural Networks

Peter A. Tass, Christian Hauptmann, and Oleksandr V. Popovych

30.1
Introduction

Synchronization is a generic phenomenon of interacting oscillators, which has been observed and studied in many fields in physics, engineering, chemistry, biology, and medicine (see e.g. [27, 39, 54, 73, 76, 99]). Synchronization processes are of crucial importance for brain function. Well-coordinated synchrony within and between neuronal populations appears to be an important mechanism for neuronal signaling and information processing [69, 73]. In contrast, pathologically strong synchronization processes may severely impair brain function as, e.g., by Parkinson's disease (PD), essential tremor, or epilepsy [15, 16, 34, 63, 92]. Parkinsonian resting tremor, for instance, appears to be caused by a population of neurons located in the thalamus and the basal ganglia. These neurons fire in a synchronized and intrinsically periodical manner at a frequency similar to that of the tremor, regardless of any feedback signals [41, 43, 52]. In contrast, under physiological conditions, these neurons fire incoherently [51]. In patients with PD this neuronal cluster acts like a pacemaker and activates premotor areas and the motor cortex [2, 96], where the latter synchronize their oscillatory activity [89] and drive muscles causing the peripheral shaking.

In patients with medically refractory movements disorders, e.g., with advanced PD or essential tremor, depth electrodes are chronically implanted in target areas like the thalamic ventralis intermedius nucleus or the subthalamic nucleus [4, 6]. Electrical deep brain stimulation (DBS) is performed by administering a permanent high-frequency (HF) ($>$ 100 Hz) periodic pulse train via the depth electrodes [4, 6]. HF DBS has been developed empirically and its mechanism is not yet fully understood [48]. It appears to strongly alter the neuronal firing and basically mimics the effect of tissue lesioning, e.g., by suppressing neuronal firing, which, in turn, suppresses the peripheral tremor [48, 95]. HF DBS is reversible and has a much lower rate of side effects than lesioning with thermocoagulation [68]. However, HF DBS may lead to side effects like dysarthria, dysesthesia, and cerebellar ataxia [95]. On the other hand, 11–15% of PD

patients have unsatisfactory outcomes concerning tremor suppression in spite of proper electrode placement [19, 42].

To improve deep brain stimulation novel stimulation techniques have been developed with methods from statistical physics and nonlinear dynamics (see [76] and references below). The goal of these techniques is to selectively counteract the pathological synchronization processes. We here present three methods which are particularly effective and robust against parameter variations and, hence, promising for therapeutic applications:

(i) *Multisite coordinated reset stimulation* (Section 30.2) [84, 85]: Brief and mild resetting stimuli are administered at different sites at subsequent times and cause an effective transient desynchronization. Desynchronized firing is maintained by repetitive administration of multisite coordinated reset stimuli.

(ii) *Linear multisite delayed feedback stimulation* (Section 30.3) [29–31]: The activity of a neuronal population is permanently registered, amplified, and fed back at different sites with different delays. By its tendency to split the whole population into entrained and phase shifted sub-populations, the multisite echo counterbalances the population's tendency to synchronize in phase, so that a robust desynchronization is achieved.

(iii) *Nonlinear delayed feedback stimulation* (Section 30.4) [57–59]: The activity of a neuronal population is permanently registered and fed back after nonlinear processing. The perturbation caused by this distorted echo causes a powerful desynchronization at minimal and practically vanishing stimulation currents. This method specifically counteracts the pathological interactions, so that the neurons' natural frequencies get restored.

A novel, theoretically fascinating and clinically highly relevant aspect emerges, if we take into account synaptic plasticity, i.e., the fact that the nervous system adapts the strength of the neurons' synaptic interaction (coupling) to the timing of the neurons' firing. As shown theoretically [32, 88, 90, 91], networks with synaptic plasticity may unlearn their tendency to produce synchronized activity. Desynchronizing stimulation may reshape the connectivity (coupling) pattern and induce long-lasting effects. This approach may lead to powerful and even curative stimulation techniques (see Section 30.5).

30.2
Multisite Coordinated Reset Stimulation

Based on Winfree's pioneering phase resetting studies of circadian rhythms [98], the effects of a pulsatile stimulus on the amplitude and, in particular, the phase dynamics of a single oscillator were analyzed in detail [23, 98, 99]. With topological methods Winfree showed that an oscillation can be annihilated by a stimulus of a critical intensity and duration administered at a critical initial phase [98, 99]. The phase resetting approach has been used to investigate the reactions of a single neuron to a pulsatile electrical stimulus; both theoretically [5] and experimentally [26].

Neuronal synchronization processes are of crucial importance under physiological [69] as well as pathological [15, 16, 34, 63, 92] conditions. Furthermore, noise is inevitable in biological systems [22]. To understand brain functioning and to design effective therapeutic stimulation techniques, which work in the presence of noise, it is necessary to understand stimulation induced synchronization and desynchronization of neuronal populations. For this reason stochastic phase resetting has been studied in both ensembles of uncoupled oscillators [74, 75] and ensembles of coupled oscillators [76] subject to noise. This leads to effectively desynchronizing stimulation techniques, such as double pulse stimulation [77, 78, 82], stimulation with a brief high-frequency pulse train followed by a single pulse [79], and stimulation with a brief low-frequency pulse train followed by a single pulse [80, 81]. These methods share one particular feature: each stimulus consists of two qualitatively different stimuli. The first stimulus is stronger and resets (restarts) the ensemble, whereas the second, weaker stimulus is a single pulse which is administered after a constant time delay and desynchronizes by hitting the cluster in a vulnerable state. All of these methods require a precise calibration of the stimulus parameters.

In contrast, multisite coordinated reset stimulation does not require any time-consuming calibration [84, 85]. This method causes an effective desynchronization and is particularly robust against parameter variations, e.g., variations of the neurons' mean frequency. Multisite coordinated reset stimulation means that a synchronized population of neurons is stimulated with a sequence of brief resetting stimuli (typically brief high-frequency stimulus trains) via different sites. The delay between the subsequent resetting stimuli equals τ/n, where $\tau \approx T$, T is the mean period of the synchronized oscillation, and n is the number of stimulation sites [84, 85]. The subsequent reset of different sub-populations induces a so-called cluster state, i.e., the whole population splits into n sub-populations which differ with respect to their mean phase. From the cluster state the neurons typically relax to a uniformly desynchronized state before they revert back to the in-phase synchronized state, if left unperturbed. Hence, to maintain a desynchronized firing, multisite coordinated reset stimuli have to be administered repetitively. Multisite coordinated reset stimulation exploits transient responses which are due to the oscillators' (pathologically strong) interactions.

We model the neuronal population with a network of N phase oscillators [17, 25, 28, 39] and, in addition, take into account stimulation and random forces [76]:

$$\dot{\psi}_j = \Omega - \frac{K}{N}\sum_{k=1}^{N}\sin(\psi_j - \psi_k) + X_j(t)\,S_j(\psi_j) + F_j(t)\,, \tag{30.1}$$

where ψ_j is the phase of the jth phase oscillator. All oscillators have the same eigenfrequency Ω and are globally coupled with strength $K > 0$. In neurons the impact of an electrical stimulus depends on the neuron's phase [5, 26]. Hence,

the stimulus is modeled by a 2π-periodic function like $S_j(\psi_j) = I \cos \psi_j$ with the intensity parameter I. Stimulus administration is modeled by

$$X_j(t) = \begin{cases} 1: & \text{neuron } j \text{ is stimulated at time } t \\ 0: & \text{else} \end{cases}. \tag{30.2}$$

The random forces $F_j(t)$ are Gaussian white noise with $\langle F_j(t) \rangle = 0$ and $\langle F_j(t) F_k(t') \rangle = D\delta_{jk}\delta(t - t')$, where D is a constant noise amplitude. For vanishing stimulation ($X = 0$), Eq. (30.1) is the well-known Kuramoto model of coupled phase oscillators [39].

A phase-dependent stimulus, like $S_j(\psi_j) = I \cos(\psi_j)$ resets the jth oscillator to a particular phase provided the intensity parameter I is large compared to the coupling strength and to the noise amplitude and provided the stimulation duration is long enough [76, 83]. Such a reset can be achieved with a strong single pulse [76, 78, 82, 86], a HF pulse train (with a pulse rate 20 times larger than the mean eigenfrequency Ω) [79] or a low-frequency pulse train (with a pulse rate similar to Ω) [80, 81]. We here use a HF pulse train for the reset.

Let us, first, assume that there is no noise ($D = 0$). A HF pulse train with $S_j(\psi_j) = I_j \cos(\psi_j + \theta)$ resets the jth neuron close to the phase $\psi_j^{\text{res}} + \theta$ [76, 83]. Hence, we could easily desynchronize the population by stimulating each neuron separately to achieve equidistant resets. For this, we would administer HF pulse trains of identical timing (i.e., $X_j(t) = X(t)$ for $j = 1,\ldots, N$) but different stimulation mechanisms $S_j(\psi_j) = I_j \cos[\psi_j + 2\pi(j-1)/N]$. After such a phase-scattering stimulation the population would be perfectly desynchronized, with a uniform distribution of the phases $\psi_j^{\text{res}} + 2\pi(j-1)/N$. However, stimulating each neuron separately would require the use of many electrodes and would easily damage or even destroy the neural tissue. Furthermore, noise makes the reset less perfect. Therefore, we choose a different approach. Instead of inducing a perfectly uniform distribution of the phases, we simply split the population into a few, say four, sub-populations which are equally spaced in a cycle $[0, 2\pi]$.

We denote as *sub-population* 1, 2, 3, and 4 the groups of neurons $j = 1,\ldots, N/4$, $j = N/4 + 1, \ldots, N/2, j = N/2 + 1, \ldots, 3N/4$, and $j = 3N/4 + 1, \ldots, N$, respectively (with N divisible by 4). To split the population in four equally spaced sub-populations we may choose qualitatively different strategies: (i) *Simultaneous stimulation* of all four sub-populations: Phase shifts of the reset neurons are induced by phase shifts of the stimulation mechanisms. We stimulate neuron j of sub-population $k = 1, \ldots, 4$ with a HF pulse train with $S_j(\psi_j) = I \cos[\psi_j + 2\pi(k-1)/4]$. (ii) The four sub-populations are *stimulated at different times with identical stimulation mechanisms S_j*. The delay between subsequent HF pulse trains is equal to $T/4$, where $T = 2\pi/\Omega$ is the period of the population without stimulation. We may stimulate neuron j of sub-population $k = 1, \ldots, 4$ at time $t' + T(k - 1)/4$ with a HF pulse train with $S_j(\psi_j) = I \cos(\psi_j)$. (iii) Strategies (i) and (ii) can be combined, e.g., by performing *two subsequent antiphase resets of pairs of sub-populations with a time delay of $T/4$* (Fig. 30.1 (a)). Sub-population 1 and 2 are stimulated simultaneously at time t', but with different polarity. A neuron of sub-population 1 is stimulated with
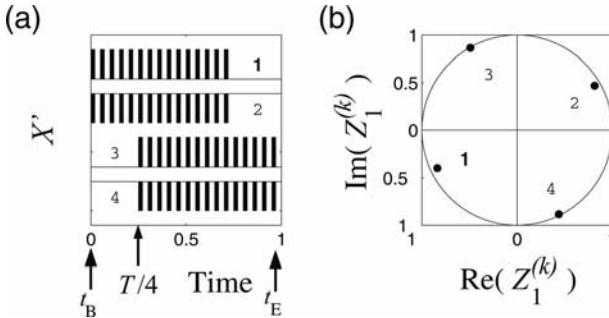
Fig. 30.1 (a) Two subsequent antiphase resets of pairs of sub-populations are achieved by administering two pairs of high-frequency (HF) pulse trains with different polarity with a time delay of $T/4$, where $T = 2\pi/\Omega$ is the period of the population. Time course and polarity of HF pulse trains is schematically indicated with $X'(t) = X(t)S_j(0)$, where the numbers indicate the sub-population to which the corresponding HF pulse train is administered. Single pulses are highlighted by shaded regions. Each HF pulse train consists of 15 single pulses with duration of 0.02, intersected by pauses of length 0.03. HF pulse trains 1 and 3 have positive polarity: $S_j(\psi_j) = I\cos(\psi_j)$, whereas HF pulse trains 2 and 4 have negative polarity: $S_j(\psi_j) = -I\cos(\psi_j)$, with $I = 30$. Stimulation starts at time $t_B = 0$ and ends at $t_E = 0.97$. (b) Stimulating model (30.1) according to (a) results in a configuration at the end of the stimulation given by $Z_1^{(k)}(t_E)$ where numbers indicate the corresponding sub-population $k = 1, \ldots, 4$. The unit circle marks the maximal range of $|Z_1^{(k)}|$. Model parameters: $N = 100, K = 2, \Omega = 2\pi$, noise amplitude $D = 0.4$.

$S_j(\psi_j) = I\cos(\psi_j)$, whereas a neuron of sub-population 2 is stimulated with $S_j(\psi_j) = I\cos(\psi_j + \pi) = -I\cos(\psi_j)$. Analogously, sub-populations 3 and 4 are simultaneously stimulated at time $t' + T/4$. A neuron of sub-population 3 is stimulated with $S_j(\psi_j) = I\cos(\psi_j)$, whereas a neuron of sub-population 4 is stimulated with $S_j(\psi_j) = -I\cos(\psi_j)$.

Variant (i) requires that we are able to modify the stimulation mechanism $S(\psi_j)$ itself. This might be difficult in an experimental application. In contrast, variants (ii) and (iii) operate with identical pulses of the same or different polarity, administered at different times. Numerically variants (i)–(iii) work comparably well. We here consider version (iii). To estimate the extent and type of synchronization of the whole population we use the cluster variables

$$Z_m(t) = R_m(t)e^{i\varphi_m(t)} = \frac{1}{N}\sum_{j=1}^{N} e^{im\psi_j(t)}, \qquad (30.3)$$

where $R_m(t)$ and $\varphi_m(t)$ are the corresponding real amplitude and real phase, where $0 \le R_m(t) \le 1$ for all times t [7, 76]. Cluster variables are convenient for characterizing synchronized states of different types: Perfect in-phase synchronization corresponds to $R_1 = 1$, whereas an incoherent state, with uniformly distributed phases, is associated with $R_m = 0$ ($m = 1, 2, 3, \ldots$). $R_1 = 0$ combined with large R_m is indicative of an m-cluster state consisting of m distinct and equally

spaced clusters, where within each cluster all oscillators have similar phase. Analogously, we use

$$Z_m^{(k)}(t) = R_m^{(k)}(t)e^{i\varphi_m^{(k)}(t)} = \frac{4}{N}\sum_{j\in\wedge_k} e^{im\psi_j(t)}\,, \tag{30.4}$$

as cluster variables for the four sub-populations separately. $k = 1, \ldots, 4$ is the index of the sub-population introduced above, m is the index referring to an m-cluster state (see Eq. (30.3)), and Λ_k is the set of indices belonging to the kth sub-population, e.g., $\Lambda_1 = \{1,\ldots,N/4\}$. With $Z_1^{(k)}$ we estimate the extent of in-phase synchronization within sub-population k. The latter is perfectly in-phase synchronized if $R_1^{(k)} = 1$.

The effect of a multisite coordinated reset is illustrated with a snapshot of $Z_1^{(k)}(t_E)$, the centers of mass of all four sub-populations at the end of the stimulation (Fig. 30.1 (b)). All four sub-populations are strongly synchronized, where their mean phases $\varphi_1^{(k)}$ are equally spaced in the cycle. $R_1^{(1)}$ and $R_1^{(2)}$ are a bit smaller than $R_1^{(3)}$ and $R_1^{(4)}$. This follows from the fact that at the end of the HF pulse trains 1 and 2 (i.e., at time $t_E - T/4$) $Z_1^{(1)}$ and $Z_1^{(2)}$ are located exactly where $Z_1^{(3)}$ and $Z_1^{(4)}$ are located at the end of the HF pulse trains 3 and 4 (i.e., at the end of the stimulation, at time t_E). Between $t_E - T/4$ and t_E sub-populations 1 and 2 spontaneously run in the counterclockwise direction through a quarter of a cycle and relax to a less synchronized state with smaller $R_1^{(1)}$ and $R_1^{(2)}$. The arrangement of $Z_1^{(1)}, \ldots, Z_1^{(4)}$ at the end of the stimulation is a symmetrical 4-cluster state of the whole population, with R_4 from (30.3) close to 1 and R_1 close to 0. The coordinated reset splits the whole populations in four distinct, symmetrically arranged sub-populations.

To understand how a stimulus-induced clustering leads to an effective desynchronization, we study the dynamics of the leading modes $Z_1, \ldots, Z_4$. We first recall the dynamical behavior of model (30.1) without stimulation (with $X(t) = 0$ in (30.2)). For large N it has been shown that noisy in-phase synchronization emerges out of the incoherent state due to a decrease of the noise amplitude D or, analogously, because of an increase of the coupling strength [39, 76]. For $K > D$ a stable limit cycle $Z_1(t) = Y\exp(i\Omega t)$ emerges, where Y is a complex constant [76]. When K exceeds its critical value $K^{\text{crit}} = D$, Z_1 from (30.3) becomes an *order parameter*, which according to the slaving principle [27] governs the dynamics of the other, stable modes Z_m ($m = 2, 3, \ldots$) on the center manifold [56]: The order parameter Z_1 acts on a slow time scale, whereas the stable modes Z_m act on a fast time scale and relax to values given by the order parameter Z_1 [27, 102]. In model (30.1) with large N this relationship reads [76]:

$$R_m \propto R_1^\nu \text{ with } \nu \geq 2,\ m = 2, 3, 4, \ldots \tag{30.5}$$

The collective dynamics will not only be visualized with the cluster variables Z_m, but also by considering the collective firing. A single firing/bursting model neuron fires/bursts whenever its phase is close to zero (modulo 2) [17, 25, 28,

39, 76]. We illustrate the collective firing with the *relative number of neurons producing an action potential or burst* at time t given by

$$n_{\text{fire}}(t) = \frac{\text{number of neurons with } \cos \varphi_j > 0.99}{N} \ . \tag{30.6}$$

$0 \le n_{\text{fire}}(t) \le 1$ for all t. $n_{\text{fire}}(t) = 0$ means that no neuron fires/bursts, while all neurons fire/burst at time t if $n_{\text{fire}}(t) = 1$. Varying the threshold parameter 0.99 in a reasonable range does not change the results.

Figure 30.2 shows the dynamics before, during and after stimulation. The phase at which the coordinated reset from Fig. 30.1 is applied to the same neuronal population is varied within one cycle. The impact of this stimulus is independent of the phase at which it is administered. At the end of the stimulation the system has reached the 4 cluster-state shown in Fig. 30.1 (a): R_4 has a value similar to the prestimulus range, whereas R_1, R_2 and R_3 are close to zero. In the poststimulus period the system does not remain in the 4 cluster-state.
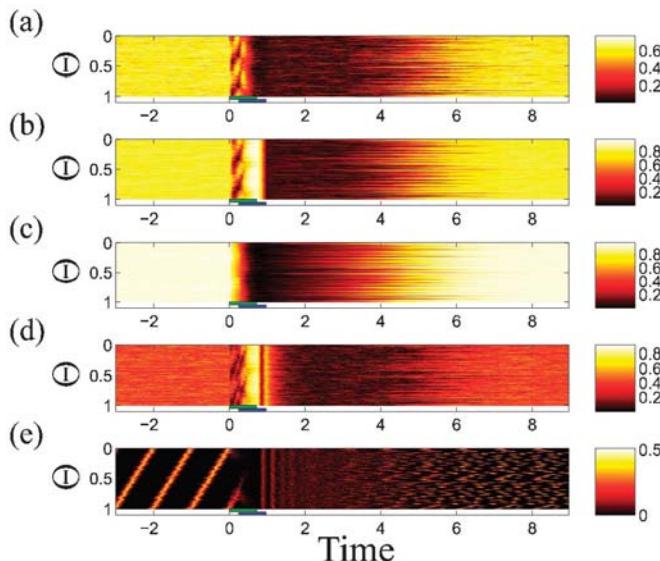
Fig. 30.2 The stimulus from Fig. 30.1 (a) is administered to the in-phase synchronized neuronal population from Eq. (30.1) at different initial phases. At the beginning of each simulation the phases are given by $\psi_j = \Psi + \Delta\psi_j$, where $\Delta\psi_j$ is normally distributed with variance $\sqrt{0.3}$. The time course of R_1 (a), R_2 (b), R_3 (c), R_4 (d) from Eq. (30.3), and the relative number of firing neurons n_{fire} from Eq. (30.6) (e) is shown in 101 simulations, where the normalized mean initial phase $\Theta = \Psi/2\pi$ is varied in equidistant steps within one cycle [0, 1]. The first 30 periods were discarded to guarantee that the stimuli hit the population in a stable synchronized state. Same stimulation parameters and model parameters as in Fig. 30.1. Stimulation starts at $t_B = 0$ and ends at $t_E = 0.97$. Pairs of HF pulse trains 1, 2 and 3, 4 are indicated by green and blue horizontal bars, respectively.

Rather due to the slaving principle R_4 rapidly decays to zero, so that the system approaches a perfectly desynchronized state characterized by $R_m = 0$ ($m = 1, 2, 3, 4, \ldots$). The vanishing R_1 suppresses R_4 according to (30.5). Without coupling (but with noise) the 4 cluster-state would decay more slowly (see [74]). From the mathematician's viewpoint the relaxation of R_4 is due to the system being attracted by the center manifold as characterized by (30.5). By imposing a 4 cluster-state, the stimulation does only half of the desynchronizing work. The rest, namely approaching a uniformly desynchronized state, is done by the system itself. In this way the coupling, which causes the synchronization, is used for improving the desynchronizing effect.

In the course of the poststimulus transient R_1 and according to (30.5) also R_2, R_3, and R_4 recover again. The system finally reaches its stable in-phase synchronized state again.

In summary, by shifting the system into an unstable 4-cluster state, the system reacts by automatically running through a desynchronized state. Finally, the system reverts back to the synchronized state, if left unperturbed. The results are stable with respect to variations of N between 20 and 1000 and more.

The effectively desynchronizing multisite coordinated reset can be used to block the resynchronization. For this, we may use three different control strategies:

(i) *Periodic administration of coordinated reset stimuli:* The most simple, open loop type of stimulation is a periodic administration of coordinated reset stimuli.

(ii) *Demand-controlled timing of the administration of identical stimuli:* Whenever the population tends to resynchronize, the same stimulus is administered (Fig. 30.3). The larger the coupling strength K, the more often a stimulus has to be administered to maintain an uncorrelated firing. In an experimental application one has to observe the synchronized oscillation during a sufficiently long period of time in order to perform a frequency analysis which yields the period T of the population in the absence of stimulation and, thus, the critical stimulation parameter $T/4$ (the time delay between the two pairs of HF pulse trains, see Fig. 30.1 (a)).

(iii) *Entrainment with periodically administered HF pulse trains of demand-controlled length:* The stimuli are periodically administered with offset times $t_n = n\nu\tau$, where $n = 0, 1, 2, 3, \ldots$ is the index labeling different stimuli, $\tau = T + \varepsilon$ is a time interval in the range of the period T of the population without stimulation, and ν is a small integer such as 2 or 3. This means we perform a $1 : \nu$ entrainment of the four sub-populations, where the spontaneous frequency of the neurons is approx. ν times larger compared to the frequency of stimulus administration. The smaller $|\varepsilon|$, the smaller is the stimulation strength necessary to achieve an entrainment.

The closed-loop variants (ii) and (iii) require that the ensembles activity can be measured appropriately. Unlike in Fig. 30.1 (a), we use HF pulse trains of demand-controlled length: The length of the HF pulse trains increases linearly between a minimal value $M_{\min}$ and a maximal value $M_{\max}$ of single pulses (except
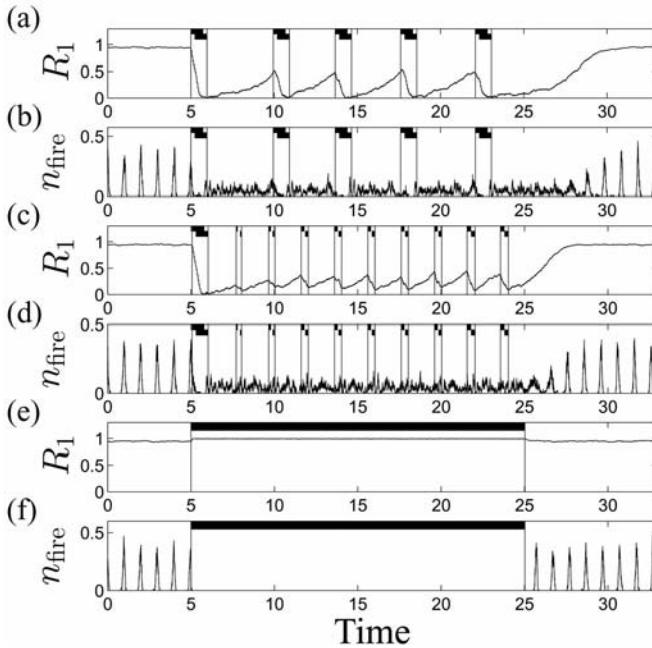
Fig. 30.3 Time course of R_1 from Eq. (30.3 (a), (c), and (e)) and of n_{fire} from Eq. (30.6) (b), (d), (f) during different types of stimulation. *Demand-controlled timing of stimulus administration* (a) and (b): As soon as the amplitude R_1 of the recovering order parameter reaches the value of 0.5, the stimulus from Fig. 30.1 (a) is administered again. *Periodical stimulation with demand-controlled length of HF pulse train* (c) and (d): The stimulus from Fig. 30.1 (a) is administered periodically, where the length of the HF pulse trains is adapted to R_1 according to Eq. (30.7) with $M_{max} = 15$ and $M_{min} = 0$. *Standard permanent HF pulse train stimulation* (e) and (f): Each neuron is stimulated with the same HF pulse train: $X_j(t) = X(t)$ in Eqs. (30.1) and (30.2). (a)–(f): Numerical integration, model parameters, and initial conditions as in Fig. 30.2. Begin and end of stimuli are indicated by *vertical lines*. (a)–(d): Upper and lower *shaded regions* correspond to pairs of HF pulse trains 1, 2 and 3, 4, respectively. (e) and (f): HF pulse train is indicated by one.

for rounding), where the latter is initially used for desynchronizing the fully synchronized population. R_1 is measured at times $t'_n = t_n - t_{max}$, where t_{max} is the maximal duration of a HF pulse train (containing M_{max} single pulses). $R_1(t'_n)$ determines the number of pulses of the HF pulse trains 1–4 of the nth stimulus according to

$$M_n = \min\left\{ \left[\frac{R_1(t'_n)(M_{max} - M_{min})}{R_1(t_0)}\right]_{\mathbb{Z}} + M_{min}, M_{max}\right\}, \qquad (30.7)$$

where $n = 0, 1, 2, 3, \ldots$, $[x]_{\mathbb{Z}}$ stands for rounding x to the nearest integer, and min $\{x_1, x_2\}$ stands for the minimum of $\{x_1, x_2\}$. The nth stimulus ends precisely at time $t_n = n\nu\tau$, whereas it starts somewhere between t'_n (for $M_n = M_{max}$)

and t_n (for $M_n = M_{\min} = 0$), depending on its duration. With this adaptive entrainment we stabilize the periodic motion of $Z_1^{(1)}$, ..., $Z_1^{(4)}$, the centers of mass of the four sub-populations. In this way only minor corrections are necessary to keep the centers of mass $Z_1^{(1)}$, ..., $Z_1^{(4)}$ sufficiently close to their corresponding attractors (Fig. 30.1(b)) at times $t_n = nv\tau$. If the suppression of R_1 is not sufficient we may (i) choose a larger intensity parameter I in $S_j(\psi_j) = I \cos \psi_j$, (ii) increase $M_{\min}$, (iii) administer the stimuli at a higher rate, i.e., decrease v, so that the inter-stimulus interval $t_{n+1} - t_n = v\tau$ gets smaller, and/or (iv) increase the duration of each single pulse of the pulse trains. The feedback value of R_1 can also be evaluated before time t'_n, especially in case of a slow order parameter dynamics (i.e., when the coupling is weak with respect to the noise). We could also use the mean of R_1 in a period of evaluation.

Applying the standard, permanent HF pulse train stimulation [4, 6] to our model (30.1) (in a first approximation) corresponds to stimulating each neuron with the same HF pulse train [$X_j(t) = X(t)$ in (30.1), (30.2)]. During a permanent HF stimulation a high-frequency entrainment of the order parameter Z_1 captures Z_1 in a small portion of the Gaussian plane [79], so that the individual neurons' firing is stopped, but no desynchronization occurs (Fig. 30.3(e) and (f)). In contrast, during stimulation R_1 is larger compared to its prestimulus level, and after stimulation the synchronous firing continues immediately. To suppress the firing with such a simple pulse train persistently, it has to be administered permanently. The number of single pulses used to suppress the firing in Fig. 30.3(e) and (f) is 5.35 and 8.02 times larger than that used for blocking the resynchronization in Fig. 30.3(a) and (b) and (c), (d), respectively. This illustrates the effectiveness of the demand-controlled multisite coordinated reset stimulation. The latter can effectively desynchronize stimulated oscillators with a signicantly smaller amount of stimulation current compared to the standard permanent HF pulse-train stimulation.

30.3
Linear Multisite Delayed Feedback

In this section we present another technique for effective and robust desynchronization of neuronal populations. As in the previous section, the presented desynchronization technique is also based on the stimulation of a strongly synchronized population of interacting oscillators. The stimulation is administered via several sites, e.g., four sites, where through each stimulation site an individual stimulation signal is applied. The individual stimulation signals are derived from the delayed mean field of the ensemble. Therefore, the macroscopic activity (mean field) of the controlled population is measured, delayed, amplified and fed back in a spatially coordinated way via the stimulation sites using different delays for each stimulation site, respectively [29–31]. More precisely, let the stimulation electrodes be E_n, $n = 1, 2, 3, 4$, where the individual stimulation signals S_n are administered via the electrodes E_n, respectively. We denote the mea-

sured mean field of the ensemble by $Z(t)$. Then the stimulation signals are de-
ned as $S_n(t) = KZ(t - \tau_n)$, where K is a stimulus amplification and τ_n, $n = 1, 2, 3,$
4 are (different) time delays. In the following the parameters K and τ are con-
sidered as the main stimulation parameters.

To investigate the effect of *linear multisite delayed feedback stimulation* we con-
sider an ensemble of coupled limit cycle oscillators stimulated with the individ-
ual stimulation terms $S_j(t)$:

$$\dot{z}_j(t) = (a_j + i\omega_j - |z_j(t)|^2)z_j(t) + CZ(t) + S_j(t) , \tag{30.8}$$

where the complex state variables of the individual oscillators are given by
$z_j = x_j + iy_j$ $(j = 1, \ldots, N$, where N denotes the number of oscillators) and
$Z(t) = \frac{1}{N}\sum_{j=1}^{N} z_j(t)$ denotes the mean field of the ensemble. Note, $S_j(t)$ indicates
the stimulation term received by the jth oscillator, while $S_n(t)$ refers to the stim-
ulation signal applied to the population through the nth electrode.

Without coupling and stimulation all oscillators of ensemble (30.8) indepen-
dently and uniformly rotate around the origin on limit cycles (radius: $\sqrt{a_j}$, fre-
quency: ω_j). The deviation of the mean field $Z(t)$ from zero is of the order of 1/
$\sqrt{N}$ [49, 54]. For increasing coupling strength ($C > 0$), the oscillators start to syn-
chronize which is characterized by large-amplitude oscillations of the mean field
$Z(t)$ (frequency: $\Omega_0 = \frac{1}{N}\sum_{j=1}^{N} \omega_j$). We will use this property of the mean field to-
gether with the mean field of order two (four) $Z_{2(4)} = N^{-1}\sum_{j=1}^{N}(z_j/|z_j|)^{2(4)}$, re-
spectively, to distinguish between synchronized, desynchronized, and clustered
states of the stimulated population of oscillators.

For the investigation of the stimulation effects we use a similar two-parameter
diagram for the averaged order parameter $\langle R(t) \rangle$ as suggested for synchroniza-
tion control by [64, 65] in the case of *linear single-site delayed feedback*, where the
stimulation signal $S(t)$ attains the form $S(t) = KZ(t - \tau)$. The stimulation is per-
formed via one stimulation electrode in such a way that all oscillators of the en-
semble receive the same stimulation signal $S_j(t) = S(t)$. For stimulation with *lin-
ear single-site delayed feedback* in a corresponding two-parameter diagram islands
of perfect desynchronization are complemented by areas of stimulation-en-
hanced synchronization [58, 64, 65] (Fig. 30.4(a)).

In contrast, in Fig. 30.4(b)–(d) where the desynchronization impact of the
stimulation with *linear multisite delayed feedback* is illustrated (see [29–31]) the
whole population is split into four sub-populations, where each of them is as-
signed to the corresponding stimulation electrode and receives the correspond-
ing stimulation signal from that electrode only. The stimulation signals S_n are
constructed from the delayed mean field of the ensemble $S_n(t) = KZ(t - \tau_n)$. We
start with time delays calculated from the following relation:

$$\tau_n = \frac{11 - 2(n-1)}{8}\tau , \ n = 1, 2, 3, 4 . \tag{30.9}$$
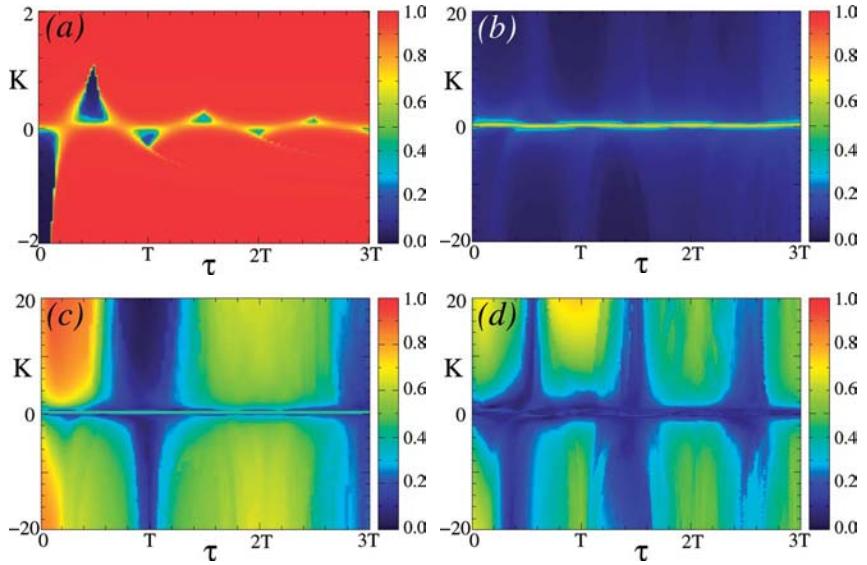
Fig. 30.4 Effect of *linear single-site delayed feedback*. The value of the averaged first order parameter $\langle R(t) \rangle$ is plotted versus delay τ and stimulus amplification K (a). Control of synchronization by *linear multisite delayed feedback*. The values of the averaged first $\langle R(t) \rangle$ (b), second $\langle R_2(t) \rangle$ (c), and fourth $\langle R_4(t) \rangle$ (d) order parameters are depicted, respectively, versus τ and K. Other parameters: $C = 0.25$, mean period of the stimulation-free ensemble $T = 5$ (mean natural frequency $\Omega_0 = 2\pi/T = 1.2566...$), Gaussian distributed individual natural frequencies ω_j (mean Ω_0, deviation $\sigma = 0.1$), number of oscillators $N = 100$ and $a_j = 1$.

As one can see, the delays τ_n are symmetrically distributed with respect to the main delay τ, where the smallest distance between neighboring electrodes is chosen as $\tau/4$. In the case, where $\tau = T$ (mean period of the ensemble), the delays τ_n are uniformly distributed over the mean period T.

For the detailed investigation of the effect of such a stimulation on the phases of ensemble (30.8) and for the calculation of the order parameters displayed in Fig. 30.4 we consider the following system:

$$\dot{\psi}_j(t) = \omega_j + CR(t) \sin[\Theta(t) + \psi_j(t)] + S_j(t), \tag{30.10}$$

where $R(t)$ is the order parameter and $\Theta(t)$ is the mean phase [39]. The corresponding stimulation term in Eq. (30.10) attains the following form:

$$S_j(t) = K \sum_{n=1}^{4} \kappa_{n,j} R(t - \tau_n) \sin[\Theta(t - \tau_n) - \psi_j(t)], \tag{30.11}$$

where the constants $\kappa_{n,j}$ define the spatial topology of the stimulus administration. $\kappa_{n,j}$ attains the values 1 or 0 depending on whether or not the oscillator j

belongs to the sub-population assigned by the stimulation electrode E_n. For example, for N coupled oscillators, we define $\kappa_{1,j}=1$ for $1 \leq j \leq N/4$ and 0 otherwise; $\kappa_{2,j}=1$ for $N/4+1 \leq j \leq N/2$ and 0 otherwise; $\kappa_{3,j}=1$ for $N/2+1 \leq j \leq 3N/4$ and 0 otherwise; and $\kappa_{4,j}=1$ for $3N/4+1 \leq j \leq N$ and 0 otherwise.

The desynchronization impact of the stimulation with *linear multisite delayed feedback* was explained in detail in [29–31]. In the present realization, we consider the following stimulation protocol. Instead of four delays τ_n, $n=1, \ldots, 4$ we use only two of them, τ_1 and τ_2. We put $\tau_3=\tau_1$ and $\tau_4=\tau_2$, where the polarity of the stimulation signals $S_3(t)$ and $S_4(t)$ is reversed: $\kappa_{3,j}=-1$ for $N/2+1 \leq j \leq 3N/4$ and 0 otherwise; and $\kappa_{4,j}=1$ for $3N/4+1 \leq j \leq N$ and 0 otherwise. Assuming that the mean field of the ensemble uniformly oscillates around zero with period τ, the alternating polarity of the signal corresponds to a shift in time by half a period. Therefore, under this condition the stimulation signal $S_3(t) = -S_1(t) = -KZ(t-\tau_1)$ approximates the stimulation signal $S_1(t+\tau/2)$ which is shifted in time by half of the period, which, in turn, is equal to $KZ(t-\tau_3)$, where τ_3 is calculated according to Eq. (30.9). Analogous arguments are applicable to the stimulation signal $S_4(t)=-S_2(t)=-KZ(t-\tau_2)$.

The results of the numerical simulations of ensemble (30.10) stimulated with *linear multisite delayed feedback* (30.11) are shown in Fig. 30.4 (b)–(d). As one can see, the in-phase synchronization in the stimulated ensemble is effectively suppressed and the averaged order parameter $\langle R(t) \rangle$ attains small values (Fig. 30.4 (b)). This indicates a symmetrical redistribution of the phases $\psi_j(t)$ over the unit circle. In Fig. 30.4 (c) and (d) the values of the averaged second $\langle R_2(t) \rangle$ and fourth $\langle R_4(t) \rangle$ order parameter are depicted versus delay τ and stimulus amplification K, respectively. One can see that either the second order parameter attains relatively large values indicating a two-cluster state, or, if the values of $\langle R_2(t) \rangle$ become small (e.g., for $\tau \approx T$), the relatively large values of the fourth order parameter indicate a four-cluster state. Therefore, the whole population splits into two or four distinct populations which have the same frequency, while their phases are equidistantly distributed within the cycle. Hence, depending on the values of the parameters τ and K, *linear multisite delayed feedback* with four stimulation sites may cause either a two-cluster state, where $\langle R(t) \rangle$ is close to zero and $\langle R_2(t) \rangle$ is maximal, or a four-cluster state, where both $\langle R(t) \rangle$ and $\langle R_2(t) \rangle$ are close to zero, but $\langle R_4(t) \rangle$ is maximal.

Two trajectories of the X-coordinate of the mean field $Z(t)$ (Fig. 30.5) illustrate the detailed behavior of the system during *linear multisite delayed feedback*. For a delay τ close to the mean period of the stimulation-free ensemble (Fig. 30.5 (a)), a four cluster state is induced by the stimulation ($C=0.25$ for $t>100$, $C=0$ else; $K=30$ for $t>200$, $K=0$ else). The value of the X-coordinate of the mean field $Z(t)$ (Fig. 30.5 (a), red curve) saturates to values close to zero, while the mean fields of higher order Z_2 (Z_4) saturate to low (high) values, respectively. As argued above such a state corresponds to a four cluster state. The subplots, which show four trajectories from each of the stimulated subsystems, illustrate the emerging four-cluster state induced by *linear multisite delayed feedback*. For $\tau=10$ we observe a two-cluster state (Fig. 30.5 (b)), as indicated by the two-dimensional diagram
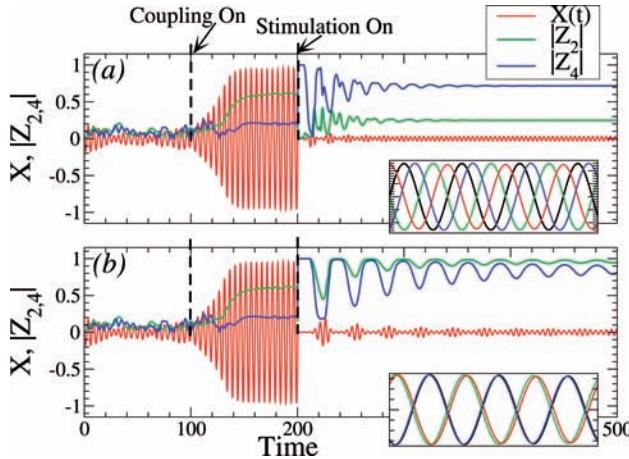
Fig. 30.5 Control of synchronization of coupled and stimulated limit-cycle oscillators. Time courses of the *X*-coordinate of the mean field $Z(t)$ (red curves). Green and red curves in the main plots are the amplitudes of the mean fields of higher order, namely, $Z_n = N^{-1} \sum_{j=1}^{N} \left(\frac{z_j}{|z_j|} \right)^n$. In the subplots four trajectories from each of the stimulated sub-system are shown for $t \in (320, 340)$. Other parameters: (a) $\tau = 5.0$, (b) $\tau = 10$, $C = 0.25$, $K = 30$, mean period of the stimulation-free ensemble $T = 5$ (mean natural frequency $\Omega_0 = 2\pi/T = 1.2566\ldots$), Gaussian distributed individual natural frequency $\omega_j(\Omega_0$, deviation $\sigma = 0.1)$, number of oscillators $N = 100$ and $a_j = 1$.

(Fig. 30.4 (c) and (d)): both Z_2 and Z_4 attain high values close to one. For considerably strong coupling (e.g., $C = 0.5$) the *linear multisite delayed feedback stimulation* method reaches its limitations and an intermittent behavior occurs. The desired two- ($\tau = 10$) or four- ($\tau = 5$) cluster state periodically alternates with a mostly desynchronized state. A noisy environment, which is inevitable for realistic systems, has capabilities to reduce the effective coupling. In such an environment intermittent behavior is not observed and *linear multisite delayed feedback* induces a robust desynchronization even for considerably strong coupling [29–31].

30.4
Nonlinear Delayed Feedback

In this section we present another technique for the control of collective dynamics in networks of interacting oscillators. As in the previous section, the present method is based on a delayed feedback loop, which is known to be an effective technique for the control of the dynamics of chaotic oscillators [35, 60, 61, 70]. The impact of a delay on the collective dynamics of coupled oscillators is intensively studied nowadays (see e.g. [18, 38, 62, 64, 67, 94, 103]). Recently, novel methods based on a linear single-site [64, 65] or linear multisite [29–31] (Section 30.3) delayed feedback were suggested for the control of synchronization. In the former realization, the linear delayed feedback method can com-

pletely desynchronize a controlled ensemble provided parameter values are chosen within bounded island-like regions complemented by areas of stimulus-enhanced synchronization. In contrast, the linear multisite delayed feedback method demonstrates greater robustness with respect to parameter variations. However, linear multisite delayed feedback induce CPG-like cluster states (see above), which are not desynchronized states. Nevertheless, CPG-like dynamics might be beneficial for other medical applications (see below).

To reliably induce complete desynchronization, we here suggest to use a nonlinear delayed feedback (NDF) for the control of the collective dynamics in oscillatory networks [57–59, 87]. The extent of synchronization can be adjusted by the NDF method to any amount ranging from complete in-phase locking to complete desynchronization. The NDF method distinguishes itself by a particular robustness with respect to system and stimulation parameter variations: A synchronized population of oscillators is stimulated with a signal which is constructed by using the delayed mean field of the ensemble nonlinearly combined with the instantaneous mean field. The stimulation results in a complete desynchronization of the oscillators and restores their natural frequencies, so that the oscillators rotate as if they were uncoupled. Simultaneously, the amplitude of the stimulation signal practically vanishes when a desynchronized state is achieved. This naturally realizes a demand-controlled character of the proposed desynchronization technique. We illustrate the discussed control method by two examples of coupled limit-cycle and phase oscillators. By means of a model equation approximating the macroscopic dynamics of the controlled ensemble, we explore the main dynamical properties of synchronization control by NDF.

The controlled network of interacting oscillators is stimulated by a signal $S(t)$ derived from the mean field of the ensemble. The mean field $Z(t)$ of the ensemble is measured and is supposed to have the form of a complex analytic signal [1] $Z(t) = X(t) + iY(t)$. The stimulation signal is then constructed by a nonlinear combination of a delayed complex conjugate mean field with the instantaneous mean field

$$S(t) = KZ^2(t)Z^*(t - \tau),\tag{30.12}$$

where K is a stimulus amplification parameter, τ is a time delay, and the asterisk denotes complex conjugacy. We illustrate the impact of the stimulation by the NDF (30.12) on the collective dynamics of an exemplary ensemble of coupled limit-cycle oscillators

$$\dot{z}_j(t) = (a_j + i\omega_j - |z_j(t)|^2)z_j(t) + CZ(t) + S(t).\tag{30.13}$$

---

[1] In the case, where only the real part $X(t)$ of the mean field $Z(t)$ is measured, the imaginary part $Y(t)$ can be obtained by, e.g., Hilbert transform $Y(t) = \pi^{-1} P.V. \int_{-\infty}^{\infty} \frac{X(s)}{t-s} ds$, where $P.V.$ denotes Cauchy principal value [54].

System (30.13) is a population of N globally coupled Landau-Stuart oscillators representing a normal form of a supercritical Andronov-Hopf bifurcation [40]. The individual limit-cycle oscillators described by the complex variables $z_j = x_j + iy_j$ have individual natural frequencies ω_j and amplitudes $\sqrt{a_j}$ and are globally coupled via their mean field $Z = N^{-1} \sum_{j=1}^{N} z_j$, where C is the parameter of the coupling strength. If the latter increases, the oscillators synchronize and start to rotate with the same frequency, where the pairwise differences between variables of individual oscillators decrease (mod 2π) [39, 47]. This phenomenon is reflected by the dynamics of the mean field which increases its amplitude in accordance with the extent of synchronization in the ensemble [39, 47, 54]. In what follows we consider two cases of (i) very strong coupling, where the oscillators (30.13) are strongly in-phase locked, and (ii) weak coupling, where most of the oscillators still remain desynchronized.

The impact of the NDF stimulation (30.12) on the globally coupled ensemble (30.13) for the two cases mentioned above is illustrated in Fig. 30.6. The population of $N = 100$ stimulated limit-cycle oscillators (30.13) is numerically simulated for strong (Fig. 30.6 (a)) and weak (Fig. 30.6 (b)) coupling among the oscillators. In the course of the simulation, the coupling (C) and the stimulation (K) are switched on at times $t = 100$ and $t = 200$, respectively. One can see that if the
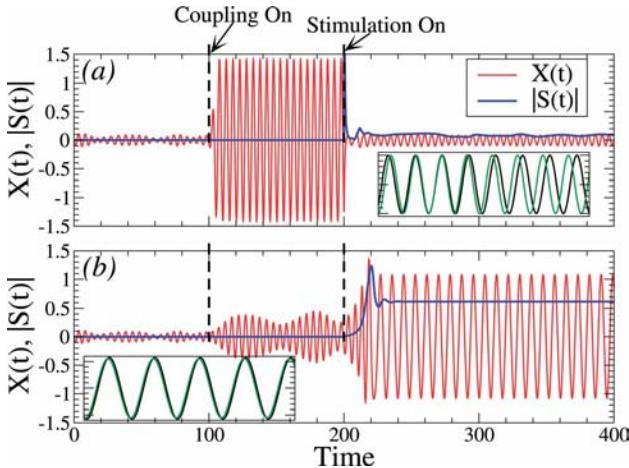
Fig. 30.6 Control of synchronization of coupled and stimulated oscillators (30.13). Time courses of the X-coordinate of the mean field $Z(t)$ (red curves) and the amplitude of the stimulation signal $|S(t)|$ (30.12) (blue curves) are plotted versus time. Coupling (C) and stimulation (K) are switched on at different times: $C = K = 0$ for $t < 100$, then (a) $C = 1$ and (b) $C = 0.15$ for $t > 100$, and, finally, (a) $K = 100$ and (b) $K = -0.5$ for $t > 200$. In the subplots two selected trajectories $x_j(t)$ of oscillators (30.13) are depicted for time $t \in (360, 400)$ (stimulated regime). The mean period of the stimulation-free ensemble (30.13) $T = 5$ (mean natural frequency $\Omega_0 = 2\pi/T = 1.2566...$), the individual natural frequencies ω_j are Gaussian distributed with mean Ω_0 and deviation $\sigma = 0.1$. The time delay $\tau = 2.5$, the number of oscillators $N = 100$, and $a_j = 1$.

coupling and stimulation are absent ($t < 100$) the mean field of the ensemble (Fig. 30.6, red curve) displays small-amplitude oscillations caused by a finite-size effect [55], which is characteristic for a desynchronized state [39, 47, 54]. The onset of strong coupling leads to a significant increase of the amplitude of the mean field (Fig. 30.6(a), where $C = 1$) reflecting an onset of strong synchronization of the oscillators. A weak coupling, on the other hand, leads to small changes in the dynamics of the mean field of ensemble (30.13) (see Fig. 30.6(b), where $C = 0.15$), and the oscillators mostly remain desynchronized. The onset of the stimulation takes place when the corresponding strongly synchronized (Fig. 30.6(a)) or weakly synchronized (Fig. 30.6(b)) dynamics is established in system (30.13). Depending on the values of the stimulation parameters K and τ of the NDF signal (30.12) the stimulation can have different effects on the oscillators. In particular, the NDF stimulation can effectively desynchronize a population of strongly coupled oscillators. This can be seen in Fig. 30.6(a), where the onset of the stimulation results in a decrease of the amplitude of the mean field, which practically reaches the level of the coupling- and stimulation-free regime. In the other case, the NDF stimulation can induce synchronization in the stimulated ensemble, which is illustrated in Fig. 30.6(b). One can see that the stimulation can provoke large-amplitude oscillations of the mean field characteristic for a synchronized dynamics.

The stimulation with the NDF signal (30.12) does not destroy the natural oscillatory activity of the individual elements of the ensemble. This follows from the insets in Fig. 30.6, where the trajectories of two selected oscillators in the stimulated regime are plotted. In accordance with the desynchronizing effect of NDF stimulation (30.12), the stimulated oscillators rotate with different frequencies and, thus, are desynchronized (see subplot in Fig. 30.6(a)). On the other hand, the synchronizing effect of NDF stimulation results in a strong in-phase synchronization of the stimulated oscillators, which is illustrated in the subplot in Fig. 30.6(b), where the trajectories of two selected oscillators of the stimulated ensemble practically coincide. In Fig. 30.6(a) another important property of the desynchronizing NDF stimulation is illustrated. As soon as a stimulation-induced desynchronized state is archived, the amplitude of the stimulation signal $|S(t)|$ (Fig. 30.6(a), blue curve) declines and reaches values of the same order of magnitude as the amplitude of the mean field. This is because of the nonlinear dependence of the stimulation signal (30.12) on the mean field. Therefore, the discussed method represents a demand-controlled technique for the desynchronization of interacting oscillators, where the stimulated system is subjected to a highly effective control at a minimal amount of stimulation force.

As mentioned above, the NDF stimulation (30.12) makes the individual frequencies $\bar{\omega}_j$ of the strongly coupled and stimulated oscillators (30.13) different from each other, in this way stabilizing a desynchronized state (Fig. 30.6(a)). To illustrate the impact of the NDF stimulation on the frequencies of the stimulated oscillators, in Fig. 30.7(a) the following frequencies of the stimulated ensemble (30.13) are depicted versus the stimulus amplification parameter K: individual frequencies $\bar{\omega}_j$ (gray dots), frequency Ω (blue curves) of the mean field $Z(t)$,
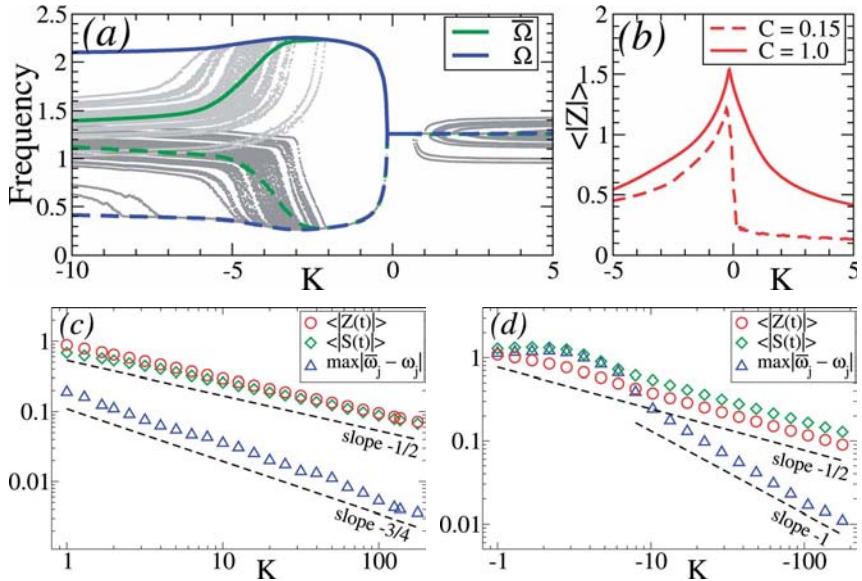
Fig. 30.7 Evolution of the frequencies and desynchronization of the coupled oscillators (30.13) stimulated with the NDF (30.12). (a) Two different realizations of the frequencies $\{\bar{\omega}_j\}$ (light and dark gray dots) of the individual oscillators, frequency Ω (solid and dashed blue curves) of the mean field $Z(t)$, and the mean of the individual frequencies $\bar{\Omega} = N^{-1}\sum_{j=1}^{N}\bar{\omega}_j$ (solid and dashed green curves) can be observed in system (30.13) for two different initial conditions. Coupling $C = 1$. The solid (dashed) green and blue curves correspond to the individual frequencies depicted by light (dark) gray dots used in two different simulations. (b) The time-averaged amplitude of the mean field $\langle|Z(t)|\rangle$ is depicted for $C = 1$ (solid red curve, corresponds to frequencies in (a)) and $C = 0.15$ (dashed red curve). In (c) and (d) the time-averaged amplitude of the mean field $\langle|Z(t)|\rangle$ (red circles), amplitude of stimulation signal $\langle|S(t)|\rangle$ (green diamonds), and the maximum of the frequency difference $\max_j|\bar{\omega}_j - \omega_j|$ (blue triangles) are depicted versus (b) positive and (c) negative values of K in log-log scale. The black dashed lines with the indicated slopes are given for comparison. Delay $\tau = 2.5$, the number of oscillators (a), (b) $N = 50$ and (c), (d) $N = 100$, and the other parameters are as in Fig. 30.6.

and the mean of the individual frequencies $\bar{\Omega} = N^{-1}\sum_{j=1}^{N}\bar{\omega}_j$ (green curves). As the parameter $K>0$ increases, the individual frequencies $\bar{\omega}_j$ diverge from each other via a sequence of frequency-splitting bifurcations, where $\bar{\omega}_j$ split, one after other, from the mean frequency Ω. This process leads to the onset of desynchronization in the stimulated ensemble, where the individual stimulated oscillators start to rotate with different frequencies. One can see in Fig. 30.7 (a) that $\Omega = \bar{\Omega}$ for $K>0$. Moreover, in this case the stimulation preserves the mean natural frequency $\Omega_0 = N^{-1}\sum_{j=1}^{N}\omega_j$, i.e. $\Omega = \Omega_0$. The situation is different for $K<0$, where NDF stimulation can lead to a multistability of stimulation-induced states in system (30.13) and can significantly detune frequencies of the stimulated ensemble. For example, we plot in Fig. 30.7 (a) two different sets of the individual frequencies $\{\bar{\omega}_j\}$ (light and dark gray dots) and the corresponding mean fre-

quencies Ω (solid and dashed blue curves) which can be realized in the stimulated ensemble (30.13) for different initial conditions for $K < 0$. The coexisting stable stimulation-induced states can be synchronous (for small values of $|K|$) or desynchronous (for large values of $|K|$), where the stimulated oscillators can rotate with the same or with different individual frequencies $\bar{\omega}_j$, respectively (Fig. 30.7 (a) for $K < 0$). Note that Ω can significantly deviate from $\bar{\Omega}$ (solid and dashed green curves in Fig. 30.7 (a)), where the mean field of the stimulated ensemble oscillates much faster (solid blue curve in Fig. 30.7 (a)) or much slower (dashed blue curve in Fig. 30.7 (a)) than the individual oscillators.

For large values of the stimulus amplification $|K|$, the extent of synchronization in the stimulated ensemble (30.13) decays as given by the time-averaged amplitude of the mean field $\langle |Z(t)| \rangle$ (red curves in Fig. 30.7 (b)). This holds both for strongly coupled (solid red curve in Fig. 30.7 (b), corresponding to the frequencies in Fig. 30.7 (a)) as well as for weakly coupled (dashed red curve in Fig. 30.7 (b)) ensembles with the difference that in the latter case there is a relatively large interval of values of K, where the synchronization among stimulated oscillators is enhanced compared to the stimulation-free regime (dashed red curve in Fig. 30.7 (b) for $K < 0$). Note, the amplitude of the mean field $\langle |Z(t)| \rangle$ (solid red curve in Fig. 30.7 (b)) is the same for both realizations of the frequencies $\{\bar{\omega}_j\}$ in Fig. 30.7 (a) obtained for two different initial conditions.

A few more important properties of the desynchronizing impact of NDF stimulation are illustrated in Fig. 30.7 (c) and (d), where the time-averaged amplitude of the mean field $\langle |Z(t)| \rangle$ (red circles), time-averaged amplitude of the stimulation signal $\langle |S(t)| \rangle$ (green diamonds), and the maximum of the frequency differences $\max_j |\bar{\omega}_j - \omega_j|$ (blue triangles) are plotted versus $|K|$ in log–log scale. One can clearly see that, as $|K|$ increases, the amplitudes of the mean field and stimulation signal decay in accordance with the following power law:

$$\langle |Z(t)| \rangle \sim \frac{1}{\sqrt{|K|}} \,, \quad \langle |S(t)| \rangle \sim \frac{1}{\sqrt{|K|}} \,. \tag{30.14}$$

Moreover, as numerical evidence suggests, the individual frequencies $\bar{\omega}_j$ of the stimulated oscillators approach the natural frequencies ω_j with the rate $|\bar{\omega}_j - \omega_j| \sim 1/K^a$, where the exponent a might depend on parameters of the stimulated system (Fig. 30.7 (c) and (d), blue triangles). Therefore, with increasing stimulus amplification $|K|$ the stimulated oscillators become effectively desynchronized, where the extent of the residual synchronization, as given by the amplitude of the mean field, decays according to Eq. (30.14). Simultaneously, the amount of the stimulation force applied to the stimulated ensemble, as given by the amplitude of the stimulation signal, decay with the same rate. Moreover, the stimulation effectively restores the individual natural frequencies of the stimulated oscillators, where all stimulated oscillators start to rotate with their natural frequencies suppressed by synchronization.

To study the phase dynamics of the stimulated ensemble (30.13), (30.12) in more detail, we consider the corresponding ensemble of phase oscillators. For

this, we substitute $z_j(t) = r_j(t) \exp(i\psi_j(t))$ into Eqs. (30.12), (30.13), and, neglecting the dynamics of the amplitudes r_j, we consider the following system for the phases ψ_j:

$$\dot{\psi}_j(t) = \omega_j + CR(t)\sin[\Theta(t) - \psi_j(t)] + KR^2(t)R(t-\tau)\sin[2\Theta(t) - \Theta(t-\tau) - \psi_j(t)].$$
(30.15)

Here, the mean field of the phase ensemble (30.15) is given by $W(t) = R(t)\exp(i\Theta(t)) = N^-\sum_{j=1}^{N}\exp(i\psi_j(t))$, where $R(t)$ is the order parameter and $\Theta(t)$ is the mean phase [8, 39]. The order parameter $R \in [0, 1]$ serves as a good indicator of the onset of synchronization in ensemble (30.15): If the phase oscillators are in-phase synchronized with pairwise phase differences tending to zero (mod 2π), then $R \to 1$.

The robustness of the discussed control method with respect to variations of system and stimulation parameters is of particular importance for its application.

We address the robustness issue by calculating the time-averaged order parameter $\langle R(t) \rangle$ of the phase ensemble (30.15) versus stimulation parameters τ and K. The results of the calculations are depicted as a two-parameter diagram in Fig. 30.8 for the two cases of strong coupling (Fig. 30.8(a), where $C = 1$) and weak coupling (Fig. 30.8(b), where $C = 0.15$). One can see in Fig. 30.8(a) that for any value of $\tau > 0$ the order parameter decays with increasing K, which indicates an onset of desynchronization in the stimulated ensemble. For a weakly coupled ensemble, the NDF stimulation can induce enhancement of synchronization in island-like regions of (τ, K)-parameter plane complemented by domain of complete desynchronization (Fig. 30.8(b)). We note here that in the above Figs. 30.6 and 30.7 the calculations are performed for a fixed delay $\tau = T/2$, where T is the mean period of the ensemble without stimulation. One can expect a similar dynamics of the mean field and the frequencies of the stimulated oscillators for other values of delay which, e.g., are multiple of $T/2$ (see Fig. 30.8).
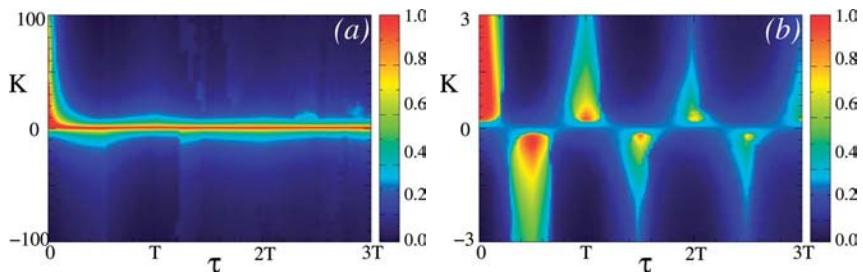
Fig. 30.8 Control of synchronization by NDF stimulation versus stimulation parameters τ and K. The values of the time-averaged order parameter $\langle R(t) \rangle$ are depicted in color ranging from 0 (blue) to 1 (red) for (a) strongly coupled ($C = 1$) and (b) weakly coupled ($C = 0.15$) ensemble of $N = 100$ stimulated phase oscillators (30.15). The natural frequencies ω_j are distributed as in Fig. 30.6. T denotes a mean natural period of ensemble (30.15) without stimulation, $T = 5$.

The dynamics of the mean field $W(t)$ of the stimulated ensemble (30.15) can be approximated by the following model equation [57, 58, 87]:

$$\dot{W}(t) = \frac{C}{2}\left(1 - |W(t)|^2\right)W(t) + i\Omega_0 W(t) + \frac{K}{2}W^2(t)W^*(t - \tau),$$ (30.16)

were $\Omega_0 = N^{-1}\sum_{j=1}^{N}\omega_j$ is the mean natural frequency of the ensemble. In a strongly synchronized regime (for large enough $C>0$ and $K=0$) the dynamics of the mean field of ensemble (30.15) for large N can be approximated by a uniform rotation on the unit circle with the frequency $\Omega=\Omega_0$ emerging in a Hopf bifurcation [39], where the amplitude of the mean field is given by the order parameter $R(t)\approx 1$. Global NDF stimulation (30.12) affects all oscillators (30.15) in the same way and is modeled by the same stimulation term in Eq. (30.16). Solutions of Eq. (30.16) of the form $W(t) = R(t)\exp(i\Theta(t))$, where $R(t)=\text{const}\neq 0$, $\Theta(t)=\Omega t + \text{const}$, can be derived from the following equations:

$$\Omega = \Omega_0 + \frac{KC\sin(\Omega\tau)}{2C - 2K\cos(\Omega\tau)}, \quad R^2 = \frac{C}{C - K\cos(\Omega\tau)}.$$ (30.17)

With the help of the model equation (30.16) one can investigate the existence, stability, and dynamical properties of stimulation-induced desynchronized states of ensemble (30.15). For example, in the stimulated ensemble (30.15) we find the same decay rate of the order parameter $\langle R\rangle$ and the amplitude of the stimulation signal $\langle |S|\rangle$ as predicted by Eq. (30.14). This decay rate can also be derived from Eq. (30.17) (Fig. 30.9 (b)). The mean frequency Ω of the NDF-induced desynchronized states of ensemble (30.15) can also be calculated from Eq. (30.17).
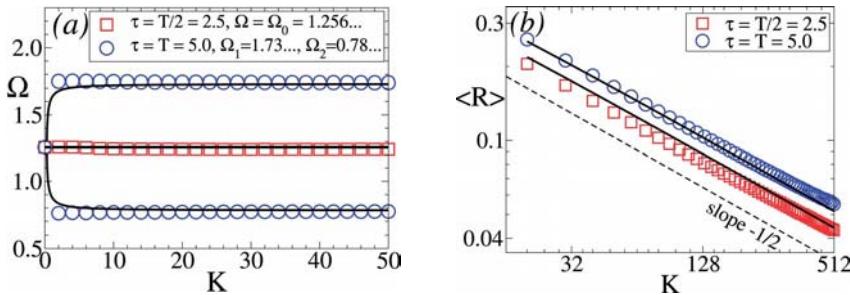
Fig. 30.9 Mean frequency Ω (plot (a)) and the time-averaged order parameter $\langle R\rangle$ (plot (b)) of the stimulation-induced desynchronized states versus stimulus amplification K. Symbols indicate the values of Ω and $\langle R\rangle$ calculated for the stimulation-induced desynchronized states of the ensemble of $N=200$ stimulated phase oscillators (30.15) for $\tau = 2.5 = T/2$ (red squares) and $\tau = 5.0 = T$ (blue circles), where $T = 2\pi/\Omega_0$ is the mean natural period of ensemble (30.15). The black solid curves are the theoretical predictions of Ω and $\langle R\rangle$ obtained from Eqs. (30.16) and (30.17) for the corresponding values of delay. Plot (b) is in a log–log scale, where the dashed line has a slope $-1/2$ and is shown for comparison. Parameter $C = 1.0$ and the natural frequencies ω_j of oscillators (30.15) are distributed as in Fig. 30.6.

In particular, the mean natural frequency Ω_0 can be preserved under stimulation $\Omega = \Omega_0$ as illustrated in Fig. 30.9 (a) for $\tau = T/2$ (red squares) (see also Fig. 30.7 (a) for $K > 0$). For other values of delay (or opposite sign of K), the feedback can induce multistability of desynchronized states, where the mean frequency of the stimulated ensemble can significantly be detuned from its original value. This phenomenon is illustrated in Fig. 30.9 (a) for $\tau = T$ (blue circles), where, depending on the initial conditions, Ω can approach, e.g., values $\Omega_1 \approx 1.73$ or $\Omega_2 \approx 0.78$ for large values of K ($\Omega_0 \approx 1.256$ in Fig. 30.9) (see also Fig. 30.7 (a) for $K < 0$). The latter property of the NDF stimulation may play an important role in the macroscopic frequency control of the stimulated populations of oscillators.

30.5
Reshaping Neural Networks

Plasticity is a fundamental property of the nervous system: In order to learn and to adapt to sensory inputs, neurons continuously adapt the strength of their synaptic connections in relation to the mutual timing properties of their firing or bursting [1, 9, 20, 33, 37, 46, 71, 93, 104]. However, plasticity may not only lead to desired learning and optimization processes. Rather, neuronal populations can learn pathologically strong interactions which may lead, e.g., to the emergence of epilepsies [50, 72]. This is well-known from the so-called kindling phenomenon [24], where preparatory stimulation induces the spontaneous production of epileptic seizures without gross morphological changes [50].

Recently, theoretical studies have initiated an approach which is targeted on unlearning pathologically strong synaptic interactions by desynchronizing brain stimulation [32, 88, 90, 91]. This approach exploits plasticity in two different ways: On the one hand, due to plasticity, desynchronizing stimulation may decrease the strength of the neurons' synapses by decreasing the rate of coincidences. On the other hand, neuronal networks with synaptic plasticity may exhibit bi- or multistability. Accordingly, by decreasing the mean synaptic weight, desynchronizing stimulation may shift a neuronal population from a stable synchronized (pathological) state to a stable desynchronized (healthy) state, where the neuronal population remains thereafter.

To illustrate this concept we present a numerical simulation where both kindling stimulation, i.e., low-frequency stimulation, and antikindling stimulation, i.e., multisite coordinated reset stimulation, are applied to a population of bursting neurons [32, 91] (Fig. 30.10).

Since the purpose of Fig. 30.10 is to illustrate and discuss a concept we omit all the details of the model, and refer the interested reader to [32, 91]. The synaptic connectivities are modified following a simplified plasticity rule with symmetric spike timing characteristics [1, 9, 36, 44, 53, 100]. In our neuronal population, which models a standard target for deep brain stimulation, synchronized states (modeling disease states) as well as a desynchronized state (modeling a
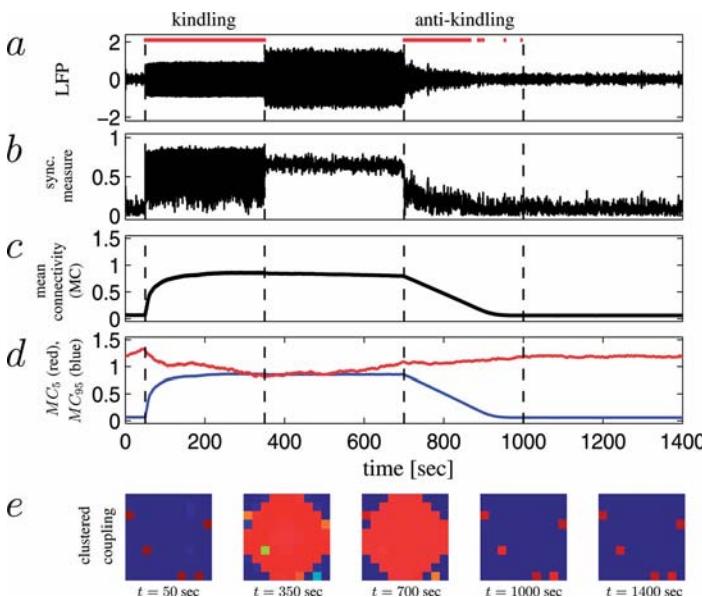
Fig. 30.10 Illustration of the effects of anti-kindling and kindling stimulation on a population of bursters in the presence of an additional weak external input: (a) local field potential (*LFP*, the stimulation epoch is indicated by a red bar and by vertical lines). (b) Synchronization measure. (c) Mean connectivity (MC). (d) Separate analysis of the mean connectivity for the five neurons affected by the weak external stochastic input (MC_5, red), the mean connectivity of the other neurons is displayed by the blue curve (MC_{95}). (e) Clustered coupling pattern calculated at different times, where the mean connectivity is evaluated for each neuron within the cluster it belongs to (MC_5 or MC_{95}). The colors indicate the amount of the averaged synaptic coupling strength (red (blue) color indicates strong (weak) coupling). For details on the used model and the parameters see [32, 91].

healthy state) are stable. The desynchronized state in our simulations is characterized by very small coupling coefficients. In realistic neuronal systems one might expect to observe among the majority of weakly coupled neurons also clusters of functionally related neurons characterized by stronger coupling. These clusters might be involved in a signal processing task induced by, for example, external sensory signals. To mimic such a situation we added a weak, exponentially correlated stochastic external signal to a small number of neurons (for details on the sensory input signal see [10, 13, 101]).

Starting from the stable desynchronized state, kindling stimulation, i.e., low-frequency stimulation presented through one centered electrode, induces a high portion of coinciding bursting activities which results in an increase of the corresponding synaptic connectivities (see Fig. 30.10(e)), the induced connectivity pattern reflects the concentric decay of the stimulation strength with distance from the centered electrode). Finally, the synchronized state is stabilized and remains thereafter (Fig. 30.10(a) and (b)). Antikindling stimulation, i.e., desyn-

chronizing multisite coordinated reset stimulation presented through four equally distributed electrodes, results in a reduction of the synaptic connectivities which, finally, ends up in a stabilization of the desynchronized state which outlasts the epoch of desynchronizing stimulation (see Fig. 30.10 (c)). If the mean synaptic connectivity is analyzed separately for the cluster of functionally related neurons (MC_5), i.e., the five neurons which receive the additional external input, and for the neurons not affected by the additional input (MC_{95}), Fig. 30.10 (d) illustrates that kindling stimulation disturbs the cluster of functionally related neurons while multisite coordinated reset stimulation leaves this cluster unperturbed, in particular the connectivities of the functionally related neurons are able to recover during the desynchronizing stimulation (Fig. 30.10 (d) and (e)).

Therapeutically rewiring stimuli of this kind [32, 88, 90, 91] shift the population into the basin of attraction of the stable desynchronized state in an extremely mild way leaving clusters of functionally related neurons unperturbed. This concept might contribute to a novel therapeutic stimulation strategy for the therapy of neurological and psychiatric diseases characterized by abnormal synchrony [21]. Instead of suppressing pathological synchronization this approach aims at reshaping neural networks in a way that they unlearn their tendency to generate pathological synchrony. According to our theoretical results [32, 88, 90, 91] this requires considerably less stimulation current as compared to standard high-frequency stimulation. Also Fig. 30.10 illustrates why we do not expect that maladaptive processes, i.e., the formation of misconnected clusters, occur. Desynchronizing stimulation specifically counteracts pathological synchrony in this way giving rise to the reemergence of physiological patterns of connectivity.

30.6
Discussion

In this chapter we presented three methods for the control of collective dynamics in ensembles of interacting oscillators. These methods are coordinated reset stimulation (Section 30.2), linear multisite delayed feedback (Section 30.3), and nonlinear delayed feedback (Section 30.4). We have shown that all three methods can effectively suppress the undesirable synchronization among oscillators, where the latter continue to exhibit their natural oscillatory activity. In contrast, high-frequency pulse train stimulation of sufficient strength blocks the individual oscillators.

The coordinated reset stimulation requires repetitive (demand-controlled or simple periodic) stimulus administration, where the stimulated oscillators are kept in a permanent transient between synchronized and desynchronized states. With such a stimulation protocol, the amount of the administered stimulation current is significantly smaller than that of the high-frequency stimulation. This allows us to expect much less side effects because of the smaller current spread

when this technique is being used for the deep brain stimulation. Multisite coordinated reset stimulation also works in simulations with realistic stimulation and interaction topologies [84, 85]. Unlike other stimulation techniques, which are based on phase resetting principles and require thorough calibration [77–82], multisite coordinated reset stimulation distinguishes itself by the absence of critical stimulation parameters, by the robustness of the desynchronizing effect, and by the quick availability (without time consuming calibration).

Linear multisite delayed feedback allows to control cluster-states in the stimulated system. On the one hand, depending on the chosen stimulation parameter τ, one can induce an N-cluster state, where N refers to the number of electrodes used for the stimulation. On the other hand, linear multisite delayed feedback stimulation provides an effective method for the control of spatiotemporal dynamics. Applied to CPGs, which are neural networks that can endogenously (i.e., without external drive) produce oscillatory patterned outputs [3, 11, 14, 45, 97], i.e., anatomically distinct, but interacting clusters of neurons, our approach might induce a coordinated sequential firing of different clusters. Different arrangements of the delays can cause different types of dynamics which might control different locomotor patterns. In this way, linear multisite delayed feedback stimulation maintains spatially patterned synchrony with minimal amounts of stimulation. Hence, linear multisite delayed feedback stimulation might be tested for the restoration of CPG activity in patients with incomplete spinal cord injury [11, 12] or gait ignition disorders [66].

By stimulation with *nonlinear delayed feedback*, the synchronization of the stimulated oscillators can effectively be enhanced, if the coupling strength and stimulus amplification are weak. On the other hand, for any coupling strength, even for very strong coupling, the synchronization can be effectively suppressed, if the stimulus amplification parameter is large enough, which is the main feature of the nonlinear delayed feedback. In the latter case, the stimulation restores the natural frequencies of the oscillators suppressed by synchronization. We approximate the decay rate of the order parameter of the stimulated ensemble and the amplitude of the stimulation signal, which characterize the extent of synchrony among the oscillators and the amount of the administered stimulation force, respectively. Both quantities decay with increasing stimulus amplification according to the power law (30.14). This scaling is extremely important for medical applications. Translated into the context of electrical brain stimulation, Eq. (30.14) means that the better the pathological synchrony is suppressed, the less stimulation current is needed. The stimulation can lead to a multistability of stimulation-induced desynchronized states, where the mean frequency of the stimulated ensemble can significantly be detuned by stimulation. This may open up a novel avenue for the frequency control of ensembles of interacting oscillators, for example, for populations of oscillatory neurons in the brain. We note that the discussed method demonstrates a great robustness with respect to system and stimulation parameter variations, which is of primary importance for applications. The NDF method also demonstrates a broad applicability and universality, which has been tested on a number of coupled networks of differ-

ent nature including ensembles of synaptically coupled bursting neurons and for a variety of stimulation protocols (see [57–59, 87]).

Desynchronizing stimulation might effectively counteract pathological neuronal synchronization processes, in order to achieve an effective suppression of symptoms. Moreover, desynchronizing stimulation might even reshape affected neuronal networks, to induce long-lasting therapeutic effects (see Section 30.5). This approach might, hence, lead to a fundamentally novel therapy for diseases characterized by pathological brain synchrony.

References

1 L.F. Abbott and S.B. Nelson. Synaptic plasticity: taming the beast. *Nat. Neurosci.*, 3:1178–1183, 2000.

2 W.W. Alberts, E.J. Wright, and B. Feinstein. Cortical potentials and parkinsonian tremor. *Nature*, 221:670–672, 1969.

3 M.C. Bellingham. Driving respiration: the respiratory central pattern generator. *Clin. Exp Pharmacol Physiol.*, 25:847–856, 1998.

4 A.L. Benabid, P. Pollak, C. Gervason, D. Hoffmann, D.M. Gao, M. Hommel, J.E. Perret, and J. de Rougemount. Longterm suppression of tremor by chronic stimulation of ventral intermediate thalamic nucleus. *The Lancet*, 337:403–406, 1991.

5 E.N. Best. Null space in the Hodgkin-Huxley equations: a critical test. *Biophys. J.*, 27:87–104, 1979.

6 S. Blond, D. Caparros-Lefebvre, F. Parker, R. Assaker, H. Petit, J.-D. Guieu, and J.-L. Christiaens. Control of tremor and involuntary movement disorders by chronic stereotactic stimulation of the ventral intermediate thalamic nucleus. *J. Neurosurg.*, 77:62–68, 1992.

7 H. Daido. Order function and macroscopic mutual entrainment in uniformly coupled limit-cycle oscillators. *Prog. Theor. Phys.*, 88:1213–1218, 1992.

8 H. Daido. Order function theory of macroscopic phase-locking in globally and weakly coupled limit-cycle oscillators. *Int. J. Bif. Chaos*, 7(4):807–829, 1997.

9 D. Debanne, B.H. Gahweiler, and S.M. Thompson. Long-term synaptic plasticity between pairs of individual CA3 pyramidal cells in rat hippocampus slice cultures. *J. Physiol.*, 507:237–247, 1998.

10 A. Destexhe, M. Rudolph, J.M. Fellous, and T.J. Sejnowski. Fluctuating synaptic conductances recreate in-vivo-like activity in neocortical neurons. *Neuroscience*, 107:13–24, 2001.

11 V. Dietz. Spinal cord pattern generators for locomotion. *Clinical Neurophysiol.*, 114:1379–1389, 2003.

12 V. Dietz and R. Müller. Degradation of neuronal function following a spinal cord injury: mechanisms and countermeasures. *Brain*, 127:2221–2231, 2004.

13 K. Dolan, A. Witt, M.L. Spano, A. Neiman, and F. Moss. Surrogates for finding unstable periodic orbits in noisy data sets. *Phys. Rev. E*, 59:5235–5241, 1999.

14 J. Duysens and H.W. van de Crommert. Neural control of locomotion; the central pattern generator from cats to humans. *Gait Posture*, 7(2):131–141, 1998.

15 R.J. Elble and W.C. Koller. *Tremor.* John Hopkins University Press, Baltimore, 1990.

16 J. Engel and T.A. Pedley. *Epilepsy: A Comprehensive Textbook.* Lippincott-Raven, Philadelphia, 1997.

17 B. Ermentrout and N. Kopell. Multiple pulse interactions and averaging in systems of coupled neural assemblies. *J. Math. Biol.*, 29:195–217, 1991.

18 U. Ernst, K. Pawelzik, and T. Geisel. Delay-induced multistable synchronization of biological oscillators. *Phys. Rev. E*, 57:2150–2162, 1998.

19 M.C. Rodriguez-Oroz et al. Bilateral deep brain stimulation in Parkinson's disease: a multicentre study with 4 years follow-up. *Brain*, 128(10):2240–2249, 2005.

20 D. E. Feldman. Timing-based LTP and LTD at vertical inputs to layer II/III pyramidal cells in rat barrel cortex. *Neuron*, 27:45–56, 2000.

21 H.-J. Freund. Long-term effects of deep brain stimulation in Parkinson's disease. *Brain*, 128:2222–2223, 2005.

22 C. Gielen and F. Moss (Eds.). *Handbook of Biological Physics, Vol. IV.* Elsevier, Amsterdam, 2001.

23 L. Glass and M. C. MacKey. *From Clocks to Chaos: the rhythms of life.* Princeton University Press, Princeton, NJ, 1988.

24 G. Goddar. Development of epileptic seizures through brain stimulation at low intensity. *Nature*, 214:1020–1021, 1967.

25 E. R. Grannan, D. Kleinfeld, and H. Sompolinsky. Stimulus-dependent synchronization of neuronal assemblies. *Neural Comp.*, 4:550–569, 1993.

26 R. Guttman, S. Lewis, and J. Rinzel. Control of repetitive firing in squid axon membrane as a model for a neurone oscillator. *J. Physiol. (London)*, 305:377–395, 1980.

27 H. Haken. *Advanced Synergetics.* Springer, Berlin, 1983.

28 D. Hansel, G. Mato, and C. Meunier. Phase dynamics of weakly coupled Hodgkin-Huxley neurons. *Europhys. Lett.*, 23:367–372, 1993.

29 C. Hauptmann, O. Popovych, and P. A. Tass. Delayed feedback control of synchronization in locally coupled neuronal networks. *Neurocomputing*, 65/66:759–767, 2005.

30 C. Hauptmann, O. Popovych, and P. A. Tass. Effectively desynchronizing deep brain stimulation based on a coordinated delayed feedback stimulation via several sites: a computational study. *Biol. Cybern.*, 93:463–470, 2005.

31 C. Hauptmann, O. Popovych, and P. A. Tass. Multisite coordinated delayed feedback for an effective desynchronization of neuronal networks. *Stoch. Dynam.*, 5(2):307–319, 2005.

32 C. Hauptmann and P. A. Tass. Therapeutic rewiring by means of desynchronizing brain stimulation. *Biosystems*, 89:173–181, 2007.

33 D. O. Hebb. *The Organization of Behavior.* Wiley, New York, 1949.

34 G. Heimer, M. Rivlin, Z. Israel, and H. Bergman. Synchronizing activity of basal ganglia and pathophysiology of Parkinsons disease. *J. Neural. Transm. Suppl.*, 70:17–20, 2006.

35 W. Just, S. Popovich, A. Amann, N. Baba, and E. Schöll. Improvement of time delayed feedback control by periodic modulation: Analytical theory of floquet mode control scheme. *Phys. Rev. E*, 67:026222, 2003.

36 A. Kepecs, M. C. W. van Rossum, S. Song, and J. Tagner. Spike-timing-dependent plasticity: common themes and divergent vistas. *Biol. Cybern.*, 87:446–458, 2002.

37 M. P. Kilgard and M. M. Merzenich. Cortical map reorganization enabled by nucleus basalis activity. *Science*, 279:1714–1718, 1998.

38 S. Kim, S. H. Park, and C. S. Ryu. Multistability in coupled oscillator systems with time delay. *Phys. Rev. Lett.*, 79:2911–2914, 1997.

39 Y. Kuramoto. *Chemical oscillations, waves, and turbulence.* Springer, Berlin, Heidelberg, New York, 1984.

40 Yu A. Kuznetsov. *Elements of applied bifurcation theory.* Springer, New York, 1998.

41 F. A. Lenz, H. C. Kwan, R. L. Martin, R. R. Tasker, J. O. Dostrovsky, and Y. E. Lenz. Single unit analysis of the human ventral thalamic nuclear group. Tremor-related activity in functionally identified cells. *Brain*, 117:531–543, 1994.

42 P. Limousin, J. D. Speelman, F. Gielen, and M. Janssens. Multicentre European study of thalamic stimulation in parkinsonian and essential tremor. *J. Neurol. Neurosurg. Psychiatry*, 66:289–296, 1999.

43 R. Llinás and H. Jahnsen. Electrophysiology of mammalian thalamic neurons in vitro. *Nature*, 297:406–408, 1982.

44 J. C. Magee and D. Johnston. A synaptically controlled, associative signal for hebbian plasticity in hippocampal neurons. *Science*, 275:209–213, 1997.

45 E. Marder and R. L. Calabrese. Roles of rhythmic motor pattern generation. *Physiol. Rev.*, 76(3):687–717, 1996.

46 H. Markram, J. Lübke, M. Frotscher, and B. Sakmann. Regulation of synaptic efficacy by coincidence of postsynaptic APs and EPSPs. *Science*, 275:213–215, 1997.

47 P. C. Matthews and S. H. Strogatz. Phase diagram for the collective behavior of limit-cycle oscillators. *Phys. Rev. Lett.*, 65:1701–1704, 1990.

48 C. C. McIntyre, M. Savasta, L. Kerkerian-Le Goff, and J. L. Vitek. Uncovering the mechanism(s) of action of deep brain stimulation: activation, inhibition, or both. *Clin. Neurophysiol.*, 115(6):1239–1248, 2004.

49 R. E. Mirollo and S. H. Strogatz. Synchronization of pulse-coupled biological oscillators. *SIAM J. Appl. Math.*, 50:1645–1662, 1990.

50 K. Morimoto, M. Fahnestock, and R. Racine. Kindling and status epilepticus models of epilepsy: rewiring the brain. *Prog. Neurobiol.*, 73:1–60, 2005.

51 A. Nini, A. Feingold, H. Slovin, and H. Bergmann. Neurons in the globus pallidus do not show correlated activity in the normal monkey, but phase-locked oscillations appear in the MPTP model of parkinsonism. *J. Neurophysiol.*, 74:1800–1805, 1995.

52 D. Pare, R. Curro'Dossi, and M. Steriade. Neuronal basis of the parkinsonian resting tremor: A hypothesis and its implications for treatment. *Neurosci.*, 35:217–226, 1990.

53 J. P. Pfister and W. Gerstner. Triplets of spikes in a model of spike timing-dependent plasticity. *J. Neurosci.*, 26:9673–9682, 2006.

54 A. Pikovsky, M. Rosenblum, and J. Kurths. *Synchronization, a universal concept in nonlinear sciences*. Cambridge University Press, Cambridge, 2001.

55 A. Pikovsky and S. Ruffo. Finite-size effects in a population of interacting oscillators. *Phys. Rev. E*, 59(2):1633–1636, 1999.

56 V. Pliss. Principal reduction in the theory of stability of motion. *Izv. Akad. Nauk SSSR Math. Ser.*, 28:1297–1324, 1964.

57 O. V. Popovych, C. Hauptmann, and P. A. Tass. Effective desynchronization by nonlinear delayed feedback. *Phys. Rev. Lett.*, 94:164102, 2005.

58 O. V. Popovych, C. Hauptmann, and P. A. Tass. Control of neuronal synchrony by nonlinear delayed feedback. *Biol. Cybern.*, 95:69–85, 2006.

59 O. V. Popovych, C. Hauptmann, and P. A. Tass. Desynchronization and decoupling of interacting oscillators by nonlinear delayed feedback. *Int. J. Bif. Chaos*, 16(7):1977–1987, 2006.

60 K. Pyragas. Continuous control of chaos by self-controlling feedback. *Phys. Lett. A*, 170:421–428, 1992.

61 K. Pyragas. Control of chaos via an unstable delayed feedback controller. *Phys. Rev. Lett.*, 86(11):2265–2268, 2001.

62 D. V. Ramana Reddy, A. Sen, and G. L. Johnston. Time delay induced death in coupled limit cycle oscillators. *Phys. Rev. Lett.*, 80:5109–5112, 1998.

63 M. Rivlin-Etzion, O. Marmor, G. Heimer, A. Raz, A. Nini, and H. Bergman. Basal ganglia oscillations and pathophysiology of movement disorders. *Curr. Opin. Neurobiol.*, 16(6):629–637, 2006.

64 M. G. Rosenblum and A. S. Pikovsky. Controlling synchronization in an ensemble of globally coupled oscillators. *Phys. Rev. Lett.*, 92:114102, 2004.

65 M. G. Rosenblum and A. S. Pikovsky. Delayed feedback control of collective synchrony: An approach to suppression of pathological brain rhythms. *Phys. Rev. E*, 70:041904, 2004.

66 F. Rubino. Gait disorders. *Neurologist*, 8(4):254–262, 2002.

67 H. G. Schuster and P. Wagner. Mutual entrainment of two limit cycle oscillators with time delayed coupling. *Prog. Theor. Phys.*, 81:939–945, 1989.

68 P. R. Schuurman, D. A. Bosch, P. M. Bossuyt, G. J. Bonsel, E. J. van Someren, R. M. de Bie, M. P. Merkus, and J. D. Speelman. A comparison of continuous thalamic stimulation and thalamotomy for suppression of severe tremor. *N. Engl. J. Med.*, 342:461–468, 2000.

69 W. Singer and C. M. Gray. Visual feature integration and the temporal correlation hypothesis. *Annu. Rev. Neurosci.*, 18:555–586, 1995.

70 J. E. S. Socolar, D. W. Sukow, and D. J. Gauthier. Stabilizing unstable periodic

orbits in fast dynamical systems. *Phys. Rev. E*, 50(4):3245–3248, 1994.

71 S. Song, K. D. Miller, and L. F. Abbott. Competitive hebian learning through spike-timing-dependent synaptic plasticity. *Nature Neurosci.*, 3(9):919–926, 2000.

72 E. Speckmann and C. Elger. The neurophysiological basis of epileptic activity: a condensed overview. *Epilepsy Res. Suppl.*, 2:1–7, 1991.

73 M. Steriade, E. G. Jones, and R. R. Llinas. *Thalamic oscillations and signaling.* Wiley, New York, 1990.

74 P. A. Tass. Phase resetting associated with changes of burst shape. *J. Biol. Phys.*, 22:125–155, 1996.

75 P. A. Tass. Resetting biological oscillators – a stochastic approach. *J. Biol. Phys.*, 22:27–64, 1996.

76 P. A. Tass. *Phase resetting in medicine and biology: stochastic modelling and data analysis.* Springer, Berlin, 1999.

77 P. A. Tass. Desynchronizing double-pulse phase resetting and application to deep brain stimulation. *Biol. Cybern.*, 85:343–354, 2001.

78 P. A. Tass. Effective desynchronization by means of double-pulse phase resetting. *Europhys. Lett.*, 53:15–21, 2001.

79 P. A. Tass. Effective desynchronization with a resetting pulse train followed by a single pulse. *Europhys. Lett.*, 55:171–177, 2001.

80 P. A. Tass. Desynchronization of brain rhythms with soft phase-resetting techniques. *Biol. Cybern.*, 87:102–115, 2002.

81 P. A. Tass. Effective desynchronization with a stimulation technique based on soft phase resetting. *Europhys. Lett.*, 57:164–170, 2002.

82 P. A. Tass. Effective desynchronization with bipolar double-pulse stimulation. *Phys. Rev. E*, 66:036226, 2002.

83 P. A. Tass. Stimulus-locked transient phase dynamics, synchronization and desynchronization of two oscillators. *Europhys. Lett.*, 59(2):199–205, 2002.

84 P. A. Tass. Desynchronization by means of a coordinated reset of neural subpopulations – a novel technique for demand-controlled deep brain stimulation. *Prog. Theor. Phys. Suppl.*, 150:281–296, 2003.

85 P. A. Tass. A model of desynchronizing deep brain stimulation with a demand-controlled coordinated reset of neural subpopulations. *Biol. Cybern.*, 89:81–88, 2003.

86 P. A. Tass. Stochastic phase resetting of two coupled phase oscillators stimulated at different times. *Phys. Rev. E*, 67:051902, 2003.

87 P. A. Tass, C. Hauptmann, and O. V. Popovych. Development of therapeutic brain stimulation techniques with methods from nonlinear dynamics and statistical physics. *Int. J. Bif. Chaos*, 16(7):1889–1911, 2006.

88 P. A. Tass and M. Majtanik. Long-term anti-kindling effects of desynchronizing brain stimulation: a theoretical study. *Biol. Cybern.*, 94(1):58–66, 2006.

89 P. A. Tass, M. G. Rosenblum, J. Weule, J. Kurths, A. Pikovsky, J. Volkmann, A. Schnitzler, and H.-J. Freund. Detection of $n:m$ phase locking from noisy data: Application to magnetoencephalography. *Phys. Rev. Lett.*, 81:3291–3294, 1998.

90 P. A. Tass and C. Hauptmann. Long-term anti-kindling effects induced by short-term, weak desynchronizing stimulation. *Nonlin. Phenom. Complex Syst.*, 9:298–312, 2006.

91 P. A. Tass and C. Hauptmann. Therapeutic modulation of synaptic connectivity with desynchronizing brain stimulation. *Int. J. Psychophysiol.*, 64:53–61, 2007.

92 P. J. Uhlhaas and W. Singer. Neural synchrony in brain disorders: relevance for cognitive dysfunctions and pathophysiology. *Neuron*, 52(1):155–168, 2006.

93 J. L. van Hemmen. Theory of synaptic plasticity. In F. Moss and S. Gielen, editors, *Handbook of Biological Physics, Vol. 4*, pages 771–823. Elsevier, Amsterdam, 2001.

94 G. D. VanWiggeren and R. Roy. Communication with chaotic lasers. *Science*, 279(5354):1198–1200, 1998.

95 J. Volkmann. Deep brain stimulation for the treatment of Parkinson's disease. *J. Clin. Neurophysiol.*, 21:6–17, 2004.

96 J. Volkmann, M. Joliot, A. Mogilner, A. A. Ioannides, F. Lado, E. Fazzini, U. Ribary, and R. Llinás. Central motor loop

oscillations in parkinsonian resting tremor revealed by magnetoencephalography. *Neurology*, 46:1359–1370, 1996.

97 E. von Holst. Über den Prozess der zentralnervösen Koordination. *Pflüg. Arch.*, 236:149–158, 1935.

98 A. T. Winfree. An integrated view of the resetting of a circadian clock. *J. Theor. Biol.*, 28:327–374, 1970.

99 A. T. Winfree. *The geometry of biological time.* Springer, Berlin, 1980.

100 G. M. Wittenberg and S. S. H. Wang. Malleability of spike-timing-dependent plasticity at the CA3-CA1 synapse. *J. Neuroscience*, 26:6610–6617, 2006.

101 J. Wolfart, D. Debay, G. Le Masson, A. Destexhe, and T. Bal. Synaptic background activity controls spike transfer from thalamus to cortex. *Nature Neurosci.*, 8:1760–1767, 2005.

102 A. Wunderlin and H. Haken. Scaling theory for nonequilibrium systems. *Z. Phys. B*, 21:393–401, 1975.

103 M. K. S. Yeung and S. H. Strogatz. Time delay in the Kuramoto model of coupled oscillators. *Phys. Rev. Lett.*, 82:648–651, 1999.

104 Q. Zhou, H. W. Tao, and M. M. Poo. Reversal and stabilization of synaptic modifications in a developing visual system. *Science*, 300:1953–1957, 2003.

31
Control of Cardiac Electrical Nonlinear Dynamics

Trine Krogh-Madsen, Peter N. Jordan, and David J. Christini

31.1
Introduction

The heart is a very complex and highly nonlinear system. Its predominant role is to function as a mechanical pump for the circulatory system. To do so, at each heart beat, the cells of the heart are stimulated by a typical propagation sequence of electrical activity. Disruption of this electrical pattern may lead to cardiac arrhythmias.

Despite the complexity of the heart, its electrical behavior can be studied using a variety of experimental and clinical techniques, and can be modeled mathematically using relatively simple systems of nonlinear differential equations. While these approaches have in recent years allowed great headway into understanding the dynamical behavior of the heart, cardiac arrhythmias such as ventricular fibrillation still claim the lives of hundreds of thousands of people each year in the United States alone [1]. Bridging the gap between understanding the mechanistic bases of arrhythmias and applying such knowledge to improve therapy presents one of the greatest challenges in the field of cardiac electrophysiology.

This chapter describes recent progress in attempting to control certain cardiac arrhythmias. In Sections 31.2 and 31.3 we give an introduction to cardiac electrophysiology and cardiac arrhythmias. A discussion on current therapies and their limitations is presented in Section 31.4. In Section 31.5, we describe recent advances toward controlling a certain type of abnormal heart rhythm called electrical alternans, which may act as a precursor for more complex and potentially lethal arrhythmias. Finally, in Section 31.6, we present recent progress in control of these more complex arrhythmias themselves. It is worth noting that chapter 32 by S. Sinha and S. Sridhar ("Controlling Spatiotemporal Chaos and Spiral Turbulence in Excitable Media") in this volume deals more specifically with control of cardiac fibrillation.

31.2
Cardiac Electrophysiology

Efficient pumping of blood throughout the body requires that the heart musculature contracts in a coordinated manner. Given that the contraction of individual myocytes is driven by electrical excitation (through a process known as excitation–contraction coupling [7]), coordinated cardiac contraction requires that different regions of the heart be electrically activated in a specific sequence. This sequential activation is facilitated by the anatomical arrangement of the heart into distinct but contiguous regions whose electrophysiological properties are markedly different [53]. Figure 31.1 illustrates the normal conduction system. A normal sequence is initiated in the natural pacemaker of the heart (the so-called sinoatrial (SA) node) when the transmembrane voltage of cells transiently increases, then decreases, over a time course of a few hundred milliseconds. This voltage change is known as an action potential. Because the SA nodal region is electrically coupled to the right atrium, activation of the SA node causes a wave of activation to spread throughout the atria. Electrical activation of the atria is soon followed by mechanical contraction of the atria.

Electrical excitation of the atria leads to activation of the atrioventricular (AV) node, the anatomical location of which is indicated in Fig. 31.1. In anatomically
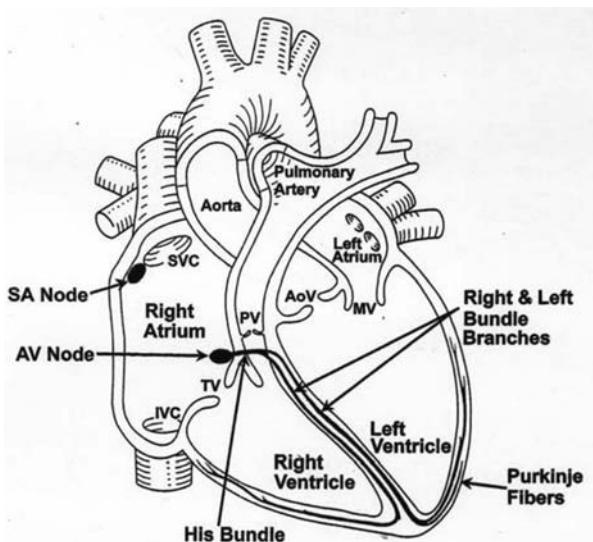
Fig. 31.1 A schematic diagram of the anatomical layout of the heart. The diagram illustrates a number of the major electrophysiological components of the heart, including the SA and AV nodes and the His-Purkinje system. PV: pulmonary vein, MV: mitral valve, TV: tricuspid valve, AoV: aortic valve, SVC: superior vena cava, IVC: inferior vena cava (reproduced from [40] with permission).

normal hearts, the AV node provides the only electrical connection between the atria and ventricles. The activation of the AV node leads to the subsequent excitation of the bundle of His, the left and right bundle branches, and the Purkinje fibers. Branches of the His-Purkinje system radiate throughout the ventricular tissue, and thus excitation of the His-Purkinje system leads to the excitation and subsequent contraction of the ventricles. The electrophysiological properties and anatomical layout of the AV node and His-Purkinje conduction system ensure that sufficient time exists for blood to flow from the atria to the ventricles before the ventricles contract. Ventricular contraction forcefully propels oxygenated blood from the left ventricle into the aorta and the systemic circulation, and deoxygenated blood from the right ventricle into the pulmonary artery and the pulmonary circulation (Fig. 31.1).

31.2.1
Restitution and Alternans

At the cellular level, the action potential is generated by the diffusion of ions through specialized channels in the cell membrane. The conductance of the membrane to the various ions present in the body varies as the channels open and close. This opening and closing generally depends nonlinearly on transmembrane potential and on time. One consequence of this is the phenomenon of restitution. Restitution is generally quantified by the restitution curve, which is a functional representation of the duration of an action potential (APD) versus the preceding rest period (the diastolic interval, or DI). An example is shown in Fig. 31.2. Such a curve reduces the high-dimensional dynamics of the cardiac cell to a simple one-dimensional approximation, expressed mathematically as the discrete map equation $\mathrm{APD}_{n+1} = f(\mathrm{DI}_n)$.
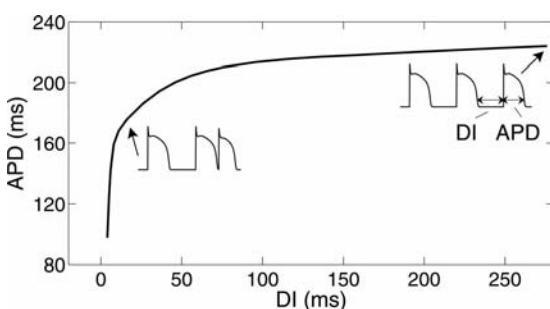
Fig. 31.2 A typical action potential duration (APD) restitution curve, generated with the Shiferaw et al. model [54] of a ventricular cell. To generate the APD restitution curve, a train of action potentials are stimulated at a constant pacing rate, followed by one premature stimulus. Thus, the diastolic interval (DI) following the penultimate action potential is varied, and the duration of the resulting action potential is plotted as a function of the preceding DI. As the action potentials in the insets demonstrate, APD shortens as DI is shortened, leading to a restitution curve with the general shape as shown.
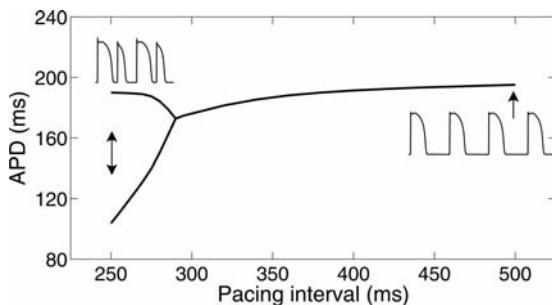
Fig. 31.3 Action potential duration bifurcation diagram, generated with the Shiferaw et al. model [54] in a one-dimensional cable. When pacing at a relatively slow rate, identical action potentials occur each time a stimulus is applied (i.e., 1:1 behavior). However, increasing the pacing rate causes the action potential behavior to bifurcate, such that for every two stimuli, two different action potentials occur (i.e., 2:2 behavior).

The APD restitution curve is generally a monotonically increasing function as shown in Fig. 31.2. This reflects the fact that if a cell is allowed less time to recover before being excited, its action potential will be shorter. During constant pacing, a stable period 1 solution usually occurs, where each APD (and DI) is the same as the previous APD (or DI). Thus, for each stimulus input there is one APD; this is typically known as a 1:1 response.

In many cells, however, a critical stimulation rate exists at which a bifurcation to a qualitatively different behavior occurs [29, 43]. When paced faster than this critical rate, a stable period-2 behavior occurs, during which the action potential duration alternates on a beat-to-beat basis and returns to a given state after every two periods (i.e., after two action potentials) instead of after one, as shown in Fig. 31.3. That is, during alternans, there is a 2:2 response – two action potentials of different duration occur for every two periodic stimuli. The particular excitation rate at which the action potential activity in a given cell bifurcates to alternans is dependent upon the membrane currents and intracellular regulatory mechanisms operating in that cell.

Our interest in alternans resides in the role of alternans as a precursor, or even as a trigger event, for more complex and potentially fatal cardiac arrhythmias. The details of the implications of APD alternans for ventricular arrhythmias will be discussed in Section 31.3.3, while research toward controlling alternans is discussed in Section 31.5.

31.3
Cardiac Arrhythmias

The normal (sinus) rhythm of cardiac activation described in Section 31.2 can be disrupted in many ways leading to very different types of cardiac arrhythmias. Arrhythmias may range from benign, to debilitating, to fatal. Some occur

as a consequence of chronic heart disease while others may be triggered in healthy hearts.

Two of the most commonly occurring and potentially lethal cardiac arrhythmias are ventricular tachycardia and ventricular fibrillation. Ventricular fibrillation is thought to be the arrhythmia typically underlying sudden cardiac death. Mainly because of their severity, much of the current research on arrhythmia control has focused on these arrhythmias.

Ventricular tachycardia and ventricular fibrillation are both so-called reentrant arrhythmias. In this section, we briefly describe these arrhythmias and discuss how they may arise.

31.3.1
Reentry

Reentrant arrhythmias occur when tissue is repeatedly activated by an activation wave that again and again reenters the same anatomical region and reactivates it. A simple model of reentry is the closed ring, shown in Fig. 31.4 A, where the activation wavefront rotates around an anatomical obstacle (e.g., scar tissue or a valve). This type of reentry can be identified by the following characteristics: (1) an area of unidirectional conduction block must exist at the time of reentry initiation, causing the activation wavefront to move in one direction only around the ring; (2) the activation wavefront must move around an anatomically distinct pathway, returning to its point of origin and then following the same path again; and (3) interruption of the reentrant circuit at any point along its path should terminate the circus movement. For a given closed circuit to form a reentrant ring, the rotation time around the ring must be longer than the recovery period of all segments of the circuit.

In the absence of an anatomical obstacle, it is still possible for circus movement reentry to occur. In such a situation, the activation wavefront rotates around a region that may be anatomically continuous, but which is functionally discontinuous. Such a situation occurs in the leading-circle/figure-of-eight/
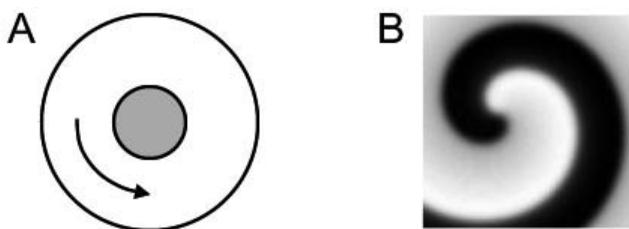
Fig. 31.4 Schematic illustration of anatomical (A) and functional (B) reentry. In anatomical reentry a wave cycles around an anatomical obstacle, while functional reentry may occur in completely homogeneous tissue, when a functional discontinuity at the tip of a spiral wave serves as a pivot point. Spiral waves may also become anchored to obstacles, causing anatomical reentry.

spiral-wave models of reentrant arrhythmias [4], where a functional discontinuity (instead of an anatomical discontinuity) serves as a pivot point about which the activation wave rotates. The functional discontinuity can be created by a region of depressed excitability (from residual or sustained refractoriness), or, in the case of spiral waves (Fig. 31.4(B)), by the high degree of curvature of the activation wavefront at the pivot point [5].

31.3.2
Ventricular Tachyarrhythmias

Some ventricular tachycardias are associated with the existence of a single reentrant circuit. This rhythm may terminate spontaneously if, for example, the wavefront catches up to the tail, or if the reentrant activity is disrupted by a different wavefront, for example one originating from the SA node. Alternatively, the reentrant circuit may destabilize and the reentrant wave may break up into multiple waves that can propagate into different regions of the ventricles. This can lead to the highly disorganized state of ventricular fibrillation.

While ventricular tachycardia can lead to excessively rapid contraction, potentially causing a reduction in the efficiency with which blood is pumped throughout the body, ventricular fibrillation leads to uncoordinated contraction and a drastic reduction in blood flow around the body. Unless defibrillation restores normal ventricular activation patterns within a few minutes of the onset of the arrhythmia, ventricular fibrillation invariably leads to death.

31.3.3
Alternans as an Arrhythmia Trigger

Initiation of ventricular tachyarrhythmias is sometimes preceded by the occurrence of alternans. As outlined below, it is possible that alternans actually causes the onset of some arrhythmias.

In tissue, alternans may occur in different spatial patterns. One type of pattern is spatially concordant alternans, where the tissue everywhere exhibits a long action potential on one beat and everywhere a short action potential on the next beat. A second type of pattern is spatially discordant alternans, where (at least) one region is out of phase and exhibits a long action potential, while for the same beat another region exhibits a short action potential. Discordant alternans may arise even in spatially homogeneous tissue, due to dynamically induced spatial variations in the conduction velocity of the propagating waves.

Discordant alternans may initiate arrhythmias through unidirectional block, which can occur when a propagating wave enters a region where a long action potential has left the tissue with too little recovery time for the wave to propagate further, while a neighboring region having had an action potential of shorter duration allows for propagation. Evidence of causality between alternans and the onset of arrhythmias has been demonstrated in experiments [10, 24, 46] and in computer simulations [24, 38, 48].

31.4
Current Treatment of Arrhythmias

Cardiac arrhythmias are currently treated using one or more of the following strategies: pharmacological treatment, implantable devices, and ablation therapy. For more details on the treatments described below, refer to [37].

31.4.1
Pharmacological Treatment

Despite a number of large clinical trials investigating the influence of an array of putative antiarrhythmic drugs, to date, only one class of drugs, β-blockers, which inhibit sympathetic nervous stimulation, have been demonstrated to be effective in preventing sudden cardiac death [33]. Some agents that block ion-specific channels have been tested in clinical trials, but they have either been proven ineffective or, worse, they have paradoxically increased mortality [59, 60]. These findings have made safety a key consideration in the development of new drugs, cardiac and otherwise, to the point where all new drugs are evaluated for inducing prolongation of the QT interval on the electrocardiogram, the most common adverse side effect. Recently, ACE inhibitors, which have long been the gold standard in treatment of high blood pressure, have shown promising results in terms of reducing the risk of sudden cardiac death [20].

Because of the limitations of current antiarrhythmic drugs, a recent book on the pharmacological treatment of cardiac arrhythmias states that the first principle of treating arrhythmias is to "avoid using antiarrhythmic drugs whenever possible" [22]. Consistent with this view, there has been an ongoing shift in emphasis in the therapies for ventricular arrhythmias, from pharmacological to nonpharmacological approaches [56]. Implantable devices (such as implantable cardioverter defibrillators) and ablative therapies have now become the therapies of choice for many patients, reflecting the demonstrated efficacy of these approaches and the recognition of the inherent risks, particularly the proarrhythmic effects, associated with long-term antiarrhythmic drug use [51].

31.4.2
Implantable Cardioverter Defibrillators

While pharmacological treatment is sometimes useful for preventing tachyarrhythmias from occurring, implantable cardioverter defibrillators (ICDs) attempt to terminate tachyarrhythmias once they have initiated. In 2003, an estimated 150,000 defibrillators were implanted in patients in the United States, with that number expected to increase in the coming years [35].

The first task of the ICD is to detect tachyarrhythmias. This is accomplished by the microprocessor, which continuously analyzes the recorded signals to determine whether an arrhythmia is occurring. Because mistakes can be deadly (in the case of a missed arrhythmia) or painful (in the case of a nonpathological

rhythm identified as a ventricular arrhythmia such that a defibrillation shock is delivered to a conscious patient), devices typically employ a combination of complementary detection techniques which examine such variables as rate, morphology, onset, regularity, and relationship of atrial and ventricular activity. Extensive research into such electrocardiogram processing techniques has greatly improved the accuracy of detection algorithms.

Once a tachyarrhythmia is detected, a suitable therapy must be delivered. The first therapeutic modality is antitachycardia pacing, which applies one or more series of suprathreshold (but not large enough to be perceptible to the patient) stimuli. Antitachycardia pacing is typically attempted for ventricular tachyarrhythmias exhibiting rates of up to 200–220 beats/minute [42] and aims to force a stimulated wave into the reentrant circuit to collide with and extinguish the reentrant wave. It was recently reported that antitachycardia pacing was effective in terminating 90% of ventricular tachyarrhythmias on which it was attempted [52].

High-energy defibrillation shocks are delivered when antitachycardia pacing fails or as primary therapy when arrhythmias such as ventricular fibrillation are detected. The defibrillation discharge typically occurs along multiple vectors, such as one defibrillation coil to another, or one defibrillation coil to the pulse generator. This approach helps ensure adequate "coverage" of the fibrillating myocardium.

Although ICDs are highly effective devices, they do have certain limitations. Up to one-third of defibrillation shocks are given at inappropriate times [6, 19, 57]. These inappropriate shocks can cause intense pain and chronic anxiety. In addition, the large shocks drain the battery of the ICD, thereby shortening the device lifetime. Improved detection algorithms may prevent unnecessary shocks from being delivered, but from the standpoint of survival, the results of a false-positive detection are likely to be far less detrimental than the results of a false-negative detection [34].

31.4.3
Ablation Therapy

Some arrhythmias can arise from a localized, abnormal region of cardiac tissue. In addition, reentrant tachyarrhythmias may require one or more critical anatomical regions of abnormal excitability or propagation to be sustained. Recognizing this fact, ablation of viable tissue in such a region can be used to treat some arrhythmias. With this technique, radiofrequency energy destroys tissue by resistive heating that creates a nonviable lesion.

Perhaps the most difficult aspect of radiofrequency catheter ablation is localization of the correct ablation site. Furthermore, especially for reentrant tachyarrhythmias, it is often necessary to reposition the catheter multiple times near the site to achieve an adequate scar, as radiofrequency lesions are relatively small in diameter and depth. The lack of depth also makes radiofrequency ablation ineffective in those situations where the abnormal region is situated well within the myocardium. This is more often the case in the ventricles than in

the atria, because of the thickness of the ventricular wall. In contrast, the much thinner atrial wall makes radiofrequency ablation useful for treatment of many atrial arrhythmias.

31.5
Alternans Control

While the ICD has been highly successful in saving lives, it has some inherent disadvantages, as discussed above. Antitachycardia pacing sometimes fails, in which case the ICD reverts to its high-energy defibrillation mode. Furthermore, defibrillation is not always successful. Hence, a preferable strategy would be a device that prevents tachyarrhythmias from occurring in the first place, by recognizing and stopping precursor events using small amplitude electrical stimuli. Control of APD alternans is one such strategy currently under investigation.

31.5.1
Controlling Cellular Alternans

Recent research has suggested that control algorithms targeted at cardiac alternans could potentially lead to an improvement in the therapeutic efficacy of implantable devices such as ICDs.

Most of this work is based on model independent, adaptive control algorithms, e.g., delayed-feedback control (DFC). In this method, which is based on the Ott-Grebogi-Yorke (OGY) [44] technique for chaos control, small perturbations are applied to the timing of the next excitation in an attempt to force the state of the system toward the (unstable) period-1 fixed point. Unlike chaos control techniques, DFC algorithms do not require a learning stage (i.e., learning the dynamics in the neighborhood of the unstable period-1 solution). This is important, because during alternans, the dynamics evolve far from the period-1 dynamics (unless the alternans amplitude is very small). Delayed-feedback control (DFC) algorithms typically require (i) knowledge of the state of the system for a very short time history, and (ii) a basic understanding of the system dynamics to ensure that the control perturbations are of the proper magnitude and polarity. These two elements allow the periodic rhythm to be stabilized by repeated adjustment of the stimulation time.

Let BCL (basic cycle length) be the time interval between two stimulations. A typical DFC algorithm for alternans control is:

$$\mathrm{BCL}_{n+1} = \begin{cases} \mathrm{BCL}^\star & \text{for} & \Delta\mathrm{BCL}_{n+1} > 0, \\ \mathrm{BCL}^\star + \Delta\mathrm{BCL}_{n+1} & \text{for} & \Delta\mathrm{BCL}_{n+1} \leq 0, \end{cases} \qquad (31.1)$$

with

$$\Delta\mathrm{BCL}_{n+1} = \frac{\gamma}{2}(\mathrm{APD}_{n+1} - \mathrm{APD}_n), \qquad (31.2)$$
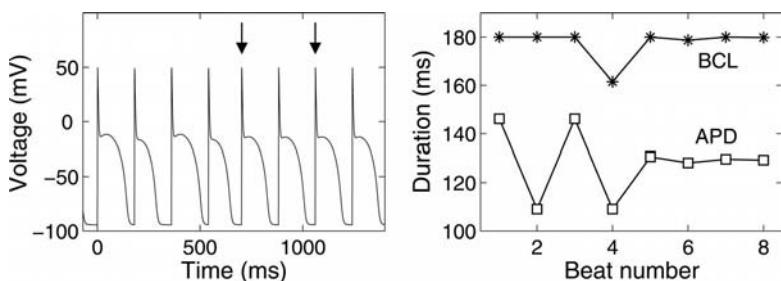
Fig. 31.5 Action potential duration (APD) alternans control in the Fox et al. model of the canine ventricular action potential [23]. Alternans is induced by rapid pacing at a basic cycle length (BCL) of 180 ms. Delayed-feedback control (DFC) is turned on after the first four action potentials. DFC works by shortening the BCL of the cycles with short APDs by delivering premature stimuli (arrows), thereby shortening the recovery interval and hence also shortening the subsequent APD. The value of the feedback gain (γ) is 1.0.

where γ is the feedback gain and BCL* is the nominal BCL. The restriction that a perturbation is only given to shorten, and not delay, the intrinsic rhythm reflects the fact that, in the heart, it is often not possible to delay the excitation: it will occur naturally without stimulation. Thus, this algorithm is said to be restricted. Both unrestricted DFC algorithms (which allow both lengthening and shortening of the BCL during control) and restricted DFC algorithms have been applied to cardiac rhythm disturbances.

An example of alternans control in a mathematical model is shown in Fig. 31.5. Essentially, the restricted algorithm works by shortening the long DI by giving a premature stimulation. This in turn shortens the long APD due to restitution, as described in Section 31.2.1. Eventually, the unstable period-1 solution is stabilized and action potentials of constant duration are established. The rate of convergence is controlled by the feedback gain.

DFC has been used experimentally to control APD alternans in small pieces (i.e., sufficiently small to be point like) of bullfrog hearts [30]. Provided that the feedback gain was within an appropriate range of values, the period-2 alternans rhythm was successfully controlled to the underlying unstable period-1 rhythm.

DFC algorithms have also been used to control a related type of alternans (atrioventricular (AV) nodal conduction alternans; a beat-to-beat alternation in the conduction time through the AV node) [12, 16, 32]. To date, AV node alternans control is the only alternans control study performed on human subjects [16].

31.5.2
Control of Alternans in Tissue

While APD alternans could be successfully eliminated in a system that does not have spatiotemporally varying repolarization and wave-propagation dynamics (the frog sections in [30] were small enough that there were no apparent spatial

variation in dynamics), research on how to control APD alternans in spatially extended systems (i.e., tissue rather than cells) is still in its infancy.

The utility of adaptive control algorithms for terminating potentially dangerous rhythms such as APD alternans will only become obvious once further research is conducted into the effectiveness of such algorithms in controlling arrhythmias spatially as well as temporally. Initial analytical work as well as computer simulations of one-dimensional fibers suggest that only in the case of spatially uniform APD alternans can alternans be terminated along the whole fiber. In cases where concordant alternans show variation in space, as well as in the more extreme cases of spatially discordant alternans, eliminating APD alternans at one site will result in APD alternans being eliminated only up to a short distance away from this stimulation site [21, 49].

Recent experiments in canine Purkinje fibers qualitatively confirm these predictions [15]. Interestingly, these experiments also showed that APD alternans of relatively small amplitude could be controlled over larger distances. Thus if one can detect the early onset of small amplitude APD alternans, control should be more easily achieved. In addition, these experiments showed that discordant alternans could be converted to concordant alternans. Since discordant alternans pose a larger risk of inducing tachyarrhythmias than concordant alternans, this finding is quite intriguing.

To date, there have been no experimental studies of the actual distance over which DFC control algorithms suppress alternans in ventricular tissue. If the distance is short, such that multiple stimulation sites are necessary in order to simultaneously suppress APD alternans in different regions of the heart, a cardiac device that fits snugly around the ventricles, perhaps similar to one (the CorCap^{TM}Cardiac Support Device, by Acorn Cardiovascular) that is now in clinical trials as a therapy for heart failure [45] could potentially be developed.

Another concern regarding APD alternans control in ventricular tissue is ionic heterogeneity. There are intrinsic differences in ionic properties, such as ion channel densities, in different regions of the ventricles, e.g., across the ventricular wall, between the apex and the base, between the left and the right ventricle, and between the posterior and the septal wall of the left ventricle [62]. At present, it is not known how this may affect the ability to control APD alternans in the ventricles. One thing to keep in mind, though, is that from a clinical point of view it would be beneficial to simply turn discordant alternans into concordant alternans, or to reduce the alternans amplitude. Complete elimination of alternans everywhere in the tissue may not be necessary in order to significantly reduce the risk of tachyarrhythmias.

31.5.3
Limitations of the DFC Algorithm in Alternans Control

In addition to the afore-mentioned complications in tissue, the DFC algorithm has certain more fundamental limitations. When DFC algorithms are used to control periodic rhythms, rapid convergence to the period-1 rhythm is achiev-

able only if the feedback gain (γ) is at or near its optimal value. The optimal value of the feedback constant is a function of the degree of instability of the fixed point [27]. Because estimation of the instability of the fixed point requires that the system state point visit the neighborhood of the fixed point, determination of the optimal feedback constant value during periodic rhythms is difficult. (Algorithms that utilize external perturbations to explore the neighborhood of the period-1 fixed point can sometimes be used to estimate this optimal value [11].) Additionally, not only does convergence rate decrease with increasing distance from the optimal proportionality constant value, but control fails when the proportionality constant lies outside an acceptable range of values. While algorithms that iteratively adapt the feedback constant to achieve control do exist [14, 31], such algorithms can be sensitive to the noise and nonstationarities that are typically present in experiments.

31.5.4
Adaptive DI Control

Although the DFC algorithms have proved effective for controlling APD alternans, an alternative approach that is based solely on cardiac electrophysiological principles has also been developed [36, 47]. This cardiac-specific control algorithm exploits the restitution properties of cardiac tissue to control both periodic and aperiodic rhythm disturbances to a period-1 rhythm, and does not require the dynamics of the system to be learned.

Consider the APD alternans occurring at a basic cycle length BCL* shown in Fig. 31.6. The AP alternates between points A and B on a beat-to-beat basis. Because $APD_n + DI_n = BCL^\star$, DI_n alternates as well. In DI control, alternans can be suppressed by perturbing BCL* on a beat-to-beat basis such that DI_n is kept at a constant target value. Due to the functional dependence of APD_{n+1} on DI_n characterized by the restitution curve, stimulation such that consecutive DIs are identical causes each subsequent AP to converge to a constant repeating morphology.

Similarly to the feedback gain (γ) in the DFC algorithm, the adaptive DI control method makes progressively smaller perturbations to the cycle length. This adaptive DI (ADI) control technique involves selecting an initial target DI and then adjusting this value on a beat-to-beat basis until the sum of the target DI and subsequent APD is equal to the original basic cycle length BCL* (i.e., $DI_n + APD_{n+1} = BCL^\star$). The target DI is adaptively lengthened on a beat-to-beat basis according to the control rule

$$DI_{n+1} = a(BCL^\star - BCL_n) + DI_n, \tag{31.3}$$

where a is a constant between 0 and 1 that controls the rate at which DI_n changes. During ADI control, the difference between the present cycle length (BCL_n) and the original cycle length ($BCL^\star$) is therefore reduced until $BCL_n = BCL^\star$, and the period-1 rhythm will have been established at the origi-
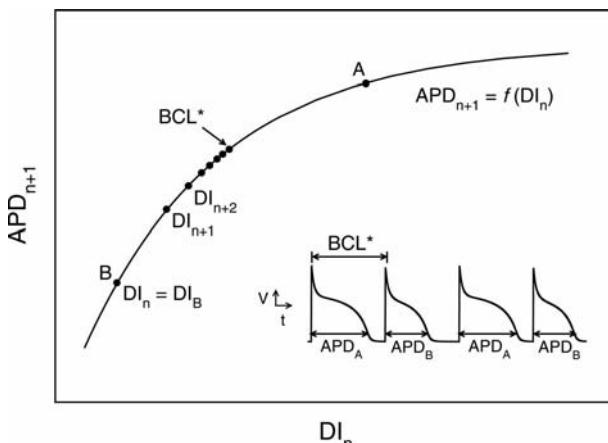
Fig. 31.6 Schematic representation of the DI and adaptive DI (ADI) control schemes. APD initially alternates between points A and B on the restitution curve during stimulation at the basic cycle length BCL*. The inset illustrates the voltage profile of this alternans rhythm prior to the onset of control. Initiation of DI control when $DI_n = DI_B$ makes every subsequent DI equal to DI_B, and hence each subsequent APD will be equal to APD_B. Alternatively, ADI control may also be initiated with the target DI set to DI_B, as $DI_B + APD_B < BCL^*$. The target DI is then lengthened according to the control rule of Eq. (31.3), such that each successive APD climbs up the restitution curve until the cycle length ($DI_n + APD_{n+1}$) is again equal to BCL*.

nal cycle length BCL*. This period-1 rhythm is the same as the unstable period-1 fixed point obtained by existing DFC algorithms. However, as Eq. (31.3) indicates, the ADI control approach is fundamentally different from DFC.

Adaptive DI control has been successful in obtaining control in numerical simulations [36]. However, there are certain limitations to the method. One concern is that DI control is based on the assumption that the AP dynamics is captured by a one-dimensional map. Recent studies have shown that intracellular calcium dynamics contributes to the development of alternans, adding to the complexity of the problem. Indeed, APD alternans may occur even when DI is fixed [17, 63]. Still, the extent to which the restitution assumption fails is under investigation and is likely to vary between cell types and species.

31.6
Control of Ventricular Tachyarrhythmias

Due to its inherent disorganization, ventricular fibrillation is much more difficult to tame with control algorithms than ventricular tachycardia or alternans. Both because antitachycardia pacing (and perhaps alternans control in future devices) sometimes fails, and because fibrillation sometimes occurs directly from sinus rhythm with no apparent warning or trigger, it is critically important

for devices to be able to defibrillate the heart. Much of the work in defibrillation research focuses on reducing the energy requirements for successful defibrillation. Smaller shocks both drain the device battery less and are less painful for the patient.

Since the dynamics of ventricular fibrillation are aperiodic, and perhaps chaotic, one way of reducing the necessary shock strength may be to apply chaos control methods. In pioneering studies, Garfinkel et al. applied OGY-type control algorithms to rabbit ventricle preparations exhibiting aperiodic, possibly chaotic, dynamics [26]. The rhythm was controlled, but to a period-3 rhythm, rather than the desired period-1 rhythm. A later mathematical study demonstrated that such control results may have resulted from mis-estimation of the period-1 rhythm [13]. In another study of aperiodic dynamics, a cardiac-specific control algorithm applied to a simulated chaotic action potential duration time series was successful in controlling the unstable period-1 rhythm at certain excitation rates [61]. Clinical realizations of these defibrillation methods are still speculative, but would almost certainly involve multiple sites for recording and stimulation.

In the remainder of this section, we will focus on termination of ventricular tachycardia. Please refer to the chapter by S. Sinha and S. Sridhar in this volume for defibrillation approaches.

31.6.1
Suppression of Spiral Waves

Because spiral waves are associated with ventricular tachycardia, several methods have been proposed for terminating spiral waves. Some of the methods are aimed at driving the spiral wave out of the tissue by local external forcing [8, 39, 41]. In the heart, the spiral would have to be forced into some nonconductive region.

Other methods have been based on feedback control. In one such simulation study, small stimuli delivered during the repolarization phase of the action potential were effective in preventing a spiral wave with alternans dynamics from breaking up into fibrillatory-like activity [49]. In other simulations, alternans-induced spiral breakup has been prevented by applying a single, well-timed stimulus during the repolarizing phase using a special algorithm based on the eigenmodes of the model equations [3].

The extent to which some of these methods for spiral wave control are feasible as therapeutic strategies remains unclear and requires further study.

31.6.2
Antitachycardia Pacing

As described in Section 31.4.2, the antitachycardia pacing modality of the ICD works quite well in many cases. The ICD is usually programmed to give either a burst of 8–10 electrical stimuli of constant frequency (faster than the reen-

trant rhythm), or a train of 8–10 stimuli with increasing frequency. Since the stimulating electrode is not necessarily situated inside the reentrant loop, it is thought that the earlier stimuli "peel back" refractoriness to allow the subsequent stimuli to enter the reentrant loop and terminate the tachycardia. However, there is no known clear physical mechanism explaining how antitachycardia pacing works in the heart.

A simple model of ventricular tachycardia is a reentrant wave traveling around a one-dimensional ring. In this model, where the stimulus site is necessarily in the reentrant circuit, it is well known how even a single stimulus may terminate the reentrant dynamics. Consider the situation in Fig. 31.7 (A), where reentrant wave is traveling around the ring. If the stimulus is given too soon after the passing of the previous wave when the tissue at the stimulus site is still refractory, the stimulus cannot induce a full action potential and has only very little effect on the reentrant wave (Fig. 31.7 (A)). On the other hand, if the stimulus is given after some delay since the passing of the previous wave, a pair of waves are generated, traveling in opposite directions away from the stimulus site (Fig. 31.7 (C)). The wave traveling in the retrograde direction to the original reentrant wave will collide with and annihilate the original wave. However, the wave traveling in the anterograde direction will continue to circulate, replacing
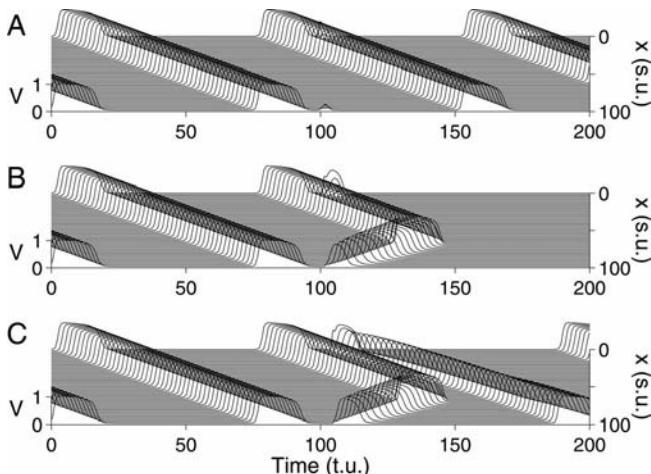
Fig. 31.7 Pacing-induced termination of reentry in a one-dimensional loop of length 100 space units (s.u.). The figure was generated using the Aliev-Panfilov version of the FitzHugh-Nagumo model [2]. The timing of the stimulus (t_s) is varied between the three panels: $t_s = 99$ time units (t.u.) (A), $t_s = 101$ t.u. (B), and $t_s = 104$ t.u. (C). When the stimulus is given too early, it does not generate new waves (A). If the stimulus is given later, two waves are induced traveling in opposite directions on the ring. One wave terminates the original reentry, but the other wave persists, such that a reentry remains (C). In contrast, if the stimulus is given within the so-called vulnerable window, the stimulus-induced wave is unidirectionally blocked and propagates in the retrograde direction only, where it will terminate the original reentry (B).

the original wave. Hence, termination was not successful. Based on continuity arguments, however, there must be an intermediate timing of the stimulus for which the reentry is terminated [28]. This happens when a well-timed stimulus causes the induced wave to be blocked unidirectionally and travel in the retrograde direction only, while the tissue in the anterograde direction is still refractory and does not allow for propagation. The wave induced by the stimulus collides with and terminates the original reentrant wave and termination is successful (Fig. 31.7 (B)).

There are several problems in terms of extrapolating this simple model to the heart. The stimulus has to fall into a narrow time interval (typically a few milliseconds), called the vulnerable window, in order for termination to be successful. In addition, the vulnerable window effectively disappears when the stimulus site is located at some distance away from the ring [55]. Finally, the heart is three dimensional, which gives additional complexities.

Still, promising work is being done in this area. Simulation studies have shown how using a pair, rather than single, stimuli increases the vulnerable window from a few milliseconds to tens of milliseconds by mechanisms other than unidirectional block [18]. Other simulation studies have shown how burst pacing with > 12 stimuli may lead to termination even when the stimulus site is located at some distance from the reentrant loop [9].

Further studies are needed to give a clear physical understanding of the mechanisms of antitachycardia pacing. It is entirely possible that such explanations will point toward new methods for improving therapy.

31.6.3
Unpinning Spiral Waves

Spiral waves associated with ventricular tachycardia are often anchored or pinned to anatomical obstacles in the heart. When pinned, the spiral wave can be very stable and would expected to be difficult to force out of the heart using the methods described in Section 31.6.1.

Simulations studies have shown that it is possible to unpin a spiral from a small obstacle using burst pacing [25]. However, for larger obstacles where the "force of attraction" between the spiral core and the obstacle is greater, it may be necessary to give a stimulus at the obstacle to unpin the spiral. In clinical situations, however, the stimulus electrode is most likely not situated exactly at the obstacle.

One potential way of circumventing this problem is the following: when an electrical field is applied to tissue with an inexcitable obstacle, a so-called virtual electrode is formed, where a region of tissue neighboring one side of the obstacle is depolarized, while a region of tissue neighboring the opposite side is hyperpolarized. If the timing is right, and the depolarization is of sufficient amplitude, a new wave is generated at the obstacle and thus inside the reentrant circuit, and the spiral is unpinned [58]. This method has been tested in preparations from rabbit hearts, where it may be even more effective than classic

antitachycardia pacing [50]. One possible limitation of this method is that the spiral may repin to the same obstacle or a different obstacle.

31.7
Conclusions and Prospects

The concept of using nonlinear dynamical control methods to control aperiodic electrical activity in animal cardiac tissue preparations was shown to be effective a decade and a half ago [26]. However, successful application of such approaches to terminate ventricular fibrillation in human hearts is still lacking. Given that there may be many spiral waves present in the ventricles during fibrillation, control methods based on application of local stimuli would likely require multiple recording and stimulation sites. While this is less practical than having a single site, it may still be possible to implement in implantable devices. Another difficulty in controlling ventricular fibrillation in vivo lies in the fact that cardiac tissue rapidly becomes ischemic during ventricular fibrillation due to lack of pumping of blood. A control algorithm would either have to rapidly terminate ventricular fibrillation, or be able to integrate the nonstationary dynamics.

Because of difficulties in controlling ventricular fibrillation, we believe that other strategies may lead to faster improvement in preventing sudden cardiac death. One approach is to attempt controlling arrhythmia precursor events such as electrical alternans. However, more research is necessary in order to determine the tissue volume over which a single electrode can control alternans. As mentioned, in contrast to fibrillation, which must be terminated in order to prevent a patient from dying, alternans need not necessarily be annihilated; a decrease in the alternans amplitude may reduce the risk of onset of ventricular tachyarrhythmias.

Another strategy to prevent sudden cardiac death is to improve antitachycardia pacing. The first step in this direction could be to determine the exact mechanisms of success versus failure of antitachycardia pacing. Utilizing such understanding might lead to the design of more effective pacing algorithms.

Because cardiac arrhythmias are characterized by complex nonlinear dynamics, tools and approaches from mathematics and physics have made, and are likely to continue making, important impacts on mechanistic understanding and therapy innovations.

References

1 *Heart disease and stroke statistics – 2005 update*. American Heart Association, Dallas, Texas, **2005.**

2 Aliev, R. A., Panfilov, A. V., *Chaos Sol. Fract. 7* (**1996**), p. 293.

3 Allexandre, D., Otani, N. F., *Phys. Rev. E* 70 (**2004**), p. 061903.

4 Antzelevitch, C., Burashnikov, A. In: Podrid, P. J., Kowey, P. R., editors, *Cardiac Arrhythmia: Mechanisms, Diagnosis, and Management*, Lippincott Williams & Wilkins, Philadelphia, **2001.**

5 Athill, C. A., Ikeda, T., Kim, Y.-H., Wu, T.-J., Fishbein, M. C., Karagueuzian, H. S., Chen, P.-S. *Circulation* 98 (**1998**), p. 1556.

6 Bardy, G. H., Lee, K. L., Mark, D. B., Poole, J. E., Packer, D. L., Boineau, R., Domanski, M., Troutman, C., Anderson, J., Johnson, G., McNulty, S. E., Clapp-Channing, N., Davidson-Ray, L. D., Fraulo, E. S., Fishbein, D. P., Luceri, R. M., Ip, J. H., *N. Engl. J. Med.* 352 (**2005**), p. 225.

7 Bers, D. M., *Excitation–Contraction Coupling and Cardiac Contractile Force*, Kluwer, Boston, **2001.**

8 Biktashev, V. N., Holden, A. V., *Chaos* 8 (**1998**), p. 48.

9 Breuer, J., Sinha, S., *Pramana. J. Phys.* 64 (**2005**), p. 553.

10 Chinushi, M., Kozhevnikov, D., Caref, E. B., Restivo, M., El-Sherif, N., *J. Cardiovasc. Electrophysiol.* 14 (**2003**), p. 632.

11 Christini, D. J., Collins, J. J., *Phys. Rev. E* 52 (**1995**), p. 5806.

12 Christini, D. J., Collins, J. J., *Phys. Rev. E* 53 (**1996**), p. R49.

13 Christini, D. J., Collins, J. J., *Chaos* 7 (**1997**), p. 544.

14 Christini, D. J., Collins, J. J., *IEEE Trans. Circ. Syst. I* 44 (**1997**), p. 1027.

15 Christini, D. J., Riccio, M. L., Culianu, C. A., Fox, J. J., Karma, A., Gilmour, Jr., R. F., *Phys. Rev. Lett.* 96 (**2006**), p. 104101.

16 Christini, D. J., Stein, K. M., Markowitz, S. M., Mittal, S., Slotwiner, D. J., Scheiner, M. A., Iwai, S., Lerman, B. B., *Proc. Natl. Acad. Sci. (USA)* 98 (**2001**), p. 5827.

17 Chudin, E., Goldhaber, J., Garfinkel, A., Weiss, J., Kogan, B., *Biophys. J.* 77 (**1999**), p. 2930.

18 Comtois, P., Vinet, A., *Chaos* 12 (**2002**), p. 903.

19 Deisenhofer, I., Kolb, C., Ndrepepa, G., Schreieck, J., Karch, M., Schmieder, S., Zrenner, B., Schmitt, C., *J. Cardiovasc. Electrophys.* 12 (**2001**), p. 134.

20 Domanski, M. J., Exner, D. V., Borkowf, C. B., Geller, N. L., Rosenberg, Y., Pfeffer, M., *J. Am. Coll. Cardiol.* 33 (**1999**), p. 598.

21 Echebarria, B., Karma, A., *Chaos* 12 (**2002**), p. 923.

22 Fogoros, R. N., *Antiarrhythmic Drugs: A Practical Guide*, Blackwell Science, Cambridge, Mass., **1997.**

23 Fox, J. J., McHarg, J. L., Gilmour, Jr., R. F., *Am. J. Physiol.* 282 (**2002**), p. H516.

24 Fox, J. J., Riccio, M. L., Hua, F., Bodenschatz, E., Gilmour, Jr., R. F., *Circ. Res.* 90 (**2002**), p. 289.

25 Fu, Y.-Q., Zhang, H., Cao, Z., Zheng, B., Ha, G., *Phys. Rev. E* 72 (**2005**), p. 046206.

26 Garfinkel, A., Spano, M. L., Ditto, W. L., Weiss, J. N., *Science* 257 (**1992**), p. 1230.

27 Gauthier, D. J., Bahar, S., Hall, G. M. In: Moss, F., Gielen, S., editors, *Handbook of Biological Physics: Neuro-Informatics, Neural Modeling*, Elsevier, New York, **2001.**

28 Glass, L., Josephson, M. E., *Phys. Rev. Lett.* 75 (**1995**), p. 2059.

29 Guevara, M. R., Ward, G., Shrier, A., Glass, L. In: IEEE Computers in Cardiology, IEEE Computer Society Press, Los Alamitos, California, **1984**, p. 167.

30 Hall, G. M., Gauthier, D. J., *Phys. Rev. Lett.* 88 (**2002**), p. 198102.

31 Hall, K., Christini, D. J., *Phys. Rev. E* 63 (**2001**), p. 046204.

32 Hall, K., Christini, D. J., Tremblay, M., Collins, J. J., Glass, L., Billette, J., *Phys. Rev. Lett.* 78 (**1997**), p. 4518.

33 Huikuri, H. V., Castellanos, A., Myerburg, R. J., *N. Engl. J. Med.* 345 (**2001**), p. 1473.

34 Ideker, R. E., Walcott, G. P., Epstein, A. E., Plumb, V. J., Kay, N., *Heart Rhythm* 2 (**2005**), p. 555.

35 Jauhar, S. and Slotwiner, D.J., *N. Engl. J. Med.* 351 (**2004**), p. 2542.

36 Jordan, P.N., Christini, D.J., *J. Cardiovasc. Electrophysiol.* 15 (**2004**), p. 1177.

37 Jordan, P.N., Christini, D.J., *Crit. Rev. Biomed. Eng.* 33 (**2005**), p. 557.

38 Karma, A., *Chaos* 4 (**1994**), p. 461.

39 Krinsky, V., Plaza, F., Voignier, V., *Phys. Rev. E* 52 (**1995**), p. 2458.

40 Lauer, M.R., Sung, R.J. In: Podrid, P.J., Kowey, P.R., editors, *Cardiac Arrhythmia: Mechanisms, Diagnosis, and Management,* Lippincott Williams & Wilkins, Philadelphia, **2001**.

41 Mantel, R.-M., Barkley, D., *Phys. Rev. E* 54 (**1996**), p. 4791.

42 Niebauer, M.J., Wilkoff, B.L. In: Zipes, D., Jalife, J., editors, *Cardiac Electrophysiology: From Cell to Bedside,* W.B. Saunders, **2000**.

43 Nolasco, J.B., Dahlen, R.W. *J. Appl. Physiol.* 25 (**1968**), p. 191.

44 Ott, E., Grebogi, C., Yorke, J.A., *Phys. Rev. Lett.* 64 (**1990**), p. 1196.

45 Oz, M.C., Konertz, W.F., Kleber, F.X., Mohr, F.W., Gummert, J.F., Ostermeyer, J., Lass, M., Raman, J., Acker, M.A., Smedira, N., *J. Thor. Card. Surg.* 126 (**2003**), p. 983.

46 Pastore, J.M., Girouard, S.D., Laurita, K.R., Akar, F.G., Rosenbaum, D.S., *Circulation* 99 (**1999**), p. 1385.

47 Patwardhan, A., Moghe, S., *Biomed. Sci. Instrum.* 37 (**2001**), p. 505.

48 Qu, Z., Garfinkel, A., Chen, P.-S., Weiss, J.N., *Circulation* 102 (**2000**), p. 1664.

49 Rappel, W.-J., Fenton, F., Karma, A., *Phys. Rev. Lett.* 83 (**1999**), p. 456.

50 Ripplinger, C.M., Krinsky, V.I., Nikolski, V.P., Efimov, I.R., *Am. J. Physiol.* 291 (**2006**), p. H184.

51 Roden, D.M., *Pacing Clin. Electrophysiol.* 26 (**2003**), p. 2340.

52 Schaumann, A., von zur Mühlen, F., Herse, B., Gonska, B.D., Kreuzer, H., *Circulation* 97 (**1998**), p. 66.

53 Schram, G., Pourrier, M., Melnyk, P., Nattel, S., *Circ. Res.* 90 (**2002**), p. 939.

54 Shiferaw, Y., Daisuke, S., Karma, A., *Phys. Rev. E* 71 (**2005**), p. 021903.

55 Sinha, S., Stein, K.M., Christini, D.J., *Chaos* 12 (**2002**), p. 893.

56 Smith, T.W., Cain, M.E. In: Zipes, D., Jalife, J., editors, *Cardiac Electrophysiology: From Cell to Bedside,* W.B. Saunders, **2004**.

57 Swerdlow, C.D., *J. Cardiovasc. Electrophysiol.* 12 (**2001**), p. 606.

58 Takagi, S., Pumir, A., Pazó, D., Efimov, I., Nikolski, V., Krinsky, V., *Phys. Rev. Lett.* 93 (**2004**), p. 058101.

59 The Cardiac Arrhythmia Suppression Trial CAST Investigators, *N. Eng. J. Med.* 321 (**1989**), p. 406.

60 Waldo, A., Camm, A., deRuyter, H., Friedman, P., MacNeil, D., Pauls, J., Pitt, B., Pratt, C., Schwartz, P., Veltri, E., *Lancet* 348 (**1996**), p. 7.

61 Watanabe, M., Gilmour, Jr., R.F., *J. Math. Biol.* 35 (**1996**), p. 73.

62 Wolk, R., Cobbe, S.M., Hicks, M.N., Kane, K.A., *Pharmacol. Ther.* 84 (**1999**), p. 207.

63 Wu, R., Patwardhan, A., *J. Cardiovasc. Electrophysiol.* 17 (**2006**), p. 87.

32
Controlling Spatiotemporal Chaos and Spiral Turbulence in Excitable Media

Sitabhra Sinha and S. Sridhar

32.1
Introduction

Excitable media denotes a class of systems that share a set of features which make their dynamical behavior qualitatively similar. These features include (i) the existence of two characteristic dynamical states, comprising a stable *resting state* and a metastable *excited state*, (ii) a *threshold* value associated with one of the dynamical variables characterizing the system, on exceeding which, the system switches from the resting state to the excited state, and (iii) a *recovery period* following an excitation, during which the response of the system to a supra-threshold stimulus is diminished, if not completely absent [1]. Natural systems which exhibit such features include, in biology, cells such as neurons, cardiac myocytes and pancreatic β cells, all of which are vital to the function of a complex living organism. Other examples of dynamical phenomena associated with excitable media include cAMP waves observed during aggregation of slime mold, calcium waves observed in Xenopus oocytes, muscle contractions during childbirth in uterine tissue, chemical waves observed in the Belusov-Zhabotinsky reaction and concentration patterns in CO-oxidation reaction on Pt(110) surface. Excitation in such systems is observed as the characteristic *action potential*, where a variable associated with the system (e.g., membrane potential, in the case of biological cells) increases very fast from its resting value to the peak value corresponding to the excited state, followed by a slower process during which it gradually returns to the resting state.

The simplest model system capable of exhibiting all these features is the generic FitzHugh-Nagumo set of coupled differential equations:

$$\mathrm{d}e/\mathrm{d}t = e(1 - e)(e - b) - g, \quad \mathrm{d}g/\mathrm{d}t = \varepsilon(ke - g), \tag{32.1}$$

which, having only two variables, is obviously incapable of exhibiting chaos. However, when several such sets are coupled together diffusively to simulate a spatially extended media (e.g., a piece of biological tissue made up of a large

number of cells), the resulting high-dimensional dynamical system can display chaotic behavior. The genesis of this *spatiotemporal chaos* lies in the distinct property of interacting waves in excitable media, which mutually annihilate on colliding. This is a result of the fact that an excitation wavefront is followed by a region, all of whose cells are in the recovery period, and which therefore cannot be stimulated by another excitation wavefront when two waves cross each other.[1] Interaction between such waves results in the creation of spatial patterns, referred to variously as *reentrant excitations* (in 1D), *vortices* or *spiral waves* (in 2D) and *scroll waves* (in 3D), which form when an excitation wavefront is broken as the wave propagates across partially recovered tissue or encounters an inexcitable obstacle [2]. The free ends of the wavefront gradually curl around to form spiral waves. Once formed, such waves become self-sustained sources of high-frequency excitation in the medium, and usually can only be terminated through external intervention. Spiral waves are associated with periodic or quasiperiodic patterns of temporal activity. As our focus is on controlling spatiotemporally chaotic activity, we shall not be discussing the many schemes proposed to terminate single spiral waves. The existence of nonlinear properties of wave propagation in several excitable media can lead to complex nonchaotic spatiotemporal rhythms. For more details on controlling such dynamical behavior refer to the chapter by Krogh-Madsen, Jordan, and Christini.

Here, we shall focus on the control of spatiotemporally chaotic patterns seen in excitable media (in 2 or 3 dimensions), that occur when under certain conditions, spiral or scroll waves become unstable and break up. Various mechanisms of such breakup have been identified,[2] including meandering of the spiral focus. If the meandering is sufficiently high, the spiral wave can collide with itself and break up spontaneously, resulting in the creation of multiple smaller spirals (Fig. 32.1). The process continues until the spatial extent of the system is spanned by several coexisting spiral waves that activate different regions without any degree of coherence. This state of *spiral turbulence* marks the onset of spatiotemporal chaos, as indicated by the Lyapunov spectrum and Kaplan-Yorke dimension [5].

Controlling spatiotemporal chaos in excitable media has certain special features. Unlike other chaotic systems, response to a control signal is not proportional to the signal strength because of the existence of a threshold. As a result, an excitable system shows discontinuous response to control as regions, which have not yet recovered from a previous excitation or where the control signal is below the threshold, will not be affected by the control algorithm at all. Also, the focus of control in excitable media is to eliminate all activity rather than to stabilize unstable periodic behavior. This is because the problem of chaos termination has great practical importance in the clinical context, as the spatiotemporally chaotic state has been associated with the cardiac problem of ventricular fi-

---

[1] Note that, unlike waves in ordinary diffusive media which dissipate as they propagate further, excitation waves are self-regenerating.

[2] For a discussion of the multiple scenarios of spiral wave breakup, see [3, 4].
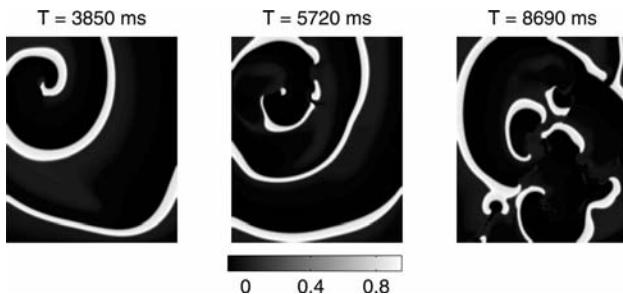
Fig. 32.1 Onset of spatiotemporal chaos in the two-dimensional Panfilov model of linear dimension $L = 256$. The initial condition is a broken plane wave that is allowed to curl around into a spiral wave (left). Meandering of the spiral focus causes wave breaks to occur (center) that eventually result in spiral turbulence, with multiple independent sources of high-frequency excitation (right).

brillation (VF). VF involves incoherent activation of the heart that results in the cessation of pumping of blood, and is fatal within minutes in the absence of external intervention. At present, the only effective treatment is electrical defibrillation, which involves applying very strong electrical shocks across the heart muscles, either externally using a defibrillator or internally through implanted devices. The principle of operation for such devices is to overwhelm the natural cardiac dynamics, so as to drive all the different regions of the heart to rest simultaneously, at which time the cardiac pacemaker can take over once again. Although the exact mechanism by which this is achieved is still not completely understood, the danger of using such large amplitude control (involving $\sim$ kV externally and $\sim$ 100 V internally) is that, not only is it excruciatingly painful to the patient, but by causing damage to portions of cardiac tissue which subsequently result in scars, it can potentially increase the likelihood of future arrhythmias (i.e., disturbances of the heart's natural rhythm). Therefore, devising a low-power control method for spatiotemporal chaos in excitable media promises a safer treatment for people at risk from potentially fatal cardiac arrhythmias.

In this chapter, we have discussed most of the recent control methods that have been proposed for terminating spatiotemporal chaos in excitable media. [3] These methods are also often applicable to the related class of systems known as oscillatory media, described by complex Landau-Ginzburg equation [7], which also exhibit spiral waves and spatiotemporal chaos through spiral breakup. We have broadly classified all control schemes into three types, depending on the nature of application of the control signal. If every region of the media is subjected to the signal (which, in general, can differ from region to region) it is termed as *global control*; on the other hand, if the control signal is applied only at a small, localized region from which its effects spread throughout the media, this is called *local control*. Between these two extremes lie control schemes

---

3) An earlier review, discussing methods proposed till 2002, can be found in [6].

where perturbations are applied simultaneously to a number of spatially distant regions. We have termed these methods as *nonglobal, spatially extended control*. While global control may be the easiest to understand, involving as it does the principle of synchronizing the activity of all regions, it is also the most difficult to implement in any practical situation. On the other hand, local control (as it can be implemented using a single control point) will be the easiest to implement but hardest to achieve.

In the next section we describe a few of the more commonly used models for studying control of spatiotemporal chaos in excitable media. Section 32.3 discusses proposed methods of global control, while Section 32.4 discusses other spatially extended schemes. The next section deals with local control methods, and we conclude with a brief section containing general discussions about chaos control and its implications.

32.2
Models of Spatiotemporal Chaos in Excitable Media

The generic FitzHugh-Nagumo model for excitable media (Eq. (32.1)) exhibits a structure that is common to most models used in the papers discussed here. Typically, the dynamics is described by a fast variable, $e(\mathbf{x}, t)$, and a slow variable, $g(\mathbf{x}, t)$, the ratio of timescales being given by ε. The resulting phase space behavior is shown in Fig. 32.2 (top). For biological cells, the fast variable is often associated with the transmembrane potential, while the slow (recovery) variable represents an effective membrane conductance that replaces the complexity of several different types of ion channels. For the spatially extended system, the fast variable of neighboring cells is coupled diffusively. There are several models belonging to this general class of excitable media which display breakup of spiral waves (in 2D) and scroll waves (in 3D), including the one proposed by Panfilov [8, 9].

$$\partial e/\partial t = \nabla^2 e - f(e) - g, \quad \partial g/\partial t = \varepsilon(e, g)(ke - g). \tag{32.2}$$

For details of the functional form of $f(e)$ and relevant parameter values, see [9].

Simpler variants that also display spiral wave breakup in 2D include (i) the Barkley model [10]:

$$\partial e/\partial t = \nabla^2 e + \varepsilon^{-1} e(1 - e)\left(e - \frac{g + b}{a}\right), \quad \partial g/\partial t = e - g, \tag{32.3}$$

the appropriate parameter values being given in [11], and (ii) the Bär-Eiswirth model [12], which differs from (32.3) only in having $\partial g/\partial t = f(e) - g$, the functional form of $f(e)$ and parameter values being as in [13]. The Aliev-Panfilov model [14] is a modified form of the Panfilov model, that takes into account nonlinear effects such as the dependence of the action potential duration on the
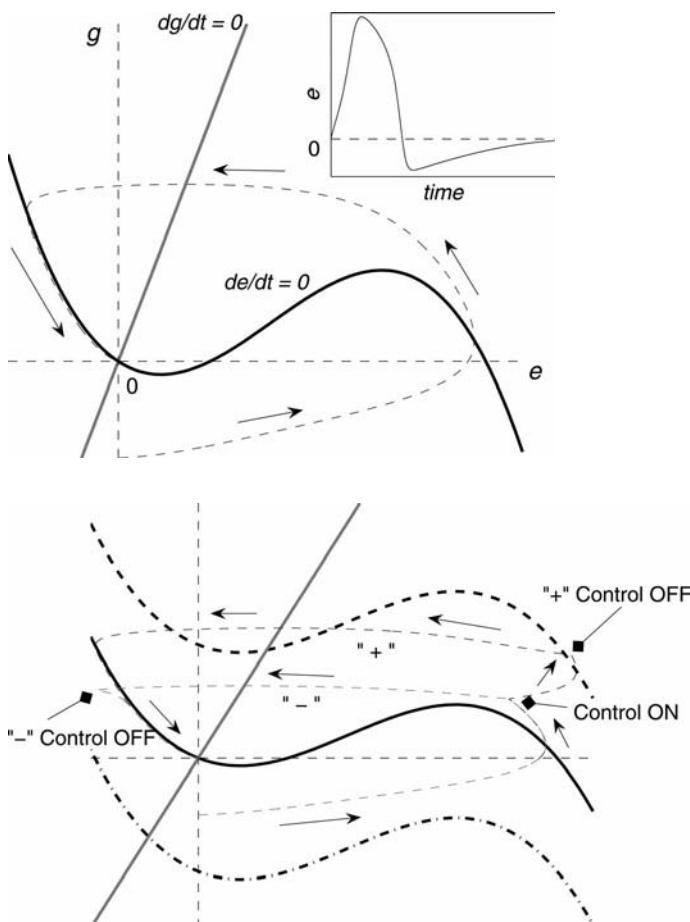
Fig. 32.2 (Top) Dynamics in the phase-space of the FitzHugh-Nagumo model, with the resulting time evolution of the action potential shown in the inset. The resting state corresponds to $e = 0, g = 0$. (Bottom) The result of applying a positive ("+") or negative ("−") additive perturbation of the same duration to the e variable: "+" control decreases the threshold and makes excitation more likely, while "−" control decreases the duration of the action potential and allows the system to recover faster. For the duration of the control signal, the e-nullcline shifts upward (downward) for positive (negative) perturbation as indicated by the dashed (dash-dotted) curve.

distance of the wavefront to the preceding waveback. It has been used for control in [15, 16].

All the preceding models tend to disregard several complex features of actual biological cells, e.g., different types of ion channels. There exists a class of models inspired by the Hodgkin-Huxley formulation of a model describing action potential in the squid giant axon, that explicitly takes such details into account. While the models described above do reproduce generic features of several excit-

able media seen in nature, these more realistic models describe many properties of specific systems, e.g., ventricular tissue. The general form of such models is described by a partial differential equation for the transmembrane potential V, $\frac{\partial V}{\partial t} + \frac{I_{\text{ion}}}{C} = D\nabla^2 V$, where C is the membrane capacitance density and D is the diffusion constant, which, if the medium is isotropic, is a scalar. I_{ion} is the instantaneous total ionic-current density, and different realistic models essentially differ in its formulation. For example, in the Luo-Rudy I model [18] of guinea pig ventricular cells, I_{ion} is assumed to be composed of six different ionic current densities, which are themselves determined by several time-dependent ion-channel gating variables whose time-evolution is governed by ordinary differential equations of the form $\frac{d\xi}{dt} = \frac{\xi_\infty - \xi}{\tau_\xi}$. Here, $\xi_\infty = a_\xi/(a_\xi + \beta_\xi)$ is the steady state value of ξ and $\tau_\xi = \frac{1}{a_\xi + \beta_\xi}$ is its time constant. The voltage-dependent rate constants, a_ξ and β_ξ, are complicated functions of V obtained by fitting experimental data.

32.3
Global Control

The first attempt at controlling chaotic activity in excitable media dates back almost to the beginning of the field of chaos control itself, when proportional perturbation feedback (PPF) control was used to stabilize cardiac arrhythmia in a piece of tissue from rabbit heart [19]. This method applied small electrical stimuli, at intervals calculated using a feedback protocol, to stabilize an unstable periodic rhythm. Unlike in the original proposal for controlling chaos [20], where the location of the stable manifold of the desired unstable periodic orbit (UPO) was moved using small perturbations, in the PPF method, it is the state of the system that is moved onto the stable manifold. However, it has been later pointed out that PPF does not necessarily require the existence of UPOs (and, by extension, deterministic chaos) and can be used even in systems with stochastic dynamics [21]. Later, PPF method was used to control atrial fibrillation in human heart [22]. However, the effectiveness of such control in suppressing spatiotemporal chaos, when applied only at a local region, has been questioned, especially as other experimental attempts in feedback control have not been able to terminate fibrillation by applying control stimuli at a single spatial location [6].

More successful, at least in numerical simulations, have been schemes where control stimuli is applied throughout the system. Such global control schemes either apply small perturbations to the dynamical variables (e or g) or one of the parameters (usually the excitation threshold). The general scheme involves introducing an external control signal A into the model equations, e.g., in the Panfilov model (Eq. (32.2)): $\partial e/\partial t = \nabla^2 e - f(e) - g + A$, for a control duration τ. If A is a small, positive perturbation, added to the fast variable, the result is an effective reduction of the threshold (Fig. 32.2, bottom), thereby making simultaneous excitation of different regions more likely. In general, A can be per-
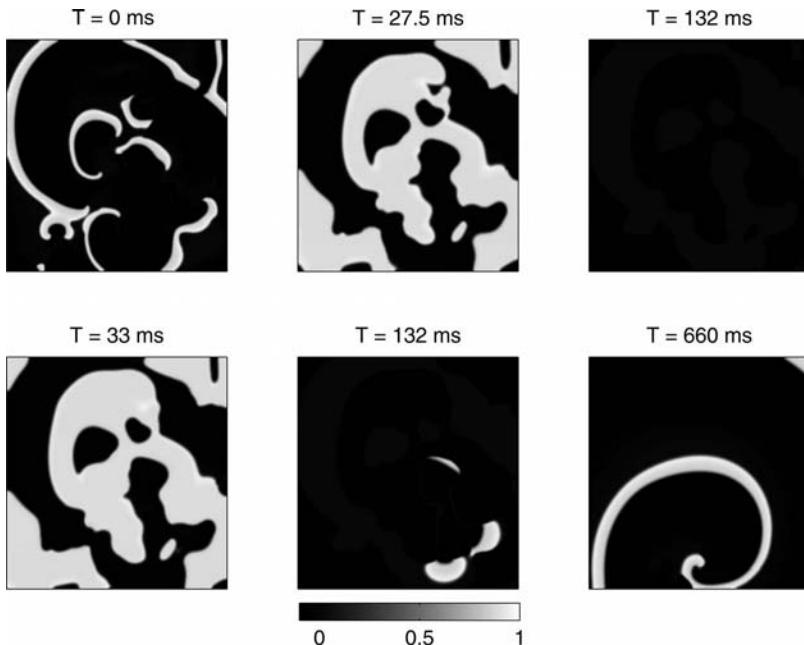
Fig. 32.3 Global control of the two-dimensional Panfilov model with $L = 256$ starting from a spatiotemporally chaotic state (top left). Pseudo-gray-scale plots of excitability e show the result of applying a pulse of amplitude $A = 0.833$ between $t = 11$ ms and 27.5 ms (top center) that eventually leads to elimination of all activity (top right). Applying the pulse between $t = 11$ ms and 33 ms (bottom left) results in some regions becoming active again after the control pulse ends (bottom center) eventually reinitiating spiral waves (bottom right).

iodic, consisting of a sequence of pulses. Figure 32.3 shows the results of applying a pulse of fixed amplitude but varying durations. While in general, increasing the amplitude, or the duration, increases the likelihood of suppressing spatiotemporal chaos, it is not a simple, monotonic relationship. Depending on the initial state at which the control signal is applied, even a high amplitude (or long duration) control signal may not be able to uniformly excite all regions simultaneously. As a result, when the control signal is withdrawn, the inhomogeneous activation results in a few regions becoming active again and restarting the spatiotemporal chaotic behavior.

Most global control schemes are variations or modifications of the above scheme. Osipov and Collins [23] have shown that a low-amplitude signal used to change the value of the slow variable at the front and back of an excitation wave can result in different wavefront and waveback velocities which destabilizes the traveling wave, eventually terminating all activity, and, hence, spatiotemporal chaos. Gray [24] has investigated the termination of spiral wave breakup by using both short- and long-duration pulses applied on the fast variable, in 2D and 3D systems. This study concluded that while short duration pulses af-

fected only the fast variable, long duration pulses affected both fast and slow variables and that the latter is more efficient (using less power) in terminating spatiotemporal chaos. The external control signal can also be periodic ($A = F \sin(\omega t)$), in which case the critical amplitude F_c required for terminating activity has been found to be a function of the signal frequency ω [15].

Other schemes have proposed applying perturbations to the parameter controlling the excitation threshold, b. Applying a control pulse on this parameter ($b = b_f$, during duration of control pulse; $b = b_0$, otherwise) has been shown to cause splitting of an excitation wave into a pair of forward and backward moving waves [13]. Splitting of a spiral wave causes the two newly created spirals to annihilate each other on collision. For a spatiotemporally chaotic state, a sequence of such pulses may cause termination of all excitation, there being an optimal time interval between pulses that results in fastest control. Another control scheme that also applies perturbation to the threshold parameter is the uniform periodic forcing method suggested by Alonso et al. [11, 25] for controlling scroll wave turbulence in three-dimensional excitable media. Such turbulence results from negative tension between scroll wave filaments, i.e., the line joining the phase singularities about which the scroll wave rotates. In this control method, the threshold is varied in periodic manner [$b = b_0 + b_f \cos(\omega t)$] and the result depends on the relation between the control frequency ω and the spiral rotation frequency. If the former is higher than the latter, sufficiently strong forcing is seen to eliminate turbulence; otherwise, turbulence suppression is not achieved. The mechanism underlying termination has been suggested to be the effective increase of filament tension due to rapid forcing, such that the originally negative tension between scroll wave filaments is changed to positive tension. This results in expanding scroll wave filaments to instead shrink and collapse, eliminating spatiotemporal chaotic activity. In a variant method, the threshold parameter has been perturbed by spatially uncorrelated Gaussian noise, rather than a periodic signal, which also results in suppression of scroll wave turbulence [26].

As already mentioned, global control, although easy to understand, is difficult to achieve in experimental systems. A few cases in which such control could be implemented include the case of eliminating spiral wave patterns in populations of the Dictyostelium amoebae by spraying a fine mist of cAMP onto the agar surface over which the amoebae cells grow [27]. Another experimental system where global control has been implemented is the photosensitive Belusov-Zhabotinsky reaction, where a light pulse shining over the entire system is used as a control signal [28]. Indeed, conventional defibrillation can be thought of as a kind of global control, where a large amplitude control signal is used to synchronize the phase of activity at all points by either exciting a previously unexcited region (advancing the phase) or slowing the recovery of an already excited region (delaying the phase) [29].

32.4
Nonglobal Spatially Extended Control

The control methods discussed so far apply control signal to all points in the system. As the chaotic activity is spatially extended, one may naively expect that any control scheme also has to be global. However, we will now discuss some schemes that, while being spatially extended, does not require the application of control to all points of the system.

32.4.1
Applying Control Over a Mesh

The control method of Sinha et al. [30] involving suprathreshold stimulation along a grid of points, is based on the observation that spatiotemporal chaos in excitable media is a long-lived transient that lasts long enough to establish a nonequilibrium statistical steady state displaying spiral turbulence. The lifetime of this transient, τ_L, increases rapidly with linear size of the system, L, e.g., increasing from 850 to 3200 ms as L increases from 100 to 128 in the two-dimensional Panfilov model. This accords with the well-known observation that small mammals do not get life-threatening VF spontaneously whereas large mammals do [31] and has been experimentally verified by trying to initiate VF in swine ventricular tissue while gradually reducing its mass [32]. A related observation is that nonconducting boundaries tend to absorb spiral excitations, which results in spiral waves not lasting for appreciable periods in small systems.

The essential idea of the control scheme is that a domain can be divided into electrically disconnected regions by creating boundaries composed of recovering cells between them. These boundaries can be created by triggering excitation across a thin strip. For two-dimensional media, the simulation domain (of size $L \times L$) is divided into K^2 smaller blocks by a network of lines with the block size ($L/K \times L/K$) small enough so that spiral waves cannot form. For control in a 3D system, the mesh is used only on one of the faces of the simulation box. Control is achieved by applying a suprathreshold stimulation via the mesh for a duration τ. A network of excited and subsequently recovering cells then divides the simulation domain into square blocks whose length in each direction is fixed at a constant value L/K for the duration of control. The network effectively simulates nonconducting boundary conditions (for the block bounded by the mesh) for the duration of its recovery period, in so far as it absorbs spirals formed inside this block. Note that τ need not be large at all because the individual blocks into which the mesh divides the system (of linear size L/K) are so small that they do not sustain long spatiotemporally chaotic transients. Nor does K, which is related to the mesh density, have to be very large since the transient lifetime, τ_L, decreases rapidly with decreasing L. The method has been applied to multiple excitable models, including the Panfilov and Luo-Rudy models (Fig. 32.4).
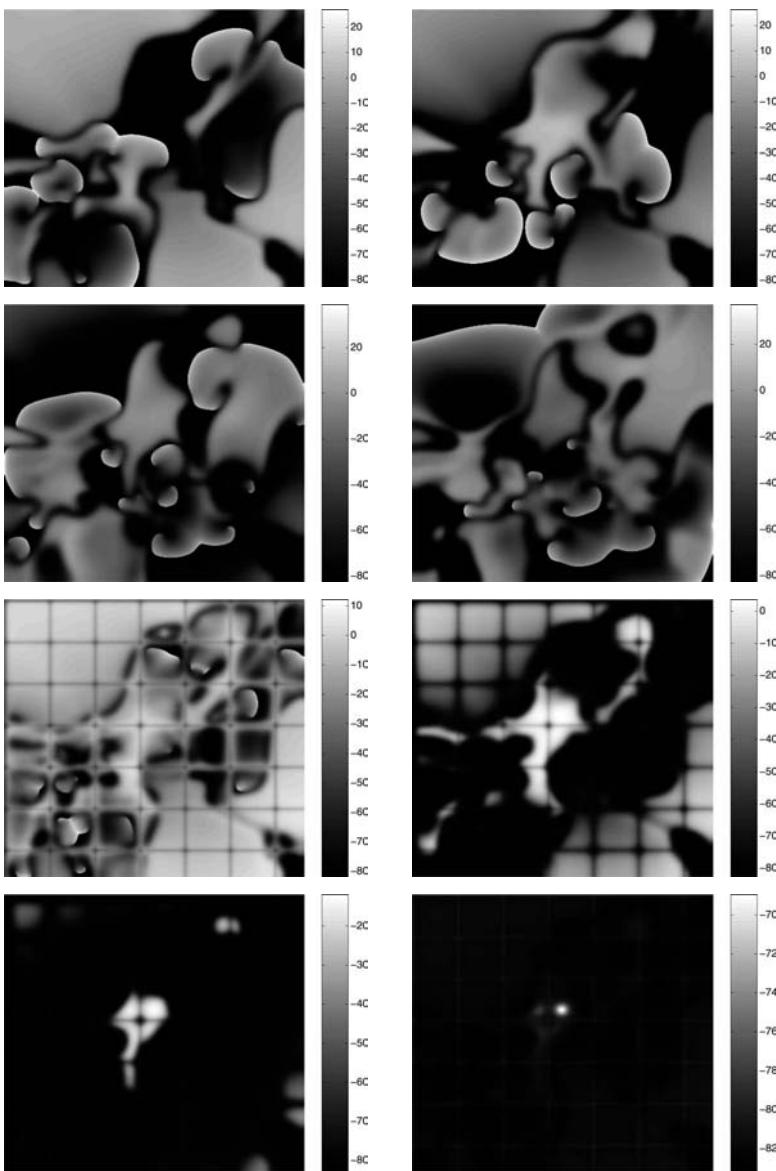
Fig. 32.4 Spatiotemporal chaos (top two rows) and its control (bottom two rows) in the two-dimensional Luo–Rudy I model with $L = 90$ mm. Pseudo-gray-scale plots of the transmembrane potential V show the evolution of spiral turbulence at times $T = 30$ ms, 90 ms, 150 ms and 210 ms (left to right, top to bottom). Control is achieved by applying an external current density $I = 150$ μA/cm^2 for $\tau = 2.5$ ms over a square mesh with each block of linear dimension $L/K = 1.35$ cm. Within 210 ms of applying control, most of the simulation domain has reached a transmembrane potential close to the resting state value; moreover, the entire domain is much below the excitation threshold. The corresponding uncontrolled case shows spatiotemporal chaos across the entire domain.

An alternative method [16] for controlling spiral turbulence that also uses a grid of control points has been demonstrated for the Aliev-Panfilov model. Two layers of excitable media are considered, where the first layer represents the two-dimensional excitable media exhibiting spatiotemporal chaos that is to be controlled, and the second layer is a grid structure also made up of excitable media. The two layers are coupled using the fast variable but with asymmetric coupling constants, with excitation pulses traveling $\sqrt{D}$ times faster in the second layer compared to the first. As the second layer consists only of grid lines, it is incapable of exhibiting chaotic behavior in the uncoupled state. If the coupling from the second layer to the first layer is sufficiently stronger than the other way round, the stable dynamics of the second layer (manifested as a single rotating spiral) overcomes the spiral chaos in the first layer, and drives it to an ordered state characterized by mutually synchronized spiral waves.

32.4.2
Applying Control Over an Array of Points

An alternative method of spatially extended control is to apply perturbations at a series of points arranged in a regular array. Rappel et al. [33] had proposed using such an arrangement for applying a time delayed feedback control scheme. However, this scheme does not control spatiotemporal chaos and is outside the scope of this review.

More recently, the authors [34] have used an array of control points to terminate spatiotemporal chaos in the Panfilov model. Figure 32.5 shows the result of applying a spatially nonuniform control scheme, which simulates an excitation wave traveling over the system, with the same wavefront velocity as in the actual medium. The control points are placed distance d apart along a regular array. At certain times, the control points at one corner of the system is stimulated, followed by the successive stimulation of the neighboring control points, such that a wave of stimulation is seen to move radially away from the site of original stimulation. This process is repeated after suitable intervals. Note that simulating a traveling wave using the array is much more effective at controlling spatiotemporal chaos than the simultaneous activation of all control points. Using a traveling wave allows the control signal to engage all high-frequency sources of excitation in the spiral turbulence regime, ultimately resulting in complete elimination of chaos. If, however, the control had only been applied locally the resulting wave could only have interacted with neighboring spiral waves and the effects of such control would not have been felt throughout the system. The efficacy of the control scheme depends upon the spacing between the points at which stimulation is applied, as well as the number of waves sent through. Traveling waves have previously been used in [35] to control spatiotemporal chaos, although in the global control context with a spatiotemporally periodic signal being applied continuously for a certain duration, over the entire system.

T = 49.5 ms

T = 104.5 ms

T = 159.5 ms

T = 214.5 ms
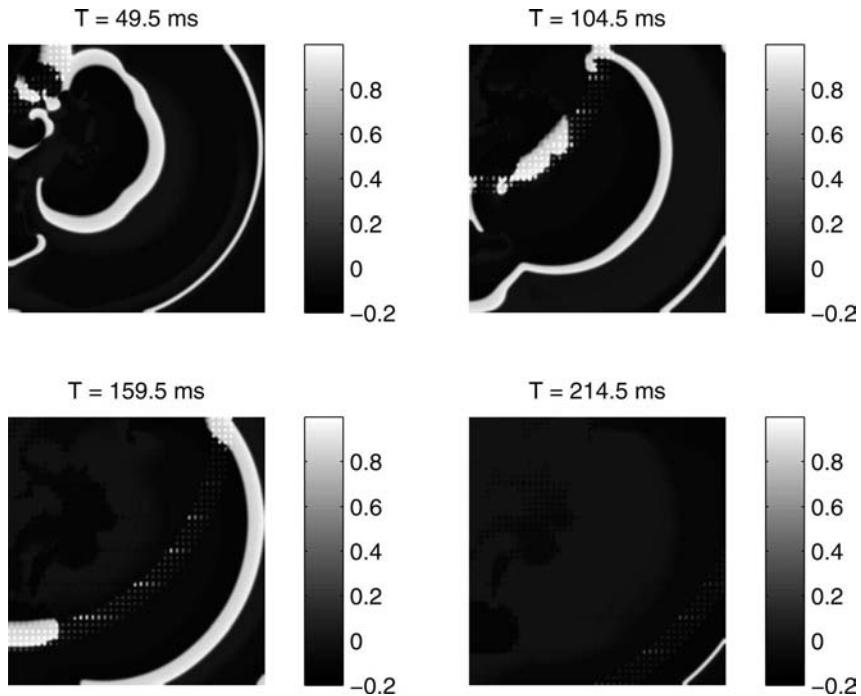
Fig. 32.5 Control of the two-dimensional Panfilov model ($L = 256$) using an array of control points with spacing $d = 6$ and strength of control stimulus $A = 2.5$. Stimulation is started at the top left corner ($T = 0$ ms) and lasts at each control point, as the wave reaches that point, for 17.9 ms. By 200 ms, the spatiotemporal chaos has disappeared and only the wave stimulated by the control points can be observed. When this wave reaches the system boundary, all excitation is terminated.

32.5
Local Control of Spatiotemporal Chaos

We now turn to the possibility of controlling spatiotemporal chaos by applying control at only a small localized region of the spatially extended system. Virtually all the proposed local control methods use *overdrive pacing*, generating a series of waves with frequency higher than any of the existing excitations in the spiral turbulent state. As low-frequency activity is progressively invaded by faster excitation, the waves generated by the control stimulation gradually sweep the chaotic activity to the system boundary where they are absorbed. Although we cannot speak of a single frequency source in the case of chaos, the relevant timescale is that of spiral waves which is limited by the recovery period of the medium. Control is manifested as a gradually growing region in which the waves generated by the control signal dominate, until the region expands to encompass the entire system. The time required to achieve termination depends

on the frequency difference between the control stimulation and that of the chaotic activity, with control being achieved faster, the greater the difference.

Stamp et al. [36] has looked at the possibility of using low-amplitude, high-frequency pacing using a series of pulses to terminate spiral turbulence. However, using a series of pulses (having various waveform shapes) has met with only limited success in suppressing spatiotemporal chaos. By contrast, a periodic stimulation protocol [37] has successfully controlled chaos in the 2D Panfilov model, as well as other models.[4] The key mechanism underlying such control is the periodic alternation between positive and negative stimulation. A more general control scheme proposed in [39] uses *biphasic pacing*, i.e., applying a series of positive and negative pulses, that shortens the recovery period around the region of control stimulation, and thus allows the generation of very high-frequency waves than would have been possible using positive stimulation alone. A simple argument shows why a negative rectangular pulse decreases the recovery period for an excitable system. The stimulation vertically displaces the e-nullcline and therefore, the maximum value of g that can be attained is reduced. Consequently, the system will recover faster from the recovery period (Fig. 32.6, bottom).

To understand how negative stimulation affects the response behavior of the spatially extended system, we can use *pacing response diagrams* indicating the relation between the control stimulation frequency f and the effective frequency f_{eff}, measured by applying a series of pulses at one site and then recording the number of pulses that reach another site located at a distance without being blocked by a region in the recovery period. Depending on the relative value of f^{-1} and the recovery period, we observe instances of $n : m$ response, i.e., m responses evoked by n stimuli. If, for any range of f, the corresponding f_{eff} is significantly higher than the effective frequency of spatiotemporal chaos, then termination of spiral turbulence is possible. As shown in [39], there are indeed ranges of stimulation frequencies that give rise to effective frequencies that dominate chaotic activity. As a result, the periodic waves emerging from the stimulation region gradually impose control over the regions exhibiting chaos. Note that there is a tradeoff involved here. If f_{eff} is only slightly higher than the chaos frequency, control takes too long; if it is too high the waves suffer conduction block at inhomogeneities produced by chaotic activity that reduces the effective frequency, and control fails.

Recently, another local control scheme has been proposed [40] that periodically perturbs the model parameter governing the threshold. In fact, it is the local control analog of the global control scheme proposed by Alonso et al. [11] discussed in Section 32.3. As in the other methods discussed here, the local stimulation generates high-frequency waves that propagate into the medium and suppress spiral or scroll waves. Unlike the global control scheme, $b_f >> b_0$, so that the threshold can be negative for a part of the time. This means that the

4) A related case of this control scheme is that proposed in [38], where the high-frequency periodic signal is applied from the boundaries.
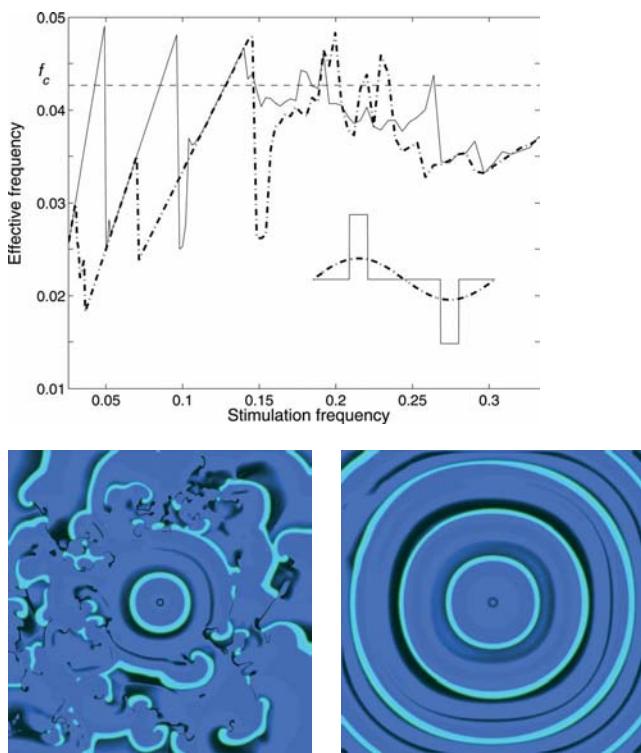
Fig. 32.6 (Top) Pacing-response diagram for the 2D Panfilov model ($L = 26$) showing relative performance of different waveforms. The dash-dotted line represents a sine wave and the solid curve represents a wave of biphasic rectangular pulses, such that they have the same total energy. Successful control occurs if the effective frequency lies above the broken line representing the effective frequency of chaos (f_c), as seen for a larger system ($L = 500$) at times $T = 1000$ (bottom left) and $T = 3800$ (bottom right) time units, where the control signal is applied only at the center of the simulation domain. The excitation wavefronts are shown in white, black marks the recovered regions ready to be excited, while the shaded regions indicate different stages of recovery.

regions in resting state can become spontaneously excited, which allow very high-frequency waves to be generated.

32.6
Discussion

Most of the methods proposed for controlling spatiotemporal chaos in excitable media involve applying perturbations either globally or over a spatially extended system of control points covering a significant proportion of the entire system. However, in most practical situations this may not be a feasible option, either for issues of implementation, or because of the high power for the control sig-

nal such methods would need. Moreover, if one is using such methods in the clinical context, e.g., terminating fibrillation, a local control scheme has the advantage that it can be readily implemented with existing hardware of the implantable cardioverter defibrillator (ICD). This is a device implanted into patients at high risk from fibrillation that monitors the heart rhythm and applies electrical treatment when necessary through electrodes placed on the heart wall. A low-energy control method involving ICDs should therefore aim towards achieving control of spatiotemporal chaos by applying small perturbations from a few local sources.

However, the problem with most local control schemes proposed so far is that they use very high-frequency waves to overdrive chaos. Such waves are themselves unstable and may breakup during propagation, resulting in reinitiation of spiral waves after the original chaotic activity has been terminated. The problem is compounded by the existence of inhomogeneities in real excitable media. Recently, Shajahan et al. [41] have found complicated dependence of spatiotemporal chaos on the presence of nonconducting regions and other types of inhomogeneities in an excitable system. Such inhomogeneities make the proposed local control schemes more vulnerable, as it is known that high-frequency pacing interacting with, e.g., nonconducting obstacles, results in wave breaks and subsequent genesis of spatiotemporal chaos [42].

The search is still on for a control algorithm for terminating spatiotemporal chaos in excitable media, that can be implemented using low power, or, that need be applied in only a small, local region of the system, and which will yet be robust, capable of terminating spiral turbulence without the control stimulation itself breaking up subsequently. The payoffs for coming up with such a method are enormous, as the potential benefits include an efficient device for cardiac defibrillation.

Acknowledgments

References

1 Keener, J., Sneyd, J., *Mathematical Physiology*, Springer, New York, **1998**

2 Jalife, J., Anumonwo, J.M., Delmar, M., Davidenko, J.M., *Basic Cardiac Electrophysiology for the Clinician*, Futura Publishing, Armonk, **1999**

3 Bär, M., Falcke, M., Or-Guil, M., in: *Lecture Notes in Physics 532*, Springer, New York, **1999**, p. 326

4 Fenton, F.H., Cherry, E.M., Hastings, H.M., Evans, S.J., *Chaos* 12 (**2002**), p. 852

5 Pandit, R., Pande, A., Sinha, S., Sen, A., *Physica A* 306 (**2002**), p. 211

6 Gauthier, D.J., Hall, G.M., Oliver, R.A., Dixon-Tulloch, E.G., Wolf, P.D., Bahar, S., *Chaos* 12 (**2002**), p. 952

7 Aranson, I.S., Kramer, L., *Rev. Mod. Phys.* 74 (**2002**), p. 99

8 Panfilov, A.V., Hogeweg, P., *Phys. Lett. A* 176 (**1993**), p. 295

9 Panfilov, A.V., *Chaos* 8 (**1998**), p. 57

10 Barkley, D., Kness, M., Tuckerman, L.S., *Phys. Rev. A* 42 (**1990**), p. 2489

11 Alonso, S., Sagués, F., Mikhailov, A.S., *Science* 299 (**2003**), p. 1722

12 Bär, M., Eiswirth, M., *Phys. Rev. E* 48 (**1993**), p. 1635

13 Woltering, M., Markus, M., *Sci. Asia* 28 (**2002**), p. 43

14 Aliev, R.R., Panfilov, A.V., *Chaos, Solitons, Fractals* 7 (**1996**), p. 293

15 Sakaguchi, H., Fujimoto, T., *Phys. Rev. E* 67 (**2003**), 067202

16 Sakaguchi, H., Kido, Y., *Phys. Rev. E* 70 (**2005**), 052901

17 Panfilov, A.V., *Phys. Rev. E* 59 (**1999**), p. 6251

18 Luo, C.H., Rudy, Y., *Circ. Res.* 68 (**1991**), p. 1501

19 Garfinkel, A., Spano, M.L., Ditto, W.L., Weiss, J.N., *Science* 257 (**1992**), p. 1230

20 Ott, E., Grebogi, C., Yorke, J.A., *Phys. Rev. Lett.* 64 (**1990**), p. 1196

21 Christini, D.J., Collins, J.J., *Phys. Rev. E* 52 (**1995**), p. 5806

22 Ditto, W.L., Spano, M.L., In, V., Neff, J., Meadows, B., Langberg, J.J., Bolmann, A., McTeague, K., *Int. J. Bif. Chaos* 52 (**2000**), p. 593

23 Osipov, G.V., Collins, J.J., *Phys. Rev. E* 60 (**1999**), p. 54

24 Gray, R.A., *Chaos* 12 (**2002**), p. 941

25 Alonso, S., Sagués, F., Mikhailov, A.S., *Chaos* 16 (**2006**), 023124

26 Alonso, S., Sancho, J.M., Sagués, F., *Phys. Rev. E* 70 (**2004**), 067201

27 Lee, K.J., Goldstein, R.E., Cox, E.C., *Phys. Rev. Lett.* 87 (**2001**), 068101

28 Muñuzuri, A.P., Pérez-Villar, V., Markus, M., *Phys. Rev. Lett.* 79 (**1997**), p. 1941

29 Gray, R.A., Chattipakorn, N., *Proc. Natl. Acad. Sci. USA* 102 (**2005**), p. 4672

30 Sinha, S., Pande, A., Pandit, R., *Phys. Rev. Lett.* 86 (**2001**), p. 3678

31 Winfree, A.T., *When Time Breaks Down*, Princeton University Press, Princeton, **1987**

32 Kim, Y.-H., Garfinkel, A., Ikeda, T., Wu, T.-J., Athill, C.A., Weiss, J.N., Karagueuzian, H.S., Chen, P.-S., *J. Clin. Invest.* 100 (**1997**), p. 2486

33 Rappel, W.-J., Fenton, F., Karma, A., *Phys. Rev. Lett.* 83 (**1999**), p. 456

34 Sridhar, S., Sinha, S., *forthcoming*

35 Peng-Ye, W., Ping, X., Hua-Wei, Y., *Chin. Phys.* 12 (**2003**), p. 674

36 Stamp, A.T., Osipov, G.V., Collins, J.J., *Chaos* 12 (**2002**), p. 931

37 Zhang, H., Hu, B., Hu, G., *Phys. Rev. E* 68 (**2003**), 026134

38 Yuan, G., Wang, G., Chen, S., *Europhys. Lett.* 72 (**2005**), p. 908

39 Breuer, J., Sinha, S., *preprint* nlin.CD/ 0406047 (**2004**)

40 Zhang, H., Cao, Z., Wu, N.-J., Ying, H.-P., Hu, G., *Phys. Rev. Lett.* 94 (**2005**), 188301

41 Shajahan, T.K., Sinha, S., Pandit, R., *preprint* nlin.PS/0606026 (**2006**)

42 Panfilov, A.V., Keener, J.P., *J. Theor. Biol.* 163 (**1993**), p. 439

Part IX
Applications to Engineering

33
Nonlinear Chaos Control and Synchronization

Henri Huijberts and Henk Nijmeijer

33.1
Introduction

Since their birth, in respectively, the work by Ott, Grebogi, and Yorke [15] and Pecora and Carroll [16], "control of chaos" and "chaos synchronization" have received an enormous interest in both theoretical and experimental studies. In both subjects the systems under consideration are characterized by the presence of nonstandard limit sets and essentially nonlinear dynamics. As a consequence control of chaotic dynamics and chaos synchronization naturally demand the application of nonlinear control techniques.

The purpose of this chapter is to present, in a tutorial way, some of the more basic tools from nonlinear geometric control as applied to the study of chaos control and synchronization. For further reading on nonlinear control we refer to, e.g., the text books [6, 8, 13, 19]. Applications of nonlinear control techniques to the study of chaos control and synchronization can be found in, e.g., [1, 4, 5, 9, 14].

This chapter is organized as follows. Section 33.2 first introduces some of the basic differential geometric concepts that are needed in nonlinear geometric control. After that, we introduce nonlinear controllability, which is one of the most fundamental concepts in nonlinear control theory. We then introduce the control methods of feedback linearization and input–output linearization, and apply them to the control of chaotic systems. In Section 33.3, we introduce Lyapunov stability theory for nonlinear dynamical systems, and illustrate how this theory can be used in the control and synchronization of chaotic systems.

33.2
Nonlinear Geometric Control

In this section we introduce and discuss a few of the main concepts and methods from the theory of nonlinear geometric control and apply them to the con-

trol of chaotic systems. We will restrict ourselves to local results and definitions on $\mathbb{R}^n$. For global results on general manifolds, see, e.g., [6, 13, 18].

33.2.1
Some Differential Geometric Concepts

For $x \in \mathbb{R}^n$, the *tangent space* $T_x\mathbb{R}^n$ at x is the set of tangent vectors to $\mathbb{R}^n$ at x. It may be shown that this implies that $T_x\mathbb{R}^n$ is isomorphic to $\mathbb{R}^n$ for every $x \in \mathbb{R}^n$. A *vector field* on $\mathbb{R}^n$ is a mapping X that assigns to each $x \in \mathbb{R}^n$ a tangent vector $X(x) \in T_x\mathbb{R}^n$. Given Cartesian coordinates $x_1, \ldots, x_n$ on $\mathbb{R}^n$, we denote by $\frac{\partial}{\partial x_i}\big|_x$ $(i \in \{1, \ldots, n\})$ the vector field that is tangent to the straight line $\ell_i = \{\bar{x} \in \mathbb{R}^n \mid \bar{x}_j = x_j (j \neq i)\}$ for every $x \in \mathbb{R}^n$. A vector field X on $\mathbb{R}^n$ is called a *smooth vector field* if for every $x \in \mathbb{R}^n$ there exist a neighborhood V of x and smooth functions $X_1, \ldots, X_n : V \to \mathbb{R}$ such that for all $\bar{x} \in V$ we have $X(\bar{x}) = \sum_{i=1}^n X_i(\bar{x})\frac{\partial}{\partial x_i}\big|_{\bar{x}}$.

Given smooth vector fields X, Y on $\mathbb{R}^n$, the *Lie bracket* of X and Y, which is denoted by $[X, Y]$, is defined by

$$[X, Y](x) := \frac{\partial Y}{\partial x}(x)X(x) - \frac{\partial X}{\partial x}(x)Y(x), \tag{33.1}$$

where

$$\frac{\partial X}{\partial x}(x) := \begin{pmatrix} \frac{\partial X_1}{\partial x_1} & \cdots & \cdots & \frac{\partial X_1}{\partial x_n} \\ \vdots & & & \vdots \\ \vdots & & & \vdots \\ \frac{\partial X_n}{\partial x_1} & \cdots & \cdots & \frac{\partial X_n}{\partial x_n} \end{pmatrix}(x)$$

and $\frac{\partial Y}{\partial x}(x)$ is defined analogously.

For smooth vector fields X, Y, and $k \in \mathbb{N}$, we define the vector field $\text{ad}_X^k Y$ recursively by $\text{ad}_X^0 Y = Y$, $\text{ad}_X^k Y = [X, \text{ad}_X^{k-1} Y]$.

Given a smooth vector field X and a smooth function $\phi : \mathbb{R}^n \to \mathbb{R}$, the *Lie derivative* of ϕ along X, which is denoted by $\mathcal{L}_X\phi$, is a smooth real-valued function on $\mathbb{R}^n$, which is given by

$$\mathcal{L}_X\phi(x) := \sum_{i=1}^n X_i(x)\frac{\partial \phi}{\partial x_i}(x). \tag{33.2}$$

A *distribution* Δ on $\mathbb{R}^n$ is a mapping that assigns to each $x \in \mathbb{R}^n$ a linear subspace of $T_x\mathbb{R}^n$. Δ is called a *smooth distribution* if for each $\bar{x} \in \mathbb{R}^n$ there exist a neighborhood V of $\bar{x}$ and a set of smooth vector fields X_i, $i \in \mathcal{I}$, where $\mathcal{I}$ is some (possible infinite) index set, such that $\Delta(x) = \text{span}_{\mathbb{R}}\{X_i(x) \mid i \in \mathcal{I}\}$ for every $x \in V$. If $\{X_i \mid i \in \mathcal{I}\}$ is a set of smooth vector fields on $\mathbb{R}^n$, then their span is the distribution defined by

$$\operatorname{span} \{X_i \mid i \in \mathcal{I}\} : x \mapsto \operatorname{span}_{\mathbb{R}} \{X_i(x) \mid i \in \mathcal{I}\}. \tag{33.3}$$

The *dimension* of a distribution Δ at $x \in \mathbb{R}^n$ is the dimension of the linear subspace $\Delta(x)$. A distribution is called *constant dimensional* if the dimension of $\Delta(x)$ does not depend on the point $x \in \mathbb{R}^n$. A distribution Δ is called *involutive* if $[X, Y] \in \Delta$, whenever $X, Y \in \Delta$.

33.2.2
Nonlinear Controllability

We consider a nonlinear control system of the form

$$\begin{cases} \dot{x} &= f(x) + \sum_{i=1}^{m} u_i g_i(x) \\ y &= h(x) \end{cases}, \tag{33.4}$$

where $x = \operatorname{col}(x_1, x_2, \ldots, x_n) \in \mathbb{R}^n$ are the states, $u = \operatorname{col}(u_1, \ldots, u_m) \in \mathbb{R}^m$ are the controls, $y = \operatorname{col}(y_1, \ldots, y_p) \in \mathbb{R}^p$ are the outputs, $f, g_1, \ldots, g_m$ are smooth vector fields on $\mathbb{R}^n$, and $h = \operatorname{col}(h_1, \ldots, h_p) : \mathbb{R}^n \to \mathbb{R}^p$ is a smooth function. The vector field f is called the *drift vector field* and the vector fields $g_1, \ldots, g_m$ are called the *control vector fields*. It is assumed that the uncontrolled system (i.e., the system (33.4) with $u \equiv 0$) is chaotic, and that the controls u are such that for any initial condition $x(0) = x^0$ the solution of (33.4) is defined on $[0, +\infty)$ and is unique. This solution will be denoted by $x(t, x^0, u)$, while the resulting output at time $t \geq 0$ will be denoted by $y(t, x^0, u)$.

We will call the system (33.4) *linear* in the coordinates x if $f(x) = Ax$, $g_i(x) = b_i$ $(i = 1, \ldots, m)$, $h(x) = Cx$, where A, b_i, C are constant matrices with appropriate dimensions. Note that a system that is linear in one set of coordinates does not necessarily need to be linear in a different set of coordinates, see, e.g., Example 33.8 for an illustration.

The system (33.4) is called (globally) *controllable* if for every $x^0, x^1 \in \mathbb{R}^n$ there exist $0 < T < +\infty$ and $u(t)$ defined on $[0, T]$ such that $x^1 = x(T, x^0, u)$, i.e., if one can steer from any initial position x^0 to any final position x^1 in finite time.

It is well known (see, e.g., [3]) that a *linear* system is globally controllable if and only if it satisfies the so-called *Kalman rank condition* ([7]):

$$\operatorname{rank}\begin{pmatrix} B & AB & \cdots & A^{n-1}B \end{pmatrix} = n. \tag{33.5}$$

Starting in the early 1970s research has also been directed toward nonlinear controllability, where the aim was to develop similar results as there are available in the linear (time-invariant) setting. However, it soon turned out that this program might be too ambitious, in that apart from a few particular generalizations, a completely parallel theory on nonlinear controllability is not feasible. Therefore, various weaker notions of nonlinear controllability have been devel-

oped in the 1970s and 1980s, all with an emphasis on computational characterizations and their implications on the system structure.

We will first define (local) nonlinear controllability.

Definition 33.1 (Local controllability)
Consider the nonlinear control system (33.4), and let $x^0 \in \mathbb{R}^n$ be given. Let V be a neighborhood of x^0. Let $R^V(x^0, T)$ denote the set of all points that can be reached from x^0 at time $T > 0$, following trajectories which remain in V for $0 \le t \le T$:

$$R^V(x^0, T) = \{x \in \mathbb{R}^n \mid \exists u : x(t, x^0, u) \in V (0 \le t \le T) \text{ and } x(T, x^0, u) = x\}.$$
(33.6)

Further, define the *V-reachable set at time T* by

$$R_T^V(x^0) = \bigcup_{\tau \le T} R^V(x^0, \tau).$$
(33.7)

Then the system (33.4) is called *locally controllable from x^0* if for every neighborhood V of x^0 and every $T > 0$ one has that $R_T^V(x^0)$ contains a neighborhood of x^0.

It will turn out that in characterizing nonlinear controllability, the Lie bracket of vector fields will play a pivotal role. To motivate this, we first consider an example.

Example 33.2 Consider the system

$$\dot{x} = u_1 g_1(x) + u_2 g_2(x),$$
(33.8)

where

$$g_1(x) = Ax, A = \begin{pmatrix} 0 & -1 & -1 \\ 1 & 0.4 & 0 \\ 0 & 0 & 0 \end{pmatrix}, \quad g_2(x) = \begin{pmatrix} 0 \\ 0 \\ 2 + (x_1 - 4)x_3 \end{pmatrix}.$$
(33.9)

Note that when $u_1 = u_2 = 1$, this system is a chaotic Rössler system. For this system, we have

$$[g_1, g_2] = \frac{\partial g_2}{\partial x} g_1 - \frac{\partial g_1}{\partial x} g_2 =$$

$$\begin{pmatrix} 0 & 0 & 0 \\ 0 & 0 & 0 \\ x_3 & 0 & x_1 - 4 \end{pmatrix} \begin{pmatrix} -x_2 - x_3 \\ x_1 + 0.4x_2 \\ 0 \end{pmatrix} -$$

$$\begin{pmatrix} 0 & -1 & -1 \\ 1 & 0.4 & 0 \\ 0 & 0 & 0 \end{pmatrix} \begin{pmatrix} 0 \\ 0 \\ 2 + (x_1 - 4)x_3 \end{pmatrix} = \tag{33.10}$$

$$\begin{pmatrix} 2 + (x_1 - 4)x_3 \\ 0 \\ -x_3(x_2 + x_3) \end{pmatrix}.$$

Since there are two independent controls, we see that the system can move instantaneously in only two independent directions, which does not result in controllability. However, an extra direction can be produced by performing a "maneuver" as follows. Choose $0 < \varepsilon \ll 1$, and choose the controls u_1, u_2 according to: $u_1 = 1, u_2 = 0$ $(0 < t \le \varepsilon)$, $u_1 = 0, u_2 = 1$ $(\varepsilon < t \le 2\varepsilon)$, $u_1 = -1, u_2 = 0$ $(2\varepsilon < t \le 3\varepsilon)$, $u_1 = 0, u_2 = -1$ $(3\varepsilon < t \le 4\varepsilon)$. It is now straightforwardly shown that for $u_1 = \pm 1, u_2 = 0$ the solutions of (33.8) satisfy

$$x(t) = \left(I + u_1 t A + \frac{1}{2} t^2 A^2 \right) x(0) + \text{h.o.t.,} \tag{33.11}$$

where "h.o.t." stands for "higher order terms." Also, it may be shown that for $u_1 = 0, u_2 = \pm 1$, the solutions of (33.8) satisfy

$$x_1(t) = x_1(0), x_2(t) = x_2(0),$$
$$x_3(t) = x_3(0) +$$
$$\left(x_3(0) + \frac{2}{x_1(0) - 4} \right) \left(u_2(x_1(0) - 4)t + \frac{1}{2}(x_1(0) - 4)^2 t^2 \right) + \text{h.o.t.}$$
$$\tag{33.12}$$

Using (33.11) and (33.12), it may then be shown that when, e.g., $x(0) = \text{col}(0, 0, 1)$, the maneuver described above results in (up to second-order terms in ε)

$$x(0) = \begin{pmatrix} 0 \\ 0 \\ 1 \end{pmatrix}, \quad x(\varepsilon) \approx \begin{pmatrix} -\varepsilon \\ -0.5\varepsilon^2 \\ 1 \end{pmatrix}, \quad x(2\varepsilon) \approx \begin{pmatrix} -\varepsilon \\ -0.5\varepsilon^2 \\ 3\varepsilon^2 - 2\varepsilon + 1 \end{pmatrix},$$

(33.13)

$$x(3\varepsilon) \approx \begin{pmatrix} -2\varepsilon^2 \\ 0 \\ 3\varepsilon^2 - 2\varepsilon + 1 \end{pmatrix}, \quad x(4\varepsilon) \approx \begin{pmatrix} -2\varepsilon^2 \\ 0 \\ -\varepsilon^2 + 1 \end{pmatrix}.$$

Comparing (33.10) and (33.13), we then see that we have

$$x(4\varepsilon) \approx x(0) + \varepsilon^2 [g_1, g_2](x(0)).$$

(33.14)

In fact it may be shown that for *any* pair of smooth input vector fields g_1, g_2 a maneuver as described above will give (33.14). Hence we see the Lie bracket of vector fields determines if and how by means of appropriate "maneuvers" new directions of movement may be produced.

Based on the above example and on the interpretation of the Lie bracket there, one might arrive at the following conjecture about (local) controllability of (33.4). Define the distribution C consisting of all repeated Lie brackets of the vector fields $f, g_1, \ldots, g_m$:

$$\begin{aligned} C = \text{span}\{ & [X_{i_k}, [\ldots, [X_{i_2}, X_{i_1}], \ldots]] \mid k \in \mathbb{N}, \\ & X_{i_1}, \ldots, X_{i_k} \in \{f, g_1, \ldots, g_m\}\}. \end{aligned}$$

(33.15)

Then the conjecture might be that (33.4) is locally controllable at $x^0 \in \mathbb{R}^n$ if $\dim(C(x^0)) = n$. However, this conjecture is only true for the so-called driftless systems, i.e., systems for which $f \equiv 0$, under a technical assumption on the set of input functions. The following example shows that the conjecture is not true in general for systems with drift.

Example 33.3 Consider the single-input nonlinear system

$$\dot{x} = f(x) + g(x)u,$$

(33.16)

where $f(x) = g_2(x)$ from Example 33.2 and $g(x) = g_1(x)$ from Example 33.2. For this system, we find that

$$[f, g] = \begin{pmatrix} -2 - (x_1 - 4)x_3 \\ 0 \\ x_3(x_2 + x_3) \end{pmatrix}, \quad [g, [f, g]] = \begin{pmatrix} 2x_2(x_2 + x_3) \\ 2 + (x_1 - 4)x_3 \\ x_3(x_1 + 0.4x_2). \end{pmatrix}$$

(33.17)

This gives that for $x^0 \in \Omega := \{x \in \mathbb{R}^3 \mid x_3 = 0\}$, we have

$$\dim(\mathrm{span}\{f(x^0), [f,g](x^0), [g,[f,g]](x^0)\}) = 3$$

and hence $\dim(C(x^0)) = 3$ for every $x^0 \in \Omega$. However, note that when $x_3 = 0$, we have that $\dot{x}_3 = 2 > 0$, which implies that from points $x^0 \in \Omega$, only points satisfying $x_3 > 0$ can be reached. Thus, the system (33.1) is not controllable from points $x^0 \in \Omega$ and hence the conjecture above is not true in general for systems with drift.

The fact that our conjecture is not true is due to the special role played by the drift vector field f in maneuvers: we cannot move "backward" along the vector field f, while we *can* move "backward" along the vector field g_i by choosing $u_i < 0$.

On the other hand, in terms of parts of the state space that can be reached, there is an essential difference between systems for which $\dim(C) = n$ and systems for which $\dim(C) < n$. This is illustrated by the following example.

Example 33.4 Consider an n-dimensional control system $\dot{x} = f(x) + g(x)u$, where the uncontrolled dynamics is chaotic and possesses a strange attractor Ω with fractal dimension $0 < d < n$. Assume that the control vector field has the form $g(x) = \phi(x)f(x)$ for some function $\phi : \mathbb{R}^n \to \mathbb{R}$, which means that $f(x)$ and $g(x)$ are linearly dependent. It is then straightforwardly shown that for any $x^0 \in \Omega$ one has that $\dim(C(x^0)) \leq 1$, and hence (33.15) is not satisfied. Furthermore, we have for every $x^0 \in \Omega$ and every control function u the vector $f(x^0) + ug(x^0)$ is tangent to Ω, which means that Ω is an invariant set for the controlled system for *any* control function u. This then implies that for any $x^0 \in \Omega$ the reachable set is a set with dimension $\bar{d} \leq d < n$.

It may be shown that the conclusion arrived in Example 33.4 holds in general: when $\dim(C(x^0)) < n$, the reachable set from x^0 is a set with empty interior (a set with dimension $\bar{d} < n$). On the other hand, it may be shown that when $\dim(C(x^0)) = n$, the reachable set from x^0 is a set with nonempty interior (an n-dimensional set). This motivates the following definitions.

Definition 33.5 (Accessibility)
1. The system (33.4) is called *locally accessible from* x^0 if $R_T^V(x^0)$ contains a nonempty open subset of $\mathbb{R}^n$ for all neighborhoods V of x^0 and all $T > 0$.
2. If the condition in 1 holds for any $x^0 \in \mathbb{R}^n$, then the system (33.4) is called *locally accessible*.
3. The system (33.4) is called *locally strongly accessible from* x^0 if for any neighborhood V of x^0 the set $R^V(x^0, T)$ contains a nonempty open subset of $\mathbb{R}^n$ for any sufficiently small $T > 0$.

We then have the following result:

Theorem 33.6 *Consider the system (33.4) and define the following distribution:*

$$
\begin{aligned}
C_0 = \operatorname{span}\big\{ & [X_{i_k}, [\ldots, [X_{i_2}, X_{i_1}], \ldots]] \mid k \in \mathbb{N} \\
& X_{i_2}, \ldots, X_{i_k} \in \{f, g_1, \ldots, g_m\}, X_{i_1} \in \{g_1, \ldots, g_m\}\big\}
\end{aligned}
\tag{33.18}
$$

Then we have the following:
1. *The system is locally accessible from $x^0 \in \mathbb{R}^n$ if $\dim(C(x^0)) = n$.*
2. *The system is locally strongly accessible from $x^0 \in \mathbb{R}^n$ if $\dim(C_0(x^0)) = n$.*

Remark 33.7 If the system (33.4) is linear, i.e., $f(x) = Ax$, where A is a constant (n, n)-matrix, and $g_i(x) = b_i \in \mathbb{R}^n$, we have

$$
[g_i, g_j] = 0 (i, j = 1, \ldots, m)
\tag{33.19}
$$

and

$$
[f, g_i] = \frac{\partial b_i}{\partial x} Ax - \frac{\partial(Ax)}{\partial x} b_i = -Ab_i \quad (i = 1, \ldots, m).
\tag{33.20}
$$

Continuing in this way, it may be shown that all repeated Lie brackets containing at least two g_i's are zero, and that

$$
\operatorname{ad}_f^k g_i = (-1)^k A^k b_i \ (k \in \mathbb{N}, i = 1, \ldots, m).
\tag{33.21}
$$

Using the Cayley-Hamilton theorem (see, e.g., [3]), this then gives that

$$
\begin{aligned}
C_0 = & \operatorname{span}\{(-1)^k A^k b_i \mid k \in \mathbb{N}, i = 1, \ldots, m\} = \\
& \operatorname{span}\{b_i, Ab_i, \ldots, A^{n-1} b_i \mid i = 1, \ldots, m\} = \\
& \operatorname{Im}\big(B \quad AB \quad \cdots \quad A^{n-1} B \big).
\end{aligned}
\tag{33.22}
$$

Thus, it follows from the Kalman rank condition (33.5) that for linear systems (global) controllability is equivalent to strong accessibility.

33.2.3
Chaos Control Through Feedback Linearization

Example 33.8 For $x \in \mathbb{R}^+ \times \mathbb{R}^+$, we consider the following nonlinear control system:

$$
\begin{cases}
\dot{x}_1 = x_1 \ln x_2, \\
\dot{x}_2 = -x_2 \ln x_1 + x_2 u.
\end{cases}
\tag{33.23}
$$

For this system, we define new coordinates $z_1 = \ln x_1$, $z_2 = \ln x_2$. Using the Chain rule, we then find that in these new coordinates the system becomes

$$\begin{cases} \dot{z}_1 = \dfrac{\dot{x}_1}{x_1} = \ln x_2 = z_2 \\[2mm] \dot{z}_2 = \dfrac{\dot{x}_2}{x_2} = -\ln x_1 + u = -z_1 + u \end{cases} \tag{33.24}$$

and thus using a state-space transformation reveals that our system is intrinsically a linear system.

Obviously, controlling a linear system is much easier than controlling a nonlinear system. Thus it might be interesting to know whether or not there exists a state space transformation that transforms a nonlinear system into a linear system. However, for chaotic systems the nonintegrability of the dynamics implies that the answer to this question is always negative. On the other hand, besides a state space transformation we also still have the freedom to apply a so-called *static-state feedback transformation* to the system. For a system (33.4) and $x^0 \in \mathbb{R}^n$, a regular static-feedback transformation around x^0 (or briefly a *regular static-state feedback* around x^0) is a control action of the form

$$u = a(x) + \beta(x)v, \tag{33.25}$$

where $a : \mathbb{R}^n \to \mathbb{R}^m$, $\beta : \mathbb{R}^n \to \mathbb{R}^{m \times m}$, $\det(\beta(x^0)) \neq 0$ and $v \in \mathbb{R}^m$ denotes new controls.

As is illustrated by the following example, application of a state space transformation *and* a static-feedback transformation may (locally) transform a chaotic system into a linear system.

Example 33.9 Consider the following Lorenz system:

$$\begin{cases} \dot{x}_1 = \sigma(x_2 - x_1), \\ \dot{x}_2 = rx_1 - x_2 - x_1 x_3 \\ \dot{x}_3 = x_1 x_2 - bx_3. \end{cases} \tag{33.26}$$

We will assume that the parameter b can be controlled around its "standard" value of $\frac{8}{3}$. Thus, we have $b = \frac{8}{3} + u$, where u denotes the control. For this system we define new coordinates $\zeta_1 = x_1$, $\zeta_2 = \sigma(x_2 - x_1)$, $\zeta_3 = \sigma\ (rx_1 - x_2 - x_1 x_3 - \sigma(x_2 - x_1))$. (It should be noted that these coordinates do not define a *global* set of new coordinates: inversion gives $x_1 = \zeta_1$, $x_2 = \frac{1}{\sigma}\zeta_2 + \zeta_1$, $x_3 = \frac{1}{\zeta_1}(rx_1 - x_2 - \zeta_2 - \zeta_3)$, and hence there is a singularity at $\zeta_1 = x_1 = 0$.) Further, on $\Omega := \{x \in \mathbb{R}^3 \mid x_1 x_3 \neq 0\}$, define a regular static-state feedback (33.25) with

$$a(x) = \frac{1}{x_1 x_3}\left[\sigma(r - x_3 + \sigma)(x_2 - x_1) - (1 + \sigma)(rx_1 - x_2 - x_1 x_3) - x_1\left(x_1 x_2 - \frac{8}{3}x_3\right)\right]$$

$$\beta(x) = \frac{1}{\sigma x_1 x_3}$$

Then it may be shown that in the new coordinates ζ the closed-loop system on Ω takes the form

$$\begin{cases} \dot{\zeta}_1 = \zeta_2 \\ \dot{\zeta}_2 = \zeta_3, \\ \dot{\zeta}_3 = v. \end{cases} \tag{33.27}$$

Thus we see that by means of appropriate state space and feedback transformations, the system (33.26) may be (locally) transformed into a linear system.

Remark 33.10 When applying the controller derived in Example 33.9 one needs to take into account the singularities that have been introduced in the design of the controller. Namely, as already indicated, in the first place there is a singularity associated with the new coordinates, and secondly there is a singularity associated with the static-state feedback. Unlike in controller design for linear control systems, it is very often difficult or even infeasible to avoid this type of singularities in controller design for nonlinear control systems. As a consequence, nonlinear control problems are often defined and solved locally (i.e., away from singularities). Obviously, when applying such local controllers globally, extra care needs to be taken, and often partial redesign and extra analysis are necessary.

Based on Example 33.9 and Remark 33.10, we formulate the following problem.

Problem 1 State space and feedback transformation into a linear system
Consider a nonlinear system (33.4) with $m = 1$. Find, if possible, an open subset $V \subset \mathbb{R}^n$, new coordinates $\zeta = \Psi(x)$ on V, and a regular static-state feedback $u = a(x) + \beta(x)v$ defined on V, such that in the new coordinates the closed-loop system takes the form

$$\dot{\zeta} = A\zeta + Bv \tag{33.28}$$

for $\zeta \in \Psi(V)$, where the system (33.28) is controllable.

A solution to this problem is given in the following result.

Theorem 33.11 *Consider the system (33.4) with $m = 1$, and let $x^0 \in \mathbb{R}^n$ satisfy $f(x^0) = 0$. Then there exist a neighborhood $V \subset \mathbb{R}^n$ of x^0, a coordinate transformation $\zeta = \Psi(x)$ on V and a regular static-state feedback $u = a(x) + \beta(x)v$ defined on V such that ζ satisfies (33.28) for $\zeta \in \Psi(V)$ if and only if*

$$\dim(\text{span}\{g(x^0), \text{ad}_f g(x^0), \ldots, \text{ad}_f^{n-1} g(x^0)\}) = n \tag{33.29}$$

and

$\text{span}\{g, \text{ad}_f g, \dots, \text{ad}_f^{n-2} g\}$ is involutive around x^0. $\qquad(33.30)$

Moreover, if (33.29) and (33.30) hold, there exist a function ϕ satisfying $\phi(x^0) = 0$ and a neighborhood V of x^0 such that

$$\mathcal{L}_{\text{ad}_f^k g} \phi(x) = 0 \quad (k = 0, 1, \dots, n-2; \forall x \in V) \qquad(33.31)$$

and

$$\mathcal{L}_{\text{ad}_f^{n-1} g} \phi(x^0) \neq 0. \qquad(33.32)$$

Given ϕ, a solution to Problem 1 around x^0 is then given by

$$\begin{cases} \zeta_i = \mathcal{L}_f^{i-1} \phi \quad (i = 1, \dots, n) \\ a(x) = -\left(\mathcal{L}_g \mathcal{L}_f^{n-1} \phi(x) \right)^{-1} \mathcal{L}_f^n \phi(x) \,. \\ \beta(x) = \left(\mathcal{L}_g \mathcal{L}_f^{n-1} \phi(x) \right)^{-1} \end{cases} \qquad(33.33)$$

Remark 33.12
1. If $f(x^0) \neq 0$, the conditions of Theorem 33.11 are equivalent to the existence of a coordinate transformation $\zeta = \Psi(x)$ and a static-state feedback $u = a(x) + \beta(x)v$ such that the closed-loop system in the coordinates ζ has the form $\dot{\zeta} = f(x^0) + A\zeta + Bv$.
2. Problem 1 and its solution can, *mutatis mutandis*, also be formulated for systems for which $m > 1$ (see e.g., [6, 13]).

Example 33.13 Consider again the Lorenz system (33.26) with $b = \frac{8}{3} + u$. For this system, we have that

$$f(x) = \begin{pmatrix} \sigma(x_2 - x_1) \\ rx_1 - x_2 - x_1 x_3 \\ x_1 x_2 - \frac{8}{3} x_3 \end{pmatrix}, \quad g(x) = \begin{pmatrix} 0 \\ 0 \\ -x_3 \end{pmatrix}. \qquad(33.34)$$

The uncontrolled system then has an unstable equilibrium at the origin, and two unstable equilibria at $\bar{x}_\pm = (\pm \bar{x}_1, \pm \bar{x}_1, r - 1)$, where $\bar{x}_1 = \sqrt{\frac{8}{3}(r-1)}$. We will now show how to use the result of Theorem 33.11 to design a controller that stabilizes the equilibrium point $\bar{x}_+$. From (33.34) it follows that

$$\mathrm{ad}_f g = \frac{\partial g}{\partial x} f - \frac{\partial f}{\partial x} g = \begin{pmatrix} 0 & 0 & 0 \\ 0 & 0 & 0 \\ 0 & 0 & -1 \end{pmatrix} \begin{pmatrix} \sigma(x_2 - x_1) \\ rx_1 - x_2 - x_1 x_3 \\ x_1 x_2 - \frac{8}{3} x_3 \end{pmatrix} -$$

$$\begin{pmatrix} -\sigma & \sigma & 0 \\ r - x_3 & -1 & -x_1 \\ x_2 & x_1 & -\frac{8}{3} \end{pmatrix} \begin{pmatrix} 0 \\ 0 \\ -x_3 \end{pmatrix} = \begin{pmatrix} 0 \\ -x_1 x_3 \\ -x_1 x_2 \end{pmatrix} \tag{33.35}$$

and similarly,

$$\mathrm{ad}_f^2 g = \begin{pmatrix} \sigma x_1 x_3 \\ -\sigma x_3 (x_2 - x_1) - x_1 (2x_1 x_2 - \frac{5}{3} x_3) \\ -\sigma x_2 (x_2 - x_1) - x_1 (rx_1 + \frac{5}{3} x_2 - 2x_1 x_3) \end{pmatrix}. \tag{33.36}$$

Due to the triangular structure of $g, \mathrm{ad}_f g, \mathrm{ad}_f^2 g$, it is straightforward to see that (33.29) holds at $\bar{x}_+$. We further have that

$$[g, \mathrm{ad}_f g] = \begin{pmatrix} 0 \\ x_1 x_3 \\ -x_1 x_2 \end{pmatrix} = \frac{2x_1 x_2}{x_3} g - \mathrm{ad}_f g \tag{33.37}$$

and thus also (33.30) holds.

It now follows from (33.34) and (33.35) that a function ϕ satisfies the conditions of Theorem 33.11 if and only if $\phi(0) = 0$ and ϕ is a nonconstant function of x_1 only. If we take $\zeta_1 = \phi(x) = x_1$, it may then be shown that the new coordinates ζ_2, ζ_3 and the static-state feedback as suggested by (33.33) are the same as in Example 33.9.

Note that it follows from the definition of ζ that $\zeta = (\bar{x}_1, 0, 0)$ if and only if $x = \bar{x}_+$. This means that stabilization of $(\bar{x}_1, 0, 0)$ for (33.27) will result in stabilization of $\bar{x}_+$ for (33.26). It is easily checked that if we choose k_0, k_1, k_2 such that the roots of the polynomial $s^3 + k_2 s^2 + k_1 s + k_0$ are in the open left half plane, we have the static-state feedback $v = -k_2 \zeta_3 - k_1 \zeta_2 - k_0(\zeta_1 - \bar{x}_1)$ will indeed stabilize the point $(\bar{x}_1, 0, 0)$ for (33.27).

33.2.4
Chaos Control Through Input–Output Linearization

Consider the system (33.4) with $m = p$. We will call the system *input–output decoupled* if, after a possible permutation of the controls, the following properties hold:
1. for each $i \in \{1, \ldots, m\}$ the output y_i is not affected by the controls u_j $(j \neq i)$,
2. the output y_i is affected by the control u_i $(i = 1, \ldots, m)$.

If the system (33.4) is not input–output decoupled, one may try to achieve this by means of a feedback $u = a(x) + \beta(x)v$, where $v \in \mathbb{R}^m$ denotes the new con-

trols. In order to express conditions under which this is possible, we define the *relative degree* r_i of the ith output y_i as the smallest integer such that

$$
\begin{cases}
\mathcal{L}_{g_j} \mathcal{L}_f^k h_i(x) = 0 \ \forall x \in \mathbb{R}^n, \ j \in \{1, \dots, m\}, \ k \in \{0, \dots, r_i - 2\} \\
\mathcal{L}_{g_j} \mathcal{L}_f^{r_i - 1} h_i(x) \neq 0 \ \text{ for some } x \in \mathbb{R}^n, \text{ and some } j \in \{1, \dots, m\}.
\end{cases}
\tag{33.38}
$$

It may then be shown that the time derivatives of the outputs y_i $(i = 1, \dots, m)$ satisfy

$$
\begin{aligned}
y_i^{(k)} &= \mathcal{L}_f^k h_i(x) & (k = 0, \dots, r_i - 1) \\
y_i^{(r_i)} &= \mathcal{L}_f^{r_i} h_i(x) + \sum_{j=1}^m u_j \mathcal{L}_{g_j} \mathcal{L}_f^{r_i - 1} h_i(x)
\end{aligned}
\tag{33.39}
$$

The relative degrees have the property that either $r_i \in \{1, \dots, n\}$ or $r_i = +\infty$. If all relative degrees of (33.4) are finite, we let $A(x)$ be the (m, m)-matrix with entries

$$
a_{ij}(x) = \mathcal{L}_{g_j} \mathcal{L}_f^{r_i - 1} h_i(x) \ \ (i, j = 1, \dots, m).
\tag{33.40}
$$

The matrix $A(x)$ is called the *decoupling matrix* of (33.4). Define

$$
\widetilde{Y} = \begin{pmatrix} y_1^{(r_1)} \\ y_2^{(r_2)} \\ \vdots \\ y_m^{(r_m)} \end{pmatrix}, \quad b(x) = \begin{pmatrix} \mathcal{L}_f^{r_1} h_1(x) \\ \mathcal{L}_f^{r_2} h_2(x) \\ \vdots \\ \mathcal{L}_f^{r_m} h_m(x) \end{pmatrix}.
\tag{33.41}
$$

It then follows from (33.39)–(33.41) that we have

$$
\widetilde{Y} = b(x) + A(x)u.
\tag{33.42}
$$

Now assume that there exists $x^0 \in \mathbb{R}^n$ such that $A(x^0)$ is invertible. This implies that there exists a neighborhood V of x^0 such that $A(x)$ is invertible for all $x \in V$. Thus, on V the following state feedback is well defined:

$$
u = A(x)^{-1}(v - b(x)),
\tag{33.43}
$$

where $v \in \mathbb{R}^m$ denotes the new controls. From (33.43) and (33.44) we then have that application of this feedback to (4) results in

$$
y_i^{(r_i)} = v_i \ \ (i = 1, \dots, m)
\tag{33.44}
$$

and thus the closed-loop systems (33.4) and (33.43) is input–output decoupled. Hence we have shown that the following holds.

Theorem 33.14 *Consider the system (33.4) with $m = p$. Assume that there exists a $x^0 \in \mathbb{R}^n$ such that $A(x^0)$ is invertible. Then there exists a neighborhood V of x^0 and a static-state feedback $u = \alpha(x) + \beta(x)v$ such that the closed-loop system is input–output decoupled on V.*

Remark 33.15 For analytic systems, the condition given in Theorem 33.14 is also a necessary condition for (local) solvability of the input–output decoupling problem. However, this is not the case for nonanalytic systems (see e.g., [13] for a counter example).

We first show that after (33.4) has been input–output decoupled using the static-state feedback (33.43), there exists a coordinate transformation that transforms (33.4) into a so-called normal form.

It may be shown that if for $x^0 \in \mathbb{R}^n$ we have $A(x^0)$ is invertible, then there exists a neighborhood V of x^0 such that the functions $\xi_{ij} = \mathcal{L}_f^{j-1} h_i$ $(i = 1, \dots, m;\ j = 1, \dots, r_i)$ are independent. Denote

$$\xi = \mathrm{col}\big(\xi_{ij} \mid i = 1, \dots, m;\ j = 1, \dots, r_i\big)$$

Defining $d := n - \sum_{i=1}^m r_i$, there then exists a function $z : V \to \mathbb{R}^d$ such that (ξ, z) forms a new set of coordinates for (33.4) on V. Using (33.39) and (33.44), and denoting $\Psi(x) = (\xi(x), z(x))$, it then follows that in the coordinates (ξ, z) the closed-loop dynamics are given by:

$$\begin{cases} \dot{\xi}_{i1} = \xi_{i2} \\ \quad \vdots \qquad\qquad\qquad (i = 1, \dots, m) \\ \dot{\xi}_{ir_i - 1} = \xi_{ir_i} \\ \dot{\xi}_{ir_i} = v_i \\ \dot{z} = \bar{f}(\xi, z) + \bar{g}(\xi, z)v \\ y_i = \xi_{i1} \qquad\qquad (i = 1, \dots, m), \end{cases} \tag{33.45}$$

where

$$\bar{f}(\xi, z) = \Big[\mathcal{L}_f z(x) - \big(\mathcal{L}_{g_1} z \cdots \mathcal{L}_{g_m} z \big)(x) A(x)^{-1} b(x) \Big]_{x = \Psi^{-1}(\xi, z)}$$

$$\bar{g}(\xi, z) = \Big[\big(\mathcal{L}_{g_1} z \cdots \mathcal{L}_{g_m} z \big)(x) A(x)^{-1} \Big]_{x = \Psi^{-1}(\xi, z)}.$$

We next show how the result of Theorem 33.14 can be used to solve the so-called *output tracking problem*. To this end, assume that sufficiently smooth desired output trajectories $y_{d1}(t), \dots, y_{dm}(t)$ $(t \geq 0)$ are given, and that we wish to design a controller such that

$$\lim_{t \to \infty} |y_i(t) - y_{di}(t)| = 0 \quad (i = 1, \dots, m). \tag{33.46}$$

Assume that the decoupling matrix of the system is invertible, and that the static-state feedback (33.43) has been applied to the system. We then choose $k_{ij} \in \mathbb{R}$ such that all roots of the polynomials $s^{r_i} + \sum_{j=0}^{r_i-1} k_{ij} s^j$ are in the open right-half plane, and let v_i in (33.44) be given by

$$v_i = y_{di}^{(r_i)} - \sum_{j=0}^{r_i-1} k_{ij}(y_i^{(j)} - y_{di}^{(j)}) \quad (i = 1, \ldots, m). \tag{33.47}$$

Defining error signals $e_i = y_{di} - y_i$ ($i = 1, \ldots, m$), it then follows from (33.44) and (33.47) that

$$e_i^{(r_i)} + \sum_{j=0}^{r_i-1} k_{ij} e^{(j)} = 0. \tag{33.48}$$

By the choice of the k_{ij}'s this gives that $e_i(t) \to 0$ as $t \to \infty$ ($i = 1, \ldots, m$), and hence (33.46) holds.

This apparently solves the output tracking problem for our system. However, there is still a matter that needs to be taken into account, as is illustrated by the following example.

Example 33.16 Consider the system (33.26) with $b = \frac{8}{3} + u$ and $y = x_3$. We then have

$$\dot{y} = \dot{x}_3 = x_1 x_2 - \frac{8}{3} x_3 - u x_3 \tag{33.49}$$

and hence the relative degree of y equals 1, while the decoupling "matrix" is given by $A(x) = -x_3$, and $b(x) = x_1 x_2 - \frac{8}{3} x_3$. Note then that we can choose $\xi = x_3$, $z = \mathrm{col}(x_1, x_2)$. Assume that we want the output to track a *constant* reference, i.e., we have $y_d(t) = \bar{y} \in \mathbb{R}$. Choosing u, v as suggested by (33.43) and (33.47), we then obtain the following closed-loop system:

$$\begin{cases} \dot{\xi} = -k(\xi - \bar{y})(k > 0), \\ \dot{z}_1 = \sigma(z_2 - z_1), \\ \dot{z}_2 = r z_1 - z_2 - z_1 \xi, \\ y = \xi. \end{cases} \tag{33.50}$$

It is clear from the differential equation for ξ that $\xi(t) \to \bar{y}$ exponentially as $t \to +\infty$. It then follows (see, e.g., [8]) that the overall stability properties of the system (33.50) are determined by the stability properties of the linear time-invariant system

$$\dot{z} = \begin{pmatrix} -\sigma & \sigma \\ r - \bar{y} & -1 \end{pmatrix} z. \tag{33.51}$$

This system is stable if and only if $\bar{y} \geq r - 1$. Thus, if $\bar{y} < r - 1$, the proposed controller *does* solve the output tracking problem, but is still useless because it leads to instability of the overall closed-loop system.

Example 33.16 illustrates that when solving the output tracking problem, one needs to take into account the stability or boundedness of some internal dynamics. For constant reference trajectories these dynamics are normally called the *zero dynamics* of the system, while for nonconstant reference trajectories these dynamics are called the *tracking dynamics* of the system. Since the closed-loop systems (33.45) and (33.47) has the property that $\xi_{ij}(t) - y_{di}^{(j-1)}(t) \to 0$ as $t \to +\infty$ exponentially, it again follows (see, e.g., [8]) that the stability properties of the closed-loop system are determined by the stability properties of the tracking dynamics, which are given by

$$\dot{z} = \overline{f}(\widetilde{Y}_d(t), z) + \overline{g}(\widetilde{Y}_d(t), z)\overline{Y}_d(t), \tag{33.52}$$

where

$$\widetilde{Y}_d(t) = \mathrm{col}\left(y_{di}^{(j)}(t) \mid i = 1, \dots, m, \ j = 0, \dots, r_i - 1\right)$$

and

$$\overline{Y}_d(t) = \mathrm{col}\left(y_{1d}^{(r_1)}(t), \dots, y_{md}^{(r_m)}(t)\right).$$

Example 33.17 Consider a controlled Lorenz system of the form $\dot{x} = f(x) + g(x)u$, $y = h(x)$, with $f(x)$ as (33.34), $g(x) = \mathrm{col}(0, 1, 0)$ and $h(x) = x_1$. For this system, we have

$$\begin{cases} \dot{y} = 10(x_2 - x_1), \\ \ddot{y} = 380x_1 - 110x_2 - 10x_1x_3 + 10u. \end{cases} \tag{33.53}$$

Thus we see that the relative degree of the system equals 2. We then have $\xi = \mathrm{col}(x_1, 10(x_2 - x_1))$ and we can take $z = x_3$, which gives that after the feedback $u = \frac{1}{10}v - 38x_1 + 11x_2 + x_1x_3$ the system in the coordinates (ξ, z) takes the form

$$\begin{cases} \dot{\xi}_1 = \xi_2, \\ \dot{\xi}_2 = v, \\ \dot{z} = \xi_1\left(\xi_1 + \frac{1}{10}\xi_2\right) - \frac{8}{3}z, \\ y = \xi_1. \end{cases} \tag{33.54}$$

Next assume that a desired output $y_d(t)$ is given. Then according to (33.47), applying the controller

$$v = \ddot{y}_d(t) - k_1(\zeta_2 - \dot{y}_d(t)) - k_0(\zeta_1 - y_d(t)), \ \ k_0, k_1 > 0 \tag{33.55}$$

will result in $|y(t) - y_d(t)| \to 0$ as $t \to +\infty$. According to (33.52), the tracking dynamics of the system are then given by

$$\dot{z} = -\frac{8}{3}z + \psi(t), \ \ \psi(t) = y_d(t)\left(y_d(t) + \frac{1}{10}\dot{y}_d(t)\right). \tag{33.56}$$

The solutions of (33.56) are given by

$$z(t) = \exp\left(-\frac{8}{3}t\right)z(0) + \int_0^t \exp\left(-\frac{8}{3}(t-\tau)\right)\psi(\tau)\mathrm{d}\tau. \tag{33.57}$$

This gives that the tracking dynamics of the system are bounded as long as $y_d(t)$ and $\dot{y}_d(t)$ are bounded. Moreover, we further see that, whatever the initial conditions of the system are, the solution $z(t)$ of the tracking dynamics will always converge to the steady state solution

$$z_{ss}(t) = \int_0^t \exp\left(-\frac{8}{3}(t-\tau)\right)\psi(\tau)\mathrm{d}\tau. \tag{33.58}$$

For example, for $y_d(t) = \sin \omega t$, one finds the steady state solution

$$z_{ss}(t) = \frac{3 + \frac{27}{16}\omega^2 - 3\cos(2\omega t) - \frac{39}{20}\omega\sin(2\omega t) - \frac{9}{40}\omega^2\cos(2\omega t)}{16 + 9\omega^2} \tag{33.59}$$

33.3
Lyapunov Design

33.3.1
Lyapunov Stability and Lyapunov's First Method

Consider an n-dimensional dynamic system of the form

$$\dot{x} = f(x), \ x \in \mathbb{R}^n, \tag{33.60}$$

where the vector field f is assumed to be smooth. Given $x_0 \in \mathbb{R}^n$, we denote by $x(t, x_0)$ the solution of (33.60) at time $t \in \mathbb{R}$ that satisfies $x(0, x_0) = x_0$. A point $\bar{x} \in \mathbb{R}^n$ is called an *equilibrium point* (or *steady state*) of (33.60) if the system is at rest at $\bar{x}$, i.e., if $f(\bar{x}) = 0$. Note that this implies that $x(t, \bar{x}) = \bar{x}$ for all $t \in \mathbb{R}$.

In many practical situations, equilibrium points represent desirable operating conditions, and due to disturbances systems will often inevitably deviate from the operating conditions. Intuitively speaking, *stability* of the equilibrium point then means that when initial deviations are small enough, the deviations will remain small, while *asymptotic stability* means that in addition the system will asymptotically return to the equilibrium point when initial deviations are small enough. To formalize these intuitive concepts, we define sets $B_\varepsilon(\overline{x})$ in the following way.

$$B_\varepsilon(\overline{x}) = \{x \in \mathbb{R}^n \mid \|x - \overline{x}\| < \varepsilon\}, \tag{33.61}$$

where $\|\cdot\|$ denotes the Euclidean norm on $\mathbb{R}^n$.

Definition 33.18 (Lyapunov stability)
1. An equilibrium point $\overline{x} \in \mathbb{R}^n$ for (33.60) is called *stable* if for every $\varepsilon > 0$ there exists a $\delta > 0$ such that for all $x_0 \in B_\delta(\overline{x})$ and all $t \geq 0$ we have that $x(t, x_0) \in B_\varepsilon(\overline{x})$.
2. An equilibrium point $\overline{x} \in \mathbb{R}^n$ for (33.60) is called *locally asymptotically stable* if it is stable and if there exists a $\eta > 0$ such that for all $x_0 \in B_\eta(\overline{x})$ we have $\lim_{t \to +\infty} \|x(t, x_0) - \overline{x}\| = 0$.
3. An equilibrium point $\overline{x} \in \mathbb{R}^n$ for (33.60) is called *globally asymptotically stable* if it is stable and if in 2. one can choose $\eta = \infty$.
4. An equilibrium point $\overline{x} \in \mathbb{R}^n$ for (33.60) is called *unstable* if it is not stable.

For linear systems, i.e., $f(x) = Ax$ in (33.60) where A is a constant $n \times n$-matrix, we have the system either has a unique equilibrium $\overline{x} = 0$ when A is invertible, or it has an infinite number of equilibria when A is not invertible. Moreover, when A is not invertible, it may be shown that the stability properties of all equilibria are the same as the stability properties of the equilibrium at the origin. The following result then gives conditions for (asymptotic) stability of the origin for linear systems.

Theorem 33.19 *Consider a linear system $\dot{x} = Ax$, where A is a constant $n \times n$-matrix.*
1. *The origin is an asymptotically stable equilibrium point for the system if and only if all eigenvalues of A are located in the open left-half plane.*
2. *The origin is a stable equilibrium point for the system if and only if all eigenvalues of A are located in the closed left-half plane and the geometric and algebraic multiplicities of eigenvalues on the imaginary axis are the same.*

Example 33.20 The simplest illustration of an unstable system with eigenvalues on the imaginary axis is a one-degree-of-freedom mechanical system exhibiting rigid body motion, i.e., a particle with equation of motion given by $\ddot{q} = 0$, where q denotes the position of the particle. Defining $x = \text{col}(q, \dot{q})$, $A = \begin{pmatrix} 0 & 1 \\ 0 & 0 \end{pmatrix}$, the equation of motion may be rewritten as $\dot{x} = Ax$. We then

have that A has an eigenvalue at zero with algebraic multiplicity equal to 2 and geometric multiplicity equal to 1. Further, it is easily checked that the solution to the equation of motion is $q(t) = q(0) + \dot{q}(0)t$, so indeed the origin is an unstable equilibrium point.

For checking stability of an equilibrium point, one normally first tries to apply *Lyapunov's first method*, which relies on the so-called *Jacobian* of f at $\overline{x}$ that is defined by

$$D_x f(\overline{x}) = \left(\frac{\partial f}{\partial x}\right)(\overline{x}). \tag{33.62}$$

Notice that $D_x f(\overline{x})$ is a constant $n \times n$-matrix.

Theorem 33.21   *Let $\overline{x} \in \mathbb{R}^n$ be an equilibrium point for (33.60). We then have the following.*
1. *If all eigenvalues of $D_x f(\overline{x})$ are located in the open left-half plane, then $\overline{x}$ is an asymptotically stable equilibrium point of (33.60).*
2. *If $D_x f(\overline{x})$ has an eigenvalue in the open right-half plane, then $\overline{x}$ is an unstable equilibrium point of (33.60).*

Note that if the eigenvalues of $D_x f(\overline{x})$ are located in the closed left-half plane and there is at least one eigenvalue on the imaginary axis, we cannot use Theorem 33.21. In this case one needs to resort to Lyapunov's direct method (or any other method) to study the stability of equilibrium points. Lyapunov's direct method will be discussed in Section 33.3.2.

33.3.2
Lyapunov's Direct Method

In Lyapunov's direct method, one uses so-called Lyapunov functions to study the stability of equilibrium points. A Lyapunov function can be interpreted as a generalization of the concept of energy functions for mechanical systems. To motivate this, we first consider a mechanical example.

Example 33.22   Consider a simple harmonic oscillator with position coordinate x and velocity v, and assume that the oscillator is subjected to a hydrodynamic force with magnitude $v|v|$. The equation of motion of the oscillator is then given by

$$\begin{cases} \dot{x} = v, \\ \dot{v} = -x - v|v|. \end{cases} \tag{33.63}$$

Consider the total energy $E(x, v)$ of the oscillator:

$$E(x, v) = \frac{1}{2}x^2 + \frac{1}{2}v^2. \tag{33.64}$$

Using the Chain rule, we find that along a solution $(x(t), v(t))$ of (33.63), the time derivative of the total energy satisfies

$$\frac{d}{dt}(E(x(t), v(t))) = x(t)\dot{x}(t) + v(t)\dot{v}(t) = -v(t)^2|v(t)| \leq 0. \tag{33.65}$$

Since the time derivative in (33.65) is nonpositive, we conclude that the total energy cannot increase. Using the form of E and Definition 33.18, this then leads to the conclusion that the origin is a stable equilibrium point for (33.63).

We will now generalize the approach in Example 33.22. For the system (33.60), consider a differentiable function $V : \mathbb{R}^n \to \mathbb{R}$. Let $x(t)$ be a solution of (33.60), and consider the value $V(x(t))$ of V along this solution. We then have that the time derivative of $V(x(t))$ satisfies

$$\frac{d}{dt}V(x(t)) = \sum_{i=1}^{n}\frac{\partial V}{\partial x_i}(x(t))\dot{x}_i(t) = \sum_{i=1}^{n}\frac{\partial V}{\partial x_i}(x(t))f_i(x(t)) = \mathcal{L}_f V(x(t)). \tag{33.66}$$

Motivated by this equality, we define the function $\dot{V} : \mathbb{R}^n \to \mathbb{R}$ by

$$\dot{V}(x) := \mathcal{L}_f V(x). \tag{33.67}$$

From (33.66) it then follows that the function $\dot{V}$ keeps track of the increase/decrease of the function V along solutions of (33.60). As a consequence of this, one can use appropriately chosen functions V and the associated function $\dot{V}$ to study the stability of equilibrium points of (33.60).

We will call a differentiable function $V : \mathbb{R}^n \to \mathbb{R}$ a *Lyapunov function* for (33.60) on $\Omega \subset \mathbb{R}^n$ if $\dot{V} \leq 0$ on Ω. If $\dot{V} < 0$ on Ω, we will call V a *strict Lyapunov function* on Ω. We further call a function $V : \mathbb{R}^n \to \mathbb{R}$ *radially unbounded* if $V(x) \to \infty$ as $\|x\| \to \infty$.

We now have the following result.

Theorem 33.23 *Consider the system (33.60), and let $\overline{x} \in \mathbb{R}^n$ be an equilibrium point for the system.*
1. *$\overline{x}$ is a stable equilibrium point of (33.60) if there exist a neighborhood U of $\overline{x}$ and a Lyapunov function V on U such that $V(\overline{x}) = 0$ and $V > 0$ on $U\backslash\{\overline{x}\}$.*
2. *$\overline{x}$ is a locally asymptotically stable equilibrium point of (33.60) if there exist a neighborhood U of $\overline{x}$ and a strict Lyapunov function V on $U\backslash\{\overline{x}\}$ such that $V(\overline{x}) = 0$ and $V > 0$ on $U\backslash\{\overline{x}\}$.*
3. *$\overline{x}$ is a globally asymptotically stable equilibrium point of (33.60) if the conditions of 2. are satisfied with $U = \mathbb{R}^n$ and a function V that is radially unbounded.*

Remark 33.24   It may be shown that in fact the conditions given in Theorem 33.23 are also *necessary conditions* (see e.g., [8]). Thus, one might hope that the necessity part of the proof gives some clues as to how to construct appropriate Lyapunov functions. However, the necessity part of the proof relies on the knowledge of the solutions of the underlying differential equation. Obviously, in most cases (like, e.g., for chaotic systems) the solutions cannot be determined explicitly, so this does not help in the construction of a Lyapunov function.

33.3.3
LaSalle's Invariance Principle

In many cases, it is easier to construct a nonstrict Lyapunov function than to construct a strict Lyapunov function. However, in practice one is mostly interested in asymptotic stability rather than just stability, and we see from Theorem 33.23 that one cannot directly use the former type of function to prove asymptotic stability. However, this *can* be done by using the so-called *LaSalle's Invariance Principle*, which we will introduce in this subsection.

Theorem 33.25 (LaSalle's Invariance Principle)
Consider the system (33.60). Assume that there exists a compact positively invariant set Ω for (33.60) and a Lyapunov function V on Ω. Define the set

$$N = \{x \in \mathbb{R}^n \mid \dot{V}(x) = 0\} \tag{33.68}$$

and let N^* denote the largest positively invariant set in N. Then every solution of (33.60) on Ω approaches N^* as $t \to +\infty$.

A specialization of Theorem 33.25 to the case of asymptotic stability of equilibrium points is the following result.

Theorem 33.26   *Consider the system (33.60) with equilibrium point $\overline{x} \in \mathbb{R}^n$. Assume that there exist a neighborhood U of $\overline{x}$ and a Lyapunov function V on U such that $V(\overline{x}) = 0$ and $V > 0$ on $U \backslash \{\overline{x}\}$. Define N as in (33.68) and let N^* denote the largest positively invariant set in N. If there exists a neighborhood $\widetilde{U} \subset U$ of $\overline{x}$ such that $N^* \cap \widetilde{U} = \{\overline{x}\}$, then $\overline{x}$ is a locally asymptotically stable equilibrium point for (33.60). Moreover, if V is radially unbounded and we can take $U = \widetilde{U} = \mathbb{R}^n$, then $\overline{x}$ is a globally stable equilibrium point for (33.60).*

The following result gives a generalization of Theorem 33.25 to the case where Ω is not necessarily compact and positively invariant.

Theorem 33.27   *Consider the system (33.60). Assume that there exists a set $\Omega \subset \mathbb{R}^n$ and a Lyapunov function V on Ω which is bounded from below on Ω. Define the set N as in (33.68), and let N^* denote the largest invariant set in N. Then every bounded solution of (33.60) on Ω approaches N^* as $t \to \infty$.*
  We will apply Theorem 33.26 to the system from Example 33.22.

Example 33.28 Consider again the system from Example 33.22 and the energy function E defined in (33.65). We then have $\dot{E}(x, v) = -v|v|$, and hence $N = \{(x, v) \in \mathbb{R}^2 \mid \dot{E}(x, v) = 0\} = \{(x, v) \in \mathbb{R}^2 \mid v = 0\}$.

We next determine N^*, the largest positively invariant set in N. Let $(x_0, v_0) \in N^*$. Since $N^* \subset N$, it follows from the definition of N that $v_0 = 0$. Further, invariance of N^* implies that for every solution $(x(t), v(t)) \in N^*$ we have that $v(t) = 0$ for all $t \geq 0$, and hence $\dot{v}(t) = 0$ for all $t \geq 0$. In particular we then have for the solution $x(t, (x_0, v_0))$ that

$$0 = \dot{v}(0, (x_0, v_0)) = -x_0 - v_0|v_0| = -x_0$$

which implies that $N^* \subset \{(0, 0)\}$. On the other hand, the fact that $(0, 0)$ is an equilibrium point gives that $\{(0, 0)\} \subset N^*$, and hence $N^* = (0, 0)$. Noting that E is radially unbounded, this then gives with Theorem 33.26 the origin is a globally stable equilibrium point for (33.63).

33.3.4
Examples

In this subsection we apply the results from Sections 33.3.2 and 33.3.3 to some examples of chaotic systems. It should be noted that in some of the examples we encounter nonautonomous dynamics, while the results developed in this section only deal with autonomous dynamics. However, the examples have been chosen in such a way that indeed using results for autonomous dynamics can be justified. However, when dealing with nonautonomous dynamics in general, one *would* need to use the parallel theory that exists for nonautonomous dynamics (see e.g., [8] for details).

Example 33.29 (Tracking control of a chaotic Duffing system [12])
Consider a controlled chaotic Duffing system of the form

$$\begin{cases} \dot{x}_1 = x_2 \\ \dot{x}_2 = -px_2 - p_1 x_1 - x_1^3 + u + q \cos \omega t, \end{cases} \tag{33.69}$$

where p, p_1, q, ω are parameters. Let a sufficiently smooth reference trajectory $x_{d1}(t)$ for x_1 be given and define error signals $e_1(t) = x_{d1}(t) - x_1(t)$, $e_2(t) = \dot{x}_{d1}(t) - x_2(t)$. Consider the static-state feedback

$$u = \ddot{x}_{d1} + p\dot{x}_{d1} + p_1 x_{d1} + x_{d1}^3 - q \cos \omega t - K_d e_2 - K_p e_1 + 3x_1 x_{d1} e_1, \tag{33.70}$$

where the parameters K_p, K_d satisfy

$$K_p > -p_1, K_d > -p. \tag{33.71}$$

It is then straightforwardly shown that after (33.70) has been applied to (33.69), the time-invariant error dynamics satisfy

$$\begin{cases} \dot{e}_1 = e_2, \\ \dot{e}_2 = -(p_1 + K_p)e_1 - (p + K_d)e_2 - e_1^3. \end{cases} \qquad (33.72)$$

We will now show that the origin is a globally asymptotically stable equilibrium point for (33.72), and hence the static-state feedback (33.70) globally solves the tracking problem for (33.69). Let $\lambda \in \mathbb{R}$ satisfy

$$0 < \lambda < p + K_d \qquad (33.73)$$

and consider the function V given by

$$V(e) = \frac{1}{2}(e_2 + \lambda e_1)^2 + \frac{1}{2}\left[(p_1 + K_p) + \lambda(p + K_d) - \lambda^2\right]e_1^2 + \frac{1}{4}e_1^4. \qquad (33.74)$$

Note that it then follows from (33.71) and (33.73) that $V > 0$ on $\mathbb{R}^2 \backslash \{0\}$ and that V is radially unbounded. We now have

$$\begin{aligned} \dot{V} &= (e_2 + \lambda e_1)(\dot{e}_2 + \lambda \dot{e}_1) + \\ &\quad \left[(p_1 + K_p) + \lambda(p + K_d) - \lambda^2\right]e_1\dot{e}_1 + e_1^3\dot{e}_1 = \cdots = \\ &\quad -(p + K_d - \lambda)e_2^2 - \lambda(p_1 + K_p)e_1^2 - \lambda e_1^4. \end{aligned} \qquad (33.75)$$

From (33.71) and (33.73) it then follows that $\dot{V} < 0$ on $\mathbb{R}^2 \backslash \{0\}$. It then follows from Theorem 33.23 that indeed u globally solves the tracking problem for (33.69).

Example 33.30 Consider a transmitter system in the form of a Lorenz system

$$\begin{cases} \dot{x}_1 = \sigma(x_2 - x_1) \\ \dot{x}_2 = rx_1 - x_2 - x_1x_3 + p \\ \dot{x}_3 = x_1x_2 - bx_3 \\ \;\; y = x_2, \end{cases} \qquad (33.76)$$

where y denotes the transmitted signal and $\sigma, r, p, b > 0$ are parameters. Also consider a receiver system of the form

$$\begin{cases} \dot{z}_1 = \sigma(y - z_1), \\ \dot{z}_2 = \rho z_1 - z_2 - z_1z_3 + \pi, \\ \dot{z}_3 = z_1z_2 - bz_3. \end{cases} \qquad (33.77)$$

First assume that the parameter p in (33.76) is unknown, and that all other parameters are known. In (33.77) we then choose $\rho = r$, and define dynamics of π by

$$\dot{\pi} = y - z_2. \qquad (33.78)$$

Define error signals $e_i = x_i - z_i$ $(i = 1, 2, 3)$, $\varepsilon_1 = p - \pi$. The error dynamics are then given by

$$
\begin{cases}
\dot{e}_1 = -\sigma e_1, \\
\dot{e}_2 = re_1 - e_2 - x_1 x_3 + z_1 z_3 + \varepsilon_1, \\
\dot{e}_3 = x_1 x_2 - z_1 z_2 - be_3, \\
\dot{\varepsilon}_1 = -e_2.
\end{cases}
\tag{33.79}
$$

The first differential equation in (33.79) implies that $e_1(t) \to 0$ exponentially as $t \to +\infty$. This means that the overall stability properties of (79) are determined by the stability properties of the $(e_2, e_3, \varepsilon_1)$-dynamics in (33.79) with $e_1 \equiv 0$:

$$
\begin{cases}
\dot{e}_2 = -e_2 - z_1 e_3 + \varepsilon_1, \\
\dot{e}_3 = z_1 e_2 - be_3, \\
\dot{\varepsilon}_1 = -e_2.
\end{cases}
\tag{33.80}
$$

Define the function $V(e_2, e_3, \varepsilon_1)$ by

$$
V(e_2, e_3, \varepsilon_1) = \frac{1}{2}(e_2^2 + e_3^2 + \varepsilon_1^2).
\tag{33.81}
$$

Then

$$
\dot{V} = e_2(-e_2 - z_1 e_3 + \varepsilon_1) + e_3(z_1 e_2 - be_3) - \varepsilon_1 e_2 = -e_2^2 - be_3^2.
\tag{33.82}
$$

This gives that V is a Lyapunov function for (33.80) on $\mathbb{R}^3$ and hence all solutions of (33.80) approach $N = \{(e_2, e_3, \varepsilon_1) \mid \dot{V} = 0\} = \{(e_2, e_3, \varepsilon_1) \mid e_2 = e_3 = 0\}$. Since we have

$$
\dot{e}_2|_{e_2 = e_3 = 0} = \varepsilon_1
\tag{33.83}
$$

this implies in a similar way to what has been done in Example 33.28 that also $\varepsilon_1(t) \to 0$ as $t \to +\infty$. Hence we have shown that when the parameter p is unknown, the systems (33.76)–(33.78) synchronize and the variable π approaches p.

Next assume that besides p also the variable r is unknown. We again consider the receiver systems (33.77) and (33.78) and add the following dynamics for ρ:

$$
\dot{\rho} = (y - z_2) z_1.
\tag{33.84}
$$

Let the error signals e_i $(i = 1, 2, 3)$ and ε_1 be defined as above, and define $\varepsilon_2 = r - \rho$. It can again be shown that $e_1(t) \to 0$ exponentially as $t \to +\infty$, and hence again the stability properties of the error dynamics are determined by the stability properties of the $(e_2, e_3, \varepsilon_1, \varepsilon_2)$-dynamics for $e_1 \equiv 0$, which in this case may be shown to be given by

$$\begin{cases} \dot{e}_2 = \varepsilon_2 z_1 - e_2 - z_1 e_3 + \varepsilon_1, \\ \dot{e}_3 = z_1 e_2 - b e_3, \\ \dot{\varepsilon}_1 = -e_2, \\ \dot{\varepsilon}_2 = -e_2 z_1. \end{cases} \tag{33.85}$$

Now consider the function

$$W(e_2, e_3, \varepsilon_1, \varepsilon_2) = \frac{1}{2} \left(e_2^2 + e_3^2 + \varepsilon_1^2 + \varepsilon_2^2 \right). \tag{33.86}$$

It may then be shown that

$$\dot{W} = -e_2^2 - b e_3^2 \tag{33.87}$$

and hence again we have $e_2(t), e_3(t) \to 0$ as $t \to +\infty$, which together with the fact that $e_1(t) \to 0$ gives that the systems (33.76) and (33.77) synchronize. We now have

$$\dot{e}_2 \big|_{e_2 = e_3 = 0} = \varepsilon_1 + \varepsilon_2 z_1, \tag{33.88}$$

which gives that we also have

$$\varepsilon_1(t) + \varepsilon_2(t) z_1(t) \to 0 (t \to +\infty). \tag{33.89}$$

Further, we have

$$\frac{d}{dt} \left(\varepsilon_1(t) + \varepsilon_2(t) z_1(t) \right)_{e_2 = e_3 = 0} = \dot{z}_1(t) \varepsilon_2(t) \tag{33.90}$$

and hence we have

$$\dot{z}_1(t) \varepsilon_2(t) \to 0 \quad (t \to +\infty). \tag{33.91}$$

Note that from (91) we can conclude that $\varepsilon_2(t) \to 0$ (and hence by (33.89) also $\varepsilon_1(t) \to 0$) for $t \to +\infty$ *only if* $\dot{z}_1(t) \not\to 0$. This means that even if the transmitter system (33.76) is chaotic, there may exist initial conditions (for example, on the stable manifold of one of the equilibria) such that ρ and π do not converge to r and p.

Remark 33.31

1. In the above example, we encountered the situation where synchronization of two systems in the presence of unknown parameters was guaranteed *irrespective of whether or not the parameters could be estimated correctly,* and parameter convergence could only be guaranteed if a certain signal satisfied some extra properties. This is a situation that is ubiquitous whenever one deals with con-

trol or synchronization problems in the presence of unknown parameters. The extra conditions guaranteeing correct parameter estimation are normally stated in terms of certain signals having to be *persistently exciting* (see e.g., [11, 17] and the references therein). Roughly speaking, this means that the signals should have a power spectrum that is not concentrated at too few peaks (cf. [2]). Due to the fact that chaotic signals have a broad power spectrum, this condition is normally satisfied when dealing with synchronization and control problems for chaotic systems, *as long as* the system is not initialized at "nongeneric" initial conditions like (stable manifolds of) equilibrium points.

2. The type of reasoning employed in the above example can be applied in a more general context by applying what is known as *Barbalat's Lemma* (see e.g., [8]).

The following two examples illustrate that the ideas behind Lyapunov's direct method can also be used to tackle other types of problems.

Example 33.32 (No finite escape time in the Rössler system)
Consider a Rössler system of the form

$$\begin{cases} \dot{x}_1 = -x_2 - x_3 \\ \dot{x}_2 = x_1 + ax_2 \\ \dot{x}_3 = c + x_3(x_1 - b), \end{cases} \tag{33.92}$$

where $a, b, c > 0$. First note that when $x_3 = 0$, we have $\dot{x}_3 = c > 0$, which implies that the set $\Omega = \{x \in \mathbb{R}^3 \mid x_3 > 0\}$ is a positively invariant set for (33.92).

It is well known that for certain parameter values the Rössler system has a bounded invariant set on which it displays complex dynamics. However, this set is not an attractor, and in fact there are solutions of the system that escape to infinity. In terms of well posedness of, e.g., synchronization or control problems it is then of importance to know whether or not there are solutions with finite escape time, i.e., whether or not there are solutions $x(t)$ for which there exists a $0 < t_0 < +\infty$ such that $\|x(t)\| \to \infty$ as $t \uparrow t_0$.

To show that on Ω there are no solutions with finite escape time, we consider the function

$$V(x) = x_1^2 + x_2^2 + x_3. \tag{33.93}$$

For this function, we then have on Ω that

$$\begin{aligned} \dot{V} &= 2x_1(-x_2 - x_3) + 2x_2(x_1 + ax_2) + 2(c + x_3(x_1 - b)) = \\ &\quad 2ax_2^2 - 2bx_3 + 2c \leq 2a(x_1^2 + x_2^2 + 2x_3) + 2c = 2aV + 2c. \end{aligned} \tag{33.94}$$

It may then be shown that this implies that $V(t) \leq W(t)$, where $W(t)$ is the solution of $\dot{W} = 2aW + 2c$, $W(0) = V(0)$, which is given by

$$W(t) = e^{2at}\left(V(0) + \frac{c}{a}\right) - \frac{c}{a}. \tag{33.95}$$

This then immediately implies that $V(t)$ is finite for every finite $t \geq 0$, which gives that (33.92) does not have solutions with finite escape time.

Example 33.33 (Bounds on the solutions of the Lorenz system [10,20])

Consider the Lorenz system

$$\begin{cases} \dot{x}_1 = 10(x_2 - x_1), \\ \dot{x}_2 = 28x_1 - x_2 - x_1 x_3, \\ \dot{x}_3 = x_1 x_2 - \frac{8}{3}x_3. \end{cases} \tag{33.96}$$

Using an appropriate Lyapunov function, we will first show that all solutions of (33.96) are bounded. Consider the function V defined by

$$V(x) = 28x_1^2 + 10x_2^2 + 10(x_3 - 56)^2. \tag{33.97}$$

For this function, we find that

$$\begin{aligned} \dot{V} &= 560x_1(x_2 - x_1) + 20x_2(28x_1 - x_2 - x_1 x_3) + \\ &\quad 20(x_3 - 56)\left(x_1 x_2 - \frac{8}{3}x_3\right) = \\ &\quad -20\left(28x_1^2 + x_2^2 + \frac{8}{3}(x_3 - 28)^2 - \frac{6272}{3}\right). \end{aligned} \tag{33.98}$$

Define the set

$$\begin{aligned} D &= \{x \in \mathbb{R}^3 \mid \dot{V}(x) \geq 0\} = \\ &\quad \left\{x \in \mathbb{R}^3 \mid 28x_1^2 + x_2^2 + \frac{8}{3}(x_3 - 28)^2 \leq \frac{6272}{3}\right\}. \end{aligned} \tag{33.99}$$

Note that the boundary of D is an ellipsoid, and hence D is a compact set. This means that we can define

$$c^* = \max\{V(x) \mid x \in D\}. \tag{33.100}$$

For $c > 0$, define sets Ω_c by

$$\Omega_c = \{x \in \mathbb{R}^3 \mid V(x) \leq c\}. \tag{33.101}$$

Since also the boundary of Ω_c is an ellipsoid, we have that Ω_c is a compact set for every $c > 0$. First note that by definition of c^* and Ω_{c^*} we have $\dot{V} < 0$ outside Ω_{c^*} and $\dot{V} \leq 0$ on the boundary of Ω_{c^*}. This implies that Ω_{c^*} is a positively in-

variant set for (33.96). Further, when $x(0) \in \mathbb{R}^n$ is such that $V(x(0)) > c^*$, we have $\dot{V}(x(0)) < 0$, which means that outside Ω_{c^*} the value of $V(x)$ is strictly decreasing. Due to compactness of Ω_c, this implies that all solutions of (33.96) are bounded.

Using the fact that all solutions are bounded, we can use Theorems 33.25 and 33.27 to derive further bounds on the solutions of (33.96). For example, consider the function W defined by

$$W(x) = \frac{x_1^2}{20} - x_3. \tag{33.102}$$

For this function, we have

$$\dot{W} = x_1(x_2 - x_1) + \frac{8}{3}x_3 = -\frac{8}{3}W - \frac{13}{15}x_1^2. \tag{33.103}$$

Define the set

$$\Pi = \{x \in \mathbb{R}^3 \mid W(x) \leq 0\}. \tag{33.104}$$

First, note that for all x satisfying $W(x) = 0$ we then have $\dot{W}(x) \leq 0$, which implies that Π is a positively invariant set for (33.96). Next assume that there exists a solution $x(t)$ for which $x(t) \notin \Pi$ for all $t \geq 0$. Note that it follows from (33.103) and (33.104) that we then have

$$\begin{aligned} x(t) \in \widetilde{\Pi} &:= \{x \in \mathbb{R}^3 \mid 0 < W(x(t)) \leq W(x(0))\} \subset \\ &\quad \{x \in \mathbb{R}^3 \mid \dot{W}(x) \leq 0\}(\forall t \geq 0). \end{aligned} \tag{33.105}$$

Since $x(t)$ is bounded, it then follows from Theorem 33.27 that $x(t)$ approaches N^*, the largest invariant set contained in the set N defined by

$$N = \{x \in \mathbb{R}^3 \mid \dot{W}(x) = 0\} = \{x \in \mathbb{R}^3 \mid x_1 = x_3 = 0\}. \tag{33.106}$$

Similarly to what has been shown in Example 33.28, it may be shown that $N^* = \{0\}$. Since the origin is an unstable equilibrium point for (33.96), this gives that we should have that $x(0)$ is on the stable manifold of the origin. Thus, we conclude that for *almost all* solutions $x(t)$ of (33.96) there exists a $t_0 \geq 0$ such that $x(t) \in \Pi$ for all $t \geq t_0$ and that for all other solutions we have $x(t) \to \Pi$ as $t \to +\infty$.

References

1 Alvarez-Ramírez, J., *Phys. Rev. E* 50 (**1994**), p. 2339.

2 Boyd, S., Sastry, S. S., *Automatica* 22 (**1986**), p. 629.

3 Chen, C.-T., *Linear System Theory and Design*, Oxford University Press, New York, **1999.**

4 Femat, R., *Chaos* 12 (**2002**), p. 1027.

5 Fuh, C.-C., Tung, P.-C., *Phys. Rev. Lett.* 75 (**1995**), p. 2952.

6 Isidori, A., *Nonlinear Control Systems (3rd edition)*, Springer, Berlin, **1995.**

7 Kalman, R., *Proceed. First IFAC Congress* (**1960**), p. 481.

8 Khalil, H. K., *Nonlinear Systems* (3rd ed.), Prentice-Hall, Upper Saddle River, NJ, **2002.**

9 Kocarev, L., Parlitz, U., Hu, B., *Chaos, Solitons Fractals* 9 (**1998**), p. 1359.

10 Leonov, G. A., Ponomarenko, D. V., Smirnova, V. B., *Frequency-Domain Methods for Nonlinear Analysis*, World Scientific, Singapore, **1996.**

11 Loría, A., Panteley, E., Popović, D., Teel, A. R., *IEEE Trans. Autom. Control* 50 (**2005**), p. 183.

12 Nijmeijer, H., Berghuis, H., *IEEE Trans. Circuits Syst. I* 42 (**1995**), p. 473.

13 Nijmeijer, H., Van der Schaft, A.J., *Nonlinear Dynamical Control Systems*, Springer, New York, **1990.**

14 Nijmeijer, H., *Physica D* 154 (**2001**), p. 219.

15 Ott, E., Grebogi, C., Yorke, J. A., *Phys. Rev. Lett.* 64 (**1990**), p. 1196.

16 Pecora, L. M., Carroll, T. L., *Phys. Rev. Lett.* 64 (**1990**), p. 821.

17 Sastry, S., Bodson, M., *Adaptive Control – Stability, Convergence, and Robustness*, Prentice-Hall, Englewood Cliffs, NJ, **1989.**

18 Sastry, S., *Nonlinear Systems – Analysis, Stability and Control*, Springer, New York, **1999.**

19 Slotine, J.-J. E., Li, W., *Applied Nonlinear Control*, Prentice-Hall, Englewood Cliffs, NJ, **1991.**

20 Swinnerton-Dyer, P., *Phys. Lett. A* 281 (**2001**), p. 161.

34

Electronic Chaos Controllers – From Theory to Applications

Maciej Ogorzałek

34.1
Introduction

The last twenty years brought a wealth of research in the domain of nonlinear dynamics. In many physical systems and their deterministic models it has been confirmed that apart from typical behaviors such as convergence to constant, periodic or quasiperiodic behaviors in some cases trajectories become aperiodic (chaotic) if their parameters, internal variables, or external signals are chosen in a specific way.

It is generally accepted that the following specific properties qualify dynamical behavior as chaotic:

- in the time evolution the solutions exhibit sensitive dependence on initial conditions. Sensitive dependence on initial conditions means that trajectories of a chaotic system starting from nearly identical initial conditions will eventually separate and become uncorrelated but remain bounded in space;
- trajectory moves over a strange attractor – a geometric invariant object which can possess fractal dimension. The trajectory passes arbitrarily close to any point of the attractor set – in the mathematical sense the trajectory is dense on the attractor or that the system is ergodic;
- chaotic behavior appears in the system as via a "route" to chaos which typically is associated with a sequence of bifurcations – qualitative changes of observed behavior when varying one or more of the parameters;
- creation of trajectories that are observable in experiments (stable in mathematical sense) via bifurcation is often accompanied by creation of unstable orbits which are invisible in experiments. Unstable orbits persist also within the chaotic attractor – the property of existence of an infinite countable number of unstable periodic orbits within an attractor is also specific for chaotic systems. Using software tools it is possible to detect some of such orbits in numerical experiments (Fig. 34.1).
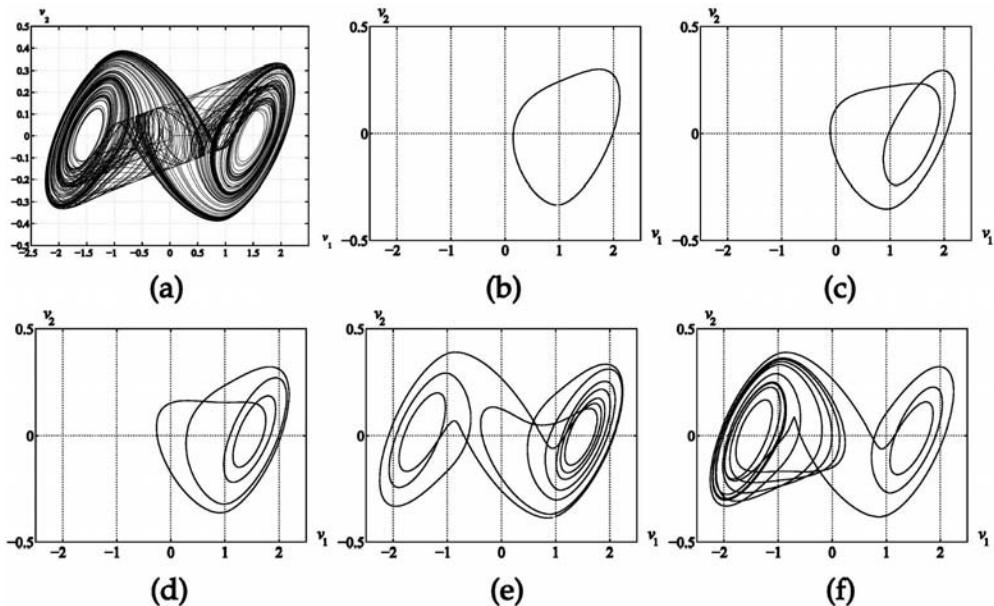
Fig. 34.1 Two-dimensional projection of the Double scroll attractor observed in Chua's circuit (a) and some of the unstable periodic orbits uncovered from it (b)–(e). The shape of these orbits resembles the overall structure of the attractor.

Sensitive dependence on initial conditions has important practical consequences. In real applications we can specify the initial conditions only with some finite accuracy ε. If two initial conditions are closer to each other than ε then they are not distinguishable in measurements. The trajectories of a chaotic system starting from such initial conditions will after a finite time diverge and become uncorrelated. Their behavior becomes unpredictable – the solutions look virtually random despite the fact they are produced by a deterministic system. One can notice that very small stimulus in the form of tiny change of parameters can have a very large effect for the system behavior. Furthermore, ergodic properties guarantee that if we choose an initial condition and a small ball of radius ε around it, the trajectory will eventually pass through this ball after a finite time (which might be however very long!).

These fundamental properties of chaotic systems are the basis of the chaos-control techniques.

34.1.1
Chaos Control

Any chaotic system from the control engineer's point of view is just as any other nonlinear systems. One could apply any method from the control engi-

neers toolkit to solve one of the typical control problems such as stabilization or tracking. The most common goal of control for chaotic systems is elimination of chaotic behavior commonly considered as causing malfunctioning, disastrous, and thus unwanted in most applications. The specific goals vary depending on a particular application. The most common goal is to convert chaotic motion into a stable periodic or constant one. We would like to avoid situations like, e.g., fibrillation or arrhythmias in medicine or hurricanes and other atmospheric disasters believed to be associated with large-scale chaotic behavior.

One can also consider conversion of unwanted chaotic behavior into another kind of chaotic motion with prescribed properties. This is the goal of chaos synchronization and many chaos-based signal transmission systems where specific types of chaotic behaviors are required as carriers or spreading codes. Alternatively one can put a requirement for changing periodic behavior into chaotic motion (which might be the goal in the case of removal of epileptic seizures). The last-mentioned type of control is often referred to as *anticontrol* of chaos.

In some cases of biomedical applications chaos is a desired state of operation. We can imagine that mixing of components in a chemical reactor would be much quicker in a chaotic state than in any other one, or chaotic signals could be useful for hiding information. In such cases, however, we need a "wanted kind" of chaotic behavior with precisely prescribed features and/or we need techniques to switch between different kinds of behavior (chaos–order or chaos–chaos).

Considering the implementation possibilities we can consider the four cases:
• variation of an existing accessible system parameter,
• change in the system design – modification of its internal structure,
• injection of an external signal(s),
• introduction of a controller (classical PI, PID, linear or nonlinear, neural, stochastic etc.).

Due to very rich dynamic phenomena encountered in typical chaotic systems, there exist a large variety of approaches to control such systems [2].

34.1.2
Fundamental Properties of Chaotic Systems and Goals of the Control

Chaotic systems possess specific properties not encountered in other nonlinear dynamical systems usually considered in control textbooks.

Route to chaos via a sequence of bifurcations gives an insight into other accessible behaviors that can be obtained by changing parameters (this may be used for redesigning the system); secondly, stable and unstable orbits that are created or annihilated in bifurcations may still exist in the chaotic range and constitute potential goals for control.

Two fundamental properties of chaotic signals and systems mentioned earlier offer interesting issues for control not available in other classes of systems:

- due to sensitive dependence on initial conditions it is possible to influence the dynamics of the systems using very small perturbations; moreover, the response of the system is very fast, and
- the existence of a countable infinity of unstable periodic orbits within the attractor offers extreme flexibility and a wide choice of possible goal behaviors for the same set of parameter values.

34.2
Requirements for Electronic Implementation of Chaos Controllers

During the last few years dozens of chaos-control techniques have been proposed (see, e.g., [2, 20, 21]). Analyzing these techniques one can easily realize that most of them are of purely academic interest – their implementation in real systems would be extremely difficult if not impossible at all. There is a general lack of easily implementable chaos-control approaches. Looking at possible applications alone it becomes obvious that chaos-control techniques and their possible implementations will greatly depend on the nature of the real process under consideration. Such systems show differences in

- speed of the phenomenon (frequency spectrum of the signals)
- amplitudes of the signals
- existence of corrupting noises, their spectrum and amplitudes
- accessibility of the signals to measurement
- accessibility of the control (tuning) parameters and
- acceptable levels of control signals.

Looking for an implementation of a particular chaos controller we must first look at the above system-induced limitations: How can we measure and process signals from the system? Are there any accessible system variables and parameters which could be used for the control task? How can we apply the control signals/connect to the system? How to choose the ones that offer the best performance for achieving control? At what speed do we need to compute and apply the control signals? What is the lowest acceptable precision of computation? Can we achieve control in real time? A slow system like a bouncing magnetoelastic ribbon (with eigenfrequencies below 1 Hz) is certainly not as demanding as a telecommunication channel (running possibly at GHz) or a laser when it comes to control.

Considering electronic implementations, one must look at several closely linked areas: sensors (for measurement of signals from a chaotic process), electronic implementation of the controllers, numerical algorithms for calculating control signals (implemented off-line using standard computers on using a microprocessor or DSP) and actuators (introducing control signals into the system). External to the implementation (but directly involved in the control process and usually fixed based on the measured signals) is finding of the goal of the control.

An obvious question arises at this point – why, despite a wealth of developed methods, we have so few successful implementations and real applications appeared?

In this chapter we try to answer at least partially this question by looking at the two most appealing methods – namely the OGY technique and OPF control. Among the approaches and methodologies for chaos control described in the literature [2, 19–21] these two approaches are of interest because they use specific properties of chaotic systems [23]:

1. Firstly, a chaotic attractor contains an infinite number of unstable periodic orbits embedded within it;
2. Secondly, there exist dense orbits in the sense that a typical trajectory on the attractor passes arbitrarily close to any point on it (it also passes arbitrarily close to any of the unstable periodic orbits);
3. In addition, these methods require very small signals to achieve control and, thus, are more realistic for implementation purposes.

From the implementation point of view these two methods are very different. OGY works on the basis of measured signals and uses a computer to find the goal of the control and make necessary calculations of the control signals – thus all the signals used in calculations are discretized both in time and space. OPF is purely analog, all operations are implemented in hardware. To consider the implementation limitations, let us first look at the principles of operation of both methods.

34.3
Short Description of the OGY Technique

The OGY control method developed by Ott, Grebogi, and Yorke [24, 25] in 1990 uses the two above-mentioned properties. The goal of control is to stabilize one of the unstable periodic orbits by perturbing a chosen (accessible) system parameter over a small range about some nominal value.

To explain in some detail the action of the OGY method, let us assume for simplicity that we have a three-dimensional continuous-time system of first-order autonomous ordinary differential equations:

$$\frac{d\mathbf{x}}{dt} = \mathbf{F}(\mathbf{x}, p), \tag{34.1}$$

where $\mathbf{x} \in R^3$ is the state and $p \in R$ is a system parameter which we can change. We also assume that parameter p can be modified within a small interval around its nominal value p_0 ($p \in [p_0 - \delta p_{max}, p_0 + \delta p_{max}]$, where δp_{max} is the maximum admissible change in the parameter p). We choose a two-dimensional Poincaré surface Σ which defines a Poincaré map $\mathbf{P}$ (for $\xi \in \Sigma$, we denote by $\mathbf{P}(\xi)$ the point at which the trajectory starting from ξ intersects Σ for the first

time). Since the vector field $\mathbf{F}$ depends on p, the Poincaré map $\mathbf{P}$ also depends on this parameter p. Thus, we have

$$\mathbf{P}\colon \mathbf{R}^2 \times \mathbf{R} \ni (\xi, p) \longrightarrow \mathbf{P}(\xi, p) \in \mathbf{R}^2. \tag{34.2}$$

Let us assume that $\mathbf{P}$ is differentiable. Say we have selected one of the unstable periodic orbits embedded in the system's attractor as a goal of our control because, for example, it offers an improvement in system performance over the original chaotic behavior. This could be the case for example of a chaotic laser intensity which is clearly an unwanted phenomenon and the effective power of the laser beam can be enhanced using control to stabilize or eliminate chaotic behavior [26]. Another example of unwanted chaotic behavior is fibrillation, where the heart pumps blood in an inefficient manner. In this application, controlling the heart beat into a nearly periodic regime is of paramount importance [11]. For simplicity, we assume that this is a period-1 orbit (a fixed point of the map $\mathbf{P}$).

Let us denote by ξ_F an unstable fixed point of $\mathbf{P}$ for $p = p_0$ ($\mathbf{P}(\xi_F, p_0) = \xi_F$). Let the first-order approximation of $\mathbf{P}$ in the neighborhood of (ξ_F, p_0) be of the form

$$\mathbf{P}(\xi, p) \approx \mathbf{P}(\xi_F, p_0) + \mathbf{A} \cdot (\xi - \xi_F) + \mathbf{w} \cdot (p - p_0), \tag{34.3}$$

where $\mathbf{A}$ is a Jacobian matrix of $\mathbf{P}(\cdot, p_0)$ at ξ_F, and $\mathbf{w} = \frac{\partial \mathbf{P}}{\partial p}(\xi_F, p_0)$ is the derivative of $\mathbf{P}$ with respect to the parameter p.

Stabilization of the fixed point is achieved by realizing feedback of the form

$$p(\xi) = p_0 + \mathbf{c}^T(\xi - \xi_F). \tag{34.4}$$

In the original description of the OGY method [24], the vector $\mathbf{c}$ is computed using the expression

$$\mathbf{c} = -\frac{\lambda_u}{\mathbf{f}_u^T \mathbf{w}} \mathbf{f}_u^T, \tag{34.5}$$

where λ_u is the unstable eigenvalue and $\mathbf{f}_u$ is the unstable contravariant corresponding left eigenvector of $\mathbf{A}$.

Thus the OGY method relies on a local linearization of the Poincaré map in the neighborhood of the chosen unstable fixed point and local linear stabilizing feedback.

An advantage of the OGY method is that all of the necessary calculations can be performed off-line on the basis of measurements (e.g., finding the unstable periodic orbits, fixing one of them as a goal of the control, computing the variables and parameters necessary for calculation of the control signal).

Once the goal of the control (unstable orbit to be stabilized) has been selected, the control signal is applied only when the observed trajectory passes

close to the fixed point (where the linearization is valid). The assumption about the existence of a dense orbit guarantees that eventually the trajectory will enter the control window. However, the time one has to wait before starting and achieving control might be very long.

It should be mentioned here that Dressler and Nitsche [8] have proposed a variant of the OGY method in which only one variable is measured in the system and other variables needed for control are reconstructed using the delayed coordinate method.

34.4
Implementation Problems for the OGY Method

When implementing the OGY method for a real-world application one has to do the following series of elementary operations:

- data acquisition – measurement of a (usually scalar) signal from the chaotic system under consideration. This operation should be performed in such a way as not to disturb the existing dynamics. For further computerized processing, measured signals must be sampled and digitalized (A/D conversion);
- selection of appropriate control parameter;
- finding unstable periodic orbits using experimental data (measured time series) and fixing the goal of control;
- finding parameters and variables necessary for control (as described above);
- application of the control signal to the system – this step requires continuous measurement of system dynamics in order to determine the moment at which to apply the control signal, i.e., the moment when the actual trajectory passes in a small vicinity of the chosen periodic orbit, and immediate reaction of the controller (application of the control pulse) in such an event.

In computer experiments, it has been confirmed that all the above-mentioned steps of OGY can be carried out successfully in a large variety of systems, achieving stabilization of even long-period orbits.

There are several problems which arise when attempting to build an experimental setup. Despite the fact that the variables and parameters can be calculated off-line, one has to consider that the signals measured from the system are usually corrupted due to noise, several nonlinear operations associated with the A/D conversion (possibly rounding, truncation, finite word-length, overflow correction, etc.). Using corrupted signal values and the introduction of additional errors by the computer algorithms and linearization used for the control calculation may result in a general failure of the method. Additionally there are time delays in the feedback loop (e.g., waiting for reaction of the computer, interrupts generated when sending and receiving data, etc.).

34.4.1
Effects of Calculation Precision

In a simple example below, we consider the case of calculating control parameters to stabilize a fixed point in the Lozi map and show how the A/D conversion accuracy and the resulting calculations of limited precision affect the possibilities for control. In the tests described below we consider the quality of computations alone, without looking at other problems like time delays in the control loop.

To be able to compare the results of digital manipulations in [22] we first computed the interesting parameters using analytical formulas and compared the results with computations based on measured time series and finite precision calculations in the case of Henon map. Let us look at the three cases compared below with the analytical results:

Reference case – analytically calculated parameters:
Coordinates of the fixed point: $(0.88794, 0.88794)$
Control vector g: $[0.40389, 0.40389]$; Jacobian eigenvalues: $-1.91322, -0.15534$
Stable direction: $[0.15350, 0.98814]$; Unstable direction: $[0.88801, -0.45981]$
Possibilities of control: successful

1. fixed point representation, 12-bit precision, rounding
   Coordinates of the fixed point: $(0.8831, 0.8810)$
   Control vector g: $[0.4352, 0.4656]$; Jacobian eigenvalues: $-1.9221, -0.0315$
   Stable direction: $[0.1156, 0.9933]$; Unstable direction: $[0.8829, -0.4696]$
   Possibilities of control: successful

2. fixed point representation, 10-bit precision, rounding
   Coordinates of the fixed point: $(0.883, 0.881)$
   Control vector g: $[0.350, 0.362]$; Jacobian eigenvalues: $-1.899, -0.021$
   Stable direction: $[0.137, 0.991]$; Unstable direction: $[0.891, -0.455]$
   Possibilities of control: often fails

3. fixed point representation, 8-bit precision, rounding
   Coordinates of the fixed point: $(0.89, 0.89)$
   Control vector g: $[0.0, 0.0]$; Jacobian eigenvalues: 0, 0
   Stable and unstable directions: Impossible to determine
   Possibilities of control: impossible

Comparing the results of computations summarized above we can easily see that if we are able to achieve an accuracy of two to three decimal digits the calculations are precise enough to ensure proper functioning of the OGY algorithm in the case of the Lozi system. To have some safety margin and robustness in the algorithm the acceptable A/D accuracy cannot be lower than 12 bit and probably it would be best to apply 16-bit conversion. This kind of accuracy is nowadays easily available using general purpose A/D converters even at speeds in the MHz range. Implementing the algorithms, one must consider the cost of implementation with growing precision and speed requirements, the

cost grows exponentially. This issue might be a great limitation when it comes to IC implementations.

34.4.2
Approximate Procedures for Finding Periodic Orbits

Another possible source of problems in the control procedure are errors introduced by algorithms for finding periodic orbits (goals of the control). Using experimental data we can only find approximations to unstable periodic orbits [1, 18, 27].

Commonly used is a simple technique proposed by Lathrop and Kostelich [18] for recovering unstable periodic orbits from an experimental time series. This procedure assumes that we have a series of successive points $\{x_i\}$, $i = 0, 1, \ldots, N$ on the system trajectory and taking any of these points x_m we search forward for the smallest positive integer k, such that $||x_{m+k} - x_m|| < \varepsilon$, where ε is the specified accuracy. It is further claimed that the orbit detected in this manner lies close to the unstable periodic orbit whose period is approximated by that of the detected sequence. Some new methods have been proposed recently [30] which could possibly improve localization procedures for unstable periodic orbits. Particularly interesting are interval arithmetics methods [9, 16] based on the interval Newton method which enable precise calculation of periodic orbit's position for systems with known mathematical models.

In laboratory experiments these orbits can either be calculated off-line using a computer program or they can be localized using hardware window comparator. In the latter case the choice is a matter of luck! the choice is just by trial-and-error.

In our experiments [23] we varied ε between 0.000001 and 0.001 and fixed the threshold for distinguishing between orbits at 0.001.

34.4.3
Effects of Time Delays

Several elements in the control loop may introduce time delays that can be detrimental to the functioning of the OGY method. Although all calculations may be done off-line, two steps are of paramount importance:
1. detection of the moment when the trajectory passes the chosen Poincaré section and
2. determination of the moment at which the control signal should be applied (close neighborhood of chosen orbit).

When these two steps are carried out by a computer with a data acquisition card, at least a few interrupts (and therefore a time delay) must be generated in order to detect the Poincaré section, take the decision of being in the right neighborhood, and to send the correct control signal.
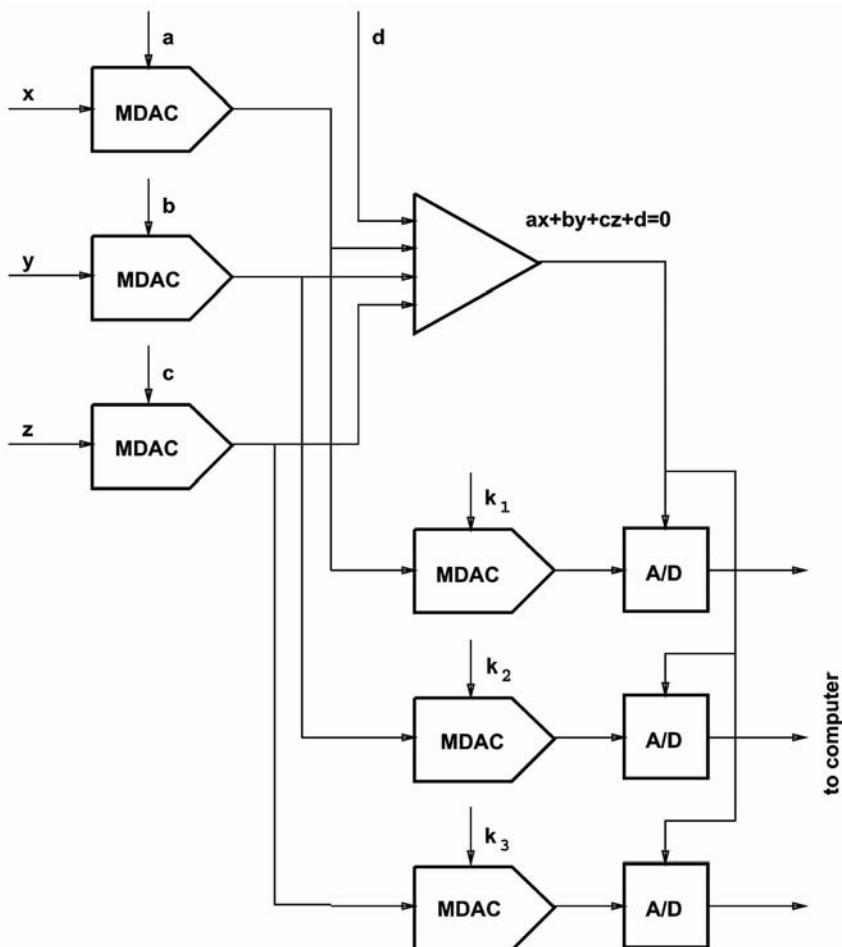
Fig. 34.2 Fast Poincaré section detector improved OGY implementation.

Most experiments with OGY control of electronic circuits have been able to achieve control when the systems were running in the 10–100 Hz range. We found out that for higher frequency systems time delays become a crucial point in the whole procedure. The failure of control was mainly due to the late arrival of the control pulse – the system was being controlled at a wrong point in state space where the formulas used for calculations were probably no longer valid; trajectory was already far away from the section plane when the control pulse arrived.

To compensate for some of the delays, we have proposed a hardware solution for a detector of the Poincaré section and vicinity detector. Block diagrams of these two pieces of equipment are shown in Figs. 34.2 and 34.3. The Poincaré section system here uses all (three in our application) state variables to simplify
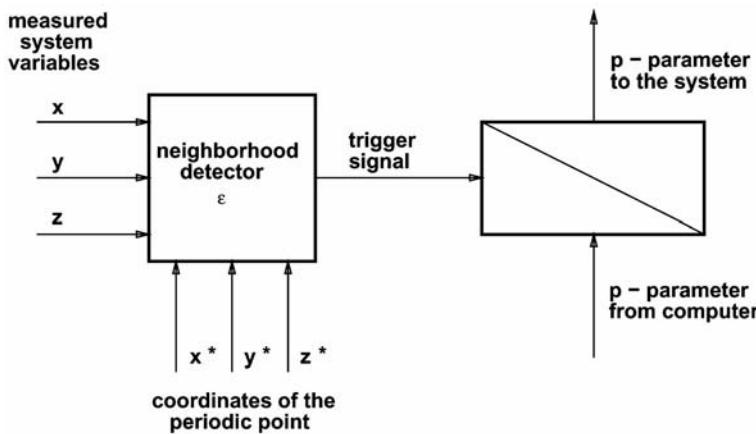
Fig. 34.3 ε-Comparator for detection of the vicinity of a desired periodic orbit.

detection. To implement this function using just one variable, delay coordinates must be introduced – realization in hardware would become much more complicated in this case if possible at all (one could think of calculating suitable time delay by a computer algorithm and saving the necessary time delayed samples in special-purpose registers).

34.5
Occasional Proportional Feedback (Hunt's) Controller

The occasional proportional feedback (OPF) technique [14, 26] can be considered as a one-dimensional version of the OGY method.

Let us describe the action of the OPF controller for the case of stabilizing a fixed point of the Poincaré map.

In the OPF method, the control signal is computed using only one variable, for example ξ_1:

$$p(\xi) = p_0 + c(\xi_1 - \xi_F). \tag{34.6}$$

Adjusting the values of c for which ξ_F is a stable fixed point of the system $\xi \mapsto \mathbf{P}(\xi, p(\xi))$ ensures proper functioning of the algorithm. In [10] we have described some theoretical results concerning the choice of coefficients and possibilities for successful OPF control. The best results can be obtained if the unstable eigenvector is parallel to the coordinate which is used to compute the control signal, and the possibility of control using the OPF technique depends on the form of the linear approximation of the system's behavior in the neighborhood of the periodic orbit.

A schematic of Hunt's implementation of the OPF control method is shown in Fig. 34.4. The window comparator, taking the input waveform, gives a logical
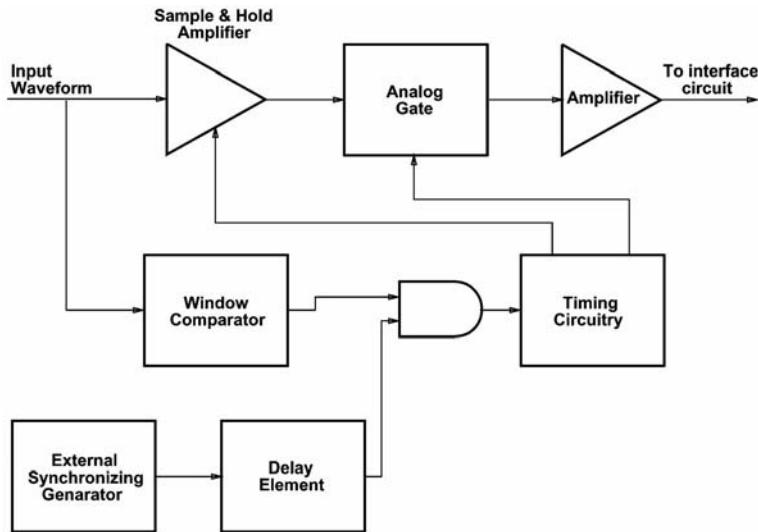
Fig. 34.4 Hunt's implementation of the OPF method.

high when the input waveform is inside the window. This is then ANDed with the delayed output from the external frequency generator. This logical signal drives the timing block which triggers the sample-and-hold and then the analog gate. The output from the gate, which represents the error signal at the sampling instant, is amplified and applied to the interface circuit which transforms the control pulse into a perturbation of the parameter p. The frequency, delay, control pulse width, window position, width and gain are all adjustable – they fix the position of the section plane, values of p_0 and c. The interface circuit depends explicitly on the chaotic system under control.

One of the major advantages of Hunt's controller over OGY is that the control law depends on just one variable and does not require any complicated calculations (as was necessary in the case of the OGY scheme) in order to generate the required control signal. All the operations can easily be performed by hardware function blocks.

The disadvantage of the OPF method is that there is no systematic method for finding the embedded unstable orbits (unlike OGY). For comparison with the OGY method let us summarize the main features of the OPF controller:

- it uses just one system variable as input;
- uses the peaks of this system variable to generate a one-dimensional map;
- a window around a fixed level sets the region where control is applied;
- peaks are located by means of a synchronizing generator, the frequency of which has to be adjusted by either a trial-and-error procedure or by consulting, for example, measured power spectra of the signals.

34.5.1
Improved Chaos Controller for Autonomous Circuits

Recently we have developed an improved chaos controller modifying the structure proposed by Hunt [10]. The modified controller uses Hunt's method without the need for an external synchronizing oscillator. Its circuit diagram is shown in Fig. 34.5. In the modified controller, the derivative of the input signal generates a pulse when it passes through zero. This pulse replaces the driving pulses from the external oscillator as the "synch" pulse for our Poincaré map. This obviates the need for the external generator and so makes the controller simpler and cheaper to build.

The variable level window comparator is implemented using a window comparator around zero and a variable level shift. Two comparators and three logic gates form the window around zero. The synchronizing generator used in Hunt's controller is replaced by an inverting differentiator and a comparator. A rising edge in the comparator's output corresponds to a peak in the input waveform. We use the rising edge of the comparator's output to trigger a monostable flip–flop. The falling edge of this monostable's pulse triggers another monostable, giving a delay. We use the monostable's output pulse to indicate that the input waveform peaked a fixed time earlier. If this pulse arrives when the output from the window comparator is high then a monostable is triggered. The output of this monostable triggers a sample-and-hold on its rising edge which samples the error voltage; on its falling edge, it triggers another monostable. This final monostable generates a pulse which opens the analog gate for a specific time (the control pulse width). The control pulse is then applied to the interface circuit, which amplifies the control signal and converts it into a perturbation of one of the system parameters, as required.
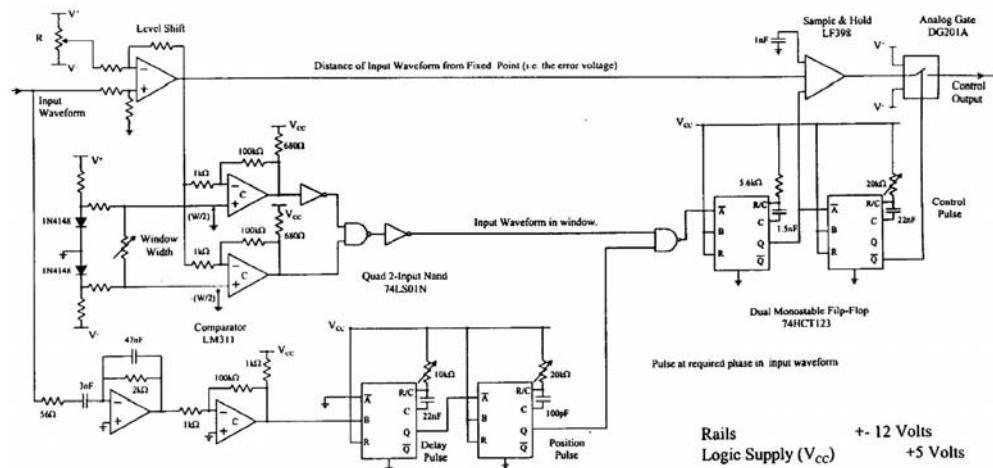
Fig. 34.5 Improved analog chaos-OPF controller without external synchronization.

V_{cc}	10 Volts	V_B	3.5 Volts
R_E	400Ω	R_L	35Ω
C_1	1μF	C_2	1μF
L	2.2mH	QI	2N2222A
V^+	12 Volts		
V^-	-12 Volts		

(a)

(b)   (c)   (d)
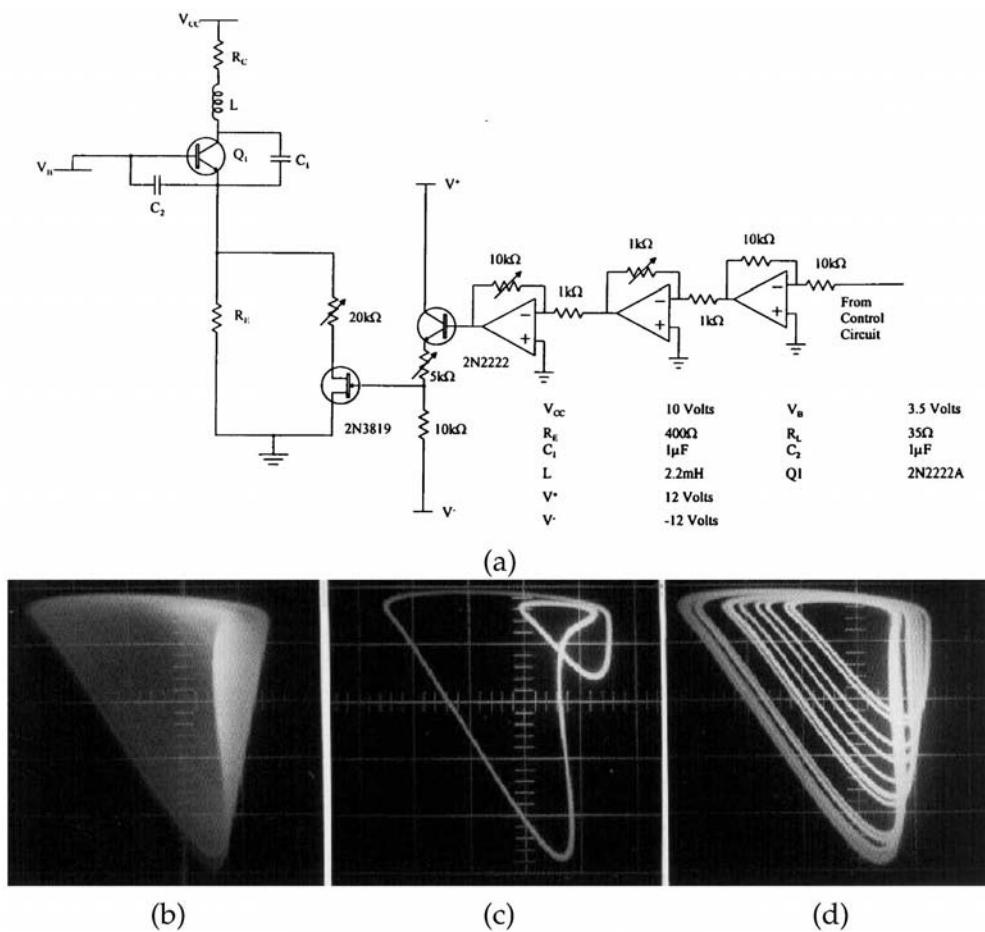
Fig. 34.6 Interface circuitry for OPF control of Colpitts oscilla-
tor and trajectories observed in the system without control
(b) and with two different choices of circuitry settings (c)–(d).

The modified controller offers, in our opinion, the simplest and most reliable implementation for chaos control. It has been tested successfully on Chua's circuit and the Colpitts oscillator working in the kHz range [10] enabling stabilization of unstable periodic orbits up to order 8. One can easily visualize adapting the scheme for controlling very fast systems. The controller implementation is cheap, simple and easy to build. IC implementation remains one of the possible future issues.

34.6
Experimental Chaos Control Systems

Any control method cannot be accepted as successful if computer simulation experiments are not followed by further laboratory tests and physical implementations. Only very few results of such tests are known – among the exceptions are: control of a green light laser [26], control of a magnetoelastic ribbon [5], and a few other examples.

34.6.1
Control of a Magnetoelastic Ribbon

Already in 1990 soon after the publication of the OGY method scientists from the Applied Chaos Laboratory at GeorgiaTech in Atlanta directed by Professor William Ditto reported on one of the first laboratory-scale successful real implementation of a chaos-control system [5]. The experimental system (see Fig. 34.7) consisted of a gravitationally buckled magnetoelastic ribbon fixed in a vertical position (clamped at the bottom end) and placed in a time-varying magnetic field having $H = H_0 + H_1 \cos(2\pi ft)$. A sensor measured the curvature of the ribbon near its base – voltage measured by this sensor was further converted to digital form and transferred to the computer carrying on the control task. H_0 has been chosen as the control parameter. Using OGY technique principles H_0 perturbations could be calculated to successfully stabilize the low-order oscillations of the beam out of its originally tuned chaotic behavior. Ditto, Rauseo, and Spano demonstrated in this experiment that chaos could be controlled in a real physical system using OGY method. It should be mentioned however that the control setup was highly susceptible to noise and disturbances. To ensure
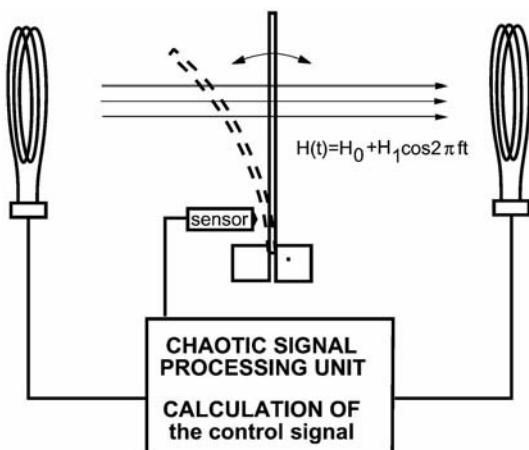
Fig. 34.7 Chaos control set-up for the magnetoelastic ribbon system.

proper functioning compensation of the Earth's magnetic field had to be placed using three pairs of mutually orthogonal Helmholtz coils. To increase the precision temperature stabilization was also very important. Successful implementation of chaos control in this particular case was possible because of very slow oscillation frequencies of the system. The eigenfrequency of the ribbon was in the range of 1 Hz !! In such a case all effects of time delays were negligible and also computer calculations were fast enough for the continuous robust operation of the system at a low-order stabilized orbit.

34.6.2
Control of a Chaotic Laser

Roy and his co-workers [26] reported on very interesting results obtained in experimental control of chaotic lasers. The goal of control was here stabilization of the chaotically varying light intensity. Roy adopted the OPF technique and was able to achieve 15-fold increase in power output achieving at the same time stable operation. Control was performed on a fast timescale of a few microseconds. Thus OGY method requiring numerical computations could not be applied. As indicated in the schematic diagram (Fig. 34.8) the choice of a suitable goal of control can be achieved by adjusting three parameters: the synchronizing frequency, the wave-form offset, and the width of the control signal. Several periodic orbits, e.g., period-1, period-4, or period-9 could be stabilized out of the chaotic regime. It should be stressed here that the laser itself is a higher dimensional system and that successful control did not require any knowledge of its model – the control task is performed on the basis of measured signal (from the photodiode) and all "computations" are done in a fast analog way. It seems that OPF controller is the only implementation alternative here.

Chaotic lasers are one of the deeply investigated chaos-control objects – many research groups worldwide work on stabilization of chaotic laser using various techniques. Interested readers should consult [33].
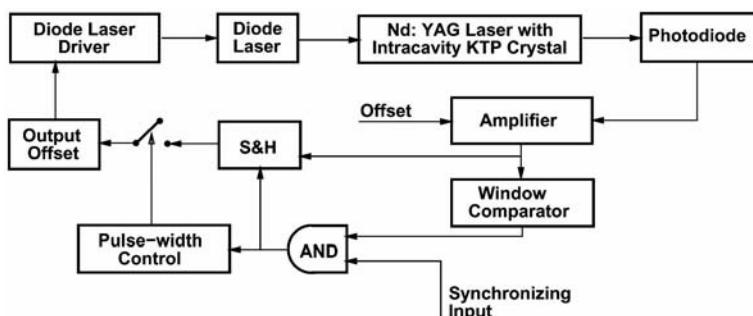
Fig. 34.8 Schematic diagram of the OPF controller driving the Nd:YAG laser system.

34.6.3
Chaos-Based Arrhythmia Suppression and Defibrillation

One of the most spectacular applications of chaos-control techniques is arrhythmia removal or defibrillation of the heart beat. Starting from many numerical experiments concerning control of arrhythmias on heart models research and exploitation of real measured signals [11, 12] in this domain has reached a stage where successful approaches have been patented [31, 32] and clinical tests are under way [7]. In the clinical setup consisted of a quadrupolar electrode catheter which was inserted via the femoral vain (FV) of the patient under test and positioned in the lateral right atrium (RA). During atrial fibrillation a pair of electrodes measured electrical activity signals which were digitized and processed in the computer. Measured time series was further used to calculate the unstable fixed point and its stable and unstable manifolds and calculate the desired control pulses. These pulses via the second pair of electrodes were applied to the atrium to control the pumping motion towards stable periodic state. The schematic of this setup is shown in Fig. 34.9. The authors [7] report on results of clinical tests performed on 25 patients. 36% consistent results of control were obtained [40], and in 24% of cases control was unsuccessful. Chaos control offers a promising alternative for quenching arrhythmia and especially fibrillation [34].
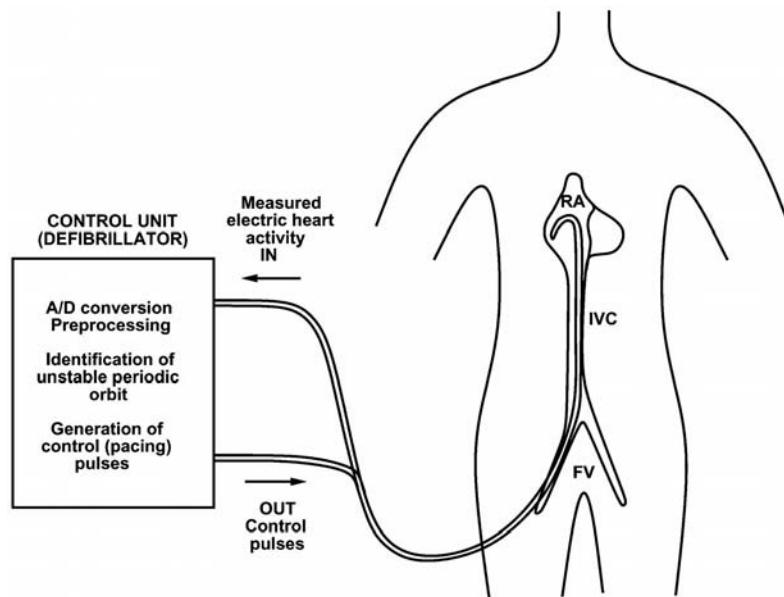
Fig. 34.9 Schematic diagram of the arrhythmia removal system.

34.7
Conclusions

In classical linear and nonlinear control problems one did not exploit existence of unstable periodic orbits, sensitive dependence on initial conditions or ergodicity of trajectories on the attractor. Chaos control techniques clearly rely on these properties. In chaos control, a target for tracking is not limited to constant vectors in the state space: it often is an unstable periodic orbit of the given system. This generally requires only tiny control to arrive at, but technically can be quite difficult due to the instability of the target. Moreover, in chaos control the terminal time is infinite to be meaningful and practical, because most nonlinear dynamical behaviors such as equilibrium states, limit cycles, attractors, and chaos are asymptotic properties. These are theoretical limitations for chaos control. There exist also several limitations imposed by electronic implementation of chaos controllers. These limitations are imposed by the speed of the considered chaotic system (highest frequency), accuracy of the measurements, errors introduced by quantization and signal processing algorithms and calculations.

Taking into account these limitations when looking for an implementation of a controller we must make a trade-off between high speed (analog implementation without possibilities of pre-specification of the goal, and a trial-and-error procedure for achieving the desired behavior) and precise knowledge of the orbit which is interesting as a goal of the control.

The modified OPF controller works well in many high-frequency systems, eliminating chaos but without prior knowledge of attainable orbits.

The OGY method is very attractive when accurate knowledge of the goal is needed (stabilized orbits offer some optimal type of performance [13]) but it is possible to implement it in very low frequency (slow) systems only.

In this study we did not consider the actuator design problem which depending on real application might pose specific problems – e.g., application of defibrillating signal to the heart might be of paramount importance far above any of the controller and algorithm design problems.

There are two interesting areas of further research and developments:
1. Hardware implementation of goal (unstable orbit) detection for use with the modifications of analog OPF method
2. development of specific hardware for use with OGY method
3. implementation of both methods in high-order (possibly hyper-chaotic) systems
4. IC implementations of controllers.

Finally, we should mention that there exist other control schemes, e.g., delayed-feedback method introduced by Pyragas [19] where certainly the controller is the cheapest possible (delay line which in some cases might be even a piece of cable!) – there is however no tuning possibilities whatsoever when it comes to real implementations. In our opinion such controllers might also find particular applications but are of little versatility and for this reason we did not look closer into them.

References

1 D. Auerbach, P. Cvitanović, J.-P. Eckmann, G. Gunaratne and I. Procaccia, "Exploring chaotic motion through periodic orbits", Phys. Rev. Letters, vol. 58, no. 23, pp. 2387–2389, 1987.

2 G. Chen and X. Dong, "From chaos to order – methodologies, perspectives and applications". World Scientific Series on Nonlinear Science, vol. 24, World Scientific, Singapore, 1998.

3 D. J. Christini, K. M. Stein, S. M. Markowitz, S. Mittal, D. J. Slotwiner, M. A. Schreiner, S. Iwai and B. B. Lerman, "Nonlinear dynamical arrhythmia control in humans", Proc. National Academy of Sciences USA, April 24, 2001.

4 N. J. Corron, B. A. Hopper and S. D. Pathel, "Limiter control of a chaotic RF transistor oscillator", Int. J. Bifur. Chaos, vol. 13, no. 4, 2003.

5 W. L. Ditto, S. N. Rauseo and M. L. Spano, "Experimental control of chaos", Phys. Rev. Letters, vol. 65, pp. 3211–3214, 1990.

6 W. L. Ditto, M. L. Spano and J. F. Lindner, "Techniques for the control of chaos", Physica D86, pp. 198–211, 1995.

7 W. L. Ditto, M. L. Spano, V. In, J. Neff, B. Meadows, J. J. Langberg, A. Bolmann and K. McTeague, "Control of human atrial fibrillation", Int. J. Bifur. Chaos, vol. 10, no. 3, pp. 593–601, 2000.

8 U. Dressler and G. Nitsche, "Controlling chaos using time delay coordinates", Phys. Rev. Lett., vol. 68, pp. 1–4, 1992.

9 Z. Galias, "Rigorous numerical studies of the existence of periodic orbits for the Henon map", J. Univ. Comp. Sci., vol. 4, no. 2, pp. 114–124, 1998.

10 Z. Galias, C. A. Murphy, M. P. Kennedy and M. J. Ogorzałek, "Electronic chaos controller", Chaos, Solitons Fractals, vol. 8, no. 9, pp. 1471–1484, 1997.

11 A. Garfinkel, M. L. Spano, W. L. Ditto and J. N. Weiss, "Controlling cardiac chaos". Science, vol. 257, pp. 1230–1235, 1992.

12 A. Garfinkel, J. N. Weiss, W. L. Ditto and M. L. Spano, "Chaos control of cardiac arrhythmias", Trends Cardiovasc. Med., vol. 5, no. 2, p. 76, 1995.

13 B. R. Hunt, E. Ott, "Optimal periodic orbits of chaotic systems", Phys. Rev. Lett., vol. 76, pp. 2254–2257, 1996.

14 E. R. Hunt, "Stabilizing high-period orbits in a chaotic system: the diode resonator", Phys. Rev. Lett., vol. 67, pp. 1953–1955, 1991.

15 E. R. Hunt, "Keeping chaos at bay", IEEE Spectrum, vol. 30, pp. 32–36, 1993.

16 R. B. Kearfott and M. Novoa, "Algorithm 681: INTBIS, a portable interval Newton/bisection package", ACM Trans. Math. Software, vol. 16, no. 2, pp. 152–157, 1990.

17 J. J. Langberg, A. Bolmann, K. McTeague, M. L. Spano, V. In, J. Neff, B. Meadows and W. L. Ditto "Chaos control of human atrial fibrillation" (preprint 1997).

18 D. P. Lathrop and E. J. Kostelich, "Characterization of an experimental strange attractor by periodic orbits", Phys. Rev. A, vol. 40, no. 7, pp. 4028–4032, 1989.

19 M. J. Ogorzałek, "Taming chaos: Part 2 – control", IEEE Trans. Circ. Syst., vol. 40, no. 10, pp. 700–706, 1993.

20 M. J. Ogorzałek, "Chaos control: How to avoid chaos or take advantage of it", J. Franklin Inst., vol. 331B, no. 6, pp. 681–704, 1994.

21 M. J. Ogorzałek, "Controlling chaos in electronic circuits,", Phil. Trans. R. Soc. London A, vol. 353, pp. 127–136, 1995.

22 M. J. Ogorzałek, "Design considerations for electronic chaos controllers", Chaos, Solitons Fractals, vol. 9, no. 1/2, pp. 295–306, 1998.

23 M. J. Ogorzałek and Z. Galias, "Characterization of chaos in Chua's oscillator in terms of unstable periodic orbits", J. Circ. Syst. Comp., vol. 3, no. 2, pp. 411–429, 1993.

24 E. Ott, C. Grebogi and J. A. Yorke, "Controlling chaos", Phys. Rev. Lett., vol. 64, no. 11, pp. 1196–1199, 1990.

25 E. Ott, C. Grebogi and J. A. Yorke, Controlling chaotic dynamical systems. In *Chaos: Soviet-American Perspectives on Nonlinear Science*, ed. D. K. Campbell, AIP, New York, 1990.

26 R. Roy, T. W. Murphy Jr., T. D. Maier, Z. Gillis and E. R. Hunt, "Dynamical

control of a chaotic laser: experimental stabilization of a globally coupled system", Phys. Rev. Lett., vol. 68, no. 9, pp. 1259–1262.

27 I. B. Schwartz, "Estimating regions of existence of unstable periodic orbits using computer-based techniques", SIAM J. Numer. Anal., vol. 20, no. 1, pp. 106–120, 1983.

28 P. So, E. Ott, S. J. Schiff, D. T. Kaplan, T. Sauer and C. Grebogi, "Detecting unstable periodic orbits in chaotic experimental data", Phys. Rev. Lett., pp. 4705, 1996.

29 M. W. Slutzky, P. Cvitanovic and D. J. Morgul, "Manipulating epileptiform bursting in the rat hippocampus using chaos control and adaptive techniques", IEEE Trans. Biomed. Eng., vol. 50, no. 5, pp. 559–570, 2003.

30 P. So, E. Ott, S. J. Schiff, D. T. Kaplan, T. Sauer and C. Grebogi, "Extracting unstable periodic orbits from chaotic time series data", Phys. Rev. E, vol. E55, pp. 5398–5417, 1997.

31 M. L. Spano, W. L. Ditto, A. Garfinkel and J. N. Weiss, "Real time cardiac arrhythmia stabilizing system", US Patent No. 5342401 (8/30/94).

32 M. L. Spano, W. L. Ditto, A. Garfinkel and J. N. Weiss, "Real time cardiac arrhythmia stabilizing system", US Patent No. 5447520 (9/05/95).

33 Control of Chaos: New perspectives in experimental and theoretical nonlinear science. Theme Issue, Int. J. Bif. Chaos, vol. 8, no. 8/9, 1998.

34 Mapping and Control of Complex Cardiac Arrhythmias, Chaos, vol. 12, no. 3, 2002.

35

Chaos in Pulse-Width Modulated Control Systems

Zhanybai T. Zhusubaliyev and Erik Mosekilde

35.1
Introduction

The chapter describes some of the nonlinear dynamic phenomena that one can observe in modern power electronic systems. The unusual character and large variety of these phenomena stem from the modification of the normal local and global bifurcations by the piecewise-smooth structure of the pulse-width modulated control systems and from the interplay of these bifurcations with various forms of border-collision bifurcations. We perform a relatively detailed analysis of two DC/DC converters with different types of pulse-width modulated control. The aim is to examine the nature of some of the main bifurcations and to describe the associated transitions to chaos. Even though engineering practice today may not live up to this standard, we consider analyses of this form to be essential elements of the design of pulse-width modulated control systems.

Power electronic systems are used to convert electrical energy from one form into another. To ensure a effective and adjustable conversion, the active devices (thyristors, power transistors, etc.) operate in a switching mode in combination with passive components such as power diodes, inductors, capacitors, and transformers. By using relatively high switching frequencies, one can reduce the size and mass of most of the passive components and thereby lower both the costs and the weights of the systems considerably.

Power electronic systems with switching operation are widely used both in the industry and in private households [7]. Examples are domestic light dimmers, switched-mode power supplies in electronic appliances and personal computers, heating and lighting controls, and electronic ballasts for fluorescent lamps. Industrial applications include induction heating, battery chargers, traction regulators in locomotives, solid-state relays and circuit breakers, offline DC power supplies, uninterruptible power supplies, conditioning for alternative energy sources, automobile electronics, and electric vehicles [9, 18, 19].

Since electrical sources can be either DC (direct current) or AC (alternating current) there are four basic types of converters: AC/DC, DC/AC, AC/AC, and

DC/DC. DC/DC converters are among the most commonly used circuits in power electronics.

The control of DC/DC converters usually applies one of the two approaches, namely *voltage-mode* control or *current-mode* control [14, 19, 28]. In voltage-mode control, the output voltage is compared with a reference to generate a control signal that drives the pulse-width modulator via some typical feedback compensation. For current-mode control, an inner current loop is used in addition to the voltage feedback loop. The aim of this loop is to force the peak inductor current to follow a reference signal which is derived from the output voltage feedback loop. The advantage of using current-mode control is often a faster response [14].

Operation of the power electronic converters is characterized by a cyclic switching of the circuit topology. The simplest version of such a converter contains two switches that connect or disconnect the voltage supplies to the load via an *LC* filter.

The nonlinearity of the system is directly related to the switching processes associated with this type of pulse-width modulation.

As mentioned above, power electronic circuits can display an unusual variety of nonlinear dynamic phenomena. These phenomena include multiple attractors, abrupt transitions associated with modified period doubling, saddle-node and torus bifurcations, the interplay between classical bifurcations and border-collision bifurcations, multiple-choice bifurcations, and new types of direct transition to chaos and nonsmooth torus destruction.

Pulse-width modulated control systems can be described by piecewise-smooth dynamical systems. The phase trajectories of such systems are "sewed" together from separate smooth parts, and one can in general distinguish between two types of bifurcations of periodic solutions.

The first type is similar to the bifurcations we know for smooth dynamical systems. These include the local bifurcations (saddle-node, pitchfork, period doubling, and Neimark-Sacker bifurcations), where a periodic orbit loses its stability as one of its multipliers (or a pair of multipliers) crosses out through the unit circle, and the global bifurcations (homo- and heteroclinic bifurcations) where a connection is established from a saddle and back to the same solution (or another saddle) along one of its stable directions (see, for example [20]). However, the bifurcation phenomena are often modified by the non-smooth character of the system. Period-doubling cascades may be truncated, providing for a transition to chaos after a finite number of period doublings. And, particularly for piecewise-linear systems, the period doubling and torus bifurcations may be abrupt such that, for example, the quasiperiodic attractor arises with a finite amplitude after a torus birth bifurcation.

The second type of bifurcations, referred to as *border-collision bifurcations* [12, 15, 16, 25–27] are connected with situations where one of the parts of the periodic trajectory becomes tangent to a sewing surface, i.e., a surface that divides the phase space into domains of different dynamics. Within each such domain the system is smooth, but the equations of motion change abruptly from one

domain to the next. This type of bifurcation, which typically involves abrupt jumps in the multipliers of the orbit, cannot occur in smooth dynamical systems.

A simple type of border-collision bifurcation consists in the continuous transformation of a solution from one type into another with preservation of the cycle period. Here, the solution type is determined by the number of sections from which the cycle is composed (or "sewed up" in the original Russian literature [12]). However, more complicated phenomena are also possible, including new types of direct transitions to chaos and the merging or disappearance of solutions of different types [4–6, 10, 30, 33, 34], transitions from one stable cycle to another through period doubling, -tripling, -quadrupling, etc., and the appearance of a denumerable set of unstable cycles together with a stable cycle. Border-collision related bifurcations also include corner collision, sliding and grazing bifurcations [11, 13, 24]. In recent works [29, 32] we have shown that border-collision bifurcations can lead to the birth of ergodic or resonant tori. Moreover, we have demonstrated that a special type of border-collision bifurcations, in which a stable periodic orbit arises simultaneously with a quasiperiodic or a phase-locked invariant torus, can occur in piecewise-smooth systems [29].

The chapter is organized as follows. In Section 35.2 we describe a DC/DC converter with pulse-width modulated control. The behavior of such a converter may be represented by a two-dimensional piecewise-smooth set of nonautonomous differential equations. We reduce the investigation of this system in studying the dynamics of a two-dimensional piecewise-smooth mapping. Due to its simplicity, this mapping allows us to perform detailed analytical and numerical bifurcation analyses.

In Section 35.3 we present the results of these analyses and study the possible transitions to chaos for the two-dimensional map. We show that the pulse-width modulated control systems can display situations where several stable periodic motions with different dynamic characteristics coexist for a wide range of parameters (see also [8]). These cycles arise in hard transitions, for example through saddle-node or border-collision bifurcations and, when changing parameters, they can undergo either a finite or an infinite sequence of period-doubling bifurcations leading to a transition to chaos.

We also give examples of complex dynamical behaviors at border-collision bifurcations such as the transition from one stable cycle to another through period doubling, the sudden jump from a periodic solution to chaos, and the direct transition from one stable periodic orbit to another with multiple periods.

Along with the period-doubling route and various forms of intermittency transitions, the formation and subsequent destruction of a two-dimensional torus is one of the classic routes to chaos in dissipative systems. Before breakdown, the resonance torus typically loses its smoothness in discrete points through folding (or winding) of the involved manifolds, and this loss of smoothness then spreads to the entire torus surface through local (e.g., saddle-node) or global (i.e., homoclinic or heteroclinic) bifurcations.

The basic theorem for the destruction of a two-dimensional torus in smooth dynamical systems was proved by Afraimovich and Shilnikov [1], and *three possi-*

ble routes for the appearance of chaotic dynamics were described. The generic character of these processes has since been confirmed numerically as well as experimentally for wide classes of both flow and discrete time systems [2, 3, 17, 20, 22, 35]. However, the transition to chaos through torus destruction in piecewise-smooth systems can display certain modifications of the Afraimovich-Shilnikov scenarios.

The purpose of the second part of this chapter is to investigate some of the mechanisms involved in torus birth and torus destruction in piecewise-smooth dynamical systems.

As a specific example we used a two-dimensional piecewise-smooth map describing the behavior of a DC/DC converter with two-level pulse-width modulated control. We first describe a border-collision bifurcation that can lead to the appearance of quasiperiodicity. We demonstrate how a two-dimensional torus can arise from a periodic orbit through a bifurcation in which two complex-conjugate Floquet multipliers jump abruptly from the inside to the outside of the unit circle. The torus may be ergodic (quasiperiodic dynamics) or resonant (phase-locked dynamics). In both cases, however, the diameter of the torus develops approximately linearly with the distance to the bifurcation point as opposed to the characteristic parabolic form of the well-known Neimark-Sacker bifurcation. Next, we consider the transition between quasiperiodic and phase-locked invariant tori and show that the involved mechanisms differ distinctly from the mechanisms known for smooth systems. Finally, we discuss how the torus is destroyed through a homoclinic bifurcation. This analysis involves the use of numerical methods that can follow the stable and unstable manifolds for the various modes.

35.2
DC/DC Converter with Pulse-Width Modulated Control

Let us consider a DC/DC buck converter with pulse-width modulation [18, 21] as an example of an electronic control system that can exhibit both a period-doubling route to chaos through smooth bifurcations and a variety of interesting border-collision bifurcations.

Figure 35.1(a) shows a schematic diagram of the considered DC/DC power converter. The switch S may be realized, for instance, by means of metal-oxide-semiconductor field-effect transistors (mosfets) that can operate with more than 50,000 switchings per second. The switching of the mosfet is controlled by a feedback logic known as a pulse-width modulation of the second kind. As the switch S opens and closes, the voltage applied to the LC filter varies between zero and the input voltage. The LC filter smoothens the signal to be applied to the load resistor R_L into a relatively constant voltage of a value lower than that of the input voltage. It is usually the object to regulate the mean output voltage to a prescribed value. This can be achieved by controlling the switching process through a feedback mechanism. A simple method, called voltage-mode control,
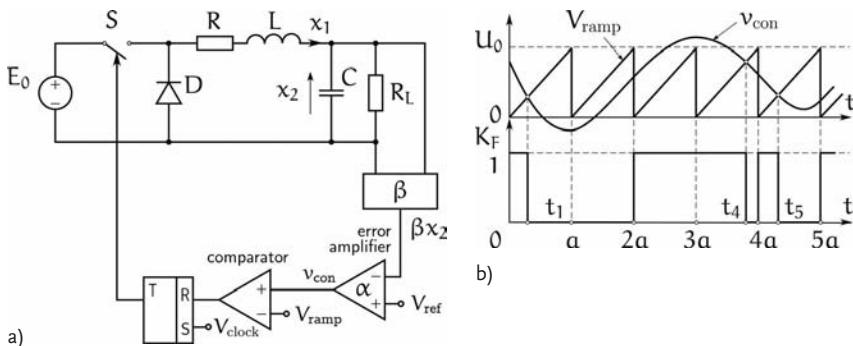
Fig. 35.1 Pulse-width modulated controlled DC/DC converter. (a) Coupling diagram. (b) Time diagrams illustrating the law of control pulse generation. The switch is turned on at the beginning of each ramp period and is turned off when the ramp voltage exceeds the value of the control signal v_{con}.

implies that a voltage proportional to the output voltage is compared with a reference voltage V_{ref} to generate a control voltage v_{con}. This control voltage is compared with a sawtooth waveform V_{ramp} to generate the switching signal K_F (Fig. 35.1 (b)). The switch is turned on at the beginning of every ramp period and is turned off when the ramp voltage exceeds the current value of the control voltage v_{con}. The behavior of such a converter is described by a set of two coupled ordinary differential equations with discontinuous right-hand sides:

$$\frac{dX}{dt} = AX + B \cdot K_F(\xi) \tag{35.1}$$

Here

$$X = \begin{bmatrix} x_1 \\ x_2 \end{bmatrix}; \ A = \begin{bmatrix} -\frac{R}{L} & -\frac{1}{L} \\ \frac{1}{C} & -\frac{1}{CR_L} \end{bmatrix}; \ B = \begin{bmatrix} \frac{E_0}{L} \\ 0 \end{bmatrix}$$

with

$$\xi(t, X) = v_{con} - V_{ramp}, v_{con} = a(V_{ref} - \beta x_2), V_{ramp} = U_0(t/a - E_1(t/a)).$$

The function $E_1(t/a)$ is defined as the integer part of its argument. x_1 and x_2 represent, respectively, the current in the inductance coil and the voltage over the capacitor of the LC filter. L and C are the inductance and the capacity of the LC filter, and R is a resistor characterizing the dissipation in the filter inductance coil and the converter. R_L is the load resistance, and E_0 is the input voltage. a is the amplification constant of the corrector, V_{ref} is the reference voltage, and β is the transfer constant of the voltage sensor. U_0 determines the amplitude of the ramp signal V_{ramp} and a is the period of this signal.

The switching function K_F takes the values of 1 or 0 depending on ξ. When $K_F = 1$ the switch S is turned on (the diode D is nonconducting), and if $K_F = 0$ then the switch is turned off (the diode D is conducting). As mentioned above, the switch is turned on at the beginning $t = (k-1)a$, $k = 1, 2, \ldots$ of each ramp period.

The switching function K_F during the kth ramp period $(k-1)\,a < t < ka$, $k = 1, 2, \ldots$ is determined by

$$K_F = \begin{cases} 1, & (k-1)\,a < t < t_k; \\ 0, & t_k < t < ka. \end{cases}$$

Here, t_k denotes the instant of time at which the switch is turned off during the kth ramp period. The value of the function ξ at the beginning of the ramp period is $\xi_{k-1} = a\big(V_{\text{ref}} - \beta x_2((k-1)a)\big) - U_0$.

If $\xi_{k-1} \leq 0$, then $t_k = (k-1)a$. In this case the duration of the pulse $\delta_k = t_k - (k-1)a$ in the kth ramp cycle is equal to 0. When $\xi_{k-1} > 0$ and the equation $\xi = 0$ has a solution, then t_k is the smallest root of the equation

$$\xi(t, X) = a\big(V_{\text{ref}} - \beta x_2(t)\big) - U_0\big(t/a - k + 1\big) = 0, (k-1)a < t < ka.$$

Finally, if $\xi(t, X(t)) > 0$ in the whole ramp period, then the pulse duration δ_k is equal to the time period a. These different conditions are illustrated in Fig. 35.1 (b) for different time intervals.

In the numerical investigations of the DC/DC converter we have assumed the following parameter values: $R = 13.5$ Ω, $L = 0.11$ H, $C = 10^{-6}$ F, $R_L = 126$ Ω, $U_0 = 5$ V, $V_{\text{ref}} = 2.5$ V, $\beta = 0.5$ and $a = 1.5 \times 10^{-4}$ s. These parameter values correspond to the values one can find in typical engineering applications [7, 18]. The amplification and transfer constants of the corrector $a > 0$ and E_0 (in V) are considered as control parameters.

With the assumed parameter values, the eigenvalues λ_1 and λ_2 of the matrix A:

$$\lambda_1, \lambda_2 = -\frac{1}{2}\left(\frac{R}{L} + \frac{1}{CR_L}\right) \mp \sqrt{\frac{1}{4}\left(\frac{R}{L} + \frac{1}{CR_L}\right)^2 - \frac{1}{LC}\left(1 + \frac{R}{R_L}\right)}$$

are real and negative, and the filter circuit does not give rise to any oscillatory response.

To simplify the analysis let us pass from the variables x_1, x_2 to the dimensionless variables w_1, w_2 through the affine transformation

$$\begin{aligned} x_1 &= \frac{E_0/L}{\lambda_1 - \lambda_2}\left(\frac{\lambda_2 + R/L}{\lambda_1}\,w_1 - \frac{\lambda_1 + R/L}{\lambda_2}\,w_2\right), \\ x_2 &= \frac{E_0/(LC)}{\lambda_2 - \lambda_1}\left(\frac{w_1}{\lambda_1} - \frac{w_2}{\lambda_2}\right). \end{aligned}$$

$$(35.2)$$

Substituting (35.2) into Eq. (35.1) and solving with respect to the derivatives we obtain [8, 30]

$$\frac{dw_1}{dt} = \lambda_1\big(w_1 - K_F(\xi)\big), \quad \frac{dw_2}{dt} = \lambda_2\big(w_2 - K_F(\xi)\big). \tag{35.3}$$

By virtue of the linearity of the electronic circuit between the switching events, the continuous-time system (35.3) may be reduced to the piecewise-smooth two-dimensional mapping [8, 30]

$$\begin{cases} w_{1k} = e^{a\lambda_1}\big(w_{1(k-1)} - 1\big) + e^{a\lambda_1(1-z_k)}, \\ w_{2k} = e^{a\lambda_2}\big(w_{2(k-1)} - 1\big) + e^{a\lambda_2(1-z_k)}, \end{cases} \quad k = 1, 2, \ldots \tag{35.4}$$

The relative pulse duration $z_k = t_k/a - k + 1$ within the time interval $(k-1)a < t < ka$ is determined by [8, 30]

$$z_k = \begin{cases} 0, & \varphi(0) \le 0, \\ z^*, & \varphi(0) > 0, \quad \varphi(1) < 0, \\ 1, & \varphi(0) > 0, \quad \varphi(1) \ge 0. \end{cases}$$

Here z^* is the smallest root of the equation

$$\varphi(z) = 0, \quad 0 < z < 1$$

with

$$\begin{aligned} \varphi(z) &= \frac{LC\lambda_1(\lambda_1 - \lambda_2)}{a\beta E_0} \cdot \xi(t, X(t)) \\ &= \vartheta(1 - w_{2(k-1)})e^{a\lambda_2 z} - (1 - w_{1(k-1)})e^{a\lambda_1 z} - \frac{Q}{a}z + q - \vartheta + 1, \\ z &= t/a - k + 1, \quad Q = \frac{U_0(\vartheta - 1)(R_L + R)}{\beta E_0 R_L}. \end{aligned}$$

$\vartheta = \lambda_1/\lambda_2$ measures the ratio of the two real and negative eigenvalues, and $q = QV_{ref}/U_0$ is an expression for the reference voltage V_{ref}.

If the eigenvalues λ_1, λ_2 are complex: $\lambda_1 = \mu + j\sigma$, $\lambda_2 = \mu - j\sigma$, the equations for the dimensionless variables w_1, w_2 take the form:

$$\frac{dw_1}{dt} = \mu w_1 - \sigma w_2 - (\mu - \sigma)K_F(\xi), \quad \frac{dw_2}{dt} = \sigma w_1 + \mu w_2 - (\mu + \sigma)K_F(\xi)$$

with

$$\xi = \vartheta w_1 - w_2 + q - \frac{Q}{a}\big(t/a - E_1(t/a)\big), \quad Q = \frac{U_0(1 - \vartheta)(R_L + R)}{\beta E_0 R_L}, \quad \vartheta = \frac{\mu + \sigma}{\mu - \sigma}.$$

The period T of a periodic mode is an integer multiple of the ramp cycle, i.e. $T = ma$, where $m = 1, 2, \ldots$. We will refer to this type of operation as a period-m cycle.

35.3
Bifurcation Analysis for the DC/DC Converter with One-Level Control

Figure 35.2 shows the domains of existence for different dynamical modes within the parameter plane (a, E_0) of the dynamical system (35.4). Here $\Pi_{k,j}$ are simply connected domains such that for any point $P \in \Pi_{k,j}$, $P = (a, E_0)$, there exists a stable cycle with the period k that varies continuously with the parameters. The index j is introduced to distinguish domains with the same k. Normal operation takes place in the parameter region $\Pi_{1,1}$

The domains $\Pi_{2^{i-1},1}$, $i = 1, 2, \ldots$ are separated by period-doubling bifurcation curves. Transverse to these curves are curves along which accumulating period-doubling cascades occur. Figure 35.3 (a) reproduces the bifurcation diagram obtained for the section $\{(a, E_0) : 30 \leq a \leq 100; E_0 = 9\}$. At the point $a = a_*$, $a_* \approx 47.7126$ the maximum multiplier of the fixed point (in absolute value) crosses the unit circle through –1 and a period-2 cycle softly arises (Fig. 35.3 (b)). With further increase of a, a period-doubling sequence leading to chaotic dynamics occurs. Besides the period-doubling route to chaos for the period-1 cycle, this diagram also illustrates the formation of a period-3 subharmonic oscillation in a saddle-node bifurcation at $a = \widehat{a}_*$, $\widehat{a}_* \approx 60.142$. Increasing the control parameter a leads to an accumulating period-doubling sequence ending with a transition to chaotic dynamics.
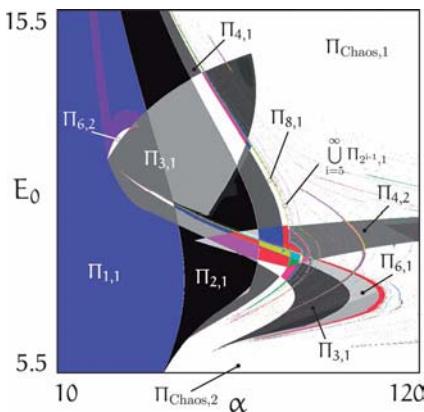
Fig. 35.2 Chart of dynamical modes in the parameter plane (a, E_0). The regions $\Pi_{k,j}$ are regions of existence for k-periodic cycles, the second index serving to distinguish between different cycles with the same periodicity. The white regions $\Pi_{\text{Chaos,1}}$ and $\Pi_{\text{Chaos,2}}$ denote regions of chaotic dynamics.

a)

b)
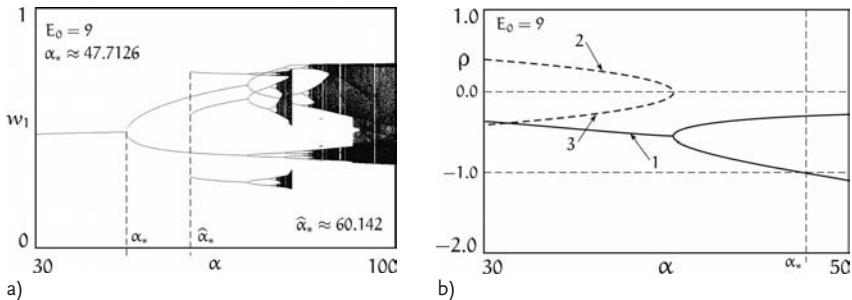
Fig. 35.3 (a) Bifurcation diagram showing the transition to chaos through an accumulating period-doubling cascade. (b) Multiplier diagram illustrating the period doubling of the 1-cycle. Full lines show the real (denoted by 1) and dotted lines the imaginary (denoted by 2 and 3) parts of the two multipliers. As a increases, the complex-conjugate multipliers of the 1-cycle turn real. In the point $a = a*$ ($a* \approx 47.7126$) the maximum multiplier of the 1-cycle (in absolute value) crosses through −1.

a)

b)
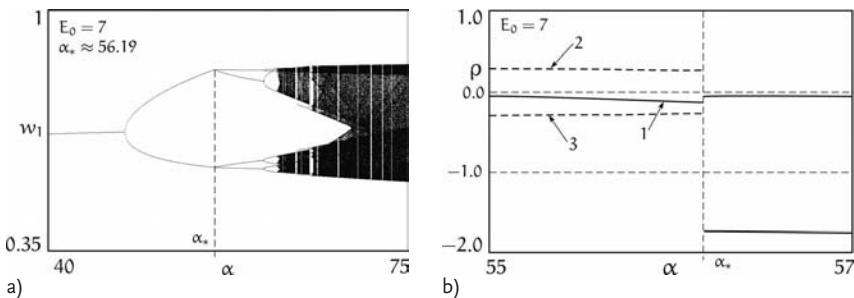
Fig. 35.4 (a) Bifurcation diagram for $E_0 = 7$ and $40 \leq a \leq 75$ illustrating the transition to chaos through a finite sequence of smooth and border-collision bifurcations. When passing through $a_* \approx 56.19$ we observe a period doubling of the 2-cycle via a border-collision bifurcation. (b) Multiplier diagram illustrating the period-doubling border-collision bifurcation for the period-2 cycle. Full lines show the real (denoted by 1) and dotted lines the imaginary (denoted by 2 and 3) parts of the complex conjugate multipliers. As a increases from values $< a_*$ to values $> a_*$ the complex multipliers abruptly become real. The absolute value of one the real multipliers is greater than unity.

The boundaries of some domains $\Pi_{k,j}$ are more complicated and typically include regions where border-collision bifurcations of different types occur, including bifurcations leading to a simple change of the solution type, fold and period-doubling border-collision bifurcations as well as more complex forms of border-collision bifurcations [30, 33]. If the parameters are varied within such domains, chaotic dynamics can arise via different sequences (usually finite) that include both smooth and border-collision bifurcations.

An example of such transitions is shown in Fig. 35.4. One can see that when the parameter a increases, the fixed point first undergoes a smooth period-doubling bifurcation: the maximum multiplier (in absolute value) of the fixed point
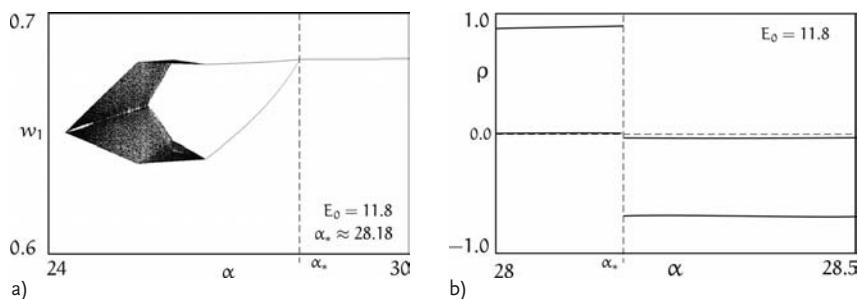
Fig. 35.5 (a) Bifurcation diagram illustrating a direct transition from a stable period-3 cycle to a period-6 cycle as a is reduced through the bifurcation point at a_*. (b) Variation of the cycle multipliers. Rather than being destabilized, the period-3 cycle disappears altogether in this bifurcation.

emerges from the unit circuit through -1. As a result, a period-2 cycle arises softly from the fixed point, and the fixed point continues to exist as a saddle.

At the bifurcation point $a = a_*$, $a_* \approx 56.19$, the 2-cycle loses its stability and transforms into a saddle 2-cycle of another type. The loss of stability for the 2-cycle is accompanied by the soft appearance of a period-4 cycle. Inspection of Fig. 35.4(b) shows how the multipliers of the 2-cycle suddenly jump. When crossing over the bifurcation point the complex multipliers of the period-2 cycle abruptly become real, and the stable period-2 focus cycle transforms into a saddle period-2 cycle. With further increase of a, the period of the 4-cycle is again doubled via a smooth period-doubling bifurcation, but the 8-cycle loses its stability through a sudden transition to chaos (see Fig. 35.4(a)).

It is also possible to find examples of a transition to chaos through a finite sequence of border-collision bifurcations. Such a transition is observed at the boundaries of the domain $\Pi_{6.2}$. Figure 35.5 displays the results of a bifurcation analysis calculated in the section $\{(a, E_0) : 24 \leq a \leq 30; E_0 = 11.8\}$. Figure 35.5(a) is the bifurcation diagram and Fig. 35.5(b) is the multiplier diagram for the period-3 and period-6 cycles. To better illustrate the bifurcation transitions we do not include all the branches of the period-3, but only a magnified vision of one of them. As one can see from the diagram, two border-collision bifurcations precede the birth of the chaotic attractor.

As the parameter a decreases from values $> a_*$ to values $< a_*$, the stable period-3 cycle transforms into a stable period-6 cycle. However, the transition to the period-6 cycle is associated with the complete disappearance of the period-3 cycle. A detailed analysis of the bifurcation behavior in Fig. 35.5(a) reveals that the transition from the period-3 cycle to the period-6 cycle occurs continuously as in normal border-collision period-doubling bifurcations. When the parameter a increases, the period-6 cycle collides with the borderline $w_1 - \vartheta w_2 - \frac{Q}{a} + q = 0$ and disappears as it merges with the period-3 cycle. Similarly, when a decreases, the period-3 cycle in the point $a = a_*$, $a_* \approx 28.18$ disappears in consequence of a violation of the conditions for its existence.

When crossing the next bifurcation point with decreasing a, the stable 6-cycle changes its type and becomes unstable in a border-collision bifurcation where a maximum (in module) multiplier jumps abruptly from the inside to the outside of the unit circle. As one can see from Fig. 35.5 (a) this loss of stability, when the period-6 cycle collides with the borderline $w_1 - \vartheta w_2 + q = 0$, leads to the appearance of a chaotic attractor.

35.4
DC/DC Converter with Two-Level Control

As an example of a piecewise-smooth dynamical system that displays a quasi-periodic route to chaos we shall consider a DC/DC converter with multilevel pulse-width modulated control [18, 21].

Converters of this type have recently attracted significant interest in the power industry, and they have been used for many different types of power conversion in high-power applications. Multilevel converters contain two or more voltage levels, and a desired output voltage can, therefore, be synthesized with less distortion and higher efficiency at lower switching frequencies and with lower voltage devices [18, 21, 23].

Figure 35.6 (a) shows the coupling diagram for a converter with two voltage levels [18]. The control system is a variant of the scheme shown in Fig. 35.1 (a), applicable when two or more input voltage levels are available. The scheme is implemented by using two ramp signals – $V_{\text{ramp}}^{(1)}$ between 0 and $U_0/2$, and $V_{\text{ramp}}^{(2)}$ between $U_0/2$ and U_0 – both driven by the same clock.

At the beginning of each ramp cycle the sample-and-hold circuit remembers the value of the corrector output signal $\psi(X)$ and holds this value during the whole ramp cycle. In Fig. 35.6 (b) the output voltage of the sample-and-hold circuit (the control voltage) is denoted as v_{con}.

If the value of v_{con} is between 0 and $U_0/2$ (zone 1), it is compared with $V_{\text{ramp}}^{(1)}$ to generate a pulse-width modulated signal $K_F^{(1)}$ that drives the switch S_1. If v_{con} is between $U_0/2$ and U_0 (zone 2), it is compared with $V_{\text{ramp}}^{(2)}$ to generate the signal $K_F^{(2)}$ which drives the second switch S_2. If $v_{\text{con}} > U_0$ then the duration of both the pulses $K_F^{(1)}$ and $K_F^{(2)}$ is equal to the ramp signal period a. In the case $v_{\text{con}} < 0$, the duration of both pulses is equal to 0. The converter output voltage v_{out} is synthesized from two voltage levels [18, 21], i.e., $v_{\text{out}} = (K_F^{(1)} + K_F^{(2)})E_0/2$.

The equations of motion for the multilevel converter take a form similar to (35.1). The difference between the two converters is associated only with the algorithm to form the switching function K_F:

$$K_F(t, X) = \sum_{s=1}^{N} K_F^{(s)};$$

$$K_F^{(s)} = \frac{1}{2N}[1 + \text{sign}(\xi_s)]; \ \xi_s(t, X) = v_{\text{con}} - V_{\text{ramp}}^{(s)}, \ v_{\text{con}} = \psi(X(\tau)),$$

$$\psi(X) = a(V_{\text{ref}} - \beta x_2), V_{\text{ramp}}^{(s)} = \frac{U_0}{N}(s - 1 + t/a - E_1(t/a)).$$
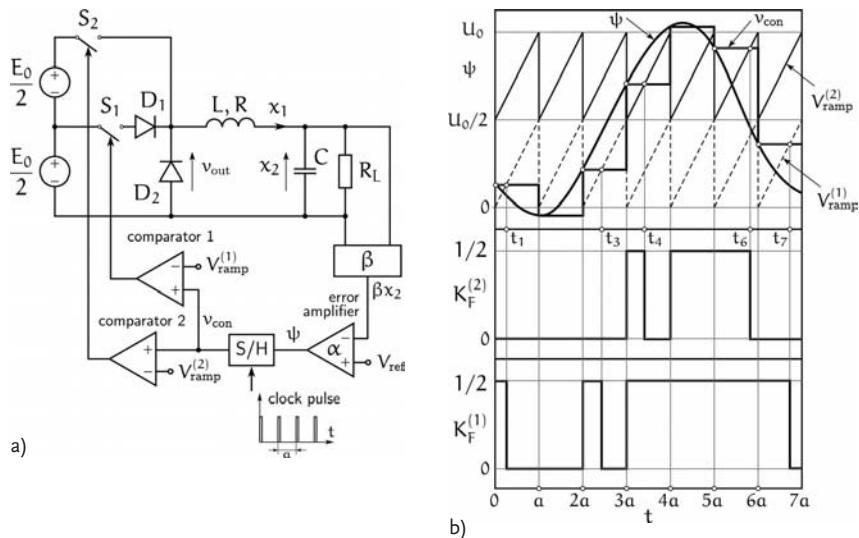
Fig. 35.6 (a) Schematic diagram of the DC–DC buck converter with two-level control. Here S/H is the sample and hold unit. (b) Generation of the switching signals S1 and S2 in a two-level controlled buck converter. This control is based on pulse-width modulation of the first kind [18]. a denotes the period of the ramp function.

Here, $\tau = aE_1(t/a) = (k-1)a$, $k = 1, 2, \ldots$ is the discrete time variable. $N = 2$ is the number of voltage levels. The function sign equals to $+1$ or -1, depending on the sign of ξ. The switching function K_F reacts to changes in the sign of the differences between the error signal v_{con} and any of the two ramp functions $V_{ramp}^{(1)}$ or $V_{ramp}^{(2)}$. We will again use the input voltage E_0 and the amplification constant of the corrector a as control parameter.

Similarly to the procedure used in Section 35.2, we can pass from the variables x_1, x_2 to the variables w_1, w_2 via the affine transformation (35.2).

The map then takes the form [30, 31]

$$\begin{cases} w_{1k} = e^{a\lambda_1}\left(w_{1(k-1)} - \frac{s_k}{N}\right) + \frac{1}{N}\left(s_k - 1 + e^{a\lambda_1(1-z_k)}\right), \\ w_{2k} = e^{a\lambda_2}\left(w_{2(k-1)} - \frac{s_k}{N}\right) + \frac{1}{N}\left(s_k - 1 + e^{a\lambda_2(1-z_k)}\right), \end{cases} \quad k = 1, 2, \ldots, \tag{35.5}$$

where the zone number s_k and the relative pulse duration z_k within the time interval $(k-1)\,a < t_k < ka$ are determined by

$$s_k = \begin{cases} 1, & \varphi_{k-1} \leq Q/(Na), \\ N, & \varphi_{k-1} > Q/(Na). \end{cases}$$

$$z_k = \begin{cases} 0, & \varphi_{k-1} < 0, \\ \frac{Na}{Q}\varphi_{k-1} - s_k + 1, & 0 \leq \varphi_{k-1} \leq Q/a, \\ 1, & \varphi_{k-1} > Q/a \end{cases}$$

with the function

$$\varphi_{k-1} = w_{1(k-1)} - \vartheta w_{2(k-1)} + q.$$

35.5
Bifurcation Analysis for the DC/DC Converter with Two-Level Control

Figure 35.7 presents a chart of the dynamical modes in the plane of control parameters (a, E_0). The domain of stability $\Pi_{1,1}$ for the fixed point is bounded to the right by the curve N_φ of a subcritical Neimark-Sacker bifurcation and from above by the curve N_φ^C of the border-collision bifurcation for the birth of a closed invariant torus (or a closed invariant curve for the discrete map). Hence, the system displays two different mechanisms of torus formation.

The Neimark-Sacker bifurcation curve N_φ is intersected by the curve N_φ^C in the point P_φ of codimension two. The domains of periodicity situated between the lines N_φ^C and N_φ represent the resonance tongues. Several of the most prominent tongues are indicated in Fig. 35.7 by their associated rotation numbers (1:4, 1:5, 1:6, 2:9, 2:11, 3:13, and 3:14). The structure of these tongues was investigated in considerable detail in some of our previous works [30, 34].

Let us now consider the behavior of the dynamical system (35.5) along the line N_φ^C.

Figure 35.8 illustrates the birth of a closed invariant curve through the border-collision bifurcation. Figure 35.8 (a) is the bifurcation diagram, calculated in the section $\{(a, E_0) : 9.14 \leq a \leq 11.14, E_0 = 9.98\}$, and Fig. 35.8 (b) shows the variation of the absolute value $|\rho|$ of the complex-conjugate multipliers $\rho_{1,2} = \rho_r \pm j\rho_j$ of the fixed point. When crossing the line N_φ^C with decreasing a the stable fixed point changes type and becomes an unstable focus in a border-collision bifurcation where a pair of complex-conjugate multipliers jump out of the unit circle. We can see how the loss of stability for the fixed point is accompanied by the soft appearance of a quasiperiodic orbit.

The range along the line N_φ^C where a border-collision transition of the form *fixed point → closed invariant curve* takes place (to the right of the point P_φ) is riddled with intervals where stable and saddle cycles, located on the closed invariant curve, arise from the fixed point. Such intervals are everywhere dense along the line N_φ^C. Each of the resonance tongues is supported by finite segments of the border-collision line N_φ^C. We suppose, however, that the total length of all intervals on N_φ^C where a quasiperiodic orbit arises is finite.

Let us first analyse what happens on the segment of the line N_φ^C, which supports the 1:5 tongue, when moving from the domain $\Pi_{1,1}$ to the resonance ton-
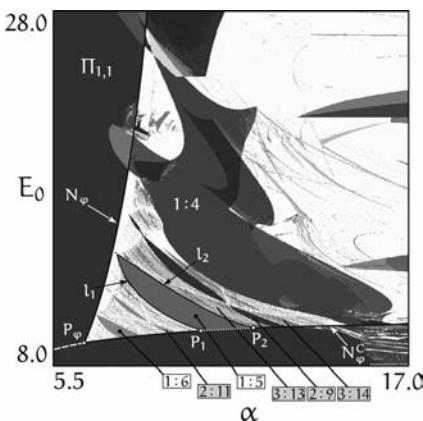
Fig. 35.7 Chart of the dynamical modes in the parameter plane (a, E_0). $\Pi_{1,1}$ is the domain of stability for the fixed point. N_φ is the Neimark-Sacker bifurcation boundary. N_φ^C is a curve of border-collision bifurcation for the birth of a closed invariant curve.
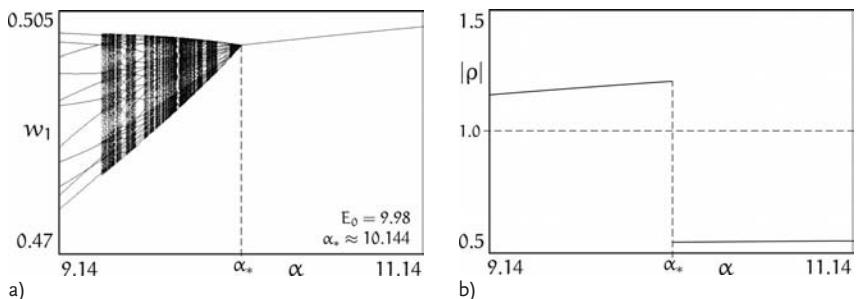
Fig. 35.8 Birth of the quasiperiodic orbit from the fixed point in a border-collision bifurcation at a_*. (a) Bifurcation diagram. (b) Variation of the absolute value of the multipliers of the fixed point. With decreasing a a pair of complex-conjugate multipliers jump from the inside to the outside of the unit circle at this bifurcation point.

gue between points P_1 and P_2 (see Fig. 35.7). Figure 35.9 (a) displays the bifurcation diagram for the section $\{(a, E_0) : 10.35 \leq a \leq 12.5, E_0 = 10.1\}$. The solid lines in this figure represent the stable 5-cycle and the dashed lines the saddle cycle. When the fixed point crosses this border, a pair of complex-conjugate multipliers of the fixed point jumps out of the unit circle. The variation of the absolute value of the multipliers with a is shown in Fig. 35.9 (b). As a result of this bifurcation the fixed point becomes an unstable focus and a closed invariant curve softly arises from it. This curve is the union of the saddle 5-cycle, its unstable manifold, and the stable period-5 focus. Figure 35.9 (c) shows the

a)

b)

c)
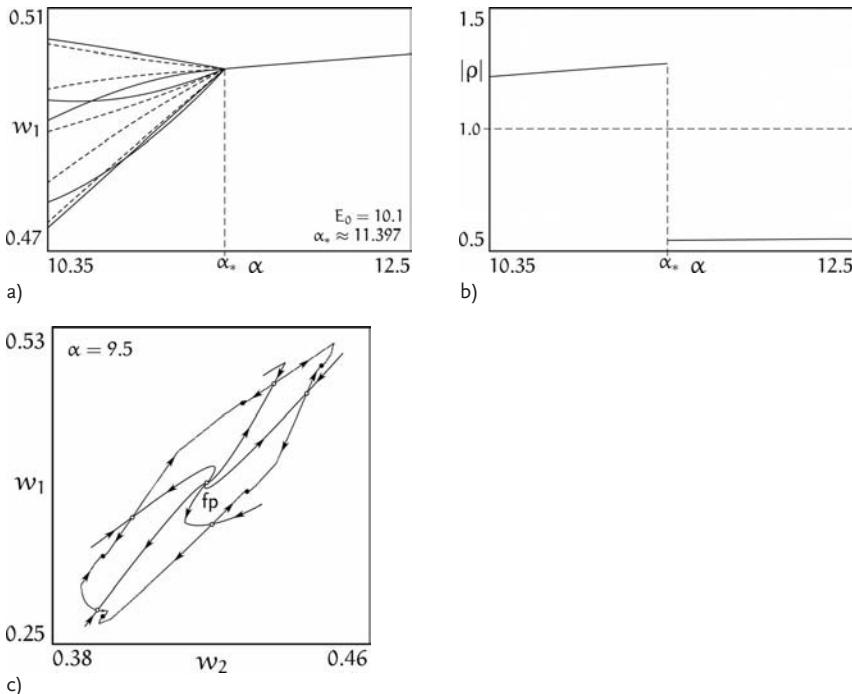
Fig. 35.9 Birth of a stable closed invariant curve from the fixed point in a border-collision bifurcation. (a) Bifurcation diagram. Solid lines mark points of the stable cycle and dashed lines show the unstable cycle. (b) Variation of the absolute value of multi-pliers for the fixed point. (c) Phase portrait for $a = 9.5$ and $E_0 = 11.8$. The closed invariant curve is the union of the unstable manifolds of the saddle cycle with the points of the stable cycle.

phase portrait within $1:5$ resonance tongue for $a = 9.5$ and $E_0 = 11.8$. The closed invariant curve is not smooth in the points of the period-5 focus. In accordance with the results obtained in our recent publications [29, 32] we thus conclude that border-collision bifurcations allow for a direct transition from a stable focus fixed point into a stable period-5 orbit of focus type. This is, obviously, a form of bifurcation that has no analog in smooth systems.

Let us hereafter turn our attention toward the transition from the mode-locking to quasiperiodicity and vice versa. As an example, Fig. 35.10 presents the results of the bifurcation analysis for the section $\{(a, E_0) : 8.0 \leq a \leq 10.5; E_0 = 11.8\}$. This section intersects the boundaries of the $1:5$ resonance tongue. The bifurcation diagram with a as parameter is presented in Fig. 35.10 (a) while the evolution of the multipliers of the stable and unstable cycles is shown in Fig. 35.10 (b).

The five times iterated map of (35.5) has five stable fixed points and the same number of saddle fixed points. As we increase or decrease a the stable and saddle fixed points collide and disappear in border-collision fold bifurcations (see
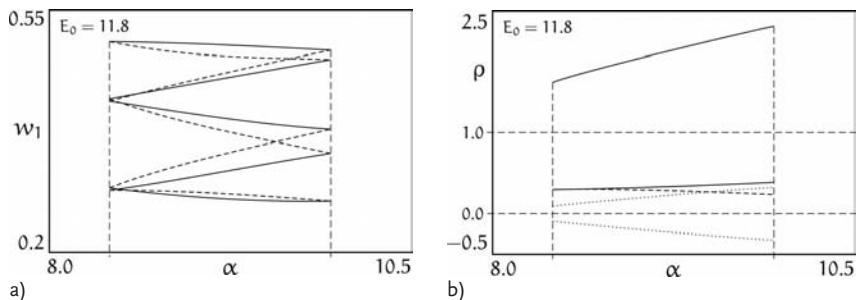
Fig. 35.10 (a) Bifurcation diagram for period-5 mode-locking window. Solid lines mark the stable cycle and dashed lines show the unstable cycle. (b) Multiplier diagram for stable and unstable period-5 cycles. Solid lines mark the multipliers of the saddle cycle, dashed and dotted lines show the real and imaginary parts, respectively, for the complex-conjugate pair of the multipliers of the stable cycle.

Fig. 35.10). In the parameter plane, these bifurcation points define two border-collision fold bifurcation lines l_1 and l_2. These lines delineate the 1:5 tongue of periodicity (see Fig. 35.7), and the two lines are supported by the curve of birth of the closed invariant curve N_φ^C in the codimension-two points P_1 and P_2, respectively.

In each tongue with the rotation number $r : q$ (see Fig. 35.7) there is an attracting closed invariant curve which is typically formed by a saddle-node connection. The unstable manifold of the period-q saddle connects to the period-q node thus forming a closed attracting curve. For other parameter values, the closed invariant curve may be associated with saddle and focus cycles [20]. With change of the parameters this closed invariant curve is destroyed through a homoclinic bifurcation. Therefore, one does not expect the closed invariant curve to exist all the way out to the curves l_1 and l_2. To study this problem in more detail let us consider the chart of dynamical modes shown in Fig. 35.7 and the bifurcation diagram presented in Fig. 35.10. As before, fp denotes the unstable fixed point, S is the period-5 saddle and F is the period-5 focus produced in the border-collision bifurcation.

A sequence of typical phase portraits illustrating the main stages of the destruction of the invariant closed curve through a homoclinic bifurcation for the 1:5 tongue are shown in Fig. 35.11. In the initial state (Fig. 35.9 (c)), the system displays a closed invariant curve that is the union of the unstable manifold of the saddle cycle of period-5 and the points of the stable and saddle period-5 cycles. As the parameter α increases, stable and unstable manifolds of the saddle cycle become tangent to each other, and this leads to the destruction of the torus and the formation of a non-transversal homoclinic orbit. Figure 35.11 (a)–(c) displays the phase portrait of the map (35.5) immediately after the "first" homoclinic tangency. With further increase of α, the stable and unstable manifolds of the period-5 saddle cycle intersect transversally to form a homoclinic structure (Fig. 35.11 (d)). The intersection of the two manifolds implies the exis-
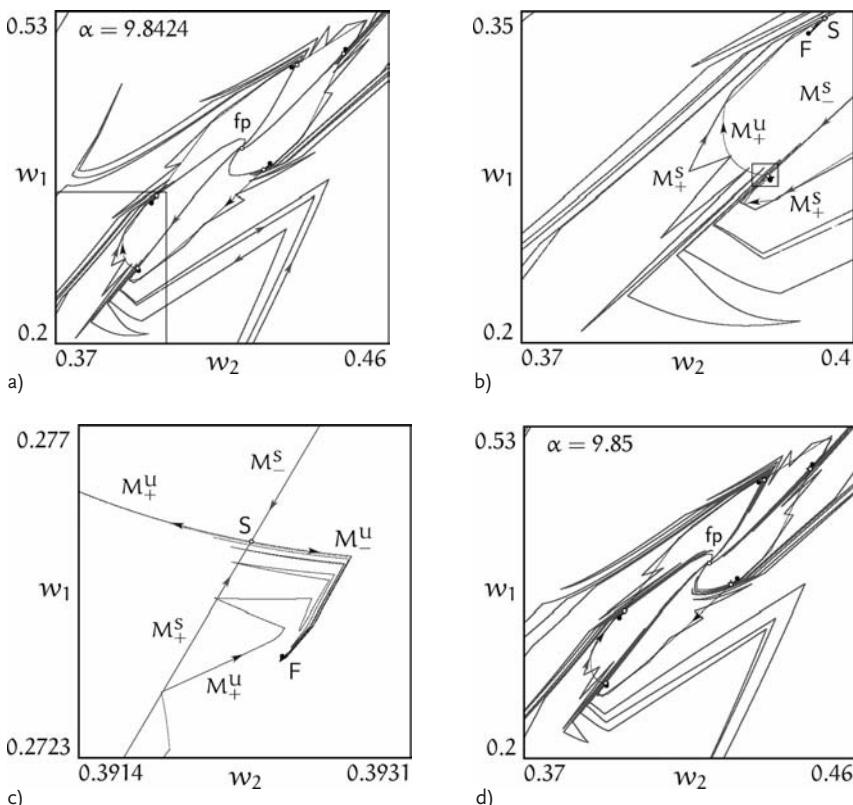
Fig. 35.11 Destruction of the closed invariant curve through a homoclinic bifurcation. (a) Phase portrait of the map (35.5) immediately after the first homoclinic tangency. (b) is a magnified part of (a), and (c) is a magnified part of (b). The stable manifolds (M_+^S and M_-^S) to the saddle point are drawn as thick lines, and the unstable manifolds (M_+^U and M_-^U) as thin lines. F is the stable period-5 focus. Parameter values are $E_0 = 11.8$ and $a = 9.8424$. (d) Homoclinic structure at $E_0 = 11.8$ and $a = 9.85$.

tence of a Smale horseshoe and, as a consequence, of a dense set of long-periodic orbits.

Figure 35.12 shows the phase portrait after the destruction of closed invariant curve. Here $a = 9.9$, $E_0 = 11.8$, and the stable period-5 cycle coexists with quasiperiodic oscillations, the trajectory of which is designated as C in the figure. The basins of attraction of these states are separated by the stable manifolds of the 5-saddle. A magnified part of the phase portrait, outlined by the rectangle in Fig. 35.12 (a), is shown in Fig. 35.12 (b). Hysteretic transitions from periodic to quasiperiodic oscillations and back are likely to occur in this parameter region.
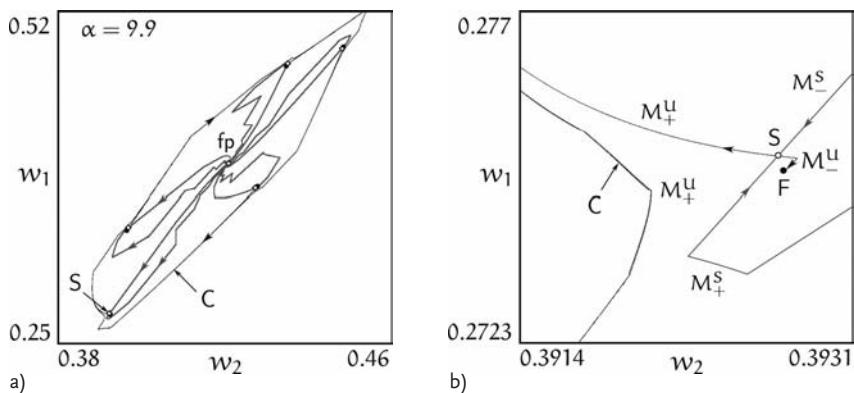
Fig. 35.12 Phase portrait of the map after the closed invariant curve is destroyed. Here the stable period-5 cycle F coexists with the quasiperiodic orbit C. The basins of attraction of periodic and quasiperiodic orbits are separated by the stable manifold of the period-5 saddle cycle. $E_0 = 11.8$ and $a = 9.9$.

35.6
Conclusions

The purpose of this chapter was to illustrate some of the complex dynamic phenomena that can arise in modern pulse-width modulated control systems. The mathematical analysis was presented in sufficient detail to allow engineers to perform similar analyses in the design of practical control systems.

By virtue of abrupt changes in circuit topology associated with the switching operation, pulse-width modulated control systems belong to a class of piecewise-smooth dynamical systems. This implies that they can exhibit a variety of complex behaviors that have no analogy in the dynamics of smooth systems. Many of these behaviors, such as truncated period-doubling cascades, period-tripling, -quadrupling, etc., bifurcations, and various forms of direct transitions to chaos are already documented in the literature. In the present chapter we demonstrated how a period-3 node, rather than being destabilized into a period-3 saddle, can disappear completely in a period-doubling bifurcation. We also showed how a focus fixed point can bifurcate directly into a period-5 focus cycle.

Similar phenomena occur in other types of piecewise-smooth systems such as, for instance, mechanical systems with impacts and stick-slip friction or economic and managerial systems with intervention and decision thresholds. The classic scenarios for torus destruction described by Afraimovich and Shilnikov may also display modifications for piecewise-smooth systems.

As specific examples, we have considered two DC/DC power electronic converters with pulse-width modulated control. The normal operation mode for this class of control systems is the regime of period-1 mode operation. Different

types of the feedback correctors may be used in order to obtain a faster response and a more accurate control. However, in practice to choose the type of feedback corrector, the parameters of the converter, and the kind of pulse-width modulation that can guarantee the desired operating mode with the proper dynamic characteristics is a difficult problem. This becomes even more complicated, of course, by the fact that under realistic conditions of operation, smaller or larger parameter changes will always take place. Such variations often lead to the loss of stability of the period-1 operating mode and to the appearance of complex dynamical behaviors, including subharmonic, quasiperiodic, or chaotic oscillations.

Moreover, pulse modulated-control systems can display situations where several stable periodic motions with different dynamic characteristics coexist within a wide range of parameters. These cycles typically arise in hard transitions, for example through saddle-node or fold border-collision bifurcations and with changing parameters they can undergo either a finite or an infinite sequence of period-doubling bifurcations, leading to the transition to chaos. As a result, we have parameter domains wherein, alongside with stable cycles, there are coexisting modes of chaotic or a quasiperiodic oscillations (see, e.g., Figs. 35.2 and 35.7). Under such conditions the action of external noise, even of low intensity, can induce a sudden transition from one dynamic state to another and, in particular, from regular to chaotic dynamics. Understanding these phenomena is extremely important for the design, prediction, and control dynamics of larger power electronic systems.

The first example we considered was a simple DC/DC converter with one-level pulse-width modulated control. The mathematical model of this converter was represented as a two-dimensional piecewise-smooth set of nonautonomous differential equations.

The first step in our investigation was to reduce the system to a two-dimensional piecewise-smooth mapping (35.4). Due to its simplicity, the mapping (35.4) allowed us to perform a detailed analytical and numerical bifurcation analysis. We showed, how the pulse-width modulated control system can exhibit both a period-doubling route to chaos through smooth bifurcations and a variety of interesting border-collision bifurcations.

Our second example was a DC/DC buck converter with two-level pulse-width modulated control. This system allowed us to describe scenarios for the transition to quasiperiodicity through border-collision bifurcations and to examine different examples of torus destruction.

Torus birth bifurcations in piecewise-smooth systems resembles the well-known Neimark-Sacker bifurcations in several respects. However, rather than through a continuous crossing of a pair of complex-conjugate multipliers of the fixed point through the unit circle, the border-collision bifurcation involves a jump of the multipliers from the inside to the outside of the unit circle. Moreover, by contrast to the parabolic growth in amplitude of the quasiperiodic oscillations characterizing a Neimark-Sacker bifurcation, we observe a linear growth in amplitude as the system moves away from the bifurcation point. The torus

may be ergodic or resonant. As mentioned above, we have also observed that the stable cycle on the resonance torus can be born as a focus rather than as a node, as it is the case for smooth systems.

Acknowledgments

References

1 V. S. Afraimovich and L. P. Shilnikov. Invariant two-dimensional tori, their breakdown and stochasticity. *Amer. Math. Soc. Transl.*, 149(2):201–212, 1991.

2 V. S. Anishchenko. *Dynamical Chaos – Models and Experiments*. World Scientific, Singapore, 1995.

3 D. G. Aronson, M. A. Chori, G. R. Hall, and R. P. McGhee. Bifurcations from an invariant circle for two-parameter families of maps of the plane: A computer-assisted study. *Comm. Math. Phys.*, 83:303–354, 1982.

4 S. Banerjee and C. Grebogi. Border collision bifurcations in two-dimensional piecewise smooth maps. *Phys. Rev. E*, 59(4):4052–4061, 1999.

5 S. Banerjee, M. S. Karthik, G. Yuan, and J. A. Yorke. Bifurcations in one-dimensional piecewise smooth maps – Theory and applications in switching circuits. *IEEE Trans. Circuits Syst. I: Fundam. Theory Appl.*, 47(3):389–394, 2000.

6 S. Banerjee, P. Ranjan, and C. Grebogi. Bifurcations in two-dimensional piecewise smooth maps – Theory and applications in switching circuits. *IEEE Trans. Circuits Syst. I: Fundam. Theory Appl.*, 47(5):633–643, 2000.

7 S. Banerjee and G. C. Verghese, editors. *Nonlinear Phenomena in Power Electronics*. IEEE Press, New York, USA, 2001.

8 V. S. Baushev and Zh. T. Zhusubaliyev. Indeterminable states of a voltage regulator with pulsewidth control. *Elect. Technol.*, 3:85–98, 1992.

9 B. K. Bose, editor. *Modern Power Electronics: Evolution, Technology, and Applications*. IEEE Press, New York, USA, 1992.

10 M. di Bernardo, C. J. Budd, and A. R. Champneys. Corner collision implies border collision. *Physica D*, 154(3/4): 171–194, 2001.

11 M. di Bernardo, C. J. Budd, and A. R. Champneys. Grazing bifurcations in *n*-dimensional piecewise-smooth dynamical systems. *Physica D*, 160:222–254, 2001.

12 M. di Bernardo, M. I. Feigin, S. J. Hogan, and M. E. Homer. Local analysis of C-bifurcations in *n*-dimensional piecewise-smooth dynamical systems. *Chaos, Solitons Fractals*, 10(11):1881–1908, 1999.

13 M. di Bernardo, P. Kowalczyk, and A. Nordmark. Bifurcations of dynamical systems with sliding: derivation of normal-form mappings. *Physica D*, 170:175–205, 2002.

14 M. di Bernardo and Ch. K. Tse. Chaos in power electronics: An overview. In G. Chen and T. Ueta, editors, *Chaos Circuits Syst.*, pp. 317–340. World Scientific, Singapore, 2002.

15 M. I. Feigin. Doubling of the oscillation period with C-bifurcations in piecewise continuous systems. *Prikl. Mat. Mekh.*, 34(5):861–869, 1970, in Russian.

16 M. I. Feigin. *Forced Oscillations in Systems with Discontinuous Nonlinearities*. Nauka, Moscow, 1994, in Russian.

17 A. I. Khibnik, D. Roose, and L. O. Chua. On periodic orbits and homoclinic bifurcations in Chua's circuit with a smooth

nonlinearity. *Int. J. Bifurcat. Chaos*, 3(2):363–384, 1993.

18 A. V. Kobzev. *Multilevel Pulse Modulation: Theory and Applications to Power Electronics*. Nauka, Novosibirsk, 1979, in Russian.

19 P. T. Krein. *Elements of Power Electronics*. Oxford University Press, New York, USA, 1998.

20 Yu. A. Kuznetsov. *Elements of Applied Bifurcation Theory*. Springer, New York, 2004.

21 J. S. Lai and F. Z. Peng. Multilevel converters – A new breed of power converters. *IEEE Trans. Ind. Appl.*, 32(3):509–517, 1996.

22 V. Maistrenko, Yu. Maistrenko, and E. Mosekilde. Torus breakdown in noninvertible maps. *Phys. Rev. E*, 67(4):046215-1-046215-6, 2003.

23 T. A. Meynard, H. Foch, P. Thomas, J. Courault, R. Jakob, and M. Nahrstaedt. Multicell converters: Basic concepts and industry applications. *IEEE Trans. Ind. Electron.*, 49(5):955–964, 2002.

24 A. B. Nordmark. Existence of periodic orbits in grazing bifurcations of impacting mechanical oscillators. *Nonlinearity*, 14:1517–1542, 2001.

25 H. E. Nusse, E. Ott, and J. A. Yorke. Border-collision bifurcations: An explanation for observed bifurcation phenomena. *Phys. Rev. E*, 49:1073–1076, 1994.

26 H. E. Nusse and J. A. Yorke. Border-collision bifurcations including "period two to period three" for piecewise smooth systems. *Physica D*, 57:39–57, 1992.

27 H. E. Nusse and J. A. Yorke. Border-collision bifurcation for piecewise smooth one-dimensional maps. *Int. J. Bifurcat. Chaos*, 5(1):189–207, 1995.

28 C. K. Tse. *Complex Behavior of Switching Power Converters*. CRC Press, Boca Raton, USA, 2003.

29 Zh. T. Zhusubaliyev, E. Mosekilde, S. M. Maity, S. Mohanan, and S. Banerjee. Border collision route to quasiperiodicity: Numerical investigation and experimental confirmation. *Chaos*, 16:023122, 2006.

30 Zh. T. Zhusubaliyev and E. Mosekilde. *Bifurcations and Chaos in Piecewise-Smooth Dynamical Systems*. World Scientific, Singapore, 2003.

31 Zh. T. Zhusubaliyev and E. Mosekilde. Birth of bilayered torus and torus breakdown in a piecewise-smooth dynamical system. *Phys. Lett. A*, 351(3):167–174, 2006.

32 Zh. T. Zhusubaliyev and E. Mosekilde. Torus birth bifurcation in a DC/DC converter. *IEEE Trans. Circuits Syst. I: Fundam. Theory Appl.*, 53(8):1839–1850, 2006.

33 Zh. T. Zhusubaliyev, E. A. Soukhoterin, and E. Mosekilde. Border-collision bifurcations and chaotic oscillations in a piecewise-smooth dynamical system. *Int. J. Bifurcat. Chaos*, 11(12):2977–3001, 2001.

34 Zh. T. Zhusubaliyev, E. A. Soukhoterin, and E. Mosekilde. Border-collision bifurcations on a two-dimensional torus. *Chaos, Solitons Fractals*, 13(9):1889–1915, 2002.

35 Zh. T. Zhusubaliyev, E. A. Soukhoterin, and E. Mosekilde. Quasiperiodicity and torus breakdown in autonomous piecewise-smooth systems. *Math. Comput. Simulation*, 73(6):364–377, 2007.

36

Transient Dynamics of Duffing System under Time-Delayed Feedback Control: Global Phase Structure and Application to Engineering

Takashi Hikihara and Kohei Yamasue

36.1
Introduction

The success of controlling chaos by Ott, Grebogi, and Yorke [1] has highly moti-vated many researchers to develop new methods for stabilizing unstable peri-odic orbits (UPOs) embedded in chaotic oscillations or vibrations. The time-de-layed feedback control (TDFC) was proposed as one of the methods for control-ling chaos in continuous dynamical systems by Pyragas [2]. This chapter focuses on this method from the viewpoint of transient dynamics based on the global phase structure of the system under control. Moreover, the possibility of applica-tion to engineering systems is also explained based on the authors' research re-sults [3–9].

In this one and half decades, there were two trends of researches related to TDFC. The theoretical stability analyses of UPOs under the control have been one of the highly important topics [10–15]. The excellent efforts summarized in the preceding chapters were made to establish the reliable corroboration of the control performance. In the same period, the performance of TDFC was experi-mentally demonstrated in diverse research fields including electronic circuits [16, 17], laser systems [18], chemical systems [19], and gas-charge systems [20]. They seemed the first significant phases of technical and theoretical discussions of TDFC. Since the middle 1990s, one of the authors has also tried to know the ability of TDFC experimentally and numerically [3, 4]. Through the experiments, remaining questions were found on the *transient* behavior after the onset of con-trol and the *domain of attraction* for target orbits in parameter and initial function space of a difference-differential equation. Just pointed out the importance of the domain and the global dynamics as rested problems [21]. Moreover, the robustness of stabilization was also the substantial topics in mechanical pendulum [3]. These persistent problems have been rested in front of us, the early enthusiastic interests on the development and analysis of TDFC being past.

In this chapter, the fundamental explanations are excluded. The readers can check them in the preceding chapters. The detail mathematical definitions are

also out of scope in this chapter. The approaches to the above-mentioned problems and the applications to nanoengineering are the main topics as a keystone of future researches.

36.2
Transient Dynamics of Transient Behavior

36.2.1
Magnetoelastic Beam and Experimental Setup

The magnetoelastic beam is well known that a chaotic vibration inherently appears in the system [22]. Here, TDFC is applied to stabilize UPOs embedded in the chaos. The experimental system was set to confirm the ability of TDFC as shown in Fig. 36.1 [3]. The time-delayed feedback signal consists of the gained difference between the memorized output and the present output. The method does not request the full set of state variables. In the experimental system, the velocity of displacement is adopted. The control signal is added to the forced sinusoidal excitation. TDFC can stabilize an UPO embedded in the chaotic attractor under the appropriate setting of time delay that coincides with the period of the UPO. Here we stabilized target UPOs whose period coincide with an integer multiplication of the forced period [23]. Once an UPO is stabilized by TDFC, the control input disappears because of the coincidence of the present state with the delayed state. In experiments, the time delay does not strictly adjusted to coincide with the forced period [4]. Of course, there remains the non-
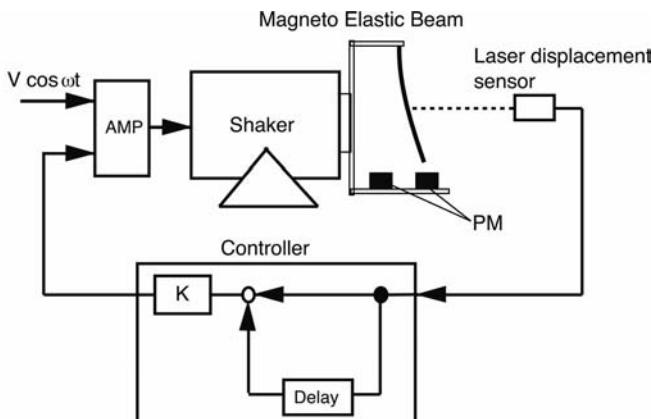
Fig. 36.1 Magnetoelastic system and control diagram of TDFC. The control signal is induced by the detected displacement and memorized one in a computer. The time delay is fixed at the period of sinusoidal force of magnetic shaker. The sinusoidal signal with the TDFC signal is amplified and supplied to the magnetic shaker as a voltage signal. Then the sign of control block is reversed.

zero control signal after the stabilization. While this does not mean the controlling chaos in a strict sense, it seems the robustness of TDFC to the parameter mismatch of time delay. This feature should strongly depend on the global structure of the configuration space related to the change of time delay. At the same time, through the experiments, we found the following questions; how the delay plays a role during transient state, what decides the length of the transient state, and how large the basin of the target UPO under control. In this chapter, we are going to discuss them according to our research results in the Duffing system with TDFC.

36.2.2
Transient Behavior

Different UPOs were experimentally stabilized under TDFC. It was, however, difficult to predict which solution was stabilized at the onset of control. When TDFC is activated, the time developed solution appears in the infinite-dimensional phase space until the control input disappears. The transient behavior is therefore affected by the infinite-dimensional global phase structure not easy to describe.

Figure 36.2 is the space–time expansion of the state space, which is adopted in order to show the feature of the dynamics in the infinite-dimensional space in [5]. The method was introduced by Arecchi, Giacomelli et al. [24, 25] to understand the time-delay dynamics as spatiotemporal dynamics. Figure 36.3 (i) and (ii) shows the space–time expansion of experimental data obtained in the magnetoelastic system with TDFC. The experimentalists have had the similar experiences in which the dynamics under control showed various transient behavior until settling to a stable state. In some cases, after the state seemed to
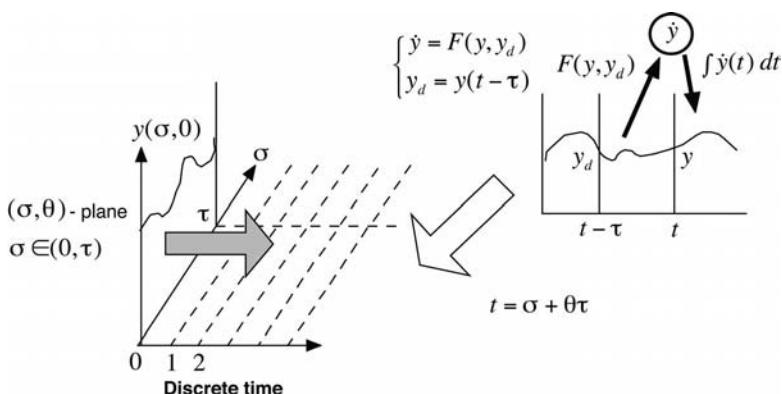
Fig. 36.2 Spatiotemporal expansion of state space. The experimentally obtained time series is divided into the phase segment. The discrete segments depict the temporal development of states and the segment of the finite space [5].
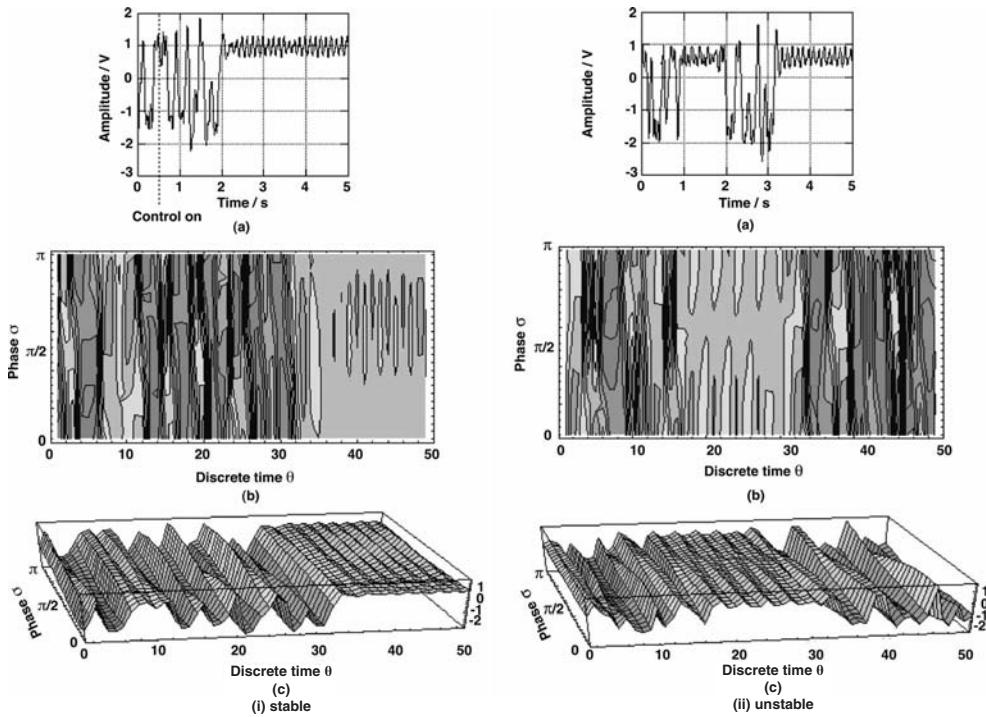
Fig. 36.3 Space-time expansion of periodic behaviors in the system with TDFC: (i) stable orbit and (ii) unstable one [5]. The contour implies the change of phase as a temporary continuous spatial variable.

converge to a target periodic orbit, it showed the divergence again as shown in Fig. 36.3. The difference of stable and unstable states can be found in the spatial waveform. A spatial node appears in the case of the unstable orbit under control as shown in Fig. 36.3 (ii).

The experimental results give us an image of state transitions in infinite-dimensional state space as propagation of discrete waves in the expanded spatio-temporal state space. The results also explain that stable and unstable solutions possibly coexist in systems under TDFC. Moreover, it suggests that there are periodic orbits which cannot be stabilized by TDFC. The experiences had been proved by the 'odd number condition' [10, 12, 13]. The condition is useful to know the ability of TDFC. From the viewpoint of dynamics, much interests are found in the transient behavior after the onset of TDFC. In this chapter, our discussions focus on the transient dynamics under TDFC.

36.3
Initial Function and Domain of Attraction

The domain of attraction for various ordinary differential equation systems has been discussed on the space of initial values and parameters. Once the values are given, the trajectory is uniquely determined in the deterministic dynamical system. The domain of attraction has provided an important information related to the robustness for initial values. However, in the system with delay, the domain of attraction should be considered in the infinite-dimensional function space. In particular, the dynamical behavior of the system with TDFC substantially depends on the initial function due to the delay at the onset of control. The initial function is determined as a segment of trajectory of the original chaotic trajectory. Figure 36.4 depicts a method for examining the domain of attraction in the discrete spatiotemporal state space.

The experimental system in Fig. 36.1 can be described by the following two well Duffing's equations with control input. That is,

$$\frac{d}{dt}\begin{pmatrix} x \\ y \end{pmatrix} = \begin{pmatrix} y \\ -\delta y(t) + ax(t) - \gamma x(t)^3 + A\cos\omega t + u(t) \end{pmatrix} \tag{36.1}$$

$$u(t) = K\{y(t-\tau) - y(t)\} \tag{36.2}$$

Here we assume that the control is activated at $t = t_0$. Then,

$$x(t_0) = x_{t_0}, \quad y(t_0) = y_{t_0}, \tag{36.3}$$
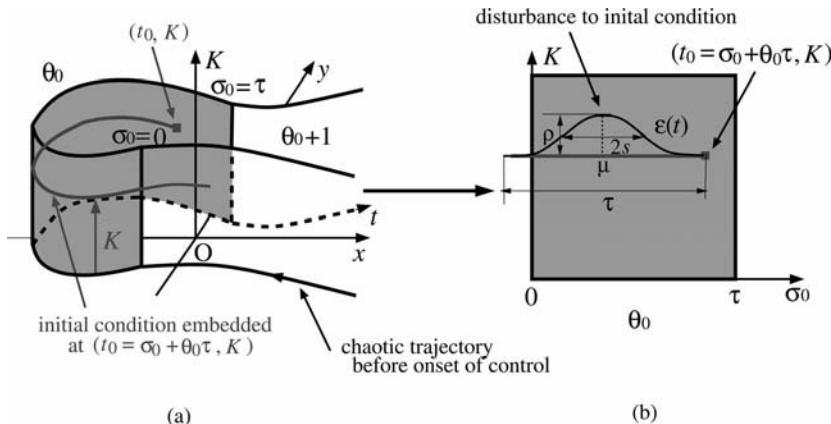
Fig. 36.4 Initial function space and disturbances [6]. The initial function is defined in (a) as a segment in $t \in |t_0 - \tau, t_0)$ of a chaotic trajectory backwardly developed from the onset time of control $t = t_0$. The disturbance is given as shown in (b). The disturbance is artificially given as a Gaussian-like function.
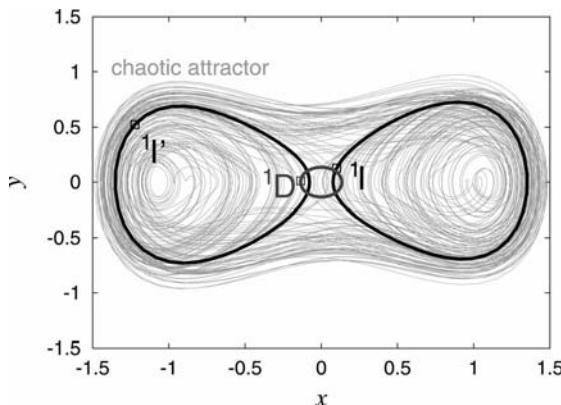
Fig. 36.5 Unstable period 2π orbits embedded in original chaotic attractor. ^{1}I and ^{1}I′ denote inversely unstable periodic orbits of the target, which are stabilized under sufficient feedback gain. ^{1}D is a directly unstable periodic embedded in chaotic attractor.

$$y(t_0) = y(t_0 + \theta), \ \theta \in [-\tau, 0) \tag{36.4}$$

are satisfied. As mentioned above, the initial function is selected from a segment of the chaotic trajectory generated by $u(t) = 0$ from the initial value $(x(0), y(0)) = (1.0, 0)$.[1] For simplicity, the angular frequency ω is set at unity. δ, a, γ, and A are fixed at 0.16, 1.0, 1.0 and 0.27, respectively. The time delay τ is adjusted to period of the target UPOs embedded in the chaotic attractor. Figure 36.5 reveals unstable period 2π orbits embedded in the original chaotic attractor. ^{1}I and ^{1}I′ denote inversely unstable periodic orbits of the target. ^{1}D is a directly unstable periodic embedded in the chaotic attractor. ^{1}I and ^{1}I′ can be stabilized by TDFC and change to stable periodic orbits. On the other hand, ^{1}D cannot be stabilized due to "the odd number condition."

The control signal converges to null when the system is stabilized at one of the target orbits. As a result of this convergence, the controlled system with time delay degenerates to the original two-dimensional system without time delay. The domain of attraction for target orbits is characterized by the infinite dimensional space under remarkable control input. That is, the estimation of the domain goes beyond the scope of linearization in the neighborhood of the original UPOs.

Figure 36.6 shows the classification of stabilized orbits on the onset time and feedback gain parameter plane [6]. The target UPOs can be stabilized through TDFC. There are, however, many other stable orbits, which have longer period

---

1) The numerical results in the following section are independent of the parameter settings and the adopted algorithm of calcula-tion. Therefore, the discussion in this section shows the typical feature of TDFC.
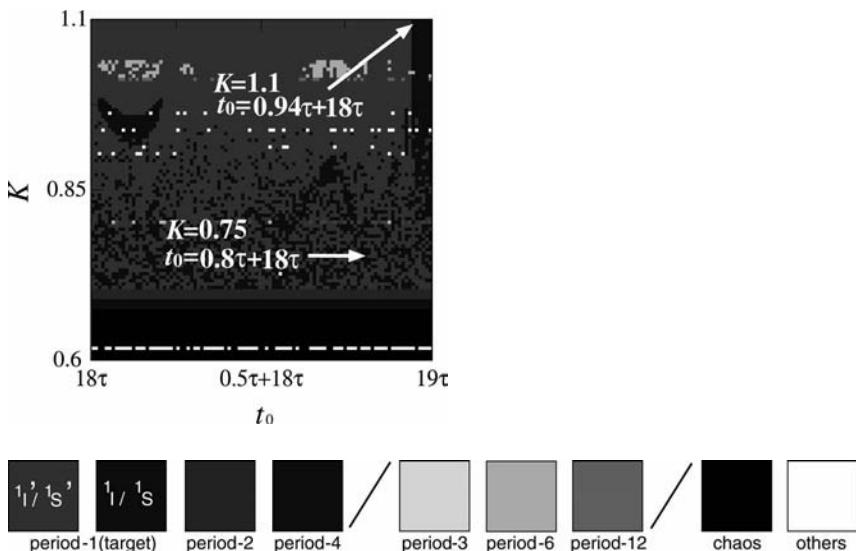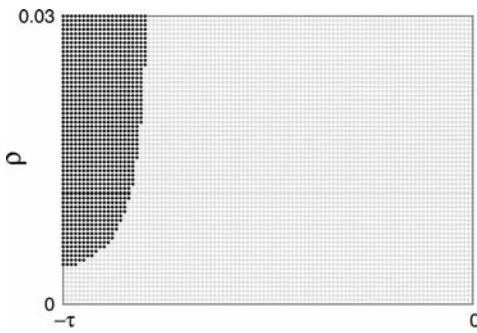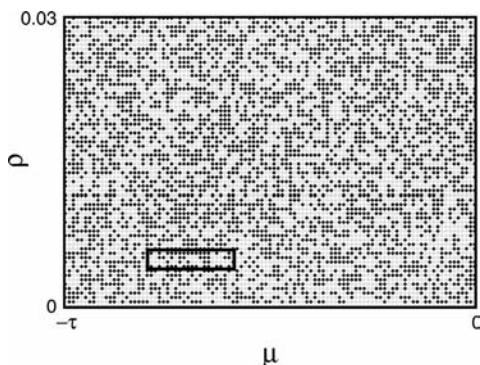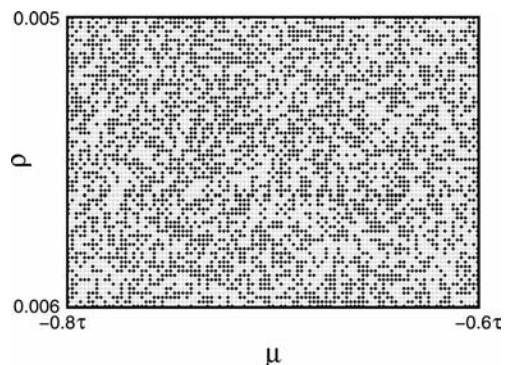
Fig. 36.6 Classification of stabilized orbits in the initial function space at $(\delta, A) = (0.16, 0.27)$. Dark and light regions correspond to each target orbit shown in Fig. 36.5.

and coexist with the targets. The previous experiment also showed that the control input could not always achieve the convergence to each UPO [4]. In order to understand the global dynamics behind this situation different external disturbances were given to the initial function as shown in Fig. 36.4. Since the period of these coexisting orbits does not coincide with 2π, the control signal $u(t)$ remains after the stabilization. Therefore, solutions are different from the target UPOs embedded in the original chaotic attractor. In other words, controlling chaos is one of the cases in which coexisting solutions are stabilized. At the parameter denoted by the arrow $(K, t_0) = (1.1, 0.94\tau + 18\tau)$, the domain of attraction due to the functional disturbance is obtained as in Fig. 36.7 (a). The boundary between two coexisting solutions is smooth. In the case the solution can be selected by the deformation of the initial function by control input. On the other hand, at the parameter $(K, t_0) = (0.75, 0.8\tau + 18\tau)$, the domain of attraction becomes as shown in Fig. 36.7 (b). Figure 36.7 (c) is the enlargement of a rectangle region in Fig. 36.7 (b). The results show that the domain of attraction is too complicated to control the convergence to each target orbit. We can thus understand that the structure of domain strongly governs the transient behavior after the onset of control.

(a) $(K, t_0) = (1.1, 0.94\tau + 18\tau)$

(b) $(K, t_0) = (0.75, 0.8\tau + 18\tau)$

(c) Enlargement of the rectangle region in (b)

Fig. 36.7 Domain of attraction in two-well Duffing system under TDFC at $(\delta, A) = (0.16, 0.27)$. The domain is obtained around the initial condition pointed by arrows in Fig. 36.6.

36.4
Persistence of Chaos

In this section, the global phase structure of the two-well Duffing system is discussed under TDFC. In the previous section, the coexistence of stable solutions under TDFC was confirmed through the numerical estimation of domain of attraction in each period-2π inversely unstable orbit. The complicated structure in domain of attraction suggested strong dependence of the transient dynamics on global structure in the infinite dimensional phase space.

A key to understanding the controlled dynamics is to investigate dynamical structures, which play a governing role in the global dynamics of the controlled system. The structure is described by a one-dimensional global unstable manifold, which provides substantial information on the global phase structure in function space [7].
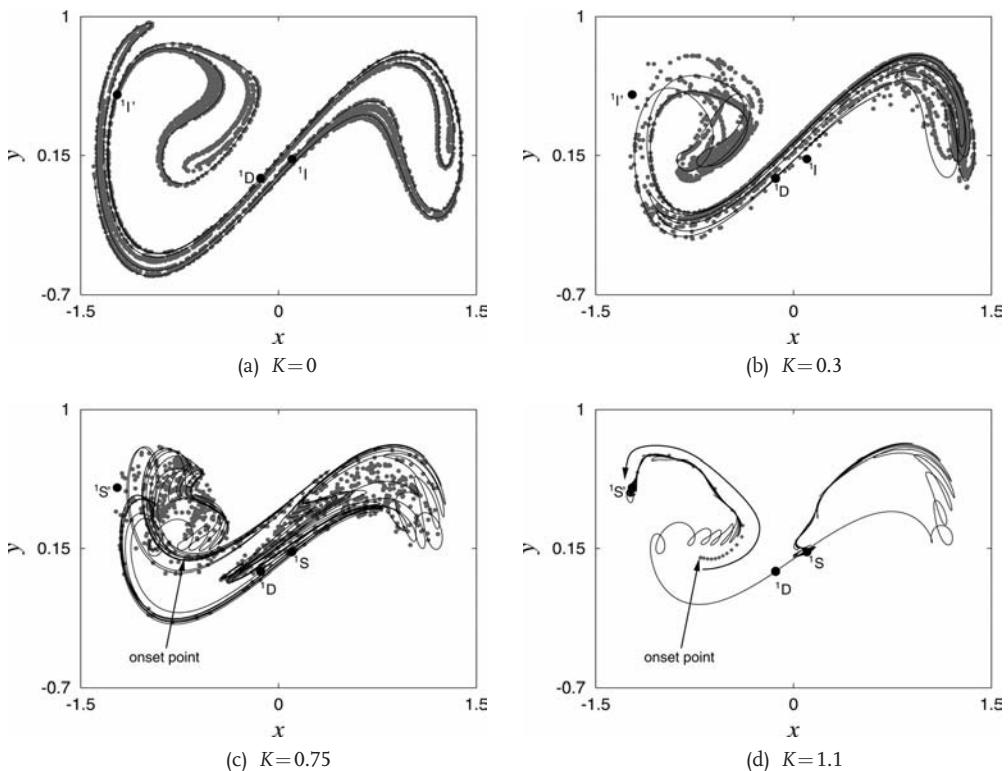
Fig. 36.8 Persistence of chaos and transient behavior based on unstable manifold [7].

The global dynamics of the two-well Duffing system is characterized by the presence of the directly unstable periodic orbit ^{1}D [22, 23]. A homoclinic intersection is confirmed in the cross section induced by stroboscopic mapping with period 2π. A chaotic invariant set, therefore, exists in the original Duffing system. The closure of the unstable manifold coincides with the chaotic attractor. The chaotic attractor includes the target UPOs and ^{1}D simultaneously.

The manifold is shown in Fig. 36.8. It is the unstable manifold of ^{1}D projected on a two-dimensional stroboscopic plane. In Fig. 36.8 (a) and (b), the target orbits are unstable and the chaotic attractor remain, as shown by gray stroboscopic points. In Fig. 36.8 (c) and (d) the targets are stable and stroboscopic points show transient behavior before the convergence to target orbits. The notation of target is changed to the stable orbits ^{1}S and ^{1}S$'$, because of their stability change. Each arrow in Fig. 36.8 (c) and (d) indicates the stroboscopic point at which the control is activated, respectively.

Once the control input is activated under $K > 0$, the original dynamics is perturbed by the control input. It implies the system changes from the original two-dimensional system to the corresponding infinite dimensional one due to

the presence of delayed input. Figure 36.8 explains that the global phase structure itself is still governed by the unstable manifold of ^{1}D, which persistently exists and keeps a unique characteristic multiplier greater than unity under TDFC because of the odd number condition.

In Fig. 36.8(b), for small feedback gain of Eq. (36.2) the target orbit is still unstable in the controlled system and the chaotic attractor remains. The unstable manifold inherits the global stretch and fold structure as the original chaotic attractor shown in Fig. 36.8(a). Both branches of the manifold once develop in opposite directions to each other, but are folded and back to ^{1}D again. It should be noted that the unstable manifold is the projection from the infinite-dimensional function space to the original two-dimensional stroboscopic plane. As the feedback gain is further increased, the two target orbits become stable. However, the stretch and fold structure of the unstable manifold is kept in Fig. 36.8(c). By considering the temporal evolution, it implies that the phase space inherits the characteristics that produce the chaotic dynamics for $K = 0$ and $K = 0.3$, while the original chaotic attractor is destroyed because of the stability change of the target orbits for $K = 0.75$. Since the chaotic dynamics remains in the controlled system, the trajectories wander irregularly between ^{1}S and ^{1}S$'$ along the unstable manifold. The characteristics can be confirmed even after the target orbits become stable by TDFC. Figure 36.9 shows the corresponding temporal change of displacement x and control input u. The displacement irregularly goes back and forth between two stable orbits under control. After the many times transition, it eventually converges to ^{1}S, although the quick convergence to a target orbit is an important performance of TDFC from the viewpoint of control.
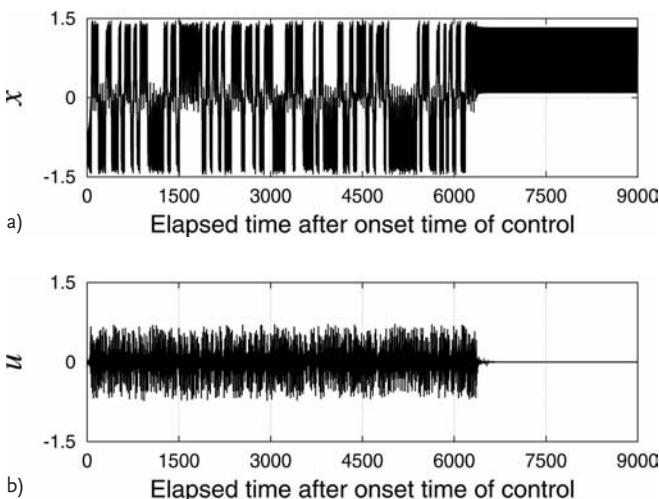
Fig. 36.9 Transient behavior (a) displacement and (b) control input after the onset of control.

The further increase of feedback gain brings the global bifurcations which completely break the homoclinic intersection appeared in original system. The simple structure of the unstable manifold for $K = 1.1$ shows the disappearance of the original chaotic invariant set and the quick convergence to the target orbits embedded in chaotic attractor.

In this section, the transient dynamics under TDFC has been discussed based on the global structure in the infinite dimensional phase space. The coexistence of UPOs which can be stabilized by TDFC gives the possibility to make the transient behavior wanders between them unexpectedly. At the same time, the persistence of transient chaotic behavior governs the performance of TDFC even in practical applications. From the engineering point of view, the transient dynamics is one of the most important characteristics, which decides the performance of the control method. This is particularly important, because the engineering systems are frequently exposed to disturbance such as noise and repeated changes of system parameters. We will note this point in the next section in an application to nanoengineering system.

36.5
Application of TDFC to Nanoengineering

Recently, nanoscience and nanoengineering are one of the hot research fields. Here we explain an example of applications of TDFC in development of atomic force microscopy having much improved performance.

36.5.1
Dynamic Force Microscopy and its Dynamics

The atomic force microscopy (AFM) [26] is nowadays widely accepted as a tool for probing nanostructures [27]. In particular, the dynamic force microscopy (DFM) [28, 29] has been developed as a flagship operating mode of the AFM for these two decades [30]. In the DFM, a microcantilever vibrating at the resonance frequency is utilized as a force sensor to detect the interaction force between the tip manufactured at the free end and a sample surface facing the tip. The topology of the sample surface is imaged by raster scan of the surface with keeping the vibration or the resonance frequency of the microcantilever constant.

In the experimental field, the researchers had recognized that there exist nonlinear oscillations including chaos in the response of AFM measurement in the late 1990s [31] and, recently, it was proved in experiments [32, 33]. The resulting oscillation modes possibly reduce the force sensitivity due to undesirable subharmonics and widely spread frequency spectrum, which are neglected in the standard configuration of the system. For the chaotic oscillation, the operating range of the DFM may be also limited by the nonperiodic and irregular motion of the microcantilever. It is, therefore, significant to develop control techniques to microcantilever oscillations for improving the performance of DFM. In this
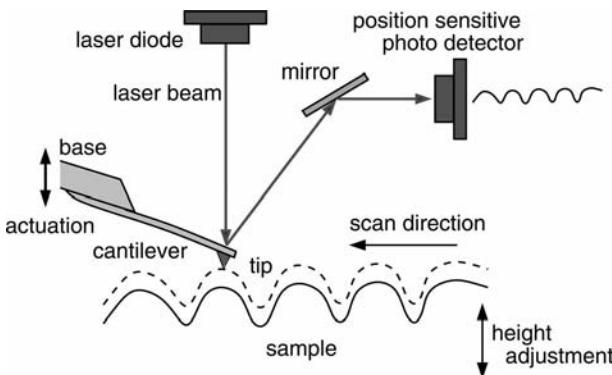
Fig. 36.10 Schematic diagram of dynamic mode atomic force microscopy.

context, some research groups have already proposed application of control techniques to restrict the oscillation [34–36].

A schematic diagram of a DFM is shown in Fig. 36.10. A microcantilever vibrating at its resonance frequency is a force sensor in the DFM and detects the variation of tip–sample interaction force as a shift of the resonance frequency. Since the interaction force depends on the mean tip–sample distance, the shift of the resonance frequency corresponds to the variation of mean tip–sample distance. The topography of a sample surface is therefore traced by raster scan of the surface by keeping the shift of resonance frequency constant. The constant shift of resonance frequency, or constant mean tip–sample distance, is achieved by adjusting the height of sample surface during the raster scan with a positioning device, such as tube scanners. The time series of signal during controlling the positioning device gives topography of the sample surface. The DFM has two major operating modes called AM–DFM [28] and FM–DFM [29], in which the variation of amplitude and frequency is detected, respectively, to estimate the shift of resonance frequency.

When the tip–sample interaction force is approximated by the Lennard–Jones potential, the first mode vibration of a microcantilever controlled by a scalar signal $u(t)$ is described by the following equation [35]:

$$\frac{d}{dt}\begin{pmatrix} x \\ y \end{pmatrix} = \left(-x - \frac{d}{(a+x)^2} + \frac{\Sigma^6 d}{30(a+x)^8} + \varepsilon(\Gamma\cos\Omega t - \Delta y) \right) + \mathbf{b}u, \qquad (36.5)$$

where x and y denote the displacement and the velocity of tip, respectively. $\mathbf{b}$ denotes a two-dimensional constant vector concerning the coupling between the control input and the state variables. The system consists of a cantilever with a nonlinear potential function, similar to magnetoelastic beam. a is the equilibrium position of tip without any other force except gravity. Γ and Ω correspond to the amplitude and the frequency of the external sinusoidal force, which is
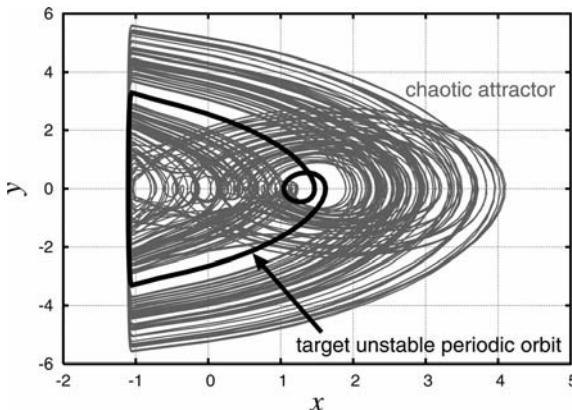
Fig. 36.11 Chaotic attractor reported in [37] and target unstable periodic orbit embedded in it. The periodic of the target is 2π which equals to the period of external driving force.

provided to the microcantilever with the damping coefficient Δ, respectively. Σ denotes a constant related to the diameter of each molecule organizing the tip and the sample. d is a constant for normalization and set at $4/27$. Finally, ε is a small parameter. In [34, 35], the existence of chaos is proved by Melnikov's method in Eq. (36.5) without control input. The chaos follows the scenario of period-doubling cascade [37].

Figure 36.11 shows a chaotic attractor reported in [37] and target unstable periodic orbit embedded in it. The period of the target is adjusted to 2π which equals to the period of external driving force. If the target orbit originating from the resonant orbit is stabilized, the possible region for measurement will be enlarged. In addition, the quick damping of the transient behavior is expected to be suppressed to increase the scanning rate of AM–DFM.

Hereafter the following coefficients are investigated according to numerical results in [37]. The damping coefficient Δ is set at 0.4 and Ω at 1.0. $\Sigma = 0.3$, $\varepsilon = 0.1$, $a = 1.2$, and $\Gamma = 20$ are given. τ is adjusted at $2\pi/\Omega$.

36.5.2
Application of TDFC

Recently, experimental studies by Jamitzky et al. and Hu et al. demonstrated chaotic vibrations of microcantilever in the actual AM–DFMs [32, 33]. Here, we numerically show that the time-delayed feedback control has a possibility to eliminate the chaotic oscillation based on Eq. (36.5). We have already numerically confirmed the possibility of the stabilization of the tapping mode chaos which Hu and Raman reported [9]. However, there are dynamical differences between these two chaotic phenomena. We, here, concentrate on the chaos which is caused by the bistable phase structure.

(a) Displacement of cantilever

(b) Control input
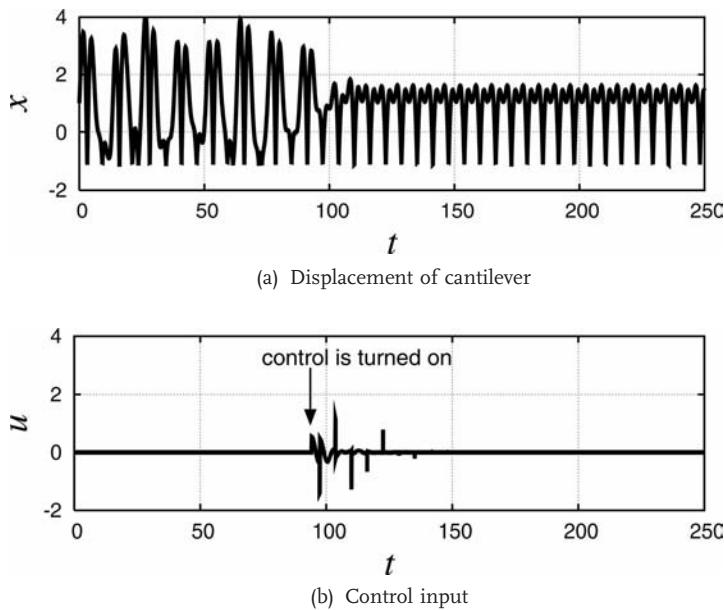
Fig. 36.12 Stabilization of target unstable periodic orbit embedded in chaotic attractor using TDFC [8].

Here, TDFC is applied to stabilize chaotic vibrations to keep the sensitivity of measurement by AM–DFM. Around the parameter region in which chaos appears, the measured topography of material surface loses the sensitivity by dynamic noise [33]. The applied control signal is given by

$$u = K(y(t - \tau) - y(t)) \tag{36.6}$$

as a difference between the current output and the past one, where τ denotes the time delay corresponding to the target orbit and K the feedback gain. Equation (36.6) implies a scalar control signal derived between the current time t and the past time $t - \tau$.

Figure 36.12 shows a numerical result of the stabilization of chaos in AM–DFM. The feedback gain K is adjusted at 0.2. After the onset of TDFC, the chaotic behavior of the tip displacement is stabilized as shown in Fig. 36.12 (a). After the transient state, the control input becomes negligible. It implies that the vibration behaves depending on the dynamics between the tip and the material surface.

36.5.3
Extension of Operating Range

TDFC is able to extend the operating range of AM–DFM. This is confirmed by Fig. 36.13. The figure shows two different toned parameter ranges. The black
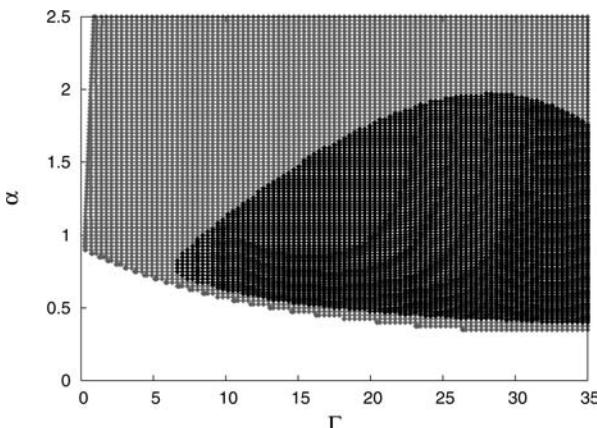
Fig. 36.13 Operating range of DFM under TDFC [8].

area displays a parameter range where the target period-2π orbit is unstable if control is not applied. It has been reported that this black area is not appropriate for the operation of AM–DFM due to the possibility of period-doubling bifurcation and the route to chaos. The gray area shows the area where the control method can keep the target period-2π orbit stable. As we can see, the gray area completely covers the black unstable area. Even in the black area, the stability of the target orbit under TDFC is completely established. Therefore, it is concluded that the control method for stabilizing target unstable orbit can eliminate the appearance of period-doubling bifurcation and subsequent chaotic oscillation. In other words, the operating range of AM–DFM is extended by applying the control method to microcantilever. Of course, there is a limitation of the parameter range, which is shown by white area. It is caused by the saddle-node bifurcation which makes the target orbit disappear in the region.

We should note that influence of surface scan on the transient dynamics of cantilever is not taken into account here. However, the transient dynamics of the cantilever is much important to improve DFM performance in addition to the stability of the target orbit under TDFC. This is because the dynamics of cantilever can show a chaotic transient state if the original chaotic dynamics persists in the controlled system as observed in the two-well Duffing system. One may face irregular and long transient behavior under control, since the tip–sample distance is repeatedly changed due to surface topography. We therefore emphasize that transient dynamics of the system under TDFC is one of the most important characteristics to be investigated for the future step to engineering application of TDFC.

**36.6
Conclusions**

In this chapter, we summarized the transient dynamics and the global phase structure which appeared in the Duffing system under TDFC and the applications to engineering system. First, it was shown that the domain of attraction in the initial function space had the complicated feature related to the coexistence of stable solutions under control. TDFC has a potential to stabilize the target orbits embedded in chaotic attractors. At the same time, there is also a potential to create multiple steady states by control. Therefore, the domain of attraction for target orbits is the most important characteristics to show the ability and robustness of the control method.

Second, it was clarified that the transient dynamics after the onset of TDFC is governed by the global phase structure in the infinite dimensional phase space. In particular the unstable manifold of the saddle, which has the same period as the target orbits, governs the transient behavior of the controlled system. The theoretical approach which ensure the local stability of the target orbits could not give any information about the transient behavior especially in the case of controlling chaos. We clearly showed how the time delay works to the global phase structure by the unstable manifold.

Finally, we showed the application of TDFC to a nanoengineering system. The family of atomic force microscopes are flag-ship devices in nanoscience and nanoengineering. The measurement is deeply affected by the interaction force between the tip and the material surface. We numerically confirmed that the unexpected nonlinear behavior of tip can be stabilized by TDFC. The application requests the quick transient behavior toward the convergence in the dynamics of cantilever. The elimination of the transient motion gives the system further sensitivity and quick scanning characteristics [8, 9].

References

1 Ott, E., Grebogi, C., and Yorke, A., *Phys. Rev. Lett. 64* (**1990**), p. 1196.

2 Pyragas, K., *Phys. Lett. A 170* (**1992**), p. 421.

3 Hikihara T. and Kawagoshi T., *Phys. Lett. A 211* (**1996**), p. 29.

4 Hikihara, T., Touno, M., and Kawagoshi, T., *Int. J. Bifurcation Chaos Appl. Sci. Eng. 7* (**1997**), p. 2837.

5 Hikihara, T. and Ueda, Y., *Chaos 9* (**1999**), p. 887.

6 Yamasue, K. and Hikihara, T., *Phys. Rev. E 69* (**2004**), p. 056209.

7 Yamasue, K. and Hikihara, T., *Phys. Rev. E 73* (**2006**), p. 036209.

8 Yamasue, K. and Hikihara, T., *Rev. Sci. Instrum. 77* (**2006**), p. 053703.

9 Yamasue, K. and Hikihara T., *Proceedings of Int. Symp. on Nonlinear Theory and its Applications* (IEICE, **2006**), p. 927.

10 Ushio, T., *IEEE Trans. Circuits Syst., I: Fundam. Theory Appl. 43* (**1996**), p. 815.

11 Konishi, K., Ishii, M., and Kokame, H., *Phys. Rev. E 54* (**1996**), p. 3455.

12 Nakajima, H. and Ueda, Y., *Physica D 111* (**1998**), p. 143.

13 Just, W., Bernard, T., Ostheimer, M., Reibold, E., and Benner, H. *Phys. Rev. Lett. 78* (**1997**), p. 203.

14 Just, W., *Physica D 142* (**2000**), p. 153.

15 Pyragas, K., *Phys. Rev. Lett*. *86* (**2001**), p. 2265.

16 Socolar, J. E. S., Sukow, D. W., and Gauthier, D. J. *Phys. Rev. E 50 (*1994), p. 3245.

17 Pyragas, K., and Tamaševičius, A., *Phys. Lett. A 180* (**1993**), p. 99.

18 Bielawski, S., Derozier, D., and Glorieux, P., *Phys. Rev. E, 49* (**1994**), p. R971.

19 Parmananda, P., Madrigal, R., Rivera, M., Nyikos, L., Kiss, I. Z., and Gáspár, V., *Phys. Rev. E, 59* (**1999**), p. 5266.

20 Pierre, T., Bonhomme, G., and Atipo, A., *Phys. Rev. Lett, 76* (**1996**), p. 2290.

21 Just, W., Reibold, E., Kacperski, K., Fronszak, P., Holyst, J. A., and Benner, H., *Phys. Rev. E 61* (**2000**), p. 5045.

22 Moon, F. C. and Holmes, P. J., *J. Sound Vib. 65* (**1979**), p. 275.

23 Ueda, Y., Nakajima, H., Hikihara, T., and Stewart, H. B., in *Dynamical Systems Approaches to Nonlinear Problems in Systems and Circuits*, SIAM, Philadelphia (**1988**), p. 128.

24 Arrechi, F. T., Giacomelli, G., Lapucci, A., and Meucci, R., *Phys. Rev. A 45* (**1992**), p. 4225.

25 Giacomelli G. and Politi, A., *Phys. Rev. Lett. 76* (**1996**), p. 2686.

26 Binning, G. Quante, C. F., and Gerber, Ch., *Phys. Rev. Lett. 56* (**1986**), p. 930.

27 Giessibl, F. J., *Rev. Mod. Phys. 75* (**2003**), p. 949.

28 Martin, Y., Williams, C. C. and Wickramasinghe, H. K., *J. Appl. Phys. 61* (**1987**), p. 4723.

29 Albrecht, T. R., Grütter, P., Horne, D., and Rugar, D., *J. Appl. Phys. 69* (**1991**), p. 668.

30 Garćia, R. and Ṕerez, R., *Surf. Sci. Rep. 47* (**2002**), p. 197.

31 Mezić, I., private communication.

32 Jamitzky, F., Stark, M., Bunk, W., Heckl, W. M., and Stark, R. W., *Nanotechnology 20* (**2006**), p. 38.

33 Hu., S. and Raman, A., *Phys. Rev. Lett. 96* (**2006**), p. 036107.

34 Ashhab, M., Salapaka M. V., Dahleh, M., and Mezić, I., *Automatica 35* (**1999**), p. 1663.

35 Ashhab, M., Salapaka M. V., Dahleh, M., and Mezić, I., *Nonlinear Dyn. 20* (**1999**), p. 197.

36 Fang, Y., Dawson D., Feemster M., and Jalili N., *Proceedings of 2002 ASME International Mechanical Engineering Congress and Exposition* (ASME, New York, **2002**), p. 33539.

37 Basso, M., Giarre, L., Dahleh, M., and Mezić, I., *J. Dyn. Syst., Meas., Control 122* (**2000**), p. 240.

Subject Index